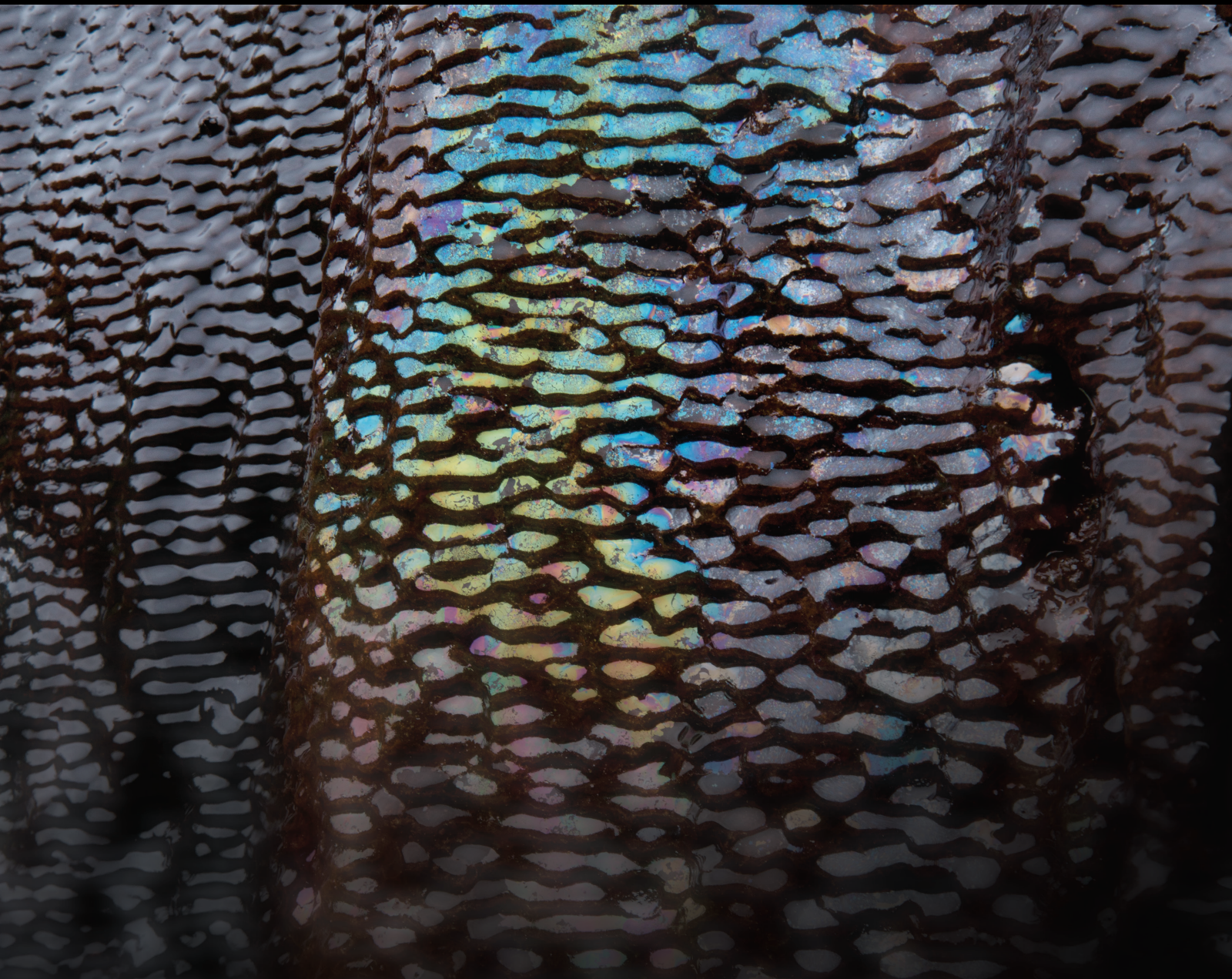


# New Advances in the Sustainability of Unconventional Oil and Gas Resources

Lead Guest Editor: Jinjie Wang

Guest Editors: Xiang Zhou and Qingwang Yuan







---

**New Advances in the Sustainability of  
Unconventional Oil and Gas Resources**



Geofluids

---

**New Advances in the Sustainability of  
Unconventional Oil and Gas Resources**

Lead Guest Editor: Jinjie Wang

Guest Editors: Xiang Zhou and Qingwang Yuan





---

Copyright © 2022 Hindawi Limited. All rights reserved.





This is a special issue published in "Geofluids." All articles are open access articles distributed under the Creative Commons Attribution License, which permits unrestricted use, distribution, and reproduction in any medium, provided the original work is properly cited.





























# Chief Editor

































Umberta Tinivella, Italy

## Associate Editors

Paolo Fulignati , Italy  
Huazhou Li , Canada  
Stefano Lo Russo , Italy  
Julie K. Pearce , Australia

## Academic Editors

Basim Abu-Jdayil , United Arab Emirates  
Hasan Alsaedi , USA  
Carmine Apollaro , Italy  
Baojun Bai, USA  
Marino Domenico Barberio , Italy  
Andrea Brogi , Italy  
Shengnan Nancy Chen , Canada  
Tao Chen , Germany  
Jianwei Cheng , China  
Paola Cianfarra , Italy  
Daniele Cinti , Italy  
Timothy S. Collett , USA  
Nicoló Colombani , Italy  
Mercè Corbella , Spain  
David Cruset, Spain  
Jun Dong , China  
Henrik Drake , Sweden  
Farhad Ehya , Iran  
Lionel Esteban , Australia  
Zhiqiang Fan , China  
Francesco Frondini, Italy  
Ilaria Fuoco, Italy  
Paola Gattinoni , Italy  
Amin Gholami , Iran  
Michela Giustiniani, Italy  
Naser Golsanami, China  
Fausto Grassa , Italy  
Jianyong Han , China  
Chris Harris , South Africa  
Liang He , China  
Sampath Hewage , Sri Lanka  
Jian Hou, China  
Guozhong Hu , China  
Lanxiao Hu , China  
Francesco Italiano , Italy  
Azizollah Khormali , Iran  
Hailing Kong, China




Karsten Kroeger, New Zealand  
Cornelius Langenbruch, USA  
Peter Leary , USA  
Guangquan Li , China  
Qingchao Li , China  
Qibin Lin , China  
Marcello Liotta , Italy  
Shuyang Liu , China  
Yong Liu, China  
Yueliang Liu , China  
Constantinos Loupasakis , Greece  
Shouqing Lu, China  
Tian-Shou Ma, China  
Judit Mádl-Szonyi, Hungary  
Paolo Madonia , Italy  
Fabien Magri , Germany  
Micòl Mastroicco , Italy  
Agnes Mazot , New Zealand  
Yuan Mei , Australia  
Evgeniy M. Myshakin , USA  
Muhammad Tayyab Naseer, Pakistan  
Michele Paternoster , Italy  
Mandadige S. A. Perera, Australia  
Marco Petitta , Italy  
Chao-Zhong Qin, China  
Qingdong Qu, Australia  
Reza Rezaee , Australia  
Eliahu Rosenthal , Israel  
Gernot Rother, USA  
Edgar Santoyo , Mexico  
Mohammad Sarmadivaleh, Australia  
Venkatramanan Senapathi , India  
Amin Shokrollahi, Australia  
Rosa Sinisi , Italy  
Zhao-Jie Song , China  
Ondra Sracek , Czech Republic  
Andri Stefansson , Iceland  
Bailu Teng , China  
Tivadar M. Tóth , Hungary  
Orlando Vaselli , Italy  
Benfeng Wang , China  
Hetang Wang , China  
Wensong Wang , China  
Zhiyuan Wang , China  
Ruud Weijermars , Saudi Arabia





Bisheng Wu , China  
Da-yang Xuan , China  
Yi Xue , China  
HE YONGLIANG, China  
Fan Yang , China  
Zhenyuan Yin , China  
Sohrab Zendeboudi, Canada  
Zhixiong Zeng , Hong Kong  
Yuanyuan Zha , China  
Keni Zhang, China  
Mingjie Zhang , China  
Rongqing Zhang, China  
Xianwei Zhang , China  
Ye Zhang , USA  
Zetian Zhang , China  
Ling-Li Zhou , Ireland  
Yingfang Zhou , United Kingdom  
Daoyi Zhu , China  
Quanle Zou, China  
Martina Zucchi, Italy

# Contents

## **Remaining Oil Distribution and Development Strategy for Offshore Unconsolidated Sandstone Reservoir at Ultrahigh Water-Cut Stage**

Chen Liu , Wensheng Zhou, Junzhe Jiang, Fanjie Shang, Hong He , and Sen Wang   
Research Article (11 pages), Article ID 6856298, Volume 2022 (2022)

## **Mechanical Properties of Different Lithological Rocks: A Case Study of the Coal Measure Strata in the Eastern Margin of Ordos Basin, China**

Xiong Jian , Wu Jianjun, Liu Junjie, Li Bing, Liu Xiangjun , and Liang Lixi  
Research Article (11 pages), Article ID 1356735, Volume 2022 (2022)


## **Research on Remaining Oil Characterization in Superheavy Oil Reservoir by Microgravity Exploration**

Qijun Lv, Aiping Zheng , Xiangjin Liang , Hongfei Chen, Shichang Ju, Yanchong Meng, Hongyuan Zhang, Guolin He, Shenshen Deng , and Junfang Li  
Research Article (10 pages), Article ID 1210780, Volume 2022 (2022)


## **Theoretical Research on the Movement Law of Water Cone Behavior in Heavy Oil Reservoirs with Bottom Water**

Kai Wang , Chenyang Tang, Tianyou Zhang, Yufei Gao, Jingyun Zou, Yan Jiang, Kuo Sun, and Yan Chen  
Research Article (9 pages), Article ID 2954973, Volume 2022 (2022)


## **Study on the Variation of Crude Oil and Flue Gas Components in Flue-Gas-Assisted Steam Flooding**

Yongzhou Wei, Xu He, Tingfeng Liu, Ming Liu, Boliang Li, Zhuangzhuang Wang, and Binfei Li   
Research Article (10 pages), Article ID 6598196, Volume 2022 (2022)



## **Experimental Study on Gas–Water Relative Permeability Characteristics of Tight Sandstone Reservoir in Ordos Basin**

Xiaoxia Ren , Aifen Li, and Asadullah Memon  
Research Article (8 pages), Article ID 1521837, Volume 2022 (2022)

## **A Method to Evaluate Gas Content with Coalbed Methane Reservoir Based on Adsorption Theory and Production Analysis**

Ruyong Feng   
Research Article (10 pages), Article ID 7341886, Volume 2022 (2022)

## **Experimental and Mechanism Study of Superheated SAGD vs. Conventional SAGD Technique: A Cost-Effective Scheme for Superheated SAGD**







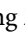

Ke Huang , Siyuan Huang , Qi Jiang, and Yang Liu  
Research Article (21 pages), Article ID 1966959, Volume 2022 (2022)

## **Plugging Performance of a New Sulfonated Tannin Gel System Applied in Tight Oil Reservoir**

Tianhan Xu , Jian Wang , Zhiwen Bai , Junheng Wang , and Peng Zhao   
Research Article (14 pages), Article ID 3602242, Volume 2022 (2022)





**A Novel Continuous Fracture Network Model: Formation Mechanism, Numerical Simulation, and Field Application**

Zixi Guo , Jinzhou Zhao , Xinhao Sun , Chengwang Wang , Dali Guo , Haoran Hu , Hongna Wang , and Qinggang Zeng 

Research Article (17 pages), Article ID 4026200, Volume 2022 (2022)

**Residual Oil Distribution Pattern in a Fault-Solution Carbonate Reservoir and Countermeasures to Improve Oil Development Effectiveness**

Peiliang Liu, Lin Jiang, Bochao Tang , Ke Ren, Mina Huang, and Chunying Geng 



Research Article (21 pages), Article ID 2147200, Volume 2022 (2022)

**Research on the Depletion and Recovery Characteristics of Fault-Karst Reservoirs**

Bochao Tang , Chunying Geng , Mina Huang, Haitao Lu, and Ke Ren

Research Article (12 pages), Article ID 1105335, Volume 2022 (2022)

**Experimental Study on Enhancing Heavy Oil Recovery by Multimedia-Assisted Steam Flooding Process**

Keyang Cheng , Zhaoting Huang, Jun Li , Taotao Luo, and Hongbo Li


Research Article (8 pages), Article ID 1968032, Volume 2022 (2022)

**Integrated Geologic Modeling of Fault-Block Reservoir: A Case Study of Ss Oil Field**

Zhipeng Xiao, Zhang Wei, Zhengyin Tang , Jianqing Guo, Ruijuan Geng, and Tuobing Gou

Research Article (16 pages), Article ID 6864786, Volume 2022 (2022)

**A Method to Improve Computational Efficiency of Productivity Evaluation with Rectangular Coalbed Methane Reservoir**

Li Chen , Sun Lichun, Sun Hansen, Feng Ruyong, Wang Cunwu, and Zhang Fang


Research Article (11 pages), Article ID 3558643, Volume 2022 (2022)

**The Viscosity of Methane in Organic Slit Nanopore of Gas-Bearing Shale by Molecular Dynamic Simulation**

Dongchen Liu , Xiaofan Chen , Na Jia , Zhimin Du , Yong Tang , Ping Yue , and Yongyi Zhou 



Research Article (11 pages), Article ID 2515152, Volume 2022 (2022)

**Experimental Study on Fracture Propagation Mechanism of Shale Oil Reservoir of Lucaogou Formation in Jimusar**

Jianmin Li, Yushi Zou , Shanzhi Shi, Shicheng Zhang, Junchao Wang, Xinfang Ma, and Xiaohuan Zhang

Research Article (11 pages), Article ID 6598575, Volume 2022 (2022)



**Graded Control Technology of Oil Stability and Water Control in Fracture-Pore Carbonate Reservoirs**

Wenqi Zhao , Lun Zhao , Junjian Li, Jue Hou, and Xuejing Guo

Research Article (11 pages), Article ID 6393277, Volume 2022 (2022)

# Contents



## **The Gravel Packing Length Determination Method and Influencing Factors Analysis in Deepwater Horizontal Wells**

Hui Huang, Min Wen, Xuesong Xing, Hao Qiu , Zening Hou, and Shengtian Zhou   
Research Article (9 pages), Article ID 2912652, Volume 2022 (2022)

## **A Novel Approach to Determine the Enriched Gas Recycling during the Enriched Gas Flooding Process**

Yan Li, Chunsheng Yu , and Kaitao Yuan  
Research Article (7 pages), Article ID 9362807, Volume 2022 (2022)



## **Experimental Study on Fe<sub>3</sub>O<sub>4</sub> Nanoparticle-Assisted Microwave Enhancing Heavy Oil**

Teng Lu , Faqiang Dang, Haitao Wang, Qingmin Zhao, and Zhengxiao Xu   
Research Article (14 pages), Article ID 6457186, Volume 2022 (2022)

## **Prediction and Analysis of PDC Bit Wear in Conglomerate Layer with Machine Learning and Finite-Element Method**

Li-qiang Wang , Ming-ji Shao , Wei Zhang , Zhi-peng Xiao , Shuo Yang , and Ming-he Yang   
Research Article (10 pages), Article ID 4324202, Volume 2022 (2022)

## **Rock Mechanical Properties and Breakdown Pressure of High-Temperature and High-Pressure Reservoirs in the Southern Margin of Junggar Basin**

Mingwei Kong, Zhaopeng Zhang , Chunyan Zhao, Huasheng Chen, Xinfang Ma , and Yushi Zou  
Research Article (14 pages), Article ID 1116136, Volume 2021 (2021)



## **Analysis of Shunted Screen Gravel Pack Process and Calculation of Friction in Deepwater Horizontal Wells**

Fei Xu, Shengtian Zhou , Chong Zhang, Yi Yu, and Zhao Dong  
Research Article (9 pages), Article ID 4651199, Volume 2021 (2021)



## **Calculation Model of Relative Permeability in Tight Sandstone Gas Reservoir with Stress Sensitivity**

Jin Yan, Rongchen Zheng, Peng Chen , Shuping Wang, and Yunqing Shi  
Research Article (12 pages), Article ID 6260663, Volume 2021 (2021)

## **Study on a Novel Water-Soluble Hydrophobically Associating Polymer as an Enhanced Heavy Oil Recovery Agent**

Dongyu Qiao, Zhongbin Ye , Xindong Wang, Yiping Zheng, Lei Tang, and Nanjun Lai   
Research Article (12 pages), Article ID 2036562, Volume 2021 (2021)

## **Advancement of Hydraulic Fracture Diagnostics in Unconventional Formations**



Ali Mahmoud, Ahmed Gowida, Murtada Saleh Aljawad , Mustafa Al-Ramadan, and Ahmed Farid Ibrahim   
Review Article (17 pages), Article ID 4223858, Volume 2021 (2021)

**Production Analysis for Fractured Vertical Well in Coal Seam Reservoirs with Stimulated Reservoir Volume**

Chen Li 

Research Article (12 pages), Article ID 1864734, Volume 2021 (2021)

**A Semianalytical Model for Analyzing the Infill Well-Caused Fracture Interference from Shale Gas Reservoirs**

Sidong Fang, Yonghui Wu , Cheng Dai, Liqiang Ma , and Hua Liu


Research Article (13 pages), Article ID 1877778, Volume 2021 (2021)

**Synthesis of a Novel Filtrate Reducer and Its Application in Water-Based Drilling Fluid for Ultra-High-Temperature Reservoirs**

Dongyu Qiao, Zhongbin Ye , Lei Tang, Yiping Zheng, Xindong Wang, and Nanjun Lai 



Research Article (11 pages), Article ID 7643826, Volume 2021 (2021)

**Experimental Study on Enhanced Condensate Recovery by Gas Injection in Yaha Condensate Gas Reservoir**

Yiming Wu, Kun Yao, Yan Liu, Xiangyun Li, Mimi Wu, Ronghong Cheng, and Bo Wang 

Research Article (15 pages), Article ID 7698970, Volume 2021 (2021)

**A New Method of Central Axis Extracting for Pore Network Modeling in Rock Engineering**

Xiao Guo , Kairui Yang , Haowei Jia, Zhengwu Tao, Mo Xu, Baozhu Dong, and Lei Liu

Research Article (20 pages), Article ID 1971622, Volume 2021 (2021)

**Experimental Study of Hydraulic Fracture Propagation Behavior during Multistage Fracturing in a Directional Well**

Yongtao Zhang, Hao Jin, Bumin Guo, Shoumei Qiu , Peng Yang, Shili Qin, Yantao Xu, and Qiang Zhang

Research Article (11 pages), Article ID 5941116, Volume 2021 (2021)



## Research Article

# Remaining Oil Distribution and Development Strategy for Offshore Unconsolidated Sandstone Reservoir at Ultrahigh Water-Cut Stage

Chen Liu <sup>1,2</sup>, Wensheng Zhou,<sup>1,2</sup> Junzhe Jiang,<sup>1,2</sup> Fanjie Shang,<sup>3</sup> Hong He <sup>4</sup>,  
and Sen Wang <sup>5</sup>

<sup>1</sup>State Key Laboratory of Offshore Oil Exploitation, Beijing 100028, China

<sup>2</sup>CNOOC Research Institute Ltd., Beijing 100028, China

<sup>3</sup>CNOOC International Limited, Beijing 100028, China

<sup>4</sup>College of Petroleum Engineering, Yangtze University, Wuhan 430100, China

<sup>5</sup>China University of Petroleum (East China), Qingdao, Shandong 266580, China

Correspondence should be addressed to Chen Liu; [liu099339@163.com](mailto:liu099339@163.com) and Hong He; [hehong1103@163.com](mailto:hehong1103@163.com)

Received 8 March 2022; Revised 17 July 2022; Accepted 23 July 2022; Published 6 September 2022

Academic Editor: Jinjie Wang

Copyright © 2022 Chen Liu et al. This is an open access article distributed under the Creative Commons Attribution License, which permits unrestricted use, distribution, and reproduction in any medium, provided the original work is properly cited.

Due to the influence of long-term waterflooding, the reservoir physical properties and percolation characteristics tend to change greatly in offshore unconsolidated sandstone reservoirs at ultrahigh water-cut stage, which can affect the remaining oil distribution. Remaining oil characterization and proper development strategy-making are of vital importance to achieve high-efficiency development of mature reservoirs. The present numerical simulation method is difficult to apply in reservoir development due to the problems of noncontinuous characterization and low computational efficiency. Based on the extended function of commercial numerical simulator, the time-varying equivalent numerical simulation method of reservoir physical properties was established, and the research of numerical simulation of X offshore oilfield with 350,000 effective grids was completed. The results show that the time-varying reservoir properties have a significant impact on the distribution of remaining oil in ultrahigh water-cut reservoir. Compared with the conventional numerical simulation, the remaining oil at the top of main thick reservoir in X oilfield has increased by 18.5% and the remaining oil in the low-permeability zone at the edge of the nonmain reservoir has increased by 27.3%. The data of coring well and the implementation effect of measures in the X oilfield are consistent with the recognition of numerical simulation, which proves the rationality of numerical simulation results. The new method is based on a mature commercial numerical simulator, which is easy to operate and has reliable results.

## 1. Introduction

Remaining oil recognition is of vital importance to achieve high-efficiency development for mature waterflooding reservoirs with high water cut. Different analysis methods such as reservoir simulation, dynamic analysis, well logging analysis, and core analysis have been applied to recognize the remaining oil [1]. Among them, reservoir simulation has become a widely used method because it is quantifiable, visualizable, and low

cost. Normally, the reservoir simulation is based on a geological model with determined physical parameters such as permeability and porosity. Parameters such as the relative permeability are calculated from the input curves. It is assumed that the determined parameters and input curves do not change during the simulation process [2]. However, during the ultrahigh water-cut development stage for unconsolidated sandstone reservoir in offshore oilfields, after long-term waterflooding, the microscopic pore-throat structure and clay content of the

reservoir will change and affect the flow of water and oil in porous media, which can have an impact on the distribution of remaining oil [3–6].

The existence of the phenomenon has been confirmed by laboratory experiments. Laboratory microscopic tests have confirmed that with the increase of water injection, the clay minerals in pores are continuously washed away by the injected water so that the shale content in the formation decreases. The secondary intergranular voids are more developed and the extralarge intergranular voids also increase [7–9]. Larger pores and throats are constructed in the medium-coarse sandstone, while pore size and throat size decrease in the silty sandstone. After long-term waterflooding, core flooding experiments show that the permeability of high-permeability cores increases and the relative permeability curve moves to the right. The residual oil saturation decreases while the irreducible water saturation increases. The oil saturation range with a two-phase flow increases. The water-phase permeability at residual oil saturation decreases. However, the permeability of the medium and low permeability cores decreases after long-term waterflooding.

The water-phase relative permeability curve shifts to the right, and also, the irreducible water saturation increases. The two-phase flow saturation range shrinks [10–12]. Besides, the well logging data from Daqing, Shengli, and other oilfields at different development stages confirm that the permeability in the medium- and high-permeability sandstone reservoirs gradually increases during waterflooding process [13, 14]. The migration simulation results of reservoir particles [15–17] based on the network modeling show that the changes of reservoir physical properties are mainly affected by factors such as injection pore volume, injection rate, fluid viscosity, degree of reservoir cementation, and clay content.

The change of the reservoir's microscopic pore-throat structure is represented by the change of parameters such as reservoir permeability, porosity, and relative permeability curve in the reservoir simulation. Previous studies indicate that reservoir porosity changes slightly during long-term waterflooding, and its impact on reservoir production can be ignored. Reservoir permeability and relative permeability curves change significantly during waterflooding and have significant impact on production. They are the two main parameters to be considered as the time-varying properties in reservoir simulation [18, 19].

The construction of time-varying reservoir simulation parameters is mainly to determine the variation law of reservoir parameters during the development process. Therefore, the proper characterization parameters of the reservoir development process are particularly important. The water cut of the reservoir has been used as time-varying reservoir simulation parameter [18]. However, the characterization method based on water-cut changes has the following problems: when the reservoir enters into high water-cut development period, although the water cut of reservoir changes slightly, the injection water can have a strong wash effect on the reservoir and the time-varying

reservoir simulation parameters change dramatically, which leads to a larger simulation error.

In order to properly characterize the change of reservoir physical properties, the water-pass multiple was proposed [20, 21]. However, the time-varying characterization method based on the water-pass volume multiple cannot eliminate the influence of grid size. For grids of different sizes, the amount of water flowing through the cross-section can be obviously different under the same water-pass volume multiple. To solve this problem, the concept of surface flux (PV/S) [22, 23] is proposed in this paper, which is the flow through a unit flow cross-sectional area. The calculation of the time-varying reservoir simulation properties can be realized by characterizing the quantitative relationship between reservoir parameters and surface flux.

Traditional commercial reservoir simulators do not consider the time-varying reservoir properties. In order to characterize the time-varying phenomenon, some approximate methods are proposed. The segmental simulation method has been proposed [24–29], which divides the simulation process into several time intervals and approximates time varying by setting different property values in each time interval. This method has a discontinuous calculation process and convergence problem. A numerical simulator that considers the time-varying phenomenon has been developed in the literature [30–37]. However, it is difficult to apply to the field case due to low computational efficiency and incomplete description of the physical model.

The time-varying phenomenon by using water-sensitive functions in the commercial numerical simulators was approximately characterized [37–44]. However, the conversion process is complex and the reliability is poor, which is difficult to accurately reflect the time-varying law of reservoir parameters. Due to the limitation of previous methods, the time-varying phenomenon has not been fully considered in reservoir simulation, which resulted in the low accuracy of remaining oil identification in the ultrahigh water-cut reservoirs. It is difficult to further improve the oil recovery without a high-quality simulation result.

Therefore, in this study, taking the example of X offshore oilfield, the X oilfield's geological properties and the time-varying reservoir properties were firstly introduced. Then, a simulation method with time-varying reservoir properties was established, and the distribution of the remaining oil in this oilfield was given. Finally, the development strategies were proposed and the field implementation was tracked.

The numerical simulation of the X oilfield with the time-varying reservoir properties has been achieved based on a commercial numerical simulator, which reveals the remaining oil distribution in the X oilfield. Compared with the results of remaining oil distribution given by conventional numerical simulation, the time-varying simulation results have been confirmed to be more consistent with the real situation of the reservoir. It also has higher accuracy and reliability. The field practice of the X oilfield provides a useful guidance for the EOR strategy-making workflow in the ultrahigh water-cut offshore unconsolidated sandstone reservoirs. Based on the development example of X oilfield, it

is suggested that sufficient attention should be paid to the time-varying reservoir properties to investigate the remaining oil distribution in mature oilfields at ultrahigh water-cut development stage. Moreover, the time-varying simulation method with higher accuracy and reliability should be paid special attention.

## 2. Characterization of Time-Varying Reservoir Property

The reservoir lithology of the X oilfield is relatively simple, dominated by fine-medium-grained feldspar quartz sandstone, followed by coarse-medium-grained feldspar lithic quartz sandstone and fine-medium-grained quartz sandstone, with the porosity of 18%-25%; the permeability is between 200~1000 ( $\times 10^{-3} \mu\text{m}^2$ ); it belongs to medium-high porosity and medium-high permeability reservoir. The oil-water distribution in the oilfield is mainly controlled by the structure, and it belongs to the anticline structural reservoir. There are 23 oil reservoirs in the vertical direction, mainly layered edge-water reservoirs. The oilfield has been exploited for nearly 20 years, the oil recovery has reached 55%, and the water cut has reached 95%. It has entered the middle and late stages of development with high water-cut and high recovery ratio. The remaining oil is highly dispersed, and it is difficult for further development.

**2.1. Characterization of Time-Varying Permeability.** Based on the core flooding experiment, the quantitative relationship between the varying factor of reservoir permeability (the ratio of actual permeability to initial permeability) and surface flux is obtained through statistical regression (Figure 1). Combined with the analysis of well logging interpretation in different development periods, it is believed that the quantitative relationship accurately and objectively reflects the long-term waterflooding variation of reservoir permeability. The logging interpretation results of different periods are basically distributed on the relationship curve, which shows a good agreement with this quantitative relationship. The X oilfield has a complete geological structure, in which there are no faults. Reservoirs distribute stably laterally with good continuity and weak heterogeneity. The interlayer differences are also small, so this time-varying pattern is universal in the X oilfield. Moreover, core flooding experimental results show that the porosity of the core is 23.0% when the surface flux is 150, which is only 2.0% higher than the initial porosity. The result is consistent with the conclusions from Song et al. [6], Chen et al. [7], and others. This change has no significant impact on reservoir development.

However, it can be seen from Figure 1 that the reservoir permeability of the X oilfield increases gradually with the increase of the surface flux. The reservoir permeability in the strong displacement zone is more than 4 times higher than the initial permeability, which is consistent with the understanding from Shengli, Daqing, and other oilfields [13, 14, 28]. It indicates that reservoir heterogeneity becomes more serious during the process of oilfield development.

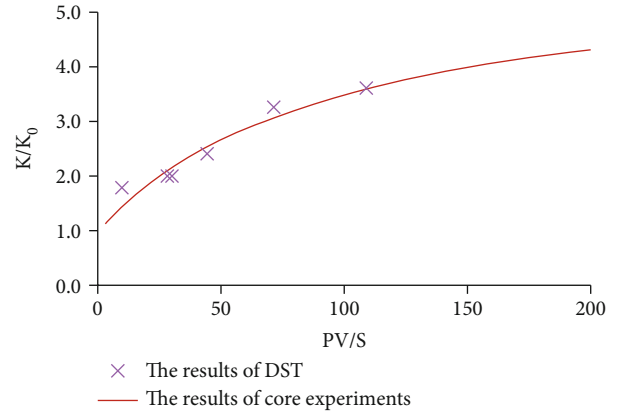


FIGURE 1: Time varying of reservoir permeability in the X oilfield.

**2.2. Characterization of Time-Varying Relative Permeability.** The time-varying characterization of relative permeability curve can be achieved by comparing the four endpoint values (initial water saturation  $S_{wi}$ , oil phase relative permeability  $K_{ro}(S_{wi})$  at initial water saturation, residual oil saturation SOWCR, and the relative permeability  $K_{rw}(S_{or})$  at residual oil saturation). Considering the degree of influence on the law of the oil-water percolation, to simplify the problem, the residual oil saturation and the endpoints of the water relative permeability at residual oil saturation are characterized [29, 30]. It can be achieved by constructing the residual oil saturation and the quantitative relationship between the relative permeability of the water phase and the areal flux at the residual oil saturation.

The core flooding experiments of the X oilfield show that long-term waterflooding will lead to a decrease in residual oil saturation, and the relative permeability of the water phase increases at residual oil saturation. However, due to the limited number of data points, it is difficult to conclude to a quantitative formula. In this paper, the reservoir engineering method is used to calculate the changing trend of relative permeability curves [30, 31]. This method firstly obtains the relationship between oil-water two-phase relative permeability ratio and water saturation through waterflooding curve and production data. Then, the exponential expression of the oil-water relative permeability is converted to a binary linear equation by applying the logarithm on both sides. In the next step, the established relationship between oil-water two-phase relative permeability ratio and water saturation is used to obtain the oil-phase index, water-phase index, and water-phase relative permeability under residual oil saturation with binary linear regression. Therefore, the exponential expression of the oil-water relative permeability can be obtained. According to field production data, the relative permeability curves of oil and water at different development stages are calculated by subsections, the relative permeability curve clusters are obtained, and then, the residual oil saturation and the water-phase relative permeability at the residual oil saturation are calculated by the regression (Figure 2).

With the increase of surface flux, the residual oil saturation of the X oilfield shows a gradual downward trend, and

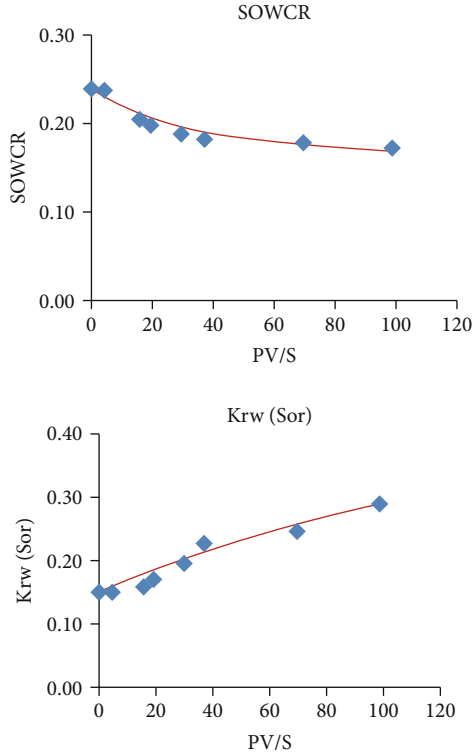


FIGURE 2: Time varying of relative permeability curve in the X Oilfield.

the residual oil saturation of the strong displacement zone can decrease from initial 0.24 to 0.18, a decrease of 25%. The relative permeability of the water phase at residual oil saturation increases with the increase of surface flux, showing a gradually increasing trend. The relative permeability of the water phase at residual oil saturation in the intensive flooding zone can increase by 93%, from initial 0.15 to 0.29. It indicates that with the deepening of oilfield development, the internal flow pattern of reservoir has changed significantly in comparison with the initial period of development. Compared with the previous research results from Shengli, Daqing, and other oilfields ([28], [14], etc.), the variation range of two endpoints (residual oil saturation and water-phase relative permeability at residual oil saturation) is more obvious under high-intensity waterflooding.

### 3. Remaining Oil Distribution considering the Time-Varying Properties

**3.1. Realization of Reservoir Simulation with Time-Varying Properties.** Based on INTERSECT, a widely used commercial numerical simulator, the study of the remaining oil distribution in the X oilfield is completed. The time-varying characterization of permeability can be achieved by adjusting the multiplication factor (MULTX, MULTY). Based on the quantitative relationship between permeability varying factor and surface flux, the characterization formula for quantitative relationship between the multiplication factors with surface flux is obtained. INTERSECT software provides a software script expansion window. PV/S is first calculated

based on the default parameters of the software. Then, input the time-varying value of the reservoir's physical properties by script, and specify the value for each step calculation, so that time-varying intergrid conductivity can be realized, and the dynamic real-time calculation of permeability is achieved. The conductivity calculation in the software is based on equation (1). In the above-mentioned time-varying method of reservoir physical properties, the multiplication factor has a cumulative effect. Thus, the multiplication factor needs to be restored to the initial value before calculating the conductivity at each time step. Table 1 is a comparison table of differences in conductivity calculation. It can be seen from Table 1 that if the cumulative effect is not eliminated, the result will obviously deviate from the accurate value.

$$\text{TRANX}_i = \frac{\text{CDARCY} \cdot \text{MLTX}_i \cdot A \cdot \text{DIPC}}{B}, \quad (1)$$

where  $\text{TRANX}_i$  is transmissibility between cell  $i$  and cell  $j$ , its neighbor in the positive  $X$ -direction;  $\text{CDARCY}$ , Darcy's constant;  $\text{MLTX}_i$ , transmissibility multiplier for cell  $i$ ;  $A$ , interface area between cell  $i$  and  $j$ ;  $\text{DIPC}$ , Dip correction; and  $B$ , planar permeability mean of cell  $i$ .

At the same time, the quantitative characterization formulas of residual oil saturation, water-phase relative permeability at residual oil saturation, and surface flux are written into the software's script editor with Python to achieve the dynamic calculation of oil-water relative permeability curve for each grid, so as to realize the time-varying characterization of oil-water relative permeability for all grids.

The production of the X oilfield has lasted for nearly 20 years, and the number of effective grids of the model was 350,000. Using the method proposed in this paper and based on INTERSECT simulator, the time-varying numerical simulation of the X oilfield has been completed in the order of whole area history matching-main production well history matching-nonmajor production well history matching. After considering the time-varying reservoir parameters, the efficiency of history matching has been significantly improved. The field production results of the simulation model in the early time steps are basically consistent with the actual production data. And only a few wells need to be properly adjusted to complete the history matching work in the later time step. At the same time, the accuracy of time-varying simulation's history matching has been significantly improved, especially in the production fluctuation period and the later period of development (Figure 3). It has achieved precise characterization of some small areas and solved the problem of water cut rising too fast, in which the original conventional simulation has always existed.

In the conventional reservoir numerical simulation, parameters such as conductivity, residual oil saturation, and water relative permeability at residual oil saturation are usually unchanged during the whole simulation process and are always the initiated values. In the numerical simulation considering time-varying reservoir physical properties, the above values will show dynamic changes with the process of reservoir development. Figure 4 shows the

TABLE 1: The differences of transmissibility with two methods.

Calculation step	PV/S	Transmissibility (actual)	Cumulative effect		Eliminate cumulative effects	
			MULTX	Transmissibility by the model	MULTX	Transmissibility by the model
Initial value	0	1	1	1	1	1
Step 1	10	1.1	1.1	$1 \times 1.1$	1.1	$1 \times 1.1/1$
Step 2	20	1.2	1.2	$1 \times 1.1 \times 1.2$	1.2	$1.1 \times 1.2/1.1$
Step 3	30	1.3	1.3	$1 \times 1.1 \times 1.2 \times 1.3$	1.3	$1.2 \times 1.3/1.2$
Step 4	40	1.4	1.4	$1 \times 1.1 \times 1.2 \times 1.3 \times 1.4$	1.4	$1.3 \times 1.4/1.3$
Step 5	50	1.5	1.5	$1 \times 1.1 \times 1.2 \times 1.3 \times 1.4 \times 1.5$	1.5	$1.4 \times 1.5/1.4$

Note: take the formula transmissibility =  $1 + (PV/S)/100$  as an example.

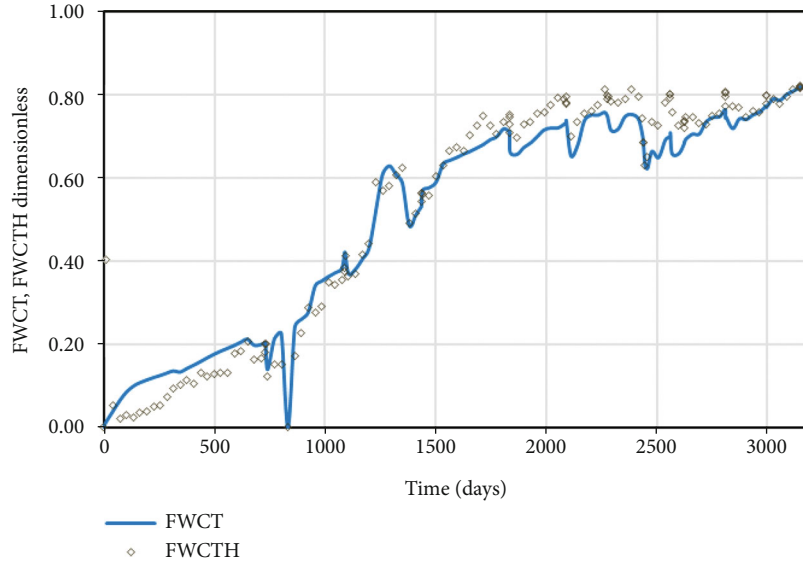


FIGURE 3: The historical matching results of the X oilfield.

comparison of parameter differences at the beginning and the end of time-varying simulation. It can be seen from Figure 4 that the proportion of grids with a conductivity value greater than 50 in the whole area increases from 3.8% at the beginning to 13.1% at the end, which indicates that the grid conductivity increases during the model operation. The residual oil saturation and the relative permeability of the water phase at residual oil saturation are the same constant value in all grids at the beginning of the model and show obvious heterogeneity at the end of the simulation, which also indicates that these two parameters show time-varying in the process of model running.

### 3.2. Remaining Oil Distribution Recognition

3.2.1. *The Main Oil Group.* ZJ-1 oil group is the main oil group in the X oilfield with sufficient edge water energy. Permeability in this group is between 500 and 1000 ( $\times 10^{-3} \mu m^2$ ). The geological reserves of this oil group are  $1132 \times 10^4 m^3$ . The current oil recovery is 61%. The comprehensive water cut is 96%. And 15 wells are in production.

Based on the time-varying reservoir simulation results, the remaining oil in the ZJ-1 oil group is mainly enriched in the structural high area, which is basically consistent with the conventional simulation results. However, there are differences in the enrichment degree in the structural high area. According to simulation results (Figure 5), the remaining geological reserves in the structural high area calculated by the conventional simulator are  $200 \times 10^4 m^3$ , of which the movable oil reserves are  $132 \times 10^4 m^3$ , while the remaining geological reserves in the structural high area of the reservoir obtained by the time-varying simulator technology are  $237 \times 10^4 m^3$ , of which the movable oil reserves were  $186 \times 10^4 m^3$ , an increase of 18.5% and 40.9%, respectively.

From the time varying of reservoir parameters during numerical simulation calculation (Figure 6), it can be seen that the middle and lower part of the ZJ-1 oil group is a strong displacement zone with a large surface flux. During the conventional numerical simulation calculation process, the reservoir conductivity and residual oil saturation are constant. In the process of time-varying simulation, the conductivity in the middle and lower part of the reservoir will



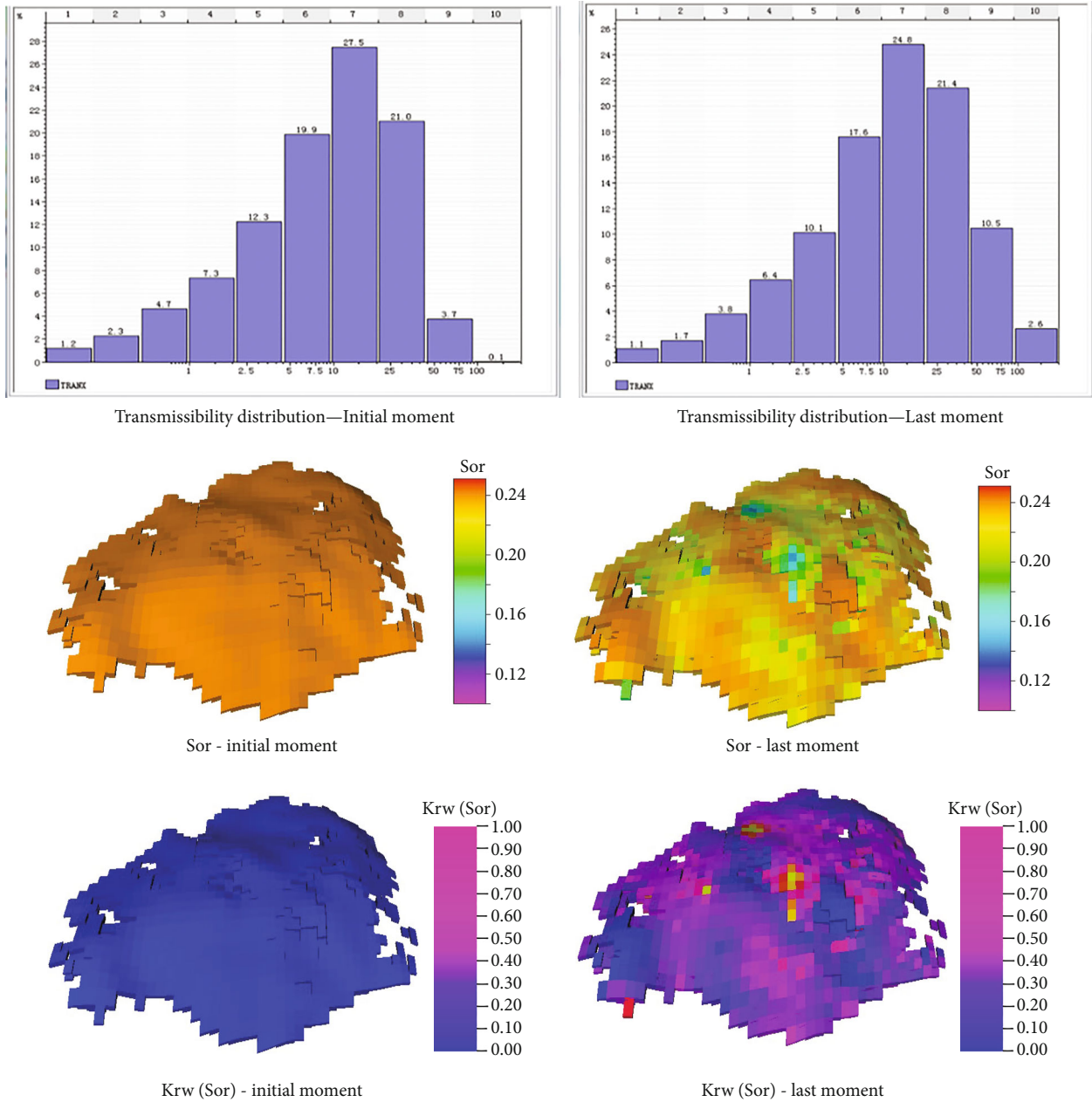


FIGURE 4: Comparison of parameters at the beginning and the end of time-varying numerical simulation.

gradually increase, and the residual oil saturation will gradually decrease, resulting in a higher recovery ratio in the middle and lower part of the reservoir than conventional numerical simulation. Therefore, the remaining oil is more enriched in the structural high area with a relatively low displacement degree.

**3.2.2. Nonmain Oil Groups.** Among the 23 oil groups in the X oilfield, except for the ZJ-1 oil group, the rest are all non-main oil groups. The geological reserves of these oil groups are small, and there are certain differences in the physical properties between these oil groups. Taking the ZJ-2 oil group as an example, the edge water energy of this oil group is sufficient, the permeability is between 200 and 1000 ( $\times 10^{-3}$

$\mu\text{m}^2$ ), and the physical properties of the eastern part of the reservoir are relatively poor. The geological reserves of this oil group are  $110 \times 10^4 \text{ m}^3$ , the current recovery ratio is 43%, the comprehensive water cut is 92%, and the production has been stopped.

It can be seen from Figure 7 that the distributions of remaining oil obtained from the traditional and time-varying simulators are basically the same and both show that there is still a certain number of recoverable reserves in the area with relatively poor physical properties in the eastern part of the reservoir. According to simulation results, the remaining geological reserves in this area calculated by conventional simulation are  $24 \times 10^4 \text{ m}^3$ , of which the movable oil reserves are  $16 \times 10^4 \text{ m}^3$ , while the remaining geological

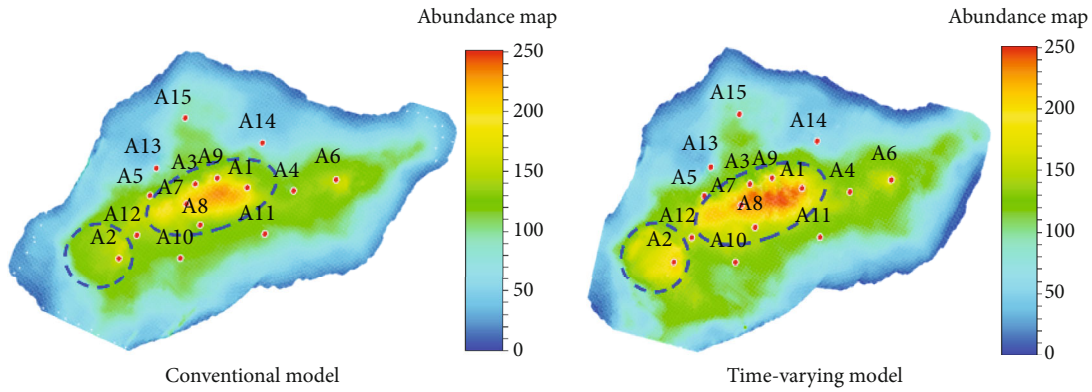


FIGURE 5: Abundance map of remaining geological reserves of ZJ-1 oil formation.

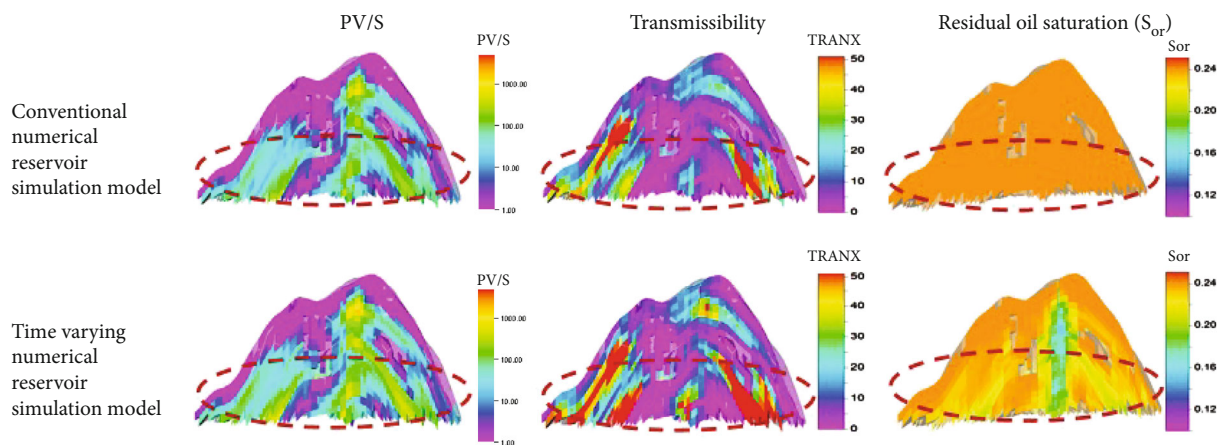


FIGURE 6: Comparison of reservoir parameters of ZJ-1 oil formation (at the end of model operation).

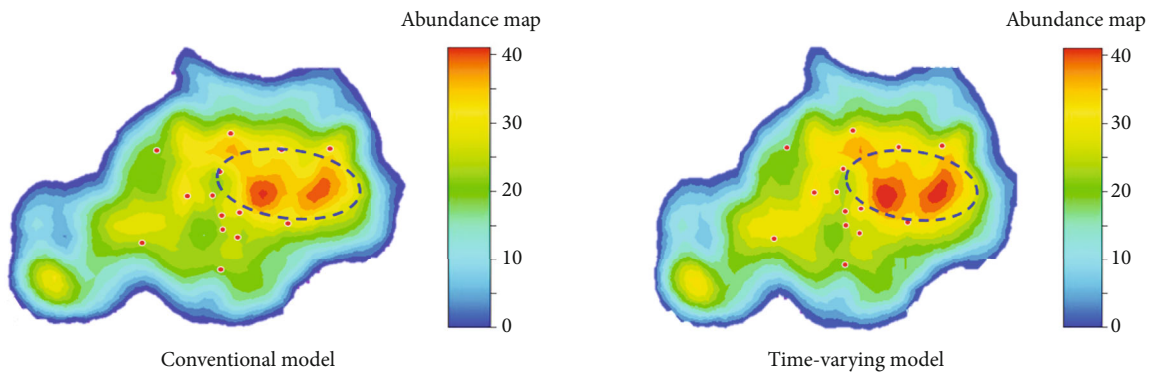


FIGURE 7: Abundance map of remaining geological reserves of ZJ-2 oil formation.

reserves in this area obtained by the time-varying simulation are  $31 \times 10^4 \text{ m}^3$ , of which the movable oil reserves are  $31 \times 10^4 \text{ m}^3$ . Oil reserves are  $25 \times 10^4 \text{ m}^3$ , an increase of 27.3% and 52.8%, respectively. Based on the remaining oil from the time-varying numerical simulation results, this area still has the potential for adjusting wells.

From the time-varying of reservoir parameters during the simulation (Figure 8), it can be seen that the high permeability zone of the ZJ-2 oil group is a strong displacement zone, and the surface flux is relatively large, so the conduc-

tivity of the high permeability zone during the time-varying simulation process will be gradually increased, while the residual oil saturation gradually decreases. So, the recovery ratio of the high permeability zone is higher than that in the conventional simulation results, and the remaining oil is more enriched in the low permeability area with a relatively low displacement degree.

3.3. Development Strategies and Field Implementation Tracking. According to the distribution of remaining oil,

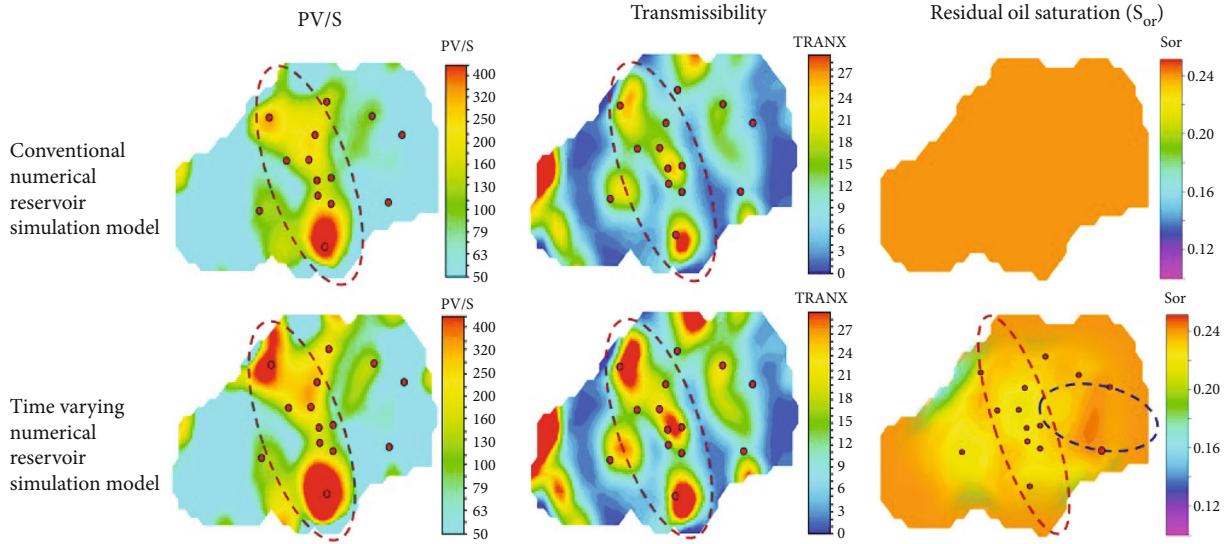


FIGURE 8: Comparison of reservoir parameters of ZJ-2 oil formation (at the end of model operation).

TABLE 2: The effect table of liquid extraction for ZJ-1 oil formation.

Well name	Current production			Liquid extraction scheme				Implementation effect		
	Liquid production rate m <sup>3</sup> /d	Oil production rate	Water cut %	Liquid extraction rate m <sup>3</sup> /d	Oil extraction rate m <sup>3</sup> /d	Water cut %	Draw down MPa	Liquid production rate m <sup>3</sup> /d	Oil production rate	Water cut %
A6	50	4.3	91.5	500	21.0	95.5	4.6	570	30.2	94.7
A8	911	54.0	94.1	215	6.0	94.7	5.1	1287	70.8	94.5
A2	1757	84.0	95.2	443	10.0	95.7	3.8	2100	98.7	95.3
A7	1273	60.0	95.3	627	16.0	96	4.6	1798	80.9	95.5
A9	399	13.0	96.8	1101	32.0	97	3.8	1659	51.4	96.9
Total	4390	215.3	—	2886	85.0	—	—	7414	332.0	—

the X Oilfield constructed a future development strategy including well production schedule optimization and adjustment wells. For the ZJ-1 main oil group, the existing well pattern control is relatively complete, and the fluid production is optimized in considering well conditions and facility capacity. The focus is on increasing the liquid production rate of wells A6, A8, A2, A7, and A9 in the structural high area (Table 2). For the nonmain oil group, it is proposed to add a new adjustment well as a test well in the area with poor physical properties in the eastern part of the ZJ-2 oil group.

After the implementation of this strategy, the ZJ-1 oil group achieved a daily oil increase of  $116.7 \text{ m}^3/\text{d}$  through an optimized production rate, and the water cut was basically consistent with prediction. When the adjustment well of the ZJ-2 oil group was in production, the initial water cut was 49.0%, and the daily oil production was  $190 \text{ m}^3/\text{d}$ . Then, the water cut reached 91.8% after 7 months of production, and the cumulative oil production was  $2.25 \times 10^4 \text{ m}^3$ . The oil volume is  $11.5 \times 10^4 \text{ m}^3$ , and based on the original

conventional simulation, the accumulative oil increase of the adjustment wells in this area is only  $4.0 \times 10^4 \text{ m}^3$  (Figure 9).

In addition, through core analysis (Figure 10), there is still a pure oil layer about 2 meters thick in the upper part of the ZJ-1 oil formation, and oil in the middle part is moderately displaced. The oil distribution is similar to the core surface of the pure water layer, which indicates that the oil in the middle and lower parts of the reservoir are very well displaced, confirming that strong waterflooding can effectively reduce the residual oil saturation.

#### 4. Conclusions

In this study, based on commercial reservoir simulator, the time-varying simulation of reservoir properties in large field cases was carried out, and a new understanding of remaining oil in ultrahigh water-cut stage was formed. The development strategies were proposed, and the field implementation were tracked. Some conclusions can be obtained as follows:



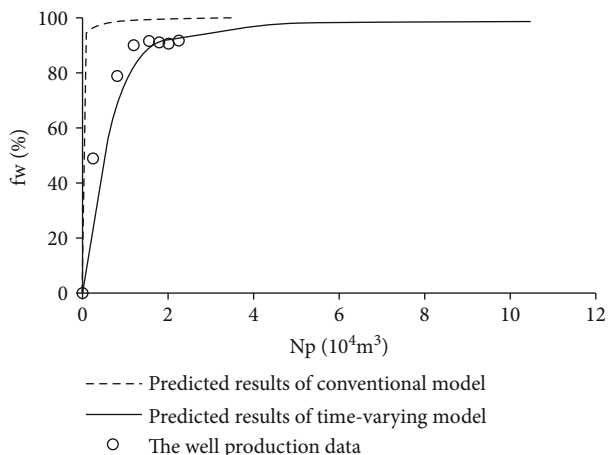


FIGURE 9: The production performance of the adjustment well in ZJ-2 oil formation.

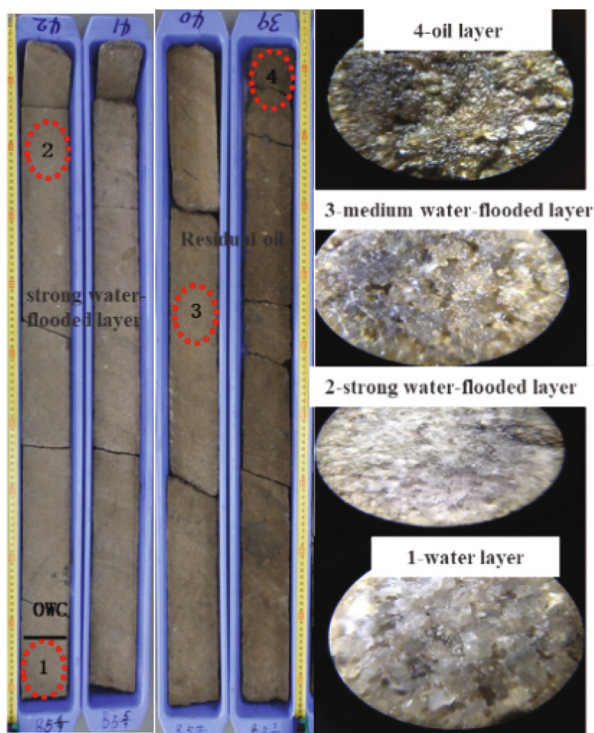


FIGURE 10: The partial coring section of ZJ-1 oil formation.

(1) The time-varying reservoir properties have a significant impact on the distribution of remaining oil in ultrahigh water-cut reservoir. The time-varying reservoir properties increase the conductivity of strong waterflooding zone, reduce the residual oil saturation, further increase the oil recovery, and correspondingly reduce the recovery of low flooding zone, which makes the remaining oil in the low flooding zone enriched. Compared with the conventional numerical simulation, the remaining oil at the top of the main thick reservoir in the X oilfield is increased by 18.5%. The remaining oil in the low-

permeability area at the edge of the nonmain reservoir is increased by 27.3%

(2) Based on the understanding that the time-varying phenomenon of reservoir physical properties affects the distribution of remaining oil in the ultrahigh water-cut stage of the reservoir, a strategy for effectively producing the remaining oil in this stage is proposed. Extracting the remaining oil at the top of the main reservoirs can be achieved by increasing the liquid production rate with existing wells. The new wells can be determined with the assistance of time-varying reservoir simulation and the improvement of understanding of the remaining oil in the low-displacement zone for nonmain reservoirs

### Data Availability

All data used to support the findings of this study are available from the corresponding authors on request.

### Conflicts of Interest

The authors declare that they have no conflicts of interest.

### Acknowledgments

This work is supported by the National Science and Technology Major Project (Grant No. 2016ZX05025-001).

### References

- [1] K. C. Khilar, R. N. Vaidya, and H. S. Fogler, "Colloidally-induced fines release in porous media," *Journal of Petroleum Science and Engineering*, vol. 4, no. 3, pp. 213–221, 1990.
- [2] Q. Feng, J. Zhang, S. Wang et al., "Unified relative permeability model and waterflooding type curves under different levels of water cut," *Journal of Petroleum Science and Engineering*, vol. 154, pp. 204–216, 2017.
- [3] Q. Sun Huanquan, F. H. Yantao, and Z. Lunmin, "Formation sensitivity characteristics study of sandstone reservoirs in Shengli oilfield," *Petroleum Exploration and Development*, vol. 27, pp. 72–75, 2000.
- [4] L. Yang, "Variation rule of macro parameters and dynamic model of oil reservoirs in continental faulted basin," *Acta Petrolei Sinica*, vol. 26, pp. 65–68, 2005.
- [5] J. Bingshan, M. Mingxue, and Q. Xiaoyan, "The mathematical simulation method of migration of fines and clay swell in elastic porous medium," *Research and Development of Hydrodynamics (Part A)*, vol. 18, pp. 9–11, 2003.
- [6] W. C. Song, H. Q. Sun, G. Sun, and S. Y. Wu, "Dynamical geological process of development liquid-taking Shengtuo oilfield as an example," *Acta Petrolei Sinica*, vol. 21, pp. 52–55, 2002.
- [7] D. Chen, J. Li, W. Zhu, and Z. Xin, "Experimental research on reservoir parameters variation after water flooding for offshore unconsolidated sandstone heavy oil reservoirs," *China Offshore Oil and Gas*, vol. 28, pp. 54–60, 2016.
- [8] S. Rui, W. Yao, and L. Jianjun, "Microscopic pore structure characterization and fluid transport visualization of reservoir rock," *Journal of Southwest Petroleum University (Science & Technology Edition)*, vol. 40, pp. 85–105, 2018.

- [9] N. Ning, Y. Li, H. Liu, and S. Zhou, "Study on influence of permeability and distribution of pore diameters in rock cores on measurement of mobile fluid saturation," *Journal of Southwest Petroleum University (Science & Technology Edition)*, vol. 40, pp. 91–97, 2018.
- [10] W. Zhizhang, C. Yi, and Y. Lei, *The Changing Rule and Mechanism of Reservoir Parameters in the Middle-Later Development Stage*, Petroleum Industry Press, Beijing, 1999.
- [11] W. Xin, D. Zong, and W. Hua, "Physical properties of marine sandstone reservoir after long-term waterflooding," *Special Oil and Gas Reservoirs*, vol. 24, pp. 157–161, 2017.
- [12] C. Hong, W. Wang, R. Lu, J. Zhong, and C. Ren, "A quantitative method to predict the dynamic variation in permeability of oil reservoirs during waterflooding and oil displacement," *Journal of Southwest Petroleum University (Science & Technology Edition)*, vol. 40, pp. 113–121, 2018.
- [13] S. Sun, J. Han, Y. Guo, and W. Zhang, "Laboratory experiment on physical properties of flooding sandstone in Shengtuo oilfield," *Journal of China University of Petroleum.*, vol. 20, pp. 33–35, 1996.
- [14] W. Yan, L. Zhengchen, and S. Yang, "Changing rules of well log interpretation permeability in different period in Daqing Placanticline," *Petroleum Geology and Oilfield Development in Daqing*, vol. 21, pp. 60–62, 2002.
- [15] O. A. Jalel, "Two-dimensional network model to simulate permeability decrease under hydrodynamic effect of particle release and capture," *Transport in Porous Media*, vol. 37, no. 3, pp. 303–325, 1999.
- [16] A. G. Siqueira, E. J. Bonet, and F. S. Shecaira, "A 3D network model of rock permeability impairment due to suspended particles in injection water," in *SPE European Formation Damage Conference*, The Hague, Netherlands, 2003.
- [17] G. Changhong, "Understanding capture of non-Brownian particles in porous media with network model," *Asia-Pacific Journal of Chemical Engineering*, vol. 3, no. 3, pp. 298–306, 2008.
- [18] L. Huiqing, *Reservoir Numerical Simulation Method*, Petroleum University Press, Shandong, 2001.
- [19] H. Q. Jiang, J. W. Gu, M. F. Chen, and M. R. Sun, "Reservoir simulation of remaining oil distribution based on time-variant reservoir model," *Petroleum Exploration and Development*, vol. 32, pp. 91–93, 2005.
- [20] C. Z. Cui, Z. L. Geng, Y. Z. Wang, Y. S. Huang, and H. Q. Liu, "Calculation model of dynamic permeability distribution and its application to water drive reservoir at high water cut stage," *Journal of China University of Petroleum*, vol. 36, pp. 118–122, 2012.
- [21] Q. Xu, Y. Chen, Y. Hou, and H. Li, "Research on numerical simulation processing mode based on reservoir time varying physical properties and seepage in extra high water cut stage," *Drilling & Production Technology*, vol. 38, pp. 41–43, 2015.
- [22] Q. Zhang, R. Jiang, P. Jiang, Z. Yao, Y. Wang, and W. Peng, "Establishment and application of oil reservoir flow-field evaluating system," *Petroleum Geology and Oilfield Development in Daqing*, vol. 33, pp. 86–89, 2014.
- [23] R. Jiang, Q. Xin, W. Teng, P. Xu, and Z. Liu, "Numerical simulation of reservoir time-variation based on surface flux," *Special Oil and Gas Reservoirs*, vol. 23, pp. 69–72, 2016.
- [24] Y. J. Gai, D. L. Lu, and Y. L. Guo, "Numerical simulation by stages about the reservoir at high water cut period," *Petroleum Geology and Recovery Efficiency*, vol. 7, pp. 54–56, 2000.
- [25] G. Boyu, P. Shimi, and H. Shuwang, "Staged numerical simulation of layer 3-member 2-Shahejie formation in district 2 of Shengtuo oilfield," *Petroleum Exploration and Development*, vol. 31, pp. 81–84, 2004.
- [26] X. Zhou, F. Al-Otaibi, and S. Kokal, "Relative permeability characteristics and wetting behavior of supercritical CO<sub>2</sub> displacing water and remaining oil for carbonate rocks at reservoir conditions," *Energy & Fuels*, vol. 33, no. 6, pp. 5464–5475, 2019.
- [27] J. Ruizhong, C. Yueming, D. Yuzhen, and Z. Yan, "Numerical simulation study on the change of physical characteristic parameters of reservoir in the second area of Shengtuo oilfield," *Petroleum Geology and Recovery Efficiency*, vol. 3, pp. 50–56, 1996.
- [28] L. Xiantai, "Study on numerical simulation technology based on time varying physical properties in min-high permeability sandstone reservoirs," *Petroleum Geology and Recovery Efficiency*, vol. 18, pp. 58–62, 2011.
- [29] Z. Jin, Q. Fang, L. Wang, and L. Zhao, "Numerical simulation method and its application when considering time-dependent effect of reservoir parameters," *Xinjiang Petroleum Geology*, vol. 37, pp. 342–345, 2016.
- [30] L. Chen, "Method for calculation the relative permeability curve of an oil reservoir considering the time-varying effect of relevant reservoir parameters," *Journal of Southwest Petroleum University (Science & Technology Edition)*, vol. 41, pp. 137–142, 2019.
- [31] Z. Jinqing, *Research on Water Drive Theory and Improvement of Reservoir Engineering Methods*, China petrochemical press, Beijing, 2019.
- [32] M. Yue, W. Zhu, H. Han, H. Song, Y. Long, and Y. Lou, "Experimental research on remaining oil distribution and recovery performances after nano-micron polymer particles injection by direct visualization," *Fuel*, vol. 212, pp. 506–514, 2018.
- [33] P. Sun, H. Xu, H. Zhu et al., "Investigation of pore-type heterogeneity and its control on microscopic remaining oil distribution in deeply buried marine clastic reservoirs," *Marine and Petroleum Geology*, vol. 123, article 104750, 2021.
- [34] W. U. Junda, L. I. Zhiping, and Y. Sun, "Neural network-based prediction of remaining oil distribution and optimization of injection-production parameters," *Petroleum Geology and Recovery Efficiency*, vol. 27, pp. 85–93, 2020.
- [35] M. Sun, C. Liu, C. Feng, and G. Zhang, "Main controlling factors and predictive models for the study of the characteristics of remaining oil distribution during the high water-cut stage in Fuyu oilfield, Songliao Basin, China," *Energy Exploration & Exploitation*, vol. 36, no. 1, pp. 97–113, 2018.
- [36] Y. Yang, S. Cai, J. Yao et al., "Pore-scale simulation of remaining oil distribution in 3D porous media affected by wettability and capillarity based on volume of fluid method," *International Journal of Multiphase Flow*, vol. 143, article 103746, 2021.
- [37] R. Li, K. D. Splinter, and S. Felder, "Aligning free surface properties in time-varying hydraulic jumps," *Experimental Thermal and Fluid Science*, vol. 126, article 110392, 2021.
- [38] M. Hashan, L. N. Jahan, S. Imtiaz, and M. E. Hossain, "Modelling of fluid flow through porous media using memory approach: a review," *Mathematics and Computers in Simulation*, vol. 177, pp. 643–673, 2020.



- [39] I. Igwe, J. Gholinezhad, and M. Sayed, "Technical implications of neglecting compositional grading effects in petroleum reservoir simulation models," *Energy & Fuels*, vol. 34, no. 2, pp. 1467–1481, 2020.
- [40] H. F. Xia, L. I. Wen-Zhuo, Y. Liu, H. Y. Zhang, and X. U. Tian-Han, "Quantitative analysis of remaining oil after weak base alkaline-surfactant-polymer flooding," *Science Technology and Engineering*, vol. 19, pp. 127–131, 2019.
- [41] S. Zhai, G. Sun, H. Chang, Q. Wu, and Y. Lei, "Study on remaining oil distribution of shallow water delta reservoir in horizontal well development: an example from Bohai oilfield," *Journal of Liaoning Shihua University*, vol. 39, pp. 53–58, 2019.
- [42] Z. Zhu, "Remaining oil distribution patterns of metamorphic buried-hill fractured reservoir based on digital core technology," *Special Oil & Gas Reservoirs*, vol. 26, p. 157, 2019.
- [43] S. Gao, S. Chen, H. Pu et al., "Fine characterization of large composite channel sandbody architecture and its control on remaining oil distribution: a case study of alkaline-surfactant-polymer (ASP) flooding test area in Xingshugang oilfield, China," *Journal of Petroleum Science & Engineering*, vol. 175, pp. 363–374, 2019.
- [44] L. U. Xiangwei, D. U. Shuheng, K. Zheng, H. Zhang, T. Sun, and H. Wang, "Fracture development characteristics in tight sandstone oil reservoir and its inspiration on remaining oil recovery: a case study on the Chang-7<sub>2-2</sub> layer of Yanchang Formation in Xin'anbian area, Ordos Basin," *Acta Scientiarum Naturalium Universitatis Pekinensis*, vol. 54, pp. 42–48, 2018.

## Research Article

# Mechanical Properties of Different Lithological Rocks: A Case Study of the Coal Measure Strata in the Eastern Margin of Ordos Basin, China

Xiong Jian <sup>1</sup>, Wu Jianjun,<sup>2</sup> Liu Junjie,<sup>1</sup> Li Bing,<sup>2</sup> Liu Xiangjun <sup>1</sup> and Liang Lixi<sup>1</sup>

<sup>1</sup>State Key Lab of Oil & Gas Reservoir Geology and Exploitation, Southwest Petroleum University, Chengdu 610500, China

<sup>2</sup>PetroChina Coalbed Methane Company Limited, Beijing 100028, China

Correspondence should be addressed to Xiong Jian; 361184163@qq.com

Received 6 January 2022; Revised 9 February 2022; Accepted 28 June 2022; Published 20 July 2022

Academic Editor: Guozhong Hu

Copyright © 2022 Xiong Jian et al. This is an open access article distributed under the Creative Commons Attribution License, which permits unrestricted use, distribution, and reproduction in any medium, provided the original work is properly cited.

In this paper, the mechanical behaviors of different lithological rocks of coal measure strata from Shanxi Formation in the eastern margin of the Ordos Basin, China, were investigated through uniaxial compression tests, and the deformation characteristics and failure modes of different lithological rocks were investigated. On this basis, the energy evolution of different lithology rocks was also discussed. The results show that there are obvious differences in the mechanical properties of different lithology rocks in coal measure strata, resulting in different wellbore instability prevention measures and fracturing measures in different lithology strata. Under the uniaxial compression condition, the peak strain of different lithological rocks is obviously different, and the denaturation characteristics are also obviously different, and the failure modes of rocks are mainly the tensile fracture mode, suggesting that the rock samples have strong brittle characteristics. With the increase of the strain, the total energy of different lithological rocks of the coal measure strata increases, and the elastic energy first increases and then decreases rapidly, whereas the dissipated energy first increases slowly and then increases rapidly. Each energy at the peak point is different, and the average total energy of shale, silty shale, siltstone, fine sandstone, and coal is  $0.022 \text{ J/cm}^3$ ,  $0.045 \text{ J/cm}^3$ ,  $0.052 \text{ J/cm}^3$ ,  $0.042 \text{ J/cm}^3$ , and  $0.003 \text{ J/cm}^3$ , respectively, indicating that there are obvious differences in the energy evolution laws of the different lithological rocks.

## 1. Introduction

In recent years, China's energy demand has increased rapidly, and its dependence on crude oil and natural gas has exceeded 70% and 40%, respectively, which has seriously affected China's energy security. For China, it is necessary to further strengthen the exploration and development of domestic oil and gas [1]. Coal measure natural gas generally refers to all kinds of natural gas existing in coal measure strata, including coalbed methane dominated by adsorption phase, tight sandstone gas dominated by free phase, and shale gas with coexistence of adsorption phase and free phase. Vertically, the coal measure strata are multilayer superimposed reservoir groups of coalbed methane, shale gas, and tight sandstone gas [2, 3]. In the process of single reservoir development, the natural gas production is lower

than expected and the resources cannot be fully utilized. The combined exploitation of natural gas in different lithological reservoirs can effectively improve the development and utilization efficiency of coal measure gas resources [4–6]. In the process of combined mining, multilayer hydraulic fracturing is implemented to improve the comprehensive development effect of coal measure natural gas [7–9]. Reservoir geomechanics parameters generally involve rock mechanics, pore pressure, in-situ stress, and other parameters, among which rock mechanics parameters are the basis of reservoir geomechanics research [10]. At the same time, rocks are composed of different mineral types and formed under complex geological processes [11]. In the process of rock deformation and failure, the accumulation and release of energy are the essence of rock failure [12, 13]. The deformation and failure process of rock mass

is an energy-driven instability phenomenon, which is closely related to the energy conversion in this process [14]. The energy evolution law of body deformation and failure has important application in hydraulic fracturing of horizontal and vertical wells. This shows that it is very necessary to investigate the laws of rock mechanics and energy evolution lithological rocks of the coal measure strata.

At present, scholars have carried out a large number of experimental studies on the mechanical properties of rock. YW. Li et al. [15], Eleni et al. [16], Piyush et al. [17], Li et al. [18], and Bagde et al. [19] conducted a lot of research on the mechanical properties of different lithology rocks such as shale, sandstone, and carbonate, and discussed the effects of confining pressure on rock mechanical properties. The fundamental reason for the differences in mechanical properties of different lithological rocks is revealed. At the same time, predecessors have also carried out a large number of experimental studies on the laws of rock energy evolution. Selahattin et al. [20] analyzed the strain fracture tendency of granite based on the post-peak energy evolution of granite. Chen et al. [21] compared and analyzed the energy evolution mechanism of Jurassic and Cretaceous argillaceous sandstone in the Northern Xinjiang, China. Jiang et al. [22] studied the effects of different water content and confining pressure on the energy evolution of mudstone based on the uniaxial and triaxial compression experiments. Yang et al. [23] studied the influences of loading mode on rock deformation characteristics and energy evolution characteristics. The above research results provide an important reference for investigating the energy evolution characteristics of different lithological rocks such as coal, marble, mudstone, and sandstone. In the eastern margin of the Ordos Basin, the vertical superposition relationship of different lithology such as coal, sandstone, shale, and limestone is complex, the horizontal lithology changes frequently [24–26], and there are obvious differences between oil and gas reservoirs with different lithology.

Therefore, taking the rocks of the coal measure strata from Shanxi formation in the eastern margin of Ordos Basin as the research object, the mechanical behaviors of different lithological rocks through uniaxial compression tests are investigated, and the compressive characteristics, deformation characteristics, and failure modes of different lithological rocks are studied, so as to reveal the mechanical properties of different lithological rocks in the coal measures. On this basis, the energy evolution laws of different lithological rocks are discussed.

## 2. Samples and Methods

**2.1. Geological Settings.** The eastern margin of Ordos Basin crosses Shanxi and Shaanxi provinces, borders Lishi fault in the East, the Yellow River and Hancheng-Heyang-Tongchuan area in the west, in a narrow and long arc belt, about 450 km long from North to South and 26~100 km wide from East to West, with a total area of  $4.5 \times 10^4 \text{ km}^2$  [24–26]. Topographically, it is a large West trending gentle slope structure with high North, low South, high East, and low West [24–26]. The coal measure strata in the study area

are the Benxi Formation, Taiyuan Formation, and Shanxi Formation from bottom to top. The sedimentary system dominated by barrier coast lagoon system is developed in the Benxi Formation and Taiyuan Formation, while the coastal shallow sea lagoon tidal delta sedimentary system is developed in Shanxi Formation, which is a typical marine land transitional facies sedimentary environment [25–28]. The coal measure strata of these different sedimentary systems have different reservoir combinations of “coalbed methane-tight sandstone gas-shale gas.” The sedimentary systems of different layer groups differ greatly, resulting in more obvious differences in the lithology developed in different layer groups, and the reservoir types of the Shanxi Formation with transitional phase sedimentary characteristics are mostly the multilayered superposition of coal-bed methane and tight gas reservoirs, interspersed with shale gas reservoirs.

**2.2. Experimental Method.** In order to investigate the differences in mechanical properties and energy evolution laws of different lithological rocks of the coal measure strata from the Shanxi Formation in the eastern margin of Ordos Basin, such as coal rocks, siltstones, and fine sandstones, shale and siltstone shale were selected as sample preparation objects. Two rock samples were drilled for each lithology and subjected to uniaxial compression test. According to the Chinese Standards GB/T 23561.7-2009 and GB/T 23561.9-2009, samples for uniaxial compression tests are cylinders with a diameter of 25 mm and length of 50 mm. The nonparallelism of the cylinder end face shall not exceed 0.05 mm, and the end face also shall be perpendicular to the axis, with a maximum deviation less than  $0.25^\circ$ . Uniaxial compression tests were carried out on rtr-1000 high-temperature and high-pressure rock triaxial mechanical test system. The maximum axial loading capacity of the test system is 1000KN and the maximum confining pressure loading capacity is 140 MPa. The RTR-1000 rock triaxial testing system can be shown in Figure 1. During the tests, the axial deformation and radial deformation were determined by the linear variable differential transducers (LVDT) and circumferential sensor, respectively.

According to the test results, the differences of uniaxial compressive strength, elastic modulus, and Poisson’s ratio of rocks with different lithology were calculated. On this basis, the energy evolution laws of different lithological rocks were discussed. During the uniaxial compression test, the displacement control mode was used during the experiment, and the strain loading rate of 0.2 mm/min was used for continuous loading of axial load until the rock samples were damaged in order to obtain the stress-strain curves. On the basis, the  $UCS$ ,  $E_s$ , and  $\nu_s$  can be calculated as follows:

$$UCS = P/A, \quad (1)$$

$$E_s = \Delta\sigma/\Delta\varepsilon, \quad (2)$$

$$\nu_s = |\varepsilon_r/\varepsilon_a|, \quad (3)$$

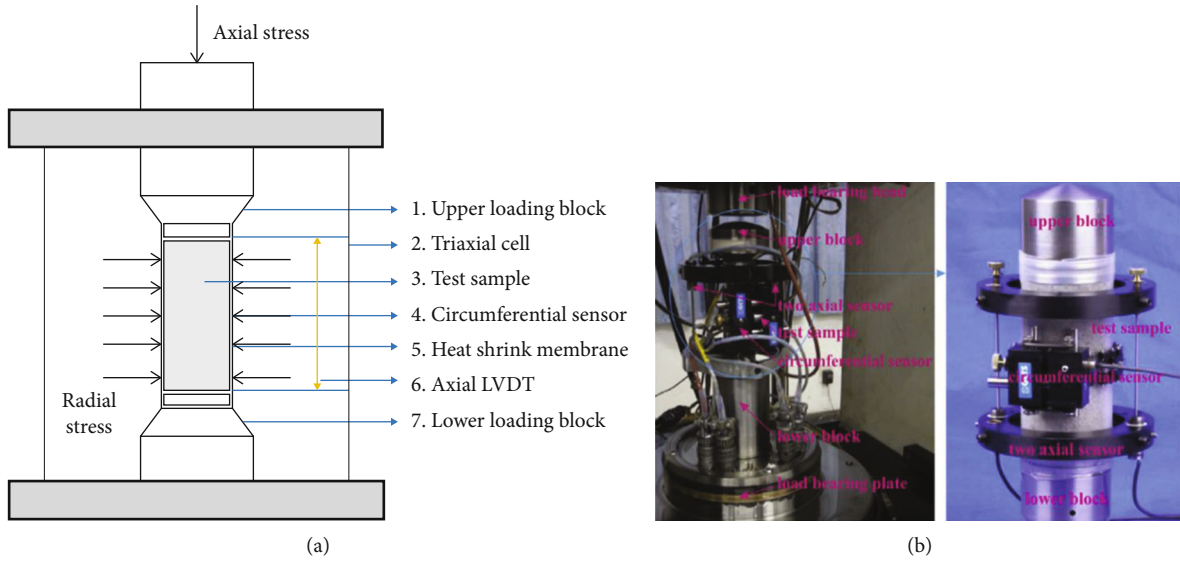


FIGURE 1: The experimental setup. (a) Schematic diagram of the sample in the triaxial cell; (b) RTR-1000 rock triaxial testing system (revised from the literature [29]).

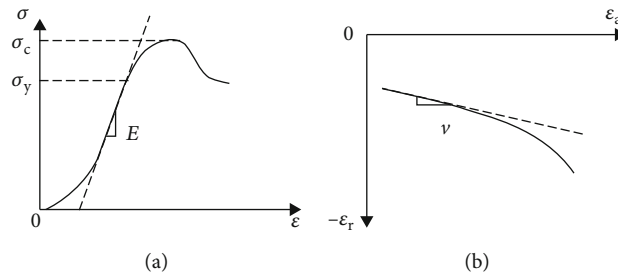


FIGURE 2: The calculation of Young's modulus (a) and Poisson's ratio (b) based on the elastic deformation stage of the stress–strain curve.

where  $P$  is the failure load, kN;  $A$  is the cross-sectional area of the sample, m;  $\Delta\sigma$  is axial stress of the elastic deformation stage of the stress–strain curve, MPa;  $\Delta\varepsilon$  is axial strain of the elastic deformation stage of the stress–strain curve, %;  $\varepsilon_r$  is radial strain of the elastic deformation stage of the stress–strain curve, %;  $\varepsilon_a$  is axial strain of the elastic deformation stage of the stress–strain curve, %. The calculation of the  $E_s$  and  $\nu_s$  parameters based on the elastic deformation stage of the stress–strain curve can be seen in Figure 2.

### 3. Results

**3.1. Failure Mode.** The failure mode of rock samples with different lithology under uniaxial compression test is shown in Figure 3. By observing Figure 3, it is found that the failure modes of different lithological rock samples are mainly splitting failure mode, which is multiple through cracks approximately parallel to the axis of the rock sample are formed on the rock samples, may be accompanied by secondary fractures that do not penetrate the rock samples. It should be noted that the local shear failure occurs in different lithological rock samples, forming multiple low angle shear fractures. At the same time, we can also see from the figure that in addition to the single or two through fractures

formed by fine sandstone, after the failure and instability of shale, silty shale, siltstone, and other rock samples, there are also multiple through fractures approximately parallel to the axis of the rock sample, and with the emergence of multiple secondary fractures, a more complex fracture network is formed. From this point of view, it shows that these rock samples have obvious brittle characteristics.

**3.2. Mechanical Properties.** Based on the uniaxial compression test, the uniaxial compressive strength, elastic modulus, and Poisson's ratio of different lithological rocks are obtained. The statistical results are shown in Figure 4, *a* presents the uniaxial compressive strength, *b* presents elastic modulus, *c* presents Poisson's ratio. As shown in Figure 4(a), we can note that the uniaxial compressive strengths of the same lithological rock samples do not differ much, but the differences in uniaxial compressive strengths of different lithological rock samples are more obvious. The uniaxial compressive strength of the rock samples varies from 8.25 to 42.68 MPa, with the average uniaxial compressive strength of 40.8 MPa for the siltstone shales, 25.3 MPa for the shales, 30.3 MPa for the siltstones, 22.3 MPa for the fine sandstones, and 8.85 MPa for the coal rocks. The order of the average uniaxial compressive strength of different lithological rocks is siltstone shales > shales > siltstones > fine

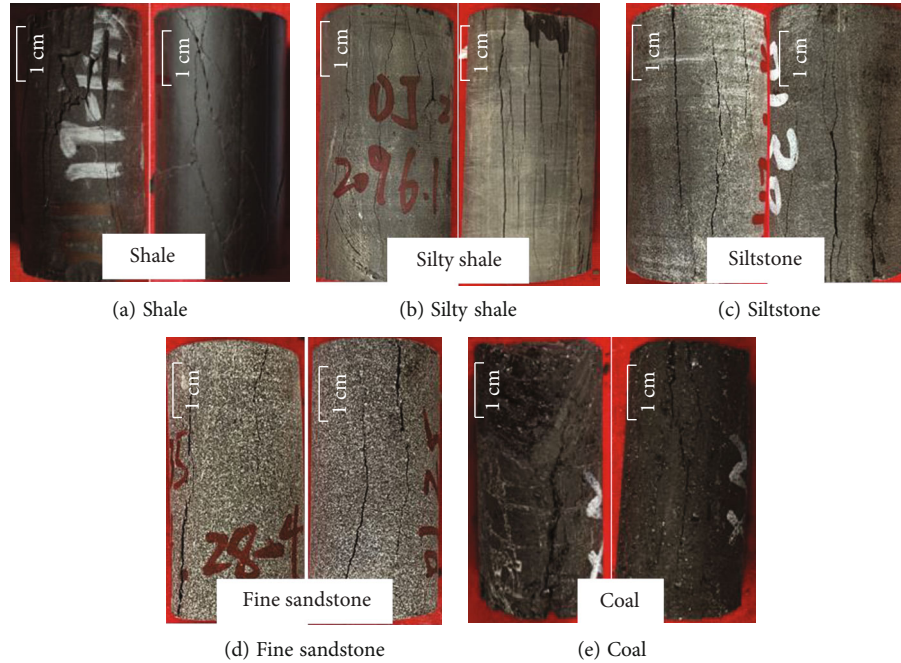


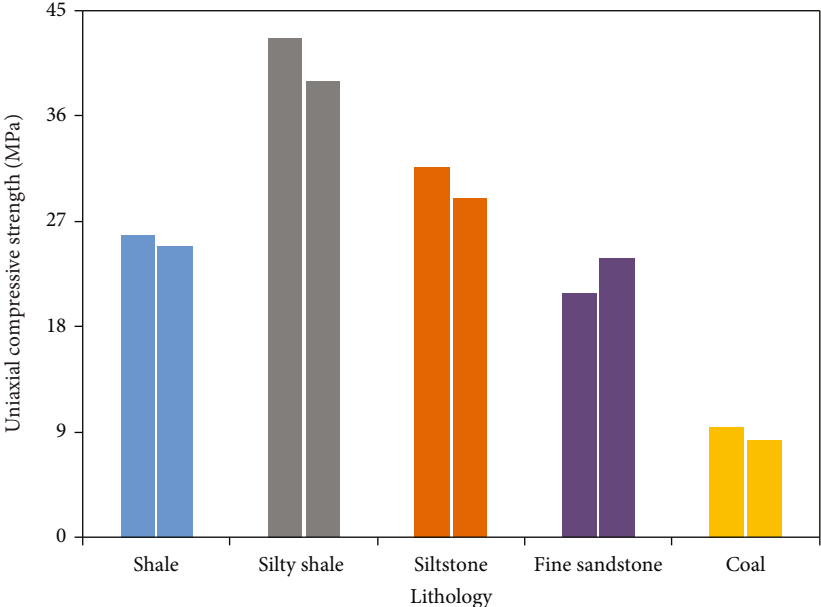
FIGURE 3: Failure mode diagram of rock samples under uniaxial compression tests.

sandstones > coal rocks. This may be related to the differences in mineral composition and structure of different lithological rocks. Meanwhile, from Figures 4(b) and 4(c), we can find that the elastic parameters in different lithological rocks differ more obviously, and the elastic modulus of shales is larger and that of coal rocks is smaller, where the elastic modulus of shales is 2-3 times that of sandstones. According to the previous research results, the differences in the elastic modulus of different lithological rocks would affect the fracture penetration ability among different lithological formations, which would affect the longitudinal upward penetration of fractures, thus affecting the extension of longitudinal fractures' height. For different lithological rocks, the sandstones with the characteristics of low elastic modulus and high Poisson's ratios are not conducive to fracturing to form fracture network. The coal rocks with the low elastic modulus and high Poisson's ratios are easy to form fracture network during fracturing transformation due to relatively developed cleats. The shales formation with high elastic modulus and low Poisson's ratios is conducive to fracture network fracturing. This shows that the vertical and horizontal distribution of rocks in different lithological formations of coal measure strata in the study area is complex, resulting in obvious differences in the vertical and horizontal distribution of elastic modulus and Poisson's ratios of rocks, which can lead to different fracturing measures for different lithological reservoirs, and different vertical penetration capacities of fractures, indicating that the differential reconstruction designs should be considered in the fracturing scheme design of different lithological reservoirs. Therefore, when selecting multilayer combined pressure of coal measure formation, interval optimization should be carried out to realize fracture height extension, and appropriate fracturing combination mode should be selected for fracturing transformation.

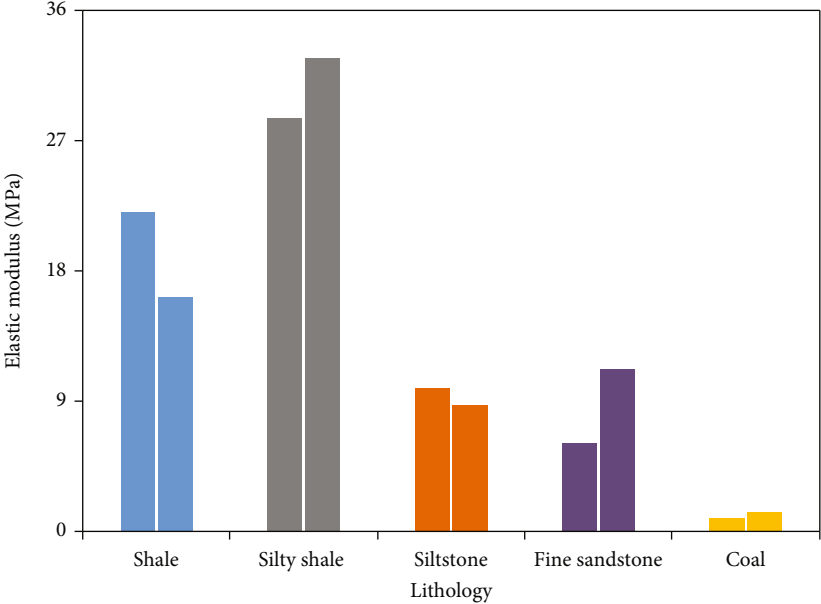
The above research results show that there are significant differences in the strength parameters and elastic parameters of different lithological rocks of the coal measure strata, combined with the characteristics of rapid spatial and temporal lithological changes, complex lithology, and frequent interstratification of the coal measure strata in the study area, which can cause more obvious differences in the distribution of strength parameters and elastic parameters in the longitudinal and lateral directions of the coal measure strata and more obvious differences among different lithological rocks. This is related to the sedimentary environment and multisource and sedimentary structure of the coal measures strata. This mechanical difference will affect the wellbore instability prevention measures and fracturing measures in different lithologic reservoir sections of coal measure strata.

**3.3. Deformation Characteristics.** Stress-strain curves of rock samples with different lithologies under uniaxial compression test are shown in Figure 5. It can be seen from Figure 5 that during the loading process, the deformation characteristics of rock samples with different lithology are obviously different. There is a compaction stage in the initial stage of coal rock, while other rock samples are relatively dense and no compaction section is found. The siltstone and fine sandstone have a long elastic deformation phase, whereas the shale and siltstone shale have a short elastic deformation phase, and the siltstone and fine sandstone do not see an obvious plastic deformation section during the loading process. The axial peak strains of siltstone shale, shale, siltstone, fine sandstone, and coal rock in the figure vary more significantly, but the peak strains of different lithological rock samples are less than 1%, which indicates that the different lithological rocks have a certain brittleness. The peak strain of the silty shale is 0.27%, that of the shale is





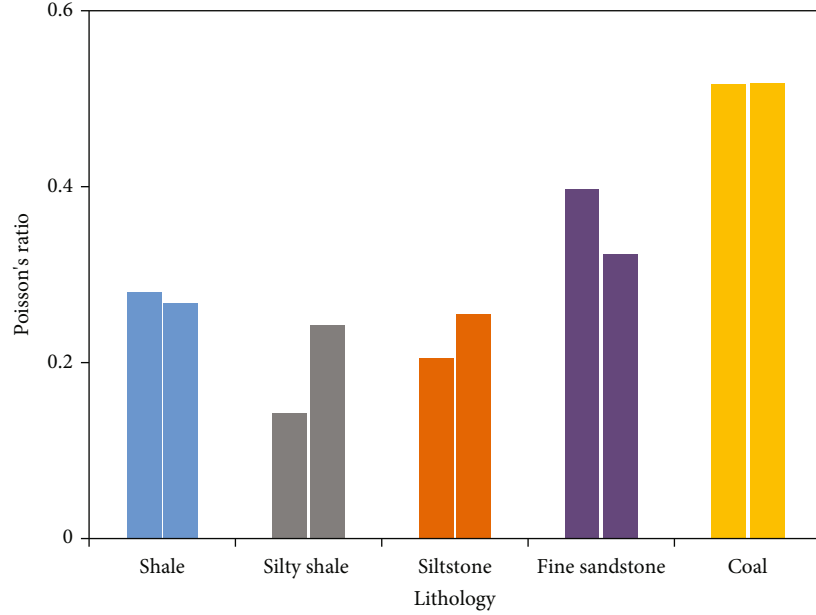
(a) Uniaxial compressive strength



(b) Elastic modulus

FIGURE 4: Continued.





(c) Poisson's ratio

FIGURE 4: Comparison of uniaxial compression test results of different lithological rock samples.

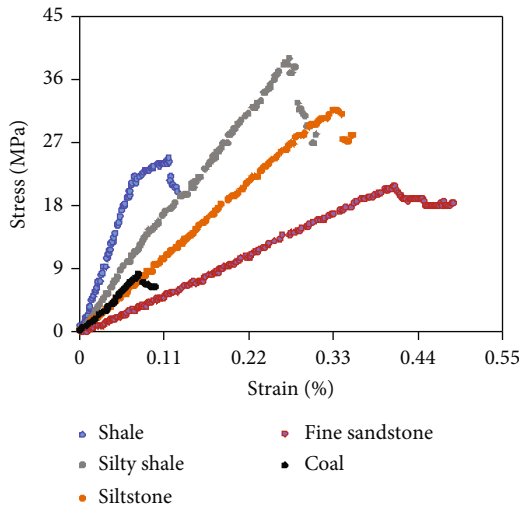


FIGURE 5: Stress-strain curves of different lithological rock samples under uniaxial compression tests.

0.11%, that of the siltstone is 0.34%, that of the fine sandstone is 0.41%, and that of the coal rock is 0.08%.

#### 4. Discussion

At the same time, according to the stress-strain curve, the total energy, elastic energy, and dissipation energy of the experimental rock sample during continuous loading are further calculated. The total energy  $U$  consists of two parts: one part is the elastic strain energy  $U_e$ , which is stored in the form of elastic deformation of the rock sample before the peak stress and can be completely released when damage occurs. The other part is the dissipated energy  $U_d$ , which is

dissipated by the plastic deformation of rock samples and the generation of microcracks before the peak stress, the penetration of the microcracks to form macroscopic cracks when failure occurs so that the energy is dissipated in large quantities, and the relative sliding that occurs between the crack surfaces also consumes energy. All kinds of energy are present simultaneously throughout the process of rock samples from force to damage, only the proportion of which varies in different cases [23]. The total energy expression is [22]:

$$U = U_e + U_d. \quad (4)$$

Under the uniaxial compression test, the total energy and elastic energy absorbed by the rock samples can be expressed, respectively, as [17]:

$$U = \int \sigma_1 d\varepsilon_1 = \sum_{i=0}^n \frac{1}{2} (\varepsilon_{i+1} - \varepsilon_{i1}) (\sigma_{1i} + \sigma_{1i+1}), \quad (5)$$

$$U_e = \frac{\sigma_1^2}{2E_0}, \quad (6)$$

where  $\sigma_1$  and  $\varepsilon_1$  are the axial stress (MPa) and axial strain (mm/mm), respectively;  $\sigma_{1i}$  and  $\varepsilon_{1i}$  are the axial stress (MPa) and axial strain (mm/mm) at point  $i$  on the axial stress-strain curve, respectively;  $E_0$  is the initial modulus of elasticity of the rock sample (MPa).

Based on the data of the axial stress, axial strain, radial strain, and confining pressure obtained from compression experiments, the energy evolution curves under various compression tests can be obtained. The energy evolution curves of some rock samples under uniaxial compression tests are shown in Figure 6. The corresponding energy

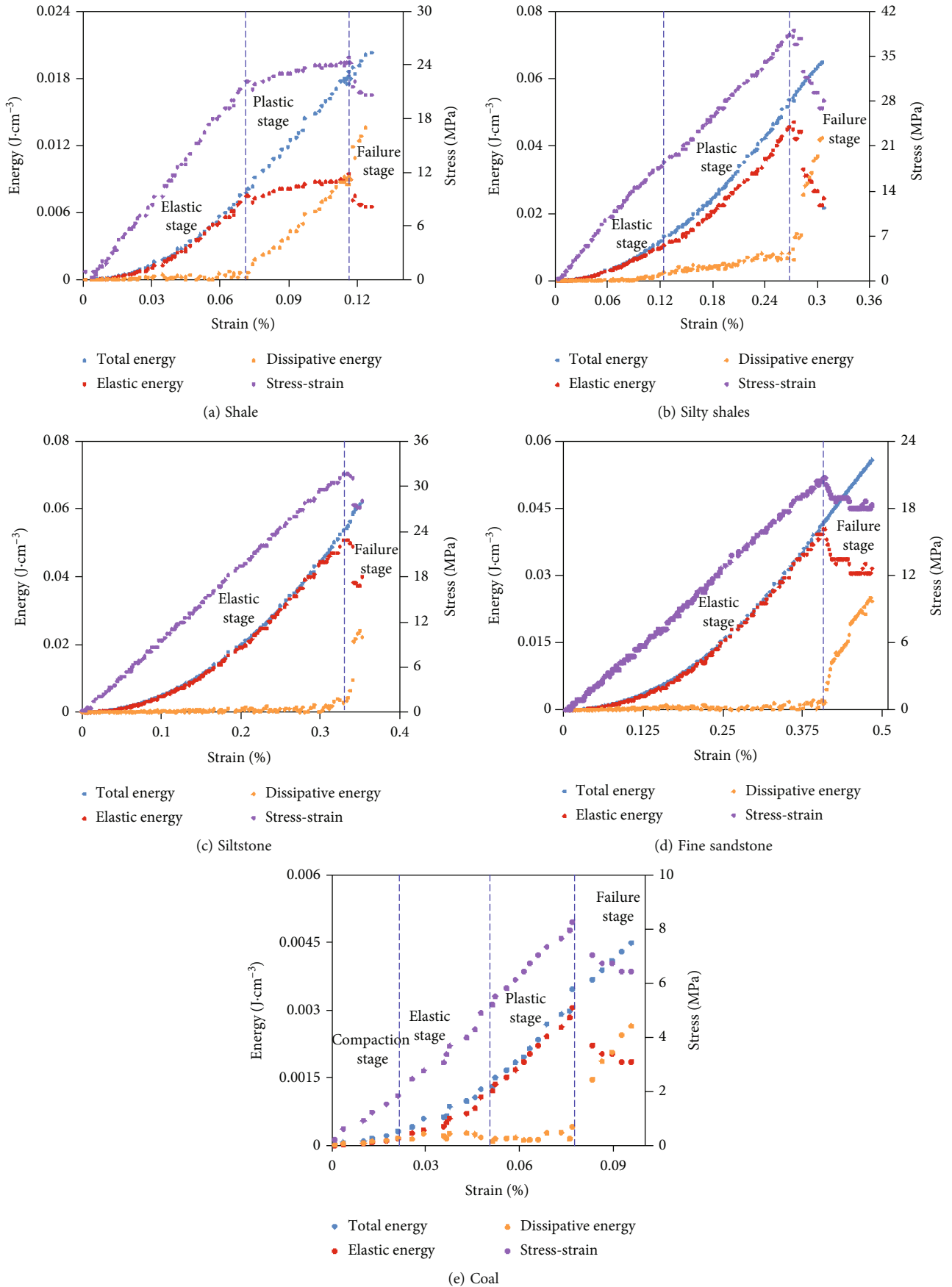


FIGURE 6: Energy evolution curves of different lithological rock samples under uniaxial compression tests.

TABLE 1: Corresponding energy parameters at the peak strain points.

No.	Lithology	$U$	$U_e$	$U_d$	$U_e/U$
1	Shale	0.02472	0.01501	0.00971	0.61
2		0.01859	0.00944	0.00915	0.51
3	Silty shale	0.03566	0.03194	0.00372	0.90
4		0.05340	0.04710	0.00629	0.88
5	Siltstone	0.05361	0.05075	0.00286	0.95
6		0.05087	0.04780	0.00307	0.94
7	Fine sandstone	0.04183	0.04044	0.00139	0.97
8		0.04129	0.04026	0.00103	0.98
9	Coal	0.00297	0.00253	0.00043	0.85
10		0.00346	0.00305	0.00041	0.88

parameters at the peak point of each rock sample are shown in Table 1. By studying the energy evolution characteristics of rock samples with different lithology, it is found that there are obvious differences in the energy evolution process and energy parameters of rock samples with different lithology. Therefore, the differences in the energy evolution laws of different lithological rock samples are further analyzed.

The energy evolution characteristics of some rock samples with different lithologies are shown in Figure 6. Combined with the stress-strain curves of rock samples, the energy evolution curves of rock samples are divided into different stages:

- (1) Compaction stage: Corresponding to the previous stage where the elastic energy is equal to the dissipated energy, in this stage, the deformation of the rock samples increases obviously under the action of low load, and the total energy of the rock samples continues to increase. The dissipated energy curves increase linearly and slowly, and the elastic energy curves increase slowly in a “concave” shape, in which the elastic energy is less than the dissipated energy. The deformation stage of rock samples is the compaction stage. This is because at the initial stage of loading, the original microcracks and micropores of the rock samples are gradually closed, and the dislocation between some internal particles needs to overcome the friction, resulting in more loss in the form of dissipated energy in the total energy, while only a small part of the energy is stored in the form of elastic performance, resulting in less energy absorbed by the rock samples. This is mainly because the cleats of coal rocks are relatively developed, while the rock samples of shale, silty shale, siltstone, and fine sandstone are relatively dense and the cracks are not developed
- (2) Elastic stage: With the continuous increase of axial load, the total energy acted on the rock samples also continues to increase, in which the elastic performance and dissipated energy show an increasing trend, and the rising trend of elastic energy is signif-

icantly greater than that of dissipated energy. When the elastic performance curve intersects with the dissipated energy curve, the deformation stage of rock samples enters the elastic stage. In this stage, the rock samples change from discontinuous state to approximately continuous state, the elastic energy rises rapidly, and the change trend of the elastic energy curve is the same as that of the total energy curve, which is approximately parallel. The rate of the increase of dissipation energy with increasing strain is very slow or approximately constant, resulting in a significant increase of the differences between the two. At this stage, most of the total energy input from the outside is converted into elastic energy and stored, whereas less energy is dissipated and lost. This stage is mainly the energy storage stage. During the loading process, obvious elastic stages can be seen in different lithological rock samples

- (3) Plastic stage: As the axial load continues to increase, the strain gradually increases, resulting in the generation of new cracks and the gradual expansion of existing cracks, and the damage of rock samples increases, which is the dissipated energy gradually increases and the growth rates are accelerated. The dissipated energy curves show a “concave” shape, whereas the elastic performance still increases, but the growth rates slow down, and the elastic energy curves show a “convex” shape. In this stage, the dissipated energy is still small, and the elastic energy still dominates and reaches the maximum at the peak strength. During loading, obvious plastic stages can be seen in the shales, silty shales, and coal rock samples, whereas there is no obvious plastic stage in the siltstone and fine sandstone samples (as shown in Table 1).
- (4) Failure stage: This stage is after the corresponding strain at the peak strength. After reaching the peak strength, the microcracks in the rock samples penetrate to form the macrocracks, resulting in the instantaneous release of elastic energy and the sharp rise of dissipated energy, resulting in the destruction and instability of the rock sample

Under uniaxial compression tests, the variation laws of the total energy before peak strain of different lithological rock samples are shown in Figure 7(a). The variation trends of total energy of different lithological rock samples in the figure before peak strain are the same, in which the total energy increases with the increase of the strain, reflecting that the rock samples continue to increase under the action of the external forces. There are differences in the total energy corresponding to different lithological rock samples under the same strain condition. For example, when the strain is about 0.1%, the total energy of different lithological rock samples is shale  $0.0149 \text{ J/cm}^3$ , silty shale  $0.0081 \text{ J/cm}^3$ , siltstone  $0.0051 \text{ J/cm}^3$ , and fine sandstone  $0.0022 \text{ J/cm}^3$ . This shows that before the failure of different lithological rock samples, at the initial stage of loading, the strain of shale is

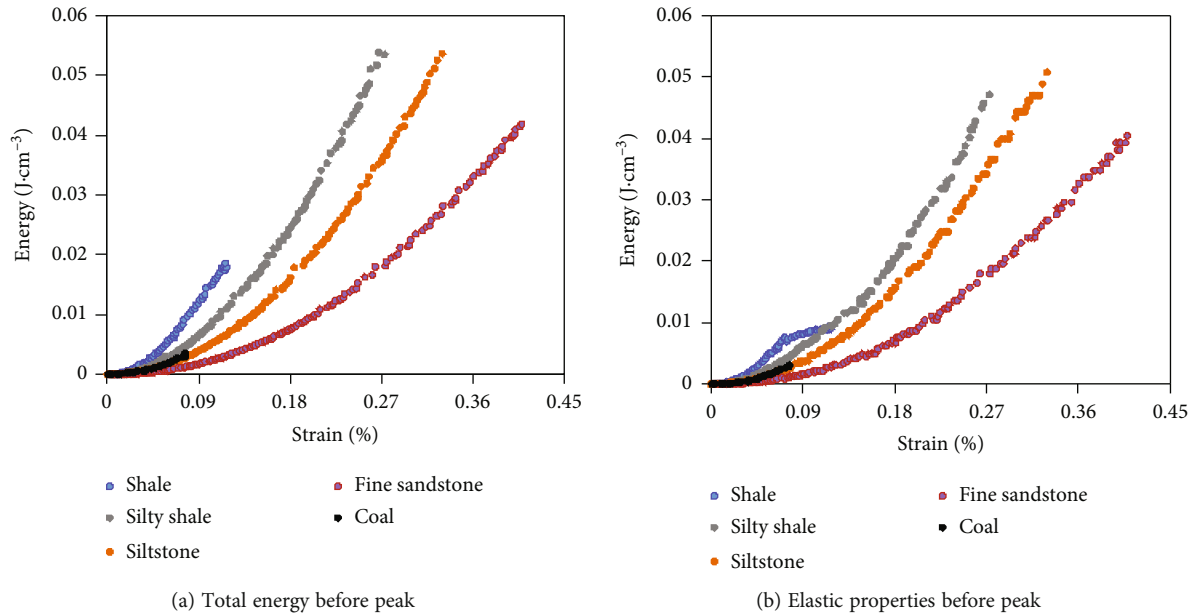


FIGURE 7: The energy parameters before peak strain of different lithological rocks under uniaxial compression tests.

the largest, while that of fine sandstone is the smallest (it should be noted that coal rocks have been damaged under low load). It can also be observed in the figure that there are obvious differences in the total energy of different lithological rock samples at the peak strain.

Under the uniaxial compression tests, the variation laws of the elastic properties before peak strain of different lithological rock samples are shown in Figure 7(b). From Figure 7(b), we can note that the variation trends of elastic energy before peak strain of different lithological rock samples are the same with Figure 7(a), indicating that the energy absorbed by the rock samples continue to increase under the continuous action of external forces. At the same time, the corresponding elastic energy of rock samples with different lithology at peak strain is very different, as shown in Table 1, which reflects the difference of absorbed energy when rock samples are damaged. Among them, the maximum average elastic energy of siltstone at the peak strength is  $0.05224 \text{ J/cm}^3$ , fine sandstone is  $0.04035 \text{ J/cm}^3$ , silty shale is  $0.03952 \text{ J/cm}^3$ , shale is  $0.0122 \text{ J/cm}^3$ , and coal rock is  $0.00279 \text{ J/cm}^3$ . This shows that when the different lithological rock samples are damaged, the energy stored in siltstone is the largest, and the coal rock is the smallest. According to Figure 7, they are reflected that the energy before peak strain is different among different lithological rocks in coal measure strata, indicating that there are differences in energy evolution laws among different lithological rock, reflecting that there is obvious heterogeneity among different lithological rocks, and there are differences in the energy consumed during destruction of different lithological rocks, which may result in different energy consumption for hydraulic fracturing of different lithological formations. This also means that customized fracturing design should be considered in the fracturing design of different lithological formations in the coal measure strata in the eastern margin of Ordos Basin.

## 5. Conclusions

In this paper, the mechanical behaviors of the rocks of the coal measure strata from the Shanxi Formation in the eastern margin of Ordos Basin are investigated, the compressive characteristics, deformation characteristics, and failure modes of different lithological rocks are studied, and the energy evolution laws of different lithological rocks are also discussed. The following conclusions were obtained:

- (1) There are obvious differences in the mechanical properties of different lithological rocks in the coal measure strata, the compressive strength of the silty shales is the largest with an average value of 40 MPa, and the compressive strength of the coals is the smallest with an average value of 8.85 MPa, resulting in the strong heterogeneity, which can cause different wellbore instability prevention measures and fracturing reconstruction measures in different lithological reservoirs
- (2) Under the uniaxial compression tests, the peak strain of different lithological rocks is obviously different, and the denaturation characteristics are obviously different. The rock failure modes are mainly the tensile fracture mode, indicating that rock samples have strong brittle characteristics
- (3) With the increase of the strain, the total energy of different lithological rocks increases, and the elastic energy first increases and then decreases rapidly, whereas the dissipated energy first increases slowly and then increases rapidly. The energy at the peak strain is different, suggesting that there are obvious differences in the energy evolution laws of different lithological rocks

## Data Availability

The data used to support the findings of this study are included within the article.

## Conflicts of Interest

The authors declare that there is no conflict of interests regarding the publication of this paper.

## Authors' Contributions

Xiong Jian contributed to the experiment, data analysis, writing-reviewing; Wu Jianjun contributed to the experiment, writing-reviewing; Liu Junjie contributed to the data analysis, writing-reviewing; Li Bing contributed to the data analysis; Liu Xiangjun contributed to the data analysis; Lixi Liang contributed to the investigation, data analysis.

## Acknowledgments

This research is supported by the Science and Technology Cooperation Project of the CNPC-SWPU Innovation Alliance (Grant No. 2020CX030000), and the Young Scientific and Technological Innovation Team of Rock Physics in Unconventional Strata of Southwest Petroleum University (No. 2018CXTD13).

## References

- [1] C. Zou, S. Pan, and Q. Hao, "On the connotation, challenge and significance of China's "energy independence" strategy," *Petroleum Exploration and Development*, vol. 47, no. 2, pp. 449–462, 2020.
- [2] Y. Li, D. Tang, P. Wu et al., "Continuous unconventional natural gas accumulations of Carboniferous-Permian coal-bearing strata in the Linxing area, northeastern Ordos basin, China," *Journal of Natural Gas Science & Engineering*, vol. 36, pp. 314–327, 2016.
- [3] Y. Li, J. Yang, Z. Pan, S. Meng, K. Wang, and X. Niu, "Unconventional natural gas accumulations in stacked deposits: a discussion of Upper Paleozoic coal-bearing strata in the east margin of the Ordos Basin, China," *Acta Geologica Sinica*, vol. 93, no. 1, pp. 111–129, 2019.
- [4] M. Shangzhi, H. Bing, Z. Jian, T. Peng, and X. Zhenyu, "Experimental research on hydraulic fracture propagation through mixed layers of shale, tight sand and coal seam," *Journal of China Coal Society*, vol. 41, no. 1, pp. 221–227, 2016.
- [5] S. Z. Meng, Y. Li, J. Z. Wang, G. Gu, Z. Wang, and X. Xu, "Co-production feasibility of "Three gases" in coal measures: Discussion based on field test well," *Journal of China Coal Society*, vol. 43, no. 1, pp. 168–174, 2018.
- [6] J. Shen, Y. Qin, B. Zhang, G. Z. Li, and Y. L. Shen, "Superimposing gas-bearing system in coal measures and its compatibility in Linxing Block, East Ordos Basin," *Journal of China Coal Society*, vol. 43, no. 6, pp. 1614–1619, 2018.
- [7] Y. Li, M. Long, L. Zuo, W. Li, and W. Zhao, "Brittleness evaluation of coal based on statistical damage and energy evolution theory," *Journal of Petroleum Science and Engineering*, vol. 172, pp. 753–763, 2019.
- [8] Y. Li, D. Jia, M. Wang et al., "Hydraulic fracturing model featuring initiation beyond the wellbore wall for directional well in coal bed," *Journal of Geophysics and Engineering*, vol. 13, no. 4, pp. 536–548, 2016.
- [9] L. I. Yuwei, L. O. Min, T. A. Jizhou, C. H. Mian, and F. U. Xiaofei, "A hydraulic fracture height mathematical model considering the influence of plastic region at fracture tip," *Petroleum Exploration and Development*, vol. 47, no. 1, pp. 184–195, 2020.
- [10] Y. Zou, S. Li, X. Ma, S. Zhang, N. Li, and M. Chen, "Effects of CO<sub>2</sub>-brine-rock interaction on porosity/permeability and mechanical properties during supercritical-CO<sub>2</sub> fracturing in shale reservoirs," *Journal of Natural Gas Science and Engineering*, vol. 49, pp. 157–168, 2018.
- [11] Y. Li, H. Li, G. Chen, K. Geng, L. Cao, and T. Liang, "On the compressional extensional tectonic environment for the formation of Jiaodong gold deposit, Shandong Province," *Geotectonics and Metallogeny*, vol. 4, no. 6, pp. 1117–1132, 2019.
- [12] Y. Li, J. Yang, Z. Pan, and W. Tong, "Nanoscale pore structure and mechanical property analysis of coal: An insight combining AFM and SEM images," *Fuel*, vol. 260, article 116352, 2020.
- [13] Y. Li, J.-Q. Chen, J.-H. Yang, J.-S. Liu, and W.-S. Tong, "Determination of shale macroscale modulus based on microscale measurement: a case study concerning multiscale mechanical characteristics," *Petroleum Science*, vol. 19, no. 3, pp. 1262–1275, 2022.
- [14] H. Wang, M. He, F. Pang, Y. Chen, and Z. Zhang, "Energy dissipation-based method for brittleness evolution and yield strength determination of rock," *Journal of Petroleum Science & Engineering*, vol. 200, 2021.
- [15] Y. Li, D. Jia, Z. Rui, J. Peng, C. Fu, and J. Zhang, "Evaluation method of rock brittleness based on statistical constitutive relations for rock damage," *Journal of Petroleum Science and Engineering*, vol. 153, pp. 123–132, 2017.
- [16] E. Stavropoulou, C. Dano, and M. Boulon, "Shear response of wet weak carbonate rock/grout interfaces under cyclic loading," *Rock Mechanics and Rock Engineering*, vol. 54, no. 6, pp. 2791–2813, 2021.
- [17] P. Rai, "A comparative investigation of inter-row delay timing vis-à-vis some rock properties on high sandstone benches," *Indian Journal of Engineering and Materials Sciences (IJEMS)*, vol. 27, no. 1, pp. 112–119, 2020.
- [18] C. Li, M. Ostadhassan, A. Abarghani, A. Fogden, and L. Kong, "Multi-scale evaluation of mechanical properties of the Bakken shale," *Journal of Materials Science*, vol. 54, no. 3, pp. 2133–2151, 2019.
- [19] P. Bagde and V. Petroš, "Fatigue properties of intact sandstone samples subjected to dynamic uniaxial cyclical loading," *International Journal of Rock Mechanics and Mining Sciences*, vol. 42, no. 2, pp. 237–250, 2005.
- [20] S. Akdag, M. Karakus, G. D. Nguyen, A. Taheri, and T. Bruning, "Evaluation of the propensity of strain burst in brittle granite based on post-peak energy analysis," *Underground Space*, vol. 6, no. 1, pp. 1–11, 2021.
- [21] Z. Chen, C. He, W. Dong, G. Ma, and C. Pei, "Physico-mechanical properties and its energy damage evolution mechanism of the jurassic and cretaceous argillaceous sandstone in northern Xinjiang," *Rock and Soil Mechanics*, vol. 39, no. 8, pp. 2873–2885, 2018.

- [22] J. Jiang, S. Chen, J. Xu, and Q. Liu, "Mechanical properties and energy characteristics of mudstone under different containing moisture states," *Journal of China Coal Society*, vol. 43, no. 8, pp. 2217–2224, 2018.
- [23] X. Yang, H. Cheng, and Y. Pei, "Study on rock deformation and post peak energy evolution under different loading modes," *Journal of Rock Mechanics and Engineering*, vol. 39, no. A2, pp. 3229–3236, 2020.
- [24] C. Hongde, L. Jie, Z. Chenggong, C. Lixue, and C. Lijun, "Discussion of sedimentary environment and its geological enlightenment of Shanxi Formation in Ordos Basin," *Acta Petrologica Sinica*, vol. 27, no. 8, pp. 2213–2229, 2011.
- [25] L. Kuang, D. O. Dazhong, H. E. Wenyuan et al., "Geological characteristics and development potential of transitional shale gas in the east margin of the Ordos Basin, NW China," *Petroleum Exploration and Development*, vol. 47, no. 3, pp. 471–482, 2020.
- [26] W. U. Jin, W. A. Hongyan, S. H. Zhensheng et al., "Favorable lithofacies types and genesis of marine-continental transitional black shale: a case study of Permian Shanxi Formation in the eastern margin of Ordos Basin, NW China," *Petroleum Exploration and Development*, vol. 48, no. 6, pp. 1315–1328, 2021.
- [27] Y. Chen, D. Ma, Y. Xia, C. Guo, F. Yang, and K. Shao, "Characteristics of the mud shale reservoirs in coal-bearing strata and resources evaluation in the eastern margin of the Ordos Basin, China," *Energy Exploration & Exploitation*, vol. 38, no. 2, pp. 372–405, 2020.
- [28] Y. Qi, Y. Ju, J. Cai et al., "The effects of solvent extraction on nanoporosity of marine-continental coal and mudstone," *Fuel*, vol. 235, pp. 72–84, 2019.
- [29] T. Ma, C. Yang, P. Chen, X. Wang, and Y. Guo, "On the damage constitutive model for hydrated shale using CT scanning technology," *Journal of Natural Gas Science and Engineering*, vol. 28, pp. 204–214, 2016.



## Research Article

# Research on Remaining Oil Characterization in Superheavy Oil Reservoir by Microgravity Exploration

Qijun Lv,<sup>1</sup> Aiping Zheng ,<sup>1</sup> Xiangjin Liang ,<sup>1</sup> Hongfei Chen,<sup>1</sup> Shichang Ju,<sup>1</sup> Yanrong Meng,<sup>1</sup> Hongyuan Zhang,<sup>1</sup> Guolin He,<sup>2</sup> Shenshen Deng ,<sup>3</sup> and Junfang Li<sup>1</sup>

<sup>1</sup>PetroChina Xinjiang Oilfield Company, Karamay, Xinjiang 834000, China

<sup>2</sup>Third Geological Brigade of Hubei Geological Bureau, Hubei 438000, China

<sup>3</sup>Beijing Zhongke Energy Geophysical Technology Co., Ltd., Beijing 100088, China

Correspondence should be addressed to Xiangjin Liang; [liangxj666@petrochina.com.cn](mailto:liangxj666@petrochina.com.cn)

Received 26 January 2022; Revised 31 March 2022; Accepted 23 May 2022; Published 18 July 2022

Academic Editor: Jinjie Wang

Copyright © 2022 Qijun Lv et al. This is an open access article distributed under the Creative Commons Attribution License, which permits unrestricted use, distribution, and reproduction in any medium, provided the original work is properly cited.

Some physical processes such as oil and gas development, metal deposit collection, and groundwater resource migration can cause density changes, for which microgravity monitoring is the most intuitive method to monitor the density change process. Based on the basic principle of microgravity measurement and the idea of multiscale separation, a multiscale, second-order, surface-fitting, residual gravity anomaly extraction method is proposed to separate superimposed microgravity fields. In this method, regional fields of different scales are fitted and calculated successively with the measurement points as the center, so as to separate the gravity anomalies produced by different-depth density bodies. Results from actual data show that this method extracts the reservoir's residual density characteristics of plane gravity anomaly on the basis of remaining oil distribution characteristics, consistent with reservoir numerical simulation results. A three-dimensional least-squares inversion of the method for extracting residual gravity anomaly was carried out, with the inversion results consistent with the results of vertical remaining oil distribution characteristics and well-test production results.

## 1. Introduction

Heavy oil is a type of high-viscosity crude oil with high asphaltene and gum content. In China, heavy oil reservoirs are important, widely distributed petroleum resources, among which the Liaohe, Shengli, and Xinjiang oilfields all have large reserves. In order to fully utilize the reservoir and improve oil recovery, it is critical to describe the characteristics of remaining oil in the process of reservoir production and then to formulate a comprehensive reservoir adjustment plan and stimulation measures.

At present, there are relatively few methods to monitor the distribution of remaining oil. Among them, microgravity exploration has become an excellent reservoir-monitoring method, having the advantages of overall monitoring, low cost, no impact on production, nondestructive monitoring, and independence from well verification. With continuous improvement in the accuracy of gravity instruments and con-

tinuous progress in technical algorithms, the applications for gravity data are expanding [1]. The gravity exploration method has gradually expanded from understanding regional structural characteristics [2], delineating rock mass range [3], indicating metallogenic prospects [4], seeking local structure [5], and determining stratigraphic rock occurrence [6] to looking for oil and gas resources [7] and describing fluid dynamic changes in oil reservoirs and other fields.

By observing changes in surface gravity data and monitoring changes in oil and gas reservoir density, microgravity exploration can effectively reflect dynamic changes in fluid in the oil and gas reservoir development process and can effectively describe the distribution of remaining oil in heavy oil reservoirs, which is an important link in the dynamic regulation of heavy oil thermal recovery—tapping the potential of remaining oil and prolonging the development life cycle of heavy oil reservoirs. Microgravity-monitoring results for the Alaska Prudhoe Bay gas field have verified that the



time-lapse microgravity anomaly can reflect density change caused by water injection in the reservoir and can guide the designs of water injection and enhanced oil recovery [8]. Subsea gravimeters have been used to monitor the height of water-gas contact in water injection gas reservoirs in offshore Norway with an accuracy of meter level [9]. In the Liaohe oilfield, time-shift microgravity monitoring has been used to quantitatively describe changing steam chamber shape during steam-assisted gravity drainage (SAGD) production, providing a reliable basis for adjusting the steam injection scheme [10]. Previous research results have shown that microgravity exploration is suitable for anomalies caused by density changes from displacement and migration of underground fluids in oil and gas reservoirs, with the key solution being to accurately separate the residual gravity anomalies representing reservoir density. At present, the commonly used gravity anomaly separation methods are the filtering method, trend analysis method, peeling method, and nonlinear method [11]. For the filtering method, if the filter is in the nonzero phase, the anomaly extreme point will shift, and there will be significant error when applied to gravity anomaly separation. Affected by the near-source field of the target source, the trend analysis method has difficulty extracting the regional anomaly; the separated local field contains the near-source field information, resulting in anomaly illusion. The premise of the peeling method is to establish a known density model, obtain the anomaly through forward modeling, and then subtract the forward-modeling anomaly from the observed anomaly to obtain the residual anomaly; the accuracy of the established density model directly affects the accuracy of the residual gravity anomaly, and although this method is invalid for regional anomalies, it is effective for near-source effects and high-frequency anomalies. The nonlinear method separates microgravity anomalies and is characterized by multiscale and locality; its disadvantage is asymmetry of surface fitting resulting in distortion of the separated anomaly shape.

In this paper, a multiscale, second-order, surface-fitting, residual gravity anomaly extraction method is proposed. This method combines the multiscale element of the nonlinear separation method and the basic principle of the surface-fitting method. Second-order surface fitting is carried out at different scales to obtain the regional field at the corresponding scale, and then, the calculated regional field is subtracted from the Bouguer gravity anomaly or the regional field at the previous scale to obtain the residual gravity anomaly at this scale. The regional field at different scales can be separated from the residual anomaly and so on, so as to obtain the residual gravity anomaly representing the density of the target area and then explain and analyze the research target. Through forward modeling and field-test verification, the accuracy and reliability of the extraction results of this method were studied in detail.

## 2. Forward Modeling

Gravity anomaly is the derivative of the additional gravity generated by the residual mass of the geological body to

TABLE 1: Forward-modeling parameters.

No.	Length (m)	Width (m)	Thickness (m)	Depth of top (m)	Residual density (g/cm <sup>3</sup> )
A1	4000	5000	1500	1500	0.15
A2	3000	7000	1500	1500	-0.10
A3	1500	3300	1500	1500	0.10
B1	400	1600	400	400	-0.25
B2	400	1000	400	400	0.25
B3	600	800	400	400	0.25
B4	600	900	400	400	0.25
B5	600	2400	400	400	-0.25
C1	100	200	100	100	0.50
C2	100	200	100	100	-0.50
C3	100	100	100	100	0.50

the unit mass at the detection point in the gravity direction. According to the formula of universal gravitation, it can be deduced that the gravity anomaly of a geological body is

$$\Delta g(x_i, y_i, z_i) = G \iiint_V \frac{\Delta \rho(x_v, y_v, z_v) \cdot (z_i - z_v)}{[(x_i - x_v)^2 + (y_i - y_v)^2 + (z_i - z_v)^2]^{3/2}} dx_v dy_v dz_v, \quad (1)$$

where  $\Delta g(x_i, y_i, z_i)$  is the derivative of gravity along the  $Z$  direction at any coordinate point  $(x_v, y_v, z_v)$ ,  $G$  is the universal gravitation constant,  $V$  is the volume of the geological body, and  $\Delta \rho(x_v, y_v, z_v)$  is the residual density difference of a volume element in the geological body coordinate  $(x_v, y_v, z_v)$ .

For a reservoir under heavy oil thermal recovery, the buried depth and thickness of the reservoir are known. According to Equation (1), the microgravity value monitored on the surface is mainly controlled by the density change in the reservoir. According to Biot's theory [12], the original density of reservoir  $\rho$  can be calculated by [13]

$$\rho = (1 - \phi) \cdot [(1 - V_{sh}) \cdot \rho_M + V_{sh} \cdot \rho_{sh}] + \phi \cdot \rho_l, \quad (2)$$

where  $\phi$  is reservoir porosity,  $V_{sh}$  is the shale content in the reservoir, and  $\rho_M$ ,  $\rho_{sh}$ , and  $\rho_l$  are rock skeleton density, argillaceous density, and liquid density in the reservoir, respectively.

After heavy oil thermal recovery development, the reservoir density can be expressed by

$$\rho = (1 - \phi) \cdot [(1 - V_{sh}) \cdot \rho_M + V_{sh} \cdot \rho_{sh}] + \phi \cdot [(1 - S_g) \cdot \rho_l + S_g \cdot \rho_g], \quad (3)$$

where  $S_g$  is the saturation after steam injection thermal recovery and  $\rho_g$  is injected steam density for thermal recovery.

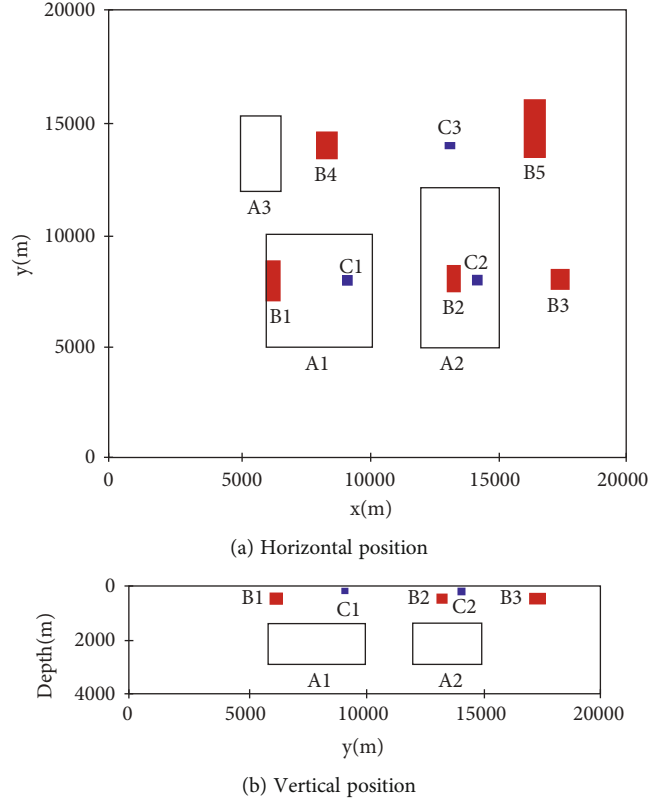


FIGURE 1: Forward modeling of geological body location.

After a period of thermal recovery, the change in reservoir density is expressed by

$$\Delta\rho = \phi \cdot (\rho_g - \rho_l) \cdot S_g. \quad (4)$$

The basic principle of microgravity monitoring for a thermal recovery reservoir can be obtained by combining Equations (4) and (1).

$$\Delta g(x_i, y_i, z_i) = G \cdot \phi \cdot S_g \iiint_V \frac{[\rho_g(x_v, y_v, z_v) - \rho_l(x_v, y_v, z_v)] \cdot (z_i - z_v)}{[(x_i - x_v)^2 + (y_i - y_v)^2 + (z_i - z_v)^2]^{3/2}} dx_v dy_v dz_v. \quad (5)$$

Equation (5) shows that for a specific reservoir, the microgravity-monitoring result is directly proportional to the steam saturation in the reservoir porosity. The formula shows the microgravity-monitoring results to be indicative of dynamic changes in fluids in the reservoir.

The Bouguer gravity anomaly obtained from surface observation is the superposition of gravity anomalies generated by all density bodies in the microgravity exploration area (including the gravity anomaly represented by Equation (5)). The gravity anomaly represented by Equation (5) is separated from the Bouguer gravity anomaly by the multi-scale, second-order, surface-fitting method. The implementation process is as follows:

Assuming the observed Bouguer gravity anomaly is  $g(x, y, 0)$ , via the multiscale nonlinear method, its expression can be

$$g_{bg}(x, y, 0) = g_{r1} + g_{l1} = g_{r2} + g_{l1} + g_{l2} = g_{r3} + g_{l1} + g_{l2} + g_{l3} \dots, \quad (6)$$

$$[\Delta g_r]_i = g_{bg} - [g_r]_i = \sum_{i=1}^n g_{li}, \quad (7)$$

where  $(x, y, 0)$  represent the ground coordinates,  $g_{l1}, g_{l2}, g_{l3}, \dots$  represent local anomalies of different scales, and  $[\Delta g_r]_i$  is the residual gravity anomaly at the  $i^{\text{th}}$  scale, where  $i = 1, 2, 3, 4$ .

The local fields  $[g_r]_i$  at different scales are obtained by the second-order surface-fitting method. Located in a small area centered on a point  $(m, n, 0)$ ,  $g_r$  can be expressed as

$$g_r = a_0 + a_1x + a_2y + a_3xy + a_4x^2 + a_5y^2, \quad (8)$$

where  $x, y$  is the distance from the point in the area to the center point. Then, the sum of error squares at each point is expressed as

$$E(g, g_r) = \sum_i \sum_j (g(i, j) - g_r(i, j))^2, \quad (9)$$

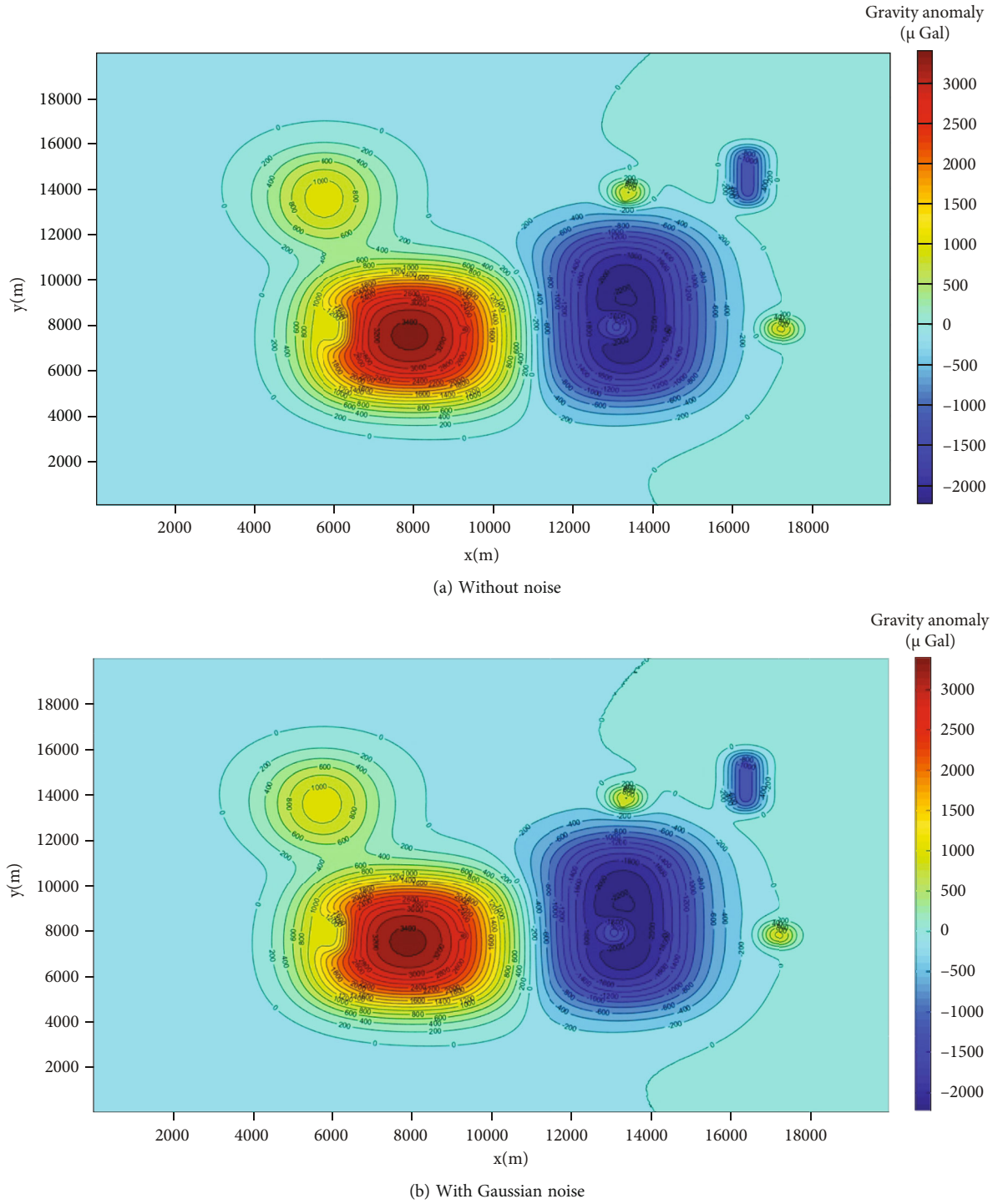


FIGURE 2: Gravity field distribution of the forward modeling.

where  $i$  and  $j$  are taken in the area with the point as the center  $(m, n)$ .

Firstly, the second-order surface coefficient  $(a_0, a_1, a_2, a_3, a_4, a_5)$  is obtained by the least-squares method, and then, the same operation is carried out for each point to obtain the regional field value of each point under the corresponding scale. Next, the residual gravity anomaly under the corresponding scale is calculated by Equation (7), and finally,

the reasonable scale is determined according to the detection target depth and relevant geological data. The residual gravity anomaly generated by density body in the depth range of microgravity detection target is obtained.

**2.1. Modeling.** In order to verify the method, a model for identifying the effect of gravity separation was adopted in this study. The model was first proposed by Guo et al.

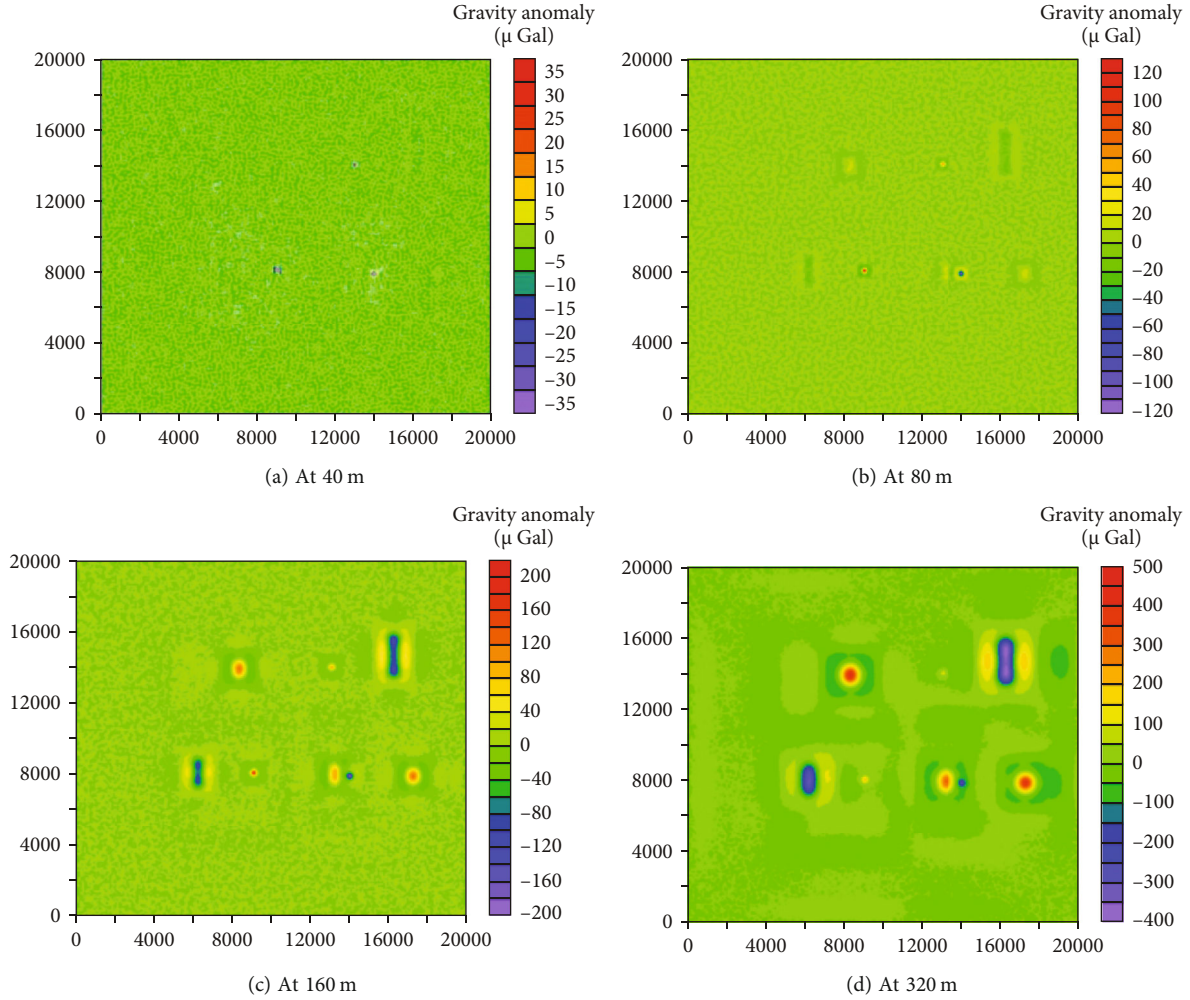


FIGURE 3: Residual gravity anomaly maps at different scales.

[14]. The model parameters are shown in Table 1, and the model distribution is shown in Figure 1.

The model is divided into 3 classes (A, B, and C) composed of 11 cuboids at different depths. The abnormal body with positive residual density simulates the deposits with high density such as metal ore, while the negative residual density simulates the karst cave, the steam cavity, and the abnormal body with low density and high porosity. For the abnormal bodies, class A represents deep background fields, such as basement fluctuation and background density body deeper than the target layer; class B represents the studied target body, which is an effective signal to be retained in the separation process; class C is removed as a shallow interference signal in some cases and is retained as a research target in some cases, such as shallow steam-channeling research.

For the model, an observation system with a sampling interval of 10 m and survey network of  $2001 \times 2001$  is used for forward-modeling simulation. The forward-modeling results are shown in Figure 2(a).

For simulating the distribution of gravity fields, random Gaussian noise with a standard deviation of  $0.2 \times 10^{-5} \text{ m/s}^2$

is added to the theoretical gravity anomaly (Figure 2(b)). Figure 2 shows the superposition results of anomalies generated by various geological bodies at different depths, testing the feasibility of the anomaly extraction method in depicting, distinguishing, and multiscale local details.

*2.2. Separated Result Analysis of Forward Modeling.* The multiscale, second-order, surface-fitting method proposed in this paper extracts the residual gravity anomalies of the gravity field generated by the model at different scales ( $2^n$  times the sampling interval). The calculation results according to Equation (7) are shown in Figure 3: among the residual gravity anomalies separated at different scales, the anomalies generated by various geological bodies are gradually displayed with the continuous increase of scales; they are consistent with geological body location.

In previous studies, Guo et al. [14] and Shi et al. [15] used a variety of methods to carry out anomaly separation experiments on the forward gravity field of the model. It was found that although these methods can extract the residual gravity anomalies generated by the model geological body, they cannot distinguish the residual gravity anomalies



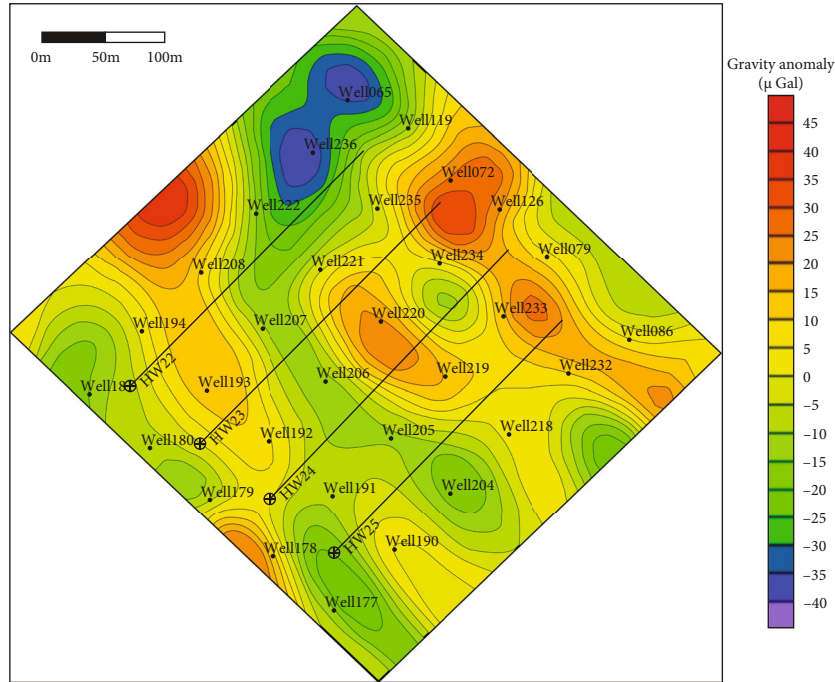


FIGURE 4: Map of microgravity-monitoring results for target reservoir.

generated by the geological body at different depths—and not at multiscale. The multiscale surface-fitting method can effectively separate the regional field at different depths from the residual field without distortion of local anomalies. The anomaly extraction results are more accurate and amplitude-preserved than other methods.

From the analysis of forward-modeling results, it can be seen that the multiscale, second-order, surface-fitting gravity anomaly extraction method proposed in this paper has the following advantages:

- (1) It is multiscale and supplies local description of anomalies without introducing abnormal distortion along the  $X$  and  $Y$  directions.
- (2) The residual gravity anomaly of each scale can reflect the gravity effect produced by the abnormal body at different depth levels. The scale can be selected according to the exploration target, and the abnormal position is clear and accurate.
- (3) It has a strong ability to suppress random noise without involving any empirical formula or parameters in anomaly extraction. Therefore, it is not susceptible to subjective influence and has a good theoretical basis and experimental effect.

### 3. Field Application

In 2019, microgravity monitoring was carried out in a heavy oil reservoir development area in Xinjiang. Using the multiscale, second-order, surface-fitting method proposed in this paper, the residual gravity anomaly representing the density body in the reservoir was extracted according to the scale determined by the buried depth range of the exploration tar-

get, and the residual oil distribution was described in slices. In addition, based on the gravity anomaly generated by the reservoir density volume extracted by multiscale surface fitting, the reservoir density volume was obtained using the three-dimensional (3D) least-squares inversion method, and the remaining oil distribution was characterized vertically. Finally, the horizontal and vertical characterization results of remaining oil distribution were verified by well data and production performance data.

*3.1. Horizontal Characterization of Remaining Oil Distribution.* The residual gravity anomaly results obtained by the multiscale, second-order, surface-fitting method representing the density in the reservoir are shown in Figure 4. On the whole, the warm-color area with a relatively high amplitude of residual gravity anomaly indicates relatively high reservoir density, high remaining oil saturation, and significant remaining oil development potential. The cold-color area with a relatively low amplitude of residual gravity anomaly indicates relatively low reservoir density, low steam sweep, low saturation of remaining oil, and low remaining oil development potential.

In order to verify the depiction results of microgravity monitoring on the plane, the reservoir density was simulated and calculated using the numerical simulation method, combined with the actual production performance data, logging, and other basic data, after which the weighted average result of reservoir density by depth was obtained. In Figure 5, the warm-color area with a relatively high density value represents high residual oil saturation. On the contrary, the cold-color area with a relatively low-density value represents low residual oil saturation. Comparing Figures 4 and 5, the distribution results from microgravity monitoring for the areas with

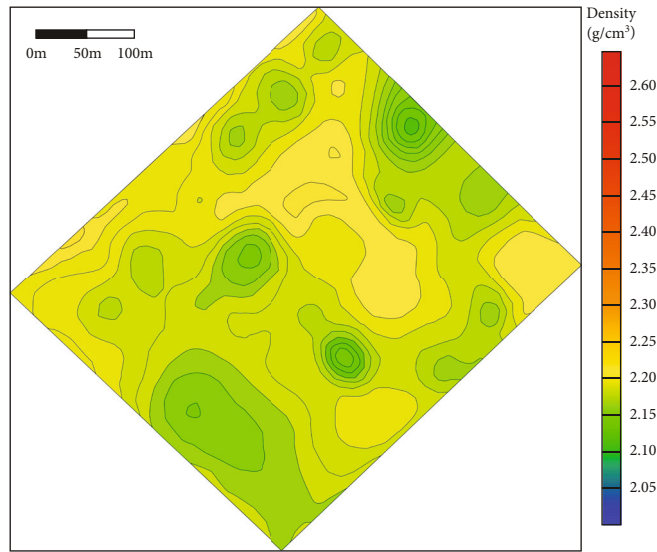


FIGURE 5: Map of weighted average of initial density volume model.

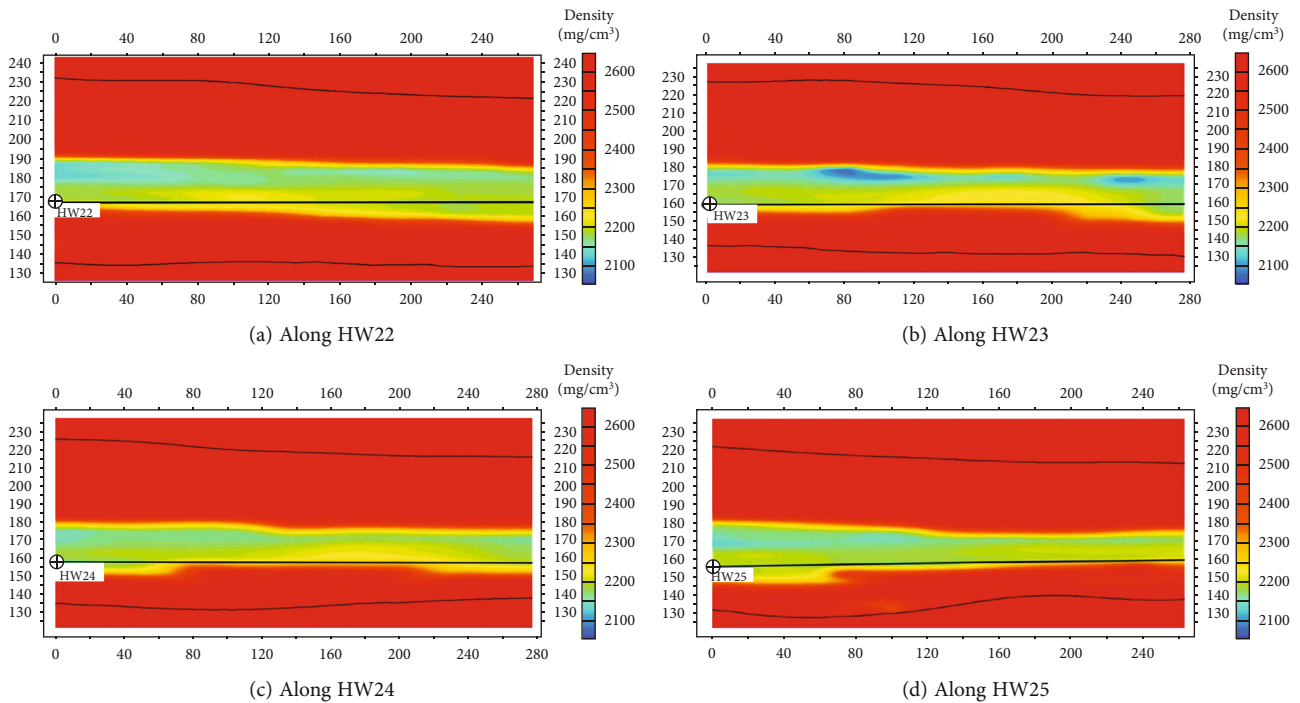


FIGURE 6: Inversion density profiles along different horizontal wells.

high and low residual oil saturations are consistent with the residual oil distribution results obtained by the numerical simulation method, verifying the residual oil distribution results from microgravity monitoring on the plane.

Therefore, the distribution of residual oil above different sections of the horizontal well can be described according to the microgravity-monitoring results, as shown in Figure 4, where the red section of the horizontal well indicates the reservoir above the well section having high residual oil saturation, the black section indicates

medium residual oil saturation, and the white section indicates low residual oil saturation.

3.2. Vertical Characterization of Remaining Oil Distribution.

Figure 6 shows the density body section along the horizontal well direction. On the whole, the reservoir density is shown to gradually decrease from the horizontal well position to the top of the reservoir, indicating a high recovery degree of the upper reservoir and the remaining oil being mainly distributed in the middle and lower parts of the reservoir. Along



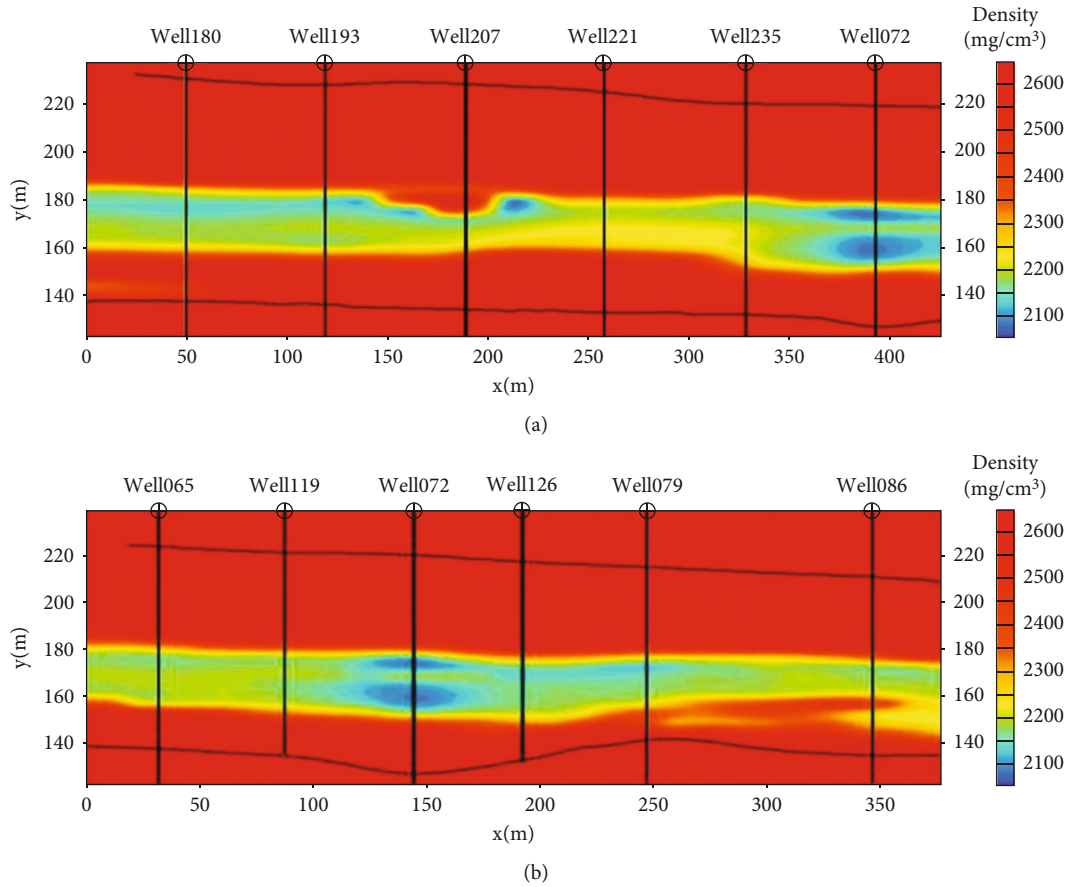


FIGURE 7: (a) Inversion section of density along source direction. (b) Inversion section of density perpendicular to source direction.

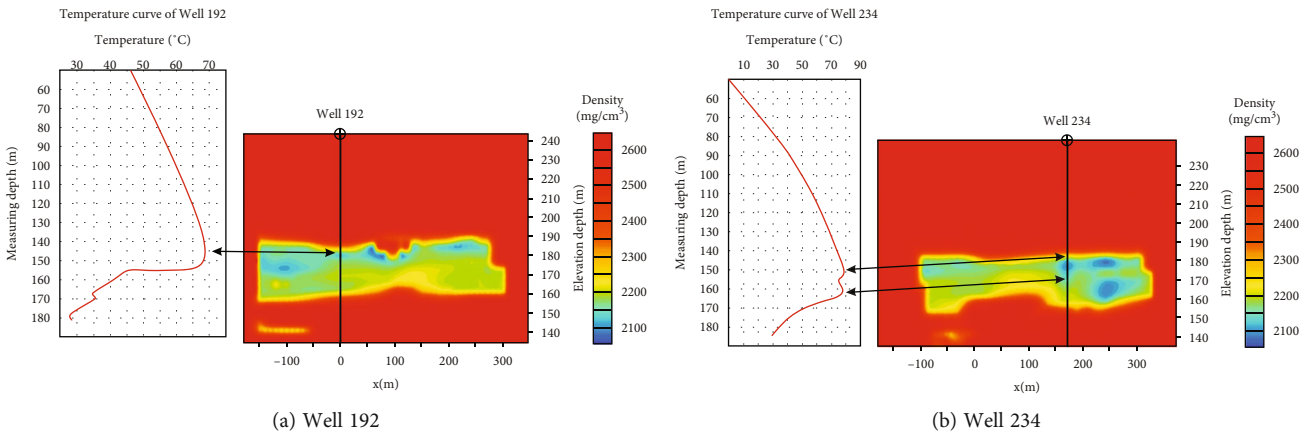


FIGURE 8: Comparison of temperature curve and inversion density profile of wells 192 and 234.

wells HW22, HW23, and HW24, the remaining oil is shown to be mainly distributed in the middle section, and along well HW25, the remaining oil is shown to be mainly distributed in the middle and end sections.

Figure 7 shows density body sections along the source direction (Figure 7(a)) and perpendicular to the source direction (Figure 7(b)). The comparison shows the reservoir density between wells along the material source direction being relatively low, indicating the degree of remaining oil

production as high and the connectivity along the material source direction being better.

As can be seen from Figures 6 and 7, the density of the reservoir decreases from bottom to top. The remaining oil is mainly distributed in the middle and lower parts of the reservoir, which are macroscopically antirhythmic in the vertical direction. At the same time, the remaining oil is affected by steam overlap, resulting in quality deficit and density reduction in the upper part of the reservoir, highly

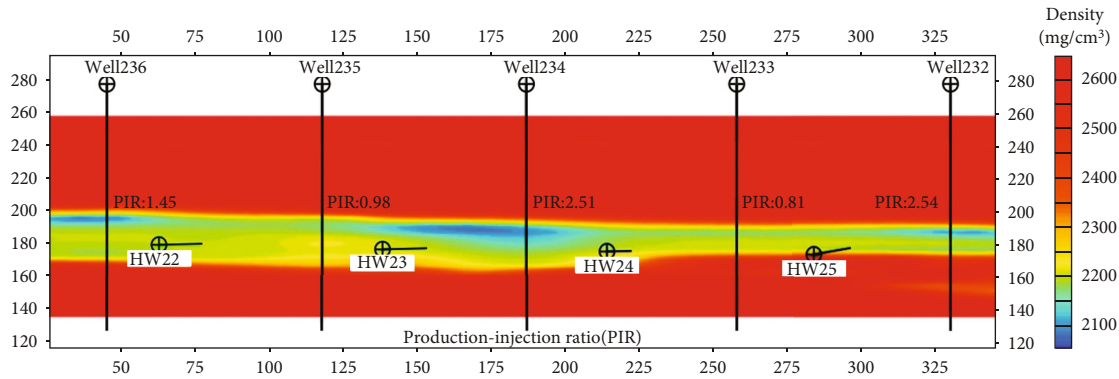


FIGURE 9: Comparison of production performance and well connectivity prediction results of well sections.

corresponding to production injection ratio and low remaining oil content. The steam sweep degree in the lower part of the reservoir is low, and oil and water accumulate in the lower part of the reservoir under the effect of gravity, which is characterized by increased mass, increased density, low production injection ratio, and high residual oil.

Well data verified the characterization results of residual oil distribution in the vertical direction from microgravity monitoring. First, temperature tests on well 192 and well 234 were used for well temperature monitoring. The peak temperature area is the steam chamber development area; the reservoir density in this area should be low. The inversion density body sections are along well 192 and well 234 (Figure 8). It can be seen that the depth range of the low-density area of the inversion density body along the well is consistent with the depth range of the low-density area of the corresponding well temperature monitoring—verifying the accuracy of extracting and characterizing the residual gravity anomaly generated by reservoir density using the multiscale, second-order, surface-fitting method.

Then, the production performance data were used to further verify the description results of residual oil distribution in the vertical direction from microgravity monitoring. The statistics of all production performance data from the microgravity exploration block show the recovery degrees of  $J_3q_2^{2-1}$  and  $J_3q_2^{2-2}$  layers to be 26.4% and 19.7%, respectively, indicating low remaining oil saturation in the upper part of the reservoir and high remaining oil saturation in the middle and lower parts. The microgravity-monitoring results for remaining oil distribution in the vertical direction are consistent with the production performance results. The single-well production performance statistics show the reservoir area with the low-production-injection-ratio well to have a relatively high reservoir density and relatively high residual oil saturation. On the contrary, the reservoir area with the high-production-injection-ratio well is shown to have a relatively low corresponding reservoir density and relatively low remaining oil saturation. It can be seen that the microgravity-monitoring results are consistent with the statistical results of single-well production performance data (Figure 9)—further verifying the accuracy of the residual gravity anomaly characterized by reservoir density extracted by multiscale, second-order surface fitting.

## 4. Conclusions

- (1) In this paper, a multiscale, second-order, surface-fitting separation method of gravity anomalies is proposed; it is suitable for separating microgravity field anomalies. This nonlinear method is more sensitive to abnormal signal changes and does not cause abnormal distortion. The anomaly extraction result is accurate, and the amplitude remains unchanged.
- (2) Compared with the traditional gravity anomaly separation method, the proposed method can effectively separate the gravity anomalies of anomaly bodies at different depths and can accurately describe the spatial distribution and edge characteristics of anomaly bodies.
- (3) The separation method was applied for a field test of microgravity residual oil characterization. The gravity anomaly representing the residual density of the reservoir extracted based on the multiscale, second-order, surface-fitting method can effectively characterize the distribution of remaining oil in the horizontal and vertical directions. The reservoir numerical simulation results and production performance data verify the reliability of the results, and the 3D density distribution provides a reliable basis for the development of remaining oil.

## Data Availability

The paper contains data supporting the results of our study.

## Conflicts of Interest

The authors declare that they have no conflicts of interest.

## Acknowledgments

This work was supported by the China National Petroleum Corporation Limited Upstream Field Forward-looking Basic Technology Research Project.

## References

- [1] A. L. Codd, L. Gross, and A. Aitken, "Fast multi-resolution 3D inversion of potential fields with application to high-resolution gravity and magnetic anomaly data from the Eastern Goldfields in Western Australia," *Computers & Geosciences*, vol. 157, article 104941, 2021.
- [2] A. V. Satyakumar, A. K. Pandey, A. P. Singh, and M. Tiwari Virendra, "Delineation of structural and tectonic features in the Mahanadi basin, eastern India: new insights from remote sensing and land gravity data," *Journal of Asian Earth Sciences*, vol. 227, article 105116, 2022.
- [3] M. B. Dejene, F. Yasuhiro, N. Jun, and S. Hakim, "Interpretation of gravity data to delineate the subsurface structures and reservoir geometry of the Aluto-Langano geothermal field, Ethiopia," *Geothermics*, vol. 94, article 102093, 2021.
- [4] K. Hassan, A. Firouz, and G. Abdolreza, "Regional magnetic and gravity structures and distribution of mineral deposits in Central Iran: implications for mineral exploration," *Journal of Asian Earth Sciences*, vol. 217, article 104828, 2021.
- [5] B. U. Camilus, A. A. Effiong, E. E. Ohara, and A. Emmanuel, "Novel technique for the interpretation of gravity anomalies over geologic structures with idealized geometries using the Manta ray foraging optimization," *Journal of Asian Earth Sciences: X*, vol. 6, article 100070, 2021.
- [6] Y. Abdelfettah, J.-J. Tiercelin, P. Tarits, S. Hautot, M. Maia, and P. Thuo, "Subsurface structure and stratigraphy of the northwest end of the Turkana Basin, Northern Kenya Rift, as revealed by magnetotellurics and gravity joint inversion," *Journal of African Earth Sciences*, vol. 119, pp. 120–138, 2016.
- [7] H. Aghajani, A. Moradzadeh, and H. Zeng, "Detection of high-potential oil and gas fields using normalized full gradient of gravity anomalies: a case study in the Tabas Basin, Eastern Iran," *Pure and Applied Geophysics*, vol. 168, no. 10, pp. 1851–1863, 2011.
- [8] J. L. Hare, J. F. Ferguson, and J. L. Brady, "The 4D microgravity method for waterflood surveillance: part IV — modeling and interpretation of early epoch 4D gravity surveys at Prudhoe Bay, Alaska," *Geophysics*, vol. 73, no. 6, pp. WA173–WA180, 2008.
- [9] M. Zumberge, H. Alnes, O. Eiken, G. Sasagawa, and T. Stenvold, "Precision of seafloor gravity and pressure measurements for reservoir monitoring," *Geophysics*, vol. 73, no. 6, pp. WA133–WA141, 2008.
- [10] Y. Li, F. Ren, L. Yang, D. Zhou, and X. Tian, "Description of steam chamber shape in heavy oil recovery using 4D microgravity measurement technology," *Petroleum Exploration and Development*, vol. 40, no. 3, pp. 409–412, 2013.
- [11] O. A. Stepanov, D. A. Koshaev, and A. V. Motorin, "Identification of gravity anomaly model parameters in airborne gravimetry problems using nonlinear filtering methods," *Gyroscopy and Navigation*, vol. 6, no. 4, pp. 318–323, 2015.
- [12] M. A. Biot, "Theory of propagation of elastic waves in a fluid-saturated porous solid," *The Journal of the Acoustical Society of America*, vol. 28, no. 2, pp. 168–178, 1956.
- [13] L. Yong, L. Zhengwen, L. Zhirong, and L. Qiong, "Study on reservoir density prediction technology," *Oil Geophysical Prospecting*, vol. 42, no. 2, pp. 216–219, 2007.
- [14] L. H. Guo, X. H. Meng, L. Shi, and Z. X. Chen, "Preferential filtering method and its application to Bouguer gravity anomaly of Chinese continent," *Chinese Journal of Geophysics*, vol. 55, no. 12, pp. 4078–4088, 2012.
- [15] S. Lei, C. Shi, J. C. X. Weimin, H. Lu, and F. Guo, "Analysis the of characteristics of gravity anomaly in the seismic area of Lushan earthquake based on preferential filtering method," *Earthquake Science*, vol. 35, no. 5, pp. 704–716, 2013.

## Research Article

# Theoretical Research on the Movement Law of Water Cone Behavior in Heavy Oil Reservoirs with Bottom Water

Kai Wang<sup>1</sup>,<sup>ORCID</sup> Chenyang Tang,<sup>1</sup> Tianyou Zhang,<sup>1</sup> Yufei Gao,<sup>1</sup> Jingyun Zou,<sup>1</sup> Yan Jiang,<sup>2</sup> Kuo Sun,<sup>1</sup> and Yan Chen<sup>1</sup>

<sup>1</sup>China National Offshore Oil Corporation Research Institute, Beijing 100028, China

<sup>2</sup>Engineering Technology Research Institute of PetroChina Huabei Oilfield Company, Hebei 062552, China

Correspondence should be addressed to Kai Wang; wangkaiupc@163.com

Received 23 January 2022; Accepted 27 April 2022; Published 17 June 2022

Academic Editor: Jinjie Wang

Copyright © 2022 Kai Wang et al. This is an open access article distributed under the Creative Commons Attribution License, which permits unrestricted use, distribution, and reproduction in any medium, provided the original work is properly cited.

Aiming at the unclear reorganization of a water cone shape, its sweep range, and water saturation distribution of horizontal well in heavy oil reservoirs with bottom water, a mathematical method was proposed in this paper to establish a microtube model and physical model with the starting pressure gradient (SPG) to study the water cone behavior. The results showed that the different water-cut stage, mobility, depth from oil-water interface (DOWI), and liquid production strength have an obvious impact on water cone behavior. Moreover, we found an interesting phenomenon on an extreme point in water saturation derivation among water cone, which could be a reason for further adjustment. Finally, we confirmed the calculation results with physical simulation, which is highly consistent. The new method proposed in this paper was significant in the water cone behavior study and has a broad application in heavy oil reservoir development in the future.

## 1. Introduction

The development of heavy oil reservoirs with bottom water is one of the big challenges in the oil and gas exploitation field worldwide [1, 2]. Developing reservoirs of this type often shows early water appearance, short water-free period, high water-cut ratio, and even violent water-cut ratio after water breakthrough, which reduces oil recovery and increases oilfield production risk [3, 4].

The core technology for developing this type of reservoirs using horizontal wells exists in the description of the water cone. The evolution of the water cone and its sweeping range has a deep influence on the developing and of adjusting project design. In the past decades, many researchers have conducted experimental, analytical, and numerical studies in the water cone behavior of horizontal wells [5–7]. However, the results of different research methods varied largely, especially for heavy oil reservoirs. For example, the sweeping range from the laboratory experiment is much lower than that from numerical simulations, because the heavy oil reservoir is similar to the low permeability res-

ervoir in the porous medium seepage, which is a non-Darcy flow with a starting pressure gradient (SPG) [8]. So, in heavy oil reservoirs, seepage can occur only if the production pressure gradient is greater than the SPG [9–11]. However, the existing commercial numerical simulation software, such as Eclipse CMG and Petrel Re, is all based on the Darcy seepage model and cannot directly characterize the non-Darcy flow in heavy oil reservoirs [12–16]. Moreover, there exists few theoretical research on the description of water cone behavior, not to mention the theoretical study considering the starting pressure gradient. All the problems mentioned above seriously influence the exact description of water cone behavior and its sweeping range in heavy oil reservoirs with bottom water, which have an impact on further development and adjustment of this type of reservoirs [17–19].

In this paper, we propose a new mathematical method to achieve the characterization of the water cone behavior in heavy oil reservoirs with bottom water. Then, we construct a microtube model and a physical model to observe the evolution of the water cone and sweeping range in this type of reservoir. The displacement path was divided through the

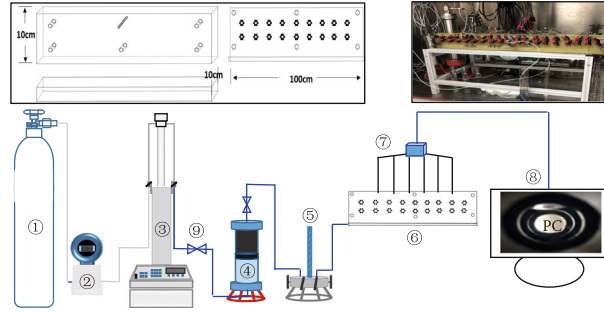


FIGURE 1: Models and experiment design of physical simulation.

analysis of the development process of the bottom water reservoir. Combined with the water-drive front equation, splitting flow equation, and Darcy equation, the expansion of the bottom water displacement area was obtained. Finally, the water cone radius, sweep range, and water saturation distribution in different positions were completely calculated. The new method proposed in this paper was significant in the water cone behavior study and has a broad application in heavy oil reservoir development in the future [20–23].

## 2. Models and Methods

**2.1. Physical Model.** The experimental setup of flowing tests consisted of a displacement pump (Teledyne ISCO, USA) used to inject fluids with different flow rates, two cylinders for formation water and model oil, an ultralarge 3D sand-pack model with a size of 100 cm×10 cm×10 cm, and a data collection system used to monitor saturation [24, 25]. Figure 1 shows a photograph of the designed 3D project, real 3D sand-pack model, and schematic of the experimental equipment, respectively. Figure 2 shows a seepage model. The similarity criteria and the main parameters are shown in Tables 1 and 2, respectively.

## 3. Results and Discussion

**3.1. Influence of Water-Cut Stage Difference on the Water Cone Behavior.** According to the above calculation process, when the mobility is 11, 33, and 64 mPa s, the movement of a water cone shape and sweeping range before and after water-drive front breakthrough were calculated, respectively, as shown in Figure 3. Meanwhile, the physical model was also simulated at the mobility of 64 mPa s, in order to calibrate the results.

The result shows that, with increasing mobility, the sweeping range of the water cone increases. From Figures 3(a) and 3(b), as the mobility increases from 11 to 64 mPa s, the water cone sweeping range increases from 60 m to 225 m. In the early stage, the movement of the water cone mainly focuses on the horizontal direction. But, after the water-drive front breakthrough, the movement of the water cone changed to a vertical direction. The water cone movement near the well was obvious while that far away from the well is limited.

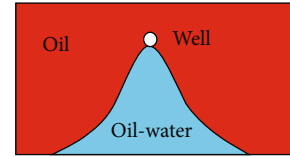


FIGURE 2: Seepage model.

From Figure 3(c), the ultralarge physical model presents the movement and water saturation distribution of the water cone at a mobility of 64 mPa s. The water cone movement shows a similar characterization with the calculated result, that is, moving horizontally firstly and then vertically. The sweeping efficiency was 0.35 initially and changed to 0.48 with water-cut reaching 98%. The distribution of water saturation through the monitor presents a relatively high value near the wellbore and a low value away from the wellbore. The reason lies in the distribution of the pressure difference on the plane. The closer it is to the well, the greater the pressure difference, and the higher the water saturation. The high water-cut was mainly contributed by the washing nearby the wellbore.

**3.2. Influence of Mobility Difference on Water Cone Behavior.** According to the above calculation process, the movement of the water cone behavior and the sweeping range were calculated, respectively, with the mobility ranging from 10 to  $90 \times 10^{-3} \mu\text{m}^2/\text{mPa s}$ . Meanwhile, the physical model with a similar principle was also conducted for the calibration of the water cone behavior and sweep range. The results are shown in Figures 4–6.

From Figures 4(a) and 4(b), with the mobility increasing or viscosity decreasing, the water cone radius increases. When the mobility changes from 10 to  $90 \times 10^{-3} \mu\text{m}^2/\text{mPa s}$ , the water cone radius increases from 48 m to 252 m. There exists a good relationship between water radius and mobility with a correlation coefficient of around 0.99.

From Figure 6, the physical simulation results showed that, with the increment of mobility, the water cone radius increased. When the mobility changes from 15 to  $60 \times 10^{-3} \mu\text{m}^2/\text{mPa s}$ , the water cone radius increases from 60 m to 200 m. The physical simulation results highly agreed with that of the calculation. In addition, all the physical simulation results showed a similar phenomenon as we discussed in



TABLE 1: Similarity criterion.

Classification	Criterion	Physical meaning
Geometric similarity	$L_1/L_2$	Ratio of length to width of the reservoir
	$L_1/H$	Ratio of reservoir length to thickness
	$\frac{L_1}{L_i}$	Ratio of reservoir length to horizontal well length
	$\Delta p/\rho_o gH; \Delta p/\rho_w gH$	The ratio of production pressure difference to gravity
Pressure similarity	$\Delta p/p_c$	The ratio of production pressure difference to capillary force
	$p_i/\bar{p}$	The ratio of reservoir pressure to the average pressure of the bottom layer
Physical similarity	$\rho_o/\rho_w$	Oil-water density ratio
	$K_{owe}\mu_w/K_{wor}\mu_o$	Oil to water mobility ratio
	$S_{wc}/S_{or}, 1/S_{or}$	The prototype is similar to the model endpoint
	$\phi$	Prototype is similar to model porosity
	$C_t/C_o, C_o/C_w$	The ratio of the comprehensive compression coefficient to the oil and water compression coefficient
Dynamic similarity	$KK_{wor}\Delta p t/\mu_w H^2 \phi S_{wc} C_t P_i, \rho_w S_{wc} \phi L_1^2 \mu_o/t \rho_o K K_{owe} \Delta p$	Darcy formula
	$L_1 L_2 K K_{wor} \rho_w g/\mu_w Q, L_1 L_2 K K_{wor} \Delta p/\mu_w QH$	Ratio of water influx to horizontal well production
	$q_o/q_w$	Ratio of oil to water production

TABLE 2: Parameter comparison of physical model with that of oilfield.

Parameter	Oilfield	Model
Thickness	20	10
Length	200	100
Width	20	10
Oil density	859.3	866.9
Water density	990	1000
Permeability	1200	2300
Pressure dropdown	3	0.006
Horizontal length	200	0.2
Well diameter	0.137	0.01
Oil production	1000	0.032

Section 3.1, that is, the distribution of water saturation through the monitor presents a relatively high value near the wellbore and a low value away from the wellbore.

From Figure 4(c), the distribution of water saturation at different positions in the water cone was calculated with oil viscosity ranging from 50 to 180 mPa s. The results showed that the water saturation in the water cone was high near the well and gradually decreased to the wings, indicating the law of first slowly declines, then rapidly declines, and finally slowly declines. With the decrease of oil viscosity, the water saturation at the same position increased, the viscosity is 50~180 mPa s, and the  $S_w$  at 100 m increased from 0.39 to 0.55. The reason lies in that the water saturation in the water cone at different positions was mainly affected by the flooding multiples. As shown in Figure 5, the relation-

ship between water saturation and flooding multiples at different positions was calculated, which shows that there was a good linear relationship between them.

As shown in Figure 4(d), when the water saturation is derived from the water cone radius, the derivative curve presents an inverted bell shape, and an extreme point exists. The extreme point decreases with the increment of oil viscosity. When the oil viscosity was 50 mPa s, the extreme point was located at the water cone radius of 113 m. When the oil viscosity was 180 mPa s, the extreme point was located at the water cone radius of 55 m.

*3.3. Influence of Distance from Oil-Water Interface (DOWI) on the Water Cone Behavior.* According to the above calculation process, the water cone shape, water saturation distribution, and sweeping radius were calculated when the DOWI was 10, 15, and 20 m, respectively. The results are shown in Figure 7.

From Figure 7(a), when the DOWI is between 10 and 20 m with a fixed mobility at  $33 \times 10^{-3} \mu\text{m}^2/\text{mPa s}$ , the water cone radius ranged from 142 to 150 m. For heavy oil reservoirs with thin bottom water, the influence of DOWI is limited. As shown in Figure 7(b), the higher the mobility, the higher the influence of DOWI. When the mobility increases to 90 with DOWI between 10 and 20 m, the water cone radius ranged from 231 to 252 m. When the mobility was 11 with the DOWI between 10 and 20 m, the water cone radius ranged only from 56 to 58 m. In Figure 7(c), the law of water saturation distribution was similar to that described in Section 3.2. However, with the increase of DOWI, the water cone radius slightly decreased, and the water saturation at the same position increased due to the increase of

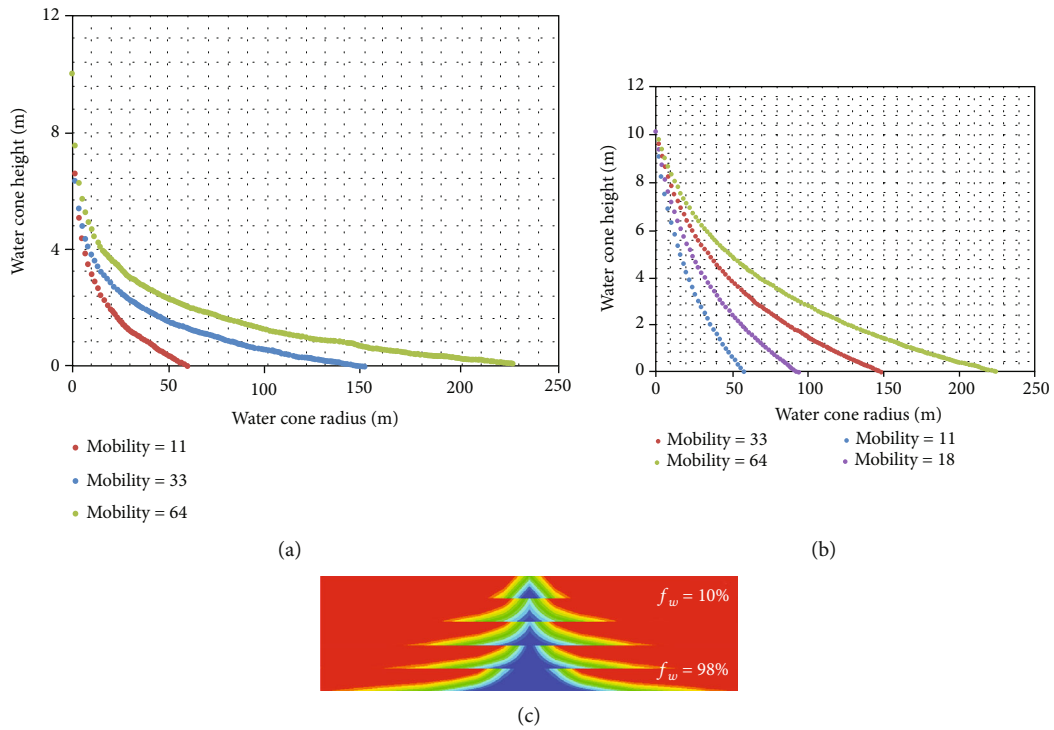


FIGURE 3: The influence of different water-cut stages on water cone behavior through mathematical calculation and physical simulation.

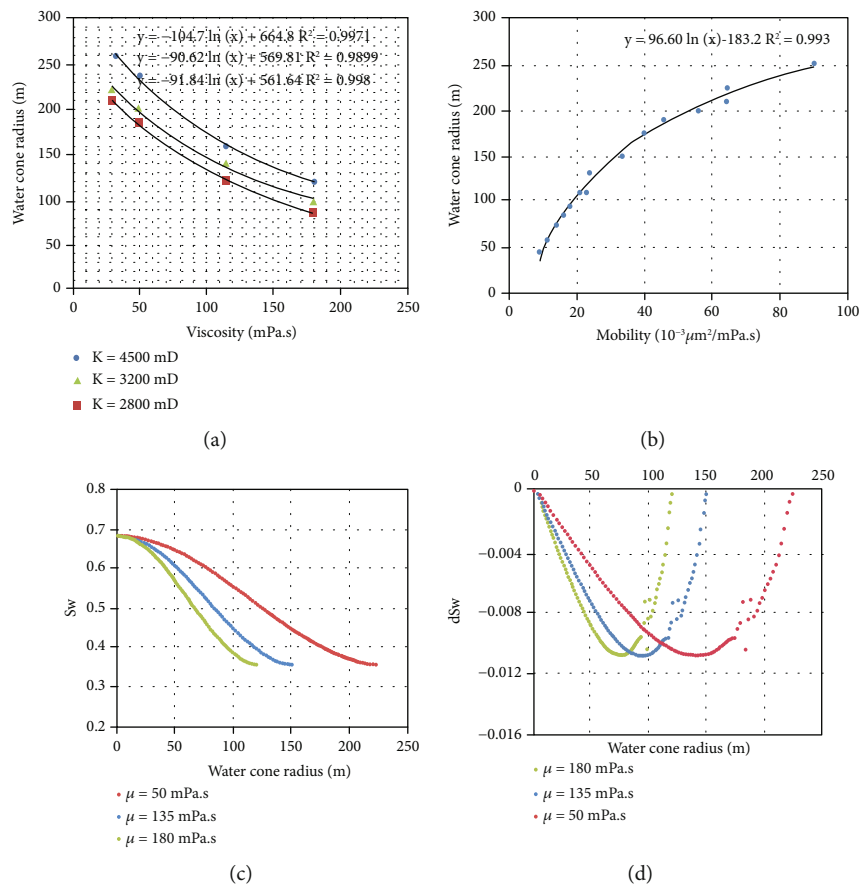


FIGURE 4: Influence of mobility on water cone behavior.

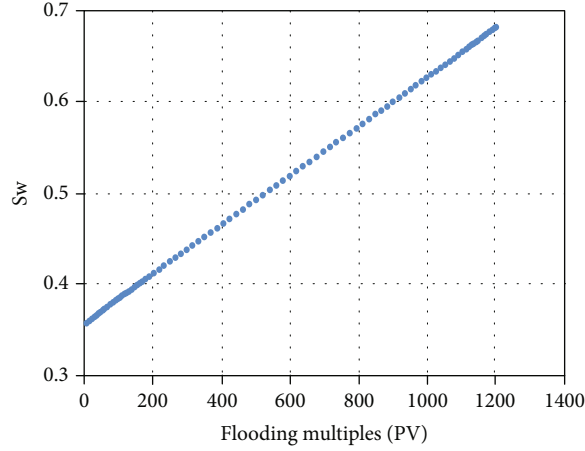


FIGURE 5: The relationship between  $S_w$  and flooding multiples.

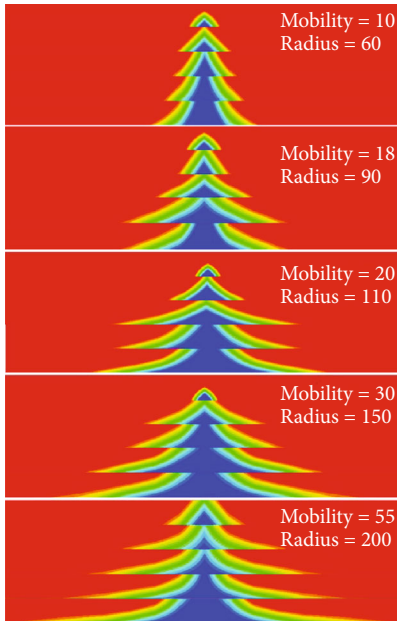


FIGURE 6: Physical simulation of water cone behavior under different mobility.

flooding multiples. As shown in Figure 7(d), the variation range of the water cone radius was limited with DOWI ranging from 10 to 20 m, and the extreme points were also highly concentrated, around 85 m.

**3.4. Influence of Liquid Production Strength on Water Cone Behavior.** According to the above calculation process, the water cone shape, water saturation distribution, and sweeping radius were calculated when the liquid production strength was 300, 500, and 1500 m<sup>3</sup>/d, respectively. The results are shown in Figure 8.

As shown in Figure 8(a), when the liquid production strength was 300~1000 m<sup>3</sup>/d with a fixed mobility of  $33 \times 10^{-3} \mu\text{m}^2/\text{mPa}\cdot\text{s}$ , the water cone radius was 100 to 150 m. For heavy oil reservoirs with thin bottom water, the liquid production strength had an obvious influence on the water

cone shape and sweep radius. From Figure 8(b), when the liquid production strength was higher than 1000 m<sup>3</sup>/d, the increase of water cone radius decreased under any mobility condition. In addition, with the increment of liquid production strength, the variation ranges of the water cone radius increased. When the liquid production strength increased from 300 to 1000 m<sup>3</sup>/d with a fixed mobility of 11, the water cone radius increased from 30 to 58 m; when the mobility was 33, the water cone radius increased greatly from 100 m to 150 m; when the mobility was 65, the water cone radius increased from 160 m to 225 m. With the increased liquid production strength, the water saturation at the same position increased. From Figure 8(c), the strength increases from 300 to 1000 m<sup>3</sup>/d, and the water saturation increases from 0.40 to 0.5 at 80 m, featured with decreasing slowly-rapidly-slowly. From Figure 8(d), the extreme point increased with the increment of the liquid production strength. When the liquid production strength is 300 m<sup>3</sup>/d, the extreme point was located at 45 m. When the liquid production strength is 1000 m<sup>3</sup>/d, it is located at 85 m.

**3.5. Influence of Adjacent Well on the Water Cone Behavior.** According to the calculation process in this paper, a model was built with DOWI of 10 m, permeability of 4500 md, oil viscosity of 135 mPa·s, and liquid production strength of 1000 m<sup>3</sup>/d. The movement of the water cone behavior and water saturation were calculated when two horizontal wells crossed at different positions. The influence degree was determined by Equation (1) to calculate the cumulative oil production. The results are shown in Figure 9.

$$\text{MAX}\{S1 \times (Sw1 - Sw0) + S2 \times (Sw1 - Sw2) - S2 \times (Sw2 - Sw0)\}. \tag{1}$$

From Figure 10, two water cones with a radius of 150 m are crossed by different well spacings of around 120 m, 85 m, and 75 m, respectively. Then the movement of water cone behavior was calculated after crossing. It can be seen that with the reduction of well spacing, the uplift of water cone between wells was more and more obvious, and the

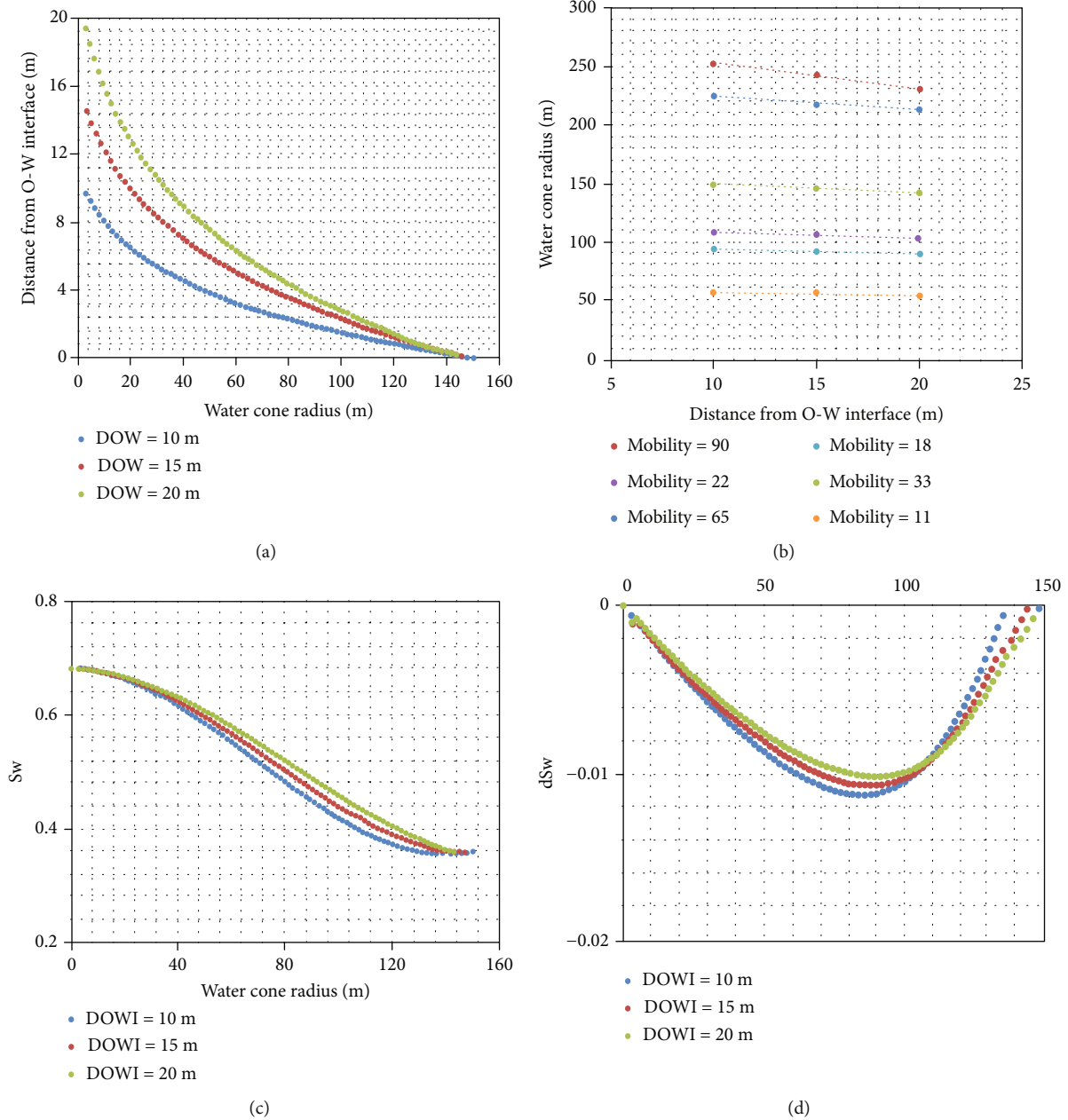


FIGURE 7: Influence of DOWI on water cone behavior.

remaining oil between wells was reduced, for the flooding multiples of the overlapping area were increased due to the joint action of two wells.

From Figure 10, the water saturation distribution between two water cones was calculated. As shown in Figure 10, with the reduction of well spacing, the water saturation in the overlapping area rises rapidly due to the joint flooding of two wells. The water saturation in the overlapping area was 0.4 when the water cone crossed at 120 m. When the overlapping area decreased to 85 m, the water saturation in the overlapping area rises to 0.6. When the well spacing further shortens, the water saturation rises to 0.68 due to the overlapping area being further flooded.

From Figure 11, the addition of an adjacent well had an obvious effect on the shape and water saturation distribution between water cones. Consistent with the calculated results, the water cone between two wells rises, and the water saturation increases. The closer the two wells, the higher the water cone, and water saturation rises due to the high-multiple flooding. The physical results confirmed what was obtained in the calculation process.

As shown in Figure 12(a), with the increment of well spacing, the cross-section oil increment first increased and then decreased. There exists a maximum cross-section oil increment. Moreover, there exists an interesting phenomenon, by comparing the intersection point of the maximum

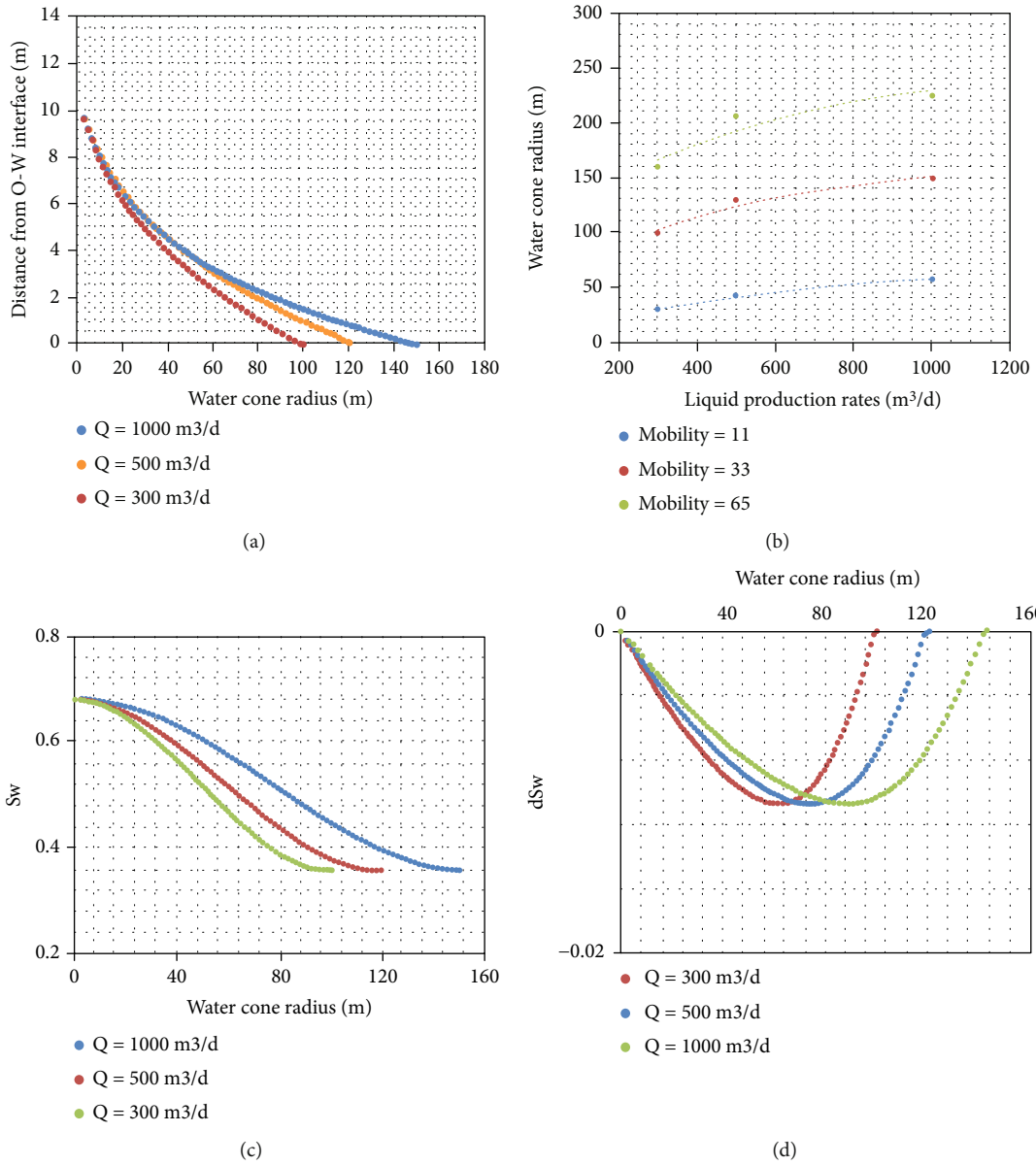


FIGURE 8: Influence of liquid production strength on the water cone behavior.

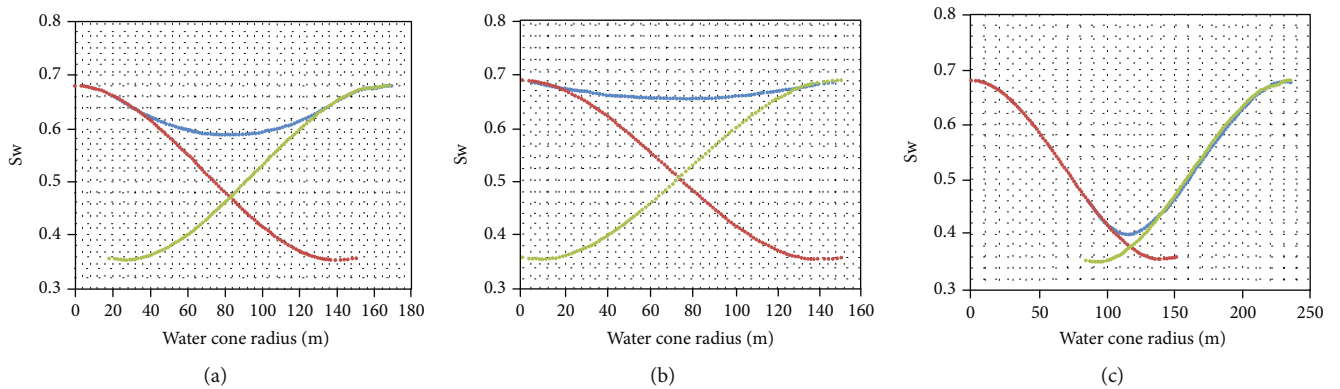


FIGURE 9: Influence of an adjacent well on the water cone behavior.



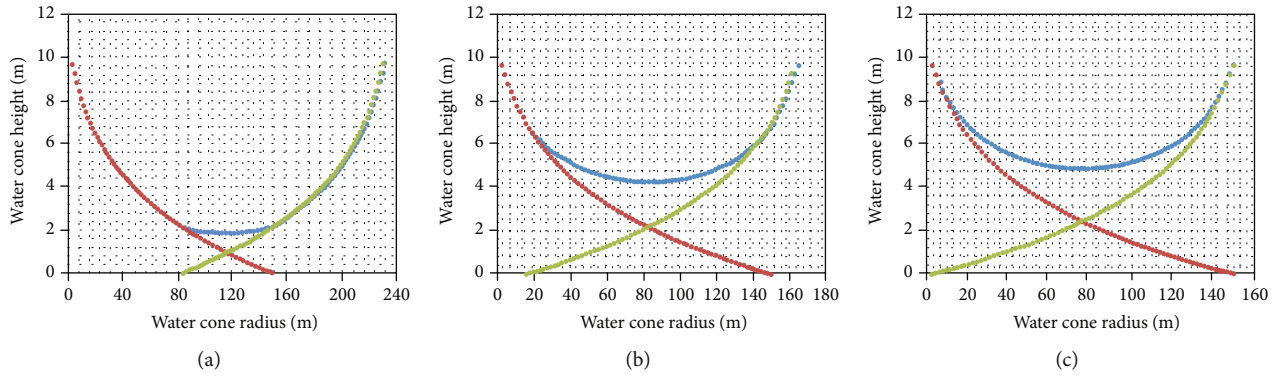


FIGURE 10: Influence of an adjacent well on the water saturation distribution in the water cone.

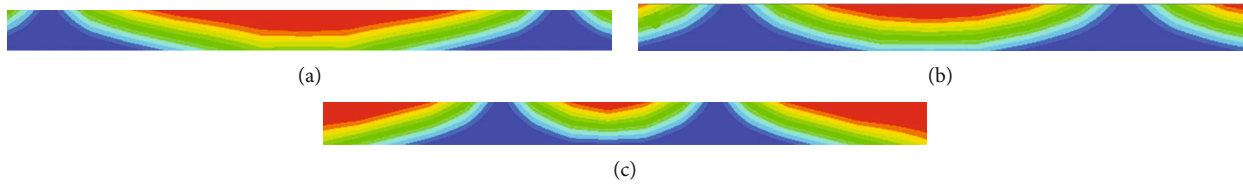


FIGURE 11: Influence of an adjacent well on the shape and water saturation distribution in the water cone through physical simulation.

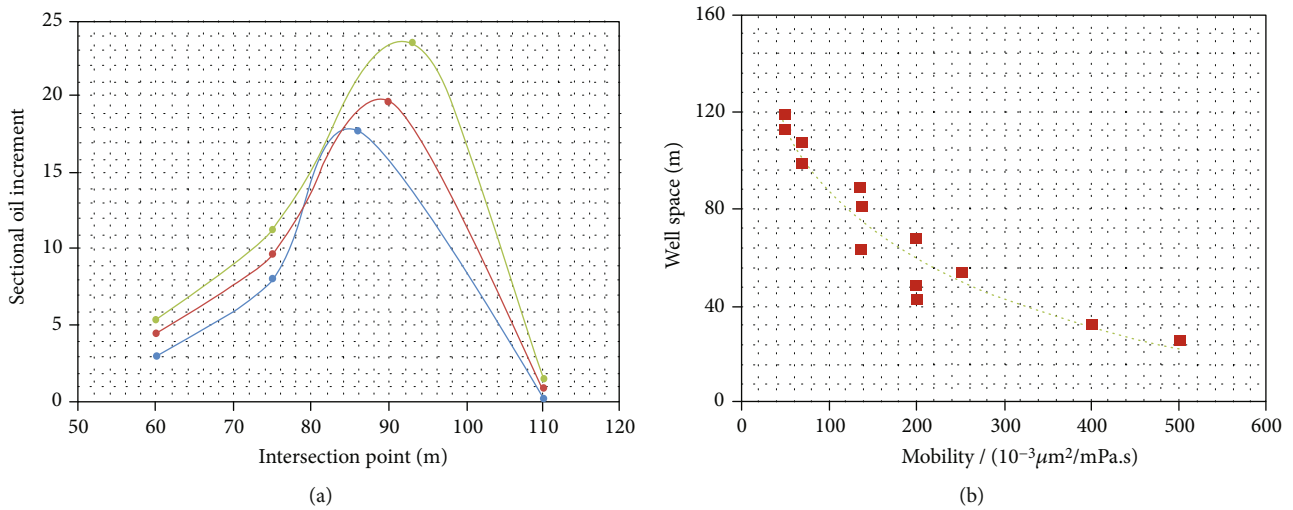


FIGURE 12: Relationship between well space and mobility.

cross-section oil increment with the extreme value of water saturation derivation in the water cone; it can be found that the two points are consistent. It provides a theoretical basis for optimizing reasonable well spacing in heavy oil reservoirs with bottom water. Figure 12(b) shows the relationship between optional well space and mobility. With the increase of oil viscosity, the reasonable well spacing decreases. When the viscosity was 100 mPa s, the optimized reasonable well spacing is 176 m. When the viscosity increases to 200 mPa s, the reasonable well spacing decreases to 120 m. With the increase of crude oil viscosity, the sweep range of the water cone decreases, which leads to a decrement in reasonable well spacing.

## 4. Conclusions

In this work, combined with the water-drive front equation, splitting flow equation, and Darcy equation, the movement of water cone behavior, its sweep range, and water saturation distribution were investigated. The summary was as follows:

- (1) The water cone shape, its sweep range, and water saturation distribution were first studied through the seepage theory considering the starting pressure gradient. The influence of the different water-cut stage, DOWI, and liquid production strength was discussed in detail and showed a good relationship

- (2) An interesting phenomenon was first found in this paper; there exists an extreme point in water saturation derivation in the water cone. It has a significant and theoretical meaning for the further adjustment
- (3) Ultralarge scale physical simulation was conducted firstly in this paper, to explore the movement behavior, sweep range, and water saturation distribution of water cone

## Data Availability

The data used to support the findings of this study are included within the article.

## Conflicts of Interest

The authors declare that they have no conflicts of interest.

## Acknowledgments

The second author and the first author contributed equally to this paper. The second institution and the first institution contributed equally to this paper.

## References

- [1] Q. You, Q. Wen, J. Fang, M. Guo, Q. Zhang, and C. Dai, "Experimental study on lateral flooding for enhanced oil recovery in bottom-water reservoir with high water cut," *Journal of Petroleum Science and Engineering*, vol. 174, pp. 747–756, 2019.
- [2] G. Zhao, C. Dai, C. Gu, Q. You, and Y. Sun, "Expandable graphite particles as a novel in-depth steam channeling control agent in heavy oil reservoirs," *Chemical Engineering Journal*, vol. 368, pp. 668–677, 2019.
- [3] D. U. Yu hong, "Study on enhanced oil recovery of Ren 11 fractured bottom water reservoir by gas injection," *Acta Petrolei Sinica*, vol. 26, no. 2, pp. 80–84, 2005.
- [4] A. E. Gill, "Circulation and bottom water production in the Weddell Sea," *Deep-Sea Research and Oceanographic Abstracts*, vol. 20, no. 2, pp. 111–140, 1973.
- [5] M. Tagavifar, R. Fortenberry, E. de Rouffignac, K. Sepehrnoori, and G. A. Pope, "Heavy-oil recovery by combined hot water and alkali/cosolvent/polymer flooding," *SPE Journal*, vol. 21, no. 1, pp. 74–86, 2016.
- [6] J. Moortgat and A. Firoozabadi, "Water coning, water, and CO<sub>2</sub> injection in heavy-oil fractured reservoirs," *SPE Reservoir Evaluation & Engineering*, vol. 20, no. 1, pp. 168–183, 2017.
- [7] A. Zakerian, S. Sarafraz, A. Tabzar, N. Hemmati, and S. R. Shadizadeh, "Numerical modeling and simulation of drilling cutting transport in horizontal wells," *Journal of Petroleum Exploration & Production Technology*, vol. 8, no. 2, pp. 455–474, 2018.
- [8] O. Weiping, S. Hedong, and Z. Mian, "Well test analysis for multistage fractured horizontal wells in tight gas reservoir considering stress sensitivity," *Acta Petrolei Sinica*, vol. 39, no. 5, pp. 570–577, 2018.
- [9] K. Wang, K. Li, Y. Gao, Y. Pan, and Q. You, "Research on water cone behavior in a heavy oil reservoir with bottom water considering the starting pressure gradient," *ACS Omega*, vol. 5, no. 27, pp. 16841–16847, 2020.
- [10] H. Wang, X. Liao, N. Lu, Z. Cai, C. Liao, and X. Dou, "A study on development effect of horizontal well with SRV in unconventional tight oil reservoir," *Journal of the Energy Institute*, vol. 87, no. 2, pp. 114–120, 2014.
- [11] W. Kai, Z. Yan, Z. Wensheng et al., "Study on the time-variant rule of reservoir parameters in sandstone reservoirs development," *Energy Sources Part A Recovery Utilization and Environmental Effects*, vol. 23, pp. 1–18, 2020.
- [12] T. Engler and D. Tiab, "Analysis of pressure and pressure derivative without type-curve matching, 6. Horizontal well tests in anisotropic media," *Journal of Petroleum Science & Engineering*, vol. 15, no. 2–4, pp. 153–168, 1996.
- [13] Y. L. Zhao, L. H. Zhang, J. X. Luo, and B. N. Zhang, "Performance of fractured horizontal well with stimulated reservoir volume in unconventional gas reservoir," *Journal of Hydrology*, vol. 512, no. 10, pp. 447–456, 2014.
- [14] Y. C. Zeng, Z. Su, and N. Y. Wu, "Numerical simulation of heat production potential from hot dry rock by water circulating through two horizontal wells at desert peak geothermal field," *Energy*, vol. 56, no. 63, pp. 92–107, 2013.
- [15] C. Dai, K. Wang, Y. Liu, H. Li, Z. Wei, and M. Zhao, "Reutilization of fracturing flowback fluids in surfactant flooding for enhanced oil recovery," *Energy & Fuels*, vol. 29, no. 4, pp. 2304–2311, 2015.
- [16] Q. Sang, Y. Li, L. Yu, Z. Li, and M. Dong, "Enhanced oil recovery by branched-preformed particle gel injection in parallel-sandpack models," *Fuel*, vol. 136, pp. 295–306, 2014.
- [17] C. Chen, J. Wan, and H. Zhan, "Theoretical and experimental studies of coupled seepage-pipe flow to a horizontal well," *Journal of Hydrology*, vol. 281, no. 1–2, pp. 159–171, 2003.
- [18] R. Zhu and L. Tao, "Boundary element method of free boundary issues of stationary water cone for gas well," *Natural Gas Industry*, vol. 24, no. 12, pp. 93–95, 2004.
- [19] N. Esmail, "Flow enhancement of medium-viscosity crude oil," *Petroleum Science & Technology*, vol. 24, no. 8, pp. 985–999, 2006.
- [20] H. L. J. Gong, "The pressure effect on rheological behavior of water content of waxy crude oil," *Petroleum Science & Technology*, vol. 29, no. 13, pp. 1344–1352, 2011.
- [21] W. C. Lee, Y. S. Lee, K. H. Kim, K. J. Lee, W. M. Sung, and J. Kim, "Investigation of gas and water coning behavior for the enhancement of oil production," *Korean Journal of Chemical Engineering*, vol. 28, no. 11, pp. 2102–2109, 2011.
- [22] S. R. Heidemann, P. Lamoureux, and R. E. Buxbaum, "Growth cone behavior and production of traction force," *Journal of Cell Biology*, vol. 111, no. 5, pp. 1949–1957, 1990.
- [23] G. S. Withers, C. D. James, C. E. Kingman, H. G. Craighead, and G. A. Banker, "Effects of substrate geometry on growth cone behavior and axon branching," *Developmental Neurobiology*, vol. 66, no. 11, pp. 1183–1194, 2006.
- [24] Z. Peng, X. H. Wen, L. Ge, L. Bo, and M. S. Wei, "Existence of flow barriers improves horizontal well production in bottom water reservoirs," *SPE Conference*, vol. SPE115348, pp. 1–15, 2008.
- [25] X. Tu, D. L. Peng, and Z. Chen, "Research and field application of water coning control with production balanced method in bottom-water reservoir," *SPE Conference*, vol. SPE105033, pp. 1–5, 2007.

## Research Article

# Study on the Variation of Crude Oil and Flue Gas Components in Flue-Gas-Assisted Steam Flooding

Yongzhou Wei,<sup>1</sup> Xu He,<sup>2</sup> Tingfeng Liu,<sup>2,3</sup> Ming Liu,<sup>2,3</sup> Boliang Li,<sup>4</sup> Zhuangzhuang Wang,<sup>5</sup> and Binfei Li <sup>4</sup>

<sup>1</sup>Binnan Oil Production Plant, Shengli Oilfield, Sinopec, Binzhou 256606, China

<sup>2</sup>Sinopec Shengli Oilfield Petroleum Engineering Technology Research Institute, Dongying 257000, China

<sup>3</sup>Shandong Provincial Key Laboratory of Heavy Oil Recovery Technology, Dongying 257000, China

<sup>4</sup>School of Petroleum Engineering, China University of Petroleum (East China), Qingdao 266580, China

<sup>5</sup>Faculty of Science, Qingdao University of Technology, Qingdao 266580, China

Correspondence should be addressed to Binfei Li; libinfei999@126.com

Received 25 February 2022; Accepted 27 May 2022; Published 9 June 2022

Academic Editor: Xiang Zhou

Copyright © 2022 Yongzhou Wei et al. This is an open access article distributed under the Creative Commons Attribution License, which permits unrestricted use, distribution, and reproduction in any medium, provided the original work is properly cited.

In heavy oil development, flue-gas-assisted steam flooding can not only improve oil recovery but also reduce carbon emissions and realize the resource utilization of flue gas. In this paper, the variation in crude oil components produced by steam flooding and flue-gas-assisted steam flooding was studied by indoor displacement experiments and component determination, and the production properties of different components in flue gas, and the influence of flue gas proportion on residual oil components was explored. The results indicate that flue gas can enhance distillation and the production of light components in the steam flooding process. When the ratio of flue gas to steam ranges from 1 : 1 to 3 : 1, the larger the proportion of flue gas injection is, the larger the scope of steam thermal sweep is, the stronger the steam distillation effect is, and the greater the content of light components in residual oil and the change value of each component at the outlet and inlet are. Due to the difference in the dissolution of N<sub>2</sub> and CO<sub>2</sub> in heavy oil, at the early stage of displacement, the retention rate of CO<sub>2</sub> in the formation in the early stage of displacement was higher, and the proportion of CO<sub>2</sub> output was lower than the initial injection proportion. With the progress of displacement, the proportion of CO<sub>2</sub> gradually increased, and the proportion of N<sub>2</sub> gradually decreased. After gas channeling occurs, the N<sub>2</sub> proportion increases and gradually approaches the injection proportion. The dissolution and precipitation of flue gas contribute to the formation of foam oil and improve the flow and production of crude oil. The research results are helpful to further understand the mechanism of flue-gas-assisted steam flooding and provide a theoretical basis for the improvement of this technology.

## 1. Introduction

With the improvement of global industrialization and the sharp increase in greenhouse gases, reducing CO<sub>2</sub> emissions has become a guide for the development of all countries [1–3]. Petroleum, natural gas, and other fossil fuels as the world's main energy source will continue for nearly half a century, and the CO<sub>2</sub> produced by fossil fuel combustion exceeds 2/3 of the total emissions [4–6]. At present, to alleviate the greenhouse effect caused by CO<sub>2</sub> emissions, CO<sub>2</sub> capture, utilization, and storage (CCUS) have attracted great

attention in various fields, especially geology and oil and gas development [7–10]. The application of CO<sub>2</sub> in crude oil development can not only realize carbon sequestration but also effectively improve oil recovery [11–15].

Globally, heavy oil is abundant and widely exploited. In the future, the exploitation of heavy oil will occupy a dominant position in oil and gas development [16–18]. However, heavy oil is developed by thermal recovery, which requires a large amount of fossil fuels to produce steam, and the boiler produces a lot of flue gas containing greenhouse gases, aggravating the greenhouse effect, which is contrary to

today's economic and green development concept. Recently, many researchers have found that the synergistic displacement of flue gas and steam can greatly improve the production of heavy oil [19–22]. Moreover, the direct recovery and utilization of the flue gas generated by the boiler avoid the complex CO<sub>2</sub> treatment process and save the cost of steam injection. It is an essential path for the oil field to carry out CO<sub>2</sub> capture, utilization, burial, and economic development of heavy oil.

Since the discovery of the application potential of flue gas, the oil displacement mechanism of flue-gas-auxiliary steam injection has attracted much attention. However, due to the large injection components in flue-gas-auxiliary steam flooding, the mechanism is very complex. High-temperature steam can decrease the viscosity of crude oil and improve the fluidity of crude oil [23–25]. The main components of flue gas are N<sub>2</sub> and CO<sub>2</sub>. N<sub>2</sub> can compensate for the formation energy deficit, maintain reservoir pressure, and increase the oil production rate [26]. CO<sub>2</sub> dissolved in heavy oil can affect the volume and viscosity of heavy oil and facilitate its expansion and overflow [27–31]. At the same time, CO<sub>2</sub> can gasify the light components in crude oil to decrease the interfacial tension and realize miscible flooding [32–35]. Wu et al. [36] explored the influence of gas on steam flooding by using the 2D visualization model, and found that in the displacement process, injected gas formed bubbles in the pore throat of the model and the Jamin effect occurred. At the same time, the gas reacted with heavy oil to improve the macrosweep area and displacement efficiency [37, 38]. Lu et al. [39] explored the influence of flue gas on steam heat dissipation characteristics by using cold condensate with a thermocouple and found that flue gas can reduce the heat dissipation rate of steam in the formation, strengthen steam seepage to the deep oil region, and expand the expansion range of the steam chamber. Although the understanding of the mechanism of flue-gas-assisted steam flooding is still deepening and improving, there are few studies on the influence of flue-gas-assisted steam flooding about the properties of crude oil, distillation, and retention characteristics of flue gas in the formation.

The change in crude oil and gas composition can directly reflect the change law of crude oil properties, the strength of distillation, and the migration characteristics of flue gas in the process of the displacement and deeply clarify the role of flue gas in strengthening steam flooding. Therefore, it is necessary to conduct research on the variation law of crude oil and gas components in this displacement. In this paper, the 1D sandpack simulation experiments of steam flooding and flue-gas-assisted flooding were carried out. In the experiment, the composition changes of heavy oil output at different periods of the two displacement patterns are compared and analyzed. The law of flue gas retention was studied by recording the gas production characteristics in the process of flue-gas-assisted steam flooding. Furthermore, the compositional changes of residual oil in flue-gas-assisted steam flooding under different flue gas-steam ratios were studied, and the effect of the flue gas ratio on steam distillation was analyzed. These findings are of extreme importance to improve the oil displacement mechanism of flue-gas-

assisted steam flooding and improve its field application effect.

## 2. Experimental Section

**2.1. Materials.** The flue gas used in the experiments was prepared by hand and was a compound of N<sub>2</sub> and CO<sub>2</sub> in molar ratios of 80% and 20%, and N<sub>2</sub> and CO<sub>2</sub> with a purity of 99.9 mol% were produced from Tianyuan, Inc., China. The crude oil used in the experiment was sampled from the Cao 20 block of Shengli Oilfield, China. The viscosity-temperature curve of the crude oil is shown in Figure 1, and the viscosity of dehydrated crude oil was 5170 mPa·s at 50.0°C. The saturated content of crude oil is 41.36 wt%, the aromatic content is 21.38 wt%, the resin content is 36.8 wt%, and the asphaltene content is 0.46 wt%. The water used to generate steam during the experiment was distilled water, which was produced by the distillation method, and the resistivity was 15 MΩ·cm. The 1D displacement model in the experiment was filled with a certain mesh of quartz sand. To ensure that the permeability of the sandpacks was between 3200 mD and 3400 mD, the model was filled with 80 mesh and 110 mesh quartz sand at 1:1. The specific dimensional data of the model are shown in Table 1.

**2.2. Apparatus.** The main contents of the experiment are a physical simulation experiment and the determination of crude oil components. The flow chart of displacement experiment is shown in Figure 2, which included mainly a steam generator, ISCO pump, gas mass-flow controller, sandpack model, intermediate container, pipeline heating belt, check valve, and back-pressure regulator (PBR). ISCO pumps (Model 100DX, Teledyne Co., Ltd., USA) provided power for flooding and controlled the injection rate of steam, heavy oil, and water with an accuracy of ±0.001 mL. The steam generator (model GL-1, Haian Petroleum Equipment Company) produces steam at a rate consistent with the rate at which distilled water is injected through the pump, the temperature range of the generated steam was 100–350°C, and its maximum pressure resistance was 25 MPa. The gas injection rate was controlled by a gas flowmeter (model Sla5861, Brooks, USA). The number of gas mass-flow controllers was the flow rate under standard conditions, which needed to be converted according to the experimental conditions. The sandpack model (Model 304, Nantong Research Instrument Co., Ltd) had a pressure resistance of 40 MPa and a temperature resistance of 300°C, with a length and an inner diameter of 60 cm and 2.54 cm, respectively, and was wrapped with a temperature-controlled heating sleeve. The check valve was set before the outlet of the gas mass-flow controller to prevent liquid backflow and damage to the gas flowmeter.

### 2.3. Experimental Procedures

#### 2.3.1. Experimental Procedure of Displacement

- (1) The sandpack model was prepared; the sandpack was filled with mixed quartz sand after ensuring that the airtightness of the sandpack was good



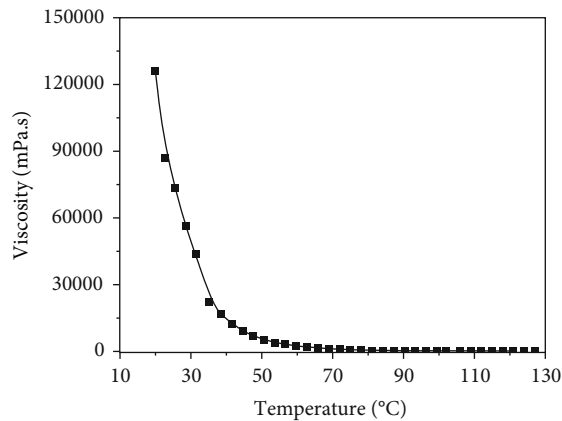


FIGURE 1: Viscosity-temperature curve.

- (2) The sandpack was saturated with water after vacuum-pumping for 4 h; then, its porosity was calculated according to the weight difference. The water flooding was carried out and the permeability of the model was determined by the Darcy equation
- (3) The sandpack was heated by the heating sleeve to a preset initial temperature of 60°C. After the model reached the set temperature, the sandpack was saturated with heavy oil at a rate of 0.5 mL·min<sup>-1</sup>. The sandpack was placed in a 60°C environment for 24 h aging after it was saturated with crude oil
- (4) The steam generator was set at 300°C for preheating, during which distilled water was injected continuously until the steam generator produced stable steam
- (5) The displacement experiments were carried out after ensuring the complete connection of the experimental devices. The back pressure was set at 2 MPa. According to the experimental scheme, the injection ratio of flue gas/steam was set as 1 : 1, 2 : 1, and 3 : 1, and the exact injection rates of flue gas and steam are shown in Table 1. When the temperature and pressure reached stability, and the water content in the output liquid exceeded 98%, it was regarded as the end of displacement
- (6) During displacement, the production characteristics of flue gas, crude oil, and water were recorded. After displacement, the oil sand in the sandpack was dug out, placed according to the position, photographed, and sampled for analysis
- (7) Four components of produced oil and residual oil in oil sand were measured
- (8) The experimental equipment was cleaned and sorted, and steps (1)–(6) were repeated for the next experiment

2.3.2. *Determination of Four Components of Heavy Oil.* The four components of heavy oil include saturates, aromatics, resins, and asphaltenes, and their content determination procedures refer to NB/SH/T 0509-2010.

- (1) The heavy oil was dissolved with n-heptane, placed in the dark, and allowed to settle for 1 h. After filtration, n-heptane was used for reflux in the precipitate to obtain the insoluble and soluble fractions
- (2) For the insoluble fraction, toluene that could dissolve the insoluble fraction was added and refluxed for more than 1 h or until the droplets were colourless. Then, asphaltenes were obtained by steaming out toluene
- (3) The soluble fraction was adsorbed on the aluminium oxide chromatographic column. The desorbed substance obtained by washing with n-heptane was saturated, while the remaining adsorbed substance was washed with toluene and toluene-ethanol in turn. The desorbed substances were aromatics and resins. The determination flow chart of the four-component contents is shown in Figure 3

### 3. Results and Discussion

3.1. *Variation Characteristics of Recovery and Displacement Pressure Difference.* Since oil recovery could directly reflect the quality of displacement and the change in displacement pressure difference could reflect the flow characteristics of heavy oil in the process of displacement from the side, the differences between steam flooding and flue-gas-assisted steam flooding were compared on oil recovery and pressure difference. The experimental data are from experiments #1 and #2 in Table 1.

Figure 4 depicts the variation in crude oil recovery and displacement pressure difference with injection volume in steam flooding and flue-gas-assisted steam flooding. The change trends of the recovery factor and flooding pressure difference under the two displacement patterns are roughly similar. The crude oil is pushed by piston propulsion at the beginning of displacement. With the increase in injection volume, oil recovery factor increases rapidly, and the displacement pressure difference increases continuously. In the middle and late stages of displacement, due to the formation of high-permeability channels, the growth rate of crude oil recovery began to slow down and gradually stabilized, and the displacement differential pressure also began to decline rapidly. The recovery factor of steam flooding is 62%, and the recovery factor of flue-gas-assisted steam flooding is 72%, which is approximately 10% higher than the recovery factor of steam flooding. The maximum flooding pressure difference of flue-gas-assisted steam flooding is 2.75 MPa, lower than 1.91 MPa of steam flooding, although the addition of flue gas increases the equivalent volume of injected fluid, the displacement differential pressure decreases to a certain extent.

There are three main reasons for the higher displacement efficiency and lower pressure of flue-gas-assisted steam



TABLE 1: Displacement experimental parameters.

Test no.	Flooding pattern	Initial temperature of sandpack (°C)	Porosity (%)	Permeability (mD)	Injection rate (mL·min <sup>-1</sup> )	
					Steam	Flue gas
#1	Steam flooding	60	35.86	3350	1	0
#2	Flue-gas-assisted steam flooding	60	33.66	3260	1	1
#3	Flue-gas-assisted steam flooding	60	33.56	3210	1	2
#4	Flue-gas-assisted steam flooding	60	33.72	3286	1	3

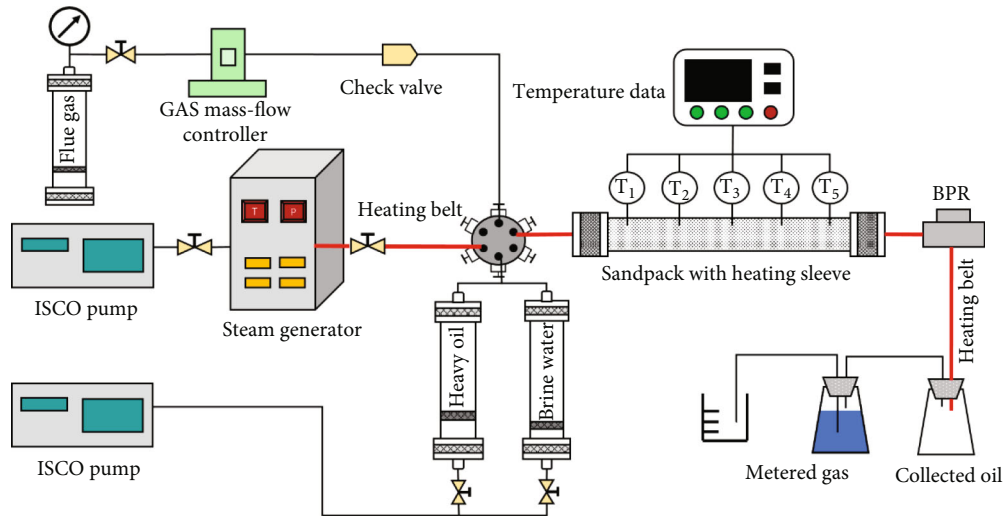


FIGURE 2: Flow chart of displacement experiment.

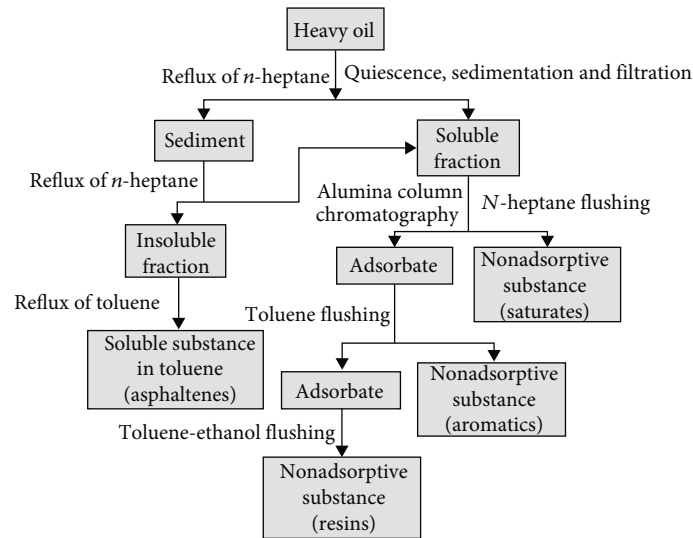


FIGURE 3: Flow chart of the four-component determination of heavy oil.

flooding: Flue gas dissolves in crude oil, which can reduce crude oil viscosity to a certain extent and improve crude oil fluidity. The high seepage capacity of flue gas can open up channels for the flow of steam and reduce the flow resistance. More importantly, flue gas, as the noncondensable gas, is able to enrich on the surface of low-temperature objects, increasing the heat transfer resistance of steam to

low-temperature objects and thus inhibiting steam condensation [40], which expands the steam heat swept volume and thick oil flowable area.

3.2. *Composition Variation Properties of Produced Crude Oil.* Among the four components of crude oil, the saturates and aromatics can be equivalent to the solvent in crude oil. The

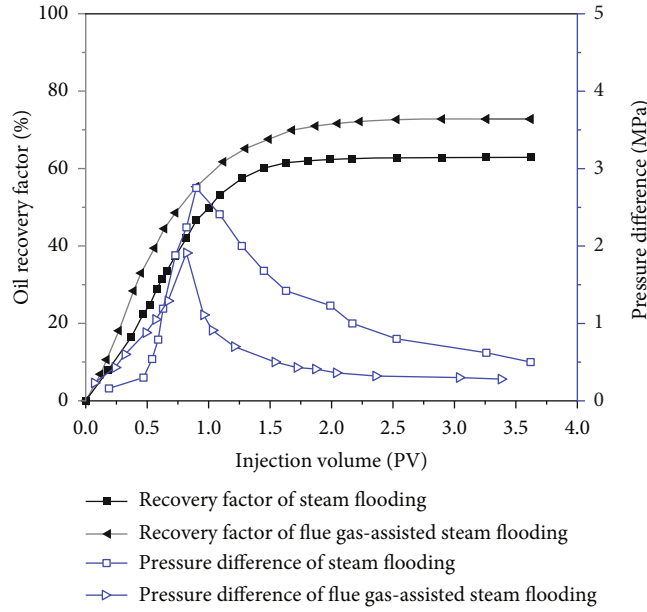


FIGURE 4: Variation curve of crude oil recovery and displacement pressure difference with injection volume.

TABLE 2: Four-component content data of produced crude oil.

Displacement pattern	Sampling stage	Saturate content (wt%)	Aromatic content (wt%)	Resin content (wt%)	Asphaltene content (wt%)
Steam flooding	Initial sample	41.36	21.38	36.8	0.46
	Before water channeling	46.24	21.51	31.82	0.43
	After water channeling	43.53	21.18	34.56	0.73
	Before gas channeling	47.71	21.8	30.08	0.41
Flue-gas-assisted steam flooding	Before water channeling	45.46	21.49	32.56	0.49
	After water channeling	43.91	21.40	34.04	0.65

higher the content is, the better the flow performance of crude oil, the lower the friction resistance between fluids and the smaller the viscosity. As polar substances in crude oil, resins and asphaltenes not only have an important impact on the pour point reduction of crude oil but also make an important contribution to the relative molecular weight and viscosity of crude oil. The experimental data in Table 2 in this section are from experiments #1 and #2 in Table 1. According to the gas and water breakthrough of the collected liquid, steam flooding was divided into two stages before and after water channeling, and flue-gas-assisted steam flooding was divided into three stages: before gas channeling, before water channeling, and after water channeling. Samples were taken in different stages of two groups of displacement experiments, and 2-3 samples were taken in each stage to determine the saturated, aromatic, resin, and asphaltene content of each sample. The measure-

ment was repeated three times, and the average value was selected.

Figure 5 shows the comparison of four components of crude oil produced in steam flooding. During the whole displacement process, compared with the initial oil sample, the content of saturates and aromatics of the produced crude oil is higher, the content of resins is lower, and the content of asphaltenes is lower than the initial oil sample before water channeling and higher than the initial oil sample after water channeling. Compared with the two stages before and after water channeling, the saturated and aromatic content decreased by 2.71 wt% and 0.33 wt%, respectively, and the total content of resins and asphaltenes increased after water channeling because in the process of flooding, light components with low viscosity and strong fluidity are extracted first. After the formation of the hyperosmotic channel, the content of light components that flow easily decreases, and

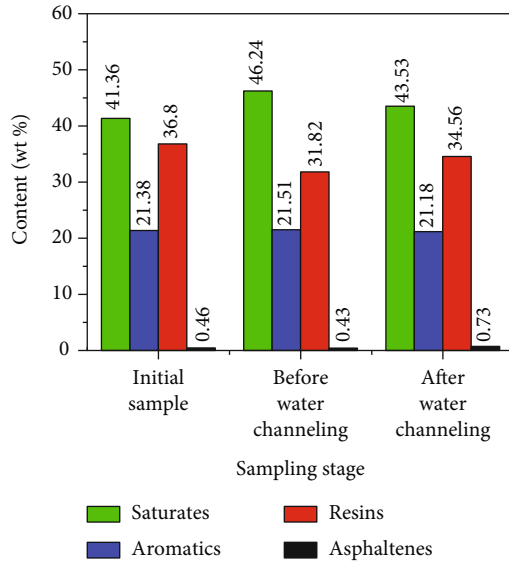


FIGURE 5: Comparison of four components of crude oil produced during steam flooding.

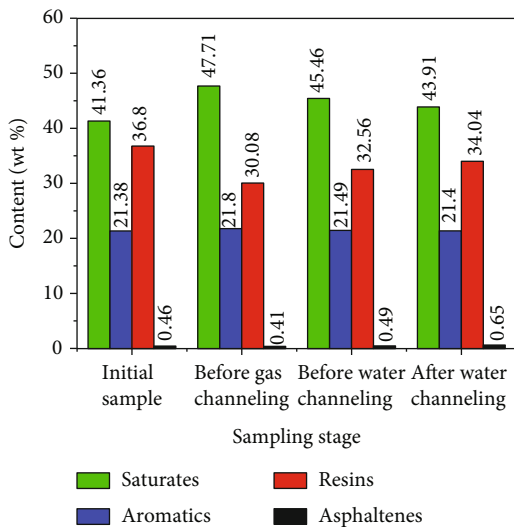


FIGURE 6: Comparison of four components of crude oil produced during flue-gas-assisted steam flooding.

the heavy components that flow with difficulty are gradually extracted under the scraping and scouring of fluid. Therefore, in the later stage of steam flooding, the produced crude oil contains less light components and more heavy components.

Figure 6 shows the comparison of four components of heavy oil produced during the process of flue-gas-assisted steam flooding. It is easier to produce light components under distillation of steam, and the content of saturated and aromatic components of the crude oil is higher than the content of saturated and aromatic components of the initial oil sample in the process of steam flooding and flue-gas-assisted steam flooding. In the process of flue-gas-assisted steam flooding, because the mobility of gas is greater than the stability of steam, gas channeling will occur before

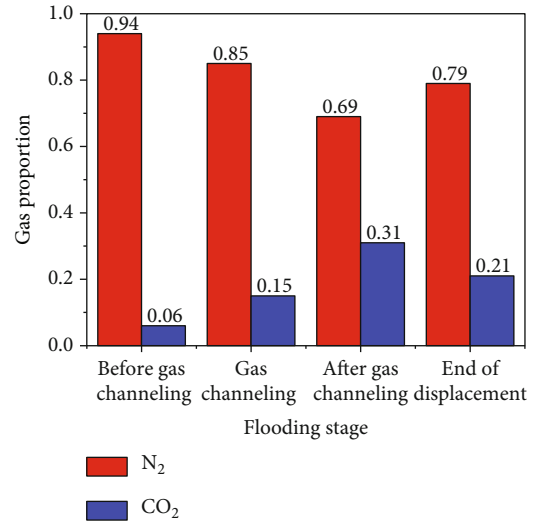


FIGURE 7: Comparison of gas components produced in different displacement stages.

the collected liquid meets water. The light component content of crude oil before gas channeling is slightly higher than that before water channeling, while the content of resins and asphaltenes is slightly lower because the flue gas has a certain solubility in crude oil. This is due to the process of gas dissolution and precipitation before gas channeling; more light components are brought to the outlet section and recovered. Comparing the two displacement patterns, the proportion of light components of oil produced by flue-gas-assisted steam flooding is higher than the proportion of light components of oil produced by steam flooding. In the process of flue-gas-assisted steam flooding, the maximum saturated hydrocarbon content is 47.71 wt%, which is 1.5% higher than the maximum saturated hydrocarbon content of steam flooding. The reason for this phenomenon is that flue gas can not only expand the transmission distance of heat carried by steam but also strengthen the distillation of steam on crude oil in the process of displacement and promote the precipitation and stripping of light components in crude oil.

**3.3. Gas Production Properties.** After the flue gas and steam are injected into the sandpack together, there are complex interactions between flue gas and oil, such as multiphase flow, gas dissolution and diffusion, and gas retention, which have an important impact on enhanced oil recovery (EOR). Therefore, the gas production law and composition change of produced gas were studied, and the influence and mechanism of gas on EOR were analyzed. The experimental data in this section are from experiment #2 in Table 1. Based on the fluid production characteristics of gas, the whole displacement process can be classified into four stages, as shown in Figure 7: before gas channeling, gas channeling, after gas channeling, and at the end of displacement.

Figure 7 presents the variation of gas components produced in each displacement stages. The proportions of N<sub>2</sub> and CO<sub>2</sub> before gas channeling are 0.94 and 0.06, respectively, and the proportions of N<sub>2</sub> and CO<sub>2</sub> in gas channeling

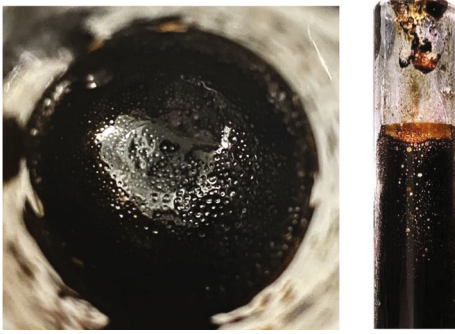


FIGURE 8: Foam form of produced oil.

are 0.85 and 0.15, respectively. After gas channeling, the proportions of  $N_2$  and  $CO_2$  are 0.69 and 0.31, respectively, and the proportions of  $N_2$  and  $CO_2$  are 0.79 and 0.21, respectively, at the close of displacement. In the early stage of displacement, the proportion difference between  $N_2$  and  $CO_2$  is easily found to be the largest because the solubility of  $CO_2$  in heavy oil is better than the solubility of  $N_2$ . Most of the  $CO_2$  in the beginning of displacement is dissolved in crude oil and retained in the sandpack model, resulting in a higher proportion of  $N_2$  output. With the progress of displacement, the proportion of  $N_2$  gradually decreases, and the proportion of  $CO_2$  gradually increases. The analysis shows that the occurrence of gas channeling will lead to a sharp drop in pressure and energy deficit in the model. At this time,  $CO_2$  dissolved in crude oil gradually precipitates, and the output proportion increases;  $N_2$  is used mostly to fill the pores and supplement the energy of the oil layer, and the output proportion decreases. At this time, the proportion of output  $N_2$  is lower than its injection proportion, and as the displacement progresses, the hypertonic channel is well developed and gradually reaches a stable state, during which the proportion of output gas gradually converges to that of injection gas, and thus there is a trend of increasing the proportion of  $N_2$  at the end of the displacement.

The above analysis and comparison illustrate that flue gas can combine the advantages of  $N_2$  and  $CO_2$ , which can not only reduce the viscosity of crude oil but also supplement model/formation energy. The dissolution and precipitation of flue gas can enhance the interaction between displacement media and crude oil and effectively promote the formation of foam oil, as presented in Figure 8.

Figure 9 depicts the retention characteristics of flue gas during flue-gas-assisted steam flooding. The flue gas retention rate refers to the ratio of the volume of flue gas trapped in the oil layer/sandpack to the total volume of flue gas injected. With the increase in injection volume, the injection and production rates of flue gas increase first and then decrease sharply, but the peak value of the flue gas production rate increases by 6.33 mL/min compared with the injection rate. The appearance of the peak value lags behind the injection rate by 0.11 PV. The retention rate of flue gas decreased slowly in the early stage, which is due mostly to the dissolution of  $CO_2$  in flue gas. When the peak gas generation rate appears, flue gas retention rate drops sharply and then gradually stabilizes, remaining at 21-23%. The occur-

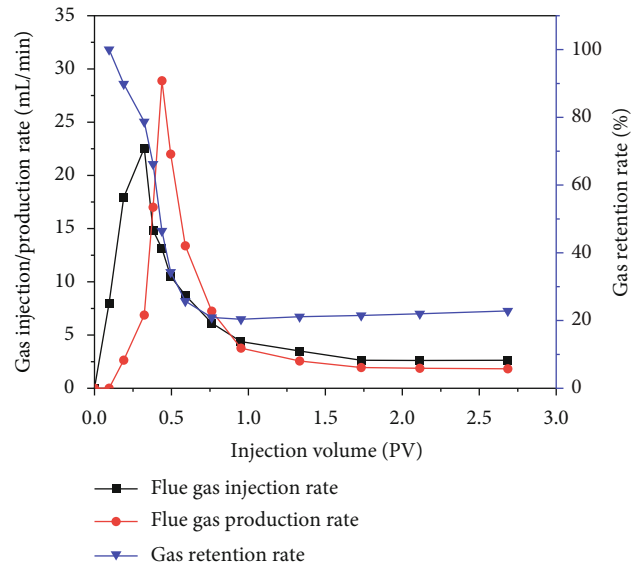


FIGURE 9: Volume variation of produced gas in flue-gas-assisted steam flooding.

rence of gas channeling greatly worsens the retention effect of flue gas, which can only be dissolved in the residual oil or fill the pores in the sandpack.

**3.4. Effect of Flue-Gas Ratio on Residual Oil Composition.** Steam distillation is crucial to enhance the development effect of heavy oil. Combined with 3.2, distillation can be seen to occur in the development process of flue-gas-assisted steam flooding. Therefore, a four-component analysis of oil sand after displacement is performed to explore the influence of the flue gas ratio to steam distillation. The experimental data in this section are from experiments #1, #2, and #3 in Table 1.

Figure 10 shows the distribution of oil sand in the one-dimensional sandpack model after flue-gas-assisted steam flooding. The colour of the oil sand gradually darkens from the entrance to exit of the model. When the ratio of flue gas to steam is 1:1, the colour of oil sand in the middle and rear of the sandpack is darker, and the colour of oil sand in the sandpack changes little after saturated oil, indicating that there is still more remaining oil at the middle and rear of the sandpack, and the distillation effect of steam is weak. When the ratio of flue gas to steam is 3:1, the lighter colour range of oil sand in the sandpack is improved to varying degrees compared with the first two groups. The higher the flue gas injection ratio is, the larger the area where the colour lightens is, and the oil sand at the same position is further cleaned. This result reflects that the increase in the ratio of flue gas can enhance the vapor transmission range and oil washing effect.

The variations of the four components in the residual oil can effectively reflect the strength of steam distillation in the displacement process. The contents of the four components were determined and analyzed for nine samples in the three groups of experiments, and the sampling locations are presented in Figure 10. Figure 11 presents the comparison of the four-component contents of residual oil under different

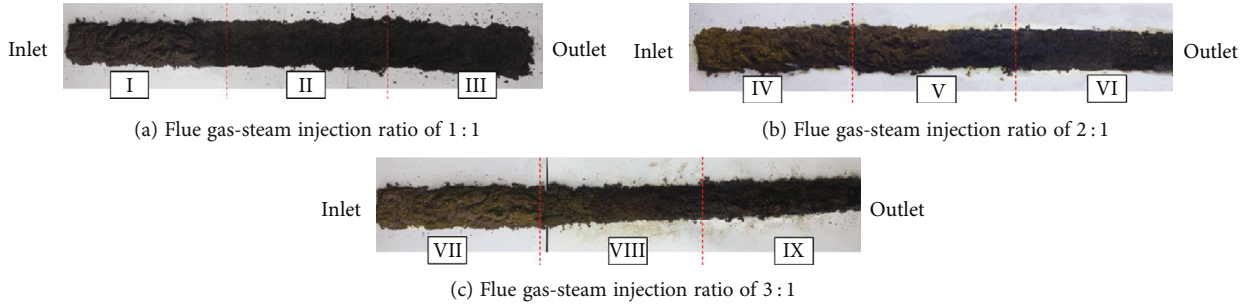


FIGURE 10: Distribution of oil sand in a one-dimensional sandpack under different injection ratios of flue gas to steam.

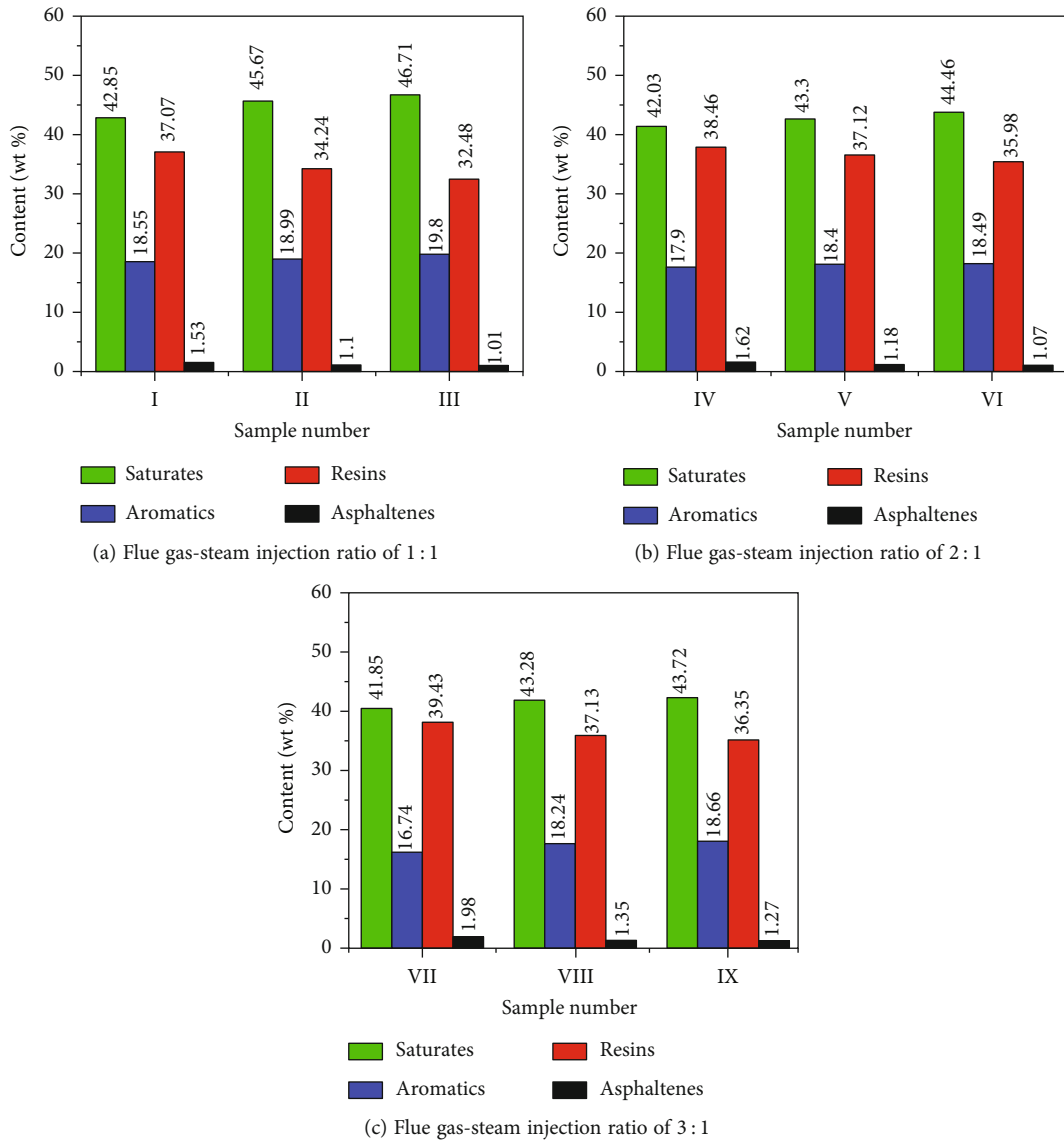


FIGURE 11: Comparison of the four-component contents of residual oil under different injection ratios of flue gas and steam.

injection ratios of flue gas and steam. In each experiment, the export, saturates, and aromatic contents in residual oil are higher, and the resin and asphaltene contents are lower because in the flue-gas-assisted steam displacement, within the scope of the spread of steam, the longer the distance the entrance is, the lower the temperature of the steam, the

steam distillation effect is weak, and the worse the effect on the extraction of the light components. The light components of the crude oil are more likely to flow than the heavy components, and the light components are more likely to be recovered after displacement and remain at the end of the core pipe, while the heavy components remain in the porous



TABLE 3: Comparison of the content of heavy and light components at the inlet and outlet.

Injection ratio of flue gas and steam	Content of light components (wt%)		Content of heavy components (wt%)		Difference between inlet and the outlet (wt%)
	Inlet	Outlet	Inlet	Outlet	
1 : 1	61.99	65.31	38.01	34.69	3.32
1 : 2	59.53	62.95	40.47	37.05	3.42
1 : 3	58.59	62.38	41.41	37.62	3.79

medium. As the amount of flue gas injection increases, the content of light components at the same position gradually reduces, and the content of crude components gradually increases, indicating the higher the flue gas injection ratio is, the stronger the steam distillation effect when the ratio of flue gas to steam is from 1 : 1 to 3 : 1.

Table 3 shows the changes in the light component and heavy component of the remaining oil at the entrance and exit at different flue gas injection ratios. Light components represent saturates and aromatics, and heavy components represent resins and asphaltenes. Numerically, the increase in the flue gas ratio not only reduces the light components at the inlet and outlet but also increases the difference between the entrance and exit. The same is true of changes in the content of heavy components, further confirming the conclusion that when the content of flue gas in the injected gas increases, the distillation effect of steam on the crude oil in the sandpack will be intensified, and the production of light components will be promoted.

#### 4. Conclusions

- (1) During steam flooding, the light components of heavy oil are easily recovered under the action of distillation. Flue gas can enhance distillation effect and increase the output proportion of light components in the process of steam flooding, increasing the recovery of steam flooding by 10%
- (2) Due to the difference in the dissolution of  $N_2$  and  $CO_2$  in heavy oil, the retention rate of  $CO_2$  in the formation in the early stage of displacement is higher, and the proportion of  $CO_2$  output is 0.06, which is lower than the initial injection proportion. After gas channeling, some dissolved  $CO_2$  begins to precipitate, and the proportion of  $CO_2$  reaches 0.31. As the displacement progresses, the proportion of  $CO_2$  gradually decreases and keeps approaching the initial injection proportion
- (3) The dissolution and release process of flue gas can help to produce foam oil. The formation of foam oil can expand the volume of original crude oil and promote the flow of crude oil while improving the output of crude oil, which reduces the maximum displacement pressure difference by 0.84 MPa

- (4) The larger the proportion of flue gas in the injected fluid is, the more significant the steam distillation effect is, the less light components in the residual oil is, and the larger the variation range of the four components of heavy oil along the sandpack is. When the proportion of flue gas to steam changes from 1 : 1 to 3 : 1, the variation of light/heavy components between the outlet and the inlet of the sandpack increases from 3.32% to 3.79%.

#### Data Availability

The underlying data support in the results of this study is reported in the figures and tables.

#### Conflicts of Interest

The authors declare that they have no known competing financial interests or personal relationships that could have appeared to influence the work reported in this paper.

#### Acknowledgments

This project is funded by the National Natural Science Foundation of China (NSFC) under the project number U20B6003 "Basic Research on Mechanisms and Key Technologies for Efficient Development of Multifunctional Thermal Complexes in Refractory Thick Oil."

#### References

- [1] G. Kindermann, M. Obersteiner, B. Sohngen et al., "Global cost estimates of reducing carbon emissions through avoided deforestation," *Proceedings of the National Academy of Sciences*, vol. 105, no. 30, pp. 10302–10307, 2008.
- [2] S. Adams and A. Acheampong, "Reducing carbon emissions: the role of renewable energy and democracy," *Journal of Cleaner Production*, vol. 240, article 118245, 2019.
- [3] M. Allen, D. Frame, C. Huntingford et al., "Warming caused by cumulative carbon emissions towards the trillionth tonne," *Nature*, vol. 458, no. 7242, pp. 1163–1166, 2009.
- [4] H. Liu, B. Tellez, T. Atallah, and M. Barghouty, "The role of  $CO_2$  capture and storage in Saudi Arabia's energy future," *International Journal of Greenhouse Gas Control*, vol. 11, pp. 163–171, 2012.
- [5] E. Rubin, J. Davison, and H. Herzog, "The cost of  $CO_2$  capture and storage," *International Journal of Greenhouse Gas Control*, vol. 40, pp. 378–400, 2015.
- [6] M. Anwar, A. Fayyaz, N. Sohail et al., " $CO_2$  capture and storage: a way forward for sustainable environment," *Journal of Environmental Management*, vol. 226, pp. 131–144, 2018.
- [7] C.-F. Tsang, S. Benson, B. Kobelski, and R. Smith, "Scientific considerations related to regulation development for  $CO_2$  sequestration in brine formations," *Environmental Geology*, vol. 42, no. 2-3, pp. 275–281, 2002.
- [8] W. Pu, B. Wei, F. Jin et al., "Experimental investigation of  $CO_2$  huff-n-puff process for enhancing oil recovery in tight reservoirs," *Chemical Engineering Research and Design*, vol. 111, pp. 269–276, 2016.
- [9] S. Bachu, "Identification of oil reservoirs suitable for  $CO_2$  -EOR and  $CO_2$  storage (CCUS) using reserves databases, with

- application to Alberta, Canada,” *International Journal of Greenhouse Gas Control*, vol. 44, pp. 152–165, 2016.
- [10] I. Kolenković and B. Saftić, “Geological storage of carbon dioxide,” *Rudarsko-geološko-naftni zbornik*, vol. 28, no. 1, pp. 9–21, 2014.
  - [11] L. Melzer, “Carbon dioxide enhanced oil recovery (CO<sub>2</sub> EOR): factors involved in adding carbon capture, utilization and storage (CCUS) to enhanced oil recovery,” *Center for Climate and Energy Solutions*, pp. 1–17, 2012.
  - [12] V. Núñez-López, R. Gil-Egui, and S. Hosseini, “Environmental and operational performance of CO<sub>2</sub>-EOR as a CCUS technology: a Cranfield example with dynamic LCA considerations,” *Energies*, vol. 12, no. 3, p. 448, 2019.
  - [13] L. Eide, M. Batum, T. Dixon et al., “Enabling large-scale carbon capture, utilisation, and storage (CCUS) using offshore carbon dioxide (CO<sub>2</sub>) infrastructure developments—a review,” *Energies*, vol. 12, no. 10, p. 1945, 2019.
  - [14] Z. Xu, S. Li, B. Li, D. Chen, Z. Liu, and Z. Li, “A review of development methods and EOR technologies for carbonate reservoirs,” *Petroleum Science*, vol. 17, no. 4, pp. 990–1013, 2020.
  - [15] Y. Xiang, C. Song, C. Li, E. Yao, and W. Yan, “Characterization of 13Cr steel corrosion in simulated EOR-CCUS environment with flue gas impurities,” *Process Safety and Environmental Protection*, vol. 140, pp. 124–136, 2020.
  - [16] P. Briggs, P. Baron, R. Fulleylove, and M. S. Wright, “Development of heavy-oil reservoirs,” *Journal of Petroleum Technology*, vol. 40, no. 2, pp. 206–214, 1988.
  - [17] R. Santos, W. Loh, A. Bannwart, and O. Trevisan, “An overview of heavy oil properties and its recovery and transportation methods,” *Brazilian Journal of Chemical Engineering*, vol. 31, no. 3, pp. 571–590, 2014.
  - [18] K. Guo, H. Li, and Z. Yu, “In-situ heavy and extra-heavy oil recovery: a review,” *Fuel*, vol. 185, pp. 886–902, 2016.
  - [19] D. Liu and W. Li, “Flue gas enhanced oil recovery (EOR) as a high efficient development technology for offshore heavy oil in China,” *Journal of Petroleum and Gas Engineering*, vol. 4, no. 5, pp. 127–142, 2013.
  - [20] L. Monte-Mor, P. Laboissiere, and O. Trevisan, “Laboratory study on steam and flue gas co-injection for heavy oil recovery,” in *Proceedings of the SPE heavy oil conference*, Canada, Alberta, Canada, June 2013.
  - [21] L. Zhong, Z. Dong, J. Hou et al., “Investigation on principles of enhanced offshore heavy oil recovery by coinjection of steam with flue gas,” in *Proceedings of the SPE Enhanced Oil Recovery Conference*, Kuala Lumpur, Malaysia, July 2013.
  - [22] R. Srivastava, S. Huang, and M. Dong, “Comparative effectiveness of CO<sub>2</sub>, produced gas, and flue gas for enhanced heavy-oil recovery,” *SPE Reservoir Evaluation & Engineering*, vol. 2, no. 3, pp. 238–247, 1999.
  - [23] C. Wu, “A critical review of steamflood mechanisms,” in *Proceedings of the SPE California Regional Meeting*, Bakersfield, California, April 1977.
  - [24] F. Kirmani, A. Raza, R. Gholami, M. Haidar, and C. S. Fareed, “Analyzing the effect of steam quality and injection temperature on the performance of steam flooding,” *Energy Geoscience*, vol. 2, no. 1, pp. 83–86, 2021.
  - [25] S. Ali, “Current status of steam injection as a heavy oil recovery method,” *Journal of Canadian Petroleum Technology*, vol. 13, no. 1, 1974.
  - [26] R. Srivastava, S. Huang, and F. Mourits, “A laboratory evaluation of suitable operating strategies for enhanced heavy oil recovery by gas injection,” *Journal of Canadian Petroleum Technology*, vol. 36, no. 2, 1997.
  - [27] S. Li, Z. Li, and X. Sun, “Effect of flue gas and *n*-hexane on heavy oil properties in steam flooding process,” *Fuel*, vol. 187, pp. 84–93, 2017.
  - [28] C. Wang, P. Liu, F. Wang, B. Atadurdyev, and M. Ovluyagulyev, “Experimental study on effects of CO<sub>2</sub> and improving oil recovery for CO<sub>2</sub> assisted SAGD in super-heavy-oil reservoirs,” *Journal of Petroleum Science and Engineering*, vol. 165, pp. 1073–1080, 2018.
  - [29] Y. Wang, X. Wu, R. Wang, and F. Lai, “Study on multiple thermal fluid applied in heavy oil development,” *Metalurgia International*, vol. 18, no. 9, p. 98, 2013.
  - [30] Q. Zhao, Z. Li, S. Wang, F. Lai, and H. Li, “Phase behavior measurements and modeling for N<sub>2</sub>/CO<sub>2</sub>/extra heavy oil mixtures at elevated temperatures,” *Industrial & Engineering Chemistry Research*, vol. 58, no. 1, pp. 428–439, 2019.
  - [31] J. Fan, J. Yang, X. Fan, and L. Wu, “Experimental study on the mechanism of enhanced oil recovery by non-condensable gas-assisted steam flooding process in extra-heavy oil reservoir,” *Energy Sources, Part A: Recovery, Utilization, and Environmental Effects*, vol. 43, no. 4, pp. 444–460, 2021.
  - [32] J. Welker, “Physical properties of carbonated oils,” *Journal of Petroleum Technology*, vol. 15, no. 8, pp. 873–876, 1963.
  - [33] S. Li, B. Li, Q. Zhang, Z. Li, and D. Yang, “Effect of CO<sub>2</sub> on heavy oil recovery and physical properties in huff-n-puff processes under reservoir conditions,” *Journal of Energy Resources Technology*, vol. 140, no. 7, 2018.
  - [34] S. Kokal and S. Sayegh, “Phase behavior and physical properties of CO<sub>2</sub>-saturated heavy oil and its constitutive fractions: experimental data and correlations,” *Journal of Petroleum Science and Engineering*, vol. 9, no. 4, pp. 289–302, 1993.
  - [35] A. Khatib, R. Earllougher, and K. Kantar, “CO<sub>2</sub> injection as an immiscible application for enhanced recovery in heavy oil reservoirs,” in *Proceedings of the SPE California Regional Meeting*, Bakersfield, California, March 1981.
  - [36] Z. Wu, L. Wang, C. Xie, and W. Yang, “Experimental investigation on improved heavy oil recovery by air assisted steam injection with 2D visualized models,” *Fuel*, vol. 252, pp. 109–115, 2019.
  - [37] A. Mohsenzadeh, M. Escrochi, M. Afraz, G. Karimi, Y. Al-Wahaibi, and S. Ayatollahi, “Non-hydrocarbon gas injection followed by steam-gas co-injection for heavy oil recovery enhancement from fractured carbonate reservoirs,” *Journal of Petroleum Science and Engineering*, vol. 144, pp. 121–130, 2016.
  - [38] R. Bora, B. Maini, and A. Chakma, “Flow visualization studies of solution gas drive process in heavy oil reservoirs with a glass micromodel,” *SPE Reservoir Evaluation & Engineering*, vol. 3, no. 3, pp. 224–229, 2000.
  - [39] T. Lu, Z. Xu, X. Ban, D. Peng, and Z. Li, “Cyclic in-situ combustion process for improved heavy oil recovery after cyclic steam stimulation,” *SPE Journal*, vol. 27, pp. 1–15, 2022.
  - [40] Z. Wang, S. Li, and Z. Li, “A novel strategy to reduce carbon emissions of heavy oil thermal recovery: condensation heat transfer performance of flue gas-assisted steam flooding,” *Applied Thermal Engineering*, vol. 205, article 118076, 2022.

## Research Article

# Experimental Study on Gas–Water Relative Permeability Characteristics of Tight Sandstone Reservoir in Ordos Basin

Xiaoxia Ren <sup>1,2</sup>, Aifen Li,<sup>3</sup> and Asadullah Memon<sup>4</sup>

<sup>1</sup>School of Science, Qingdao University of Technology, Qingdao 266525, China

<sup>2</sup>Shandong Key Laboratory of Oilfield Chemistry, China University of Petroleum (East China), Qingdao 266580, China

<sup>3</sup>School of Petroleum Engineering, China University of Petroleum (East China), Qingdao 266580, China

<sup>4</sup>Department of Petroleum and Natural Gas Engineering, Mehran University of Engineering and Technology, Jamshoro, 76062 Sindh, Pakistan

Correspondence should be addressed to Xiaoxia Ren; [renxiaoxia1010@163.com](mailto:renxiaoxia1010@163.com)

Received 18 February 2022; Accepted 22 May 2022; Published 8 June 2022

Academic Editor: Xiang Zhou

Copyright © 2022 Xiaoxia Ren et al. This is an open access article distributed under the Creative Commons Attribution License, which permits unrestricted use, distribution, and reproduction in any medium, provided the original work is properly cited.

Accurate measurement of relative permeability curve is the basis for evaluating gas reservoir performance. The unsteady-state method could bring significant measurement error for low-permeability cores. However, it is difficult to control the constant gas flow rate in the traditional steady-state method, which obstacles the experimental operation. In this study, an improved steady-state method was proposed. First, the pressure value obtained from the experiment, when the gas permeability no longer changed with the average pressure on the rock core, was set as the testing pressure. Then, the gas was injected under constant pressure, and the water was injected with a constant flow rate. Finally, the relative permeability values of gas and water phases were calculated based on Darcy's law. Comparative analysis of the results of the relative permeability curves under formation pressure and pressure with negligible slip effect indicates that the relative permeability curves are the same in gas and water phases, proving the feasibility of the new method. Further, the results were compared with those of the test method at normal pressure, the water-phase relative permeability showed no significant change, the relative permeability of gas phase was larger, the two-phase flow area became wider, and the irreducible water saturation was lower than that at the normal pressure. This result reflects that pressure does not significantly affect the flow of wetting phase but tremendously influences the nonwetted phase under low pressure. The relationship between relative permeability and water saturation is linear in the semilogarithmic coordinate diagram and can be described by using the following relationship:  $\ln(k_{rg}/k_{rw}) = aS_w + \ln b$ . With the decrease in the core permeability, relative permeability curve, and isotonic point moved to the right, irreducible water saturation gradually increased, and residual gas saturation decreased, indicating that the smaller permeability induced a lower gas-phase flow capacity.

## 1. Introduction

Gas–water relative permeability is of great significance in the industrial research on natural gas. Relative permeability can be obtained by direct measurement, capillary pressure curve, production data analysis, and indirect calculation methods by using the empirical formulas [1, 2]. Over the past decades, various experiments have been developed and conducted to systematically explore the gas–water relative permeability curves [3–6]. Currently, steady-state and unsteady-state methods are commonly used to obtain relative permeability at the labora-

tory scale [2]. In the steady-state method, two fluids are simultaneously injected into the core, and their permeability is calculated separately, according to Darcy's law [7, 8]. Abaci et al. [9] injected a mixture of gas and liquid into a vertical artificial sandstone column at room temperature and pressure to measure relative permeability of gas and liquid. The results showed that when water saturation decreased slightly, the relative permeability of water decreased sharply, and the relative permeability of the gas phase at irreducible water saturation was higher than that of the water phase at residual gas saturation. Donald et al. [10] improved the fluid saturation test by

X-ray computed tomography (CT) scanning technology under indoor conditions. The calculation formula for the steady-state method was simple, and the saturation could be measured directly based on Darcy's law. However, it was challenging to maintain the constant gas flow rate by conventional methods, which brought errors into the measurement results.

In contrast, in the unsteady-state method, the displacing phase is injected into the saturated core along with the wetting phase [11–13]. Berry et al. [14] conducted a series of constant-velocity unsteady-state gas–liquid displacement tests on four reservoir sandstone cores with similar porosity, permeability, and lithological characteristics under reservoir conditions. For short-core experiments, if the unsteady-state method is used, the dead volume generally accounts for about 33% of the pore volume of the core [15]. Thus, this effect cannot be ignored, significantly impacting data processing.

Furthermore, the effect of pressure was also studied. However, scholars have different opinions on the effects of overlying strata pressure on relative permeability [16, 17]. Some of the early studies in this area was done by Fatt and Mo et al. [18, 19] and Thomas and Ward [20]. They supposed that the overlying strata pressure would not affect the relative permeability of gas and water phases. However, some literature studies indicated that overlying strata pressure significantly affected the gas–water permeability curves for both gas and water phases [19, 21–25]. Some literature studies also reported that pressure significantly affected the nonwetted phase under the overlying pressure; however, it did not significantly affect the wetting phase [26, 27]. This could be attributed to the increase in the overlying strata that binds sand grains tightly together, resulting in a decrease in the pore throat diameter. For a defined water saturation, this results in redistribution of the wetting phase to occupy more pore throats, which indicates that this cannot cause any significant changes in the water-phase relative permeability (e.g., in water-wet sandstone); however, results in more oil flow blockages thus reduce the relative permeability of nonwet phase [28, 29].

The unsteady-state method often provides errors in measuring gas–water relative permeability curve due to volume measurement, and the influence of pressure on gas–water relative permeability is seldom considered in the currently used test methods. Therefore, based on the traditional steady-state method to measure relative permeability, in this study, the steady-state method is improved and modified. Considering the influence of the formation pressure, the relative permeability curve can be measured by the improved steady-state method, during which water is injected at constant flow as gas is injected at constant pressure. The test results at normal pressure were compared with those at formation pressure to verify the feasibility of this method.

## 2. Materials and Methods

*2.1. Experimental Specimens and Conditions.* The specimens used in the experiment were obtained from Sulige gas field, Ordos, Inner Mongolia, with a core diameter of 2.5 cm and length of no more than 5.0 cm. The dimensions, porosities, and permeabilities of the core samples are presented in

Table 1. The porosity and permeability were tested under  $N_2$  at 25°C. The experimental temperature was set to the formation temperature of 95°C. Water used was prepared according to the components of output crude oil at the mouth of a well after electric dehydration, and it showed the density of 1.025 g·cm<sup>-3</sup> and the viscosity of 0.334 mPa·s, at 95°C. The components and viscosity of water for experimental use were found to be almost the same as those under the formation conditions, which could avoid plugging damage caused by incompatibility of injected water.

The wettability of all cores was tested by contact angle measurements with the Kruss DSA-100 drop shape analyzer. A photograph was taken using a camera when a drop of water attached to the surface of a solid. The contact angle between the water and the solid was then calculated.

The confining pressure was set as formation, atmospheric, and pressure with negligible slip effect, respectively.

### 2.2. Experimental Equipment and Process

*2.2.1. Experimental Setup.* Figure 1 shows the simulated displacement equipment used for providing high temperature and high reservoir pressure in the test. The system mainly includes displacement pump, humidifier, core holder, gas–water separator, and gas–water metering device.

#### 2.2.2. Experimental Process

- (a) By testing gas permeability of rock specimens under different backpressures, the pressure value  $P_N$  (under which gas permeability does not change with pressure) was obtained
- (b) A core saturated with formation water was placed in a core holder at 95°C and the backpressure of  $P_N$ . Formation water was passed through the rock specimen at the constant flow rate ( $q_w$ ). When the system reached stability, the upstream pressure ( $P_1$ ) was recorded, and water permeability was calculated
- (c) Water driven by gas: gas was injected into the core to gradually increase upstream pressure to  $P_1$ . Displacement was continued at constant pressure  $P_1$  until no water was produced, and the gas-phase permeability with irreducible water ( $S_{wc}$ ) was calculated. The core was sealed, with the conditions reduced to laboratory conditions, and then the core was taken out and weighed to calculate the irreducible water saturation of the core
- (d) Simultaneous injection of gas and water: the gas pressure was constant  $P_1$ , and water was simultaneously injected at a constant flow rate of  $q_w/20$ . When the system reached pressure equilibrium, the gas flow rate was recorded, and the effective permeability of the water and gas phases was calculated. Then, the core was weighed following the method mentioned in the previous step, and the water saturation was calculated



TABLE 1: Basic data of core used in gas–water permeability experiment.

Core number	Length/cm	Diameter/cm	Porosity/%	Perm-plug method/ $(10^{-3}\mu\text{m}^2)$	Dry weight/g	Wet weight/g	Saturated water/mL	Contact angle/°
1	4.240	2.540	17.710	1.896	47.920	51.504	3.497	45.05
2	4.058	2.540	13.629	1.024	52.140	54.664	2.462	49.38
3	4.324	2.530	9.473	0.703	52.717	54.463	1.899	37.65
4	4.549	2.533	15.970	0.516	53.614	56.784	3.093	50.36
5	3.380	2.540	8.140	0.360	42.911	44.116	1.176	32.15
6	3.658	2.536	5.132	0.194	47.300	48.112	0.792	40.56
7	3.681	2.540	3.030	0.130	48.262	48.758	0.484	38.21
8	4.424	2.540	6.240	0.090	57.503	58.557	1.028	36.77

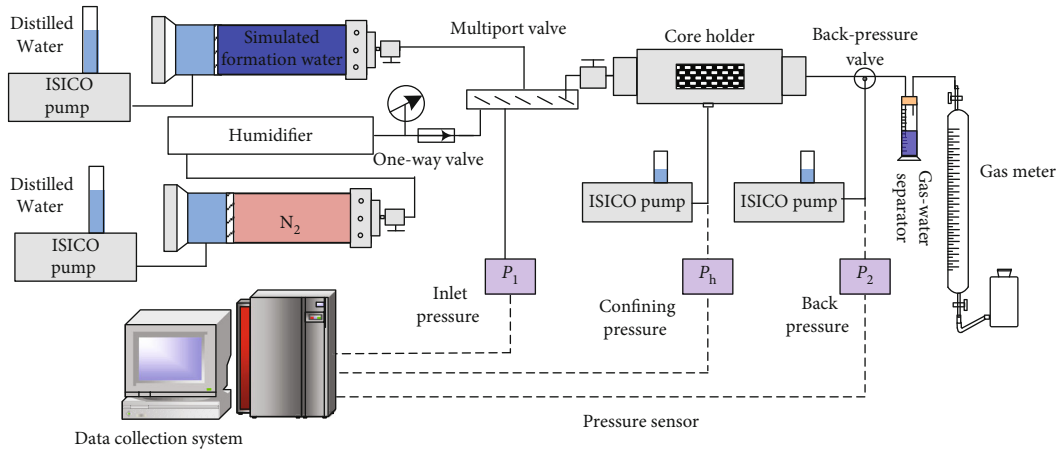


FIGURE 1: Flow chart of gas–water phase permeability test by the improved steady-state method.

(e) The water flow rate was adjusted to  $q_w/10$ , and the gas pressure was kept constant  $P_1$ . Then, the above-mentioned step  $d$  was repeated

(f) The gas source was closed, water was injected with a flow rate of  $q_w$ , and then the water-phase relative permeability under residual gas saturation ( $S_{gr}$ ) was calculated

**2.3. Experimental Data Processing Methods.** Considering the variation of water and gas volume with temperature and pressure, it is necessary to adjust water and gas production at room temperature and normal pressure to that at high temperature and high pressure. Therefore, the formula for calculating the gas–water-phase permeability curve by a steady-state method was improved as follows:

The volume of liquid under formation conditions is represented as follows:

$$Q_w = Q_{L_0} \cdot B_w, \quad (1)$$

where  $Q_w$  denotes the flow rate of water under experimental conditions,  $\text{cm}^3 \cdot \text{s}^{-1}$ ,  $Q_{L_0}$  is the flow rate of water under room temperature and normal pressure,  $\text{cm}^3 \cdot \text{s}^{-1}$ , and  $B_w$  is water volume coefficient under experimental conditions.

Therefore, after reaching stability, according to Darcy's law, liquid-phase permeability is represented as follows:

$$k_w = \frac{Q_{L_0} B_w \mu_w L}{A(p_1 - p_2)}, \quad (2)$$

where  $k_w$  is the liquid-phase permeability,  $\text{cm}^2$ ,  $\mu_w$  denotes water-phase viscosity under experimental conditions,  $\text{mPa} \cdot \text{s}$ ,  $L$  and  $A$  are the core length and cross-section, with the units of  $\text{cm}$  and  $\text{cm}^2$ , respectively, and  $P_1$  and  $P_2$  denote upstream and downstream pressure of core holder at steady gas and water discharge, respectively,  $10^{-1} \text{MPa}$ .

Figure 2 shows schematic illustration for gas permeability, and Darcy's formula is expressed as follows:

$$Q_g = -\frac{k_g A dp}{\mu_g dL}, \quad (3)$$

where  $Q_g$  is the flow rate of gas under experimental conditions,  $\text{cm}^3 \cdot \text{s}^{-1}$ ,  $k_g$  is the gas permeability,  $\text{cm}^2$ ,  $\mu_g$  denotes gas viscosity under experimental conditions,  $\text{mPa} \cdot \text{s}$ ,  $A$  represents core cross-section,  $\text{cm}^2$ , and  $dp/dL$  is the pressure gradient,  $10^{-1} \text{MPa} \cdot \text{cm}^{-1}$ .



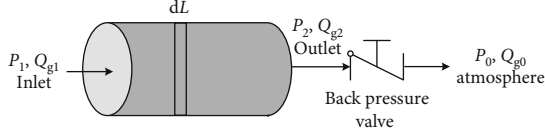


FIGURE 2: Schematic representation of flow process.

From the gas state formula, on the ground,

$$p_0 Q_{g0} = nRT_0, \quad (4)$$

where  $p_0$  is the atmospheric pressure,  $10^{-1}$  MPa,  $Q_{g0}$  is the flow rate of gas under room temperature and normal pressure,  $\text{cm}^3 \cdot \text{s}^{-1}$ ,  $n$  is the amount of substance, mol,  $R$  denotes proportionality coefficient,  $\text{J} \cdot (\text{mol} \cdot \text{K})^{-1}$ , and  $T_0$  is the room temperature, K.

Under the ground,

$$pQ_g = nzRT, \quad (5)$$

where  $p$  is the experimental mean pressure,  $10^{-1}$  MPa,  $Q_g$  is the flow rate of gas under experimental condition,  $\text{cm}^3 \cdot \text{s}^{-1}$ ,  $z$  is the compression factor of gas at experimental temperature and pressure, and  $T$  is the experimental temperature, K.

Then,

$$Q_g = \frac{p_0 Q_0 z T}{p T_0} = - \frac{k_g A}{\mu_g} \frac{dp}{dL}. \quad (6)$$

Gas permeability could be obtained by separating the calculus of variations as follows:

$$k_g = \frac{2\mu_g p_0 Q_{g0} z T L}{A T_0 (p_1^2 - p_2^2)}. \quad (7)$$

In this study, the gas-phase permeability under irreducible water is considered as absolute permeability:

$$k_{rg} = \frac{k_g}{k}, \quad (8)$$

$$k_{rw} = \frac{k_w}{k}, \quad (9)$$

where  $k_{rg}$  and  $k_{rw}$  denote relative permeability of gas and water, respectively, and  $k$  is the absolute permeability,  $\text{cm}^2$ . Average water saturation is as follows:

$$S_w = \frac{m_i - m_o}{V_p \rho_w} B_w, \quad (10)$$

where  $S_w$  indicates mean water saturation,  $m_i$  and  $m_o$  denote core mass before and after experiment, respectively,  $\rho_w$  represents density of water at room temperature,  $\text{g} \cdot \text{cm}^{-3}$ , and  $V_p$  is the pore volume of sample,  $\text{cm}^3$ .

### 3. Results and Discussion

**3.1. Relation between Gas Permeability and Average Core Pressure.** Average pore pressure could affect core permeability due to the Klinkenberg effect [2, 30]. Therefore, in this study, the influence of pressure on gas permeability was tested before conducting experiments on relative permeability.

The experimental results show that gas permeability first decreased rapidly with the increase of average pore pressure and then decreased slowly with the further increase of the pressure. When a specific pressure was reached, there was no significant change in permeability, even with the continuous increase in the pressure. Figure 3 shows that when the average pressure reached 4.25 MPa, the change in permeability became negligible. Therefore, it is reasonable to set backpressure of 5.0 MPa to eliminate slippage effect for gas–water relative permeability test, which is closer to formation conditions.

**3.2. Comparison of Gas–Water Phase Permeability Curves under Different Backpressures.** In order to verify the effectiveness of this method, experiments were conducted on the relative permeability of core 7 under different backpressure conditions, as shown in Figure 4. The results reveal that there is no significant difference among the three curves for the water phase, which indicates that pressure has no apparent influence on water-phase relative permeability. Noteworthy, relative permeability curves at the backpressure of 5 and 28 MPa are the same in gas and water phases, thus proving the feasibility of the new method. Compared with the gas-phase relative permeability curve under normal pressure, the two-phase penetration area increased, the gas-phase relative permeability became slightly larger, and the irreducible water saturation was lower than that at the normal pressure, which shows that pressure significantly influences gas-phase relative permeability at low pressure.

The improved method can provide the accurate gas–water permeability under the condition of lower pressure than the actual reservoir pressure, which is of great significance to design development scheme for tight gas reservoir, and for the prediction of production performance and reservoir simulation.

**3.2.1. Effects of Different Permeabilities on Gas–Water Permeability Curve.** Figure 5 shows the test results of the gas–water permeability curve of core No. 4. With the increase of water saturation, the gas-phase relative permeability shows the variation trend of first decreasing rapidly and then decreasing slowly, while the water-phase relative permeability first increases slowly and then rapidly. The gas–water two-phase penetration area of the low-permeability core was relatively narrow, with irreducible water saturation of 63.69% and residual gas saturation of 14.95%. The water saturation corresponding to the isotonic point was higher (about 78%), while the gas–water-phase relative permeability at the isotonic point was lower, about 0.12.

Figure 6 shows gas–water permeability curves of three cores with different permeabilities. The changing trend of the gas–water permeability curve was the same for conditions with different core permeabilities, and the characteristic parameters

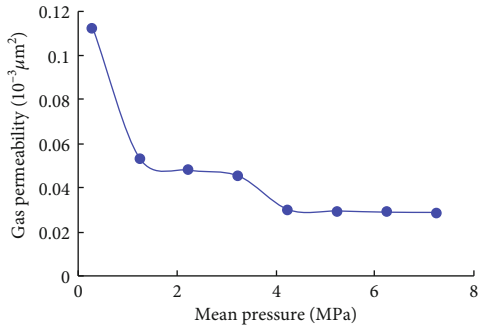


FIGURE 3: Change of gas permeability with test pressure.

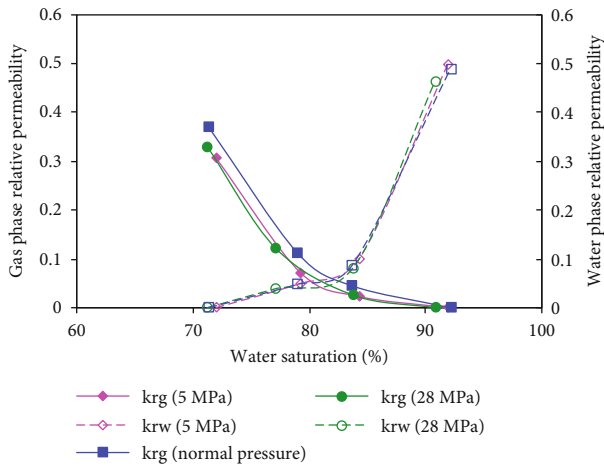


FIGURE 4: Influence of pressure on gas-water relative permeability curves.

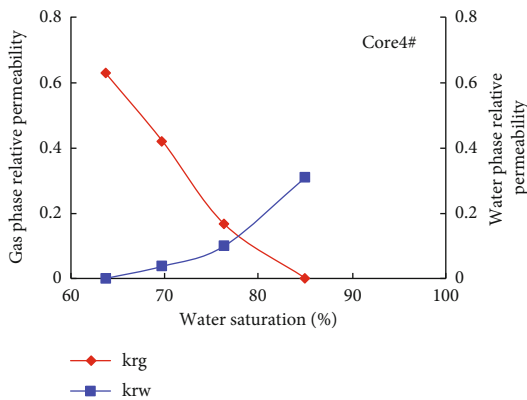


FIGURE 5: Results of the gas-water permeability curve of core No. 4.

of the gas-water permeability curve changed significantly. The gas-phase permeability curve moved to the right in the same coordinate system with the decrease in permeability. The irreducible water saturation increased, the residual gas saturation decreased, the isotonic point moved to the right, and the two-phase region narrowed. At low permeability, the water-phase relative permeability at residual gas saturation increased compared to gas-phase relative permeability at irreducible water saturation [30, 31].

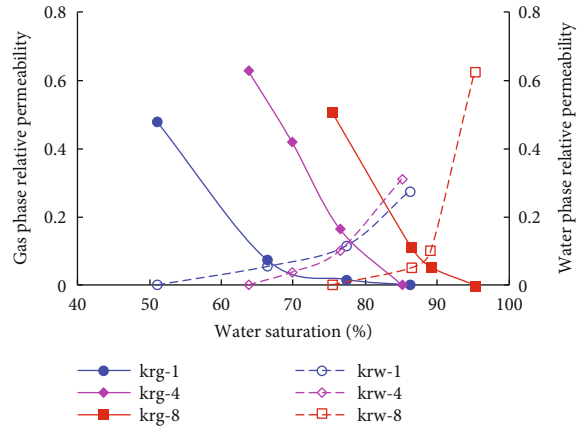


FIGURE 6: Gas-water permeability curves of cores with different permeabilities.

X-ray analysis results show that the average clay content of cores with a permeability greater than 0.13 mD was 14%, and that of cores with permeability less than 0.13 mD was 8%. Clay minerals are susceptible to speed sensitivity. The gas flow rate was higher than that of water; thus, gas was more susceptible to speed sensitivity when passed through the pores. Moreover, clay content in low permeability core was high; thus, it was easy for the clay minerals to plug the pores, which led to the decrease of gas permeability.

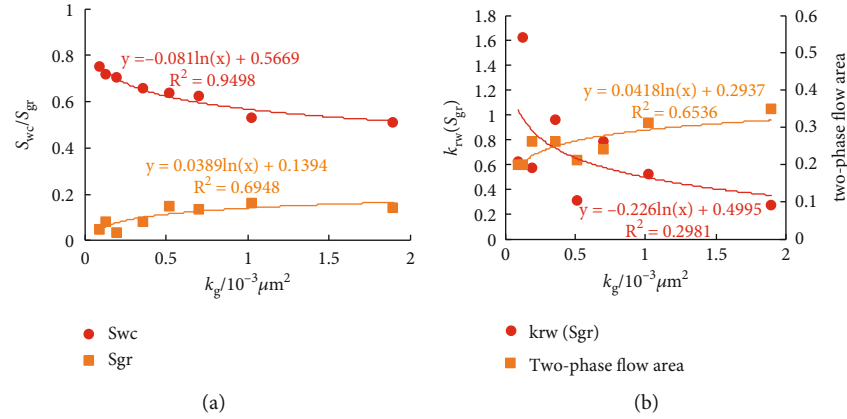
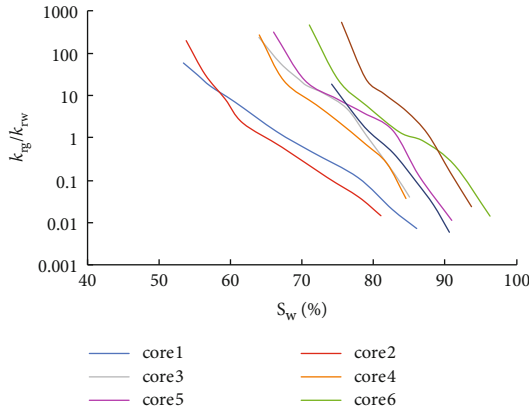
The characteristic parameters for gas-water relative permeability of cores with different permeabilities are listed in Table 2, and the results are presented in Figure 7.

Figure 7(a) exhibits that the irreducible water saturation increases, and residual gas saturation decreases with the decrease in permeability. Notably, all rocks are hydrophilic; therefore, water is the wetting phase, and gas is the nonwetting phase. Before the test, rock was saturated with water, and thus water occupied all pores and throats. When the gas entered the pores under external pressure, the gas could only overcome the capillary force and enter the main pore throat because of the preoccupation of all the percolating channels with water. The smaller the rock permeability, the fewer the larger pore throats. When water reentered the core and displaced the gas, the gas in the mainstream channel could be easily carried away with only a small amount left. Therefore, the smaller permeability induces minor residual gas saturation.

The two-phase flow area narrowed with the decrease in the core permeability (Figure 7(b)). The two-phase flow area reflects the flowability of two-phase fluid in the pore. The decrease of the two-phase flow area indicated a decrease in pore size and poor pore connectivity. Figure 7(b) demonstrates that the water-phase relative permeability under residual gas saturation tends to increase gradually with the decrease of rock permeability. When core permeability was below  $0.13 \times 10^{-3} \mu\text{m}^2$ , the water-phase relative permeability at residual gas saturation was higher than gas-phase relative permeability at irreducible water saturation. This indicates that the lower permeability induces an increased influence of irreducible water saturation on gas permeability.

TABLE 2: Experiments results of the core samples.

Core No.	$k_g/10^{-3}\mu\text{m}^2$	$S_{wc}$	$S_{gr}$	Absolute permeability $k_g(S_{wc})/10^{-3}\mu\text{m}^2$	$k_{rw}(S_{gr})$	Two-phase flow range
1	1.896	0.510	0.139	0.480	0.275	0.351
2	1.024	0.531	0.159	0.977	0.525	0.310
3	0.703	0.625	0.135	0.813	0.783	0.240
4	0.516	0.637	0.150	0.629	0.310	0.214
5	0.360	0.656	0.082	0.921	0.966	0.261
6	0.194	0.706	0.031	0.924	0.573	0.264
7	0.130	0.720	0.081	0.307	1.629	0.200
8	0.090	0.753	0.048	0.508	0.625	0.198

FIGURE 7: Relationship between characteristic value and permeability of gas-water relative permeability curves: (a) relationship between  $S_{wc}/S_{gr}$  and  $k_g$  and (b) relationship between  $k_{rw}(S_{gr})$ /two-phase flow area and  $k_g$ .FIGURE 8: Relationship between  $k_{rg}/k_{rw}$  and  $S_w$  of cores with different permeabilities.

The relationship between relative permeability and water saturation is shown in Figure 8. Clearly, the curve is linear in the semilogarithmic coordinate diagram and can be described by the relation  $\ln(k_{rg}/k_{rw}) = aS_w + \ln b$ , where  $a$  and  $b$  are constants [32–34]. With the increase of water saturation, the relative permeability ratio of the gas-water phase decreases exponentially. When the ratio is 1, the corresponding saturation is the water saturation at the isotonic point. Moreover, the core permeability decreases, and the

isotonic point moves to the right. Further, the slope of the eight curves is higher, which indicates that the relative permeability ratio of gas to water decreases rapidly, and the gas-phase permeability is poor. The slope increases gradually with the decrease of permeability, indicating that the smaller permeability induces a lower gas-phase flow capacity.

#### 4. Conclusions

- (1) By changing the simultaneous gas-water constant velocity injection mode to gas constant pressure injection and liquid constant flow injection, respectively, an improved steady-state method for determining the gas-water relative permeability of low-permeability sandstones was proposed in this study. This method simulates the formation temperature and determines the backpressure value when the gas permeability no longer changes with the average pore pressure. With this pressure value considered as backpressure, gas was injected at constant pressure, water was injected at constant flow, and relative permeability was calculated by using Darcy's formula. Notably, this method could avoid the errors caused by volume measurement in the unsteady-state method and the errors caused by inaccurate control of gas flow rate in the traditional steady-state method

- (2) There was no obvious difference between the gas water relative permeability curve measured by this method and that under formation conditions. Compared with the test method at normal pressure, the relative permeability of the water phase did not exhibit any significant change, the gas-phase relative permeability was larger, and the two-phase flow area was wider, which indicates that pressure significantly influences gas-phase relative permeability at low pressure
- (3) With the decrease in the core permeability, relative permeability curve, and isotonic point moved to the right, irreducible water saturation gradually increased, and residual gas saturation decreased. When core permeability was below 0.13 mD, the water-phase relative permeability under residual gas saturation was higher than the gas-phase relative permeability at irreducible water saturation

### Data Availability

The data used to support the findings of this study are available from the first author upon request.

### Conflicts of Interest

The authors declare that there are no conflicts of interest regarding the publication of this paper.

### Acknowledgments

This work was supported by the National Natural Science Foundation of China (NSFC) 52104026.

### References

- [1] S. Chen, J. Zhang, D. Yin, X. Cheng, and N. Jiang, "Relative permeability measurement of coal microchannels using advanced microchip technology," *Fuel*, vol. 312, Article ID 122633, p. 122633, 2022.
- [2] A. Li, *Petrophysics*, China University of Petroleum Press, Dongying, 2015.
- [3] J. Wang, M. Dong, and J. Yao, "Calculation of relative permeability in reservoir engineering using an interacting triangular tube bundle model," *Particuology*, vol. 10, no. 6, pp. 710–721, 2012.
- [4] A. J. Babchin, R. Bentsen, B. Faybishenko, and M. B. Geilikman, "On the capillary pressure function in porous media based on relative permeabilities of two immiscible fluids: application of capillary bundle models and validation using experimental data," *Advances in Colloid and Interface Science*, vol. 233, no. 462, pp. 176–185, 2016.
- [5] B. Xiao, J. Fang, and F. Ding, "Prediction of relative permeability of unsaturated porous media based on fractal theory and Monte Carlo simulation," *Energy & Fuels*, vol. 26, no. 11, pp. 6971–6978, 2012.
- [6] N. Zhang, B. Yan, Q. Sun, and Y. Wang, "Improving multiscale mixed finite element method for flow simulation in highly heterogeneous reservoir using adaptivity," *Journal of Petroleum Science & Engineering*, vol. 154, pp. 382–388, 2017.
- [7] Y. Wu, K. Pruess, and Z. Chen, "Buckley-Leverett flow in composite porous media," *SPE Advanced Technology Series*, vol. 1, no. 2, pp. 36–42, 1993.
- [8] A. Afanasyev, "Fluid displacement in a dual-permeability medium with local capillary equilibrium," *Transport in Porous Media*, vol. 135, no. 2, pp. 513–533, 2020.
- [9] S. Abaci, J. Edwards, and B. Whittaker, "Relative permeability measurements for two phase flow in unconsolidated sands," *International Journal of Mine Water*, vol. 11, no. 2, pp. 11–26, 1992.
- [10] D. Macallister, K. Miller, S. K. Graham, and C. Yang, "Application of X-ray CT scanning to determine gas/water relative permeabilities," *SPE Formation Evaluation*, vol. 8, no. 3, pp. 184–188, 1993.
- [11] D. Dong, "Processing method to the data of relative permeability in unsteady state displacement," *Journal of Southwest Petroleum University Science & Technology Edition*, vol. 36, pp. 110–116, 2014.
- [12] X. Ren, A. Li, S. Fu, and S. Wang, "Experimental study on the oil-water relative permeability relationship for tight sandstone considering the nonlinear seepage characteristics," *Journal of Petroleum Science and Engineering*, vol. 161, pp. 409–416, 2018.
- [13] X. Chen and D. Dicarolo, "A new unsteady-state method of determining two-phase relative permeability illustrated by CO<sub>2</sub>-brine primary drainage in berea sandstone," *Advances in Water Resources*, vol. 96, pp. 251–265, 2016.
- [14] F. Berry, A. Little, and R. Skinner, "Differences in gas/oil and gas/water relative permeability," *Proceedings of the SPE/DOE Enhanced Oil Recovery Symposium*, SPE-24133-MS, France, 1992.
- [15] W. Hu, S. Yang, G. Liu, Z. Wang, P. Wang, and H. Lei, "A new correction method for oil-water relative permeability curve on the basis of resistivity and water saturation relationship," *Transport in Porous Media*, vol. 109, no. 3, pp. 527–540, 2015.
- [16] M. Meng, Z. Qiu, R. Zhong, Z. Liu, Y. Liu, and P. Chen, "Adsorption characteristics of supercritical CO<sub>2</sub>/CH<sub>4</sub> on different types of coal and a machine learning approach," *Chemical Engineering Journal*, vol. 368, pp. 847–864, 2019.
- [17] M. Meng and Z. Qiu, "Experiment study of mechanical properties and microstructures of bituminous coals influenced by supercritical carbon dioxide," *Fuel*, vol. 219, pp. 223–238, 2018.
- [18] I. Fatt, "The effect of overburden pressure on relative permeability," *Journal of Petroleum Technology*, vol. 5, no. 10, pp. 15–16, 1953.
- [19] S. Mo, S. He, G. Lei, S. Gai, and Z. Liu, "Effect of the drawdown pressure on the relative permeability in tight gas: a theoretical and experimental study," *Journal of Natural Gas Science and Engineering*, vol. 24, pp. 264–271, 2015.
- [20] R. Thomas and D. Ward, "Effect of overburden pressure and water saturation on gas permeability of tight sandstone cores," *Journal of Petroleum Technology*, vol. 24, no. 2, pp. 120–124, 1972.
- [21] J. Fang, P. Guo, X. Xiao et al., "Gas-water relative permeability measurement of high temperature and high pressure tight gas reservoirs," *Petroleum Exploration and Development*, vol. 42, no. 1, pp. 92–96, 2015.
- [22] X. Guo, Z. Du, Y. Jiang, L. Sun, X. Liu, and N. Zhang, "Can gas-water relative permeability measured under experiment conditions be reliable for the development guidance of a real HPHT

- reservoir,” *Natural Gas Industry*, vol. 34, no. 6, pp. 60–64, 2014.
- [23] S. Mo, S. He, G. Lei, G. Liu, and S. Gai, “Theoretical and experimental analysis of gas-water relative permeability in tight gas,” *Natural Gas Geoscience*, vol. 26, no. 11, pp. 2149–2154, 2015.
- [24] J. Shen, Y. Qin, Y. Li, and G. Wang, “Experimental investigation into the relative permeability of gas and water in low-rank coal,” *Journal of Petroleum Science and Engineering*, vol. 175, pp. 303–316, 2019.
- [25] X. Zhang, C. Wu, and S. Liu, “Characteristic analysis and fractal model of the gas-water relative permeability of coal under different confining pressures,” *Journal of Petroleum Science and Engineering*, vol. 159, pp. 488–496, 2017.
- [26] C. Adenutsi, Z. Li, W. Aggrey, and B. Toro, “Performance of relative permeability and two-phase flow parameters under net effective stress in water wet porous media: a comparative study of water–oil versus silica nanofluid–oil,” *Arabian Journal for Science and Engineering*, vol. 43, no. 11, pp. 6555–6565, 2018.
- [27] B. Lai and J. Miskimins, “A new technique for accurately measuring two-phase relative permeability under non-Darcy flow conditions,” *Journal of Petroleum Science and Engineering*, vol. 127, pp. 398–408, 2015.
- [28] L. Wang, Z. Li, C. D. Adenutsi, and C. Wang, “An experimental study of the effect of three metallic oxide nanoparticles on oil-water relative permeability curves derived from the JBN and extended JBN methods,” *Journal of Petroleum Science and Engineering*, vol. 233, Article ID 107257, 2020.
- [29] H. Sidiq, “UPSCALING gas-water relative permeability measurements from ambient to reservoir CONDITIONS,” *Journal of Porous Media*, vol. 22, no. 8, pp. 975–985, 2019.
- [30] X. Zhao, Z. Qiu, B. Sun, S. Liu, X. Xing, and M. Wang, “Formation damage mechanisms associated with drilling and completion fluids for deepwater reservoirs,” *Journal of Petroleum Science and Engineering*, vol. 173, pp. 112–121, 2019.
- [31] L. Shunshu, P. Yuhui, W. Xinshan et al., “Characteristics and classification of gas-water relative permeability curves of tight sandstone reservoirs in Sulige gas field,” *Journal of Xi’an Shiyou University(Natural Science Edition)*, vol. 30, no. 6, pp. 55–61+9, 2015.
- [32] W. Tian, A. Li, X. Ren, and Y. Josephine, “The threshold pressure gradient effect in the tight sandstone gas reservoirs with high water saturation,” *Fuel*, vol. 226, pp. 221–229, 2018.
- [33] Y. Guo, H. Liu, A. Gao, Z. Hu, X. Hue, and H. Zhou, “Research and application effect analysis on water-drive characteristic curve for water-drive gas reservoir,” *Oil Drilling & Production Technology*, vol. 35, no. 3, pp. 63–65, 2013.
- [34] H. Liu, *Principles of Reservoir Engineering*, China University of Petroleum Press, Dongying, China, 2015.



## Research Article

# A Method to Evaluate Gas Content with Coalbed Methane Reservoir Based on Adsorption Theory and Production Analysis

Ruyong Feng 

CNOOC Research Institute Ltd., CNOOC Building, Yard 6, Taiyanggong South Street, Chaoyang District, Beijing, China

Correspondence should be addressed to Ruyong Feng; fengruiyong@qq.com

Received 17 January 2022; Revised 25 February 2022; Accepted 29 April 2022; Published 3 June 2022

Academic Editor: Xiang Zhou

Copyright © 2022 Feng Ruyong. This is an open access article distributed under the Creative Commons Attribution License, which permits unrestricted use, distribution, and reproduction in any medium, provided the original work is properly cited.

In the process of coalbed methane development, the gas content not only determines the reserves of methane in coal reservoir but also is the most important geological parameter affecting the production of coalbed methane. The gas content directly determines whether coalbed methane can be developed efficiently. However, in the current development evaluation process, it is very difficult to accurately predict the gas content in coal seams. An efficient and accurate method to predict gas content has not been found yet. This is mainly restricted by the development mode and technology of coalbed methane. In the current low-cost development model, gas content test data are relatively scarce. Under such circumstances, it is difficult to accurately evaluate the distribution of CBM gas content in the whole area. At the same time, the gas content of coalbed is the key parameter for efficient development of coalbed methane. Under normal circumstances, gas content heterogeneity will result in a large gap between development effects in different regions. At present, there is no evaluation method for gas content parameters of coal reservoir. Under this background, the key parameters of coalbed methane development in southern Qinshui Basin were evaluated. On the basis of systematically summarizing and understanding the development law of coalbed methane in different types of coal reservoirs, a gas content evaluation method based on adsorption theory and production dynamic analysis is proposed. Combined with the coalbed methane production model and isothermal adsorption model, the critical desorption pressure can be calculated accurately by using the bottom hole pressure when casing pressure occurs in production wells. The critical desorption pressure correction model of coalbed methane was innovatively established. Langmuir equation was used to accurately characterize the adsorption characteristics of coalbed methane. Forming a new method for gas content prediction in the case of fewer coring wells. The gas content evaluation technology coupled with isothermal adsorption theory and production dynamic analysis saves the development cost of coalbed methane and improves the prediction accuracy of coal seam gas content in noncoring wells. At the same time, there is a good relationship between the predicted results and the measured gas content at well points. The coincidence rate reached 97.37%. This technology can effectively improve the prediction accuracy of coal seam gas content. This technique is suitable for the productivity evaluation of coalbed methane reservoir. It can also provide scientific basis for the development and reserve evaluation of coalbed methane reservoirs at home and abroad.

## 1. Introduction

Coalbed methane is the methane gas in coal seam. There are two main ways of coalbed methane occurrence in coal seam: free and adsorption. The methane in coal seam is mainly in adsorption state, and there is little free gas. The gas content and structure are the main factors affecting CBM production [1]. Whether in the exploration stage or in the development stage, how to evaluate the gas content of coalbed methane becomes particularly important. Coal is an organic reservoir, and CBM reserves are calculated by gas content rather than saturation of free gas in pores. At present, coalbed methane

is a kind of gas field with poor economic benefit and needs to be developed with low cost. In the process of development, gas content testing is less. It is necessary to find an effective method to evaluate the distribution of gas content in the CBM reservoir.

Different scholars have carried out a lot of research work on the adsorption characteristics of methane molecules by coal. Anderson et al. first measured the desorption/adsorption isotherms curve of methane, nitrogen, carbon dioxide, and other gases in coal seams by volume method and found hysteresis [2]. Joubert et al. perfected the volume method and established the relationship between adsorption capacity

and coal moisture content [3]. Kim further established the adsorption correlation formula including moisture, gray level, coal rank, pressure, and temperature, which is mainly used to evaluate the adsorption of shallow and low pressure coalbed methane [4]. Langmuir isothermal adsorption equation is widely used at present. So far, for coal samples filled with pure gas of different coal rank and geological age, all adsorption data measured in experiments can actually be described by Langmuir equation [5]. Gregory and Karen also found the limitations of Langmuir model through experiments. The adsorption characteristics of water-bearing coal seam under high pressure were studied by volume method to simulate formation temperature, and the adsorption experimental data were correlated with Langmuir model. The results show that the experimental gas content is higher than the actual gas content. The desorption isotherm measured in the experiment has obvious hysteresis phenomenon. The experimental results show that Langmuir model is not suitable for fitting isothermal adsorption experimental data under high pressure [6]. An adsorption model with different concepts is needed to study the effect of temperature on gas content of coalbed methane. Langmuir adsorption theory assumes that adsorbed gas covers the surface of coal matrix. Dubinin's theory is basically contrary to Langmuir's theory. It assumes that adsorbed gas fills the pores of coalbed. Considering the influence of temperature on adsorbed gas volume, two equations, namely, Dubinin-Astakhov equation and Dubinin-Radushkevich equation, are derived according to Dubinin theory. Both equations show that the adsorbed gas volume decreases exponentially with temperature. Dubinin-Astakhov equation and Dubinin-Radushkevich equation can correct isothermal adsorption curve and CBM content to another appropriate temperature condition by Dubinin equation and Kirchhoff equation. Two constants in Dubinin-Radushkevich equation and three constants in Dubinin-Astakhov can be calculated using the adsorption data measured in the experiment. The CBM content at the required temperature and pressure is then calculated [7]. Freundlich equation can be used for monolayer adsorption, especially in medium pressure range. Its form is relatively simple, and calculation is also more convenient, so it is widely used. However, the constants in the equation have no clear physical significance and cannot explain the mechanism of adsorption. The above equations are used to characterize the adsorption behavior of coal to methane molecules. Through analysis and comparison of the assumptions, operating conditions, and characterization equations of different models, it is believed that Langmuir equation can accurately characterize the adsorption characteristics of coalbed methane. Methane is adsorbed on the surface of coal matrix by single molecular layer, and the correlation coefficient of isothermal adsorption curve fitted by measured adsorption amount under different pressures is greater than 0.99, accurately characterizing the adsorption behavior of coalbed methane. Based on the isothermal adsorption curve of coal seam measured by exploration well, the corresponding critical desorption pressure is calculated according to the gas content of coal seam. Based on the relationship between measured gas content and critical desorp-

tion pressure, gas content can be calculated by critical desorption pressure.

There are currently three methods for predicting gas content to supplement evaluation. One is to evaluate the gas content of reservoir by inversion method of elastic parameters of seismic data. Xiaolong et al. selected coal samples with different coal rank and coal quality, combined with laboratory testing and actual drilling data analysis, and determined that the modulus attribute was sensitive to the detection of ton coal gas content. At the same time, density is more sensitive to gas content than compressional wave velocity. Based on this, the inversion method of coalbed methane three-parameter elastic modulus (relative change of Lamet constant, shear modulus, and density) based on seismic data was established [8]. Xinping and Fuyi analyzed that seismic data and coalbed AVO technology can be used to predict the reserve enrichment and high permeability positions of reservoirs, which can provide a basis for deployment of exploration and development wells. Using logging data to conduct preevaluation and reevaluation before and after fracturing in coalbed methane wells can avoid capital waste, achieve the goal of improving the success rate of drilling and single well production, and achieve commercial production [9]. Jinshan and Weiyao analyzed the existing CBM drilling data and 3D seismic data. Through correlation fitting, the prediction model of floor elevation and gas content of No. 8 coal seam in Karoo Basin of Africa and the predicted gas content of No. 8 coal seam are obtained, and then compared with the measured gas content of the coal seam drilling data, the prediction accuracy is more than 85% [10]. Zijing et al. proposed an improved BP neural network prediction method characterized by artificial bee colony algorithm. The prediction results are basically consistent with the variation trend of gas content in each well, and the prediction accuracy is high [11]. Lutong et al. found a seismic sedimentology method to reveal the sedimentary microfacies of high frequency sequences in the coal-bearing Shanxi Formation of the Zhongyu area in the central-western of the Qinshui Basin [12]. The other is to evaluate gas content by logging characteristics. The literature of Jie et al. is based on the geological, logging, and coal test data of No. 3 and No. 15 coal seams in the southern Qinshui Basin. The gas content is calculated by regression analysis, Langmuir coal rank equation, KIM method, and BP neural network method, and the results are compared. Generally, the logging interpretation method would have a good application effect to evaluate the coalbed methane content in the south block of Qinshui Basin [13]. Zhang et al. proposed a zonal gas content prediction method based on the impact of geological factors on gas content. Combined with a large number of laboratory test data, the influence of sedimentary, structural, and hydrodynamic conditions on the gas content of coal seam is analyzed, and the main controlling factors are obtained. Through fuzzy hierarchy analysis, the difference of geological factors is quantified and the geological partition is realized. Principal component analysis is introduced in each partition. A large number of conventional logging curves in the field were fully utilized to conduct multiple regression and establish a prediction model for coal seam gas content

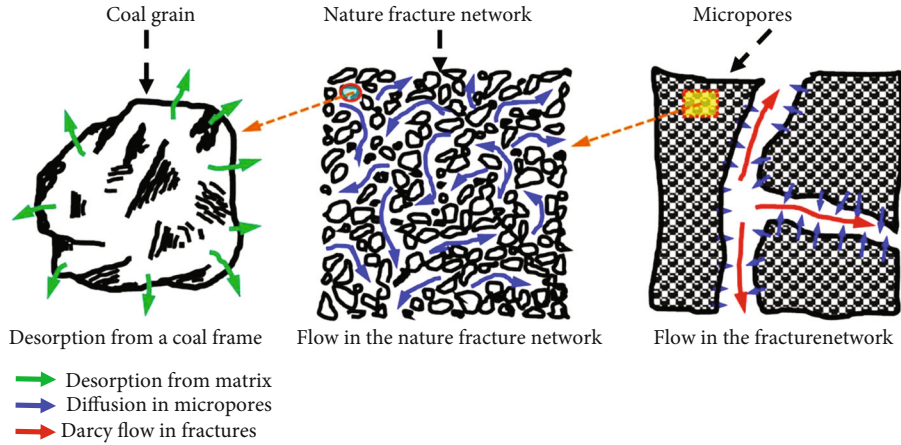


FIGURE 1: Desorption and diffusion in the matrix and Darcy flow in the fracture.

[14]. Li et al. proposed to use the cross entropy algorithm to determine the global optimal parameters of support vector machine and build the best prediction model to predict the porosity, permeability, and gas content of an unexplored block in the southern Qinshui Basin driven by well-seismic joint data [15]. In order to solve the problem of quantitative interpretation of coal seam gas content, Chi et al. used coal logging data and coal core desorption data as input and output parameters to build a depth confidence network and then predict coal seam gas content. The results show that depth confidence network has the best prediction effect, followed by probabilistic statistical method, and SVM is the worst [16]. Based on the logging response characteristics of coal seam gas content, Tao et al. analyzed the correlation between logging parameters and gas content, proposed the logging parameter optimization strategy combining mean impact value technology and least squares support vector machine technology, optimized the logging parameters, and constructed a set of logging model suitable for coal seam gas content prediction [17]. Banerjee and Chatterjee developed a methodology to identify prospective coal seam by establishing multiple regression models between geophysical well log parameters and organic and inorganic contents from laboratory-tested core samples for one seam [18]. The third is to establish the regression relationship between thickness, depth, thickness, and gas content. Min et al., taking Jincheng mining area as an example, analyzed the influencing factors of CBM content based on the basic theory of CBM geology and the improved slope degree of grey incidence. Furthermore, the coalbed methane content is predicted by grey multivariable static model GM(0,N) and compared with the results of multiple regression analysis. The results show that the main influencing factors of CBM content determined by grey correlation analysis with improved slope correlation degree are reliable. The prediction of coal seam gas content by GM(0,N) model requires less sample data, simple principle, convenient calculation, and high prediction accuracy [19]. Xiangrong and Haijiang analyzed the control effect of coal seam gas content based on the geological data of coal field exploration and borehole test data of coalbed methane wells, combined with the characteristics of regional geological back-

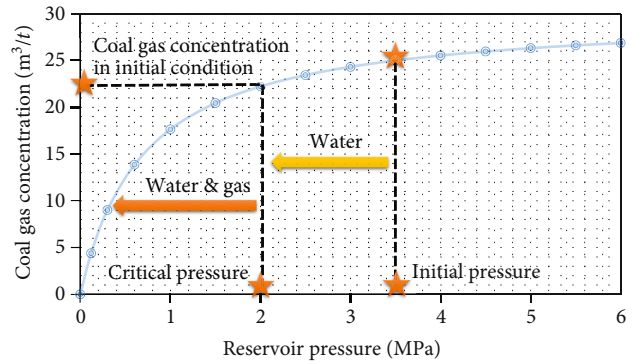


FIGURE 2: Gas content change during coalbed methane development.

ground. Through correlation analysis and multivariate statistics, the main controlling factors of coal seam gas content are obtained. The mathematical model of coalbed methane gas content prediction is established, which has important guiding value for coalbed methane development [20]. According to Xiaoming et al., taking the geological strength index as the link, the thickness, gas content, permeability, and brittleness index of different coal structures in a coal seam section were quantitatively characterized. Based on an analytical hierarchy process, a system for the evaluation of coal reservoir CBM production potential was constructed considering different coal structure in coal seam sections [21]. Hui et al. introduce a parameter fault scale to quantify the scale of faults, which is described by fault length, fault throw, and the investigated area and propose a horizontal grid method to determine the faulting influence on current gas content [22].

## 2. Coalbed Methane Adsorption Model and Applicability

### 2.1. Assumptions

- (1) The adsorption model of gas is isothermal adsorption; it follows the isothermal adsorption equation [23]

- (2) The adsorption of gas in coalbed methane is unsaturated
- (3) The gas present in coal seams is only methane
- (4) The temperature in the coal seam is constant
- (5) The boundary of reservoir is closed boundary with no external gas source supply and no gas escape

**2.2. Adsorption Model.** Adsorbed gas is adsorbed in coal matrix in a dynamic equilibrium way. In the development process, with the decrease of reservoir pressure, adsorbed gas is gradually resolved from adsorbed state into free gas. Free gas flows into the natural fracture system through diffusion, and eventually methane gas flows into the hydraulic fracture through the natural fracture and eventually into the wellbore (Figure 1) [24].

For unsaturated coalbed methane reservoirs, in the original state, the reservoir pressure is greater than the critical desorption pressure. During production, the pressure in the formation is gradually reduced through an earlier drainage process. When the formation pressure decreases to the critical desorption pressure, the gas begins to desorption and enters into the natural fracture system to participate in the flow and is finally mined (Figure 2). Therefore, the production system of drainage and production is the characteristic of coalbed methane development.

The adsorption curve of high-rank coal in southern Qinshui basin belongs to type I. Langmuir isothermal adsorption equation can be used to describe the adsorption and desorption of coalbed methane. According to the T2 spectrum characteristics of coal samples, the pores in the coal seam are mainly dominated by adsorption pores, followed by seepage pores and small fracture pores (Figure 3). According to the isothermal adsorption test data, the fitting relationship between the isothermal adsorption test data of coalbed methane in Qinshui Basin and Langmuir isothermal adsorption curve is very good (Figure 4 and Table 1).

The decision coefficient is defined as

$$DC = b_i^2 + 2 \sum_{j \neq i} b_i r_{ij} b_j. \quad (1)$$

Based on isothermal adsorption theory, Langmuir equation was used to establish the calculation method of gas content. Langmuir equation can be expressed as

$$V = \frac{PV_L}{P + P_L}. \quad (2)$$

The coal gas content corresponding to the original reservoir pressure is the maximum adsorption capacity of coal seam, that is, the saturated gas content. In unsaturated coalbed methane reservoirs, the measured gas content is less than saturated gas content. When the coal reservoir pressure decreases to the corresponding pressure of the gas content, the coalbed methane begins to change into free state after coal desorption. Therefore, the measured gas content of coal seam corresponds to the critical desorption pressure. Gas

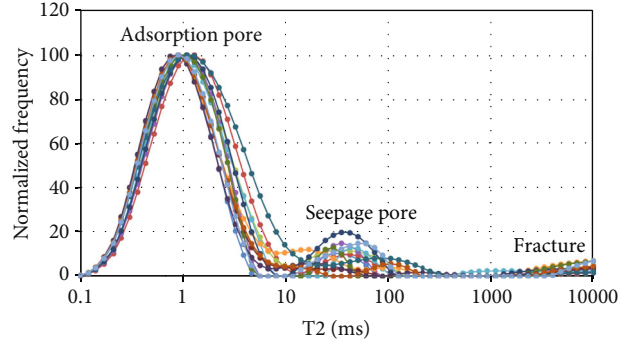


FIGURE 3: T2 spectrum characteristics of No. 3 coal in SZ block.

content calculation formula (2) shows that when the pressure is the critical desorption pressure, the corresponding gas content is the original gas content of coal seam. The gas content of coal seam can be calculated according to the critical desorption pressure.

$$V_i = \frac{P_c V_L}{P_c + P_L}. \quad (3)$$

**2.3. Method Application Conditions.** The method presented in this paper can accurately predict the gas content of the block, but it also needs to be combined with relevant geological parameters and production data. Therefore, in the process of use, the target area needs to have certain conditions:

- (1) There are parameter wells evenly distributed throughout the target area, and the isothermal adsorption test is carried out for parameter wells. The density of parameter wells determines whether the isothermal adsorption equation is accurate
- (2) The reservoir depth and drilling technology are basically the same in the whole area, which is conducive to reducing the error of converting bottom hole flow pressure to critical desorption pressure

### 3. Gas Content Calculation

According to Equation (3), the most important parameter in the calculation of gas content is the formation pressure near the wellbore when gas is seen. According to the percolation mechanism of the reservoir, the pressure is funneled in the formation, with the lowest pressure near the bottom and the highest pressure at the boundary. Therefore, the formation pressure at the bottom of the well is the critical desorption pressure of the coal seam. However, there is an error between the critical desorption pressure and the formation pressure at the bottom of the hole when gas is detected, because the flow cannot be accurately monitored instantaneously. How to correct this error is the key to calculate the critical desorption pressure accurately.

At present, there are two main errors in measuring bottom hole flow pressure when gas is detected. One is affected by the well storage effect. When coalbed methane around the



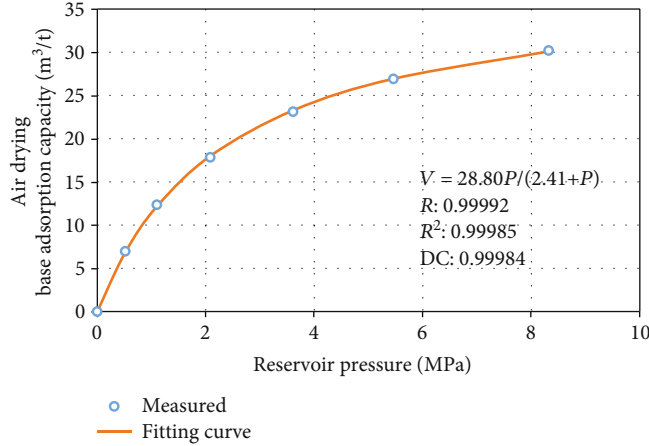


FIGURE 4: Fitting diagram of gas content in SZ block.

TABLE 1: Data from 7 samples from 2 wells.

The sample	The correlation coefficient	Correlation coefficient squared	Decision coefficient
Sample 1	0.9999	0.9999	0.9998
Sample 2	0.9999	0.9999	0.9998
Sample 3	0.9999	0.9997	0.9997
Sample 4	0.9995	0.9991	0.9991
Sample 5	0.9997	0.9995	0.9995
Sample 6	0.9947	0.9894	0.9889
Sample 7	0.9996	0.9992	0.9992

well begins to desorption into the wellbore, it needs to rise to the oil casing annulus through the wellbore liquid column and then be detected by the wellhead pressure gauge. This process can result in delayed detection. When we detect casing pressure at the wellhead, it is already past the well storage stage, which can cause errors. The second is the accuracy of the wellhead pressure gauge. When the pressure range in the wellbore is small, the pressure gauge cannot detect the pressure. When the pressure is detected by the pressure gauge, the bottom hole pressure is already below the critical desorption pressure. Therefore, the data need to be corrected when calculating the critical desorption pressure.

Through the analysis of the causes of the errors, it can be found that the main factors affecting the test errors include pressure gauge specifications, well structure, and coal seam depth. Under the same conditions, linear regression can be used for correction (Figure 5). The same regression equation can be used to correct critical desorption pressure in the same block, where pressure gauge specifications, well structure, and depth are essentially the same.

According to Langmuir isothermal equation and linear regression equation, gas content and can be expressed as

$$V_c = \frac{aPV_L + bV_L}{aP + P_L + b} \tag{4}$$

### 4. Field Application

4.1. *Gas Content Calculation in SZ Block.* SZ block is located in the south of Qinshui Basin. The main coal seam for development is No. 3 coal of Shanxi Formation. The block is a monoclinical structure, low in the east and high in the west, gentle in the east, fault-fold area in the middle, and relatively developed faults in the north. The sedimentary environment is delta plain facies, located in interdistributary bay, which is favorable for coal forming environment.

4.2. *Calculation of Relationship between Gas Content and Bottom Hole Pressure in Gas Well.* The block covers an area of 388.3 km<sup>2</sup>, but there are only 20 isothermal adsorption test wells. The test data include gas content and critical desorption pressure (Table 2).

The critical desorption pressure and gas content were regressed by the test data in Table 2. The critical desorption pressure has a good correlation with gas content, and it accords with Langmuir isothermal adsorption curve equation (Figure 6). This indicates that the adsorption properties of coal reservoirs in the block are similar with little difference. The gas content can be calculated using the critical desorption pressure by regression Langmuir equation. Langmuir equation of SZ block is

$$V = \frac{26.32P}{1.65 + P} \tag{5}$$

Currently, 9 of the wells listed in Table 2 are in production. All 9 wells have produced gas (Table 3). The bottom hole pressure of the whole area can be corrected by the bottom hole pressure and the measured critical desorption pressure of 9 wells (Figure 7). Through regression, the relationship between critical desorption pressure and bottom hole flow pressure when gas is seen is

$$P_c = 1.3050P_g - 0.0435. \tag{6}$$

According to formulas (5) and (6), the relationship between gas content in SZ block of Qinshui basin and



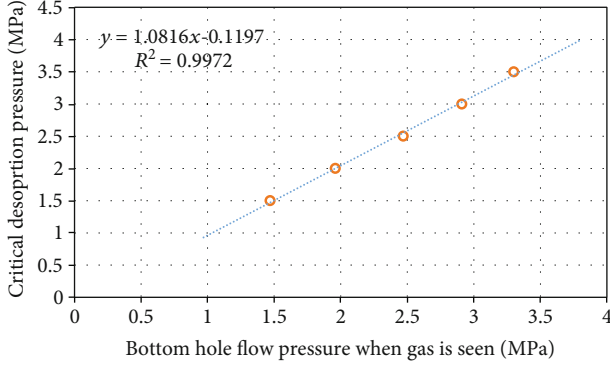


FIGURE 5: Linear regression corrects critical desorption pressure.

TABLE 2: Critical desorption pressure and gas content of SZ block.

Well name	Critical pressure (MPa)	Gas content (m <sup>3</sup> /t)
SZN02	0.63	8.33
SZN05	0.61	6.82
SZN09	0.99	7.18
SZN16	1.63	14.27
SZS01	0.93	9.27
SZS02	0.80	8.48
SZS03	1.63	14.13
SZS04	0.69	8.79
SZS05	0.70	7.50
SZS06	1.21	7.59
SZS07	3.32	19.16
SZS09	0.79	11.01
SZS11	2.30	14.91
SZS11-1	2.42	13.71
SZS12	0.59	7.50
SZS13	0.91	9.83
SZS15	0.20	2.34
SZS17	1.90	13.06
SZS19	1.80	15.50
SZS20	0.31	4.90

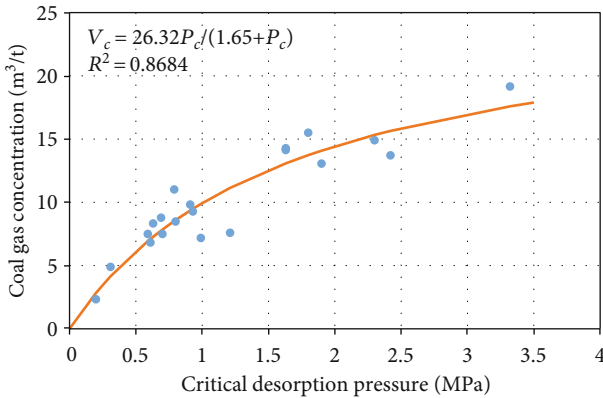


FIGURE 6: Relationship between critical desorption pressure and gas content.

TABLE 3: Critical desorption pressure and bottom hole pressure at begin of gas flow.

Well name	Critical pressure (MPa)	BHP when gas is seen (MPa)
SZN16	1.63	1.25
SZS01	0.93	0.71
SZS03	1.63	1.08
SZS04	0.69	0.61
SZS06	1.21	0.98
SZS11	2.30	1.66
SZS13	0.91	0.52
SZS17	1.90	1.50
SZS20	0.31	0.21

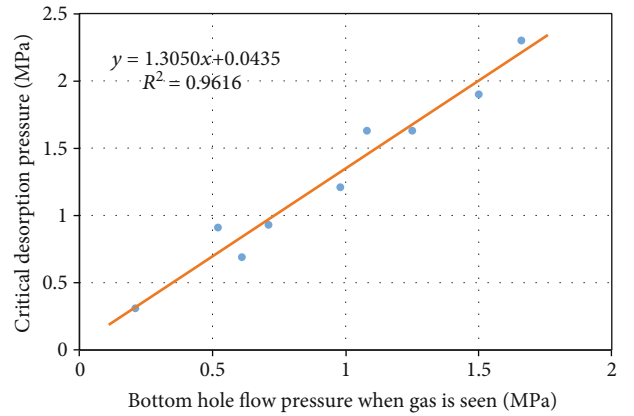


FIGURE 7: Relationship between critical desorption pressure and bottom hole pressure at begin of gas flow.

bottom flow pressure of gas well can be obtained as follows:

$$V_c = \frac{34.3476P_g - 1.1449}{1.3050P_g + 1.6065} \quad (7)$$

4.3. *The Calculation Results.* Take the calculation results of No. 3 coal in block W of SZ block as an example. Block W covers an area of 21.2 km<sup>2</sup>, with two gas content test wells and 171 drainage and production wells, 160 of which have gas. The calculated and tested gas content results of the two production wells are shown in Table 4. A total of 136 gas-producing wells with smooth production curve were selected. According to the bottom hole pressure and formula (7) of 136 wells, the initial gas content data of each well point were obtained, and the gas content of the plane of block W was evaluated (Figure 8).

4.4. *Gas Content Calculation in pH Block.* pH block is located in the southeast slope belt of Qinshui Basin, and the main coal seam is No. 3 coal of Shanxi Formation. pH block is located in delta front, favorable coal forming environment, and thick coal belt development area. The block area is 17 km<sup>2</sup>. The structure of the demonstration area is simple, with north-

TABLE 4: Comparison of calculated and tested gas content in block W.

Well name	Tested gas content (m <sup>3</sup> /t)	Calculated gas content (m <sup>3</sup> /t)	Error (%)
SZS01	9.27	9.38	1.2
SZS03	14.13	14.09	0.3

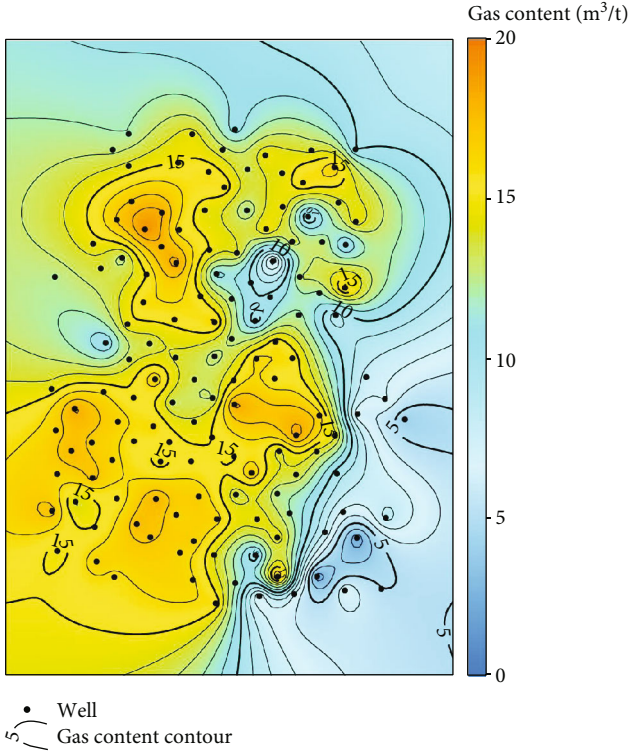


FIGURE 8: Gas content contour of W block for 3# coal seam of SZ block.

south folds and pH syncline in the middle. The top surface of the area is low in the middle and high in the two wings.

4.5. Calculation of Relationship between Gas Content and Bottom Hole Pressure in Gas Well. The correlation between the critical desorption pressure and the bottom flow pressure of No. 3 coal in pH block is analyzed through the test data of parameter well. The linear regression diagram of critical desorption pressure and bottom flow pressure in gas well was established (Figure 9). Through correlation analysis, the relationship between critical desorption pressure and bottom flow pressure of No. 3 coal in pH block can be obtained as follows:

$$P_c = 1.3263P_g + 0.7131. \quad (8)$$

There are a lot of gas content test data in pH block. Through the laboratory gas content test data, isothermal adsorption curves of different areas can be obtained. Due to the small area of the whole pH block, the coal seam is evenly distributed and the heterogeneity is weak, and there

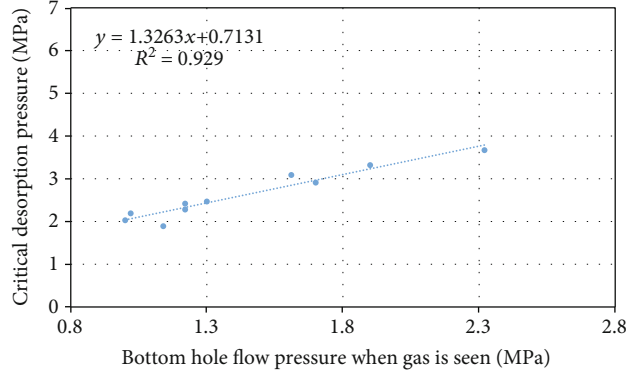


FIGURE 9: Relationship between critical desorption pressure and bottom hole pressure at begin of gas flow.

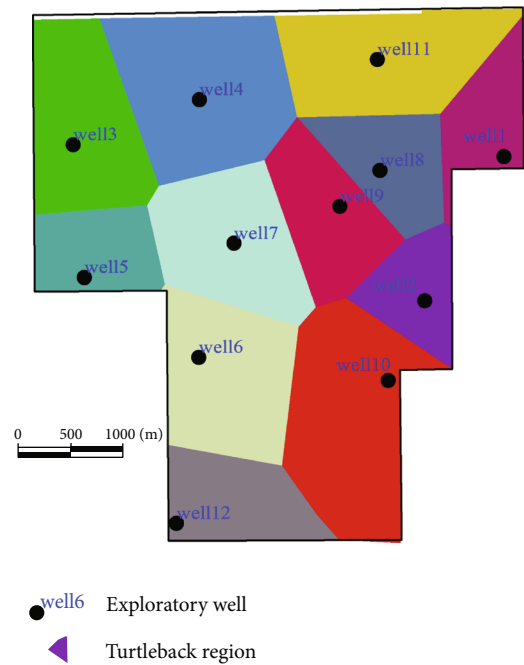


FIGURE 10: Isothermal adsorption curves of different regions with pH block.

is no fault in the whole area. Geologically, the pH block can be considered as a whole. Therefore, the zoning is mainly based on the location of the test well. The well control range of the test well is used as the basis for zoning. Different isothermal adsorption curves were used for each small area to calculate data more accurately (Figure 10).

4.6. The Calculation Results. Combined with the isothermal adsorption curves of each block and formula (8), the gas content of the current production wells in pH block can be calculated, and then, the gas content of the whole area can be evaluated (Figure 11).

The calculated results are compared with the measured results. The error can be controlled within 8% by using this method. Compared with the six wells, the average error of gas content calculation by this method is 2.63%. The method provided in this paper has high accuracy in calculation

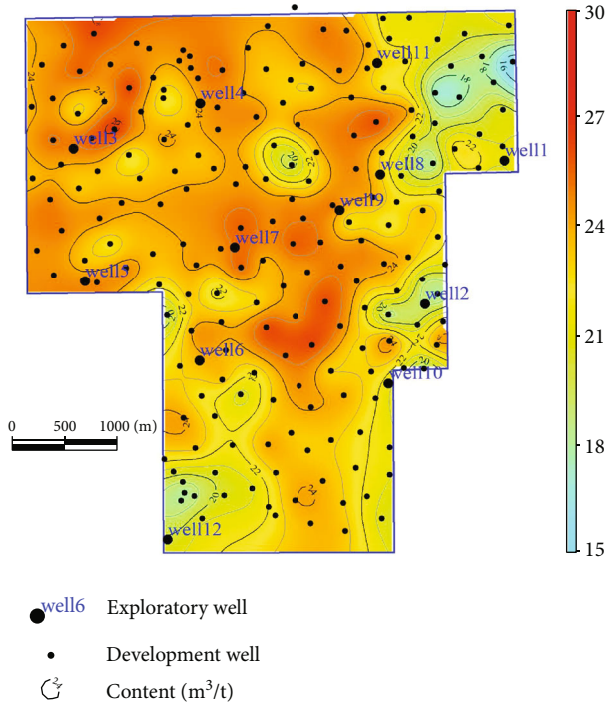


FIGURE 11: Calculation results of gas content in pH block.

TABLE 5: Comparison of measured gas content with calculated gas content.

Well name	Measured gas content (m <sup>3</sup> /t)	Calculated gas content (m <sup>3</sup> /t)	Error
Well 1	30.9	29.6	4.2%
Well 2	27.6	28.1	1.8%
Well 3	27.8	27.6	0.7%
Well 4	15.91	15.75	1.0%
Well 5	10.73	10.63	0.9%
Well 6	9.45	10.13	7.2%

(Table 5). The error in Table 5 are defined as

$$\text{Error} = \frac{|\text{Measured gas content} - \text{Calculated gas content}|}{\text{Measured gas content}} \times 100\%. \quad (9)$$

## 5. Article Innovation

In the development of coalbed methane reservoirs, gas content has always been an important parameter for evaluating coal reservoirs. However, due to the limitations of the low-cost development model, the measured data of gas content are less. Most of the development wells use indirect forecasting. There are currently three evaluation methods, but they are all pure geological evaluations, ignoring the production data of coalbed methane wells. In this paper, an innovative method is proposed to combine experimental testing with production dynamics to calculate the gas content of coal seams. There are two main innovation points:

- (1) Through the analysis of T2 spectroscopic characteristics of coal samples, the pore distribution characteristics of coal reservoirs are clarified. Combined with the isothermal adsorption test data, the applicability of the Langmuir isothermal adsorption equation is verified. This is a prerequisite for the use of methods
- (2) By inverting the adsorption-desorption process in the coal seam, the gas content of the coal seam under the original conditions was obtained. By means of the critical desorption pressure of the coal seam and the bottom hole pressure of the gas appears under the same completion method of the proposed contract block, the bottom hole pressure of the gas appears can be corrected and the prediction accuracy of the method can be improved

## 6. Conclusion

On the basis of systematically summarizing and understanding the development law of different types of coal reservoirs, this paper puts forward an evaluation method of coal seam gas content based on adsorption theory. The critical desorption pressure is calculated by bottom hole pressure when casing pressure occurs in production well. Langmuir equation was used to accurately characterize the adsorption characteristics of coalbed methane. A new method for accurately calculating coal seam gas content based on production data is developed. Through the above analysis, the following conclusions can be summarized.

- (1) Langmuir isothermal adsorption equation can be used to describe the adsorption and desorption of coalbed methane in high-rank coal in southern Qinshui Basin. The pores in coal seam are mainly dominated by adsorption pores, followed by seepage pores and small fissure pores. The measured data show that the fitting relationship between isothermal adsorption test data and Langmuir isothermal adsorption curve is very good
- (2) The critical desorption pressure is different from the bottom hole flow pressure at gas exposure. This difference is mainly affected by three factors: pressure gauge specification, well structure, and coal seam depth. Within the same block, the three factors are basically the same. The bottom hole pressure at gas exposure can be corrected to the critical desorption pressure by linear regression
- (3) The gas content error of reservoir calculated by the corrected bottom hole pressure at gas exposure of gas well is small. In the case of abundant isothermal adsorption curves in the whole region, the calculated results are compared with the measured results. Compared with the six wells, the average error of gas content calculation by this method is 2.63%. The method provided in this paper has high accuracy in calculation

### Symbols

$V$ : Volume gas content,  $\text{m}^3/\text{ton}$   
 $P$ : Reservoir pressure, MPa  
 $V_L$ : Langmuir volume,  $\text{m}^3/\text{ton}$   
 $P_L$ : Langmuir pressure, MPa  
 $P_O$ : Adsorbent saturated vapor pressure, MPa  
 $V_m$ : BET equation for monolayer adsorption capacity,  $\text{m}^3/\text{ton}$   
 $C$ : Constants related to the heat of adsorption and the liquefaction of the adsorbed gas  
 $V_0$ : Langmuir volume under the standard conditions,  $\text{m}^3/\text{ton}$   
 $R$ : Universal gas constant,  $\text{MPa}\cdot\text{m}^3/(\text{lb}\cdot\text{mole}\cdot\text{k})$   
 $T$ : Absolute temperature, k  
 $\beta$ : Adsorption gas affinity coefficient, dimensionless  
 $E$ : Characteristics of the energy,  $\text{MPa}\cdot\text{m}^3/(\text{lb}\cdot\text{mole})$   
 $n$ : Integer, usually between 1 and 4, dimensionless  
 $V_f$ : Freundlich coefficient 1, dimensionless  
 $n_f$ : Freundlich coefficient 2, dimensionless  
 $V_i$ : Initial volume gas content,  $\text{m}^3/\text{ton}$   
 $P_c$ : Critical desorption pressure, MPa  
 $V_c$ : Volume gas content,  $\text{m}^3/\text{ton}$   
 $a$ : Regression coefficient 1, dimensionless  
 $b$ : Regression coefficient 2, dimensionless  
 $DC$ : The decision coefficient  
 $b_i$ : Regression coefficient  
 $r_{ij}$ : Correlation coefficient.

### Data Availability

The data are all original; if you need any data in the article, please send me an email (email address: fengruiyong@qq.com).

### Conflicts of Interest

The author declares that there are no conflicts of interest.

### References

- [1] S. Tao, D. Z. Shang, H. Hu, Y. M. Lv, and X. L. Zhao, "Analysis on influence factors of coalbed methane wells productivity and development proposals in southern Qinshui Basin," *Journal of China Coal Society*, vol. 36, no. 2, pp. 194–198, 2018.
- [2] R. B. Anderson, J. Bayer, and L. Hofer, "Equilibrium sorption studies of methane on Pittsburgh seam and Pocahontas no. 3 seam coal," *Advances in Chemistry*, vol. 55, no. 24, pp. 386–399, 1966.
- [3] J. I. Joubert, C. T. Grein, and D. Bienstock, "Sorptions of methane in moist coal," *Fuel*, vol. 52, no. 3, pp. 181–185, 1973.
- [4] A. G. Kim, *Estimating Methane Content of Bituminous Coal Beds from Adsorption Data*, US Bureau of Mines Report of Investigations, 1977.
- [5] Y. Dan, J. P. Seidle, and W. B. Hanson, *Gas Sorption on Coal and Measurement of Gas Content*, Instituto Fernando el Católico, 1993.
- [6] J. B. Gregory and C. R. Karen, "Hysteresis of methane coal sorption isotherms," in *SPE Annual Technical Conference and Exhibition*, pp. 375–383, New Orleans, Louisiana, 1986.
- [7] C. R. Clarkson, R. M. Bustin, and J. H. Levy, "Application of the mono/multilayer and adsorption potential theories to coal methane adsorption isotherms at elevated temperature and pressure," *Carbon*, vol. 35, no. 12, pp. 1689–1705, 1997.
- [8] G. Xiaolong, L. Xuan, D. Chunmeng, B. Haijun, X. Xuhua, and X. Jing, "Research on CBM geophysical prediction," *Natural Gas Geoscience*, vol. 28, no. 2, pp. 287–295, 2017.
- [9] C. Xinpeng and C. Fuyi, "A discussion on the technical model guided by prediction in CBM exploration and development in China," *China Offshore Oil and Gas*, vol. 25, no. 5, pp. 31–34, 2013.
- [10] L. Jinshan and Z. Weiyao, "A prediction for the gas content of coalbed methane in African Karoo basin based on 3D seismic bottom elevation simulation," *China Mining Magazine*, vol. 27, no. 12, pp. 173–182, 2018.
- [11] Z. Zijing, W. Haibo, and Z. Pingsong, "Prediction of coal seam gas content based on ABC-BP model," *Coal Geology & Exploration*, vol. 49, no. 2, pp. 152–158, 2021.
- [12] C. Lutong, C. Suoliang, and Y. Yanbin, "Application of seismic sedimentology in predicating sedimentary microfacies and coalbed methane gas content," *Journal of Natural Gas Science and Engineering*, vol. 69, article 102944, 2019.
- [13] H. Jie, Z. Changchun, Y. Yuqing, Z. Guohua, and W. Wenwen, "Comparison study on evaluation methods of coalbed methane gas content with logging interpretation," *Coal Science and Technology*, vol. 43, no. 12, pp. 157–161, 2015.
- [14] C. Zhang, Y. Wang, N. Xiaoming, and T. Beijing, "Research on prediction method of coal seam gas content based on geological division," *Journal of Henan Polytechnic University (Natural Science)*, vol. 36, no. 2, pp. 22–29, 2017.
- [15] B. Li, H. Hui, C. Xiangqian, and Y. Dezhi, "Prediction of coalbed methane parameters driven by well-seismic data," *Journal of Heilongjiang University of Science & Technology*, vol. 29, no. 2, pp. 196–200, 2019.
- [16] H. Chi, L. Xinhu, L. Xiaojun, L. Jian, and G. Jie, "Research for coal seam gas content well logging interpretation based on deep belief network," *Coal Geology Of China*, vol. 33, no. 3, pp. 70–78, 2021.
- [17] C. Tao, Z. Zhansong, Z. Xueqing et al., "Prediction model of coalbed methane content based on well logging parameter optimization," *Coal Geology & Exploration*, vol. 49, no. 3, pp. 227–235, 2021.
- [18] A. Banerjee and R. Chatterjee, "A methodology to estimate proximate and gas content saturation with lithological classification in coalbed methane reservoir, Bokaro field, India," *Natural Resources Research*, vol. 30, no. 3, pp. 2413–2429, 2021.
- [19] T. Min, Z. Yongjun, and Z. Pengcheng, "Application of grey system theory in prediction of coalbed methane content," *Coal Geology & Exploration*, vol. 36, no. 2, pp. 24–27, 2008.
- [20] L. Xiangrong and Z. Haijiang, "Analysis of main controlling factors of gas content for no. 4 coal seam in Huijiahe-Xiaozhuang mine field and modeling prediction," *China Coalbed Methane*, vol. 14, no. 2, pp. 3–8, 2017.
- [21] N. Xiaoming, T. Xuebin, Y. Sen, X. Bin, and F. Xiaokang, "Evaluation of coal reservoir coalbed methane production potential in considering different coal structures in a coal seam section: a case study of the Shizhuang north block in the Qinshui basin," *Environmental Earth Sciences*, vol. 80, no. 19, pp. 1–6, 2021.
- [22] W. Hui, Y. Yanbin, H. Chencheng, L. Dameng, and C. Yidong, "Fault development characteristics and their effects on current

gas content and productivity of no. 3 coal seam in the Zhengzhuang field, southern Qinshui basin, North China,” *Energy & Fuels*, vol. 35, no. 3, pp. 2268–2281, 2021.

- [23] C. R. Clarkson and R. M. Bustin, “The effect of pore structure and gas pressure upon the transport properties of coal: a laboratory and modeling study. 1. Isotherms and pore volume distributions,” *Fuel*, vol. 78, no. 11, pp. 1333–1344, 1999.
- [24] L. Chen, D. Zhenzhen, and L. Xiang, “A production analysis for fractured vertical well in rectangular coal reservoirs,” *Oil and Gas Science and Technology*, vol. 73, no. 1, pp. 1–10, 2018.



## Research Article

# Experimental and Mechanism Study of Superheated SAGD vs. Conventional SAGD Technique: A Cost-Effective Scheme for Superheated SAGD

Ke Huang <sup>1</sup>, Siyuan Huang <sup>1</sup>, Qi Jiang,<sup>1,2</sup> and Yang Liu<sup>3</sup>

<sup>1</sup>Petroleum and Natural Gas Engineering Department, Southwest Petroleum University, China

<sup>2</sup>Department of Chemical and Petroleum Engineering, Schulich School of Engineering, University of Calgary, Canada

<sup>3</sup>Research Institute of Petroleum Exploration and Development, PetroChina, China

Correspondence should be addressed to Siyuan Huang; huangsiy2013@163.com

Received 3 November 2021; Revised 10 March 2022; Accepted 21 March 2022; Published 27 April 2022

Academic Editor: Qingwang Yuan

Copyright © 2022 Ke Huang et al. This is an open access article distributed under the Creative Commons Attribution License, which permits unrestricted use, distribution, and reproduction in any medium, provided the original work is properly cited.

Steam-assisted gravity drainage (SAGD) is one of the steam injection techniques to exploit heavy oil and extra heavy oil resources, where the nature of steam is crucial to the production efficiency. Replacing saturated steam with superheated steam can effectively improve the steam quality at the bottom of the well and the production efficiency. In this study, based on the 2-D SAGD experiments, the recovery mechanisms of SAGD under the 220°C saturated steam and 260°C (superheated degree of 40°C) and 300°C (superheated degree of 80°C) superheated steam are compared and analyzed. The numerical model was developed based on experimental results, and the influence of steam superheated degree on the recovery degree of the SAGD process was further investigated. The physical experiment results and numerical simulation results show that the advantages of high enthalpy and large specific volume of superheated steam are significant at the horizontal expansion stage of the steam chamber stage compared to those of saturated steam. However, although the superheated steam can improve the recovery degree, the economic efficiency may decrease with the addition of superheated steam since it requires higher energy to generate the superheated steam. Thus, the SOR (steam-oil ratio) cannot appropriately describe the energy and economic efficiency when superheated steam is considered. Therefore, the cumulative FOR (fuel-oil ratio) is proposed, and the optimal superheated degree, optimal injection strategy, and its relation with the recovery mechanisms are studied. The results indicate that using superheated steam at 80°C superheated degree during the steam chamber horizontal expansion stage can increase the recovery factor around 12% and also reduce the cumulative FOR around 5.3 compared to the conventional SAGD strategy.

## 1. Introduction

With the increasing demand for oil resources, unconventional oil resources have gained more attention [1, 2]. Heavy oil is one of the unconventional resources which is characterized by its high viscosity at reservoir temperature. The thermal EOR (enhanced oil recovery) technology has been widely applied to develop the heavy oil reservoirs [3, 4]. In the 1980s, Butler [5] proposed the SAGD (steam-assisted gravity drainage) technique, which is considered an efficient and commercially successful technology for heavy oil development. The main mechanism of SAGD relies on the gravity

force which is caused by the density difference between steam and heavy oil. During the SAGD process, the steam is injected from the bottom of the reservoir and rises to the top to form a steam chamber. The heavy oil viscosity is reduced by heat exchange with steam, and the heated oil and condensed water are produced with the aid of gravity forces. The SAGD technology is different from steam flooding. During the steam flooding process, oil viscosity is still high except which in contact with steam, resulting in a high-pressure gradient between the production well and the injection well. However, the SAGD technology mainly relies on the gravity force, where the oil around the steam

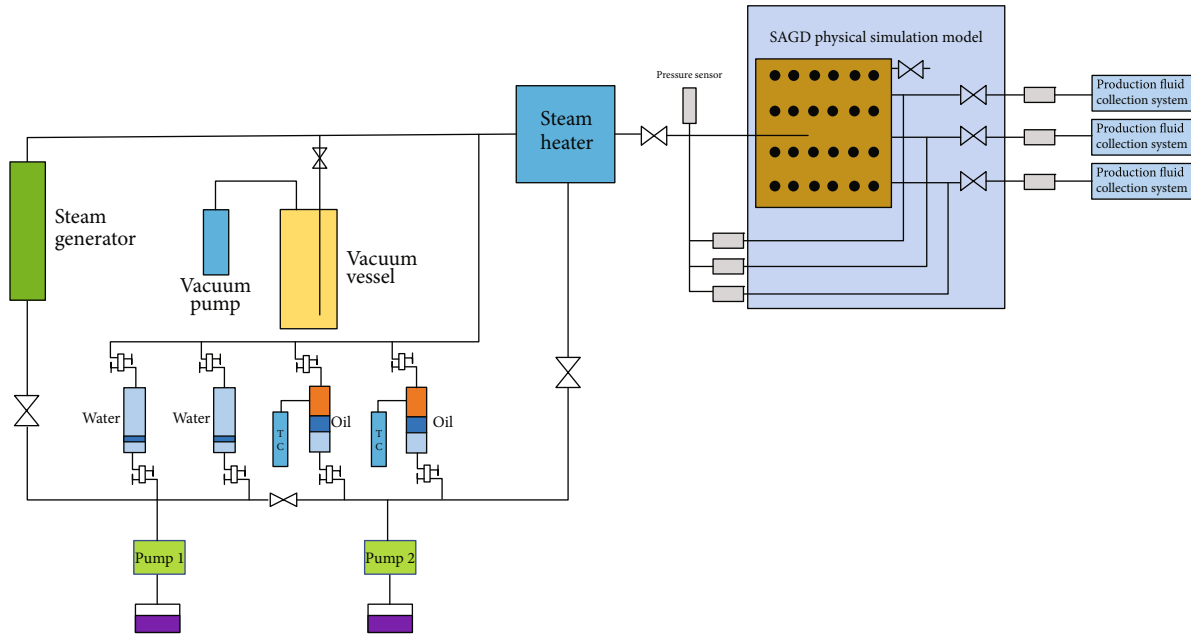


FIGURE 1: Schematic diagram of the SAGD 2-D physical simulation experiment system.

chamber maintains at the heated state and thus can be easily produced. With the expansion of the steam chamber volume, the oil flowing rate is increased as well [6, 7]. One of the critical factors for SAGD is to maintain the steam chamber temperature. In order to enhance the steam quality, superheated steam can be used to replace the saturated steam.

The mechanism of superheated steam to enhance oil recovery mainly includes the following four aspects: viscosity reduction, distillation, aquathermolysis reaction, and reservoir reconstruction. The mechanism of viscosity reduction by superheated steam at high temperature has been fully studied. Most experimental results show that the viscosity reduction effect of superheated steam is better than that of ordinary saturated steam. The higher the superheated degree, the more obvious the decrease in crude oil viscosity [8–14]. In terms of the distillation, the light components account for most of the distillation products, and the heavy components are still liquid [15–21]. Butler [22] shows that the steam superheated degree and light component content are very important to steam distillation rate. Vafaei et al. [23] show that the superheated steam can greatly improve the steam distillation rate, and the higher the content of light components in crude oil components, the stronger the distillation effect. In terms of the aquathermolysis reaction, compared with ordinary steam, superheated steam of the same quality can bring more heat into the formation and provide better temperature conditions, and the aquathermolysis reaction of heavy oil is more intense. Through the experiment of heavy oil aquathermolysis reaction, Clark and Hyne [24], Muraza [25], and Wu et al. [26] show that under high-temperature conditions, after the pyrolysis reaction between heavy oil and steam, the chain breaks occur in the molecules of heavy oil components, the light hydrocarbons increase, and the heavy hydrocarbons decrease. The content of carbon

atoms decreased, and the content of hydrogen atoms increased significantly. Lamoureux-Var and Lorant [27] and Liu et al. [28] believe that when the ordinary steam is injected, the aquathermolysis reaction of heavy oil is generally not very intense, so the aquathermolysis reaction is also an important mechanism for the difference between superheated steam and ordinary steam. In terms of the reservoir reconstruction, Fan [29] scanned the microstructure of oil sand before and after the action of superheated steam by using an electron microscope. The comparison of pore structure distribution shows that the rock pore surface after the action of superheated steam is flatter and smoother. When superheated steam is injected into the formation, strong scouring of reservoir rocks at high temperature will cause migration and cracking of reservoir rock mineral particles and even dissolution of soil minerals, smooth the reservoir rock pore throat channel, improve reservoir rock structure, improve reservoir rock permeability, and reduce residual oil saturation [30].

The superheated SAGD technique has been extensively studied. Badea and Daripa [31] studied the recovery efficiency of the superheated SAGD and conventional SAGD; the results show that the superheated steam can lower the steam-oil ratio. Fredman [32] conducted numerical simulation on the huff and puff preheating stage of SAGD using superheated steam. The results show that the cumulative oil production increases with the increase in the superheated degree, which was mainly due to the steam chamber expansion and reservoir temperature increment. Wu et al. [33] also studied the mechanisms of superheated steam enhanced oil recovery. They stated that the greater heat enthalpy and larger specific volume and latent heat of vaporization are the main characteristics for superheated steam, which result in higher production and economic performance. Also, the



(a) The appearance of the model



(b) The interior of the model and the location of the wells

FIGURE 2: Physical simulation model.

superheated steam is often used to replace the steam in the late stage of SAGD. There are many studies similar to the above scholars, most of which are based on the numerical simulation experiments. The conclusions are that superheated steam can significantly reduce steam consumption and improve economic benefits.

The economic benefits of superheated steam are also widely studied. Gates and Larter [34] proposed a thermal efficiency parameter for the steam injection technique, which is the ratio of theoretical SOR to actual SOR. The theoretical SOR is the ratio of the equivalent amount of steam required to raise the temperature from reservoir temperature





FIGURE 3: Oil sands in the model.

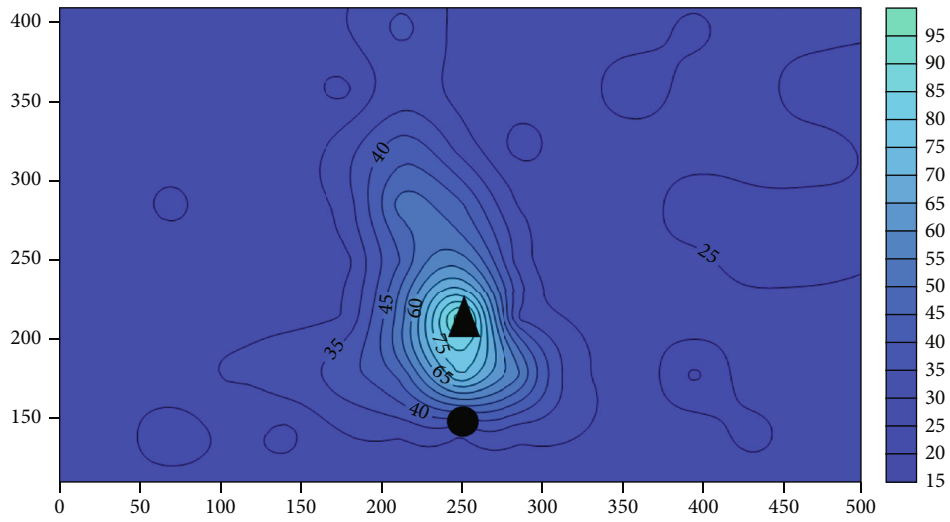
TABLE 1: Similarity parameters of the field and experiment.

Parameter name	Field scale	Laboratory scale
Well pattern	Double horizontal well	Double horizontal well
Shaft radius (m, cm)	0.1	0.3
Injection production horizontal well spacing (m, cm)	5	4
Horizontal well length (m, cm)	850	4
Distance from the production well to reservoir bottom (m, cm)	1.5	1.5
Oil layer thickness (m, cm)	21	30
Porosity (%)	32	32
Initial oil saturation (%)	80	80
Absolute permeability ( $10^{-3} \mu\text{m}^2$ )	3000	210000
Crude oil viscosity at $15^\circ\text{C}$ (mPa·s)	2500000	2500000
Injection steam temperature ( $^\circ\text{C}$ )	220	220/260/300
Steam quality	0.7	0.7
Steam injection rate (t/d, mL/min)	300	46

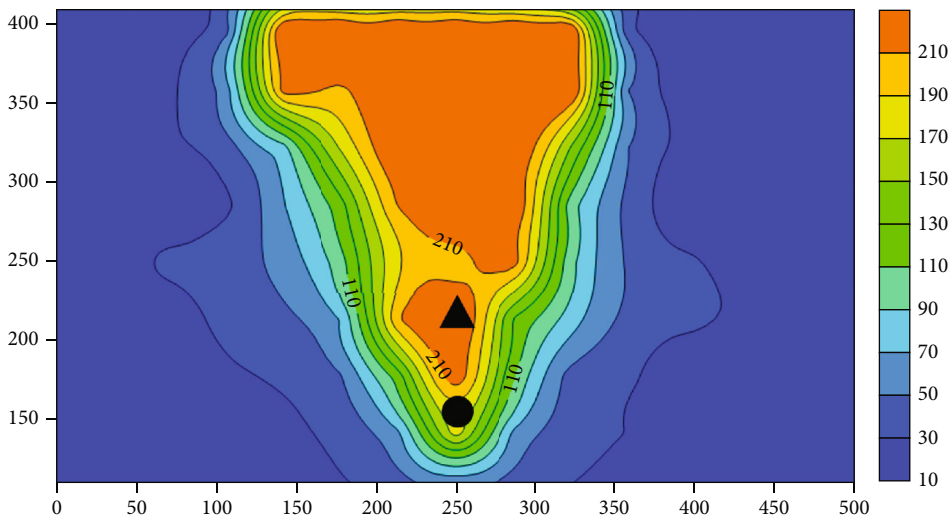
TABLE 2: Experimental schemes.

Experiment	Steam type	Steam temperature ( $^\circ\text{C}$ )	Steam pressure (kPa)
Group 1	Saturated steam	220	2350
Group 2	Superheated steam	260	2350
Group 3	Superheated steam	300	2350

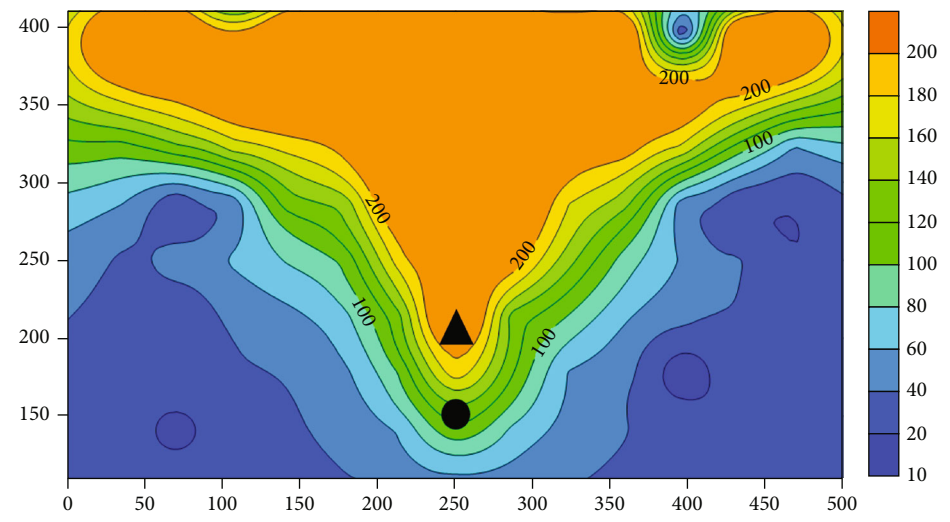
to steam temperature to the oil volume. It was stated that the average thermal efficiency of actual SAGD projects is about 30%. Alharthy et al. [35] used energy gain to evaluate the recovery efficiency for the SAGD process, where the energy gain is defined as the ratio of the energy produced to the energy injected. The concept of energy gain is more capable of reflecting the energy efficiency of the SAGD process than SOR. Pinto et al. [36] also used the ratio of the energy produced to the energy injected to evaluate the SAGD performance. They also claimed that using energy gain can better reflect the energy efficiency of the SAGD process. Wang [37] used the ratio of the difference between injected steam energy and produced water energy to the injected steam



(a) Temperature distribution at the initial stage (220°C)



(b) Temperature distribution at the maximum oil production rate (220°C)



(c) Temperature distribution when the SOR is 10 (220°C)

FIGURE 4: Temperature distribution in different periods (220°C).



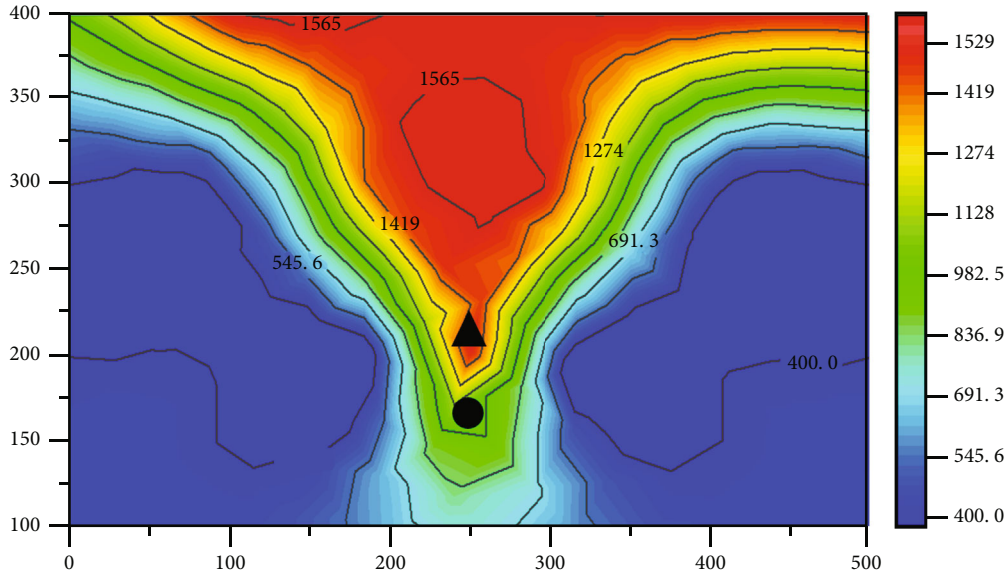


FIGURE 5: Pressure distribution at the end of the experiment (220°C, kPa).

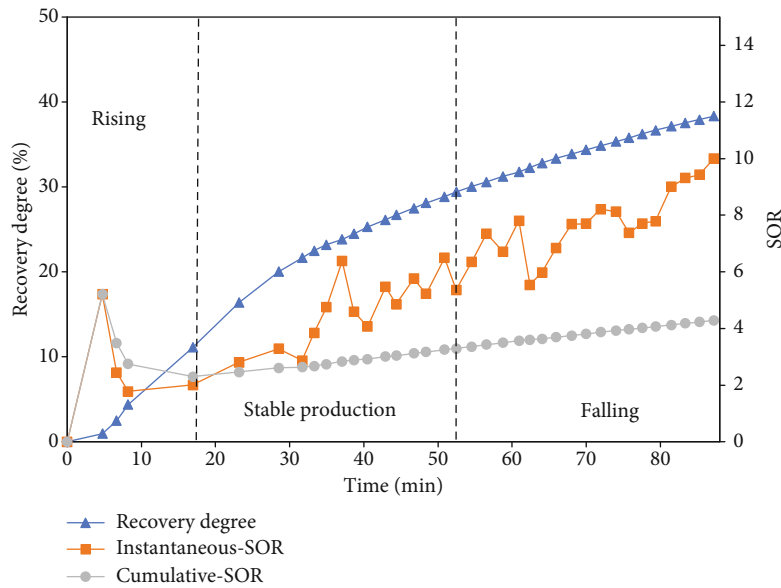


FIGURE 6: The recovery degree and SOR of 220°C saturated SAGD.

energy. In order to evaluate the energy efficiency for the superheated SAGD process, the ratio of the energy produced to the energy injected is adopted rather than SOR. Although the studies have proven that superheated steam has a stronger potential to improve heavy oil recovery compared with saturated steam, whether superheated steam has an economic advantage compared with saturated steam is worthier of attention and answer. The SOR is often used as a key economic indicator for the steam recovery process. However, it cannot reflect the actual energy efficiency when it comes to the superheated steam. For instance, although the SOR value of superheated steam is lower than that of saturated steam because superheated steam recovers more oil than saturated steam, the energy consumption required to produce superheated steam is also higher than that required

to produce saturated steam. Therefore, Liang et al. [38] and Yuan et al. [39] used the cumulative enthalpy of injected steam to represent the cost instead of the volume of injected steam. They proposed the cumulative enthalpy-oil ratio (EOR) to evaluate the cost of superheated steam. However, using cumulative EOR is not very intuitive to evaluate the energy efficiency and cannot be very convenient to help the on-site decision-making; it is necessary to use another indicator to evaluate the energy efficiency of superheated steam recovery.

Based on the 2-D SAGD experiments, this paper compares and analyzes the recovery mechanisms of SAGD under 220°C saturated steam and 260°C (superheated degree of 40°C) and 300°C (superheated degree of 80°C) superheated steam. The numerical model was developed which was

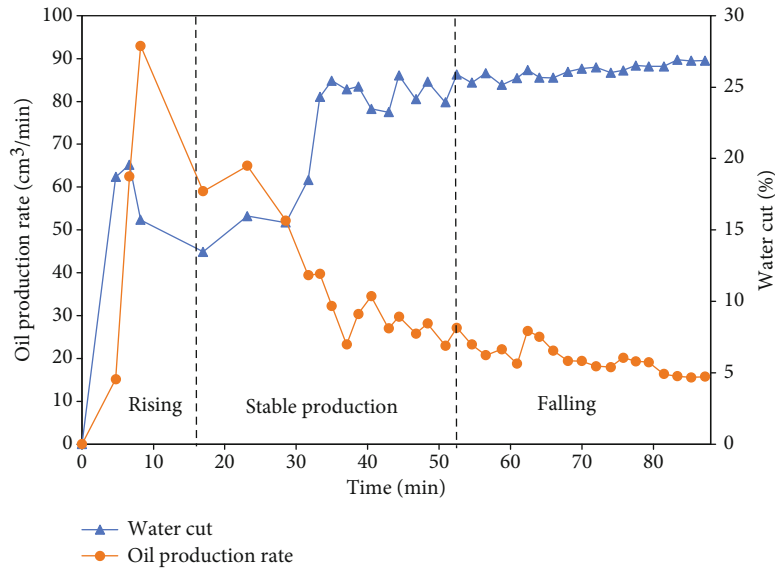


FIGURE 7: The oil production rate and water cut of 220°C saturated SAGD.

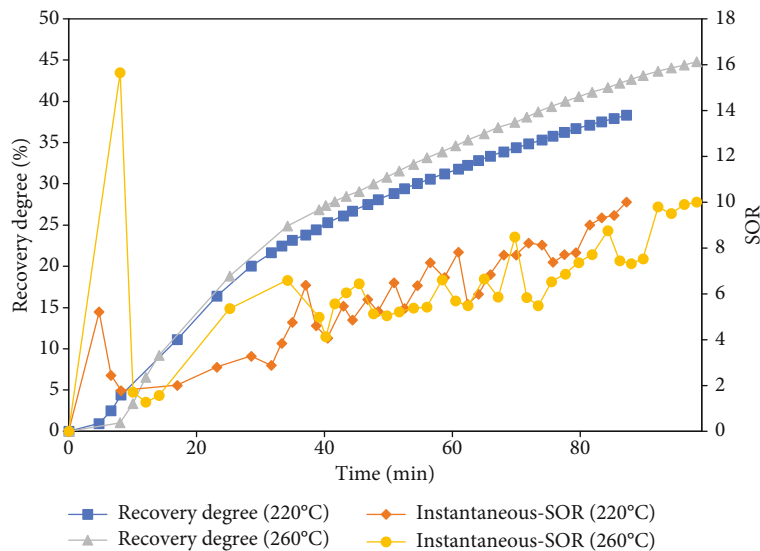


FIGURE 8: Comparison of superheated SAGD (260°C) and saturated SAGD (220°C).

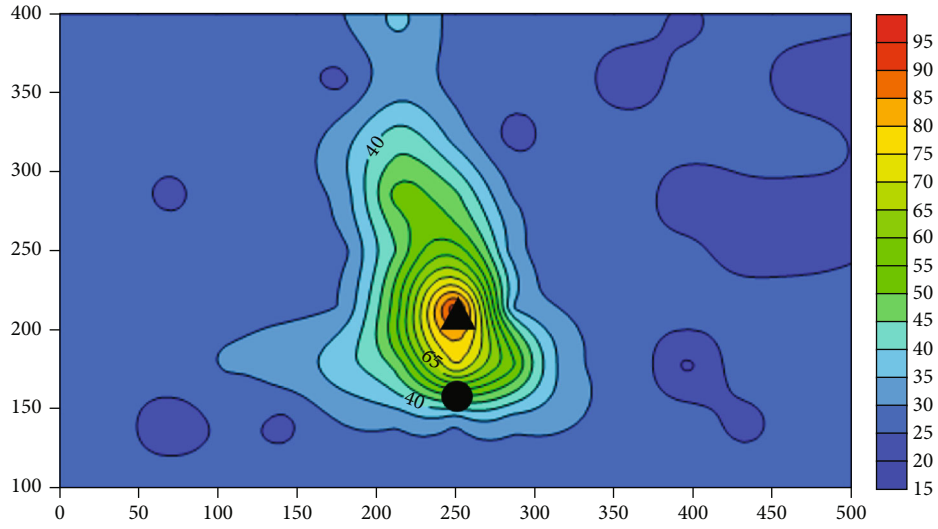
verified based on experimental results, and the influence of superheat degrees on SAGD and detailed recovery mechanisms were further investigated. The cumulative fuel-oil ratio (FOR) is proposed to investigate the optimal superheat degree and its relation with the recovery mechanisms. Also, the optimal superheated steam and saturated steam combination strategy is investigated, and the superheated steam enhancing recovery mechanisms for the SAGD technique is proposed.

## 2. SAGD Physical Experiment Study

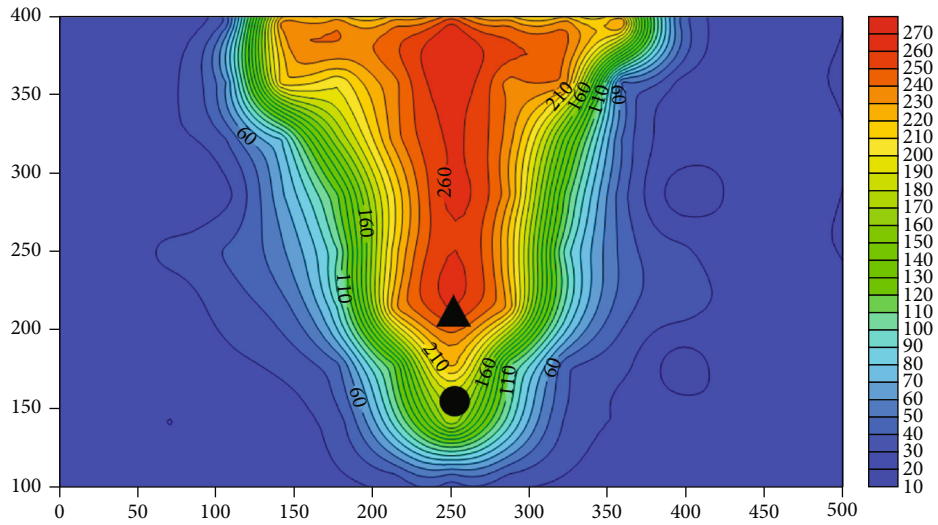
*2.1. Physical Experiment System.* The SAGD physical experiments are carried out through a 2-D SAGD system. The maximum internal temperature tolerance is 450°C. The size

of the model is 500 × 500 × 40mm, and the maximum working pressure of the model is 25000 kPa. The physical simulation system is shown in Figure 1, and the model is displayed in Figure 2.

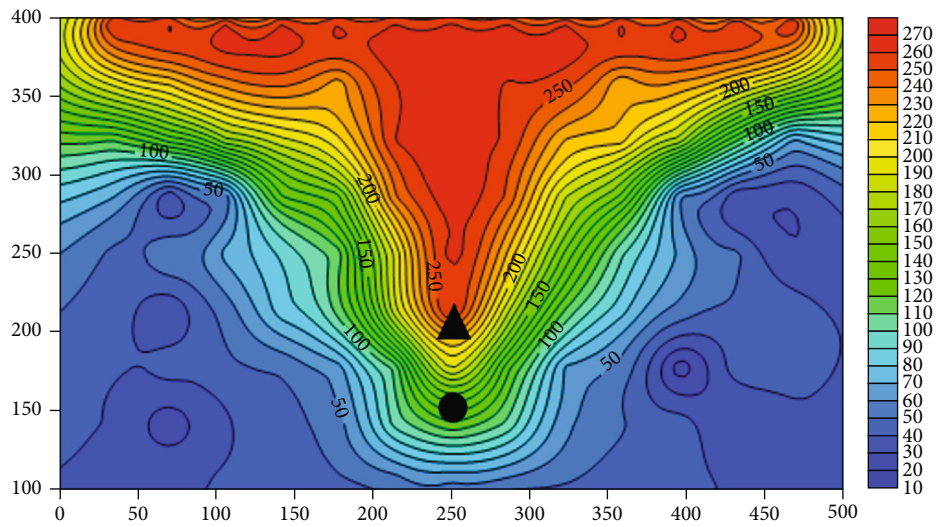
Thermal insulation materials are coated on the inner surface of the model to reduce heat loss. The quartz sand is used to simulate the reservoir rock. The pressure and temperature monitoring probes are placed evenly in the model, which connect to the computer to show the real-time temperature and pressure distribution. The steam generator in Figure 1 can produce the saturated steam; then, the saturated steam will be heated to superheated steam by the steam heater. When steam reaches the experimental condition, it will be injected into the SAGD physical simulation model. The heavy oil used in the experiments is from Xinjiang,



(a) Temperature distribution at the end of preheating (260°C)



(b) Temperature distribution at the maximum oil production rate (260°C)



(c) Temperature distribution when the SOR is 10 (260°C)

FIGURE 9: Temperature distribution in different periods (260°C).

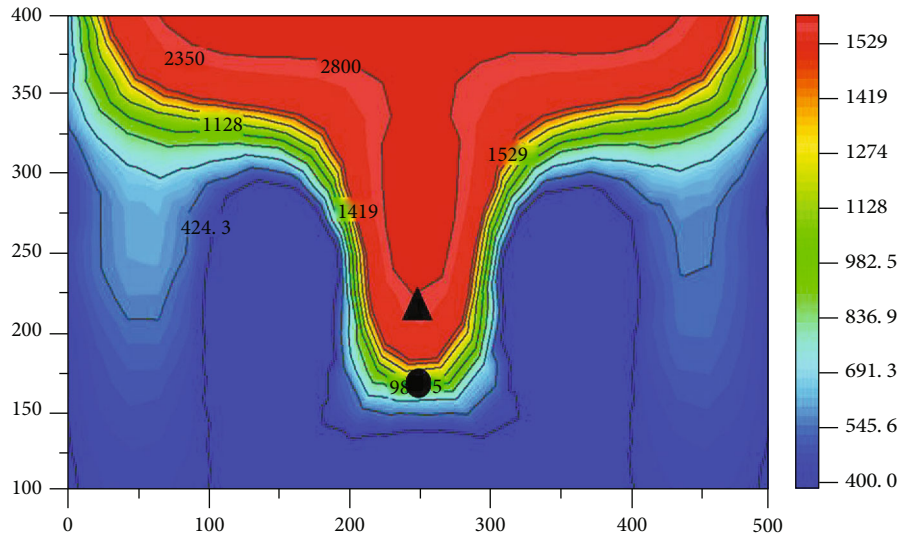


FIGURE 10: Pressure distribution at the end of the experiment (260°C, kPa).

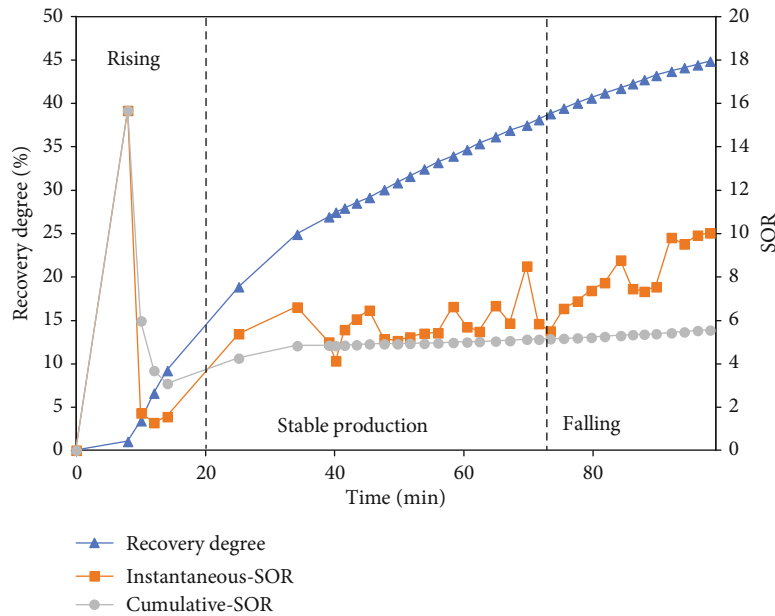


FIGURE 11: The recovery degree and SOR of 260°C superheated SAGD.

China, and the API is 10. Figure 3 shows the sample of oil sand filled in the physical experiment.

**2.2. Experimental Method.** The experiment is based on a SAGD well group in Xinjiang, and according to the SAGD similarity rule, the laboratory-scale parameters are obtained, which are shown in Table 1.

Table 2 shows the experimental schemes. The operating pressure was 2350 kPa, and the steam temperature was 220°C (saturated steam), 260°C (superheated degree of 40°C), and 300°C (superheated degree of 80°C), respectively.

**2.3. Experimental Procedures.** The experimental procedures are as follows:

- (1) Material preparation. Prepare quartz sand and crude oil according to the experimental design. Check all devices and equipment to ensure they are in good condition
- (2) Model filling. Fill the model with mixed oil sand at a designed ratio and compact. When the oil sand is filled, fill the clay into the model to simulate the overburden rock
- (3) Check the air tightness of the model. Pressurize the model with nitrogen, stabilize the pressure at 5000 kPa and maintain it for more than 24 h, and use a surfactant to detect whether there is air leakage at each outlet port of the model

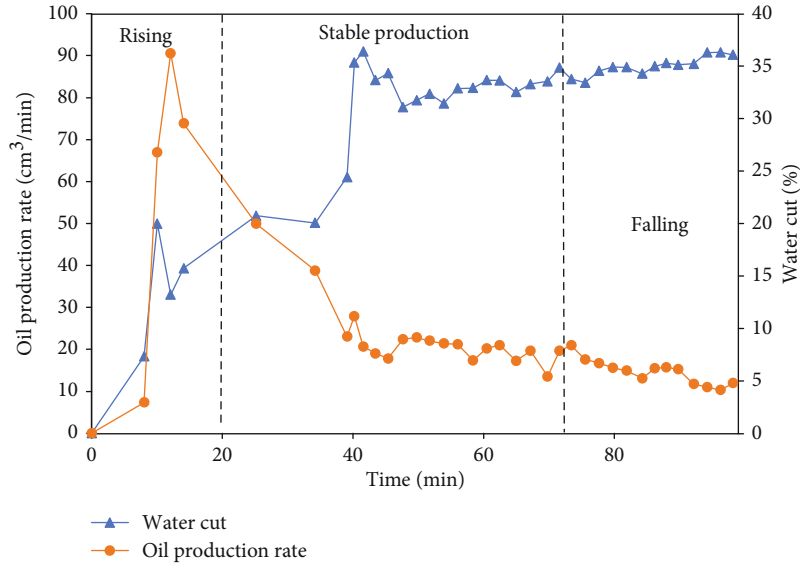


FIGURE 12: The oil production rate and water cut of 260°C superheated SAGD.

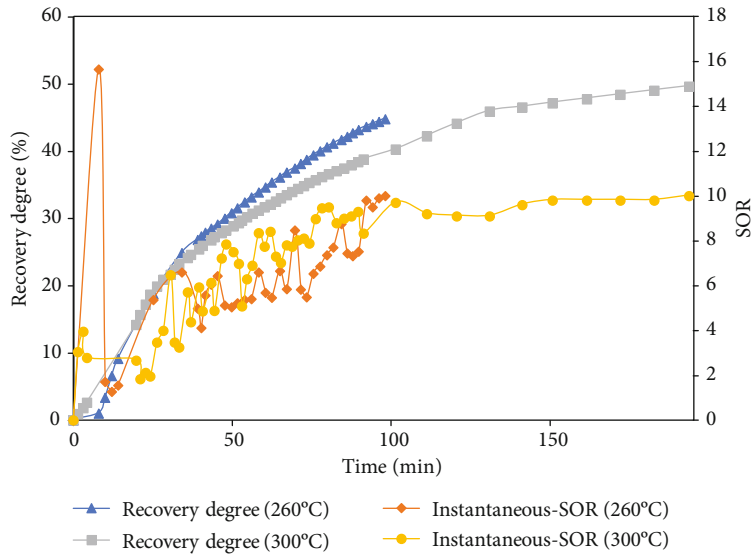


FIGURE 13: Comparison of superheated SAGD (260°C) and superheated SAGD (300°C).

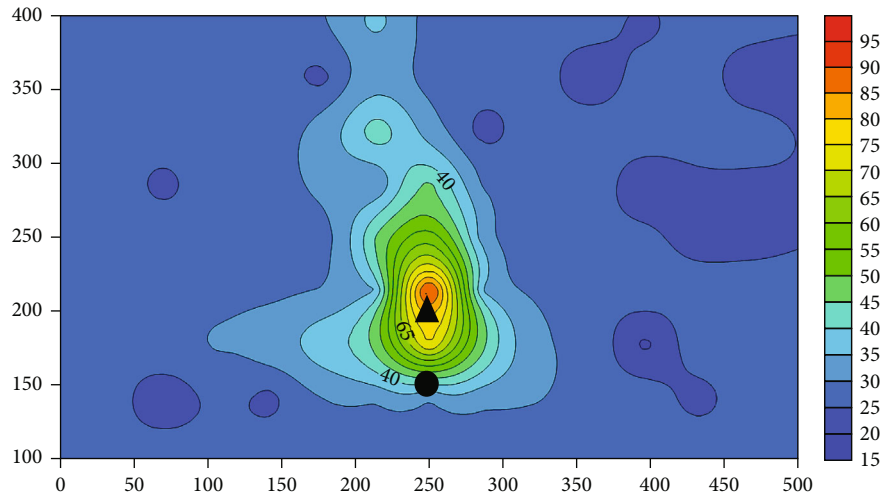
- (4) Model initialization. Put the model in the oven and heat the model to make the whole model temperature reach 90°C
- (5) Experimental operation. During the experiment, the monitoring system will monitor the temperature and pressure of the model body, steam generator outlet, and thermostat in real time. The production fluid collection system will collect and measure the produced liquid. The experiment will stop when the SOR is 10

### 3. Experimental Results of SAGD Physical Simulation

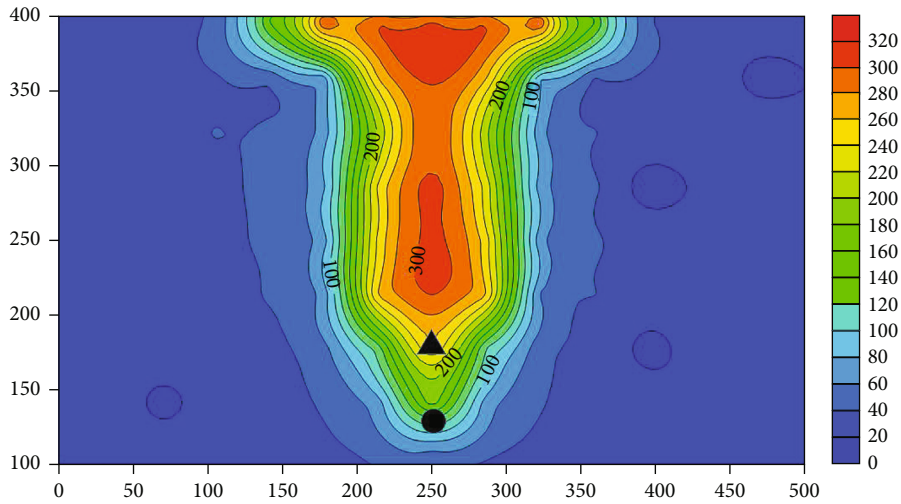
3.1. 220°C Saturated SAGD. Figures 4–7 show the temperature distribution, the pressure distribution, and the produc-

tion performance of the 220°C saturated SAGD experiment. Based on the results of the experiment, the SAGD process can be divided into three stages: rising stage, stable production stage, and falling stage. In the rising stage, the steam rapidly moves upward due to density differences and the entire steam chamber has a small contact area with crude oil, so the oil is produced mainly from the area between the injection well and the production well, which corresponds to the fact that the average water cut is about 50% and the recovery degree is 11.1%. In the stable production stage, the steam chamber reaches the overburden layer when the peak oil production rate was reached. And then the steam chamber begins to horizontally expand, which lasted about 35 min. The average water cut is 81%, and the average SOR is 4.6. Moreover, the average oil production rate is 8 cm<sup>3</sup>/min, and the recovery degree is 18.3%. In the

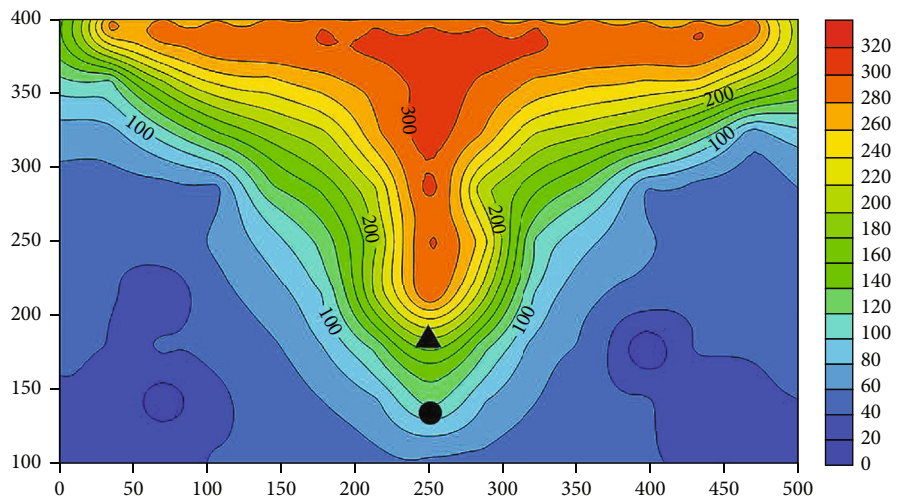




(a) Temperature distribution at the end of preheating (300°C)



(b) Temperature distribution at the maximum oil production rate (300°C)



(c) Temperature distribution when the SOR is 10 (300°C)

FIGURE 14: Temperature distribution in different periods (300°C).

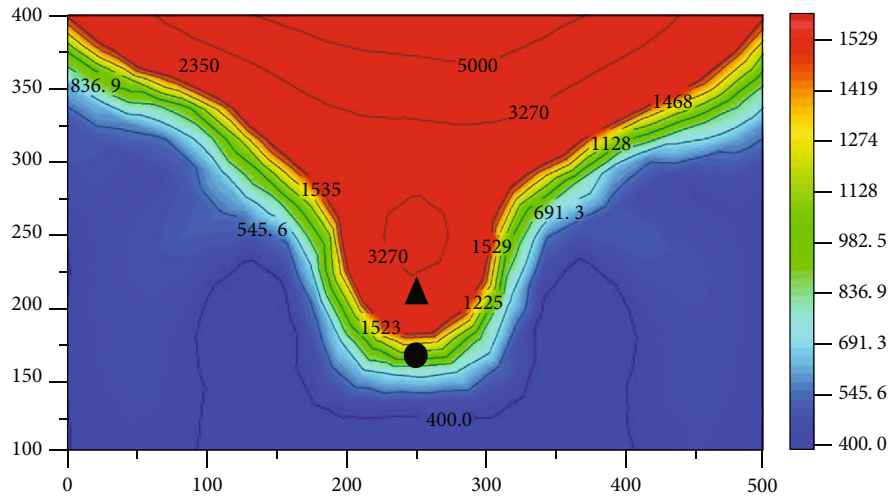


FIGURE 15: Pressure distribution at the end of the experiment (300°C, kPa).

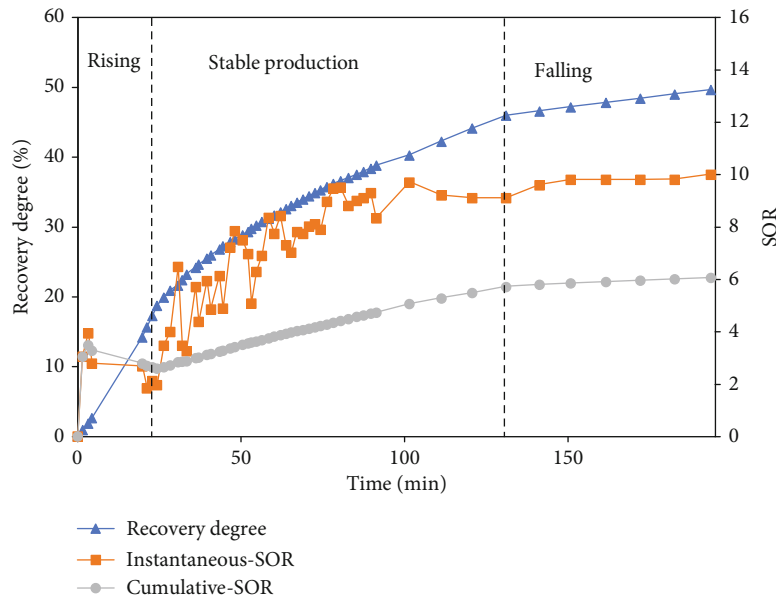


FIGURE 16: The recovery degree and SOR of 300°C superheated SAGD.

falling stage, the steam chamber expands to the both sides of the boundary. With the injection of steam, the steam chamber slowly falls downward along the boundary. The average water cut increases to around 90%, and the oil production rate decreases rapidly. The recovery degree is 8.9%. The final recovery degree of this experiment is 38.3%, and the cumulative SOR is 4.3. The SOR continues to rise during the experiment, and it eventually rises to 10 at the end of this experiment.

**3.2. 260°C Superheated SAGD.** It can be observed from Figure 8 that the final recovery degree of 260°C superheated SAGD is about 44.8%, which is about 6.5% higher than that of 220°C saturated SAGD and the SOR is lower. Obviously, the SAGD process is enhanced significantly when the superheated steam is used. Figures 8–11 show the temperature

distribution, the pressure distribution, and the production performance of the 260°C superheated SAGD experiment. It can be seen that the steam chamber development pattern for 220°C saturated SAGD and 260°C superheated SAGD is similar, which can also be divided into three stages. As shown in Figure 9(b), the steam chamber is larger and the temperature of the steam chamber is higher, which is caused by the fact that superheated steam carries more heat and has a higher temperature. Moreover, it can be proven from Figures 9(c) and 10 that superheated steam exists in the steam chamber. Due to the promotion of the steam chamber by superheated steam, the maximum oil production rate of 260°C superheated SAGD is higher, which reaches 37 cm<sup>3</sup>/min. Also, it is observed from Figure 12 that 260°C superheated SAGD has a higher average oil production rate and a lower average water cut during the stable production stage.

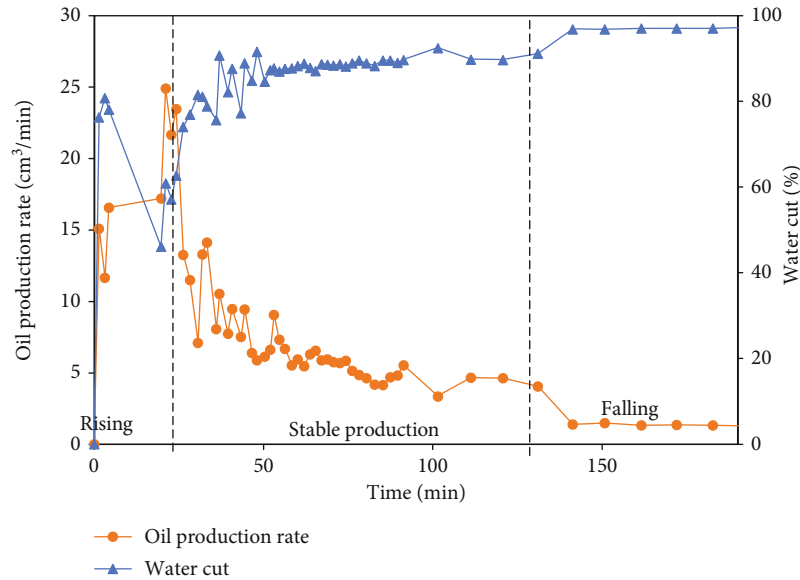


FIGURE 17: The oil production rate and water cut of 300°C superheated SAGD.

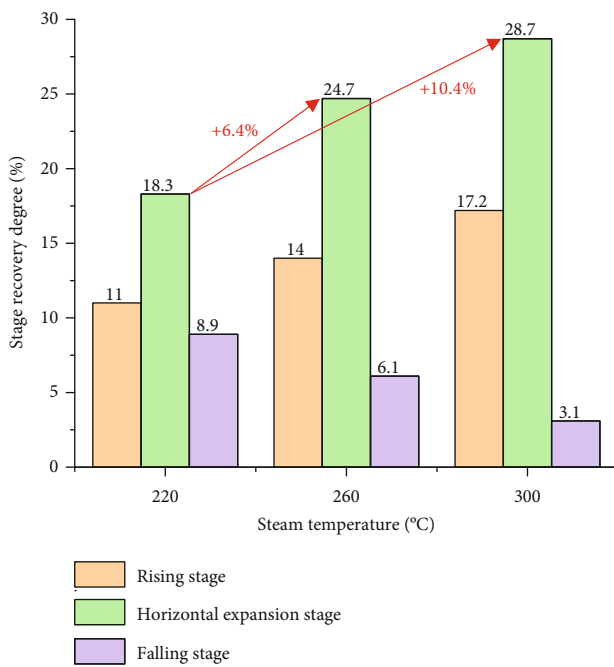


FIGURE 18: Stage recovery degrees at different steam temperatures.

**3.3. 300°C Superheated SAGD.** It can be found from Figure 13 that the final recovery degree of 300°C superheated SAGD is 49.6%, which is 4.8% higher than that of 260°C superheated SAGD. And, it is worth noting that the production time of 300°C superheated SAGD is significantly longer. Distinctly, the increase in superheated degree of the superheated steam improves the SAGD production performance. Figures 14–17 show the temperature distribution, the pressure distribution, and the production performance of the 300°C superheated SAGD experiment. It can be seen that the average temperature of the steam chamber is only about 280°C at the end of the experiment, which is due to the heat

loss of the superheated steam which is significantly higher than that of 220°C saturated SAGD. Compared with 220°C saturated SAGD and 260°C superheated SAGD, the steam chamber of 300°C superheated SAGD is much larger and the temperature in the center of the steam chamber is higher. What is more, based on Figures 14(c) and 15, it can be proven that the superheated degree in the steam chamber of 300°C superheated SAGD is higher than that of 260°C superheated SAGD. And it can be seen from Figures 16 and 17 that the stable production stage lasts about 107 min, which is much longer than that of the two previous experiments. So, it is obvious that the increase in the superheated degree has a great potential to improve the degree of reservoir exploitation.

**3.4. Summary of Physics Experiment.** Figure 18 shows the recovery degrees at different stages for SAGD tests. It shows that the horizontal expansion stage of the steam chamber in the SAGD process contributes the most to the final recovery degree. Also, the superheated steam has an obvious improvement in the recovery degree. When the 220°C saturated steam is converted to the 260°C superheated steam, the recovery degree at the horizontal expansion stage increased by 6.4%. When the 300°C superheated steam is used, the recovery degree at the horizontal expansion stage is 10.4% higher than that of the 220°C saturated steam. This is because when the steam chamber rises to the top, as the steam chamber expands, the pressure of the steam chamber decreases, and the advantages of large enthalpy and large specific volume of superheated steam are fully utilized. However, Figure 18 shows that as the steam temperature rises, the recovery degree decreases during the falling stage. This is because the superheated steam can advance the peak of oil production, a large amount of crude oil has been extracted in the previous stages, and reservoir is depleted later. Table 3 shows the cumulative steam injection, cumulative oil production, and cumulative SOR of the three

TABLE 3: Experimental results of cumulative SOR.

Experiment	Temperature (°C)	Cumulative steam (cm <sup>3</sup> )	Cumulative oil (cm <sup>3</sup> )	Cumulative SOR
Group 1	220	4505.55	881.11	5.11
Group 2	260	5710.00	1030.42	5.54
Group 3	300	6900.81	1140.47	6.05

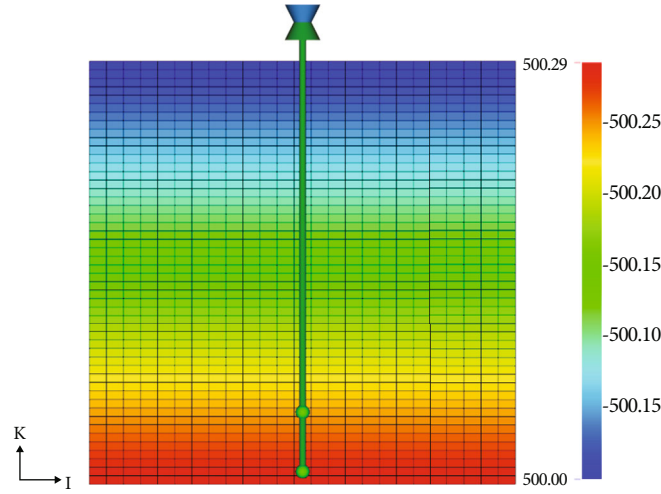


FIGURE 19: I-K view of the model.

TABLE 4: Relevant parameters of the SAGD model.

Parameter name	Numerical model
Reservoir depth (m)	200
Reservoir thickness (cm)	30
Horizontal well length (cm)	4
Crude oil viscosity (mPa·s)	$1.5 \times 10^4$
Porosity (%)	32
Permeability ( $10^{-3} \mu\text{m}^2$ )	210000
Oil saturation (%)	80
Water saturation (%)	20
Initial reservoir pressure (kPa)	400
Initial reservoir temperature (°C)	18

experiments. It shows that the cumulative oil production increases with the increase in superheated degree, while the cumulative SOR is also gradually increasing. This is because the heat loss of the physical simulation experiment is more than that of the actual oil reservoir, which caused a higher cumulative SOR. In particular, in the superheated steam experiments, the temperature of the steam chamber is higher; the heat loss is more than that of the saturated steam experiment. Although the advantages of superheated steam are also reflected in the results of laboratory experiments, the advantages of superheated steam in actual oil reservoirs will be more obvious.

In summary, physical experiments prove that the superheated steam has the ability to enhance oil recovery and show that the contribution of superheated steam to enhancing oil recovery is mainly at the horizontal expansion stage

TABLE 5: Thermophysical parameters of the rock and fluid in the SAGD numerical model.

Parameter name	Numerical model
Crude oil thermal conductivity	$1.15 \times 10^4 \text{ J/m} \cdot \text{day} \cdot ^\circ\text{C}$
Rock thermal conductivity	$6.6 \times 10^5 \text{ J/m} \cdot \text{day} \cdot ^\circ\text{C}$
Water thermal conductivity	$5.35 \times 10^4 \text{ J/m} \cdot \text{day} \cdot ^\circ\text{C}$
Crude oil thermal expansion coefficient	$4.8 \times 10^{-7} \text{ } ^\circ\text{C}^{-1}$
Crude oil compression coefficient	$7.3 \times 10^{-7} \text{ kPa}^{-1}$
Formation compression coefficient	$9.6 \times 10^{-6} \text{ kPa}^{-1}$
Thermal capacity of the rock	$2.35 \times 10^6 \text{ J/m}^3 \cdot ^\circ\text{C}$
Thermal conductivity of upper and lower formations	$2.35 \times 10^6 \text{ J/m}^3 \cdot ^\circ\text{C}$
Crude oil thermal conductivity	$1.47 \times 10^5 \text{ J/m} \cdot \text{day} \cdot ^\circ\text{C}$

of the steam chamber. However, due to the limitation of physical experimental equipment and huge heat loss, the amount of steam injected in the superheated steam experiments is too large. The cumulative SOR cannot truly reflect the effect of superheated steam in the actual reservoir. Therefore, the following study will use CMG to establish a numerical model to study the steam chamber development and energy efficiency of superheated SAGD and select the best steam injection scheme for superheated SAGD.

#### 4. SAGD Numerical Simulation Experiment

4.1. Establishment of the Numerical Model. Based on the physical simulation experiments, a two-dimensional

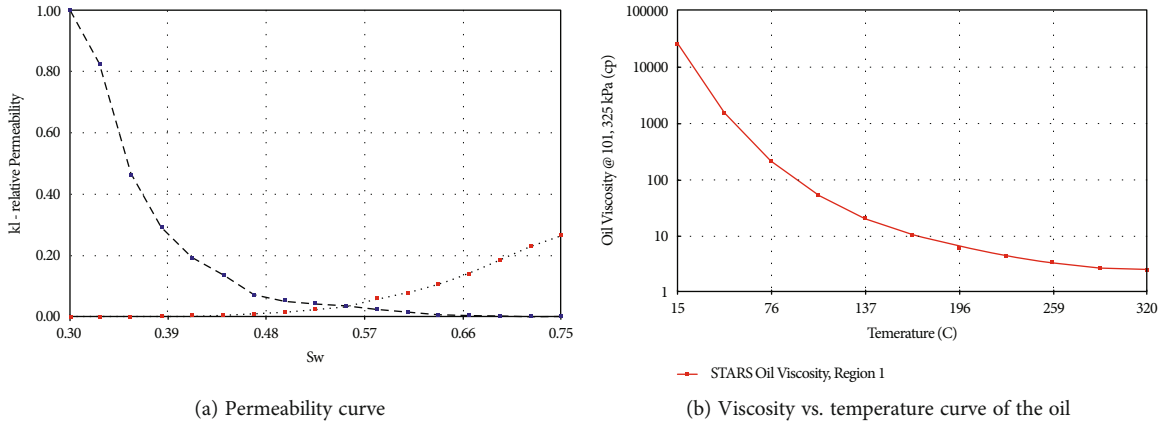


FIGURE 20: Fluid's property curve.

numerical simulation model was established through the STARS module of CMG. The grid design of the numerical model is  $I \times J \times K = 25 \times 1 \times 50$ , the grid size is  $2 \text{ cm} \times 4 \text{ cm} \times 0.6 \text{ cm}$ , the porosity is 0.32, and the oil saturation is 0.8. The model is a homogeneous model, and the permeability in all directions is equal. Figure 19 shows the  $I$ - $K$  view of the model, and the green dots indicate the locations of the wells. The distance between the wells is 1.5 cm. Table 4 shows the physical property parameter of the numerical model. The physical property parameters of the rock and fluids are shown in Table 5, and Figure 20 shows the physical property curve of the fluid.

4.2. *The Effect of the Superheated Degree on SAGD.* In this section, the 220°C saturated SAGD experiments and the superheated SAGD experiments with superheated degrees of 20°C, 40°C, 60°C, 80°C, and 100°C were set to study the effect of the superheated degree on SAGD. The steam chamber development and production performance under different superheated degrees were investigated. Moreover, the effect of the superheated degree on the cumulative SOR was obtained.

Figure 21 shows the cumulative SOR under different superheated degrees. It is observed that the cumulative SOR decreased with the increase in the superheated degree. In particular, the cumulative SOR decreases greatly from 220°C saturated SAGD to 320°C superheated SAGD, which is reduced by 10.0%. Besides, Figures 22–25 show the temperature distribution and the production performance of the numerical simulation experiments. In the rising stage, it can be seen that the increase in the superheated degree does not improve the SAGD performance, which corresponds to the same average oil production rate, steam chamber volume, and steam injection rate of the saturated SAGD and the superheated SAGD. However, in the horizontal expansion stage, it is obvious that the average oil production rate of superheated SAGD is significantly higher than that of saturated SAGD. Among them, the oil production rate of 320°C superheated SAGD reaches  $21.5 \text{ cm}^3/\text{min}$  at the highest, and the average oil production rate of 220°C saturated SAGD is  $15.5 \text{ cm}^3/\text{min}$ . It can be seen from Figure 24 that the volume of the steam chamber in the superheated SAGD

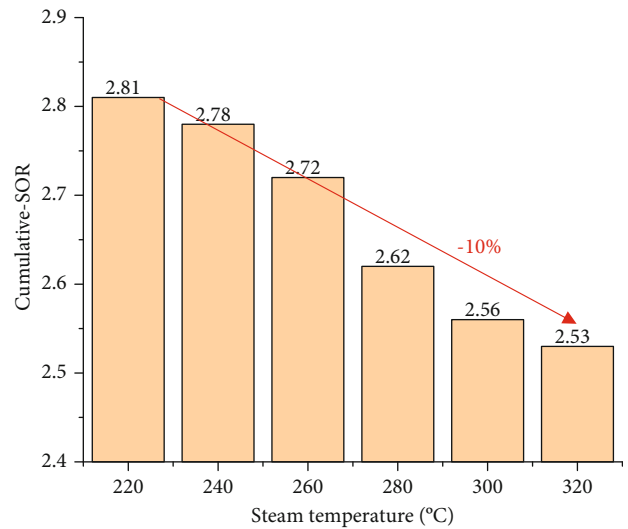


FIGURE 21: Cumulative SOR at different steam temperatures.

is significantly larger than that of the saturated SAGD. Nevertheless, Figure 25 shows that the average steam injection rate of saturated SAGD is  $36 \text{ cm}^3/\text{min}$ , while the minimum steam injection rate of superheated SAGD is  $27.5 \text{ cm}^3/\text{min}$ , which indicates that the use of superheated steam can significantly reduce the amount of steam injection. This is caused by the fact that the same volume of superheated steam can carry more heat. Obviously, it can be found that the superheated steam can greatly improve SAGD performance during the horizontal expansion stage, and this improvement continues to the falling stage.

In a word, numerical simulation results show that the use of superheated steam can greatly reduce the cumulative SOR. Moreover, the increase in the superheated degree does not improve the SAGD performance during the rising stage. However, in the horizontal expansion stage, the superheated steam can greatly save the steam injection and improve the SAGD performance significantly. The SAGD performance improves more obviously with the increase in the superheated degree. In the falling stage, the superheated steam can also improve the SAGD performance, but the rate of



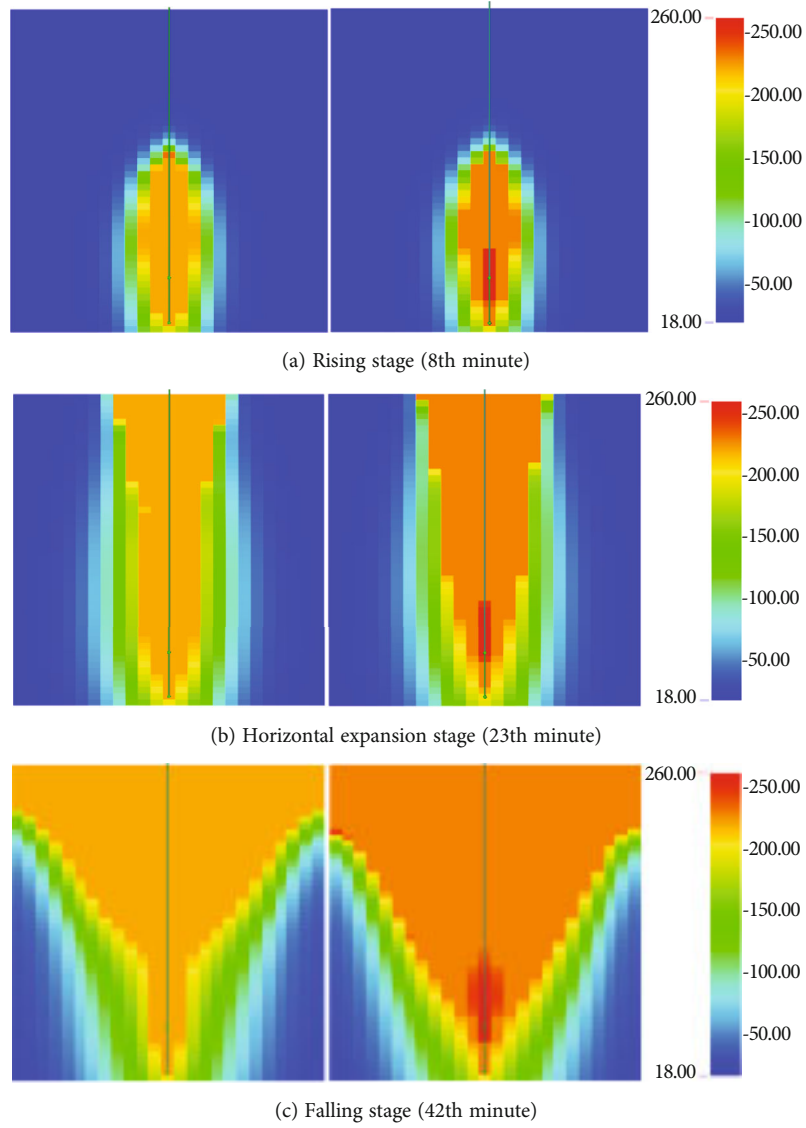


FIGURE 22: Temperature distribution in different periods of 220°C saturated SAGD (left) and 320°C superheated SAGD (right).

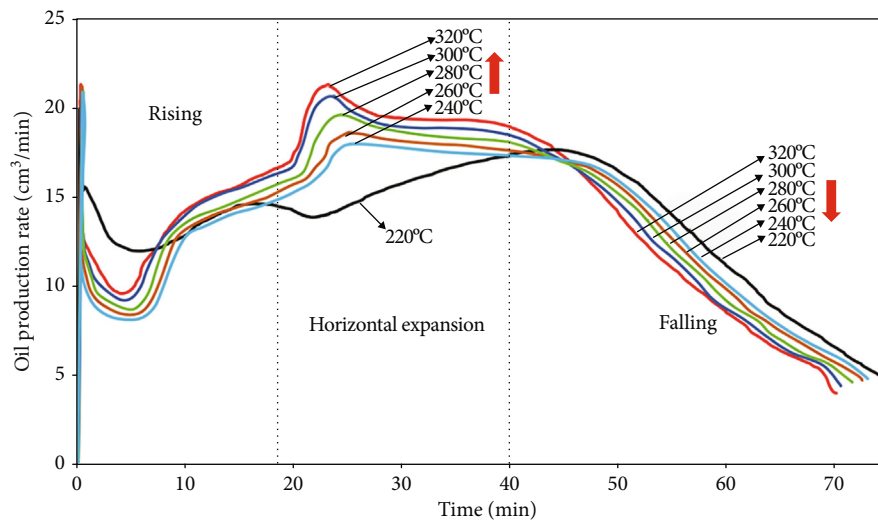


FIGURE 23: Oil production rate at different steam temperatures.

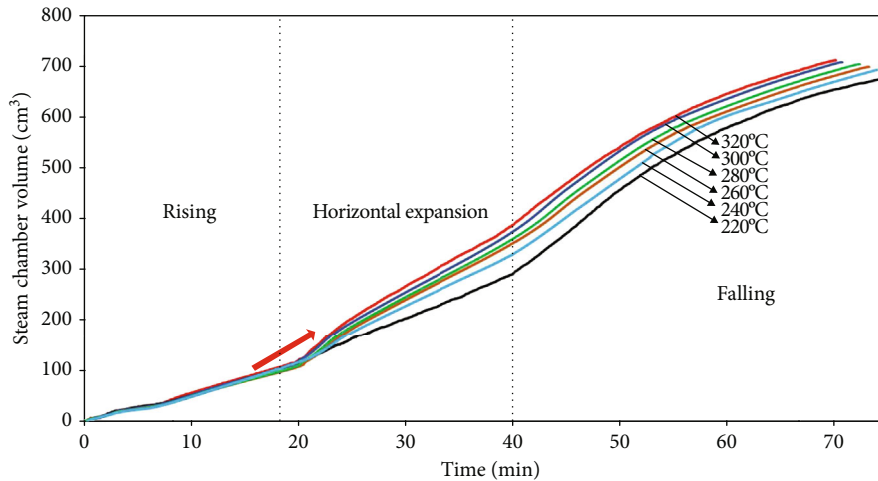


FIGURE 24: Steam chamber volume at different steam temperatures.

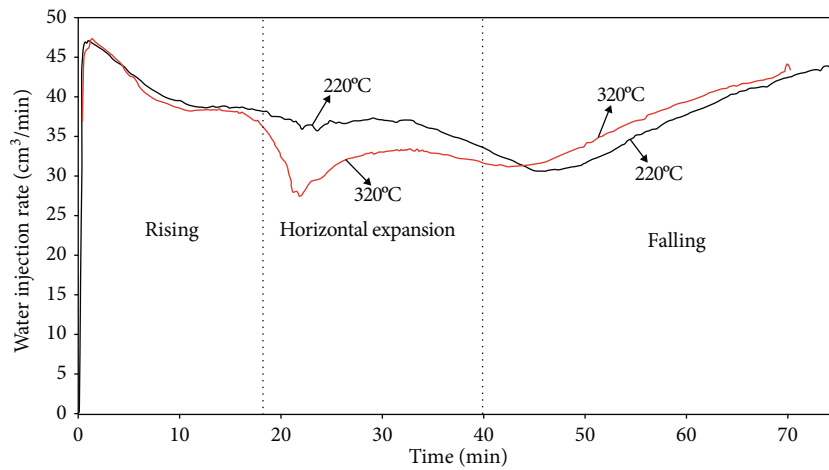


FIGURE 25: Steam injection rate at different steam temperatures.

TABLE 6: Steam injection strategy optimization.

Case	Rising	Horizontal expansion	Falling
1		220°C saturated steam	
2		320°C superheated steam	
3			320°C superheated steam
4	220°C saturated steam	320°C superheated steam	220°C saturated steam

steam injection is higher, which is due to the more heat loss of the superheated steam.

4.3. *Optimization of the Steam Injection Strategy for Superheated SAGD.* In this section, numerical simulation experiments are set to optimize the steam injection strategy for superheated SAGD. So, the purpose of this experiment is to study at which stage superheated steam can be used to obtain the greatest economic benefit. As shown in Table 6, case 1 and case 4 can show the effect of the superheated steam only used during the horizontal expansion stage, case 2 and case 3 can show the effect of the super-

heated steam only used during the rising stage, and case 3 and case 4 can show the effect of the superheated steam only used during the falling stage. Moreover, the effect of the superheated steam used during the horizontal expansion stage and the falling stage can be observed from case 1 and case 3. All tests were performed under 320°C superheated steam. The simulation will stop when the SOR is 10.

Based on Figure 26, the ratio of the volume of fuel consumed to the volume of steam produced in each case was calculated, and the results are shown in Figure 27. It is obvious that using cumulative SOR to evaluate the economic benefits of each case is not applicable, because the

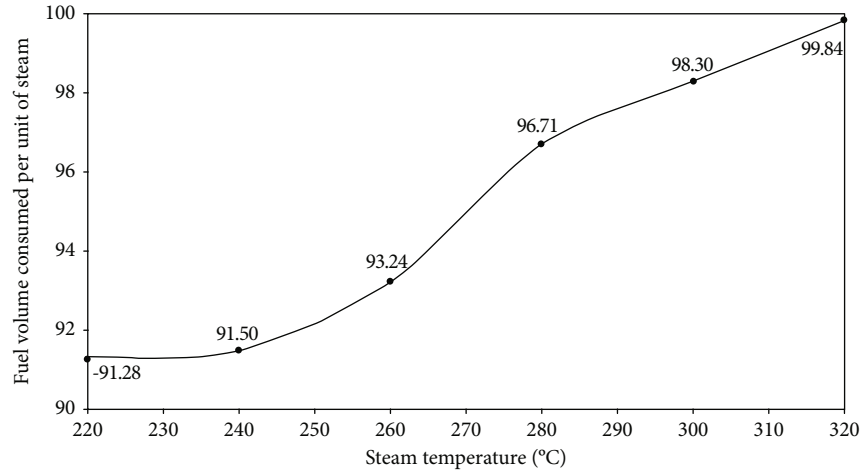


FIGURE 26: The volume of fuel consumed to produce a unit volume of steam in different temperatures [40].

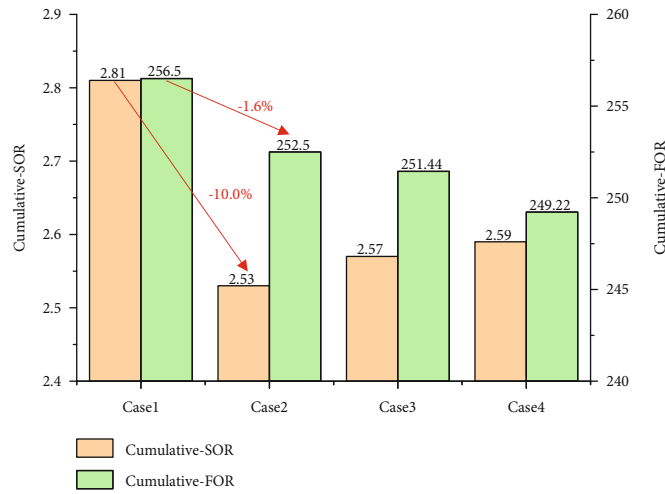


FIGURE 27: Cumulative SOR and cumulative FOR in different cases.

production costs of saturated steam and superheated steam are not the same. It can be found from Figure 27 that the cumulative FOR can better reflect the actual economic benefits. Based on the cumulative FOR, two key conclusions can be drawn. First, the use of the superheated steam does not greatly improve economic efficiency as shown by cumulative SOR. Compared with case 1, the cumulative SOR of case 2 is reduced by 10.0%, but the cumulative FOR is only reduced by 1.6%. Second, the cumulative FOR of case 4 is the lowest, indicating that the economic benefits of using superheated steam only during the horizontal expansion stage are higher than those of using superheated steam all the time.

Figures 28 and 29 show the oil production rate and the steam chamber volume of different cases. It can be observed that the average oil production rates during the horizontal expansion stage of case 3 and case 4 increased rapidly after injecting 320°C superheated steam during the horizontal expansion stage, increasing from 14.6 cm<sup>3</sup>/min to 19.5 cm<sup>3</sup>/min. Figure 30 shows that the steam chamber is fully expanded due to the high enthalpy and large specific volume of the superheated steam after injection of superheated

steam. At the end of the horizontal expansion stage, the volume of the steam chamber of case 1 is only 290 cm<sup>3</sup>, and the volume of the steam chamber of case 3 and case 4 is both 360 cm<sup>3</sup>. In the falling stage, case 3 used 320°C superheated steam at this stage and case 4 used 220°C saturated steam. Apparently, it can be found from Figures 28 and 29 that the use of superheated steam at the falling stage has little effect on SAGD production.

To sum up, the best use time of superheated steam is during the horizontal expansion stage of the steam chamber, which corresponds to the fact that the volume of the steam chamber increases rapidly and the advantage of superheated steam is significant. Moreover, the superheated degree needs to be determined by the FOR again.

Next, the superheated degree of the steam used during the horizontal expansion stage is optimized by using cumulative FOR. Table 7 shows the optimal schemes of the superheated degree. It can be found from Figure 30 that as the temperature of the superheated steam rises, the cumulative FOR first decreases and then rises, which is due to the fact that the steam chamber becomes larger and larger with the

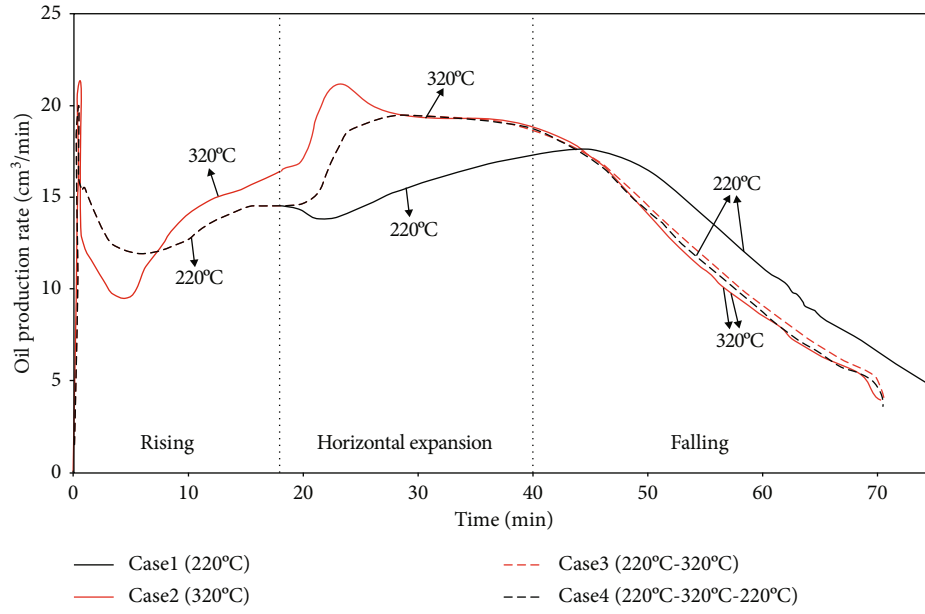


FIGURE 28: Oil production rate in different steam injection strategies.

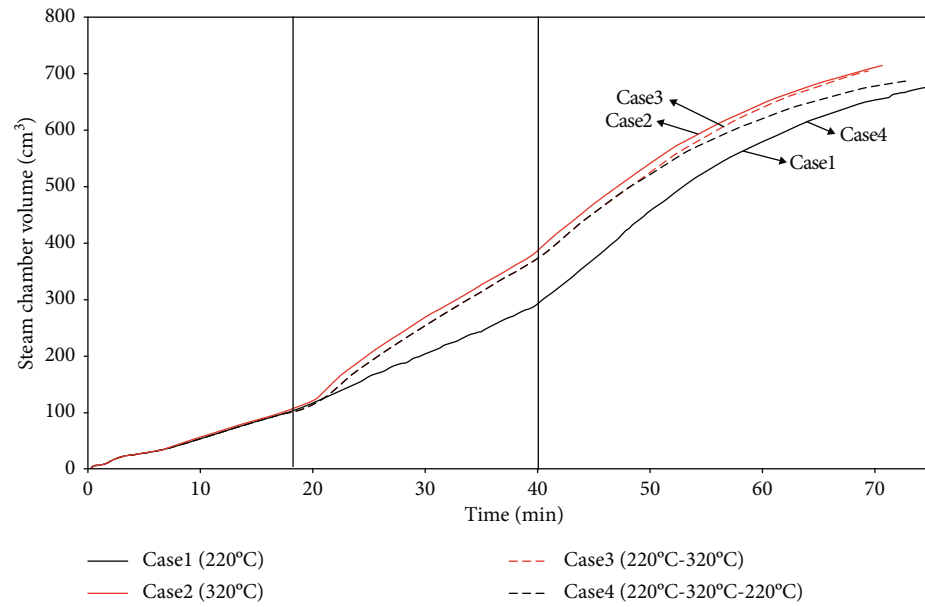


FIGURE 29: Steam chamber volume in different steam injection strategies.

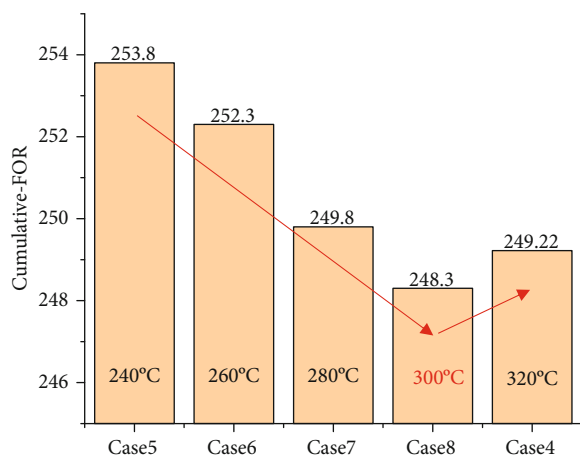


FIGURE 30: The cumulative FOR in different cases.

TABLE 7: Optimization of the superheated degree.

Case	Rising	Horizontal expansion	Falling
5		240°C superheated steam	
6	220°C saturated steam	260°C superheated steam	220°C saturated steam
7		280°C superheated steam	
8		300°C superheated steam	

increase in superheated degree during the horizontal expansion stage, and more oil can be produced. However, the increase in the superheated degree increases the cost per unit of steam, so the cumulative FOR rises later. The cumulative FOR of case 8 is 248.3, which is the lowest. Therefore, based on the cumulative FOR, case 8 is the most cost-effective scheme. The cumulative FOR of case 8 is 248.3, which is the lowest.

In summary, due to the high enthalpy and large specific volume of the superheated steam, the best use time of superheated steam is during the horizontal expansion stage of the steam chamber, which corresponds to the fact that the volume of the steam chamber increases rapidly and the advantage of superheated steam is significant. Compared with the traditional cumulative SOR, the cumulative FOR can better reflect the actual economic benefits of SAGD production and provide suggestions for the formulation of making SAGD program schemes.

## 5. Conclusions

- (1) The superheated steam can significantly enhance the recovery factor compared to the saturated steam, especially during the steam chamber horizontal expansion stage. Also, the recovery factor increases with the increment of superheat degree; when super-

heated degree 80°C is used, around 10.4% recovery degree increment is reached

- (2) Although the superheated steam can improve the recovery degree, the economic efficiency may decrease with the addition of superheated steam. Therefore, it is suggested to use the FOR to optimize the injection strategy, where the FOR can more directly show the energy cost in the production process and optimize the steam injection strategy
- (3) Compared to the conventional SAGD operation, the optimized superheated SAGD strategy can increase recovery degree around 12% and reduce FOR around 5.3

## Data Availability

The data of the research results of this paper are reflected in this paper.

## Conflicts of Interest

The authors declare no conflict of interest regarding the publication of this manuscript.

## References

- [1] A. Xu, L. Mu, Z. Fan et al., "Mechanism of heavy oil recovery by cyclic superheated steam stimulation," *Journal of Petroleum Science and Engineering*, vol. 111, pp. 197–207, 2013.
- [2] Z. Ping, S. Bingzhong, Z. Donghui, and W. Junhua, "Ground simulation experiment of superheated steam high temperature oil displacement in heavy oil wells," *Oil and Gas Field Surface Engineering*, vol. 33, no. 6, pp. 39–40, 2014.
- [3] H. Jie, W. Tao, and W. Yong, "Experiment on distillation mechanism of superheated steam drive," *Oil and Gas Field Surface Engineering*, vol. 33, no. 9, pp. 15–16, 2014.
- [4] G. Xiaotian, W. Guansheng, S. Dehuang, and G. Xuntao, "Experimental study on distillation mechanism of superheated steam drive in heavy oil reservoir," *Journal of Petroleum and Natural Gas*, vol. 32, no. 3, pp. 344–346, 2010.
- [5] R. M. Butler, "A new approach to the modelling of steam-assisted gravity drainage," *Journal of Canadian Petroleum Technology*, vol. 24, no. 3, pp. 42–51, 1985.
- [6] L. Chuntao, Q. Genbao, W. Shuhong, Y. Kequan, and Y. Yuping, "Properties of superheated steam and its application in huff and puff development of heavy oil reservoir – taking the salt heavy oil reservoir of Kenjiyak oilfield in Kazakhstan as an example," *Xinjiang Petroleum Geology*, vol. 29, no. 4, pp. 495–497, 2008.
- [7] G. Qunli, "Research and test on superheated steam drive development of shallow extra heavy oil – taking well block Louzi 27 as an example," *Petroleum Geology and Engineering*, vol. 136, no. 2, pp. 76–78, 2011.
- [8] G. Bin, L. Riyi, W. Zeyu, M. Qiang, and W. Xinwei, "Experiment and mechanism analysis of superheated steam improving oil displacement effect," *Xinjiang Petroleum Geology*, vol. 40, no. 4, pp. 481–485, 2019.
- [9] T. Songlin, "Discussion and improvement of heat loss factors of steam huff and puff in heavy oil production," *Enterprise guide*, vol. 40, no. 1, p. 291, 2011.



- [10] Z. Yuqiang, L. Xiaoping, C. Li, L. Xiaohui, and W. Qin, "Analysis of wellbore heat loss in steam injection development of heavy oil reservoir," *Drilling and Production Technology*, vol. 13, no. 7, p. 77, 2006.
- [11] L. Hongbo, "Feasibility study on a method to improve the thermal efficiency of steam injection boiler in oil field," *Special Oil and Gas Reservoir*, vol. 13, no. 6, pp. 98–100+110, 2006.
- [12] S. Fengrui, Y. Yodong, L. Xiangfang, C. Mingqiang, and Z. Ming, "Prediction model of heating radius and productivity of superheated steam huff and puff horizontal wells," *Special Oil and Gas Reservoirs*, vol. 24, no. 2, pp. 120–124, 2017.
- [13] Z. Yuqiang, L. Shuzhi, W. Qin, R. Yong, and L. Xiaohui, "Overview of heavy oil steam stimulation," *Special Oil and Gas Reservoirs*, vol. 13, no. 6, pp. 5–9, 2006.
- [14] D. Jinyang, C. Fulan, G. Zhanjun, and X. Xinde, "New analysis of energy utilization of thermal recovery boilers," *China Science and Technology News*, vol. 13, no. 14, p. 147, 2013.
- [15] R. M. Butler, G. S. McNab, and H. Y. Lo, "Theoretical studies on the gravity drainage of heavy oil during in-situ steam heating," *The Canadian Journal of Chemical Engineering*, vol. 59, no. 4, pp. 455–460, 1981.
- [16] M. Nukhaev, V. P. Pimenov, A. Shandrygin, and V. V. Ter-tychnyi, "A new analytical model for the SAGD production phase," in *SPE annual technical conference and exhibition*, San Antonio, TX, USA, 2006.
- [17] J. Sharma and I. D. Gates, "Multiphase flow at the edge of a steam chamber," *Canadian Journal of Chemical Engineering*, vol. 88, no. 3, 2010.
- [18] M. Irani and S. Ghannadi, "Understanding the heat-transfer mechanism in the steam-assisted gravity-drainage (SAGD) process and comparing the conduction and convection flux in bitumen reservoirs," *SPE Journal*, vol. 18, no. 1, pp. 134–145, 2013.
- [19] J. Rabb and C. Palmgren, "Pressure transient analysis in SAGD," *Journal of Canadian Petroleum Technology*, vol. 44, no. 9, pp. 16–22, 2005.
- [20] A. Zamani, B. R. James, and R. H. Hite, "Use of pressure transient analysis for monitoring SAGD steam chamber development," in *Proceedings of the SPE Heavy Oil Conference, SPE165489-MS*, Calgary, Canada, June 2013.
- [21] H. S. Carslaw and J. C. Jaeger, *Conduction of Heat in Solids*, Oxford Science Publications, 1959.
- [22] R. M. Butler, "Rise of interfering steam chambers," *Journal of Canadian Petroleum Technology*, vol. 26, no. 3, pp. 70–75, 1987.
- [23] M. T. Vafaei, R. Eslamloueyan, L. Enfeali, and S. Ayatollahi, "Analysis and simulation of steam distillation mechanism during the steam injection process," *Energy & Fuels*, vol. 23, no. 1, pp. 327–333, 2009.
- [24] P. D. Clark and J. B. Hyne, "Studies on the chemical reactions of heavy oils under steam stimulation conditions," *AOSTRA Journal of Research*, vol. 6, pp. 29–39, 1990.
- [25] O. Muraza, "Hydrous pyrolysis of heavy oil using solid acid minerals for viscosity reduction," *Journal of Analytical and Applied Pyrolysis*, vol. 114, pp. 1–10, 2015.
- [26] W. Chuan, C. Yanling, W. Yuanqing, and Y. Chao, "Study on upgrading and viscosity reduction of Shengli super heavy oil by catalytic hydrothermal cracking," *Oilfield Chemistry*, vol. 26, no. 2, pp. 121–123, 2009.
- [27] V. Lamoureux-Var and F. Lorant, "H<sub>2</sub>S artificial formation as a result of steam injection for EOR: a compositional kinetic approach," *ITOHOS International Thermal Operations and Heavy Oil Symposium*, 2005.
- [28] L. Yongjian, Z. Liguang, J. Shengjian, S. Xianli, and G. Yuning, "Research progress of heavy oil recovery technology by hydrothermal cracking," *Journal of Fuel Chemistry*, vol. 26, no. 1, pp. 117–122, 2004.
- [29] F. Hongfu, "Research and application of hydrothermal cracking reaction of Liaohe heavy oil," Daqing Petroleum Institute, 2002.
- [30] F. Hongfu, L. Yongjian, and Z. Xiaofei, "Study on composition change of heavy oil under the action of steam," *Journal of fuel chemistry*, vol. 20, no. 3, pp. 269–272, 2001.
- [31] L. Badea and P. Daripa, "A domain embedding method using the optimal distributed control and a fast algorithm," *Numerical Algorithms*, vol. 36, no. 2, pp. 95–112, 2004.
- [32] T. P. Fredman, "A boundary identification method for an inverse heat conduction problem with an application in iron-making," *Heat and Mass Transfer*, vol. 41, no. 2, pp. 95–103, 2004.
- [33] Y. Wu, D. Ma, S. Liu, H. Wang, and X. Zhao, "EOR of superheated steam injection in shallow heavy oil reservoir: a case study," in *Proceedings of the CPS/SPE International Oil & Gas Conference and Exhibition, SPE131224*, Beijing, China, June 2010.
- [34] I. Gates and S. Larter, "Energy efficiency and emissions intensity of SAGD," *Fuel*, vol. 115, pp. 706–713, 2014.
- [35] N. Alharthy, H. Kazemi, R. Graves, and J. Akinboyewa, "Energy gain efficiency in steam-assisted gravity drainage (SAGD)," in *SPE Annual Technical Conference and Exhibition*, Florence, Italy, 2010.
- [36] H. Pinto, X. Wang, and I. Gates, "On the ratio of energy produced to energy injected in SAGD: long-term consequences of early stage operational decisions," *Journal of Petroleum Science and Engineering*, vol. 199, 2021.
- [37] W. Jiazheng, "Mechanism analysis and numerical simulation of SAGD oil displacement process," Northeast Petroleum University, 2012.
- [38] G. Liang, S. Liu, Y. Liu, Y. Luo, B. Han, and J. Huang, "The potential evaluation of superheated steam with high degree assisted gravity drainage process in oil sands project," in *Proceedings of the Abu Dhabi International Petroleum Exhibition & Conference*, p. 18, Abu Dhabi, UAE, 2017.
- [39] R. Yuan, Z. Yang, B. Guo, X. Wang, L. Zhang, and R. Lin, "Potential analysis of enhanced oil recovery by superheated steam during steam-assisted gravity drainage," *Energy Technology*, vol. 9, no. 7, pp. 2100135–2100135, 2021.
- [40] W. Hongyuan, "Energy consumption of overheated steam generator during SAGD development in Liaohe oil field," *Resources and Industries*, vol. 19, no. 4, pp. 18–21, 2017.

## Research Article

# Plugging Performance of a New Sulfonated Tannin Gel System Applied in Tight Oil Reservoir

Tianhan Xu <sup>1</sup>, Jian Wang <sup>1</sup>, Zhiwen Bai <sup>2</sup>, Junheng Wang <sup>1</sup> and Peng Zhao <sup>1</sup>

<sup>1</sup>State Key Laboratory of Oil and Gas Reservoir Geology and Exploitation, Southwest Petroleum University, Sichuan Province, China

<sup>2</sup>Baikouquan Oil Plant, Xinjiang Oilfield Company, CNPC, Karamay, Xinjiang 834000, China

Correspondence should be addressed to Jian Wang; 404674469@qq.com

Received 2 November 2021; Revised 5 March 2022; Accepted 22 March 2022; Published 23 April 2022

Academic Editor: Jinjie Wang

Copyright © 2022 Tianhan Xu et al. This is an open access article distributed under the Creative Commons Attribution License, which permits unrestricted use, distribution, and reproduction in any medium, provided the original work is properly cited.

In this study, based on the high-temperature characteristics of Western China tight oil reservoirs, a phenolic-larch tannin, temperature-resistant, plugging agent was synthesized by changing the mass fractions of larch tannin, double cross-linking agent, and accelerator. Young's modulus of the dispersed gel was directly measured by an atomic force microscope, and the macroscopic plugging performance was evaluated by a physical simulation experiment of the artificially fractured natural core from Western China tight oil oilfield, thereby establishing a mapping relationship between the two. Research indicates that the formula of the high-temperature-resistant tannin system optimized by the experiment is 3.0% sulfonated tannin + 3.0% formaldehyde cross-linking agent + 1.0% phenol cross-linking agent + 0.05%  $\text{MnSO}_4$  accelerator; the mechanical strength of the tannin gel and its plugging performance have a linear relationship. When Young's modulus rises from 18.74 to 63.89 KPa, the plugging rate rises from 94.11% to 97.44%.

## 1. Introduction

Given the increasing difficulty of conventional oil and gas exploration and development, the development of unconventional resources such as tight oil and gas has become inevitable [1, 2]. Tight oil storage and seepage conditions are poor, and fracturing is generally used to connect the pores in the reservoir and expand the seepage area. However, this mode of development will aggravate the difference in matrix-fracture seepage flow and form a flow channel. Therefore, after long-term fracturing development, reservoir regulation is required to change the original seepage channel, increase the swept volume, and achieve the purpose of increasing oil well production [3, 4]. Current research mostly uses polyacrylamide cross-linked polyvalent metal ion ( $\text{Cr}^{3+}$ ,  $\text{Al}^{3+}$ ,  $\text{Zr}^{4+}$ , etc.) gel to block gas flow channels [5, 6], but this gel is affected by high temperature and  $\text{Ca}^{2+}$  and  $\text{Mg}^{2+}$ , which will cause the plugging agent to fail. At present, there are few studies on organic cross-linking agent gels (formaldehyde, phenol, etc.), and most of them focus on the use of a single cross-linking agent to synthesize the gel

[7–9]. Compared with metal ions and a single organic cross-linking agent, double organic cross-linking agent gel has higher thermal stability through covalent bond cross-linking and is more suitable for high-temperature, unconventional oil reservoirs [10–12].

Due to the high temperature and high pressure of unconventional tight oil reservoirs in Xinjiang and the characteristics of ultralow porosity and ultralow permeability reservoirs, conventional plugging agents are difficult to plug, and the effective plugging time is not long, and the plugging effect is extremely poor. In this study, based on the high-temperature characteristics of the tight oil reservoirs in Xinjiang tight oil reservoir, a phenolic-larch tannin temperature-resistant plugging agent was synthesized by changing the mass fractions of larch tannin, double cross-linking agent, and accelerator.

Wang et al. [13–15] have made a high-temperature blocking agent capable of resisting 250°C by mixing sulfonated tannin extract with phenol, formaldehyde, or paraformaldehyde. Fangeng et al. [16] used tannin extract as raw material to react with phenol and formaldehyde and

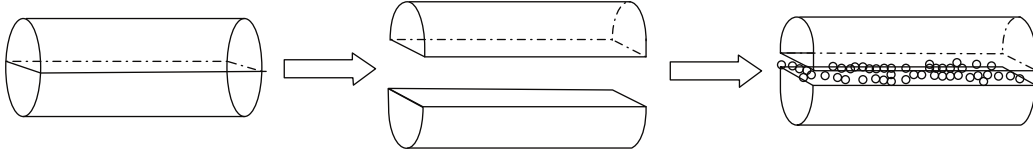


FIGURE 1: Physical treatment of natural cores.

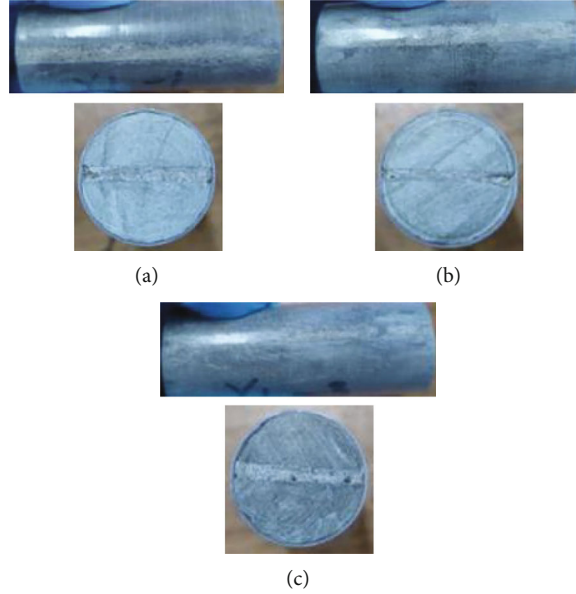


FIGURE 2: Artificially fractured natural core.

TABLE 1: Summary of physical properties of the cores applied in this study.

Core number	Length (cm)	Diameter (cm)	Porosity (%)	Permeability ( $10^{-3} \mu\text{m}^2$ )
Core #1	6.77	2.62	10.72	1726.1
Core #2	6.04	2.64	8.02	1688.3
Core #3	6.70	2.57	7.37	1696.3

then used transition metal salts such as inorganic salts  $\text{MnSO}_4$ ,  $\text{TiCl}_4$ , and tannin extract. The chelation reaction occurs to promote the cross-linking reaction, and the gel is formed in the range of  $170\sim 280^\circ\text{C}$  and pH value of  $4\sim 9$ , and a good blocking effect is achieved. Dezhi et al. [17] also used tannin extract as raw material to prepare a water plugging agent suitable for high-temperature profile control. It was determined by experiments that after adding an accelerator, a selective plugging agent with enhanced strength of the plugging agent can be obtained with the increase of temperature, which can be applied to high-temperature formations. Han et al. [18] have obtained a profile control and water plugging agent that can withstand high temperatures of  $300^\circ\text{C}$  through experimental research using tannin extract as raw material. After field tests in Liaohe Oilfield, they obtained a good production increase effect, and at the same time, the water yield also decreased.

Gel dispersion is obtained by shearing and grinding the synthesized gel to a state where the particles are stably dispersed in an aqueous solution [19]. The dispersed gel is easy to inject because it has low viscosity and controllable particle size; it can be elastically deformed, spontaneously aggregate in the pore throat, and migrate to the deep part of the reservoir [20–25], which can avoid the dilution of formation water during pumping and formation shearing and migration. Compared with other granular plugging control agents, dispersed gel has better stratum adaptability [26, 27].

Plugging performance is an important index to evaluate the application of gel dispersion in the oil field, which is mainly affected by the characteristics of the dispersed gel [28]. At present, research on the mechanical properties of gel-plugging agents mostly has involved the performance of large-particle-size gel [29–31]. The mechanical properties of dispersed gels have not been systematically studied. The ability of dispersed gels with different mechanical properties to resist deformation after being squeezed during the migration process is different, which affects the blocking effect. At present, the gel strength code (GSC) method and rheological parameter method are generally used to characterize the strength of bulk gel [32–34], but there are few studies on directly characterizing the mechanical properties of the dispersed gel itself. Therefore, this paper introduces micro-nano-scale Young's modulus, which reflects the ability of the dispersed gel to resist deformation after being

TABLE 2: Experiment reagents used in this study.

Base tannin	Cross-linking agent		Accelerator	pH conditioner
Larch tannin (tannin content 60%, nontannin content 35%, and insoluble matter content 5%)	Formaldehyde (analytical pure)	Phenol (analytical pure)	MnSO <sub>4</sub> (analytical pure)	Sodium hydroxide (analytical pure)



(a) YP-1 high-temperature, high-pressure gel performance test device



(b) Atomic force microscope

FIGURE 3: Instruments used in the experiment.

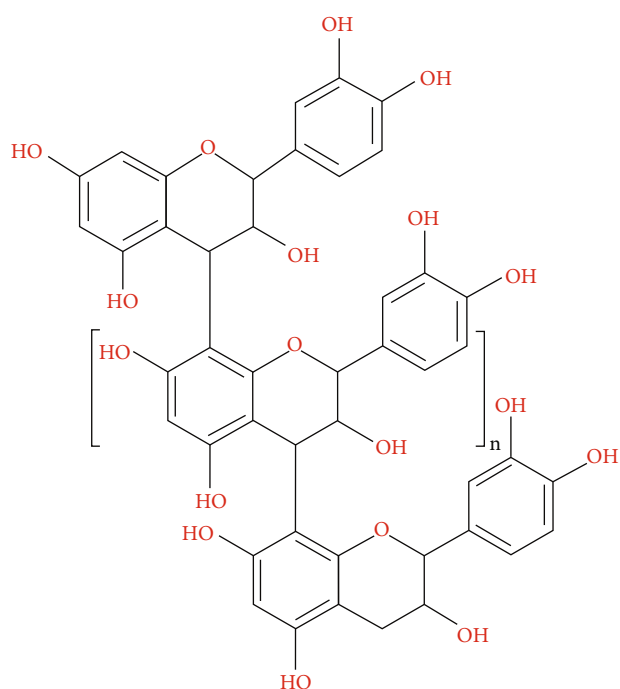


FIGURE 4: Polyprocyanidin [42].

compressed when it migrates in the porous medium and directly quantifies the mechanical properties of the gel. Traditional measurement methods of Young's modulus include the optical lever stretching method, pulse excitation method, and acoustic resonance method [35–37], but none of these methods can be used to characterize micro-nano-scale materials. With the development of nanomechanical measure-

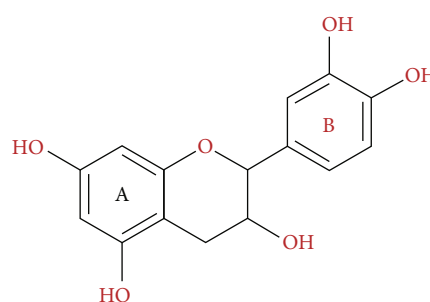


FIGURE 5: Procyanidin monomer [42].

ment technology, the atomic force microscope has become the most advanced and intuitive method for measuring small-scale materials [38–41].

Different from previous literature, the three new insights in this study mainly focus on the strengthening of the sulfonated larch gel structure system through the paraintermediate, the relationship between the gel storage modulus and Young's modulus of its dispersion, and the relationship between its mechanical strength and its macroscopic plugging performance. In this paper, by optimizing the mass fractions of four reagents (tannin, formaldehyde, phenol, and manganese sulfate) to synthesize temperature-resistant sulfonated larch gel, the relationship between the mechanical strength of sulfonated larch gel and the plugging performance was studied through three artificially fractured core flow experiments. The formula of the high-temperature-resistant tannin system optimized by the experiment is as follows: 3.0% sulfonated tannin + 3.0% formaldehyde cross-linking agent + 1.0% phenol cross-linking agent + 0.05% MnSO<sub>4</sub> accelerator. Secondly, the mechanical strength of the

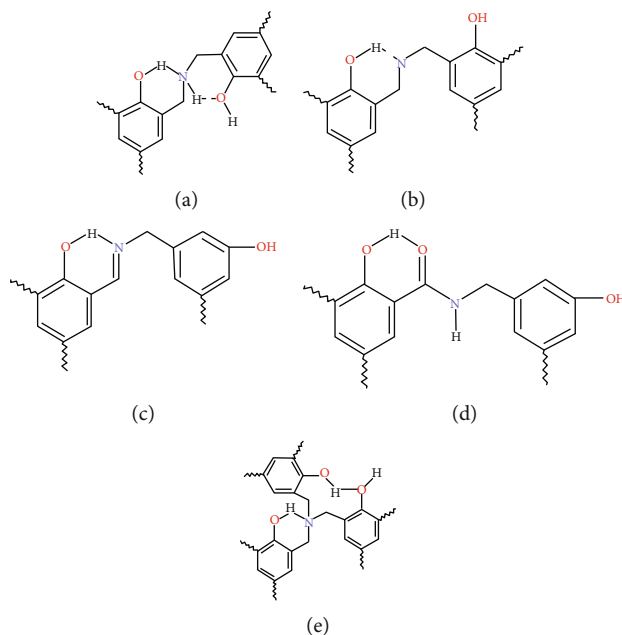


FIGURE 6: Structural intermediate in the cross-linking process.

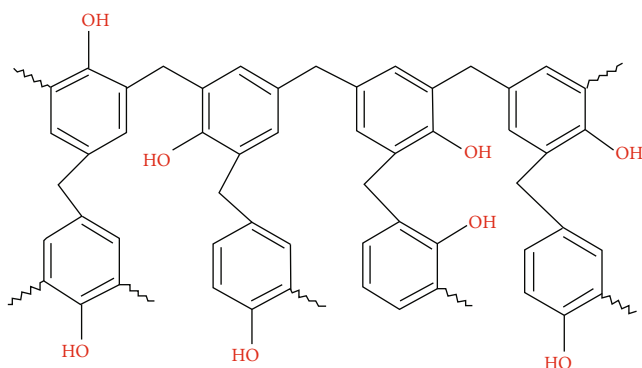


FIGURE 7: Novolac-type phenolic resin forms a network-like strengthening structure.

tannin gel and its plugging performance have a linear relationship. When Young's modulus rises from 18.74 to 63.89 kPa, the plugging rate rises from 94.11% to 97.44%.

## 2. Materials and Methods

**2.1. Materials.** In this study, artificially fractured natural cores (3.15 in) were used to conduct macroscopic plugging performance evaluation experiments. The cores were cut from the Xinjiang oilfield tight oil reservoir. The core was first cut in half along the midline and filled with quartz sand to simulate postfracturing fractures. Use a small amount of epoxy resin and heat-shrinkable tubing for fixing to ensure the overall strength of the core. The preparation process is shown in Figures 1 and 2. The properties (permeability and porosity) of the cores are listed in Table 1. The brine used in this study was simulated formation water. The salinity of the brine was 7197.77 mg/L.

The reagents used in this experiment are shown in Table 2.

The instruments used in this study were a JB200-SH electric stirrer (speed range of 0 to 8000 rpm); YP-1 high-temperature, high-pressure gel performance test device (Figure 3(a)); Keysight 7500 atomic force microscope (AFM) (Figure 3(b)); oven; electronic balance (accuracy of 0.001 g); and ground flask, beaker, dropper, suction ball, glass rod, graduated cylinder, etc.

### 2.2. Methods

**2.2.1. Preparation Principle of Larch Tannin Gel.** The main component of larch tannin is condensed tannin, its chemical composition is polyanthocyanidin, the average molecular weight is about 2800 (determined by vapor phase osmometry (VPO)), and the average degree of polymerization is 9 to 10. Its specific configuration is shown in Figures 4 and 5. Larch tannin has a higher molecular weight and a higher viscosity, and the length of the  $-\text{CH}_2-$  cross-linked bond generated by formaldehyde is not long enough to form sufficient cross-links between the reaction points, resulting in insufficient bonding strength. Therefore, a second cross-linking agent, phenol, was added in this study. The phenol molecules can react with the formaldehyde cross-linking agent in the main body of the gel-forming solution, and the formed structure can be interlaced with the main network structure formed by larch tannin to make the system whole. The structure is more compact, and the strength is greatly improved.

The reaction rate is significantly affected by temperature and accelerator. Therefore, an accelerator,  $\text{MnSO}_4$ , was added in this study to accelerate the reaction process, such that the main network structure formed by larch tannin and the novolac phenolic resin-reinforced structure were



TABLE 3: Observation method to evaluate gel standards.

Level	Status description	Classification
A	The gel viscosity is the same as the initial viscosity, and no gel is formed by visual inspection	No gel formed
B	The gel viscosity is slightly higher than the initial polymer viscosity	
C	Upside down has obvious flow	Weak gel
D	There is a small amount of gel that does not flow quickly	
E	The gel does not flow easily	
F	The gel can only flow in a small area at the top	Medium gel
G	The gel flow is about halfway down	
H	The surface of the gel is slightly deformed when inverted	
I	The surface of the gel is not deformed when inverted	Strong gel



FIGURE 8: Breakthrough vacuum experimental device [44].

formed almost at the same time and that their structures were intertwined to make the system whole. The overall structure was more compact, and the strength was greatly improved. It continued to decompose during the heating and curing process, and there may be a variety of ortho-to-position intermediate structures during the cross-linking process [43], as shown in Figure 6.

Under the application of high temperature, the various intermediates formed by the mixture system composed of low-molecular-weight oligomers and various hydroxymethyl phenols will gel, and various intermediates will exist in the main body of larch tannin. Interlacing each other in the network structure makes the overall structure of the system more compact and greatly improves the strength. Its possible reinforcement network configuration is shown in Figure 7.

### 2.2.2. Preparation and Characterization of Larch Tannin Gel.

The following steps were taken to prepare the larch tannin gel: Add the dry larch tannin powder to clear water at room temperature, stir with an electric stirrer for 2 hours to fully dissolve it, and prepare a 0.3% to 7% tannin solution. Add formaldehyde with a mass fraction of 2.2% to 3.6% to the tannin solution, stir it evenly, and let it stand for 10 minutes. Add 0.5% to 3.0% phenol to the tannin solution, and stir well. Add 0.01% to 0.1%  $\text{MnSO}_4$  with a mass fraction of 0.01% to 0.1%, stir evenly, and put it in a constant temperature oven at 248°F for 24 hours.

The strength grade of the gel in the ground bottle was observed by visual inspection (Table 3) and measured by the vacuum penetration method (Figure 8). A HAAKE MARS III rotational rheometer was used to measure the storage modulus,  $G'$ , of the gel. The gel was aged at 302°F

for 30 days, the change in gel strength grade was observed every day, and the change in storage modulus was measured by the rheological parameter method.

Gel strength was measured by the breakthrough vacuum method [44]. The experimental setup is shown in Figure 8. Connect the blue-cap bottle containing the gel to the vacuum breakthrough experimental device as shown in Figure 1; insert the tip of the 1 mL pipette 1 cm below the surface of the gel. Start the vacuum pump. Slowly adjust the knob to increase the vacuum degree of the system. When the air breaks through the gel, the maximum reading of the vacuum gauge on the vacuum gauge is the breakthrough vacuum degree of the gel. It is referred to as the BV (breakthrough vacuum) value; each sample is repeatedly measured 3 times. Its arithmetic mean is taken as its final BV value. The larger the BV value, the higher the strength, on the contrary, the lower the strength.

At room temperature, an appropriate amount of the bulk gel was transferred onto a mica sheet, and the sample was scanned using the tapping mode of an atomic force microscope to characterize the microscopic morphology of the gel.

### 2.2.3. Preparation of Dispersed Gel and Its Young's Modulus Measurement.

Gel with different mass fractions of the cross-linking agent and clean water was added to a colloid pulverizer at a ratio of 1 : 1, and the micro-nano-scale dispersed gel with similar particle size was obtained by controlling the rate and time of cyclic shearing.

The test probe model SCANASYST-FLUID was selected, the elastic constant was 0.7 N/m, the Thermal Tune method was used to correct the elastic coefficient, and the scan rate was set to 1 Hz. The peak force mode of the atomic force microscope was used to measure in a liquid environment, and the relationship curve between the force and the distance between the probe and the dispersed gel sample was obtained. The distance between the probe and the dispersed gel sample was equivalent to the deformation of the dispersed gel sample. By fitting and calculating the DMT mechanical model, Young's modulus ( $E$ ) of the micro-nano-scale dispersed gel could be obtained [45]:

$$F = \frac{4}{3} E \sqrt{R \delta_s^3} + F_a, \quad (1)$$

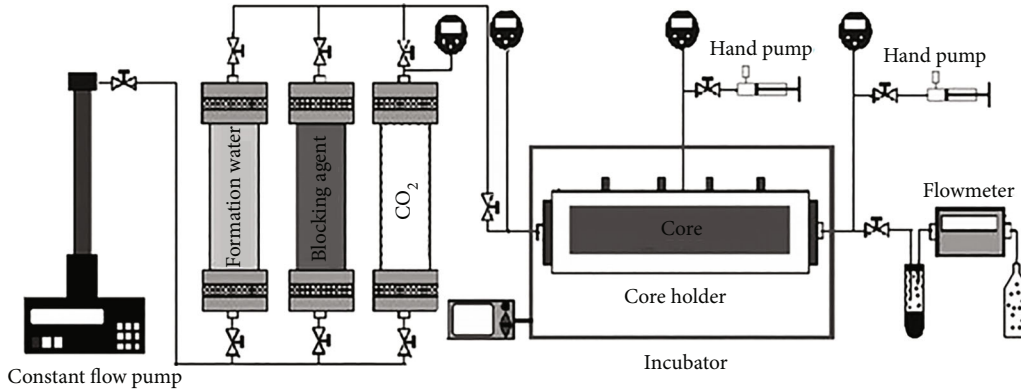


FIGURE 9: Single-core physical experiment flow chart.

where  $F$  is the force between the tip and the sample,  $E$  is the DMT modulus,  $R$  is the radius of the tip,  $\delta_s$  is the amount of sample deformation, and  $F_a$  is the adhesion force on the sample.

**2.2.4. Evaluation of the Plugging Performance of Dispersed Gel.** At room temperature, a single-core physical experiment was performed to determine the initial permeability of the natural core by water flooding. The dispersed gel was continuously injected into the natural core at a rate of 0.5 mL/min until the liquid injection volume reached 1 PV, and then, subsequent water flooding was performed at a constant speed until the pressure at the output end of the natural core was stable; the pressure change at the injection end of the natural core was recorded. The injection pressure, the plugging efficiency ( $\epsilon$ ), and the residual resistance coefficient ( $F_{rr}$ ) were used to characterize the plugging ability of the dispersed gel to the large pore throats in the reservoir. The flow chart of the experiment is shown in Figure 9.

### 3. Results and Discussion

#### 3.1. Gel Strength

**3.1.1. Effect of Tannin Concentration.** Tannin is the main body of the whole system, and its concentration directly affects the gel-forming performance of the plugging agent. Simulated formation water was used in the experiment to maintain the formaldehyde cross-linking agent concentration of 3.0%, the phenolic accelerator (P1) concentration of 1.5%, the inorganic salt accelerator concentration of 500 mg/L (unchanged), and the change in tannin concentration (0.3% to 7%). The experimental results were recorded and investigated for the gelation of the tannin system under different tannin concentrations. The experimental results are shown in Figure 10.

The experimental results show that a small amount of tannin does not gel. It can be gelatinized in the range of 0.3% to 7% by a mass fraction. When the mass fraction of the cross-linking agent is less than 0.3%, it is not enough to form a network structure with sufficient strength, but sporadic small micelles are formed, resulting in no gelling. As the concentration of tannin increases, the gelation time of

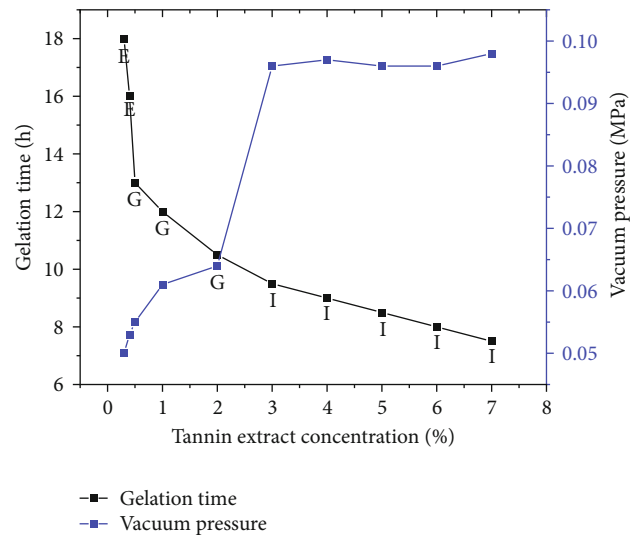


FIGURE 10: The effect of tannin concentration on the gel formation and strength of the system.

the system is gradually shortened, and the gel strength gradually increases. When the mass fraction reaches 3.0%, the gelation time of the entire system is 10 hours, the gel strength is level I, and the vacuum test can reach 0.095 MPa. Meeting the evaluation criteria and continuing to increase the tannin concentration, the gel strength does not change much, so the preferred tannin concentration is 3.0%, and the actual gel formation diagram is shown in Figure 11.

**3.1.2. Effect of Formaldehyde Cross-Linking Agent Concentration.** After keeping the temperature at 120°C, pH at 10 to 11, tannin concentration at 3.0%, phenol cross-linking agent concentration at 1.0%, and inorganic salt accelerator ( $\text{MnSO}_4$ ) concentration at 0.05% (unchanged) and changing the formaldehyde cross-linking agent concentration (2.2% to 3.6%), the experimental results were recorded and investigated for gel formation of the tannin system under different cross-linking agent concentrations. The experimental results are shown in Figure 12.

The experimental results show that the concentration of the formaldehyde cross-linking agent has a significant effect

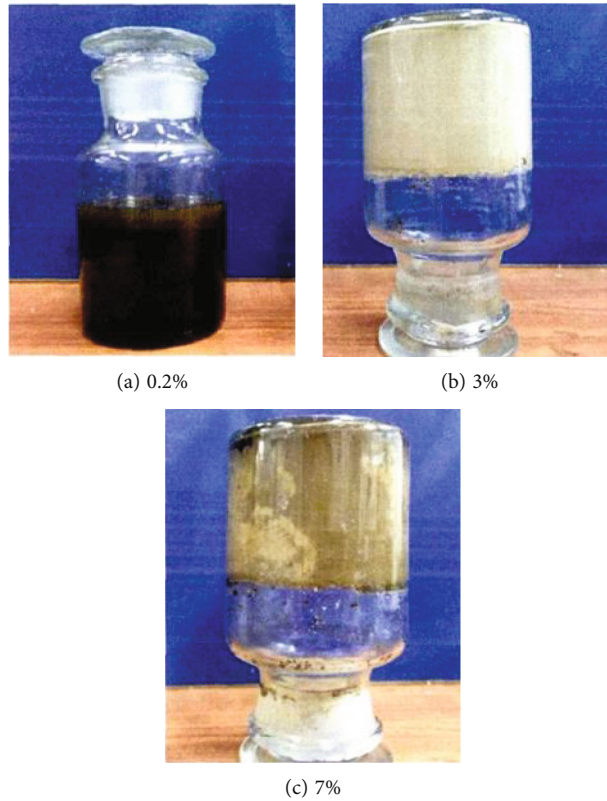


FIGURE 11: Performance of the gel under different tannin concentrations.

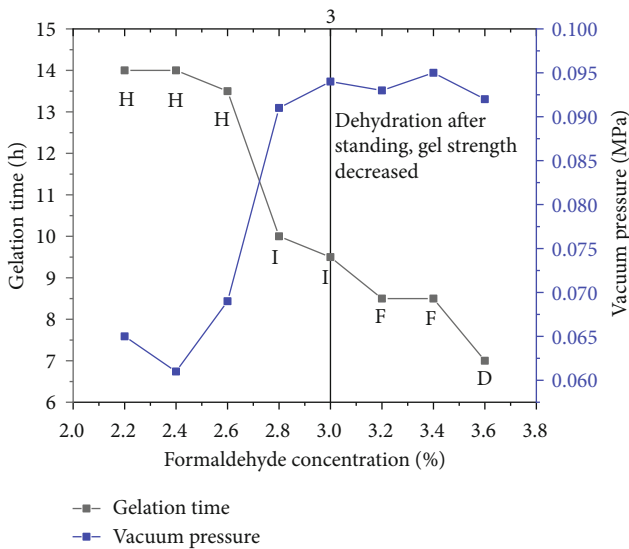


FIGURE 12: The effect of formaldehyde cross-linking agent concentration on the gel formation and strength of the system.

on the gel-forming effect of the entire system. As the concentration of the cross-linking agent increases, the gel-forming time gradually decreases, and the gel-forming strength first increases and then decreases. This is because when the concentration of tannin is constant, the number of reactive

groups is determined. As the concentration of the cross-linking agent increases, the reaction speed increases, the gel-forming time is shortened, and the gel strength increases. However, when the cross-linking agent concentration is too high, the system will be excessively cross-linked, the gel is easily dehydrated, and the strength becomes low. When the cross-linking agent concentration is 2.8% to 3.0%, the gel-forming time of the system is 9.5 hours, and the gel strength is level I, which meets the evaluation standard. Therefore, the preferred concentration of the formaldehyde cross-linking agent is 3.0%.

Experiments have found that when the content of the aldehyde cross-linking agent reaches 3.2% and above, the formed gel is prone to dehydration after a period of time, and then, the gel strength is greatly reduced. This phenomenon is caused by over-cross-linking of the cross-linking agent.

### 3.1.3. Effect of Phenol Cross-Linking Agent Concentration.

After keeping the tannin concentration at 3.0%, the formaldehyde cross-linking agent concentration at 3.0%, and the accelerator ( $MnSO_4$ ) concentration at 0.05% (unchanged) and changing the phenol concentration (0.5% to 3.0%), the experimental results were recorded and investigated for the gelation of the tannin system under different phenol cross-linking agent concentrations. The experimental results are shown in Figure 13.

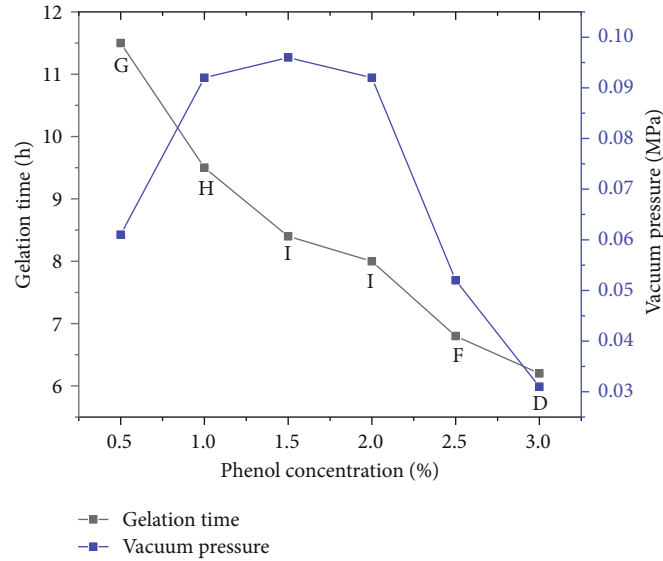


FIGURE 13: The effect of phenol cross-linking agent concentration on the gel formation and strength of the system.

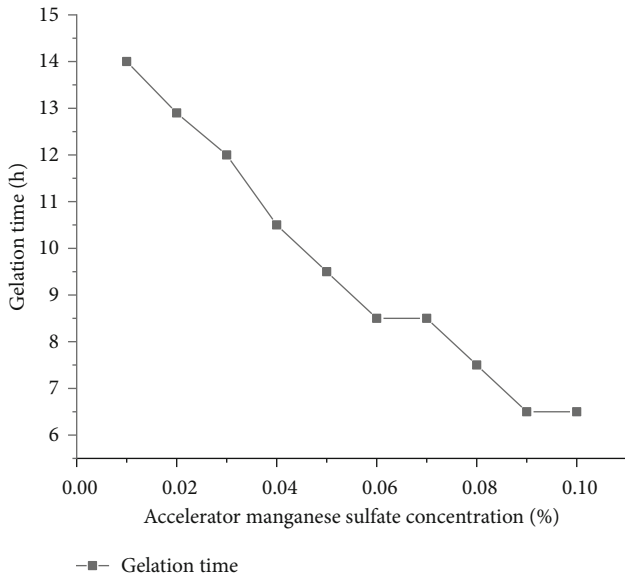


FIGURE 14: The effect of accelerator concentration on the gel-forming effect of the system.

The experimental results show that the performance of the plugging agent varies with the phenol cross-linking agent, similar to that of the formaldehyde cross-linking agent. When the concentration of the phenol cross-linking agent is less than 0.5%, the cross-linking strength of the system is too low; when the concentration is 1.0% to 2.0%, the greater the concentration of phenol cross-linking agent, the shorter the gelation time of the system and the stronger the gel formed. However, when its concentration exceeds 2.0%, the gel strength of the system is weakened because when the concentration of the phenol cross-linking agent is low, it cannot form an effective network structure with the sulfonated tannin and can only interact with the formaldehyde cross-linking agent at a local position. The interac-

tion of molecules involved in the cross-linking reaction results in poor gelation strength of the system. With the gradual increase in the concentration of the phenol cross-linking agent, more molecules can react with the formaldehyde cross-linking agent in the main body of the gel-forming solution, and the formed structure can be interlaced with the main network structure formed by the sulfonated tannin to make the system whole. The structure is tighter, and the strength gradually increases, but when the concentration of the phenol cross-linking agent exceeds a certain value, too many formaldehyde cross-linking agent molecules will preferentially react with the phenol cross-linking agent, weakening the main structure of the system and leading to a blocking agent. The strength is slightly reduced. Therefore, the concentration of the phenol cross-linking agent is preferably 1.0%.

**3.1.4. Effect of  $MnSO_4$  Accelerator Concentration.** After the sulfonated tannin reacted with phenol, the inorganic salt  $MnSO_4$  was used to chelate the tannin to promote the cross-linking reaction. In the experiment, Western China tight oilfield formation water was used to prepare the solution, keeping the tannin concentration at 3.0%, the formaldehyde cross-linking agent concentration at 3.0%, the phenol cross-linking agent concentration at 1.0%, and the accelerator concentration between 0.01% and 0.1%. The experimental results were recorded and investigated for the gelation of the tannin system under different accelerator concentrations. The experimental results are shown in Figure 14.

The experimental results show that as the concentration of the accelerator increases, the gelation time is gradually shortened, the gelation strength does not change much, and the strength level (I) basically remains unchanged because the transition metal salt has a chelation reaction with tannin to promote the cross-linking reaction. When the concentration of the cross-linking agent is constant,



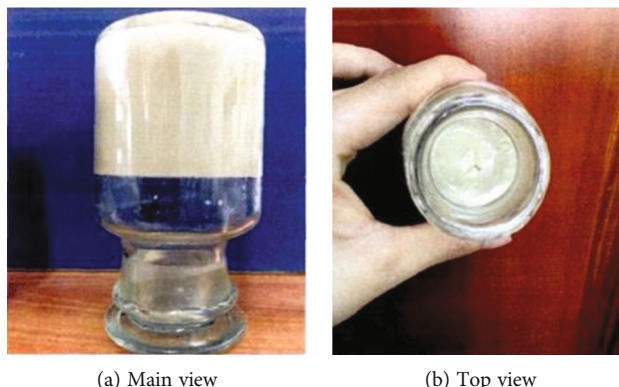


FIGURE 15: Preferred accelerator concentration tannin gel (accelerator 0.05%).

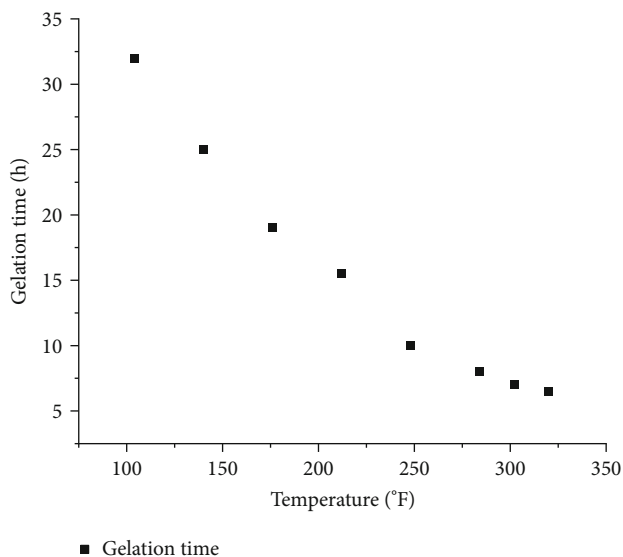


FIGURE 16: The effect of temperature on the gel-forming effect of the system.

adding the accelerator can increase the reaction speed of the system and shorten the gel-forming time. When the concentration of the accelerator is 0.05%, the gel-forming effect of the system meets the evaluation criteria. Considering the actual economic benefits, the preferred accelerator concentration is 0.05%. The actual gel-forming diagram is shown in Figure 15.

### 3.2. Gel Strength

#### 3.2.1. Effect of Temperature.

After taking the preferred formula (- 3.0% sulfonated tannin + 3.0% formaldehyde cross-linking agent + 1.0% phenol cross-linking agent + 0.05% accelerator) and placing it in a thermostat at different temperatures, the experimental results were recorded and investigated for the temperature resistance of the system. The gel was prepared at 104°F, 140°F, 176°F, 212°F, 248°F, 284°F, 302°F, and 320°F. The gelation time was used as an indicator to evaluate the gelling ability of the bulk gel. The results are shown in Figure 16. The experimental results show that the tannin

system cannot be gelled at 104°F. It can be gelled under the temperature conditions of 140°F to 320°F. When the temperature is between 140°F and 248°F, the strength of the gel is H grade, and when the temperature is before 248°F-320°F, the gel strength is I grade. As the temperature increases, the gelation time of the system decreases, indicating that the system has good temperature resistance stability.

3.2.2. Effect of Aging Time. The gel was aged at 302°F for 30 days. The storage modulus was used as an indicator to evaluate the stability of the bulk gel. The results are shown in Figure 17. The experimental results show that gels with 2.4% and 3.2% cross-linking agent mass fraction will decrease the mechanical strength of the gel to a certain extent as the aging time increases. The higher the cross-linking agent mass fraction, the more obvious the decrease in gel storage modulus. The storage modulus of the bulk gel with 3.0% tannin and 2.8% cross-linking agent mass fraction decreased from 2.74 to 2.54 Pa within 30 days. The storage modulus of the gel with 3.0% tannin and 3.0% cross-linking agent mass fraction decreased rapidly in the first 15 days (from 4.85 to 3.41 Pa); the later storage modulus decreased slightly and finally decreased to 3.13 Pa. However, the gel with 3.0% tannin and 3.2% cross-linking agent mass fraction was completely dehydrated when it was aged for 13 days. This shows that the dense structure in the gel can slow the release rate of bound water to a certain extent, but as the mass fraction of cross-linking agent increases, the degree of intermolecular cross-linking reaction increases. When the mass fraction of the cross-linking agent is too high, the formation reaction of multinuclear hydroxyl bridge ions moves relatively quickly to the right, resulting in excessive cross-linking. During a certain aging time, the spatial network structure of the gel system is destroyed due to syneresis, and the final strength is significantly reduced. Therefore, the gel with too high a mass fraction of cross-linking agent has poor stability and is not suitable for reasonable and effective control of the reservoir.

3.2.3. Effect of pH Value. After taking the preferred formula (- 3.0% sulfonated tannin + 3.0% formaldehyde cross-linking agent + 1.0% phenol cross-linking agent + 0.05% accelerator),



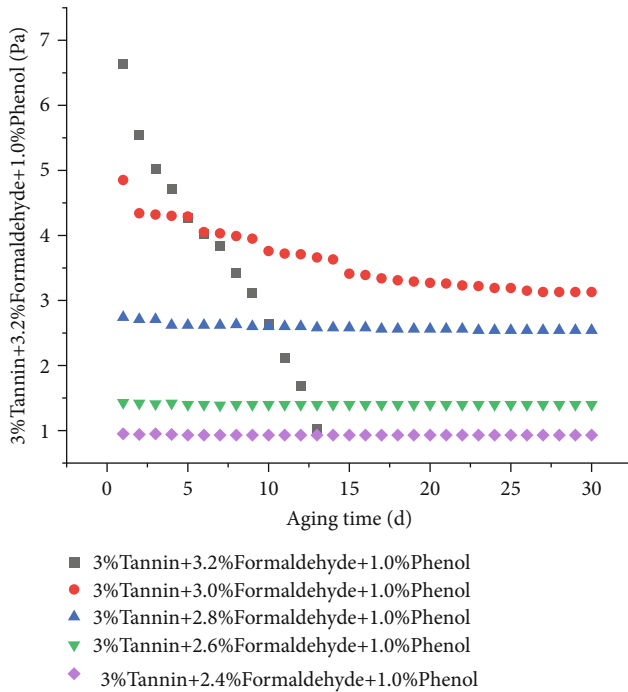


FIGURE 17: Change trend of gel strength with aging time.

adjusting the pH of the system, and placing it in a thermostat, the experimental results were recorded and investigated for the effect of pH on the performance of the tannin system. The experimental results are shown in Figure 18. With the increase in pH value, the gelation time of the tannin system gradually decreases, and the gel strength first increases and then decreases. This is because the B ring in the tannin system only reacts when the pH value is higher than 10 or in the presence of metal ions. A pH value higher than 10 will reduce the gelation time, and the network structure of the system will be affected in a strongly alkaline environment. If it is destroyed, it cannot be cross-linked or the cross-linked structure fails, which reduces the strength of the system. The experimental results also confirm this point; that is, under the same conditions as other components, without adjusting the pH value, the tannin solution (pH = 3 – 5) is not easy to gel, and the strength of the plugging agent is relatively weak.

The reaction of tannin and formaldehyde mainly occurs in the A ring, as shown in Figure 19(a). When the pH value is higher than 10, the B ring can react with formaldehyde [46], as shown in Figure 19(b).

Therefore, the suitable pH value of the tannin system is 6 to 10. At the same time, if the blockage needs to be removed at a later stage, an acid solution of pH < 5 or an alkaline solution of pH > 10 can be used to remove the blockage.

Through experimental screening, the final optimized formula of the high-temperature-resistant tannin system is as follows: 3.0% sulfonated tannin + 3.0% formaldehyde cross-linking agent + 1.0% phenol cross-linking agent + 0.05%  $\text{MnSO}_4$  accelerator.

**3.2.4. Effect of Erosion Resistance.** The core parameters used and the experimental results are shown in Table 4. The 6 PV

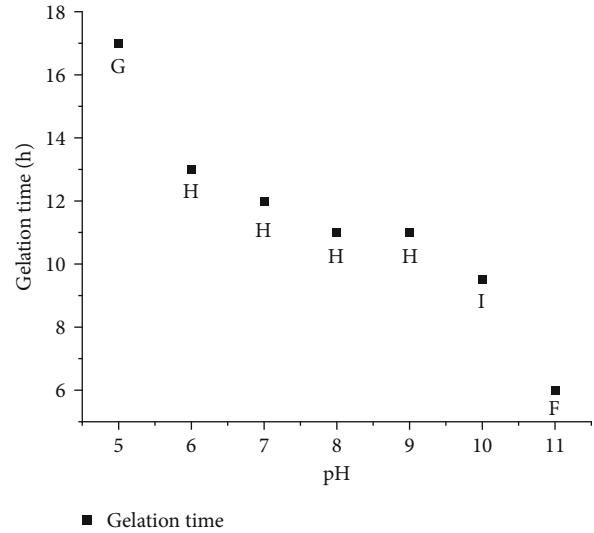


FIGURE 18: The change trend of gel strength with pH.

was continuously displaced by water injection at a constant flow rate, the pressure changes were recorded, and the scour resistance of the plugging agent was investigated. The variation of injection pressure with injection amount is shown in Figure 20.

The experimental results show that the injection pressure first increases and then decreases with the increase of the injected water. When the injection amount is 1.0 PV, the injection pressure reaches the maximum value, and the plugging rate can still reach 93.8% when the injection amount is 6 PV, indicating that the tannin extract system has good erosion resistance.

**3.3. Characterization of Young's Modulus of Dispersed Gel.** According to the gel-forming performance test results of the gel-forming liquid with different cross-linking agent concentrations, it was found that when the mass fraction of the sulfonated tannin is controlled at 3.0%, the mass fraction of the cross-linking agent increases from 2.2% to 2.4%, the macrostrength code assesses the gel at level H, and the storage modulus value measured by the rheological parameter method rises from 0.95 to 1.41 Pa. Then, the difference in the mechanical properties of the dispersion prepared by shearing the gel with the same strength code and different storage moduli will further increase, which will impact the effect of the dispersed gel in plugging the reservoir.

Therefore, Young's modulus ( $E$ ) of the dispersed gel was measured using the peak force mode of an atomic force microscope. Because the dispersed gel sample belongs to the state of soft particles and is dispersed in the liquid phase, a probe with a small elastic constant (1.0 N/m) was selected for measurement in a liquid environment. The force-distance curve of each pixel in the imaging process of the dispersed gel in a liquid environment was recorded in real time, and Young's modulus of the micro-nano-scale dispersed gel was obtained by fitting calculation. Because the micro-nano-scale dispersed gel particles were low-viscosity samples, there was a certain adhesive force when the needle tip interacted with the dispersed gel sample, but it was small.

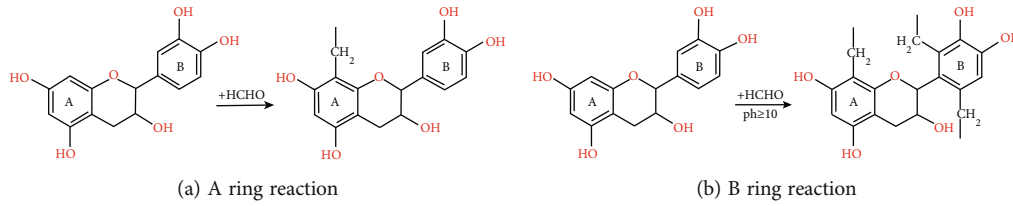


FIGURE 19: The reaction formula of tannin and formaldehyde.

TABLE 4: Erosion resistance performance evaluation test results.

Core number	Permeability ( $10^{-3} \mu\text{m}^2$ )	Injection blocking agent (PV)	After continuous displacement of 6 PV water permeability ( $10^{-3} \mu\text{m}^2$ )	Blocking rate (%)
Core #1	1726.1	0.5	106.5	93.8

Therefore, the Hertz model was not considered [47]. The JKR model under high adhesion experimental conditions is not suitable for characterizing Young's modulus of dispersed gel [48]. Therefore, Young's modulus of the micro-nano-scale dispersed gel was obtained by fitting the calculation of the DMT model [49]. During the experiment, parameter settings such as the peak force of each dispersed gel sample were always consistent with the test area.

Figure 21 shows the variation of the gel storage modulus and Young's modulus of the dispersed gel with the mass fraction of the cross-linking agent. It can be seen from the figure that when the mass fraction of the cross-linking agent is between 2.4% and 3.2%, as the mass fraction of the cross-linking agent increases, Young's modulus of the dispersed gel increases from 15.9 to 63.3 kPa, showing a linear increase. This trend is consistent with the change law of gel storage modulus on a macroscale. This linear increase law can be explained as when the mass fraction of the cross-linking agent increases, the cross-linking density between the polymer and the cross-linking agent increases greatly, the gel space network structure becomes denser, and the strength increases. The fracture of the prepared dispersed gel at the joint is relatively reduced, its phase deformation ability is reduced accordingly, and Young's modulus of the dispersed gel measured under the same peak force increases.

Young's modulus of micro-nano-scale dispersed gel is obviously higher than that of macroscale gel. The change in geometrical scale will lead to a significant increase in the order of molecules [50] and, at the same time, will increase the surface tension and thus change the mechanical properties of the sample. The storage modulus of the gel was measured by a dynamic shear rheometer under sinusoidal shear oscillation. It was used to indicate the storage of the gel's shear deformation capacity, that is, the elasticity of the gel. Young's modulus of the dispersed gel is measured by an atomic force microscope. The external load of atomic force microscopes (AFM) directly acts on the surface of the dispersed gel sample. Its Young's modulus represents the ability

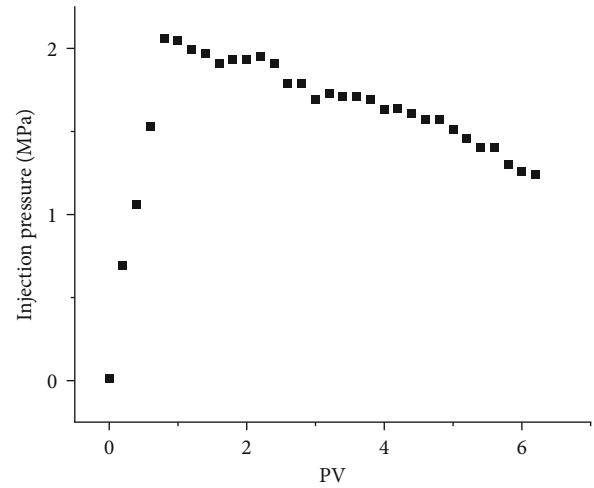


FIGURE 20: Plugging agent scour test.

of the dispersed gel to withstand unidirectional compressive stress and produce compression deformation.

The flexible particles of dispersed gel are not affected by the shear of the formation when they migrate in the porous medium and may be subjected to compression effects such as shape deformation when they pass through the pore throat [51]. When controlling the dominant channel and plugging the high-permeability layer, the gel may also be squeezed. Therefore, measuring Young's modulus of the dispersed gel under compression can be used to effectively and quantitatively characterize its mechanical strength. Under the combined influence of the two factors of geometric scale and physical principle, the measured Young's modulus of the dispersed gel and the storage modulus of the gel cannot be directly compared numerically, but there is a linear relationship between them.

### 3.4. Evaluation of the Plugging Performance of Dispersed Gel.

The artificially fractured core made from the natural core of the tight oil reservoir was used for physical simulation testing, and the prepared tannin dispersion was injected into the natural core. The injection pressure at a flow rate of 0.1 mL/min was investigated to characterize the injection performance and plugging performance of the dispersed gel. The change in the experimental residual resistance coefficient is shown in Table 3. When the mass fraction of the cross-linking agent increases from 2.6% to 2.8%, Young's modulus of the dispersed gel rises from 18.74 to 36.06 kPa, indicating that the two systems have little difference. With the further increase of the mass fraction of the cross-

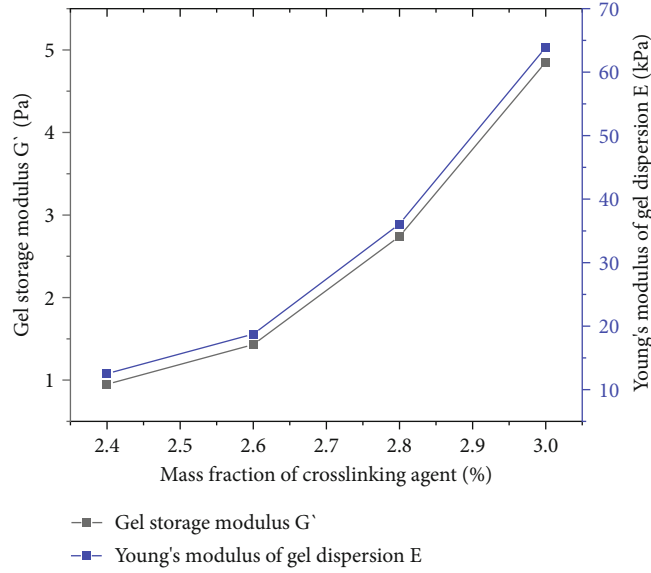


FIGURE 21: Variation of gel storage modulus and dispersed gel's Young's modulus with the mass fraction of cross-linking agent.

TABLE 5: Blocking rate of tannin plugging agent.

Core number	Mass fraction of formaldehyde (%)	Gel storage modulus $G'$ (Pa)	Young's modulus of dispersed gel $E$ (kPa)	$K_{w0}$ ( $10^{-3} \mu\text{m}^2$ )	$K_{w2}$ ( $10^{-3} \mu\text{m}^2$ )	Frr	Blocking rate (%)
Test #1	2.6	1.43	18.74	1726.1	101.8	16.95	94.11
Test #2	2.8	2.74	36.06	1688.3	87.8	19.22	94.82
Test #3	3.0	4.85	63.89	1696.3	43.3	39.17	97.44

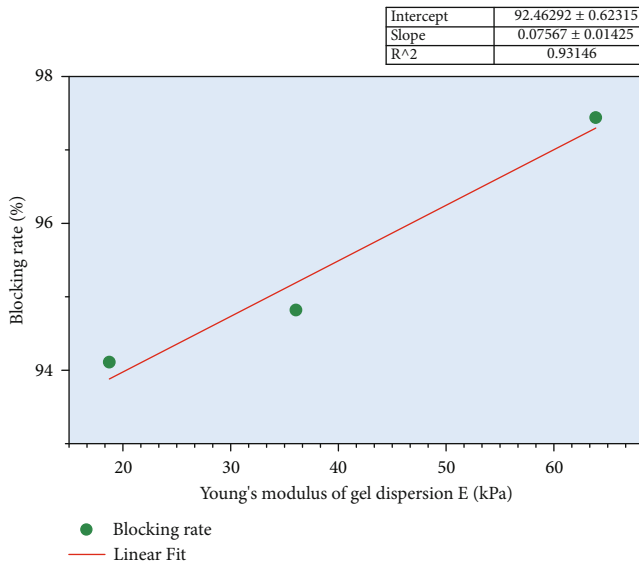


FIGURE 22: The plugging rate of dispersed gel varies with Young's modulus.

linking agent to 3.0%, Young's modulus of the dispersed gel increases relatively dramatically, and the residual drag coefficient also increases significantly. The experimental results are shown in Table 5. The plugging rate of different formulations of the plugging agent is above 94%, and the plugging rate of the preferred formulation is above 97%, indicating

that the tannin system has good plugging performance and can meet the needs of reservoirs. As shown in Figure 22, Young's modulus of the dispersed gel has a good linear relationship with the core plugging rate. Under the premise of ensuring the stability of the body gel, Young's modulus of the dispersed gel increases, and the plugging effect is better.

## 4. Conclusions

The conclusions of this study are listed as follows.

- (1) Through experimental screening, the final optimized formula of the high-temperature-resistant tannin system is 3.0% sulfonated tannin + 3.0% formaldehyde cross-linking agent + 1.0% phenol cross-linking agent + 0.05%  $\text{MnSO}_4$  accelerator
- (2) Young's modulus of the corresponding dispersed gel can be adjusted by adjusting the gel formula. When the mass fraction of tannin is 3.0% and the mass fraction of cross-linking agent increases from 2.4% to 3.0%, the cross-linking density increases, and the storage modulus of the gel increases from 1.43 to 4.85 Pa. Young's modulus of the dispersed gel obtained by physical shearing of the gel increases from 18.74 to 63.89 kPa
- (3) When Young's modulus of the dispersed gel increases from 18.74 to 63.89 kPa, the blocking rate

increases from 94.11% to 97.44%. Seeking the range of Young's modulus corresponding to excellent application performance of the dispersed gel provides a theoretical basis for improving the unconventional ability of dispersed gel to control tight oil reservoirs

## Data Availability

The data that support the findings of this study are available on request from the corresponding author. The data are not publicly available due to privacy or ethical restrictions.

## Conflicts of Interest

The authors declare that they have no conflicts of interest.

## Acknowledgments

This research was funded by the National Natural Science Foundation of China, grant number 52174035.

## References

- [1] C. Cheng, X. Li, and H. T. Qian, "Anisotropic failure strength of shale with increasing confinement: behaviors, factors and mechanism," *Materials*, vol. 10, no. 11, 2017.
- [2] Z. B. Zhang and X. Li, "The shear mechanisms of natural fractures during the hydraulic stimulation of shale gas reservoirs," *Materials*, vol. 9, no. 9, 2016.
- [3] X. Zhang and Y. Zhang, "Experimental and numerical investigation on basic law of dense linear multihole directional hydraulic fracturing," *Geofluids*, vol. 2021, Article ID 8355737, 19 pages, 2021.
- [4] J. Zou, Y.-Y. Jiao, F. Tan, J. Lv, and Q. Zhang, "Complex hydraulic-fracture-network propagation in a naturally fractured reservoir," *Computers and Geotechnics*, vol. 135, 2021.
- [5] B. J. Bai, J. Zhou, and M. F. Yin, "A comprehensive review of polyacrylamide polymer gels for conformance control," *Petroleum Exploration and Development*, vol. 42, no. 4, pp. 525–532, 2015.
- [6] Z. Dong, Y. Li, M. Lin, and M. Li, "Rheological properties of polymer micro-gel dispersions," *Petroleum Science*, vol. 6, no. 3, pp. 294–298, 2009.
- [7] T. Ichibouji, T. Miyazaki, E. Ishida et al., "Influence of cross-linking agents on apatite-forming ability of pectin gels," *20th International Symposium on Ceramics in Medicine*, vol. 361, pp. 559–562, 2007.
- [8] V. Purcar, D. Donescu, M. Ghiurea, S. Serban, C. Petcu, and C. Podina, "The effect of different cross-linking agents on the properties of hybrid films," *Optoelectronics and Advanced Materials-Rapid Communications*, vol. 3, no. 3, pp. 204–209, 2009.
- [9] H. Yamamoto, Y. Hirata, and H. Tanisho, "Cross-linking and insolubilization studies of water-soluble poly(l-ornithine)," *International Journal of Biological Macromolecules*, vol. 16, no. 2, pp. 81–85, 1994.
- [10] C. Anger, F. Deubel, S. Salzinger et al., "Organic-inorganic hybrid nanoparticles via photoinduced micellation and siloxane core cross-linking of stimuli-responsive copolymers," *ACS Macro Letters*, vol. 2, no. 2, pp. 121–124, 2013.
- [11] T. Liang, Z. Fan, Q. Liu, J. Wang, and J. Xu, "The study on double cross-linking gel plugging system," *IOP Conference Series: Materials Science and Engineering*, vol. 274, no. 1, 2017.
- [12] X. Wei, X. Li, X. Xue, and L. Ding, "Preparation and laboratory evaluation of a new type of cross-linking agent for acid fracturing fluid system," *Advanced Materials Research*, vol. 347, pp. 995–1000, 2011.
- [13] L. H. Wang, H. F. Xia, P. H. Han et al., "Synthesis of new PPG and study of heterogeneous combination flooding systems," *Journal of Dispersion Science and Technology*, vol. 43, no. 2, pp. 164–177, 2022.
- [14] X. Han, L. H. Wang, H. F. Xia, P. Han, R. Cao, and L. Liu, "Mechanism underlying initiation of migration of film-like residual oil," *Journal of Dispersion Science and Technology*, 2021.
- [15] H. F. Xia, L. H. Wang, P. H. Han, R. Cao, S. Zhang, and X. Sun, "Microscopic residual oil distribution characteristics and quantitative characterization of producing degree based on core fluorescence analysis technology," *Geofluids*, vol. 2021, Article ID 8827721, 17 pages, 2021.
- [16] C. Fangeng, H. Ling, and M. Baoqi, "Preparation of modified rubber bowl tannin extract for high temperature blocking agent," *Journal of Xi'an Shiyou University*, vol. 1, pp. 67–73, 1990.
- [17] L. Dezhi, Y. Fei, W. Rongjun, and D. Ming, "Study on high temperature blocking agent of larch tannin extract," *Xinjiang Oil and Gas*, vol. 8, Supplement 1, pp. 82–89, 2012.
- [18] X. Han, I. Kurnia, Z. Chen, J. Yu, and G. Zhang, "Effect of oil reactivity on salinity profile design during alkaline-surfactant-polymer flooding," *Fuel*, vol. 254, article 115738, 2019.
- [19] X. Sun, J. Zhao, T. Chen, and X. Liu, "Colloidal particle size of fumed silica dispersed in solution and the particle size effect on silica gelation and some electrochemical behaviour in gelled electrolyte," *Journal of Solid State Electrochemistry*, vol. 20, no. 3, pp. 657–664, 2016.
- [20] A. J. Gravelle and A. G. Marangoni, "Effect of matrix architecture on the elastic behavior of an emulsion-filled polymer gel," *Food Hydrocolloids*, vol. 119, article 106875, 2021.
- [21] M. T. Lopez-Lopez, L. Y. Iskakova, and A. Y. Zubarev, "To the theory of shear elastic properties of magnetic gels," *Physica A: Statistical Mechanics and its Applications*, vol. 486, pp. 908–914, 2017.
- [22] J. Q. Leng, M. Z. Wei, and B. J. Bai, "Review of transport mechanisms and numerical simulation studies of preformed particle gel for conformance control," *Journal of Petroleum Science and Engineering*, vol. 206, article 109051, 2021.
- [23] I. Kurnia, G. Y. Zhang, X. Han, and J. Yu, "Zwitterionic-anionic surfactant mixture for chemical enhanced oil recovery without alkali," *Fuel*, vol. 259, 2020.
- [24] Z. Chen, X. Han, I. Kurnia, J. Yu, G. Zhang, and L. Li, "Adoption of phase behavior tests and negative salinity gradient concept to optimize Daqing oilfield alkaline-surfactant-polymer flooding," *Fuel*, vol. 232, pp. 71–80, 2018.
- [25] A. M. S. Lala and N. A. A. El-Sayed, "Controls of pore throat radius distribution on permeability," *Journal of Petroleum Science and Engineering*, vol. 157, pp. 941–950, 2017.
- [26] S. M. Lin and L. X. Gu, "Influence of crosslink density and stiffness on mechanical properties of type I collagen gel," *Materials*, vol. 8, no. 2, pp. 551–560, 2015.

- [27] Y. Qin, R. Q. Liao, S. S. Luo, and J. Li, "The thermal gelation behavior and performance evaluation of high molecular weight nonionic polyacrylamide and polyethyleneimine mixtures for in-depth water control in mature oilfields," *Materials*, vol. 13, no. 18, 2020.
- [28] S. Zhao, D. Zhu, and B. Bai, "Experimental study of degradable preformed particle gel (DPPG) as temporary plugging agent for carbonate reservoir matrix acidizing to improve oil recovery," *Journal of Petroleum Science and Engineering*, vol. 205, article 108760, 2021.
- [29] R. Pandey and J. C. Conrad, "Gelation in mixtures of polymers and bidisperse colloids," *Physical Review E*, vol. 93, no. 1, 2016.
- [30] Y. Yao, M. Wei, and W. Kang, "A review of wettability alteration using surfactants in carbonate reservoirs," *Advances in Colloid and Interface Science*, vol. 294, 2021.
- [31] Y. Yao, M. Wei, and B. Bai, "Descriptive statistical analysis of experimental data for wettability alteration with surfactants in carbonate reservoirs," *Fuel*, vol. 310, article 122110, 2022.
- [32] J. Fang, J. Wang, Q. Wen et al., "Research of phenolic crosslinker gel for profile control and oil displacement in high temperature and high salinity reservoirs," *Journal of Applied Polymer Science*, vol. 135, no. 14, article 46075, 2018.
- [33] L. Romero-Zeron, F. Manalo, and A. Kantzas, "Characterization of crosslinked gel kinetics and gel strength by use of NMR," *SPE Reservoir Evaluation & Engineering*, vol. 11, no. 3, pp. 439–453, 2008.
- [34] S. Zhang, J. Guo, Y. Gu, Q. Zhao, R. Yang, and Y. Yang, "Polyacrylamide gel formed by Cr(III) and phenolic resin for water control in high-temperature reservoirs," *Journal of Petroleum Science and Engineering*, vol. 194, article 107423, 2020.
- [35] D. Hou, W. Zhang, P. Wang, M. Wang, and H. Zhang, "Mesoscale insights on the structure, mechanical performances and the damage process of calcium-silicate-hydrate," *Construction and Building Materials*, vol. 287, article 123031, 2021.
- [36] K. Mayumi, C. Liu, Y. Yasuda, and K. Ito, "Softness, elasticity, and toughness of polymer networks with slide-ring crosslinks," *Gels*, vol. 7, no. 3, p. 91, 2021.
- [37] I. Zafeiri, A. Beri, B. Linter, and I. Norton, "Mechanical properties of starch-filled alginate gel particles," *Carbohydrate Polymers*, vol. 255, article 117373, 2021.
- [38] S. Backes and R. von Klitzing, "Nanomechanics and nanorheology of microgels at interfaces," *Polymers*, vol. 10, no. 9, 2018.
- [39] A. Tanaka, H. Nakashima, Y. Kashimura, and K. Sumitomo, "Fabrication of a gel-supported lipid membrane array on a silicon substrate," *Japanese Journal of Applied Physics*, vol. 53, no. 1, 2014.
- [40] G. Li, J. Zhang, and X. Sun, "Preparation of superhydrophilic polyethersulfone by sol-gel method," *Advanced Materials Research*, vol. 785-786, pp. 1547–1550, 2013.
- [41] N. Wu, L. Chen, Q. Wei, Q. Liu, and J. Li, "Nanoscale three-point bending of single polymer/inorganic composite nanofiber," *Journal of the Textile Institute*, vol. 103, no. 2, pp. 154–158, 2012.
- [42] Y. Zhao and N. Yan, "Recent development in forest biomass derived phenol formaldehyde (PF) resol resin for wood adhesives application," *Journal of Biobased Materials and Bioenergy*, vol. 8, no. 5, pp. 465–480, 2014.
- [43] M. Derradji, J. Wang, and W. Liu, "X-functional phthalonitrile monomers and polymers," in *Phthalonitrile Resins and Composites*, pp. 107–174, Elsevier B.V, 2018.
- [44] Z. Hongtao, J. Han, C. Jinyuan, L. Xuehui, Z. Yanguang, and J. Kunpeng, "Viscosity quantitative breakthrough vacuum degree method for rapid determination of jelly strength," *Petroleum Drilling and Production Technology*, vol. 37, no. 5, pp. 116–119, 2015.
- [45] M. Satheesh Chandran and C. P. Reghunadhan Nair, "Maleimide-based Alder-Enes," in *Handbook of Thermoset Plastics*, pp. 459–510, Elsevier B.V, 2014.
- [46] J. Li, C. Li, W. Wang, W. Zhang, and J. Li, "Reactivity of larch and valonia tannins in synthesis of tannin-formaldehyde resins," *BioResources*, vol. 11, no. 1, pp. 2256–2268, 2016.
- [47] E. Dintwa, E. Tijskens, and H. Ramon, "On the accuracy of the Hertz model to describe the normal contact of soft elastic spheres," *Granular Matter*, vol. 10, no. 3, pp. 209–221, 2008.
- [48] I. I. Argatov, G. S. Mishuris, and V. L. Popov, "An approximate JKR model of elliptical contact between thin incompressible elastic coatings covering rigid cylinders," *Tribology Letters*, vol. 64, no. 1, 2016.
- [49] S. N. Ramakrishna, P. C. Nalam, L. Y. Clasohm, and N. D. Spencer, "Correction to study of adhesion and friction properties on a nanoparticle gradient surface: transition from JKR to DMT contact mechanics," *Langmuir*, vol. 35, no. 34, pp. 11242–11242, 2019.
- [50] E. Masoero, E. Del Gado, R. J. M. Pellenq, S. Yip, and F.-J. Ulm, "Nano-scale mechanics of colloidal C-S-H gels," *Soft Matter*, vol. 10, no. 3, pp. 491–499, 2014.
- [51] W. Zhao, H. Liu, J. Wang et al., "Investigation of restarting pressure gradient for preformed particle gel passing through pore-throat," *Journal of Petroleum Science and Engineering*, vol. 168, pp. 72–80, 2018.



## Research Article

# A Novel Continuous Fracture Network Model: Formation Mechanism, Numerical Simulation, and Field Application

Zixi Guo <sup>1</sup>, Jinzhou Zhao <sup>1</sup>, Xinhao Sun <sup>2</sup>, Chengwang Wang <sup>3</sup>, Dali Guo <sup>1</sup>,  
Haoran Hu <sup>4</sup>, Hongna Wang <sup>5</sup>, and Qinggang Zeng <sup>6</sup>

<sup>1</sup>State Key Laboratory of Oil and Gas Reservoir Geology and Exploitation, Southwest Petroleum University, Chengdu, Sichuan 610500, China

<sup>2</sup>CNPC Western Drilling Engineering Company Limited, Karamay, Xinjiang 834009, China

<sup>3</sup>PetroChina Coalbed Methane Company Limited, Chaoyang, Beijing 100028, China

<sup>4</sup>PetroChina Southwest Oil & Gas Field Company, Chengdu 610051, China

<sup>5</sup>CNPC Exploration Software Company Limited, Beijing 100080, China

<sup>6</sup>Sichuan Kehong Oil & Gas Engineering Company Limited, Chengdu 610051, China

Correspondence should be addressed to Zixi Guo; [guozixi@vip.163.com](mailto:guozixi@vip.163.com) and Jinzhou Zhao; [zhaojinzhou\\_swpu@163.com](mailto:zhaojinzhou_swpu@163.com)

Received 25 January 2022; Accepted 23 March 2022; Published 19 April 2022

Academic Editor: Mohammed Fattah

Copyright © 2022 Zixi Guo et al. This is an open access article distributed under the Creative Commons Attribution License, which permits unrestricted use, distribution, and reproduction in any medium, provided the original work is properly cited.

After a shale gas reservoir is fractured, hydraulic fractures interweave with natural fractures to form a fracture network. Numerical simulation based on the continuous fracture network model is a relatively economical and convenient method to predict fracture network morphology and size in the field application. However, some important factors, such as fracture height variation and filtration loss, have not been considered in the past continuous fracture network models. Therefore, this paper is aimed at establishing a novel continuous fracture network model to improve simulation accuracy. Firstly, this paper established a method to judge whether natural fractures develop or not. Then, a novel continuous fracture network model considering fracture height variation and asymmetry, filtration loss, fluid flow, and other key factors was established, and the forward algorithm and inverse algorithm of the model were proposed. At last, this model was applied in a field case to verify accuracy, and the average accuracy is more than 90%. Compared with the traditional Meyer software, the average error of prediction was reduced by 7.86%.

## 1. Introduction

Hydraulic fracturing has been used commonly in the development of shale gas reservoirs to initiate several dominant hydraulic fractures from the wellbore [1–4]. The technique is aimed at opening the widely existing natural fractures in the shale formation and generating the largest possible hydraulic fracture network for transporting hydrocarbon to the wellbore [5–9]. Thus, accurate knowledge of the fracture initiation and propagation of hydraulic fractures is significant for optimizing the fracturing treatment design and, ultimately, improving well productivity [10–12].

Many key parameters affect the complexity of a fracture network, including the existence of natural fractures, anisotropy of stress, and heterogeneity of rock properties [13, 14].

Moreover, simulating hydraulic fracture propagation in a formation with preexisting natural fractures is very complex and requires proper consideration of key physical elements, including fracture propagation [15], fluid flow in the fracture networks [16], fracture height growth [17], interaction between hydraulic and natural fractures [18], and proppant transport in the fracture networks [19]. Microseismic and other geophysical methods are the main techniques for monitoring a fracture network in a shale reservoir [20]. However, the uncertainty of microseismic events and the high cost of fracture monitoring make the implementation of these techniques difficult for multiple wells [21].

Numerical simulation is a relatively economical and convenient method to predict fracture morphology and size [22]. Different modeling approaches have been developed

recently to simulate fracture networks, mainly divided into the discrete fracture network model [23, 24] and the continuous fracture network model. The main difference between these two models is that the discrete model fully considers the influence of natural fractures, while the continuous model uses the orthogonal fracture model to approximately describe the natural fracture network. In theory, the discrete model is closer to reality. However, in field applications, natural fracture diagnosis is limited by technology and high cost. Therefore, both methods have their own research value. This paper is aimed at developing and applying a new continuous fracture network model.

The important breakthroughs in the development of fracture network models are summarized below: In 2008, Olson presented a continuous fracture network model capable of predicting hydraulic fracture propagation and interaction with preexisting natural fractures [25]. However, the model is based on fracture mechanics alone and does not include fluid flow or proppant transport. From 2009 to 2010, Xu et al. proposed a wire-mesh model to estimate fracture network dimensions and proppant placement in a network [26, 27]. This model has the advantage of fast computation speed due to being a semianalytical solution. But its fracture network pattern (i.e., fracture spacing) is relatively simple in simulating the geometric shape of fractures. In addition, the wire-mesh model neglects changes in fracture height and filtration of fracturing fluid. After 2011, Meyer established a relatively complete continuous fracture network model and developed commercial software [28], but its core problem was that the algorithm of model was not fully published, and this model did not take into account asymmetry of fracture height. In recent years, the discrete fracture network (DFN) model proposed by Meyer has been improved and extended by many scholars [29, 30]. For example, in 2017, Nejadi et al. proposed history matching and uncertainty quantification of DFN models in fractured reservoirs [31]. In 2020, Yao et al. discussed the role of natural fracture characteristics on the performance of hydraulic fracturing for deep energy extraction using DFN [32]. In 2021, Hyman and Dentz discussed the transport upscaling under flow heterogeneity and matrix-diffusion in three-dimensional DFN [33]. The development of the fracture network model is summarized in Table 1.

From the above literature review, a number of remaining challenges need to be resolved. To properly simulate the propagation of continuous fractures developed during hydraulic fracturing and get more accurate simulation results, a new model is needed. Therefore, this work researches the mechanical mechanism associated with fracture network formation based on fracture mechanics and proposes a kind of extended model of a continuous fracture network. This study establishes a mathematical model of the fracture network, including equations of width, fracture length, and fracture height. The model solves a system of equations governing fracture deformation, height growth, fluid flow, and proppant transport so as to predict the size of a complicated fracture network more accurately.

The paper is organized as follows. Firstly, it provides mechanical condition requirements related to fracture net-

work formation to determine whether natural fractures have developed or not. Secondly, it establishes a continuous fracture network extension model according to the propagation law of continuous fracture networking and considers the change in fracturing fluid filtration and fracture height. Finally, it uses field experimental data to verify the accuracy of the model.

## 2. Mechanical Mechanism of Fracture Network Formation Based on Fracture Mechanics

Warpinski et al. [28, 34, 35] pointed out that fracture networks are the result of interaction between hydraulic fractures and natural fractures; researchers have held that a continuous fracture network consists of one main fracture and several branch fractures, as shown in Figure 1. The key to fracture network formation lies in the fact that branch fractures develop around the main fracture [36, 37]. Some natural fractures develop, while some do not. This work studied the mechanical mechanism of reservoir formation with and without natural fracture development.

*2.1. Mechanical Condition Requirements for Reservoir Formation with Natural Fracture Development.* For reservoirs with natural fracture development, when the net pressure in the main fracture of a certain length increases after its formation, a natural fracture or weak plane opens, and then, a fracture network is formed. At present, the linear criterion put forward by Warpinski and Teufel [38, 39] is the most widely used fracture propagation criterion. The mechanical condition requirements for the formation of branch fractures in a fracture network can be analyzed based on the fracture propagation of a naturally fractured reservoir. Figure 2 shows a diagram of a reservoir fracture network with natural fracture development.

The closed natural fracture (or weak plane) is acted on by the maximum horizontal principal stress ( $\sigma_H$ ) and minimum horizontal principal stress ( $\sigma_h$ ) of the far-field, and its angle from the maximum horizontal principal stress is  $\theta$  ( $0 < \theta < (\pi/2)$ ).

According to the 2D linear elastic theory, shear stress and normal stress can be expressed as follows [40]:

$$\tau = -\frac{\sigma_H - \sigma_h}{2} \sin 2\theta, \quad (1)$$

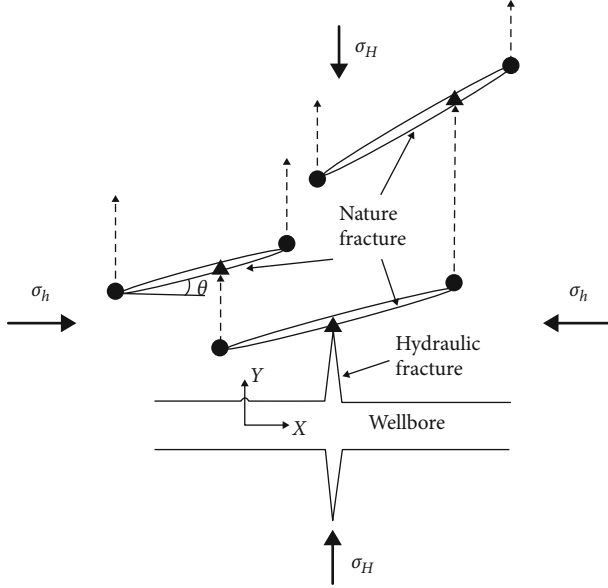
$$\sigma_n = \frac{\sigma_H + \sigma_h}{2} - \frac{\sigma_H - \sigma_h}{2} \cos 2\theta. \quad (2)$$

According to the Warpinski criterion widely applied to fracture propagation of naturally fractured reservoirs, when the fluid pressure of a natural fracture is larger than its normal stress, fracture extension will occur [41] as follows:

$$p(t) > \sigma_n + \Delta p_{nf}(t), \quad (3)$$

TABLE 1: Comparison of different continuous fracture network models.

Reference	Time	Base	Innovation
Olson [25]	2008	Original	Continuous fracture network model
Xu et al. [26, 27]	2009	CFN	Semianalytical solution model
Meyer et al. [28]	2011	CFN	Relatively complete model and software
Nejadi et al. [31]	2017	DFN	History matching and uncertainty quantification
Yao et al. [32]	2020	DFN	Role of natural fracture characteristics
Hyman and Dentz [33]	2021	DFN	Transport upscaling under flow heterogeneity and matrix-diffusion



- Fracture turning point
- ▲ Fracture branch point
- ←- The extension direction of the branch fracture after steering

FIGURE 1: Schematic diagram of the formation of a fracture network.

$$\Delta p_{nf}(t) = \frac{4[p(t) - p_0]}{\pi} \sum_{n=0}^{\infty} \frac{1}{2n+1} * \exp \left[ -\frac{(2n+1)^2 \pi^2 k_{nf} t}{4\phi_{nf} \mu C_i L_f^2} \right] \cdot \sin \frac{(2n+1)\pi}{2}. \quad (4)$$

When two fractures intersect, the hydraulic fracture end is connected with the natural fracture, and fracturing fluid floods into the natural fracture. The pore pressure of the natural fracture's near wall is as follows:

$$p(t) = \sigma_h + p_{net}(t). \quad (5)$$

By substituting Equations (2) and (5) into Equation (3), the net pressure required for the tension fracture of the natural fracture is as follows:

$$p_{net}(t) > \frac{\sigma_H - \sigma_h}{2} (1 - \cos 2\theta) + \Delta p_{nf}(t). \quad (6)$$

When  $\theta = (\pi/2)$ , the net pressure reaches the maximum:

$$p_{max} = (\sigma_H - \sigma_h) + \Delta p_{nf}(t). \quad (7)$$

According to the Warpinski criterion, when the pressure in the natural fracture is low, normal stress acting on the fracture surface is pressure stress, and the fracture is closed. When the shear stress acting on the natural fracture is high, the shear slip of the natural fracture will occur easily [42]:

$$|\tau| > \tau_0 + K_f(\sigma_n - p(t)). \quad (8)$$

Effective shear stress ( $\tau_e$ ) acting on fracture surface is as follows:

$$\tau_e = |\tau| - \tau_0 - K_f(\sigma_n - p(t)). \quad (9)$$

The fracture criterion of a compression shear fracture is as follows:

$$K_{II} = K_{IIc}, \quad (10)$$

$$K_{II} = \tau_e \sqrt{\pi l}. \quad (11)$$

By substituting Equations (1), (2), and (11) into Equation (9), we get critical pressure ( $p_c$ ) for the occurrence of shear slip and branch fracture formation:

$$p_c = \frac{1}{K_f} \left( \frac{K_{IIc}}{\sqrt{\pi l}} + \tau_0 \right) + \frac{\sigma_H + \sigma_h}{2} - \frac{\sigma_H - \sigma_h}{2} \left( \cos 2\theta + \frac{\sin 2\theta}{K_f} \right). \quad (12)$$

According to Equation (12), when  $\theta = (\pi/2)$ , the net pressure is the largest, and  $p_{max}$  is as follows:

$$p_{max} = \Delta\sigma + \frac{\tau_0}{K_f}. \quad (13)$$

The natural fracture surface is unbounded ( $\tau_0 = 0$ ). Net pressure required for shear slip is horizontal principal stress difference ( $\Delta\sigma$ ).

According to Equations (7) and (13), maximum net pressure is positively correlated with  $\Delta\sigma$ . Therefore, the reduction in initial horizontal stress difference can help expand the fracture network fully.

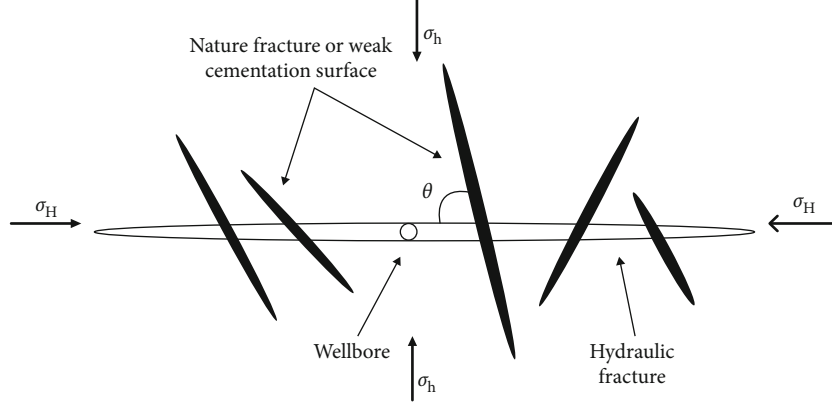


FIGURE 2: Schematic diagram of a naturally fractured reservoir fracture network.

The calculation formula for the difference between two horizontal principal stresses of a reservoir can be derived based on the maximum horizontal principal stress formula [(36)]:

$$\Delta\sigma = 2\sigma_h - P_i - P_f + S_t. \quad (14)$$

Therefore, according to  $\Delta\sigma$ , combined with the net pressure in the fracture propagation model, a judgment can be made on whether a fracture network can be formed.

**2.2. Mechanical Condition Requirements for Reservoir Formation without Natural Fracture Development.** For a reservoir formation without natural fracture development, branch fractures in the rock body are required for fracture network formation [43]. According to the mechanical model shown in Figure 3, there is an elliptical fracture in the infinite field with the major semiaxis  $L_f$  and the minor semiaxis  $w$ . At infinity, the major semiaxis is acted on by pressure stress ( $\sigma_H$ ) and the minor semiaxis ( $\sigma_h$ ); there is uniform pressure action in the fracture.

Boundary conditions:

At  $y = 0, |x| < l_f$ ,

$$\sigma_y = -p_{\text{net}}, \tau_{xy} = 0. \quad (15)$$

At  $\sqrt{x^2 + y^2} \rightarrow \infty$ ,

$$\sigma_x \rightarrow \sigma_H, \sigma_y \rightarrow \sigma_h, \tau_{xy} \rightarrow 0. \quad (16)$$

Expressions of  $\sigma_x$ ,  $\sigma_y$ , and  $\tau_{xy}$  can be obtained according to the solutions for plane problems of elastic mechanics. Stress distribution on the fracture surface is expressed as follows:

$$\begin{cases} \sigma_\theta = -\frac{1-3m^2+2m\cos 2\theta}{1+m^2-2m\cos 2\theta} p_{\text{net}} + \frac{1-m^2-2m+2\cos 2\theta}{1+m^2-2m\cos 2\theta} \sigma_h + \frac{1-m^2+2m+2\cos 2\theta}{1+m^2-2m\cos 2\theta} \sigma_H, \\ \sigma_p = -p_{\text{net}}, \\ \tau_{p\theta} = 0, \end{cases} \quad (17)$$

where  $m = (l_f - w)/(l_f + w)$ .

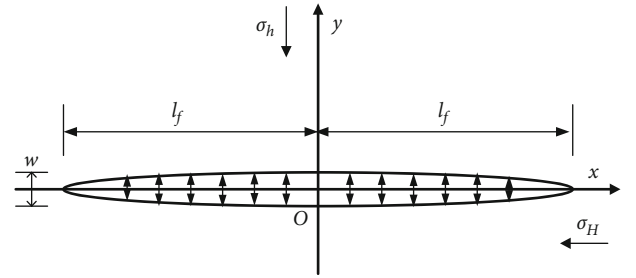


FIGURE 3: Schematic diagram of a naturally fractured reservoir fracture network.

Because  $l_f \gg w$ ,  $m \approx 1$ , and putting into Equation (8), we obtain the following:

$$\sigma_\theta = p_{\text{net}} - \sigma_h + \sigma_H. \quad (18)$$

According to the elastic failure criterion, setting  $\sigma_\theta = -S_t$ , we obtain the following:

$$p_{\text{net}} = -(\sigma_H - \sigma_h) - S_t. \quad (19)$$

Therefore, when the value of net pressure in a fracture is larger than  $(\sigma_H - \sigma_h) + S_t$ , the fracture in the rock body breaks and forms branch fractures, and then, a fracture network is formed.

To sum up, mechanical condition requirements for a fracture network in a naturally fractured reservoir lie in net pressure in the constructed fracture exceeding the horizontal principal stress difference of the reservoir. For a fracture network in a reservoir without natural fracture development, mechanical condition requirements lie in the fracture breaking in the rock body and the value of net pressure in the fracture being larger than the sum of horizontal principal stress difference and reservoir tensile strength.

### 3. Continuous Fracture Network Modeling

The physical model of network fractures is shown in Figure 4, which is composed of two clusters of orthogonal equally spaced vertical fractures. They are elliptical in the transverse direction, but the fracture height is not constant in the longitudinal

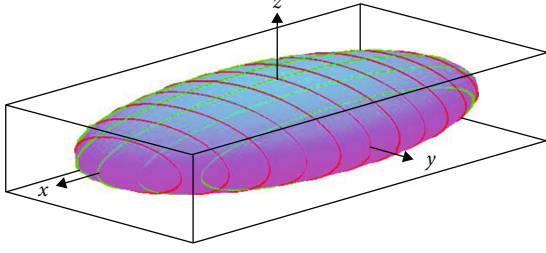


FIGURE 4: Schematic diagram of a continuous fracture network.

direction, so they can be asymmetric in the upper and lower directions. The advantage of this physical model is that when the distribution of natural fractures is not clear, natural fractures and other factors are contained in the model, and it is a reasonable approximation of fractures in complex networks.

**3.1. Building Fracture Network Modeling.** In order to establish the mathematical model of the fracture network, the coordinate system was established. The origin of the coordinates was taken as the shaft injection point, the  $x$  axis was the direction of the maximum horizontal principal stress, and the  $y$  axis was the direction of the minimum horizontal principal stress. Suppose that the half-length of elliptical network fracture on  $x$  axis and  $y$  axis is  $L_x$  and  $L_y$ , respectively, and the fracture spacing on  $x$  axis and  $y$  axis is  $d_x$  and  $d_y$ , respectively, then the number of fractures parallel to  $x$  axis and  $y$  axis is  $2n_y + 1$  and  $2n_x + 1$ , where

$$n_m = \text{int} \left( \frac{L_m}{d_m} \right) \quad (m = x, y). \quad (20)$$

According to the elliptic equation, the half-length of the  $j$  th fracture parallel to the  $x$  axis is

$$L_{xj} = L_x \sqrt{1 - \left( \frac{j d_y}{L_y} \right)^2} \quad (j = 0, \pm 1, \dots, \pm n_y). \quad (21)$$

The half-length of the  $i$  th fracture parallel to the  $y$  axis is

$$L_{yi} = L_y \sqrt{1 - \left( \frac{i d_x}{L_x} \right)^2} \quad (i = 0, \pm 1, \dots, \pm n_x). \quad (22)$$

In the process of network fracture propagation, the fluid flows from the center of the ellipse to the edge of the ellipse and presents laminar flow in the fracture. The mathematical model describing network fracture propagation is established by considering fracture fluid filtration and fracture height variation.

**3.1.1. Volumetric Equilibrium Equation.** According to the principle of mass conservation and ignoring fluid compressibility and initial filtration loss of fracturing fluid, the volume of fracturing injection is equal to the sum of the volume of network fractures and the filtration loss volume of fracturing fluid, that is

$$\int_0^t q(\tau) d\tau = (V_{fx}(t) + V_{fy}(t)) - (V_{lx}(t) + V_{ly}(t)), \quad (23)$$

where  $V_{fx}$  and  $V_{fy}$  are the volume of fractures parallel to  $x$  axis and  $y$  axis, respectively.  $V_{lx}$  and  $V_{ly}$  are the filtration volume of fracturing fluid for fractures parallel to  $x$  axis and  $y$  axis, respectively.

According to the morphology and composition of the fracture network, the cross-section of fractures parallel to the  $x$  axis is approximately elliptical, and the volume of fractures is

$$V_{fx} = \sum_{j=-n_y}^{n_y} \int_{-L_{xj}}^{L_{xj}} \frac{\pi}{4} w_{xj} h_{xj} dx, \quad (24)$$

where  $w_{xj}$  is the fracture width of the  $j$  th fracture parallel to the  $x$  axis.  $h_{xj}$  is the fracture height of the  $j$  th fracture parallel to the  $x$  axis.

Similarly, the volume of the fracture parallel to the  $y$  axis is

$$V_{fy} = \sum_{i=-n_x}^{n_x} \int_{-L_{yi}}^{L_{yi}} \frac{\pi}{4} w_{yi} h_{yi} dy, \quad (25)$$

where  $w_{yi}$  is the fracture width of the  $i$  th fracture parallel to the  $y$  axis.  $h_{yi}$  is the fracture height of the  $i$  th fracture parallel to the  $y$  axis.

The volume of the fracture is equal to the sum of the volume of fractures parallel to the  $x$  axis and the volume of fractures parallel to the  $y$  axis, that is:

$$V_f = \sum_{j=-n_y}^{n_y} \int_{-L_{xj}}^{L_{xj}} \frac{\pi}{4} w_{xj} h_{xj} dx + \sum_{i=-n_x}^{n_x} \int_{-L_{yi}}^{L_{yi}} \frac{\pi}{4} w_{yi} h_{yi} dy. \quad (26)$$

According to the morphology and composition of the fracture network, the fracturing fluid filtration volume of fractures parallel to the  $x$  axis can also be obtained by the following equation:

$$V_{lx} = \sum_{j=-n_y}^{n_y} \int_{-L_{xj}}^{L_{xj}} \int_0^t \frac{2h_{xj} C_L}{\sqrt{t - \tau_0(s)}} ds dx. \quad (27)$$

The fracturing fluid filtration volume of the fracture parallel to the  $y$  axis is

$$V_{ly} = \sum_{i=-n_x}^{n_x} \int_{-L_{yi}}^{L_{yi}} \int_0^t \frac{2h_{yi} C_L}{\sqrt{t - \tau_0(s)}} ds dy. \quad (28)$$

**3.1.2. Fracture Width Equation.** In the  $j$  th fracture parallel to the  $x$  axis, considering the variation of crustal stress in the longitudinal direction, when the fracture penetrates the upper and lower layers ( $h_{xj} \geq H_p$ ), the net pressure distribution in the fracture is



$$\Delta p_{xj}(z) = \begin{cases} p_{xj} - \sigma_{hu} & a_{xj} \leq z \leq l_{xj} \\ p_{xj} - \sigma_h & b_{xj} \leq z \leq a_{xj} \\ p_{xj} - \sigma_{hl} & -l_{xj} \leq z \leq b_{xj} \end{cases} \quad (j = 0, \pm 1, \dots, \pm n_y), \quad (29)$$

where

$$\begin{aligned} l_{xj} &= \frac{h_{xj}}{2} = \frac{h_{xju} + h_{xjl}}{2}, \\ a_{xj} &= \frac{H_p + h_{xjl} - h_{xju}}{2}, \\ b_{xj} &= \frac{-H_p - h_{xjl} + h_{xju}}{2}. \end{aligned} \quad (30)$$

According to the elastic deformation theory, the net pressure in the fracture is decomposed into the sum of even stress distribution and odd stress distribution, and then, the fracture width profile is calculated by the England and Green formulas. After deduction, the fracture width is

$$\begin{aligned} w_{xj} &= \frac{4(1-\nu^2)l_{xj}}{E} (p_{xj} - \sigma_h) - \frac{4(1-\nu^2)l_{xj}}{\pi E} (\sigma_{hu} - \sigma_h) \\ &\cdot \left( \cos^{-1} \frac{a_{xj}}{l_{xj}} - \frac{a_{xj}}{l_{xj}} \ln \frac{l_{xj} + \sqrt{l_{xj}^2 - a_{xj}^2}}{a_{xj}} \right) - \frac{4(1-\nu^2)l_{xj}}{\pi E} (\sigma_{hl} - \sigma_h) \\ &\cdot \left( \cos^{-1} \frac{b_{xj}}{l_{xj}} - \frac{b_{xj}}{l_{xj}} \ln \frac{l_{xj} + \sqrt{l_{xj}^2 - b_{xj}^2}}{b_{xj}} \right) \quad (j = 0, \pm 1, \dots, \pm n_y). \end{aligned} \quad (31)$$

When the fracture does not penetrate the overlying and underlying strata ( $h_{xj} < H_p$ ) or the longitudinal variation of crustal stress is ignored, the fracture width of the  $j$ th fracture parallel to the  $x$  axis is

$$w_{xj} = \frac{2(1-\nu^2)h_{xj}}{E} (p_{xj} - \sigma_h) \quad (j = 0, \pm 1, \dots, \pm n_y). \quad (32)$$

Similarly, when the fracture penetrates the upper and lower layers ( $h_{yi} \geq H_p$ ) or the longitudinal variation of crustal stress is ignored, the fracture width of the  $i$ th fracture parallel to the  $y$  axis is

$$\begin{aligned} w_{yi} &= \frac{4(1-\nu^2)l_{yi}}{E} (p_{yi} - \sigma_H) - \frac{4(1-\nu^2)l_{yi}}{\pi E} (\sigma_{Hu} - \sigma_H) \\ &\cdot \left( \cos^{-1} \frac{a_{yi}}{l_{yi}} - \frac{a_{yi}}{l_{yi}} \ln \frac{l_{yi} + \sqrt{l_{yi}^2 - a_{yi}^2}}{a_{yi}} \right) - \frac{4(1-\nu^2)l_{yi}}{\pi E} (\sigma_{Hl} - \sigma_H) \\ &\cdot \left( \cos^{-1} \frac{b_{yi}}{l_{yi}} - \frac{b_{yi}}{l_{yi}} \ln \frac{l_{yi} + \sqrt{l_{yi}^2 - b_{yi}^2}}{b_{yi}} \right) \quad (i = 0, \pm 1, \dots, \pm n_x), \end{aligned} \quad (33)$$

where

$$\begin{aligned} l_{yi} &= \frac{h_{yi}}{2} = \frac{h_{yiu} + h_{yil}}{2}, \\ a_{yi} &= \frac{H_p + h_{yil} - h_{yiu}}{2}, \\ b_{yi} &= \frac{-H_p - h_{yil} + h_{yiu}}{2}. \end{aligned} \quad (34)$$

When the fracture does not penetrate the upper and lower layers ( $h_{yi} < H_p$ ) or the longitudinal variation of crustal stress is ignored, the fracture width of the  $i$ th fracture parallel to the  $y$  axis is

$$w_{yi} = \frac{2(1-\nu^2)h_{yi}}{E} (p_{yi} - \sigma_H) \quad (i = 0, \pm 1, \dots, \pm n_x). \quad (35)$$

**3.1.3. Fracture Height Equation.** According to the theory of linear elastic fracture mechanics, when the fracture penetrates the upper and lower layers ( $h_{xj} \geq H_p$ ), the stress intensity factor at the upper and lower ends of the  $j$ th fracture parallel to the  $x$  axis is

$$K_{Iu} = \frac{1}{\sqrt{\pi l_{xj}}} \int_{-l_{xj}}^{l_{xj}} \Delta p_{xj} \sqrt{\frac{l_{xj} + z}{l_{xj} - z}} dz, \quad (36)$$

$$K_{Il} = -\frac{1}{\sqrt{\pi l_{xj}}} \int_{l_{xj}}^{-l_{xj}} \Delta p_{xj} \sqrt{\frac{l_{xj} - z}{l_{xj} + z}} dz. \quad (37)$$

According to the net pressure distribution in the fracture and let  $K_{Iu} = K_{ICu}$  and  $K_{Il} = K_{ICl}$ , the fracture height equation of the  $j$ th fracture parallel to the  $x$  axis is

$$\begin{aligned} \sqrt{\pi l_{xj}} K_{ICu} &= \pi l_{xj} \left( p_{xj} - \frac{\sigma_{hu} + \sigma_{hl}}{2} \right) \\ &+ (\sigma_{hl} - \sigma_h) \left( \sqrt{l_{xj}^2 - b_{xj}^2} - l_{xj} \sin^{-1} \frac{b_{xj}}{l_{xj}} \right) \\ &- (\sigma_{hu} - \sigma_h) \left( \sqrt{l_{xj}^2 - a_{xj}^2} - l_{xj} \sin^{-1} \frac{a_{xj}}{l_{xj}} \right), \\ \sqrt{\pi l_{xj}} K_{ICl} &= \pi l_{xj} \left( p_{xj} - \frac{\sigma_{hu} + \sigma_{hl}}{2} \right) \\ &- (\sigma_{hl} - \sigma_h) \left( \sqrt{l_{xj}^2 - b_{xj}^2} + l_{xj} \sin^{-1} \frac{b_{xj}}{l_{xj}} \right) \\ &+ (\sigma_{hu} - \sigma_h) \left( \sqrt{l_{xj}^2 - a_{xj}^2} + l_{xj} \sin^{-1} \frac{a_{xj}}{l_{xj}} \right). \end{aligned} \quad (38)$$

When the fracture does not penetrate the upper and lower layers ( $h_{xj} < H_p$ ) or the longitudinal variation of crustal stress is ignored, the fracture height equation of the  $j$ th fracture parallel to the  $x$  axis is

$$K_{IC} = (p_{xj} - \sigma_h) \sqrt{\pi l_{xj}} \quad (j = 0, \pm 1, \dots, \pm n_y). \quad (39)$$

Similarly, when the fracture penetrates the upper and lower layers ( $h_{yi} \geq H_p$ ), the fracture height equation of the  $i$ th fracture parallel to the  $y$  axis is

$$\begin{aligned} \sqrt{\pi l_{yi}} K_{ICu} &= \pi l_{yi} \left( p_{yi} - \frac{\sigma_{Hu} + \sigma_{Hl}}{2} \right) \\ &+ (\sigma_{Hl} - \sigma_H) \left( \sqrt{l_{yi}^2 - b_{yi}^2} - l_{yi} \sin^{-1} \frac{b_{yi}}{l_{yi}} \right) \\ &- (\sigma_{Hu} - \sigma_H) \left( \sqrt{l_{yi}^2 - a_{yi}^2} - l_{yi} \sin^{-1} \frac{a_{yi}}{l_{yi}} \right), \\ \sqrt{\pi l_{yi}} K_{ICl} &= \pi l_{yi} \left( p_{yi} - \frac{\sigma_{Hu} + \sigma_{Hl}}{2} \right) \\ &- (\sigma_{Hl} - \sigma_H) \left( \sqrt{l_{yi}^2 - b_{yi}^2} + l_{yi} \sin^{-1} \frac{b_{yi}}{l_{yi}} \right) \\ &+ (\sigma_{Hu} - \sigma_H) \left( \sqrt{l_{yi}^2 - a_{yi}^2} + l_{yi} \sin^{-1} \frac{a_{yi}}{l_{yi}} \right). \end{aligned} \quad (40)$$

When the fracture does not penetrate the upper and lower layers ( $h_{yi} < H_p$ ) or the longitudinal variation of crustal stress is ignored, the fracture height equation of the  $i$ th fracture parallel to the  $y$  axis is

$$K_{IC} = (p_{yi} - \sigma_H) \sqrt{\pi l_{yi}} \quad (i = 0, \pm 1, \dots, \pm n_x). \quad (41)$$

**3.1.4. Fluid Flow Equation.** According to the mechanics through porous media, the fluid flow equation in the  $j$ th fracture parallel to  $x$  axis is

$$\pi \lambda \frac{\partial \phi}{\partial t} = \frac{1}{x} \frac{\partial}{\partial x} \left( \frac{\eta(1 + \xi) x w_{xj} k_{fxj}}{\mu d_x} \frac{\partial p_{xj}}{\partial x} \right) \quad (j = 0, \pm 1, \dots, \pm n_y), \quad (42)$$

where  $\xi$  is the axial ratio of the  $x$  axis to the  $y$  axis,  $\xi = L_x/L_y$ .  $\eta$  is the complete elliptic integrals of the second kind,  $\eta = \int_0^{\pi/2} \sqrt{1 - (1 - \xi^2) \sin^2 s} ds$ .  $k_{fxj}$  is the permeability of the  $j$ th fracture parallel to the  $x$  axis.

Considering the flow in the fracture is in laminar, the permeability of the  $j$ th fracture parallel to the  $x$  axis is

$$k_{fxj} = \frac{\pi^2 h_{xj}^2 (p_{xj} - \sigma_h)}{48 E^2}. \quad (43)$$

Substitute into the fluid flow equation, it can be obtained:

$$\frac{\partial \phi}{\partial t} = \frac{\pi^2 (1 - v^2) \eta (1 + \xi)}{24 \lambda E^3 \mu x d_x} \frac{\partial}{\partial x} \left( x h_{xj}^3 (p_{xj} - \sigma_h)^3 \frac{\partial p_{xj}}{\partial x} \right). \quad (44)$$

Considering the change of porosity with pressure, it is represented by rock compression coefficient, that is

$$C_R = \frac{1}{\phi} \frac{d\phi}{dp}. \quad (45)$$

Integrate the above equation and the porosity can be obtained by:

$$\phi = \phi_0 e^{C_R(p - p_0)}, \quad (46)$$

where  $p_0$  is the initial pressure.

Expand the above equation by series, omit the infinitesimal of higher order, and get

$$\phi = \phi_0 [C_R(p - p_0)], \quad (47)$$

so get

$$\frac{\partial \phi}{\partial t} = \phi_0 C_R \frac{\partial p}{\partial t}. \quad (48)$$

Thus, in the  $j$ th fracture parallel to the  $x$  axis, the fluid flow equation is

$$\frac{\partial p_{xj}}{\partial t} = A_x(x) \frac{\partial}{\partial x} \left( B_x(p_{xj}, x) \frac{\partial p_{xj}}{\partial x} \right) \quad (j = 0, \pm 1, \dots, \pm n_y), \quad (49)$$

where

$$\begin{aligned} A_x(x) &= \frac{\pi^2 (1 - v^2) \eta (1 + \xi)}{24 \phi_0 C_R \lambda E^3 \mu x d_x}, \\ B_x(p_{xj}, x) &= x h_{xj}^3 (p_{xj} - \sigma_h)^3. \end{aligned} \quad (50)$$

The initial conditions and boundary conditions are

$$\begin{cases} p_{xj}|_{t=0} = \sigma_h \\ p_{xj}|_{x=L_{xj}} = \sigma_h, \quad \frac{\partial p_{xj}}{\partial x}|_{x=L_{xj}} = 0 \end{cases}. \quad (51)$$

Similarly, in the  $i$ th fracture parallel to the  $y$  axis, the fluid flow equation is

$$\frac{\partial p_{yi}}{\partial t} = A_y(y) \frac{\partial}{\partial y} \left( B_y(p_{yi}, y) \frac{\partial p_{yi}}{\partial y} \right) \quad (i = 0, \pm 1, \dots, \pm n_x), \quad (52)$$

where

$$\begin{aligned} A_y(y) &= \frac{\pi^2 (1 - v^2) \eta (1 + \xi)}{24 \phi_0 C_R \lambda E^3 \mu y d_y}, \\ B_y(p_{yi}, y) &= y h_{yi}^3 (p_{yi} - \sigma_H)^3. \end{aligned} \quad (53)$$

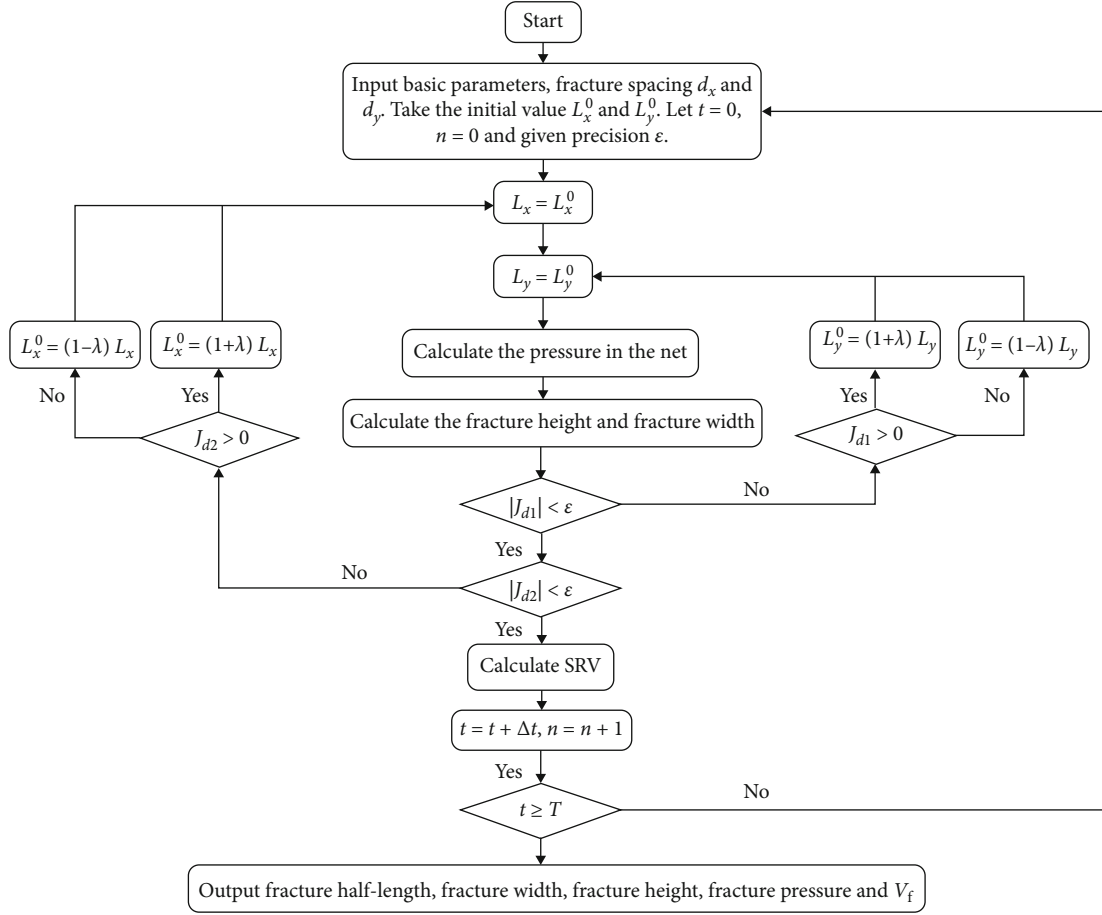


FIGURE 5: Flow chart of the forward algorithm for numerical solution.

The initial conditions and boundary conditions are

$$\begin{cases} p_{yi}|_{t=0} = \sigma_H \\ p_{yi}|_{y=L_{yi}} = \sigma_H, \frac{\partial p_{yi}}{\partial y}|_{y=L_{yi}} = 0 \end{cases} \quad (54)$$

**3.1.5. Coupling Conditions.** Each fracture of the network (whether parallel to  $x$  axis or  $y$  axis) is relatively independent and interrelated, constituting a complex network fracture system. Each fracture is described by its own fluid flow equation, fracture width equation, and fracture height equation and is controlled by volume balance equation. At the same time, there is coupling condition; that is, the pressure at the origin of coordinates is equal, expressed as

$$p_{x0}|_{x=0} = p_{y0}|_{y=0} \quad (55)$$

### 3.2. Numerical Solution of the Fracture Network Model

**3.2.1. Difference Method for Fluid Flow Equations.** It is a nonlinear partial differential equation for the fluid flow equation of the  $j$ th fracture parallel to the  $x$  axis. We use the implicit scheme difference method to solve it, and the nonlinear prob-

lem is solved by the coefficient freezing method. Thus, the left end of the fluid flow equation is discretized as follows:

$$\frac{\partial p_{xj}}{\partial t} \approx \frac{[p_{xj}]_k^{n+1} - [p_{xj}]_k^n}{\Delta t} \quad (56)$$

The right end of the fluid flow equation is discretized as follows:

$$\begin{aligned} A_x \frac{\partial}{\partial x} \left( B_x \frac{\partial p_{xj}}{\partial x} \right) \\ \approx [A_x]_k^n \frac{[B_x]_{k+1/2}^n \left( ([p_{xj}]_{k+1}^{n+1} - [p_{xj}]_k^{n+1}) / \Delta x \right) - [B_x]_{k-1/2}^n \left( ([p_{xj}]_k^{n+1} - [p_{xj}]_{k-1}^{n+1}) / \Delta x \right)}{\Delta x} \end{aligned} \quad (57)$$

where  $\Delta t$  is the time step and  $\Delta x$  is the length step in the  $x$  direction.

$$\begin{aligned} [B_x]_{k+1/2}^n &\approx \frac{[B_x]_{k+1}^n + [B_x]_k^n}{2}, \\ [B_x]_{k-1/2}^n &\approx \frac{[B_x]_k^n + [B_x]_{k-1}^n}{2}. \end{aligned} \quad (58)$$

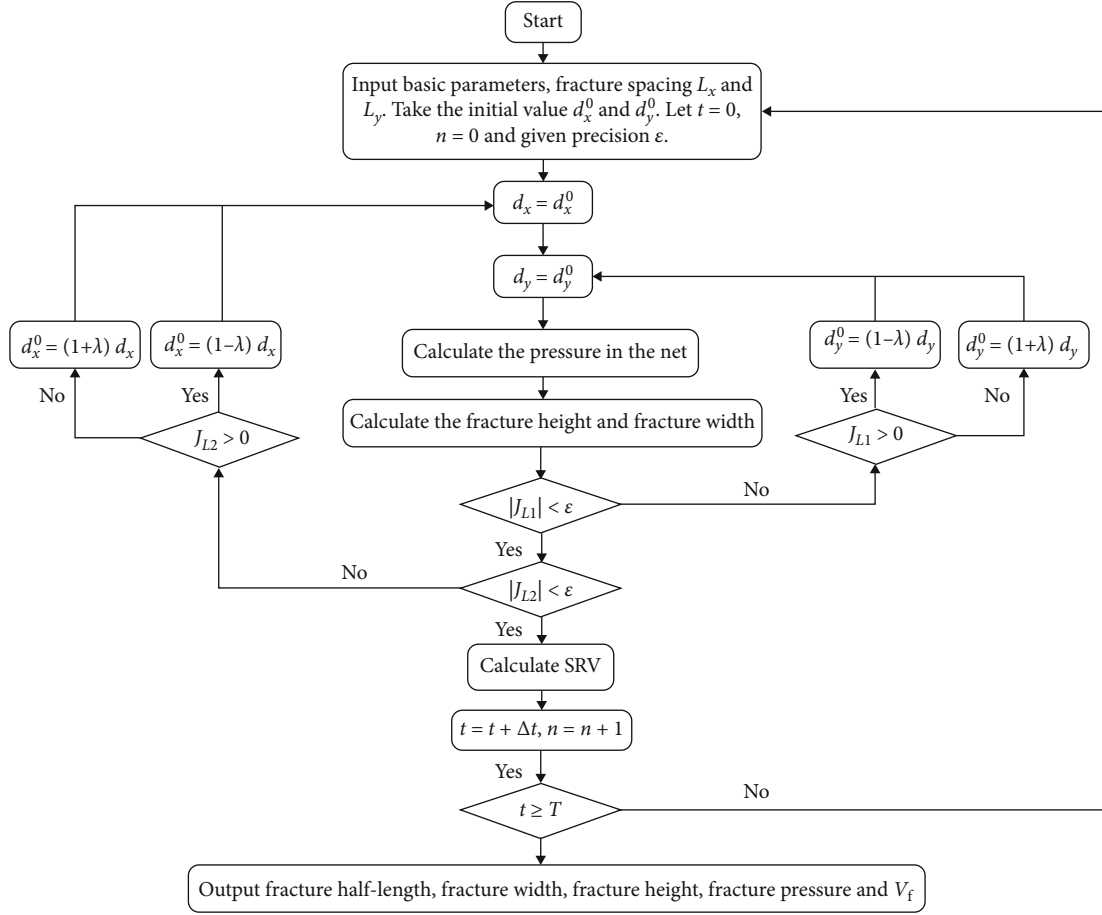


FIGURE 6: Flow chart of the inverse algorithm for numerical solution.

Thus, the difference equation of the fluid flow equation is

$$\begin{aligned}
 & -\frac{\Delta t [A_x]_k^n [B_x]_{k+1/2}^n}{(\Delta x)^2} [p_{xj}]_{k+1}^{n+1} \\
 & + \left( 1 + \frac{\Delta t [A_x]_k^n ([B_x]_{k+1/2}^n + [B_x]_{k-1/2}^n)}{(\Delta x)^2} \right) \\
 & \cdot [p_{xj}]_k^{n+1} - \frac{\Delta t [A_x]_k^n [B_x]_{k-1/2}^n}{(\Delta x)^2} [p_{xj}]_{k-1}^{n+1} = [p_{xj}]_k^n.
 \end{aligned} \quad (59)$$

These are tridiagonal linear equations with dominant diagonal, which can be solved by the catch-up method combined with their initial conditions and boundary conditions.

Similarly, for the  $i$ th fracture parallel to the  $y$  axis, the difference equation of the fluid flow equation (3-108) can be expressed as follows:

$$\begin{aligned}
 & -\frac{\Delta t [A_y]_k^n [B_y]_{k+1/2}^n}{(\Delta y)^2} [p_{yi}]_{k+1}^{n+1} + \left( 1 + \frac{\Delta t [A_y]_k^n ([B_y]_{k+1/2}^n + [B_y]_{k-1/2}^n)}{(\Delta y)^2} \right) \\
 & \cdot [p_{yi}]_k^{n+1} - \frac{\Delta t [A_y]_k^n [B_y]_{k-1/2}^n}{(\Delta y)^2} [p_{yi}]_{k-1}^{n+1} = [p_{yi}]_k^n,
 \end{aligned} \quad (60)$$

where  $\Delta y$  is the length step in the  $y$  direction.

TABLE 2: Reservoir and construction parameters.

Parameter	Value
Depth (m)	1837
Permeability ( $10^{-3} \mu\text{m}^2$ )	0.19
Porosity (%)	8.25
Thickness (m)	12
Poisson's ratio	0.24
Elastic modulus (MPa)	32891
Fracture spacing of $x$ axis (m)	32.6
Fracture spacing of $y$ axis (m)	18.7
Fracturing fluid viscosity (mPa.s)	1.1
Filtration coefficient ( $\text{m}/\text{min}^{0.5}$ )	0.0012
Injection rate ( $\text{m}^3/\text{min}$ )	12
Injection time of fracturing fluid (min)	126

**3.2.2. Forward Algorithm for the Numerical Solution.** The main purpose of establishing and solving the fracture network model is known basic parameters (such as elastic modulus  $E$ , Poisson's ratio  $\nu$  and other rock parameters, fracturing fluid viscosity  $\mu$ , injection rate  $q$ , injection time  $T$ , and other construction parameters); by solving the model, the fracture network parameters can be obtained (such as half-length  $L_x$  and  $L_y$ , fracture width, fracture height, and  $V_f$ ).

TABLE 3: Rock mechanics parameters.

Parameter	Overburden layer	Production layer	Underburden layer
Horizontal minimum principal stress (MPa)	29.50	28.34	31.63
Horizontal maximum principal stress (MPa)	33.89	32.06	35.72

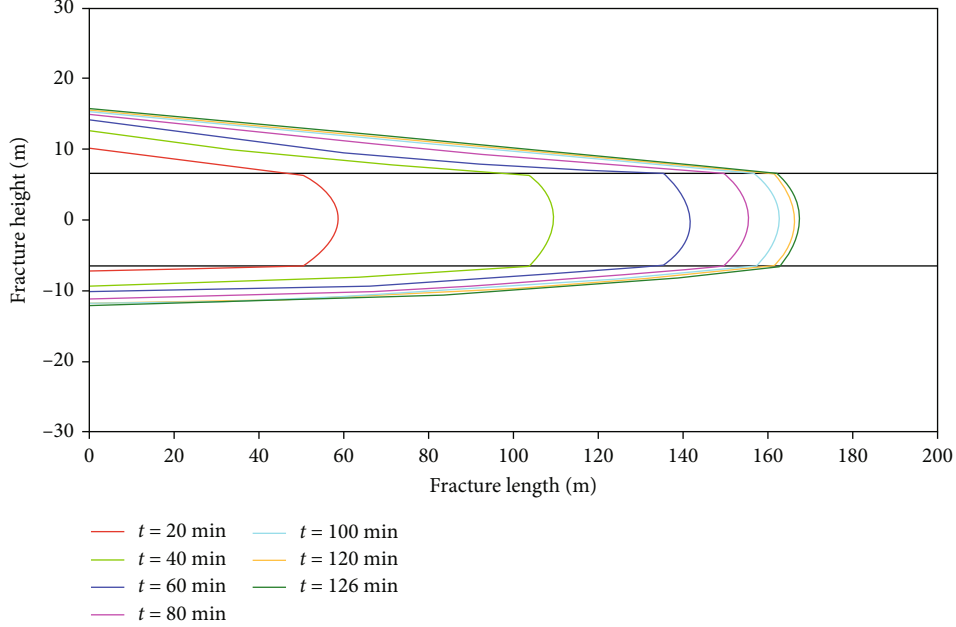


FIGURE 7: Fracture height profile extension.

It is not hard to see that each fracture of the network is described by its own fluid flow equation, fracture height equation, and fracture width equation, which is a complete mathematical model. In other words, under the condition of known basic parameters, fracture spacing ( $d_x$  and  $d_y$ ) and fracture half-length ( $L_x$  and  $L_y$ ), the fracture length, fracture width, and fracture height and pressure in each fracture can be calculated by using this model. Therefore, by using the volume balance equation and coupling conditions (the pressure is equal at the intersection), the algorithm is established to obtain some parameters of the fracture spacing and the fracture half-length.

The forward algorithm in this paper is to obtain the half-length ( $L_x$  and  $L_y$ ) of fracture network, the length, width, height, pressure, and  $V_f$  of each fracture under the condition of known basic parameters and fracture spacing ( $d_x$  and  $d_y$ ).

The specific step of the forward algorithm is as follows:

- (1) The coupling conditions are transformed to construct the following function:

$$J_{d1}(L_x, L_y) = p_{x0}|_{x=0} - p_{y0}|_{y=0}. \quad (61)$$

As you can see that for any  $L_x$  and  $L_y$ ,  $J_{d1}$  can be calculated

by the function. Theoretical analysis and practical calculation show that if  $J_{d1} = 0$ , then  $L_x = L_y$ . Therefore, for a fixed value  $L_x$ , according to the condition  $J_{d1} = 0$ , it is easy to calculate the value of  $L_y$  by iterative method. At this time, the iteration formula is designed as follows:

$$L_y = (1 \pm \lambda)L_x, \quad (62)$$

where  $\lambda$  is the iteration factor which is set to 0.1 during trial calculation.

- (2) According to the volume equilibrium equation, the following function is constructed:

$$J_{d2}(L_x) = \int_0^t q(\tau) d\tau - (V_{fx}(t) + V_{fy}(t)) + (V_{lx}(t) + V_{ly}(t)). \quad (63)$$

It is not difficult to see that for any value of  $L_x$ , since the value of  $L_y$  is determined by the condition  $J_{d1} = 0$ ,  $J_{d2}$  is just a function of  $L_x$ . Theoretical analysis and practical calculation show that if  $J_{d2} = 0$ , then the value of  $L_x$  reaches volumetric balance. Therefore, according to the condition  $J_{d2} = 0$ , it is easy to calculate the value of  $L_x$  by iterative method. At this time, the iteration formula is designed as follows:



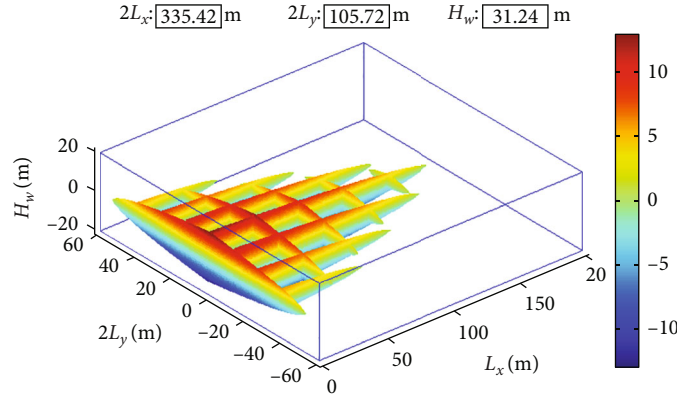


FIGURE 8: Numerical simulation results of the continuous fracture network. The change of color in the figure represents the change of fracture height.

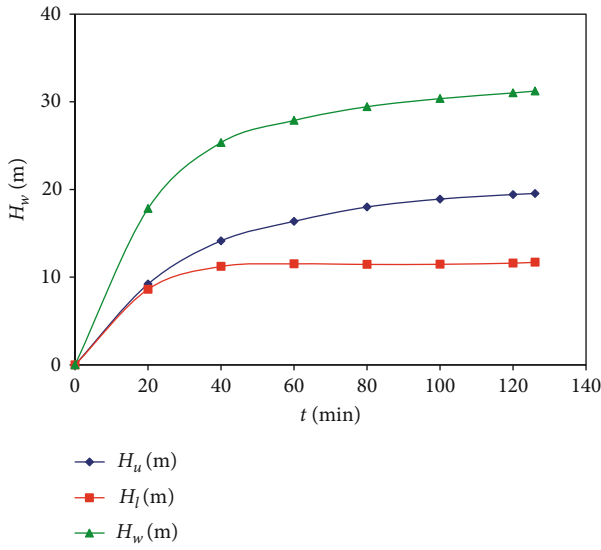


FIGURE 9: Relationship between height and time.

$$L_x = (1 \pm \lambda)L_x. \quad (64)$$

- (3) The forward algorithm advances step by step by time step  $\Delta t$ . Because the implicit difference method is used to solve the fluid flow equation, the numerical calculation is unconditionally stable. However, the smaller the time step, the higher the accuracy of the calculation result

To sum up, the forward algorithm designed is shown in Figure 5.

**3.2.3. Inverse Algorithm for the Numerical Solution.** The forward algorithm for the numerical solution of the network fracture model requires the fracture spacing ( $d_x$  and  $d_y$ ) to be input as known parameters. Usually, the forward algorithm is used to check and invert the microseismic data of nearby wells, borrowing the fracture spacing of adjacent wells.

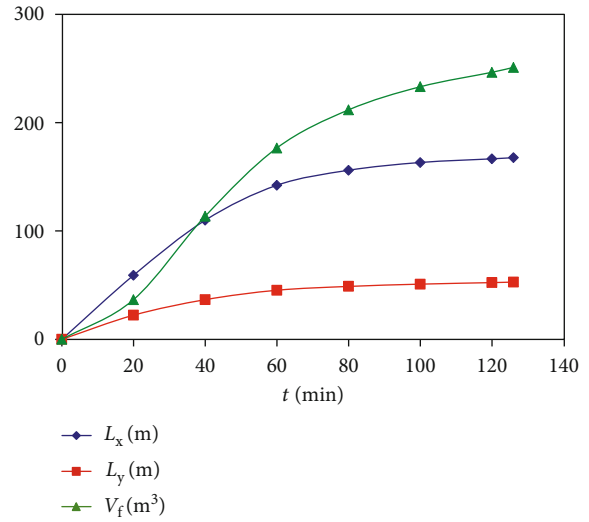


FIGURE 10: Change of  $L_x$ ,  $L_y$ , and  $V_f$  with time.

In fact, parameter inversion is the inverse problem of parameter forward modeling, and the inversion algorithm is different with different parameters. The inversion algorithm in this paper is to obtain the fracture spacing ( $d_x$  and  $d_y$ ), the fracture length, the fracture width, the fracture height, the pressure in the fracture, and  $V_f$  of each fracture through the algorithm under the condition that the basic parameters and the half-length ( $L_x$  and  $L_y$ ) of the fracture network are known.

The inversion algorithm of the fracture network numerical solution is similar to the forward algorithm, which is briefly described here. Take the coupling conditions of equal pressure at the origin of coordinates and construct the following function:

$$J_{L1}(d_x, d_y) = p_{x0}|_{x=0} - p_{y0}|_{y=0}. \quad (65)$$

The following iterative formula is adopted:

$$d_y = (1 \pm \lambda)d_y. \quad (66)$$

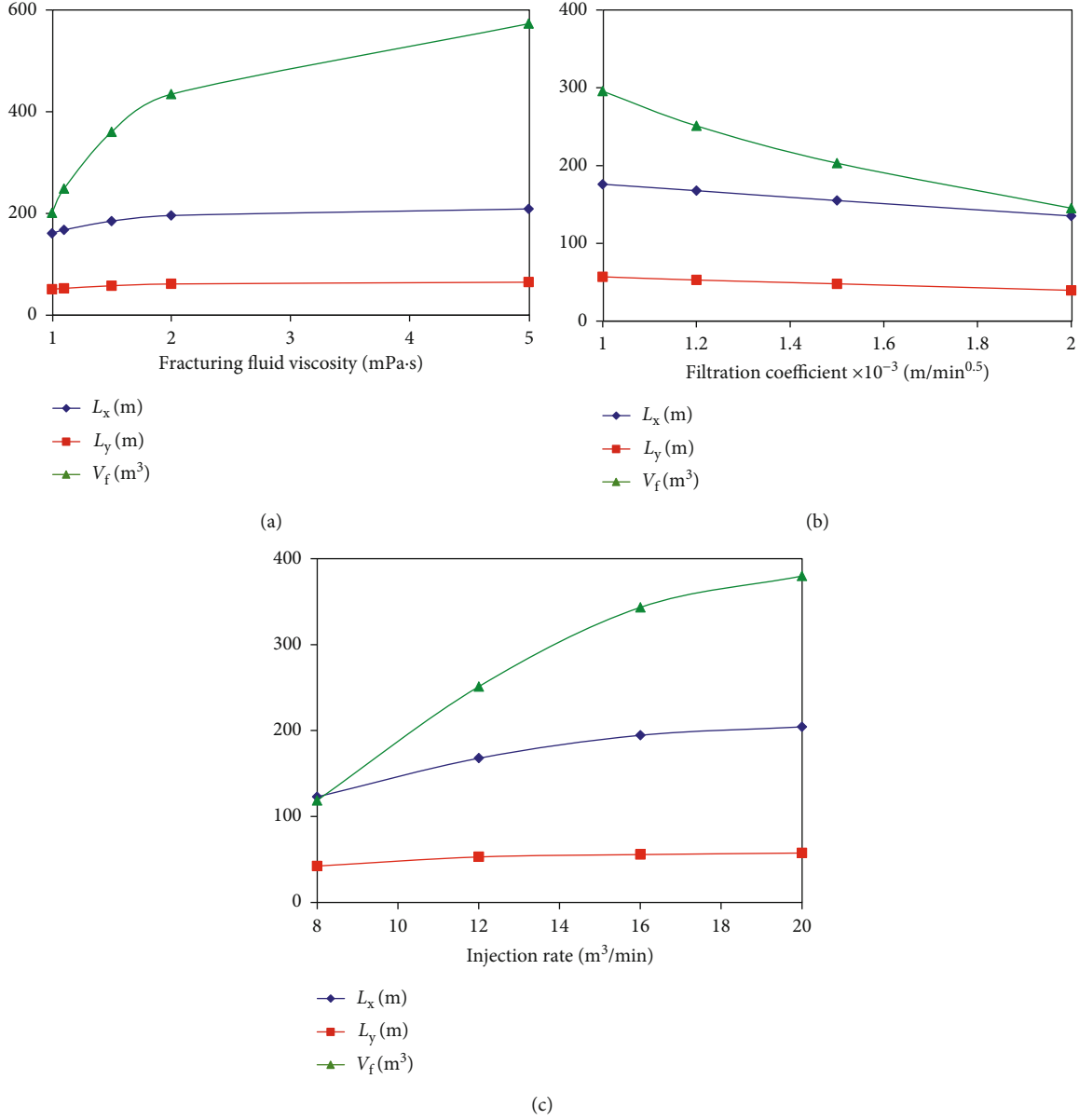


FIGURE 11: (a) Change of  $L_x$ ,  $L_y$ , and  $V_f$  with fracturing fluid viscosity at 126 min. (b) Change of  $L_x$ ,  $L_y$ , and  $V_f$  with filtration coefficient at 126 min. (c) Change of  $L_x$ ,  $L_y$ , and  $V_f$  with injection rate at 126 min.

At the same time, according to the volume equilibrium equation, the following function is constructed:

$$J_{L2}(d_x) = \int_0^t q(\tau) d\tau - (V_{fx}(t) + V_{fy}(t)) + (V_{lx}(t) + V_{ly}(t)). \quad (67)$$

The following iterative formula is adopted:

$$d_x = (1 \pm \lambda) d_x. \quad (68)$$

Therefore, the process of the inversion algorithm is shown in Figure 6.

## 4. Results and Discussion

**4.1. Application.** Take the well H03-11 as an example. The proposed continuous fracture network mechanics and model from this research have been applied to this well. The main parameters used during the simulation process for well H03-11 are listed in Tables 2 and 3.

The formation of this well belongs to a naturally fractured developed reservoir, with the value of net pressure in the fracture larger than  $(\sigma_H - \sigma_h) + S_t$ . According to the mechanical mechanism of fracture network formation proposed in this paper, well H03-11 can form a fracture network. Therefore, the continuous fracture network model established in this paper is appropriate for simulations of fracture propagation within well H03-11. Using the

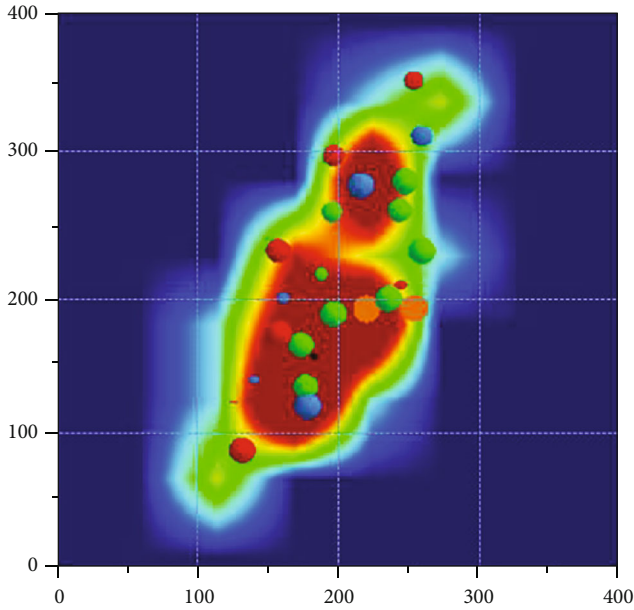


FIGURE 12: Results of microseismic monitoring of well H03-11.

continuous fracture network model, the growth of fracture height was calculated. As shown in Figure 7, the heights of the upper and lower extensions are 19.53 m and 11.71 m, respectively. Therefore, the height of the fracture is 31.24 m.

$L_x$  and  $L_y$  are the half-length of the fracture in the  $x$  and  $y$  directions, respectively.  $H$  is the fracture height. The calculated results of the continuous fracture network are shown in Figure 8.  $2L_x$  is 335.42 m,  $2L_y$  is 105.72 m, and  $H$  is 31.24 m.

**4.2. Verification and Discussion.** The height of a fracture network changes with time as shown in Figure 9. The total injection time of well H03-11 is 126 minutes. At the early time stage, the fracture height increases rapidly. The later-time fracture height grows slowly. In the production process, the height changes, so considering height variation, the simulation results are more accurate.

We discuss the changes of  $L_x$ ,  $L_y$ , and  $V_f$  with different times; the results are shown in Figure 10. It can be seen from Figure 10 that the  $L_x$  and  $L_y$  increase rapidly at the early time stage and grow slowly at later-time. The growth of  $V_f$  is S-shaped; that is, the first growth is slow, the middle growth is fast, and the latter is slow.

We also discussed the influence of fracturing fluid viscosity, filtration coefficient, and injection rate on  $L_x$ ,  $L_y$ , and  $V_f$ . The results are shown in Figure 11. It can be seen from Figure 11 that (1) the higher the viscosity and injection rate are, the better the effect of reservoir simulation is. The larger the filtration coefficient is, the worse the effect of reservoir simulation is. (2) Viscosity has little effect on  $L_x$  and  $L_y$ , but a greater effect on  $V_f$ , only because viscosity has a greater effect on fracture height. (3) The injection rate has a great influence on  $V_f$ , indicating that the injection rate

should be increased in field case under the premise of ensuring safety.

Microseismic monitoring technology is the main method for accurate fracture network design. In order to verify the accuracy of the continuous fracture network model in this paper, the fracture was monitored by microseismic monitoring technology; the results are shown in Figure 12. An industry-accepted technology, Meyer, was employed to predict the dimension of fractures with the same well H03-11 data. Calculated by the forward algorithm of continuous fracture network model, Meyer and the microseismic monitoring results are compared in Table 4.

As shown in Table 4, the prediction accuracy of the continuous fracture network is higher than that of Meyer. This is because the influence of fracture height and filtration coefficient is not taken into account in the Meyer. From the discussion in Figure 11, we know that these two factors have a great influence on the prediction results.

In order to further prove the prediction accuracy of the continuous fracture network model in the field case, we applied this model to a horizontal well TP12-06. The model in this paper is only used to predict the size of fractures, and the directions of fractures are calculated by the pressure field model. The results of microseismic monitoring of TP12-06 are shown in Figure 13(a). The comparison between the prediction results of microseismic monitoring and continuous fracture network model is shown in Figure 13(b) and Table 5. The average error of prediction of fracture length and fracture width is 3.64% and 5.70%, respectively.

## 5. Conclusion

This work contributes to a novel continuous fracture network model. The findings from this study allow the following conclusions to be drawn:

- (1) By comprehensively considering the development situations of natural fractures, this study provides mechanical condition requirements related to fracture network formation. The mechanical condition requirements for a fracture network in a naturally fractured reservoir lie in net pressure in a constructed fracture exceeding the horizontal principal stress difference of the reservoir. For a fracture network in a reservoir without natural fracture development, the condition requirements lie in the fracture breaking in the rock body and the value of net pressure in the fracture being larger than the sum of horizontal principal stress difference and reservoir tensile strength
- (2) A continuous fracture network model was established based on the mechanical mechanism for fracture network formation. A geometric fracture network model was constructed with the main fracture and branch fractures, mathematical equations were established to simulate geometric parameters

TABLE 4: Comparison of prediction results of well H03-11 by different technologies.

Applied technology	$2L_x$		$2L_y$		$H$	
	Result (m)	Error (%)	Result (m)	Error (%)	Result (m)	Error (%)
Microseismic monitoring	324		114		29	
Meyer	362.29	11.82	96.71	15.16	24.62	15.10
Continuous fracture network	335.42	3.52	105.72	7.26	31.24	7.72

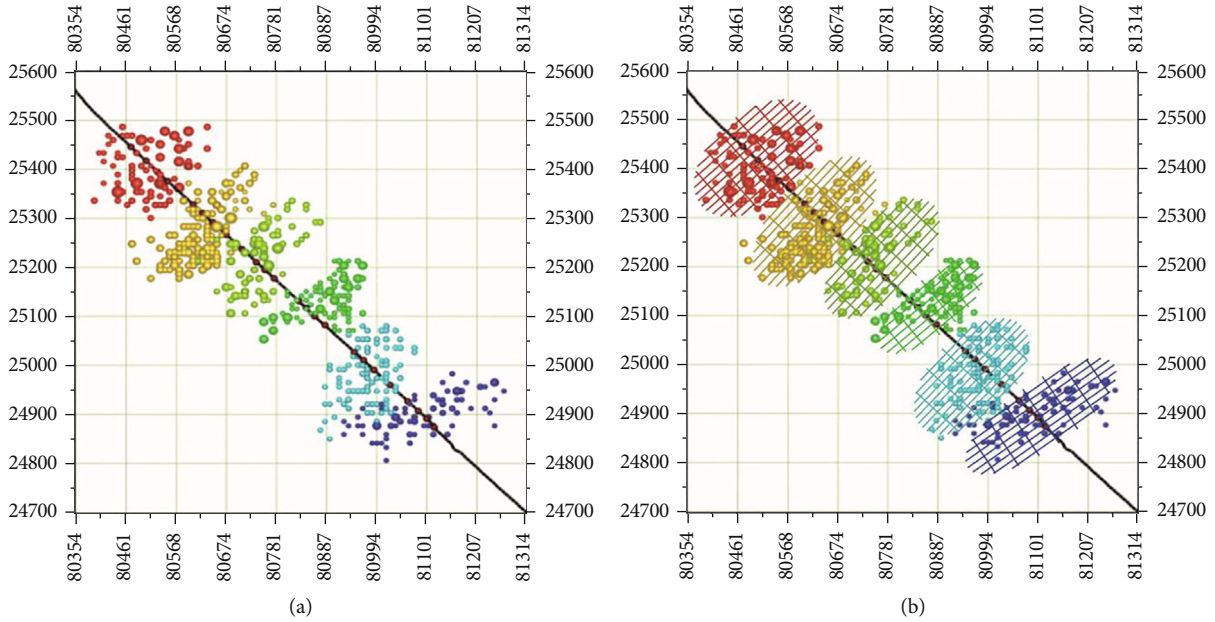


FIGURE 13: (a) Results of microseismic monitoring of TP12-06. (b) Comparison of prediction results of microseismic monitoring and continuous fracture network model.

TABLE 5: Comparison of prediction results of well TP12-06 by different technologies.

Cluster	Fracture length			Fracture width			Azimuth (°)
	Microseismic monitoring (m)	Simulation result (m)	Error (%)	Microseismic monitoring (m)	Simulation result (m)	Error (%)	
1	372	384.47	3.35	142	134.67	5.16	71
2	304	317.83	4.55	151	142.89	5.37	33
3	291	302.58	3.98	193	181.49	5.96	49
4	302	309.59	2.51	201	191.73	4.61	36
5	332	343.72	3.53	143	136.64	4.45	56
6	314	326.39	3.94	210	191.82	8.66	56
Average			3.64			5.70	

of a shale gas continuous fracture network, and related calculation methods were derived

- (3) In this study, a numerical simulation program of a continuous fracture network was developed, overall consideration was made for an increase in fracture height and filtration of fracturing liquid, and a simulation study was performed on a continuous fracture network. Actual microseismic monitoring data verifies the accuracy of this model. The simulation results are of great significance for fracturing design optimization of shale gas fracture networks

## 6. Recommendations

In future research, the following aspects can be further explored:

- (1) The junction of fracture is assumed to be noninterference, but there is fracture interference in the actual situation, so this study needs to be added in the future
- (2) It is assumed that fractures are perpendicular to each other. However, for an oblique fracture, how to establish a model in accordance with the real situation is worthy of further discussion

## Nomenclature

$\sigma_H$ :	Maximum horizontal principal stress, MPa
$\sigma_h$ :	Minimum horizontal principal stress, MPa
$\theta$ :	Angle from the maximum horizontal principal stress, dimensionless
$\tau$ :	Shear stress, MPa
$\sigma_n$ :	Normal stress, MPa
$t$ :	Time, min
$p(t)$ :	Pressure in fracture, MPa
$p_{nf}(t)$ :	Normal net pressure in fracture, MPa
$k_f$ :	Permeability, $10^{-3} \mu\text{m}^2$
$\phi_f$ :	Porosity, dimensionless
$L_f$ :	Length of a natural fracture, m
$K_f$ :	Coefficient of friction on the surface of a natural fracture, dimensionless
$\tau_e$ :	Effective shear stress, MPa
$S_t$ :	Tensile strength, Pa
$L_x$ :	Half-length of elliptical network fracture on $x$ axis, m
$L_y$ :	Half-length of elliptical network fracture on $y$ axis, m
$d_x$ :	Fracture spacing on $x$ axis, m
$d_y$ :	Fracture spacing on $y$ axis, m
$V_{fx}$ :	Volume of fractures parallel to $x$ axis, $\text{m}^3$
$V_{fy}$ :	Volume of fractures parallel to $y$ axis, $\text{m}^3$
$V_{lx}$ :	Filtration volume of fracturing fluid for fractures parallel to $x$ axis, $\text{m}^3$
$V_{ly}$ :	Filtration volume of fracturing fluid for fractures parallel to $y$ axis, $\text{m}^3$
$w_{xj}$ :	Fracture width of the $j$ th fracture parallel to the $x$ axis, m
$h_{xj}$ :	Fracture height of the $j$ th fracture parallel to the $x$ axis, m
$w_{yi}$ :	Fracture width of the $i$ th fracture parallel to the $y$ axis, m
:	Fracture height of the $i$ th fracture parallel to the $y$ axis, m
$H_p$ :	Fracture thickness, m
$p_{xj}$ :	Pressure of the $j$ th fracture parallel to the $x$ axis, MPa
$p_{yi}$ :	Pressure of the $i$ th fracture parallel to the $y$ axis, MPa
$K_{Iu}$ :	Stress intensity factor of upper fracture, $\text{MPa}\cdot\text{m}^{0.5}$
$K_{Il}$ :	Stress intensity factor of lower fracture, $\text{MPa}\cdot\text{m}^{0.5}$
$K_{ICu}$ :	Fracture toughness of upper rock, $\text{MPa}\cdot\text{m}^{0.5}$
$K_{ICl}$ :	Fracture toughness of lower rock, $\text{MPa}\cdot\text{m}^{0.5}$
$K_{IC}$ :	Fracture toughness, $\text{MPa}\cdot\text{m}^{0.5}$
$\xi$ :	Axial ratio of the $x$ axis to the $y$ axis, dimensionless
$\eta$ :	Complete elliptic integrals of the second kind, dimensionless
$C_R$ :	Rock compressibility, Pa $^{-1}$
$p_0$ :	Initial pressure, MPa
$\Delta t$ :	Time step, min
$\Delta x$ :	Length step in the $x$ direction, m
$\Delta y$ :	Length step in the $y$ direction, m
$\lambda$ :	Iteration factor which is set to 0.1 during trial calculation, dimensionless.

## Data Availability

The data used to support the findings of this study are included in the article.

## Conflicts of Interest

The authors confirm that this article content has no conflict of interest.

## Acknowledgments

This work was supported financially by the Science and Technology Cooperation Project of the CNPC-SWPU Innovation Alliance and Study on Production Law and Technology Policy of Coalbed Methane Reservoir (2017E-1405).

## References

- [1] J. Zhang and S. Yin, "A three-dimensional solution of hydraulic fracture width for wellbore strengthening applications," *Petroleum Science*, vol. 16, no. 4, pp. 808–815, 2019.
- [2] W. Cheng, Y. Jin, and M. Chen, "Reactivation mechanism of natural fractures by hydraulic fracturing in naturally fractured shale reservoirs," *Journal of Natural Gas Science and Engineering*, vol. 23, pp. 431–439, 2015.
- [3] J. Wang, H. Q. Liu, G. B. Qian, and Y. C. Peng, "Mechanisms and capacity of high-pressure soaking after hydraulic fracturing in tight/shale oil reservoirs," *Petroleum Science*, vol. 18, no. 2, pp. 546–564, 2021.
- [4] L. Yangying, *Proceedings of the International Field Exploration and Development Conference 2019*, Springer Series in Geomechanics and Geoengineering, Springer Singapore, 2020.
- [5] M. J. Mayerhofer, E. P. Lonon, N. R. Warpinski, C. L. L. Cipolla, D. Walser, and C. M. M. Rightmire, "What is stimulated reservoir volume?," *SPE Production & Operations*, vol. 25, no. 1, pp. 89–98, 2010.
- [6] M. Chen, S. Zhang, S. Li, X. Ma, X. Zhang, and Y. Zou, "An explicit algorithm for modeling planar 3D hydraulic fracture growth based on a super-time-stepping method," *International Journal of Solids and Structures*, vol. 191–192, pp. 370–389, 2020.
- [7] Z. Zhang, S. Zhang, Y. Zou, X. Ma, N. Li, and L. Liu, "Experimental investigation into simultaneous and sequential propagation of multiple closely spaced fractures in a horizontal well," *Journal of Petroleum Science and Engineering*, vol. 202, article 108531, 2021.
- [8] M. Aslannezhad, A. Kalantariasl, Z. You, S. Iglauer, and A. Keshavarz, "Micro-proppant placement in hydraulic and natural fracture stimulation in unconventional reservoirs: a review," *Energy Reports*, vol. 7, pp. 8997–9022, 2021.
- [9] G. Feng, Y. Zhu, S. Chen et al., "Supercritical methane adsorption on shale over wide pressure and temperature ranges: implications for gas-in-place estimation," *Energy & Fuels*, vol. 34, no. 3, pp. 3121–3134, 2020.
- [10] Z. Guo, Y. Chen, X. Zhou, and F. Zeng, "Inverting fracture parameters using early-time production data for fractured wells," *Inverse Problems in Science and Engineering*, vol. 28, no. 5, pp. 674–694, 2020.
- [11] D. Wang, Z. You, R. L. Johnson Jr. et al., "Numerical investigation of the effects of proppant embedment on fracture



- permeability and well production in Queensland coal seam gas reservoirs,” *International Journal of Coal Geology*, vol. 242, article 103689, 2021.
- [12] D. Wang, Z. You, M. Wang, Q. Li, and L. Wu, “Numerical investigation of proppant transport at hydraulic-natural fracture intersection,” *Powder Technology*, vol. 398, p. 117123, 2022.
- [13] W. D. Wang, Y. L. Su, Q. Zhang, G. Xiang, and S. M. Cui, “Performance-based fractal fracture model for complex fracture network simulation,” *Petroleum Science*, vol. 15, no. 1, pp. 126–134, 2018.
- [14] I. Mohammed, T. O. Olayiwola, M. Alkathim, A. A. Awotunde, and S. F. Alafnan, “A review of pressure transient analysis in reservoirs with natural fractures, vugs and/or caves,” *Petroleum Science*, vol. 18, no. 1, pp. 154–172, 2021.
- [15] Y. Wang, B. Hou, D. Wang, and Z. Jia, “Features of fracture height propagation in cross-layer fracturing of shale oil reservoirs,” *Petroleum Exploration and Development*, vol. 48, no. 2, pp. 469–479, 2021.
- [16] N. Huang, R. Liu, Y. Jiang, and Y. Cheng, “Development and application of three-dimensional discrete fracture network modeling approach for fluid flow in fractured rock masses,” *Journal of Natural Gas Science and Engineering*, vol. 91, p. 103957, 2021.
- [17] V. J. Pandey and V. Rasouli, “Fracture height growth prediction using fluid velocity based apparent fracture toughness model,” *Rock Mechanics and Rock Engineering*, vol. 54, no. 8, pp. 4059–4078, 2021.
- [18] N. Makedonska, S. Karra, H. S. Viswanathan, and G. D. Guthrie, “Role of interaction between hydraulic and natural fractures on production,” *Journal of Natural Gas Science and Engineering*, vol. 82, article 103451, 2020.
- [19] Q. Zeng and J. Yao, “Numerical simulation of fracture network generation in naturally fractured reservoirs,” *Journal of Natural Gas Science and Engineering*, vol. 30, pp. 430–443, 2016.
- [20] X. Yu, J. Rutledge, S. Leaney, and S. Maxwell, “Discrete-fracture-network generation from microseismic data by use of moment-tensor- and event-location-constrained hough transforms,” *SPE Journal*, vol. 21, no. 1, pp. 221–232, 2016.
- [21] X. Liu, Y. Jin, B. Lin, Q. Zhang, and S. Wei, “An integrated 3D fracture network reconstruction method based on microseismic events,” *Journal of Natural Gas Science and Engineering*, vol. 95, article 104182, 2021.
- [22] Z. Guo, J. Zhao, Z. You, Y. Li, S. Zhang, and Y. Chen, “Prediction of coalbed methane production based on deep learning,” *Energy*, vol. 230, p. 120847, 2021.
- [23] K. Wu and J. E. Olson, “A simplified three-dimensional displacement discontinuity method for multiple fracture simulations,” *International Journal of Fracture*, vol. 193, no. 2, pp. 191–204, 2015.
- [24] O. Olorode, B. Wang, and H. U. Rashid, “Three-dimensional projection-based embedded discrete-fracture model for compositional simulation of fractured reservoirs,” *SPE Journal*, vol. 25, no. 4, pp. 2143–2161, 2020.
- [25] J. E. Olson, “Multi-fracture propagation modeling: applications to hydraulic fracturing in shales and tight gas sands,” in *The 42nd US rock mechanics symposium (USRMS)*, San Francisco, California, 2008.
- [26] W. Xu, J. H. Le Calvez, and M. J. Thiercelin, “Characterization of hydraulically-induced fracture network using treatment and microseismic data in a tight-gas sand formation: a geomechanical approach,” in *SPE tight gas completions conference*, San Antonio, Texas, USA, 2009.
- [27] W. Xu, M. Thiercelin, U. Ganguly et al., “Wiremesh: a novel shale fracturing simulator,” in *In International oil and gas conference and exhibition in China*, Beijing, China, 2010.
- [28] N. R. Warpinski and L. W. Teufel, “Influence of geologic discontinuities on hydraulic fracture propagation (includes associated papers 17011 and 17074),” *Journal of Petroleum Technology*, vol. 39, no. 2, pp. 209–220, 1987.
- [29] G. Ma, M. Li, H. Wang, and Y. Chen, “Equivalent discrete fracture network method for numerical estimation of deformability in complexly fractured rock masses,” *Engineering Geology*, vol. 277, article 105784, 2020.
- [30] O. L. Manzoli, L. F. A. Borges, E. A. Rodrigues, P. R. Cleto, M. A. Maedo, and L. A. G. Bitencourt Jr., “A new discrete fracture approach based on the use of coupling finite elements for modeling fluid transport in naturally fractured porous media,” *Computer Methods in Applied Mechanics and Engineering*, vol. 386, article 114112, 2021.
- [31] S. Nejadi, J. J. Trivedi, and J. Leung, “History matching and uncertainty quantification of discrete fracture network models in fractured reservoirs,” *Journal of Petroleum Science and Engineering*, vol. 152, pp. 21–32, 2017.
- [32] W. Yao, S. Mostafa, Z. Yang, and G. Xu, “Role of natural fractures characteristics on the performance of hydraulic fracturing for deep energy extraction using discrete fracture network (DFN),” *Engineering Fracture Mechanics*, vol. 230, article 106962, 2020.
- [33] J. D. Hyman and M. Dentz, “Transport upscaling under flow heterogeneity and matrix-diffusion in three-dimensional discrete fracture networks,” *Advances in Water Resources*, vol. 155, article 103994, 2021.
- [34] J. C. Lorenz, N. R. Warpinski, and L. W. Teufel, “Natural fracture characteristics and effects,” *The Leading Edge*, vol. 15, no. 8, pp. 909–911, 1996.
- [35] H. Zhao, M. Chen, Y. Jin, D. Yunhong, and W. Yonghui, “Rock fracture kinetics of the fracture mesh system in shale gas reservoirs,” *Petroleum Exploration and Development*, vol. 39, no. 4, pp. 498–503, 2012.
- [36] J. Zhao, L. Ren, and Y. Hu, “Controlling factors of hydraulic fractures extending into network in shale formations,” *Journal of Southwest Petroleum University (Science & Technology Edition)*, vol. 35, no. 1, p. 1, 2013.
- [37] X. Zhao, L. Liu, J. Hu, X. Zhou, and M. Li, “The tectonic fracture modeling of an ultra-low permeability sandstone reservoir based on an outcrop analogy: a case study in the Wangyao Oilfield of Ordos Basin, China,” *Petroleum Science*, vol. 11, no. 3, pp. 363–375, 2014.
- [38] N. R. Warpinski and L. W. Teufel, “Influence of geologic discontinuities on hydraulic fracture propagation (includes associated papers 17011 and 17074 ),” *Journal of Petroleum Technology*, vol. 39, no. 2, pp. 209–220, 1987.
- [39] C. Lu, Y. Lu, J. Guo, and L. M. Liu, “Stability of the formation interface under the impact of hydraulic fracture propagation in the vicinity of the formation interface,” *Petroleum Science*, vol. 17, no. 4, pp. 1101–1118, 2020.
- [40] Y. Cheng, X. Chang, Y. Sun, and S. Wang, “Research on fracture network propagation pattern of shale reservoir based on fracture mechanics,” *Natural Gas Geoscience*, vol. 25, no. 4, pp. 603–611, 2014.
- [41] L. Ren, R. Lin, J. Zhao, K. W. Yang, Y. Q. Hu, and X. J. Wang, “Simultaneous hydraulic fracturing of ultra-low permeability

sandstone reservoirs in China: mechanism and its field test,” *Journal of Central South University*, vol. 22, no. 4, pp. 1427–1436, 2015.

- [42] L. Zhao, F. Liu, P. Wang, P. L. Liu, Z. F. Luo, and N. Y. Li, “A review of creation and propagation of complex hydraulic fracture network,” *Oil and Gas Geology*, vol. 35, no. 4, pp. 562–569, 2014.
- [43] L. Li and S. Lee, “Efficient field-scale simulation of black oil in a naturally fractured reservoir through discrete fracture networks and homogenized media,” *SPE Reservoir Evaluation & Engineering*, vol. 11, no. 4, pp. 750–758, 2008.

## Research Article

# Residual Oil Distribution Pattern in a Fault-Solution Carbonate Reservoir and Countermeasures to Improve Oil Development Effectiveness

Peiliang Liu, Lin Jiang, Bochao Tang , Ke Ren, Mina Huang, and Chunying Geng 

*Sinopec Northwest Oilfield Company, Xinjiang Urumqi 830011, China*

Correspondence should be addressed to Bochao Tang; tangbochao1008@163.com

Received 5 November 2021; Revised 8 February 2022; Accepted 17 February 2022; Published 15 April 2022

Academic Editor: Xiang Zhou

Copyright © 2022 Peiliang Liu et al. This is an open access article distributed under the Creative Commons Attribution License, which permits unrestricted use, distribution, and reproduction in any medium, provided the original work is properly cited.

Because of the strong random distribution of fractures and caves, fault-solution carbonate reservoirs exhibit significantly different flow mechanisms and development methods from conventional carbonate reservoirs. Natural elastic and edge-bottom water flooding are the main processes for developing fault-solution reservoirs. The rapid decline in production and the complex residual oil distribution are major challenges for oil production. This study is aimed at (1) assessing the residual oil migration law, (2) determining the residual oil distribution characteristics, and (3) identifying the main controlling factors using numerical simulation, to provide suggestions for enhancing oil recovery. The results showed that fractures are the main channel for oil flow and the main path of bottom water coning in the fault-solution reservoirs. The channeling of bottom water along high-angle fractures is the main reason for the decline in oil production. In addition, bottom water coning and gas/water injection are the key factors affecting the distribution of residual oil, while the irregular development of fractures and caves is the main factor causing diversified distribution patterns of the residual oil. The residual oil distribution patterns of fault-solution reservoirs include 4 types, namely, attic, bottom water rising and blocking, separated fracture-cavity, and pores near high-conductivity channel types. For tapping the potential of residual oil, several approaches can be used, namely, deploying new wells or using sidetracking of old wells in the loft and the separated fracture-cavity reservoirs. In addition, the attic residual oil type can also be developed using drainage oil recovery or gas injection for oil replacement. Liquid lift pump, water shutoff, and water cone restrain can also be used to tap residual oil from rising bottom water. Optimizing profile control and water shutoff measures and adjusting the injection and production relationship can be effective approaches for developing residual oil in the pores and cracks beside the high diversion channel.

## 1. Introduction

Fault-solution reservoirs are important components of deep carbonate oil and gas resources in China. They are mainly controlled by dissolution and strike-slip fault zones at different levels. These reservoirs are characterized by segmented accumulation along the fault zone, vertical penetration, and intermittent spatial distribution [1, 2]. Fault-solution oil reservoirs are independent of the regional unconformity levels and structural locations. Hydrocarbon is filled vertically along the Tongyuan fault zone to form reservoirs and migrates in a “T” shape along with the fracture network sys-

tem related to the fault zone, which are the characteristics of vertical transportation and accumulation, segmented accumulation, and differential accumulation [3, 4]. The main zones of fault-solution reservoirs are characterized by high oil and gas resources, with high productivity of oil wells. Indeed, they are characterized by large and small faults with large and small reservoirs, respectively, while the absence of faults results in the lack of oil accumulation. The controlled reserves and development characteristics of different wells in the same fault-solution reservoir are different. The size of caves in the well-controlled and the degree of interwell connectivity can determine the single well productivity and

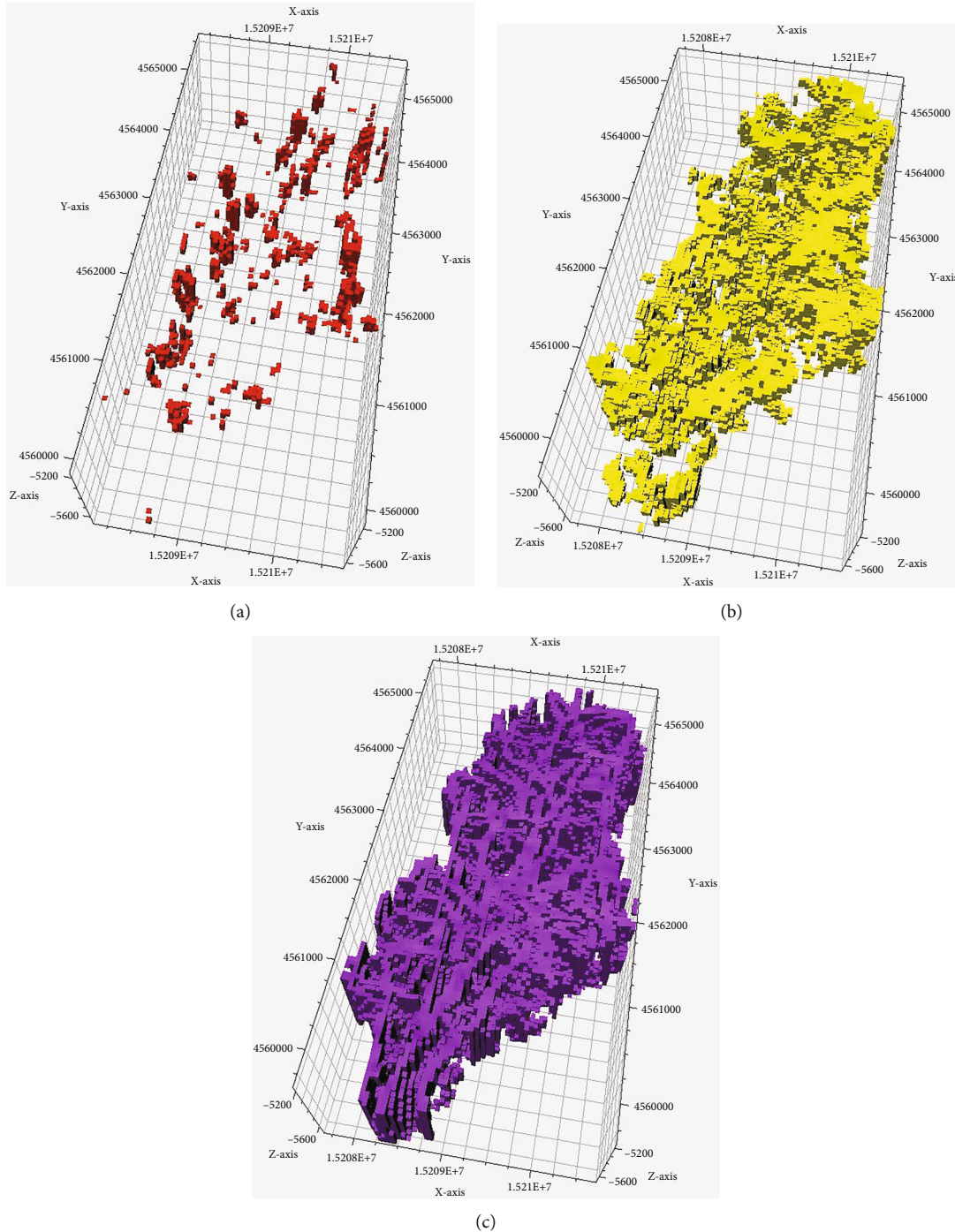


FIGURE 1: Distribution characteristics of L11 unit reservoirs.

residual oil distribution.

The Middle-Lower Ordovician carbonate strata in the Tahe Oilfield have experienced multiphase tectonic movements, forming a series of fault systems of different levels and multiphase superimposition and developing abundant fault-solution reservoirs [5]. Oil reservoirs are mainly composed of fractures caused by tectonic deformation, pore structures, caves, and fractures, formed by the karstification process. Indeed, large caves are the most important storage space, while fractures constitute not only the storage spaces

but also the main seepage channels. The carbonate has no significant storage and permeability matrix. The reservoir spaces are diverse in shape, large in size, uneven in distribution, and highly heterogeneous, resulting in a complex distribution of residual oil in oilfield development. Therefore, it is important to improve the development effect by further investigating the distribution pattern of the residual oil in the reservoir and improving the comprehensive management of the reservoir to exploit the potential of the residual oil. Indeed, numerous researchers have investigated the



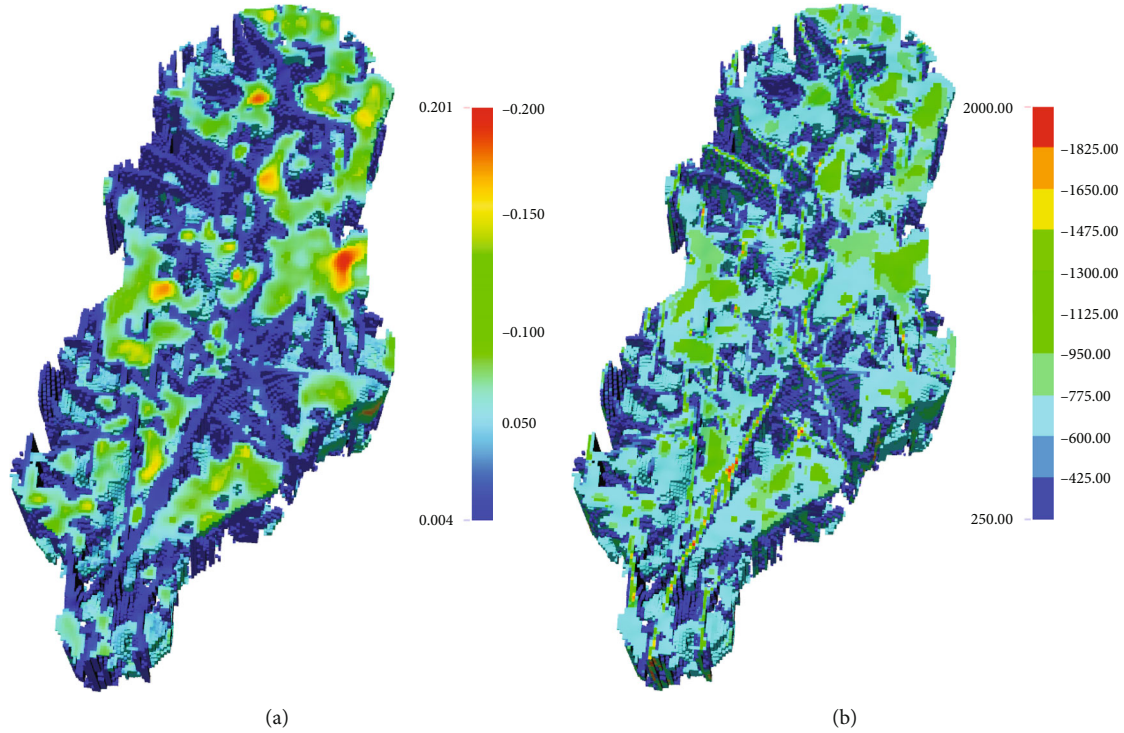


FIGURE 2: Porosity and permeability fields of L11 unit.

TABLE 1: Physical parameters of the numerical simulation model of the L11 unit.

Model parameter	Value	Model parameter	Value
Reservoir temperature	140°C	Reservoir pressure	67 MPa
Rock compressibility	$4.93 \times 10^{-5}$ 1/MPa	Fluid compressibility	$13.2 \times 10^{-4}$ 1/MPa
Porosity	0.01-0.28%	Permeability	0-2000 mD
Water multiple	10	Oil volume factor	1.167

residual oil in clastic and carbonate fractured reservoirs. For carbonate fractured-cavity reservoirs, many scholars have used indoor mechanism model experiments and numerical simulation methods. The distribution characteristics of residual oil have been explored and studied, and some distribution laws of residual oil have been preliminarily summarized [6].

Wang et al. [7] studied the distribution characteristics and laws of remaining oil in fractured-cavity carbonate reservoirs through experiments and numerical simulations. Rong et al. [8] divided the remaining oil into 4 categories and 5 subcategories based on the distribution characteristics of the residual oil through the detailed description of the reservoir and the analysis of the production performance test data. Ameri et al. [9] suggested that the residual oil can be extracted by water, surfactant, and gas flooding in the buried hill fractured reservoir matrix. Zheng et al. [10] used various data, such as cores, logging, seismic, and production performance, to determine the multiscale characteristics, reservoir types, spatial morphology, and distribution laws of fracture-cavity carbonate reservoirs. The model and the configuration relationship with production wells were studied, the influence of various factors on the distribution of residual oil

was analyzed, and the main controlling factor model on the residual oil distribution after the water flooding was established. Liu et al. [11] proposed a method for building fractured porous media models for macroscopic experimental simulation of reservoirs and presented an application example of simulation of the development process of fractured porous media reservoirs. Due to the different physical properties of the reservoirs, problems such as water intrusion and unclear distribution of residual oil arise, compromising the successful development of the water-flooding process in carbonate reservoirs. Li et al. [12] used an interlayer heterogeneous and anisotropic physical model to conduct a three-dimensional water flooding experiment and to quantitatively characterize the water-conducting states, water flooding mechanisms, and residual oil distribution of the bottom water-bearing carbonate porous reservoir. In recent years, studies on residual oil distribution and enhanced oil recovery in carbonate reservoirs worldwide have mainly focused on fractured reservoirs, while studies on fractured-cavity reservoirs in my country have focused on bottom water flooding, based on laboratory experiments and numerical simulations. There is a lack of systematic studies on the distribution pattern of residual oil in fault-



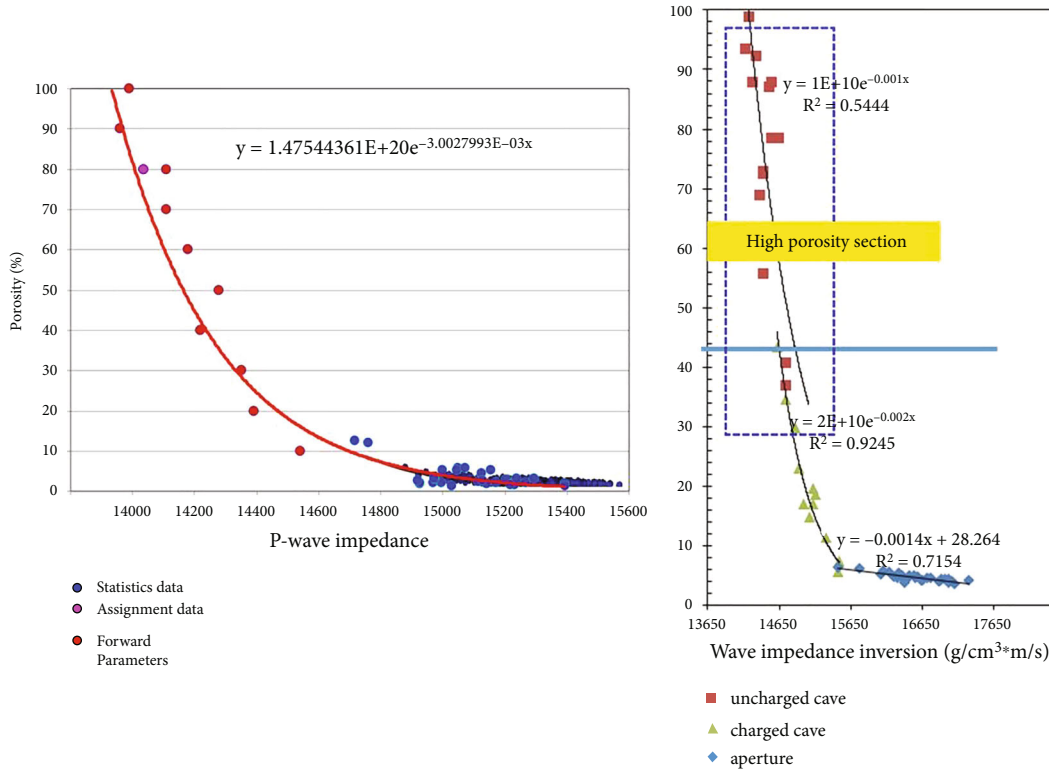


FIGURE 3: Reserve fitting porosity correction.

karst carbonate reservoirs and on enhanced oil recovery methods in the later stage of the water flooding development process.

Unit L11 is a typical fault-solution fracture-cavity carbonate reservoir. Since its development in 2009, it has been experiencing several phases of natural energy and water/gas injection development. The current production and comprehensive water cut rates are 10.2 and 70%, respectively. However, there are several development challenges, including high water cut, low recovery rate, and low recovery degree [13]. Several researchers have used numerical simulation to study the typical unit of L11 and to reveal the residual oil distribution characteristics of fault-solution reservoirs, in order to provide suggestions for further improving the recovery factor, forming and stimulating potential residual oil stimulation of the fault-solution fracture-cavity reservoir in the Tahe Oilfield, and providing technical support for the efficient production of residual oil in fault-solution reservoirs [14].

## 2. Implementation of a Numerical Simulation Model for Fault Solution

Based on the geological data of the L11 unit, the model was divided according to the type of reservoir, while the corresponding porosity and permeability parameters, as well as phase permeability curves, were used to implement the numerical model of the typical unit of fault-solution reservoir [15, 16].

TABLE 2: L11 unit reserve fitting parameters.

Type	Geological reserves ( $\times 10^4 \text{ m}^3$ )	Numerical simulation reserves ( $\times 10^4 \text{ m}^3$ )	Relative error (%)
Caves	1100	1113	0.3
Cavities	900	902	0.2
Fractures	89	91.4	2.7
Total	2099	2106.4	0.4

*2.1. Geological Characteristics of L11 Unit.* The L11 unit is located in the tension zone of the L12CX main fault, with a large communication depth. The NW-oriented secondary faults form a compression and transformation on the main fault. The surface layer developed NEE- and NW-oriented secondary faults. In addition, the primary and secondary faults are superimposed, the degree of fragmentation is large, and the dissolution foundation and the filling conditions are good. The L11 unit is a typical fault-solution fracture-cavity reservoir. The L11 reservoir is developed in segments along the primary and secondary faults, with a large scale and vertical depth. The reservoirs developed along the faults and converge with the primary faults.

There are 14 wells in the well-block pressure and can be divided into 4 well groups based on the previous understanding of connectivity: (1) group L1: L10X, L11X, and L1X; (2) group L110: L18 and L110X; (3) group L11: L11, L18X, L12X, and L16CH; and (4) group L13: L19, L18H, and L13CH. L14 and L15X wells have not been established Unicom.

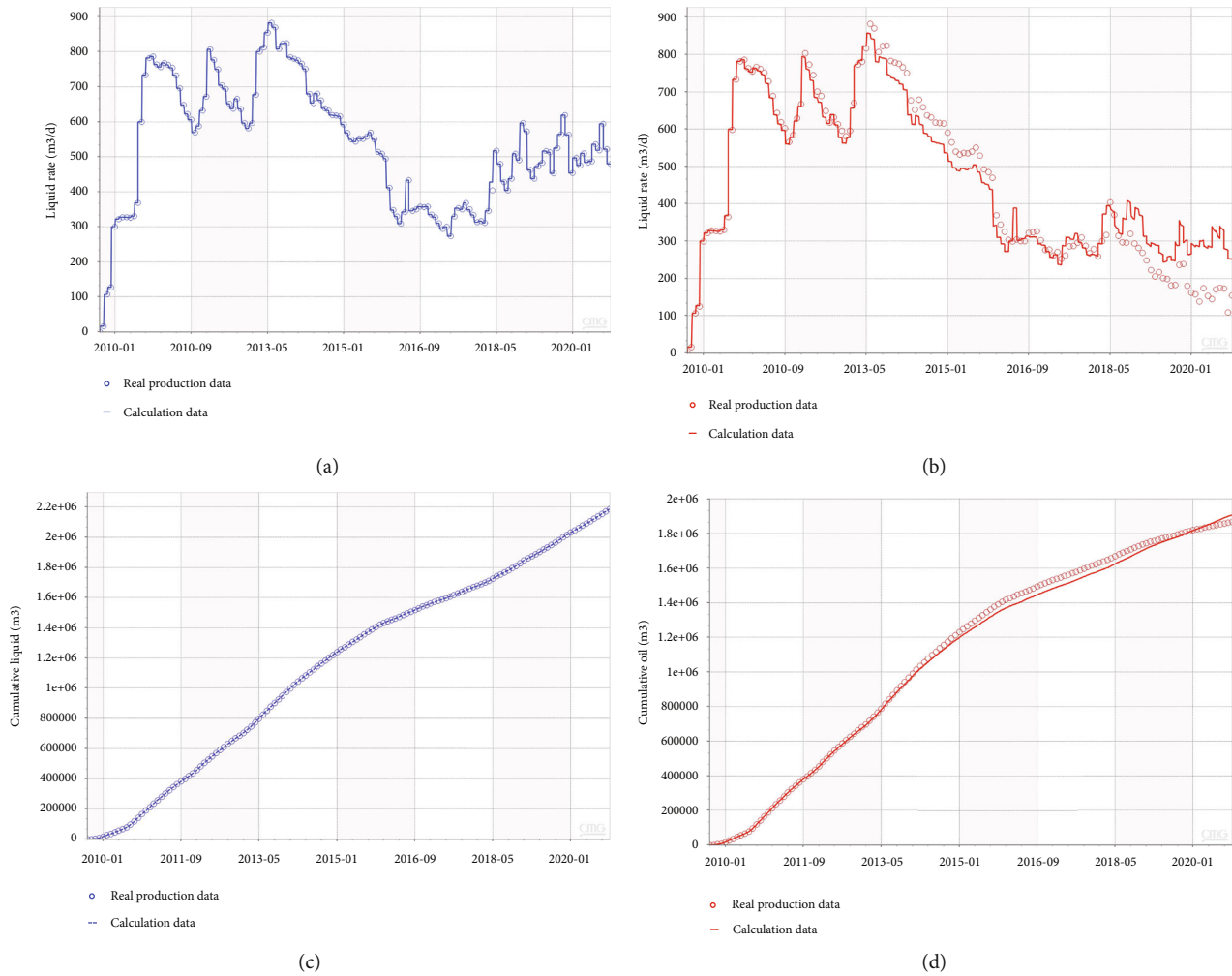


FIGURE 4: Fluid production and oil production fitting curves of the L11 unit.

2.2. *Implementation of the Numerical Simulation Model.* Based on the development characteristics, porosity, and permeability of the L11 unit, three types of reservoirs were first distinguished: caves, cavities, and fractures; then, a numerical model of the L11 unit was implemented [17, 18]. The distribution characteristics of reservoir types are shown in Figure 1. The size and number of the model grid were  $25\text{ m} \times 25\text{ m} \times 3\text{ m}$  and 4561216 ( $124 \times 242 \times 152$ ), respectively.

*Grid reservoir definition principle:* loyal to the well point reservoir type, caves and fractures are given priority, cavities second, and the reservoir type of each grid is unique.

Part of the grid in the model is a superposition of multiple reservoirs. The porosity and permeability characteristics of these grids were processed. The permeability is determined by the dominant channel method. The maximum value of the superimposed reservoir permeability was considered the permeability of the grid, while the pore degree was determined using the direct summation method [19]. The porosity and permeability distribution of the model is shown in Figure 2.

The reservoir and oil-water physical parameters of the digital simulation model are shown in Table 1. The positions and trajectories of the wells, as well as the perforation hori-

zons in the model, were obtained using the actual data of the L11 unit. Taking into account the different flow laws of pores and fractures, as well as the characteristics of the numerical simulation model, the permeability curve was used to reflect the flow characteristics of different reservoirs. The bottom water energy was stimulated using the water-oil volume ratio method.

2.3. *History Fitting and Model Verification.* The history matching process is based on historical data production and adjusting reservoir parameters to establish a model that represents as much as possible the true behavior of the reservoir. The L11 unit reservoir showed significant differences in porosity and permeability [20]. The porosity values can be adjusted using the inversion relationship of the parameters and statistical methods, and they can be corrected during reserve fitting. On the other hand, there is currently no unified theory for adjusting permeability, and it needs to be carried out correction during production dynamic fitting.

The established mathematical model was used to calculate the unit geological reserves. In addition, the porosity, net-to-gross ratio, and oil-water saturation were adjusted based on the characteristics of the reservoir type and the

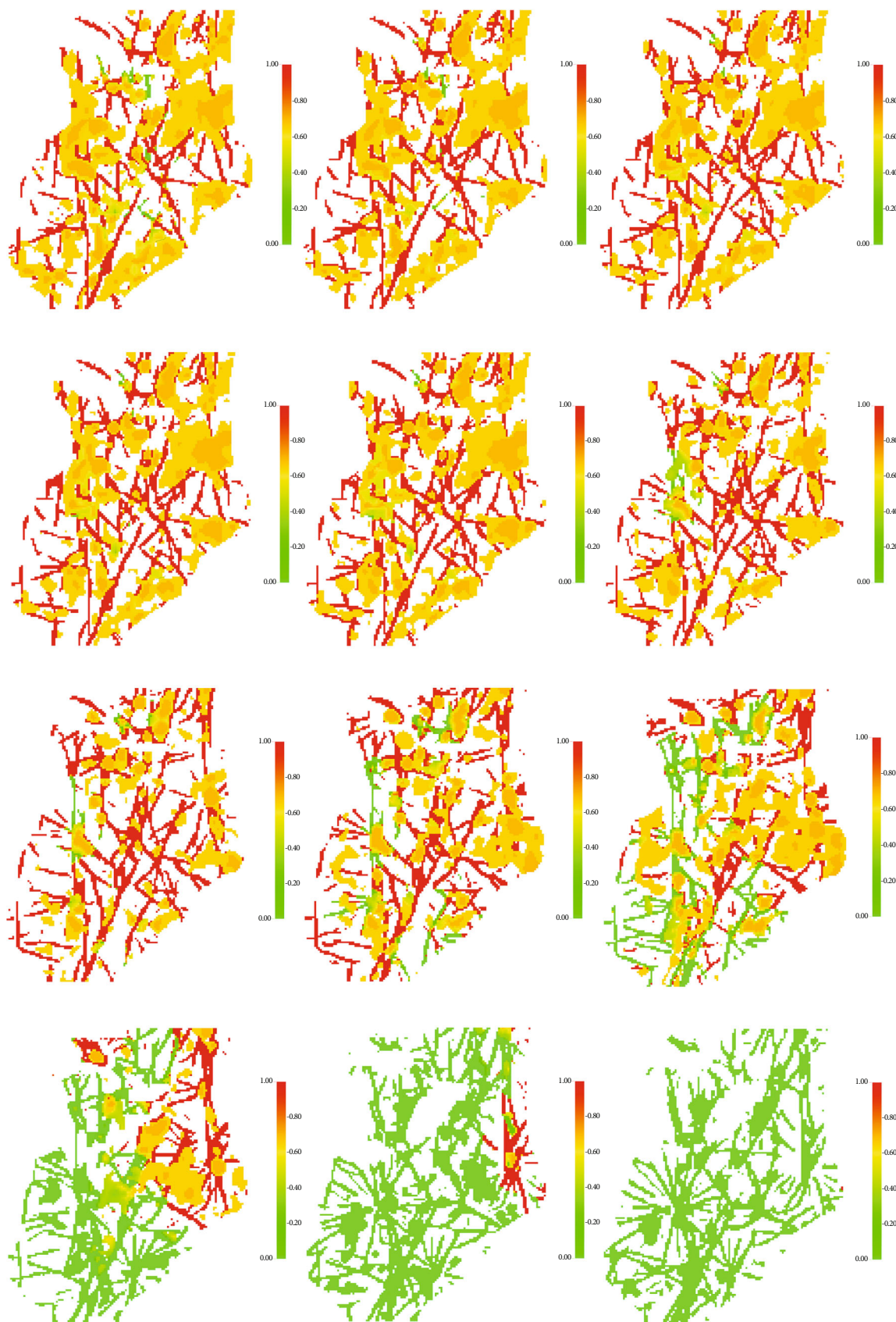


FIGURE 5: Residual oil distribution in different depth planes of the L11 unit (k from 1 to 40).

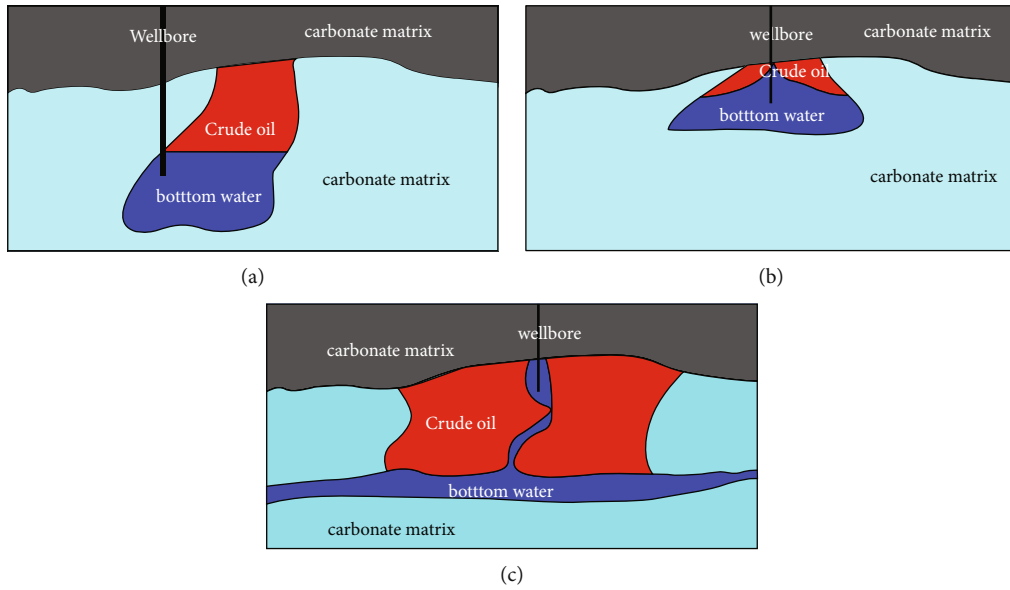


FIGURE 6: Well point residual oil mode.

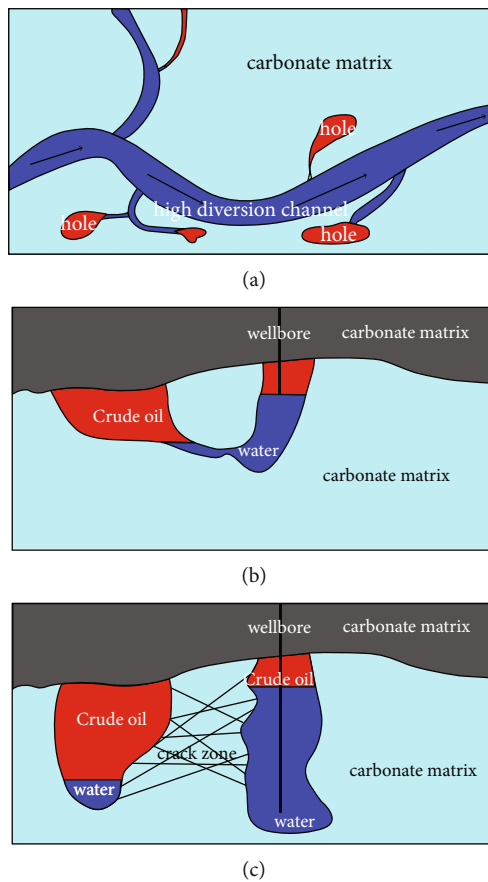


FIGURE 7: Residual oil pattern between wells.

seismic logging combined with statistical methods, while the actual geological reserves were used as the basis for reserve fitting. After matching the production history data, the constant liquid production was used for fitting the oil production index. By modifying the relative permeability, the

production history of the whole district was fitted. Then, based on seismic logging data and stimulation measures, single-well production fitting was performed. In addition, the original digital model was revised to establish a more consistent model by adjusting the near-well permeability,

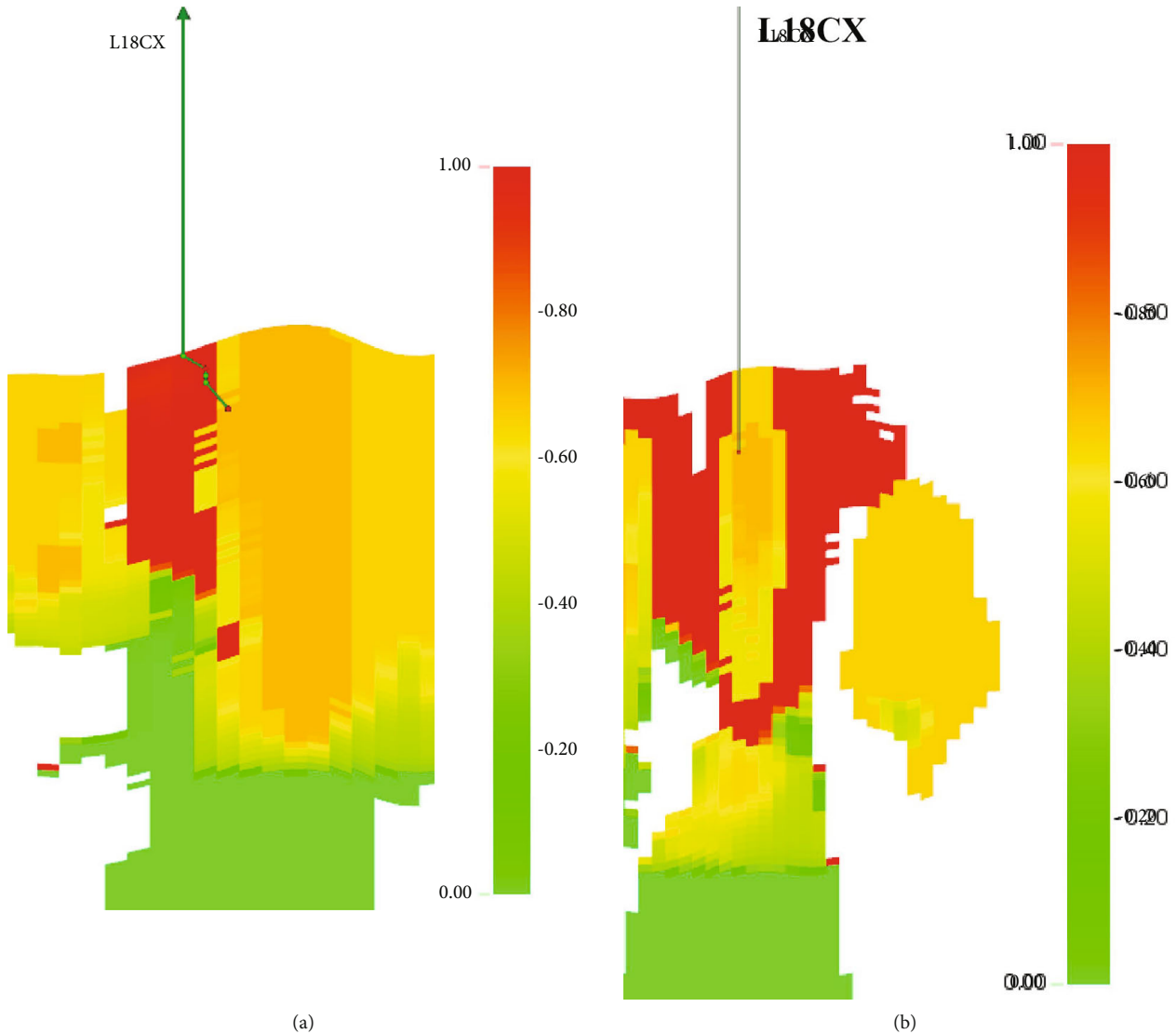


FIGURE 8: Residual oil distribution characteristics of the well L18CX.

the connection relationship, and the degree of connection between the well, surrounding reservoirs, and water bodies [21, 22]. The digital simulation model of production dynamics provides a reliable basis for the analysis of residual oil distribution and the study of countermeasures to improve the development effect.

**2.3.1. Reserve Fitting.** The unit geological reserve, the actual geological reserve, and the relative error were  $2106.4 \times 10^4$ ,  $2099 \times 10^4 \text{ m}^3$ , and 0.4%, respectively. The results showed good reserve fitting. The calibration basis for porosity in the fitting process is shown in Figure 3. Table 2 reports the reserve fitting situation of reservoir types in the L11 unit.

**2.3.2. Production History Matching.** Figure 4 shows the fitted temporal production rates of fluid and oil in the L11 unit block. The liquid and oil production rates were consistent with the actual production data. Moreover, the cumulative liquid and oil production rates were in line with the actual

production rates. The results revealed that the single-well production fitting rate reached more than 90%. The adjusted digital model based on geological data and stimulation operations can reflect the characteristics and current situation of the L11 unit and serve as the basis for assessing the residual oil distribution characteristics and adjustment countermeasures.

### 3. Analysis of Residual Oil Distribution Mode

Study the produced reserves under different injection-production conditions during the development process of the L11 fault-dissolution fracture-cavity unit, analyze the residual oil migration rules, and summarize the main controlling factors of residual oil distribution under different development methods. Study the residual oil distribution at different development stages in the water-drive gas reservoir, summarize the main concentration positions of the residual oil after the development effect deteriorates, determine the



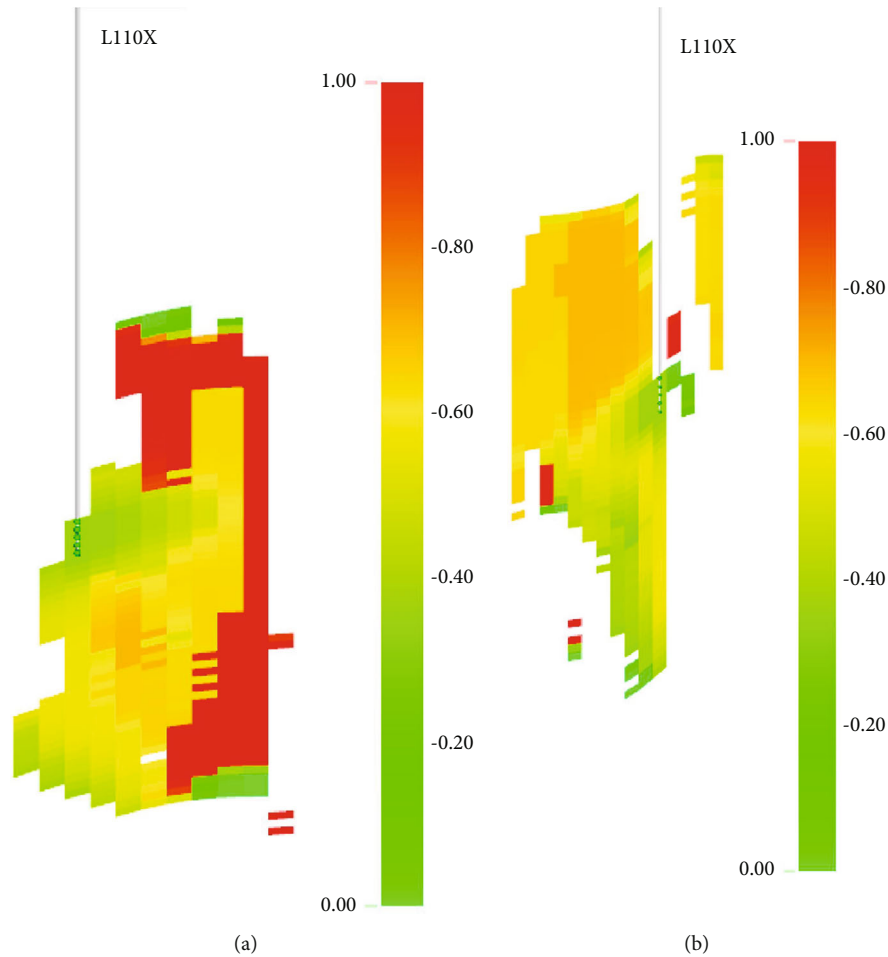


FIGURE 9: Residual oil distribution characteristics in the L110X well.

residual oil distribution and main control factor analysis methods, and provide a research base for the formulation of countermeasures to improve the development effect [23].

### 3.1. Residual Oil Distribution Characteristics of the L11 Unit.

The L11 unit has abundant residual oil reserves and great potential for subsequent adjustment and development. The residual oil distribution at different depths of the L11 unit, from production to May 2021, is shown in Figure 5. In the upper part of the unit, wells L18, L110X, TP157, L19, TP188, L18H, and L13CH formed clear gas caps, and the crude oil corresponding to the upper of the reservoir was produced to a certain extent. However, as the depth of the reservoir increases, the influence of the gas cap weakens rapidly. Moreover, it was observed disappearance of the gas cap influence at  $k=5$ . With increasing depth, the high-angle fractures communicate with the bottom water, leading to bottom water coning in the wells L11X, L11, and L18X ( $k=7\sim 10$ ). At  $k=15$ , clear bottom water cones appeared in wells L11 and L14. In the process, a mixed distribution of oil and water was formed, leading to dispersing and distribution of the residual oil. In the interval  $k=20\sim 30$ , the wells L1X, L12X, L16CH, L18H, and L13CH showed obvious bottom water coning. Since then, as the depth increases, the

degree of water flooding of the production well became increasingly severe until it was completely flooded ( $k=80$ ).

Fractures in fault-solution fracture-cavity reservoirs are the main channel for oil and gas flow and the main path of bottom water coning. The bottom water channeling along high-angle fractures is the main reason for the decline in the L11 unit production, while bottom water coning and gas/water injection development are the key factors affecting the residual oil distribution in the L11 unit. In addition, the irregular development of fractures and caves represents the main factors that cause the diversified residual oil distribution patterns. To assess the main controlling factors of residual oil in the L11 unit, the residual oil distribution pattern of each production well was analyzed and classified [24].

### 3.2. Residual Oil Distribution Pattern and the Main Controlling Factors

**3.2.1. Residual Oil Distribution Pattern.** According to the distribution location and formation mechanism, the residual oil distribution pattern of the L11 unit includes 4 types (Figures 6 and 7). There are two types of residual oil at the well points, namely, loft-type and bottom water rising blocking type (including bottom water cone ingress blocking and

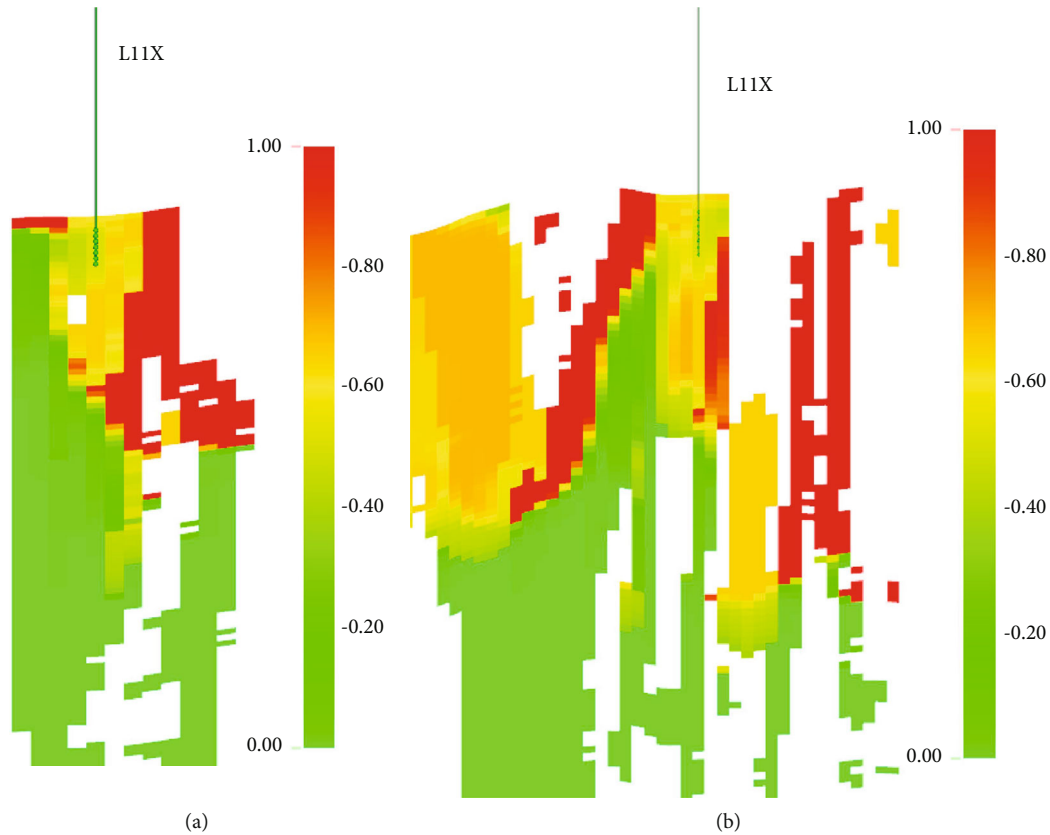


FIGURE 10: Residual oil distribution characteristics of the L11X well.

bottom water intrusion blocking types). In addition, two types of residual oil between wells are distinguished, namely, separated fracture-cavity type (including oil-separation and near-fracture cave types) and pore/slit type near high diversion channels [25].

(1) *Loft-Type*. Loft-type residual oil refers to the residual oil that cannot be directly produced from the fractured-vuggy reservoir above the top of the production interval of the oil well. In the production well, above the oil-water interface of the fractured-vuggy in the production interval, with the production of crude oil, the oil-water interface in the lower part of the reservoir continues to rise [26]. As the oil-water interface rises to the production interval, flooding occurs in the production interval of the oil well, resulting in the presence of attic-type residual oil in the upper fissures that were difficult to recover, as revealed in L18CX, L14, and L13CH wells. As shown in Figure 8, well L18CX is a side-drilling well of well L18, designed to develop cavern reservoirs shielded by the bottom water channel. The well was successfully sidetracked to the upper edge of the cavernous reservoir, showing a good production rate. At present, the residual oil is mainly karst cave residual oil. Indeed, fractures were developed near the well; thus, restraining and delaying the penetration of bottom water along the fractures is the key to ensuring stable production of the well [27].

(2) *Bottom Water Rising and Blocking Type*. Bottom water rising and blocking residual oil refers to the residual oil that

cannot be directly produced around the flooded oil well due to bottom water rising, blocking the residual oil [28]. The formation of two types of residual oil with bottom water rising and blocking type is summarized:

- (1) The bottom water cone enters the residual oil of the sealing type. In reservoirs with pores and fractures, the bottom water rises in a cone-shaped distribution at the bottom of the well, and crude oil around the well cannot be produced, forming a water cone that blocks the residual oil, as revealed in well L110X.

As shown in Figure 9, well L110X is located in the north-central part of the L11 unit. The area where this well is located is controlled with caves and fractures. During the development process, the bottom water coning causes a decline in production, resulting in the dispersion of the residual oil on the upper part of the cave [29, 30].

- (2) The bottom water flees into the residual oil of the blocking type. There are cracks near the bottom of the well that communicates with the deep bottom water. During the production process, the deep water quickly penetrates the bottom of the well along the cracks, with a pressure difference, causing flooding of the oil well. Because the water in the cracks enters linearly, after the oil well is flooded, wells mainly produce water, with the presence of significant residual oil amount blocked by the bottom

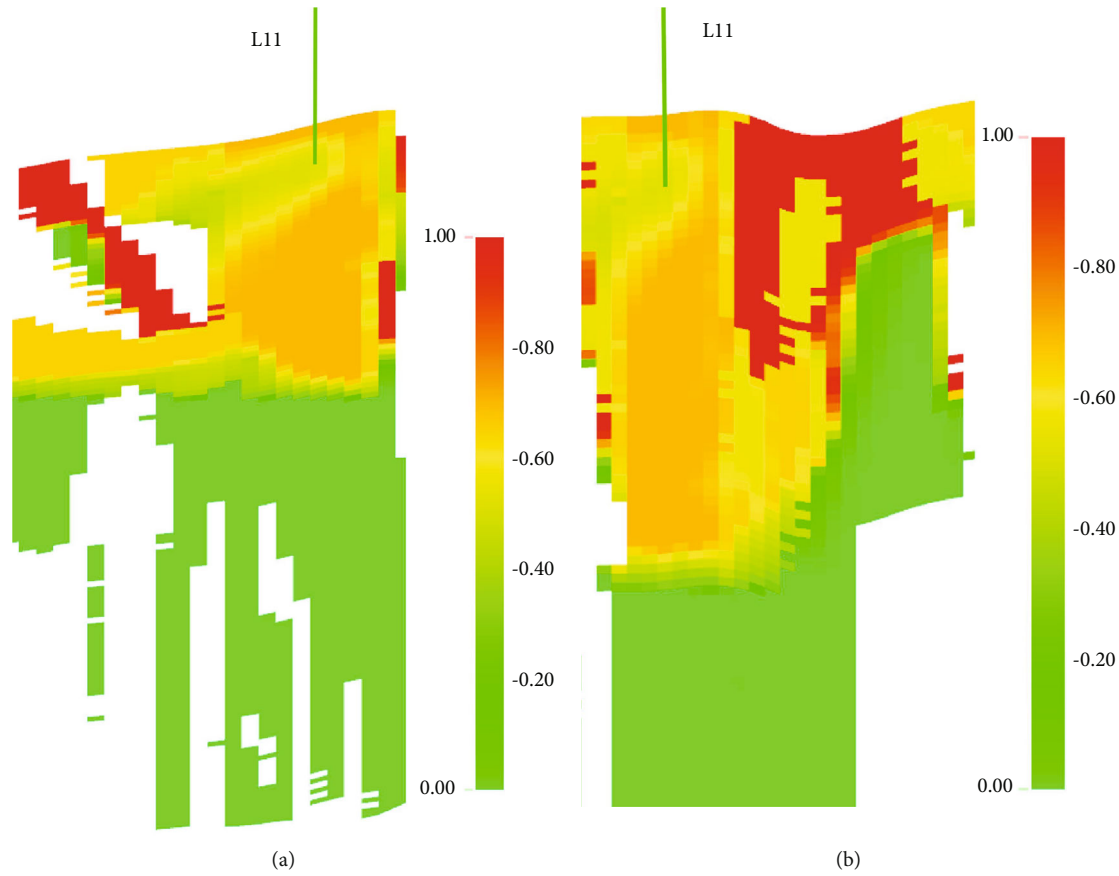


FIGURE 11: Distribution characteristics of residual oil in the L11 well.

water that cannot be directly produced around the oil well, as observed in L11X, L1X, L11, L18X, L12X, L16CH, L19, and L18H wells. The distribution characteristics of this type of residual oil were analyzed, using L11X and L11 wells as examples. As shown in Figure 10, well L11X is located in the northern part of the L11 unit. The area where the well is located is characterized by the presence of fractures and karst caves. Indeed, the well connects the karst cave reservoirs through the fractures. During the production process, the bottom water penetrates along the fractures, causing partial water flooding in the production well section and protecting the crude oil in the karst caves, resulting in dispersed and lumpy residual oils.

As shown in Figure 11, well L11 is located in the west of the unit, where karst caves and abundant crude oil reserves were developed. The well is connected to the top of the cave, and the cracks between the cave and the bottom water body are developed. Before 2017, L11 was the main production well in the block. During the production process, the bottom water flowed into the wellbore through high-angle fractures, shielding the crude oil in the middle and lower parts of the caves, thus resulting in a substantially lower output. Indeed, the residual oil is mainly shielded block-shaped residual oil.

(3) *Hole Type Near High Diversion Channel*. The residual oil of pores and fractures near the high conductivity channel refers to the residual oil in low-developed pores and fractures near the water channel along the fault. The large-scale fractures are high-conductivity channels allowing the bottom water to flow into carbonate fracture-cavity reservoirs. In fact, these parts are easily flooded by water. Porous and fractured reservoirs, which are associated with high-conductivity channels and have a low degree of development, are located on nonflowing channels, resulting in a high retention rate of residual oil. As illustrated in Figure 12, there are clear channels between L18 and L110X wells.

(4) *Separated Fracture-Cavity Type*. Separated fracture-vuggy residual oil refers to the residual oil in the fracture-vuggy assembly that is not directly connected to the strong water-flooded fracture-vuggy in the transverse direction. Fracture-cavity bodies in carbonate fracture-vuggy reservoirs are mostly geometrically complexes. Inside the fracture-cavity, there are connected channels with different degrees of connectivity. Indeed, this fracture-cavity is the main storage space of crude oil and may have a certain degree of separation in the horizontal direction. According to the type of fracture-cavity separation, it can be divided into separated and near-fracture-cavity residual oils.

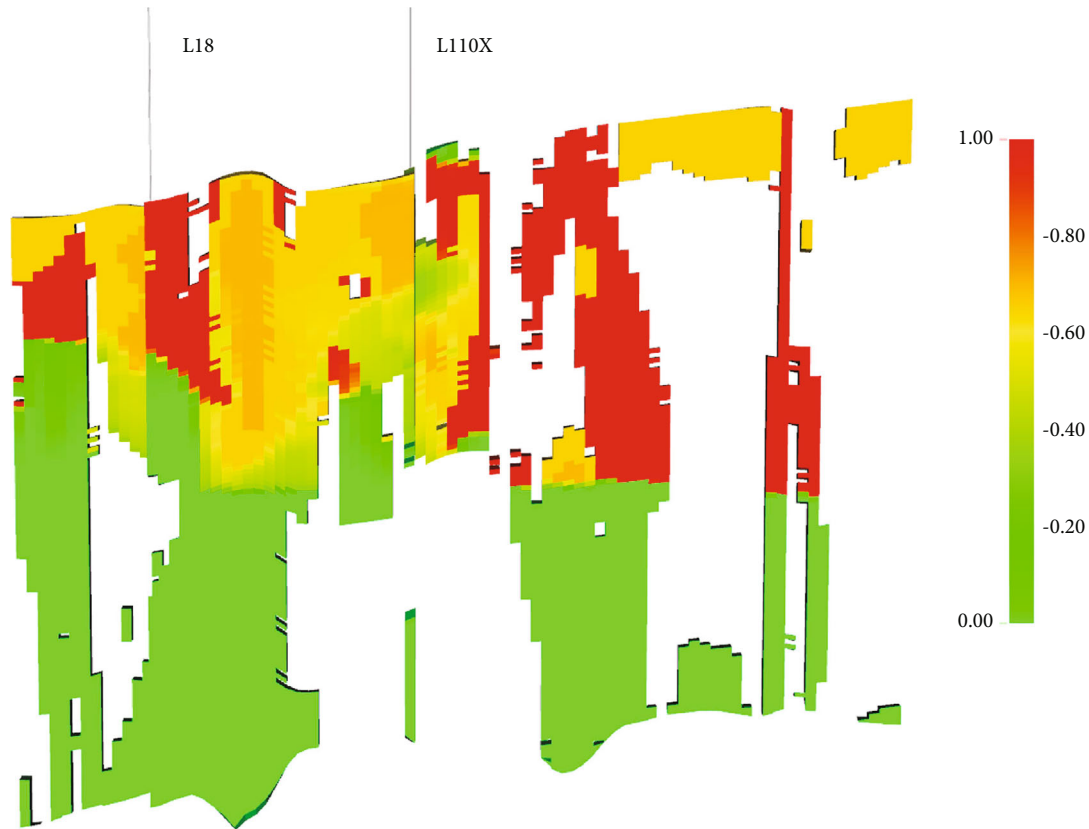


FIGURE 12: Distribution characteristics of residual oil in the L110X well.

The separated residual oil refers to the fractured “U”-shaped cave, where one side is exploited with high water flooding, and the other side is not well controlled. Because each fractured-vuggy is laterally separated by nonpermeable matrix rock blocks or low-developed reservoirs, the deep reservoirs are connected, forming a separate “U”-shaped connected fractured-vuggy. In this type of fractured caverns, when drilling on one side of the “U”-shaped fractured-vuggy is put into production, the oil-water interface may gradually rise and flood along with the production, while the other side of the fractured “U”-shaped fractured-vuggy cannot be flooded. The oil-water interface in the well-controlled fracture-cavity may remain at the overflow point, where the two fracture cavities are connected; thus, the upper crude oil cannot be produced, forming a separated fracture-type residual oil. Indeed, L10X and L11X wells present some evidence of the separated residual, as shown in Figure 13.

The near fractured-vuggy type refers to the residual oil in uncontrolled and low-connected fractures and caves. Each fractured-vuggy is laterally separated by nonpermeable matrix rock blocks or connected by small fractures or pore-type reservoirs; thus, the degree of connectivity is considered relatively low and fluids cannot directly flow through, forming a near-fracture-type separated fractured-vuggy. In this type of separated fracture-cavity, the fluid cannot flow directly after producing the crude oil in one fracture cavity. The other fracture-cavity cannot be produced by conventional methods, and the separated fracture-cavity type

residual oil is formed, as illustrated in Figure 14 between wells L11 and L12X and between wells L12X and L16CH.

**3.2.2. Main Controlling Factors of Residual Oil.** A numerical simulation was performed on the L11 unit. According to the analysis of static and residual oil simulation results, the distribution of residual oil in the reservoir is related to the development degree of the reservoir, the position of the structure, the positional relationship between the fracture and the reservoir, and the oil well-operating conditions. The connectivity between karst caves and reservoirs is poor, and the fractures communicate with the water body, causing a rapid tapering of the bottom water into the well section, thus shielding the cave area by the upper part of the oil well and the bottom water to enrich the residual oil [29]. The main controlling factors of the residual oil are summarized as follows:

(1) *Vertical Reservoir Connectivity.* L11 fractured-vuggy reservoirs have vertical fractures of different sizes. The development of fractures may improve the permeability of the reservoir near the well. In addition, the fractures that communicate with the bottom water are crucial for the coning of the bottom water. During the production process, the cracks that have good communication with the bottom water are opened, forming a water cone and advantageous water channels between the production section of the oil well and the bottom water. For reservoirs with good vertical

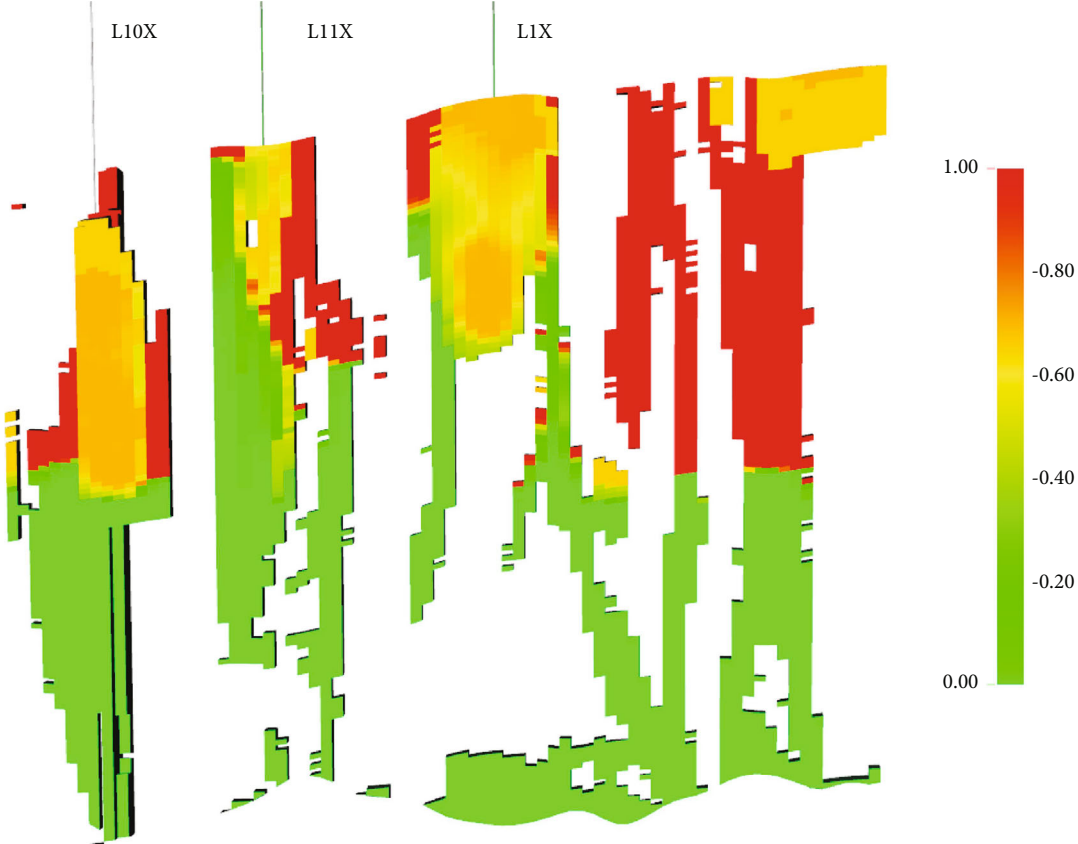


FIGURE 13: Residual oil distribution between L10X and L11X wells.

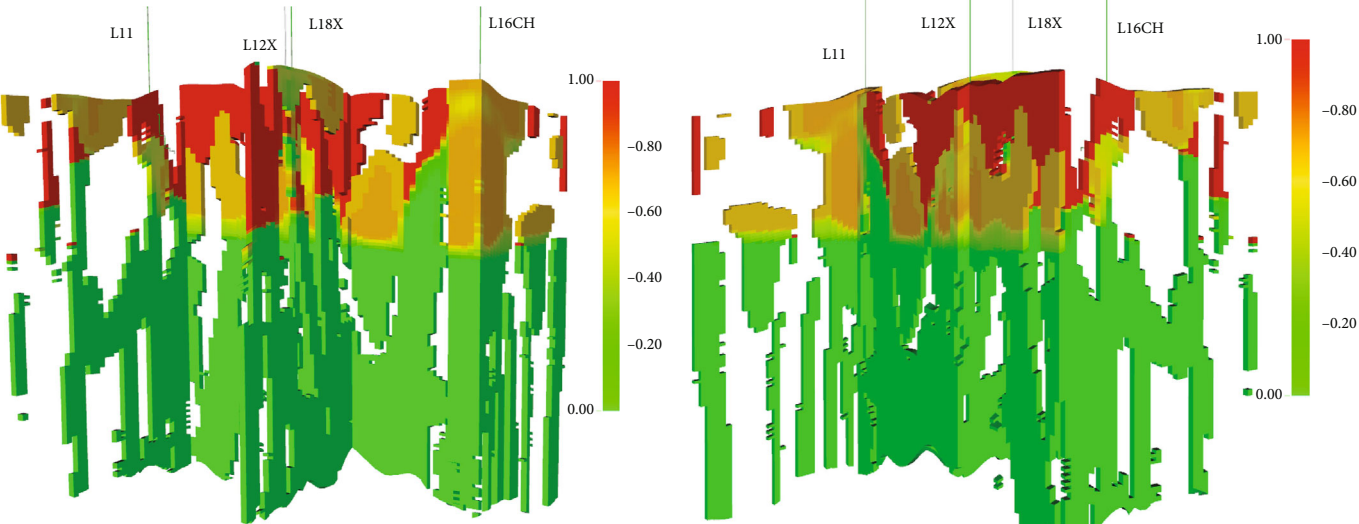


FIGURE 14: Residual oil distribution between L11, L12X, and L16CH wells.



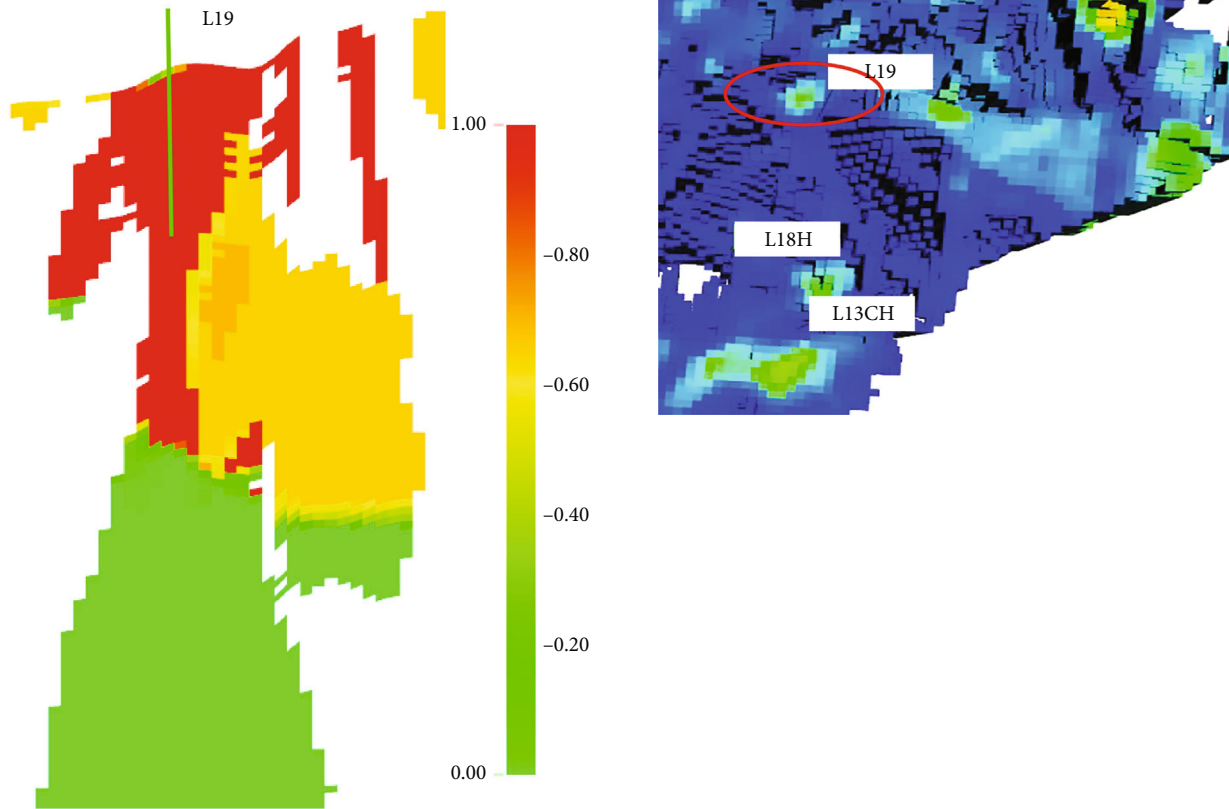


FIGURE 15: Residual oil near the L19 well.

connectivity, the development of fractures becomes the main influencing factor controlling the distribution of residual oil. Indeed, the residual oil is mainly distributed in dissolved caves that are not connected to the fractures or shielded caves by bottom water channeling.

(2) *Single Well Working System.* Fractured-vuggy reservoirs can form dispersed residual oil following injection of bottom water, artificial water, or gas due to the heterogeneity of the reservoir. This type of residual oil is characterized by a large dispersion range and low oil saturation, making development difficult.

#### 4. Countermeasures and Schemes for Enhancing Oil Recovery

In the middle and late stages of the development of fracture-cavity reservoirs in fault solution, as the water cut increases, the development effect may gradually deteriorate, and the oil-water relationship becomes more complicated. To improve the development effect, it is necessary to formulate countermeasures to tap the potential of the residual oil between the control well and the well according to the residual oil distribution pattern. In general, the potential of various types of residual oil in uncontrolled fractured caverns between wells and large well spacing can be exploited by deploying new wells or using sidetracking in old wells. Conventional measures are mainly used to exploit the potential of remaining oil distribution at wells, taking into account

the distribution characteristics of the residual oil. These measures can be summarized as follows:

4.1. *Deploying New Wells or Using Sidetracking in Old Wells Allowing for Effective Control of the Residual Oil of the Loft-Type and the Separated Fracture-Cavity Type with a Large Well Spacing.* Well L19 is located in the central and southern parts of the L11 unit. The well-controlled area is characterized by fractures, connecting the cave reservoir and the bottom water body. During the production process, the bottom water channeled through the fractures, causing rapid flooding in the production well section and distribution of the residual oil in the bottom water channeling (Figure 15).

The sidetracking development of this well was carried out inside the shielded cave, and the new sidetracking well was produced with a fixed rate of  $60 \text{ m}^3/\text{day}$ . The results of the 3-year production simulation, as well as comparison and analysis of the effect of increasing production of the measured wells, are reported in Figure 16.

After the sidetracking of the well L19, the upward trend of bottom water was better delayed, while the possibility of shielding the residual oil from the bottom water was improved. When the new well allocates  $60 \text{ m}^3/\text{day}$ , the oil production rate can be stabilized above  $40 \text{ m}^3/\text{day}$ , corresponding to a cumulative oil of  $26480 \text{ m}^3$  for 1.5 years (validity period). During the production process, a bottom water ridge gradually occurred at the heel of the sidetracked horizontal well, leading to a significant decrease in the oil production rate. Therefore, when developing sidetracking in

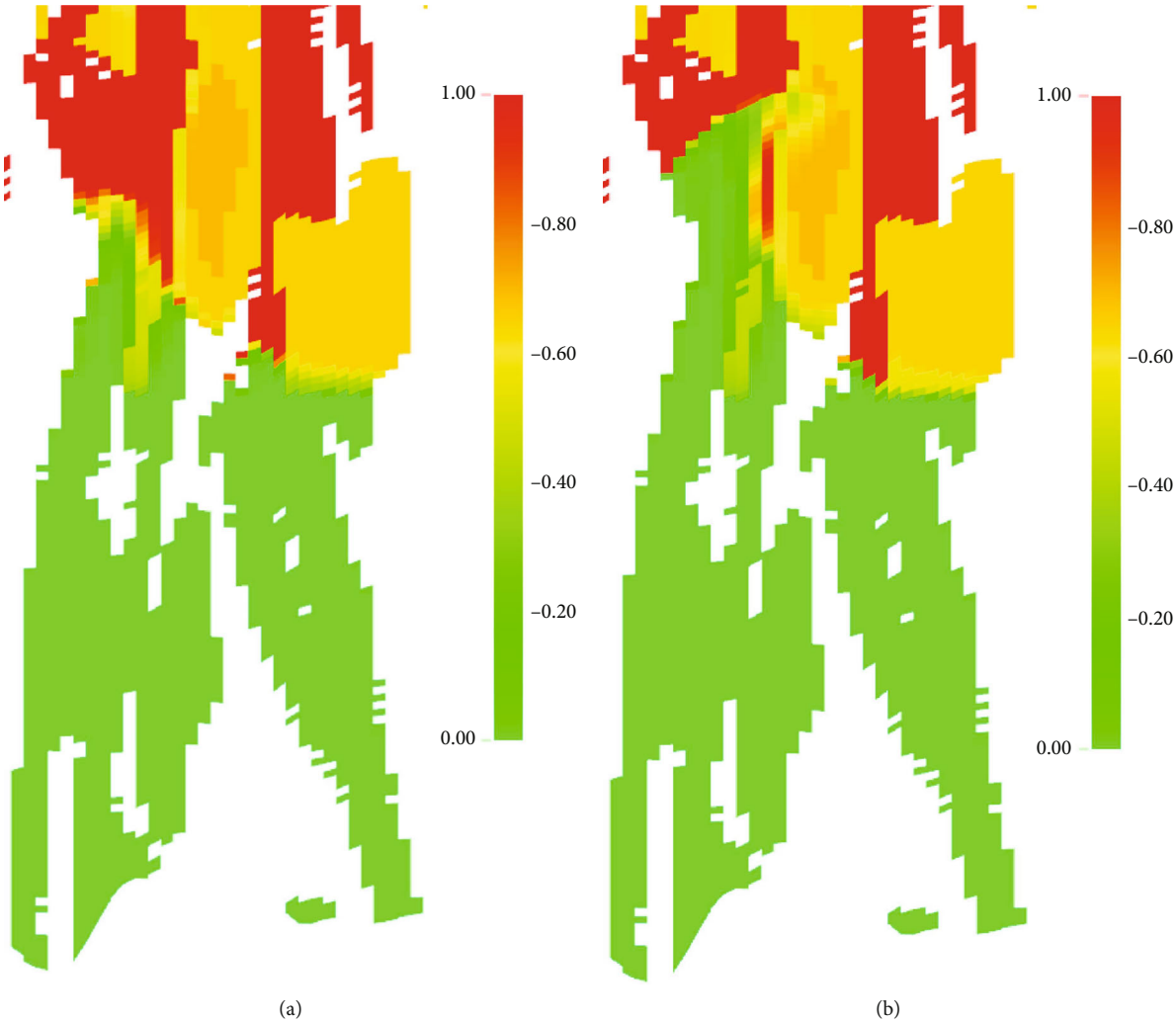


FIGURE 16: Sidetracking effect on the residual oil near the L19 well.

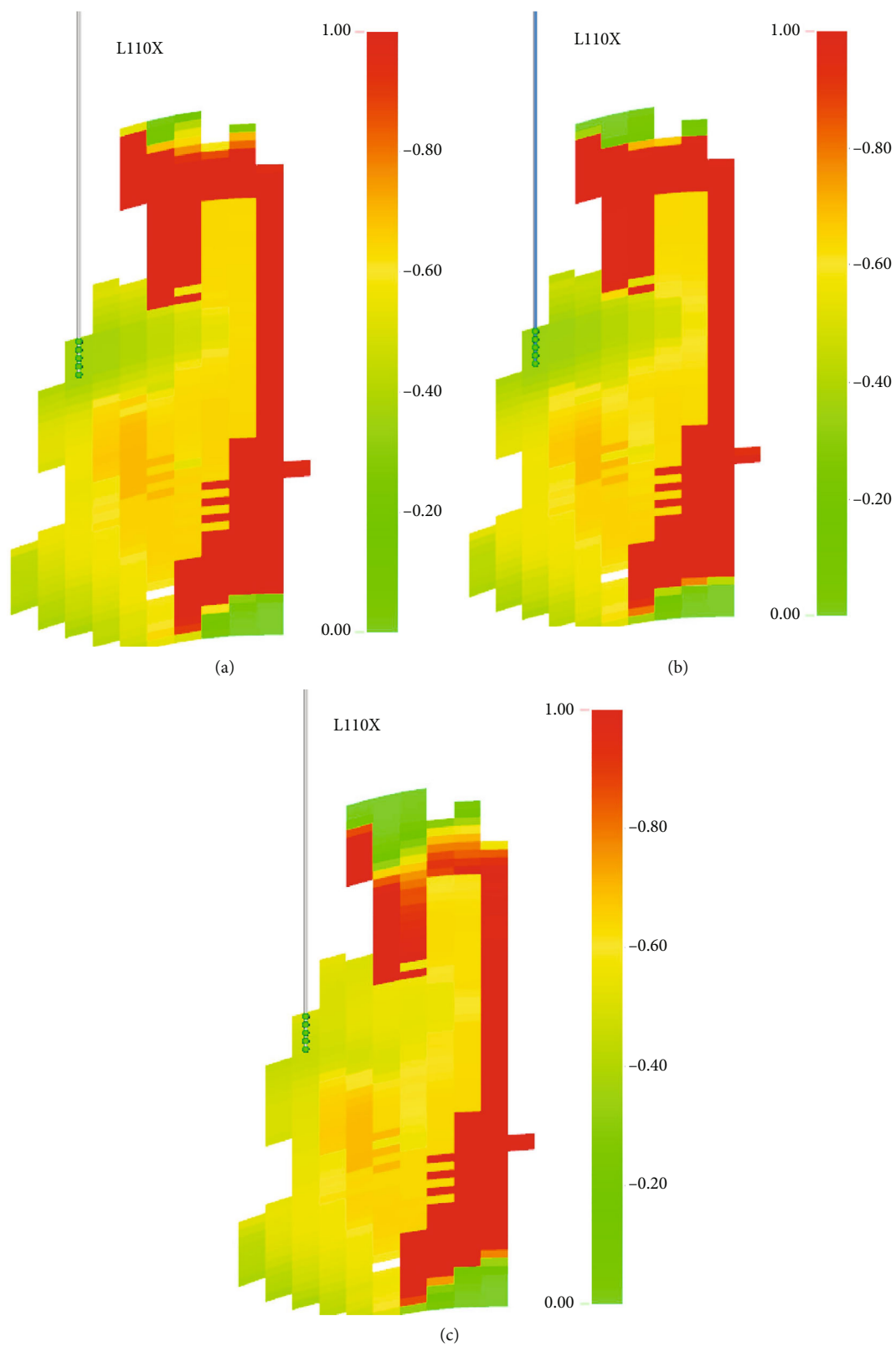


FIGURE 17: Influence of gas injection development on oil-water distribution characteristics of the L110X well.

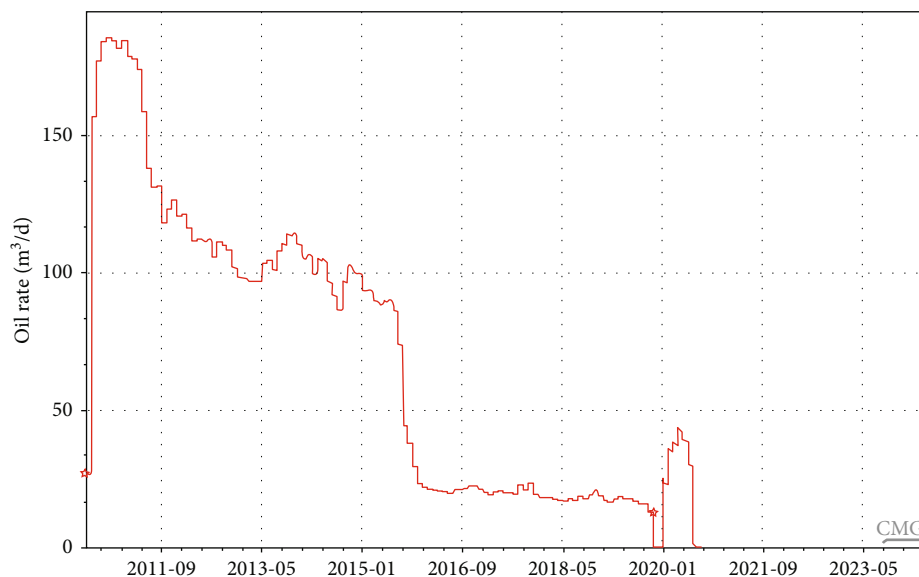


FIGURE 18: L110X well gas injection development increasing effect.

the fracture-developed area, it is recommended to compound corresponding plugging measures to extend the high and stable production period of sidetracking.

**4.2. Exploiting of Attic Residual Oil Using Drainage Oil Extraction and Gas Injection.** For the attic-type residual oil formed in the upper part of the generation interval, where the oil-water interface rises at the late stage of production in nonconstant volume fractures, conventional drainage cannot lower the oil-water interface, but it can be exploited by gas injection in oil. In addition, by injecting nitrogen into the suffocating well, the nitrogen may rise to the top of the attic under the action of gravity and accumulate to fill the attic space, causing a decrease in the gas-oil and oil-water interfaces. In addition, the well may become open when the oil-water interface sinks to the bottom of the production well, resulting in continuous crude oil production (Figure 17).

The well-controlled area of the L110X well consists of controlled caves and fractures. During the development process, the bottom water coning caused a decline in production, thus resulting in dispersion of the residual oil on the top of the cave. The well was developed by gas injection to produce the crude oil from the top of the cave. In addition, the oil-water interface was adjusted by the gas injection process, and the bottom water was used to shield the residual oil. From August 2020 to April 2021, several rounds of gas injection with water and drilling were carried out. The numerical simulation results showed that the gas injection and water rates were 42000 and 40 m<sup>3</sup>/day, respectively, in June 2021. After the well was simmered in January, the liquid production rate was fixed at 80 m<sup>3</sup>/day. After multiple rounds of gas injection with water in the well L110X, a clear gas cap was formed, showing the temporal evolution of the residual oil production.

After multiple rounds of gas injection with water in the well L110X, a clear gas cap was formed, as shown in

Figure 18. After the well is braised, the oil-water interface was redistributed and the bottom water cone was effectively removed. After the well is opened for production, the effect of increasing production is obvious. The oil production rate can reach 40 m<sup>3</sup>/d, and the oil production rate before the measures is 20 m<sup>3</sup>/d. After the well is opened for production within 2 months, the increase in production can reach more than 1000 t.

**4.3. Use of Pumps to Lift Liquid, Jam Water, Pressure Cone, Unit Water Injection Drive, and Other Measures to Tap the Bottom Water to Rise and Block the Residual Oil.** Due to the differences in the mechanism of bottom water rise and the distribution of residual oil, there are various methods for tapping the potential of bottom water ascending and blocking residual oil. For the residual oil of the cone-in-blocking type, the conventional shut-in cone pressure or deep water plugging measures are mainly used to collapse the water cone and restore the production capacity of the oil well. The conventional water plugging method is not effective for bottom water penetration and residual oil blocking due to the linear characteristics of bottom water rise and the similar oil and water paths. By considering foam and other selective water plugging agents or using connected adjacent wells, water injection can laterally drive residual oil near the oil well and be blocked as a result of the good effect of the bottom water.

In the design of the numerical simulation scheme, the conductivity between the grids at the bottom of the production well was modified to simulate the injection of gel in actual production to establish an artificial partition to delay the rise of the bottom water, increase the extent of the bottom water, and reduce the residual oil distribution. On the other hand, in the L11 unit model, an artificial partition was established for the high water cut production in well L15X (the partition was 6 m from the bottom of the well, while the diameter of the partition was 60 m); then, the

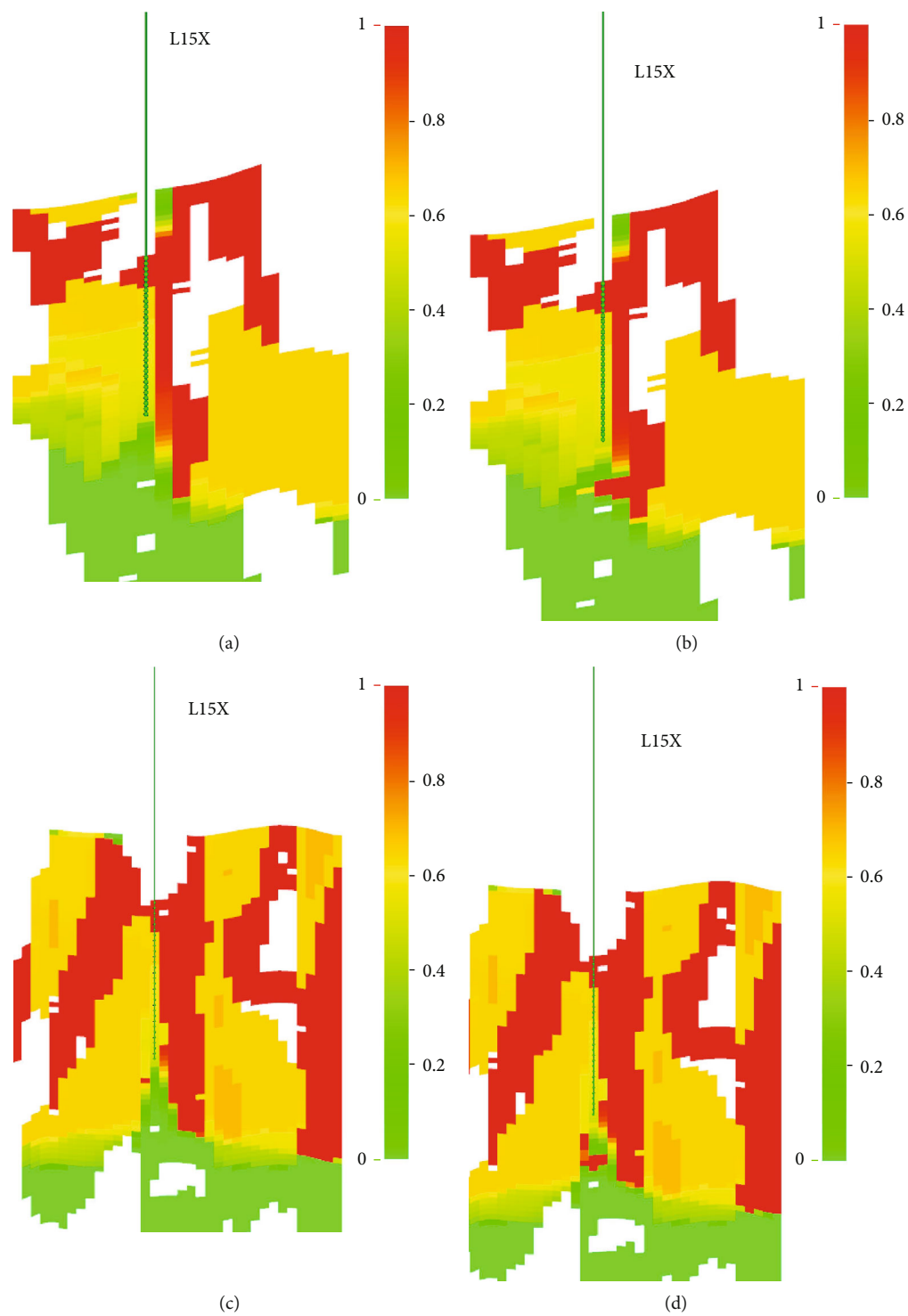


FIGURE 19: The influence of bottom hole artificial baffle on residual oil distribution.



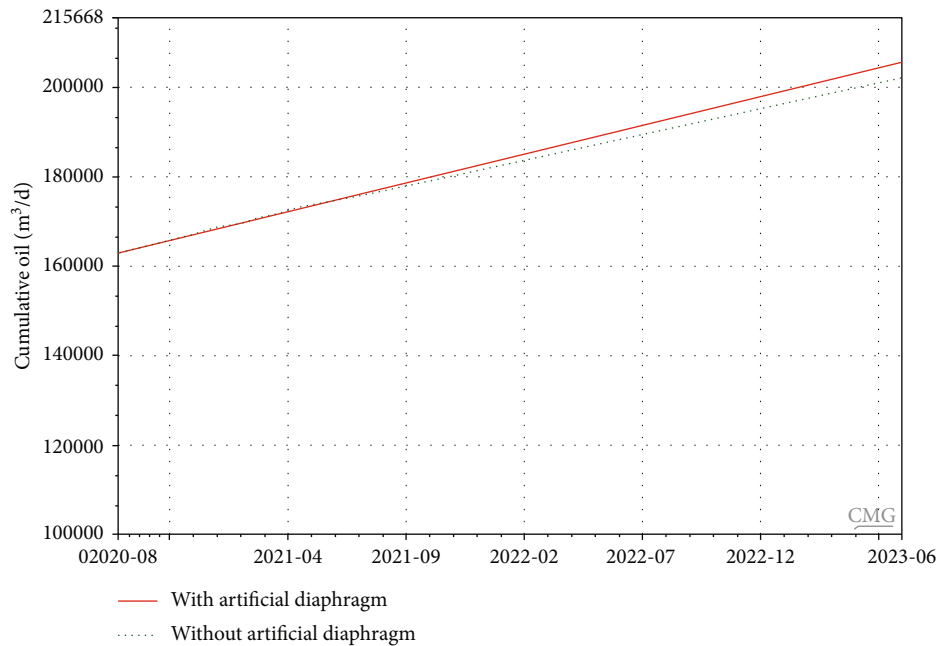


FIGURE 20: Effect of artificial diaphragm on increasing production in the well L15X.

production was started at a constant liquid production rate. The liquid production rate was determined based on the average liquid production rate of the well during 1 year ( $50 \text{ m}^3/\text{d}$ ). Figure 19 shows the simulation results of 2 years of production before and after the implementation of the measures.

After adding the artificial partition, the rising trend of the bottom water of the L15X well was more delayed, and the extent of the bottom water's impact on the residual oil in the near-well reservoir was increased (Figure 20). At a production rate of  $50 \text{ m}^3/\text{day}$ , the rate of oil production after the measures was increased by  $5 \text{ m}^3/\text{day}$  compared to that of no measures, corresponding to a cumulative oil amount of  $1696 \text{ m}^3/\text{year}$ . Therefore, an artificial bottom hole barrier can be an effective measure to remove bottom water coning and improve the residual oil production degree.

## 5. Conclusions

- (1) Fractures are the main channel for oil and gas flow in fault-solution reservoirs, as well as the main path of bottom water coning. The channeling of bottom water along high-angle fractures is the main reason for the decline in the oil production of typical units. Bottom water coning and gas/water injection development are the key factors affecting the distribution of residual oil. In addition, the irregular development of fractures and caves are the main factors causing the diverse distribution patterns of residual oil
- (2) The residual oil distribution patterns of fault-solution reservoirs include 4 types of residual oil, namely, attic and bottom water upblocking types at well point (including bottom water cone-inlet blocking and bottom-water channeling blocking types)

and separated fracture-cavity (including oil-separating and near-fracture-cavity types), and pore-fracture types near the high conductivity channel between wells

- (3) According to the residual oil distribution pattern, approaches to exploiting the potential residual oil were formulated. By deploying new wells or using sidetracking of old wells, it is possible to effectively control the residual oil of the loft and fracture-cavity separated oil types with a large well spacing. Drainage oil extraction or gas injection can be used to replace and exploit the potential attic residual oil. In addition, a liquid lift pump, jam water, press cones, and other measures can be used to tap the bottom water to rise and block the residual oil. By optimizing oil and water well-plugging measures, adjusting the injection and production structure, changing the direction of liquid flow, and tapping the potential residual oil in the pores and cracks beside the high diversion channel, residual oil can be further exploited

## Data Availability

Data used in this study will be available upon reasonable request.

## Conflicts of Interest

The authors declare that they have no conflicts of interest.

## Acknowledgments

This research was funded by the National Science and Technology Major Project of China (2016ZX05053) and the

Science and Technology Department Project of Sinopec-China Petroleum (P11089).

## References

- [1] F. Tian, Q. Jin, X. B. Lu et al., "Multi-layered Ordovician paleokarst reservoir detection and spatial delineation: a case study in the Tahe Oilfield, Tarim Basin, Western China," *Marine and Petroleum Geology*, vol. 69, pp. 53–73, 2016.
- [2] X. M. Zhou and M. H. Shahzad Kamal, "Experimental study on the relationship between carbonate reservoir quality index and dynamic parameters of chemical solutions for oil recovery practice," *Energy & Fuels*, vol. 33, no. 10, pp. 9747–9758, 2019.
- [3] E. Artun, T. Ertekin, R. Watson, and B. Miller, "Performance evaluation of cyclic pressure pulsing in a depleted, naturally fractured reservoir with stripper-well production," *Liquid Fuels Technology*, vol. 29, no. 9, pp. 953–965, 2011.
- [4] C. F. Guo, H. B. Li, Y. Tao, L. Y. Lang, and Z. X. Niu, "Water invasion and remaining gas distribution in carbonate gas reservoirs using core displacement and NMR," *Journal of Central South University*, vol. 27, no. 2, pp. 531–541, 2020.
- [5] A. Goudarzi, M. Delshad, K. K. Mohanty, and K. Sepehrnoori, "Surfactant oil recovery in fractured carbonates: experiments and modeling of different matrix dimensions," *Journal of Petroleum Science & Engineering*, vol. 125, pp. 136–145, 2015.
- [6] Y. Li, D. P. Wan, and J. M. Liu, "Remaining oil enrichment areas in continental waterflooding reservoirs," *Petroleum Exploration and Development*, vol. 32, no. 3, pp. 91–96, 2005.
- [7] J. Wang, H. Q. Liu, J. Xu, and H. F. Zhang, "Formation mechanism and distribution law of remaining oil in fracture-cavity reservoir," *Petroleum Exploration and Development*, vol. 39, no. 5, pp. 624–629, 2012.
- [8] Y. S. Rong, J. Z. Zhao, X. B. Lu, X. H. Li, and X. B. Li, "Remaining oil distribution patterns and potential-tapping countermeasures in carbonate fracture-cavity reservoir," *Acta Petrolei Sinica*, vol. 35, no. 6, pp. 1138–1146, 2014.
- [9] A. Ameri, R. Farajzadeh, V. S. Suicmez, M. Verlaan, and J. Bruining, "Effect of non-equilibrium gas injection on the performance of (immiscible and miscible) gas–oil gravity drainage in naturally fractured reservoirs," *Energy & Fuels*, vol. 27, no. 10, pp. 6055–6067, 2013.
- [10] S. Q. Zheng, M. Yang, Z. J. Kang et al., "Controlling factors of remaining oil distribution after water flooding and enhanced oil recovery methods for fracture-cavity carbonate reservoirs in Tahe Oilfield," *Petroleum Exploration and Development*, vol. 46, no. 4, pp. 786–795, 2019.
- [11] T. Bochao, C. Geng, M. Huang, H. Lu, and K. Ren, "Research on the Depletion and Recovery Characteristics of Fault-Karst Reservoirs," *Geofluids*, Article ID 1105335, 12 pages, 2022.
- [12] S. Q. Li, Y. T. Liu, X. Liang, Y. Li, Z. W. Yuan, and C. S. Jian, "An investigation on water flooding performance and pattern of porous carbonate reservoirs with bottom water," *Journal of Petroleum Science & Engineering*, vol. 200, article 108353, 2021.
- [13] K. D. Pennell, G. A. Pope, and L. M. Abriola, "Influence of viscous and buoyancy forces on the mobilization of residual tetrachloroethylene during surfactant flushing," *Environmental Science and Technology*, vol. 30, no. 4, pp. 1328–1335, 1996.
- [14] K. Qian, S. L. Yang, H. E. Dou, Q. Wang, L. Wang, and Y. Huang, "Experimental investigation on microscopic residual oil distribution during CO<sub>2</sub> huff-and-puff process in tight oil reservoirs," *Energies*, vol. 11, no. 10, p. 2843, 2018.
- [15] S. Ayatollahi, F. H. Boukadi, A. S. Al-Bemani, R. S. Al-Maamari, and M. A. Al-Wadhahi, "Investigation of thermal gas-oil gravity drainage (GOGD) in fractured carbonate reservoirs," in *SPE Middle East Oil and Gas Show and Conference*, Kingdom of Bahrain, 2005.
- [16] D. Y. Yuan, J. R. Hou, Z. J. Song, Y. Wang, M. Luo, and Z. Y. Zheng, "Residual oil distribution characteristic of fractured-cavity carbonate reservoir after water flooding and enhanced oil recovery by N<sub>2</sub> flooding of fractured-cavity carbonate reservoir," *Journal of Petroleum Science and Engineering*, vol. 129, pp. 15–22, 2015.
- [17] G. J. Wang, J. C. Zhang, S. Kou, and Q. Zhang, "Models for residual oil distribution of carbonate reservoir in Yanling Oilfield," *Journal of the University of Petroleum, China*, vol. 23, no. 4, pp. 26–28, 1999.
- [18] P. H. Nelson, "Pore-throat sizes in sandstones, tight sandstones, and shales," *AAPG Bulletin*, vol. 93, no. 3, pp. 329–340, 2009.
- [19] J. Wang, H. Q. Liu, J. Zhang et al., "Experimental investigation on water flooding and continued EOR techniques in buried-hill metamorphic fractured reservoirs," *Journal of Petroleum Science and Engineering*, vol. 171, no. 12, pp. 529–541, 2018.
- [20] L. Yang, "The theory and method for development of carbonate fractured-cavity reservoirs in Tahe Oilfield," *Acta Petrolei Sinica*, vol. 34, no. 1, pp. 115–121, 2013.
- [21] L. Yang, Z. J. Kang, Z. J. Xue, and S. Q. Zheng, "Theories and practices of carbonate reservoirs development in China," *Petroleum Exploration and Development*, vol. 45, no. 4, pp. 712–722, 2018.
- [22] Z. C. Liu, "Analyses of the remained oil and EOR methods for Tahe paleokarst reservoirs," *Petroleum Geology & Oilfield Development in Daqing*, vol. 34, no. 2, pp. 62–68, 2015.
- [23] Y. S. Liu, Y. T. Liu, Q. C. Zhang et al., "Large-scale physical simulation experimental study on thick carbonate reservoirs," *Petroleum Geology and Recovery Efficiency (in Chinese)*, vol. 27, no. 4, pp. 117–125, 2020.
- [24] Y. F. Yang, S. B. Cai, J. Yao et al., "Pore-scale simulation of remaining oil distribution in 3D porous media affected by wettability and capillarity based on volume of fluid method," *International Journal of Multiphase Flow*, vol. 143, article 103746, 2021.
- [25] T. Akai, A. M. Alhammadi, M. J. Blunt, and B. Bijeljic, "Modeling oil recovery in mixed-wet rocks: pore-scale comparison between experiment and simulation," *Transport in Porous Media*, vol. 127, no. 2, pp. 393–414, 2019.
- [26] S. W. Mao, Z. D. Bao, X. X. Wang et al., "Origin of carbonate cements and reservoir evolution of tight sandstone in the Upper Triassic Yanchang Formation, Ordos Basin, China," *Australian Journal of Earth Sciences*, vol. 66, no. 8, pp. 1175–1194, 2019.
- [27] R. Marathe, M. L. Turner, and A. Fogden, "Pore-scale distribution of crude oil wettability in carbonate rocks," *Energy & Fuels*, vol. 26, no. 10, pp. 6268–6281, 2012.

- [28] M. Y. Cai, Y. L. Su, L. Li, Y. M. Hao, and X. G. Gao, "CO<sub>2</sub>-fluid-rock interactions and the coupled geomechanical response during CCUS processes in unconventional reservoirs," *Geofluids*, vol. 2021, Article ID 6671871, 22 pages, 2021.
- [29] H. I. Petersen, B. Holland, H. P. Nytoft et al., "Geochemistry of crude oils, seepage oils and source rocks from Belize and Guatemala: indications of carbonate-sourced petroleum systems," *Journal of Petroleum Geology*, vol. 35, no. 2, pp. 127–163, 2012.
- [30] V. Anand, R. Freedman, S. Crary, C. C. C. Minh, and R. L. L. Terry, "Predicting effective permeability to oil in sandstone and carbonate reservoirs from well-logging data," *SPE Reservoir Evaluation and Engineering*, vol. 14, no. 6, pp. 750–762, 2011.

## Research Article

# Research on the Depletion and Recovery Characteristics of Fault-Karst Reservoirs

Bochao Tang , Chunying Geng , Mina Huang, Haitao Lu, and Ke Ren

*Sinopec Northwest Oilfield Company, Xinjiang, Urumqi 830011, China*

Correspondence should be addressed to Bochao Tang; tangbochao1008@163.com

Received 22 September 2021; Accepted 22 November 2021; Published 31 March 2022

Academic Editor: Xiang Zhou

Copyright © 2022 Bochao Tang et al. This is an open access article distributed under the Creative Commons Attribution License, which permits unrestricted use, distribution, and reproduction in any medium, provided the original work is properly cited.

A fractured-vuggy carbonate reservoir is a special reservoir formed by long-term physical, chemical, and geological processes. Its reserves are large in scale and widely distributed, showing the characteristics of free flow-seepage coupling. Conventional simulation is usually simplified by equivalent permeability, which cannot reflect the actual development characteristics. Given this, the flow in caves and fractures is treated with free flow, using the Navier–Stokes equation. The seepage simulation is used for other areas, and the Darcy formula is used. Finally, the simulation results are obtained by coupling, and the influence of oil production speed, fracture-cavity size, fracture-cavity location, dynamic viscosity, permeability, and other factors on bottom pressure is analyzed to effectively guide the field development. The results show that the production pressure of fractured-vuggy reservoirs diffuses from the central fractured-vuggy area to the surrounding matrix, and the pressure increases from the fractured-vuggy area to the surrounding matrix. The flow velocity in the seepage area is relatively stable and flows gently into the middle fracture cavity from all directions. There will be eddy current in the free-flow area. Different factors have different effects on the development. The oil production speed and oil dynamic viscosity are positively correlated with it, while the formation permeability is negatively correlated with it. The size and location distribution of fracture cavity will also have a certain impact. Simulation in advance can effectively avoid some reservoir development problems.

## 1. Introduction

The oilfield reservoirs experienced multiphase tectonic movement and karstification, covered in Ordovician, under the influence of soluble rock seam between the growth of body piercing and fault belt; the tectonic deformation belt formed the good matching relationship, mostly occurring in deep fault belt as its core dissolution expansion of favorable reservoir trap formation, which resulted in the formation of fractured-vuggy reservoirs with fault-controlled karst characteristics [1–5]. As a new type and target of deep marine carbonate oil and gas exploration and development, it is urgent to clarify the production characteristics of this type of reservoir to provide a theoretical basis for the efficient development of crude oil in this type of reservoir [6, 7]. Fractured-vuggy reservoirs in fault-solution reservoirs are developed along the main fault zone, which is banded and diverged in some parts. The main reservoir space is a large

cave, the fracture zone is wide, and the vertical faults with high angle are developed. In the early stage of mining, the main mining is exhaustion, and the phenomenon of water flooding occurs due to the channeling flow of bottom water along the fault zone [8–10]. Therefore, the understanding of the production characteristics (including dynamic variation characteristics of pressure field and dynamic variation characteristics of velocity field) in fractured-vuggy reservoirs in the early stage of depletion is helpful to provide flow field analysis for controlling water flooding caused by bottom water coning and then to take water control measures. However, different from conventional carbonate reservoirs, the main reservoir space and flow space of faulted fluid reservoirs are large caves, surrounded by fracture zones and fractures. The flow law of crude oil in faulted fluid reservoirs cannot be uniformly described by the traditional Darcy seepage theory [11–13]. A typical single cavity melt broken seam hole reservoir geological model of karst cave inside the

free flow of oil displacement by N-S equation was built using COMSOL physical field coupling numerical simulation software. The fracture zone and fracture around the cave unified seepage area were described by Darcy formula, which were equivalent to two junction coupled area via BJS conditions. The evolution law of pressure field and velocity difference in the exploitation of solvent reservoir is analyzed, and the influence of exploitation speed, location, size, and viscosity of crude oil and permeability on solvent reservoir is studied.

## 2. Establishment of a Mathematical Model of Free Flow-Seepage Coupling in Fractures and Caves

A faulted solution reservoir is a special fractured-vuggy reservoir. Influenced by multistage geological tectonic movement and karstic action, its reservoir space is mostly large karst caves and dissolution pores located in the fracture zone and the fault is the main flow channel, as shown in Figure 1. When fluid flows in fault-solution reservoirs, its flow characteristics are a complex free flow-seepage-combined flow system, including the free-flow region of the cave system, the seepage region composed of matrix rock blocks and fractures, and the coupling region between the two regions using BJS conditions [14, 15].

*2.1. Flow Equation in Free-Flow Region.* When the fluid flows in a large space, the fluid has little influence on the matrix, and the flow at this time is called free flow. When the fluid flows in the fracture reservoir cave system, it is free to flow [16, 17]. The law describing the relationship between stress and strain is the conservation of dynamic quantity. The fluid motion is controlled by the continuity equation and the momentum equation, which are expressed in vector form as follows:

$$\frac{\partial \rho}{\partial t} + \nabla \cdot (\rho u) = 0, \quad (1)$$

$$\rho \frac{\partial u}{\partial t} + \rho(u \cdot \nabla)u = \rho f + \nabla \cdot \sigma, \quad (2)$$

where  $\rho$  is the density ( $\text{kg/m}^3$ ),  $u$  is the fluid velocity ( $\text{m/s}$ ),  $\nabla$  is the gradient operator,  $f$  is the physical force per unit mass ( $\text{m/s}^2$ ), and  $\sigma$  is the fluid stress tensor (Pa). For the sake of simplicity, we will consider only Newtonian fluids. The density of a slightly compressible fluid can be assumed to be almost constant, i.e., incompressible. Therefore, the controlled fluid motion equation can be summed up as the N-S equation, which is described as follows:

$$\nabla \cdot u = 0, \quad (3)$$

$$\rho \frac{\partial u}{\partial t} + \rho(u \cdot \nabla)u = \rho f - \nabla p_f + \mu \nabla^2 u, \quad (4)$$

where the  $pf$  is the pressure (Pa) and  $u$  is the fluid viscosity (Pa-s). In addition, the stress tensor  $\sigma$  of incompressible Newtonian fluid satisfies the following equation:

$$\sigma = -p_f I + 2\mu \varepsilon, \quad (5)$$

where  $I$  is the unit tensor and  $\varepsilon$  is the strain rate, which satisfies

$$\varepsilon = \frac{1}{2} (\nabla u + u \nabla). \quad (6)$$

*2.2. Flow Equation in the Seepage Zone.* The flow of fluid through porous media is called percolation. A porous medium is a material consisting of a solid skeleton and interconnected pores, fractures, or capillary tubes of various types [18]. In this paper, the seepage zone includes a macroscopic fracture system and porous rock matrix. The flow of fluid through large fractures should be described as free flow because there is more space in large fractures. However, the flow model in the crack can be simplified to a parallel-plate laminar flow model and described as a Darcy formula form with equivalent flows. Therefore, the flow of the fluid in the matrix rock block and fracture system is treated as seepage flow in this paper, which follows the classical Darcy's law and develops along the direction of mass conservation. The viscosity and compressibility of the fluid are considered, and the molecular force and physical-chemical action are not considered. The formula is shown as follows:

$$v = -\frac{K}{\mu} (\nabla p_d - \rho f), \quad (7)$$

$$\frac{\partial(\rho \Phi)}{\partial t} + \nabla \cdot (\rho v) = 0, \quad (8)$$

where  $V$  is the Darcy velocity, the average volume velocity ( $\text{m/s}$ ), and  $K$  is the permeability tensor ( $\text{m}^2$ ),  $p_d$  is the average pore pressure (Pa), and  $\Phi$  is the porosity of porous media. Boundary conditions of the equation include two parts: pressure condition (equation (9)) and fluid flux conditions (equation (10)):

$$p_d = p_D, \text{ on } \Gamma_D, \quad (9)$$

$$n \cdot \frac{K}{\mu} (\nabla p_d - \rho f) = q_N, \text{ on } \Gamma_N. \quad (10)$$

$p_D$  is the specific pressure on the pressure boundary  $\Gamma_D$  and  $q_N$  is a specific value or expression of the inward Darcy flux ( $\text{m/s}$ ) on the fluid flux boundary  $\Gamma_N$ .

*2.3. Coupled Boundary Conditions of Percolation and Free Flow.* Suitable interface conditions should be introduced at the interface between the seepage zone and the free-flow zone. In this paper, the depletion and production process of a single-vuggy reservoir is simulated. It is a single first-order field problem using BJS condition coupled with Darcy equation and N-S equation [19–21]. At the junction of the seepage zone and free flow, the pressure field and velocity field satisfy



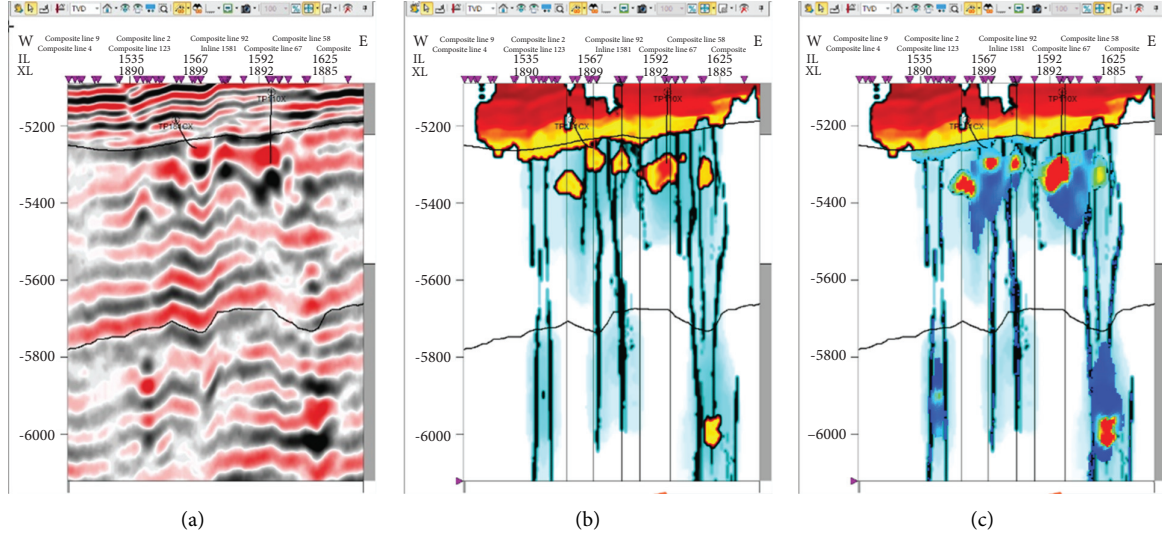


FIGURE 1: A fault-solution reservoir in Tahe Oilfield: (a) original seismic map, (b) attribute fusion map, and (c) porosity fusion map.

$$P_f(X) = P_d(X), \quad X \in \Omega, \quad (11)$$

$$u_f(X) = u_d(X), \quad X \in \Omega, \quad (12)$$

where  $\Omega$  is the boundary between the seepage zone and free flow,  $P_f$  is the pressure in the free-flow region,  $P_d$  is the pressure in the seepage zone,  $u_f$  is the velocity in the free-flow region, and  $u_d$  is the velocity of the seepage zone.

Initial conditions include initial formation pressure  $P = P_0$  and initial formation temperature  $T = T_0$ . Boundary conditions include outlet boundary conditions satisfying bottom hole constant flow production  $u_w = q_0$ , elastic reservoir conditions meet the compressibility of fluid and rock, and energy depletion is provided by the elastic reservoir.

### 3. Establishment of Geological Model of Fractured-Vuggy Reservoir

Because the reservoir is modified by multiple karst, the storage space is mostly dissolution holes and large caves formed along the fracture zone, so COMSOL software is used to establish the typical karst caves, with a geological model of single karst fracture-cave reservoir controlled by fault and a single-phase flow process of crude oil during reservoir depletion production process.

According to the formation fluid parameters, using COMSOL software, firstly, a cuboid with the length of 100 m, the width of 100 m, and height of 50 m is built to simulate the matrix of fault-controlled karst fractured-vuggy reservoir enveloping a single cave body. Then, a cube cave with a side length of 10 m was constructed in the center. Finally, a cylindrical production pipe through the internal karst cave and the external space is constructed, with an inner diameter of 0.08 m and a height of 22.5 m. The fracture-cavity area and the production pipe are selected to construct a union and form a combination. The edge of the whole mold is selected, and the boundary condition is set as no-slip geological models.

Based on the 3D geological model in Figure 2(a), fluid properties are preliminarily used at a density of 900 kg/m<sup>3</sup>, the dynamic viscosity is 0.1 Pa·s, the initial mining pressure is 40 MPa, and the mining outlet speed is controlled to 0.001 m/s. For the porous media matrix, the porosity rate is set to 0.005, and the permeability is set to  $5 \times 10^{-15}$  m<sup>2</sup>. Secondly, in the water storage model, set the compressibility of the fluid as  $4 \times 10^{-9}$  [1/Pa], the effective compressibility of the matrix is  $4 \times 10^{-10}$  (1/Pa). The tetrahedral mesh was used for 3D mesh division. The whole geometry was selected from the list of several solid layers and calibrated to fluid dynamics. The maximum element size was 9.19 m, the minimum element size was 0.2 m, the maximum element growth rate was 1.25, the curvature factor was 0.8, the narrow area resolution was 0.5, and the number of iterations was 4. After the parameters are set, grid construction is carried out to form the geological model grid of single-vuggy fault-controlled karst fractured-vuggy reservoir as shown in Figure 2(b). The complete grid contains 114,861 domain units, 4084 boundary units, and 660 edge units. In the calculation process, the output time of the 3D model is set at 300 days.

To facilitate the comparative analysis of the flow pattern and pressure variation characteristics of the porous media matrix zone in the free-flow area around the bottom of the well and in the seepage area, a longitudinal section was cut along the center of the well, as shown in Figure 2(c). The two-dimensional profile mesh was divided by a triangular mesh. The entire geometry was selected from the list of geometric solid layers and calibrated to fluid dynamics. The maximum element size was 6.7 m, the minimum element size was 6 m, the maximum element growth rate was 1.2, the curvature factor was 0.4, the narrow area resolution was 1, and the number of iterations was 8. After the parameters are set, grid construction is carried out. The complete grid contains 7684 domain units and 504 boundary units. The calculation process is analyzed according to the output time of the two-dimensional model is 6 days per unit.

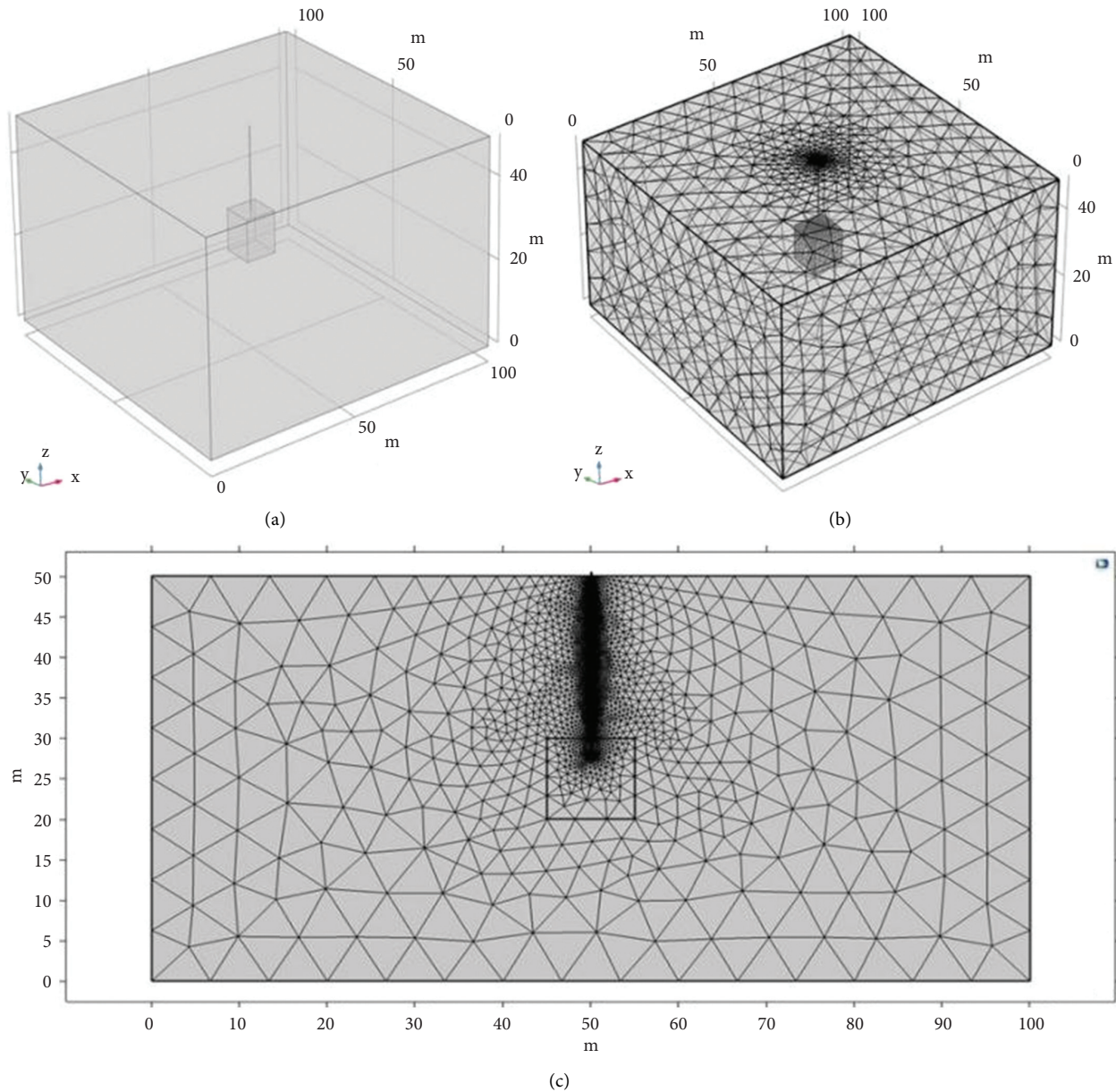


FIGURE 2: Single-cavity fault-controlled karst fracture-cavity reservoir geological model (a), geological model grid (b), and two-dimensional grid unit along the longitudinal section of the well center (c).

## 4. Results and Discussion

**4.1. Evolution Characteristics of Pressure Field and Velocity Field.** Based on the free flow-seepage-coupled fractured-vuggy reservoir, this paper analyzes the characteristics of the development process of the fractured-vuggy reservoir from two aspects of fluid pressure and velocity:

- (1) For pressure analysis, select a point at the bottom of the production pipe, which is located at the upper part of the fracture hole and can typically represent the pressure change of the whole fracture hole. In addition, for the whole reservoir matrix area, the change of the overall pressure field from beginning to end can be seen through the change of tone, as well as

the pressure comparison between the free-flow area and the seepage area at the same time.

- (2) For the analysis of velocity, streamline with arrows is used to clearly illustrate the flow direction of the fluid. Meanwhile, the density of the streamline in the velocity field can also show the velocities in different regions, and the shape of the streamline can intuitively reflect the flow state of the fluid.

To make the simulation results more convincing, the flow of the fluid in the free-flow region and the seepage region is mainly affected by the pressure brought by gravity and matrix, and the viscous force has little influence on the fluid. Only the dynamic viscosity of the extracted oil is

considered, and the influence of the viscous force is not studied too much.

According to experience, in the process of reservoir development, the pressure field in the pure seepage zone will be wide at the top and narrow at the bottom, but from the actual simulation, it can be seen that the upper and lower widths of the pressure field in the fractured-vuggy reservoir are not significantly different but appear column. The lateral width of the lower pressure field is likely widened due to the relationship between the fracture-cavity region. The pressure change spreads from the bottom center of the production line to the periphery. Under the assumed physical numerical conditions, the pressure of fractured vuggy decreases with the development of reservoir production. By comparing the vuggy and porous media areas, it can be seen that the pressure in the free-flow area is always lower than that in the seepage zone at any time of reservoir production (Figure 3).

Further comparative analysis of the two-dimensional velocity fields in different periods (Figure 4) shows that the color distribution of the velocity fields is relatively uniform, indicating that the overall velocity distribution is stable. According to the second figure in Figure 3, an obvious velocity peak appears at the bottom of the oil production pipe between 0 and 1 d and then decreases and becomes stable. The flow line of the porous media area is relatively straight, the upper part is straight, the lower part is curved, and it gently merges into the middle fracture-cavity area from all directions. The flow line of the free-flow fracture-hole area is spiral, and the eddy current phenomenon is present.

From the 3D pressure diagram (Figure 5), it can be seen that the pressure distribution also presents a cup-shaped or column-shaped structure, which diffused from the center of the slit to the surrounding, and presents a petal-like at a certain moment. The pressure decreases rapidly at the center of the upper surface of the matrix, while the pressure decreases slowly at the center of the lower surface. The upper part of the side of the square matrix is not a single trend change, but a wave shape. Considering the square matrix, oil products will affect each other at the vertex of the cube during the mining process, and the closer it is to the vertex, the greater the degree of influence.

From the 3D view, a 3D drawing group was built to describe the seam hole area. The uniform density streamline was added with a 0.05 interval distance. The 3D velocity field streamline data of the free flow area at day 60 were selected for simulation analysis, as shown in Figure 6. It can be seen from the figure that the central flow line of the free flow area is more concentrated, and the edge flow line is more scattered, intuitively showing the shape of a funnel. At the same time, there is also an obvious vortex flowing into the center in the middle and upper area, which is consistent with the spiral flow line in the previous two-dimensional section.

In order to analyze the coupling situation of free flow-percolation, based on the model constructed in this paper, the central cube is selected in the three-dimensional model for analysis. With low coupling complex, the pressure decreases fast, so the coupling situation of free flow-seepage can be reflected by the change of surface pressure to some extent. Datas on day 60 were selected as the research object,

and the results are shown in Figure 7. The cube corner position, especially the lower pressure, drops slowly, which indicates that the coupling complexity is relatively high. The central position pressure drops rapidly, indicating a low coupling complexity. The two views below are the upper surface and the bottom surface of the square, respectively. The area of the blue low-pressure area on the upper surface is significantly larger than that on the bottom surface, and the same result can be obtained.

#### 4.2. Analysis of Influencing Factors of Mining Characteristics.

The formation of carbonate reservoir is more complex than other reservoir types because the geological hole is the main space of the oil storage and oil speed. The subjective factors such as oil production speed and wellhead pressure, and the objective factors such as oil attribute, seam cave type, and matrix permeability all have an important influence on the development of seam cave carbonate reservoir. Song et al. based on this model studied the influence of gravity, fracture opening, water injection rate, and other factors on fluid flow characteristics and oil displacement effect [19]. This paper selected several typical factors for reference to analyze the influence law of different factors on mining characteristics [20–26].

**4.2.1. Mining Rate.** In the development and production process of oil and gas fields, while maintaining stable harvesting, a high mining speed should be selected as far as possible to ensure the actual production efficiency, so as to meet the national and social demand for oil. Therefore, selecting an appropriate and reasonable oil recovery speed will not only improve the reservoir development efficiency but also achieve the best overall economic effect [27–29]. To analyze the influence of oil recovery rate on the development of fractured-vuggy reservoirs, this paper sets the oil recovery rate as 172.8 m/d, 86.4 m/d, and 43.2 m/d, and the pressure field and velocity field distribution of different production rates are obtained, as shown in Figure 8(a). It can be seen from the figure that, in the production process of fractured-vuggy reservoirs, the production rate will affect the change of bottom hole pressure. At the same time, the blue low-pressure area will appear earlier when the speed is higher. As shown in Figure 8(b), the changing trend of bottom hole pressure decreases with time, and the faster the oil recovery rate, the faster the change of bottom hole pressure. The slower the recovery rate, the slower the change in bottom hole pressure. In the seepage zone, the flow rate is stable. In the free-flow region, the maximum value appears at 0.2 d and 3 d. When the oil recovery rate reaches 172.8 m/d, the bottom hole pressure will be pumped to 0 MPa in about 2.5 d. Continuing the production will cause negative pressure, which will affect the production. Therefore, the proper oil recovery rate should be selected to avoid negative pressure in the actual development process.

**4.2.2. Location of Karst Cave.** Both caves and fractures are formed in the stratum after long-term physical and chemical action, and their positions are random. The depth of the



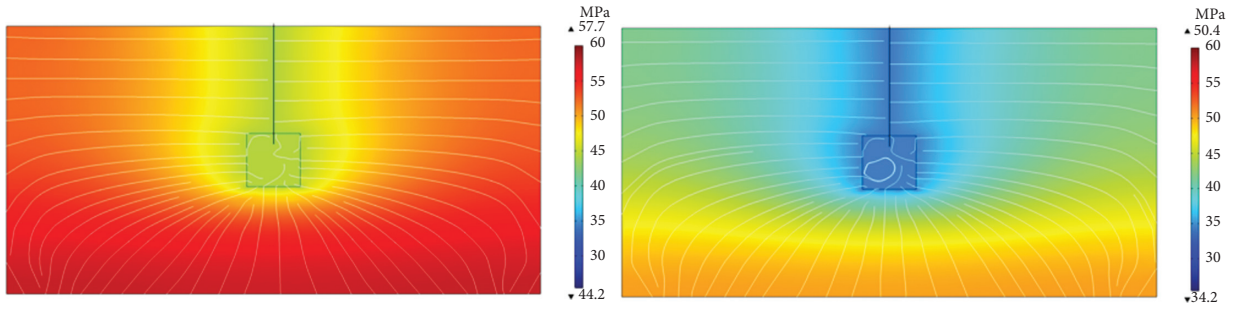


FIGURE 3: Comparison of two-dimensional pressure field distribution at the initial stage and later stage.

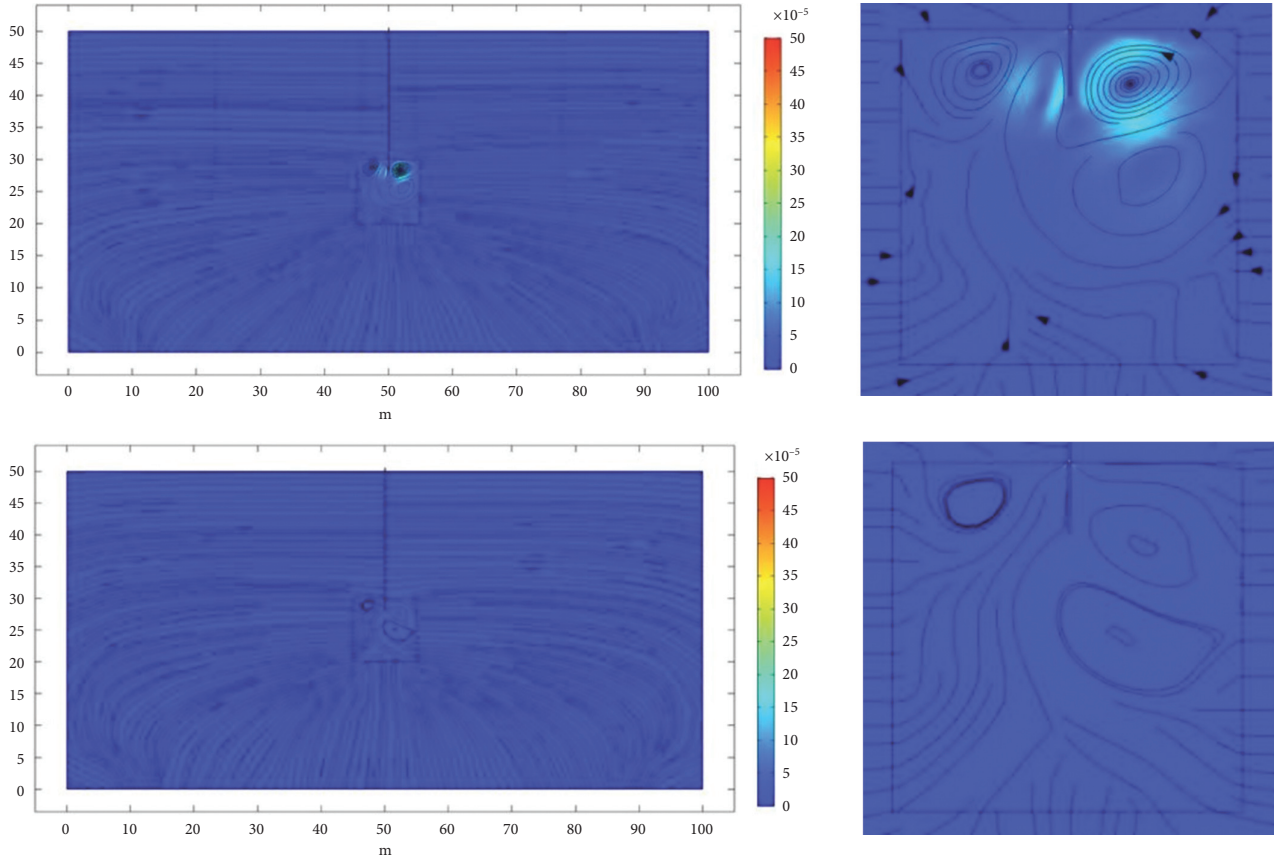


FIGURE 4: Comparison of two dimensional velocity field distribution in different periods.

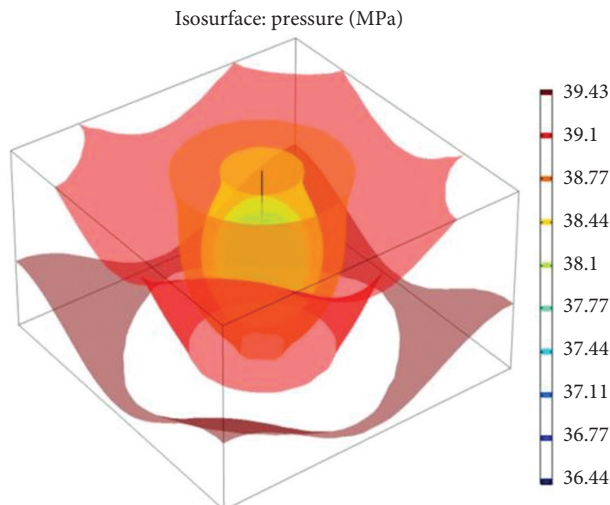


FIGURE 5: Distribution of 3D pressure field on the 60th day.

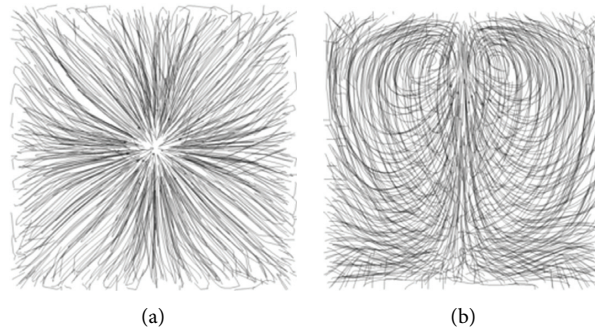


FIGURE 6: Streamline distribution of velocity field in different views: (a) top view of  $x$ - $y$  axis and (b) left view of  $y$ - $z$  axis.

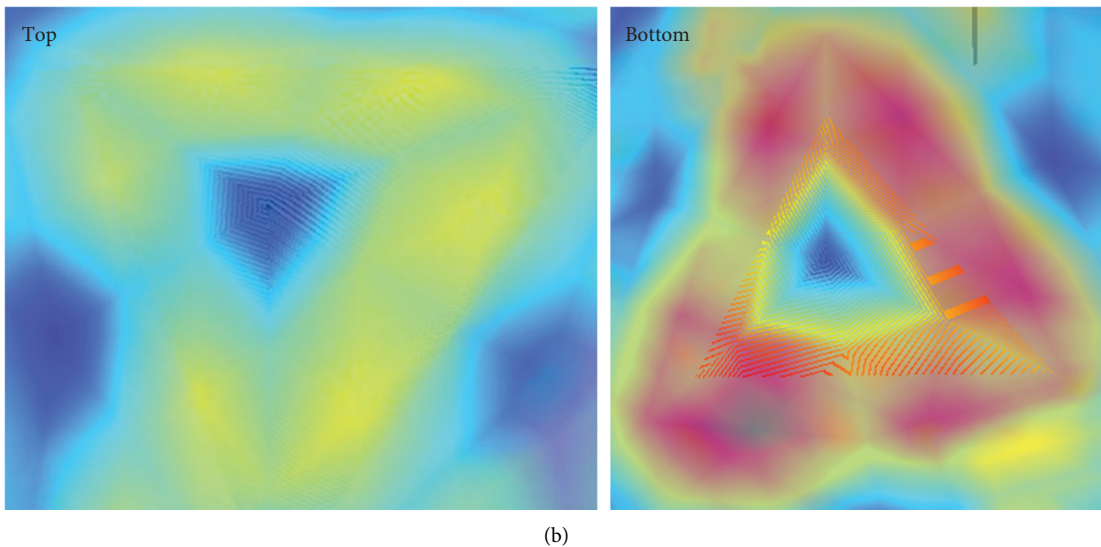
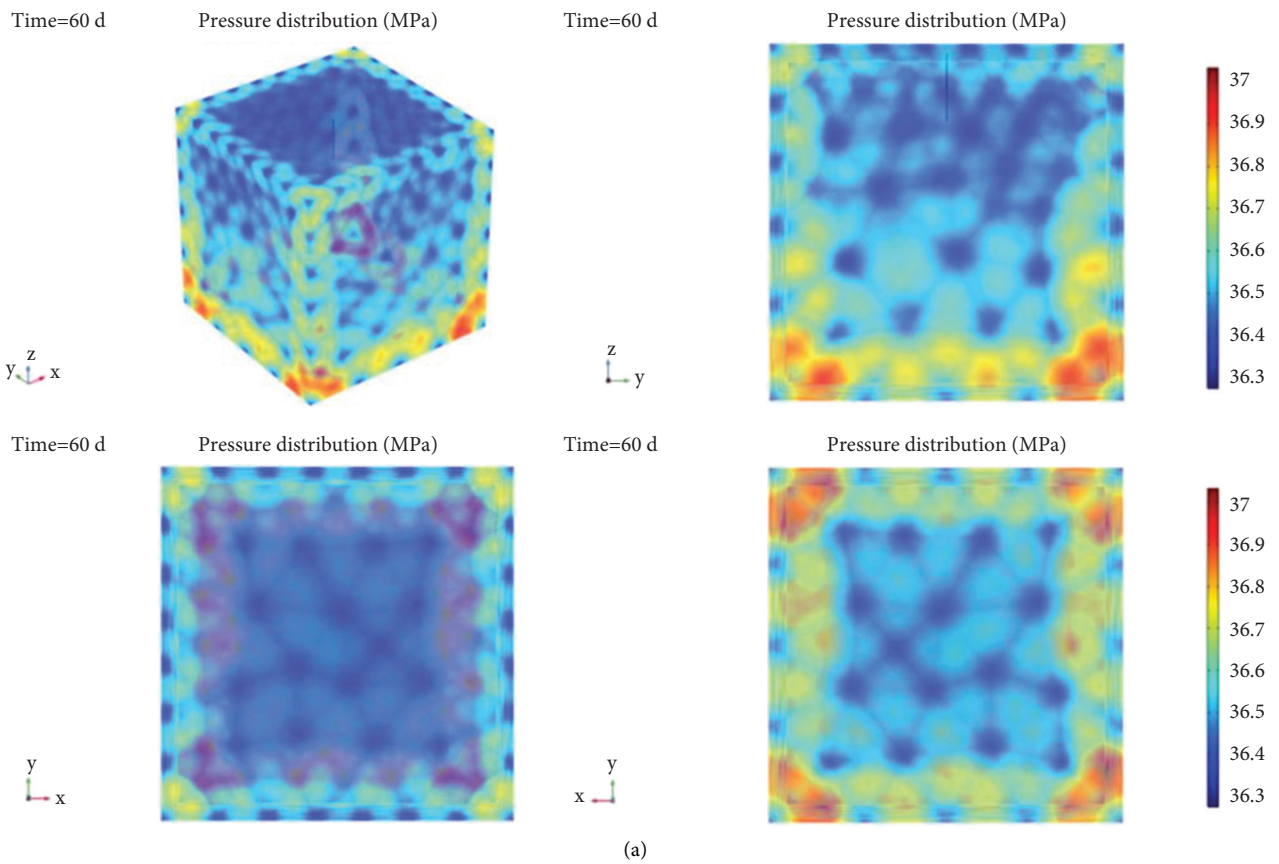


FIGURE 7: Three-dimensional coupling distribution: (a) different perspectives and (b) enlargement of vertices.



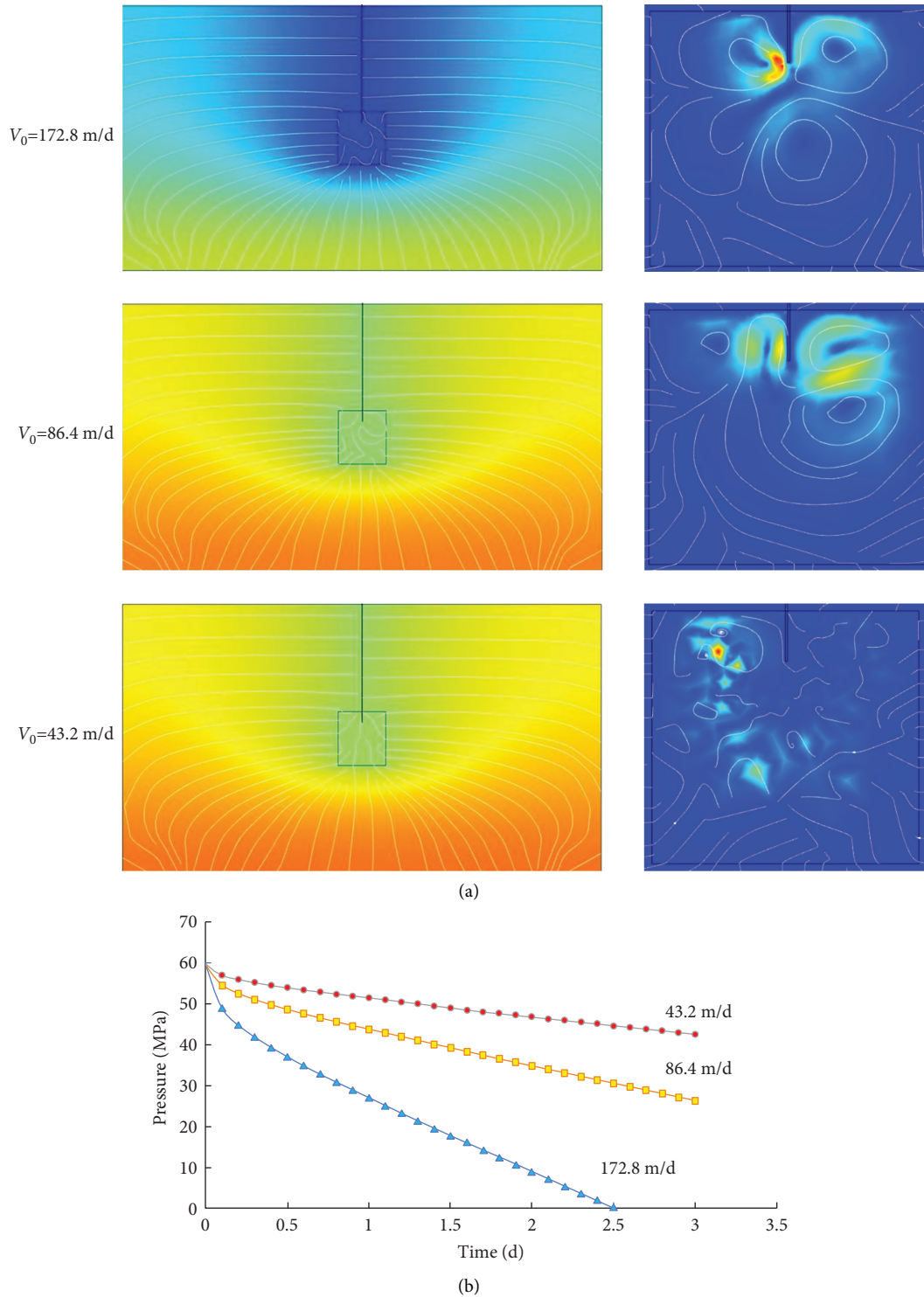


FIGURE 8: Distribution of pressure and velocity field at different mining rates (a) and pressure comparison of different oil recovery rates (b).

fracture-cave area also affects the burial depth of the reservoir [30, 31]. To analyze the influence of fracture-cavity positions on the development of fracture-cavity reservoirs, this paper selects three fracture-cavity positions in the upper part, the middle part, and the lower part for simple comparative analysis (Figure 9(a)).

The pressure distribution map on the left can be used to determine that when the oil reservoir is shallow, that is, the fracture-cavity area is close to the upper part, the streamline at the lower part of the matrix is bent more, and the pressure spreading range is smaller. When the oil reservoir is deep, that is, the fracture-cavity area is close to the lower part of the

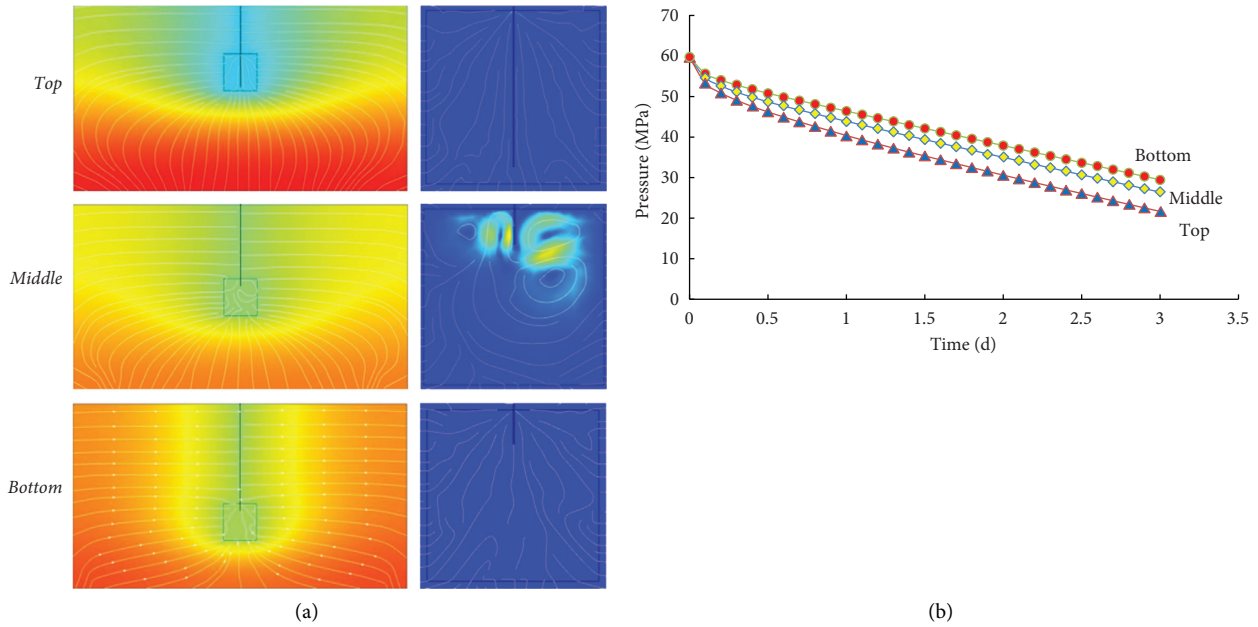


FIGURE 9: Distribution of pressure and velocity field at different fracture-cavity positions (a) and pressure comparison of different fracture-hole positions (b).

matrix, the streamline bending degree of the lower part of the matrix is smaller, and the range of pressure diffusion is larger. According to the pressure variation diagram of different fracture positions (Figure 9(b)), it can be seen that the position of the fracture has a certain influence on the reservoir development process to some extent. When the fracture is located at a higher position, the pressure drops quickly and the flow line in the fracture area is stable. When the cavity is located at a lower position, the pressure drops more slowly. As for the change of flow velocity, there is no great difference in the flow velocity of the three positions, and the flow line in the fracture-hole area is messy. Compared with the middle position, there is no obvious spiral flow line in the free-flow area of the upper and lower fractures.

**4.2.3. Cave Size.** To analyze the influence of the size of the slit on the development, the simulation completed the analysis by fixing the central position of the slit and changing the side length of the square slit region. The side length of the slit region was assumed to be 10 m, 20 m, and 30 m, respectively (Figure 10(a)). The larger the size of the fracture means that the contact area between the free-flow zone and the seepage zone increases, that is, the area of the coupling zone between the two increases. Therefore, the larger the size of the fracture, the faster the reservoir flow and the faster the pressure drop; the smaller the size of the fracture, the slower the reservoir flow and the slower the pressure drop. In the seepage zone, the flow rate is stable. In the free flow region, the maximum value appears at 0.2d and 0.6d, respectively. Meanwhile the larger the edge length, the more obvious the vortex flow and the larger the vortex range. According to the one-dimensional map of pressure change, in the early stage of mining, the pressure drops slower when the size of the fracture cavity is larger, and faster when the size of the fracture cavity is

smaller. Late in mining, from the pressure variation (Figure 10(b)), after about 2.5 d, this trend will have a change, if seam hole size is larger, the pressure drop, and if seam hole size is small, the pressure drop, but overall, the size of the slot hole size will have little impact on the bottom hole pressure, and bottom hole pressure continues to fall over time.

**4.2.4. Crude Oil Viscosity.** Crude oil viscosity refers to the internal friction resistance caused by oil in the process of flow. It is a very important parameter for oil and gas transportation, accumulation, and development of oil and gas fields. The crude oil viscosity of 7 mPa·s, 5 mPa·s, and 1.28 Pa·s was selected for simulation analysis, and the results are shown in Figure 11.

Figure 11(a) shows that the bottom hole pressure drops faster at the viscosity of 5 mPa·s and 7 mPa·s, resulting in an earlier blue low-pressure zone compared with the initial standard of 1.28 Pa·s. According to the velocity field cloud diagram on the right side of Figure 11(a), the flow velocity is relatively stable in the seepage zone. In the free-flow region, the maximum value occurs at 0.2 d. Figure 11(b) shows that the viscosity of crude oil affects the bottom hole pressure. The greater the viscosity, the faster the pressure decreases. The lower the viscosity, the slower the pressure reduction, which is consistent with previous conclusions. When the viscosity of crude oil is 7 mPa·s, the pressure will reach 0 at 2.5 d. When the viscosity gradually increases, the folding point due to the elastic pressure of the matrix gradually becomes unclear. In the figure, when the dynamic viscosity is 7 mPa·s, the folding line is approximately a parabola with an upward opening.

**4.2.5. Permeability of Matrix Fracture Zone.** Fractured-vuggy carbonate reservoirs are widely distributed throughout the world. However, the geological strip is different

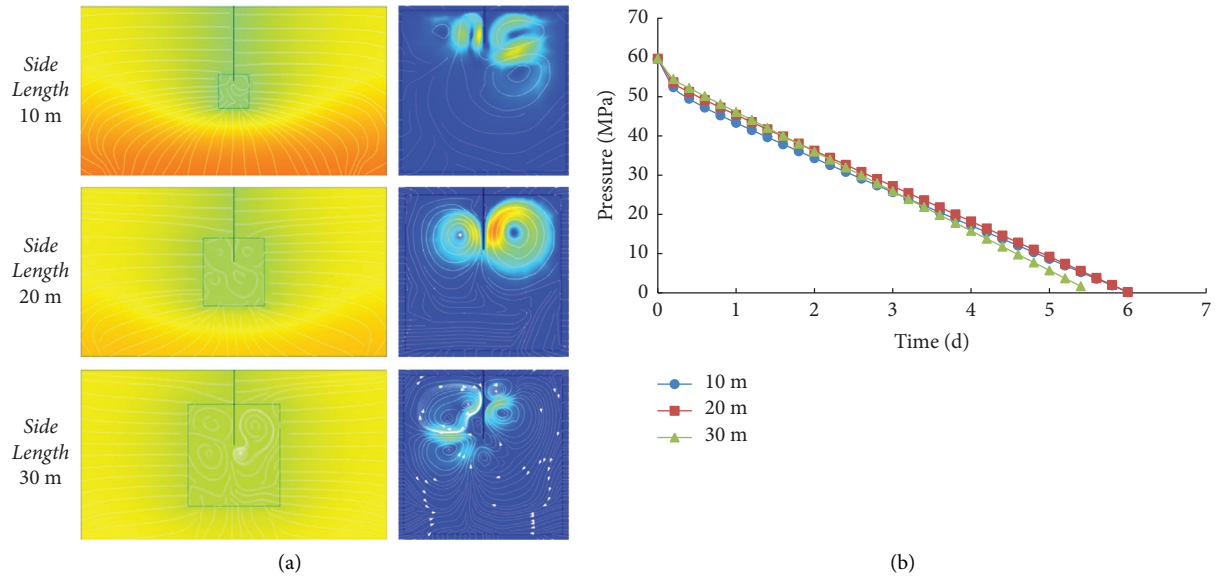


FIGURE 10: Distribution of pressure and velocity field with different sizes of fractures (a) and pressure of different fractures and hole sizes with production time (b).

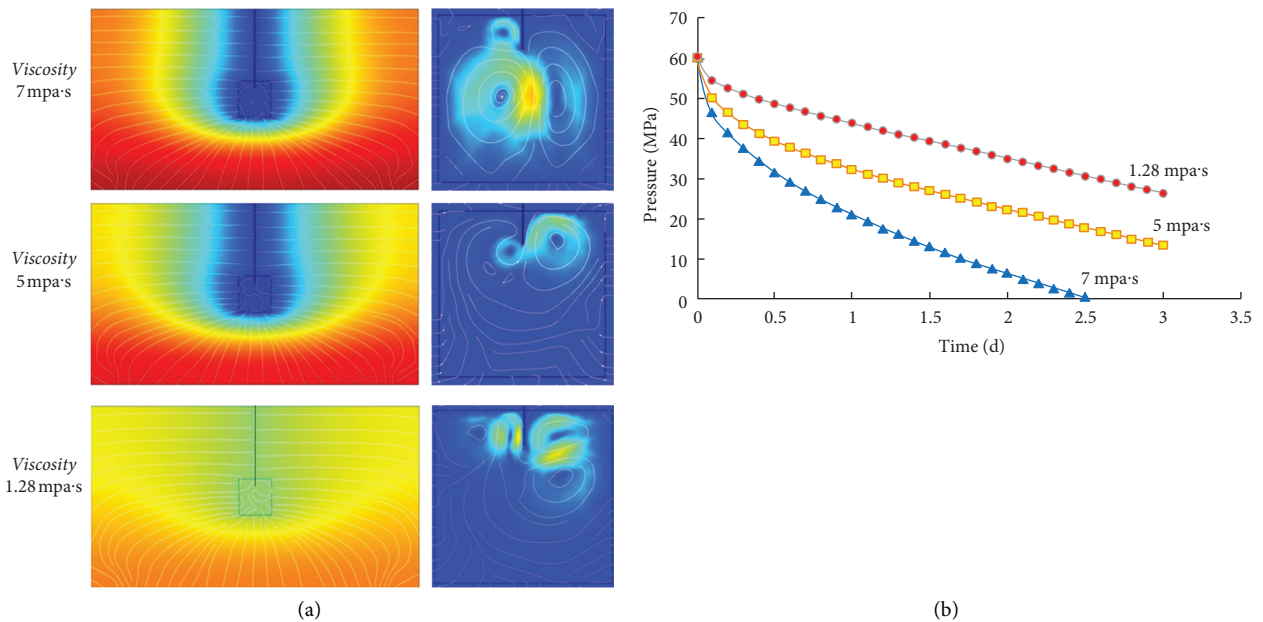


FIGURE 11: Distribution of pressure and velocity fields with different dynamic viscosity (a) and pressure comparison of different dynamic viscosity (b).

in different parts of the world and therefore needs to be considered in the development process. In this paper, the influence of matrix permeability on development was considered separately. Permeability is a parameter representing the ability of rock itself to conduct liquid. After several parameter changes, 10 mD, 1 mD, and 0.5 mD permeability were finally selected for analysis. It can be seen from Figure 12(a) that the size of matrix permeability will affect the change of bottom hole pressure. At the same time, when the permeability is low, the cyan part will appear earlier in the middle fracture-hole area, indicating that the pressure drops quickly; on the contrary, when the permeability is high, the pressure drops slowly. In

addition, it can be seen from the one-dimensional pressure diagram (Figure 12(b)) that the higher the permeability is, the slower the pressure drops. The lower the permeability is, the faster the pressure decreases. After about 0.4 d, the slope gradually slows down and tends to be stable. Considering the elastic pressure of the matrix mentioned above, it can be further concluded that the higher the permeability is, the smaller the elastic pressure is. The lower the permeability, the greater the elastic pressure. When the permeability is higher, the streamline distribution is more uniform. When the permeability is low, in the free-flow area, the maximum value appears at 0.2 d.

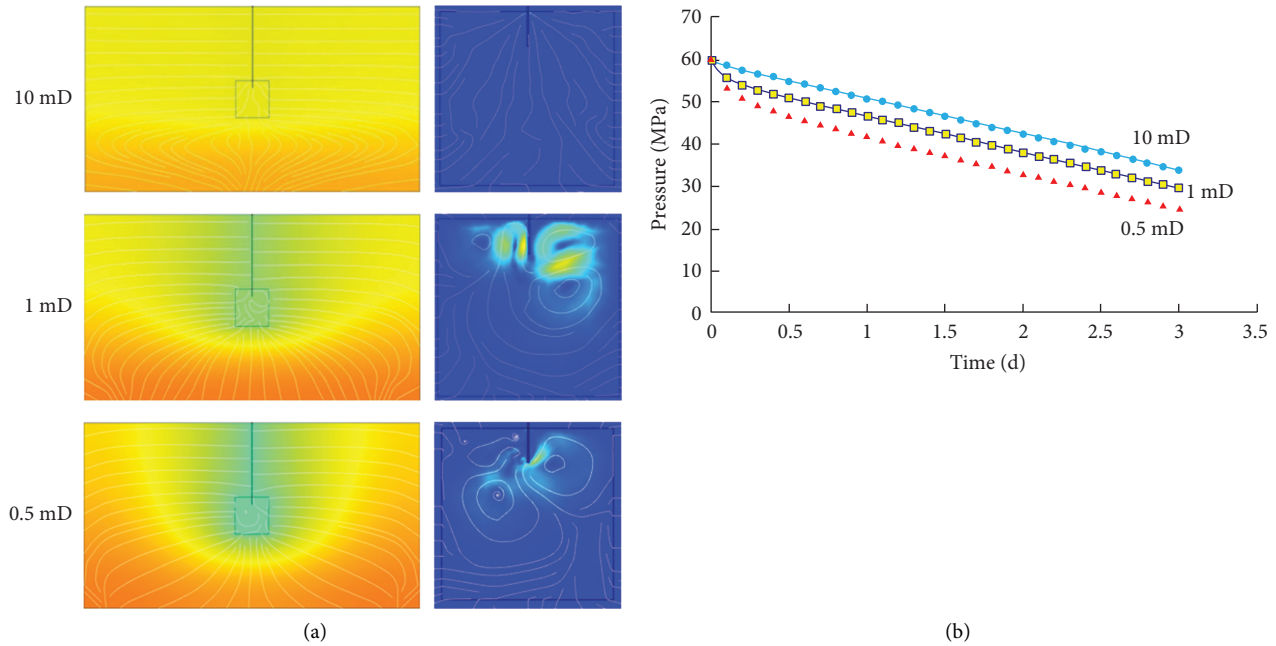


FIGURE 12: Distribution of pressure and velocity fields with different permeability (a) and pressure comparison of different permeability (b).

## 5. Conclusion

Large karst cave-fracture zone is the main oil storage space of seam cave-type carbonate reservoir. In this paper, the three-dimensional cavity model is established for the cavity reservoir simulation of free flow-seepage coupling. And reasonable fluid data and conditions are selected as simulation examples for the failure development of fracture-vug type reservoir. The results show that the simulation method can directly reflect the development characteristics of field operation under real conditions, so as to effectively guide the field development, which has certain significance for the continuous and efficient development of seam reservoir and relieve the energy tension.

- (1) In the development process of fractured-vuggy reservoirs, the production pressure of the reservoir spreads from the central fractured-vuggy area to the surrounding matrix. The two-dimensional section presents the cup shape and the three-dimensional petal shape. The pressure increases from the fractured-vuggy area to the surrounding area. For different oil properties and geological conditions, the declining trend of bottom hole pressure is different, so it is necessary to detect well the variation of strata pressure in actual depletion exploitation. Through the pressure curve, it can be analyzed that due to the elastic force of the matrix, the bottom hole pressure will appear at the initial bending point, and the geological conditions will have an impact on it.
- (2) For the change of reservoir velocity in the development process, the seepage zone is relatively stable and gently flows into the central fracture-cavity area from all directions. Vortices will appear in the free-

flow area, and at the early stage of the development process, areas with increased velocity will appear at random locations. On the whole, taking the horizontal plane where the fracture-hole area is as the standard, the upper streamline is dense and the flow velocity is fast, while the lower streamline is sparse and the flow velocity is slow.

- (3) Many factors can affect the development of seam-type reservoir, such as oil recovery speed and oil dynamic viscosity are positively correlated, the permeability is negative, and the size and position distribution of the hole will also have a certain impact. Therefore, according to different geological conditions and reservoir attributes, different mining methods should be adopted in the actual operation process to achieve the best effect.

## Data Availability

The data used to support the findings of this study are included within the supplementary information files.

## Conflicts of Interest

The authors declare that there are no conflicts of interest regarding the publication of this manuscript.

## Acknowledgments

This research was funded by the National Science and Technology Major Project of China (2016ZX05053) and the Science and Technology Department Project of Sinopec-China Petroleum (P11089). The authors acknowledge the technical support provided by the China University of Petroleum (East China) in using COMSOL software.



## References

- [1] L. Guo, S. L. Wang, L. M. Sun, Z. H. Kang, and C. J. Zhao, "Numerical simulation and experimental studies of karst caves collapse mechanism in fractured-vuggy reservoirs," *Geofluids*, vol. 2020, p. 21, Article ID 8817104, 2020.
- [2] Z. Q. Huang, X. Zhou, L. J. Liu, T. Huang, J. Yao, and X. G. Wang, "Hervé Jourde, "Numerical modeling for coupled hydro-mechanical processes in fractured-vuggy carbonate reservoirs," *Journal of China University of Petroleum*, vol. 44, no. 01, pp. 96–105, 2020.
- [3] X. B. Lu, W. G. Hu, Y. Wang et al., "Characteristics and development practice of fault-karst carbonate reservoirs in Tahe area, Tarim Basin," *Oil & Gas Geology*, vol. 36, no. 03, pp. 347–355, 2015.
- [4] Z.-Q. Huang, J. Yao, and Y.-Y. Wang, "An efficient numerical model for immiscible two-phase flow in fractured karst reservoirs," *Communications in Computational Physics*, vol. 13, no. 2, pp. 540–558, 2013.
- [5] Y. Li, Z. J. Kang, Z. J. Xue, and S. Q. Zheng, "Theories and practices of carbonate reservoirs development in China," *Petroleum Exploration and Development*, vol. 45, no. 4, pp. 669–678, 2018.
- [6] C. N. Zou, J. H. Du, and C. C. Xu, "Formation, distribution, resource potential and discovery of the Sinian-Cambrian giant gas field, Sichuan Basin, SW China," *Petroleum Exploration and Development*, vol. 41, no. 3, pp. 278–293, 2014.
- [7] R. Zhu, Z. H. Lou, and S. F. Niu, "Occurrence of formation water and measures for water control of Ordovician reservoirs in Tahe Oilfield," *Journal of Zhejiang University (Engineering Science)*, vol. 42, no. 10, pp. 1843–1848, 2008.
- [8] X. R. Lv, J. F. Sun, W. X. Wu et al., "Internal architecture characterization of fractured-vuggy carbonate reservoirs: a case study on the Ordovician reservoirs, Tahe Unit S67, Tarim Basin," *Oil & Gas Geology*, vol. 42, no. 03, pp. 728–737, 2021.
- [9] F. Tian, X. R. Luo, and W. Zhang, "Integrated geological-geophysical characterizations of deeply buried fractured-vuggy carbonate reservoirs in Ordovician strata, Tarim Basin," *Marine and Petroleum Geology*, vol. 99, pp. 292–309, 2018.
- [10] G. H. Wu, L. H. Gao, Y. T. Zhang, C. Z. Ning, and E. Xie, "Fracture attributes in reservoir-scale carbonate fault damage zones and implications for damage zone width and growth in the deep subsurface," *Journal of Structural Geology*, vol. 118, 2018.
- [11] N. Zhang, J. Yao, S. Xue, and Z. Huang, "Multiscale mixed finite element, discrete fracture-vug model for fluid flow in fractured vuggy porous media," *International Journal of Heat and Mass Transfer*, vol. 96, no. 5, pp. 396–405, 2016.
- [12] J. Yao, Z. Q. Huang, Z. S. Wang, Y. J. Li, and C. C. Wang, "Mathematical model of fluid flow in fractured vuggy reservoirs based on discrete fracture-vug network," *Acta Petrolei Sinica*, vol. 31, no. 5, pp. 815–819, 2010.
- [13] Q. Sun, N. Zhang, M. Fadlelmula, and Y. Wang, "Structural regeneration of fracture-vug network in naturally fractured vuggy reservoirs," *Journal of Petroleum Science and Engineering*, vol. 165, pp. 28–41, 2018.
- [14] S. Q. Zheng, Y. Li, and H. F. Zhang, "Fracture -cavity net work model for fracture -cavity carbonate reservoir," *Journal of China University of Petroleum*, vol. 34, no. 3, pp. 72–79, 2010.
- [15] Y. Basar, D. Weichert, and J. Petrolito, "Nonlinear continuum mechanics of solids: fundamental mathematical and physical concepts," *Applied Mechanics Reviews*, vol. 54, no. 6, pp. B98–B99, 2001.
- [16] A. Cesmelioglu, "Analysis of the coupled Navier-Stokes/Biot problem," *Journal of Mathematical Analysis and Applications*, vol. 456, no. 2, pp. 970–991, 2017.
- [17] Y. Li, *Development Theories and Methods of Fracture-Vug Carbonate Reservoirs*, Academic Press, Cambridge, MA, UK, 2017.
- [18] Z. Huang, J. Yao, Y. Li, C. Wang, and X. Lü, "Permeability analysis of fractured vuggy porous media based on homogenization theory," *Science China Technological Sciences*, vol. 53, no. 3, pp. 839–847, 2010.
- [19] I. Ambartsumyan, E. Khattatov, I. Yotov, and P. Zunino, "A Lagrange multiplier method for a Stokes-Biot fluid-poroelastic structure interaction model," *Numerische Mathematik*, vol. 140, no. 2, pp. 513–553, 2018.
- [20] S. Badia, A. Quaini, and A. Quarteroni, "Coupling Biot and Navier-Stokes equations for modelling fluid-poroelastic media interaction," *Journal of Computational Physics*, vol. 228, no. 21, pp. 7986–8014, 2009.
- [21] M. A. Murad, J. N. Guerreiro, and A. F. D. Loula, "Micro-mechanical computational modeling of secondary consolidation and hereditary creep in soils," *Computer Methods in Applied Mechanics and Engineering*, vol. 190, no. 15-17, pp. 1985–2016, 2001.
- [22] J. Yang and J. Hou, "Experimental study on gas channeling characteristics of nitrogen and foam flooding in 2-D visualized fractured-vuggy model," *Journal of Petroleum Science and Engineering*, vol. 192, 2020.
- [23] J. Yang, J. R. Hou, and M. Qu, "Experimental study the flow behaviors and mechanisms of nitrogen and foam assisted nitrogen gas flooding in 2-D visualized fractured-vuggy model," *Journal of Petroleum Science and Engineering*, vol. 194, 2020.
- [24] T. Liang and J. R. Hou, "Fluids flow behaviors of nitrogen and foam-assisted nitrogen floods in 2D visual fault-karst carbonate reservoir physical models," *Journal of Petroleum Science and Engineering*, vol. 200, 2021.
- [25] T. Liang, J. Hou, M. Qu et al., "Flow behaviors of nitrogen and foams in micro-visual fracture-vuggy structures," *RSC Advances*, vol. 11, no. 45, pp. 28169–28177, 2021.
- [26] F. M. M. Fadlelmula, S. Qian, and Y. Wang, "Separable multiple-point geostatistical modeling of three-dimensional discrete fracture-vug networks," in *Proceedings of the Abu Dhabi International Petroleum Exhibition & Conference*, Abu Dhabi, UAE, November 2016.
- [27] J. Liu, M. Wu, and R. Song, "Study on simulation method of multi-scale fractures in low permeability reservoirs," *Journal of Southwest Petroleum University (Science & Technology Edition)*, vol. 39, no. 4, pp. 90–97, 2017.
- [28] Y.-L. Li, F. Wu, X.-P. Li, X.-H. Tan, X.-H. Hu, and Q. Yang, "Displacement efficiency in the water flooding process in fracture-vuggy reservoirs," *Journal of Petroleum Exploration and Production Technology*, vol. 7, no. 4, pp. 1165–1172, 2017.
- [29] Y. Ning, C. Wei, and G. Qin, "A unified grayscale lattice Boltzmann model for multiphase fluid flow in vuggy carbonates," *Advances in Water Resources*, vol. 124, pp. 68–83, 2019.
- [30] D. Han, T. Li, Q. Tang, B. Yu, and D. Sun, "A Galerkin-free/equation-free model reduction method for single-phase flow in fractured porous media," *Energy Science & Engineering*, vol. 8, no. 6, pp. 1997–2010, 2020.
- [31] Z. Li, T. Chen, and Y. Ning, "Numerical simulation of waterflooding process using lattice Boltzmann method to estimate relative permeability for fractured unconventional reservoirs," in *Proceedings of the SPE Middle East Oil and Gas Show and Conference*, Manama, Bahrain, March 2019.



## Research Article

# Experimental Study on Enhancing Heavy Oil Recovery by Multimedia-Assisted Steam Flooding Process

Keyang Cheng <sup>1,2</sup>, Zhaoting Huang,<sup>3</sup> Jun Li <sup>2</sup>, Taotao Luo,<sup>2</sup> and Hongbo Li<sup>4</sup>

<sup>1</sup>School of Petroleum Engineering, Northeast Petroleum University, Daqing, China

<sup>2</sup>School of Petroleum and Natural Gas Engineering, Chongqing University of Science and Technology, Chongqing, China

<sup>3</sup>Exploration and Development Research Institute, PetroChina Tarim Oilfield Company, Korla, China

<sup>4</sup>Tazhong Oil and Gas Development Department, PetroChina Tarim Oilfield Company, Korla, China

Correspondence should be addressed to Keyang Cheng; 2012905@cqust.edu.cn and Jun Li; 2011927@cqust.edu.cn

Received 25 October 2021; Accepted 25 January 2022; Published 31 March 2022

Academic Editor: Xiang Zhou

Copyright © 2022 Keyang Cheng et al. This is an open access article distributed under the Creative Commons Attribution License, which permits unrestricted use, distribution, and reproduction in any medium, provided the original work is properly cited.

Aiming to reduce the negative effect of steam channeling in the late stage of steam flooding applied in heavy oil reservoirs, experimental studies were carried out on selective plugging of solid particles, added to single-medium- and multimedia-assisted steam flooding. This work also explored the mechanisms of enhancing heavy oil recovery by applying plugging agent- and multimedia-assisted steam flooding and its optimized injection parameters. Through solid particle plugging experiments, this study clarifies the high-efficiency solid particle plugging mechanism, with an optimized slug size of 0.40 PV and plugging ratio of over 98%. Through single-medium- and multimedia-assisted steam flooding experiments, this study confirms that gas-assisted steam flooding has an effect of synergistic oil displacement and that a CO<sub>2</sub> with urea solution-assisted steam flooding method achieves the best production performance. Its oil recovery factor is 10.7% higher than that of the steam flooding process. Parallel sand pack models with a permeability difference of more than 10 times were used to mimic a heavy oil reservoir with high-permeability channels, and the selective plugging of solid particles was carried out. The plugging ratio of high-permeability formation reached 91.20%, playing an effective plugging role. Solid particle plugging is less effective to the low-permeability formation, with the plugging ratio at only 32.39%. Based on the selective plugging of solid particles, a plugging agent- and multimedia-assisted steam flooding experiment was conducted, the high-permeability formation was effectively plugged, and the swept volume of the low-permeability formation increased significantly. The final recovery factor of the high-permeability formation was enhanced by 11%, and the recovery factor of the low-permeability formation increased by 3 times, reaching 36.38%. Therefore, solid particle plugging effectively alleviates the impact of high-permeability formation caused by permeability difference during steam flooding.

## 1. Introduction

Heavy oil resources are becoming increasingly essential to meet the growing energy demand in the world [1]. At present, thermal-based heavy oil recovery methods, including SAGD, steam huff-n-puff, and steam flooding, are still effective methods for the exploitation of heavy oil resources [2, 3], which is why they are dominant in oil fields. However, because of the significant differences in density and viscosity between heavy oil and steam [4, 5], conventional enhanced oil recovery methods lead to problems such as steam fingering and channeling [6, 7]. In

this situation, the injected steam only flows through high-permeability areas and bypasses most of the remaining oil [8], resulting in a low recovery factor [9]. Particularly for the reservoir with thin oil pay zone, the SAGD process cannot be applied in this reservoir economically. So that in order to develop the oil reserves in this reservoir, steam flooding process is usually carried out. To boost the oil recovery, it is important to alleviate the negative effect of steam channeling in heavy oil development, in terms of how to plug the channel and increase the steam sweep volume. Scholars have carried out studies on injecting different media to enhance oil recovery, such as solid

particle plugging, gas-phase foam plugging, and liquid-phase plugging.

Solid particle plugging has the following advantages: low cost, high-temperature resistance, high plugging strength, long-acting time, etc. Zhao et al. prepared coated particles suitable for high-temperature, high-salinity reservoirs. They believed particle migration to be closely related to reservoir permeability [10]. Zhao et al. developed an expandable quartz particle that can effectively block high-permeability channels under high-temperature conditions and force steam into the low-permeability area. This study showed that under the action of polymers, the suspension performance of the solid particle plugging system is greatly improved [11].

Based on solid particle plugging, researchers conducted CO<sub>2</sub>-assisted steam flooding to enhance heavy oil recovery. Li et al. studied the effect of CO<sub>2</sub> on the physical properties of a heavy oil-water system [12]. During the steam flooding process, the crude oil was generally emulsified and water-in-oil (W/O) emulsion was formed, which increased the viscosity of crude oil. However, CO<sub>2</sub> has a de-emulsification effect that significantly decreases the viscosity of emulsified crude oil [13, 14]. Another plugging agent is urea solution; once urea solution is injected into the reservoir, it reacts to generate NH<sub>3</sub> and CO<sub>2</sub> under high temperature. This improved heavy oil recovery factor occurs through in situ gas production [15]. Liu et al. used three-dimensional (3D) physical models to carry out experimental research on urea-assisted steam flooding and urea foam agent-assisted steam flooding [16]. The results showed that urea reacts in situ, generating NH<sub>3</sub> and CO<sub>2</sub> and increasing oil recovery factor by 9.85% and 16.08%, respectively, compared with steam flooding. Wang et al. carried out experimental research on urea-assisted steam flooding with high-pressure, high-temperature models [17]. The results showed the injection of urea solution to enhance the oil recovery factor between 2.4% and 18.8%. Li et al. conducted urea-assisted steam flooding experiments and numerical simulation studies using a one-dimensional (1D) physical model [9]. The results showed the gas generated by the urea reaction to maintain pressure in an oil reservoir and to increase oil recovery factor by 10% to 20%. Dahbag carried out a numerical simulation study to improve heavy oil recovery using a 5% to 10% hot urea solution [18]. The results showed the urea solution to change the formation wettability, improve the relative permeability of the oil phase, and delay water breakthrough.

Urea-assisted steam flooding improves heavy oil recovery factor mainly by the following mechanisms: (1) CO<sub>2</sub> generated in situ expands the steam sweep volume and enhances the thermal efficiency [19, 20]. (2) The generated ammonia and the acidic compounds in heavy oil asphaltene react to form surfactants [21]. (3) The generated surfactants reduce the oil-water interfacial tension and change the reservoir rock wettability. (4) The generated surfactant in situ forms W/O emulsion bounded in porous media, which relieves the effect of steam channeling in high-permeability reservoirs and increases the sweep volume [12]. (5) The generated surfactants combine with CO<sub>2</sub> to generate foam [22], which plugs the high-permeability channel and increases the steam sweep coefficient [19]. (6) The urea

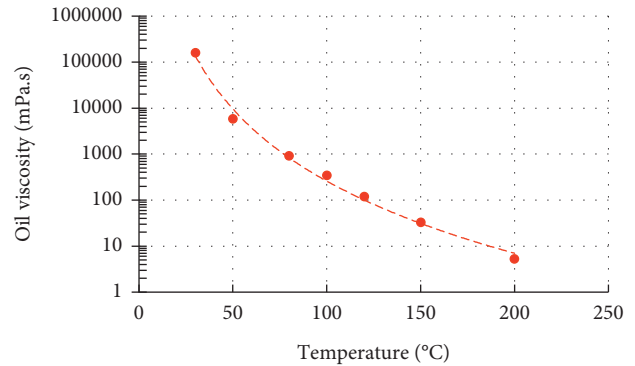


FIGURE 1: Crude oil viscosity-temperature curve.

solution reacts with naphthenic acid in the asphalt under high temperature to form an in situ surfactant that emulsifies the oil phase [23] and to form W/O emulsion at the displacement front, which restricts viscous fingering and channeling [24]. (7) Because the polar charges in the solution will be adsorbed on the rock surface [25], the use of urea solution will change reservoir wettability and make it more water wet; this is good for displacing crude oil out of the reservoir.

Analyzing the mechanism of urea-assisted steam flooding to enhance heavy oil recovery, it has been found that urea combines the mechanisms of condensate gas, non-condensate gas, and chemical agents, making urea a great choice for assisting steam flooding, but in the process of replenishing formation energy, urea exhibits a pattern different from that of non-condensate gas. For the non-condensate gas injection process, pressure spreads from surface to reservoir, and sweep efficiency is very limited. However, for the urea solution, pressure maintenance is based on the reaction in the reservoir. The urea solution can move to the deep formation of the reservoir to increase the remote pressure. Further, the gas generated after the reaction has a longer distance action, which reaches more residual oil and improves the sweep efficiency [26, 27]. It can be seen that in enhancing heavy oil recovery, urea-assisted steam flooding has broader application prospects.

## 2. Experimental Section

According to the realities of the on-site steam flooding process for heavy oil fields, the injected high-temperature steam causes dominant channels or high-permeability formation in the reservoir, which leads to the channeling of subsequent medium injection and makes further enhancing heavy oil recovery impossible. This study used solid particles to carry out experiments on plugging ratio for high-permeability formation to clarify the effect of solid particle plugging on a parallel sand pack model with a significant difference in permeability. Meanwhile, this study conducted research on medium-assisted steam flooding to improve heavy oil recovery, including CO<sub>2</sub>, urea solution, and other single-medium-assisted steam flooding experiments, as well as research on multimedia-assisted steam flooding experiments.

TABLE 1: SARA of the crude oil sample.

Property	Saturates	Aromatics	Resins	Asphaltenes	Unrecovered
Measured (%)	36.97	22.25	19.92	18.81	2.05

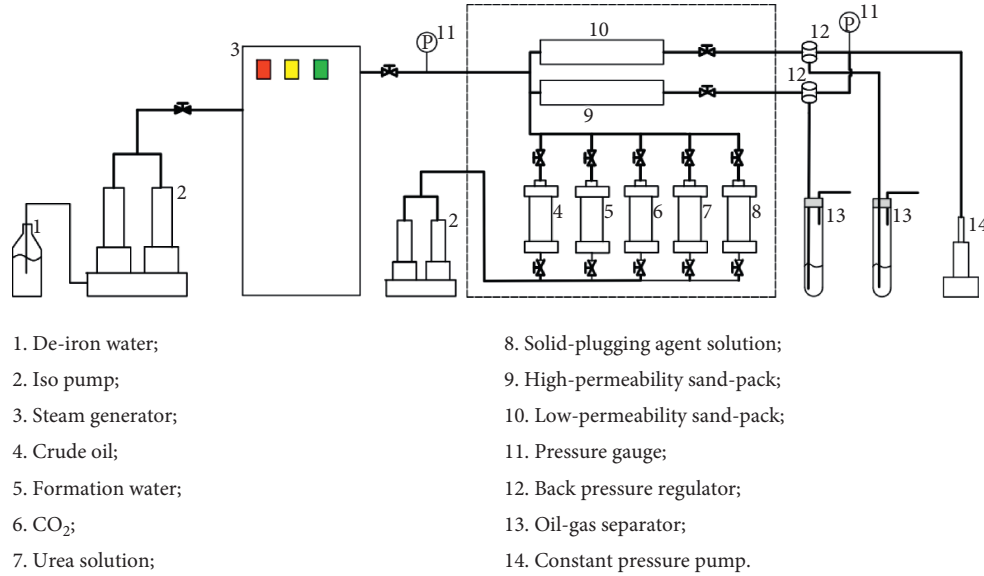


FIGURE 2: Schematic of multimedia-assisted steam flooding process. (1) De-iron water; (2) iso-pump; (3) steam generator; (4) crude oil; (5) formation water; (6) CO<sub>2</sub>; (7) urea solution; (8) solid plugging agent solution; (9) high-permeability sand pack; (10) low-permeability sand pack; (11) pressure gauge; (12) back pressure regulator; (13) oil-gas separator; and (14) constant pressure pump.

**2.1. Materials.** Crude oil was collected from heavy oil fields in western China. The viscosity of crude oil at 50°C was 5862 MPa, the crude oil viscosity-temperature curve is shown in Figure 1. A saturate-aromatic-resin-asphaltene (SARA) analysis of the crude oil is shown in Table 1. The salinity of the formation water was 9586 mg/L. The CO<sub>2</sub> gas concentration was 99.9%, and the urea purity was 99.99%.

**2.2. Experimental Setup.** In this study, the experimental setup of multimedia-assisted steam flooding to improve heavy oil recovery is shown in Figure 2. The device included the following:

- (1) Injection system: constant speed displacement pump, steam generator, transfer containers.
- (2) Displacement system: sand pack model, pressure sensor, high-temperature and high-pressure oven.
- (3) Data collection system: computer, data converter.
- (4) Gas-liquid separation system: gas-liquid separator, back pressure regulator, constant pressure control pump.

The sand packs and transfer containers were located in the oven, and the pressure in the models was maintained using the back pressure regulars. The test range of the oven was 20 to 300°C with an accuracy of  $\pm 0.5^\circ\text{C}$ . The range of the steam generator was 20 to 400°C with an accuracy of  $\pm 0.5^\circ\text{C}$ . The liquid meter accuracy was 0.1 mL. The inner diameter of

the 1D sand pack model was 3.8 cm, and the length was 30 cm. The particle size of quartz sand was 20 to 100 mesh.

**2.3. Experimental Procedure.** To study the role played by multimedia in the multimedia-assisted steam flooding process, it was applied in high-permeability formation for plugging and profile control. This study carried out the following experiments: high-permeability sand pack model plugging experiments and single-medium and multimedia-assisted steam flooding experiments. The specific experimental processes can be summarized as follows.

### 2.3.1. Plugging Experiment

- (1) The one-dimensional (1D) sand pack model is filled with quartz sand to establish a high-permeability model.
- (2) Then, the measurement of the physical properties of the model (pore volume, porosity, and permeability) was conducted.
- (3) The sand pack was vacuumed, and then, the pore volume and porosity were determined by the water volume saturated in the sand pack. Different injection rates were employed in the sand pack, and Darcy's law was applied to determine the average permeability under the different injection rates.

- (4) Solid plugging agent solutions in different pore volumes (PVs) are injected, the permeability of the plugged sand pack is measured, and the plugging ratio is calculated.
- (5) The injection volume of the solid plugging agent is changed, the above experimental steps are repeated, and the injection volume is optimized.

### 2.3.2. Single-Medium-Assisted Steam Flooding Experiment

- (1) The packed sand pack model is saturated with crude oil until no water is displaced out of the model, and the original oil saturation and original water saturation are calculated. In total, 2 PV of crude oil was injected.
- (2) Steam and single medium are injected into the sand pack model, and the single-medium-assisted steam flooding experiments are conducted. The experiment is stopped once water cut of the steam flooding reaches 95%.

### 2.3.3. Multimedia-Assisted Steam Flooding Experiment

- (1) Two sand pack models with a significant permeability difference as a parallel model system are packed. The higher-permeability sand pack is used to mimic the formation where steam channeling is dominant during steam injection.
- (2) The properties (PV, porosity, permeability, oil saturation, water saturation) of the physical model are measured using the above methods.
- (3) The steam flooding experiment is conducted as the base case. Solid particle plugging agent is used to plug high-permeability sand pack model, and then, multimedia-assisted steam flooding experiment and plugging agent with multimedia-assisted steam flooding experiment are carried out.

## 3. Results and Discussion

**3.1. Experiment on Solid Particle Plugging Ratio.** Five sets of physical sand pack models were filled with 20 to 100 mesh quartz sand. After sand packing, the permeability of the model was measured in the range of 2576 to 2718 mD. Different sand pack models were injected with different volumes of plugging agent, and then, the permeability was measured and plugging ratio was determined. The experimental results are shown in Table 2 and Figure 3.

From the experimental results, one can find that good plugging performance by the plugging agent in the high-permeability sand pack model was achieved. With the volume increase in injected solid particle plugging agent, the plugging ratio increased. When the injection volume reached 0.10 PV, the plugging ratio was 88.28%, essentially successfully plugging the high-permeability formation to a large extent. With the injection of the plugging agent, the plugging effect was significantly improved. When 0.40 PV plugging agent was injected, the plugging rate reached 98.75%. When the injected plugging agent volume exceeded

TABLE 2: Plugging effect experiments with different sand pack models.

PV <sub>inj</sub> (PV)	K <sub>ini</sub> (mD)	K <sub>plug</sub> (mD)	R <sub>plug</sub> (%)
0.1	2576	302	88.28
0.2	2631	185	92.97
0.3	2596	127	95.11
0.4	2633	63	97.61
0.5	2718	45	98.34

Note. PV<sub>inj</sub>—injection volume of solid particle plugging; K<sub>ini</sub>—initial permeability; K<sub>plug</sub>—permeability after plugging; R<sub>plug</sub>—plugging ratio.

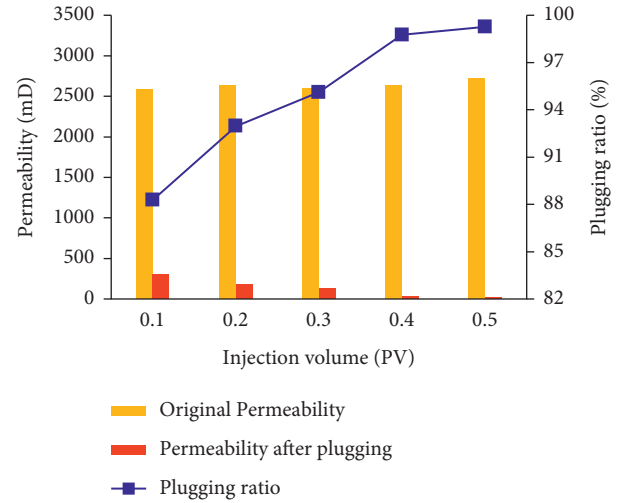


FIGURE 3: Plugging ratio with different models under different conditions.

0.40 PV, the plugging ratio of the sand pack model did not increase too much. Therefore, the optimized injection volume of the plugging agent in this study was found to be 0.40 PV, and the permeability of the sand pack model decreased from 2633 to 63 mD.

**3.2. Screening Injected Medium.** To optimize the injection medium for the media-assisted steam flooding process, this study implemented experimental research on different media-assisted steam flooding processes. When the water cut reached 95% in the steam flooding process, different types of media, such as CO<sub>2</sub>, urea solution (30% concentration), and CO<sub>2</sub> + urea solution, were used in the flooding experiments. The slug size was 0.20 PV, the experimental temperature was 200°C, a back pressure regulator was used to make sure that the pressure in the model was lower than the steam-saturated vapor pressure at 200°C, which is 1.55 MPa, and the steam displacement rate was 3 mL/min. The oil displacement volume was recorded, and the recovery factor was calculated. The production performances are shown in Table 3 and Figure 4.

The experimental results indicate that, when the medium was injected for displacement after steam flooding, good production performance was obtained, with the recovery factor being 3.37% to 10.70% higher than the steam flooding process. CO<sub>2</sub>-assisted steam flooding improved heavy oil



TABLE 3: Statistics of physical properties and displacement performance for different sand pack models.

Test	PV (cm <sup>3</sup> )	Φ (%)	K (mD)	So (%)	IM	Rs/o (cm <sup>3</sup> /cm <sup>3</sup> )	RF (%)
#1	117.68	34.59	3089	75.36	Steam	0.073	48.68
#2	106.15	31.20	2756	70.81	CO <sub>2</sub> + steam	0.074	52.05
#3	125.13	36.78	3261	72.65	Urea + steam	0.084	57.73
#4	116.87	34.35	2938	68.77	CO <sub>2</sub> + urea + steam	0.082	59.38

Note. PV—pore volume; Φ—porosity; K—permeability; So—oil saturation; IM—injection medium; Rs/o—oil-steam ratio; RF—recovery factor.

recovery to a certain extent. Urea-assisted steam flooding greatly increased the recovery factor by 9.05%. This can be attributed mainly as follows:

- (1) The mechanisms of CO<sub>2</sub>-assisted steam flooding process are viscosity reduction, dissolution, and expansion, CO<sub>2</sub> extraction of light hydrocarbons, enhanced steam sweep volume, gravity differentiation, etc.
- (2) CO<sub>2</sub> has an overlap and thermal insulation effect. Because of the difference in density between CO<sub>2</sub> and steam, CO<sub>2</sub> will flow to the upper formation. Because CO<sub>2</sub> is a non-condensate gas and its thermal conductivity is relatively low, the heat transmission rate of steam overlying formation is reduced, and the heat loss is reduced significantly. Thus, the heat efficiency of steam injection is improved effectively.
- (3) The generated free gas merges with crude oil in the reservoir to form foamy oil, which plays a role of plugging to a certain extent, as shown in Figure 5.

From Figure 4, one can find that the CO<sub>2</sub> + urea solution-assisted steam flooding process achieves the best production performance, with the recovery factor being 10.7% higher than that of the steam flooding process. This is mainly due to the following:

- (1) Urea decomposes into NH<sub>3</sub> and CO<sub>2</sub> under high temperature (200°C), and CO<sub>2</sub> could reduce steam condensation. Meanwhile, gas volume expansion under high temperature supplements formation energy and greatly increases displacement pressure.
- (2) The NH<sub>3</sub> generated from the decomposition of urea reacts with acidic substances in the crude oil after being dissolved in water to form a surfactant. The surfactant reduces the capillary force at the oil-water interface and promotes the flow of residual oil.
- (3) The generated CO<sub>2</sub> in the urea decomposition process and the injected CO<sub>2</sub> have a synergistic oil displacement in the steam flooding process.
- (4) Emulsification occurs in the process of urea-assisted thermal recovery. The emulsified oil droplets block the pore throats, which block the high-permeability zone. The displacement fluid then flows into the unswept throats, and thus, the sweep coefficient is increased.

3.3. *Multimedia-Plugging-Assisted Steam Flooding.* For heavy oil reserves developed by steam flooding process,

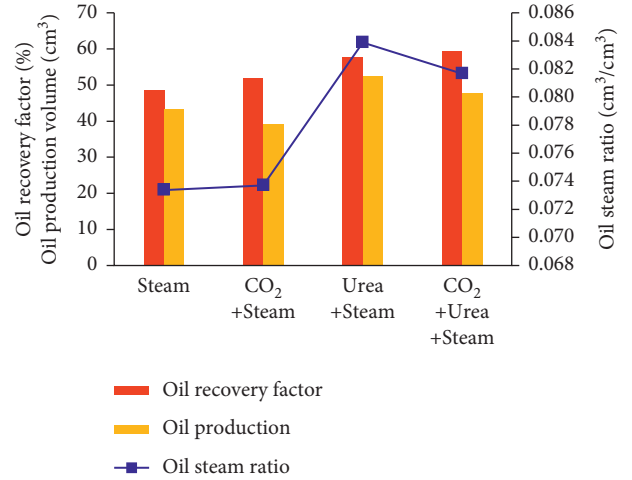


FIGURE 4: Comparison of production performance with different medium-assisted steam flooding processes.

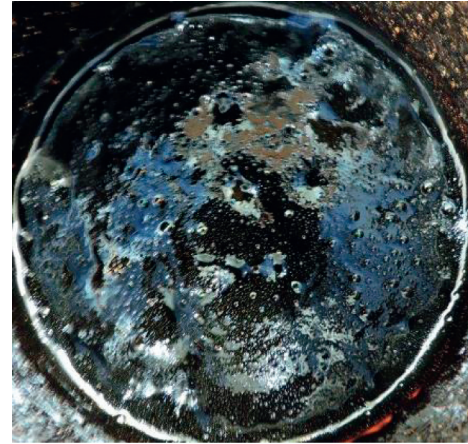


FIGURE 5: Foamy oil in the experiment.

high-permeability channels are formed by long-term steam flooding process, which seriously affects the heavy oil production performance. To study the influence of different high-permeability formations on the production performance of steam injection, parallel displacement experiments of different sand pack models with a permeability difference of 10 times were conducted in this study. The properties and displacement effects are shown in Table 4.

In the experiments, the permeabilities of the parallel sand pack models were 5713 and 565 mD. Steam flooding was firstly implemented on the parallel sand pack model. After the water cut at the outlet of the sand pack model achieved 95%, the steam flooding process was stopped. Then,



TABLE 4: Physical properties and development effects of sand pack models with different permeabilities.

Test	PV cm <sup>3</sup>	Φ (%)	So (%)	K (mD)		RF (%)		
				K <sub>ini</sub>	K <sub>plug</sub>	SF	SF/plug	SF/CO <sub>2</sub> / urea
#5	115.03	33.81	75.08	5713	503	50.15	52.78	61.13
	98.32	28.9	71.26	565	382	10.08	28.96	36.38

Note. PV—pore volume; Φ—porosity; So—oil saturation; K—permeability; RF—recovery factor; K<sub>ini</sub>—initial permeability; K<sub>plug</sub>—permeability after plugging; SF—steam flooding; SF/plug—steam flooding after plugging; SF/CO<sub>2</sub>/urea—mixture of CO<sub>2</sub> and urea-assisted steam flooding.

the solution of solid plugging agent was injected into the sand pack models, and in total, 0.40 PV plugging agent was employed, and the differences in the permeabilities are shown in Figure 6.

This was reflected in the experiments when steam flooded the parallel sand pack model; the high-permeability sand pack model (5713 mD) was prone to steam channeling. The injected steam passed by the high-permeability formation directly to the production end, resulting in low oil displacement efficiency in the low-permeability sand pack, with the recovery factor at only 10.08%. To relieve steam channeling, it is suggested to use the aforementioned optimized solid particle plugging agent to plug the sand pack model. Because the plugging agent has certain selective plugging properties, it will first plug high-permeability sand pack models. Figure 6 indicates that the plugging ratio of the high-permeability sand pack reached 91.20% after injecting 0.40 PV plugging agent. This effectively plugged the high-permeability formation, and thus, steam channeling was controlled. Solid particle plugging agents were less harmful to low-permeability formation, with the plugging ratio at only 32.39%.

Once the solid plugging agent was injected into the model, 0.20 PV of CO<sub>2</sub> + urea was combined for multimedia-assisted steam flooding. The experimental temperature was 200°C, and the steam displacement rate was 3 mL/min. The production performance of the plugging agent + multimedia combination was evaluated, as shown in Figure 7.

It can be seen from the results (as shown in Figure 7) that after steam flooding process, the oil recovery factors for high-permeability and low-permeability sand packs were 50.15% and 10.08%, respectively. Once the sand pack model was plugged, the recovery factor of high-permeability reservoir was increased by 2.63%, and the recovery factor of low-permeability reservoir was improved by 18.88%, which is because the steam injected in the early stage preferentially flowed into the high-permeability formation, leading to a higher recovery factor of the high-permeability sand pack model and resulting in less improvement in recovery factor after plugging. Before plugging, the steam sweep efficiency of the low-permeability sand pack model was low, with the recovery factor at only 10.08%. After plugging, the permeability difference in parallel sand pack models was reduced, with greatly improved sweep efficiency and recovery factor.

Based on the profile improvement of the sand pack model, 0.20 PV CO<sub>2</sub> + urea solution combined media were

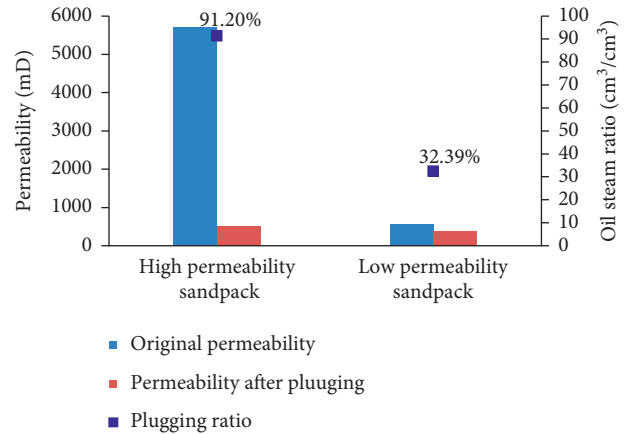


FIGURE 6: Comparison of plugging ratio before and after plugging with different-permeability sand pack models.

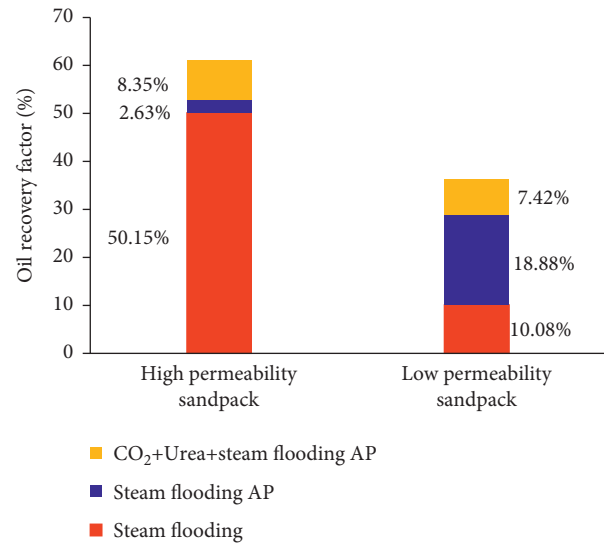


FIGURE 7: Comparison of production performance before and after plugging with different-permeability sand pack models. AP—after plugging.

injected to carry out the plugging agent + multimedia oil displacement experiment shown in Table 4 and Figure 7. It can be seen from the results that the oil recovery factor of the two sand pack models was improved after the injection of multimedia. The recovery factor of the high-permeability formation increased by 8.35%, and the recovery factor of the low-permeability formation improved by 7.42%. It can be seen by these experiments that the plugging agent + multimedia channeling obviously improves oil recovery factor for highly oil-saturated reservoirs. Crude oil in low-permeability reservoirs is swept effectively with this method. The experimental results indicate that under the condition of a significant permeability difference, the plugging agent and multimedia can still produce crude oil in medium- and low-permeability reservoirs. The solid particle plugging agent still has good plugging performance for high-permeability formation and obviously improves reservoir recovery.

## 4. Conclusions

In this study, plugging agent study, single-media-assisted steam flooding experiment, and multimedia-assisted steam flooding experiment were conducted with the following conclusions obtained:

- (1) The solid particle plugging agent has good injection ability, the optimized slug size is 0.40 PV, and the plugging ratio is above 98%.
- (2) The medium-assisted steam flooding process improves heavy oil recovery factor compared with steam flooding, and gas-assisted steam flooding meets synergistic oil displacement effect. The CO<sub>2</sub> + urea solution-assisted steam flooding method achieves the best production performance, with the recovery factor of 10.70% higher than that of the steam flooding process.
- (3) With the selective plugging properties of the solid particle plugging agent, the plugging ratio of the high-permeability formation can reach 91.20%, playing a role in plugging effectively. The solid particle plugging agent is less harmful to low-permeability formation with a plugging ratio of 32.39%.
- (4) After plugging, the permeability difference in the parallel sand pack model is remarkably reduced, which improves the sweep efficiency, and thus, the recovery factor is greatly enhanced. Compared with the original sand pack model and the sand pack model after plugging, the oil recovery factor for high-permeability sand pack is improved by 10.98%, and the recovery factor for low-permeability sand pack is improved by 26.30%.

## Data Availability

All data and research results supporting this study are included in the manuscript.

## Conflicts of Interest

The authors declare that they have no conflicts of interest.

## Acknowledgments

The authors would like to acknowledge the Chongqing Natural Science Foundation (cstc2020jcyj-msxmX0573) and the Science and Technology Research Project of Chongqing Municipal Education Commission (KJQN201901538) for their financial support.

## References

- [1] I. D. Gates, "Solvent-aided steam-assisted gravity drainage in thin oil sand reservoirs," *Journal of Petroleum Science and Engineering*, vol. 74, no. 4, pp. 138–146, 2010.
- [2] S. Huang, X. Chen, H. Liu et al., "Experimental and numerical study of steam-chamber evolution during solvent-enhanced steam flooding in thin heavy-oil reservoirs," *Journal of Petroleum Science and Engineering*, vol. 172, pp. 776–786, 2019.
- [3] A. Zare and A. A. Hamouda, "Coinjection of C6, C7, and CO<sub>2</sub> with steam to improve low-pressure SAGD process," *Fuel*, vol. 238, pp. 394–401, 2019.
- [4] A. Xu, L. Mu, Z. Fan et al., "Mechanism of heavy oil recovery by cyclic superheated steam stimulation," *Journal of Petroleum Science and Engineering*, vol. 111, pp. 197–207, 2013.
- [5] Y. Liu, X. Liu, J. Hou, H. A. Li, Y. Liu, and Z. Chen, "Technical and economic feasibility of a novel heavy oil recovery method: geothermal energy assisted heavy oil recovery," *Energy*, vol. 181, pp. 853–867, 2019.
- [6] L. S. Cheng, L. Liang, Z. X. Lang, and X. S. Li, "Mechanistic simulation studies on the steam-foam drive in superviscous oil reservoirs," *Journal of Petroleum Science and Engineering*, vol. 41, no. 1–3, pp. 199–212, 2004.
- [7] J. Gong, M. Polikar, and R. J. Chalaturnyk, "Fast SAGD and geomechanical mechanisms," in *Proceedings of the Canadian International Petroleum Conference*, Calgary, Canada, June 2002.
- [8] M. Al-Gosayir, T. Babadagli, J. Leung, and A. M. Al-Bahlani, "In-situ recovery of heavy-oil from fractured carbonate reservoirs: optimization of steam-over-solvent injection method," *Journal of Petroleum Science and Engineering*, vol. 130, pp. 77–85, 2015.
- [9] Y.-B. Li, Y.-Q. Zhang, C. Luo et al., "The experimental and numerical investigation of in situ re-energization mechanism of urea-assisted steam drive in superficial heavy oil reservoir," *Fuel*, vol. 249, no. 6, pp. 188–197, 2019.
- [10] F. Zhao, Z. Li, J. Wu, J. Hou, and S. Qu, "New type plugging particle system with high temperature & high salinity resistance," *Journal of Petroleum Science and Engineering*, vol. 152, pp. 317–329, 2017.
- [11] G. Zhao, C. Dai, C. Gu, Q. You, and Y. Sun, "Expandable graphite particles as a novel in-depth steam channeling control agent in heavy oil reservoirs," *Chemical Engineering Journal*, vol. 368, pp. 668–677, 2019.
- [12] S. Li, Q. Wang, and Z. Li, "Stability and flow properties of oil-based foam generated by CO<sub>2</sub>," *SPE Journal*, vol. 25, no. 1, pp. 416–431, 2020.
- [13] Y. M. Liu, L. Zhang, S. R. Ren, B. Ren, S. T. Wang, and G. R. Xu, "Injection of nitrogen foam for improved oil recovery in viscous oil reservoirs offshore Bohai Bay China," in *Proceedings of the SPE Improved Oil Recover Conference*, Tulsa, OK, USA, April 2016.
- [14] P. Emeka, M. Naylor, S. Haszeldine, and A. Curtis, "CO<sub>2</sub>/Brine surface dissolution and injection: CO<sub>2</sub> storage enhancement," *SPE Projects. Facilities. Construction*, vol. 6, no. 01, pp. 41–53, 2011.
- [15] M. Zirrahi, H. Hassanzadeh, and J. Abedi, "Experimental and modeling studies of MacKay River bitumen and water," *Journal of Petroleum Science and Engineering*, vol. 151, pp. 305–310, 2017.
- [16] P. Liu, Y. Zhou, P. Liu, L. Shi, X. Li, and L. Li, "Numerical study of herringbone injector-horizontal producer steam assisted gravity drainage (HI-SAGD) for extra-heavy oil recovery," *Journal of Petroleum Science and Engineering*, vol. 181, Article ID 106227, 2019.
- [17] S. Wang, C. Chen, B. Shiau, and J. H. Harwell, "In-situ CO<sub>2</sub> generation for EOR by using urea as a gas generation agent," *Fuel*, vol. 217, pp. 499–507, 2018.
- [18] M. Bin Dahbag, A. Al-Gawfi, and H. Hassanzadeh, "Suitability of hot urea solutions for wettability alteration of bitumen reservoirs – Simulation of laboratory flooding experiments," *Fuel*, vol. 272, 2020.
- [19] B. Rostami, P. Pourafshary, A. Fathollahi et al., "A new approach to characterize the performance of heavy oil recovery

- due to various gas injection,” *International Journal of Multiphase Flow*, vol. 99, pp. 273–283, 2018.
- [20] R. A. DeRuiter, L. J. Nash, and M. S. Singletary, “Solubility and displacement behavior of a viscous crude with CO<sub>2</sub> and hydrocarbon gases,” *SPE Reserv. Eng. (Society Pet. Eng)*, vol. 9, no. 2, pp. 101–106, 1994.
- [21] S. Wang, M. J. Kadhum, C. Chen, B. Shiao, and J. H. Harwell, “Development of in situ CO<sub>2</sub> generation formulations for enhanced oil recovery,” *Energy & Fuels*, vol. 31, no. 12, pp. 13475–13486, 2017.
- [22] T. Lu, Z. Li, S. Li, P. Wang, Z. Wang, and S. Liu, “Enhanced heavy oil recovery after solution gas drive by water flooding,” *Journal of Petroleum Science and Engineering*, vol. 137, pp. 113–124, 2016.
- [23] M. Dong, Q. Liu, and A. Li, “Displacement mechanisms of enhanced heavy oil recovery by alkaline flooding in a micromodel,” *Particuology*, vol. 10, no. 3, pp. 298–305, 2012.
- [24] M. J. Pitts, K. Wyatt, and H. Surkalo, “Alkaline-polymer flooding of the david pool, Lloydminster Alberta,” in *Proceedings of the SPE Symp Improved Oil Recovery*, pp. 1–6, Lloydminster, Canada, April 2004.
- [25] B. Azinfar, M. Zirrahi, H. Hassanzadeh, and J. Abedi, “Characterization of heavy crude oils and residues using combined gel permeation chromatography and simulated distillation,” *Fuel*, vol. 233, pp. 885–893, 2018.
- [26] S. Wang, Q. Yuan, M. Kadhum et al., “In situ carbon dioxide generation for improved recovery: Part II. Concentrated Urea solutions,” in *Proceedings of the SPE Symp Improved Oil Recovery Conference*, Tulsa, Oklahoma, USA, April 2018.
- [27] M. BinDahbag, M. Zirrahi, and H. Hassanzadeh, “Injection of hot urea solutions as a novel process for heavy oil recovery — A proof-of-concept experimental study,” *Journal of Industrial and Engineering Chemistry*, vol. 95, pp. 244–251, 2021.

## Research Article

# Integrated Geologic Modeling of Fault-Block Reservoir: A Case Study of Ss Oil Field

Zhipeng Xiao,<sup>1</sup> Zhang Wei,<sup>1</sup> Zhengyin Tang ,<sup>2</sup> Jianqing Guo,<sup>1</sup> Ruijuan Geng,<sup>1</sup> and Tuobing Gou<sup>1</sup>

<sup>1</sup>Exploration and Development Research Institute of TuHa Oilfield Company, CNPC, Hami, China

<sup>2</sup>Key Laboratory of Tectonics and Petroleum Resources, (China University of Geosciences), China

Correspondence should be addressed to Zhengyin Tang; 1632512357@qq.com

Received 19 January 2022; Accepted 17 February 2022; Published 12 March 2022

Academic Editor: Andrea Brogi

Copyright © 2022 Zhipeng Xiao et al. This is an open access article distributed under the Creative Commons Attribution License, which permits unrestricted use, distribution, and reproduction in any medium, provided the original work is properly cited.

The Ss oil field is found in the Turpan-Hami Basin's Taipei Sag's arc structural belt. This reservoir has a complicated character that has a significant impact on reservoir modeling and production prediction. This is a fault-block reservoir with ultralow permeability and low porosity that is divided by 57 faults. A static model was constructed by Petrel software based on reinterpretation of original log and core data and seismic information so as to clarify the spatial distribution of oil and water in the reservoir and to fit the development history of the later simulated reservoir. The integrated geological modeling approach is described in this work using the Ss reservoir as an example. A 3D structural model was built based on the spatial cutting relationship between the layer model and the fault, and the model's quality was improved by breakpoint data, which more correctly depicted the structural properties of the research area. The lithofacies model was built within the restrictions of sedimentary facies using the sequential Gaussian simulation (SGS) stochastic modeling approach, which is paired with variogram data analysis to achieve the range value. To obtain the porosity and permeability model, the empirical formula of porosity and permeability, the SGS method, and the variation range value was input into the lithofacies model. It is important to note that the input lithofacies and property models have values of the same range. To gain the water saturation model, the distinct  $S_w$  function formulas of the S1 ~ S4 layer derived from the  $J(S_w)$  function were fed into the software. The NTG model was created according to the lower limit of porosity, which is 11%. The merging of detailed reservoir description and simulation led to the establishment of the Ss reservoir geological model. In the plane, the scale of the geological model has reached the meter level and decimeter level in the longitudinal direction. It also offers a framework for optimum reservoir modeling for complex fault-block reservoirs. This method improves the accuracy and precision of the model by reflecting the reservoir's heterogeneity and the oil-water distribution. It could provide more details for future reservoir research such as fine reservoir simulation.

## 1. Introduction

Fault-block oil and gas reservoirs are intricate and trapped reservoirs produced by fault [1]. Faults are a vital part in fault-block reservoirs, as faults regulate the majority of the reservoir's main attributes [2, 3]. Many faults of various grades, orientations, periods, and mechanical qualities occur in the oil field, cutting and fracturing the structure to produce smaller fault-blocks, which are made up of fault-block groups of various forms and genesis [4]. Reservoir heterogeneity, poor connectivity, substantial lateral shifts,

and complex fluid connections are all hallmarks of fault-block reservoirs. Recent studies have shown that faults and their structures have important effects on fluid distribution and reservoir permeability.

Faults are the fundamental building blocks of fault-block reservoirs. Many researchers already have relevant knowledge for studying the fault structure. Based on extensive research using mine practice and laboratory methods, Liotta et al. [5] believe that when the structure interacts with the fault, the axial permeability of the fault increases locally, allowing formation fluids to migrate. Siler et al. [6] simulated



fault slip and historical stress transfer, and they said that stress changes caused by fault slip are important for determining the permeability enhancement and the size of structural discontinuities. According to Brogi et al. [7], faults can act as conduits for formation fluid migration. Smeraglia et al. [8] focused at the active faults in the southern Apennines and thought that the highly permeable fluid conduits were found in the area where the faults fit. Thus, this paper uses a fault-block reservoir composed of fault elements to model 3D geology. The 3D geological modeling research is significant for fluid spatial distribution and seepage studies.

The approach a geological model is created, and scaled-up has a major effect on the simulation grid's final performance, specifically when there is a lot of variability in the reservoir [9]. Fault-block oil and gas reservoirs are more challenging to analyze and classify due to their genesis. Fault-block oil and gas reservoirs are more challenging to analyze and recognize due to their construction [10]. For reservoir geological modeling, determining how to properly and effectively characterize the spatial distribution characteristics of each fault is a complex process.

The ultimate purpose of the geological model's creation is to provide reservoir simulation services. The geological model was established with extensive geological data such as reservoir seismic, well logging, and core, and the generated grid finely illustrates the reservoir's geological properties. In fact, the simulated grid was typically coarsened cell of reservoir flow characteristics with flow unit characteristics [9–11]. As a result, once the geological model is mostly complete, the constructed grid must be coarsened before it can be imported into the simulator.

At present, most research on geological modeling is limited to conventional oil reservoirs, with few introductions to integrated fault-block reservoirs of a case study [12–16]. The Ss reservoir is a low-amplitude dome anticline reservoir dominated by sedimentary facies from the fan delta and braided river delta. The primary oil-producing formations are the Upper Qiketai J2q sand units and the Lower Sanjianfang J2s sand units. It is buried at a depth of 2800–3200 meters, with the water-oil contact at the depth of -2500 meters (shown in Figure 1). Porosity is 12.5%, and permeability is 6.2 mD. The viscosity and density of formation crude oil are 0.39 mPa·s and 0.66 g/cm<sup>3</sup>, respectively. The geological model was accomplished in this study after within most latest geological information and development data of the study area, which supplied some reference concepts for later similar research on fault-block oil and gas reserves. Furthermore, it represents research methods for the block's remaining oil development in the future. The study is related to a range of dynamic and static geological data from the Ss reservoir, including seismic, logging, and core analysis, as well as a detailed summary of the work area. Petrel software was utilized to do this geological modeling workflow in the area when combined with detailed geological data. Quantitatively expose the 3D distribution of lithology and facial attributes of reservoirs in the Ss reservoir, as well as the distribution and favorable regions of reserve, in the modeling system.

The first chapter of the study discusses the current understanding about fault-block reservoirs in geologic modeling. The study area's history and geological setting are detailed in the second part. The third section is a quick overview of modeling methodological approach. The fourth and fifth parts present the results of the geological modeling, as well as comments and conclusions.

## 2. Geological Setting and Study Area

**2.1. Location and Development.** The Ss reservoir is located in the Taipei Sag of the Turpan-Hami Basin, with Qiuling reservoir to the west and Wenmi reservoir to the east, in the arc structural belt. The reservoir was discovered in the 1950s, but development did not begin until the late 1980s, and production began in the early 1990s [17]. Figure 2 depicts total oil production, total fluid production, and total water content over period.

**2.2. Geologic Structure.** The Ss structure is a short-axis northwest-trending anticline with a long axis of 9.15 kilometres a short axis of 5.2 kilometres [17, 18]. The reservoir has a closed range of 328.5 meters, a closed area of 38.0 kilometres, and 57 faults. The overall terrain of Ss reservoir is higher in the north and lower in the south, with a small uplift and a nose-like structure in the middle that gradually descends to the two flanks. Figure 3 depicts the recognition of seismic attribute slices such as coherent body, ant body, and tectonic steering filter, as well as how the interpretation results are used to estimate the study area's fault distribution characteristics. Finally, the investigated area's fault structure distribution is confirmed (shown in Figure 4).

**2.3. Layered.** The primary oil-producing formations are the Upper Qiketai J2q sand units and the Lower Sanjianfang J2s sand units, with an oil layer depth of 2800 m to 3200 m. The J2s of the Sanjianfang formation are divided into oil group SI and SII, applying sequence stratigraphic analysis method and the short-term base level cycle [19]. According to the sedimentary rhythm and lithological variation surface, SI oil group is sorted into S<sub>1</sub> and S<sub>2</sub> sand units, and SII is sorted into S<sub>3</sub>, S<sub>4</sub>, and S<sub>5</sub> sand units. Each sand unit is divided into single layer sand for modeling and research purposes, with the specific division results be provided in Table 1. The oil units Q1 are 56.3 meters thick, SI is 105.8 meters thick, and SII is 178 meters thick. In the study area, the productive layer's original oil saturation ranges from 58 to 68.5 percent.

**2.4. Porosity and Permeability.** In the study area, in-layer heterogeneity is not obvious but the interlayer heterogeneity is very strong [20]. The majority of pore types are secondary. The results of the test suggest that the reservoir rocks have a high degree of hydrophilicity from 14 cores wettability, which is advantageous for water injection development and enhanced oil recovery. The laboratory measured relative permeability curves and normalized them to generate three rock type curves using 33 sample cores with various permeability levels (Figure 5). The Sanjianfang formation's mean permeability and porosity were proved to be 6 mD and



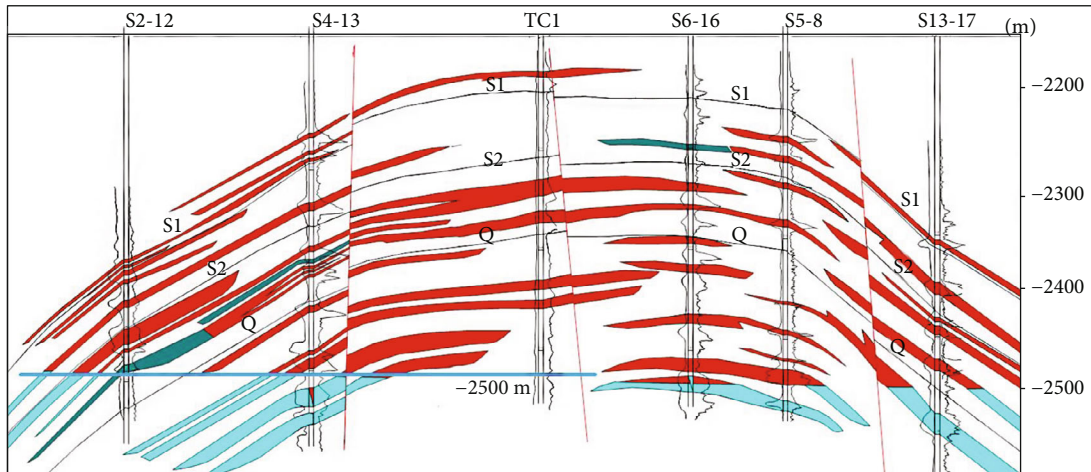


FIGURE 1: Geological structure of Ss reservoir.

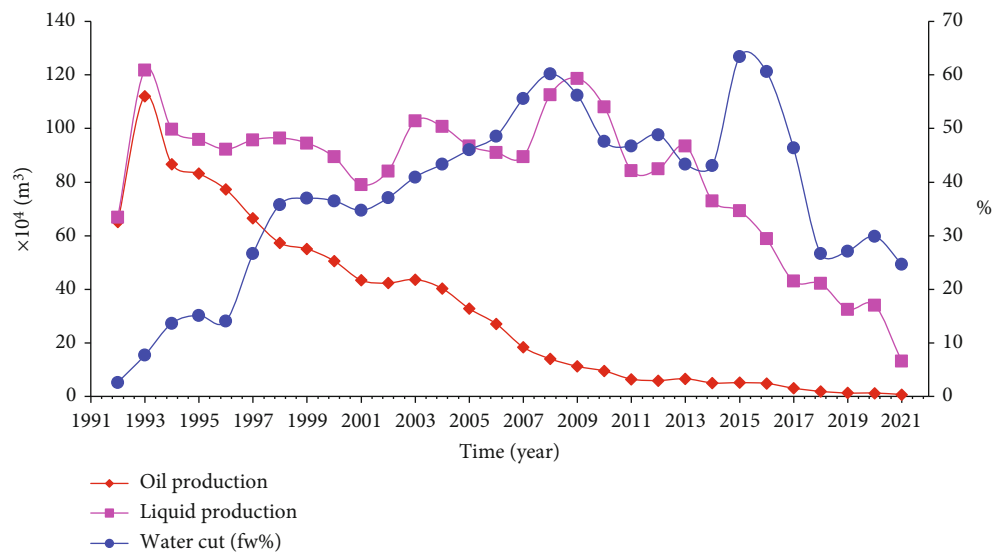


FIGURE 2: The Ss historical production.

13%, respectively, as shown in Figure 6. The reservoir is characterized by low porosity and ultralow permeability.

negative anomaly system (the normal geothermal gradient is  $3^\circ\text{C}/100 \text{ m}$ ).

**2.5. Fluid Properties.** Table 2 shows the general fluid properties under initial reservoir conditions as well as the simulation’s initialization parameters. The light density, low viscosity, and substantial gas content of crude oil account for its properties [17]. The reservoir has a low associated methane content, but a significant intermediate hydrocarbon ( $\text{C}_2 \sim \text{C}_5$ ) content. The salinity of the formation water is not high; the water type is  $\text{NaHCO}_3$  and  $\text{CaCl}_2$ , with  $\text{NaHCO}_3$  having a salinity of 2000~5000 ppm and  $\text{CaCl}_2$  having a salinity of 10000~22000 ppm. The initial reservoir pressure is 28.8 MPa, and the pressure coefficient is 0.97, indicating a normal pressure system. The saturation pressure is 18.2 MPa, the reservoir temperature is  $86^\circ\text{C}$ , and the geothermal gradient is  $2.5^\circ\text{C}/100 \text{ m}$ , as a low temperature

### 3. Materials and Methods

The reservoir geological model is the quantitative expression of diverse geological properties in 3D space and the integration of comprehensive geological research results [21]. As demonstrated in Figure 7, geological modeling necessitates a comprehensive set of a framework. Applying Petrel of 3D modeling software, to make a fault and structural model, facies-controlled model, and property model based on all available geological study results.

Deterministic and stochastic reservoir modeling is the two most commonly used methodologies for reservoir modeling [22–24]. Linear interpolation, inverse square weighted average of distance, kriging method, and seismic

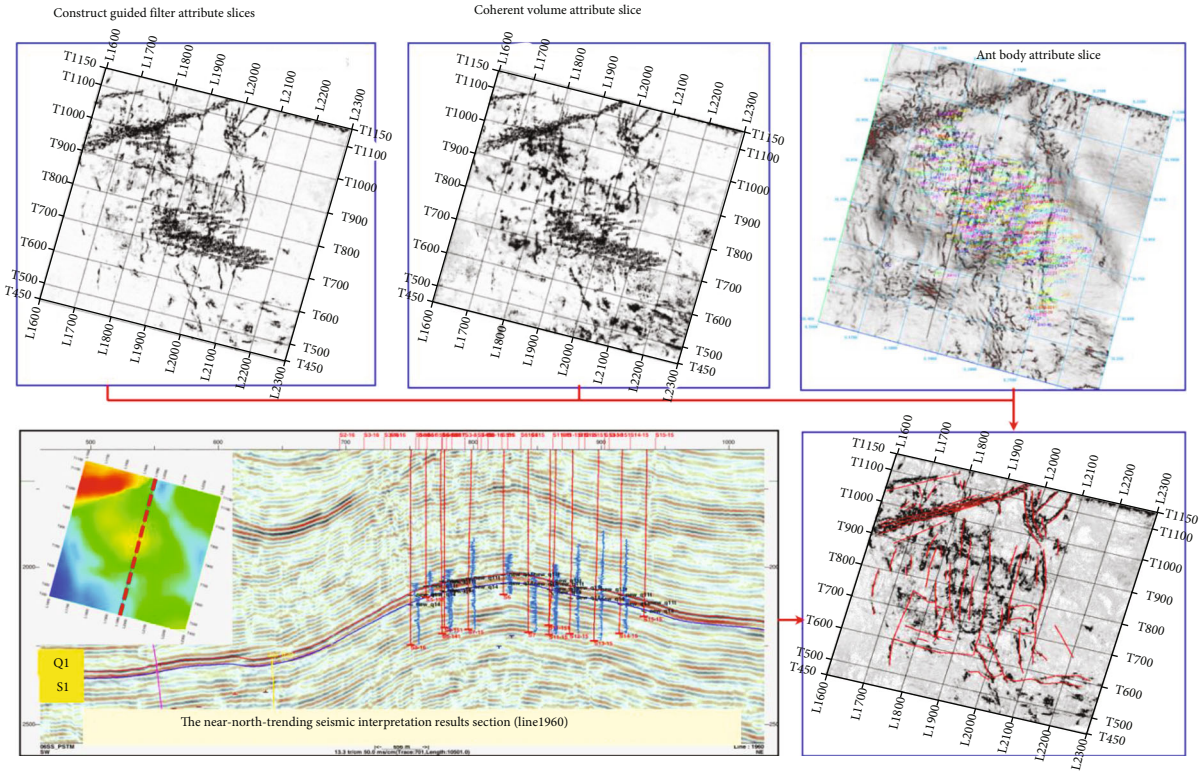


FIGURE 3: Fault combination and fault system interpretation.

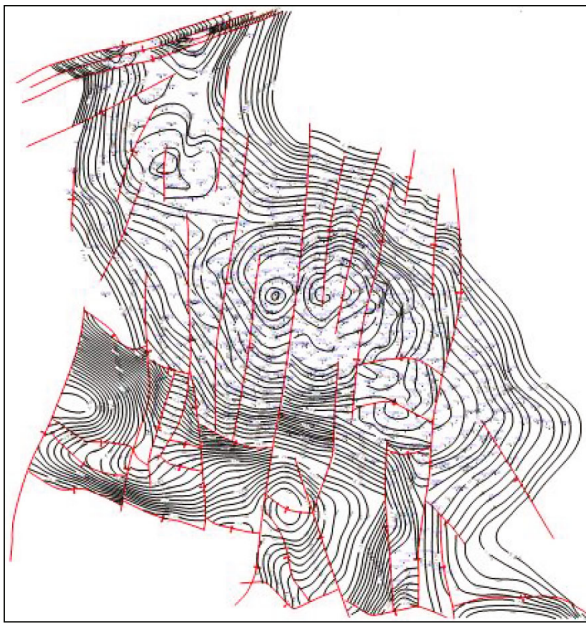


FIGURE 4: The structure of the study area.

reservoir prediction are among the techniques used in deterministic modeling [25]. The deterministic modeling method is distinguished by the fact that only one output can be obtained by entering a set of parameters. The Kriging interpolation approach may reflect the variogram properties of sand formations of various derivation; however, it is overburdened when dealing with complex fault-block reservoirs.

TABLE 1: Sand layer division of Ss reservoir.

Oily section	Oil group	Sand units	Single layer units
$J_2q$	Q <sub>1</sub>	Q <sub>1</sub>	4
	SI	S <sub>1</sub>	3
S <sub>2</sub>		5	
$J_2s$	SII	S <sub>3</sub>	5
		S <sub>4</sub>	3
		S <sub>5</sub>	4
Total	3	6	24

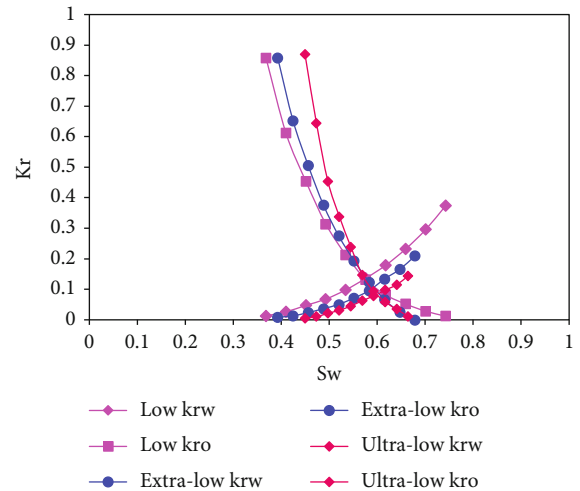


FIGURE 5: Relative permeability curves of three types.

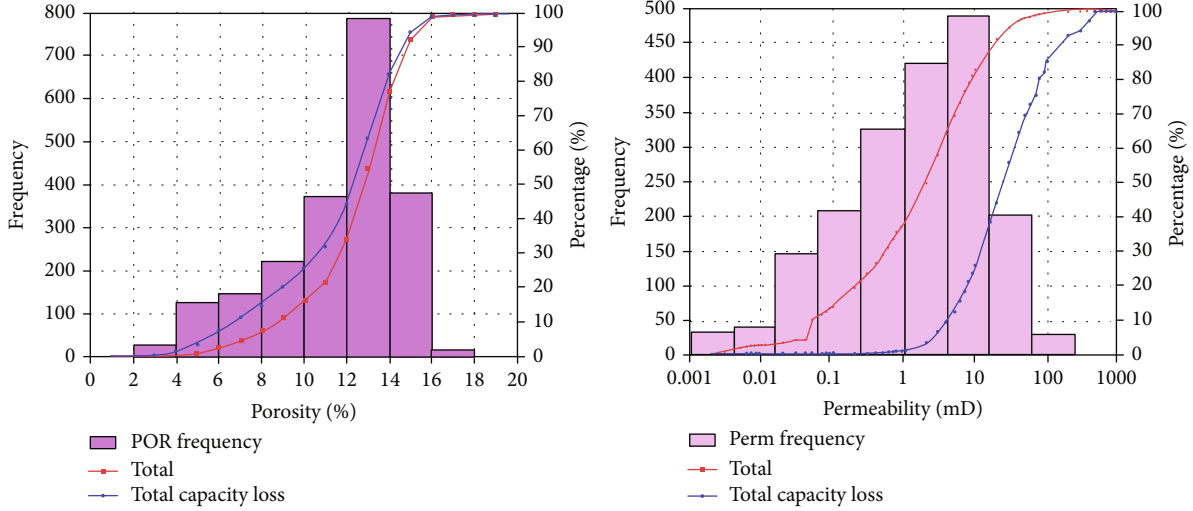


FIGURE 6: Histogram of porosity (a) and permeability (b) distribution.

TABLE 2: General fluid properties at initial reservoir conditions and initialization parameters used in the modeling.

Parameter	Value
Oil density	0.6597 g/cm <sup>3</sup>
Oil viscosity	0.3879 mPa-s
Oil bubble point pressure	18.2186 MPa
Oil compression factor( <i>c<sub>o</sub></i> )	16.7486 × 10 <sup>-4</sup> MPa <sup>-1</sup>
Gas density	1.04 kg/m <sup>3</sup>
Water formation	NaHCO <sub>3</sub> , CaCl <sub>2</sub>
Water viscosity	0.3246 mPa-s
Reservoir pressure	28.84 MPa
Reservoir temperature	86°C
Geothermal gradient	2.5 °C/100 m
Depth of water-oil contact	-2500 m

The application of stochastic simulation technology to establish multiple alternative reservoir space parameter forecasts with equal probability of reservoir spatial distribution models is based on known information together with random function theory [26, 27]. Multiple stochastic results generated using the stochastic simulation method can better capture the varied nature of reservoir attribute spatial distribution [28]. Advanced stochastic modeling methods and facies-controlled modeling approaches are needed to construct geological models based on the research objective, depth, and accuracy requirements of the study area.

The fault model is a three-dimensional fault plane that is based on seismic interpretation and fault data to determine fault distribution in space [29]. The layer structure model uses the interpolation method and layered data to build the top and bottom surface models of each isochronous layer [30]. The layer model is a three-dimensional representation of the stratum interface. After merging the space of each layer model, the constructed fault model can be loaded to acquire the reservoir's 3D spatial framework.

Stochastic modeling simulation requires two types of parameters. The conditional parameter is the original geological information. The other category is statistical characteristic parameters, which comprise lithology index variation coefficient, petrophysical variation function, and probability density function [31]. The most advanced method currently used to determine these values is variogram analysis with stratigraphic comparison.

The variogram quantifies the spatial variability of regionalized variables. It reflects the fact that the degree of spatial variability varies with distance and direction. It builds a corresponding theoretical variogram model using limited spatial observations of regionalized variables to reveal the variable's main structural characteristics [31]. Taking the lithofacy interpretation data on the well point as the control point, the horizontal and vertical variation functions of the five lithologic facies of the 24 single sand layers were analyzed, and the variable gradient function model curves were fitted so that various statistical characteristic parameters were relatively well determined, as shown in Table 3. The variogram model curves obtained by analyzing the lateral and vertical variograms of the five lithofacies with the properties of 24 sand layers are depicted in Figure 8.

Following the completion of structural and lithofacies modeling, property modeling, which includes porosity, permeability, water saturation, and NTG models, is performed. Variogram analysis and stochastic modeling method optimization are required in porosity and permeability modeling, as well as when the lithofacies model is established. Accurate modeling of water saturation variation in the transition zone is critical for reservoir simulation and determining original oil in place [32]. There was no complete set of resistivity logs available to generate capillary pressures ( $P_{cr}$ ) [33].  $P_{cHg}$  data for rock samples were available, which was then converted to the  $P_{cr}$  in the following equation.

$$P_{cr} = \frac{\sigma_r \cos \theta_r}{\sigma_l \cos \theta_l} \cdot P_{cHg}, \quad (1)$$



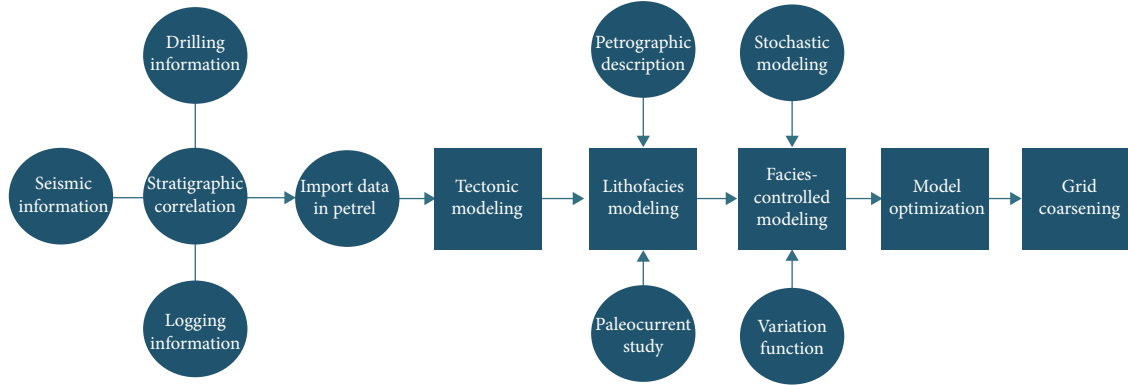


FIGURE 7: The workflow used for the entire modeling procedure.

TABLE 3: The variogram fits the input parameter value.

Parameter	Value
Major range	600 meters
Minor range	380meters
Vertical range	3 meters
Major azimuth	SE45°
Vertical dip	90°

where  $P_{cr}$  and  $P_{cHg}$  are under formation conditions and laboratory conditions capillary pressure (MPa);  $\sigma_r$  and  $\sigma_l$  are the interfacial tension under the formation conditions and laboratory (mN/m);  $\theta_r$  and  $\theta_l$  are the capillary angle under the formation and laboratory, respectively. Table 4 provides specific value of the above parameters.

Because of the large density differences between oil and gas and the lack of an initial gas cap in the reservoir, the capillary pressure between them was ignored. Equation (2) was used to convert the obtained capillary pressure data to depth:

$$H = H_O - H_{FWL} = \frac{100P_{cr}}{\rho_w - \rho_o}, \quad (2)$$

where  $H$  is the height of oil, m;  $H_{FWL}$  is height above the free water level, m;  $\rho_w$  is water density,  $g/cm^3$ ; and  $\rho_o$  is oil density,  $g/cm^3$ .

Finally, eq. (3) [34, 35] is used to transform the capillary pressure curve under oil reservoir circumstances to the  $J$  function in consistent units:

$$J(S_w) = \frac{P_{cr}}{\sigma_r \cos \theta_r} \cdot \sqrt{\frac{k}{\phi}}, \quad (3)$$

where  $K$  is permeability (md);  $\phi$  is fractional porosity, %.

Figure 9 shows water saturation and capillary pressure curves for multiple rock samples from S1 to S4.

Data preparation is essential before the modeling work begins. 502 well position and well trajectory data were sorted by the researchers. Fine geological stratification data, logging interpretation curves, seismic tectonic surface and fault data, lithology curves, paleo-current direction data, and other

information are also included. Various test data (such as oil test and production data), fluid property data, and production dynamic data must also be prepared.

An orthogonal grid system was used to establish the model grid in the study area. The grid step length is 20 meters on the 2D surface, and a total of  $348 \times 345$  grids are divided. With an average step length of 0.2 meters, it approaches the decimeter level in the longitudinal direction. As a result, a total of 1730 microlayers are separated longitudinally from the upper of the Q sand group to the lower of the S5 sand group, resulting in a total of  $348 \times 345 \times 1730$  cells in the 3D modeling. The total number of cells exceeds 200 million. Because the geological model is so detailed, it cannot be directly loaded into the simulator for simulation testing. On the one hand, machine capacity and computer power are significant challenges; on the other hand, they are insignificant for research simulation. As a result, work on coarsening the cell is also required. To check for invalid cells, cell height and volume models were constructed after coarsening the cell of the geological model.

## 4. Results and Discussion

**4.1. Fault Modeling.** The fault model is a 3D fault plane that is based on seismic interpretation and fault data to determine fault distribution in space. The layer structure model uses the interpolation method and layered data to build the top and bottom surface models of each isochronous layer. The layer model is a 3D representation of the stratum interface. After superimposing the space of each layer model, the constructed fault model can be loaded to acquire the reservoir's 3D spatial framework.

According to the result of the seismic investigation and interpretation, the study area has 57 faults of various magnitude, with a rather basic fault structure. Applying seismically interpreted fault data to construct each fault plane and analyze the contact and cutting relationships between the faults, a fault model for the entire oil area of the Ss was established, as shown in Figure 10.

**4.2. Structural Modeling.** From the upper Q to the lower S5 sand, the geological stratification of the study area is divided into 6 layer units and 24 small strata. Although well

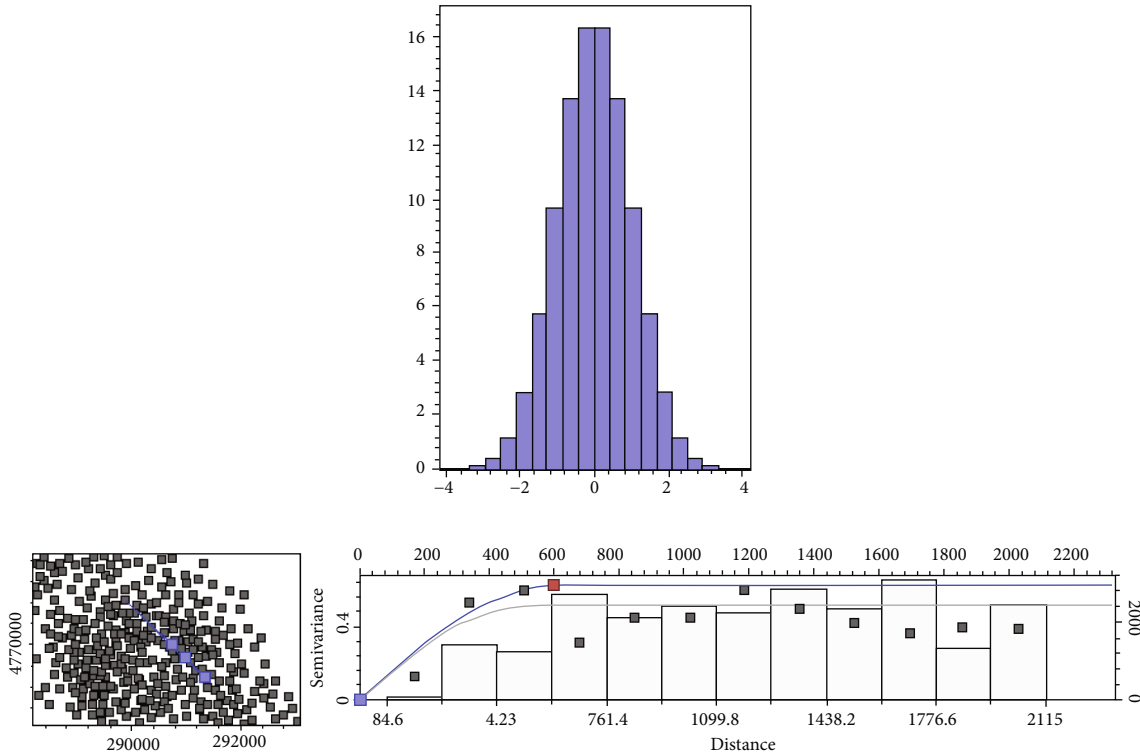


FIGURE 8: Normalization and matching in variogram analysis.

TABLE 4: Wetting angle and interfacial tension value [34, 35].

Environment	System	Capillary angle $\theta$ ( $^{\circ}$ )	Interfacial tension $\sigma$ ( $\text{mNm}^{-1}$ )
Laboratory	Gas-water	0	72
	Oil-water	30	48
	Gas-mercury	140	480
	Gas-oil	0	24
Formation	Water-oil	30	30
	Water-gas	0	50

geological stratification data is quite reliable, predicting the value obtained between wells is problematic. Four tiers of upper and lower oil groups were developed based on the interpretation surface data of seismic interpretation in the study (Figure 11) in order to make the structure correspond to the details of wells and reflect the overall trend of seismic interpretation. The four layers were adjusted and reconstructed using the layered data from 502 wells, and the layered thickness surface of 24 single sand layers was established. Finally, a 3D structural model of the Ss was created by merging four layer models, layered thickness planes, and fault models (Figure 12).

**4.3. Lithofacies Modeling.** The sandstone is categorized into four lithofacies by studying the sedimentary facies of the Ss reservoir: glutenite, medium to coarse sandstone, packsand, and siltstone. To create a 3D lithofacies model, the paper used a combination of stratigraphic lithology and strati-

graphic contrast division, log facies analysis, and lithofacies curve interpretation in the study area, as well as paleocurrent direction and advanced stochastic modeling technologies.

The stochastic modeling approach was screened based on variogram analysis, employing logging interpretation of lithofacies data at the well locations as hard information, and a more suitable sequential inertia indicator method was applied to construct 24 layers of 3D lithofacies model. The lithofacies model of the study region is displayed in 3D in Figure 13, and the lithofacies model of the  $s_2^3$  layer is shown in Figure 14.

**4.4. Property Modeling.** The 3D facies model is used to model the petrophysical parameters. Under the control of conditional wells, statistically evaluate parameters of the standard deviation, probability distribution, and variogram in the facies model, using sequential Gaussian simulation (SGS) to produce the requisite 3D parameter model. The



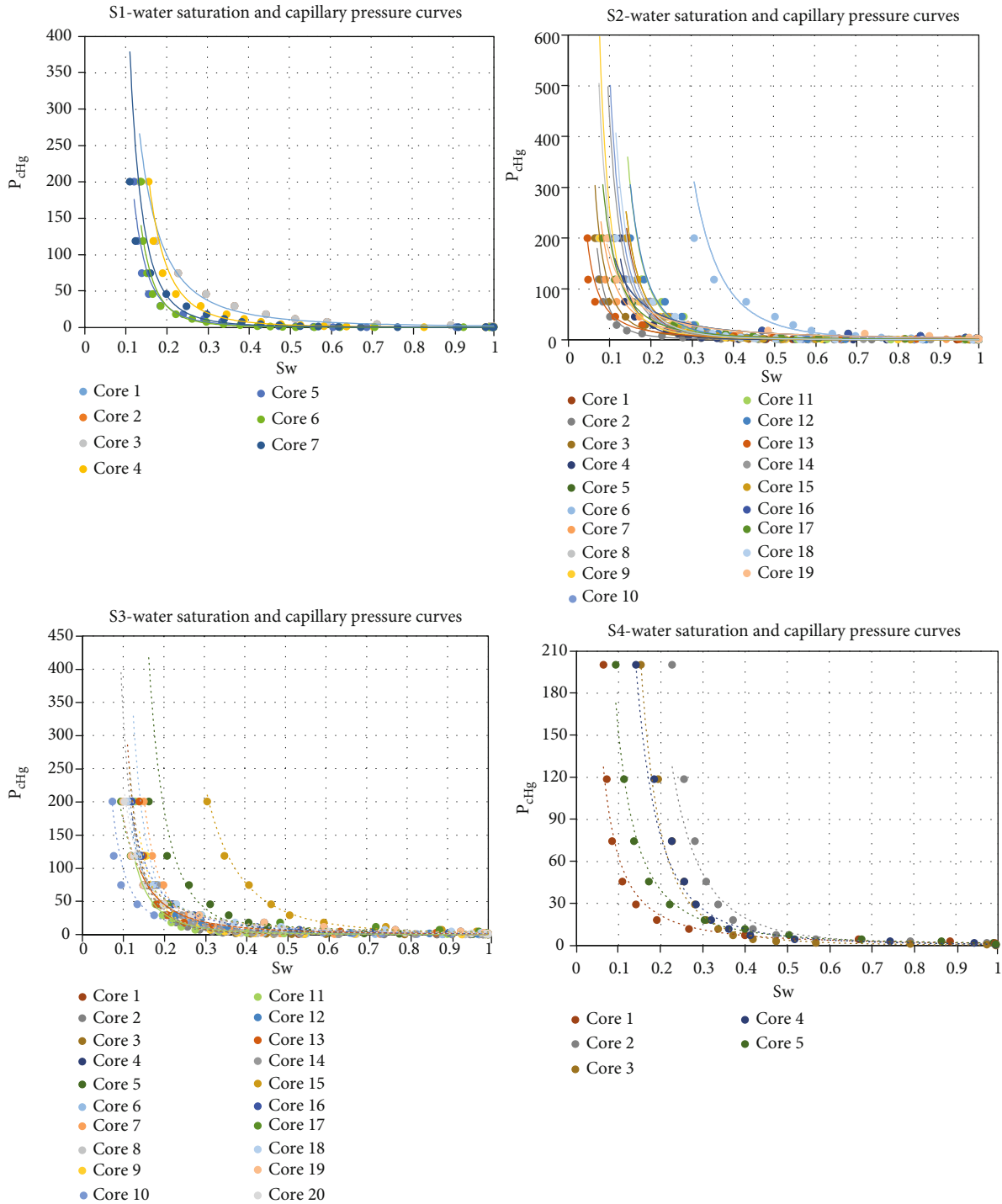


FIGURE 9: S1 to S4 water saturation and capillary pressure curves.

SGS [36] algorithm provides two benefits. It is first carried out in a sequential manner from one pixel to the next. Second, in addition to the original data, the conditional data utilized to build the conditional probability distribution function of a pixel includes all simulated data.

The porosity is the fundamental parameter that reveals the reservoir capacity's relative size. Porosity accuracy is directly related to the precision of key metrics such as saturation,

which is critical in the appraisal and computation of reservoir reserves. The link Eq. (4) between AC and porosity was established using core analysis porosity and logging electrical parameters of the core layer. The relationship between AC and formation porosity is shown in Figure 15(a).

$$\Phi_C = 0.001811 \times AC - 0.2964 (R^2 = 0.832 N = 97), \quad (4)$$

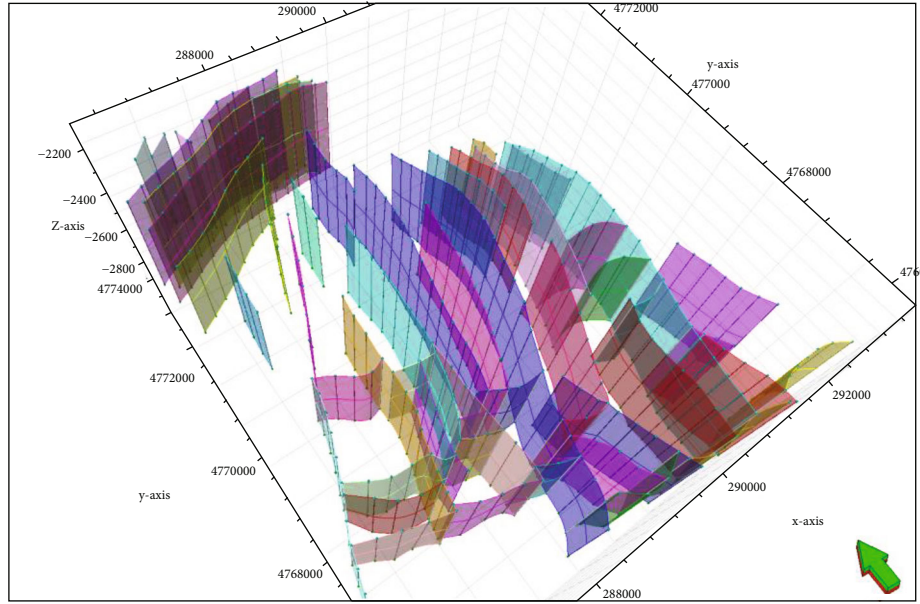


FIGURE 10: Fault model of the study area.

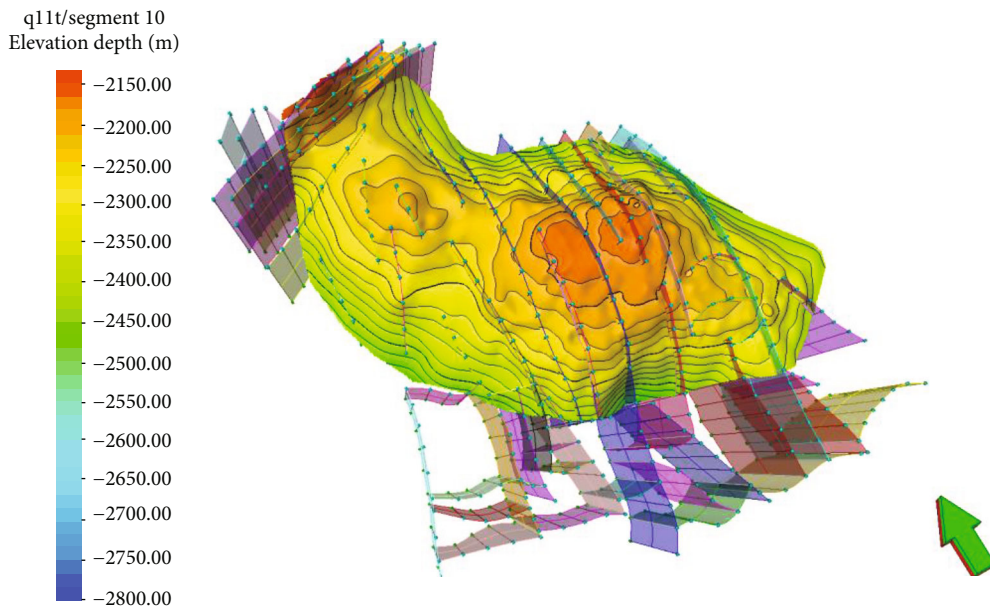


FIGURE 11: Top structure of the study area.

Where  $\Phi_C$  is the porosity,  $AC$  is the acoustic time difference.

As demonstrated in Figure 15(b), permeability and porosity have a particular relationship. An empirical Eq. (5) for the intersecting permeability of the porosity and permeability of the Ss reservoir is established based on the porosity and permeability data from the core analysis in the research region.

$$K = 0.01097 \times e^{(0.4356 \times \Phi)} \quad (R^2 = 0.8039 \ N = 139), \quad (5)$$

where  $K$  is the permeability of reservoir, and  $\Phi$  is the porosity.

The porosity of mudstone is zero, according to the lithofacies model, when Eq. (4) is used to compute the porosity of sandstone. Discretize the calculated porosity into a property while also setting the porosity of the mudstone and inter-layer to low-value ranges of 0~001. The porosity of sands was distributed according to the real data range, which was combined with the log interpretation of the property parameter data of wells point as the hard data, and 24 layers of 3D porosity models were built using the SGS technique (shown

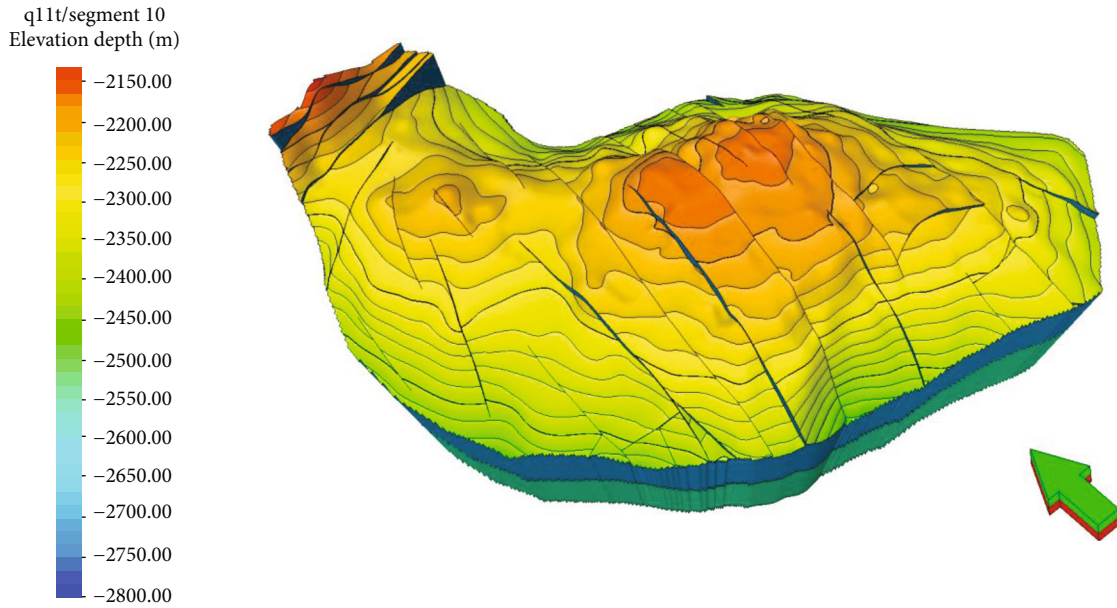


FIGURE 12: 3D structural model of the study area.

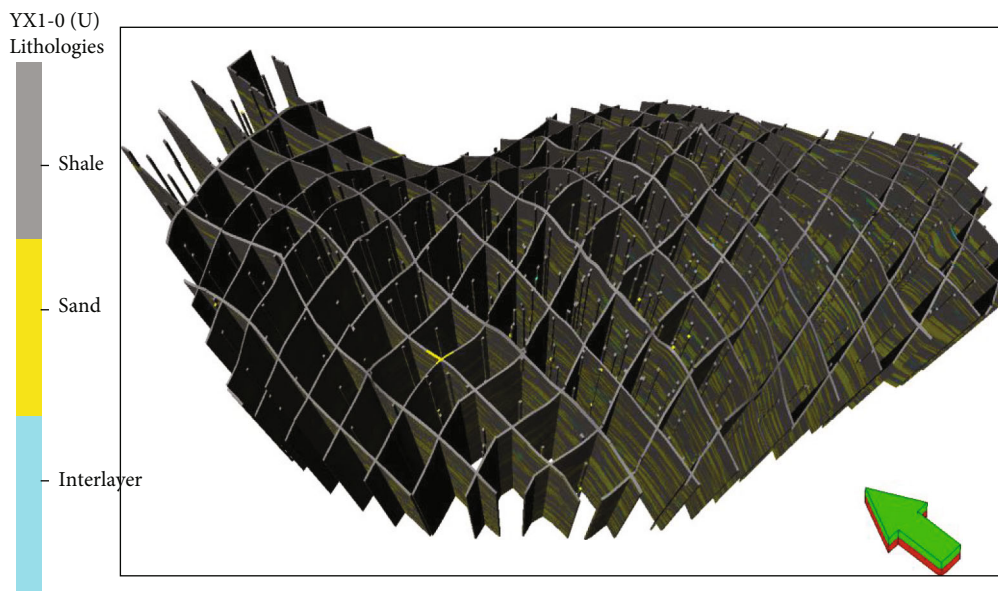


FIGURE 13: 3D lithofacies model of the study area.

in Figure 16(a)). Given the link between permeability and porosity, developing permeability models is consistent with the above strategy (shown in Figure 16(b)). The longitudinal porosity and permeability model distributions are shown in Figures 16(c) and 16(d), respectively.

Water saturation was computed in every cell of the 3D grid using the height above free water level concept, which was modeled using capillary pressure curves assigned to each reservoir rock type (RRT) in this study. Reservoir rock cores were investigated, and the relationship between capillary

force and water saturation ( $S_1$  to  $S_4$ ) was determined under experimental settings, as shown in Figure 9. The  $J(S_w)$  function and water saturation model ( $S_w$ ) of ( $S_1 \sim S_4$ ) sand units are shown in Table 5. The following is a more detailed explanation of the approach. To begin, Eq. (1) converts the capillary force value measured under experimental conditions into the equivalent value under formation conditions. Second, Eq. (3) was implemented to create a series of  $J(S_w)$  values, and then multiple regression matching was used to determine the relationship between  $J(S_w)$  and ( $S_w$ ). Finally,

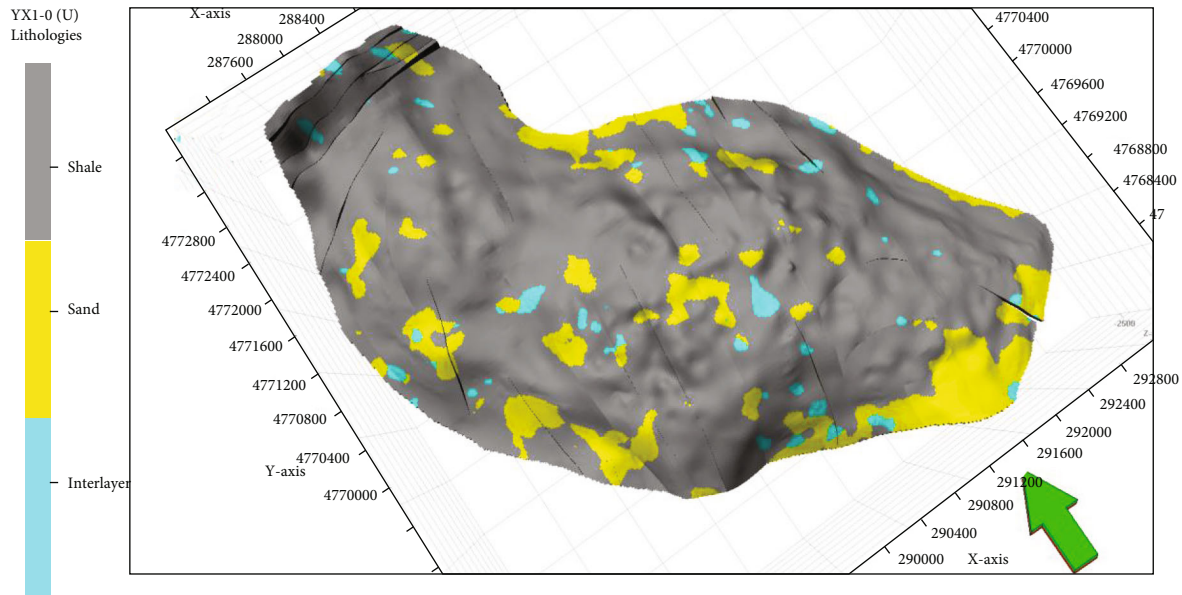


FIGURE 14: Lithofacies model of  $s_2^3$  layer in the study area.

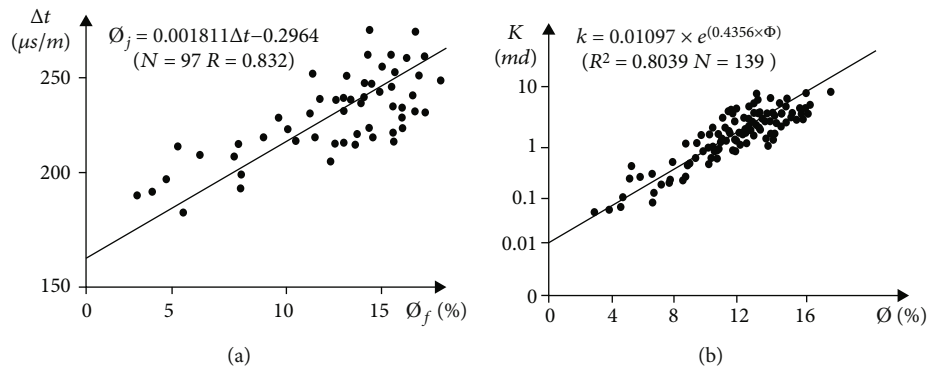


FIGURE 15: Relation of AC and porosity (a) and relation of permeability and porosity (b).

by integrating Eqs. (2) and (3), the ( $S_w$ ) function is obtained, which shows the relation between water saturation, formation porosity and permeability, and oil column height of distinct oil layer units. To establish the water saturation model, the derived ( $S_w$ ) functional relationship was entered into Petrel modeling software. Exhibition of modeled longitudinal cross-sections (S1 to S4) of the water saturation models in primary reservoir regions is shown in Figure 17.

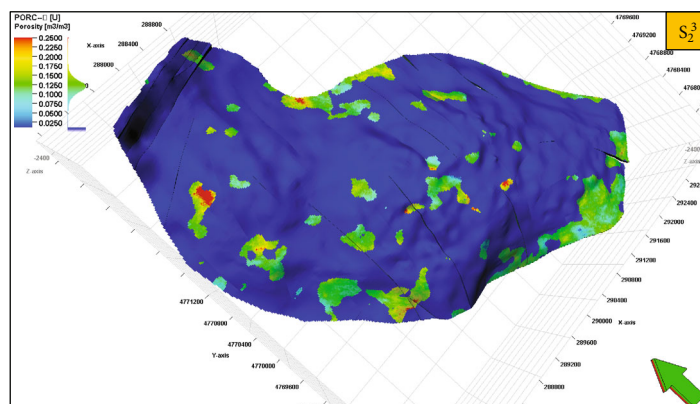
This method improved the petrophysical model's accuracy. When compared to the Archie technique, the calculation accuracy of the water saturation model derived by solving the different levels is greatly improved, and it can disclose the change in saturation near the oil-water interface.

Furthermore, as compared to the simple assignment method's water saturation model, the  $S_w$  function model can better expose the original reservoir saturation and give a solid foundation for simulation.

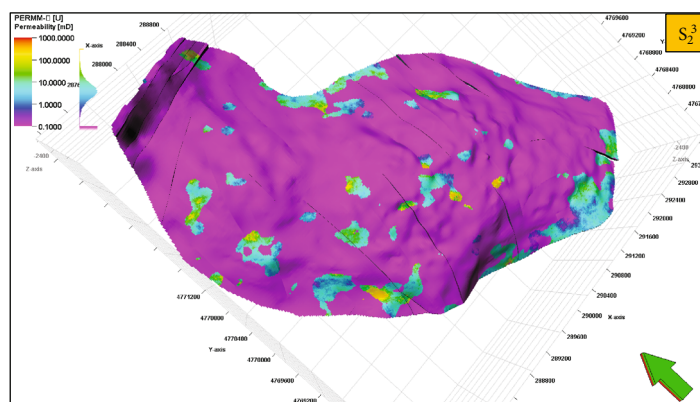
**4.5. Net to Gross Modeling.** The term “cut-off” refers to a collaborative effort by geological researchers to determine a value that will distinguish non-reservoir rock (mudstone) from reservoir rock [11]. The NTG defines the effective to rock thickness ratio of the reservoir [37]. In this study, geological reserve prove only related to porosity, hence, NTG is primarily controlled by the lower limit of porosity. The intersection diagram of porosity and permeability of Ss reservoir (Figure 18), the lower limit of porosity as  $\varnothing_0$  is 11%. The syntax in the model is NTG = if (Por  $\geq$  11%, 1, 0). Figure 19 illustrates the NTG model of  $S_2^3$ .

**4.6. Calculation of Reserves.** The calculation of geological reserves is an initial test of the model's quality after it has been established. The thorough results of the initial geological model reserve calculation for the study area are shown in Table 6. The calculated reserves of the initially geological model are  $3969 \times 10^4 \text{ m}^3$ , which is 3.5% deviation than the

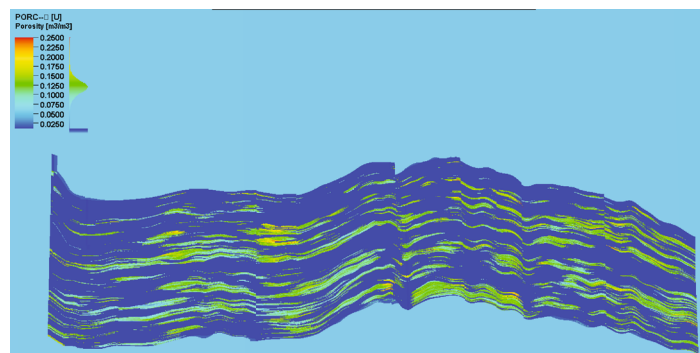




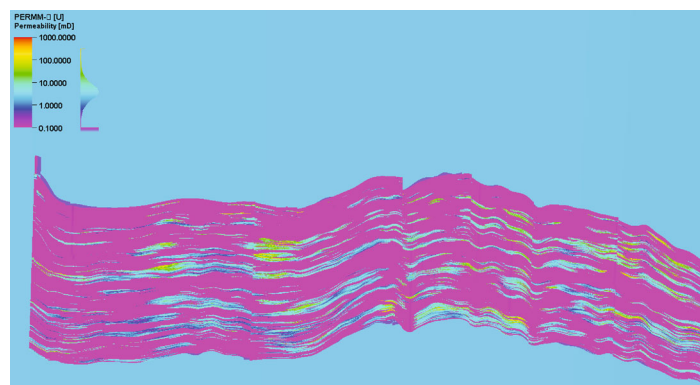
(a)



(b)



(c)



(d)

FIGURE 16: Porosity (a) and permeability (b) model of  $s_2^3$  layer, longitudinal section of the porosity (c) and permeability (d) model.



TABLE 5: ( $S_w$ ) and  $J(S_w)$  function of (S1 ~ S4) sand units.

Sand units	$J$ -function ( $J(S_w)$ )	$(S_w)$ function
S1	$J(S_w) = 0.0838 \times S_w^{-3.3} R^2 = 0.8951$	$S_w = 1.1206638 \left( \frac{1}{h} \times \sqrt{\frac{\varnothing}{k}} \right)^{\frac{1}{3.445}}$
S2	$J(S_w) = 0.0968 \times S_w^{-2.648} R^2 = 0.7405$	$S_w = 1.287414 \left( \frac{1}{h} \times \sqrt{\frac{\varnothing}{k}} \right)^{\frac{1}{2.719}}$
S3	$J(S_w) = 0.1247 \times S_w^{-2.692} R^2 = 0.7315$	$S_w = 1.294725 \left( \frac{1}{h} \times \sqrt{\frac{\varnothing}{k}} \right)^{\frac{1}{2.496}}$
S4	$J(S_w) = 0.3421 \times S_w^{-2.146} R^2 = 0.8768$	$S_w = 1.295409 \left( \frac{1}{h} \times \sqrt{\frac{\varnothing}{k}} \right)^{\frac{1}{2.56}}$

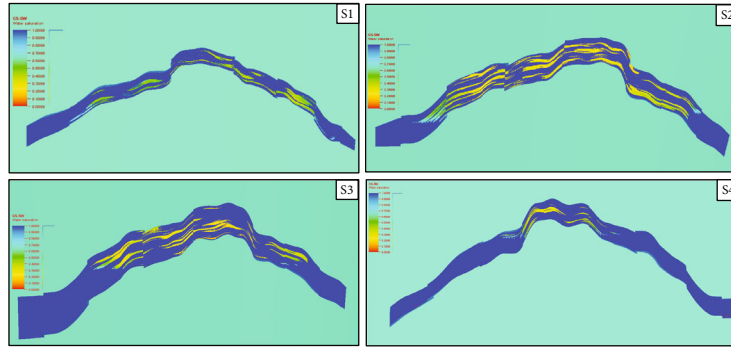


FIGURE 17: Longitudinal cross-sections of the S1 ~ S4 water saturation models.

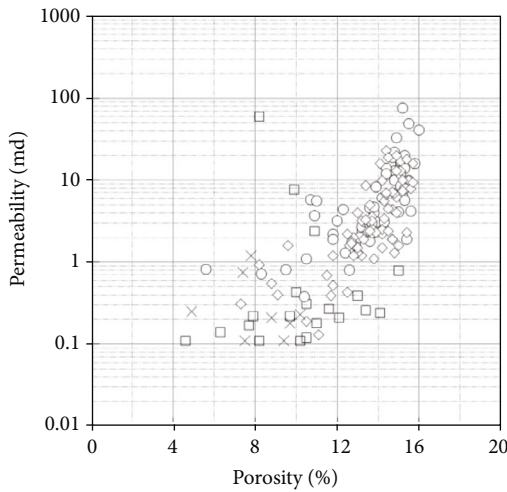


FIGURE 18: Intersection diagram of porosity and permeability.

geological reserves of  $4114 \times 10^4 \text{ m}^3$ , which conform the error range of model requirements.

4.7. Model Coarsening. The geological modeling work is nearly complete now that the structural, lithofacies, and property models have been completed. The goal of finishing

the modeling work is to make a proper support structure for simulation. The lithofacies model, porosity model, and permeability model were coarsened in order to allow the geological model to be entered into the simulator to finish the simulation study work. The coarsening process varies based on the qualities of attribute parameters [38].

The geological model was coarsened to allow the output model grids to be appropriate to simulation work and to minimize the process of modifying parameters throughout the simulation process. The vertical distribution frequency of single sand is adopted by the cells coarsening of the lithofacies model. A weighted arithmetic average approach is used to coarsen the porosity and permeability models. The grid step length was coarsened to  $50 \times 50$  meters on the 2D surface, and a total of  $139 \times 138$  grids were divided. The 1730 microlayers are coarsened 72 layers in the longitudinal direction through the three small layers of each single sand unit as the boundary coarsening condition. After coarsening, the total number of cells in the output model is  $139 \times 138 \times 72$ . The stratified reserves are rematched when the model is coarsened. The coarsened model reserve is calculated to be  $4121 \times 10^4 \text{ m}^3$ . The deviation between the simulation results of coarsened model and the geological reserves is only 0.2%. This demonstrates that the model's reserves estimate through grid coarsening is more reasonable than noncoarsening, the coarsened model more appropriate for research.

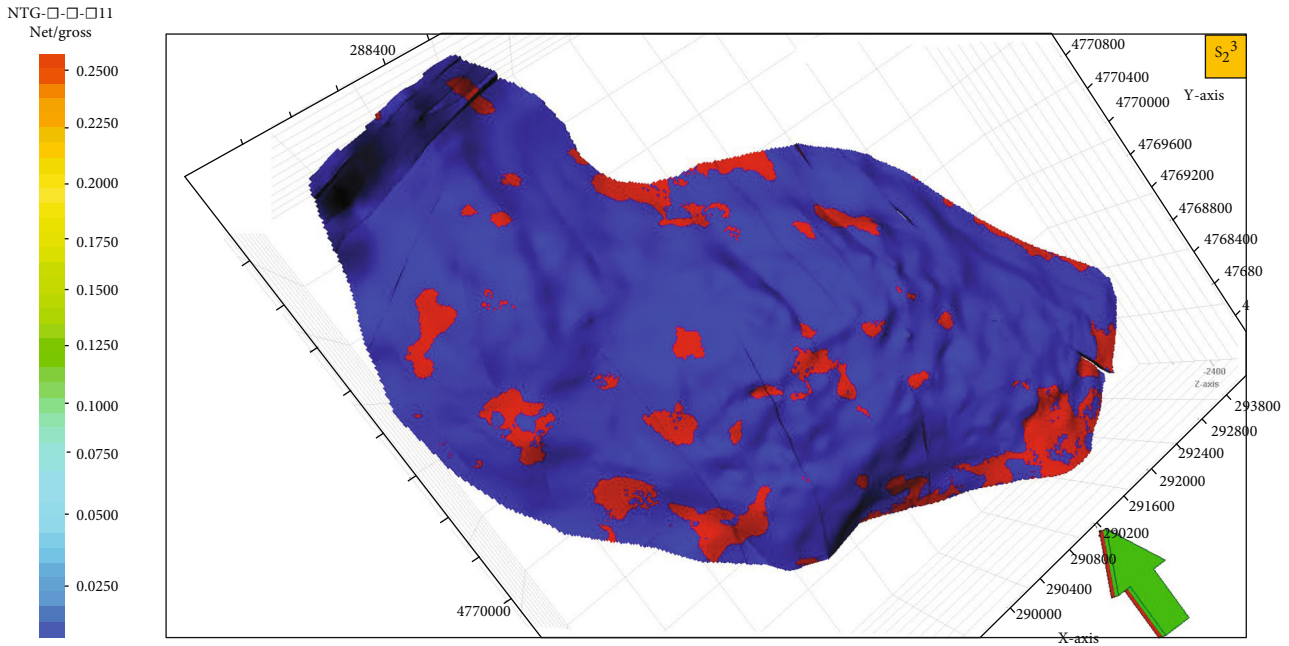


FIGURE 19: The NTG model of  $S_2^3$ .

TABLE 6: Reserve matching result of Shansan 3D model.

Sand units	$Q_1$	$S_1$	$S_2$	$S_3$	$S_4$	$S_5$	Total
Match reserve $\times 10^4 \text{m}^3$	618	879	1495	737	148	88	3969

## 5. Conclusion

- (1) The integration of detailed reservoir description and simulation led to the creation of the  $S_s$  reservoir geological model. In the plane, the geological model has reached the meter level, and in the longitudinal direction, it has reached the decimeter level. The grid step length on the 2D surface was 20 meters, and a total of  $348 \times 345$  grids were separated. In the longitudinal direction, the 1730 microlayers are divided longitudinally from the upper of the Qiketai to the lower of the  $S_5$  sand group, and the total number of nodes in the 3D modeling is  $348 \times 345 \times 1730$  cells. The 3D model reserves match is  $3969 \times 10^4 \text{m}^3$ , which is 3.5% deviation than the geological reserves of  $4113 \times 10^4 \text{m}^3$ . The results show that the model meets the accuracy and research purpose requirements
- (2) Advanced stochastic simulation methods are used to solve the complex fault-block model, which visually displays the spatial distribution characteristics of the reservoir and improves the fine description of the reservoir, as part of reservoir modeling research that closely combines the formation and sand body distribution characteristics of the  $S_s$  reservoir. This gives a parametric model for simulation due to its precision. The properties of complicated fault-block reservoir are extremely important to research

- (3) The study not only offers fault-block reservoir modeling approaches but it also publishes a vast number of geological data bodies in the study region, including 430 production well history data and reservoir material properties, as well as proposing directions for future geological research.
- (4) Through the application of variogram analysis to acquire a great grasp of sand bodies, geological study, lithofacies simulation, and physical parameter simulation become a trinity. The spatial distribution of lithofacies and petrophysical parameters is adequately displayed in lithofacies modeling and property modeling, and geological research and reservoir modeling are closely coupled to make the subsequent simulation results more realistic and dependable.

## Data Availability

The oil field geological description, except the information presented in the manuscript, used to support the findings of this study is restricted by the Safety Law of Petrel China. However, other data such as the depth or reservoir fluid description used to support the findings are currently under embargo while the research findings are commercialized. Requests for data, 12 months after publication of this article, will be considered by the corresponding author.

## Conflicts of Interest

The author(s) declare(s) that they have no conflicts of interest.

## Acknowledgments

The authors thank Tuha Oilfield Research Institute for providing the detailed geological background and date of the reservoir.

## References

- [1] X. Zhuang and S. Huang, "Establishment of fine 3D geological model of fault-block reservoir," *Application of Petrochemical Industry*, vol. 38, no. 11, pp. 79–82, 2019.
- [2] X. Pan, J. Li, L. Zhou, J. Gong, Y. H. Chen, and Q. C. Chen, "Structural modeling of oil and gas reservoirs in complex fault-block groups and its application," *Fault-Block Oil and Gas Fields*, vol. 2008, no. 6, pp. 53–54–53–58, 2018.
- [3] D. Jinhu, S. Yi, and Q. Wang, "Exploration practice and understanding of subtle reservoirs in Huabei Oil field," *China Petroleum Exploration*, vol. 2003, no. 1, pp. 1–10–1–15, 2003.
- [4] P. Gillespie, T. Skov, and P. La Pointe, "Use of an ant-tracking algorithm for fractured reservoir modeling workflow," in *Conference on Fractured Reservoirs*, Geological Society of London Burlington House, pp. 16–17, London, 2004.
- [5] D. Liotta, A. Brogi, G. Ruggieri, and M. Zucchi, "Fossil vs. active geothermal systems: a field and laboratory method to disclose the relationships between geothermal fluid flow and geological structures at depth," *Energies*, vol. 14, no. 4, article 933, 2021.
- [6] D. L. Siler, N. H. Hinz, and J. E. Faulds, "Stress concentrations at structural discontinuities in active fault zones in the western United States: implications for permeability and fluid flow in geothermal fields," *Bulletin*, vol. 130, no. 7–8, pp. 1273–1288, 2018.
- [7] A. Brogi, M. C. Alcicek, D. Liotta, E. Capezzuoli, M. Zucchi, and P. F. Matera, "Step-over fault zones controlling geothermal fluid-flow and travertine formation (Denizli Basin, Turkey)," *Geothermics*, vol. 89, article 101941, 2021.
- [8] L. Smeraglia, A. Giuffrida, S. Grimaldi et al., "Fault-controlled upwelling of low-T hydrothermal fluids tracked by travertines in a fold-and-thrust belt, Monte Alpi, southern apennines, Italy," *Italy. Journal of Structural Geology*, vol. 144, article 104276, 2021.
- [9] A. Asadi-Eskandar, H. Rahimpour-Bonab, S. Hejri, K. Afsari, and A. Mardani, "Consistent geological-simulation modeling in carbonate reservoirs, a case study from the Khuff Formation. Persian Gulf," *Journal of Petroleum Science and Engineering*, vol. 109, pp. 260–279, 2013.
- [10] B. Lv and Y. Luo, *Bo Wang, et al.*, IOS Press, Natural fractures characteristics of the carboniferous volcanic reservoir in northwestern margin of Junggar Basin, 2021.
- [11] I. O. Kohshour, M. Ahmadi, and C. Hanks, "Integrated geologic modeling and reservoir simulation of Umiat: a frozen shallow oil accumulation in national petroleum reserve of Alaska," *Journal of Unconventional Oil and Gas Resources*, vol. 6, pp. 4–27, 2014.
- [12] H. E. Zhiliang, S. U. N. Jianfang, G. U. O. Panhong, W. E. I. Hehua, L. Y. U. Xinrui, and H. A. N. Kelong, "Construction of carbonate reservoir knowledge base and its application in fracture-cavity reservoir geological modeling," *Petroleum Exploration and Development*, vol. 48, no. 4, pp. 824–834, 2021.
- [13] A. A. Radwan, M. A. Abdelwahhab, B. S. Nabawy, K. H. Mahfouz, and M. S. Ahmed, "Facies analysis-constrained geophysical 3D-static reservoir modeling of Cenomanian units in the Aghar oilfield (Western Desert, Egypt): insights into paleoenvironment and petroleum geology of fluviomarine systems," *Marine and Petroleum Geology*, vol. 136, article 105436, 2022.
- [14] J. Zheng, P. A. N. Wenqing, S. H. E. N. Anjiang et al., "Reservoir geological modeling and significance of Cambrian Xiaoerblak Formation in Keping outcrop area, Tarim Basin, NW China," *Tarim Basin, NW China, Petroleum Exploration and Development*, vol. 47, no. 3, pp. 536–547, 2020.
- [15] H. V. Thanh, Y. Sugai, R. Nguele, and K. Sasaki, "Integrated workflow in 3D geological model construction for evaluation of CO<sub>2</sub> storage capacity of a fractured basement reservoir in Cuu Long Basin. Vietnam," *International Journal of Greenhouse Gas Control*, vol. 90, article 102826, 2019.
- [16] T. A. N. Xuequn, L. I. U. Yunyan, Z. H. O. U. Xiaozhou, L. I. U. Jiandang, R. Zheng, and J. I. A. Chao, "Multi-parameter quantitative assessment of 3D geological models for complex fault-block oil reservoirs," *Petroleum Exploration and Development*, vol. 46, no. 1, pp. 194–204, 2019.
- [17] F. Bai, "Study on geological characteristics and development technology of Ss oilfield," *Sinopec*, vol. 11, pp. 39–40, 2017.
- [18] Y. C. An, "Reservoir Characteristics of Ss Oilfield," in *North-east University of Petroleum, China*, Northeast University of Petroleum Press, 2011.
- [19] L. Liu, "Small layer correlation of Sanjianfang formation in Ss oilfield, Xinjiang," *Sedimentation and Tethys Geology*, vol. 3, pp. 25–32, 2000.
- [20] G. Luo, "Fine Reservoir Description in Ss Oilfield," in *Daqing Petroleum Institute, China*, Daqing Petroleum Institute Press, 2010.
- [21] O. Lerat, P. Nivlet, B. Doligez et al., "Construction of a stochastic geological model constrained by high-resolution 3D seismic data-application to the Girassol field, offshore Angola," in *SPE Annual Technical Conference and Exhibition*, Anaheim, California, U.S.A., Nov 2007.
- [22] M. Varga, A. Schaaf, and F. Wellmann, "GemPy 1.0: open-source stochastic geological modeling and inversion," *Geoscientific Model Development*, vol. 12, no. 1, pp. 1–32, 2019.
- [23] A. Cáceres, X. Emery, L. Aedo, and O. Gálvez, "Stochastic geological modeling using implicit boundary simulation," in *Proceedings of the 2nd International Seminar on Geology for the Mining Industry GEOMIN*, p. 21, Antofagasta, Chile, 2011.
- [24] O. Rashad, A. N. El-Barkooky, A. El-Araby, and M. El-Tonbary, "Deterministic and stochastic seismic inversion techniques towards a better prediction for the reservoir distribution in NEAG-2 Field, north Western Desert, Egypt," *Egyptian Journal of Petroleum*, vol. 31, no. 1, pp. 15–23, 2022.
- [25] W. B. Zhang, T. Z. Duan, and Y. F. Liu, "Application status and development trend of quantitative geological modeling technology," *Geological Science and Technology Information*, vol. 38, no. 3, pp. 264–275, 2019.
- [26] Y. Lin, G. Zhang, M. Huang, and B. Wang, "Stochastic simulation and inversion method based on random medium theory and gradual deformation algorithm," in *SEG/AAPG/SEPM First International Meeting for Applied Geoscience & Energy*, Denver, Colorado, USA, Sep-Oct 2021OnePetro.
- [27] G. Latouche and V. Ramaswami, "Introduction to Matrix Analytic Methods in Stochastic Modeling," in *Society for Industrial and Applied Mathematics*, United States, Technometrics, 1999.

- [28] M. Finkelstein and J. H. Cha, *Stochastic Modeling for Reliability. Shocks, Burn-in and Heterogeneous Populations. Springer Series in Reliability Engineering*, Springer, London, 2013.
- [29] D. J. Andrews, "A stochastic fault model: 1. static case," *Journal of Geophysical Research: Solid Earth*, vol. 85, no. B7, pp. 3867–3877, 1980.
- [30] L. Zhu, M. Li, C. Li et al., "Coupled modeling between geological structure fields and property parameter fields in 3D engineering geological space," *Engineering Geology*, vol. 167, pp. 105–116, 2013, (In Chinese).
- [31] L. Y. Faust, "A velocity function including lithologic variation," *Geophysics*, vol. 18, no. 2, pp. 271–288, 1953.
- [32] S. G. Ghedan, B. M. Thiebot, and D. A. Boyd, "Modeling original water saturation in the transition zone of a carbonate oil reservoir," *SPE Reservoir Evaluation & Engineering*, vol. 9, no. 6, pp. 681–687, 2006.
- [33] J. Amyx, M. D. Bass, and L. R. Whiting, *Petroleum Reservoir Engineering Physical Properties*, McGraw-Hill Companies, 1960.
- [34] Y. Yongliang, "A method of establishing oil saturation model based on J function," *Journal of Colleges and Universities of Petrochemical Industry*, vol. 27, no. 5, pp. 69–71, 2014.
- [35] C. Chen, H. Cai, H. J. Liao, D. W. Qin, B. Chen, and X. Huang, "Geological modeling method of saturation constrained by J function in offshore oil and gas fields," *Petroleum Geology and Engineering*, vol. 30, no. 1, pp. 103–105, 2016.
- [36] J. M. Mayer, D. Stead, I. de Bruyn, and M. Nowak, "A sequential Gaussian simulation approach to modelling rock mass heterogeneity," in *48th US Rock Mechanics/Geomechanics Symposium*, Minneapolis, Minnesota, June 2014.
- [37] P. H. Widjaja and D. Noeradi, "3D properties modeling to support reservoir characteristics of W-ITB field in Madura Strait area," *Bulletin of the Marine Geology*, vol. 25, no. 2, pp. 77–88, 2016.
- [38] M. J. King, K. S. Burn, P. Wang et al., "Optimal coarsening of 3D reservoir models for flow simulation," *SPE Reservoir Evaluation & Engineering*, vol. 9, no. 4, pp. 317–334, 2006.

## Research Article

# A Method to Improve Computational Efficiency of Productivity Evaluation with Rectangular Coalbed Methane Reservoir

Li Chen <sup>1</sup>, Sun Lichun,<sup>1</sup> Sun Hansen,<sup>1</sup> Feng Ruyong,<sup>1</sup> Wang Cunwu,<sup>1</sup> and Zhang Fang<sup>2</sup>

<sup>1</sup>CNOOC Research Institute Ltd., CNOOC Building, Yard 6, Taiyanggong South Street, Chaoyang District, Beijing, China

<sup>2</sup>Exploration and Development Research Institute of Liaohe Oilfield Company, 97 Huibin Street, Xinglongtai District, Panjin City, Liaoning Province, China

Correspondence should be addressed to Li Chen; [lichen1125@foxmail.com](mailto:lichen1125@foxmail.com)

Received 10 January 2022; Revised 8 February 2022; Accepted 19 February 2022; Published 11 March 2022

Academic Editor: Jinjie Wang

Copyright © 2022 Li Chen et al. This is an open access article distributed under the Creative Commons Attribution License, which permits unrestricted use, distribution, and reproduction in any medium, provided the original work is properly cited.

Computational efficiency is the key factor to be considered in the productivity evaluation of rectangular coalbed methane reservoir. There are three main factors affecting the calculation speed: the nonlinearity of the material balance equation of coalbed methane reservoir, the poor conductivity of fractures cannot be considered as infinite conductivity fractures, and the Duhamel convolution is needed in history fitting and boundary image inversion. At present, there is no method to quickly evaluate the productivity of finite conductivity fracture model in rectangular coalbed methane reservoir. Diffusion equation of matrix is generated by the Fick diffusion law. The Darcy seepage law is used to build the seepage equation of fractured system in coalbed methane reservoir. In order to transform the calculation result of infinite conductivity fracture into finite conductivity fracture, fracture conductivity factor is employed in this paper. The applicability of fracture conductivity factor in the whole production process is clarified. It is clear that the factor is prone to calculation errors when the time is small, and the calculation fluctuates greatly. According to the characteristics of the Riley method and discrete method, an accurate and efficient analytical solution calculation process is designed. This will make the calculation results accurate. A production evaluation method of rectangular coalbed methane reservoirs with fractured vertical well and finite conductivity fracture is proposed. The purpose of quickly and accurately predict well production capacity is reached. The geological parameters are recombined, and new coalbed methane reservoir flow parameters are defined. Through parameter sensitivity analysis, the influence of different flow characteristic parameters on gas production is clarified. The dimensionless transfer constant and dimensionless storage capacity affect the appearance time of desorption and diffusion and the storage capacity of the fracture system, respectively. The dimensionless desorption constant describes the strength of desorption and diffusion. The influence of fracture conductivity factor on production is studied. It is clarified that its impacts are different in the early stage and the later stage of production. There is a limit to the fracture conductivity factor. When the limit is exceeded, the fracture conductivity factors no longer affect the production of a single well. The findings of this study can understand the percolation stage of finite conductivity fractured wells with rectangular coalbed methane reservoir and can also guide fracturing design and writing in the field. The research results enrich the productivity evaluation model of coalbed methane reservoir. In the end, a set of production evaluation method is put forward suitable for the well in rectangular coalbed methane reservoirs with fractured vertical well and finite conductivity fracture. In this paper, the influence of fracture conductivity on single well productivity in rectangular coalbed methane reservoir is quantitatively evaluated for the first time. By improving the calculation method and optimizing the calculation path, the productivity evaluation calculation speed of finite conductivity fractured wells in rectangular coalbed methane reservoir is optimized without affecting the calculation accuracy. The new method can be applied directly to productivity evaluation software, which has the significance of popularization.



## 1. Introduction

Coalbed methane is considered as one of the dangerous sources in coal mining. There are two main occurrence modes of CBM in coal seam: adsorbed gas and free gas. Free gas exists in the same form as conventional gas reservoirs. Under the condition of original formation, adsorbed gas is mainly adsorbed in coal rock matrix [1]. With the early drainage of coalbed methane wells, the formation pressure gradually decreases. When formation pressure reaches the critical desorption pressure, the adsorbed gas will gradually separate from the coal rock matrix and become free gas. Current research shows that the porosity of coal seam is small, usually less than 1%. The production contribution of coalbed methane is mainly adsorbed gas. The separation and migration of free gas must be considered when evaluating the capacity of coalbed methane reservoir.

The Langmuir isothermal adsorption equation is used to describe the dynamic balance between free gas and adsorbed gas. Fick's diffusion law is used to describe the process of free gas entering the natural fracture system of coal seam by diffusion. Fick's first diffusion law describes quasisteady-state diffusion, and Fick's second diffusion law describes unsteady diffusion. The analytical solution model of coalbed methane productivity is based on the dual-medium model of conventional gas reservoirs proposed by Warren and Root [2] and De Swaan [3]. Anbarci and Ertekin [4] introduced the Langmuir isothermal adsorption equation based on molecular motion theory to describe the desorption process of adsorbed gas. The Fick diffusion equation of mass transfer was introduced to describe the process of desorption gas migration from coal matrix to fracture system. The introduction of these two equations greatly increases the accuracy of CBM seepage model. With the wide application of reservoir reconstruction technology in unconventional gas reservoir development, Nie et al. [5] and Yu-Long [6] analyzed the analytical solution of the model with artificial fracture and analyzed its flow stage and pressure production change. Li et al. [7] studied the seepage characteristics of coalbed methane reservoir and the productivity characteristics with the presence of stimulated reservoir volume. Fu [8] studied the influence of hydraulic fracturing of coal seam on roof rupture and instability by physical simulation experiment. Based on the production characteristics of coalbed methane wells in Hancheng field, Zhiming et al. [9] summarized three typical models of coalbed methane production. Jun et al. [10] explored the geological control factors that govern the productivity of coalbed methane wells on a small scale. By using the method of geological analysis and grey correlation analysis, the geological and drainage data of 26 coalbed methane production wells over 5 years in Zhengcun block were systematically analyzed. Based on the basic unit of the dual-pore model, Long and Rigui [11] deduced the shape factors suitable for the dual-pore model of coalbed methane reservoir by considering the Darcy flow, molecular diffusion movement, gas desorption effect, slippage effect, and other seepage mechanisms. Lijun et al. [12] put forward the concept of controllable horizontal well design, realizing the design objectives of controllable well, easy to transform, fast

and efficient, and widely adaptable. Bo et al. [13] systematically described the key drilling technology successfully implemented for tree-like horizontal well, which provides a new means for the efficient development of coalbed methane. In recent years, nitrogen foam fracturing has been used in more and more CBM wells, and good results have been achieved. Nitrogen foam fracturing can increase the conductivity of fractures.

Wei [14] constructed a conceptual model of discrete fracture network using unstructured perpendicular bisection grid, established a mathematical model considering shale gas reservoir permeability, Darcy flow, diffusion, and adsorption/desorption stress sensitivity, derived and obtained nonlinear numerical equation of production decline, obtained production decline curve, and identified the flow stage of the model. Li X. et al. [15] evaluated the productivity of nitrogen foam fracturing CBM wells through production data analysis and found that nitrogen foam fracturing had significantly better effect than hydraulic fracturing. Based on logging, experimental testing, and drainage data of a research area in Qinshui Basin, Qiao et al. [16] carried out research on coalbed methane reservoir productivity prediction technology and calculated the weight of each reservoir parameter affecting coalbed methane reservoir productivity through grey correlation analysis method. A polynomial exponential model is established by using four parameters of gas content, ash content, porosity, and permeability to predict coalbed methane reservoir productivity. Li [17] introduced a special quasitime function to solve the nonlinear problem of CBM material balance equation. Using the newly defined parameters to characterize the asymmetry of hydraulic fractures, the productivity evaluation model and its analytical solution with different degrees of symmetry of fractures are obtained. The permeability of coalbed methane reservoir is low according to well test. The seepage range of coalbed methane wells for hydraulic fracturing is almost limited to the rectangular area with hydraulic fracture as the center line. At present, the hydraulic fracture in the model proposed by most scholars is a hyperpermeability channel. The fracture is assumed to have infinite conductivity, with fluid from the reservoir instantaneously flowing into the wellbore with equal flow throughout the fracture and no pressure drop. Actual hydraulic fractures do not have infinite conductivity. Especially for the soft stratum such as coal seam, the hydraulic fracture conductivity is generally small. Fracture conductivity should be considered in the evaluation of single well productivity and gas reservoir development potential. In productivity evaluation, the finite conductivity characteristics of rectangular boundary and fracture will bring a huge amount of calculation. The increase of calculation will affect the application of the model in gas reservoir development.

Previous studies mainly focused on circular boundary and rarely involved rectangular boundary. But according to the seismic data, rectangular boundary is more common in coal seam. Taking the no. 1 coalbed methane block as an example, it is found that the fracture conductivity coefficient of fractured vertical wells is generally between 1 and 10, and 38% of wells are suitable for rectangular boundary model.

Under the influence of reservoir structure, fracture conductivity coefficient of fractured vertical wells in no. 2 coalbed methane block is generally below 5, and 27% of wells are suitable for rectangular boundary model. Based on the rectangular boundary, this paper increases the applicability of the model and enriches the productivity evaluation model of coalbed methane. In addition, previous studies mainly focused on increasing the accuracy of the model while ignoring the calculation speed of the model. However, due to the complexity of coalbed methane, the calculation amount of the productivity evaluation model is increased, so the previous model is still in the theoretical stage, with few applications. In this paper, the fracture conductivity conversion factor is introduced to optimize the calculation path, avoid the error caused by the fracture conductivity conversion factor, and greatly increase the calculation speed. The model presented in this paper can be embedded into current productivity evaluation software to achieve direct application.

First, the methodology is presented. Then, the gas migration model in the matrix was determined by the Langmuir equation and Fick diffusion law. The gas flow model in the natural fracture system was determined by the flow material balance equation, and the fracture conductivity conversion factor was introduced to solve the seepage problem of finite conductivity fractures. Then, the conclusion is analyzed, including the influence of fracture conductivity on production and the sensitivity of parameters. The calculation path of capacity evaluation is optimized, and the calculation speed is increased without affecting the calculation accuracy. Finally, the model is used to fit the historical production data and forecast the future production of a coalbed methane well in Bowen Basin.

## 2. Methodology

In order to simplify the seepage model, important assumptions need to be made:

- (1) The gas reservoir is a constant temperature
- (2) The properties of each point in the gas reservoir are consistent
- (3) Hydraulically fractured vertical wells are located in the middle of the gas reservoir (Figure 1).
- (4) Gas is desorbed from the matrix and diffused into the natural fracture system. The Darcy flow is followed in a natural fracture system (Figure 2)
- (5) Hydraulic fracture is a finite conductivity fracture
- (6) Vertical well production mode is constant pressure production or constant flow rate production
- (7) The coalbed methane reservoir is rectangular with a closed boundary or a constant pressure boundary
- (8) Unsteady and quasisteady gas diffusion occurs in the matrix micropore system of coal seam (Figure 3)
- (9) The gas reservoir does not percolate vertically

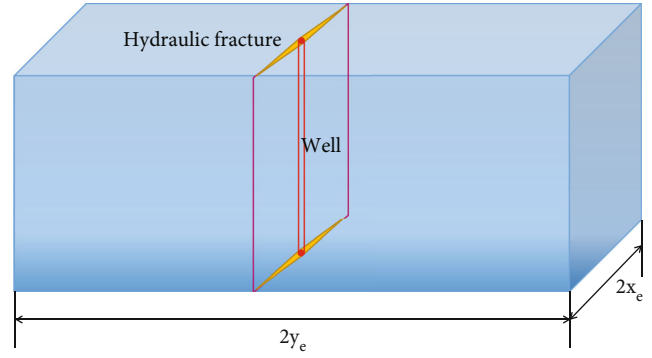


FIGURE 1: Hydraulically fractured wells located in the middle of the rectangular coalbed methane reservoir.

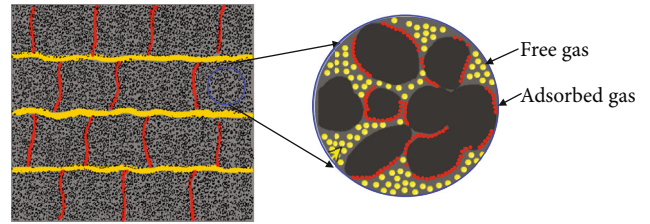


FIGURE 2: The adsorbed gas and free gas in coalbed methane.

**2.1. Model Establishment and Solution.** Anbarci and Ertekin [4] proposed a coalbed methane reservoir seepage model based on the conventional double porosity model. In this model, the fracture is an infinite conductivity fracture. In this article, fractured well with finite conductivity in rectangular-shaped coalbed methane reservoirs was discussed, using the spherical matrix to describe the transient steady state sorption and using the cubic matrix to describe the pseudosteady-state sorption.

**2.2. Modeling Flow in the Nature Fracture.** Free gas and desorbed gas flow together in coalbed methane reservoirs are different from conventional gas reservoirs. This makes the material balance equation become nonlinear equation. The material balance equation in the nature fracture is as follows:

$$\frac{1}{r} \frac{\partial}{\partial r} \left( r \frac{p}{\mu z} \frac{\partial p}{\partial r} \right) = \frac{\phi c_g p}{kz} \frac{\partial p}{\partial t} + \frac{p_{sc} T}{kT_{sc}} \frac{\partial V}{\partial t}. \quad (1)$$

Equation (1) is a nonlinear equation. At present, there is no accurate analytical solution for nonlinear equation, so it needs to be solved by numerical method.

$$\frac{1}{r} \frac{\partial}{\partial r} \left( r^2 D \frac{\partial C}{\partial r} \right) = \frac{\partial C}{\partial t}, \quad (2)$$

$$\frac{\partial C}{\partial t} = D \frac{\partial^2 C}{\partial r^2}.$$

Associated with diffusion equation and dimensionless transformation, the solution of formula (1) in Laplace space is as follows:

$$\frac{1}{r_D} \frac{\partial}{\partial r_D} \left( r_D \frac{\partial \widetilde{\psi}_D}{\partial r_D} \right) = f(s) \widetilde{\psi}_D. \quad (3)$$

Unsteady diffusion:

$$f(s) = \omega s + \frac{(1-\omega)}{\lambda} \sigma \left( \sqrt{\lambda s} \coth \sqrt{\lambda s} - 1 \right). \quad (4)$$

Quasisteady-state diffusion:

$$f(s) = \omega s + \frac{(1-\omega)}{\lambda} \sigma \frac{s}{s+1/\lambda}. \quad (5)$$

**2.3. Fracture Conductivity Conversion Factor.** In rectangular CBM reservoir model with finite conductivity fractures, the computational speed is the key to application. In order to consider the conductivity of fracture without increasing the amount of calculation, the fracture conductivity conversion factor can be used to transform the calculation results of infinite conductivity fracture to finite conductivity fracture. The transformation formula is [18] as follows:

$$s \widetilde{p}_{wD} = s \widetilde{p}_{wDinf} + s \widetilde{f}(C_{fD}). \quad (6)$$

$\widetilde{p}_{wDinf}$  is the calculation result of infinite conductivity fracture, and  $\widetilde{f}(C_{fD})$  is convert conductivity factor for fracture. According to the calculation results of Riley [18], this factor can be expressed as follows:

$$s \widetilde{f}(C_{fD}) = 2\pi \sum_{n=1}^{\infty} \frac{1}{n^2 \pi^2 C_{fD} + 2\sqrt{n^2 \pi^2 + s}} + \frac{0.4063\pi}{\pi(C_{fD} + 0.8997) + 1.6252s}. \quad (7)$$

### 3. Result and Discussion

**3.1. Analysis of Fracture Conductivity.** Even under the condition of the same geological characteristics, the hydraulic fracture conductivity is different. Due to the large gas flow in the early stage, fracture conductivity becomes the bottleneck of single well productivity. The influence mainly occurs in the early stage of production. With the increase of fracture conductivity, energy consumption decreases and single well productivity increases at the same flow rate. When the dimensionless conductivity factor of fracture is about 12, the conductivity of fracture almost no longer affects the productivity of single well. With proper fracturing technology, the conductivity factor of hydraulic fracture can easily reach 12. There is no need to increase the fracturing scale to pursue fracture conductivity. For most CBM reservoirs, the dimensionless fracture conductivity factor is usually less than 12, and its impact on single well productivity must be considered during productivity evaluation (Figure 4).

**3.2. Parameter Sensitivity Analysis.** In order to better describe the flow in the reservoir, it is necessary to recombine the geological parameters into flow characteristic parameters. Flow characteristic parameters mainly include dimensionless transfer constant  $\lambda$ , dimensionless storage

capacity  $\omega$ , and dimensionless desorption constant  $\sigma$ . In addition, always with the well storage coefficient and well skin factor, these five parameters are used to analyze the pressure sensitivity of coalbed methane. The basic parameters of sensitivity analysis are shown in Table 1. Parameter sensitivity analysis based on the closed gas reservoir model.

The dimensionless transfer constant  $\lambda$  is directly proportional to permeability and analytical time constant and inversely proportional to reservoir porosity, gas viscosity, fracture half-length, and gas compressibility. Because the desorption time is inversely proportional to the dimensionless desorption constant, dimensionless transfer constant is inversely proportional to the desorption intensity. The larger the dimensionless transfer constant is, the later the “descent” feature in the pressure curve appears, and the later the desorption and diffusion control stage appear. Therefore, dimensionless transfer mainly affects the time when desorption and diffusion occur and has a weaker effect on the degree of desorption and diffusion (Figure 5(a)).

The dimensionless storage capacity  $\omega$  is directly proportional to the porosity of the fracture system and reflects the storage capacity of fracture system. Contrary to the conventional dual-porous media model reflecting the storage capacity of the matrix, the dimensionless storage capacity represents the proportion of gas flow in the reservoir from the fracture system. When the dimensionless storage capacity is high, the more gas from the fracture system is produced, and the less gas will be diffused from the matrix. In this case, the desorption and diffusion of coalbed methane reservoir are not obvious. The pressure derivative curve is different than that of conventional dual porosity reservoir, and the “downward concave” shape of pressure derivative becomes smaller. In the early stage, as the seepage occurs in natural fractures, the pressure drop decreases for gas reservoirs with large storage capacity, the linear flow time increases, and the desorption diffusion is delayed and the time becomes shorter (Figure 5(b)).

The dimensionless desorption constant  $\sigma$  mainly describes the strength of desorption and diffusion. It is directly proportional to Langmuir volume, production rate, and original reservoir pressure. The original reservoir pressure determines the Langmuir volume. The greater the original pressure, the gas adsorbed in the coal seam will increase. Therefore, Langmuir volume also represents the ability of gas desorption in the matrix to recharge the fracture system. The larger the Langmuir volume, the faster the gas concentration changes in the reservoir. All of these will lead to the enhancement of desorption and diffusion, which makes the “sag” phenomenon of the pressure derivative curve stronger (Figure 5(c)).

The well storage coefficient mainly affects the early stage of production. Well storage coefficient reflects the size of well storage effect. It determines both the degree and the duration of well storage effect. If the well storage effect is too large, it will cover the linear flow stage and make the production directly enter into the CBM desorption and diffusion stage (Figure 5(d)).

The skin factor mainly affects the pressure drop in the transition stage of well storage. After the wellbore storage

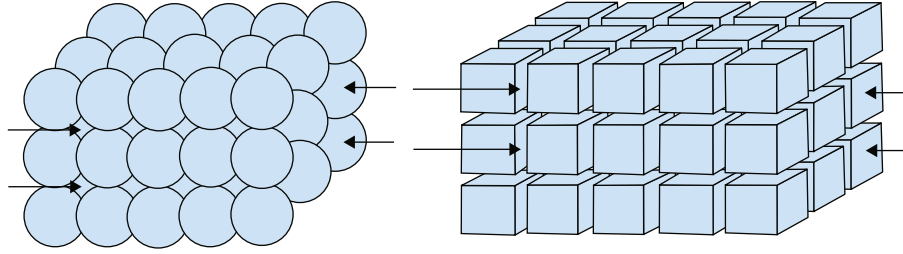


FIGURE 3: Unsteady state (a) and pseudosteady state (b) sorption/diffusion.

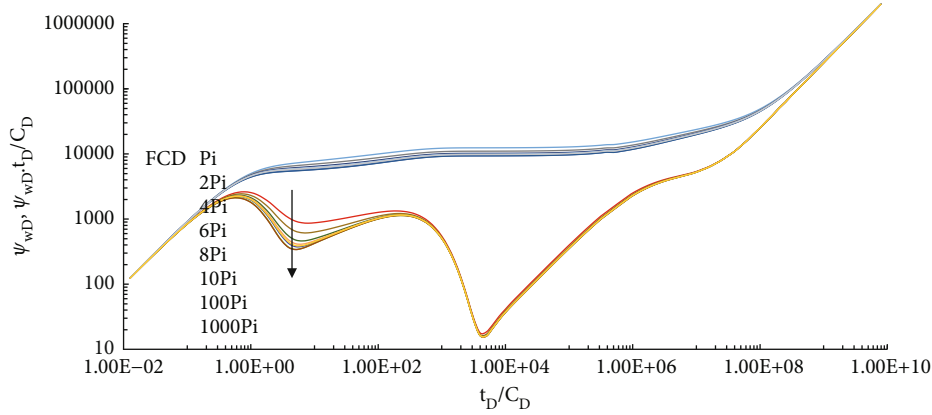


FIGURE 4: Different dimensionless bottomhole pressure with different dimensionless fracture conductivity.

TABLE 1: The basic parameters with sensitivity analysis.

$\sigma$	$\omega$	$\lambda$	$C_D$	$s$	$x_{eD}$	$\gamma_{eD}$
500	0.5	500	10	5	100	50

phase, it evolves into the wellbore transition phase. The skin effect appears. Skin factor mainly affects the transition stage between well storage stage and unsteady flow stage. The skin factor represents the degree of contamination near the well. At the same flow rate, an increase in skin factor will lead to an increase in near-wellbore pressure drop (Figure 5(e)).

**3.3. Verification of the Fracture Conductivity Conversion Factor.** Figure 6 shows comparison of calculation time under different fracture conductivity conditions. The Riley method (1991) and the discrete method are for the same mathematical model. It can be seen from the figure that the Riley method has a greater computational speed advantage. The average calculation speed of the Riley method is 19 times fast as that of discrete method. This is because the Riley method does not need to discretize the cracks during the calculation process. So the Riley method does not need to solve a system of equations at every time step. This greatly saves calculation time. In addition, with the increase of fracture conductivity, the error between the Riley method and the discrete method gradually decreases. As the fracture conductivity increases from 1 to 100 (Figure 6), the errors between model A and model B are 2.8%, 1.6%, 1%, 0.6%, and 0.4%, respectively. All the errors were less than 3% (note: fitting error is defined as  $|\text{value}_{\text{Riley method}} - \text{value}_{\text{discrete method}}| / \text{value}_{\text{discrete method}}$ ).

But there are some problems when using the Riley method. The curves of the same color in Figure 7 represent the results of calculations using different methods with the same conversion factor. The curves represent the results of calculation using accurate discrete method. The dotted curve represents the results of calculation using the Riley method. However, when the time is small, the method is prone to errors. When the dimensionless time is less than  $1.0E-4$ , the error caused by the Riley method is larger. When the dimensionless time is more than  $1.0E-4$ , the calculation result of the Riley method is consistent with discrete method. Moreover, when the dimensionless conductivity of the fracture is greater than 100, the results of Riley method and discrete method are consistent. If the fracture conductivity factor is greater than 100, the calculated results of the two methods are consistent. At this time, considering the calculation speed, the Riley method is preferred.

In practice, the Riley method can be combined with discrete method. When the dimensionless time is less than  $1.0E-4$ , more accurate but time-consuming discrete method can be used. In this case, the time is relatively small and does not affect the overall computing speed. If the dimensionless time is greater than  $1.0E-4$ , the Riley method can be used. According to the study in this paper, the accuracy of the Riley method is guaranteed at this time (Figure 8). In this way, the combination of the two methods ensures the accuracy and efficiency of calculation. In addition, the variables in the calculation are dimensionless, so the calculation process is not limited by the geological characteristics of the gas reservoir itself. Before there is dimensional change, it is a purely mathematical problem.

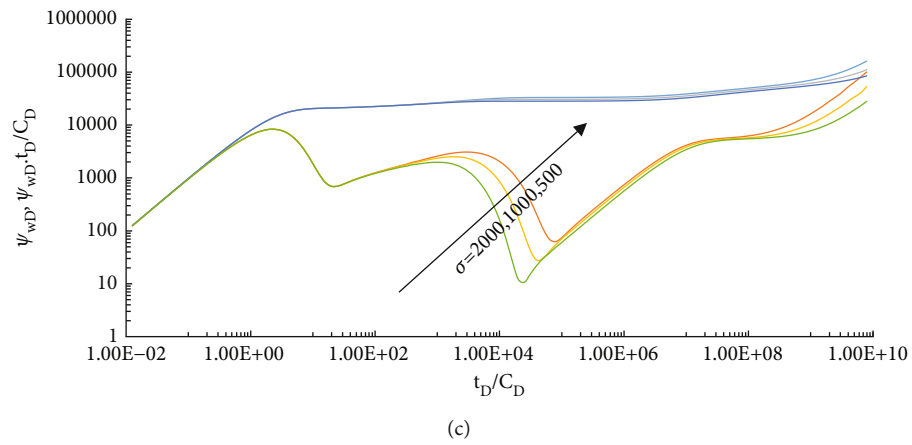
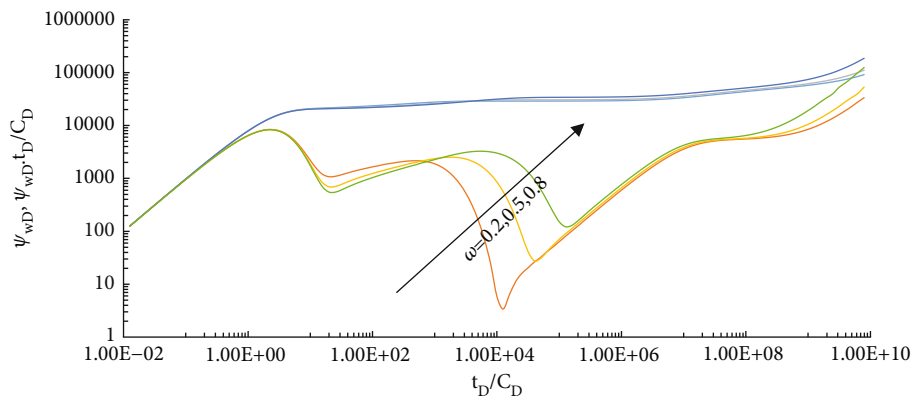
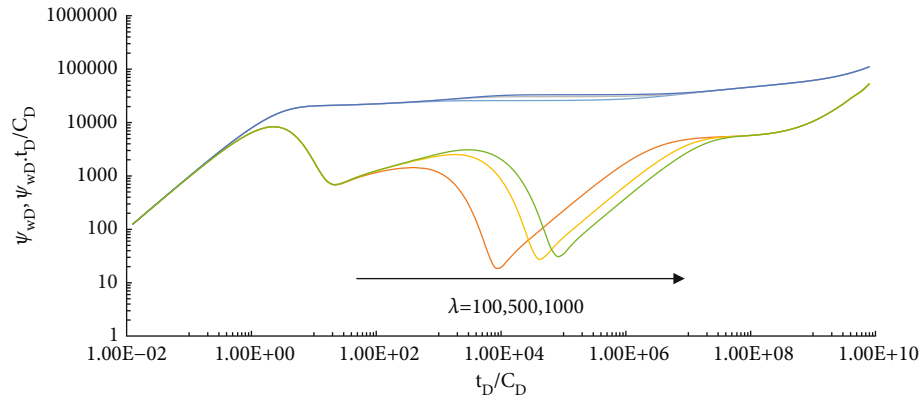
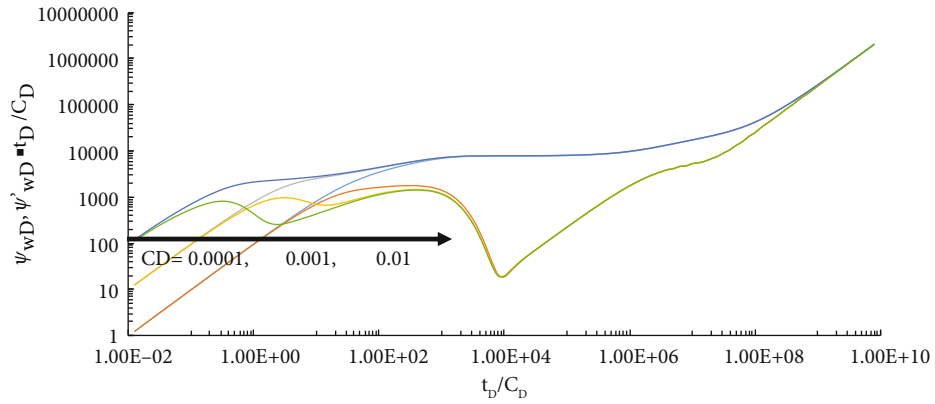
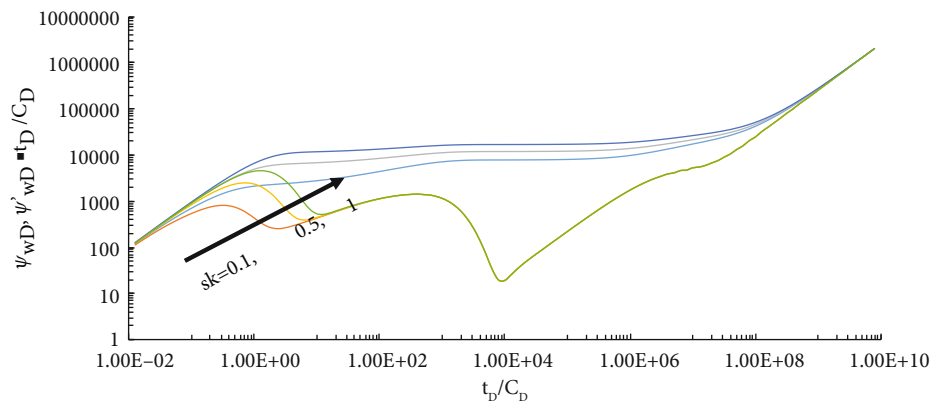


FIGURE 5: Continued.





(d)



(e)

FIGURE 5: (a) Influence of cross-flow coefficient on the pseudopressure and pseudopressure derivative. (b) Influence of storage ratio on the pseudopressure and pseudopressure derivative. (c) Influence of desorption constant on the pseudopressure and pseudopressure derivative. (d) Influence of well storage coefficient on the pseudopressure and pseudopressure derivative. (e) Influence of skin coefficient on the pseudopressure and pseudopressure derivative.

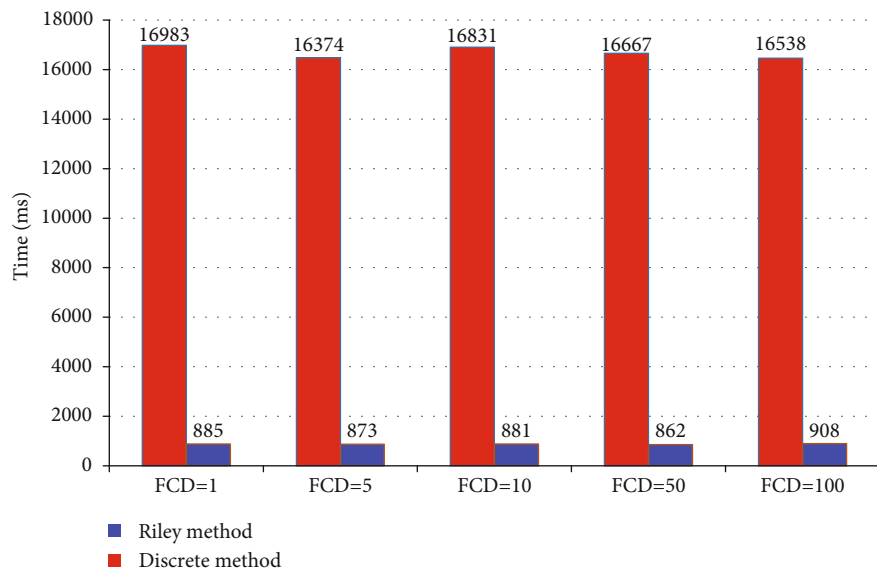


FIGURE 6: Comparison of calculation time between the Riley method and discrete method.

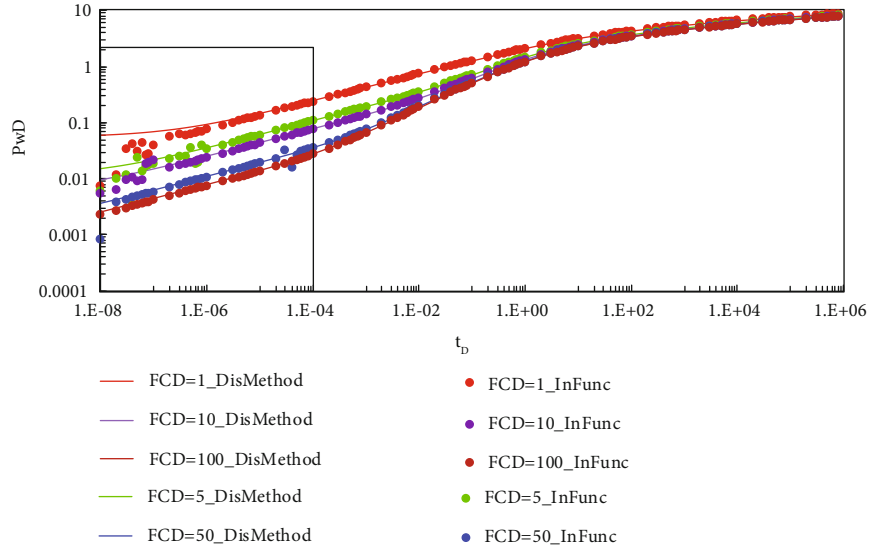


FIGURE 7: The Riley method causes errors when the time is small.

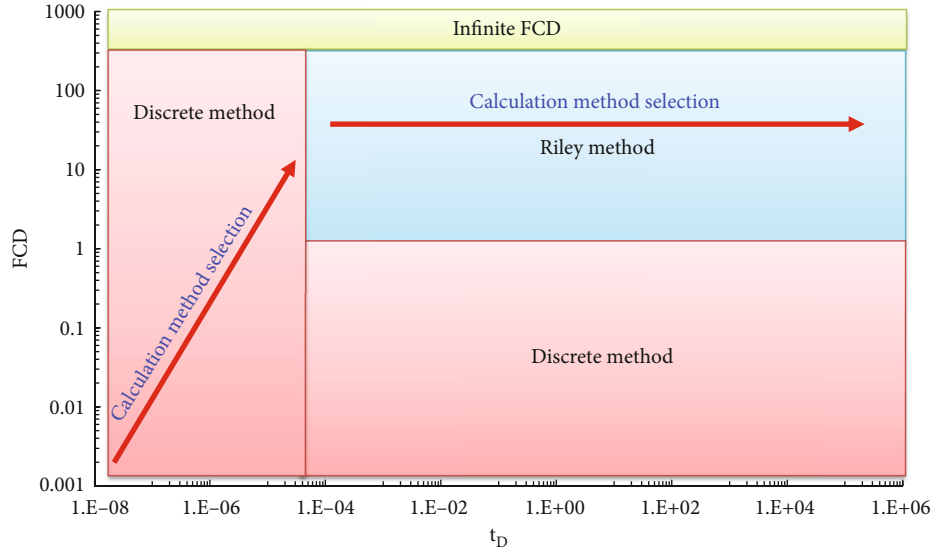


FIGURE 8: The calculation method selection between the Riley method and discrete method.

TABLE 2: Example of single well basic data.

$p_{ic}$ (MPa)	$s$	$k$ (md)	$\rho_g$ ( $\text{g}\cdot\text{m}^{-3}$ )	$x_e$ (m)	$y_e$ (m)	$h$ (m)
2.08	0	3.37	1.47	800	800	10
$R_w$ (m)	$T$ (k)	$\varphi$	$V_L$ ( $\text{cm}^3\cdot\text{g}^{-1}$ )	$L_f$ (m)	$P_L$ (MPa)	$C_f$ ( $\text{kp}^{-1}$ )
0.3	287.15	0.2	9.97	160	1.15	$2.9e^{-6}$

#### 4. Field Application

The example well is a CBM fracturing vertical well in Bowen Basin, Western Australia. The basic data of the well are shown in Table 2. According to the seismic data, there are sealing faults around the well. It can be approximated as a rectangular gas reservoir. The model in this paper is used for productivity evaluation. The Duhamel convolution is

used to fit the well production, accumulated production, and bottomhole flow pressure with the productivity equation. Under the optimal fitting parameters, the fitting error of production is 8.9% (Figure 9), the fitting error of cumulative production is 1.8% (Figure 9), and the fitting error of pressure is 17.7% (Figure 10). The evaluation results are in line with the basic understanding of gas reservoir, and the error is small. Based on the historical matching, the future

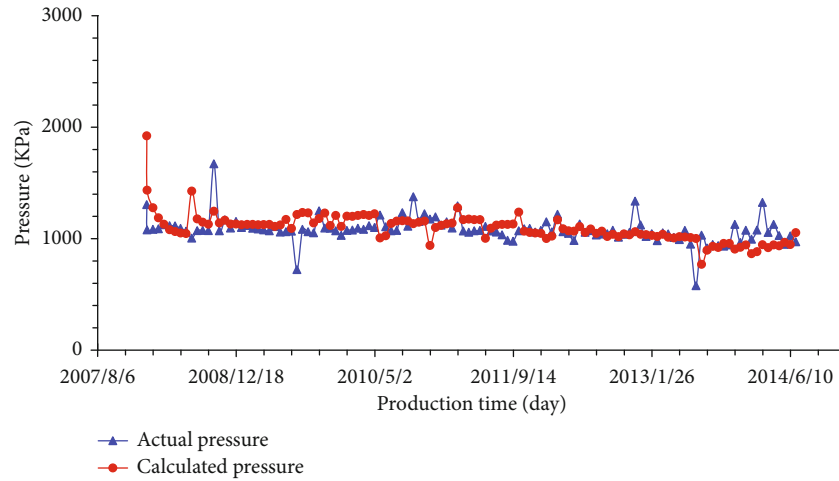


FIGURE 9: Fitting of production and cumulative production in a single well.

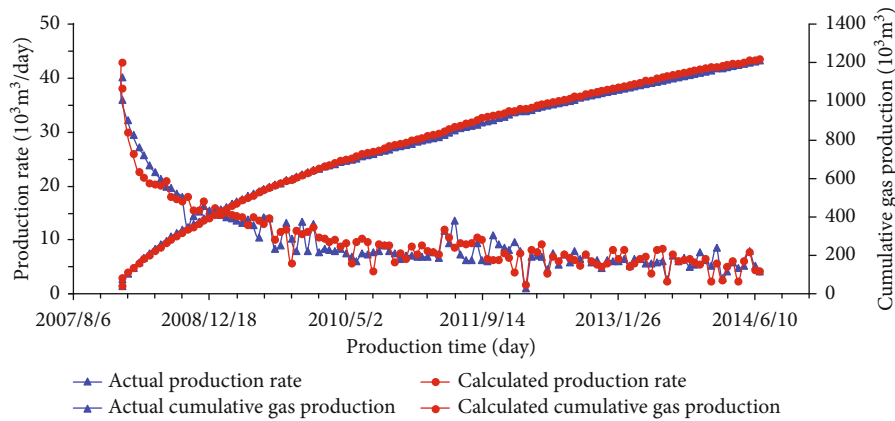


FIGURE 10: Single well pressure fitting.

production of the well can be predicted and the productivity of the well can be evaluated (note: fitting error is defined as  $|\text{value}_{\text{actual}} - \text{value}_{\text{calculated}}|/\text{value}_{\text{actual}}$ ).

### 5. Summary and Conclusions

- (1) The main parameters affecting the pressure curve of CBM can be recombined as dimensionless transfer constant, dimensionless storage capacity, dimensionless desorption constant, well storage coefficient, and skin factor. The dimensionless transfer constant mainly affects the time when desorption and diffusion occur and has a weaker effect on the degree of desorption and diffusion. The dimensionless storage capacity reflects the storage capacity of the fracture system, and the dimensionless desorption constant describes the strength of desorption and diffusion. Well storage coefficient and skin coefficient affect the initial stage of production
- (2) The bottleneck effect of fracture conductivity mainly occurs in the early stage of production. Single well productivity increases with fracture conductivity.

When the dimensionless conductivity factor of fracture is over 12, the conductivity of fracture almost no longer affects the productivity of single well

- (3) By optimizing the calculation method, the productivity evaluation and calculation speed of finite conductivity fractured wells in rectangular coalbed methane reservoir can be significantly improved. The calculation results show that the calculation speed can be improved 18 to 19 times, while the calculation error can be controlled within 3%.
- (4) For vertical wells with low conductivity fractures, the productivity evaluation model of fractured vertical wells with limited conductivity fractures can matched better with the field production data. Under the optimal fitting parameters, the fitting errors of production, cumulative production, and pressure are 8.9%, 1.8%, and 17.7%, respectively. The evaluation results are more accurate and reliable

### Abbreviations

$r$ : Radius of coalbed methane reservoir, m

$p$ :	Gas reservoir pressure, MPa
$\mu$ :	Gas viscosity in the gas reservoir, mpa·s
$Z$ :	Gas deviation factor, dimensionless
$\phi$ :	Reservoir porosity, dimensionless
$c_g$ :	Coal compressibility, MPa <sup>-1</sup>
$k$ :	Reservoir permeability, D
$t$ :	Time variable, h
$p_{sc}$ :	Pressure under standard conditions, MPa
$T$ :	Gas reservoir temperature, K
$T_{sc}$ :	Temperature under standard conditions, K
$V$ :	Average matrix gas concentration, m <sup>3</sup> /m <sup>3</sup>
$C$ :	Volumetric gas concentration in the microspores, m <sup>3</sup> /m <sup>3</sup>
$D$ :	Diffusion coefficient, m <sup>3</sup> /s
$r_D$ :	Dimensionless radius
$\psi$ :	Pseudopressure, MPa <sup>2</sup> /cp
$\psi_D$ :	Dimensionless pseudo-pressure, dimensionless
$\psi_i$ :	Pseudopressure under initial conditions, MPa <sup>2</sup> /cp
$t_D$ :	Dimensionless time variable, dimensionless
$L_f$ :	Half-length of hydraulic fracture, m
$L_D$ :	Dimensionless length, dimensionless
$\tilde{\psi}_D$ :	Dimensionless pseudo-pressure into Laplace place, dimensionless
$s$ :	Laplace variable, dimensionless
$x_{eD}$ :	Dimensionless reservoir length of the $x$ coordinates, dimensionless
$y_{eD}$ :	Dimensionless reservoir length of the $y$ coordinates, dimensionless
$L$ :	Reference length, in this paper $L$ equal to half of the fracture length, m
$p_L$ :	Langmuir pressure, MPa
$C_D$ :	Dimensionless wellbore storage coefficient
$C_{fD}$ :	Dimensionless fracture conductivity
$\tilde{p}_{wD}$ :	Dimensionless bottomhole pressure with finite conductivity fracture
$\tilde{s}\tilde{p}_{wDinf}$ :	Dimensionless bottomhole pressure with infinite conductivity fracture.

### Intermediate Variable

$$\begin{aligned} \sigma &: p_L V_L \tilde{p}_i q_D / (p_L + p)(p_L + p_i)(p_i + p) \\ \Lambda &: \phi \mu c_g + (p_{sc} T \mu z / T_{sc} q_D \tilde{p}_i^2) \\ \omega &: \phi \mu c_g / \Lambda \\ \lambda &: k \tau / \Lambda L_f^2 \\ \gamma &: \sqrt{f(s)} \\ \psi &: 2 \int_0^p (p / \mu z) dp \end{aligned}$$

### Dimensionless

$$\begin{aligned} \psi_D &: (\pi k h T_{sc} / p_{sc} q_{sc} T) (\psi_i - \psi) \\ t_D &: k t / \Lambda L_f^2 \\ L_D &: L / L_f \end{aligned}$$

### Data Availability

The data are all original; if you need any data in the article, please send me an email (email address: lichen1125@foxmail.com).

### Conflicts of Interest

The authors declare no potential conflicts of interest with respect to the research, authorship, or publication of this article.

### References

- [1] J. Seidle, *Fundamentals of Coalbed Methane Reservoir Engineering*, Petroleum Industry Press, Beijing, 2016.
- [2] J. E. Warren and P. J. Root, "The behavior of naturally fractured reservoirs," *Society of Petroleum Engineers Journal*, vol. 3, no. 3, pp. 245–255, 1963.
- [3] A. De Swaan, "Analytic solutions for determining naturally fractured reservoir properties by well testing," *Society of Petroleum Engineers Journal*, vol. 16, no. 3, pp. 117–122, 1976.
- [4] K. Anbarci and T. Ertekin, "A comprehensive study of pressure transient analysis with sorption phenomena for single-phase gas flow in coal seams," in *SPE Annual Technical Conference and Exhibition*, pp. 411–423, New Orleans, Louisiana, 1990.
- [5] R. S. Nie, Y. F. Meng, J. C. Guo, and Y. L. Jia, "Modeling transient flow behavior of a horizontal well in a coal seam," *International Journal of Coal Geology*, vol. 92, pp. 54–68, 2012.
- [6] Z. Yu-Long, Z. Lie-Hui, F. Guo-Qing, Z. Bo-Ning, and K. Bo, "Performance analysis of fractured wells with stimulated reservoir volume in coal seam reservoirs," *Oil & Gas Science and Technology*, vol. 71, pp. 1–18, 2016.
- [7] L. Chen, "Production analysis for fractured vertical well in coal seam reservoirs with stimulated reservoir volume," *Geofluids*, vol. 2021, 12 pages, 2021.
- [8] F. Junhui, "Study and application of influence law of coal seam hydraulic fracturing on rock movement," *Coal Engineering*, vol. 50, no. 1, pp. 56–59, 2018.
- [9] T. Zhiming, L. Peng, L. Na, Y. Wei, and Z. Liang, "Analysis of coalbed methane production characteristics and main geological control factors in Hancheng mining area," *Coal Engineering*, vol. 50, no. 4, pp. 126–131, 2018.
- [10] T. Jun, Z. Yang, Y. Yang, Z. Zhengguang, and L. Shuaishuai, "Analysis on main control factors for production of CBM wells on a smaller scale: a case study on Zhengcun well, Fanzhuang bloc," *Coal Engineering*, vol. 50, no. 5, pp. 82–86, 2018.
- [11] C. Long and X. Rigui, "Derivation and proven the shape factor in unconventional gas reservoir," *Coal Engineering*, vol. 50, no. 7, pp. 147–151, 2018.
- [12] L. Lijun, C. Biwu, L. Zongyuan, Z. Bo, L. Jiafeng, and L. Bin, "Huabei oilfield CBM drilling situation and development direction," *Coal Engineering*, vol. 51, no. 10, pp. 77–81, 2019.
- [13] Z. Bo, L. Yuanyong, S. Chen, C. Shuqing, Z. Wu, and Q. Cunhua, "Research on key drilling technology of CBM tree-like horizontal well," *Coal Engineering*, vol. 51, no. 1, pp. 47–50, 2019.
- [14] M. Wei, Y. Duan, M. Dong, Q. Fang, and M. Dejam, "Transient production decline behavior analysis for a multi-fractured horizontal well with discrete fracture networks in shale gas reservoirs," *Journal of Porous Media*, vol. 22, no. 3, pp. 343–361, 2019.
- [15] X. Li, D. Zhang, and S. Li, "A multi-continuum multiple flow mechanism simulator for unconventional oil and gas recovery," *Journal of Natural Gas Science and Engineering*, vol. 26, pp. 652–669, 2015.

- [16] L. Qiao, P. Wang, L. Chen, X. Ji, Y. Cui, and H. Su, "Productivity prediction of coalbed methane reservoir by logging data based on polynomial index model," *Journal of Chengde Petroleum College*, vol. 23, no. 4, pp. 35–39, 2021.
- [17] C. Li, "Evaluation on productivity of asymmetric hydraulic fractured vertical wells in coalbed methane reservoirs," *Special Oil & Gas Reservoirs*, vol. 28, no. 2, pp. 96–101, 2021.
- [18] M. F. Riley, W. E. Brigham, and R. N. Horne, "Analytic Solutions for Elliptical Finite-Conductivity Fractures," in *SPE Annual Technical Conference and Exhibition*, pp. 6–9, Dallas, Texas, 1991.
- [19] R. Al-Hussainy, H. J. Ramey, and P. B. Crawford, "The flow of real gases through porous media," *Journal of Petroleum Technology*, vol. 1, pp. 624–636, 1966.



## Research Article

# The Viscosity of Methane in Organic Slit Nanopore of Gas-Bearing Shale by Molecular Dynamic Simulation

Dongchen Liu <sup>1</sup>, Xiaofan Chen <sup>1</sup>, Na Jia <sup>2</sup>, Zhimin Du <sup>1</sup>, Yong Tang <sup>1</sup>, Ping Yue <sup>1</sup>, and Yongyi Zhou <sup>3</sup>

<sup>1</sup>State Key Laboratory of Oil and Gas Reservoir Geology and Exploitation, Southwest Petroleum University, Chengdu 610500, China

<sup>2</sup>Faculty of Engineering and Applied Science, University of Regina, Regina, SK S4S0A2, Canada

<sup>3</sup>North China Branch, SINOPEC, Zhengzhou 450006, China

Correspondence should be addressed to Xiaofan Chen; chenxf@swpu.edu.cn

Received 3 November 2021; Revised 5 January 2022; Accepted 18 January 2022; Published 27 February 2022

Academic Editor: Qingwang Yuan

Copyright © 2022 Dongchen Liu et al. This is an open access article distributed under the Creative Commons Attribution License, which permits unrestricted use, distribution, and reproduction in any medium, provided the original work is properly cited.

Non-Darcy flow is observed in the shale gas reservoir because it is rich in organic nanopores. Generally, the permeability of shale gas reservoirs is modified because of non-Darcy flow. However, the viscosity is much less concerned. It has been verified that the viscosity of dilute gas depends on the size of the pore. In this paper, the viscosity of methane in organic slit nanopore is determined with equilibrium molecular dynamics (EMD) simulation. The result shows that the viscosity of bulk methane would decrease with dropping down pressure, while the confined effect would make the viscosity of methane in the organic slit nanopore lesser than that of the bulk phase, and it decreases severely at low pressure. The confined dense gas viscosity model is obtained by theoretical derivation. The EMD results were fitted with this model to obtain the viscosity correction method for dense methane in organic slit nanopores. The dimensionless viscosity ( $\mu_{eff}/\mu_b$ ) would decrease sharply with the Knudsen number between 0.1 and 10. Unlike the confined effect on the dilute gas, the potential contribution of the dense gas and the wall also affects its viscosity. Because of the confined effect on the dense methane, the flow capacity of methane is enhanced 1.5 times at least with the pore being smaller than 10 nm and the pressure being lower than 5 MPa. It means that keeping a low reservoir pressure helps to improve the flow of shale gas. This work can improve the understanding of the importance of gas viscosity with the non-Darcy flow in shale gas reservoirs.

## 1. Introduction

The problem of modeling the transport of fluid in confined spaces has been attracting the attention of scientists and engineers for over a century because of its importance in a variety of applications and industrial interests [1]. Especially, the topic gained attention in the last decades in the petroleum development area as the shale gas reservoir was developed successfully. The flux of gas through the pore is composed of viscous donation and diffusion donation [2]. The transport of gas becomes more complex because of the presence of adsorption [1].

Generally, Darcy's law is used to depict the viscous flow process of fluid in the pore. As shown in equation (1), the permeability and viscosity determine the velocity of the fluid

in the pores at a specific pressure gradient [3]. Permeability is the ability of a porous material to allow fluids to pass through it, which depends on the porosity, tortuosity, connection, shape, and pore sizes of the porous material. The permeability ( $k$ ) of the circular pore and the slit pore can be derived from the Navier–Stokes equation, which are  $r_p^2/8$  and  $w^2/12$ , individually. Viscosity reflects a fluid's resistance to flow under a specific differential pressure [3], which is generally affected by the pressure, temperature, and fluid species.

$$v = -\frac{k}{\mu} \frac{dp}{dx} \quad (1)$$

Most of the shale gas reservoir pores are nanopores that are in the range of 2~50 nm, with pressures between

2~50 MPa and temperatures between 20~140 °C [4, 5]. Darcy's law should be modified in shale gas development because shale gas experiences multiscale flow at shale gas reservoir conditions. Thus, many methods are proposed to modify the permeability of a shale gas reservoir [5–9]. However, there are much fewer concerns about the viscosity of shale gas.

Gas is classified as dilute gas and dense gas by  $\delta$  [10].  $\delta$  is defined as equation (2).

$$\delta = \frac{d}{\sigma}, \quad (2)$$

$$d = \sqrt[3]{\frac{Zk_B T}{p}}.$$

When  $\delta \geq 7$ , the gas is in the dilute regime. As molecular spacing decreases, the dense gas regime develops ( $\delta < 7$ ). For dilute gas, the density of the gas is too small, and the kinetic-potential and potential-potential contributions are zero because the potential shear stress becomes zero. At this time, the viscosity of the dilute gas equals the kinetic-kinetic contributions according to the Chapman–Enskog formula, which is independent of pressure (or density) [11]. Because of the effect of potential, the viscosity of dense gas would increase with pressure (or density) [11]. Several methods for calculating the dense gas viscosity have been proposed [12–15]. Based on the developed viscosity calculation theory [12], a semiempirical formula is proposed [14], which is consistent with the experimentally measured data from 37.8 to 171.2°C and 0.1013 to 55.158 MPa. The standard deviation of calculation is  $\pm 2.69\%$ , and the maximum deviation is approximately 8.99% [14].

The existence of the Knudsen layer would affect the effective viscosity of the fluid. The free path area adjacent to a pore wall is referred to as the Knudsen layer, and the viscosity of the Knudsen layer is less than that in the bulk phase [16]. The effect of the Knudsen layer on the viscosity of a dilute gas was identified [17–23]. The measured viscosity of the dilute gas in the Knudsen layer of nanopores is reported to be smaller than that measured in the bulk phase [20–23], and the effective viscosity value decreases with increasing Knudsen number [17–19]. Beskok found that unless the boundary condition was modified, the Navier–Stokes equation could not depict the velocity profile of the dilute gas in the pore when the Knudsen number is bigger than 0.1. He assumed that the viscosity could be expressed as the Bosanquet-type of approximation with a Knudsen number. Based on this thought, Beskok used the Navier–Stokes equation and general slip boundary condition to fit with the direct simulation Monte Carlo (DSMC) results to get the viscosity of the dilute gas in different shape pores [17]. NEMD simulations were used to mimic the Poiseuille flow of methane in the organic or inorganic pores of shale [24–26]. NEMD showed that the gas flux was improved in the nanopore. Chen et al. concluded that the decrease of viscosity and slip effect led to the improvement of gas flux [25].

Lv et al. got a new viscosity of the dilute gas in the cylindrical pore using the effective volume diffusion

hydrodynamics method to fit with the results of the linearized Boltzmann equation and the BGK model of the Boltzmann equation [19]. Michalis et al. performed DSMC simulations and used the Green–Kubo relationship to calculate the viscosity of dilute nitrogen in the transition regime, the result of which showed that the value of viscosity depended on the Kn value [18]. On the basis of the Green–Kubo relationship, Fei et al. derived an expression of viscosity with the Knudsen number, which was usable when Kn was less than 0.5 [27]. According to the best knowledge of the authors, there is no such theory that derives an analytical equation to describe the viscosity of the dense fluid, not to mention the viscosity of the dense gas in nanopores [28]. Molecular dynamics (MD) simulation is a good method to study the viscosity of the fluid in the nanopores. Both equilibrium molecular dynamics (EMD) and nonequilibrium molecular dynamics (NEMD) can be utilized to calculate the viscosity of the dense fluid in nanopores [11]. The time-related correlation functions, such as the Green–Kubo relations, are usually applied to estimate the fluid (includes dilute gas and dense fluid) transport parameters, such as viscosity, diffusivity, and thermal conductivity, while the transport parameters are expressed as the integrals of time-correlated functions to the corresponding thermodynamic fluxes (stress tensor, velocity, and heat current) [29] in EMD [30–32]. In the NEMD method, through a simulation of the dense gas flow in the pore, the velocity distribution and shear stress across the pore are generated, by which the viscosity of the fluid can be evaluated using Newton's law of internal friction [31–38]. The EMD and NEMD simulation methods can generate the same results [31, 39]. Zhang et al. [30] used the equilibrium molecular dynamics simulation (EMD) to study the viscosity of the methane liquid in silicate pores. The result showed that the viscosity of the methane liquid was affected by the temperature, density, and pore width. In this paper, the EMD method is chosen.

More than 90% composition of the shale gas is methane, which stays in the nanoporous shale in a dense state [40]. It is important to clarify the viscosity of the dense methane gas in the gas-bearing shale to describe the shale gas flow. Gas-bearing shale is rich in organic pores [1, 4]. Therefore, this paper is going to concentrate on the determination of the viscosity of methane at different states (dilute and dense states) in organic nanopores in shale reservoir conditions.

This paper is organized as follows: section 2 provides the calculation detail for the methane viscosity in equilibrium molecular dynamics simulations. In Section 3, the viscosity of methane in the bulk phase is calculated, and the results are compared by applying the Chapman–Enskog theory, the Lee function, and the EMD methods, firstly. After that, the effective viscosity of dense methane in the organic pore is determined using the EMD method. Next, a theory model is promoted to fit the result of the MD simulation. This method uses the experiential controlling coefficient,  $\alpha$ , which reflects the effect of the Knudsen layer on gas viscosity. The value of the coefficient  $\alpha$  is 2.75, which is a little bit bigger than the results of the dilute gas [10, 18, 20]. It may be caused by the interaction of gas and pore wall. The results show that the flow capacity of dense methane in the organic pore would be

improved at low pressure, which indicates that reducing the reservoir pressure helps improve the flow of the shale gas. Finally, the key conclusions are presented in Section 4.

## 2. Molecular Dynamics (MD) Simulations

The LAMMPS<sup>TM</sup> (large-scale atomic/molecular massively parallel simulator) was used to perform the EMD simulations [41].

**2.1. Force Field.** The available force field models for methane include TraPPE-UA [42], TraPPE-EH [43], Optimized Potentials for Liquid Simulations (OPLS) [44], and others. These models can accurately predict the critical parameters, the relations among the pressure-volume-temperature (PVT), viscosity, and the diffusion coefficients of methane. TraPPE-UA is a union atomic model that saves considerable time when compared to other models that calculate at the same scale, and therefore, it is used in this study. Two parallel graphene sheets are used to represent the organic slit pore of the gas-bearing shale [45–47]. The width of the organic pore is adjusted by the distance of two graphene sheets. 12–6 Lennard–Jones potential function (Equation (3)) is used in the intermolecular interaction, and detailed parameters are presented in Table 1. The cutoff radius in the present study is assumed to be  $5\sigma$ .

$$U_{ij}(r_{ij}) = 4\varepsilon_{ij} \left[ \left( \frac{\sigma_{ij}}{r_{ij}} \right)^{12} - \left( \frac{\sigma_{ij}}{r_{ij}} \right)^6 \right]. \quad (3)$$

The interaction potential between the methane molecules and C atoms follows the Lorentz–Berthelot rules and is calculated by equations (4) and (5).

$$\sigma_{ij} = \frac{\sigma_i + \sigma_j}{2}, \quad (4)$$

$$\varepsilon_{ij} = \sqrt{\varepsilon_i \varepsilon_j}. \quad (5)$$

**2.2. Viscosity Calculation.** Using the kinetic theory concept, viscosity can be described in relation to the transfer of the momentum between the different layers of fluid moving at different velocities at the microscopic level [32]. The Green–Kubo function, developed by Green [48] and Kubo [49], can be used to calculate the fluid transportation properties. Shear viscosity can be calculated by the integration of an autocorrelation function of the off-diagonal elements in the stress tensor  $\tau_{\alpha\beta}$ , as shown in equation (6) [29].

$$\mu_{\alpha\beta} = \frac{1}{k_B V T} \int_0^\infty \langle \tau_{\alpha\beta}(t_0) \tau_{\alpha\beta}(t) \rangle dt. \quad (6)$$

The microscopic expression of shear stress is presented in equation (7).

$$\tau_{\alpha\beta}(t) = -\frac{1}{V} \left( \sum_{i=1}^N m v_{\alpha,i} v_{\beta,i} + \sum_{i=1}^{N-1} \sum_{j=i+1}^N r_{\alpha,ij} F_{\beta,ij} \right), \quad (7)$$

TABLE 1: TraPPE-UA potential parameters [42]].

Molecule	Symbol	$M_w$ (g/mol)	$\varepsilon$ (kcal/mol)	$\sigma$ (Å)	$q$ (e)
Methane	CH <sub>4</sub>	16.04276	0.293905	3.73	0
Wall	C	12.0107	0.055604	3.4	0

where  $v_{\alpha,i}$  is the velocity in  $\alpha$  direction of molecule  $i$ . The shear stress of fluid in the pore can be mathematically represented as equation (8).

$$\tau_{\alpha\beta}(t) = -\frac{1}{V} \left( \sum_{i=1}^N m v_{\alpha,i} v_{\beta,i} + \sum_{i=1}^{N-1} \sum_{j=i+1}^N r_{\alpha,ij} F_{\beta,ij} + \sum_{i=1}^N \sum_{j=1}^M r_{\alpha,ij} F_{\beta,ij} \right). \quad (8)$$

For the bulk phase, all the off-diagonal elements in the stress tensor are equal. For the gas confined in the slit pore because of the interaction between the wall and the fluid atoms,  $\mu_{xz}$  and  $\mu_{yz}$  are enhanced compared with  $\mu_{xz}$ . The viscosity of the gas confined in the slit pore can be written as equation (9) [32].

$$\mu = \frac{1}{2k_B V T} \sum_{i=1}^N \int_0^\infty \langle \tau_{xz}(t_0) \tau_{xz}(t) \rangle + \langle \tau_{yz}(t_0) \tau_{yz}(t) \rangle dt. \quad (9)$$

**2.3. The Width of Slit Pore.** Figure 1 shows the typical solid-fluid potential in a slit pore with the physical width  $L$ . Because of the repulsion between the gas and the wall, the gas molecule can only access the region with width  $L'$ .  $L'$  is defined as the accessible pore width, as shown in equation (10), [50] which corresponds to the pore size from the experiment [51]. Therefore,  $L'$  is going to be used to calculate the Knudsen number of simulation data.

$$L' = L - 2z_0 + \sigma_f. \quad (10)$$

$L$  is the physical width of the pore, which is the distance between the center of the atoms at the surface of the two walls, Å;  $\sigma_f$  is the effective collision radius of the fluid, and Å;  $z_0$  is the distance at which the solid-fluid potential is zero. The potential distribution of methane in the slit pore is counted by moving a methane molecule in the pore, and the  $z_0$  is 3.03 Å for the pore with 10 Å width and 3.05 Å for pore with a width between 25~400 Å.

**2.4. Simulation Details.** The workflow to calculate the viscosity of confined methane by molecular simulation is shown in Figure 2.

The viscosity of methane at the temperature of 343 K, the pressure from 1 MPa to 16 MPa, and the in-pore width from 1 nm to 40 nm was simulated. The length and width of the slit pore were 4.26~42.6 nm and 4.92~49.2 nm and were adjusted so that a sufficient number (>600) of methane molecules was contained in the box. Figure 3 shows a snapshot of the simulation to illustrate the geometry of the system. For the simulation of the methane molecules inside the channel, the confinement was only in

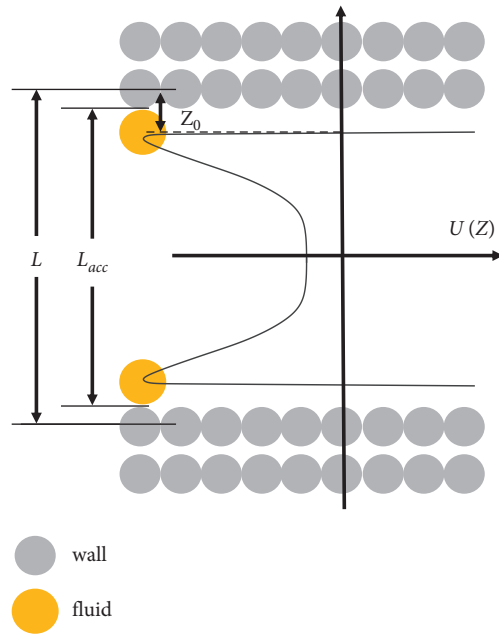


FIGURE 1: Definition of the accessible pore width  $L'$  and the physical pore width  $L$ .

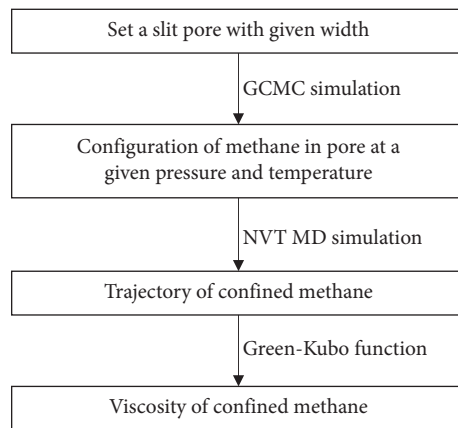


FIGURE 2: The sketch of workflow to calculate the viscosity of confined methane by molecular simulation.

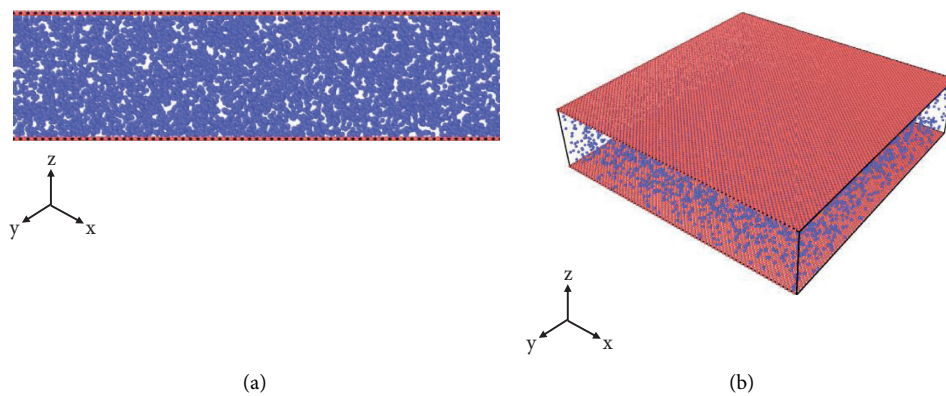


FIGURE 3: Snapshots of methane in slit nanopore (blue: methane atoms, red: C atoms). (a) Slit pore model profile. (b) Slit pore model 3D diagram.

the  $z$ -direction, perpendicular to the channel walls, and the periodic boundary conditions were applied in the  $x$ - and  $y$ -direction.

Firstly, the grand canonical ensemble Monte Carlo (GCMC) method is used to get a configuration of methane in a specific pore under a defined temperature and pressure. The GCMC method simulates gas molecules in the pore exchange with an imaginary ideal gas reservoir at the specified temperature and chemical potential ( $\mu$ ) [52]. It also attempts Monte Carlo (MC) moves (translations and molecule rotations) within the simulation cell or region. Eventually, the potential and temperature of the gas in the pores are equal to the imaginary ideal gas reservoir. The chemical potential is related to pressure ( $p$ ) and fugacity coefficient ( $\phi$ ) as shown in Appendix A. The fugacity coefficient is obtained from the RK EOS in Appendix B. 0.1 to 1 million Monte Carlo move steps are run to get equilibrium, and then 1 million Monte Carlo move steps are run to the product equilibrium configuration. Secondly, the average configuration of GCMC in the production process is set as the initial configuration in the NVT ensemble molecular dynamic simulation. At the NVT ensemble, the number of molecular and system volume, the number of molecules, and the volume of the simulation box remain constant. The system temperature is controlled at a defined value by the Nose–Hoover method [32]. The equation of motion is integrated using velocity-Verlet scheme in every time step until the system achieves a steady-state with time running. In this study, the system is run to reach equilibrium in the last 4 ns, with each time step of 1 fs. Finally, the stress correlation function data is collected after equilibrium is acquired. The Green–Kubo equation is used to calculate the viscosity. The dump time ( $T_d$ ), which is the integration upper bond of the Green–Kubo equation, is a vital parameter to calculate viscosity. Theoretically, it is infinity. As emphasized by Stadler et al., the statistical error increases very rapidly [53]. Some authors proposed to choose dump time as the time for which the TAF first crosses the zero value [54]. In this paper, the dump time is correctly and suitably chosen by trying to assume the continuity of the functions and of their derivatives. Using this criterion, the dump time was chosen, which ranged from 3000 to 16,000 fs for different cases in this study. The sampling interval is 10 steps. The collection time is 400 times the dump time. To obtain accurate viscosity data, each data point was the average of 10 independent simulation outcome results [55].

### 3. Results and Analysis

**3.1. Bulk Gas Viscosity.** Bulk methane viscosity at different pressures and 343 K was calculated using the Chapman–Enskog formula in Appendix C, the Lee equation in Appendix D<sub>2</sub> and the molecular simulation method. As Figure 4 shows, the methane viscosity varied slightly at low-pressure ranges but increased in high-pressure ranges. The results of the MD method matched well with the experimental data reported by NIST values [56], demonstrating that the MD simulation results were valid and reliable at shale gas reservoir conditions.

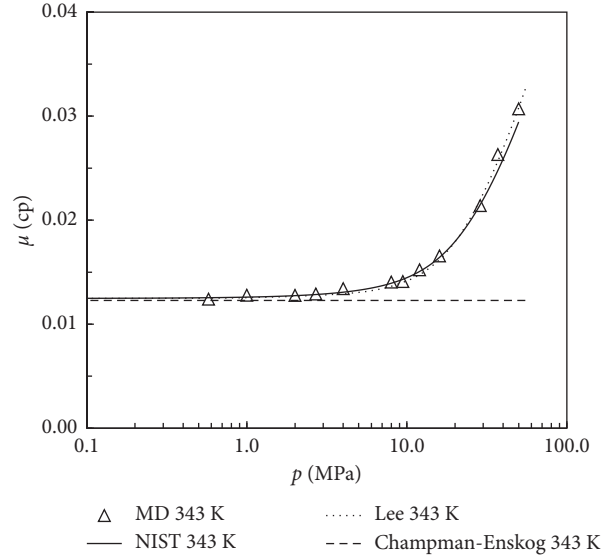


FIGURE 4: Comparison of bulk methane viscosity results by using different methods.

**3.2. Gas Viscosity in Slit Nanopore.** The effective gas viscosity for different pore widths at 1, 2, 4, 8, 12, and 16 MPa was simulated using the MD method described in Section 2, and the results are plotted in Figure 5.

Confine spaces may decrease the effective viscosity of methane. In the pore, the effective viscosity of gas decreased with the decreasing pore width, while in the smaller pores, the pore width has more effect on effective gas viscosity. Figure 6 reflects that the confined effect would make the effective viscosity of methane decrease at least 10% for pore size less than 40 nm when the pressure is 4 MPa. It means that the confined effect on viscosity should be paid more attention to. The viscosity change rate increases as pressure decreases. For small pores, the trend is even more pronounced.

There are two differences in effective viscosity between bulk gas and confined gas. Firstly, the effective viscosity of the confined gas decreases more rapidly than the bulk phase with decreasing pressure. Secondly, while the viscosity of the bulk gas is independent of pressure when the pressure is lower than 2 MPa, the viscosity of the confined gas decreases rapidly with decreasing pressure. The reasons for these differences are complex and will be further analyzed in the next section.

**3.3. The Relationship between Viscosity and Knudsen Number ( $Kn$ ).** The shear stress of fluid in the pore can be mathematically represented as equation (11).

$$\tau_{\alpha\beta}(t) = -\frac{1}{V} \left( \sum_{i=1}^N m v_{\alpha,i} v_{\beta,i} + \sum_{i=1}^{N-1} \sum_{j=i+1}^N r_{\alpha,i,j} F_{\beta,i,j} + \sum_{i=1}^N \sum_{j=1}^M r_{\alpha,i,j} F_{\beta,i,j} \right). \quad (11)$$

There are three major components contributing to the above equation: kinetics contribution, potential contribution, and wall contribution.



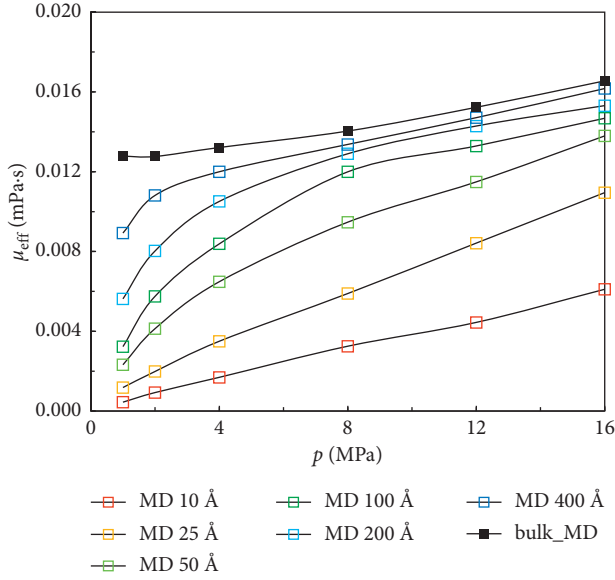


FIGURE 5: The gas viscosity in the slit pore with pressure for different width pores at 343.15 K (the symbols denote the viscosity of methane in organic slit nanopore. Lines are drawn as a guide to the eye).

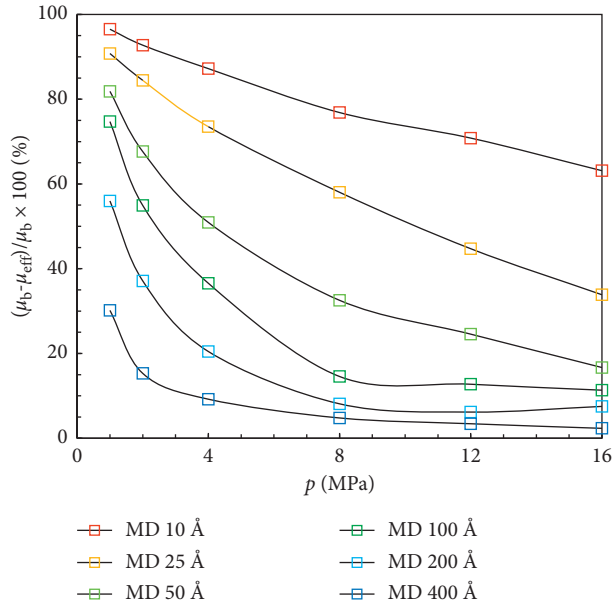


FIGURE 6: The gas viscosity changes rate in the slit pore with pressure for different width pores at 343.15 K (the symbols denote the viscosity of methane in organic slit nanopore. Lines are drawn as a guide to the eye).

In equation (12), which combines equation (11) with equation (6), the viscosity is divided into several different contribution groups.

$$\begin{aligned} \mu(p, T, L) = & \mu_{kk}(T, L) + \mu_{kp_g}(\rho, T, L) + \mu_{p_g p_g}(\rho, T, L) \\ & + \mu_{kp_w}(\rho, T, L) + \mu_{p_g p_w}(\rho, T, L). \end{aligned} \quad (12)$$

In equation (12), there are six viscosity contributions that depended on temperature and density. When the density

limits to 0, the effective viscosity of the dilute gas becomes  $\mu_{kk}$ . In this limit, the other terms on the right-hand side of equation (12) are zero because the potential shear stress becomes zero.  $\mu_{kp_g}$  and  $\mu_{p_g p_g}$  are the potential gas viscosities that are dependent on the potential shear stress between the gas molecules.  $\mu_{kp_w}$  and  $\mu_{p_g p_w}$  depend on the potential shear stress between the gas and the wall.

Because of the presence of the Knudsen layer, the effective viscosity of the dilute gas reduces and decreases with increasing the Knudsen number, which is expressed as a function of the Knudsen number equation (13).  $\alpha$  is the viscosity coefficient reflecting the effect of the Knudsen effect on viscosity, which is affected by the shape of the pore and is taken as 2 for slit pores [18].

$$\mu_{eff} = \mu_{kk} = \mu_0(T) \frac{1}{1 + \alpha Kn} \quad (13)$$

According to equation (12), the effective viscosity of dense gas can be expressed as equation (14). The detailed derivation is given in Appendix E.

$$\mu_{eff}(\rho, T, L) = \mu_b(\rho, T) \frac{1}{1 + \alpha Kn} + h(\rho, T, L). \quad (14)$$

Equation (16) shows that there is no direct functional relationship between the effective viscosity and the Knudsen number. Therefore, to clarify the effect of the Knudsen number on the effective viscosity, the relative viscosity is defined,  $\mu_{eff}/\mu_b$ . The relative viscosities of dilute and dense gases can be written as equation (15) and equation (16).

$$\frac{\mu_{eff}}{\mu_0(T)} = \frac{1}{1 + \alpha Kn}, \quad (15)$$

$$\frac{\mu_{eff}(Kn)}{\mu_b(\rho, T)} = \frac{1}{1 + \alpha Kn} + \frac{h(\rho, T, L)}{\mu_b(\rho, T)}. \quad (16)$$

The semilog plot of relative viscosity obtained by the MD method and the Knudsen number is shown at Figure 7. The Knudsen number of methane can be acquired from Appendix F. As we know, when the value is below 0.001, it is a continuous flow, and when it falls between 0.001 and 0.1, a slip flow occurs. When the Knudsen number is greater than 0.1 but less than 10, it is a transition flow. A Knudsen number greater than 10 indicates that a free molecular flow is forming [10]. As shown in Figure 7, the results of relative viscosity with different width pores appear the same trend that the relative viscosity decrease with increase in  $Kn$ . Notably, the relative viscosity appears at different change rates with the Knudsen number in different regimes: when  $Kn$  is less than 0.1, relative viscosity slowly decreases with  $Kn$  increasing; however, effective viscosity decreases quickly with increase in  $Kn$  when  $Kn$  is between 0.1 and 10.

Michalis et al. [18] used equation (15) to depict the effective viscosity of confined dilute Nitrogen gas and got  $\alpha = 2$ . As shown in Figure 7, it is noteworthy that the relative viscosity of the dense gas in the organic slit pores obtained from the MD simulations in this paper is lower than that of the dilute gas obtained from Michalis et al. [18]. It means that the steeper drop in the relative viscosity of the dense gas occurs at the position where the Knudsen number is smaller.

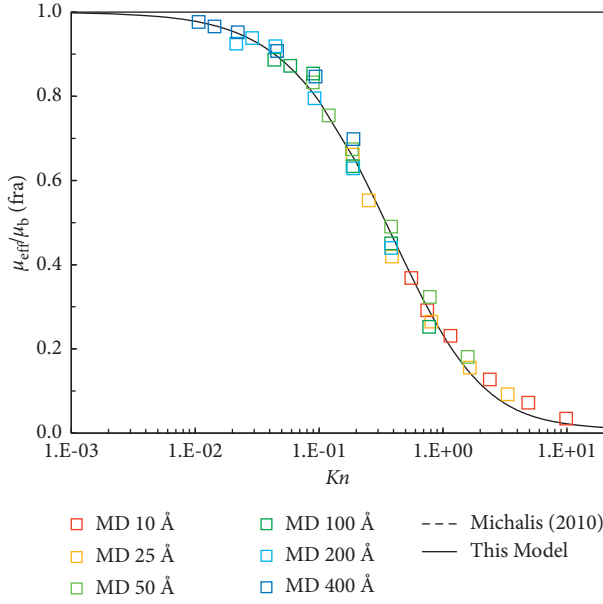


FIGURE 7: The relative viscosity ( $\mu_{\text{eff}}/\mu_b$ ) with Kn (the symbols represent the result of MD simulation, the black lines is the result of this model, the dash line is the results of dilute methane gas by the methods in the literatures).

Equation (15) could fit the MD results well. 2.901 is for  $\alpha$ , while  $R^2 = 0.990$ . The last term on the right side of equation (16) has a good correlation with the Knudsen number and tends to increase and then decrease. It is assumed that this term has the following equation (17) functional form.

$$\frac{h(\rho, T, L)}{\mu_b(\rho, T)} = -\frac{1}{aKn\sqrt{2\pi}} \exp\left(-\frac{(\ln(Kn) - b)^2}{(2a^2)}\right). \quad (17)$$

$\alpha$  is assumed to be the same with Michalis et al. [18]. The relative viscosity of dense methane in organic matter slit pores was fitted with equations (16) and (17), and the results of the fit are shown in the black solid line of Figure 6 with coefficients  $a = 1.563$ ,  $b = 2.143$ , and deterministic coefficient  $R^2 = 0.993$ . This difference is because of the fact that the relative viscosity of the dense gas has one more contribution from the dense gas potential and the wall potential than that of the dilute gas.

**3.4. Analysis of the Flow Capacity Improvement.** The flow capacity is defined as permeability divided by viscosity. The effect of viscosity on the flow capacity could be described by  $\mu_b/\mu_{\text{eff}}$ , which is shown in Figure 8. The flow capacity increases as the pressure decrease. When the pressure is 1 MPa, the flow capacity is 28.7 times that calculated by the bulk gas viscosity in 1 nm pore.

## 4. Summary and Conclusions

Gas-bearing shale is rich in organic nanopores. This paper determined the viscosity of methane in organic slit nanopores by EMD simulations at shale gas reservoir conditions. The result shows that the viscosity of the shale gas is affected

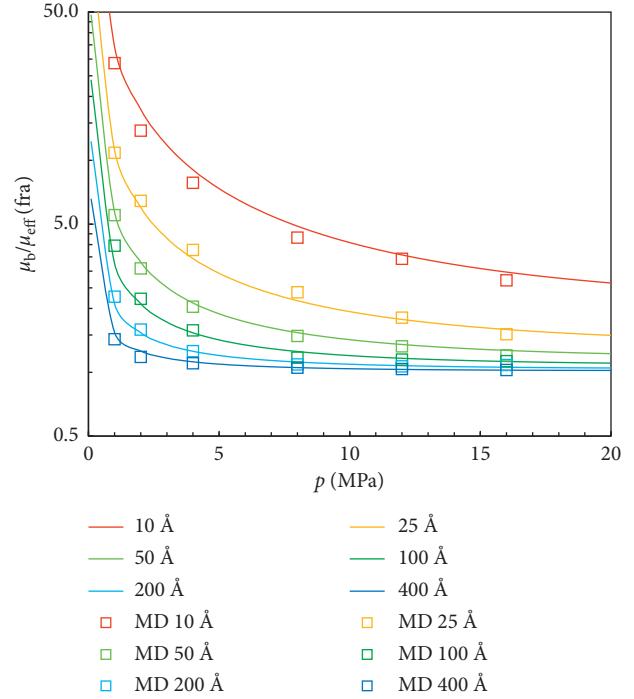


FIGURE 8: The multiple of gas flow capacity increased in the slit pore with pressure for different width pores at 343.15 K (the symbols represent the result of MD simulation, and the lines are the result of equation (16)).

by the presence of nanopores. We obtained the restricted dense gas viscosity model by theoretical analysis. We use this model to fit the EMD results to obtain the viscosity correction formula for dense methane in the organic slit nanopore.

The conclusions drawn are as follows:

- (1) Confine spaces may decrease the effective viscosity of methane. In the pore, the effective viscosity of gas decreased with decreasing pore width, while in the smaller pores, pore width has more effect on effective gas viscosity. The confined effect would make the effective viscosity of methane decrease at least 10% for pore size less than 40 nm when the pressure is 4 MPa, which means that the confined effect on viscosity should be paid more attention to.
- (2) There are two differences in effective viscosity between bulk gas and confined gas. Firstly, the effective viscosity of the confined gas decreases more rapidly than the bulk phase with decreasing pressure. Secondly, while the viscosity of the bulk gas is independent of pressure when the pressure is lower than 2 MPa, the viscosity of the confined gas decreases rapidly with decreasing pressure.
- (3) The viscosity of a confined dense gas devotes by kinetic contribution, the potential of gas contribution, and the potential of wall contribution. A viscosity model of confined dense gas is promoted, and specific model parameters are obtained by fitting EMD results, which can be used to characterize the

effective viscosity of dense methane under shale gas reservoir conditions.

- (4) The confinement effect causes the methane flow capacity in the reservoir to increase. As this pressure decreases, the effect of the confinement effect on the methane flow capacity increases rapidly. Keeping a low pressure can decrease the viscosity of shale gas, which is beneficial to improving the flow capacity of shale gas.

The confinement effects on the viscosity of shale gas should not be negligible, and viscosity correction is recommended for shale gas flow description. In this paper, a viscosity correction method for dense methane in organic matter slit pores is provided. The proposed method still has shortcomings, which could be improved later, such as the diverse types and complex morphology of real shale pores, however, the target of this paper has been achieved, which is only for organic matter slit pores.

## Appendix

### A. Chemical Potential

The chemical potential of dense methane is written as (A.1) [51] follows:

$$\mu = k_B T \ln \left( \frac{\Lambda^3 \phi p}{k_B T} \right), \quad (\text{A.1})$$

$$\Lambda = \sqrt{\frac{h^2}{2\pi m k_B T}}. \quad (\text{A.2})$$

### B. Redlich–Kwong Equation of State

The Redlich–Kwong equation of state (RK EOS), which is shown as equations (B.1) and (B.2), is used in calculating the density and fugacity of light hydrocarbons with different polarities (nonpolar, middle polar, and highly polar) [57, 58].

$$p = \frac{RT}{v-b} - \frac{a}{\sqrt{T}v(v+b)}, \quad (\text{B.1})$$

$$a = 0.42748 \frac{R^2 T_c^{5/2}}{P_c}, \quad (\text{B.2})$$

$$b = 0.08664 \frac{RT_c}{P_c}. \quad (\text{B.3})$$

The compressibility factor of RK EOS is determined by equations (B.2) and (B.4)<sub>2</sub>

$$Z^3 - Z^2 + (A - B - B^2)Z - AB = 0, \quad (\text{B.4})$$

$$A = 0.42748 \frac{P_r}{T_r^{5/2}}, \quad (\text{B.5})$$

$$B = 0.08664 \frac{P_r}{T_r}. \quad (\text{B.6})$$

For methane gas,  $T_C$  is 190.6 K,  $p_C$  is 4.599 MPa, molecular mass is 16.04 g/mol, and  $\omega$  is 0.012 [59].

The fugacity coefficient of RK EOS is determined by equation (B.7) [60].

$$\ln \phi = Z - 1 - \ln(Z - B) - \frac{A}{B} \ln \frac{Z + B}{Z}. \quad (\text{B.7})$$

### C. Chapman–Enskog Formula

There are numerous pieces of research on the viscosity of dilute gas, which contains the methodologies of bulk gas and gas in the pore [18, 61]. A formula to estimate the dilute gas viscosity at low pressure was proposed and shown in equation (C.1) [18].

$$\mu = \frac{5}{16} \frac{\sqrt{mk_B T / \pi}}{\delta^2}. \quad (\text{C.1})$$

### D. Lee Function

The correlation about viscosity from Lee is a common method, which is shown in equations (D.1) to (D.2) [14].

$$\mu_b = 10^{-4} K \exp(X \rho_g^Y), \quad (\text{D.1})$$

$$K = \frac{(22.650 + 0.0388 M_w) T^{1.5}}{209.2 + 19.26 M_w + 1.8 T}, \quad (\text{D.2})$$

$$X = 3.448 + \frac{986.4}{T} + 0.01009 M_w, \quad (\text{D.3})$$

$$Y = 2.447 - 0.2224 X. \quad (\text{D.4})$$

### E. The Effective Viscosity of Dense Gas in Slit Pore

By bringing equation (13) into (12) and splitting the second and third terms on the right-hand side of equation (12), equation (12) can be rewritten as equation (E.3).

$$\begin{aligned} \mu_{\text{eff}}(\text{Kn}) = & \mu_{kk,b}(T) \frac{1}{1 + \alpha \text{Kn}} + \mu_{kp_g,b}(\rho, T) \frac{1}{1 + \alpha \text{Kn}} + f(\rho, T, L) \\ & + \mu_{p_g p_g,b}(\rho, T) \frac{1}{1 + \alpha \text{Kn}} + g(\rho, T, L) + \mu_{p_w}(\rho, T, L). \end{aligned} \quad (\text{E.1})$$

Let

$$\begin{aligned} h(\rho, T, L) = & f(\rho, T, L) + g(\rho, T, L) + \mu_{p_w}(\rho, T, L), \\ \mu_b(\rho, T) = & \mu_{kk,b}(T) + \mu_{kp_g,b}(\rho, T) + \mu_{p_g p_g,b}(\rho, T). \end{aligned} \quad (\text{E.2})$$

Then, the effective viscosity can be further rewritten as follows:

$$\mu_{\text{eff}}(\text{Kn}) = \mu_b(T) \frac{1}{1 + \alpha \text{Kn}} + h(\rho, T, L). \quad (\text{E.3})$$

## F. Knudsen Number

The Knudsen number is defined as equation (F.1) [10].

$$\text{Kn} = \frac{\lambda}{L}, \quad (\text{F.1})$$

$$\lambda = \frac{1}{\sqrt{2}\pi\sigma^2 n}. \quad (\text{F.2})$$

The characteristic length ( $L$ ) of a pore that is used in the criterion to classify flow regimes is the radius ( $r_p$ ) for a circular pore and the width ( $w$ ) for a slit pore.

The density of methane is calculated by equation (F.3). For a dense gas, the compressibility factor is identified by RK EOS. However, the compressibility factor is 1 for dilute gas.

$$n = \frac{P}{Zk_B T}. \quad (\text{F.3})$$

## Nomenclature

### Notations

- $a$ : A parameter of the Redlich–Kwong equation of state  
 $b$ : A parameter of the Redlich–Kwong equation of state  
 $\bar{c}$ : Mean velocity of molecule in the system  
 $d$ : Average intermolecular distance, Å/fs  
 $h$ : Planck constant,  $6.62607004 \times 10^{-34} \text{ m}^2\text{kg/s}$  or J·s  
 $k$ : Permeability of pore,  $\text{m}^2$   
 $m$ : Molecular mass, g/molecule  
 $n$ : The number density of gas, molecules/ $\text{m}^{-3}$   
 $n_0$ : The number density of gas at standard condition, molecules/ $\text{m}^{-3}$   
 $p$ : Pressure of fluid, Pa  
 $r$ : The vector between two molecules  
 $r_p$ : The radius of circular pore, m  
 $t$ : Time, s  
 $u$ : The speed of the stream layer, m/s  
 $v$ : The average flow rate in pore when it is in Darcy's law, m/s  
 $v$ : The velocity of atom when it is in the Green–Kubo function, Å/fs  
 $v$ : The molar volume when it is in the Redlich–Kwong equation of state,  $\text{m}^3/\text{mol}$   
 $w$ : The width of slit pore, m  
 $x$ : The position at flow direction, m  
 $y$ : The location of the stream layer, m  
 $A$ ,  $B$ : The coefficients for equation of state  
 $A$ : The cross-area of pore, m  
 $F$ : The intermolecular forces, N  
 $L$ : The physical width of the pore, m  
 $L'$ : The effective width of pore, m  
 $M$ : The total number of wall molecules  
 $N$ : The total number of fluid molecules in the system  
 $T$ : System temperature, K

$U$ : The van der Waals potential between two atoms, Kcal/mol

$V$ : System volume,  $\text{m}^3$

$Z$ : A compressibility factor of real gas

$\text{Kn}$ : The Knudsen number

$M_w$ : Relative molecular mass, g/mol

$\bar{\cdot}$ : Averaging for the system

*Greek symbol*

$\alpha$ : The coefficient of viscosity

$\delta$ : Rarefied gas criterion. When  $\delta \geq 7$ , the gas is in the dilute regime

$\epsilon$ : The potential well of Lennard–Jones potential model

$\lambda$ : The mean free path, m

$\mu$ : The viscosity of fluid, Pa s

$\rho$ : Density,  $\text{g}/\text{cm}^3$

$\sigma$ : The molecular effective collision diameter, m

$\sigma_T$ : Tangential accommodation coefficient

$\tau$ : Shear stress,  $\text{N}/\text{m}^2$

$\phi$ : Fugacity coefficient, fraction

$\omega$ : The acentric factor of fluid

$\Lambda$ : de Broglie wavelength, m

*Subscripts*

$b$ : The parameter of bulk phase

$c$ : The parameter under the effect of confinement

$C$ : The parameter at the critical point

$i, j$ : Molecule number

$p$ : The parameter of gas in pore

$r$ : The reduced parameter

eff: The effective parameter

$\alpha, \beta$ : Coordinate direction

0: The parameter when Kn approaches 0

$\infty$ : The parameter when Kn approaches infinity

*Constant*

$k_B$ : Boltzmann constant,  $1.381 \times 10^{-23} \text{ m}^2\cdot\text{kg}\cdot\text{s}^{-2}\cdot\text{K}^{-1}$

$R$ : Ideal gas constant,  $8.314 \text{ J}/(\text{mol K})$ .

## Data Availability

The raw data required to reproduce these findings cannot be shared at this time as the data are also a part of an ongoing study. If someone is interested in our work, the result can be repeated by the details of the model, and the methods of data processing are described in the paper.

## Conflicts of Interest

The authors declare that they have no conflicts of interest.

## Acknowledgments

This work was supported by China Postdoctoral Science Foundation (No. 2019M650965), China National Major Projects (Nos. 2016ZX05010-002-002 and 2016ZX05048-002), and The Fund of SKL of Oil & Gas Reservoir Geology and Exploitation Engineering (No. PLN2019020). The first author would also like to acknowledge the China Scholarship Council (CSC) for providing financial support for him to study at the Faculty of Engineering and Applied Science of the University of Regina as a coeducation Ph.D. student.

## References

- [1] S. K. Bhatia, M. R. Bonilla, and D. Nicholson, "Molecular transport in nanopores: a theoretical perspective," *Physical Chemistry Chemical Physics*, vol. 13, no. 34, pp. 15350–15383, 2011.
- [2] F. Javadpour, "Nanopores and apparent permeability of gas flow in mudrocks (shales and siltstone)," *Journal of Canadian Petroleum Technology*, vol. 48, no. 08, pp. 16–21, 2009.
- [3] E. G. Leonov and V. I. Isaev, *Applied Hydroaeromechanics in Oil and Gas Drilling*, Wiley Online Library, Hoboken, NJ, USA, 2010.
- [4] J. Rouquerol, D. Avnir, C. W. Fairbridge et al., "Recommendations for the characterization of porous solids (technical report)," *Pure and Applied Chemistry*, vol. 66, no. 8, pp. 1739–1758, 1994.
- [5] R. Nazari Moghaddam and M. Jamiolahmady, "Slip flow in porous media," *Fuel*, vol. 173, pp. 298–310, 2016.
- [6] F. Civan, "Effective correlation of apparent gas permeability in tight porous media," *Transport in Porous Media*, vol. 82, no. 2, pp. 375–384, 2009.
- [7] K. Wu, X. Li, C. Wang, W. Yu, and Z. Chen, "Apparent permeability for gas flow in shale reservoirs coupling effects of gas diffusion and desorption," in *Proceedings of the 2nd Unconventional Resources Technology Conference*, Denver, CO, USA, August 2014.
- [8] M. Kazemi and A. Takbiri-Borujeni, "An analytical model for shale gas permeability," *International Journal of Coal Geology*, vol. 146, pp. 188–197, 2015.
- [9] L. Wu, M. T. Ho, L. Germanou et al., "On the apparent permeability of porous media in rarefied gas flows," *Journal of Fluid Mechanics*, vol. 822, pp. 398–417, 2017.
- [10] G. A. Bird and J. Brady, *Molecular Gas Dynamics and the Direct Simulation of Gas Flows*, Clarendon Press Oxford, Oxford, UK, 1994.
- [11] K. Meier, A. Laesecke, and S. Kabelac, "Transport coefficients of the Lennard-Jones model fluid. I. Viscosity," *The Journal of Chemical Physics*, vol. 121, no. 8, pp. 3671–3687, 2004.
- [12] M. Born and H. Green, "A general kinetic theory of liquids I. The molecular distribution functions," *Proceedings of the Royal Society of London Series A Mathematical and Physical Sciences*, vol. 188, no. 1012, pp. 10–18, 1946.
- [13] J. A. Jossi, L. I. Stiel, and G. Thodos, "The viscosity of pure substances in the dense gaseous and liquid phases," *AIChE Journal*, vol. 8, no. 1, pp. 59–63, 1962.
- [14] A. L. Lee, M. H. Gonzalez, and B. E. Eakin, "The viscosity of natural gases," *Journal of Petroleum Technology*, vol. 18, no. 08, pp. 997–1000, 1966.
- [15] R. P. Sutton, "Fundamental PVT calculations for associated and gas-condensate natural gas systems," in *Proceedings of the SPE Annual Technical Conference and Exhibition*, October 2005.
- [16] J. Xie, M. Borg, L. Gibelli, O. Henrich, D. Lockerby, and J. Reese, "Effective mean free path and viscosity of confined gases," *Physics of Fluids*, vol. 31, p. 7, Article ID 072002, 2019.
- [17] A. K. Beskok, "A model for flows in channels, pipes, and ducts at micro and nano scales," *Microscale Thermophysical Engineering*, vol. 3, no. 1, pp. 43–77, 1999.
- [18] V. K. Michalis, A. N. Kalarakis, E. D. Skouras, and V. N. Burganos, "Rarefaction effects on gas viscosity in the Knudsen transition regime," *Microfluidics and Nanofluidics*, vol. 9, no. 4-5, pp. 847–853, 2010.
- [19] Q. Lv, E. Wang, X. Liu, and S. Wang, "Determining the intrinsic permeability of tight porous media based on bivelocity hydrodynamics," *Microfluidics and Nanofluidics*, vol. 16, no. 5, pp. 841–848, 2014.
- [20] D. A. Lockerby, J. M. Reese, and M. A. Gallis, "Capturing the Knudsen layer in continuum-fluid models of nonequilibrium gas flows," *AIAA Journal*, vol. 43, no. 6, pp. 1391–1393, 2005.
- [21] J. M. Reese, Y. Zheng, and D. A. Lockerby, "Computing the near-wall region in gas micro-and nanofluidics: critical Knudsen layer phenomena," *Journal of Computational and Theoretical Nanoscience*, vol. 4, no. 4, pp. 807–813, 2007.
- [22] Z. L. Guo, B. C. Shi, and C. G. Zheng, "An extended Navier-Stokes formulation for gas flows in the Knudsen layer near a wall," *Europhysics Letters (EPL)*, vol. 80, no. 2, Article ID 24001, 2007.
- [23] C. R. Lilley and J. E. Sader, "Velocity profile in the Knudsen layer according to the Boltzmann equation," *Proceedings of the Royal Society A: Mathematical, Physical and Engineering Sciences*, vol. 464, no. 2096, pp. 2015–2035, 2008.
- [24] Z. Jin and A. Firoozabadi, "Flow of methane in shale nanopores at low and high pressure by molecular dynamics simulations," *The Journal of Chemical Physics*, vol. 143, no. 10, Article ID 104315, 2015.
- [25] J. Chen, H. Yu, J. Fan et al., "Channel-width dependent pressure-driven flow characteristics of shale gas in nanopores," *AIP Advances*, vol. 7, no. 4, Article ID 045217, 2017.
- [26] M. Kazemi and A. Takbiri-Borujeni, "Modeling and simulation of gas transport in carbon-based organic nano-capillaries," *Fuel*, vol. 206, pp. 724–737, 2017.
- [27] F. Fei, J. Fan, and J. Jiang, "Solid wall effect on the transport coefficients of gases," *Science China Physics, Mechanics and Astronomy*, vol. 55, no. 6, pp. 927–932, 2012.
- [28] H. O. Baled, I. K. Gamwo, R. M. Enick, and M. A. McHugh, "Viscosity models for pure hydrocarbons at extreme conditions: a review and comparative study," *Fuel*, vol. 218, pp. 89–111, 2018.
- [29] J. M. Haile, *Molecular Dynamics Simulation: Elementary Methods*, Wiley, Hoboken, NJ, USA, 1992.
- [30] H. Zhang, B.-J. Zhang, and J.-J. Zhang, "Shear viscosity of simple fluids in porous media: molecular dynamics simulations and correlation models (II) – methane in silicate pores," *Chemical Physics Letters*, vol. 397, no. 1-3, pp. 233–236, 2004.
- [31] G. Arya, E. J. Maginn, and H.-C. Chang, "Efficient viscosity estimation from molecular dynamics simulation via momentum impulse relaxation," *The Journal of Chemical Physics*, vol. 113, no. 6, pp. 2079–2087, 2000.
- [32] S. Derakhshan, M. Rezaee, and H. Sarrafha, "A molecular dynamics study of description models for shear viscosity in nanochannels: mixtures and effect of temperature," *Nanoscale and Microscale Thermophysical Engineering*, vol. 19, no. 3, pp. 206–220, 2015.
- [33] J. A. Thomas and A. J. H. McGaughey, "Effect of surface wettability on liquid density, structure, and diffusion near a solid surface," *The Journal of Chemical Physics*, vol. 126, no. 3, Article ID 034707, 2007.
- [34] M. Horsch, J. Vrabec, M. Bernreuther, and H. Hasse, *Poiseuille Flow of Liquidmethane in Nanoscopic Graphite Channels by Molecular Dynamics Simulation*, Begel House Inc., Danbury, CT, USA, 2009.
- [35] A. P. Markesteijn, R. Hartkamp, S. Luding, and J. Westerweel, "A comparison of the value of viscosity for several water models using Poiseuille flow in a nano-channel," *The Journal of Chemical Physics*, vol. 136, no. 13, Article ID 134104, 2012.
- [36] D. J. Evans and G. Morriss, *Statistical Mechanics of Nonequilibrium Liquids*, Cambridge University Press, Cambridge, UK, 2008.



- [37] W. G. Hoover, *Computational Statistical Mechanics*, Elsevier, Amsterdam, Netherlands, 2012.
- [38] F. Müller-Plathe, “Reversing the perturbation in nonequilibrium molecular dynamics: an easy way to calculate the shear viscosity of fluids,” *Physical Review E*, vol. 59, no. 5, p. 4894, 1999.
- [39] G. Galliéro, C. Boned, and A. Baylaucq, “Molecular dynamics study of the Lennard–Jones fluid viscosity: application to real fluids,” *Industrial & Engineering Chemistry Research*, vol. 44, no. 17, pp. 6963–6972, 2005.
- [40] J. G. Speight, *Shale Gas Production Processes*, Elsevier, Amsterdam, Netherlands, 2013.
- [41] S. Plimpton, “Fast parallel algorithms for short-range molecular dynamics,” *Journal of Computational Physics*, vol. 117, no. 1, pp. 1–19, 1995.
- [42] M. G. Martin and J. I. Siepmann, “Transferable potentials for phase equilibria. 1. United-atom description of n-alkanes,” *The Journal of Physical Chemistry B*, vol. 102, no. 14, pp. 2569–2577, 1998.
- [43] B. Chen and J. I. Siepmann, “Transferable potentials for phase equilibria. 3. Explicit-hydrogen description of normal alkanes,” *The Journal of Physical Chemistry B*, vol. 103, no. 25, pp. 5370–5379, 1999.
- [44] W. L. Jorgensen, D. S. Maxwell, and J. Tirado-Rives, “Development and testing of the OPLS all-atom force field on conformational energetics and properties of organic liquids,” *Journal of the American Chemical Society*, vol. 118, no. 45, pp. 11225–11236, 1996.
- [45] M. Kazemi and A. Takbiri-Borujeni, “Flow of gases in organic nanoscale channels: a boundary-driven molecular simulation study,” *Energy & Fuels*, vol. 30, no. 10, pp. 8156–8163, 2016.
- [46] Y. A. Hao, J. Fan, J. Xia, H. Liu, and H.-A. Wu, “Multiscale gas transport behavior in heterogeneous shale matrix consisting of organic and inorganic nanopores,” *Journal of Natural Gas Science and Engineering*, vol. 75, 2020.
- [47] Z.-Z. Li, T. Min, Q. Kang, Y.-L. He, and W.-Q. Tao, “Investigation of methane adsorption and its effect on gas transport in shale matrix through microscale and mesoscale simulations,” *International Journal of Heat and Mass Transfer*, vol. 98, pp. 675–686, 2016.
- [48] M. S. Green, “Markoff random processes and the statistical mechanics of time-dependent phenomena,” *Journal of Chemical Physics*, vol. 20, no. 8, pp. 1281–1295, 2004.
- [49] R. Kubo, “Statistical-mechanical theory of irreversible processes. I. general theory and simple applications to magnetic and conduction problems,” *Journal of the Physical Society of Japan*, vol. 12, 1997.
- [50] D. D. Do and H. D. Do, “Evaluation of 1-site and 5-site models of methane on its adsorption on graphite and in graphitic slit pores,” *The Journal of Physical Chemistry B*, vol. 109, no. 41, pp. 19288–19295, 2005.
- [51] P. Pascual, P. Ungerer, B. Tavitian, and A. Boutin, “Development of a transferable guest-host force field for adsorption of hydrocarbons in zeolites. II. Prediction of alkenes adsorption and alkane/alkene selectivity in silicalite,” *Journal of Physical Chemistry B*, vol. 108, 2004.
- [52] D. Frenkel and B. Smit, *Understanding Molecular Simulation: From Algorithms to Applications*, Elsevier, Amsterdam, Netherlands, 2001.
- [53] R. Stadler, D. R. Bowler, D. Alfè, and M. J. Gillan, “Tight binding molecular dynamics studies of the viscosity of liquid selenium,” *Journal of Physics: Condensed Matter*, vol. 12, no. 24, pp. 5109–5119, 2000.
- [54] Y. Zhang, G. Guo, and G. Nie, “A molecular dynamics study of bulk and shear viscosity of liquid iron using embedded-atom potential,” *Physics and Chemistry of Minerals*, vol. 27, no. 3, pp. 164–169, 2000.
- [55] Z. Fan, L. F. C. Pereira, H.-Q. Wang, J.-C. Zheng, D. Donadio, and A. Harju, “Force and heat current formulas for many-body potentials in molecular dynamics simulations with applications to thermal conductivity calculations,” *Physical Review B*, vol. 92, no. 9, Article ID 094301, 2015.
- [56] National Institute of Standards and Technology, *Thermophysical Properties of Fluid Systems*, National Institute of Standards and Technology, Gaithersburg, MD, USA, 2020.
- [57] R. R. Tarakad, C. F. Spencer, and S. B. Adler, “A comparison of eight equations of state to predict gas-phase density and fugacity,” *Industrial & Engineering Chemistry Process Design and Development*, vol. 18, no. 4, pp. 726–739, 1979.
- [58] K. Marnasidou, G. Takidis, and M. Stamatoudis, “Comparison of fourteen generalized equations of state to predict gas-phase fugacity,” *Chemical Engineering Communications*, vol. 187, no. 1, pp. 149–159, 2007.
- [59] N. De Nevers, *Physical and Chemical Equilibrium for Chemical Engineers*, John Wiley & Sons, Hoboken, NJ, USA, 2012.
- [60] A. Bahadori, *Fluid Phase Behavior for Conventional and Unconventional Oil and Gas Reservoirs*, pp. 521–533, Elsevier, Amsterdam, Netherlands, 2017.
- [61] S. Chapman and T. G. Cowling, *The Mathematical Theory of Non-uniform Gases: An Account of the Kinetic Theory of Viscosity, Thermal Conduction and Diffusion in Gases*, Cambridge University Press, Cambridge, UK, 1953.

## Research Article

# Experimental Study on Fracture Propagation Mechanism of Shale Oil Reservoir of Lucaogou Formation in Jimusar

Jianmin Li,<sup>1</sup> Yushi Zou ,<sup>2</sup> Shanzhi Shi,<sup>1</sup> Shicheng Zhang,<sup>2</sup> Junchao Wang,<sup>1</sup> Xinfang Ma,<sup>2</sup> and Xiaohuan Zhang<sup>2</sup>

<sup>1</sup>Engineering Technology Institute, Petro China Xinjiang Oilfield Company, Xinjiang 834000, China

<sup>2</sup>State Key Laboratory of Petroleum Resources and Prospecting, China University of Petroleum (Beijing), Beijing 102249, China

Correspondence should be addressed to Yushi Zou; [zouyushi@126.com](mailto:zouyushi@126.com)

Received 19 September 2021; Revised 16 January 2022; Accepted 4 February 2022; Published 27 February 2022

Academic Editor: Xiang Zhou

Copyright © 2022 Jianmin Li et al. This is an open access article distributed under the Creative Commons Attribution License, which permits unrestricted use, distribution, and reproduction in any medium, provided the original work is properly cited.

The lithology of shale oil reservoir of Lucaogou Formation in Junggar Basin, China shows great variation in a vertical direction and develops bedding planes (BPs). In such formation, rock properties and fabrics have a significant impact on stimulation effects. To clarify the fracture propagation mechanism in a vertically heterogeneous reservoir, an experimental study on fracture propagation in layered rock samples with complex lithology has been conducted. The effect of layers on the height of hydraulic fractures (HFs) was analysed based on triaxial hydraulic fracturing simulation system combined with mineral and mechanical characteristics analysis. The research shows that when the HF is initiated in siltstone layer, it tends to penetrate BPs with the dimensionless fracture height of more than 0.74. When HF is initiated in mudstone layer, the vertical growth of HFs tends to be terminated at the BPs, and the fracture height is constrained. The greater the thickness of the interlayer is, the more likely the HFs tend to be cut off at the interface and propagate along the interface, resulting in the limited fracture height. Under high horizontal stress difference, HFs are relatively straight. Due to the high permeability of BPs and the low viscosity of fracturing fluid, the fluid leakoff into BPs is observed, which is not conducive to the vertical propagation of HFs. Increasing the viscosity of fracturing fluid facilitates HFs to penetrate the high-permeability BPs and improves the vertical stimulated volume of shale oil reservoir.

## 1. Introduction

The shale oil reservoir of Lucaogou Formation in Junggar Basin was deposited in the salinized lake basin sedimentary environment after the closure of residual sea. During the sedimentary period of Lucaogou Formation, the lake basin was in the environment of continuous transformation of deep and shallow water. Due to the influence of structure and climate, the vertical lithology of the reservoir varies greatly in a vertical direction, and the BPs are developed [1–3]. The influence of BPs on HFs propagation behavior and stimulated volume is not clearly understood. Consequently, the selection of fracturing process and engineering parameters mainly lacks theoretical support, and the height of HFs and vertical stimulated volume are limited [4]. Therefore, it is of great significance to study the interaction mechanism between geological interface and HFs and the

theory of fracture propagation in a vertical heterogeneous reservoir.

International scholars have conducted a large number of experimental studies on the mechanism of HF propagation [5–9]. The HF propagation behavior in layered rock formations was first studied by Daneshy [10], who found that the HF will penetrate the bonding interface, but the unbonded interface will stop the HF, which is independent of the difference of mechanical properties between the two layers. Wu et al. [11] studied the propagation form of HFs in layered media through plexiglas. It was found that when HFs propagate from rigid media to soft media, the fractures will penetrate the interlayer interface. When the HF propagates from soft medium to rigid medium, the fracture will be cut off or deflected. The fracture mechanics analysis at the interface can be used to judge whether the fracture can penetrate the layer. Athavale and Miskimins [12] used

cement and sandstone to make layered rock samples to study the fracture propagation dynamics of layered formation. The experiment found that radial HF were formed in homogeneous samples and complex fractures were formed in thin multi-laminated samples, which were caused by the difference of interlaminar mechanical properties, namely, interfacial shear slippage and strength of the interface. In the experiment, the similarity criteria established by Bunger et al. [13] and Pater et al. [14] were successfully applied, and quasi-static propagating HF were formed in the laboratory. Heng et al. [15] conducted true triaxial hydraulic fracturing simulation test on shale outcrop, finding that when hydraulic fractures encounter BPs, and observed three types of responses of HF: (1) stagnation on weak BPs, (2) crossing strong BPs, and (3) deflecting from weak BPs. Whether the HF penetrates through or deflects from the BPs mainly depends on the mechanical properties of BPs. Compared with the shale reservoir deposited in marine environment with stable distribution in North America, the shale reservoir formed in continental environment in China, subjected to complex tectonic movement, was characterized by complex lithology and ample mineral types [16, 17]. Therefore, it is necessary to study the fracture propagation behavior in reservoirs where lithology varies greatly in a vertical direction.

At present, a series of laboratory fracturing experiments on the HF propagation in layered formation have been carried out; however, most of the experiments were carried out on artificial cores and field outcrops, while there were relatively few studies on the HF propagation on the downhole cores of thin-interbedded shale oil reservoirs with BPs. Therefore, it is necessary to further carry out laboratory physical simulation research on thin-interbedded shale oil reservoir to encounter the exploration and development needs of reservoirs with complex geological structure in different blocks in China. Through the XRD analysis and brittleness evaluation of downhole cores, the petrophysical properties of complex lithology were studied to support fracture propagation experiments. After that, a set of true triaxial fracturing simulation experimental devices was applied for fracturing physical simulation experiment with layered samples. Then fracture propagation mechanism of shale oil reservoir of Lucaogou Formation in Jimusar Basin was analysed.

## 2. Petrophysical Properties

**2.1. XRD Analysis of Reservoir Rock Samples.** The sample was prepared from the downhole core (10 cm in diameter) of Lucaogou Formation in Junggar Basin from the same well. Before the fracturing simulation experiment, the mineral composition and basic physical parameters of the rock sample were tested.

The mineral composition of 31 samples was tested. As shown in Figure 1, the main mineral components of shale oil in Lucaogou Formation are quartz and carbonate, with a content of 20% to 90%. The content of clay minerals, less than 10%, is relatively small. The average content of the main minerals of quartz is 22.44%, plagioclase feldspar 27.38%,

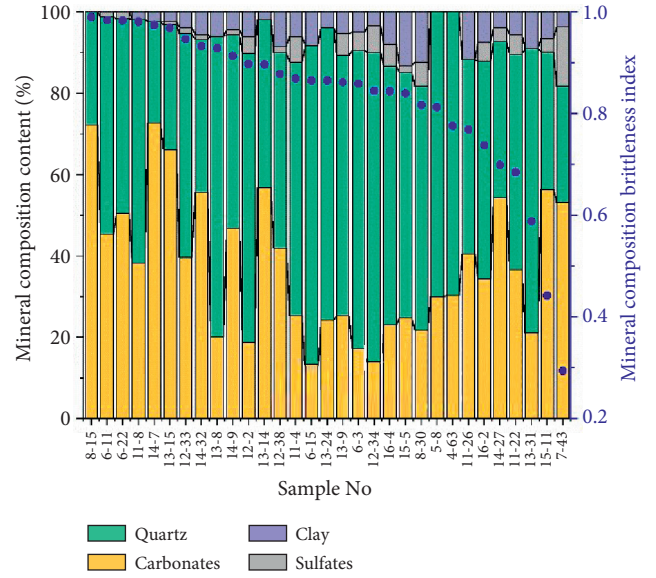


FIGURE 1: Mineral composition and brittleness evaluation results of cores in shale oil reservoir of Lucaogou Formation.

dolomite 28.58%, calcite 10.37%, and clay minerals 5.85%. Based on previous studies [18–21], quartz minerals (quartz, potassium feldspar, and plagioclase) and carbonate minerals (dolomite) are used as brittle minerals to calculate and analyse the brittleness index (formula (1)) of rock mineral composition in shale oil reservoir of Lucaogou Formation in Jimusar Basin.

$$B_M = \frac{m_{\text{qua}} + m_{\text{pf}} + m_{\text{pla}} + m_{\text{dol}}}{m_{\text{total}}}, \quad (1)$$

where  $m_i$  is the weight fraction of component,  $i$  is qua is quartz, pf is potassium feldspar, pla is plagioclase, and dol is dolomite.

The results in Figure 1 show that except for a few cores with higher content of clay minerals and sulfate minerals and a low mineral composition brittleness index, the mineral composition brittleness index of other cores is all higher than 0.6, with little difference.

**2.2. Brittle Characteristics of Rocks with Different Lithology in Lucaogou Formation.** In order to explore the influence of BPs on rock brittleness, standard cores of 5 cm in length and 2.5 cm in diameter were drilled in different directions for the same downhole core. Triaxial compression mechanical tests were carried out for cores in directions parallel and vertical to BPs. The experimental results are shown in Figure 2.

From the stress-strain curve, it can be seen that the micritic dolomite sample (sample #12–34 vertical core) that is perpendicular to BP direction presented obvious ductile characteristics. After reaching the peak stress of 130 MPa, there is no obvious damage behavior with the increase of strain, and there is no sudden drop in load. The micritic dolomite (sample #12–34 parallel core) parallel to the BP direction shows strong brittleness characteristics. After reaching the peak stress of 228 MPa, fracture appears

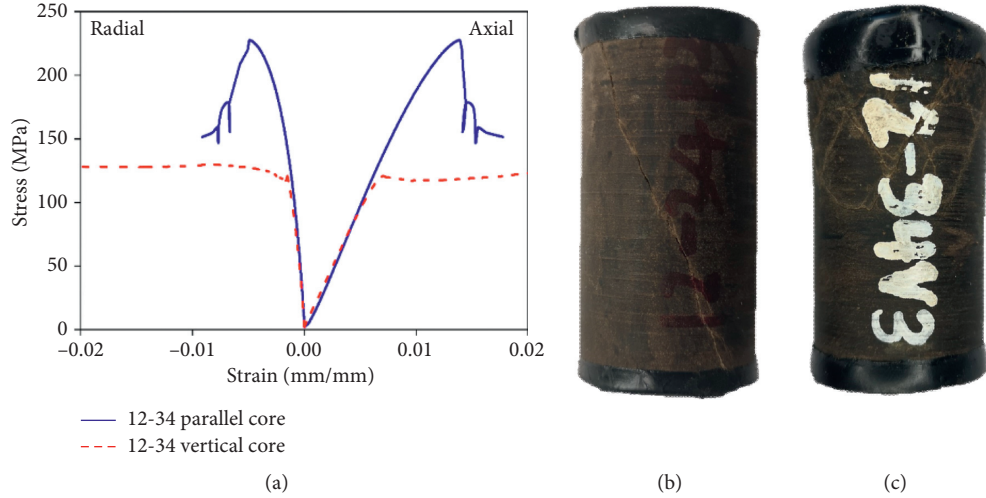


FIGURE 2: Brittle characteristics of rocks in different BP directions: (a) stress-strain curve; (b) fracture geometry in cores parallel to BP direction; (c) fracture geometry in cores perpendicular to BP direction.

obviously, the loading capacity decreases greatly, the post-peak stress decreases rapidly, and the residual stress is about 150 MPa. The vertical core volume strain is  $4.19 \times 10^{-3}$ , and the parallel core volume strain is  $-5.06 \times 10^{-4}$ . This indicates that the vertical core occurred plastic deformation and volume compression. Parallel cores produced macroscopic fractures and exhibited volume expansion. From the fracture geometry of rock samples, it can also be found that macro shear fractures appear in the rock samples in the direction parallel to BPs, while the rock samples in the direction perpendicular to BPs show expansion deformation behavior. Based on the energy evolution analysis of full stress-strain curve, many scholars put forward the method that can best reflect the brittle characteristics of rock [22–25]. High brittleness means that the sample stores more absorbed energy in the form of elastic strain energy before the peak, rock failure depends more on the release of elastic strain energy, and the consumption of elastic strain energy is more thorough after the peak value. According to this definition, the brittleness index  $B$  (composed of  $B_1$ ,  $B_2$ , and  $B_3$ , formula (2)–(5)) proposed by Li et al. [26] is used to evaluate the brittleness of rock energy evolution of Lucaogou Formation. The brittleness index for sample (#12–34 parallel core) in the direction parallel to BPs is 0.67, and that of sample (#12–34 vertical core) in the direction perpendicular to BPs is 0.

Comprehensive analysis shows that BPs anisotropy has a great impact on the mechanical properties and brittleness characteristics of rock samples. The brittleness of rock samples in the direction parallel to BPs in the same downhole rock core is greater than that of the samples in the direction perpendicular to BPs.

Prepeak stage: the higher the proportion of input energy stored in the form of elastic properties, the higher the brittleness [26].

$$B_1 = \frac{U_p^e}{U_p} = \frac{(1/2E) \left\{ (\sigma_p + \sigma_c)^2 + 2\sigma_c^2 - 2\nu [2(\sigma_p + \sigma_c)\sigma_c + \sigma_c^2] \right\}}{\int_0^{\epsilon_{ap}} \sigma_a d\epsilon_a + \sigma_c \epsilon_{vp}}, \quad (2)$$

where  $U_p^e$  and  $U_p$  are the elastic strain energy and absorbed energy, respectively;  $E$  is the Young's modulus;  $\sigma_p$ ,  $\sigma_a$ , and  $\sigma_c$  are the peak stress, axial stress, and confining pressure;  $\epsilon_a$  and  $\epsilon_{vp}$  are the axial strain and volumetric strain, respectively;  $\nu$  is the Poisson's ratio;  $B_1$  is prepeak brittleness index.

Postpeak stage: the higher the proportion of released elastic energy in the process of driving rock fracture, the higher the brittleness.  $W > 0$ , class I curve (brittle plastic);  $w < 0$ , class II curve (super brittle) [26].

$$B_2 = \begin{cases} \frac{\Delta U^e}{W + \Delta U^e} = \frac{(1/E)(\sigma_p + \sigma_r + 2\sigma_c - 4\nu\sigma_c)}{(-1/M_a)[\sigma_p + \sigma_r + 2\sigma_c - 4\sigma_c(-M_a/M_r)] + (1/E)(\sigma_p + \sigma_r + 2\sigma_c - 4\nu\sigma_c)}, & W > 0, \\ 1, & W \leq 0, \end{cases} \quad (3)$$

where  $W$  is the extra energy,  $\sigma_r$  is the residual stress,  $M_a$  is the axial softening modulus,  $M_r$  is the radial softening modulus, and  $B_2$  is postpeak brittleness index.



Residual stage: the more thoroughly the elastic energy is released, the higher the brittleness [26].

$$B_3 = 1 - \frac{U_r^e}{U_p^e} = 1 - \frac{(\sigma_r + \sigma_c)^2 + 2\sigma_c^2 - 2\nu[2(\sigma_r + \sigma_c)\sigma_c + \sigma_c^2]}{(\sigma_p + \sigma_c)^2 + 2\sigma_c^2 - 2\nu[2(\sigma_p + \sigma_c)\sigma_c + \sigma_c^2]}, \quad (4)$$

where  $U_r^e$  is the residual energy, and  $B_3$  is the residual brittleness index.

Therefore, the total brittleness index is calculated by the following equation [26]:

$$B = \frac{3}{\sum_{i=1}^3 (1/B_i)}. \quad (5)$$

The brittleness of rocks with different lithology of Lucaogou Formation was calculated based on the stress-strain data obtained from triaxial compression experiment. It can be found in Figure 3 that the reservoir rocks of Lucaogou Formation have strong heterogeneity, and the brittleness of rocks with different lithology has a wide range of variation, including argillaceous siltstone, sandy dolomite, and shale. The average energy evolution brittleness index of pelitic siltstone was 0.77, dolomitic siltstone 0.68, mud shale 0.61, dolomitic mudstone 0.43, micritic dolomite 0.45, and sandy dolomite 0.68. Among them, the energy evolution brittleness index of pelitic siltstone, mud shale, and sandy dolomite is higher than 0.6, dolomitic siltstone and micritic dolomite is medium, greater than 0.5, and dolomitic mudstone is low, less than 0.5. In order to explore the fracture propagation mechanism of rocks with complex lithology and different brittle characteristics of continental shale oil, the physical simulation experiment of fracture propagation has been carried out.

### 3. Physical Simulation Experiment of Fracture Propagation

**3.1. Experimental Apparatus and Preparation of Layered Samples.** A set of true triaxial fracturing simulation experimental devices is applied for fracturing physical simulation experiment. The device is mainly composed of liquid supply system, stress loading system, real-time data monitoring and acquisition system, and rock chamber and acoustic emission acquisition system. The experimental device is shown in Figure 4.

Preparation process of fracturing test sample is shown in Figure 5. Firstly, the downhole cores with the diameter of 100 mm were cut into discs, which then were bonded to form thin-interbedded cylindrical samples by epoxy with the height of 10 cm (divided into 3 layers:  $L_1 = 2$  cm,  $L_2 = 6$  cm, and  $L_3 = 2$  cm). Finally, the cylindrical sample is cut into 8 cm × 8 cm × 10 cm cube. At the center of surface with the size of 8 cm × 8 cm, a borehole of 5.3 cm was drilled with a drill bit (outer diameter of 1.5 cm) to place the simulated wellbore. A steel pipe (simulated wellbore) with an outer diameter of 1.3 cm, an inner diameter of 0.6 cm, and a length of 4.3 cm is cemented in the borehole with epoxy. An open hole section (OHS) with a length of 1 cm at the bottom of the

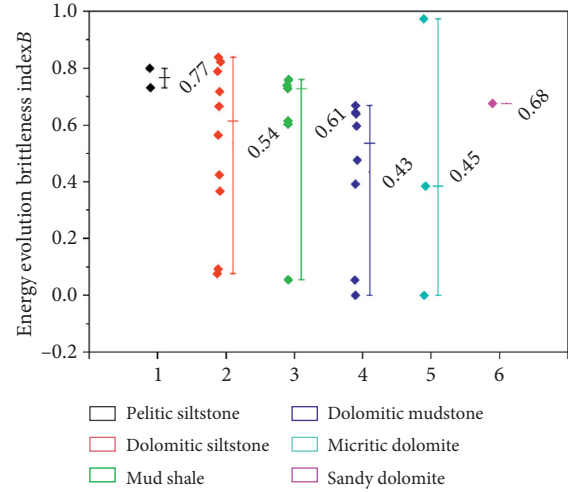


FIGURE 3: Energy evolution brittleness index of rocks with different lithology.



FIGURE 4: Small-size triaxial fracturing simulation system.

well was left unsealed. The standard small-size downhole fracturing physical model is shown in Figure 5(d).

**3.2. Experimental Method and Scheme.** The minimum horizontal principal stress is applied to simulate the three-dimensional in-situ stress state of a vertical well  $\sigma_h$ , maximum horizontal principal stress  $\sigma_H$  is perpendicular to the shaft axis, and vertical stress  $\sigma_V$  is parallel to the shaft axis (Figure 5(d)). The fracturing simulation experiment is carried out with the fracturing fluid added with the yellow fluorescent agent to observe the HF geometry. In the process of fracturing simulation, the double-cylinder constant speed and pressure pump is used to inject the fracturing fluid from the intermediate container into the wellbore at a constant injection rate, and the wellhead pressure is recorded by the pressure sensor and transmitted to the computer. When the wellhead pressure drops rapidly and does not increase pressure, it indicates that the HF starts to fracture and extends to the sample surface. At this time, the pump is stopped. After the experiment, the rock sample is taken out, the surface fracture geometry is determined according to the distribution of fluorescent agent solution on the sample surface, and the fracture initiation and propagation



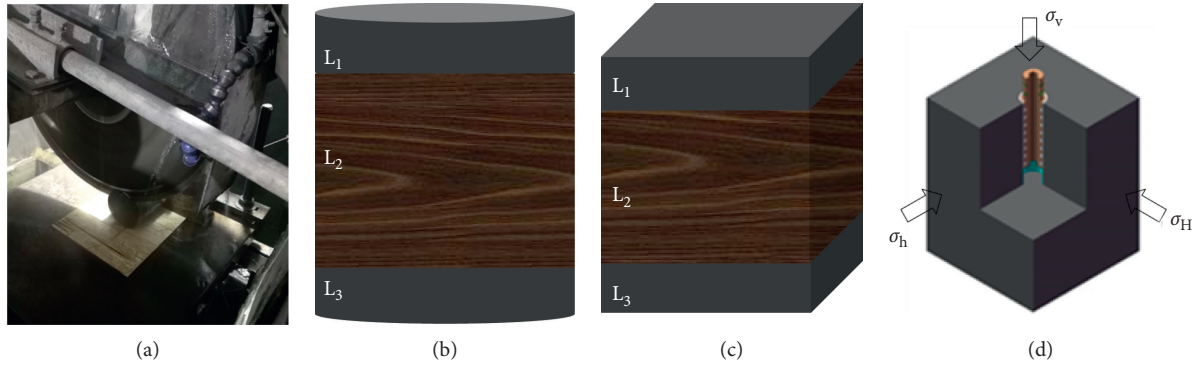


FIGURE 5: Fabrication process of small-size model. (a) Cutting discs from downhole cores. (b) Bonding of different lithology. (c) Cutting cylindrical samples into the cube. (d) Drilling and completion.

characteristics combined with the wellhead injection pressure curve are analysed.

The experiment mainly considers the effects of reservoir lithology, interlayer thickness, horizontal stress difference, and fracturing fluid viscosity on HF propagation, and a total of 7 groups of experiments are carried out. Table 1 lists the parameters used during the fracturing experiments.

## 4. Experimental Results and Analysis

**4.1. Injection Pressure versus Time Curves Characteristics.** Samples 1–3 were the comparison of different lithologies, samples 2 and 4 were the comparison of different horizontal stress differences, samples 5 and 6 were the comparison of different layer thicknesses, and samples 3 and 7 were the comparison of different fracturing fluid viscosities. Figure 6 shows the injection pressure versus time curves during the fracturing experiments. The specific parameters are given in Table 1. When the fluid was injected into the wellbore, the injection pressure increased rapidly from zero with the injection time. The injection pressure then reached a peak value, namely, breakdown pressure. Afterward, the injection pressure decreased sharply, indicating that HF was initiated from OHS. HF continued to propagate at a propagate pressure that fluctuated above and below the minimum horizontal stress ( $\sigma_h = 2$  MPa) until the pump was shut-in. The pressure curve patterns of different experiments were significantly different, especially in terms of pressurization rate and breakdown pressure. These findings will be discussed in the subsequent subsections.

**4.2. Influence of Reservoir Lithology Difference.** The basic physical property research shows that the mechanical properties of rock samples with different lithology of Lucaogou Formation in Junggar Basin are obviously different [27, 28]. In this section, the influence of reservoir lithology difference is considered. The rock properties used for the three samples were measured by Triaxial compression test and Brazilian disc test and are listed in Table 2. The lithology of sample #1 is pelitic siltstone, the lithology of sample #2 is the combination of silty mudstone in the middle layer and dolomitic siltstone 1 in the interlayer, and the

lithology of sample #3 is the combination of dolomitic siltstone 2 in the middle layer and siltstone in the interlayer.

Under the condition of injection rate of 20 mL/min, according to injection pressure versus time curves (Figure 6), the breakdown pressure was 8.94 MPa in sample #1, and the fracture height was 10 cm (Figure 7(a)), which penetrates the whole sample. In sample #2, the breakdown pressure was 15.1 MPa, and the fracture height was 6.4 cm (Figure 7(b)). In sample #3, the breakdown pressure was 25.6 MPa, and the fracture height was 7.4 cm (Figure 7(c)). The experimental results show that the greater young's modulus and tensile strength of middle layer and interlayer rocks, the greater breakdown pressure of samples. The breakdown pressure of high-strength sample #3 was 1.86 times greater than that of sample one. Moreover, the greater strength of the rock sample, the higher fluid flow resistance in the fracture of the sample. The propagate pressure was 1.58 MPa in sample #1, 2.05 MPa in sample #2, and 4.5 MPa in sample #3. The propagate pressure was increased by 1.84 times, which was due to the narrow fracture and narrow liquid flow channel of rock with high strength.

Through analysing the local fracture propagation pattern (Figure 8), the influence of BPs on fracture propagation can be observed more intuitively. In the pelitic siltstone of sample #1, when the BP was activated, the HF directly penetrates the BP. In the silty mudstone of sample #2, when the HF encounters BP 1, it activates the BP, turns to propagate along the BP, and then initiates again to continue to propagate along the direction of horizontal maximum principal stress, which soon encounters BP 2. After opening BP 2, it propagates along the horizontal BP to the boundary and fails to penetrate BP 2. Its width is less than that of sample #1. The BP opening width in sample #2 is greater than that of sample #1. It shows that BPs in mudstone are easier to open and have a greater barrier effect on the vertical propagate of HFs.

In the nonlayered low Young's modulus and low-strength sample, the fracture starts from the OHS, propagates up and down the wellbore, and penetrates the whole sample, and two horizontal BPs are opened. However, in the high-strength sample, the fracture tends to propagate to the upper part of the wellbore and fails to penetrate the whole

TABLE 1: Parameters used during the fracturing experiments.

Sample number	Layer thickness: $L_1/L_2/L_3$ (cm)	Injection rate (mL/min)	Viscosity (mPa·s)	Horizontal stress difference (MPa)
1	10	20	100	13
2	2/6/2	20	100	13
3	2/6/2	20	100	13
4	2/6/2	20	100	18
5	3/4/3	5	100	13
6	2/6/2	5	100	13
7	2/6/2	20	3	13

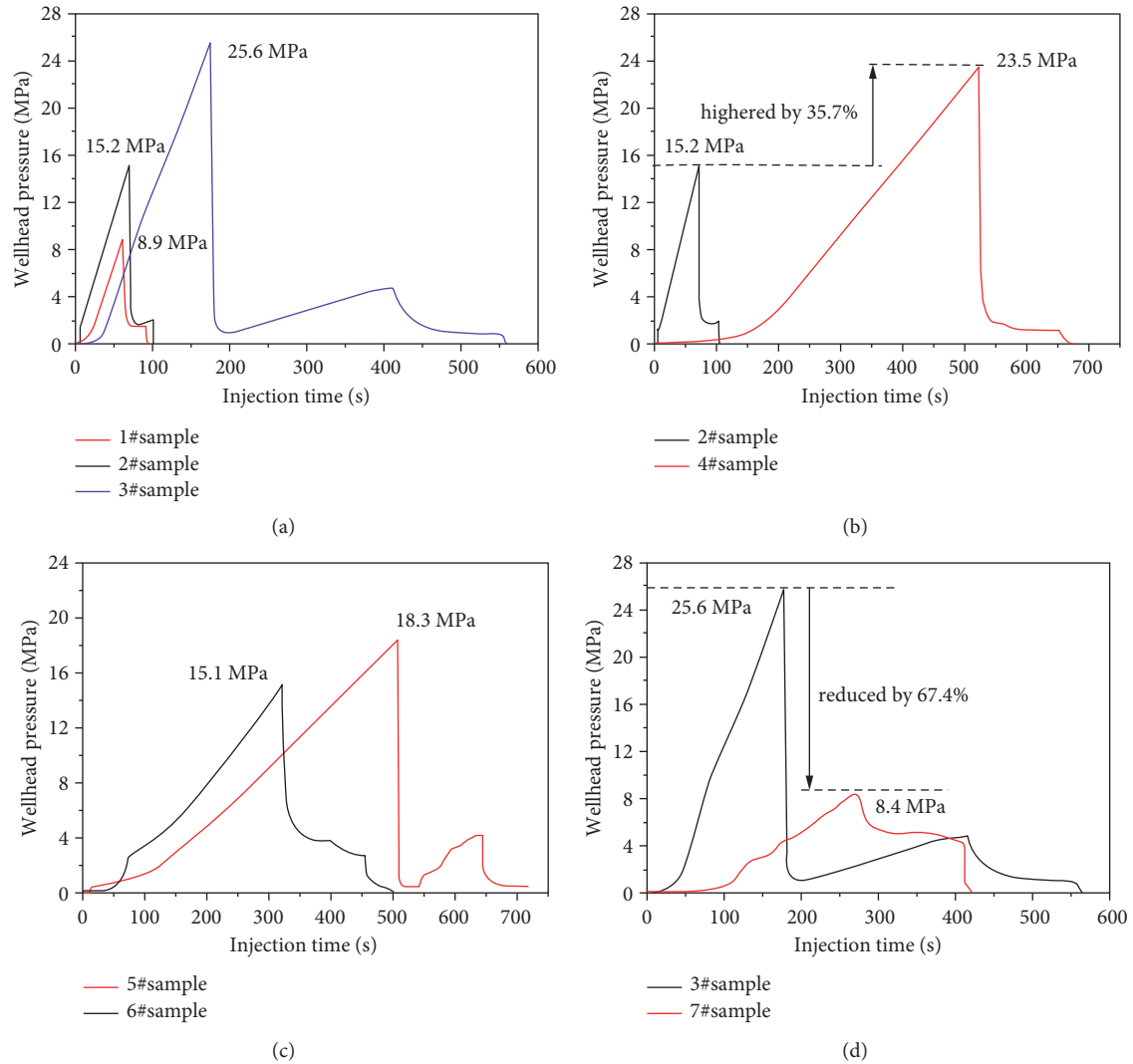


FIGURE 6: Comparison of injection pressure versus time curves characteristics under different influencing factors. (a) Different lithology; (b) different horizontal stress difference; (c) different layer thickness; (d) different fracturing fluid viscosity.

TABLE 2: Statistical table of downhole rock sample properties.

Rock name	Young's modulus (GPa)	Tensile strength (MPa)
Pelitic siltstone	12	6
Silty mudstone	15.64	6.49
Dolomitic siltstone 1	6.16	5.1
Dolomitic siltstone 2	20.2	6.79
Siltstone	33.53	8.49

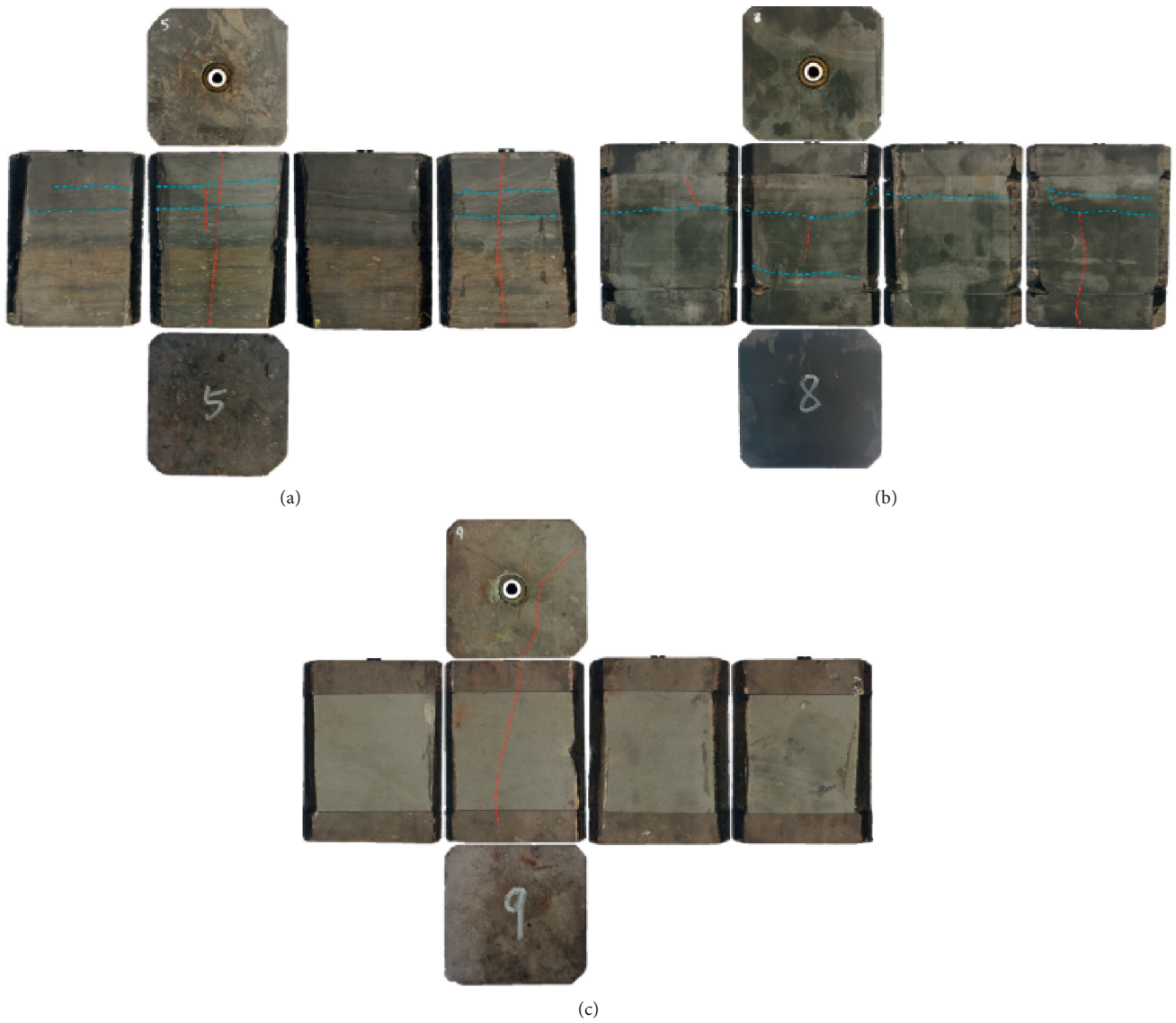


FIGURE 7: Fracture geometry and pressure curves of different lithologies. (a) Sample #1. (b) Sample #2. (c) Sample #3.

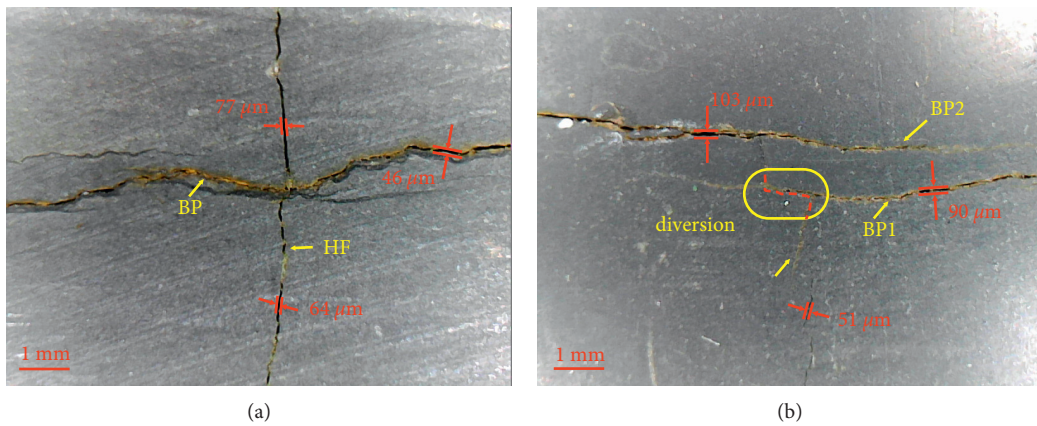


FIGURE 8: BP propagation behavior of HF with different lithology. (a) The HF penetrating the BP in sample #1. (b) HF cutting off by BP in sample #2.



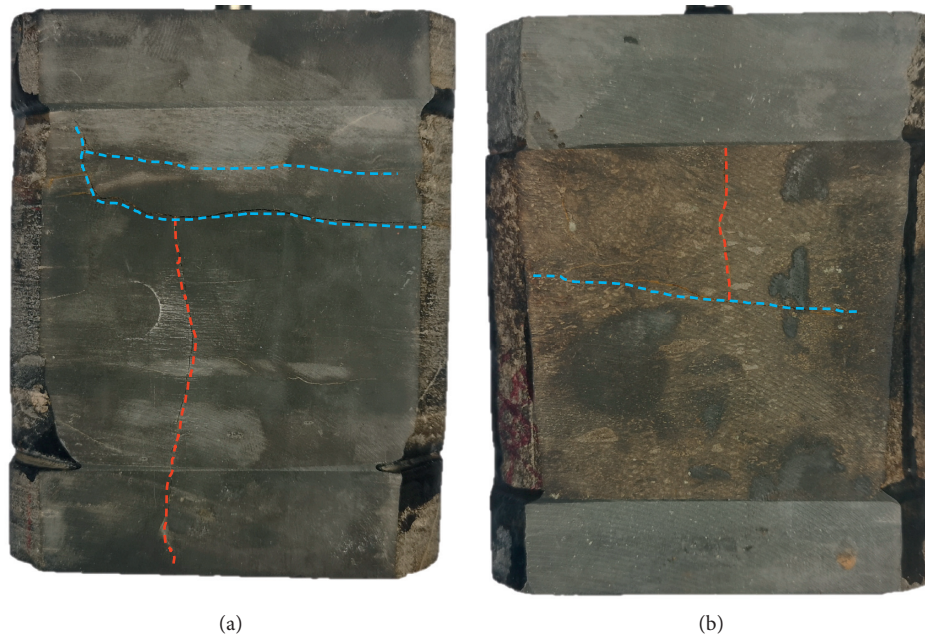


FIGURE 9: Fracture geometry under different horizontal stress difference. (a) Sample #2: horizontal stress difference 13 MPa. (b) Sample #4: horizontal stress difference 18 MPa.

sample. The strength increases, and the fracture height shows a downward trend. Without opening the BP, the fractures can penetrate the bonding interface of the reservoir. However, sample #2 failed to reach the bonding interface of the upper layer due to the propagation between the upper two BPs. When the HF is initiated in argillaceous siltstone, it tends to propagate through BP, and the dimensionless fracture height (HF height/sample height) is higher than 0.74. When HF is initiated in mudstone, the vertical growth of HF tends to terminate at BPs, and the fracture height is constrained. This is mainly because the BPs of mudstone are more developed and the cementation strength is lower.

**4.3. Influence of Horizontal Stress Difference.** The horizontal stress difference has an important impact on the complex fracture geometry of natural fracture-developed reservoir. Generally, the smaller the horizontal stress difference is, the easier it is to form a complex fracture network. For the reservoir with well-developed BP and underdeveloped natural fractures, the impact of horizontal stress difference on fracture propagation needs to be further studied. This section analyses the impact of horizontal stress difference on fracture propagation geometry. As shown in Figure 9, under the conditions of injection rate of 20 mL/min and viscosity of 100 mPa·s, the breakdown pressure was 15.16 MPa in sample #2 under the horizontal stress difference of 13 MPa, forming an HF with a height of 6.4 cm, opening two horizontal BPs, and penetrating the interface of the lower bonding layer. Under the horizontal stress difference of 18 MPa, the breakdown pressure was 20.57 MPa in sample #4, forming an HF with a height of 3 cm. The fracture is more straight and fails to penetrate the interface of the upper bonding

layer. A horizontal BP is formed in the middle, and the HF was cut off by the BP. The experimental results show that the horizontal stress difference increases, the HF is more straight, the propagation is more difficult, the vertical growth of HF tends to terminate at the interface, and the fracture height is small. The horizontal stress difference increases by 5 MPa, the breakdown pressure increases by 35.7%, and the HF height decreases by 37.5%.

**4.4. Influence of Interlayer Thickness.** The influence of interlayer thickness on the vertical propagation of HFs is still unknown [16]. This section mainly considers the influence of interlayer thickness on fracture geometry. When the thickness of the interlayer is 3 cm, the fracture geometry of sample #5 is shown in Figure 10(a). The HF fails to penetrate the upper bonding interface, and the fracturing fluid is leaking off from the bonding interface, with a fracture height of 7.4 cm. When the thickness of the interlayer is 2 cm, the fracture geometric characteristics of sample #6 are shown in Figure 10(b). The HF penetrates through the upper and lower bonding interfaces, penetrates the whole sample, opens two horizontal BPs in the middle layer, with complex fracture geometry, and the fracture height reaches 10 cm. The pressure curve is shown in Figure 6(c). The breakdown pressure was 15.1 MPa in sample #5 and 18.28 MPa in sample #6. There is little difference in the strength of rock samples between the two groups, and the breakdown pressure is similar. The experimental results show that with the increase of interlayer thickness, the HF tends to terminate at the reservoir interlayer interface and propagate horizontally along the interlayer interface, and the fracture height is limited. The interlayer thickness increases by 50%, and the HF height decreases by 26%.

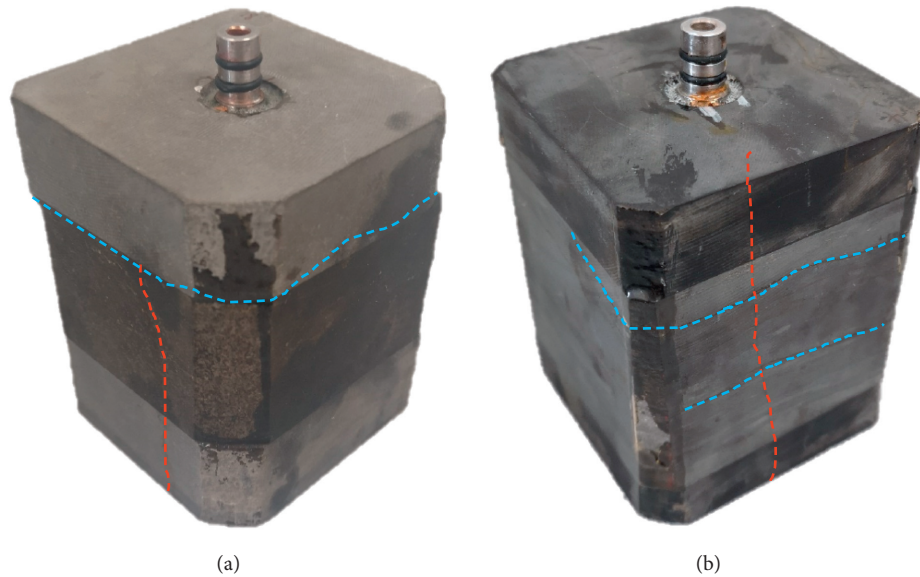


FIGURE 10: Fracture geometry characteristics of samples with different interlayer thicknesses. (a) Sample #5. (b) Sample #6.

**4.5. Effect of Fracturing Fluid Viscosity.** The performance of fracturing fluid mainly includes frictional characteristics, rheological characteristics, and leakoff. Viscosity can be used as a comprehensive index and is an important physical parameter of fracturing fluid. This section mainly considers the influence of liquid viscosity on fracture propagation. Under the condition of high viscosity of fracturing fluid (100 mPa·s), the breakdown pressure was 25.59 MPa (Figure 6(d)), the bottom hole pressure growth rate was fast, the breakdown pressure was high, the HF propagated sufficiently vertical and penetrated the bonding interface, and fracture height reached 7.4 cm. Under the condition of low viscosity of fracturing fluid (3 mPa·s), the breakdown pressure of the sample was 8.35 MPa, which is 67.4% lower than that of high viscosity fracturing fluid, formed a vertical HF with a height of only 3.1 cm (Figure 11). A natural BP was activated at the upper and lower parts respectively, and the vertical propagation of the fracture was seriously limited. When the fracturing fluid viscosity was 100 mPa·s, the fracture height increases by 1.39 times compared with the fracturing fluid viscosity of 3 mPa·s.

The experimental results show that the viscosity of fracturing fluid has an important impact on the HF propagation of BP development samples. Due to the strong permeability of BP and the low viscosity of fracturing fluid, the liquid is easy to leak off along the BP, which is not conducive to the vertical propagate of HFs. Increasing the viscosity of fracturing fluid is helpful for the fracture to penetrate the excessively permeable BP and significantly improve the vertical propagation of fractures. However, under the condition of high viscosity fracturing fluid, HFs are difficult to activate BP, and the fracture geometry is single. In order to improve the fracture control volume, the combined fracturing method of high viscosity fracturing fluid and low viscosity fracturing fluid can be considered.

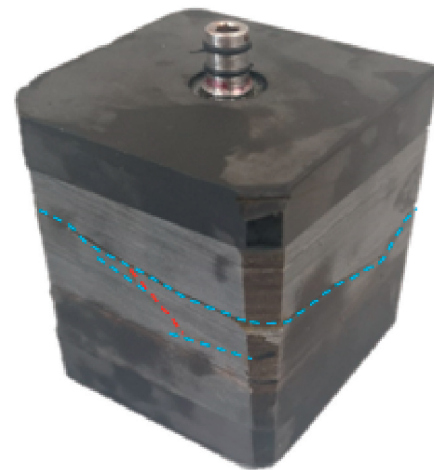


FIGURE 11: Fracture geometry under viscosity 3 mPa·s.

The high viscosity fracturing fluid breaks through the BP barrier, and low viscosity fracturing fluid activates the BP.

## 5. Conclusion

In this study, the laboratory fracturing simulation experiment was carried out on the downhole core samples of Lucaogou Formation, Junggar Basin, China. Fracture propagation behavior in thin-interbedded rock samples was analysed. The findings are summarized as follows:

- (1) In the high-strength sample, HFs tend to propagate to the upper part of the wellbore. The greater the strength is, the smaller the fracture height would be. When HFs initiate in argillaceous siltstone, HFs tend to penetrate BPs, and the dimensionless fracture height is more than 0.74. When HFs initiate in



mudstone, the vertical propagation of HF tends to be terminated at the BPs, and fracture height is constrained.

- (2) The greater the thickness of the interlayer is, the more likely HF tends to be terminated at the interface of the interlayer, propagate along the interface, and have a limited fracture height.
- (3) With the increase of horizontal stress difference, the geometry of HF tends to be simple and straight, which is not conducive to the formation of branch fractures.
- (4) The viscosity of fracturing fluid has a significant impact on the HF propagation in the BP-developed samples. Due to the high permeability of BP and the low viscosity of fracturing fluid, the fluid filtration occurs along the BPs, which is not conducive to the vertical propagation of HF. Increasing the viscosity of fracturing fluid facilitates fractures penetrating through the high-permeability BPs.

## Data Availability

The data that support the findings of this study are available on request from the corresponding author. The data are not publicly available due to privacy or ethical restrictions.

## Conflicts of Interest

The authors declare that they have no conflicts of interest.

## References

- [1] D. Zhi, Y. Tang, Z. Yang et al., "Geological characteristics and accumulation mechanism of continental shale oil in Jimusar sag, Junggar Basin," *Oil & Gas Geology*, vol. 40, no. 03, pp. 524–534, 2019.
- [2] C. Zou, S. Pan, Z. Jing et al., "Shale oil and gas revolution and its impact," *Acta Petrolei Sinica*, vol. 41, no. 01, pp. 1–12, 2020.
- [3] H. Nie, F. He, and S. Bao, "Peculiar geological characteristics of shale gas in China and its exploration countermeasures," *Natural Gas Industry*, vol. 31, no. 11, pp. 111–116 + 132, 2011.
- [4] Z. Yang, L. Hou, S. Lin, X. Luo, S. Wu, and J. Cui, "Geologic characteristics and exploration potential of tight oil and shale oil in lucaogou formation in Jimsar sag," *China Petroleum Exploration*, vol. 23, no. 04, pp. 76–85, 2018.
- [5] S. Zhang, T. Guo, T. Zhou, Y. Zou, and S. Mu, "Fracture propagation mechanism experiment of hydraulic fracturing in natural shale," *Acta Petrolei Sinica*, vol. 35, no. 03, pp. 496–503 + 518, 2014.
- [6] S. Stanchits, J. Burghardt, and A. Surdi, "Hydraulic fracturing of heterogeneous rock monitored by acoustic emission," *Rock Mechanics and Rock Engineering*, vol. 48, no. 12, pp. 2513–2527, 2015.
- [7] Y. S. Zou, S. C. Zhang, T. Zhou, Z. Xiang, and T. Guo, "Experimental investigation into HF network propagation in gas shales using CT scanning technology," *Rock Mechanics and Rock Engineering*, vol. 49, 2015.
- [8] M. Chen, F. Pang, and Y. Jin, "Experiments and analysis on hydraulic fracturing by a large-size triaxial simulator," *Chinese Journal of Rock Mechanics and Engineering*, vol. 19, pp. 868–872, 2000.
- [9] J. Zhou, M. Chen, Y. Jin, and G. Zhang, "Experimental study on propagation mechanism of HF in naturally fractured reservoir," *Acta Petrolei Sinica*, vol. 28, no. 5, pp. 109–113, 2007.
- [10] A. A. Daneshy, "HF propagation in layered formations," *Society of Petroleum Engineers Journal*, vol. 18, no. 1, pp. 33–41, 1978.
- [11] H. Wu, A. Chudnovsky, J. W. Dudley, and G. K. Wong, "A map of fracture behavior in the vicinity of an interface," in *Proceedings of the American Rock Mechanics Association*, Wollongong, Australia, 2004.
- [12] A. S. Athavale and J. L. Miskimins, "Laboratory hydraulic fracturing tests on small homogeneous and laminated blocks," in *US Rock Mechanics Symposium*, Taylor & Francis, London, UK, 2008.
- [13] A. P. Bungler, E. Detournay, and D. I. Garagash, "Toughness-dominated hydraulic fracture with leak-off," *International Journal of Fracture*, vol. 134, no. 2, pp. 175–190, 2005.
- [14] C. D. Pater, M. P. Cleary, T. S. Quinn, D. T. Barr, D. E. Johnson, and L. Weijers, "Experimental verification of dimensional analysis for hydraulic fracturing," *SPE Production & Facilities*, vol. 9, no. 4, pp. 230–238, 1994.
- [15] S. Heng, X. Liu, X. Li, X. Zhang, and C. Yang, "Experimental and numerical study on the non-planar propagation of hydraulic fractures in shale," *Journal of Petroleum Science and Engineering*, vol. 179, pp. 410–426, 2019.
- [16] H. Jin, J. He, Y. Gao, Y. Dong, D. Xu, and Y. Li, "Difficulties and countermeasures of shale oil development in lucaogou formation of jimsar sag," *Xinjiang Petroleum Geology*, vol. 40, no. 04, pp. 379–388, 2019.
- [17] W. Zhao, S. Hu, L. Hou et al., "Types and resource potential of continental shale oil in China and its boundary with tight oil," *Petroleum Exploration and Development*, vol. 47, no. 01, pp. 1–10, 2020.
- [18] D. M. Jarvie, R. J. Hill, T. E. Ruble, and R. M. Pollastro, "Unconventional shale-gas systems: the mississippian barnett shale of north-central Texas as one model for thermogenic shale-gas assessment," *AAPG Bulletin*, vol. 91, no. 4, pp. 475–499, 2007.
- [19] F. P. Wang and J. F. Gale, "Screening criteria for shale-gas systems," *Gulf Coast Association of Geological Societies Transactions*, vol. 59, pp. 779–793, 2009.
- [20] J. Li, "Analysis on mineral components and frangibility of shales in dongying depression," *Acta Sedimentologica Sinica*, vol. 31, no. 4, pp. 616–620, 2013.
- [21] X. C. Jin, S. N. Shah, J. C. Roegiers, and B. Zhang, "Fracability evaluation in shale reservoirs—an integrated petrophysics and geomechanics approach," in *Proceedings of the SPE Hydraulic Fracturing Technology Conference*, The Woodlands, Texas, USA, February 2014.
- [22] B. Tarasov and Y. Potvin, "Universal criteria for rock brittleness estimation under triaxial compression," *International Journal of Rock Mechanics and Mining Sciences*, vol. 59, pp. 57–69, 2013.
- [23] C. Ai, J. Zhang, Y. W. Li, J. Zeng, X.-L. Yang, and J.-G. Wang, "Estimation criteria for rock brittleness based on energy analysis during the rupturing process," *Rock Mechanics and Rock Engineering*, vol. 49, no. 12, pp. 4681–4698, 2016.
- [24] J. Zhang, A. Chi, Y. W. Li, M. G. Che, R. Gao, and J. Zeng, "Energy-based brittleness index and acoustic emission characteristics of anisotropic coal under triaxial stress condition," *Rock Mechanics and Rock Engineering*, vol. 51, 2018.
- [25] I. Rahimzadeh Kivi, M. Ameri, and H. Molladavoodi, "Shale brittleness evaluation based on energy balance analysis of

- stress-strain curves,” *Journal of Petroleum Science and Engineering*, vol. 167, pp. 1–19, 2018.
- [26] N. Li, Y. S. Zou, S. C. Zhang et al., “Rock brittleness evaluation based on energy dissipation under triaxial compression,” *Journal of Petroleum Science and Engineering*, vol. 183, 2019.
- [27] K. Xi, Y. Cao, R. Zhu et al., “Rock types and characteristic of tight oil reservoir in permian lucaogou formation, Jimsar sag,” *Acta Petrolei Sinica*, vol. 36, no. 12, pp. 1495–1507, 2015.
- [28] J. He, C. J. Okere, G. Su et al., “Formation damage mitigation mechanism for coalbed methane wells via refracturing with fuzzy-ball fluid as temporary blocking agents,” *Journal of Natural Gas Science and Engineering*, vol. 90, 2021.

## Research Article

# Graded Control Technology of Oil Stability and Water Control in Fracture-Pore Carbonate Reservoirs

Wenqi Zhao <sup>1</sup>, Lun Zhao <sup>1</sup>, Junjian Li,<sup>2</sup> Jue Hou,<sup>1</sup> and Xuejing Guo<sup>1</sup>

<sup>1</sup>PetroChina Research Institute of Petroleum Exploration & Development, China National Petroleum Corporation, Beijing 100083, China

<sup>2</sup>China University of Petroleum, Beijing 102249, China

Correspondence should be addressed to Lun Zhao; zhaolun@petrochina.com.cn

Received 18 November 2021; Accepted 17 January 2022; Published 8 February 2022

Academic Editor: Xiang Zhou

Copyright © 2022 Wenqi Zhao et al. This is an open access article distributed under the Creative Commons Attribution License, which permits unrestricted use, distribution, and reproduction in any medium, provided the original work is properly cited.

In view of the prominent problems of extremely strong heterogeneity, fracture development of different scales, and serious rapid water channelling in the process of water injection development in fracture-pore carbonate reservoirs, a comprehensive treatment method of oil stabilizing and water controlling is proposed, which includes fracture classification control, combination of adjustment and plugging, and wettability change. Based on the static and dynamic test data, the characteristics of reservoir fracture development and fracture scales are described in detail. By means of reservoir engineering and numerical simulation, the water flooding rule under different grade fracture reservoir conditions is studied, the influence of different levels of fractures on water injection development is evaluated, and the improvement effect of different control methods on water drive sweep is demonstrated. Research shows that a large amount of remaining oil trapped in pores is affected by fracture water channelling, which makes it difficult to use effectively. The water flooding sweep characteristics of reservoirs with different scales of fractures are quite different, and large-scale fractures are the main reason for ineffective water injection. The hierarchical control techniques of plugging large-scale fractures, intervening and adjusting small- and medium-scale fractures, and changing the wettability of microscale pore media can significantly extend the water flooding spread range and effectively improve oil well production. The research results have been applied in the field and achieved good results. This technology can provide theoretical guidance and a technical basis for the comprehensive treatment of oil stabilization and water control in fractured-porous carbonate oil and gas reservoirs.

## 1. Introduction

As one of the most important oil and gas reservoirs globally, carbonate reservoirs account for an increasing proportion of oil and gas reserves and production. However, carbonate reservoirs are complex, bringing difficulties in hydrocarbon exploitation. Carbonate reservoir development technology has become a challenge and an important research area in global and domestic oil development [1–5]. To date, experiences in developing complex carbonate reservoirs are limited both at home and abroad [6–9]. Carbonate reservoirs have various types of pores, mainly including large-scale cavities, small-scale pores, and multiscale fractures. Fractured carbonate reservoirs commonly have internal preferential pathways, resulting in severe water channelling

problems and poor development results. Consequently, oil stabilization and water control are essential for the oil recovery of fractured carbonate reservoirs. Reservoir development practice at home and abroad shows that plugging technology is an essential means to improve water drive effect. The injection of chemical agents to block the dominant flow channel can adjust the liquid production profile, alleviate the internal contradictions in the reservoir, and improve the effect of oilfield development, but the plugging technology of carbonate reservoirs is not mature enough. The existing methods are difficult to implement and cannot truly combine the real geological characteristics of the oilfield. The process and selection of chemicals are relatively simple, and the reservoir is only generally blocked at the macrolevel. Therefore, the previous technology cannot really

play profile control water, alleviating reservoir contradictions. It is difficult to achieve hierarchical control and achieve the desired development effect.

This paper takes the fractured-porous carbonate reservoirs in the T oilfield at the eastern margin of the Pre-Caspian Basin as an example to study the characteristics of fractures and the principle of water flooding in different levels of fractured reservoirs. The purpose is to propose a graded regulation method for stabilizing oil and controlling water in fractured-porous carbonate reservoirs. This proposed method can effectively block the large-scale media to avoid the rapid influx of injected water, effectively intervene the medium- and small-scale media to inhibit the seepage velocity of injected water, and improve the rock wettability of microscale media to improve the water drive efficiency. The suggested method is closely combined with the reservoir geological characteristics and development law and has stronger pertinence. It can effectively improve the production and absorption profile, expand the swept volume of water flooding, and improve the macroscopic swept range and microscopic oil displacement efficiency. This has important practical significance for improving oilfield development effects.

*1.1. Geological Characteristic of Carbonate Reservoirs.* Structures of the Pre-Caspian Basin can be found in Figure 1. More than 90% of the oil and gas reserves in the Pre-Caspian Basin are from carbonate reservoirs. The strata of the basin can be divided into two sets, which are above-salt and subsalt strata. All currently discovered carbonate reservoirs are located below the salt layer. Two oil-bearing reservoirs, Carboniferous KT-I and KT-II, are developed. Lithology at the eastern margin of the basin is complex [10–14]. Limestone and dolomite are dominated by minor gypsum and others.

The carbonate reservoirs in the Pre-Caspian Basin are influenced by sedimentary, diagenetic, and tectonic processes, resulting in various reservoir space types, such as pores, fractures, and caves. Based on the observation of cores, thin sections, and scanning electron microscopic photos, it shows that pores are the dominant oil accumulation space. The volume of the pores accounts for 94% of the total volume of the space. Fractures and caves are 5% and 1%, respectively. Large-scale fractures and cavities are relatively abundant.

According to the dip angle, the fractures can be divided into low angle, oblique, and high angle, as shown in Table 1. Based on core and image logging data, the number of different types of fractures is counted. The statistical results are shown in Figure 2. The results show that the low-angle fractures account for 80.5% and 57.5% in core and imaging logging data. Oblique fractures account for 14.6% and 35.8% in core and imaging logging data, and high-angle fractures account for 4.9% and 6.7% in core and image logging data. In general, low-angle fractures are dominated.

According to the opening size, the fractures are divided into large-scale fractures, mesoscale fractures, small-scale fractures, and microscale fractures, as shown in Table 2. The

number of fractures with different opening sizes is counted based on imaging logging, as shown in Figure 3. The results show that the proportions of large-scale, mesoscale, small-scale, and microscale fractures in the reservoir are 4.7%, 52.5%, 42.5%, and 0.4%, respectively. In general, mesoscale and small-scale fractures are dominated.

The types of reservoir accumulation space and space combination are complex. According to the development degree and space combination, the reservoir space can be divided into five types based on core observation and well logging response. The five types of reservoir space include the porous-cavernous-fractured composite type, porous-cavernous type, porous type, fractured-porous type, and fractured type. The proportions of each type are 6.2%, 5.3%, 44.9%, 42.6%, and 1.0%, respectively. In general, the fractured pore type is dominated.

## 2. Seepage Characteristics of Water Injection in Different Types of Reservoirs

In order to better understand the effect of water flooding, seepage characteristics of water injection in reservoirs with fractured, fractured-porous, and porous-cavernous spaces are discussed by using microfluidic technology [15–18]. The first step is to select the typical thin section that represents various types of reservoirs and design a model based on pore-throat structure extraction and image stitching, as shown in Figure 4. Then, the microfluidic water drive experiment is carried out to analyze the water injection seepage characteristics of different types of reservoirs. During the microfluidic experiment, the thin section is first injected with kerosene for saturation, and then, at one end of the thin section, water is injected at an injection rate of  $1 \mu\text{L}/\text{min}$  to displace kerosene, and the other end is the production end. During the experiment, the displacement process is recorded by using a high-power camera.

Analyzing the thin reservoir section with the pore space type shows that the maximum, minimum, and average pore sizes are  $613 \mu\text{m}$ ,  $6.1 \mu\text{m}$ , and  $63.4 \mu\text{m}$ , respectively. The main pore size distribution is below  $200 \mu\text{m}$ . The porous reservoir is heterogeneous, which can be observed from the water flooding test of the oil-saturated thin section, as shown in Figure 5. The injected water is relatively fully affected by the thin section when it enters the pores and throats. The front of the injected water is relatively uniform. The flooded water has a wider sweep area and low penetration speed. The flooding effect is mainly affected by the pore size, pore distribution, and connectivity of the pore and throat. The recovery rate of this model is 43.7%.

Compared with the porous reservoir, the fractured-porous reservoir is more heterogeneous. The maximum, minimum, and average pore sizes are  $754 \mu\text{m}$ ,  $10.2 \mu\text{m}$ , and  $122.9 \mu\text{m}$ , respectively. The main pore size distribution is below  $250 \mu\text{m}$ . The opening degree of fractures is different in various places, enhancing the heterogeneity of the reservoir. It can be observed from the water flooding test of the oil-saturated thin section, as shown in Figure 6. The injected water first enters the matrix around the injection point and then the fractures. Finally, the injected water rapidly

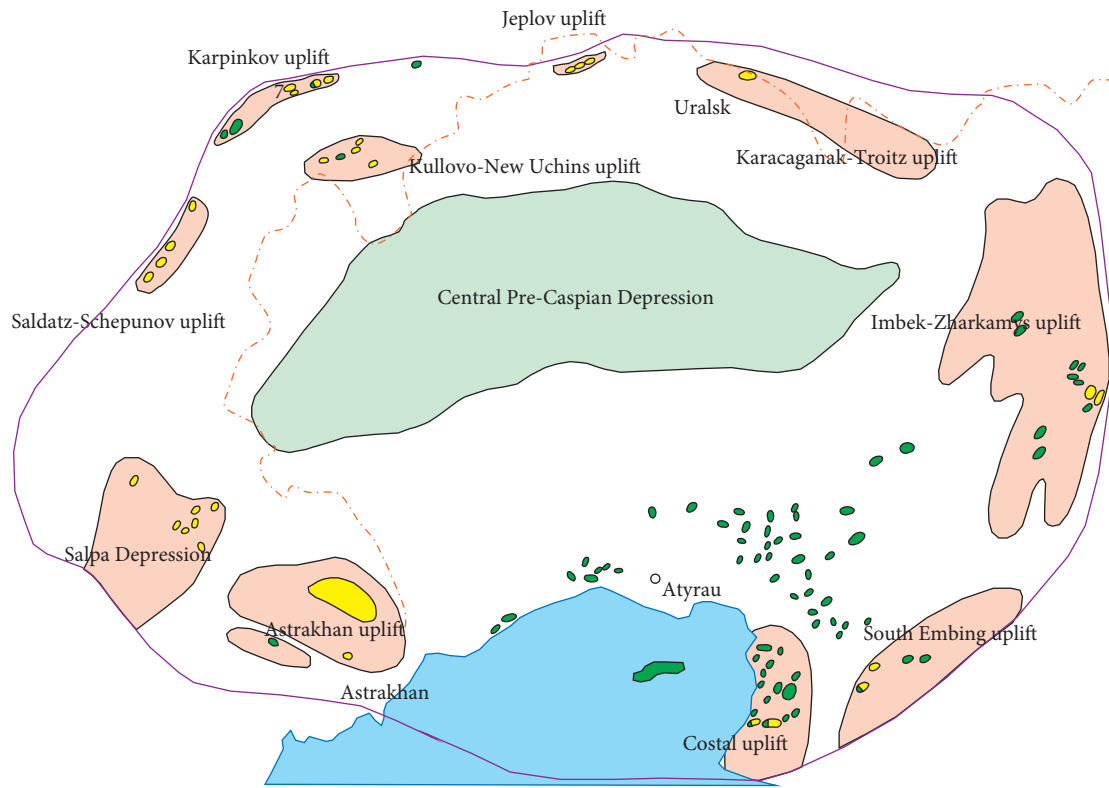


FIGURE 1: Structures of the Pre-Caspian Basin.

TABLE 1: Fracture dip angle and fracture types.

Fracture dip angle	>70°	35°–70°	<35°
Fracture type	High-angle fracture	Oblique fracture	Low-angle fracture

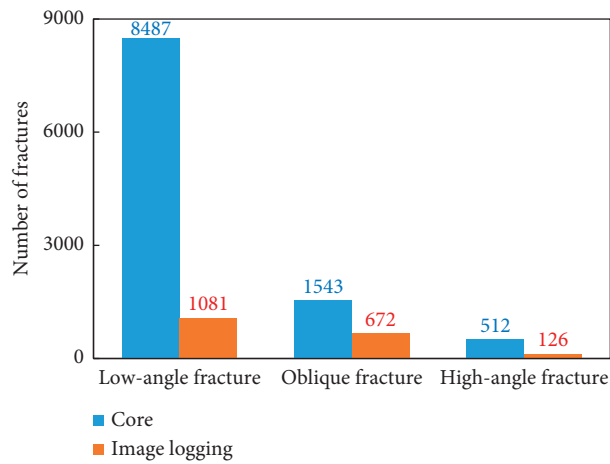


FIGURE 2: Numbers of the fractures with different types.

TABLE 2: Fracture opening size and fracture type.

Fracture opening size (mm)	<0.001	0.001–0.01	0.01–0.1	>0.1
Fracture type	Microscale	Small-scale	Mesoscale	Large-scale



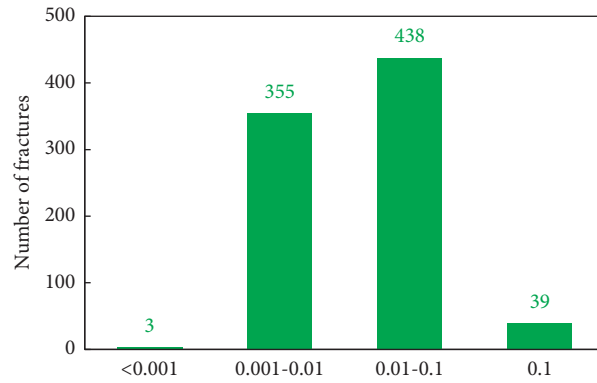


FIGURE 3: Numbers of the fractures with different opening sizes.

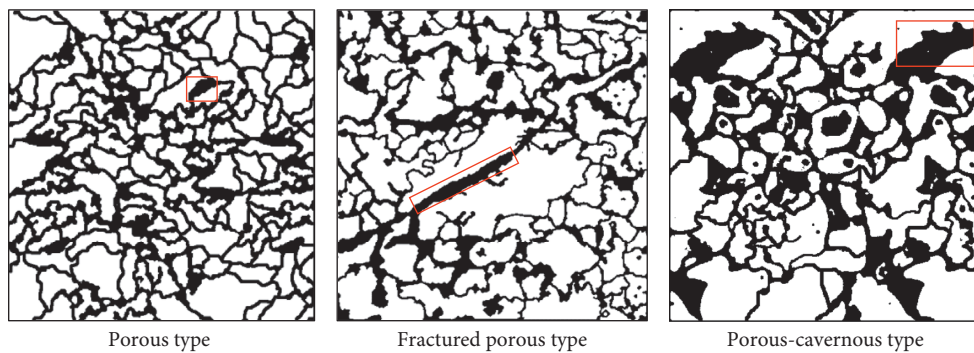


FIGURE 4: Experimental models of microfluid in different space types of reservoirs (pores, fractures, and caves are marked in the red box). (a) Porous type. (b) Fractured-porous type. (c) Porous-cavernous type.

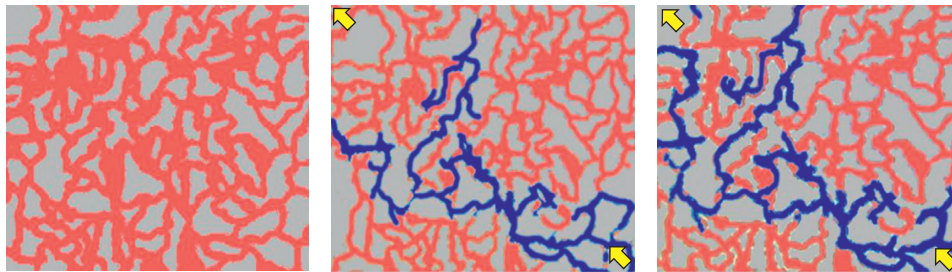


FIGURE 5: Schematic diagram of the early, middle, and late stages of water injection in porous reservoirs.

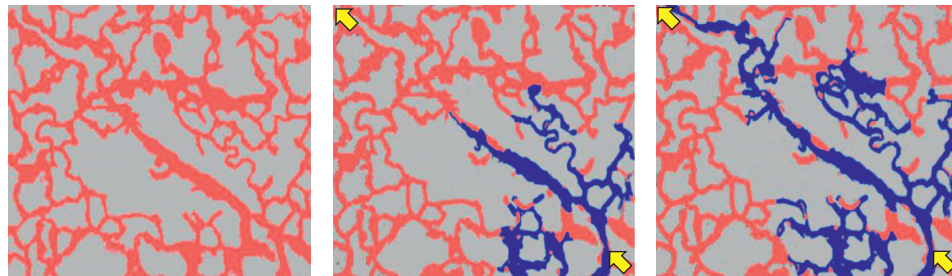


FIGURE 6: Schematic diagram of the early, middle, and late stages of water injection in fractured-porous reservoirs.

advances along the cracks. Simultaneously, part of the injected water sweeps the surrounding areas with better connectivity. After the water breakthrough, the scope of the

injected water does not increase. The oil in the fractures is effectively displaced, whereas the matrix has a poorer oil displacement effect. The recovery rate of this model is 35.4%.

The reservoir with the porous-cavernous space type also shows strong heterogeneity. The maximum, minimum, and average pore sizes are  $1031\ \mu\text{m}$ ,  $13.1\ \mu\text{m}$ , and  $123.7\ \mu\text{m}$ , respectively. The main pore size distribution is below  $550\ \mu\text{m}$ . The injected water easily enters the large cavities and gradually displaces the oil from the cavities to the surrounding pores with good connectivity. This can be observed from the water flooding test of the oil-saturated thin section, as shown in Figure 7. The swept area of the injected water decreases. The cavities mainly play a role in storage. The water flooding effect is mainly affected by the degree of connectivity between the cavities and the throats. The recovery rate of this model is 38.6%.

From the above analyses, it can be seen that the water flooding effects of different types of reservoirs are different. Due to the presence of fractures and cavities, the injected water flows fast, and the swept area is small. Therefore, the fractures and cavities determine the effect of water flooding development. For the T oilfield, cavities are relatively small. Consequently, fractures are the key to stabilizing oil and controlling water in the T oilfield.

In order to better understand the role of fractures in the water flooding process, digital core simulation methods were used to simulate the porous, fractured-porous, and fractured reservoirs [19–23], as shown in Figure 8. The results show that the development of fractures is the main factor influencing the effect of water flooding. Table 3 shows that the water flood recovery rates of fractured and fractured-porous reservoirs are around 17%, significantly lower than the 40% recovery rate of porous reservoirs. The remaining movable oil in fractured-porous reservoirs is significantly higher than that in porous reservoirs. Therefore, improving the effectiveness of water flooding in fractured reservoirs is the direction of adjustment of oilfield water injection development.

### 3. Graded Water Flooding Control of Fractured Reservoirs with Variable Opening Sizes

**3.1. Water Flooding Effect of Fractures with Different Opening Sizes.** The porosity and permeability of 1991 cores from 10 wells in the study area were measured by using an overburden pressure porosity and permeability tester to simulate formation conditions, including 171 fractured cores and 1820 nonfractured cores. Based on the analysis of the relationship between porosity and permeability of cores, it can be seen that fractures can significantly improve the permeability of the reservoir, especially when the porosity is less than 10%, as shown in Figure 9. The fractures can increase the permeability of the reservoir by 10 to 100 times.

Although fractures can improve the conductivity of fluids in the reservoir, the injected water easily flows along with the fractures, resulting in a large amount of oil being immobilized in the matrix and unable to be recovered. In order to better understand the role of fractures with different opening sizes in the water flooding process, the embedded discrete fracture numerical simulation method is used to analyze the sweep characteristics of water flooding. The fracture opening sizes are designed to be 0.001 mm,

0.005 mm, 0.01 mm, 0.05 mm, 0.1 mm, and zero, as shown in Figure 10. Under the condition of 0.4 times the pore volume, when water drive development is carried out in the reservoir without fractures and with a fracture opening of 0.001 mm, the injected water advances more evenly, the water drive front edge is relatively flat, no obvious water channelling hardly occurs, and the water drive has a wide range. When the opening size is greater than 0.005 mm, water channelling occurs. There is a tongue at the front edge of the water drive, and the fracture begins to affect the water flow velocity, which has an adverse impact on the effect of water injection development. It shows that the fracture improves the conductivity of the reservoir, and with the increase of opening, the conductivity of the reservoir increases, and the channelling speed of injected water becomes faster. The water channelling is obvious when the opening size is 0.1 mm, and the swept area of water flooding is limited. The difference of permeability grade between the fracture and the matrix becomes larger, and the injected water rapidly rushes into the production end along the fracture, resulting in poor water drive development effect.

As is shown in Figure 11, the water flooding sweep coefficient of the nonfracture model can reach 62.5%. With the increase of the fracture opening size, the water flooding sweep coefficient gradually decreases. When the opening size increases to over 0.01 mm, the water flooding sweep coefficient decreases significantly. When the fracture opening size is 0.1 mm, the water flooding sweep coefficient is only 31.3%. Therefore, the water flooding effect of fractures with variable opening sizes is different. When the fracture opening size is under 0.001 mm, there is no obvious penetration of the injected water. When the fracture opening size reaches more than 0.01 mm, the water injection effect starts to deteriorate significantly. When the reservoir has large-scale fractures with an opening size of more than 0.1 mm, the injected water shows obvious channelling, which easily leads to ineffective water injection.

**3.2. Profile Control of Fractures with Different Opening Sizes.** According to the aforementioned research results, the water flooding features of fractured reservoirs of variable opening sizes are different. The roles of fractures with variable opening sizes played in water injection development are also different. Therefore, it is necessary to conduct different order control on fractures to understand the effectiveness of water injection. The numerical simulation model of fractured reservoirs with fracture openings of 0.1 mm (large-scale), 0.01 mm (medium- to small-scale), and 0.001 mm (micro-scale) is designed. Flexible gels, nano-microspheres, and wettability modifiers are used to inject into reservoir samples at 0.5 times the fracture volume, 0.5 times the fracture volume, and 0.2 times the matrix volume, respectively. Then, samples are flooded with water. The concentration of modifiers in fractured reservoirs with variable opening sizes and the oil saturation after adjustment are shown in Figures 12–14.

Based on the distribution pattern of the chemical agent after the flexible gel flooding, it shows that, as the fracture

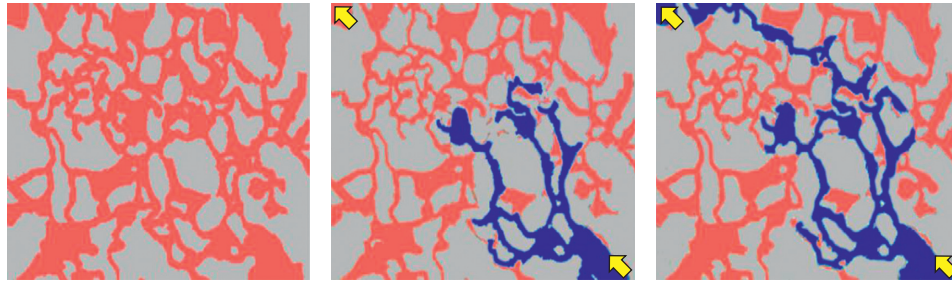


FIGURE 7: Schematic diagram of the early, middle, and late stages of water injection in a porous-cavernous reservoir.

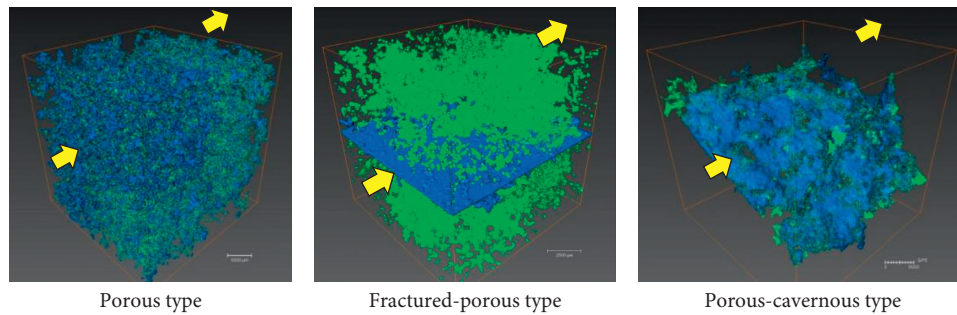


FIGURE 8: Digital core simulation of movable remaining oil distribution in different types of reservoirs. (a) Porous type. (b) Fractured-porous type. (c) Porous-cavernous type.

TABLE 3: Porosity and remaining oil saturation of different types of reservoirs.

Reservoir type	Total porosity (%)	Connected porosity (%)	Effective porosity (%)	Irreducible water saturation (%)	Residual oil saturation (%)	Movable remaining oil saturation (%)	Recovery rate (%)
Porous type	12.47	10.81	5.39	32.02	24.72	16.05	40
Fractured type	5.25	1.43	0.54	49.40	40.28	1.66	17.1
Fractured-porous type	13.48	11.82	4.13	38.04	31.34	20.13	16.9

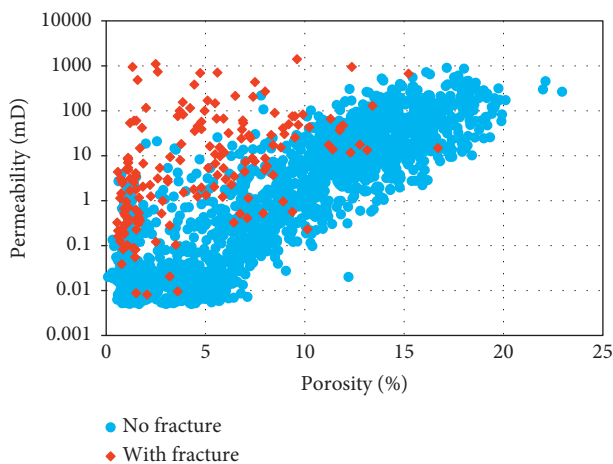


FIGURE 9: The relationship between porosity and permeability of cores.

size and profile depth decrease, the sweep coefficient of large-scale, medium-small-scale, and microscale fractured reservoirs increases to 11.4%, 5.2%, and 2.5%, respectively.

The large-scale fracture has the largest increase in the sweep coefficient. The large-scale fractures can achieve deep profile control and flooding. The water channelling problem is controlled after the fractures are deeply controlled.

Based on the distribution pattern of the chemical agent after the nano-microsphere controlling and flooding, it shows that nano-microspheres can migrate into large-scale and medium-small-scale fractures. In microscale fractured reservoirs, the chemical agent is concentrated around the injection well. After nano-microsphere profile control and flooding, the large-scale, medium-small-scale, and microscale fractured reservoir sweep coefficients are increased by 4.8%, 8.5%, and 2.5%, respectively. The sweep coefficient of the small-medium-scale fractured reservoir has the largest increase. Although nano-microspheres can realize deep adjustment and flooding of large-scale fractures, they have limited fracture control. They cannot effectively control the channelling of injected water in large-scale fractures. For small- and medium-scale fractured reservoirs, nano-microspheres can achieve deep adjustment and flooding and obvious control over medium-small-scale fractures and uniform water flooding results.



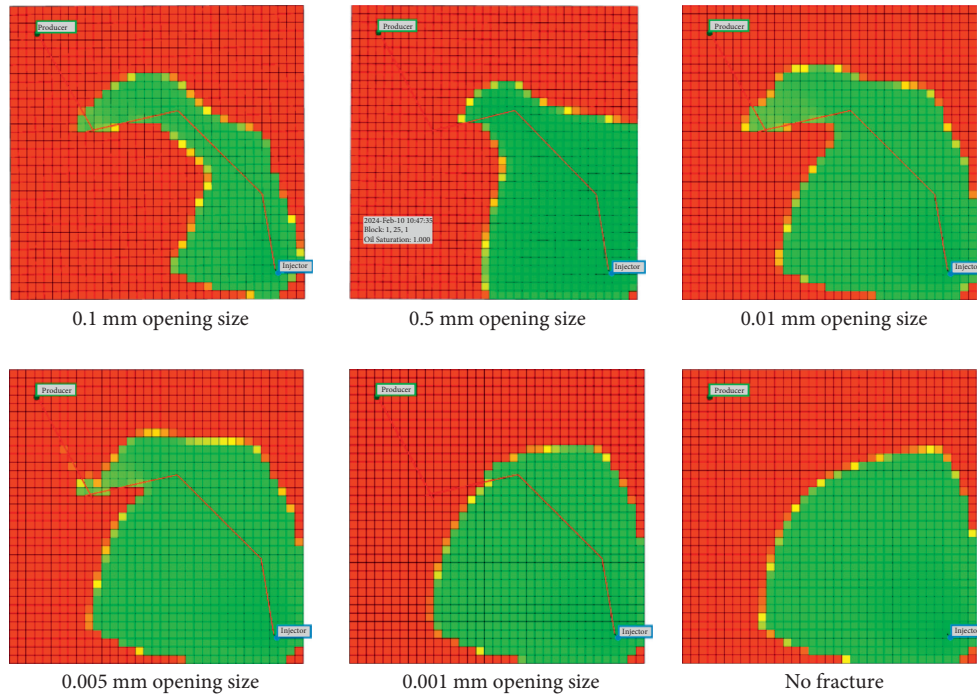


FIGURE 10: Oil saturation distribution of water flooding in reservoirs with different fracture openings. (a) 0.1 mm opening size. (b) 0.5 mm opening size. (c) 0.01 mm opening size. (d) 0.005 mm opening size. (e) 0.001 mm opening size. (f) No fracture.

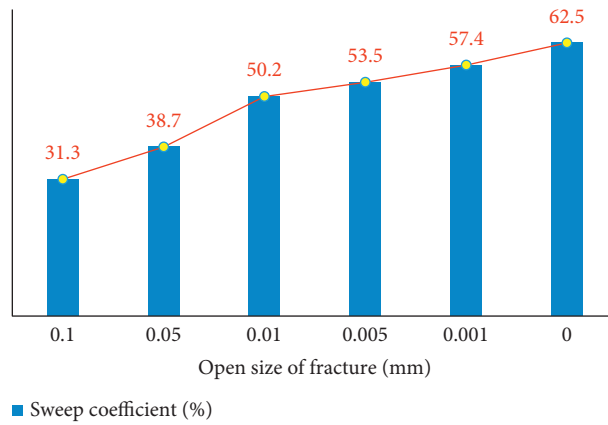


FIGURE 11: Water flooding sweep coefficients of fractured reservoirs with variable opening sizes.

Based on the distribution pattern of the surfactant injection, it shows that the surfactant can migrate into the fractures with different scales. In the microscale fractures, the agent is relatively enriched around the injection well. After surfactant injection, the large-scale, medium-small-scale, and microscale fractured reservoir sweep coefficients are increased by 4.8%, 8.5%, and 2.5%, respectively. The sweep coefficient of the microscale fractured reservoir has the largest increase. Surfactants can effectively improve the wettability of rocks in microscale fractured reservoirs. The oil in the matrix pores can be recovered, significantly improving the water flooding effect of microscale fractured reservoirs.

From the above analysis, it can be seen that the control methods of fractured reservoirs with variable fracture sizes

are different. Large-scale, small-medium-scale, and micro-scale fractured reservoirs can be controlled with flexible gels, nano-microspheres, and surfactants to achieve better water flooding results.

### 3.3. Control Method for Oil Stabilization and Water Control.

The research mentioned above shows that low angle is mainly developed in the study area. Water channelling easily occurs during water injection. The direction of water flooding is complicated, which seriously reduces oil production. Therefore, effective control of fractures is the key to stabilizing oil and controlling water in fractured-porous carbonate reservoirs. Fractures with variable scales are developed in the oilfield. The effects of fractures with different

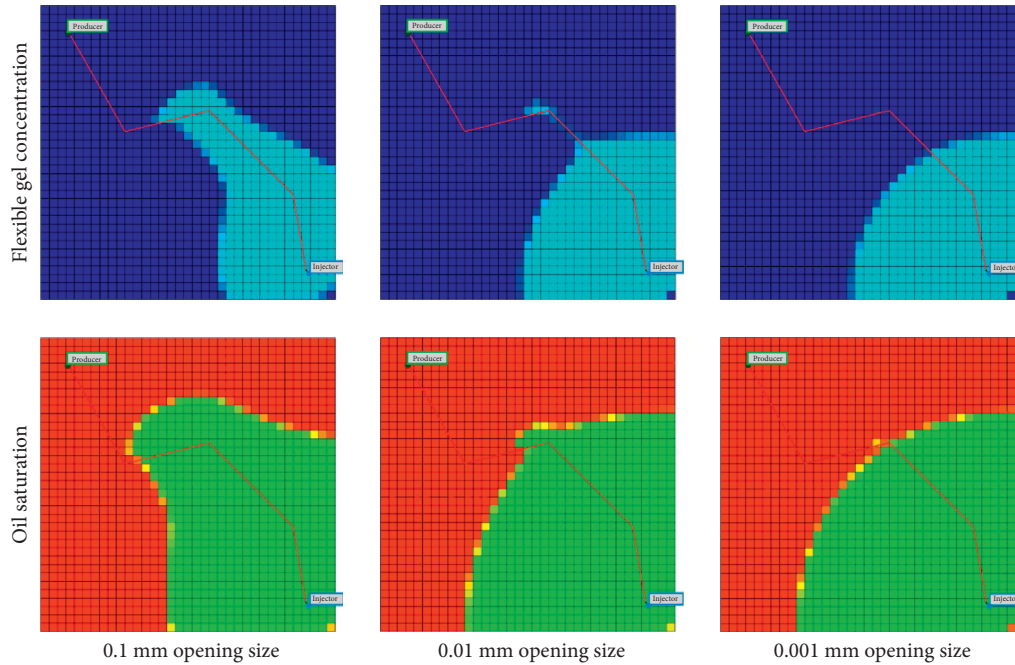


FIGURE 12: Distribution of chemical agent concentration and oil saturation after control and flooding with flexible gel in fractured reservoirs with variable opening sizes.

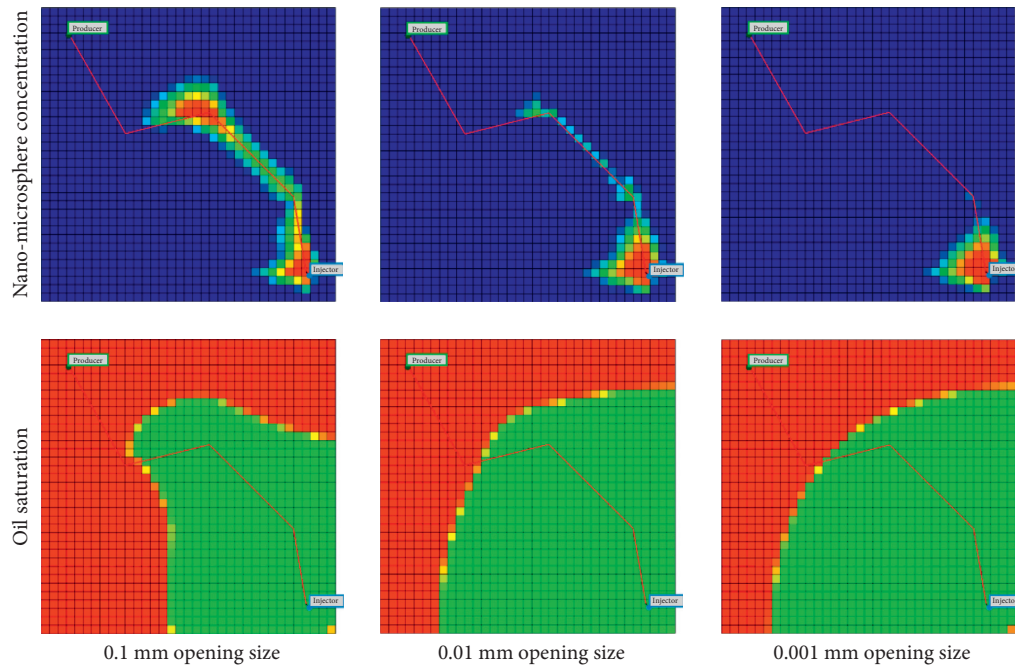


FIGURE 13: Chemical agent concentration and oil saturation distribution after control and flooding with nano-microspheres in fractured reservoirs with variable opening sizes.

scales in the water flooding are quite different. Different control strategies should be adopted for different scale fractures based on the profile control results of variable fractures.

Large-scale fractures are the main channel for the rapid penetration of injected water, which can easily cause ineffective water injection. Large-scale fractures need to be

effectively plugged and effectively solve the channelling problem. Small-medium-scale fractures are secondary channels for injected water intrusion. The flow rate of injected water is relatively fast, which largely affects the effect of water injection. Effective intervention needs to be taken to suppress the seepage rate of injected water. Microscale fractures and matrices are the main oil accumulation areas,



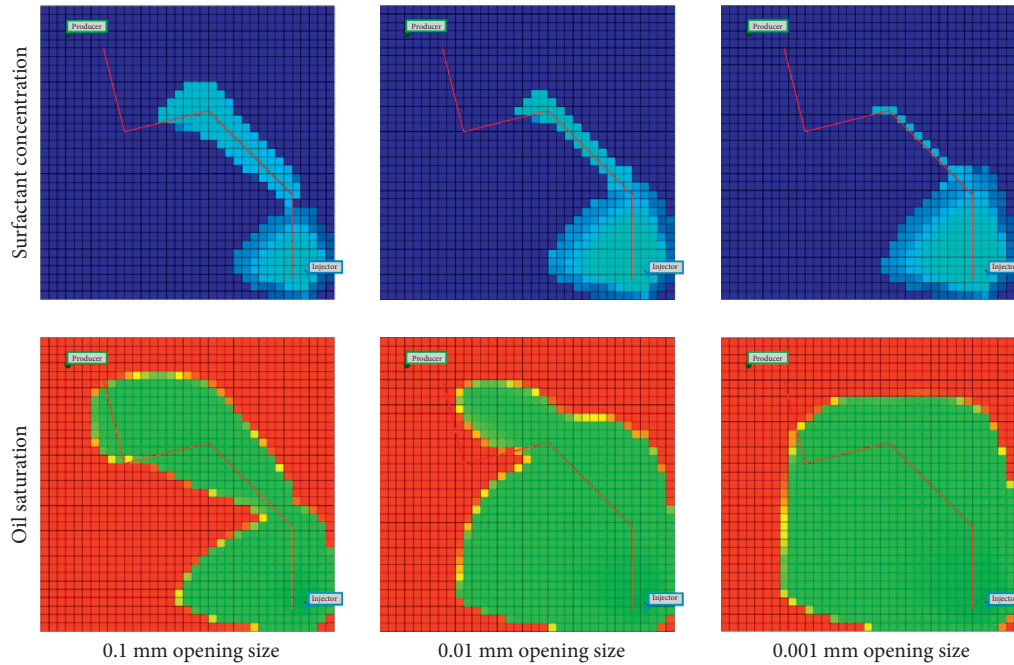


FIGURE 14: Distribution of chemical agent concentration and oil saturation after surfactant injection in fractured reservoirs with variable opening sizes.

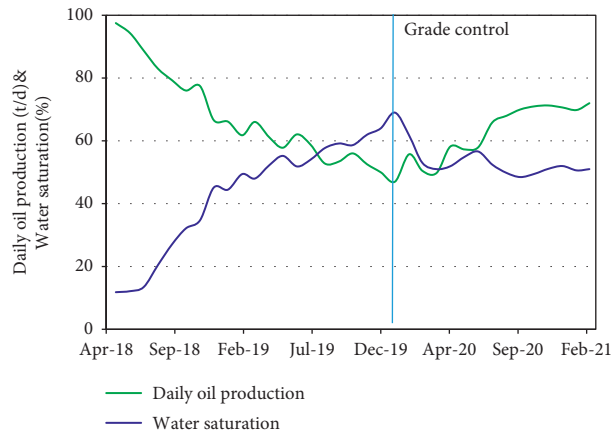


FIGURE 15: Production performance of wells in the pilot test area.

which are key to enhancing productivity. The wettability of rocks needs to be improved to increase water flooding efficiency.

Due to the presence of multiscale fractures in the reservoir, it is necessary to perform hierarchical control on fractures with different scales and use multiple control agents and slugs for comprehensive intervention in order to form a grading control method for oil stabilization and water control. The first plug uses flexible gel to block large-scale fractures. The second plug uses a nano-microsphere to adjust small-medium-scale fractures. The third plug uses surfactant to change the wettability of the microscale pore and block the channelling. The purpose is to adjust the secondary preferential channel and to reduce the flow resistance of the matrix. Consequently, macroswept volume is expanded. The

microdisplacement efficiency is improved. Finally, the goal of oil stabilization and water control can be achieved.

#### 4. Application Result

The technology was carried out in January 2020 in the T oilfield at the eastern margin of the Pre-Caspian Basin. The graded control technology has been implemented in four water injection wells and ten surrounding oil wells. As depicted in Figure 15, the development effect has been significantly improved. The oil production increases 4 t/d based on the calculation result of the declining method. The water cut has dropped by 18%. 279 tonnes of oil will be increased. Due to the good performance, it is ready to expand the test scale within the entire oilfield.

China operates about 20 carbonate oil reservoirs in Central Asia. This technology can be applied to the development of carbonate hydrocarbon reservoirs in Kazakhstan, providing technological support for enhancing oil recovery in Central Asia. To date, experiences in the development of complex carbonate reservoirs through water injection are limited both at home and abroad. This technology can be used for Sino-foreign cooperation projects in Kazakhstan, Oman, Turkmenistan, Iraq, and Syria, making a contribution to oil stabilization and water control in complex carbonate oil and gas fields.

## 5. Conclusions

This paper reveals the seepage characteristics of different types of reservoirs and factors affecting oil development based on the reservoir characteristics, water flooding principles, physical simulation, and digital core displacement experiment. The purpose is to understand the role of fractures in water flooding and the water flooding effect after fracture adjustment. Finally, graded control technology is proposed for oil stabilization and water control in fractured reservoirs with variable scale fractures. The specific conclusions are as follows:

- (1) Reservoir types in the study area are diverse. The seepage characteristics of different types of reservoirs are different. The seepage rate of injected water in porous reservoirs is relatively slow—the water flooding front advances more uniformly. The swept area is wide. The water flooding development effect is good.
- (2) The presence of fractures enhances the heterogeneity of the reservoir—fractures with various dip angles cut each other to form a complex networked fracture system. The water channelling problem is serious. A large amount of the remaining oil has been sealed in the matrix. The water flooding direction is complicated and severely reduces oil production. Fracture is the main factor that affects the effect of reservoir water flooding. Improving the swept area of fractured reservoirs is the direction of water flooding development and adjustment.
- (3) The water flooding features and effects of fractured reservoirs with different fracture scales are different. When the fracture opening size reaches the medium-small scale or above, the water channelling will affect oil development. Water injection is invalid.
- (4) The application of flexible gel to block large-scale fractures, nano-microspheres to block small-medium-scale fractures, and surfactants to change the wettability of microscale pores has been promoted in oilfields. It shows that this technology can effectively improve the effect of water injection and increase oilfield recovery. The application prospects of the technology are abroad, which can provide a technical basis for the comprehensive treatment of oil stabilization and water control in complex carbonate oil and gas fields at home and abroad.

## Data Availability

The data used to support the findings of this study are included within the article.

## Conflicts of Interest

The authors declare that there are no conflicts of interest regarding the publication of this paper.

## References

- [1] B. Zhang and J. Liu, "Classification and characteristics of karst reservoirs in China and related theories," *Petroleum Exploration and Development*, vol. 36, no. 1, pp. 19–36, 2009.
- [2] S. J. Mazzullo and G. V. Chilingarian, "Chapter 9 Hydrocarbon reservoirs in karsted carbonate rocks," *Developments in Petroleum Science*, vol. 44, pp. 797–865, 1996.
- [3] Y. Liu, Z. Tian, and R. Guo, "Review and prospective of rock-typing for complex carbonate reservoirs," *Progress in Geophysics*, vol. 32, no. 5, pp. 2057–2064, 2017.
- [4] R. P. Major and M. H. Holtz, "A new meshless local Petrov-Galerkin (MLPG) approach in computational mechanics," *Computational Mechanics*, vol. 22, pp. 117–127, 1990.
- [5] Y. Li, Z. Kang, Z. Xue, and S. Zheng, "Theories and practices of carbonate reservoirs development in China," *Petroleum Exploration and Development*, vol. 45, no. 4, pp. 669–678, 2018.
- [6] Z. Jin, X. Tan, and R. Guo, "Pore structure characteristics and control factors of carbonate reservoirs: the cretaceous Mishrif formation, halfaya oilfield, Iraq," *Acta Sedimentologica Sinica*, vol. 36, no. 5, pp. 981–994, 1998.
- [7] Y. Liu, B. Liu, and D. Liu, "Analytic model of single well production performance in triple porosity medium reservoirs," *Journal of Oil and Gas Technology*, vol. 33, no. 2, pp. 123–127, 2011.
- [8] Y. Li, Y. Hu, and B. Li, "Influencing factors of deliverability of horizontal wells in carbonate gas condensate reservoirs," *Petroleum Geology and Recovery Efficiency*, vol. 16, no. 2, pp. 85–87+116–117, 2009.
- [9] W. Zhao, L. Zhao, and X. Wang, "Phase behavior characteristics and water-flooding development technical policy of weakly volatile oil in carbonate reservoirs," *Petroleum Exploration and Development*, vol. 43, no. 2, pp. 281–286, 2016.
- [10] Q. Yang, J. Zhang, and T. Hao, "Seismic stepped prediction methods of sub-salt carbonate reservoirs in pre-caspian basin," *Natural Gas Geoscience*, vol. 25, no. 8, pp. 1216–1266, 2014.
- [11] L. He, L. Zhao, and J. Liu, "Complex relationship between porosity and permeability of carbonate reservoirs and its controlling factors: a case of platform facies in pre-caspian basin," *Petroleum Exploration and Development*, vol. 41, no. 2, pp. 206–214, 2014.
- [12] J. Zhang, "Seismic stepped prediction methods of sub-salt carbonate reservoirs in pre-caspian basin," *Marine Geology Frontiers*, vol. 27, no. 7, pp. 50–56, 2011.
- [13] L. Liu, Y. Zhu, and A. Hu, "Petroleum geology of pre-salt sediments in pre-caspian basin," *Journal of Southwest Petroleum Institute*, vol. 24, no. 3, pp. 11–15, 2002.
- [14] S. Wang, L. Zhao, X. Cheng, Z. Fan, and L. He, "Geochemical characteristics and genetic model of dolomite reservoirs in the eastern margin of the pre-caspian basin," *Petroleum Science*, vol. 9, no. 2, pp. 161–169, 2012.
- [15] C. Yu, L. Mi, and C. Wang, "Percolation characteristics investigation of microscopic remaining oil in water flooding

- reservoir with ultra-high water cut,” *Fault-block Oil & Gas Field*, vol. 23, no. 05, pp. 592–594+598, 2016.
- [16] J. Li, H. Sun, and H. Jiang, “Application of microfluidic models in oil and gas field development,” *Petroleum Science Bulletin*, vol. 3, no. 03, pp. 284–301, 2018.
- [17] H. J. Vogel, K. Roth, and S. Shen, “Quantitative morphology and network representation of soil pore structure,” *Advances in Water Resources*, vol. 24, no. 3, pp. 233–242, 2001.
- [18] J. Li, Y. Liu, and Y. Gao, “Effects of microscopic pore structure heterogeneity on the distribution and morphology of remaining oil,” *Petroleum Exploration and Development*, vol. 45, no. 6, pp. 1043–1052, 2018.
- [19] G. Cheng, J. Yin, and Y. Liu, “3D digital rock core reconstruction based on casting slice image,” *Science Technology and Engineering*, vol. 15, no. 18, pp. 16–21, 2015.
- [20] J. Yao, X. Zhao, and Y. Yi, “The current situation and prospect on digital core technology,” *Petroleum Geology and Recovery Efficiency*, vol. 12, no. 6, pp. 52–54, 2005.
- [21] X. Zhao, J. Yao, and J. Tao, “A method of constructing digital core by simulated annealing algorithm,” *Applied Mathematics-A Journal of Chinese Universities Series A*, vol. 22, no. 2, pp. 127–133, 2007.
- [22] Y. Zhu, G. Tao, and W. Fang, “Application of image processing technique in digital core modeling,” *Journal of Oil and Gas Technology*, vol. 29, no. 5, pp. 54–57, 2007.
- [23] I. Verri, A. Della Torre, G. Montenegro et al., “Development of a digital rock physics workflow for the analysis of sandstones and tight rocks,” *Journal of Petroleum Science and Engineering*, vol. 156, pp. 790–800, 2017.

## Research Article

# The Gravel Packing Length Determination Method and Influencing Factors Analysis in Deepwater Horizontal Wells

Hui Huang,<sup>1</sup> Min Wen,<sup>1</sup> Xuesong Xing,<sup>1</sup> Hao Qiu ,<sup>1</sup> Zening Hou,<sup>1</sup> and Shengtian Zhou <sup>2</sup>

<sup>1</sup>CNOOC Research Institute co., Ltd., Beijing 100028, China

<sup>2</sup>China University of Petroleum, Shandong, Qingdao 266580, China

Correspondence should be addressed to Hao Qiu; haoqiu216@163.com

Received 23 October 2021; Accepted 8 December 2021; Published 18 January 2022

Academic Editor: Jinjie Wang

Copyright © 2022 Hui Huang et al. This is an open access article distributed under the Creative Commons Attribution License, which permits unrestricted use, distribution, and reproduction in any medium, provided the original work is properly cited.

Horizontal well gravel packing is the most commonly used sand control technology in offshore oil and gas fields. For extreme conditions such as deepwater, low fracture pressure formations, and long horizontal well bore length, targeted and cost-effective measures are required. According to the friction models in different stages of gravel packing process of horizontal well, the corresponding friction is calculated and compared. According to the calculation, during the entire packing process, the washpipe/screen annular friction is the largest in  $\beta$  wave packing stage, which reflects that higher packing pressure is required in this stage, and the formation fracture pressure is easily broken at this stage. According to the equilibrium flow velocity, the calculation method and flow chart of  $\alpha$ -wave sand bed height were put forward. The criterion and calculation method of packing length were designed. The influencing factors of viscosity, density and leakage rate of carrier fluid on  $\alpha$ -wave packing length were discussed. The quantitative analysis was carried out. The design and calculation method of  $\alpha$ - $\beta$  wave packing length considering the successful completion of  $\alpha$  wave packing and the successful completion of  $\beta$  wave reverse packing was put forward. The corresponding software was compiled to discuss and calculate the quantitative analysis of the factors affecting the  $\alpha$ - $\beta$  wave packing length, such as the density of carrier fluid, gravel density and washpipe/screen ratio. For specific conditions, certain criteria and methods can be used to design and optimize horizontal well gravel packing length.

## 1. Introduction

With the increase of oil and natural gas demand and the progress of horizontal well drilling and completion technology, increasing the length of horizontal well to improve production has become increasingly popular, especially in the development of offshore oil and gas fields. In order to reduce the number of offshore platforms and costs, horizontal well technology has been used extensively. However, for offshore oil and gas fields, most of them are in extreme conditions, such as deepwater, ultra-deepwater, long or ultra-long horizontal wellbore section, and unconsolidated oil and gas reservoirs with low fracture pressure gradient. Most of these wells require sand control, and horizontal well gravel pack sand control is the most common completion method. Horizontal well gravel pack consists of two important stages, namely the  $\alpha$  wave packing stage and  $\beta$  wave packing stage [1]. The  $\alpha$  wave packing stage is the forward packing process

for the equilibrium dune at the bottom of the wellbore [2]. When  $\alpha$  wave packing front reaches the toe of the horizontal wellbore or when the top of the sedimentary sand bed reaches the upper of the casing or wellbore, gravel particles in slurry cannot move forward, at this point the  $\alpha$  wave packing stage stop. Gravel particles begin to reverse pack from the toe of the wellbore in the upper part of the already formed  $\alpha$  wave sand bed to the heel of the horizontal section. This process is called the  $\beta$ -wave pack stage. The carrier fluid enters the washpipe/screen annulus through the deposited gravel and screen, enters the washpipe at the inlet of the wellbore toe, and returns to the surface.

Although the horizontal gravel pack has been widely recognized as a reliable sand control technology, there are significant risks associated with current horizontal gravel pack operations. For extreme reservoir conditions, if wellbore length is short, the expected production will not be achieved. However, if the horizontal wellbore length is long, the height

of sand bed may be too high in the process of  $\alpha$  wave packing stage, or the formation fracture pressure may be exceeded in  $\beta$  wave packing stage. So the entire horizontal wellbore section cannot be fully packed and effective sand control effect cannot be achieved [3]. Especially for the unconsolidated sandstone reservoir, the long horizontal well, the deepwater and low fracture pressure formations. Premature sand bridge may occur before the gravel pack reaches the toe of the horizontal section, resulting in failure of the operation. This is mainly because the horizontal wellbore packing section is long, and sufficient pump rate is required to transport gravel to the toe of the wellbore, which results in higher pump pressure. The formation can be easily fractured due to low fracture gradient, resulting in the leakoff of carrier fluid to the formation during the packing process. If the pump rate is low, the carrying capacity of carrier fluid to carry gravel is insufficient. Both of these conditions can lead to premature bridging and pack failure, which can make the packing process very complicated and difficult to control. The gravel packing length is a particularly important for the target. If wellbore length design is too short to meet its expected production, if the wellbore length is too long to complete entire gravel packing. To date, there is no design and calculation method for gravel packing length in horizontal wells. Therefore, for specific conditions, it is necessary to design and calculate the horizontal well gravel packing length, and analyze the influence of construction parameters on the packing length, which is of great significance for reasonable design and optimization.

## 2. Calculation of Equilibrium Velocity in $\alpha$ -Wave Packing Stage

Horizontal gravel packing is essentially a solid/liquid two-phase flow process that carrier fluid carrying gravel particles. When a fluid-gravel mixture is pumped through the pipe until a cross over tool where the flow will be diverted to the wellbore/screen annulus. The transport of solids in the form of a slurry has been used many years and the flow of a slurry differs from that homogeneous liquids [4]. The flow process of carrier fluid carrying gravel particles in a horizontal wellbore can present several different flow characteristics. Generally these can be divided into following kinds: symmetric suspension, asymmetric suspension, sedimentation with a moving bed of particulates, deposited stationary bed with saltation and complete settling of the particles from the liquid. Due to its complexity, the project is generally not on the study of specific flow pattern, but uses the concept of critical or equilibrium velocity. From the initial equilibrium sand dune [1, 5–7] to the  $\alpha$ - $\beta$  wave theory proposed by Penberthy in 1996, the  $\alpha$ - $\beta$  wave packing theory has been adopted by the industry.

According to the actual packing tool combination, the carrier fluid mainly carries gravel forward in the wellbore annulus in the packing process. While part of the carrier fluid will be diverted into the washpipe/screen annulus through the screen, and the other part of the carrier fluid will leak into the formation around the wellbore through the wellbore wall. Due to the increase of wellbore annulus cross

section area, carrier fluid shunt and carrier fluid leakage, the carrying capacity of carrier fluid decreases, some gravel particles will deposit and fall down to form sand dune. Under the condition of constant wellhead pump rate, the suspension and settlement of gravel particles in the wellbore annulus will reach a critical state. The sedimentary dune under this critical condition is called the critical sand bed, and the corresponding flow velocity is the equilibrium flow velocity in the  $\alpha$  wave packing stage, which is an important parameter to calculate the height of the  $\alpha$  wave sand bed. Chen et al. [8, 9] compared three equilibrium flow velocities according to the results of Gruesbeck, Penberthy and Oroskar et al.

Gruesbeck model

$$v_* = 15v_s \left[ \frac{r_H v_s \rho_l}{\mu_l} \right]^{0.39} \left[ \frac{d_p v_s \rho_l}{\mu_l} \right]^{-0.73} \left[ \frac{\rho_p - \rho_l}{\rho_l} \right]^{0.17} [C_*]^{0.14} \quad (1)$$

Penberthy model

$$v_* = \max(v_1, v_2) \quad (2)$$

Where

$$v_1 = \left[ 0.0251 g d_p \left( \frac{\rho_p - \rho_l}{\rho_l} \right) \left( \frac{D_H \rho_m}{\mu_l} \right)^{0.775} \right]^{0.816} \quad (3)$$

$$v_2 = 1.35 \left[ \frac{2g D_H (\rho_p - \rho_l)}{\rho_l} \right]^{0.25}$$

Oroskar and Turian model

$$\frac{v_*}{\sqrt{g d_p (s-1)}} = \left\{ 5C_* (1 - C_*)^{2n-1} \left( \frac{D_H}{d_p} \right) \left( \frac{D_H \rho_l \sqrt{g d_p (s-1)}}{\mu_l} \right)^{\frac{1}{8}} \frac{1}{x} \right\}^{8/15} \quad (4)$$

Where  $v_*$  -critical or equilibrium velocity, m/s;  $v_s$  -settling velocity of gravel particles, m/s;  $r_H$  -hydraulic radius, m;  $\rho_l$ 、 $\rho_p$ 、 $\rho_m$  - carrier fluid density, gravel density and slurry density, respectively, kg/m<sup>3</sup>;  $d_p$  -gravel particle diameter, m;  $D_H$  -hydraulic diameter, m;  $\mu_l$  -carrier fluid viscosity, Pa·s;  $C_*$  -gravel particle volume concentration under equilibrium condition, m<sup>3</sup>/m<sup>3</sup>;  $g$  -gravity acceleration, m/s<sup>2</sup>;  $x$  - the correction factor for dissipation of turbulent energy, which can be written as follows:

$$x = \frac{4}{\pi} \gamma \exp\left(\frac{-4\gamma^2}{\pi}\right) + \frac{\sqrt{\pi}}{2} \operatorname{erfc}\left(\frac{2\gamma}{\sqrt{\pi}}\right) \quad (5)$$

In this relation  $\gamma$  is the ratio of particle settling velocity to critical velocity. In the calculation,  $x$  is determined for a range of values for  $\gamma$ . For the settling velocity it is observed and for a reasonable range of critical velocities(0.018 to 1.6185 m/s),  $x \approx 0.96$ ;  $s$  -the solid/liquid density ratio,  $s = \rho_p/\rho_l$ .



TABLE 1: simulation parameters.

Simulation calculation parameter list			
Horizontal section length(m)	600	Washpipe OD(in)	3.8
Vertical depth(m)	3720	Washpipe ID(in)	3.22
Fracture gradient(MPa/100 m)	1.59	Carrier fluid leakoff ratio	5%
Openhole diameter(in)	8.75	Design initial pump rate(bpm)	5.6
String OD(in)	4.11	Sand ratio(ppg)	0.5
String ID(in)	3.2	Gravel diameter(mm)	0.33
Screen OD(in)	6.2	Gravel volume density(kg/m <sup>3</sup> )	1260
Screen ID(in)	4.5	Apparent gravel density(kg/m <sup>3</sup> )	2200
Formation pressure(MPa)	44.2	Carrier fluid density(kg/m <sup>3</sup> )	1300

The three equilibrium velocity correlations (1), (2) and (4) above are applicable to different situations. The equation (1) demonstrates that the equilibrium velocity depends on the particle concentrations, fluid viscosity, inertial, gravitational, and buoyant forces that act on the particles transported over the equilibrium bank. Four dimensionless groups that include forces are: the Reynolds number based on the open channel above the  $\alpha$  wave bank, the Reynolds number based on the particle diameter, dimensionless density difference between the particle and the fluid, and the particle concentration. The equation (2) utilized a different equilibrium velocity model to predict transport velocity in a field-scale physical model by using gravel of the sizes 40/60, 20/40, and 12/20 U.S. mesh. The equation (4) developed by Oroskar and Turian, accounted for dissipation of turbulent energy. Based on the application range of three correlation formulas, parameters can be optimized and the corresponding equilibrium flow velocity can be calculated.

### 3. Calculation of Flow Friction Resistance at Different Stages and $\alpha$ Wave Sand Bed Height

*3.1. The Flow Friction Resistance in  $\alpha$ - $\beta$  Wave Packing Stage.* In the gravel packing process of horizontal wells, the slurry and carrier fluid flow through different locations, at different times and at different packing stages, accompanied by pressure loss and corresponding flow resistance. Especially in the gravel packing process of deepwater horizontal wells, the control of packing pressure is very important. In long horizontal wells under the environment of low formation fracture pressure, the high packing pressure will fracture formation, causing large amounts carrier fluid into the formation. In  $\alpha$  wave packing stage, most of the carrier fluid flow in the wellbore/screen annulus. In  $\beta$  wave packing stage, carrier fluid radial flow through the screen and into the washpipe/screen annulus axial flow and finally in the wellbore toe back into the wash pipe. As the  $\beta$ -wave packing stage progresses, the flow distance of carrier fluid increases gradually in the washpipe/screen annulus, so the wellbore pressure and pump pressure increase rapidly in this stage. When the  $\beta$ -wave reverse packing reaches the heel of the wellbore, the packing pressure reaches the maximum value.

For the specific calculation model of flow resistance in each stage, can refer to reference [10].

According to the friction model corresponding to different stages, the corresponding software is compiled to calculate the gravel packing operation parameters given for a certain horizontal well. The specific simulation parameters are shown in Table 1.

It can be seen from Figure 1 that:(1) slurry injection stage: The maximum friction resistance occurs in drill string during slurry injection stage, followed by flow friction resistance in washpipe. Since there is no sand bed formed in horizontal wellbore annulus during slurry injection stage, only pure fluid flows, so the horizontal wellbore friction resistance is relatively small. (2) the  $\alpha$  packing stage: due to the long drill string length in deepwater formation, the friction resistance in the drill string is still the biggest, but the proportion is slightly lower. The friction resistance in the wash pipe stays the same, but the proportion has decreased. As the formed sand bed move forward gradually in the  $\alpha$  packing stage, the friction resistance in the upper sand bed increases gradually, and carrier fluid friction resistance at sand bed front gradually reduce; (3) the  $\beta$  wave packing stage: in the reverse packing process, flow length for carrier fluid in washpipe/screen annulus increases gradually, friction resistance increases rapidly. Meanwhile, for the sand bed covered screen, in the process of the reverse packing, flow length decreases, and the seepage velocity through sand bed increases, the flow friction will increase. While the friction resistance proportion for slurry injection in the drill string decreases.

Overall, pressure loss occurs mainly in the  $\beta$  reverse packing stage, especially when the  $\beta$  wave approaches the heel of the horizontal well. The carrier fluid flows through the long distance and the narrow washpipe/screen annulus and enters washpipe at the inlet of wellbore toe. A rapid increase in friction resistance leads a rapid increase in packing pressure. It is easy to break through the formation fracture pressure. Once the formation fracture pressure is broken through, a large amount of carrier fluid will leak into the formation, resulting in packing failure.

*3.2. Calculation of  $\alpha$  Wave Sand Bed Height.* The design of  $\alpha$  wave sand bed height is a key step in the gravel packing of the entire horizontal well [11, 12]. In this process, premature

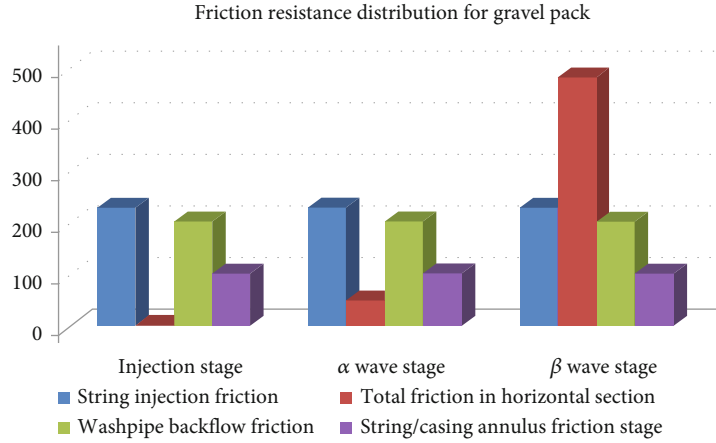


FIGURE 1: Comparison and analysis of 3-stage friction distribution of gravel packing in horizontal Wells.

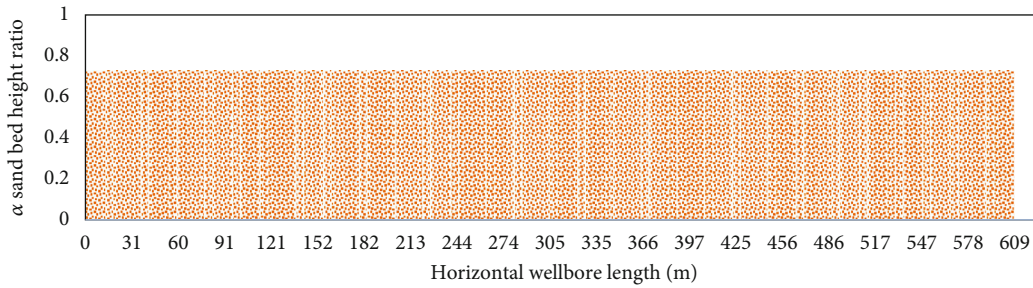


FIGURE 2: Calculation result for  $\alpha$  wave sand bed height.

sand bridge is prone to be formed if the designed sand bed is too high. The gravel concentration in wellbore/screen annulus will increase with the carrier fluid leakage along packing process, resulting in high sand bed height. According to the critical sand bed theory of  $\alpha$ - $\beta$  wave packing, the calculation method and calculation process of  $\alpha$  wave sand bed height are realized. The specific calculation process is as follows:

① Given the size parameters of the well structure, washpipe and screen system;

② Select carrier fluid (density and viscosity), gravel parameters and specific pump rate  $Q$ ;

③ The horizontal section was separated into  $N$  sections and the packing calculation was carried out step by step;

④ For packing section  $i_{th}$ , according to initial pump rate  $Q$ , the amount of leakage rate calculated before  $(i-1)_{th}$ ,  $q_p$  and the former  $(i-1)$  section enters the washpipe/screen annulus return flow rate  $q_r$ , Calculate the actual flow rate of section  $i_{th}$ ,  $Q_i = Q - q_p - q_r$ ;

⑤ According to the actual flow  $Q_i$  of section  $i_{th}$  and the current sand bed height  $h$ , the wellbore annular cross-sectional area  $S$  was calculated, and the velocity  $v$  of sand bed upper was obtained;

⑥ According to the equilibrium of velocity model in (1), determine the actual velocity and the equilibrium flow velocity, whether to meet  $|v - v^*| < \varepsilon$ , if yes, then the sand bed height  $h = h + dh$ , if not, return to step ⑤ recalculate until the accuracy of critical velocity is satisfied, and record as the equilibrium sand bed height at section  $i_{th}$ ;

⑦ Step by step as above ④-⑥, until the packing reaches the  $N_{th}$  stage, complete.

Using the basic data in Table 1 and according to the above calculation process, the corresponding software was compiled to calculate the sand bed height, as shown in Figure 2.

As can be seen from Figure 2, if there is no loss of carrier fluid, the  $\alpha$  wave sand bed height along wellbore is in a straight line; if the carrier fluid leakoff ratio along the wellbore into the around reservoir is low (5%), the the  $\alpha$  wave sand bed height is basically a constant along the wellbore. In this case, as long as the the  $\alpha$  wave sand bed height is designed within a safe range, the  $\alpha$  wave stage can be completed. If the carrier fluid leakoff is high, the amount of carrier fluid in the wellbore annulus along the wellbore will be reduced. The carrying capacity of carrier fluid will be reduced, resulting in premature settlement of excess gravels, which makes the the  $\alpha$  wave sand bed height increase rapidly, and it is easy to cause premature sand bridge and packing failure.

#### 4. Determination Method of Packing Length in $\alpha$ Wave Packing Stage

Premature bridge can occur if pump rate is too low and carrier fluid is not sufficient to support gravel to the toe of the wellbore in  $\alpha$  wave packing stage. If there is a leakoff of carrier fluid along the path, the slurry flow rate will be reduced, and the carrying capacity of carrier fluid will be reduced. To

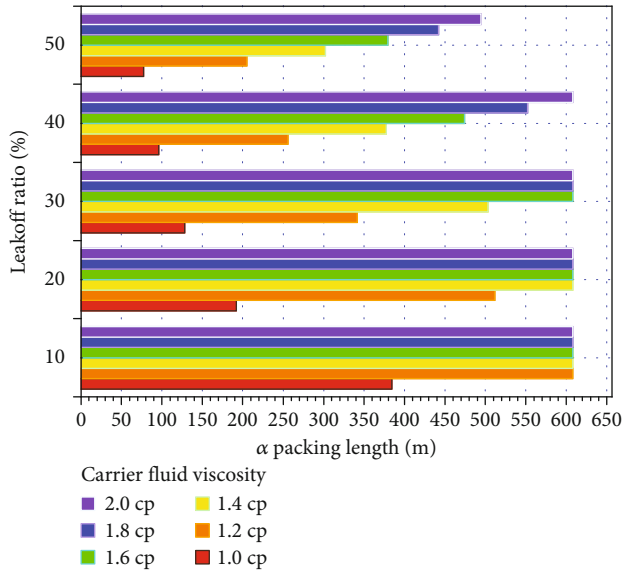


FIGURE 3: Effect of viscosity and leakoff on  $\alpha$  wave packing length.

be able to carry gravel to the toe of the wellbore, there needs sufficient flow rate and energy to guide the carrier fluid through the toe inlet into the washpipe and then return along the washpipe. Experimental studies and field operation data show that [2], for the determined gravel concentration, the apparent velocity of carrier fluid at the toe of wellbore should not be less than 1 ft/s [2]. If the apparent velocity is lower than this, the  $\alpha$  wave packing process will stop and reverse packing will begin. At this time, an effective means is to reduce the sand ratio appropriately [13].

According to different string structure and packing parameters, the upper limit of sand dune ratio (sand bed height/wellbore diameter) can be set as 0.8. If the sand dune ratio exceeds this value during the  $\alpha$  wave packing process, it is considered that a sand bridge is formed, resulting in early plugging and the  $\alpha$  wave packing process is ended. The  $\beta$  wave reverse packing starts at plugging location and the length from the heel of wellbore to plugging location is  $\alpha$  wave packing length. There are many factors influencing the length of  $\alpha$  wave packing [12–16], including pump rate, sand ratio, carrier fluid leakoff, washpipe/screen ratio, carrier fluid viscosity, fluid density and gravel density. For gravel packing of long horizontal wells in deepwater, the successful completion of  $\alpha$  wave packing is an important first step.

Using the basic data in Table 1, designed the upper limit of sand dune ratio is 0.8, carrier fluid leakoff ratio separately: 10%, 20%, 30%, 40%, 50%, carrier fluid viscosity were taken: 1.0, 1.2, 1.4, 1.6, 1.8, 2.0 cp, respectively, to calculate the effect of leakoff rate, carrier density and viscosity on the length of  $\alpha$  wave packing.

Figure 3 shows the change of  $\alpha$  wave packing length under different combinations of carrier fluid viscosity and carrier fluid leakoff ratio. For low viscosity carrier fluid, gravel transport mainly depends on the flow rate of carrier fluid to provide carrying capacity. If the leakoff rate is higher, the flow rate in annulus will decrease and more gravel will settle. The sand dune ratio will be higher than

designed value in advance and premature sand bridge will occur. At this time, the  $\alpha$  wave packing length is shorter. With the increase of the viscosity of the carrier, the suspension capacity of carrier fluid is increased and keeps a certain amount of gravel in suspension.

Although the leakoff rate of the carrier fluid increases, the gravel can still be carried forward by the viscosity of the carrier fluid. With the increase of the viscosity of the carrier fluid, the corresponding  $\alpha$  wave packing length is longer. The larger the leakoff rate, the shorter the  $\alpha$  wave packing length under the same viscosity of the carrier fluid.

Figure 4 shows the influences of different carrier fluid densities and leakoff ratio on the  $\alpha$  wave packing length. Conventional gravel was used at this time, and the carrier fluid densities were, respectively, 1.250, 1.275, 1.300, 1.325 and 1.350sg, the  $\alpha$  packing length increases with the increase of the carrier fluid density, because the density difference between the carrier fluid and gravel particles decreases. When the leakoff ratio is greater than 20%, the corresponding carrier fluid density cannot achieve the desired wellbore length.

### 5. Determination Method of Complete Packing Length of $\alpha$ - $\beta$ Wave Packing

Under certain parameters, ideal gravel pack requirement is that the  $\alpha$  wave packing and  $\beta$  wave reverse packing can be successfully completed. As the previous 3, complete  $\alpha$  packing must meet  $\alpha$  sand dune ratio should not exceed the value of design and sufficient return rate at the inlet of washpipe [17, 18]. Throughout the  $\beta$ -wave reverse packing stage, the packing pressure increases dramatically due to the rapid increase friction in washpipe/screen annulus. Once the packing pressure exceeds the formation fracture pressure, a large amount of carrier fluid is lost. The distance from the pressure breakthrough point to the toe of the wellbore is called the  $\beta$ -wave reverse packing length. If  $\alpha$  packing length is equal to the horizontal section length from the heel to the toe of the horizontal wellbore, while the  $\beta$  wave reverse packing length is equal to the horizontal section length from the toe to the heel of the horizontal wellbore, known as  $\alpha$ - $\beta$  wave complete packing length. Whether early sand bridge in  $\alpha$  wave packing stage, or pressure breakthrough of formation fracture pressure in  $\beta$  wave packing stage, all is not completed successfully  $\alpha$ - $\beta$  packing. In general, the packing length is the length of  $\alpha$ - $\beta$  wave successfully completed. The principle of designing the packing length is: the dune ratio in the process of  $\alpha$  wave packing is lower than 0.8, and the packing pressure in the process of  $\beta$  wave packing is less than the formation fracture pressure. According to this design principle, the corresponding software is compiled, and the calculation is carried out by using the basic data in Table 1, and some factors affecting the packing length are analyzed.

For conventional gravel (2.2sg gravel density), the leakoff ratio was set to 5% with three different densities of carrier fluids: 1.25sg, 1.30sg, and 1.35sg. Figure 5 shows the corresponding simulation results.

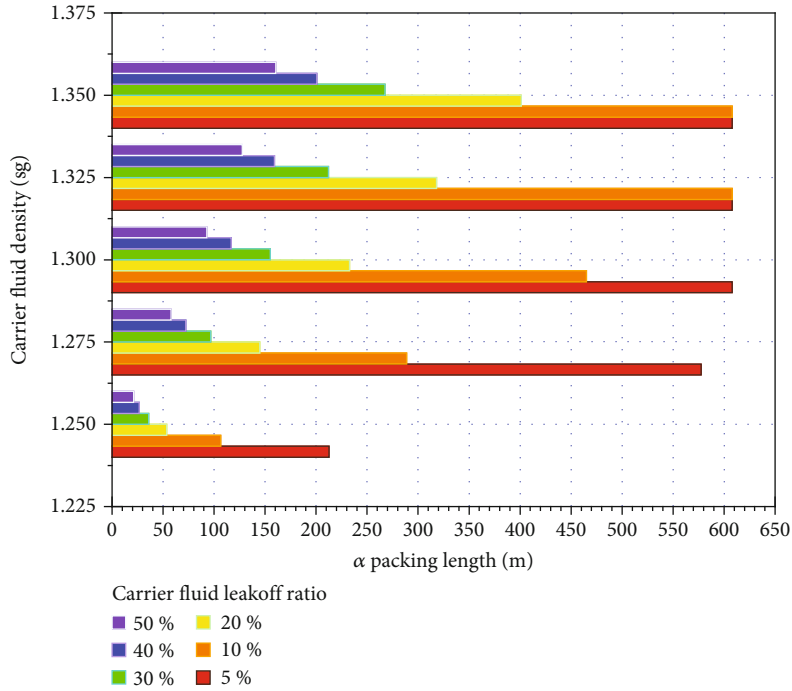


FIGURE 4: Influence of density and leakoff of carrier fluid on  $\alpha$  packing length.

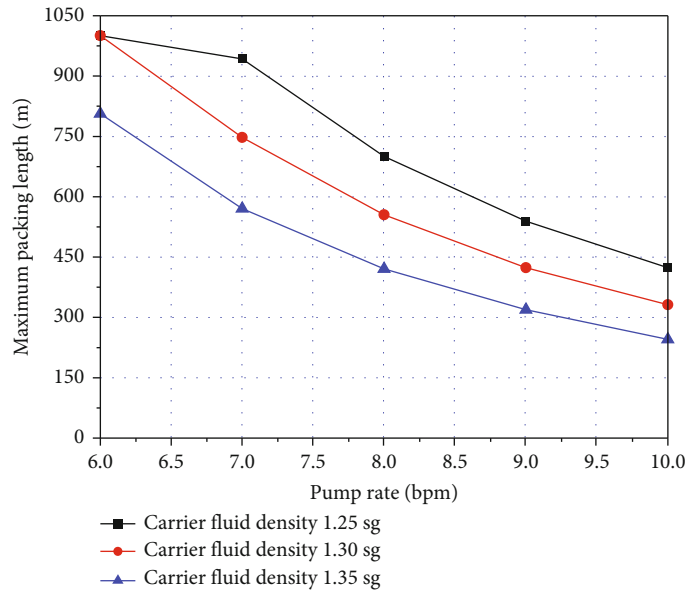


FIGURE 5: Influence of pump rate and fluid density on maximum packing length.

It can be seen from Figure 5 that, with the increase of pump rate, the packing lengths corresponding to the densities of the three carrier fluid gradually decrease. Although it is helpful for  $\alpha$  wave packing because of the increase of pump rate, packing pressure increases rapidly in the  $\beta$  wave packing stage, and it is easy to break through the formation rupture pressure. If the pump rate is lower than 6.0 bpm, sand bridge will be formed early in the  $\alpha$  wave packing stage, and effective  $\alpha$  wave packing length cannot be reached. Under the condition of a certain pump rate, the complete  $\alpha$ - $\beta$  wave packing length decreases with the increase of the

density of carrier fluid. This is because the high density of carrier fluid in the  $\beta$  wave packing stage leads to high friction in washpipe/screen annulus, resulting in rapid growth of packing pressure, which leads to early pressure breakthrough and reduces the  $\beta$  wave reverse packing length. The density of carrier fluid was 1.3sg, and Figure 6 simulated the effect of four different gravel densities on the pack length.

It can be seen from Figure 6 that for higher pump rate, the  $\alpha$ -wave sand bed height can be controlled to successfully complete the  $\alpha$ -wave packing stage. However, for  $\beta$ -wave

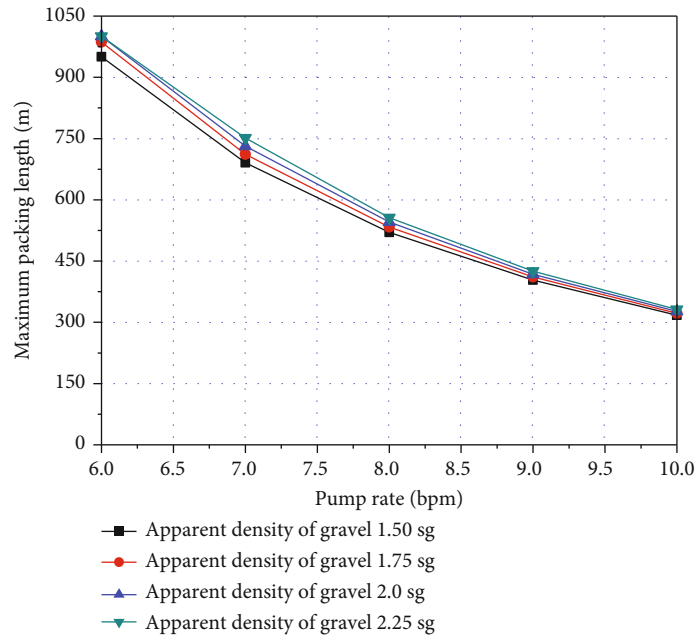


FIGURE 6: Effect of different gravel density on packing length.

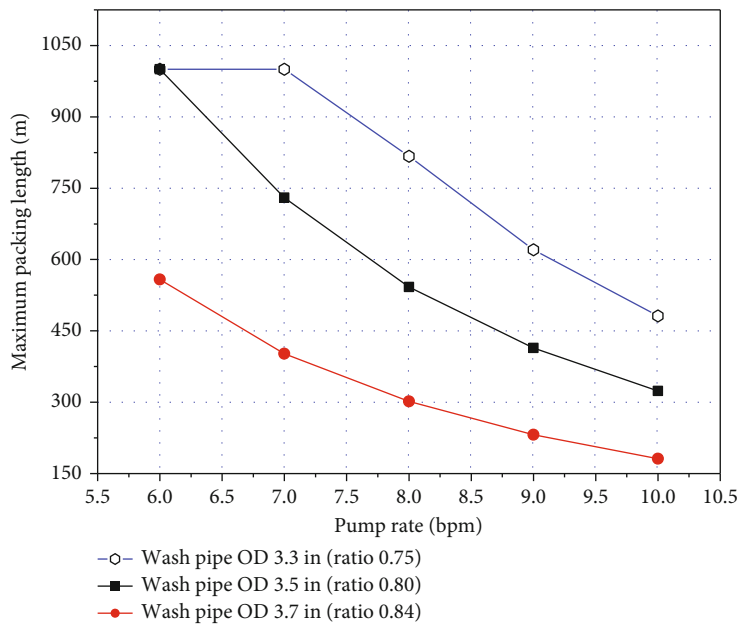


FIGURE 7: Change of packing length with pump rate under washpipe/screen (screen ID: 4.4in).

packing stage, the reverse packing length of  $\beta$ -wave is mainly affected by the packing pressure [19, 20]. With the increase of pump rate, the complete  $\alpha$ - $\beta$  wave packing length decreases.

The influence of screen and washpipe size on gravel pack length is discussed below. Screen ID is 4.4in, washpipe OD is 3.3in, 3.5in and 3.7in, respectively, and basic calculation parameters are shown in Table 1. According to the complete  $\alpha$ - $\beta$  wave packing length method designed above, the change of packing length with pump rate is calculated under three different washpipe/screen ratios (washpipe OD/screen ID).

Three cases of washpipe/screen ratio were 0.75, 0.80 and 0.84. If the screen size does not change, the greater washpipe/screen ratio is (that is, the greater the wash pipe diameter), the smaller the clearance of washpipe/screen annulus is. Flow friction resistance in the washpipe/screen annulus will increase and can ensure more carrier fluid in the wellbore/screen annulus. The carrying capacity of carrier fluid increases. Increased carrying capacity in the wellbore annulus helps with  $\alpha$  wave packing. During  $\beta$ -wave packing, especially late in the  $\beta$ -wave packing process, because the carrier fluid has to flow through the narrow washpipe/screen



annulus, which is longer in long horizontal wellbore, the high pressure loss will be caused. This increases the  $\beta$ -wave packing pressure, which can easily exceed the formation fracture. On the contrary, if the washpipe/screen ratio is small, the washpipe/screen annulus becomes larger. At this time, more carrier fluid will be diverted to the washpipe/screen annulus, and then enters the washpipe at the toe entrance. Due to more carrier fluid diversion, the carrying capacity of carrier fluid in the wellbore/screen annulus is reduced, and early sand blocking is easy to occur. Can be seen from the Figure 7, with the increase of the washpipe/screen ratio,  $\alpha$ - $\beta$  complete packing length decreases. This is because the packing pressure increases rapidly in the  $\beta$ -wave stage after the increase of the washpipe/screen ratio, resulting in the shortening of the length of the  $\beta$ -wave reverse packing and the decrease of the length of the complete  $\alpha$ - $\beta$  wave packing. For specific horizontal gravel pack, parameters such as washpipe/screen ratio need to be optimized. According to experiment and field experience, the washpipe/screen ratio is generally about 0.8.

## 6. Conclusions

- (1) According to the mechanism of gravel packing in horizontal wells, precise calculation and analysis of friction resistance in different stages are carried out. In the entire packing stage, the packing pressure increases rapidly in the  $\beta$  wave packing stage and it is easy to break through the formation fracture pressure
- (2) Based on the equilibrium flow velocity calculation model, the calculation method and calculation process of  $\alpha$  wave sand bed height are presented
- (3) The characteristics of  $\alpha$  -wave sand bed is studied, especially in the gravel packing of long horizontal well in deepwater. The conditions of forming stable  $\alpha$ -wave equilibrium sand bed are studied. The calculation model and process of  $\alpha$  -wave packing length are established, and the quantitative variation law of parameters affecting  $\alpha$  -wave packing length is discussed
- (4) The design principle and method of complete  $\alpha$ - $\beta$  wave packing length are put forward, and the influencing of parameters such as carrier fluid density, carrier fluid viscosity, pump rate and washpipe/screen ratio on complete  $\alpha$ - $\beta$  wave packing length are analyzed by using the software
- (5) By using the established model and method, gravel packing parameters can be optimized to provide support for the success of field gravel packing construction

## Data Availability

This is a theoretical work for which no data need to be made available.

## Conflicts of Interest

The authors declare that they have no conflicts of interest.

## Acknowledgments

This work was supported by the National Natural Science Foundation of China Project "Basic Research on Wellbore Pressure Control in Deep Water Oil and Gas Drilling and Production (no. 51734010)".

## References

- [1] C. Gruesbeck, W. M. Salathiel, and E. E. Echols, "Design of gravel packs in deviated wellbores," *Journal of Petroleum Technology*, vol. 31, no. 1, pp. 109–115, 1979.
- [2] W. L. Penberthy, K. L. Bickham, H. T. Nguyen, and T. A. Paulley, "Gravel placement in horizontal wells," in *SPE Formation Damage Control Symposium*, Lafayette, LA, 1996.
- [3] Z. Chen and R. Novotny, "The dynamic bottomhole pressure management: A necessity to gravel packing long horizontal wells with low fracture gradients," in *Paper SPE 96396, presented at the 2005 SPE Annual Technical Conference*, pp. 9–12, Dallas, Texas, U.S.A., October 2005.
- [4] G. W. Govier and K. Aziz, *The Flow of Complex Mixtures in Pipes*, Robert E. Krieger Publishing Co. Inc., Huntington, NY, 1972.
- [5] A. R. Oroskar and R. M. Turian, "The critical velocity in pipeline flow of slurries," *AIChE Journal*, vol. 26, no. 4, pp. 550–558, 1980.
- [6] J. X. Forrest, "Horizontal gravel packing studies in a full-scale model wellbore," in *Paper SPE 20681, presented at the 1990 SPE Annual Technical Conference*, pp. 23–26, New Orleans, LA, September, 1990.
- [7] S. D. E. Jr, "Gravel-pack studies in a full-scale, high-pressure wellbore model," in *Paper SPE 16890, presented at the 1987 SPE Annual Technical Conference*, pp. 27–30, Dallas, 1987.
- [8] Z. Chen, "Horizontal well gravel packing: Dynamic alpha wave dune height calculation and its impact on gravel placement job execution," in *Paper SPE 110665, presented at the 2007 SPE Annual Technical Conference*, pp. 11–14, Anaheim, California, U.S.A., November 2007.
- [9] Z. Chen, R. J. Novotny, R. Farias, A. Mendez, C. A. Pedroso, and L. H. Fernandes, "Gravel packing deep water long horizontal wells under low fracture gradient," in *Paper SPE 90552, presented at the SPE Annual Technical Conference*, pp. 26–29, Houston, Texas, September 2004.
- [10] A. L. Martins, J. V. M. de Magalhaes, A. Calderon, and C. M. Chagas, "A mechanistic model for horizontal gravel pack displacement," in *Paper SPE 82247, presented at the SPE European Formation Damage Conference*, pp. 13–14, The Hague, The Netherlands, May 2003.
- [11] L. Aifen and Y. Liu, "Numerical simulation study of gravel packing in horizontal well," *Acta Petrol Et Sinica*, vol. 23, no. 1, pp. 102–107, 2002.
- [12] Z. Shengtian, L. Zhaomin, and D. Changyin, "The advances of numerical simulation for gravel packing in horizontal wells," *Mechanics in Engineering*, vol. 31, no. 3, pp. 9–15, 2009.
- [13] J. Jeanpert, T. Banning, C. Abad, I. Mbamalu, and J. Hardy, "Successful installation of horizontal openhole gravel-pack completions in low fracture gradient environment: A case

- history from deepwater West Africa,” in *Paper SPE-189492-MS, presented at the SPE International Conference and Exhibition on Formation Damage Control*, Lafayette, Louisiana, U.S.A., 2018.
- [14] D. J. Attong and W. V. C. DeLandro, “Case History: Pushing The Limit On Long Horizontal Gravel Packs,” in *Paper SPE 36087, presented at the Fourth Latin American and Caribbean Petroleum Engineering Conference*, pp. 23–26, Port of Spain, Trinidad, April 1996.
- [15] K. Alexander, D. Bruce, C. Williamson et al., “Evolution of Open-Hole Gravel Pack Methodology in a Low Frac-Window Environment: Case Histories and Lessons Learned From the Kraken Field Development,” in *Paper SPE-195937-MS, presented at the SPE Annual Technical Conference*, Calgary, Alberta, Canada, October 2019.
- [16] T. Hubert, M. T. Chembou, N. Dupouy, R. Ilyasov, C. M. Nkala, and B. Reilly, “Optimised pumping design for 100% pack efficiency in open-hole gravel packs: A field study from Offshore Republic of Congo,” in *Paper SPE-202291-MS, presented at the SPE Asia Pacific Oil & Gas Conference*, Perth, Australia, October 2020.
- [17] J. A. Firth, H. Hanid, and P. M. Saldungary, “Novel techniques enable successful gravel packing of long horizontal North Sea wells,” in *SPE Europec*, Amsterdam, 2020.
- [18] V. Gupta, J. Jeanpert, C. John et al., “Analysing critical elements in openhole gravel pack treatment design cycle: Case study in Indian ultra-deepwater,” in *SPE Asia Pacific Oil & Gas conference and Exhibition*, Perth, Australia, November 2020.
- [19] F. C. Colbert, A. L. Costa, R. F. Gachet, F. M. Garcia, and A. J. Neto, “Sand control technology for extend-reach wells: Best practices from the longest gravel packs performed Offshore Brazil,” in *International Petroleum Exhibition & Conference*, Abu Dhabi, UAE, November 2017.
- [20] M. P. Coronado and T. G. Corbett, “Beta-wave pressure control enables extended-reach horizontal gravel packs,” in *2001 SPE annual technical conference and exhibition*, New Orleans, Louisiana, October 2001.

## Research Article

# A Novel Approach to Determine the Enriched Gas Recycling during the Enriched Gas Flooding Process

Yan Li,<sup>1</sup> Chunsheng Yu ,<sup>2</sup> and Kaitao Yuan<sup>1</sup>

<sup>1</sup>Dingbian Oil Production Plant of Yanchang Oilfield Co., Ltd., China

<sup>2</sup>Southwest Petroleum University, China

Correspondence should be addressed to Chunsheng Yu; [yuchunsheng\\_2000@163.com](mailto:yuchunsheng_2000@163.com)

Received 19 October 2021; Revised 3 December 2021; Accepted 21 December 2021; Published 14 January 2022

Academic Editor: Qingwang Yuan

Copyright © 2022 Yan Li et al. This is an open access article distributed under the Creative Commons Attribution License, which permits unrestricted use, distribution, and reproduction in any medium, provided the original work is properly cited.

A novel approach was proposed for calculating the enriched gas recovery factor based on the theory of two-phase isothermal flash calculations. First, define a new parameter, pseudo formation volume factor of enriched gas, to represent the ratio of the surface volume of produced mixture gas to underground volume of enriched gas. Two logarithmic functions were obtained by matching the flash calculation data, to characterize the relationships between pseudo formation volume factor and the produced gas-oil ratio. These two functions belong to the proportion of liquefied petroleum gas in enriched gas; the proportion is greater than 50% and less than 50%, respectively. Given measured gas-oil ratio and produced gas volume, underground volume of produced enriched gas can be calculated. Injection volume of enriched gas is known; therefore, recovery factor of enriched gas is the ratio of produced to injected volume of enriched gas. This approach is simply to calculate enriched gas recovery factor, because of only needs three parameters, which can be measured directly. New approach was compared to numerical simulation results; mean error is 12%. In addition, new approach can effectively avoid the influence of lean gas on the calculation of enriched gas recycling. Three stages of enriched gas recovery factors in field Z were calculated, and the mean error is 5.62% compared to the field analysis, which proves that the new approach's correctness and practicability.

## 1. Introduction

Tight sandstone reservoirs are widely distributed in China. However, they are characterized by low permeability, complex pore structures, and high ratio of nano- to micropore radius, which results in poor development efficiency and low primary recovery [1–3]. As one of the main technologies of tertiary oil recovery, gas flooding has been successfully applied in many oilfields and shows a good performance [4, 5]. Gas injection EOR technologies that have been employed in industrial applications mainly include carbon dioxide flooding, air flooding, nitrogen flooding, hydrocarbon gas flooding, and flue gas flooding [6–8]. Enriched gas is a kind of hydrocarbon gas mixed by natural gas (NG) and liquefied petroleum gas (LPG) in a certain proportion. The purpose is to reduce the minimum miscible pressure of natural gas and crude oil by mixing with LPG.

The first field test of LPG miscible flooding was implemented in 1956, and the oil recovery was increased by more

than 12% [9, 10]. Breakthrough of continuous gas injection is the key challenge that affects oil recovery [11, 12]. Produced gas reinjection is one commonly used technology [13, 14]. Yang et al. [15] analyzed the mixture of CO<sub>2</sub> and dissolved gas reinjection by conducting computed tomography (CT) scan experiments, and it revealed that CO<sub>2</sub> content determines the extent of enhanced oil recovery. Chen et al. [16] studied the influence of CO<sub>2</sub> content in the reinjected mixture gas on the near miscible pressure through slim tube experiments. Only when the CO<sub>2</sub> content reached a certain proportion could the near miscible flooding of the reinjected gas be occurred [17]. The mentioned above studies show that CO<sub>2</sub> content in the reinjected mixture gas determines the oil recovery efficiency. Similarly, a certain proportion of enriched gas is needed to achieve efficient development. The gas produced from the process of enriched gas flooding is a mixture of solution gas and enriched gas; in addition, the ratio of enriched gas to solution gas in the mixture varies along with the reservoir heterogeneity, well pattern, and well

spacing. Therefore, it is difficult to obtain the accurate value for enriched gas recovery (EGR).

EGR is usually measured indoor by using gas chromatography (GC) or mass spectrometry (MS) [18–20] but not applied to the field. Flash calculation is one of the basic constituents of gas-liquid equilibrium calculation, which is used to calculate the compositional ratio of gas phase to the liquid phase at a given temperature, and pressure provided the total composition of the system is known [21–23]. Lee et al. [19] quantified the mass transfer mechanism in a rich-gas injection EOR process. Subsequently, combined with the molar composition of injected LPG and dry gas, the overdetermined equations were established, and the LPG quantity was calculated by the least square method. This method requires that the composition of the produced gas is known. However, the fact is that the produced gas composition always varies with time, which implies that this calculation method is debatable. In this paper, a novel approach was proposed to calculate the EGR factor based on the theory of two-phase isothermal flash calculation. Two logarithmic functions were obtained by matching the flash calculation data, which characterizes the relationships between pseudo formation volume factor (PFVF) and the produced gas-oil ratio (GOR). Given the value of GOR and produced gas volume, underground volume of produced enriched gas can be calculated. The volume of injected enriched gas is known; therefore, EGR is the volumetric ratio of produced to injected enriched gas. Our new approach only needs three parameters, i.e., GOR, produced gas volume, and injected enriched gas volume, which can be measured directly in field enriched gas flooding process. Thereby, this method can be easily used by reservoir engineers. In order to prove the validity of our novel approach, numerical simulation results were compared, and the mean error is 12%. In addition, the new approach can effectively avoid the influence of lean gas on the calculation of enriched gas recycling. Three stages of enriched gas recovery factors in field Z were calculated, and the mean error is 5.62% compared to the field analysis, which proves that the new approach's correctness and practicability.

**1.1. Isothermal Flash Calculation Theory.** Flash separation is known as contact separation or one-time degassing [24]. This separation method mimics the process when the produced oil and gas enter the separator at one time or directly into the large tank for degassing. Oil and gas reach equilibrium instantly, and the separated gas and oil always stay in contact during the separation process, which means that the total composition of the system remains unchanged (Figure 1).

Two-phase flash calculation method is widely adopted in the existing software of compositional model. And this method excludes the water phase and calculates the oil-gas two-phases flash separation of the mixture [25].

One mole of mixture with known composition reaches phase equilibrium at specific temperature and pressure and separates into two phases, i.e., oil and gas. The basic equations describing this process are as follows.

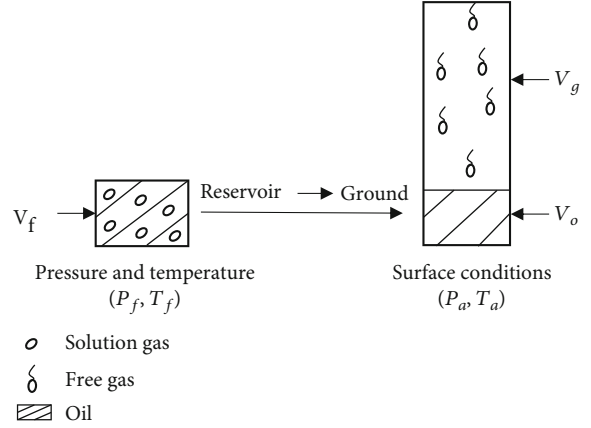


FIGURE 1: Flash separation schematic diagram.

Total material conservation is expressed as

$$L + V = 1, \quad (1)$$

where  $L$  represents molar composition of oil phase and  $V$  is molar composition of gas phase.

The material conservation of component  $i$  is expressed as

$$Lx_i + Vy_i = z_i (i = 1, 2, \dots, n), \quad (2)$$

where  $x_i$  is the mole fraction of component  $i$  in oil phase,  $y_i$  is the mole fraction of component  $i$  in gas phase,  $z_i$  is the total mole fraction in the mixture of oil and gas, and  $n$  is the number of components.

When the hydrocarbon system reaches phase equilibrium, the fugacity of each component in the system is equal in gas and liquid phases

$$f_{iL} = f_{iV} (i = 1, 2, \dots, n), \quad (3)$$

where  $f_{iL}$  and  $f_{iV}$  are fugacities of component  $i$  in oil and gas phases, respectively.

The constraint equation is

$$\sum_{i=1}^n x_i = 1 (i = 1, 2, \dots, n). \quad (4)$$

Equations (1) to (4) contain  $(2n + 2)$  functions, which have  $(2n + 2)$  unknowns. Fugacity of component  $i$  is calculated by the Peng-Robinson equation of state [26].

**1.2. EGR Model.** Underground volume of enriched gas  $V_y$  in a mixture under formation pressure and temperature can be calculated by the two-phase flash calculation method. The surface volume  $V_{ys}$  and GOR of the separated gas are calculated by flashing the mixture to surface conditions.

The PFVF of the enriched gas is defined as  $B_y$ ,

$$B_y = \frac{V_y}{V_{ys}}. \quad (5)$$

TABLE 1: Flash calculation results of PFVF and GOR of different composition of enriched gas mixed with crude oil in different proportions.

Enriched gas (LPG : NG, %)	Flash calculation parameters	Composition of reservoir fluids (oil : enriched gas, %)				
		95 : 5	90 : 10	80 : 20	50 : 50	10 : 90
59.1 : 40.9	$B_y/10^{-3}$	0.831	1.164	1.577	3.207	4.565
	GOR/sm <sup>3</sup> /rm <sup>3</sup>	63.82	73.97	94.19	415.09	1650.44
51 : 49	$B_y/10^{-3}$	0.869	1.196	1.663	3.301	4.635
	GOR/sm <sup>3</sup> /rm <sup>3</sup>	64.02	74.1	95.86	421.55	1694.875
41 : 59	$B_y/10^{-3}$	0.983	1.807	3.085	5.163	6.156
	GOR/sm <sup>3</sup> /rm <sup>3</sup>	65.06	76.53	99.72	433.34	1758.36
37.1 : 62.9	$B_y/10^{-3}$	0.983	1.407	2.085	4.163	6.156
	GOR/sm <sup>3</sup> /rm <sup>3</sup>	65.32	77.07	100.87	436.96	1779.44
35.2 : 64.8	$B_y/10^{-3}$	0.991	1.419	2.101	4.188	6.307
	GOR/sm <sup>3</sup> /rm <sup>3</sup>	65.45	77.33	101.42	438.69	1789.46
34.8 : 65.2	$B_y/10^{-3}$	0.997	1.429	2.117	4.215	6.343
	GOR/sm <sup>3</sup> /rm <sup>3</sup>	65.47	77.39	101.54	439.05	1791.55

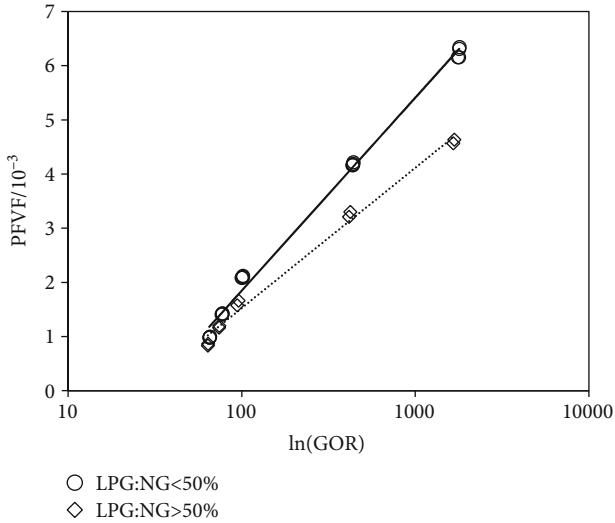


FIGURE 2: Relationships between PFVF and GOR. The dashed line indicates LPG : NG > 50%, and the solid line is LPG : NG < 50%.

Due to the miscible or near miscible characteristics of enriched gas contacts with crude oil, C3-C4 hydrocarbons in enriched gas constantly dissolve into crude oil, and light components in crude oil are extracted to free gas. This phenomenon results in complex composition of produced gas, which cannot be simply treated as a mixture of enriched gas and solution gas [6, 27]. Therefore,  $B_y$  is not the real formation factor of enriched gas, so it is named as pseudo formation volume factor.

PFVF and GOR are intrinsically related to each other; hence, functional relationships between  $B_y$  and GOR are given by

$$B_y = F(\text{GOR}). \quad (6)$$

So far, given the GOR, that the PFVF  $B_y$  can be calculated by equation (6). In the real oilfield production process, the gas

TABLE 2: Comparison of expansion coefficients.

Block	Enriched gas (LPG : NG, %)	Expansion coefficient		
		Measured values	Calculated values	Rel. error/%
IV	59.8 : 40.2	199.86	217.51	8.83
	41 : 59	159.63	170.35	6.72
	37.1 : 62.9	150.22	159.25	6.02
IA-top	59.8 : 40.2	150.815	151.208	0.26
	41 : 59	142.717	145.779	2.15
IA-bottom	59.8 : 40.2	239.69	257.756	7.54
	41 : 59	197.965	207.562	4.85

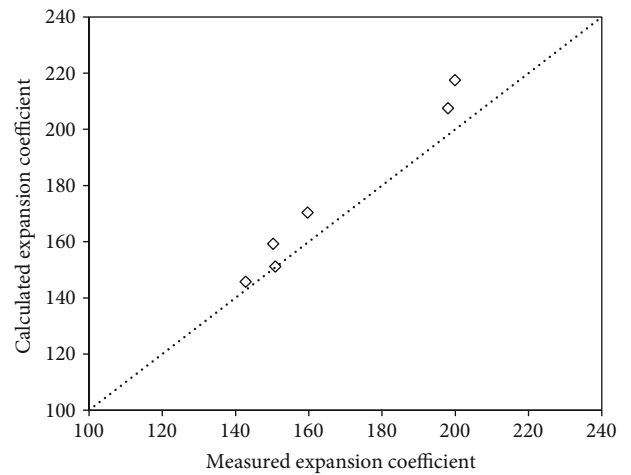


FIGURE 3: Comparison of calculated expansion coefficient against the measured values. The dashed lines indicate relative errors equal to zero.



TABLE 3: Parameter design of numerical simulation model.

Grid direction	Grid numbers	Step size/ m	Permeability/ mD	Porosity/ %	Oil saturation/ %	Formation pressure/ MPa	Saturated pressure/ MPa
X	150	1	1.09				
Y	1	100	1.09	11.05	41.35	10.5	10.2
Z	7	3.1	0.107				

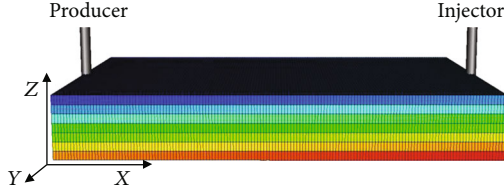


FIGURE 4: The 3D grid model of reservoir simulation.

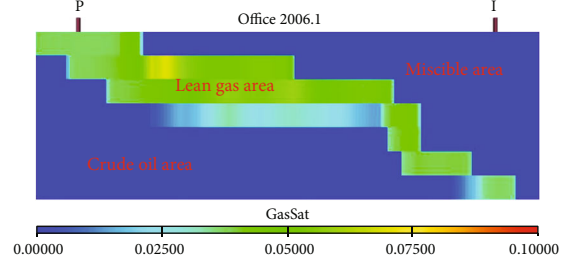


FIGURE 7: Gas saturation profile of enriched gas flooding.

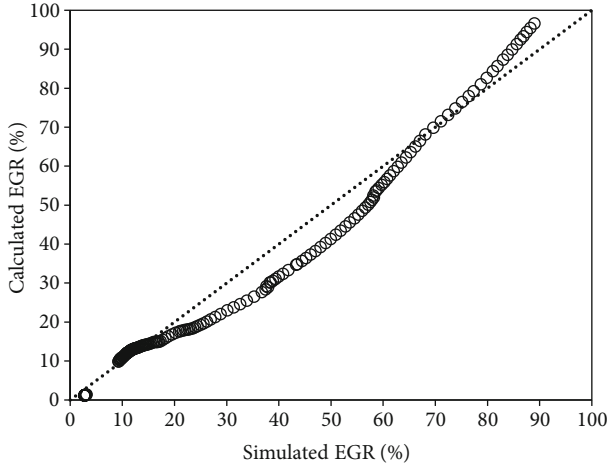


FIGURE 5: Comparison of calculated EGR against the simulated values, LPG : NG &lt; 50%. The dashed lines indicate relative errors equal to zero.

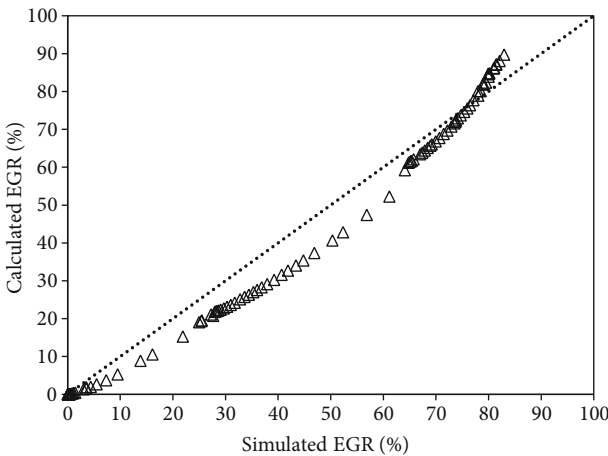


FIGURE 6: Comparison of calculated EGR against the simulated values, LPG : NG &gt; 50%. The dashed lines indicate relative errors equal to zero.

volume  $V_{ys}$  produced from wellhead can be measured; thereby, the underground enriched gas volume  $V_y$  can be obtained through equation (5). Injected volume of enriched gas  $V_{gl}$  is known; finally, enriched gas recovery  $R_g$  can be calculated as

$$R_g = 100 \times \frac{V_y}{V_{gl}}. \quad (7)$$

The above analysis shows that key point to calculate EGR factor is to obtain the functional relationships between the PFVF of enriched gas and the produced GOR. In the following, the way to obtain the functional relationships is delineated, and one application to an enriched gas flooding in tight sandstone reservoir is provided.

Taking the enriched gas flooding in oilfield Z as an example, the reservoir pressure is 10.5 MPa, formation temperature is 34.2°C, and the average permeability is 1.09 mD. Six proportions of enriched gas were tested in the laboratory, and the molar ratios of LPG to natural gas are 59.1:40.9, 51:49, 41:59, 37.1:62.9, 35.2:64.8, and 34.8:65.2, respectively. In pilot test, three proportions of enriched gas were implemented; they are 59.8:40.2, 41:59, and 37.1:62.9, respectively. Due to the influence of formation heterogeneity, enriched gas is not evenly distributed in the formation during gas flooding. Consequently, the produced GOR will vary with time. Therefore, the PFVF and GOR were calculated by different crude oil to enriched gas ratios. Molar ratios of crude oil to enriched gas are 95:5, 90:10, 80:20, 50:50, and 10:90, respectively. Flash calculation results are shown in Table 1.

In order to obtain the functional relationships between PFVF and GOR, a relationship diagram (Figure 2) was drawn. From Figure 2, the following conclusions can be obtained: PFVF increases with GOR; when the proportion of LPG in the enriched gas is more than 50%, the PFVF and the GOR follow a logarithmic relationship; when the proportion of LPG in the enriched gas is less than 50%, the

TABLE 4: Injection and production data of enriched gas flooding in the field Z and calculated EGRs.

Injection stage	Enriched gas (LPG:NG, %)	Injection volume (rm <sup>3</sup> )	GOR	Produced gas (10 <sup>3</sup> m <sup>3</sup> )	PFVF (10 <sup>-3</sup> )	Production volume (rm <sup>3</sup> )	EGR (%)
Stage 1	59.8:40.2	145.8	883	19.35	4.26	82.48	56.57
Stage 2	41:59	479.5	370	66.91	4.29	287.21	59.89
Stage 3	37.1:62.9	556.9	950	71.38	5.68	405.06	72.73

PFVF and GOR follow another logarithmic relationship. When the proportion of LPG in the enriched gas is more than 50%, the relative volume increases slightly than LPG proportion is less than 50%; this is mainly because the higher LPG proportion is, the more easily miscible flooding occurred. 50% of LPG in enriched gas was used as the demarcation point in this research; it is related to the composition of crude oil and the reservoir situations (temperature and pressure).

Based on Figure 2, logarithmic fitting method is adopted to obtain the functional relationships between PFVF and GOR when the proportion of LPG is less than 50% and more than 50% in enriched gas, respectively, as described in equations (8) and (9). In addition, the fitting precisions of equations (8) and (9) are 0.9943 and 0.9922, respectively, which meet the needs of engineering application.

$$B_{y1} = 1.547 \ln(\text{GOR}_1) - 5.2768, \quad (8)$$

$$B_{y2} = 1.124 \ln(\text{GOR}_2) - 3.6497. \quad (9)$$

## 2. Results and Discussion

**2.1. Comparison of Expansion Coefficients.** In order to verify the robustness of our flash calculation method, we compared the expansion coefficient of enriched gas between measured values and calculated ones. Measured values were taken from the pilot test of enriched gas miscible flooding in oilfield Z of Algeria. Miscible flooding was carried out in three blocks, block IV, block IA-top, and block IA-bottom. Expansion coefficient is the reciprocal of the formation volume factor of enriched gas under standard conditions. As shown in Table 2, the calculated error for different proportions of LPG in enriched gas is between 4 and 8%. From Figure 3, it indicates that the calculated expansion coefficients are slightly higher than measured values. This is probably because the actual measured pressure and temperature may be lower than the calculated value due to the pressure and temperature loss of the measuring instrument, resulting in low measurement results. The relative error increases with the increase of LPG proportion. The underlying reason is that as the proportion of LPG increases, the percentage of C3-C4 increases in enriched gas, and its compressibility is greater than that of natural gas, thus magnifying the calculation error.

**2.2. Comparison of EGR Calculation Results and That from Numerical Simulations.** Numerical simulation model was established to simulate the EGR factors with different injected LPG:NG proportions. The Eclipse composition simulator v2006 of Schlumberger was used for numerical

simulation, which can simulate multicomposition flash calculation and enriched gas flooding. A number of grids in the directions of X, Y, and Z are 150, 1, and 7, respectively, and the step sizes are 1, 100, and 3.1 meters, respectively. The model represents a tight sandstone reservoir with the average permeability of 1.09 mD, and porosity is 11.05%. Other parameters of the model are shown in Table 3, and Figure 4 is the three-dimensional grid model.

Two scenarios were simulated, i.e., scenario 1 and scenario 2. The injected proportion of LPG:NG of scenario 1 is 41:59, which represents that the LPG:NG < 50%, and equation (8) is employed to calculate EGR. Scenario 2 with LPG:NG is 59:41, which indicates the LPG:NG > 50%, and equation (9) is used to calculate EGR. Enriched gas injection volumes of the both scenarios are 100 rm<sup>3</sup>/d; minimum bottom hole pressure of production well is slightly higher than saturation pressure to ensure that solution gas is not released.

Numerical simulation results and calculated values are compared in Figures 5 and 6, respectively. Mean errors are 11.22% and 12.21% for Figures 5 and 6, respectively. Error analysis shows that when EGR is less than 10%, the errors of both functions are greater than 50%. The main reason is that the proposed approach is based on the flash calculation theory. However, the numerical simulation approach takes account of the dynamic process of light hydrocarbon extraction and heavy hydrocarbon dissolution. As shown in Figure 7, gas saturation profile falls into three regions. The first region corresponds to the miscible process of crude oil and enriched gas. The second one is lean gas area which is extracted from crude oil, and the third one is crude oil area. Because of the light hydrocarbon extracted from the crude oil, EGR is high in the early stage of enriched gas flooding. In this stage, lean gas is mainly produced, and C3-C4 are not largely produced. In other words, the proposed approach avoids the influence of lean gas production on the calculation of EGR in the early stage of enriched gas flooding.

**2.3. Field Application.** The production data of the pilot test with one injection well and one production well in oilfield Z was used to calculate the EGR. Table 4 displays the injection and production performance of the three stages' enriched gas injection. According to the molar composition of injected enriched gas, equation (9) was used to calculate the enriched gas PFVF in the first stage, and equation (8) was used to calculate the enriched gas PFVF in the second and third stages. Enriched gas PFVFs in the first, second, and third stages were calculated to be  $4.26 \times 10^{-3}$ ,  $4.29 \times 10^{-3}$ , and  $5.68 \times 10^{-3}$ , respectively. Given the PFVFs of enriched gas, the underground volumes of enriched gas

produced in three stages are calculated according to the gas production from wellhead in each stage, and the underground volumes are  $82.48 \text{ m}^3$ ,  $287.21 \text{ m}^3$ , and  $405.06 \text{ m}^3$ , respectively. Thus, the EGRs in three stages are 56.57%, 59.89%, and 72.73%, respectively, with an average value of 63.07%. EGR of three gas injection stages obtained by chromatographic analysis in the field is 59.71%, and the error between the approach proposed in this paper and the results from the field is 5.62%.

A simple approach is proposed in this article to calculate the EGR of unconventional reservoir enriched gas displacement. It should be noted that the functional relationships between PFVF and GOR are not applicable to all reservoirs and should be recalculated according to the compositions of crude oil for the certain reservoir.

### 3. Conclusions

Based on the two-phase flash calculation theory of oil and gas, a novel approach was proposed to predict the EGR. PFVF of enriched gas was defined, and the logarithmic functions between the PFVF and GOR were established. As a consequence, the approach of EGR calculation for unconventional reservoir enriched gas displacement was obtained. The results obtained from this new approach were compared with that from numerical simulations, and the mean error is 12%. In addition, the new approach can effectively avoid the influence of lean gas on the calculation of EGR.

Flash calculation results of different proportion of LPG in enriched gas show that when the proportion of LPG in the enriched gas is more than 50%, the PFVF and GOR follow a logarithmic relationship; when the proportion of LPG in the enriched gas is less than 50%, the PFVF and GOR follow another logarithmic relationship. Hence, the relationships between PFVF and GOR can be described by two functions. According to the different composition of the enriched gas, the corresponding function is selected to calculate the PFVF.

New approach has been used to calculate the EGR of enriched gas in three stages of enriched gas flooding in a low permeability and tight oilfield. The error is 5.62% compared to the results of field analysis data, which proves the correctness and practicability of this approach.

### Data Availability

Data supporting the results of our study are in the article.

### Conflicts of Interest

We declare that we do not have any commercial or associative interest that represents a conflict of interest in connection with the work submitted.

### Acknowledgments

This study was carried out with the Open Fund of State Key Laboratory of Oil and Gas Reservoir Geology and Exploita-

tion (Southwest Petroleum University) (Grant No. PLN2020-22) for its financial supports which we gratefully acknowledge.

### References

- [1] Y. Song, Q. Luo, Z. Jiang, W. Yang, and D. Liu, "Enrichment of tight oil and its controlling factors in central and western China," *Shiyou Kantan Yu Kaifa/Petroleum Exploration and Development*, vol. 48, pp. 421–433, 2021.
- [2] L. Sun, C. Zou, A. Jia et al., "Development characteristics and orientation of tight oil and gas in China," *Petroleum Exploration and Development*, vol. 46, pp. 1073–1087, 2019.
- [3] C. Yu, Q. Jiang, N. Su, and L. Chang, "Predicting the permeability of tight sandstone utilizing experimental and mathematical modeling approaches," *Journal of Energy Resources Technology, Transactions of the ASME*, vol. 143, no. 2, pp. 1–9, 2021.
- [4] J. I. Lee, E. L. Astete, and T. F. Jerhoff, "Performance review of Brazeau River Nisku dry-gas miscible-flood projects," *SPE Reservoir Engineering (Society of Petroleum Engineers)*, vol. 9, no. 1, pp. 29–34, 1994.
- [5] L. Wang, Y. Tian, X. Yu et al., "Advances in improved/enhanced oil recovery technologies for tight and shale reservoirs," *Fuel*, vol. 210, pp. 425–445, 2017.
- [6] W. Chengjun and L. Xiaorui, "The empirical and theoretical miscible characterization method in gas-enhanced oil recovery," *Geofluids*, vol. 2018, Article ID 7841948, 9 pages, 2018.
- [7] V. S. Rios, L. O. S. Santos, F. B. Quadros, and D. J. Schiozer, "New upscaling technique for compositional reservoir simulations of miscible gas injection," *Journal of Petroleum Science and Engineering*, vol. 175, pp. 389–406, 2019.
- [8] A. Ebrahimi, E. Khamehchi, and J. Rostami, "Investigation of hydrocarbon and non-hydrocarbon (CO<sub>2</sub>, N<sub>2</sub>) gas injection on enhanced oil recovery in one of the Iranian oil fields," *Technology*, vol. 2, no. 4, pp. 209–222, 2012.
- [9] L. L. Harbert, P. W. Reed, R. K. Bray, and J. N. Dew, "Progress report of LPG injection in the Meadow Creek Unit, Lakota B Reservoir," *Journal of Petroleum Technology*, vol. 11, no. 7, pp. 26–29, 1959.
- [10] R. A. Fitch, "Experimental and calculated performance of miscible floods in stratified reservoirs," *Journal of Petroleum Technology*, vol. 16, no. 11, pp. 1289–1298, 1964.
- [11] A. Hildenbrand, S. Schlömer, and B. M. Krooss, "Gas breakthrough experiments on fine-grained sedimentary rocks," *Geofluids*, vol. 2, no. 1, 23 pages, 2002.
- [12] L. Xu, W. M. Ye, Y. G. Chen, B. Chen, and Y. J. Cui, "A new approach for determination of gas breakthrough in saturated materials with low permeability," *Engineering Geology*, vol. 241, pp. 121–131, 2018.
- [13] F. Du and B. Nojabaei, "A diffusion-based compositionally-extended black oil model to investigate produced gas reinjection EOR in Eagle Ford," *Fuel*, vol. 306, article 121711, 2021.
- [14] D. G. Raheem, B. Yilmaz, U. Kayahan, and S. Özdoğan, "Effect of recycled flue gas ratio on combustion characteristics of lignite oxy-combustion in a circulating fluidized bed," *Energy and Fuels*, vol. 34, no. 11, pp. 14786–14795, 2020.
- [15] S. L. Yang, H. Chen, D. Z. Hang, H. Lu, X. Zhang, and S. B. Lv, "Mechanism of produced gas reinjection during CO<sub>2</sub> Flooding

- by chromatographic analysis,” *Journal of Dispersion Science and Technology*, vol. 34, no. 3, pp. 342–346, 2013.
- [16] H. Chen, S. L. Yang, S. S. Ren et al., “Crude oil displacement efficiency of produced gas re-injection,” *International Journal of Green Energy*, vol. 10, no. 6, pp. 566–573, 2013.
- [17] H. Yu, X. Lu, W. Fu et al., “Determination of minimum near miscible pressure region during CO<sub>2</sub> and associated gas injection for tight oil reservoir in Ordos Basin, China,” *Fuel*, vol. 263, article 116737, 2020.
- [18] D. Cosovanu, M. Llovera, G. Villorbina, R. Canela-Garayoa, and J. Eras, “A simple and fast method for metabolomic analysis by gas liquid chromatography–mass spectrometry,” *Metabolomics*, vol. 17, no. 2, 2021.
- [19] S. T. Lee, H. Lo, and B. T. Dharmawardhana, “Analysis of mass transfer mechanisms occurring in rich gas displacement process,” *SPE Annual Technical Conference and Exhibition*, no. - article 18062, pp. 47–62, 1988.
- [20] Y. Kawajiri, “Model-based optimization strategies for chromatographic processes: a review,” *Adsorption*, vol. 27, no. 1, pp. 1–26, 2021.
- [21] A. Lucia, B. M. Bonk, R. R. Waterman, and A. Roy, “A multi-scale framework for multi-phase equilibrium flash,” *Computers and Chemical Engineering*, vol. 36, pp. 79–98, 2012.
- [22] A. Lucia, L. Padmanabhan, and S. Venkataraman, “Multiphase equilibrium flash calculations,” *Computers and Chemical Engineering*, vol. 24, no. 12, pp. 2557–2569, 2000.
- [23] W. X. Jin, S. C. Low, and S. C. M. Yu, “Some experimental observations on the single and multi-phase flow patterns in a model flash evaporation chamber,” *International Communications in Heat and Mass Transfer*, vol. 26, no. 6, pp. 839–848, 1999.
- [24] C. H. Whitson and S. B. Torp, “Evaluating constant-volume depletion data,” *Journal of Petroleum Technology*, vol. 35, no. 3, pp. 610–620, 1983.
- [25] R. M. Enick, G. D. Holder, and R. Mohamed, “Four-phase flash equilibrium calculations using the Peng-Robinson equation of state and a mixing rule for asymmetric systems,” *SPE Reservoir Engineering (Society of Petroleum Engineers)*, vol. 2, no. 4, pp. 687–694, 1987.
- [26] D.-Y. Peng and D. B. Robinson, “A new two-constant equation of state,” *Industrial & Engineering Chemistry Fundamentals*, vol. 15, no. 1, pp. 59–64, 1976.
- [27] P. Luo, W. Luo, and S. Li, “Effectiveness of miscible and immiscible gas flooding in recovering tight oil from Bakken reservoirs in Saskatchewan, Canada,” *Fuel*, vol. 208, pp. 626–636, 2017.

## Research Article

# Experimental Study on Fe<sub>3</sub>O<sub>4</sub> Nanoparticle-Assisted Microwave Enhancing Heavy Oil

Teng Lu <sup>1,2</sup>, Faqiang Dang,<sup>2</sup> Haitao Wang,<sup>1</sup> Qingmin Zhao,<sup>1</sup> and Zhengxiao Xu <sup>2</sup>

<sup>1</sup>State Energy Center for Shale Oil Research and Development, China

<sup>2</sup>School of Petroleum Engineering, China University of Petroleum (East China), China

Correspondence should be addressed to Teng Lu; luteng@upc.edu.cn

Received 26 September 2021; Accepted 24 November 2021; Published 12 January 2022

Academic Editor: Xiang Zhou

Copyright © 2022 Teng Lu et al. This is an open access article distributed under the Creative Commons Attribution License, which permits unrestricted use, distribution, and reproduction in any medium, provided the original work is properly cited.

Nanoparticle-assisted microwave heating of heavy oil has the advantages of fast temperature rise and high thermal efficiency. Compared with traditional heating methods, it can reduce viscosity in a shorter time. In addition, the heavy components in the heavy oil are cracked into light components at high temperatures (this high temperature cannot be reached by conventional heating methods). This process is irreversible and avoids the problem of viscosity recovery of heavy oil after the temperature is reduced. Through absorbing microwave heating experiments, study the effect of nanoparticles on the improvement of the ability of heavy oil to absorb waves and raise temperature; through the heavy oil upgrading experiment and the four-component analysis experiment, the effect of adding hydrogen donor to assist microwave on the viscosity reduction of heavy oil upgrading by nanoparticles was studied, and the problem of viscosity recovery was determined; Through the gravity drainage experiment, the mechanism of nanoparticle-assisted microwave to improve the recovery of heavy oil is studied, and the influence of water content, nanocatalyst, and microwave power on the production of drainage is analyzed. The results show that nanoparticles can improve the wave absorption and heating capacity of heavy oil, and adding 0.6 wt% of nanomagnetic iron oxide catalyst can increase the heating rate of heavy oil in microwave by 60.6%; nanoparticle-assisted microwave heating method can effectively upgrade heavy oil and reduce viscosity. The experimental conditions are 2 wt% tetralin mass concentration, 0.5 wt% nano-Fe<sub>3</sub>O<sub>4</sub> particle mass concentration, microwave heating time 50-60 min, and microwave power 539 W. Under this experimental condition, the viscosity is reduced by 40%. This method has viscosity recovery problems, but final viscosity reduction effect is still very significant. Obtaining the mechanism of nanoparticle-assisted microwave to enhance oil recovery, one of which is that nanoparticles improve the wave absorption and heating capacity of heavy oil and increase the heating speed of heavy oil; the second is that the nanoparticles form local high temperature under the action of microwave, which catalyzes the hydrocracking reaction between the heavy components in the heavy oil and the hydrogen donor, upgrading and reducing the viscosity of the heavy oil, and accelerating the production of heavy oil.

## 1. Introduction

With the depletion of conventional oil, the world's population continues to grow, and the world's industrialization and motorization levels increase, and how to meet energy supply and demand has become a huge challenge facing the world. The world has huge reserves of heavy oil, and Venezuela, Canada, the United States, Brazil, Mexico, China, Russia, and the Middle East have large amounts of heavy oil. According to the report of the International Energy Agency, the world's total oil reserves are about 9-13 trillion barrels,

and heavy oil and ultraheavy oil account for 40% of the world's oil reserves, about 4-5 trillion barrels of oil [1].

Heavy oil is also called heavy oil. It not only has the characteristics of high viscosity and high specific gravity but also has low hydrogen to carbon ratio, high asphaltene content, high carbon residue, sulfur, nitrogen and heavy metal content, and high acid value [2, 3]. The difficulty in heavy oil production is high viscosity. Heating and upgrading are two effective ways to reduce viscosity.

With the continuous development of microwave technology, microwave heating technology has also been introduced



into the production of heavy oil reservoirs. Its main purpose is to use the advantages of microwave heating, volume heating, and selective heating to heat the oil reservoir [4–6]. The efficiency of microwave heating depends on the dielectric loss constant of the heated material. Water, activated carbon, transition metals, and their oxides are strong microwave absorbing materials, while heavy oil absorbs microwaves very poorly [7]. Therefore, strong absorbing materials must be added to improve the absorbing ability of heavy oil. Some preliminary exploratory experiments have proved the technical advantages of microwave and nanoparticles in improving the recovery rate of unconventional oil reservoirs [8–13].

In recent years, scientists have proved through experiments that  $\text{Fe}_3\text{O}_4$  particles can be used as a heavy oil adsorbent and catalyst compared with other nanoparticles, which can reduce the viscosity of heavy oil more effectively [14–21]. For example, a molecular sieve supported  $\text{Fe}_3\text{O}_4$  catalyst was synthesized by microwave means. The synergistic effect of  $\text{Fe}_3\text{O}_4$  and molecular sieve catalyzed the cracking of heavy oil. After 6 hours of reaction at  $200^\circ\text{C}$ , the viscosity reduction rate reached 92% [15]. Although the nanoparticle-assisted microwave performed well in the experiment of heating and viscosity reduction of heavy oil, it did not solve the problem of viscosity recovery. Nanoparticles will form localized high temperature after absorbing microwaves [22], which provides conditions for the addition of hydrogen donors to reform and viscosity reduction of heavy oil cracking. It can also further improve and reduce viscosity on the basis of heating and viscosity reduction, which greatly increases, and improve the viscosity reduction rate and effectively solve the problem of viscosity recovery.

This paper studies the mechanism of nanoparticle-assisted microwave heavy oil upgrading and enhanced oil recovery. First, the mechanism of nanoparticle-enhanced heat utilization efficiency of heavy oil is studied through the wave absorption and heating experiment of heavy oil. It is found that nanoparticles can improve the wave absorption and heating of heavy oil. It is found that the location of the nanoparticles during the microwave heating process will form a local high temperature, and the local high temperature provides a temperature condition for the cracking of heavy oil; then, a microwave-nanoparticle heavy oil upgrading and viscosity reduction study has been carried out, which proves that the method can be effectively upgraded and reduce the viscosity of heavy oil. Obtained the mechanism of nanoparticle-assisted microwave heavy oil to enhance oil recovery. The addition of catalyst improves the wave absorption and heating capacity of heavy oil, increases microwave energy utilization, and accelerates the heating rate of the oil reservoir in the microwave field, thereby using the viscosity-temperature characteristics of heavy oil to reduce the viscosity of heavy oil accelerates the exploitation of heavy oil; the nanoparticles form a high-temperature field under the action of microwave to catalyze the hydrocracking reaction between the heavy components in the heavy oil and the hydrogen donor to achieve the purpose of upgrading and reducing viscosity. These studies provide technical references for nanoparticle-assisted microwave heavy oil upgrading and enhanced oil recovery technologies and are of great

significance to the development of technologies for further enhancing the recovery of heavy oil reservoirs.

## 2. Experiment

### 2.1. Materials and Instruments

**2.1.1. Materials.** Ultraheavy oil from Venezuela was used in these experiments, and Table 1 summarizes its properties. The  $\text{Fe}_3\text{O}_4$  nanoparticles with particles sizes of 20 nm, 100 nm, and  $10\ \mu\text{m}$  were used (Aladdin Corporation). Tetrahydronaphthalene was used as the hydrogen donor ( $>98\ \text{wt}\%$  purity, Sinopharm Group). n-Heptane, petroleum ether, toluene, anhydrous ethanol, and neutral alumina were purchased from Sinopharm Group.

**2.1.2. Instrument.** The experimental device mainly includes microwave heater (Midea M1-L1213B, microwave power 231 385 539 700w, microwave frequency 2455 MHz, Qingdao Midea Co. Ltd. of China), Anton Paar rheometer, as shown in Figure 1, and oil drain system (oil drain funnel, glass beads, and oil receiving beaker), as shown in Figure 2.

### 2.2. Methods

**2.2.1. Heating Test of Heavy Oil Using Nanoparticle-Assisted Microwaves.** First, heavy oil was placed in a constant-temperature oven and heated to  $80^\circ\text{C}$  to make the heavy oil flowable, followed by its transfer into a 50 mL beaker. Second,  $\sim 45\ \text{g}$  of heavy oil was weighed, and a certain concentration of the nanoparticles was added into the beaker. Third, the mixture was cooled to room temperature after stirring it well. Next, the beaker was placed in an M1-L1213B microwave heater (Midea, China; microwave frequency of 2450 MHz and maximum power of 700 W), the corresponding microwave power was set, and heating was started; and heavy oil was sampled out, and its temperature was measured every 2 min of heating. The temperature measurement was completed when the heavy oil was heated to  $\sim 110^\circ\text{C}$ .

**2.2.2. Local High-Temperature Experiment.** First, place the heavy oil in a heating thermostat and heat it to  $80^\circ\text{C}$  to increase the temperature of the heavy oil and reduce its viscosity to flow, and transfer it to a 250 mL beaker; second, after the heavy oil drops to room temperature, place the beaker in a microwave heater for heating and measure the heating curve of the heavy oil without adding nanoparticles; take out the beaker, wait until the heavy oil is lowered to room temperature, add a small amount of nanoparticles to the beaker A, then place the beaker in a microwave heater for heating, and measure the temperature at two points A and B every 2 minutes until the temperature is reached; when reaching  $90^\circ\text{C}$ , the temperature rise curve at two points is obtained.

**2.2.3. Upgrading of Heavy Oil Using Nanoparticle-Assisted Microwaves.** First, the heavy oil sample was placed in a constant-temperature heating incubator and heated to  $80^\circ\text{C}$  to make the heavy oil warm to its flowable state. Second, the heated heavy oil was transferred to a 50 mL weighing

TABLE 1: Properties of ultraheavy oil from Venezuela.

Density at 50°C ( $\text{kg}\cdot\text{m}^{-3}$ )	Viscosity at 25°C ( $\text{mPa}\cdot\text{s}$ )	Viscosity at 50°C ( $\text{mPa}\cdot\text{s}$ )	Saturates (wt%)	Aromatics (wt%)	Resin (wt%)	Asphaltenes (wt%)
976.5	1380000	100400	25.70	35.25	27.05	12.00



FIGURE 1: Antonpa rheometer.



FIGURE 2: Heavy oil gravity drainage device.

bottle for weighing  $\sim 45$  g of heavy oil. Third, the catalyst and hydrogen donor were added to reach certain mass contents, and the mixture was stirred until a homogeneous system was formed, and then cooled to room temperature. The weighing bottle was placed into a microwave heater; the microwave power and heating time were set; the oil sample was removed after heating; and relevant measurements were performed after cooling, including the viscosity measurement of crude oil viscosity and four-component test.

Viscosity measurement of crude oil: a planar laminar system of an MCR rheometer (Anton Paar, Austria) was used, and the test parameters were set to a speed of  $170 \text{ s}^{-1}$  and a temperature range of 20–100°C.

Four-component determination: first, asphaltenes were removed from the oil sample, followed by the dilution and dissolution of the sample with 10 mL of petroleum ether. Second, an adsorption column was connected to an ultraconstant temperature water bath, and the temperature of the circulating water was maintained at 50°C. Third, the lower

end of the adsorption column was plugged with a small amount of degreased cotton, the column was filled with alumina till 7 cm below the circulating water level of the column, and then 30 mL of petroleum ether was added to prewet the adsorption column after tapping. As all the petroleum ether for prewetting entered the alumina layer, the diluted sample was added, and petroleum ether was used to wash the conical flask thrice. The washing solution was poured into the adsorption column. After all the sample solution entered into the alumina layer, the solution was covered with 3 cm thick alumina. Each component was rinsed, and its mass was recorded at the end of the experiment for calculating the proportion of four components in the sample [15, 16].

**2.2.4. Gravity Drainage Test of Heavy Oil under Microwave Heating.** The oven temperature was set to 80°C, and the beaker with heavy oil was placed in an oven for heating. The connection of the gravity drain device is shown in Figure 3. After the heavy oil reached a flowable state, the heavy oil was removed into a 250 mL beaker, and the sample was measured with a mass of  $m_1$ . According to  $m_1$ , the chemicals with the corresponding mass percentages were added and stirred with a glass rod; the weight of this sample was designated as  $m_2$ . The glass bead with a mass of  $m_3$  was weighed, the glass beads were mixed with the heavy oil, transferred into a drainage funnel, and the mass of residual heavy oil in the beaker was measured to be  $m_4$ . The mass difference between  $m_2$  and  $m_4$  corresponded to the total amount of heavy oil in the drainage funnel and the mass of the oil-receiving beaker, which was measured as  $m_5$ . As the heavy oil in the drainage funnel cooled to room temperature, the drainage system was placed into a microwave heater, the microwave power was set, and the experiment was started. During the experiment, the drainage system was taken out every 2 min, and the mass of the oil-receiving beaker was measured to be  $m_6$  using an analytical balance.  $m_6 - m_5$  referred to the mass of output oil. An infrared thermometer was used to measure the temperature of the heavy oil (T1) until the recovery amount of the heavy oil did not increase, and the experiment was completed. According to the measurement data, the production curve was drawn, and the effect of each influencing factor on the microwave drainage experiment of heavy oil was compared and analyzed. Figure 1 shows the schematic of the microwave gravity drainage experiment of heavy oil.

### 3. Results and Discussion

#### 3.1. Research on the Mechanism of Nanoparticles to Enhance the Heat Utilization Efficiency of Heavy Oil

##### 3.1.1. Research on Nanoparticles to Improve the Absorbing and Heating Ability of Heavy Oil.

The experimental

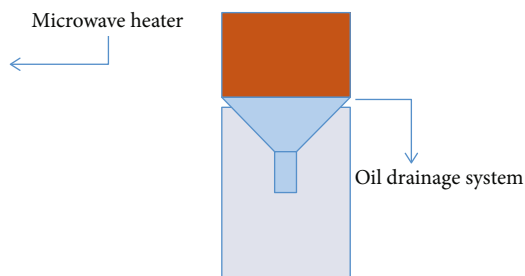


FIGURE 3: Schematic of the gravity drainage test of heavy oil under microwave heating.

nanoparticle is 100 nm  $\text{Fe}_3\text{O}_4$ , the microwave power is 539 W, and the curve of the temperature of the heavy oil with time when the nanoparticle of different mass concentration is added is obtained, as shown in Figure 4.

It can be found from Figure 4 that under the condition of an initial temperature of  $24^\circ\text{C}$ , the oil sample with nano- $\text{Fe}_3\text{O}_4$  nanoparticles added has a higher temperature than the crude oil sample heated by microwave for the same time. As the mass concentration of nano- $\text{Fe}_3\text{O}_4$  nanoparticles increases, the time it takes to reach the same temperature is shorter. This is because nano- $\text{Fe}_3\text{O}_4$  nanoparticles have a large dielectric constant and have a stronger absorbing effect on microwaves, indicating that the addition of nano- $\text{Fe}_3\text{O}_4$  nanoparticles improves the wave-absorbing and heating ability of heavy oil.

**3.1.2. Microwave-Nanoparticle Local High-Temperature Experimental Research.** The nanoparticle used in the experiment is 100 nm  $\text{Fe}_3\text{O}_4$ , and the microwave power is set to 539 W. In the experiment, the heating curve of the microwave heating heavy oil as it is and the heating curve of the two points A and B after adding nanoparticles are shown in Figure 5.

Observing Figure 5, it can be found that the heating rate of point A is faster than that of point B, and the heating rate of heavy oil is the slowest. This is because the nanoparticles of point A quickly convert microwave energy into heat energy. Point A is the first to heat up to form a local high temperature and drive the thick oil. The overall temperature of the oil accelerates, so the heating rate of point B is faster than that of the original control group of heavy oil. This shows that during the microwave heating process, the location of the nanoparticles will form a local relatively high temperature, which provides a temperature condition for the cracking of heavy oil.

### 3.2. Nanoparticle-Assisted Microwave Heavy Oil Upgrading and Viscosity Reduction

**3.2.1. Microwave-Nanoparticle Heavy Oil Upgrading Verification Experiment.** The nanoparticles used in the experiment were 100 nm magnetic iron oxide nanoparticles, and the hydrogen donor was tetralin. The viscosity-temperature curves of the four groups of heavy oil samples after microwave treatment are shown in Figure 6.

Comparing the original heavy oil and the heavy oil with only nanoparticles, it can be found that the viscosity of the heavy oil in the control group with only nanoparticles is increased. Due to the high-temperature environment, the long chain of the heavy components is broken, but because there is no hydrogen supplementation, it cannot happen. Hydrogenation reaction, so the broken long chain will recombine. And because the experimental environment is not sealed, the light components in the heavy oil evaporate and lose at high temperatures, so the viscosity becomes higher; comparing the original heavy oil and the heavy oil with only hydrogen donors, it can be found that the viscosity of the control group with only hydrogen donors has decreased. The analysis believes that the viscosity reduction effect of tetralin is due to the dilution and viscosity reduction effect of tetralin, and it may also be modified by heating to the cracking temperature. Four-component analysis is required for further verification; observing the viscosity reduction system of the experimental group, the experimental group can find that the viscosity reduction effect of the experimental group with heavy oil added to the viscosity reduction system is the best. Analysis suggests that the viscosity reduction of heavy oil occurred during the process, and the reduction of asphaltene content resulted in a significant decrease in viscosity.

In order to further verify the experimental results, a four-component analysis test was carried out to calculate the proportion of the four components. The results are shown in Figure 7.

Comparing experiments 1# and 2#, the aromatic content increased, and the rest decreased, but the overall change was small, mainly because the added hydrogen donor was an aromatic hydrocarbon, and the decrease in viscosity of the control group was mainly due to the effect of dilution. Comparing experiment 1# and 3#, the light components are reduced, mainly because the addition of nanoparticles provides a high-temperature environment, and the hydrogenation reduction reaction cannot occur under the condition of high temperature without hydrogen donor, and because of the high temperature, the light components are volatilized loss. Comparing experiment 1# and 4#, the asphaltenes are obviously reduced, and the gums are increased. This is because the asphaltenes will be partially converted to gums during the upgrading process, and the content of asphaltenes is the main influence on the viscosity of heavy oil. This also explains the reason for the significant drop in viscosity in the viscosity-temperature curve.

**3.2.2. Research on Viscosity Recovery of Microwave-Nanoparticle Heavy Oil Upgrading.** The hydrogen donor used in the experiment was tetralin, the nanoparticles were 100 nm  $\text{Fe}_3\text{O}_4$  particles, the microwave heating power was set to 539 W, and the microwave heating reaction time was 60 min.

The viscosity-temperature curve of the thick oil obtained in the third group of upgrading experiments was measured, the viscosity-temperature curve of the retained heavy oil samples was measured again at 3 days, 7 days, and 14 days

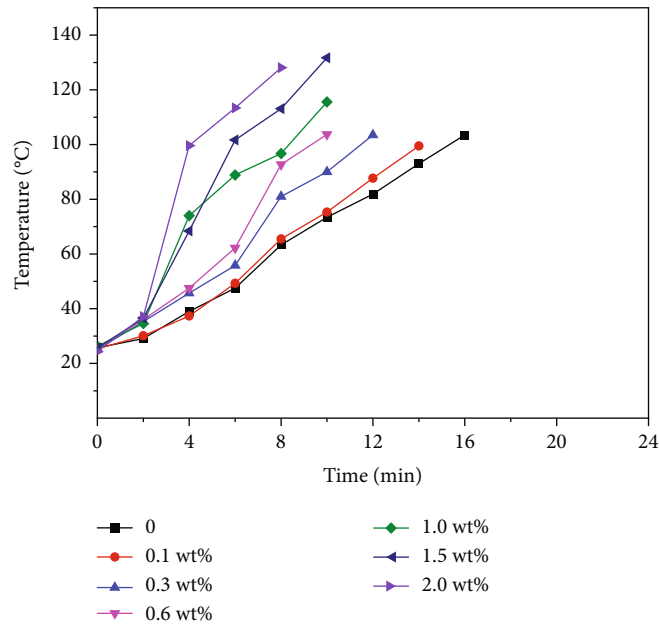


FIGURE 4: Temperature curves of heavy oil with time under different mass fractions of nanoparticles.

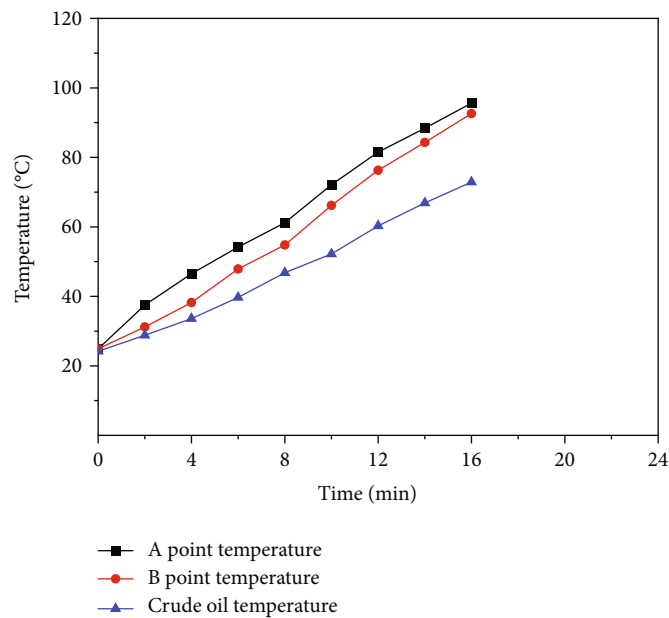


FIGURE 5: Temperature curve of heavy oil heated by microwave with time.

after the end of the experiment, and the viscosity of the modified heavy oil was observed. The recovery situation, the experimental results are shown in Figure 8.

At present, the commonly used index to evaluate the viscosity reduction ability is the viscosity reduction rate, that is, the percentage of the viscosity reduction of the super heavy oil after adding the viscosity reducer. In order to express its viscosity reduction effect more intuitively, compare the viscosity and viscosity reduction rate of heavy oil at 50°C. The results are shown in Figure 9.

Observing Figures 8 and 9, it can be found that within seven days after the microwave-nanoparticle heavy oil upgrading experiment, the viscosity has a relatively obvious recovery, but on the 14th day, it is found that the viscosity of the heavy oil remains stable, and the viscosity is still much lower after recovery. The viscosity of heavy oil is diluted by adding 5 wt% hydrogen donor as it is. Experiments have proved that there is viscosity recovery in microwave-nanoparticle heavy oil upgrading and viscosity reduction, but its viscosity reduction effect is still significant.

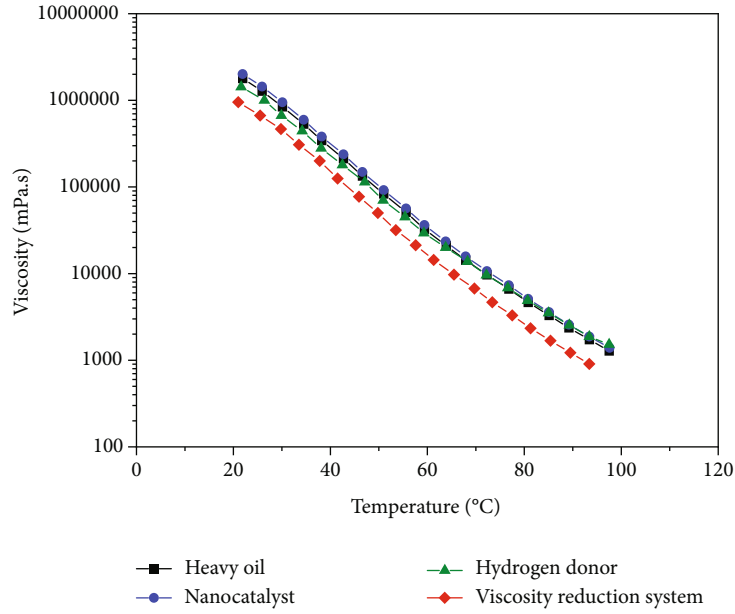


FIGURE 6: Viscosity-temperature curves of heavy oil obtained from each group of experiments.

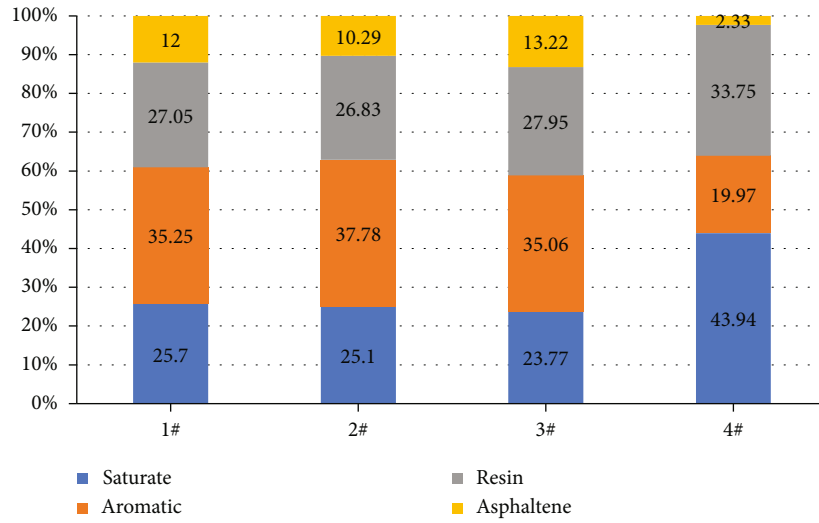


FIGURE 7: The proportion of four components.

### 3.3. Nanoparticle-Assisted Microwave Heavy Oil Enhanced Oil Recovery Research

3.3.1. *The Influence of Water Content on the Microwave Heavy Oil Drainage Experiment.* According to the temperature data measured in the experiment, the regression data obtains the linear slope of one yuan, that is, the heating rate of the heavy oil in the porous medium during the oil drainage process, as shown in Table 2. It is observed that when the water content is increased to 5%, there is a significant increase in the heating rate, while the increase in the water content from 5% to 10% reduces the heating rate of the heavy oil. The addition of water can effectively improve the wave absorption and heating capacity of the reservoir, but

the increase in water cut has little effect on the increase in heating rate.

Calculate the recovery factor of the heavy oil in each group of experiments, and get the curve of the recovery factor of heavy oil drainage experiment with time under different water cuts, as shown in Figure 10. It is observed that the two groups of experimental curves with a moisture content of 5% and 10% are similar, and the production time is significantly shortened compared with the control group without moisture.

Calculate the oil production rate of each group of experimental heavy oil and obtain the curve of the oil production rate of the heavy oil drainage experiment with time under different water cuts, as shown in Figure 11. It is observed



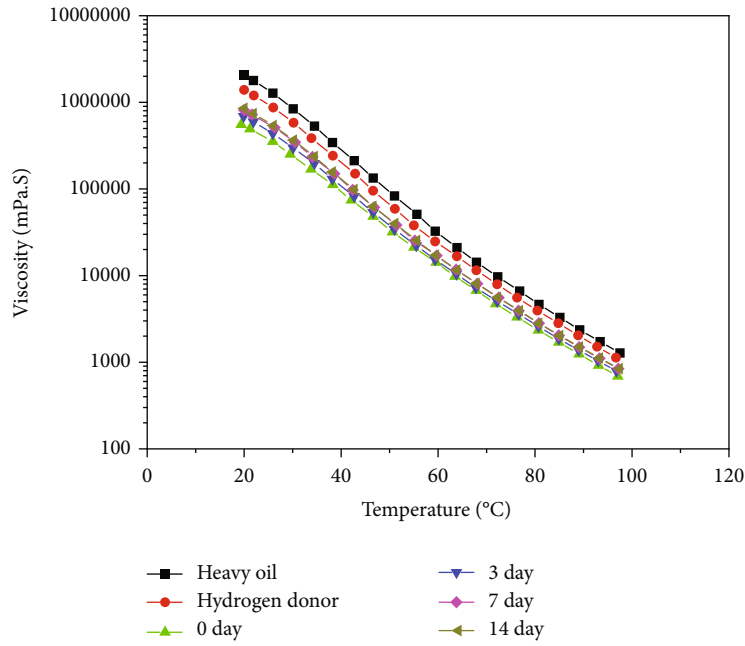


FIGURE 8: Viscosity-temperature curves of heavy oil obtained from each group of experiments.

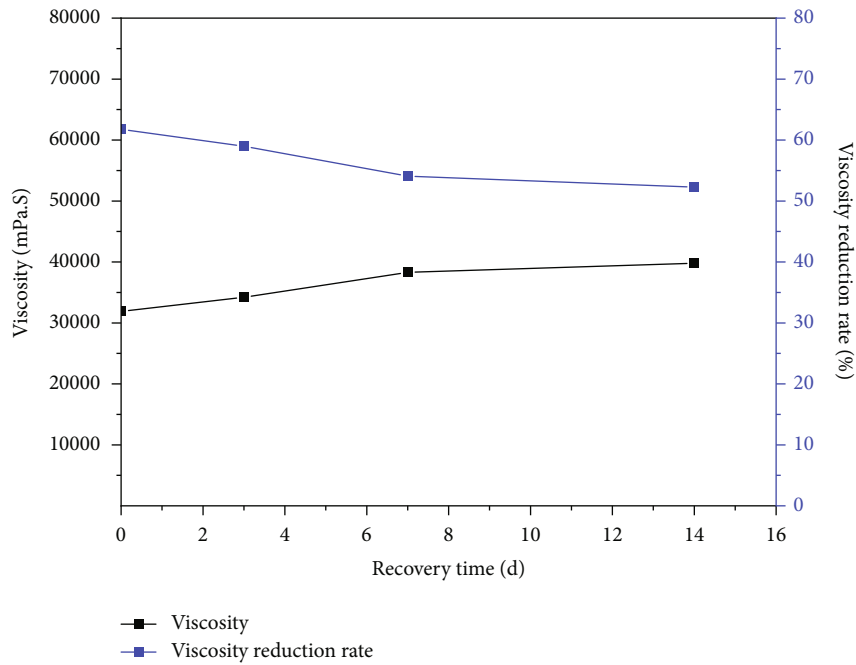


FIGURE 9: Viscosity and viscosity reduction rate curve changes with recovery time after reaction.

TABLE 2: Experimental heating rate under different moisture content.

Serial number	Water cut (%)	Heating rate (°C/min)
1#	—	3.132
2#	5	5.2545
3#	10	5.1164

that the two sets of experiments with water can reach the high-speed production period earlier. The analysis suggests that the wave absorption and heating ability of the heavy oil are improved after the addition of water, which accelerates the temperature rise of the heavy oil, and then the viscosity decreases rapidly, so the fluidity of the heavy oil enhances so the oil production rate can reach the peak earlier.

Take the data of 8 minutes and 16 minutes of each experiment for comparative analysis. At 8 minutes and 16

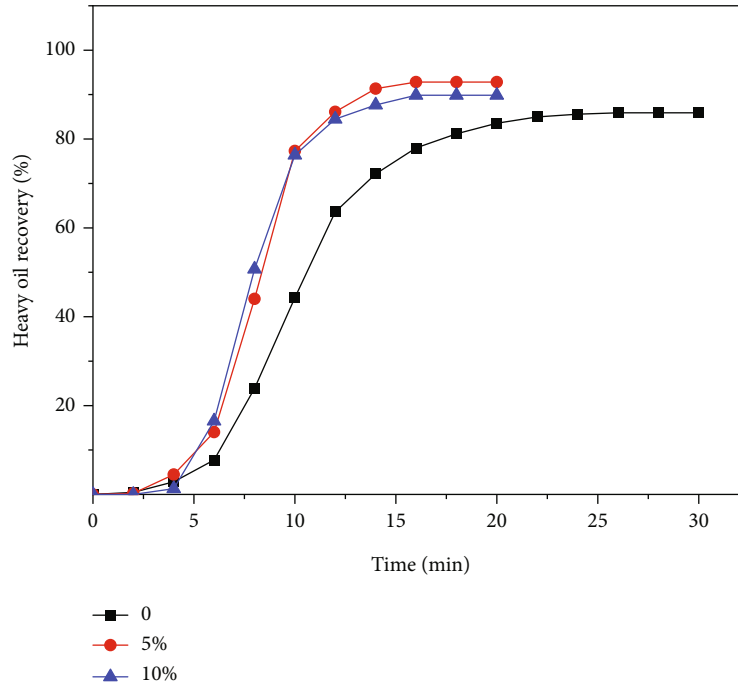


FIGURE 10: The experimental heavy oil recovery curves of each group under different water content.

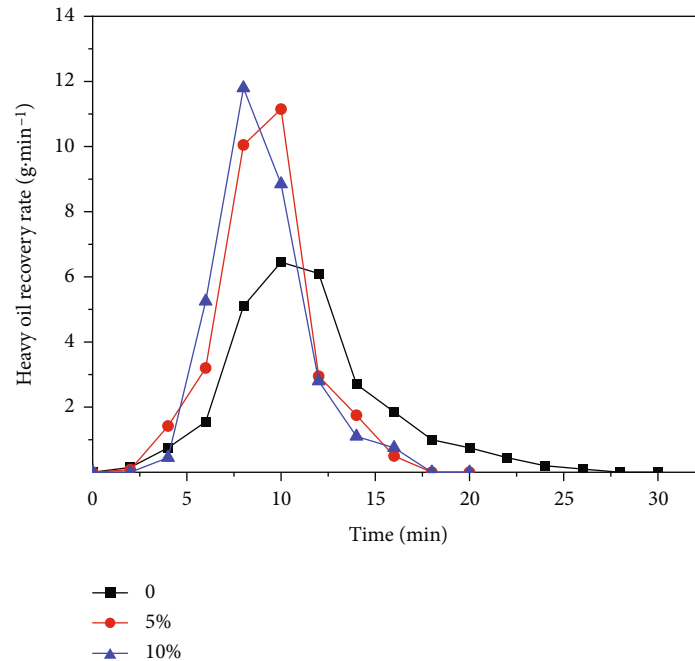


FIGURE 11: The experimental heavy oil recovery rate curves of each group.

minutes, 2# and 3# are the water-bearing experimental groups, and the temperature is about 10°C higher than that of the 1# heavy oil original sample group, which proves the addition of water accelerates the heating rate of the heavy oil drainage system and improves the wave absorption and heating ability of the heavy oil system; comparing the recovery factor and oil production rate at 8 minutes, it can be found that the 2# and 3# water-bearing experimental groups

are thick. The oil is about twice as much as the control group, because the addition of water increases the heating speed of the heavy oil system, the viscosity of the heavy oil increases, the fluidity increases, the gravity driving effect is enhanced, and the faster oil production rate can be achieved. Corresponding to an increase in oil recovery; comparing the oil production rate and recovery efficiency of each group of experiments at 16 minutes, it can be found that the oil

production of the experimental groups with water cuts of 5% and 10% has slowed down and the oil recovery has reached the maximum, while the original heavy oil control group is still in production; comparing the production time, the time used in the experimental group with 5% and 10% water content is 10 minutes shorter than that of the original heavy oil, which proves that the presence of water accelerates production; the final recovery rate is in terms of water content in the latter two groups of experiments, although there is boiling and evaporation during the experiment, the final recovery rate is higher than that of the original heavy oil control. The analysis believes that the addition of water increased the final recovery rate of heavy oil.

In summary, it is believed that the presence of water in the heavy oil system can effectively improve the wave absorption and heating capacity of the heavy oil, speed up the temperature rise of the reservoir, make the heavy oil heated quickly reduce the viscosity, enhance the fluidity of the heavy oil, and accelerate the gravity drainage of the heavy oil.

*3.3.2. The Influence of Nanoparticle Size on Microwave Heavy Oil Drainage Experiment.* According to the temperature data measured in the experiment, the regression data obtains the linear slope of one yuan, that is, the heating rate of the heavy oil in the porous medium is physically simulated during the oil drainage process. The heating rate of the heavy oil with different size nanoparticles is shown in Table 3. It is observed that the addition of 20 nm and 100 nm magnetic iron oxide nanoparticles has similar lifting effects on the heavy oil system, while the 10  $\mu\text{m}$  nanoparticles have little effect on the improvement of the heating rate of the heavy oil system.

Calculate the recovery factor of each group of experimental heavy oil and obtain the curve of heavy oil recovery overtime in the heavy oil drainage experiment under different particle size nanoparticles, as shown in Figure 12. It was observed that the two experimental curves with nanoparticles were similar, and the curves of the experimental group with micron nanoparticles were between the nanometer and the original. The production of the two types of nanoparticles was the fastest, and the final recovery efficiency of the four groups of experiments was similar.

The oil production rate of each group of experimental heavy oil was calculated, and the oil production rate of the heavy oil drain experiment with different particle diameters of nanoparticles was obtained with time, as shown in Figure 13. It was observed that the oil production rate of the two groups of experiments with nanometer-sized nanoparticles reached the maximum earlier, nanometer-level.

At 8 minutes and 16 minutes, the temperature of the experimental group with nanosized nanoparticles was the highest, followed by microsized magnetic iron oxide nanoparticles. Nano- and microsized magnetic iron oxide nanoparticles improved the absorption of the heavy oil drainage system during the heavy oil drainage experiment. The improvement effect of the wave heating ability, nanometer level is better than micron level.

TABLE 3: Heating rate of each group.

Serial number	Catalyst particle size	Heating rate ( $^{\circ}\text{C}/\text{min}$ )
1#	—	3.0916
2#	20 nm	5.3358
3#	100 nm	5.4348
4#	10 $\mu\text{m}$	4.3886

Comparing the recovery rate and oil production rate at 8 minutes, it can be found that the experimental group with nanometer-sized nanoparticles has a faster oil production rate and a higher recovery rate, followed by the micron level. The analysis believes that because the nanoscale nanoparticles assisted heavy oil to heat up faster in the microwave, the viscosity of the heavy oil decreases faster, the fluidity of the heavy oil increases, and the oil drainage production is accelerated by the action of gravity displacement.

Comparing the oil recovery and oil production rate of each group of experiments at 16 minutes, the two groups added nanosized nanoparticles in the experimental group have the slowest oil production rate, and the recovery factor is close to the final recovery factor, and then observe the production time to further confirm. The addition of nanosized nanoparticles effectively shortens the production time. Micron-sized nanoparticles have the same effect, but the effect is inferior to that of nanosized nanoparticles. In terms of ultimate oil recovery, the final oil recovery of the four groups of experiments is similar, and the addition of nanoparticles has no effect on the ultimate oil recovery.

In summary, the addition of magnetic iron oxide nanoparticles to the heavy oil system during the microwave gravity drainage experiment can effectively speed up the temperature of the system, accelerate the rate of oil production, and shorten the production time, and the effect of nanosized nanoparticles is better than microsized nanoparticles.

*3.3.3. The Influence of Nanoparticle Mass Concentration on Microwave Heavy Oil Drainage Experiment.* According to the temperature data measured in the experiment, the regression data obtains the linear slope of one yuan, that is, the heating rate of the heavy oil in the porous medium during the physical simulation of the oil drainage process, as shown in Table 4. It can be found that as the mass concentration of nanoparticles increases, the heating rate increases significantly.

The recovery factor of each group of experimental heavy oil was calculated, and the recovery factor of heavy oil drainage experiment with different nanoparticle mass concentrations was obtained with time, as shown in Figure 14. It can be found that as the mass concentration of nanoparticles increases, the oil drainage experiment can reach the maximum recovery factor earlier, the production time is shortened, and the final recovery factor is similar.

Calculate the oil production rate of each group of experimental heavy oil and obtain the curve of the oil production rate of the heavy oil drainage experiment with time under different nanoparticle mass concentrations. As shown in

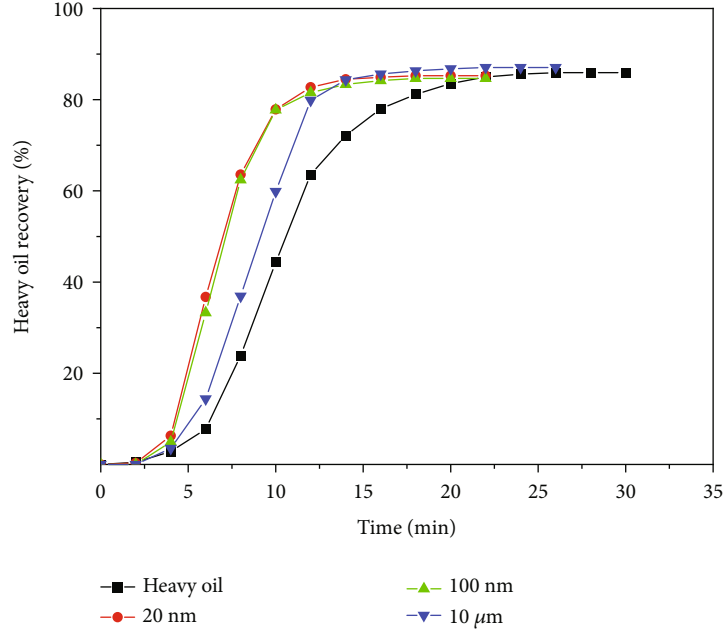


FIGURE 12: The experimental heavy oil recovery curves of each group under different water content.

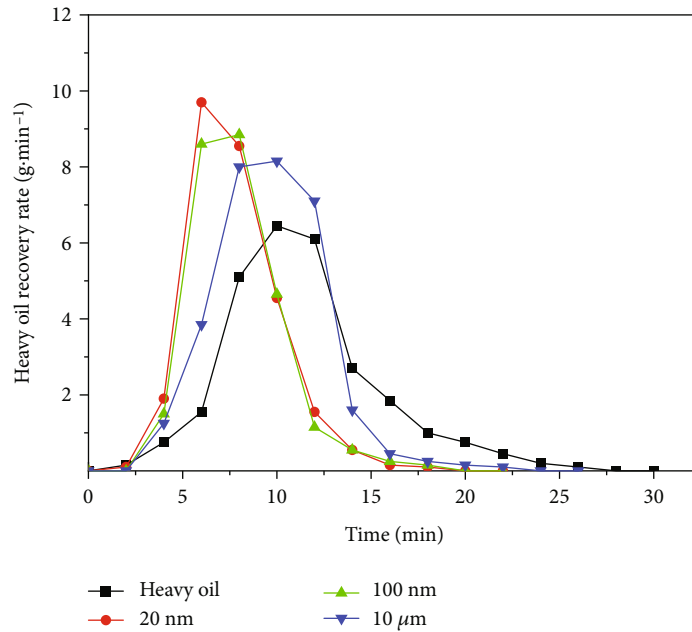


FIGURE 13: The experimental heavy oil recovery rate curves of each group under different water content.

TABLE 4: Experimental heating rate under different catalyst mass concentration.

Serial number	Mass (%)	Heating rate (°C/min)
1#	—	3.09
2#	0.1	5.34
3#	0.5	5.43

Figure 15, it can be found that the higher the nanoparticle mass concentration added, the higher the production rate.

At 8 minutes and 16 minutes, the higher the mass concentration of nanoparticles added, the faster the temperature of the measured heavy oil drainage system will rise. The higher the mass concentration of nanoparticles, the better the effect of improving the wave absorption and heating capacity of the heavy oil drainage system during the heavy oil drainage experiment.

Comparing the recovery rate and oil production rate at 8 minutes, it can be found that the higher the mass

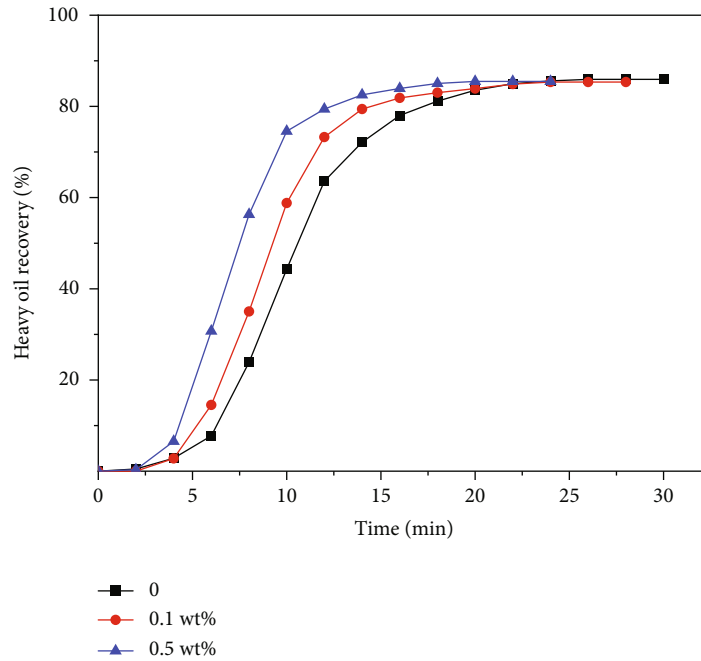


FIGURE 14: The experimental heavy oil recovery curves of each group under different mass fractions of nanoparticles.

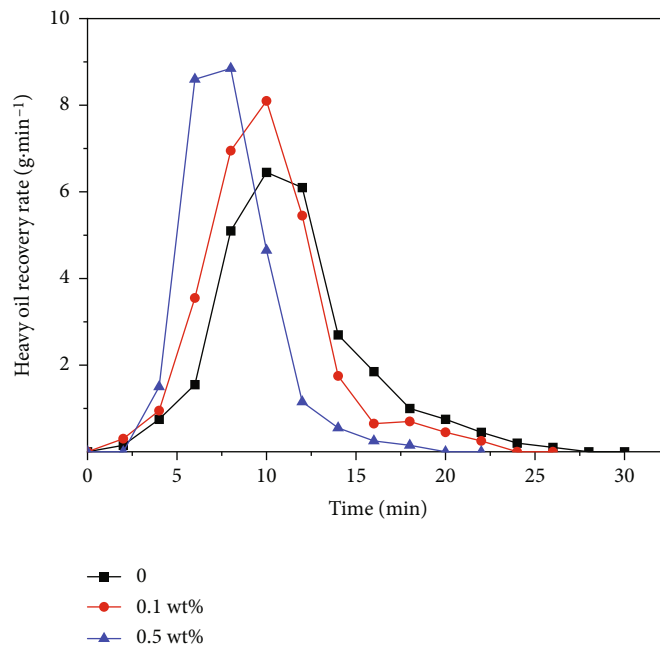


FIGURE 15: The experimental heavy oil recovery rate curves of each group under different mass fractions of nanocatalysts.

TABLE 5: Different microwave power experiment heating rate.

Serial number	Microwave power (W)	Heating rate (°C/min)
1#	385	3.0916
2#	539	4.2282
3#	700	5.2621

concentration of rice nanoparticles in the experimental group, the higher the oil production rate and oil recovery rate. This is because when the temperature rises faster, the viscosity of the heavy oil decreases faster, the fluidity is rapidly enhanced, the gravity drive is more obvious, and the rate of oil production is accelerated.

Comparing the recovery factor and oil production rate of each group of experiments at 16 minutes, it can be found that the higher the mass concentration of rice nanoparticles, the slower the oil production rate, and the closer the



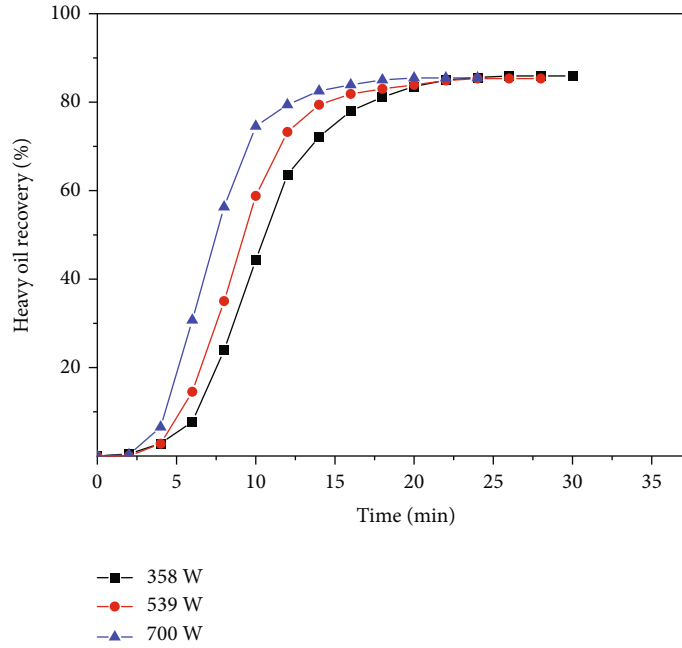


FIGURE 16: The experimental heavy oil recovery curves of each group under different microwave power.

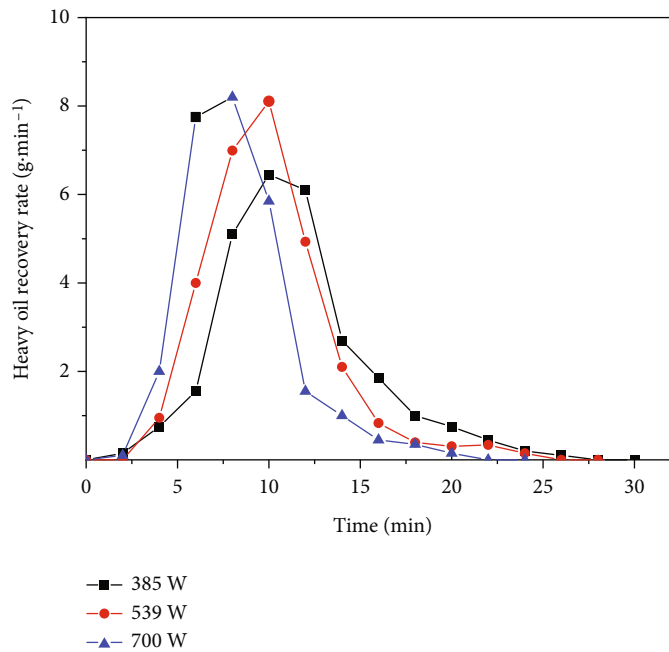


FIGURE 17: The experimental heavy oil recovery rate curves of each group under different microwave power.

recovery factor is to the final recovery factor. By observing the production time, it can be further determined that the higher the mass concentration of nanoparticles, the shorter the production time; in terms of the final recovery factor, the three sets of experiments have similar final recovery factors, and the addition of nanoparticles has no effect on the final recovery factor.

In summary, adding nanoparticles to the heavy oil system can effectively speed up the temperature of the heavy

oil system, accelerate the oil production rate, and shorten the production time during the microwave gravity drainage experiment. The higher the amount added, the more obvious the improvement effect.

3.3.4. *The Influence of Microwave Power on Microwave Heavy Oil Drainage Experiment.* According to the temperature data measured in the experiment, the regression data obtains a linear slope of one yuan, that is, physical

simulation of the heating rate of heavy oil in porous media during oil drainage. As shown in Table 5, it is found that as the microwave power increases, and the heating rate increases.

The recovery factor of each group of experimental heavy oil is calculated, and the recovery factor of the heavy oil drain experiment with different microwave power numbers is obtained with time, as shown in Figure 16. It can be found that with the increase of microwave power, the heavy oil drainage experiment can reach the maximum recovery factor earlier, the production time is shortened, and the final recovery factor is similar.

Calculate the oil production rate of each group of experimental heavy oil and obtain the oil production rate of heavy oil drainage experiment with time under different nanoparticle mass concentrations, as shown in Figure 17. It can be found that as the microwave power increases, the production speed can reach the fastest value earlier.

Comparing the temperature data at 8 minutes and 16 minutes, it is found that the higher the microwave power, the faster the heating of the heavy oil system will be. The higher the microwave power, the more energy is provided for the heavy oil system, and the heating of the heavy oil system is accelerated.

Comparing the recovery factor and oil production rate at 8 minutes, it can be found that the higher the microwave power of the experimental group, the faster the oil production rate and the higher the recovery factor. This is because when the temperature rises faster, the viscosity of the heavy oil decreases faster, the fluidity increases rapidly, and the rate of oil discharge and oil production speeds up due to the action of gravity driving.

Comparing the recovery factor and oil production rate of each group of experiments at 16 minutes, it can be found that the higher the microwave power, the slower the oil production rate, and the closer the recovery factor is to the final recovery factor. Observing the production time, it can be further determined that the higher the microwave power, the shorter the production time; in terms of the final recovery factor, the final recovery factors of the three experiments are similar, and the microwave power has no effect on the final recovery factor.

To sum up, the higher the microwave power, the more energy can be provided to the oil reservoir, which can accelerate the temperature of the oil reservoir, thereby accelerating production and shortening the production time.

#### 4. Conclusion

- (1) The mechanism of nanoparticles to enhance the heat utilization efficiency of heavy oil is obtained. Nanoparticles can effectively improve the wave absorption and heating capacity of heavy oil, and the improvement effect will be enhanced with the increase of the amount of addition. In addition, during the microwave heating process, the location of the nanoparticles will form a high-temperature field. This local high temperature provides temperature conditions for the cracking of heavy oil

- (2) It is proved that the method of nanoparticle-assisted microwave heating of heavy oil can effectively upgrade oil and reduce the viscosity of heavy oil, reducing the asphaltene content and viscosity of the heavy oil
- (3) The method of nanoparticle-assisted microwave upgrading and viscosity reduction of thick oil has the problem of viscosity recovery, the final viscosity reduction rate is stabilized at 50%, and the viscosity reduction effect is still very obvious
- (4) Completed the research on the factors affecting the gravity drainage of microwave heavy oil. Water and nanoparticles can improve the wave absorption and heating capacity of heavy oil, accelerate the heating of heavy oil, and reduce the viscosity of heavy oil rapidly, thereby shortening the production time of heavy oil drainage and accelerating the production of heavy oil

#### Abbreviations

IEA: International Energy Agency.

#### Data Availability

The data used to support the findings of this study are included within the article.

#### Conflicts of Interest

The authors declare no competing financial interest.

#### Acknowledgments

This work was supported by the National Key Research and Development Program of China (2018YFA0702400), Major Scientific and Technological Projects of CNPC (ZD2019-183-008). We are grateful to the researchers at the Foam Fluid Enhanced Oil & Gas Production Engineering Research Center in Shandong Province and UPC-COSL Joint Laboratory on Heavy Oil Recovery for their kind help in this study.

#### References

- [1] A. Belani, "Management: it's time for an industry initiative on heavy oil," *Journal of Petroleum Technology*, vol. 58, no. 6, pp. 40–42, 2006.
- [2] Z. X. Xu, S. Y. Li, B. F. Li, D. Q. Chen, Z. Y. Liu, and Z. M. Li, "A review of development methods and EOR technologies for carbonate reservoirs," *Petroleum Science*, vol. 17, no. 4, pp. 990–1013, 2020.
- [3] W. Heim, F. Wolf, and J. Savery, "Heavy oil recovering: U.S. Patent 4, 456, 06," 1984.
- [4] S. Mutyala, C. Fairbridge, J. R. J. Paré, J. M. R. Bélanger, S. Ng, and R. Hawkins, "Microwave applications to oil sands and petroleum: a review," *Fuel Processing Technology*, vol. 91, no. 2, pp. 127–135, 2010.
- [5] A. K. Jha, N. Joshi, and A. Singh, "Applicability and assessment of micro-wave assisted gravity drainage (Mwagd) applications

- in Mehsana heavy oil field, India,” in *SPE Heavy Oil Conference and Exhibition*, Kuwait City, Kuwait, 2011.
- [6] J. Robinson, E. Binner, A. Saeid, M. Al-Harashseh, and S. Kingman, “Microwave processing of oil sands and contribution of clay minerals,” *Fuel*, vol. 135, pp. 153–161, 2014.
- [7] M. Fortuny, C. B. Oliveira, R. L. Melo, M. Nele, R. C. Coutinho, and A. F. Santos, “Effect of salinity, temperature, water content, and pH on the microwave demulsification of crude oil emulsions,” *Energy & Fuels*, vol. 21, no. 3, pp. 1358–1364, 2007.
- [8] Y. H. Shokrlu and T. Babadagli, “Effects of nano-sized metals on viscosity reduction of heavy oil/bitumen during thermal applications,” in *Canadian Unconventional Resources and International Petroleum Conference*, vol. 137540, Calgary, Alberta, Canada, 2010.
- [9] Y. Hamed Shokrlu and T. Babadagli, “In-situ upgrading of heavy oil/bitumen during steam injection by use of metal nanoparticles: a study on in-situ catalysis and catalyst transportation,” *SPE Reservoir Evaluation & Engineering*, vol. 16, no. 3, pp. 333–344, 2013.
- [10] Y. H. Shokrlu and T. Babadagli, “Viscosity reduction of heavy oil/bitumen using micro- and nano-metal particles during aqueous and non-aqueous thermal applications,” *Journal of Petroleum Science and Engineering*, vol. 119, pp. 210–220, 2014.
- [11] Y. H. Shokrlu and T. Babadagli, “Transportation and interaction of nano and micro size metal particles injected to improve thermal recovery of heavy-oil,” in *SPE Annual Technical Conference and Exhibition*, vol. 146661, Denver, Colorado, USA, 2011.
- [12] Y. Hamed Shokrlu, Y. Maham, X. Tan, T. Babadagli, and M. Gray, “Enhancement of the efficiency of in situ combustion technique for heavy-oil recovery by application of nickel ions,” *Fuel*, vol. 105, pp. 397–407, 2013.
- [13] J. Greff and T. Babadagli, “Use of nano-metal particles as catalyst under electromagnetic heating for viscosity reduction of heavy oil,” in *International Petroleum Technology Conference*, vol. 14720, Bangkok, Thailand, 2011.
- [14] N. N. Nassar, A. Hassan, L. Carbognani, F. Lopez-Linares, and P. Pereira-Almao, “Iron oxide nanoparticles for rapid adsorption and enhanced catalytic oxidation of thermally cracked asphaltenes,” *Fuel*, vol. 95, pp. 257–262, 2012.
- [15] F. Iskandar, P. Fitriani, S. Merissa, R. R. Mukti, and A. Khairurrijal, “Fe<sub>3</sub>O<sub>4</sub>/zeolite nanocomposites synthesized by microwave assisted coprecipitation and its performance in reducing viscosity of heavy oil,” in *5TH NANOSCIENCE AND NANOTECHNOLOGY SYMPOSIUM*, vol. 1586, pp. 132–135, Indonesia, 2013.
- [16] D. Lin, H. H. Zhu, Y. N. Wu et al., “Morphological insights into the catalytic aquathermolysis of crude oil with an easily prepared high-efficiency Fe<sub>3</sub>O<sub>4</sub>-containing catalyst,” *Fuel*, vol. 245, pp. 420–428, 2019.
- [17] Z. S. Zhang, H. D. Li, H. Sui, L. He, and X. Li, “Synthesis and application of hydrophilically-modified Fe<sub>3</sub>O<sub>4</sub> nanoparticles in oil sands separation,” *RSC Advances*, vol. 8, no. 28, pp. 15813–15824, 2018.
- [18] S. H. Siregar, K. Wijaya, E. S. Kunarti, and A. Syoufian, “Kinetics adsorption of heavy oil spills in rivers on magnetite-(CTAB-montmorillonite) adsorbent,” in *13th Annual Joint Conference on Chemistry (JCC), Diponegoro Univ, Chem Dept*, Semarang, Indonesia, September 2018.
- [19] D. F. Chen, Y. M. Li, M. T. Bao et al., “Magnet-responsive silica microrods as solid stabilizer and adsorbent for simultaneous removal of coexisting contaminants in water,” *ACS Sustainable Chemistry & Engineering*, vol. 7, no. 16, pp. 13786–13795, 2019.
- [20] J. E. Aristizabal-Fontal, F. B. Cortes, and C. A. Franco, “Viscosity reduction of extra heavy crude oil by magnetite nanoparticle-based ferrofluids,” *Adsorption Science & Technology*, vol. 36, no. 1-2, pp. 23–45, 2018.
- [21] K. H. Wu, W. C. Huang, W. C. Hung, and C. W. Tsai, “Sorption and regeneration of expanded graphite/Fe<sub>3</sub>O<sub>4</sub> composite for removal of oil pollution from the water,” *Materials Express*, vol. 11, no. 4, pp. 579–585, 2021.
- [22] H. Will, P. Scholz, and B. Ondruschka, “Heterogeneous gas-phase catalysis under microwave irradiation—a new multi-mode microwave applicator,” *Topics in Catalysis*, vol. 29, no. 3/4, pp. 175–182, 2004.

## Research Article

# Prediction and Analysis of PDC Bit Wear in Conglomerate Layer with Machine Learning and Finite-Element Method

Li-qiang Wang <sup>1</sup>, Ming-ji Shao <sup>2</sup>, Wei Zhang <sup>2</sup>, Zhi-peng Xiao <sup>2</sup>, Shuo Yang <sup>2</sup>,  
and Ming-he Yang <sup>3</sup>

<sup>1</sup>Department of Petroleum Engineering, Shengli College, China Petroleum University, Shandong Dongying 257061, China

<sup>2</sup>Exploration and Development Research Institute of TuHa Oilfield Company, CNPC, Xinjiang Hami 839009, China

<sup>3</sup>Department of Petroleum Engineering, Yangtze University, Hubei Wuhan 430000, China

Correspondence should be addressed to Li-qiang Wang; 281035925@qq.com

Received 26 September 2021; Revised 21 November 2021; Accepted 6 December 2021; Published 10 January 2022

Academic Editor: Jinjie Wang

Copyright © 2022 Li-qiang Wang et al. This is an open access article distributed under the Creative Commons Attribution License, which permits unrestricted use, distribution, and reproduction in any medium, provided the original work is properly cited.

Polycrystalline diamond compact (PDC) bits experience a serious wear problem in drilling tight gravel layers. To achieve efficient drilling and prolong the bit service life, a simplified model of a PDC bit with double cutting teeth was established by using finite-element numerical simulation technology, and the rock-breaking process of PDC bit cutting teeth was simulated using the Archard wear principle. The numerical simulation results of the wear loss of the PDC bit cutting teeth, such as the cutter angle, temperature, linear velocity, and bit pressure, as well as previous experimental research results, were combined into a training dataset. Then, machine learning methods for equal-probability gene expression programming (EP-GEP) were used. Based on the accuracy of the training set, the effectiveness of this method in predicting the wear of PDC bits was demonstrated by verifying the dataset. Finally, a prediction dataset was established by a Latin hypercube experiment and finite-element numerical simulation. Through comparison with the EP-GEP prediction results, it was verified that the prediction accuracy of this method meets actual engineering needs. The results of the sensitivity analysis method for the gray correlation degree show that the degree of influence of bit wear is in the order of temperature, back dip angle of the PDC cutter, linear speed, and bit pressure. These results demonstrate that when an actual PDC bit is drilling hard strata such as a conglomerate layer, after the local high temperature is generated in the formation cut by the bit, appropriate cooling measures should be taken to increase the bit pressure and reduce the rotating speed appropriately. Doing so can effectively reduce the wear of the bit and prolong its service life. This study provides guidance for predicting the wear of a PDC bit when drilling in conglomerate, adjusting drilling parameters reasonably, and prolonging the service life of the bit.

## 1. Introduction

With increasing oil and gas exploration in China, many glutenite reservoirs have been discovered, among which a representative oilfield is the Mahu oilfield in the Xinjiang oil region. At the bottom of the Badaowan Formation in the oilfield, the gravels are well developed, with a thickness of 100–350 m, and the ability to drill is poor. The formation lithology of the Karamay Formation changes greatly in the horizontal direction, there are many longitudinal intercalations, the glutenite particle size is uneven, and bit selection is diffi-

cult. Other glutenite reservoirs share this feature. The hard gravel makes it difficult to drill [1, 2].

Although polycrystalline diamond compact (PDC) bits have the advantages of high rock-breaking efficiency, strong wear resistance, and a long service life, when drilling in a conglomerate formation, the wear rate of the cutting teeth increases sharply, easily leading to bit failure. Therefore, to enhance the rock-breaking ability, accurately predicting the bit wear and reducing the adverse effects is important.

In research on the PDC bit wear law in conglomerate layers, experimental methods and numerical simulation

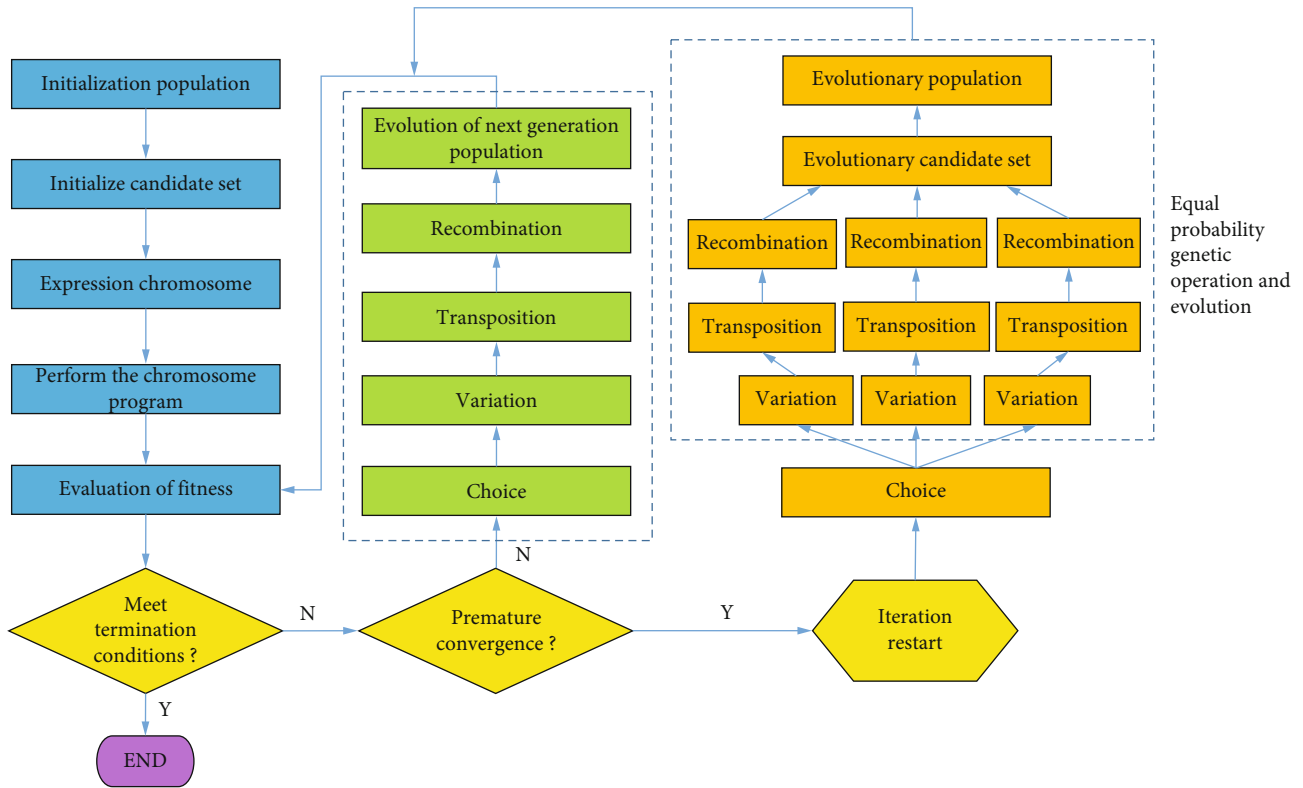


FIGURE 1: Flowchart of EP-GEP [19].

methods, such as the finite-element method, have mainly been used. In experimental research, standard wear parts or composite chips are generally used for grinding tests to obtain the wear laws of diamond bits in different rock media, such as the influences of rock properties, normal pressure, cutting line speed, and wear chord length on the amount of wear of the composite [3–7]. In comprehensive research through experiments and numerical simulations, the experimental method is generally used to study the influences of different factors, such as the cutting angle of the PDC coring bit, outcrop, linear velocity, and rock sample properties, on the wear law of composite cutting teeth. Then, the feasibility of wear law is verified using the numerical simulation method [8, 9]. The above research mainly addressed the wear law of the drill bit using the experimental method, which has played a positive role in promoting research in this field. However, the influence of temperature on bit wear has not been considered, and the experimental method or combined experimental and numerical simulation verification cannot accurately predict the wear of the PDC drill under the combined action of various factors in high-temperature and high-pressure environments. Therefore, not only is in-depth study of the bit wear law under different temperatures needed, but also it is particularly important to select appropriate prediction methods to predict bit wear under different working conditions to achieve efficient drilling and prolong the service life of bits.

Among the many prediction methods, machine learning has developed rapidly in recent years and has good develop-

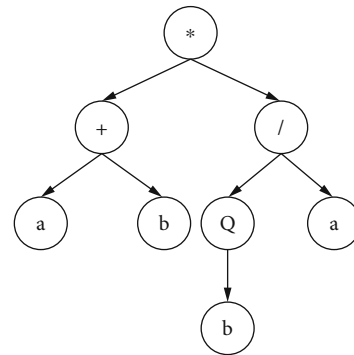


FIGURE 2: Expression tree corresponding to Equation (2).

ment prospects [10–13]. Gene expression programming (GEP) is based on the genetic algorithm (GA) and genetic programming (GP), which has excellent performance in knowledge mining, function discovery, optimization, and prediction [14]. Using a machine learning modeling tool, an explicit model with a simple structure and high prediction accuracy can be obtained through evolution without it being necessary to know the structure and parameters of the model in advance, thereby reducing the difficulty of establishing the prediction model and avoiding the preset model structure based on the regression method. Then, the subjectivity of parameters is determined using a statistical method [15]. At present, the GEP method has been



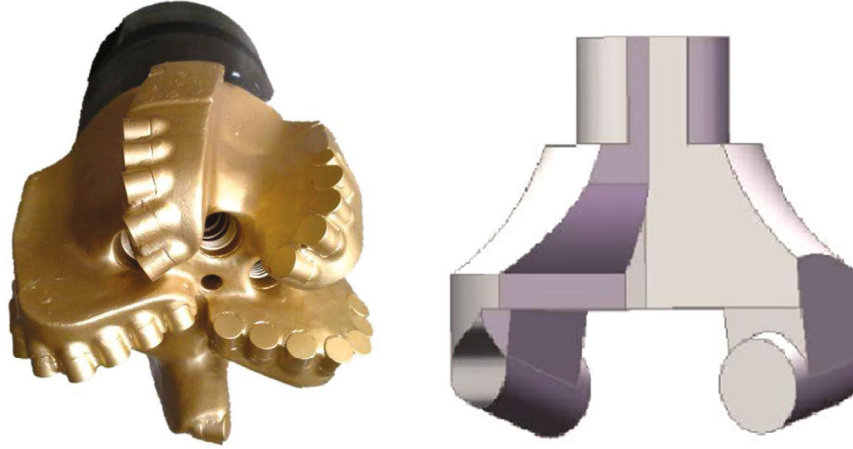


FIGURE 3: Simplified model of PDC bit with double cutting teeth.

successfully applied in many disciplines and fields [16–18]. It has not been reported that the GEP machine learning method has been used to predict bit wear. To predict the bit wear accurately under different working conditions, realizing the purpose of efficient drilling and prolonging the service life of the bit, it is necessary to study the GEP machine learning modeling method and its prediction effectiveness.

## 2. Equal-Probability Gene Expression Programming Algorithm (EP-GEP)

GEP combines the advantages of GAs and GP. In the form of expression, it inherits the simple and fast characteristics of the fixed-length linear coding of the GA. In terms of gene expression (semantic expression), it inherits the flexible and changeable characteristics of the GP tree structure, and it solves complex problems with simple coding two to four orders of magnitude faster than the traditional machine learning evolutionary algorithm [15].

However, the traditional GEP method has some problems, such as nondirectional evolution and premature convergence in the process of knowledge mining, which can easily fall into the local optimum and reduce the efficiency and quality of the overall optimal solution. Therefore, it is necessary to mitigate these defects. The proposed EP-GEP method can improve the convergence efficiency and solution quality of the algorithm.

The flow of the EP-GEP optimization calculation is shown in Figure 1. First, a certain number of chromosome individuals are randomly generated to form the initial population. Second, the candidate set is established by selecting excellent individuals in the initial population. According to the bit wear analysis, the best fitness function of the individual in the group suitable for the problem expression is selected. The responsiveness of each individual in the group is assessed. Then, the individual is selected, mutated, inserted, and recombined, and other genetic operations are carried out to produce new offspring and form new groups. Then, they enter the next round of the optimization pro-

cess. If local precocious convergence occurs, the algorithm enters the calculation process of equal-probability gene expression optimization (taking three equal probability individuals as an example in Figure 1), generating new offspring to form a new population, and they enter the next round of optimization calculation. Then, the above optimization calculation process is repeated until the iteration termination condition is satisfied.

**2.1. Gene Structure.** The target of EP-GEP is a chromosome (genome) composed of a single gene or multiple genes. The gene in EP-GEP is a simplification of the gene principle in biology. The gene in EP-GEP is composed of a head and tail. The head can be composed of a function symbol ( $F$ ) and a terminal symbol ( $t$ ), whereas the tail can only be composed of terminal symbol  $t$ . The chromosome (or individual) in EP-GEP is composed of one or more genes of equal length, and multiple genes are connected by a connection function. Each individual represents a candidate solution to the problem to be solved. Several of these chromosomes constitute the entire population.

The relationship between tail length  $t$  and head length  $h$  is

$$t = h \times (n - 1) + 1, \quad (1)$$

where  $n$  represents the maximum number of variables required by the function character (for example, open-ended operation,  $n = 1$ ; multiplication or addition operation,  $n = 2$ ).

For example, the expression tree corresponding to Equation (2) is shown in Figure 2.

$$(a + b) * \left( \frac{b^{1/2}}{a} \right). \quad (2)$$

The parsing rule of the expression tree is from top to bottom and from left to right, until the node is the terminator. The gene after the termination point is the noncoding

TABLE 1: Attribute parameters of polycrystalline diamond and conglomerate.

Parameter name	Polycrystalline diamond	Conglomerate
Density ( $\text{kg}\cdot\text{m}^{-3}$ )	3520	2540
Elastic modulus (MPa)	$8.9 \times 10^5$	$5.4 \times 10^4$
Poisson's ratio	0.07	0.27
Thermal conductivity ( $\text{J}\cdot\text{m}^{-1}\cdot\text{s}^{-1}\cdot\text{C}^{-1}$ )	543.0	3.5
Specific heat capacity ( $\text{J}\cdot\text{kg}^{-1}\cdot\text{C}^{-1}$ )	790.0	800.0
Coefficient of thermal expansion ( $10^{-6}\text{C}$ )	2.5	52.0
Compressive strength (MPa)	270.0	67.6
Wear coefficient	$3 \times 10^{-7}$	$3 \times 10^{-7}$

region of the chromosome, so it is no longer in operation. Here, the function character set is  $\{*, +, /, Q\}$  ( $Q$  is the square-root operation), and the terminator set is  $\{a, b\}$ . If the head length  $h$  of the gene is 6, then, according to Equation (1), the tail length  $t$  is 7, and the total length of the gene is 13 [20].

**2.2. Genetic Operator.** EP-GEP creates an initial population in the algorithm, and each chromosome in the population represents a solution to the problem. Then, a series of genetic operations are carried out to generate new high-fitness offspring individuals to obtain better solutions. The basic genetic operators of EP-GEP include selection, mutation, inversion, insertion, root insertion, gene transformation, single point recombination, two-point recombination, and gene recombination [19].

**2.3. Fitness Function.** To obtain the best solution, it is necessary to evaluate the environmental adaptability of the newly generated chromosomes. Similar to other machine learning evolutionary algorithms, EP-GEP uses the fitness function value (i.e., fitness) to evaluate the quality of chromosomes. Sometimes, the fitness function can be defined according to the solution of the problem. The commonly used fitness functions in the symbolic regression are the complex correlation coefficient method, relative hits, absolute hits, mean square error (MSE), root MSE (RMSE), absolute mean difference, relative variance, relative root mean square error, and relative absolute value difference.

In this study, the RMSE was obtained using the fitness function expressed in the following equation.

$$\text{RMSE} = \sqrt{\frac{1}{m} \sum_{j=1}^m (y_j - \hat{y}_j)^2}. \quad (3)$$

#### 2.4. Finite-Element Simulation Model

**2.4.1. Simplified Model of Cutting Teeth.** Among the main parameters affecting the rock-breaking efficiency of the PDC bit, the back dip angle mainly represents the cutting ability of the cutting teeth for the formation. The role of the side angle is to produce a pushing force on the cuttings to discharge them, and the circumferential angle determines

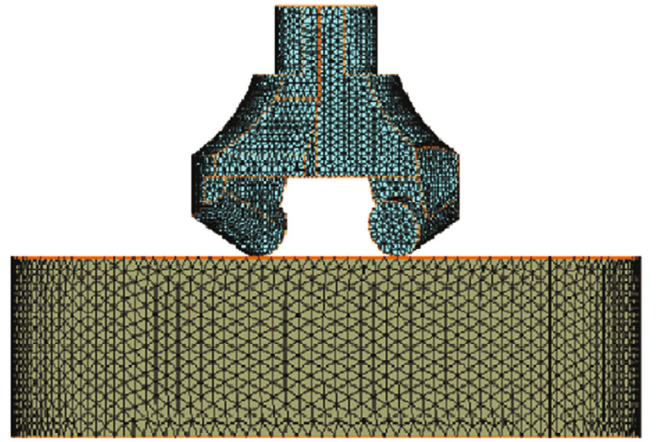


FIGURE 4: Mesh generation of finite-element model for rock breaking of PDC bit with double cutting teeth.

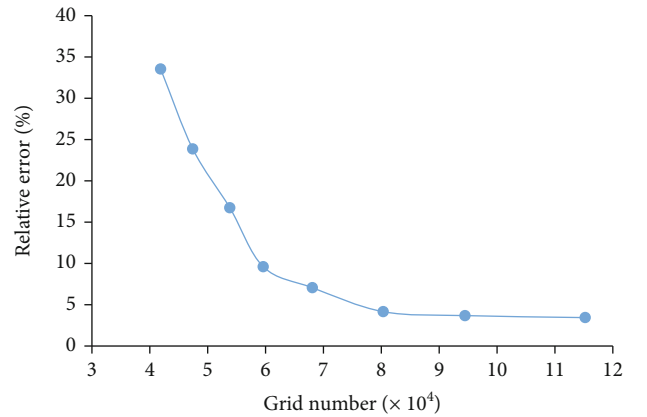


FIGURE 5: Influence of grid number on simulation accuracy.

the distribution of the cutting teeth. The finite-element software used was MSC Marc. When finite-element software is used to model and simulate the all the PDC bit cutting teeth, there are two problems. First, the model is more complex. Because there are many factors affecting the rock breaking by a bit, it is difficult to highlight the role of the back dip angle of the cutting teeth of the bit in rock breaking. Second,

TABLE 2: Experimental parameters of EP-GEP.

Parameter	Value	Parameter	Value
Population size	78	Length of head	9
Gene number	6	Mutation rate	0.00138
Recombination rate	0.00277	One-point recombination rate	0.00277
Two-point recombination rate	0.00277	Transposition rate	0.00277
Root insertion sequence transposition rate	0.00546	Insertion sequence transposition rate	0.00546
Link function fitness function	*	Fitness function	RMSE

calculation is difficult, leading to the nonconvergence phenomenon, which affects the stability and reliability of the simulation results. Based on previous research and the above two considerations, the entire cutting tooth model is simplified to a double cutting tooth model (see Figure 3). The basic parameters of the simplified model are as follows: the side angle is  $25^\circ$ , the diameter of the composite chip is 13.4 mm, and the maximum diameter of the bit is 60 mm [21].

#### 2.4.2. Material Parameters and Basic Assumptions

(1) *Material Parameters.* The material property parameters of the conglomerate and PCD are shown in Table 1.

(2) *Basic Assumptions.* The classical Archard wear model was used to simulate the wear of the PDC bit [22]. Because the maximum diameter of the PDC bit with double cutting teeth is 60 mm, to reduce the influence of rock side loading on rock breaking, according to Saint Venant's principle [23], a cylindrical rock sample with a diameter of 180 mm and a height of 40 mm was used to simulate the actual formation rock. In addition, the formation rock was assumed to be isotropic, and the influence of the drilling fluid on the cutting tooth wear was ignored. The failure criterion of the rock was the linear Mohr–Coulomb criterion. The confining pressure was loaded on the side of the rock in the form of stress, and thermal/structural analysis was selected for the analysis task.

2.4.3. *Grid Size and Accuracy Control.* A 10-node tetrahedral mesh was adopted, and the mesh was refined. The mesh division of the finite-element model for the rock breaking of the PDC bit with double cutting teeth is shown in Figure 4. When the rock sample is broken and deformed, mesh redivision technology is used to solve the subsequent simulation problems.

When the PDC bit crown top ( $r = 100$  mm) had an off-cutting tooth loading pressure of  $1.5 \times 10^3$  N and rotating speed of 120 r/min, the wear volume of the PDC bit was  $19.70 \text{ mm}^3$  when the composite was scrapped. The errors in the simulation results under different grid numbers were compared according to the results of the physical simulation experiment. It was found that, when the mesh number was greater than  $8.00 \times 10^4$ , the wear of the cutting teeth tended to be stable. Considering the calculation accuracy and simulation time, the mesh size was 1.6 mm, the mesh number was

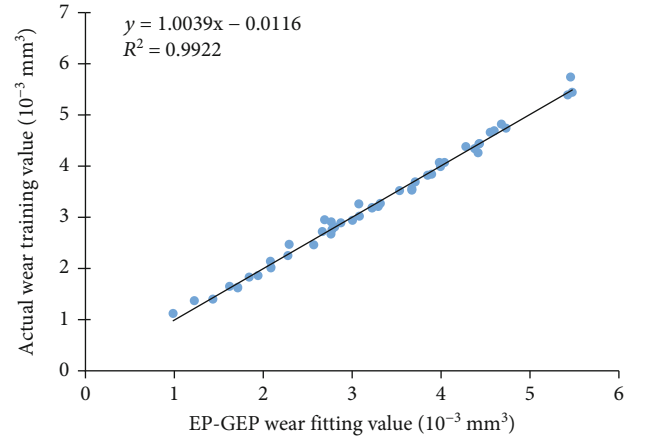


FIGURE 6: Comparison between wear amount of training dataset and EP-GEP fitting value.

$9.44 \times 10^4$ , and the cutting tooth wear was  $18.98 \text{ mm}^3$ . Compared with the experimental data in a previous report [5], the relative error was 3.67% (Figure 5).

#### 2.5. PDC Bit Wear Dataset

2.5.1. *Single-Factor Wear Dataset.* The finite-element numerical simulation method was used to fix three of the four variables of the bit cutting teeth, such as the back angle, temperature, linear velocity, and bit pressure, to simulate the change law of bit wear when the other variable changes. For example, when the inclination angle, temperature, and linear speed of the cutting teeth are fixed, different bit pressures are set, and the wear amount of the bit is determined by simulation. This can be expressed as

$$y = \{\alpha, T, v, x\}, \quad (4)$$

where  $y$  is the bit wear,  $\alpha$  is the back angle of the cutting teeth,  $T$  is the temperature,  $v$  is the linear speed, and  $x$  is the weight on the bit.

Equation (4) can be further expressed as the following vector form:

$$(\alpha, T, v, x, y). \quad (5)$$

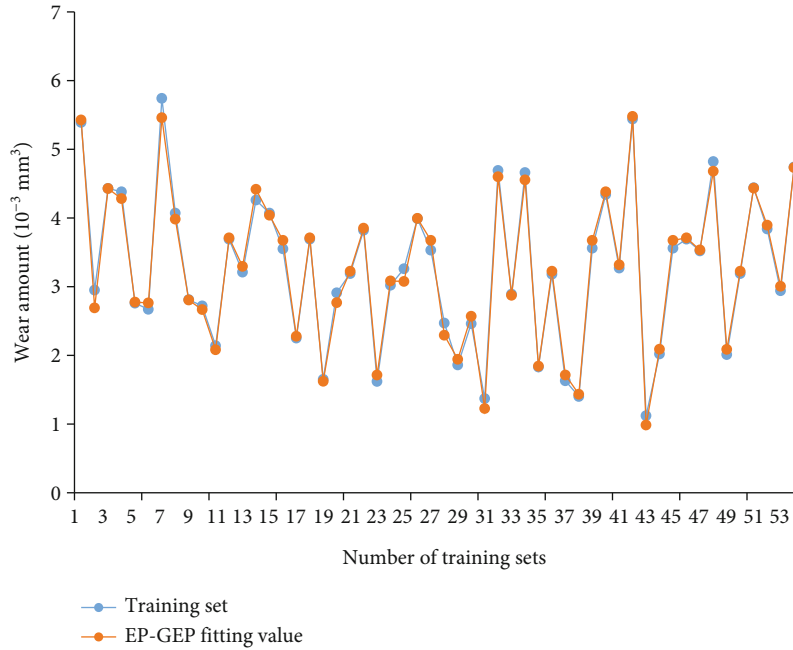


FIGURE 7: Comparison of training set wear and EP-GEP fitting value.

The effects of other single variables on bit wear can be studied similarly.

The dataset in the form of Equation (5) and the previous experimental data were combined into a single-factor wear dataset, which was a part of the machine learning training set.

**2.5.2. Multifactor Wear Dataset.** The finite-element numerical simulation method was used to fix one of the four variables of the bit cutting teeth (the back angle, temperature, linear velocity, and bit pressure) to simulate the change law of bit wear when the other three variables change. For example, when the back angle of the cutting teeth was fixed as a variable, different temperatures, linear velocities, and bit pressures were set to determine the wear amount of the bit through simulation. This can be expressed as

$$y = \{\alpha, x_1, x_2, x_3\}, \quad (6)$$

where  $y$  is the bit wear,  $\alpha$  is the back angle of the cutting teeth,  $x_1$  is the temperature,  $x_2$  is the linear speed, and  $x_3$  is the weight on the bit.

Equation (6) can be further expressed in the following vector form:

$$(\alpha, x_1, x_2, x_3, y). \quad (7)$$

The influences of other variables on the bit wear can be studied similarly.

The dataset of Equation (7) and that of single-factor wear were combined to establish a complete machine learning training set.

### 3. Results and Analysis

**3.1. EP-GEP Time Series Model Training.** Fifty-four groups of data from 80 groups were used for the EP-GEP time series training. The experimental parameters are shown in Table 2. The remaining 26 sets of data were used for validation.

After training, the  $R^2$  value of the model was 0.9922, as shown in Figures 6 and 7.

The expression tree structure of individual genes is shown in parts (1)–(6) in Figure 8.

**3.2. EP-GEP Model Validation.** The model was compared with the validation dataset to verify the prediction ability of the EP-GEP model. A comparison between the wear amount of the validation set and the EP-GEP prediction value is shown in Figure 9, and the relative error comparison results are shown in Figure 10.

As shown in Figure 9, the validation set is basically consistent with the EP-GEP prediction results, and the gap is small. Figure 10 reveals that the relative error between the prediction results of the EP-GEP model and the verification set is small, with a maximum relative error of 9.49%, a minimum of 0.13%, and an average of 3.64%. This shows that the model established by the EP-GEP method can accurately fit the bit wear.

**3.3. EP-GEP Model Prediction.** To highlight the generality of the model, an irregular real number was selected for the value of the influencing factors. All parameters were covered according to the Latin hypercube experimental design method. In Table 3, the predicted value of the EP-GEP model and the results of finite-element simulation are compared. The maximum relative error is  $-7.01\%$ , the minimum

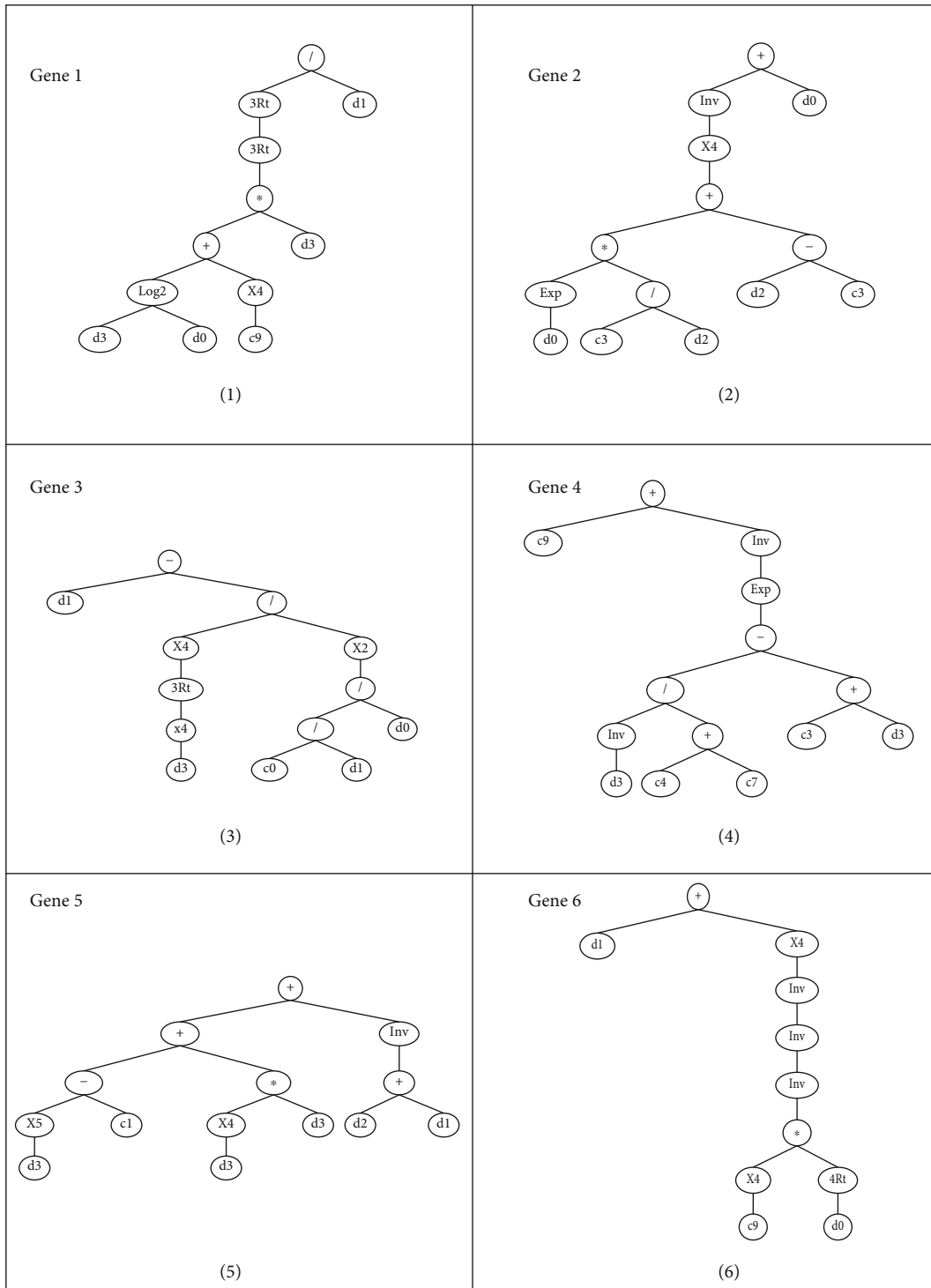


FIGURE 8: Expression trees of genes 1–6.

error is  $-0.47\%$ , and the average relative error is  $-0.99\%$ . From the perspective of prediction accuracy, the model can meet the demand of PDC bit wear prediction research.

3.4. Sensitivity Research Based on Deng's Gray Relational Analysis. The sensitivity of each influencing factor to the

wear amount in Table 3 was analyzed by Deng's correlation degree method and the gray correlation theory [24, 25].

If  $X_i$  is a system factor and its observation data at the  $k$ -th moment is  $x_i(k)$ , then the behavior sequence of the factor  $X_i$  is  $X_i = (x_i(1), x_i(2), \dots, x_i(n))$ . Here,  $X_0$  is the reference sequence, and  $X_1$  is the comparison sequence.



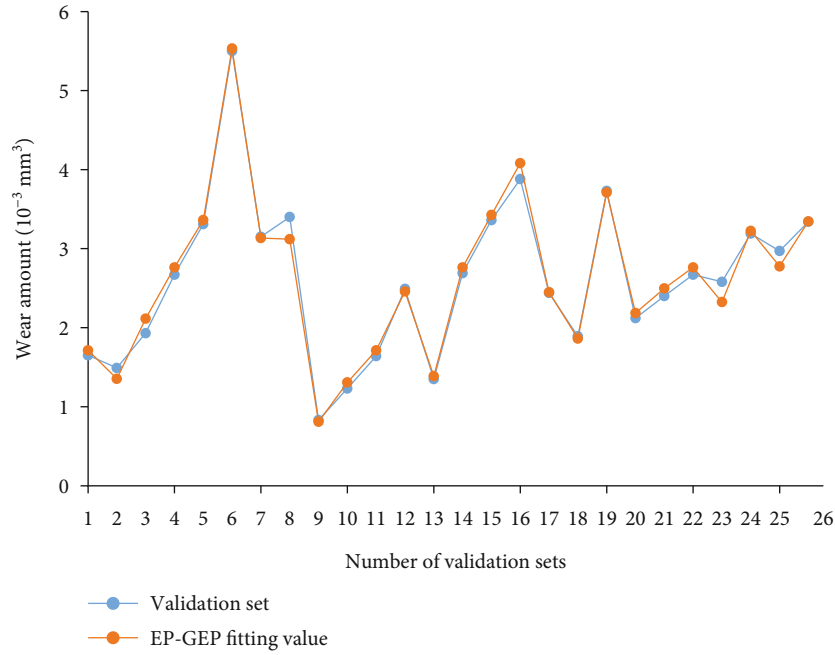


FIGURE 9: Comparison of wear amount of verification set and EP-GEP prediction value.

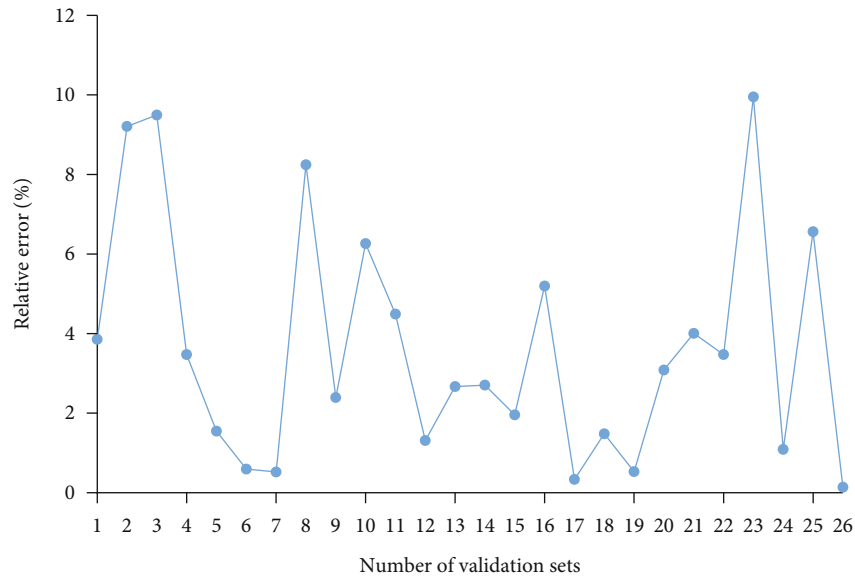


FIGURE 10: Comparison of relative error between verification set and EP-GEP.

If  $\gamma(x_0(k), x_i(k))$  is the real number, then the calculation formula of Deng's correlation degree is as follows:

$$\gamma(x_0(k), x_i(k)) = \frac{\min_i \min_k |x_0(k) - x_i(k)| + \xi \max_i \max_k |x_0(k) - x_i(k)|}{|x_0(k) - x_i(k)| + \xi \max_i \max_k |x_0(k) - x_i(k)|}, \quad (8)$$

$$\gamma(X_0, X_i) = \frac{1}{n} \sum_{k=1}^n \gamma(x_0(k), x_i(k)). \quad (9)$$

Equation (9) is the average value of  $\gamma(x_0(k), x_i(k))$  when the four axioms of the gray relation are satisfied [25]. When  $\gamma(X_0, X_i)$  is the gray relational degree of  $X_1$  to  $X_0$ ,  $\gamma(x_0(k), x_i(k))$  is the gray correlation coefficient of  $X_1$  to  $X_0$ .

The results show that Dun's correlation degrees of the cutter inclination angle  $\alpha$ , temperature  $T$ , linear velocity  $V$ , and bit pressure  $P$  on wear are 0.7032, 0.7208, 0.7159, and 0.7138, respectively. According to Deng's correlation degree, the temperature has the greatest influence on the bit wear during rock breaking, followed by the rake angle of the

TABLE 3: Comparison of relative error between EP-GEP model predicted value and finite-element simulation result.

Serial number	$\alpha$ ( $^{\circ}$ )	$T$ ( $^{\circ}\text{C}$ )	$V$ ( $\text{m}\cdot\text{s}^{-1}$ )	$P$ (N)	EP-GEP ( $\text{V}/\text{mm}^3$ )	Relative error with the simulated value of finite-element method (%)
1	12	120	0.07	1580	1.722	-2.433
2	12	220	0.13	1870	2.601	-3.302
3	12	340	0.23	2060	4.343	1.592
4	12	430	0.27	2265	5.730	-2.873
5	12	550	0.29	2775	8.023	2.368
6	17	120	0.13	2060	2.599	2.757
7	17	220	0.23	2265	3.741	3.885
8	17	340	0.27	2775	5.156	-6.776
9	17	430	0.29	1580	5.855	2.073
10	17	550	0.07	1870	2.907	3.174
11	22	120	0.23	2775	4.155	3.243
12	22	220	0.27	1580	3.712	-2.722
13	22	340	0.29	1870	4.979	-6.980
14	22	430	0.07	2060	2.515	-7.010
15	22	550	0.13	2265	4.263	-0.585
16	27	120	0.27	1870	2.826	0.626
17	27	220	0.29	2060	3.650	-6.791
18	27	340	0.07	2265	2.226	-5.063
19	27	430	0.13	2775	3.390	-2.726
20	27	550	0.23	1580	5.346	6.506
21	33	120	0.29	2265	2.138	-5.392
22	33	220	0.07	2775	1.776	4.279
23	33	340	0.13	1580	1.810	-0.501
24	33	430	0.23	1870	3.220	-1.587
25	33	550	0.27	2060	4.639	-0.468

cutting teeth, linear velocity, and bit pressure [21]. Therefore, when the PDC bit is drilling in hard formations, such as gravel, reducing the local high temperature generated by bit cutting and maintaining the high-bit-pressure and low-rotation-speed mode can reduce bit wear and prolong service life to a certain extent.

#### 4. Conclusions

- (1) Through the verification of the experimental results and the sensitivity analysis of the mesh number and on the basis of verifying the accuracy of the numerical simulation model, finite-element prediction results of wear under different cutting tooth caster angle, temperature, linear velocity, and bit pressure were introduced into a machine learning training dataset
- (2) The EP-GEP machine learning method was used to carry out modeling and prediction research. Through a comparative analysis of the model effectiveness and prediction ability, it was proven that the EP-GEP model has good prediction accuracy

- (3) The results of EP-GEP wear prediction and gray correlation sensitivity analysis show that, after the actual PDC bit cuts the formation to produce a local high temperature, taking appropriate cooling measures, appropriately increasing the bit pressure, and reducing the rotating speed can effectively reduce the bit wear and prolong the service life

#### Data Availability

The data used to support the findings of this study are available from the corresponding author upon request.

#### Conflicts of Interest

The authors declare no potential conflicts of interest with respect to the research, authorship, or publication of this article.

#### Acknowledgments

This study was supported by the Scientific Research Development Plan of Shandong Province (j18ka205), the Scientific Research Start-Up Fund for Introducing High-Level Talents

from the Shengli College of China University of Petroleum (Beijing) (kq2019-005), and the Key R&D Program of Dongying City in Shandong Province (2018kjc).

## References

- [1] L. Zongyu, Z. Fei, and L. Ming, "Key drilling technology for glutenite tight oil horizontal wells in Mahu oilfield, Xinjiang," *Petroleum Drilling Technology*, vol. 47, no. 2, pp. 9–14, 2019.
- [2] L. Li, Z. Lubin, and Z. Lingzhan, "Drilling and completion technology for efficient development of Mahu low permeability reservoir," *Xinjiang Petroleum Science and Technology*, vol. 27, no. 2, pp. 1–6, 2017.
- [3] C. A. Cheatham and D. A. Loeb, "Effects of field wear on PDC bit performance," in *SPE/IADC Drilling Conference*, Louisiana, USA, 1985.
- [4] D. A. Glowka, "Implications of thermal wear phenomena for PDC bit design and operation," in *SPE Annual Technical Conference and Exhibition*, Nevada, USA, 1985.
- [5] Z. Deyong, Y. Jun, and X. Cheng, "A modified determination method of rock's abrasiveness for well drilling using diamond bits," *Journal of China University of Petroleum*, vol. 40, no. 4, pp. 73–80, 2016.
- [6] Z. H. Shaohe, X. Xiaohong, and F. Hhaijiang, "PDC abrasion rule affected by height of protrusion and linear velocity," *Journal of Central South University*, vol. 41, no. 6, pp. 2173–2177, 2010.
- [7] I. H. Michaels, M. Mostofi, and T. Richard, "An experimental study of the wear of polycrystalline diamond compact bits," in *SPE 53rd U.S. Rock Mechanics/Geomechanics Symposium*, New York, USA, 2019.
- [8] X. Xiaohong, *The study on the cutter's abrasion rule of PDC coring bit*, Central South University, Changsha, China, 2011.
- [9] G. M. Gouda, M. Maestrami, and M. A. A. Saif, "A mathematical model to compute the PDC cutter wear value to terminate PDC bit run," in *SPE Middle East Oil and Gas Show and Conference*, Manama, Bahrain, 2011.
- [10] D. Weber, T. F. Edgar, and L. W. Lake, "Improvements in capacitance-resistive modeling and optimization of large scale reservoirs," in *Paper presented at the SPE Western Regional Meeting*, San Jose, California, 2009.
- [11] J. Li, Z. Lei, and S. Li, "Optimizing water flood performance to improve injector efficiency in fractured low-permeability reservoirs using streamline simulation," in *Paper presented at the SPE Kingdom of Saudi Arabia Annual Technical Symposium and Exhibition*, Dammam, Saudi Arabia, 2016.
- [12] M. Khan, S. Alnuaim, and Z. Tariq, "Machine learning application for oil rate prediction in artificial gas lift wells," in *Paper presented at the SPE Middle East Oil and Gas Show and Conference*, Manama, Bahrain, 2019.
- [13] C. Noshi, M. Eissa, and R. Abdalla, "An intelligent data driven approach for production prediction," in *Paper presented at the Offshore Technology Conference*, Houston, Texas, 2019.
- [14] C. Ferreira, "Gene expression programming: a new adaptive algorithm for solving problems," *Complex Systems*, vol. 13, no. 2, pp. 87–129, 2001.
- [15] Z. Kisi, "Comparative analysis of ozone level prediction models using gene expression programming and multiple linear regression," *Geofizika*, vol. 30, no. 30, pp. 43–74, 2013.
- [16] C. Zhou, W. Xiao, and T. M. Tirpak, "Evolving accurate and compact classification rules with gene expression programming," *IEEE Transactions on Evolutionary Computation*, vol. 7, no. 6, pp. 519–531, 2003.
- [17] N. D. Hoang and D. Tien Bui, "Spatial prediction of rainfall-induced shallow landslides using gene expression programming integrated with GIS: a case study in Vietnam," *Natural Hazards*, vol. 92, no. 3, pp. 1871–1887, 2018.
- [18] J. Jedrzejowicz, P. Jedrzejowicz, and I. Wierzbowska, "Implementing gene expression programming in the parallel environment for big datasets' classification," *Vietnam Journal of Computer Science*, vol. 6, no. 2, pp. 163–175, 2019.
- [19] L. Wang, M. Shao, G. Kou et al., "Time series analysis of production decline in carbonate reservoirs with machine learning," *Geofluids*, vol. 2021, 8 pages, 2021.
- [20] C. Ferreira, *Gene Expression Programming: Mathematical Modeling by an Artificial Intelligence*, Springer, Berlin, 2006.
- [21] H. Peng, G. Feng, Z. Liwei, W. Lili, and Y. Minghe, "Study on the wear law of PDC bits in conglomerate," *China Petroleum Machinery*, vol. 48, no. 7, pp. 1–6, 2020.
- [22] J. F. Archard, "Contact and rubbing of flat surfaces," *Journal of Applied Physics*, vol. 24, no. 8, pp. 981–988, 1953.
- [23] R. A. Toupin, "Saint-Venant's principle," *Archive for Rational Mechanics and Analysis*, vol. 18, no. 2, pp. 83–96, 1965.
- [24] J. L. Deng, "Figure on difference information space in grey relational analysis source," *Journal of Grey Systems*, vol. 16, no. 2, pp. 121–139, 2004.
- [25] J. L. Deng, *Course of Grey System Theory*, Huazhong University of Technology Press, 1990.

## Research Article

# Rock Mechanical Properties and Breakdown Pressure of High-Temperature and High-Pressure Reservoirs in the Southern Margin of Junggar Basin

Mingwei Kong,<sup>1</sup> Zhaopeng Zhang<sup>1,2</sup>, Chunyan Zhao,<sup>1</sup> Huasheng Chen,<sup>1</sup> Xinfang Ma<sup>1,2</sup>, and Yushi Zou<sup>2</sup>

<sup>1</sup>Engineering Technology Institute, PetroChina Xinjiang Oilfield Company, 834000, China

<sup>2</sup>State Key Laboratory of Petroleum Resources and Prospecting, China University of Petroleum, (Beijing), 102249, China

Correspondence should be addressed to Xinfang Ma; [maxinfang@cup.edu.cn](mailto:maxinfang@cup.edu.cn)

Received 18 October 2021; Revised 5 December 2021; Accepted 8 December 2021; Published 29 December 2021

Academic Editor: Qingwang Yuan

Copyright © 2021 Mingwei Kong et al. This is an open access article distributed under the Creative Commons Attribution License, which permits unrestricted use, distribution, and reproduction in any medium, provided the original work is properly cited.

The mechanical properties of the high-temperature and high-pressure reservoirs in the southern margin of Junggar Basin have not been clearly understood, which correspondingly results in uncertainties when predicting the breakdown pressure. To address this issue, firstly, rock mechanical experiments under high temperature, high confining pressure, and high pore pressure were carried out. Secondly, empirical formulas related to the transformation of dynamic and static mechanical parameters in the regional strata were proposed. Finally, the existing prediction model for the formation breakdown pressure was improved by taking the wellbore seepage and thermal stress into consideration. Results show that under the reservoir condition of high temperature and high pressure, the rock sample tends to form closed shear cracks. High temperature causes thermal damages and the reduction of the compressive strength and elastic modulus, while the combined effects of high confining pressure and pore pressure enhance the compressive strength and plasticity of the rock sample simultaneously. Based on the correlation analysis, it is found that the static elastic modulus is linearly related to the dynamic value, while static Poisson's ratio is a quadratic function of the dynamic value. These fitting functions can be used to obtain the profiles of static elastic modulus and Poisson's ratio based on their dynamic values from the logging interpretation. Besides, the improved prediction model for the rock breakdown pressure can yield more accurate results indicated by the error less than 2%. Therefore, the proposed breakdown pressure prediction model in this study can provide theoretical guidance in the selection of fracturing truck groups and the design of the pumping schedule for high-temperature and high-pressure reservoirs.

## 1. Introduction

Breakthroughs have been made for oil and gas exploration of tight sandstones in Sikeshu sag in the southern margin of Junggar Basin [1–3], revealing that multiple sets of high-quality sandstone reservoirs exist in the lower assemblage of the southern margin [4–7]. The average reservoir depth is approximately 5800–6000 m, and the pressure coefficient is 1.6–2.3 [8]. Thus, it is a typical high-temperature and high-pressure ultradeep reservoir [1, 8]. Based on the current theoretical understanding, under the complex conditions of high temperature, high pore pressure, and high tectonic stress in the deep reservoir, rock mechanical properties are different

from those of shallow formations to some extent [9, 10]. For instance, the rock deformation and failure modes may transit from elasticity and brittleness in shallow reservoirs to elastoplasticity and ductility in deep reservoirs [9]. Under this circumstance, the rock mechanical properties of shallow formations obtained under conventional test conditions (i.e., high temperature and high pressure are not taken into account) are unable to represent the real in situ geomechanical properties in the deep reservoirs. From the perspective of petroleum engineering, the rock mechanical properties are associated with the successful implementations of drilling, completion, production, and workover operations [11]. Using inaccurate rock mechanical properties to design the drilling

scheme may have a negative effect on the wellbore stability, probably leading to the borehole collapse during drilling [11]. Also, the predictions of breakdown pressure and fracture propagation geometry involved in designing the hydraulically fracturing scheme heavily depend on the accurate measurement of mechanical properties of target layers [12]. To effectively explore and develop oil and gas resources in Sikeshu sag, it is necessary to have a comprehensive knowledge of in situ geomechanical properties of the ultradeep reservoirs with high temperature, high pore pressure, and high tectonic stress.

So far, a large number of studies have been carried out on the rock mechanical properties of the deep rock mass [13–21]. Zhang et al. [13] tested the variation of rock mechanical properties from the room temperature to high temperature (600–800°C) for various rocks and found that the elastic modulus generally decreases with the increase of temperature, but the effect of temperature on the compressive strength is complex. Some experts believe that this complex effect is attributed to the deformation of rock mineral particles under the high temperature [14] and the heterogeneity of mesoscale damages [15]. Tian et al. [16] and Wan et al. [17] found that the temperature affects the rock mechanical properties in a piecewise manner, and there is a temperature threshold, above which the elastic modulus and compressive strength reduce significantly. Deng et al. [18] and Kumari et al. [19] investigated the effects of confining pressures on the mechanical properties of sandstone and granite under high temperature, respectively, and found that the rock strength typically increases with the increase of confining pressure, while the brittleness gradually decreases, and the sample failure mode transforms from the tensile failure of vertical joints and fissures under the low confining pressure to the shear failure of multiple shear bands under the high confining pressure (90–120 MPa). Zhou et al. [20] tested the mechanical properties of sandstones by considering the coupling behaviour among the temperature, confining pressure, and pore pressure and found that under the constant confining pressure, the rock strength and elastic modulus decrease with the increase of pore pressure. Pan et al. [21] further pointed out that as the pore pressure in carbonate rock increases, the cohesion increases and the internal friction angle decreases. According to previous studies mentioned above, the rock mechanical properties of deep reservoirs are comprehensively influenced by the coupling among the temperature, tectonic stress, and pore pressure. To reflect the in situ geomechanical properties of deep formations, none of those three factors can be neglected while conducting rock mechanical tests.

In situ rock mechanical properties can be used to evaluate the breakdown pressure of reservoirs, which is a key parameter for in situ stress assessment and hydraulic fracturing design. For exploratory vertical wells in targeted blocks of the southern margin, the hydraulic fracturing technique is usually utilized for the formation testing and the breakdown pressure should be assessed in advance for the selection of fracturing truck groups and the design of the pumping schedule. For the open-hole completion, the stress distribution at the wellbore is generally regarded as a result of the superposition of the wellbore internal pressure, in situ

stress, and additional stress induced by the fracturing fluid filtration [22]. The rock will be fractured as the stress distribution meets a certain failure criterion. For formations at shallower depths, the linear failure criterion based on the Mohr-Coulomb model is mostly used [23], but this model is too simplified to accurately predict the breakdown pressure in the deep and complex environments [24]. Hubbert-Willis (H-W) formula [25] and Haimson-Fairhurst (H-F) formula [26] are prediction models based on the tensile failure criterion, which can estimate the upper and lower limits of the formation breakdown pressure, respectively. Different from the H-W model, the H-F model considers the poroelastic effect by assuming that the rock is permeable and fluid flows through the rock mass once injected into the wellbore [24]. On these foundations, Eaton [27], Stephen [28], Anderson et al. [29], and Huang [30] successively put forward calculation methods of the breakdown pressure, which are suitable for the field application. Ito and Hayashi [31] assumed that the fracture is initiated inside the rock instead of on the borehole wall and further proposed the point stress failure criterion based on the fracture characteristic length and gave a reasonable explanation to the influences of the borehole size and pressurization rate on the breakdown pressure. Due to the difference in stress distribution around the wellbore between the perforated completion and open-hole completion, breakdown pressure prediction models for the perforation completion were proposed, in which the perforation is taken as a cylinder orthogonal to the wellbore [22]. Considering the influences of the induced stress and natural fractures, Guo et al. [32] proposed a model for predicting the stress distribution on the surface of perforation channels in a horizontal well. Based on the fracture mechanics theory, Fan et al. [33] deduced the stress intensity factor at the perforation tip and accurately predicted the breakdown pressure and fracture initiation angle. Afterward, more sophisticated combined stress and energy criteria were proposed [34, 35]. Although some fracture mechanics-based models and combined models can give accurate predicted values, the mathematical expressions in the models are complex and numerical simulations are usually required for solutions, which is not adaptive to the field application.

This study focuses on the rock mechanical properties and breakdown pressure prediction of ultradeep reservoirs in the southern margin, Junggar Basin. Currently, in situ geomechanical properties of the targeted ultradeep reservoirs are usually dynamically examined through the logging interpretation, and there is lack of adequate and reliable laboratory static data of rock samples under high pressure and high temperature. Even though some pilot tests [36, 37] have been carried out to understand the rock mechanical characteristics under high temperature and high pressure, a holistic knowledge of the in situ geomechanical properties are still needed. Besides, most of the previous studies [13–19] took the concept of “effective stress” to set the experimental confining pressure during conducting compression tests, without the consideration of pore pressures. Some studies [20, 21] that accounted for the pore pressure adopted a limited range of 0–30 MPa, which cannot represent the actual pore pressure (e.g., over 60 MPa) in ultradeep reservoirs.



Consequently, to understand the in situ geomechanical characteristics of ultradeep formations, rock mechanical tests should be performed under a similar temperature-pressure condition to that of the reservoir, with the consideration of the coupling effects of high temperature, high confining pressure, and high pore pressure. As for the breakdown pressure prediction, the conventional models (e.g., H-W and H-F models) suitable for the field application did not incorporate the component of the thermal stress. The thermal stress is taken as the additional stress caused by the temperature change at the wellbore wall during injecting the fracturing fluid. A large temperature gradient may be caused at the wellbore wall due to the high temperature (e.g., over 150°C) in ultradeep reservoirs, which may induce a comparable additional stress that cannot be ignored. Therefore, considering the effect of thermal stress, an improved prediction model is proposed in this study to reduce the deviation of the predicted value from the measured value obtain from the real-time pressure curve.

The Jurassic formations in Sikeshu sag of Junggar Basin, including Badaowan, Sangonghe, Xishanyao, Toutunhe, and Qigu formations, have great potential to explore and develop. Among them, thick Toutunhe formation shows promising hydrocarbon accumulation potential and is a key candidate for the following exploration [1]. Taking the Toutunhe formation as the research object, this paper intends to perform a series of triaxial compression tests to evaluate the in situ rock mechanical properties by considering the coupling effects of the high temperature and high pressures (i.e., including the high confining pressure and high pore pressure) of ultradeep reservoirs. Afterward, an existing breakdown pressure prediction model was improved to give more accurate predictions for the breakdown pressure of ultradeep reservoirs on the basis of the acquired in situ geomechanical parameters. This paper is aimed at laying a theoretical foundation for the selection of “sweet spots for fracturing” and the optimization of the pumping schedule.

## 2. Materials and Methods

*2.1. Geological Overview.* Four sets of source rocks (i.e., Permian, Jurassic, Cretaceous, and Paleogene rock systems) are developed in the piedmont thrust belt in the southern margin of Junggar Basin, which has rich oil and gas resources. Vertically, three sets of mudstone and gypsum mudstone caprocks (i.e., Neogene taxihe formation, Paleogene Anjihaihe formation, and Cretaceous Tugulu group) are developed, which can be divided into upper, middle, and lower reservoir-cap assemblages [1]. The Toutunhe formation of lower assemblage in the Sikeshu sag includes the thick taupe glutenite formation, which contains the interbedding of medium-coarse grained sandstone and medium-fine grained sandstone, mixed with a small amount of argillaceous medium-fine grained sandstone and sandy mudstone [38]. The reservoir depth is nearly 6200 m, the average porosity is 15.4%, the permeability is 0.3-33.9 mD, the formation pressure coefficient is 1.6-2.3, and the formation temperature is about 150°C. Thus, it is a high-

temperature and high-pressure ultradeep reservoir with moderate porosity and permeability. Thin slice analysis shows that the sandstone of the Toutunhe formation belongs to the lithic sandstone or feldspathic lithic sandstone, and the mineral clastic mainly includes quartz and feldspar, with the contents of 29.33%-37% and 16.5%-27%, respectively. The rock debris is mainly composed of sedimentary rocks and magmatic rocks, accounting for 17%-78%. The content of the matrix is low, the cement is mainly calcite, and the cementation type is mostly porous cementation. In addition, the in situ stress test results show that the vertical stress of the Toutunhe formation sandstone reservoir is 174.0-184.1 MPa, the maximum horizontal principal stress is 154.5-175.8 MPa, and the minimum horizontal principal stress is 149.4-155.6 MPa.

*2.2. Rock Mechanical Test under High Temperature and High Pressure.* The samples are collected from the Toutunhe formation in the Sikeshu sag, including the argillaceous siltstone, medium-fine grained sandstone, and glutenite. Both Brazilian splitting and triaxial compression tests under high temperature and high pressure were conducted to evaluate the mechanical properties of reservoir rocks. According to the International Society of Rock Mechanics (ISRM) standards [39], samples for Brazilian splitting tests are cylinders with a diameter of 25 mm and length of 13 mm, and samples for triaxial compression tests are cylinders with a diameter of 25 mm and length of 50 mm. The nonparallelism of the cylinder end face shall not exceed 0.05 mm, and the end face also shall be perpendicular to the axis, with a maximum deviation less than 0.25°.

GCTS RTR-2000 triaxial rock mechanics test system was used, as shown in Figure 1. The experimental procedure for the Brazilian splitting tests can be referred to the ISRM standards [39], and the procedure for the triaxial compression test is described specifically as follows. At first, simultaneously increase the confining pressure (horizontal stress) and axial stress (vertical stress) such that the rock sample is under hydrostatic pressure. At this time, the horizontal stress is equal to axial stress. Then, the pore pressure is increased while the confining pressure and axial stress are maintained constant by the servomechanism. At the time when the pore pressure reaches the target value, the effective confining pressure is the same as the effective vertical stress. Afterward, the axial stress is increased to commence the triaxial test. During the axial compression, the confining pressure and pore pressure are kept constant by the servomechanism, meaning that effective confining pressure does not change and the effective axial stress increases with the increase of the axial stress. During the test, a curve of the deviatoric stress versus the axial strain or radial strain is recorded simultaneously. According to the working conditions of the apparatus, the experimental temperature was set to 150°C, the confining pressure was set to 110 MPa, and the pore pressure was set to 80 MPa. In this way, both the effective confining pressure and effective vertical stress are 30 MPa before the triaxial compression test starts. Based on the procedure described above, the deep formation condition can be realized in the laboratory. Two samples were

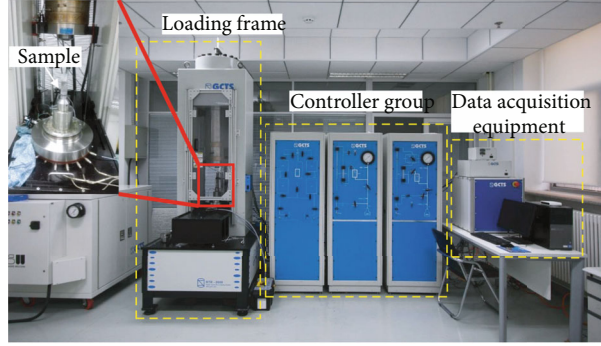


FIGURE 1: Schematic of GCTS RTR-2000 triaxial rock mechanics test system.

TABLE 1: Test scheme and results of high-temperature and high-pressure rock mechanical properties of rock samples from Toutunhe formation in the Sikeshu sag.

No.	Lithology	Confining pressure $p_c$ (MPa)	Temperature $T$ ( $^{\circ}\text{C}$ )	Pore pressure $p_p$ (MPa)	Tensile strength $\sigma_t$ (MPa)	Elastic modulus $E$ (GPa)	Poisson's ratio $\nu$	Compressive strength $\sigma_c$ (MPa)
1#		110	150	80		21.91, 19.11	0.402, 0.388	369.0, 290.3
2#		90	150	60		21.31, 19.44	0.387, 0.398	359.6, 274.4
3#	Argillaceous siltstone	60	150	30	6.86, 8.79 9.58, 6.81	18.64, 20.12	0.377, 0.396	258.2, 206.0
4#		30	150	0	4.33, 6.46 6.10, 8.41	18.97, 16.11	0.394, 0.380	205.0, 177.2
5#		110	25	80		28.64, 27.92	0.191, 0.213	415.7, 379.1
6#		30	25	0		32.93, 34.91	0.221, 0.221	258.2, 285.8
7#		110	150	80		26.83, 24.69	0.273, 0.265	359.0, 331.2
8#		90	150	60		28.33, 21.31	0.268, 0.260	290.2, 302.4
9#	Medium-fine grained sandstone	60	150	30	5.27, 8.47 6.46, 5.43	25.64, 22.27	0.261, 0.245	260.3, 256.9
10#		30	150	0		24.55, 19.57	0.248, 0.237	222.2, 208.3
11#		110	25	80		13.29, 15.26	0.226, 0.194	258.7, 256.9
12#		30	25	0		26.26, 30.13	0.242, 0.261	289.2, 287.7
13#		110	150	80		35.23, 35.09	0.232, 0.220	403.4, 431.8
14#		90	150	60		38.68, 30.43	0.238, 0.217	377.6, 341.7
15#	Glutenite	60	150	30		34.06, 36.41	0.231, 0.206	346.2, 290.8
16#		30	150	0	3.70, 6.92 7.82, 5.60	34.71, 33.62	0.217, 0.194	239.6, 269.0
17#		110	25	80		35.56, 16.91	0.259, 0.184	436.0, 253.2
18#		30	25	0		38.60, 40.43	0.338, 0.191	256.8, 260.0

tested in each experimental group to reduce the contingency of the results. The test scheme is shown in Table 1.

**2.3. Corrected Breakdown Pressure Prediction Model.** In this paper, considering a two-dimensional case in which a borehole is drilled at the center of an infinite plane formation, a corrected prediction model for the formation breakdown pressure was proposed based on Huang's model [30]. The breakdown pressure model proposed by Huang improved Eaton's formula [27], as presented in

$$p_f = p_p + \left( \frac{2\nu}{1-\nu} - a + 3b \right) (\sigma_v - \alpha p_p) + \sigma_t, \quad (1)$$

where  $p_f$  is the formation breakdown pressure, MPa;  $p_p$  is the initial pore pressure, MPa;  $\nu$  is rock Poisson's ratio;  $a$  is the tectonic stress coefficient corresponding to the maxi-

um horizontal principal stress  $\sigma_H$ ;  $b$  is the tectonic stress coefficient corresponding to the minimum horizontal principal stress  $\sigma_h$ ;  $\alpha$  is the Biot elastic coefficient;  $\sigma_v$  is the formation vertical stress, MPa; and  $\sigma_t$  is the rock tensile strength, MPa. The above model can be decomposed into two stress terms separately caused by the in situ stress and wellbore internal pressure, which can be described as follows:

$$\sigma_{\theta\theta}^{(1)} = \left( \frac{2\nu}{1-\nu} - a + 3b \right) (\sigma_v - \alpha p_p) + 2p_p, \quad (2)$$

$$\sigma_{\theta\theta}^{(2)} = -p_i, \quad (3)$$

where  $\sigma_{\theta\theta}^{(1)}$  is the stress term caused by the in-situ stress, MPa;  $\sigma_{\theta\theta}^{(2)}$  is the stress term caused by the wellbore internal pressure, MPa; and  $p_i$  is the fluid pressure in the wellbore,

MPa. Equation (1) ignores the influence of the fluid infiltration into the rock stratum. Thus, two additional stresses, which are caused by the seepage effect of fracturing fluid at the wellbore wall and the temperature variation around the borehole, are not considered. However, the influences of the above two additional stresses cannot be ignored in the high-temperature and high-pressure ultradeep reservoir. Based on the theoretical analysis by Haimson and Fairhurs [26], the circumferential additional stress caused by the seepage effect of fracturing fluid is expressed by

$$\sigma_{\theta\theta}^{(3)} = -\frac{\alpha(1-2\nu)}{1-\nu} \left[ \frac{1}{r^2} \int_{r_w}^r p_n(r) r dr - p_n(r) \right], \quad (4)$$

where  $\sigma_{\theta\theta}^{(3)}$  is the circumferential additional stress caused by the seepage effect of fracturing fluid, MPa;  $r$  is the distance from the center of the wellbore, m;  $r_w$  is the wellbore radius, m; and  $p_n(r)$  is the formation net pressure at radius  $r$ ,  $p_n(r) = p(r) - p_p$ , MPa. Assuming that the formation net pressure at the wellbore wall is  $p_n(r_w) = p_w - p_p$ , the circum-

ferential additional stress caused by the seepage effect of fracturing fluid at the wellbore can be presented as follows:

$$\sigma_{\theta\theta}^{(3)} = \frac{\alpha(1-2\nu)}{1-\nu} (p_w - p_p). \quad (5)$$

Li et al. [40] adopted Equation (6) to represent the influence of the temperature variation at the wellbore wall on breakdown pressure. This paper stipulates that the compressive stress is positive and the tensile stress is negative.

$$\sigma_{\theta\theta}^{(4)} = -\frac{E\alpha_m}{3(1-\nu)} (T_0 - T_w), \quad (6)$$

where  $\sigma_{\theta\theta}^{(4)}$  is the additional stress caused by the temperature variation at the wellbore wall, Pa;  $E$  is the rock elastic modulus, MPa;  $\alpha_m$  is the rock thermal expansion coefficient,  $^{\circ}\text{C}^{-1}$ ;  $T_w$  is the fracturing fluid temperature,  $^{\circ}\text{C}$ ; and  $T_0$  is the initial formation temperature,  $^{\circ}\text{C}$ . By summing up Equations (2), (3), (5), and (6) and adopting the maximum tensile stress criterion, we can obtain a corrected formation breakdown pressure prediction model, as shown in Equation (7)

$$p_f = \frac{((2\nu/(1-\nu)) - a + 3b)(\sigma_v - \alpha p_p) + (2 - \alpha(1-2\nu)/(1-\nu))p_p - ((E\alpha_m\Delta T)E\alpha_m\Delta T/(3(1-\nu)3(1-\nu)) + \sigma_t}{1 - \alpha((1-2\nu)1 - 2\nu/(1-\nu)1 - \nu)}, \quad (7)$$

where the elastic modulus  $E$  and Poisson's ratio  $\nu$  in Equation (7) are replaced by the empirical formula for the transformation between the dynamic and static mechanical parameters; then, the formation breakdown pressure can be predicted according to the logging and geological data.

### 3. Results and Discussions

#### 3.1. Rock Mechanical Properties under High Temperature and High Pressure

**3.1.1. Measured Values of Rock Mechanical Parameters.** The results in Table 1 show that the average tensile strength of argillaceous siltstone, medium-fine grained sandstone, and glutenite are  $7.17 \pm 1.58$  MPa,  $6.41 \pm 1.28$  MPa, and  $6.01 \pm 1.55$  MPa, respectively. In general, the tensile strength of argillaceous siltstone is larger than that of medium-fine grained sandstone and glutenite. In the deep formation condition, i.e., the confining pressure  $p_c$  is 110 MPa, temperature  $T$  is  $150^{\circ}\text{C}$ , and pore pressure  $p_p$  is 80 MPa; the average elastic modulus, Poisson's ratio, and compressive strength of argillaceous siltstone are 20.51 GPa, 0.395, and 329.7 MPa, respectively; the average elastic modulus, Poisson's ratio, and compressive strength of medium-fine grained sandstone are 25.76 GPa, 0.269, and 345.1 MPa, respectively; and the average elastic modulus, Poisson's ratio, and compressive strength of glutenite are 35.16 GPa, 0.226, and 417.6 MPa, respectively. The aforementioned results

reveal that the mechanical properties of various lithologic strata are significantly different under high temperature and high pressure. Specifically, the elastic modulus and compressive strength of argillaceous siltstone are the lowest, followed by the medium-fine grained sandstone and glutenite. However, Poisson's ratio of argillaceous siltstone is the highest, while glutenite has the lowest one, with that of medium-fine sandstone falling in between.

#### 3.1.2. Rock Deformation Characteristics and Failure Modes.

By comparing the whole stress-strain curves (see Figure 2) and failure modes (see Figure 3) of samples of different lithologies under varying temperatures and pressures, it was found that under the conventional condition (i.e.,  $p_c$  is 30 MPa,  $T$  is  $25^{\circ}\text{C}$ , and  $p_p$  is 0 MPa), the deviatoric stress of argillaceous siltstone and medium-fine sandstone dropped by 57.4% and 81.1%, respectively, after passing the peak, and the macroscopic shear fractures can be seen on the sample surface, indicating shearing brittle failures. However, the deviatoric stress of glutenite gradually decreased after passing the peak, and closed tensile cracks can be seen on the local surface of the sample, presenting low brittleness.

Keeping the effective confining pressure (30 MPa) constant and only introducing the high pressure (i.e.,  $p_c$  is 110 MPa,  $T$  is  $25^{\circ}\text{C}$ , and  $p_p$  is 80 MPa), the peak stress and peak strain of the stress-strain curve and the compressive

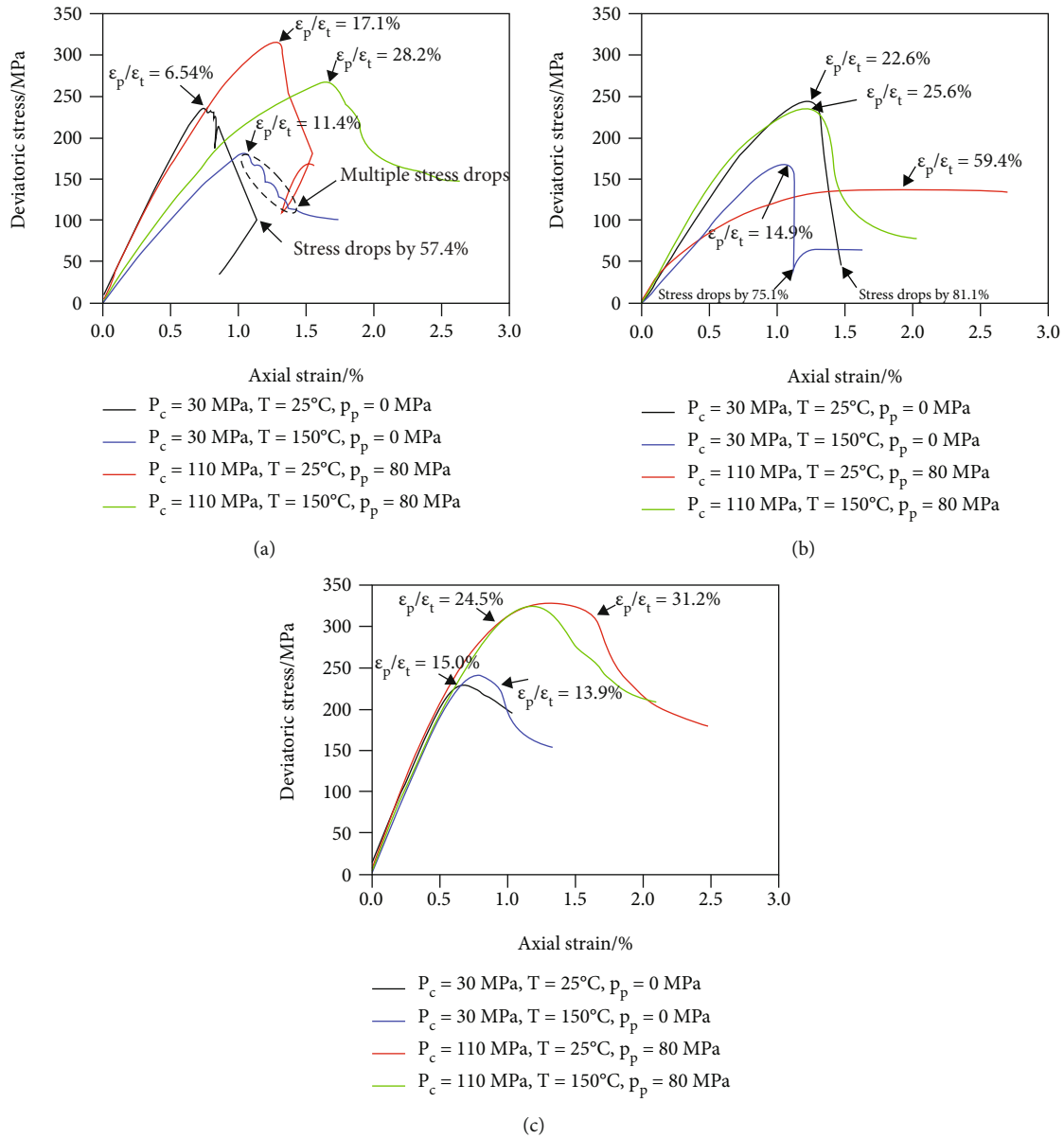


FIGURE 2: Whole stress-strain curves of samples with different lithologies under high temperature and high pressure. (a) Argillaceous siltstone. (b) Medium-fine grained sandstone. (c) Glutenite.

strength for argillaceous siltstone and glutenite significantly increased compared with the conventional test condition. For example, the proportion of the plastic strain ( $\epsilon_p/\epsilon_t$ ) for argillaceous siltstone and glutenite increased from 6.5% to 17.1% and from 15.0% to 24.5%, respectively. As a result, the plastic deformation was enhanced, and closed shear cracks could be observed on the sample surface. The proportion of the plastic strain for medium-fine grained sandstone accounted for 59.4%, and the curve after the peak tends to be flat, indicating the occurrence of the plastic creep; and there is no obvious crack on the sample surface. The above phenomena show that under the conditions of high confining pressure and pore pressure, the plastic deformation of rock samples tends to be enhanced, and an oblique shearing plane usually occurred for the primary failure.

Keeping the effective confining pressure (30 MPa) constant and only introducing the high temperature (i.e.,  $p_c$  is 30 MPa,  $T$  is  $150^\circ\text{C}$ , and  $p_p$  is 0 MPa), the elastic modulus and compressive strength of argillaceous siltstone, medium-fine grained sandstone, and glutenite tended to decrease (see Table 1) compared with the conventional test condition. Specifically, the elastic modulus of argillaceous siltstone decreased from 33.92 GPa to 17.54 GPa, with that of medium-fine grained sandstone decreasing from 28.20 GPa to 22.06 GPa and that of glutenite decreasing from 39.52 GPa to 34.17 GPa. Additionally, the average compressive strength of argillaceous siltstone decreased from 272.0 MPa to 191.1 MPa, with that of medium-fine grained sandstone decreasing from 288.5 MPa to 215.3 MPa and that of glutenite slightly decreasing from 258.4 MPa to





FIGURE 3: Illustrations of failure modes of samples with different lithologies under high temperature and high pressure.

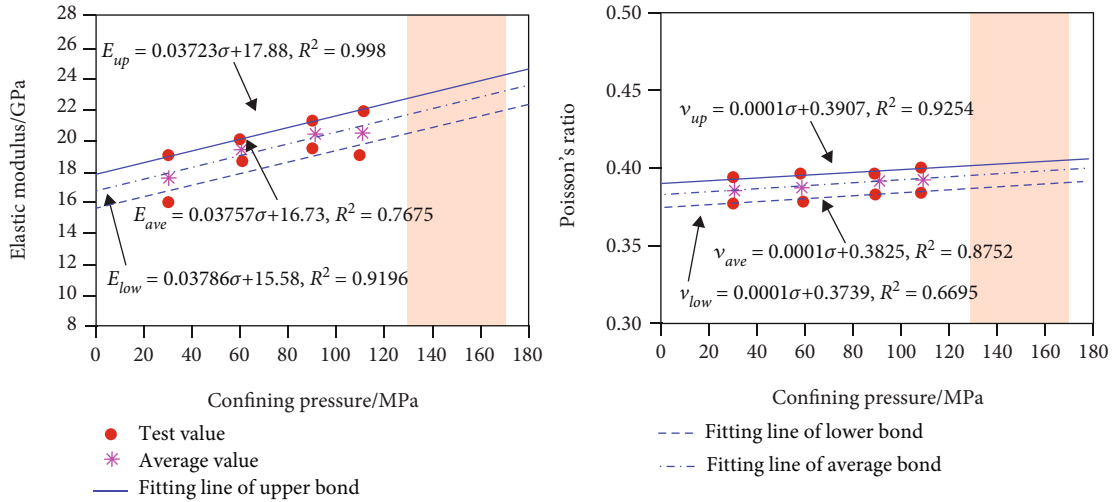
254.3 MPa. Different from the results under the high pressure, the plastic deformation of medium-fine grained sandstone and glutenite was not enhanced, and the proportion of the plastic strain of argillaceous siltstone just increased slightly by 4.86%. Besides, there were multiple stress drops after passing the peak stress in the whole stress-strain curve of argillaceous siltstone, as shown in Figure 2(c), indicating that multiple failures may occur in the sample. Consequently, multiple intersecting or parallel closed shearing cracks were formed on the sample surface. As for medium-fine grained sandstone, the deviatoric stress dropped significantly by 75.1% after passing the peak, with an oblique shearing plane formed on the sample surface, indicating a brittle failure.

Under the high temperature, the rock sample tended to be softened, which was reflected by a gradual strength weakening, and meanwhile, was accompanied by multiple failures. This is because mineral grains can expand due to the increase of temperature and there exist differences in the value of the thermal expansion coefficient among various minerals, which may cause the difference in the magnitude of the thermal strain among these minerals and further induce the generation of shearing micro-cracks [15, 16]. Hence, the macroscopic strength of the rock sample can be weakened. Moreover, local microcracks were gradually connected to form multiple macroscopic shearing bands during loading the sample [19], which were reflected by multiple stress drops in the whole stress-strain curve. For glutenite under the high temperature, the deviatoric stress gradually decreased after passing the peak, without macrocracks on

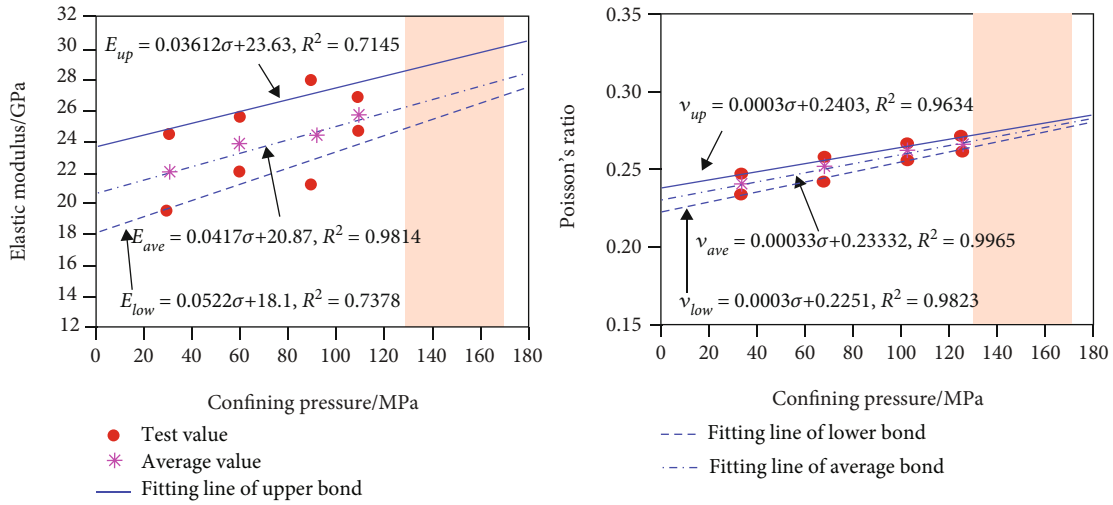
the sample surface, and in the meantime, with a slight decrease of the compressive strength. This is because glutenite contains gravels with high strengths, and the temperature of  $150^\circ\text{C}$  has not reached the thermal damage threshold of the gravel. Although the matrix of glutenite was fractured by local microcracks produced under the high temperature, the gravel still possessed the bearing capacity. Additionally, there was probably slippage between the gravel and matrix during load the glutenite sample, causing meso-scale damages along the gravel interface.

It is necessary to point out that the rock mechanical properties of deep reservoirs are determined by the coupling among the temperature, in situ stress, and pore pressure. According to the experimental results, when the effective confining pressure is constant, increasing the confining pressure or pore pressure tends to enhance the compressive strength and plastic deformation of rock samples, while the high temperature tends to soften the rock, causing the elastic modulus and compressive strength of rock samples to decrease. However, the comprehensive effect of the confining pressure, pore pressure, and temperature on rock mechanical properties is complicated. For argillaceous siltstone, the elastic modulus of the rock sample under high temperature and high pressure is lower than that under the conventional condition, while Poisson's ratio and compressive strength are larger than those under the conventional condition. For medium-fine grained sandstone, the compressive strength under high temperature and high pressure is larger than that under the conventional condition, but the elastic modulus and Poisson's ratio are similar to those

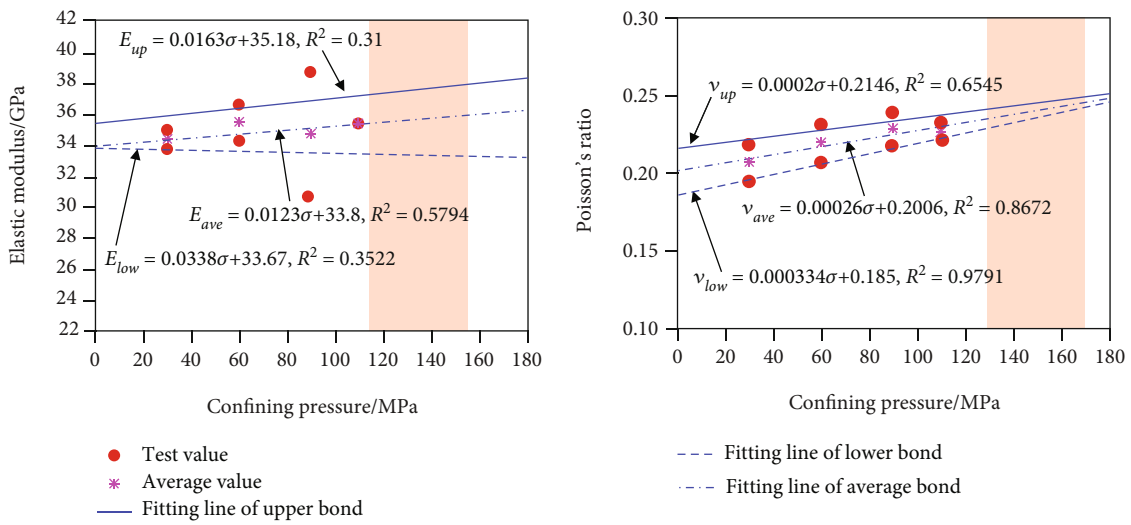




(a) Argillaceous siltstone ((A) elastic modulus and (B) Poisson's ratio)



(b) Medium-fine grained sandstone ((A) elastic modulus and (B) Poisson's ratio)



(c) Glutenite ((A) elastic modulus and (B) Poisson's ratio)

FIGURE 4: Extrapolation of mechanical parameters of samples with different lithologies (the red area is the corresponding confining pressure range of the reservoir).

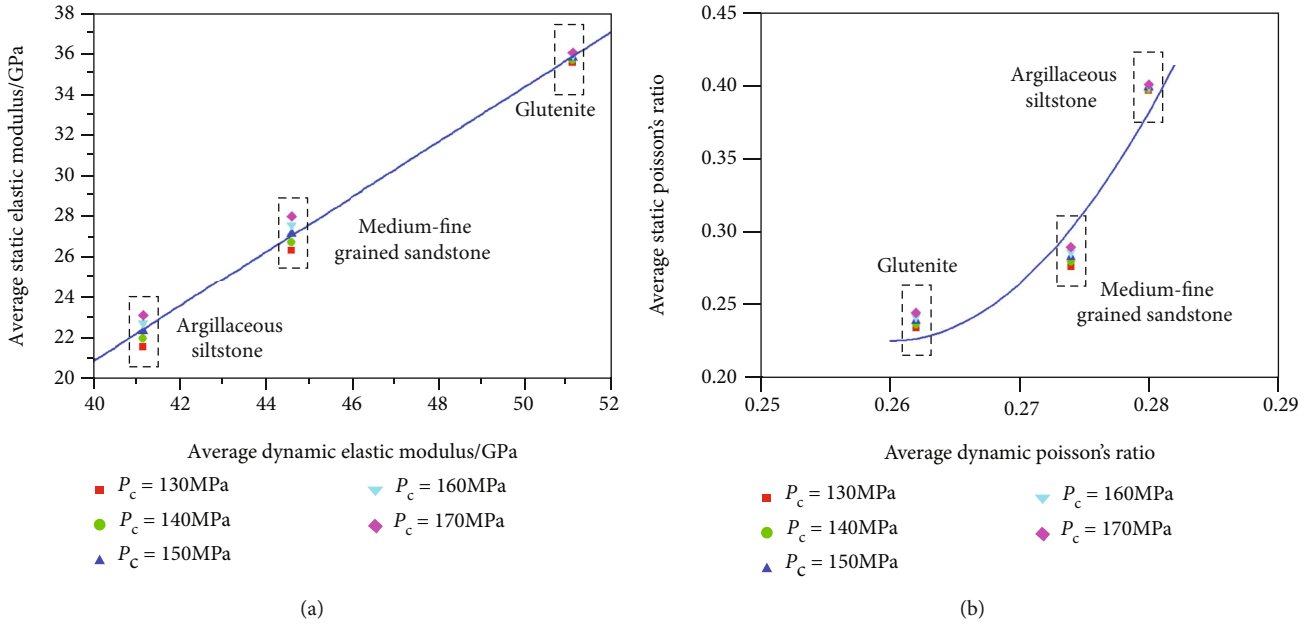


FIGURE 5: Dynamic and static mechanical parameter transformation. (a) Transformation for the elastic modulus. (b) Transformation for Poisson's ratio.

under the conventional condition. As for glutenite, the variation trend of the compressive strength under high temperature and high pressure is similar to that of argillaceous siltstone and medium-fine grained sandstone. Compared with glutenite sample under the conventional condition, however, the elastic modulus and Poisson's ratio under high temperature and high pressure are smaller. Apart from the lithology possibly causing the difference in mechanical properties, some studies point out that rock mechanical properties may vary in a piecewise manner under high temperature and high pressure due to a potential threshold temperature, which complicates the variation law of mechanical parameters [13, 17]. The experimental results also show that from the conventional test condition (i.e., low confining pressure and room temperature) to the condition of the high temperature, high confining pressure, and high pore pressure, the rock failure mode tends to transit from forming shearing macro-cracks to forming shearing closed damaged cracks, and meanwhile, transit from the shearing brittle failure to the mesoscale structural damage accompanied by the enhanced plastic deformation.

**3.1.3. Empirical Formula for Transformation of Dynamic and Static Mechanical Parameters.** Due to the limitation of the apparatus performance, the real in situ stress condition cannot be achieved in laboratory rock mechanical tests. Because the pressure coefficient of the Toutunhe formation ranges from 1.6 to 2.3, the corresponding formation pressure is about 100-140 MPa. Please note that the in situ stress is approximately 130-170 MPa, then, the corresponding effective confining pressure is about 30 MPa, which is the same as that adopted in the rock mechanical test. Thus, the rock mechanical parameters under 130-170 MPa confining pressure (i.e., the in situ stress condition) can be obtained by

extrapolating the test results in laboratories (i.e., the results of Nos. 1~4#, 7~10#, and 13~16#). The extrapolation results are shown in Figure 4.

It can be seen from Figure 4 that both the elastic modulus and Poisson's ratio increased approximately linearly with the increase of the confining pressure. The fitting results show that the lower bound of the elastic modulus of glutenite decreased as the confining pressure increased. This trend was caused by the abnormally low measured value under 90 MPa confining pressure. In addition, the matching degree of the linear extrapolation correlation for the elastic modulus and Poisson's ratio of glutenite is lower than that of argillaceous siltstone and medium-fine grained sandstone. In the future, this linear extrapolation correlation needs to be further verified for glutenite. Figure 4 shows that under the reservoir condition (i.e., 130-170 MPa confining pressure), the elastic modulus of argillaceous siltstone is 20.50-24.21 GPa and Poisson's ratio is 0.387-0.404; for medium-fine grained sandstone, the elastic modulus is 24.89-29.77 GPa and Poisson's ratio is 0.273-0.279; as for glutenite, the elastic modulus is 33.06-37.96 GPa and Poisson's ratio is 0.228-0.249. To facilitate the field application, empirical formulas for the transformation between dynamic mechanical parameters obtained from the logging interpretation of sampling wells and static mechanical parameters obtained from laboratory tests were established, as indicated in Figure 5. It was known from Figure 5 that the average dynamic elastic modulus of argillaceous siltstone is 41.78 GPa and average dynamic Poisson's ratio is 0.280; the average dynamic elastic modulus of medium-fine grained sandstone is 44.59 GPa and average dynamic Poisson's ratio is 0.274; and the average dynamic elastic modulus of glutenite is 51.09 GPa and average dynamic Poisson's ratio is 0.262. Comparing the dynamic mechanical parameters with the corresponding

TABLE 2: Basic parameters of the sensitivity analysis for the corrected breakdown pressure prediction model.

Parameters	Values	Parameters	Values
Elastic modulus $E$ (GPa)	18-40	Fracturing fluid temperature $T_w$ ( $^{\circ}\text{C}$ )	25
Poisson's ratio $\nu$	0.18-0.40	Initial formation temperature $T_0$ ( $^{\circ}\text{C}$ )	100-200
Vertical stress $\sigma_v$ (MPa)	160	Rock thermal expansion coefficient $\alpha_m$ ( $1/^{\circ}\text{C}$ )	0.00004
Pore pressure $p_p$ (MPa)	100-150	Tectonic stress coefficient $a$	0.6
Biot elastic coefficient	0.8	Tectonic stress coefficient $b$	0.11
Tensile strength $\sigma_t$ (MPa)	7		

static mechanical parameters for samples with various lithologies, it is found that there is a good linear correlation between the dynamic and static elastic modulus (as shown in Equation (8)), while the correlation between the dynamic and static Poisson's ratio can be characterized by a quadratic function (as shown in Equation (9)). These two equations can be given as follows:

$$E_s = 1.3373E_d - 32.62, \quad (8)$$

$$\nu_s = 384.7\nu_d^2 - 200\nu_d + 26.22, \quad (9)$$

where  $E_s$  is the static elastic modulus, GPa;  $E_d$  is the dynamic elastic modulus, GPa;  $\nu_s$  is the static Poisson's ratio; and  $\nu_d$  is the dynamic Poisson's ratio.

### 3.2. Breakdown Pressure Prediction

**3.2.1. Parametric Sensitivity Analysis.** In this section, the sensitivity analysis on the rock breakdown pressure was carried out based on Equation (7). Four factors, i.e., the formation rock elastic modulus, Poisson's ratio, pore pressure, and formation temperature, were analyzed. The simulation parameters are shown in Table 2, and the simulation results of the sensitivity analysis are shown in Figure 6.

As can be seen from Figure 6(a), when the elastic modulus increases from 18 GPa to 40 GPa, the breakdown pressure decreases by about 27.2%, which is due to the additional stress caused by the wellbore temperature variation. When the temperature difference is kept constant, the larger the elastic modulus is, the higher the additional tensile stress is, and the lower the breakdown pressure is. Li et al. [40] believe that this additional stress term is sensitive to the lithology and found that the influence of the temperature variation on the breakdown pressure of hard brittle shale and limestone formations with a high elastic modulus and low Poisson's ratio was far greater than that of loose sandstone and soft mudstone with a low elastic modulus and high Poisson's ratio. According to the experimental results in this paper, the predicted average elastic moduli of argillaceous siltstone, medium-fine grained sandstone, and glutenite under the confining pressure of 160 MPa are 22.74 MPa, 27.54 MPa, and 35.78 MPa, respectively, and the corresponding breakdown pressures are 169.3 MPa, 158.8 MPa, and 140.7 MPa, respectively. The wellbore temperature variation has the greatest impact on the breakdown pressure of glutenite. Therefore, for the deep formation under the high confining pressure, the low elastic modulus

and the high confining pressure amplify the influence of the additional stress term caused by the wellbore temperature variation, which cannot be ignored in the breakdown pressure prediction.

Figure 6(b) reveals that the breakdown pressure is positively correlated with Poisson's ratio. When Poisson's ratio increases from 0.18 to 0.40, the breakdown pressure increases by about 54.7%. Based on the results shown in Figure 4, when the temperature and effective confining pressure are kept constant, Poisson's ratio increases as the confining pressure increases. In this paper, Poisson's ratios of argillaceous siltstone, medium-fine grained sandstone, and glutenite under the confining pressure of 160 MPa are estimated to be 0.399, 0.286, and 0.242, respectively. The corresponding breakdown pressures are 214.0 MPa, 169.9 MPa, and 154.8 MPa, respectively. The larger Poisson's ratio is, the stronger the rock deformation is, which means that  $\varepsilon_p/\varepsilon_t$  increases. Under the reservoir condition adopted in this paper (i.e.,  $p_c$  is 110 MPa,  $T$  is  $150^{\circ}\text{C}$ , and  $p_p$  is 80 MPa),  $\varepsilon_p/\varepsilon_t$  of argillaceous siltstone, medium-fine grained sandstone, and glutenite are 28.2%, 25.6%, and 24.5%, respectively, which will be higher under the real reservoir condition, suggesting that the plastic deformation is stronger. Guo et al. [41], considering the elastoplastic characteristics of rocks, studied the hydraulic fracturing in a vertical well with the open-hole completion and found that the breakdown pressure of the plastic formation is higher than that of the elastic brittle formation, which is consistent with the variation trend shown in Figure 6(b). To summarize, the higher the Poisson's ratio is, the stronger the plastic deformation is, and the higher the breakdown pressure is.

It can be revealed from Figure 6(c) that the rock breakdown pressure increases with the pore pressure when keeping the other parameters constant. For example, when the pore pressure increases from 100 MPa to 150 MPa, the breakdown pressure increases by 46.6%. The contributions of the pore pressure include the wellbore internal pressure and additional stress caused by the seepage at the wellbore wall. At the same depth, the larger the pore pressure is, the higher the bottom-hole pressure is, leading to the increase of the formation net pressure ( $p_n$ ) at the borehole wall. Thus, the net stress caused by the wellbore internal pressure and the additional stress caused by the seepage at the borehole wall will increase, and the formation breakdown pressure will correspondingly increase. On the other hand, when the confining pressure keeps constant, the increase of the pore pressure may lead to the decrease of the effective confining

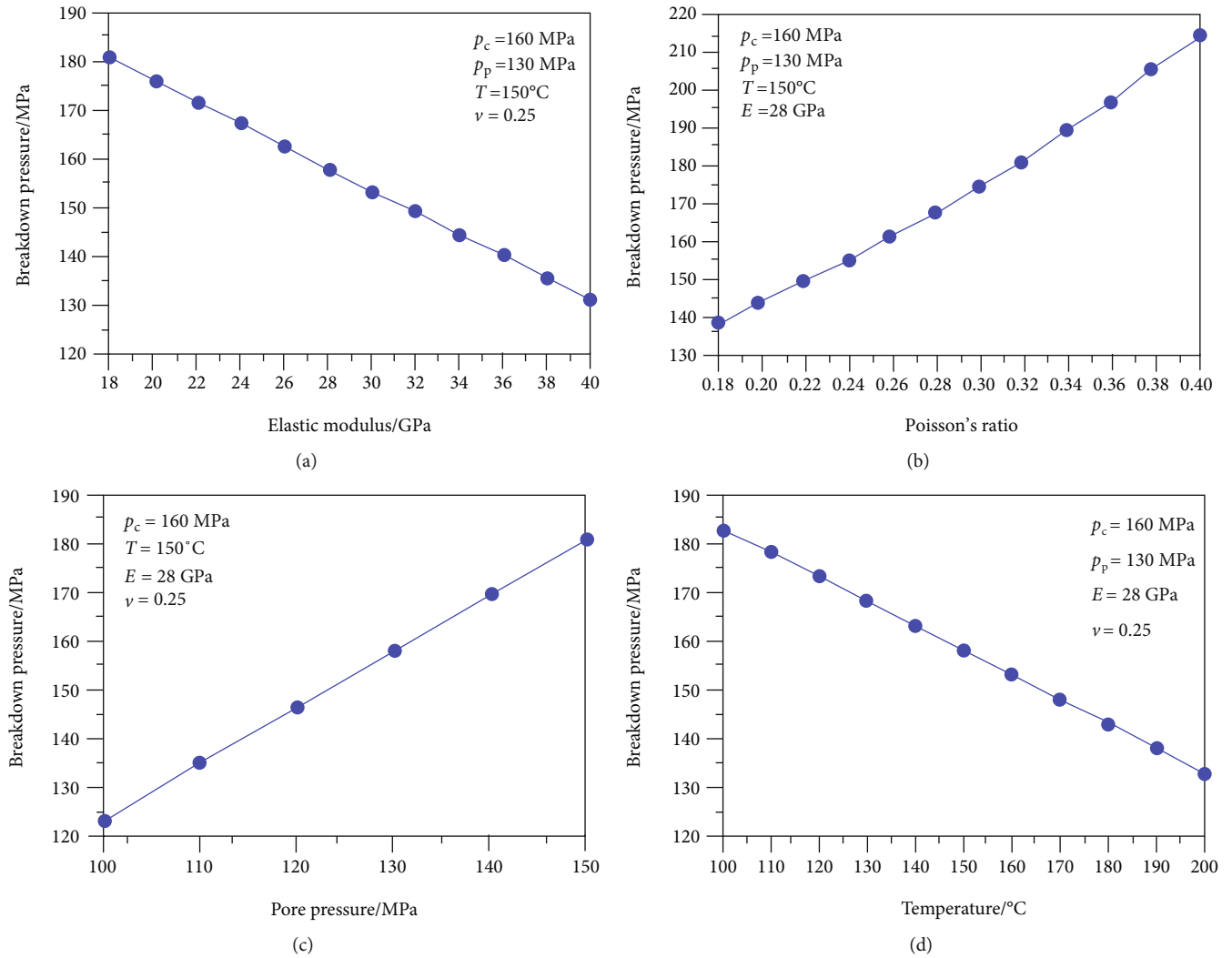


FIGURE 6: Parametric sensitivity analysis of the formation breakdown pressure. (a) Effect of elastic modulus. (b) Effect of Poisson's ratio. (c) Effect of pore pressure. (d) Effect of formation temperature.

pressure. Pan et al. [21] pointed out that when the effective confining pressure decreases, the elastic modulus of rocks tends to decrease, thus weakening the effect of the thermal stress caused by the wellbore temperature variation. Figure 6(d) further reflects the influence of the formation temperature variation on the rock breakdown pressure. When the other parameters kept constant, the breakdown pressure decreases with the increase of formation temperature. The injection of the fracturing fluid under the high temperature leads to a large temperature difference inside the rock, enhancing the thermal stress. At the same time, the thermal expansion coefficients of various minerals are different, which results in differences in the thermal strain among different minerals. In addition, the local thermal cracking could further reduce the formation breakdown pressure. It should be noted that the influence of the temperature variation on rock mechanical parameters is not considered in Figure 6(d). The effect of the temperature on rock mechanical properties is complex. Zhang et al. [42] pointed out that with the increase of temperature, the Poisson's ratio

of rocks tends to decrease first and then increase, while the elastic modulus tends to increase first and then decrease. The changes of elastic modulus and Poisson's ratio affect the formation breakdown pressure in turn. Therefore, while considering the effect of the thermal stress, it is also necessary to comprehensively consider the influence of the temperature variation on the elastic modulus and Poisson's ratio of rocks around the wellbore.

**3.2.2. Field Application.** In this section, the corrected model was verified against an actual case. Well Xihu 1 is an exploration vertical well in the Xihu anticline of the Sikeshu sag, piedmont thrust belt in the southern margin of Junggar Basin. The mechanical test has been carried out for Jurassic Qigu formation, and the breakdown pressure monitored in the treatment is about 144 MPa. The well depth at the target layer is 6139.0-6160.0 m, the temperature of the target layer is  $140^\circ\text{C}$ , and the formation pressure is 116-120 MPa. Based on the logging interpretation of stimulation stage, the average dynamic elastic modulus is about 49.46 GPa, average

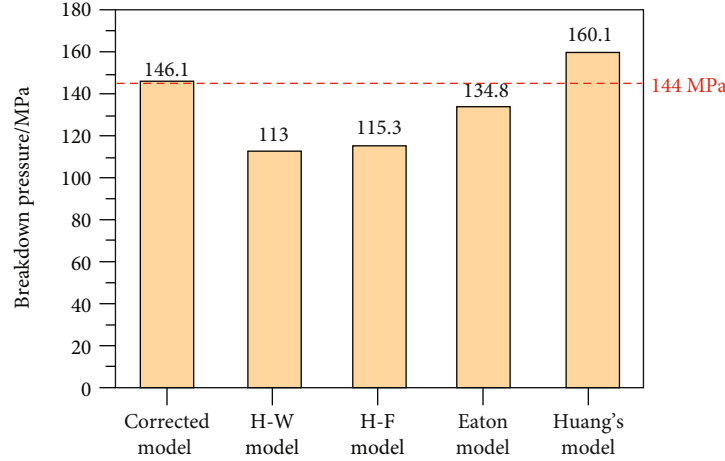


FIGURE 7: Prediction results of the breakdown pressure by different models.

dynamic Poisson's ratio is 0.27, the minimum horizontal principal stress is 123-140 MPa, and the average tensile strength is 10.13 MPa. The tectonic stress coefficients corresponding to the maximum and minimum horizontal principal stresses are 0.6 and 0.11, respectively. Other necessary parameters are consistent with those in Table 2. We adopt the proposed empirical formulas for the transformation between the dynamic and static mechanical parameters and the corrected breakdown pressure model to predict the breakdown pressure in the target formation. Meanwhile, the predicted value was comprehensively compared with those by other models such as the H-W model [25], H-F model [26], Eaton model [27], and Huang's model [30]. The prediction results are shown in Figure 7.

It can be seen from Figure 7 that the predicted values of the formation breakdown pressure given by the H-W model and H-F model are 113 MPa and 115.3 MPa, respectively, which are nearly 30 MPa lower than the measured value, with an error of about 20.8%. The predicted value of the Huang's model is 160.1 MPa, which is about 16 MPa higher than the measured value, with an error of 11.1%. The predicted value from the Eaton model is 134.8 MPa, about 10 MPa lower than the measured value, and the prediction error is about 6.4%. By contrast, the predicted value from the corrected model is 146.1 MPa, which is only 2.1 MPa higher than the measured value, with an error of 1.46%. It shows that considering the seepage effect at the wellbore wall and the thermal stress will improve the prediction accuracy. The empirical formula for the transformation between dynamic and static mechanical parameters and the corrected breakdown pressure model proposed in this paper have demonstrated promising applicability.

#### 4. Conclusions

Aiming at the ultradeep reservoir in Sikeshu sag on the southern margin of Junggar Basin, the evaluation of rock mechanical properties was performed under a similar temperature-pressure condition to that of the ultradeep reservoir, with the consideration of the coupling effects of high temperature, high confining pressure, and high pore pres-

sure. Besides, an improved prediction model for the formation breakdown pressure was proposed by taking the wellbore seepage and thermal stress into consideration. The primary findings can be summarized as follows:

- (a) While keeping the effective confining pressure constant, under high confining pressure and high pore pressure, the rock compressive strength tends to be enhanced. Meanwhile, the peak strain and proportion of plastic strain are both increased, with the plasticity also enhanced. However, high temperature is inclined to softening the rock, resulting in meso-scale thermal damages and the reduction of the compressive strength and elastic modulus. Besides, the rock failure mode tends to transit from forming shearing macroscopic fractures under the conventional mechanical condition to forming a single or multiple closed shearing cracks under high temperature and high pressure
- (b) Keeping the effective confining pressure constant, the static elastic modulus and Poisson's ratio of the deep strata are approximately linearly correlated to the confining pressure. There is also a linear correlation between the static and dynamic elastic modulus, while there is a quadratic correlation between the static and dynamic Poisson's ratio. These fitting functions can be used to obtain the profiles of static elastic modulus and Poisson's ratio based on their dynamic values from the logging interpretation
- (c) The thermal stress caused by the temperature variation at the wellbore wall has a great effect on the reduction of the breakdown pressure in the hard brittle deep high-temperature formation with a high elastic modulus and low Poisson's ratio. Considering the influences of the seepage at the wellbore wall and the thermal stress, the corrected breakdown pressure prediction model can give more accurate prediction results than some other classical models. The proposed model in this study can provide theoretical guidance in the selection of fracturing truck groups



and the design of the pumping schedule for high-temperature and high-pressure reservoirs

## Data Availability

The data used to support the findings of this study are available from the corresponding author upon request.

## Conflicts of Interest

The authors declare that there is no conflict of interest regarding the publication of this paper.

## Authors' Contributions

Conceptualization was done by M.W. and X.F. Methodology was done by Y.S. Formal analysis was performed by Z.P. and C.Y. Investigation was conducted by Z.P. and C.Y. Resources were acquired by M.W., C.Y., and H.S. Writing—original draft preparation was done by Z.P. Writing—review and editing was done by Y.S. Visualization was done by H.S. Supervision was done by X.F. Project administration was done by M.W. and X.F. All authors have read and agreed to the published version of the manuscript.

## Acknowledgments

This study was supported by the National Natural Science Foundation of China (51974332).

## References

- [1] J. H. Du, D. M. Zhi, J. Z. Li et al., "Major breakthrough of well Gaotan 1 and exploration prospects of lower assemblage in southern margin of Junggar Basin, NW China," *Petroleum Exploration and Development*, vol. 46, no. 2, pp. 205–215, 2019.
- [2] Y. B. Zhang, M. J. Wang, Z. L. Du, and Q. D. Yuan, "Main oil source rocks and oil-source correlation in the Sikesu sag, the southern margin of Junggar Basin," *Marine Geology Frontiers*, vol. 36, no. 12, pp. 39–48, 2020.
- [3] D. S. Yang, L. X. Xiao, G. H. Yan, W. E. I. Lingyun, W. A. N. G. Xin, and W. A. N. G. Xinqiang, "Structural characteristics and petroleum exploration in Sikesu sag, southern margin of Junggar Basin," *Xinjiang Petroleum Geology*, vol. 40, no. 2, pp. 138–144, 2019.
- [4] Z. Yang, Q. Y. Li, X. F. Qi, and D. Yang, "A new possible giant hydrocarbon generated formation: the Upper Triassic source rock in Southwestern Junggar Basin, NW China," *Marine and Petroleum Geology*, vol. 88, pp. 575–586, 2017.
- [5] D. W. Lei, J. Zhang, N. G. Chen, and B. L. Xiang, "Conditions for gas pooling in the lower assemblage in the southern margin of the Junggar Basin and the exploration prospect of large hydrocarbon fields," *Natural Gas Industry*, vol. 32, no. 2, pp. 16–22, 2012.
- [6] L. C. Kuang, X. L. Wang, J. Zhang, and H. P. Xia, "Structural modeling of the Huoerguosi-Manasi-Tugulu thrust belt at the southern margin of the Junggar Basin and the discovery of the Mahe gas field," *Natural Gas Industry*, vol. 32, no. 2, pp. 11–16, 2012.
- [7] X. Y. Li, Y. Shao, and T. M. Li, "Three oil-reservoir combinations in south marginal of Junggar Basin, Northwest China," *Petroleum Exploration and Development*, vol. 30, no. 6, pp. 32–34, 2003.
- [8] X. Q. Si, B. Yuan, H. J. Guo, X. U. Yang, C. H. E. N. Nenggui, and P. E. N. G. Bo, "Reservoir characteristics and main controlling factors of cretaceous Qingshuihe formation in the southern margin of Junggar Basin," *Xinjiang Petroleum Geology*, vol. 41, no. 2, pp. 38–45, 2020.
- [9] J. Yao, C. Q. Huang, W. Z. Liu, Y. Zhang, Q. Zeng, and X. Yan, "Key mechanical problems in the development of deep oil and gas reservoirs," *SCIENTIA SINICA Physica, Mechanica & Astronomica*, vol. 48, 2018.
- [10] J. C. Guo, Z. H. Hao, and Q. L. Lu, "Research progress in key mechanical theories of deep shale network fracturing," *Natural Gas Industry*, vol. 41, no. 1, pp. 102–117, 2021.
- [11] K. Oladoyin, F. Gabriella, and S. István, "Formation susceptibility to wellbore instability and sand production in the Pannonian Basin, Hungary," in *The 52nd US Rock Mechanics / Geomechanics Symposium* American Rock Mechanics Association.
- [12] M. J. Economides and K. G. Nolte, *Reservoir Stimulation*, John Wiley & Sons, Ltd., Third edition, 2000.
- [13] L. Y. Zhang, X. B. Mao, and A. H. Lu, "Experimental study on the mechanical properties of rocks at high temperature," *Science in China Series E: Technological Sciences*, vol. 52, no. 3, pp. 641–646, 2009.
- [14] Q. Sun, Z. Z. Zhang, L. Xue, and S. Y. Zhu, "Physico-mechanical properties variation of rock with phase transformation under high temperature," *Chinese Journal of Rock Mechanics and Engineering*, vol. 32, no. 5, pp. 935–942, 2013.
- [15] A. S. Chiarelli, J. F. Shao, and N. Hoteit, "Modeling of elastoplastic damage behavior of a claystone," *International Journal of Plasticity*, vol. 19, pp. 23–45, 2003.
- [16] H. Tian, T. Kempka, S. Yu, and M. Ziegler, "Mechanical properties of sandstones exposed to high temperature," *Rock Mechanics and Rock Engineering*, vol. 49, no. 1, pp. 321–327, 2016.
- [17] Z. J. Wan, Y. S. Zhao, F. K. Dong, Z. Feng, N. Zhang, and J. Wu, "Experimental study on mechanical characteristics of granite under high temperatures and triaxial stresses," *Chinese Journal of Rock Mechanics and Engineering*, vol. 27, no. 1, pp. 72–77, 2008.
- [18] H. Deng, M. Zhang, T. H. Deng, and Q. Zhang, "A triaxial compression test of tight quartz sandstone under high temperature and high confining pressure," *Oil & Gas Geology*, vol. 38, no. 6, pp. 1172–1179, 2017.
- [19] W. G. P. Kumari, P. G. Ranjith, M. S. A. Perera et al., "Mechanical behaviour of Australian Strathbogie granite under in-situ stress and temperature conditions: an application to geothermal energy extraction," *Geothermics*, vol. 65, pp. 44–59, 2017.
- [20] Q. C. Zhou, H. B. Li, C. H. Yang, H. S. MA, and L. J. CHEN, "Experimental study on thermo-mechanical and hydro-mechanical coupling of sandstone for west route of south-to-north water transfer project," *Chinese Journal of Rock Mechanics and Engineering*, vol. 24, no. 20, pp. 3639–3645, 2005.
- [21] L. H. Pan, S. C. Zhang, L. J. Cheng et al., "Experimental study on mechanical property of carbonate under the effect of confining pressure and pore pressure," *Journal of Xi'an Shiyou University*, vol. 29, no. 5, pp. 17–20, 2014.

- [22] S. M. Liao, C. Y. She, Y. Sang, and J. C. Guo, *Theory and Technology of Fracture Network Fracturing in Tight Gas Reservoir*, Petroleum Industry Press, 2016.
- [23] J. Xie, H. M. Wu, Y. S. Lou, and X. P. Zhai, "Fracture pressure prediction model of high temperature and high pressure formation in deep water area of the South China Sea," *Fault-Block Oil and Gas Field*, vol. 28, no. 3, pp. 378–382, 2021.
- [24] K. H. S. M. Sampath, M. S. A. Perera, and P. G. Ranjith, "Theoretical overview of hydraulic fracturing break-down pressure," *Journal of Natural Gas Science and Engineering*, vol. 58, pp. 251–265, 2018.
- [25] M. K. Hubbert and D. G. Willis, "Mechanics of hydraulic fracturing," *AIME Petroleum Transactions*, vol. 210, no. 1, pp. 153–168, 1957.
- [26] B. Haimson and C. Fairhurst, "Initiation and extension of hydraulic fractures in rocks," *Society of Petroleum Engineers Journal*, vol. 7, no. 3, pp. 310–318, 1967.
- [27] B. Eaton, "Fracture gradient prediction and its application in oilfield operations," *Journal of Petroleum Technology*, vol. 21, no. 10, pp. 1353–1360, 1969.
- [28] R. D. Stephen, "Prediction of fracture pressures for wildcat wells," *Journal of Petroleum Technology*, vol. 34, no. 4, pp. 863–872, 1982.
- [29] R. A. Anderson, D. S. Ingram, and A. M. Zanier, "Determining fracture pressure gradients from well logs," *Journal of Petroleum Technology*, vol. 25, no. 11, pp. 1259–1268, 1973.
- [30] R. Z. Huang, "Discussion on prediction model of formation fracture pressure," *Journal of East China Petroleum Institute*, vol. 4, pp. 335–347, 1984.
- [31] T. Ito and K. Hayashi, "Physical background to the breakdown pressure in hydraulic fracturing tectonic stress measurements," *International Journal of Rock Mechanics and Mining Sciences & Geomechanics Abstracts*, vol. 28, no. 4, pp. 285–293, 1991.
- [32] T. K. Guo, S. C. Zhang, W. L. Liu, and L. Wenxu, "Initiation pressure of multi-stage fracking for perforated horizontal wells of shale gas reservoirs," *Natural Gas Industry*, vol. 33, no. 12, pp. 87–93, 2013.
- [33] Y. Fan, Y. L. Zhao, Z. M. Zhu, C. L. Zhou, and X. S. Zhang, "Theoretical study of break down pressures and fracture initiation angles based on model containing wellbore and perforations," *Journal of Central South University (Natural Science)*, vol. 50, no. 3, pp. 669–679, 2019.
- [34] B. Lecampion, "Modeling size effects associated with tensile fracture initiation from a wellbore," *International Journal of Rock Mechanics and Mining Sciences*, vol. 56, pp. 67–76, 2012.
- [35] P. Cornetti, N. Pugno, A. Carpinteri, and D. Taylor, "Finite fracture mechanics: a coupled stress and energy failure criterion," *Engineering Fracture Mechanics*, vol. 73, no. 14, pp. 2021–2033, 2006.
- [36] X. R. Luo, L. J. Liu, and X. Y. Li, "Overpressure distribution and pressuring mechanism on the southern margin of the Junggar Basin, northwestern China," *Chinese Science Bulletin*, vol. 51, no. 19, pp. 2383–2390, 2006.
- [37] Y. X. Liu, H. Y. Zhou, J. C. Guo, and J. Wang, "Mechanical characteristics and influencing factors of shallow igneous rocks in Junggar Basin," *IOP Conference Series: Earth and Environmental Science*, vol. 861, 2021.
- [38] B. Yuan, X. M. Dong, X. T. Guan et al., "Analysis of characteristics of tight sandstone reservoir with porous-fissure dual medium in Toutunhe formation of Sikeshu sag," *Acta Scientiarum Naturalium Universitatis Pekinensis (Natural Science)*, vol. 56, no. 3, pp. 449–459, 2020.
- [39] R. Ulusay, *The ISRM Suggested Methods for Rock Characterization, Testing and Monitoring: 2007-2014*, Springer International Publishing, 2015.
- [40] S. G. Li, J. G. Deng, B. H. Yu, and L. J. Yu, "Formation fracture pressure calculation in high temperatures wells," *Chinese journal of rock mechanics and engineering*, vol. 24, pp. 5669–5673, 2005.
- [41] J. C. Guo, S. G. He, Y. Deng, and Z. Zhao, "New stress and initiation model of hydraulic fracturing based on nonlinear constitutive equation," *Journal of Natural Gas Science and Engineering*, vol. 27, pp. 666–675, 2015.
- [42] P. Zhang, B. Mishra, and K. A. Heasley, "Experimental investigation on the influence of high pressure and high temperature on the mechanical properties of deep reservoir rocks," *Rock Mechanics and Rock Engineering*, vol. 48, no. 6, pp. 2197–2211, 2015.

## Research Article

# Analysis of Shunted Screen Gravel Pack Process and Calculation of Friction in Deepwater Horizontal Wells

Fei Xu,<sup>1</sup> Shengtian Zhou ,<sup>2</sup> Chong Zhang,<sup>1</sup> Yi Yu,<sup>1</sup> and Zhao Dong<sup>1</sup>

<sup>1</sup>CNOOC China Limited, Zhanjiang Branch, Zhanjiang, Guangdong 524957, China

<sup>2</sup>China University of Petroleum, Qingdao, Shandong 266580, China

Correspondence should be addressed to Shengtian Zhou; [stzhou2008@163.com](mailto:stzhou2008@163.com)

Received 22 September 2021; Accepted 15 November 2021; Published 12 December 2021

Academic Editor: Xiang Zhou

Copyright © 2021 Fei Xu et al. This is an open access article distributed under the Creative Commons Attribution License, which permits unrestricted use, distribution, and reproduction in any medium, provided the original work is properly cited.

Shunted screen gravel packing is a kind of technology which is difficult to complete gravel packing with the conventional method in low fracture pressure formation and long wellbore length condition. According to the characteristics of LS 17-2 deepwater gas field, the shunted screen packing tool was designed and the gravel packing process and packing mechanism were analyzed. The variation law of the flow friction, flow rate distribution in multichannel, and other parameters of the shunted screen gravel packing were analyzed and calculated. The friction calculation model of different stages of gravel packing was established. A gravel packing simulation software was developed to simulate the friction in different stages of shunted screen gravel packing. The parameters such as sand-dune ratio, pumping sand amount, packing length, and packing time in the process of packing were also calculated. In deepwater horizontal well gravel packing, the results show that the friction ratio of the string is the largest in the stage of injection and  $\alpha$ -wave packing. While the friction increases rapidly in the stage of  $\beta$ -wave packing because the carrier fluid needs to flow through the long and narrow washpipe/screen annulus. Particularly when the  $\beta$ -wave packing is near the beginning of the open hole, the packing pressure reaches the maximum. The calculated results are in good agreement with the measured results of the downhole pressure gauge. The model and software can provide technical support for the prediction and optimization of gravel packing parameters in the future.

## 1. Introduction

For offshore deepwater oil and gas reservoir development, in order to reduce the number of wells and obtain higher sand-free production, sand control measures need to be taken. Gravel packing is the most commonly used sand control technology in the oil and gas industry [1–3]. In a conventional gravel pack, gravel slurry is injected into the wellbore/screen annulus, where gravel is packed into the wellbore/screen annulus to control formation sand entry into the wellbore. Due to the leakage of carrier fluid into the formation or shunt into the washpipe/screen annulus, the cross-section flow rate of carrier fluid decreases gradually along the flow direction, thus reducing the sand-carrying capacity of carrier fluid. The gravel in the wellbore/screen annulus is often blocked in advance, resulting in the premature sand bridge in the wellbore/screen annulus, especially in the long wellbore or low fracture pressure formation. For

these special cases, despite the use of low-density gravel, the addition of drag reducers to the carrier fluid, multiple  $\alpha$ -wave or multiple  $\beta$ -wave packing, and other targeted countermeasures [4–7]. However, these methods can not ensure the success of gravel packing in some extreme cases. In the 1990s, shunted screen gravel packing was put forward [8], which was mainly used in casing gravel packing completion initially. With the extensive use of open hole completion gravel packing in offshore, gravel packing with shunted screen was gradually applied to open hole completion [9–22]. Although this technology is being used more and more widely, most of the field applications of this technology have not been specifically studied on the mechanism of shunted screen gravel packing. Particularly on the basis of this particular structural design, there is no quantitative description of the friction of each part of the shunted screen gravel packing. This paper mainly discusses the mechanism of shunted screen gravel packing, set up multichannel flow

model, and friction calculation model for different flow stages. The corresponding software was developed to calculate flow parameters of the shunted screen multichannel and the friction calculation at the different stages. The calculated results are in good agreement with the data of LS 17-2 deepwater gas field in the South China Sea, which provides technical support for the design of shunted screen gravel packing in the future.

## 2. Gravel Packing Mechanism of Shunted Screen

The shunted screen pipe design is shown in Figure 1. Two types of tubes are welded outside the screen pipe in the wellbore/screen annulus, one is the transport tube and the other is the packing tube. The transport tube forms a continuous nonperforated pipe along the length of the screen pipe assembly. These transport tubes lead the slurry into the packing tube with the packing port through the multibranch pipe between each screen pipe joint, and then, the slurry flows to the wellbore/screen annulus through the packing tube. Both the transport tube and the packing tube are rectangular in cross section. Compared with the packing tube, the transport tube usually has a larger flow cross-section area. The cross section of the shunted screen pipe is shown in Figure 2.

The present design includes three transport tubes and two packing tubes, which are distributed in the wellbore/screen annulus as shown in Figure 2.

In the process of gravel packing, due to the loss of carrier fluid to the formation or flowing to the washpipe/screen annulus, the sand-carrying capacity of carrier fluid decreases, the gravel concentration in the wellbore/screen annulus increases, and a large amount of gravel will deposit in this annulus. At this time, the wellbore/screen annulus may be blocked, forming a sand bridge. So the flow resistance in the wellbore/screen annulus will increase, and the slurry will be then led along the lower resistance channel into the shunted screen, across the blockage, and into the annulus behind the sand bridge to continue packing, as shown in Figure 3.

## 3. The Establishment of Multichannel Mathematical Model

Consider shunt system, it is a multichannel flow path system. The slurry into the wellbore/screen annulus from a crossover tool located in the beginning of the open hole flow along the wellbore/screen annulus. Carrier fluid may leak off into formation, and it also diverts through the screen into the washpipe/screen annulus. Once the blockage occurs in the wellbore/screen annulus, there is increased flow resistance. Meanwhile, the slurry will pass through the transport tube, enter the packing tube at the joint, and pack behind the plugging point. Suppose  $Q_p$ ,  $Q_w$ , and  $Q_s$  are the wellbore/screen annulus flow rate, the washpipe/screen annulus flow rate, and the transport pipe flow rate, respectively,  $m^3/s$ .  $Q_{pw}$ ,  $Q_{pr}$ , and  $Q_{ps}$  represent the flow rate per unit length of



FIGURE 1: Shunted screen structure diagram.

the wellbore annulus through the screen to the washpipe/screen annulus, the leakage rate per unit length into the formation and into transport pipe flow rate, respectively,  $m^2/s$ .  $P_p$ ,  $P_w$ ,  $P_s$ , and  $P_r$ , respectively, represent the wellbore/screen annulus pressure, washpipe/screen annulus pressure, transport tube pressure, and reservoir pressure, Pa. There are the following conservation equations [15].

### 3.1. Mass Conservation Equation of Carrier Fluid.

$$\begin{cases} \frac{\partial Q_p}{\partial x} + Q_{pw} + Q_{ps} + Q_{pr} = 0, \\ \frac{\partial Q_w}{\partial x} - Q_{pw} = 0, \\ \frac{\partial Q_s}{\partial x} - Q_{ps} = 0, \end{cases} \quad (1)$$

where  $Q_{pw}$ ,  $Q_{pr}$ , and  $Q_{ps}$  are functions of pressure difference of each flow channel, respectively, which can be expressed as

$$\begin{cases} Q_{pw} = f_{pw}(P_p - P_w), \\ Q_{ps} = f_{ps}(P_p - P_s), \\ Q_{pr} = f_{pr}(P_p - P_r), \end{cases} \quad (2)$$

where  $f_{pw}$ ,  $f_{ps}$ , and  $f_{pr}$  are the specific functional relation between flow rate and pressure difference.

### 3.2. Mass Conservation Equation of Gravel.

$$\begin{cases} \frac{\partial(Q_p c_p)}{\partial x} + \frac{\partial(A_p c_p)}{\partial t} + Q_{ps} c_{ps} = 0, \\ \frac{\partial(Q_s c_s)}{\partial x} + \frac{\partial(A_s c_s)}{\partial t} - Q_{ps} c_{ps} = 0, \end{cases} \quad (3)$$

where  $A_p$  and  $A_s$  are the cross-sectional areas of the wellbore/screen annulus and the transport tube,  $m^2$ ;  $c_p$  and  $c_s$  are the gravel concentration in the wellbore/screen annulus and the transport tube, respectively, dimensionless; and  $c_{ps}$



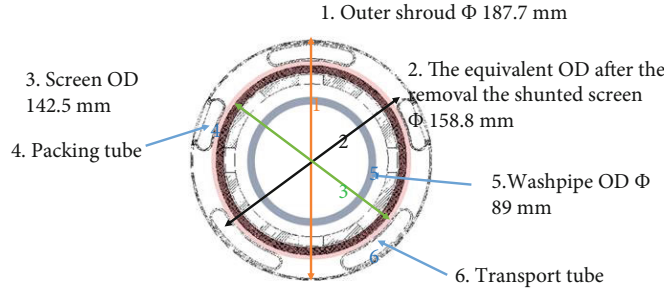


FIGURE 2: Shunted screen cross section.

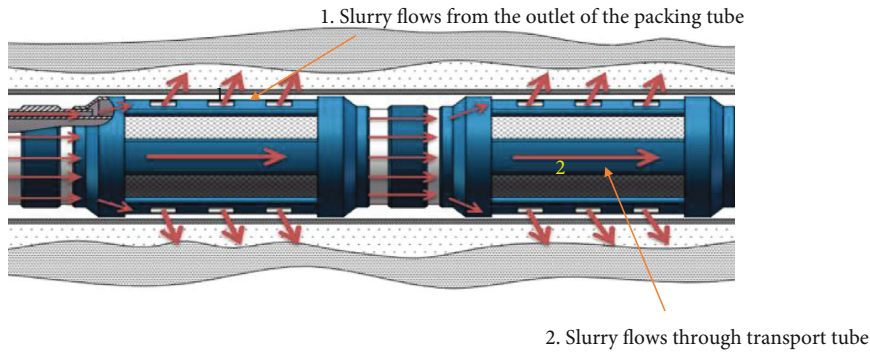


FIGURE 3: Principle of alternate path screen flow passage.

is the gravel concentration from the wellbore/screen annulus into the transport tube, dimensionless.

### 3.3. Momentum Conservation Equation.

$$\begin{cases} \rho_p \frac{Q_p}{A_p} \frac{\partial}{\partial x} \left( \frac{Q_p}{A_p} \right) = -\frac{\partial P_p}{\partial x} - F_p(Q_p), \\ \rho_w \frac{Q_w}{A_w} \frac{\partial}{\partial x} \left( \frac{Q_w}{A_w} \right) = -\frac{\partial P_w}{\partial x} - F_w(Q_w), \\ \rho_s \frac{Q_s}{A_s} \frac{\partial}{\partial x} \left( \frac{Q_s}{A_s} \right) = -\frac{\partial P_s}{\partial x} - F_s(Q_s). \end{cases} \quad (4)$$

Once the specific relationship between  $Q_{pw}$ ,  $Q_{pr}$ , and  $Q_{ps}$  and pressure difference in (2) and the relationship between  $F_p(Q_p)$ ,  $F_w(Q_w)$ , and  $F_s(Q_s)$  and respective flow rate in (4) are determined, the equations composed of (1) and (4) can solve  $P_p$ ,  $P_w$ ,  $P_s$ ,  $Q_p$ ,  $Q_w$ , and  $Q_s$  and then substitute them into (3) to calculate the gravel concentration in the wellbore/screen annulus and transport tube.

During the gravel packing process of the shunted pipe, the slurry is transported from top to bottom along the wellbore, and the flow rate is related to the friction resistance. Therefore, the smaller the cross-sectional area, the less the flow rate. Whether the packing tube transmits the slurry is automatically adjusted according to the flow resistance. When the flow resistance in the wellbore/screen annulus is small, the packing tube does not transmit or transmits at the same time. Then, the shunted pipe must transmit once

the sand bridge form in the wellbore/screen annulus. The packing of the section in front of the sand bridge is a complicated process. That is, part of the slurry is packed with  $\beta$ -wave and part of the slurry is packed to the lower part along the shunted pipe, which is continuous and simultaneous. The flow and packing process are based on the relationship between friction resistance and flow rate. The flow relationship is automatically adjusted, where the friction is large, the flow is less, and the slurry flow rate is less.

## 4. Friction Resistance Analysis for Gravel Packing System

Shunted screen gravel packing is a very effective gravel packing completion technology for the special situation of low formation fracture pressure and long wellbore length. The low fracture formation pressure requires that the packing pressure should not be too high in the gravel packing process, so as to avoid fracturing the formation and causing serious loss of carrier fluid. To complete the gravel packing of long wellbore, the carrier fluid should have sufficient sand carrying capacity to carry gravel to the end of the wellbore. Otherwise, the gravel may deposit too much when the slurry flows in the wellbore/screen annulus. If the height of the sand bed is too high, a sand bridge will form in the wellbore/screen annulus and the packing will stop. Sufficient sand-carrying capacity requires a sufficient pump rate, which will result in higher packing pressure. Therefore, for the horizontal open hole gravel packing, it is necessary to have the corresponding pump rate safety interval. For



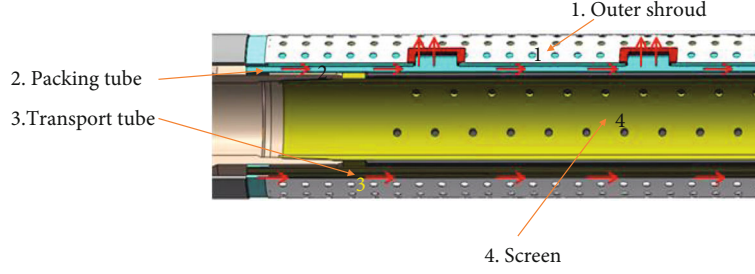


FIGURE 4: Schematic diagram of alternate path screen gravel packing.

TABLE 1: Basic parameters of A10H well in LS 17-2 gas field.

Parameter	Numerical value	Parameter	Numerical value
Open hole section (m)	3854.6-4198	Formation leakage rate (%)	4.80
Wellbore length (m)	343.4	Open hole diameter (in)	8.54
Vertical depth of horizontal section (m)	3424	Pump rate (bpm)	5.6
Reservoir pressure (MPa)	40.4	Sand ratio (ppg)	0.5
Drill pipe	5-7/8" drill pipe + 5" drill pipe	Density of carrier fluid (kg/m <sup>3</sup> )	1350
Equivalent outer diameter of screen tube (in)	6.25	Apparent density of gravel (kg/m <sup>3</sup> )	2400
Washpipe (in)	3-1/2		

extreme conditions, such as deepwater and low fracture pressure formations, such safety zones may not exist with conventional techniques. According to its unique design, the shunted screen gravel packing is equipped with transport tubes and packing tubes in the wellbore annulus. According to the self-adaptability of flow resistance, the slurry flow of different channel is automatically adjusted. If it is blocked, it will shunt the blockage through the transport tube and continue to the annulus behind the sand bridge through the packing tube. Therefore, the calculation and analysis of friction resistance are particularly important in different packing stages.

When designing gravel packing tools in the LS 17-2 gas field in the South China Sea, a pressure gauge was installed on the washpipe in order to timely and accurately analyze the changes in bottom hole pressure. Based on the packing mechanism and the friction calculation model at each stage and the actual basic data on site, the frictional resistance at each stage was calculated and the calculation results were compared with the on-site construction data in this paper. The shunted screen gravel packing diagram is shown in Figure 4.

The open hole gravel packing in horizontal wells can be divided into three stages: slurry injection stage,  $\alpha$ -wave packing stage, and  $\beta$ -wave packing stage [23].

**4.1. Friction Loss in String.** In the slurry injection stage, slurry flows along the string after injection at the wellhead, and the flow resistance in the string can be calculated according to the flow position of the slurry front. Friction loss in the string is

$$\Delta P_i = \frac{32f\rho_m Q_p^2 L_i(t)}{\pi^2 D_c^5} + \frac{32f\rho_f (L_c - L_i(t))}{\pi^2 D_c^5}. \quad (5)$$

**4.2. Friction Loss of Open Hole Wellbore during  $\alpha$ -Wave Packing Stage.** Once the slurry enters the wellbore/screen annulus, the frontier position of slurry is the demarcation point. Along the flow direction, slurry flows behind the frontier position, and liquid flows in the front of the frontier position. This stage is the  $\alpha$ -wave packing stage, and the flow resistance at this stage is

$$\Delta P_\alpha = \frac{2f\rho_m Q_p^2 L_\alpha(t)}{A_{up}^2 D_{up}} + \frac{2f\rho_f Q_p^2 (L - L_\alpha(t))}{A_{an}^2 D_{an}}. \quad (6)$$

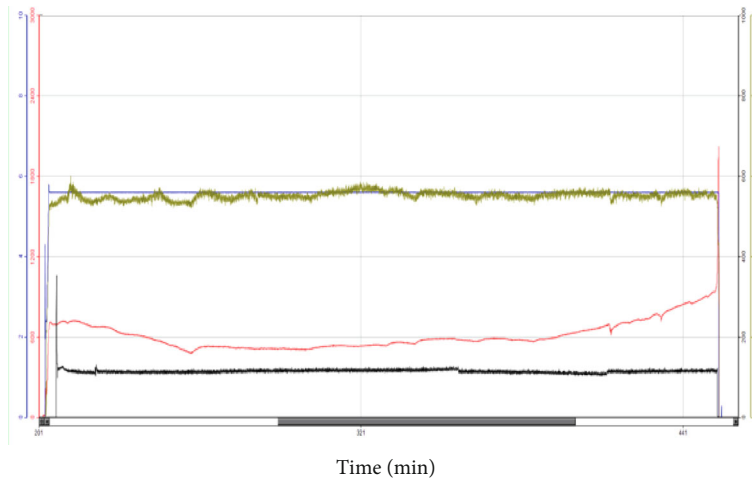
**4.3. Friction Loss of Open Hole Wellbore during  $\beta$ -Wave Packing Stage.** After  $\alpha$ -wave packing reaches the toe of the wellbore, the  $\beta$ -wave reverse packing stage begins. The flow resistance of this stage is as follows:

$$\Delta P_\beta = \frac{2f\rho_m Q_p^2 (L - L_\beta(t))}{A_{up}^2 D_{up}} + \frac{32f\rho_f Q_p^2 L_\beta(t)}{\pi^2 (2/3)^{1/2} (D_i^2 - D_e^2)^2 (D_i - D_e)}, \quad (7)$$

where  $\Delta P_i$ ,  $\Delta P_\alpha$ , and  $\Delta P_\beta$  are friction loss, Pa;  $Q_p$  is the pump rate, m<sup>3</sup>/s;  $L_c$  is the depth of casing shoe, m;  $L_i(t)$  is the depth of slurry injection at  $t$ , m;  $\rho_m$  and  $\rho_f$  are the density of slurry and carrier liquid, respectively, kg/m<sup>3</sup>;  $D_c$  is the diameter of string, m;  $L$ ,  $L_\alpha(t)$ , and  $L_\beta(t)$  are wellbore length and  $\alpha$ -wave packing front distance at time  $t$ ,  $\beta$ -wave front distance at time  $t$ , m;  $A_{up}$  and  $A_{an}$  are the cross-sectional area of the upper part of the sand bed and the cross-sectional area of the wellbore/screen annulus, m<sup>2</sup>;  $f$  is the friction coefficient;  $D_{up}$  and  $D_{an}$  are the hydraulic diameter of the upper channel of the sand bed and the hydraulic diameter of wellbore/screen annulus, m;  $D_i$  and  $D_e$  are the

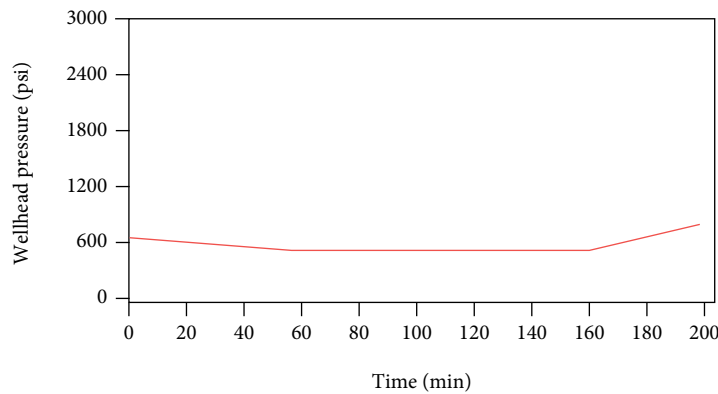
TABLE 2: Comparison of simulation results and operation results.

Parameter	Model calculation results	Construction results	Errors and remarks
$\alpha$ -Wave packing length (m)	343.4	343.4	No error, packing can be completed
$\beta$ -Wave packing length (m)	343.4	343.4	No error, packing can be completed
Total packing time (min)	195.03	251	100% packing is considered in the simulation, while 138% packing is achieved in the actual operation, so the simulation time is less than the actual packing time
Total sand consumption (lbs)	16371.8365	16509 (100% packing), 22800 (138% packing)	Error < 1%
$\alpha$ -Wave sand dune ratio	0.7921	0.79	Error < 1%



- Pack pressure (psi)
- Pump rate (bbl/min)
- Sand rate (lb/min)
- Annulus return rate (bbl/min)

(a) Sand control construction curve



- Wellhead pressure

(b) Simulation calculation of wellhead pressure curve

FIGURE 5: Comparison of simulation results and construction results.

inner diameter of screen pipe and the outer diameter of washpipe, respectively, m.

Given the actual data and combined with formulas (5), (6), and (7), the friction calculation at different stages can

be carried out. The prediction and optimization can be made by comparing the calculated results with the operation results of the actual downhole pressure gauge in the field.

TABLE 3: Construction and simulation results in different packing stages.

	Model calculation results	Sand control construction results	Error and remarks
When starting to add sand, the wellhead pump pressure (psi)	670.95	697	Error < 5%
$\alpha$ -Wave packing start pressure (psi)	528.3456	501	Error < 5%
$\alpha$ -Wave packing average pressure (psi)	542.346	525	Error < 5%
$\beta$ -Wave packing average pressure (psi)	567.1467	580	Error < 5%
Pressure before screenout (psi)	812.75	940	The simulation calculation considers 100% packing, but the actual construction reaches 138%, which leads to some errors
Compared with the wellhead pump pressure curve, it can be seen that the simulation results have high accuracy and can meet the requirements			

TABLE 4: Downhole pressure gauge data logging.

Serial number	Packing state	Lower outside-inside difference (psi)	Upper outer-inner difference (psi)	Top-bottom external difference (psi)	Bottom-up internal difference (psi)
1	Prepump stage	3	1	-41	39
2	Began to sand	34	176	25	118
3	$\alpha$ -Wave packing	50	190	13	127
4	$\alpha$ -Wave packing	48	184	10	126
5	Stage 3-4	43	179	20	116
6	$\beta$ -Wave initiation	45	180	19	116
7	Screenout	51	390	216	123

TABLE 5: Simulation results of friction distribution at each packing stage.

	Injection stage	$\alpha$ -Wave stage	$\beta$ -Wave stage
String injection friction (max), psi	181.8335892	181.8338831	181.8338831
Total friction in horizontal section (max), psi	1.380201471	29.54096242	285.8021072
Backflow friction of washpipe (max), psi	119.5657029	119.5657029	119.5657029
Annular friction between string and casing (max), psi	81.82761718	81.82761718	81.82761718

## 5. Filed Case Histories and Application

*5.1. Comparative Analysis of Packing Simulation Results and Construction Results.* LS 17-2 gas field is a deepwater gas field in the South China Sea. Water depth is approximately 1252~1530 m, and the reservoir buried depth is approximately 3200~3400 m. The reservoir pressure coefficient is approximately 1.19~1.21, and reservoir pressure is approximately 39.0~40.3 MPa. The reservoir temperature is approximately 85~95.1°C, and the permeability is approximately 89.0~2512.3 mD; the average permeability is 543.0 mD. The physical properties are high porosity~extra high porosity, high permeability~extra high permeability. The median particle size is between 67.0 and 250.0  $\mu\text{m}$ . The clay content is approximately 21.0%~27.0%. Using the prediction methods of acoustic time difference, B index, and S index, there is a great risk of sand production. So gravel packing is recommended for sand control. There are 11 development wells (6 horizontal wells and 5 vertical wells) in LS 17-2 gas field, with a total footage of 41171 m. An average well depth is

3743 m, and a maximum well depth is 4054 m. A maximum horizontal displacement is 927 m, and a maximum well inclination is 90°. A shunted screen is used for gravel packing in well A10H, and a pressure gauge is installed above and below the washpipe of the downhole packing tool to monitor the pressure change in the packing process in real time.

Corresponding gravel packing process and mechanism, the calculation software was developed to calculate and simulate the friction at different stages of the packing process. The parameters of the  $\alpha$ - $\beta$  wave packing stage and the screenout pressure and then compared with the construction results were calculated and analyzed. The basic parameters of well A10H are shown in Table 1.

The simulation calculation results are shown in Table 2. From the data in the table, it can be seen that the simulation calculation results of  $\alpha$ - $\beta$  packing length and  $\beta$ -wave packing length are completely consistent with the operation results. If the total packing time is considered 100% packing in theory, the error between the calculation results and the

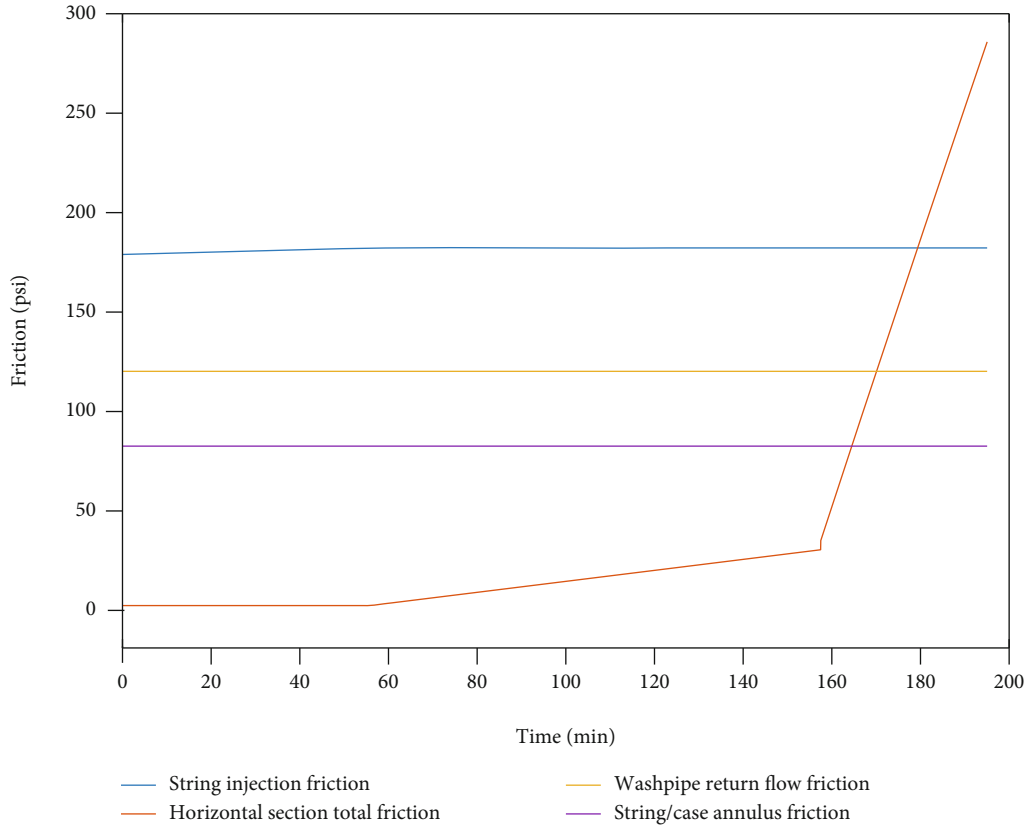


FIGURE 6: Friction distribution at different packing position vs. time.

operation results is less than 10%. At the same time, the total sand consumption and sand dune ratio error are both less than 1%.

5.2. Comparative Analysis of Packing Pressure. According to the friction calculation models at different stages, the corresponding software was compiled and calculated. The comparison of the packing pressure calculated by the simulation and the on-site operation results is shown in Figure 5. It can be seen from the figure that the pressure change trend tends to be consistent. At the same time, the pressure calculation and operation results before starting to add sand,  $\alpha$ -wave packing,  $\beta$ -wave packing, and screenout are shown in Table 3. The error is less than 5%; the simulation accuracy is high and can meet the requirements.

Table 4 shows the data recording results of the downhole pressure gauge. According to the design position of the pressure gauge, numerical simulation calculations were carried out using the compiled software. The calculation results are shown in Table 5.

As can be seen from Tables 4 and 5, the calculation simulation results and the downhole pressure gauge test results are as follows: the maximum value of the external difference between upper and lower is 20 psi at the  $\alpha$ -wave stage, which is roughly the horizontal packing friction and the calculated value is 29.54 psi. This calculation result should be reasonable considering the deviation of position. The maximum difference between upper and lower was 216 psi in the  $\beta$ -wave stage, and the calculated value of packing friction resis-

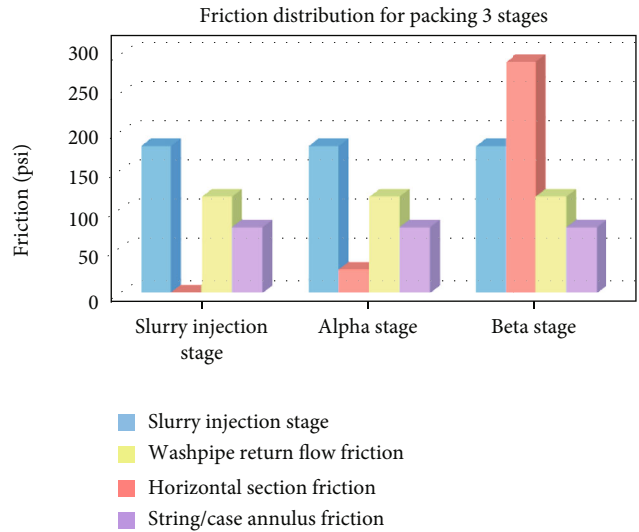


FIGURE 7: Friction distribution in three packing stages.

tance in the horizontal section was 285.802 psi. The internal difference between the bottom and top is about 120 psi, which roughly reflects the friction resistance of the washpipe, and the calculated value is 119.5657 psi, which are within manageable margins of error.

Figure 6 shows the calculated and simulated frictional distribution at different positions of gravel packing with packing time. It can be seen that the total frictional

distribution in the horizontal section increases rapidly in the  $\beta$ -wave stage, resulting in high packing pressure and easy fracturing formation.

Figure 7 is to calculate the slurry injection stage,  $\alpha$ -wave and  $\beta$ -wave packing stage corresponding friction calculation contrast. It can be seen that in deepwater wells, in the slurry injection stage and  $\alpha$ -wave packing stage, the string friction proportion is the largest. During the  $\beta$ -wave packing stage, with the need of carrier fluid through a long narrow wash-pipe/screen annulus, friction increases quickly. Therefore, this packing stage is the stage of maximum of packing pressure.

## 6. Conclusions

- (1) Shunted screen gravel pack uses its unique design structure, when there is a sand bridge in the wellbore annulus, according to the flow resistance and flow adaptability, the slurry can be introduced across the sand bridge to pack the back of the annulus. This technology is suitable for gravel packing in low fracture pressure formations and long horizontal wells
- (2) According to the mechanism analysis of shunted screen gravel packing technology and the friction calculation model established, the developed gravel packing simulation software can accurately predict the change of friction in the packing process. According to the friction at different positions, the flow direction of slurry in the transport pipe and wellbore annulus can be judged and then the change of flow parameters in the transport pipe can be calculated. The calculated results are in good agreement with the construction results
- (3) Through mutual checking of the data obtained from the downhole pressure gauge and the results of simulation calculation, the packing effect can be further predicted and the parameters can be optimized to ensure the success of gravel packing in the field

## Data Availability

All data, models, and code generated or used during the study appear in the submitted article.

## Conflicts of Interest

The authors declare that they have no conflicts of interest.

## Acknowledgments

This work was financially supported by the Scientific Research Project of CNOOC (China) Co. Ltd: Key technology research on drilling and completion of 20 million cubic meters of oil field in the west of South China Sea (CNOOC-KJ135ZDXM38ZJ05ZJ). We sincerely thank other persons in the China University of Petroleum for helping with the model established.

## References

- [1] Z. Chen, R. J. Novotny, R. Farias, A. Mendez, C. A. Pedroso, and L. H. C. Fernandes, "Gravel packing deep water long horizontal wells under low fracture gradient," in *Paper presented at the SPE Annual Technical Conference and Exhibition*, pp. 1–18, Houston, Texas, 2004.
- [2] Z. Shengtian, L. Zhaomin, and D. Changyin, "The advances of numerical simulation for gravel packing in horizontal wells," *Mechanics and Practice.*, vol. 31, no. 3, pp. 9–15, 2009.
- [3] Z. Chen, "The application of light and ultra-light weight proppant in horizontal well sand control: unified model and case histories," in *Paper presented at the SPE Deepwater Drilling and Completions Conference*, pp. 1–12, Galveston, Texas, USA, 2012.
- [4] A. T. Jardim Neto, F. G. M. Prata, J. R. R. Gomez, C. A. A. Pedroso, M. O. O. Martins, and D. N. N. Silva, "Ultralightweight proppants: an effective approach to address problems in long horizontal gravel packs offshore Brazil," *SPE Drilling & Completion*, vol. 27, no. 4, pp. 613–624, 2012.
- [5] R. Farias, J. Li, A. Vilela, and R. S. Aboud, "Openhole horizontal gravel packing offshore Brazil: best practices and lessons learned from 72 operations," in *Paper presented at the Latin American & Caribbean Petroleum Engineering Conference*, pp. 1–19, Buenos Aires, Argentina, 2007.
- [6] B. Baser, S. Shenoy, B. Gadiyar, S. Jain, and M. Parlar, "An alternative method of dealing with pressure: friction reducer for water packing of long horizontal open holes in low-fracturing-gradient environments," *SPE Drilling & Completion*, vol. 25, no. 3, pp. 300–308, 2010.
- [7] W. Meng, S. Zhou, D. Jiang et al., "Research on low-density gravel packing technique plan for long horizontal wells in offshore sup-shallow gas pools," *China Offshore Oil and Gas.*, vol. 31, no. 3, pp. 147–151, 2019.
- [8] L. G. Jones, C. S. Yeh, T. J. Yates, D. W. Bryant, M. W. Doolittle, and J. C. Healy, "Alternate path gravel packing," in *Paper presented at the SPE Annual Technical Conference and Exhibition*, pp. 391–398, Dallas, Texas, 1991.
- [9] C. S. Yeh, S. Clingman, B. A. Dale et al., "Unlocking the limits of extreme length in alternate path gravel packing," in *IPTC 12549, International Petroleum Technology Conference*, pp. 1–13, Kuala Lumpur, Malaysia, 2008.
- [10] B. N. Rao and A. M. Amin, "A flow simulator for the design of extreme-length gravel packs utilizing alternate-path technology," in *Paper presented at the SPE International Symposium and Exhibition on Formation Damage Control*, p. SPE-128068-MS, Lafayette, Louisiana, USA, 2010.
- [11] A. Kumar, B. Gadiyar, M. Langlais, G. Woiceshyn, A. Dikshit, and M. Parlar, "Development and qualification of enhanced shunted screens for openhole gravel packing of long intervals," in *Paper presented at the SPE Annual Technical Conference and Exhibition, Virtual*, p. SPE-201731-MS, Denver, Colorado, USA, 2020.
- [12] J. Jeanpert, T. Banning, C. Abad, I. Mbamalu, and J. Hardy, "Successful installation of horizontal openhole gravel-pack completions in low fracture gradient environment: a case history from deepwater west Africa," in *Paper presented at the SPE International Conference and Exhibition on Formation Damage Control*, p. SPE-189492-MS, Lafayette, Louisiana, USA, 2018.
- [13] M. T. Hecker, M. D. Barry, C. M. Sweeney, S. P. Arnold, and C. S. Yeh, "Extending openhole gravel packing capability:



- initial field installation of internal shunt alternate path technology,” in *Paper presented at the SPE Annual Technical Conference and Exhibition*, p. SPE-135102-MS, Florence, Italy, 2010.
- [14] B. N. Rao, A. M. Amin, R. Van Petegeg, and J. Broussard, “On the hydraulics of inverted flow path gravel pack operations,” in *Paper presented at the SPE International Symposium and Exhibition on Formation Damage Control*, p. SPE-151803-MS, Lafayette, Louisiana, USA, 2012.
- [15] A. Mimouna, A. Verma, and M. N. Guddati, “Generalized framework to simulate gravel packing in wellbore completions,” in *Paper presented at the Offshore Technology Conference*, p. OTC-28683-MS, Houston, Texas, USA, 2018.
- [16] L. G. Jones, R. J. Tibbles, L. Myers, D. Bryant, J. Hardin, and G. Hurst, “Gravel packing horizontal wellbore with leak-off using shunts,” in *Paper presented at the SPE Annual Technical Conference and Exhibition*, p. SPE-38640-MS, San Antonio, Texas, 1997.
- [17] P. M. Saldungaray, J. C. Troncoso, and B. T. Santoso, “Simultaneous gravel packing and filter cake removal in horizontal wells applying shunt tubes and novel carrier and breaker fluid,” in *Paper presented at the SPE Middle East Oil Show*, p. SPE-68205-MS, Manama, Bahrain, 2001.
- [18] K. Godwin, B. Gadiyar, and H. Riordan, “Simultaneous gravel packing and filtercake cleanup with shunt tubes in open-hole completions: a case history from the Gulf of Mexico,” in *Paper presented at the SPE Annual Technical Conference and Exhibition*, p. SPE-71672-MS, New Orleans, Louisiana, 2001.
- [19] G. Hurst, S. D. Cooper, W. D. Norman et al., “Alternate path completions: a critical review and lessons learned from case histories with recommended practices for deepwater applications,” in *Paper presented at the SPE International Symposium and Exhibition on Formation Damage Control*, p. SPE-86532-MS, Lafayette, Louisiana, 2004.
- [20] A. Dikshit, A. Kumar, M. Langlais, B. Gadiyar, G. Woiceshyn, and M. Parlar, “Extending openhole gravel-packing intervals through enhanced shunted screens,” *SPE Drilling and Completion*, vol. 36, no. 2, pp. 445–458, 2021.
- [21] P. Pillai, C.-C. Lin, J. Brege et al., “Industry first openhole alternate path gravel pack completion in HPHT environment: fluid development and caase history,” in *Paper presented at the SPE Annual Technical Conference and Exhibition*, p. SPE-206048-MS, Dubai, UAE, 2021.
- [22] S. Saebi, “The evolution of completion designs using alternate path (shunt-tubes) technology,” in *Paper presented at the SPE Oil and Gas India Conference and Exhibition*, p. SPE-155129-MS, Mumbai, India, 2012.
- [23] A. L. Martins, J. V. M. de Magalhaes, A. Calderon, and C. M. Chagas, “A mechanistic model for horizontal gravel pack displacement,” *SPE Journal*, vol. 10, no. 3, pp. 229–237, 2005.

## Research Article

# Calculation Model of Relative Permeability in Tight Sandstone Gas Reservoir with Stress Sensitivity

Jin Yan,<sup>1</sup> Rongchen Zheng,<sup>1</sup> Peng Chen <sup>1,2</sup> Shuping Wang,<sup>1</sup> and Yunqing Shi<sup>1</sup>

<sup>1</sup>State Key Laboratory of Shale Oil and Gas Enrichment Mechanisms and Effective Development, Beijing 100083, China

<sup>2</sup>School of Geosciences, Yangtze University, Hubei, Wuhan 430100, China

Correspondence should be addressed to Peng Chen; ccpeng2008@126.com

Received 6 September 2021; Revised 3 November 2021; Accepted 24 November 2021; Published 10 December 2021

Academic Editor: Jinjie Wang

Copyright © 2021 Jin Yan et al. This is an open access article distributed under the Creative Commons Attribution License, which permits unrestricted use, distribution, and reproduction in any medium, provided the original work is properly cited.

During the development of tight gas reservoir, the irreducible water saturation, rock permeability, and relative permeability change with formation pressure, which has a significant impact on well production. Based on capillary bundle model and fractal theory, the irreducible water saturation model, permeability model, and relative permeability model are constructed considering the influence of water film and stress sensitivity at the same time. The accuracy of this model is verified by results of nuclear magnetic experiment and comparison with previous models. The effects of some factors on irreducible water saturation, permeability, and relative permeability curves are discussed. The results show that the stress sensitivity will obviously reduce the formation permeability and increase the irreducible water saturation, and the existence of water film will reduce the permeability of gas phase. The increase of elastic modulus weakens the stress sensitivity of reservoir. The irreducible water saturation increases, and the relative permeability curve changes little with the increase of effective stress. When the minimum pore radius is constant, the ratio of maximum pore radius to minimum pore radius increases, the permeability increases, the irreducible water saturation decreases obviously, and the two-phase flow interval of relative permeability curve increases. When the displacement pressure increases, the irreducible water saturation decreases, and the interval of two-phase flow increases. These models can calculate the irreducible water saturation, permeability and relative permeability curves under any pressure in the development of tight gas reservoir. The findings of this study can help for better understanding of the productivity evaluation and performance prediction of tight sandstone gas reservoirs.

## 1. Introduction

With more and more tight gas reservoirs are put into development around the world, tight gas reservoirs have become an important part of the current natural gas production. Tight sandstone gas is an unconventional natural gas resource, which exists in tight sandstone reservoirs, and its permeability is generally less than 0.1 mD [1–3]. Such reservoirs generally have no natural capacity or extremely low capacity, and they can only be exploited under certain economic and technical conditions. Because most of tight sandstone gas reservoirs are firstly tight and then accumulate, they have obvious characteristics of near-source accumulation. Due to the influence of factors such as sedimentation, accumulation, and reservoir physical properties, the occurrence state of formation water is diverse in tight gas reser-

voirs. In the production process, gas well produces water, which severely restricts the benefit of gas reservoir development [4, 5]. In addition, the reservoir is prone to stress-sensitive effects, which results in a rapid decline. Therefore, it is necessary to study the change characteristics of permeability and relative permeability curve during the development of tight sandstone gas reservoirs.

When the effective stress is increased in tight gas reservoirs, the pores will undergo elastic and plastic deformation, and the stress-sensitive effect will cause the porosity and permeability to decrease. Many scholars have studied the mechanism of reservoir stress sensitivity through physical simulation methods [6–10]. These experimental results show that the permeability decreases significantly and the porosity changes little with the increase of confining pressure [10–12]. These physical simulation experiments are

only suitable for research on specific objects under given conditions and cannot reflect the change characteristics of reservoir physical properties during the development of gas reservoir. On the basis of rock mechanics, some scholars construct a mathematical model of permeability changing with confining pressure and have realized effective prediction of permeability during the decrease of reservoir pressure [13, 14]. Through experimental data fitting, some scholars have constructed the relationship model between permeability and effective stress, which mainly include exponential model, logarithmic model, and linear relationship model [15–17]. These models based on experimental data only reveal the relationship between permeability and effective stress and do not reflect the mechanism of stress-sensitive effects. Based on the theory of elastic mechanics, some models are established to describe the mechanism of stress sensitivity. Cao and Lei establish a permeability model in tight reservoirs, which considers the stress sensitivity based on the Hertz contact deformation principle [18]. Xu constructs digital core samples with different porosity and different pore size distributions by the four-parameter random growth model and gives a permeability model using elastic mechanics theory [19]. Although the above models can calculate the formation permeability, it is not suitable for multiphase fluids and cannot obtain the relative permeability curve of two-phase flow. At present, most gas-water phase relative permeability curves are obtained through core experiments. Due to the limitation of experimental conditions, the measured relative permeability curve cannot simulate the characteristics of two-phase flow after stress sensitivity in tight reservoirs [20, 21]. Some scholars establish two-phase relative permeability calculation models based on different methods. Yan et al. constructs the permeability model and the relative permeability model using numerical core technology and lattice Boltzmann method, which can calculate the core relative permeability curve by  $T_2$  spectrum, but these methods cannot be used in stress-sensitive reservoirs [22]. Based on the capillary bundle model and fractal theory, Lei et al. construct a two-phase flow model considering stress sensitivity, but the model does not consider the influence of water film in a tight sandstone gas reservoir [23]. Due to the hydrophilicity of formation, bound water films are widespread in tight sandstone gas reservoirs [24]. Derjaguin and Churaev use DLVO theory to establish a thickness model of fluid film and explain the influence factors of water film thickness [24]. Su et al. use the capillary bundle model and the fractal theory to establish the irreducible water saturation calculation model with the influence of stress sensitivity and analyze the influence of water film thickness on the irreducible water saturation of tight reservoirs [25].

The above studies show that water film and stress-sensitive effect are common in tight reservoirs and have a significant impact on the fluid flow capacity (Figure 1). At present, only one of them is considered in some calculation models of permeability and relative permeability in tight reservoirs, and it is urgent to establish relevant mathematical models considering both water film and stress sensitivity. Based on the capillary bundle model and the fractal theory,

this paper constructs a model of irreducible water saturation under the given pressure differences and gives a permeability model and a calculation model of relative permeability curve considering the stress sensitivity and water film in tight sandstone gas reservoirs. These models are used to discuss the influence of some factors on irreducible water saturation, permeability, and relative permeability curve.

## 2. Mathematical Model

*2.1. Model of Irreducible Water Saturation.* In nature, both the part and the whole of an object have self-similarity, which conforms to the principle of fractal. In tight sandstone reservoirs, the pore structure also has fractal characteristics, and the size distribution of pore can be characterized as follows [26]:

$$N(r) = \int_r^{r_{\max}} f(r) dr = \left( \frac{r_{\max}}{r} \right)^{D_f}, \quad (1)$$

where  $N(r)$  is the capillary number,  $r$  is the radius of capillary,  $r_{\max}$  is the maximum radius of capillary,  $f(r)$  is the distribution function of capillary bundle, and  $D_f$  is the pore area fractal dimension.

By deriving from the above formula, the expression of capillary bundle quantity function  $f(x)$  can be obtained as follows:

$$f(r) = D_f r_{\max}^{D_f} r^{-D_f-1}. \quad (2)$$

According to the rock characteristics of tight reservoirs and the fractal principle, the fractal dimension  $D_f$  can be written as [26]

$$D_f = d - \frac{\ln \phi}{\ln (r_{\min}/r_{\max})}, \quad (3)$$

where  $d$  is the Euclidean dimension,  $d=2$  in two-dimensional space.  $\phi$  is the porosity, and  $r_{\min}$  is the minimum radius of capillary.

The core is simplified as a capillary bundle model. Due to the certain curvature of the pore in the core, the length of capillary bundle is generally greater than the apparent length. According to the fractal theory, there is self-similarity between the actual length and the characteristic length of capillary bundle, and the actual length of capillary bundle can be expressed as [26]

$$L(r) = (2r)^{1-D_T} L_0^{D_T}, \quad (4)$$

where  $D_t$  is the tortuosity fractal dimension, and it is [26]

$$D_T = 1 + \frac{\ln \bar{\tau}}{\ln (L_0/2\bar{r})}, \quad (5)$$

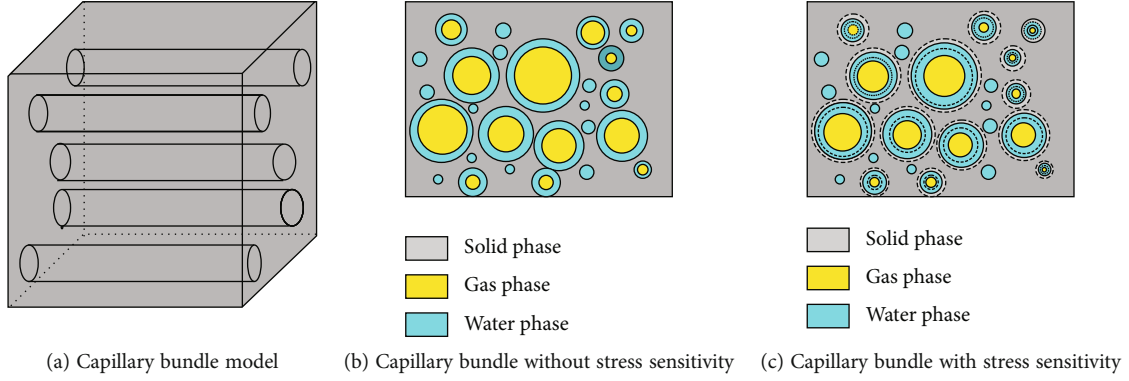


FIGURE 1: The distribution of gas and water in capillary bundle model [25].

where  $\bar{\tau}$  is the average tortuosity, and  $L_0$  is the capillary characteristic length. They can be written as [27, 28]

$$\bar{\tau} = \frac{1}{2} \left[ 1 + \frac{1}{2} \sqrt{1-\phi} + \frac{\sqrt{(1-\sqrt{1-\phi})^2 + 0.25(1-\phi)}}{1-\sqrt{1-\phi}} \right], \quad (6)$$

$$\frac{L_0}{2\bar{\tau}} = \frac{D_f - 1}{\sqrt{D_f}} \sqrt{\frac{1-\phi}{4\phi} \frac{\pi}{2-D_f} \frac{r_{\max}}{r_{\min}}}. \quad (7)$$

Regarding the core as a capillary bundle model, the bound water includes the immovable water in the thin capillary tubes and the water film retained water in the general capillary tubes. Immovable water in the thin capillaries mainly refers to the water that does not flow in these capillaries when the displacement pressure is less than the capillary pressure. In general, due to the hydrophilicity of rocks and minerals, a layer of water film is produced on the wall of wide capillary tubes. The irreducible water saturation is the sum of immovable water saturation and water film retention water saturation, which can be written as

$$S_{wc} = S_{wn} + S_{wf}, \quad (8)$$

where  $S_{wc}$  is the irreducible water saturation,  $S_{wn}$  is the immovable water saturation in fine capillaries, and  $S_{wf}$  is the water saturation of water film.

In thin capillaries, the water cannot flow due to the capillary force, and the capillary is completely saturated with water. According to the capillary bundle model and the fractal principle, the water content volume in the part of capillary bundle can be written as

$$\begin{aligned} V_{wn} &= \int_{r_{\min}}^{r_{\max}} \pi r^2 L(r) f(r) dr - \int_{r_c}^{r_{\max}} \pi r^2 L(r) f(r) dr \\ &= \int_{r_{\min}}^{r_c} \pi r^2 L(r) f(r) dr, \end{aligned} \quad (9)$$

where  $V_{wn}$  is the immovable water volume in fine capillaries, and  $r_c$  is the minimum flow pore radius under a certain dis-

placement pressure in the capillary bundle model. The capillary force in the capillary is equal to the displacement pressure, which can be expressed as

$$r_c = \frac{2\sigma \cos \theta}{p_d}, \quad (10)$$

where  $\sigma$  is the interfacial tension,  $\theta$  is the wetting angle, and  $p_d$  is the displacement pressure.

The interfacial tension is affected by factors such as temperature, pressure, fluid composition, and other factors. For the gas-water interfacial tension, the calculation formula is [29]

$$\sigma = \frac{1.8(137.78 - T)}{206} [\sigma(23.33) - \sigma(137.78)] + \sigma(137.78), \quad (11)$$

where  $T$  is the temperature,  $\sigma(23.33) = 76 \exp(-0.0362575 p)$ ,  $\sigma(137.78) = 52.5 - 0.87018 p$ .

In thick capillaries, the surface of pores is covered by a layer of water film. Li et al. analyze by microtube experiments that the thickness of water film has a linear relationship with fluid viscosity and a power function relationship with capillary radius. The water film thickness formula can be expressed as [25]

$$\delta = \begin{cases} r \times 0.25763 e^{-0.261r} (\nabla p)^{-0.419} \mu_w & \nabla p < 1 \text{ MPa/m}, \\ r \times 0.25763 e^{-0.261r} \mu_w & p > 1 \text{ MPa/m}, \end{cases} \quad (12)$$

where  $\delta$  is water film thickness,  $\nabla p$  is the pressure gradient, and  $\mu$  is the viscosity of water.

Since the viscosity of water is mainly affected by temperature, relevant scholars have given the relationship between viscosity and temperature [30]:

$$\mu_w = 0.001792 \exp \left[ -1.94 - 4.8 \frac{273.15}{T} + 6.74 \left( \frac{273.15}{T} \right)^2 \right]. \quad (13)$$

In a capillary with water film, the retained water volume of water film is equal to the total volume of capillary minus the gas filling volume, which can be expressed as

$$V_{wf} = \int_{r_c}^{r_{\max}} \pi [r^2 - (r - \delta)^2] L(r) f(r) dr, \quad (14)$$

where  $V_{wf}$  is the water volume of water film.

The volume of total bound water in a capillary bundle model is

$$\begin{aligned} V_{wc} &= V_{wn} + V_{wf} \\ &= \int_{r_{\min}}^{r_c} \pi r^2 L(r) f(r) dr + \int_{r_c}^{r_{\max}} \pi [r^2 - (r - \delta)^2] L(r) f(r) dr. \end{aligned} \quad (15)$$

The irreducible water saturation in the capillary bundle model is the ratio of the total irreducible water volume to the pore volume, which can be expressed as

$$\begin{aligned} S_{wc} &= \frac{V_{wn} + V_{wf}}{V_p} \\ &= \frac{\int_{r_{\min}}^{r_c} \pi r^2 L(r) f(r) dr + \int_{r_c}^{r_{\max}} \pi [r^2 - (r - \delta)^2] L(r) f(r) dr}{\int_{r_{\min}}^{r_{\max}} \pi r^2 L(r) f(r) dr}, \end{aligned} \quad (16)$$

where  $V_p$  is the pore volume.

**2.2. Model of Irreducible Water Saturation with Stress Sensitivity.** In the development of gas reservoirs, the decrease of formation pressure will lead to pore compression, pore radius reduces, and rock permeability decreases. According to Hertzian contact theory, the relationship between capillary radius and effective stress is as follows [31]:

$$r' = r \left\{ 1 - 4 \left[ \frac{3\pi(1 - \nu^2) P_{eff}}{4E} \right]^\beta \right\}, \quad (17)$$

where  $E$  is the elastic modulus,  $\nu$  is the Poisson's ratio,  $\beta$  is a constant, and the superscript  $'$  is the relevant parameters after stress sensitivity.

After the stress sensitivity effect occurs, the pore volume of capillary bundle model will change, the model constructed by Harari characterizes the relationship between porosity and effective stress, and it is written as [32]

$$\phi' = 1.09 \phi p_{eff}^{-0.0152}. \quad (18)$$

According to equations (17) and (18), the porosity and radius of rock will decrease after the stress-sensitive effect

occurs. The pore area fractal dimension with stress sensitivity effect can be written as

$$D'_f = d - \frac{\ln \phi'}{\ln (r'_{\min}/r'_{\max})}. \quad (19)$$

The tortuosity fractal dimension with stress sensitivity effect can be expressed as

$$D'_T = 1 + \frac{\ln \bar{r}'}{\ln (L'_0/2r')}, \quad (20)$$

where  $\bar{r}'$  and  $L'_0/2r'$  can be written as

$$\bar{r}' = \frac{1}{2} \left[ 1 + \frac{1}{2} \sqrt{1 - \phi'} + \frac{\sqrt{(1 - \sqrt{1 - \phi'})^2 + 0.25(1 - \phi')}}{1 - \sqrt{1 - \phi'}} \right], \quad (21)$$

$$\frac{L'_0}{2r'} = \frac{D'_f - 1}{\sqrt{D'_f}} \sqrt{\frac{1 - \phi'}{4\phi'} \frac{\pi' r'_{\max}}{2 - D'_f r'_{\min}}}. \quad (22)$$

The volume of bound water is the sum of the volume of water in the thin capillaries after radius changes and the volume of formation water in the thick capillaries, which can be expressed as

$$V'_{wc} = \int_{r'_{\min}}^{r_c} \pi r'^2 L'(r) f'(r) dr + \int_{r_c}^{r'_{\max}} \pi [r'^2 - (r - \delta)^2] L'(r) f'(r) dr. \quad (23)$$

After the formation pressure drops, the irreducible water saturation is equal to the ratio of irreducible water saturation to the changed pore volume, so it is

$$S'_{wc} = \frac{\int_{r'_{\min}}^{r_c} \pi r'^2 L'(r) f'(r) dr + \int_{r_c}^{r'_{\max}} \pi [r'^2 - (r - \delta)^2] L'(r) f'(r) dr}{\int_{r'_{\min}}^{r'_{\max}} \pi r'^2 L'(r) f'(r) dr}. \quad (24)$$

The formation water will expand due to its elastic energy, and its elastic compressibility can be expressed as [33]

$$C_w = 145.03 \times 10^{-6} (a + b + c^2), \quad (25)$$

where  $C_w$  is the elastic compressibility of water,  $a$ ,  $b$ , and  $c$  are the coefficients, and they can be written as

$$a = 3.8546 - 1.9435 \times 10^{-2} p, \quad (26)$$

$$b = -0.01052 + 6.9179 \times 10^{-5} p, \quad (27)$$

$$c = 3.9267 \times 10^{-5} - 1.2763 \times 10^{-7} p. \quad (28)$$



After the formation pressure drops, the volume of movable water is equal to the volume of formation water after hydro elastic expansion minus the volume of bound water. It is written as

$$\Delta V_w = (1 + C_w \Delta p) V_w - V'_{wc}, \quad (29)$$

where  $\Delta V_w$  is the increased volume of movable water after stress sensitivity, and  $\Delta p$  is the pressure drop.

The movable water saturation can be expressed as

$$\Delta S_w = \frac{(1 + C_w \Delta p) V_w - V'_{wc}}{\int_{r'_{\min}}^{r'_{\max}} \pi r^2 L'(r) f'(r) dr}. \quad (30)$$

**2.3. Permeability Model.** In the capillary bundle, it is assumed that the pressure difference at both ends of the capillary bundle is  $\Delta p$ , and according to Poiseuille's law, the fluid flow in a single capillary bundle is

$$q = \frac{\pi r^4 \Delta p}{8 \mu L(r)}, \quad (31)$$

where  $q$  is the flow of single capillary.

The total flow of the core is the sum of all capillary flows in the capillary bundle model. The flow can be expressed as

$$\begin{aligned} Q &= \int_{r_{\min}}^{r_{\max}} \frac{\pi r^4 \Delta p}{8 \mu L(r)} f(r) dr \\ &= \int_{r_{\min}}^{r_{\max}} \frac{\pi r^4 \Delta p}{8 \mu (2r)^{1-D_T} L_0^{D_T}} D_f r_{\max}^{D_f} r^{-D_f-1} dr \\ &= \frac{\pi D_f r_{\max}^{D_f} (r_{\max}^{3+D_T-D_f} - r_{\min}^{3+D_T-D_f})}{8 \mu \times 2^{1-D_T} L_0^{D_T} (3 + D_T - D_f)} \Delta p, \end{aligned} \quad (32)$$

where  $Q$  is the total flow of capillary bundle model.

According to Darcy's law, the flow can be expressed as

$$Q = \frac{KA \Delta p}{\mu L}, \quad (33)$$

where  $K$  is the permeability, and  $A$  is the cross-sectional area.

By introducing equation (32) in equation (33), the permeability of rock can be calculated. The permeability can be expressed as

$$K = \frac{2^{D_T} \pi D_f r_{\max}^{D_f} (r_{\max}^{3+D_T-D_f} - r_{\min}^{3+D_T-D_f})}{16 A L_0^{D_T-1} (3 + D_T - D_f)}. \quad (34)$$

According to the fractal principle, there are

$$A = \frac{\pi D_f r_{\max}^2}{\phi(2 - D_f)}, L_0 = \sqrt{A} = \sqrt{\frac{\pi D_f r_{\max}^2}{\phi(2 - D_f)}}. \quad (35)$$

Stress sensitivity is common in tight reservoirs. After the stress sensitivity occurs, the porosity and radius will decrease, and its permeability will also decrease. Considering the influence of stress-sensitivity effect, the permeability expression can be written as

$$K' = \frac{2^{D_T'} \pi D_f' r_{\max}^{D_f'} (r_{\max}^{3+D_T'-D_f'} - r_{\min}^{3+D_T'-D_f'})}{16 A' L_0'^{D_T'-1} (3 + D_T' - D_f')}, \quad (36)$$

where the cross-sectional area  $A'$  and the capillary characteristic length  $L_0'$  with stress sensitivity can be expressed as

$$A' = \frac{\pi D_f'^2 r_{\max}^2}{\phi'(2 - D_f')}, L_0' = \sqrt{A'} = \sqrt{\frac{\pi D_f'^2 r_{\max}^2}{\phi'(2 - D_f')}}. \quad (37)$$

**2.4. Relative Permeability Model.** As a flow capacity curve describing multiphase fluid flowing in rock core at the same time, relative permeability curve is widely used in the development of oil and gas reservoirs. Many scholars study the relative permeability curve by mathematical model and physical simulation experiment [33–37]. Tsakiroglou proposes the analytical solution of the relative permeability by network simulations in porous reservoirs [38]. Based on the fractal theory, a relative permeability model is built in fracture networks, which is a function of saturation of water and gas [39]. Based on percolation theory and effective medium theory in, a model of two-phase permeability curve is established using the bimodal fractal model [40]. These studies provide a good idea for the application of fractal theory in relative permeability curve, but they do not consider the influence the water film and stress-sensitive effect. In tight gas reservoir, water film and stress-sensitive effect have an obvious influence on gas flow, and it is necessary to establish a calculation model of relative permeability.

Considering the influence of water film thickness on gas flow, the flow radius is equal to the pore radius minus the water film thickness. The permeability of gas phase and water phase can be calculated by Poiseuille's law and Darcy's law, and they can be written as [23]

$$K_g = \frac{2^{D_T} \pi (1 - S_w) D_f r_{\max}^{D_f}}{16 A L_0^{D_T-1}} \int_{r_{wg}}^{r_{\max}} (r - \delta)^{2+D_T-D_f} dr, \quad (38)$$

$$K_w = \frac{2^{D_T} \pi S_w D_f r_{\max}^{D_f}}{16 A L_0^{D_T-1}} \int_{r_c}^{r_{wg}} (r - \delta)^{2+D_T-D_f} dr, \quad (39)$$

where  $K_g$  is the permeability of gas phase,  $K_w$  is the permeability of water phase, and  $S_w$  is the water saturation.

Relative permeability is the ratio of phase permeability to inherent permeability, simultaneous equations (34), (38),

TABLE 1: Comparison of results between core experiment and model.

Well	Depth (m)	Length (cm)	Diameter (cm)	Porosity	Irreducible water saturation			Permeability		
					Experiment	Model	Error (%)	Experiment	Model	Error (%)
D16	2868	2.832	2.534	7.85	0.4471	0.4624	3.42	0.3228	0.3316	2.73
					0.4166	0.3977	4.53			
					0.3503	0.3467	1.02			
					0.2917	0.2976	2.03			
D22	2773	2.153	2.542	7.14	0.5126	0.5152	0.51	0.2328	0.2553	9.66
					0.4384	0.4451	1.54			
					0.3655	0.3936	7.69			
					0.3277	0.3424	4.49			

and (39), and the relative permeability of gas phase and water phase can be expressed as

$$K_{rg} = \frac{K_g}{K} = (1 - S_w)(3 + D_T - D_f) \frac{\int_{r_{wg}}^{r_{\max}} (r - \delta)^{2+D_T-D_f} dr}{r_{\max}^{3+D_T-D_f} - r_{\min}^{3+D_T-D_f}}, \quad (40)$$

$$K_{rw} = \frac{K_w}{K} = S_w(3 + D_T - D_f) \frac{\int_{r_c}^{r_{wg}} (r - \delta)^{2+D_T-D_f} dr}{r_{\max}^{3+D_T-D_f} - r_{\min}^{3+D_T-D_f}}, \quad (41)$$

where  $K_{rg}$  is the relative permeability of gas phase, and  $K_{rw}$  is the relative permeability of water phase.

After the occurrence of stress sensitivity, the pore structure changes and relevant parameters change, but the calculation principle of relative permeability remains unchanged. The relative permeability of gas phase and water phase can be expressed as

$$K'_{rg} = \frac{K'_g}{K'} = (1 - S'_w)(3 + D'_T - D'_f) \frac{\int_{r'_{wg}}^{r'_{\max}} (r - \delta)^{2+D'_T-D'_f} dr}{r'_{\max}^{3+D'_T-D'_f} - r'_{\min}^{3+D'_T-D'_f}}, \quad (42)$$

$$K'_{rw} = \frac{K'_w}{K'} = S'_w(3 + D'_T - D'_f) \frac{\int_{r'_c}^{r'_{wg}} (r - \delta)^{2+D'_T-D'_f} dr}{r'_{\max}^{3+D'_T-D'_f} - r'_{\min}^{3+D'_T-D'_f}}. \quad (43)$$

### 3. Model Validation

Nuclear magnetic resonance experiments can test the distribution characteristics of water in different pores. According to test results under different displacement pressures, the distribution of water saturation in rocks under different displacement pressures can be obtained. The irreducible water saturation of two cores under different displacement pressure is tested by nuclear magnetic resonance experiments, and the related parameters and experimental results are shown in Table 1. At the same time, the maximum pore

radius, the minimum pore radius, and the ratio between them can be calculated using the  $T_2$  spectrum curve. Based on the proposed irreducible water saturation model and permeability model, the water saturation and permeability of the core under different pressure can be obtained according to these characteristic parameters (Table 1). Comparing the irreducible water saturation and permeability calculated by the model with the core test results, it is found that the maximum error of the irreducible water saturation under different displacement pressure is 7.69%, the minimum error is 0.51, and the average is 3.15%. The maximum error of the permeability is 9.66%, the minimum error is 2.73%, and the average is 6.2%. The results of these models and the experimental results have relatively small errors, and these models can be used to predict irreducible water saturation and permeability under different displacement pressures.

This paper also gives a relative permeability model based on the fractal principle. The relative permeability curve calculated by the model is compared with the results of Li's model and Lei's model [23, 24]. In the calculation, the porosity is 0.2, the irreducible water saturation is 0.24, and the ratio of the maximum pore radius to the minimum pore radius is 100. The results show that the model is basically similar to the results of Li's model and Lei's model (Figure 2). The relative permeability of gas phase in this model is slightly lower than that of Lei's model without considering water film, indicating that the existence of water film has a certain influence on relative permeability curve. The relative permeability model proposed in this paper can meet the needs of practical applications.

### 4. Analysis and Discussion

In the section, the relevant parameters under given conditions are calculated by using the irreducible water saturation model, permeability model, and relative permeability model. The effects of rock elastic modulus, Poisson's ratio, the ratio of maximum pore radius to minimum pore radius, and minimum flowable pore radius on irreducible water saturation, permeability, and relative permeability are discussed.

*4.1. Elastic Modulus.* Elastic modulus is one of basic parameters to measure elastic deformation of rock, and its value

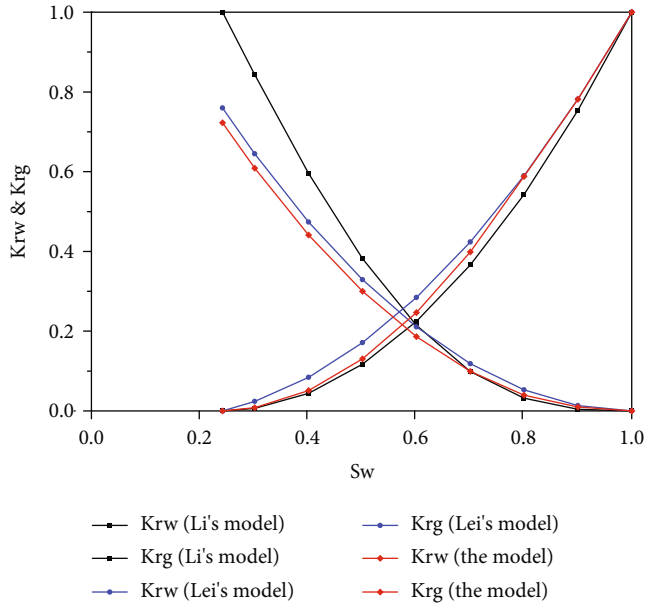


FIGURE 2: Results comparison of different relative permeability models with this model.

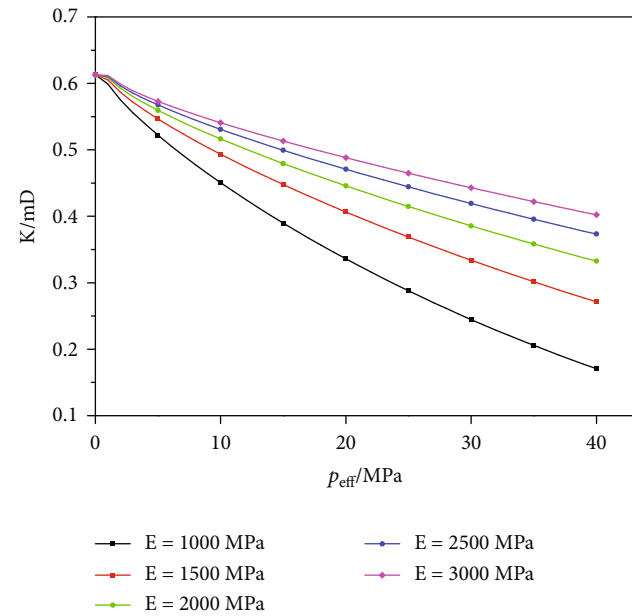


FIGURE 3: Relationship curve between permeability and effective stress under different elastic modulus.

reflects the degree of compressibility. When effective stress is certain, the larger the elastic modulus is, and the smaller the compressibility of rock is. Figure 3 shows the relationship between permeability and effective stress under different elastic modulus. With the increase of elastic modulus, the elasticity decreases, and the deformation amplitude of pore radius under the same effective stress decreases. Therefore, the larger the elastic modulus is, the larger the permeability retention value is. Figure 4 is the relationship between irreducible water saturation and effective stress under different elastic modulus. With the increase of elastic modulus, irre-

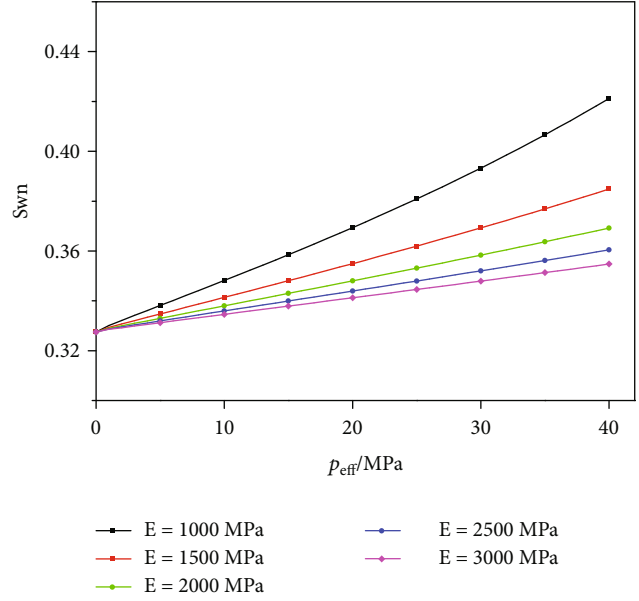


FIGURE 4: Relationship curve between irreducible water saturation and effective stress under different elastic modulus.

ducible water saturation decreases. This is due to the increase of elastic modulus, the number of nonflowing capillaries decreases under the same stress, so the irreducible water saturation decreases. When the effective stress increases, capillaries with radius less than the minimum flowable pore radius increase, and the irreducible water saturation increases. When the elastic modulus and effective stress changes in the capillary bundle, the capillary radius changes little. While the relative permeability curve mainly reflects the structural characteristics in the pore, the relative permeability curve changes little (Figure 5).

**4.2. Poisson's Ratio.** Poisson's ratio is other basic parameters to measure elastic deformation of rock, which represents the ratio of transverse strain to axial strain. Figure 6 is the relationship curve between permeability and effective stress under different Poisson's ratios. Poisson's ratio has little effect on rock permeability. With the increase of Poisson's ratio, the permeability increases to a certain extent, but the increase is very small, which indicates that the size of Poisson's ratio has little effect on the elastic compression of rock pores. Figure 7 shows the relationship curve between irreducible water saturation and effective stress under different Poisson's ratios. Since Poisson's ratio has little effect on elastic compression of rock pores, Poisson's ratio has little effect on irreducible water saturation. With the increase of Poisson's ratio, irreducible water saturation decreases slightly under the same effective stress, and Poisson's ratio has little effect on relative permeability curve.

**4.3. Ratio of Maximum Pore Radius to Minimum Pore Radius.** When the porosity and minimum pore radius are certain, the ratio of maximum pore radius to minimum pore radius represents the pore scale distribution interval. The larger the pore distribution interval is, the larger the radius

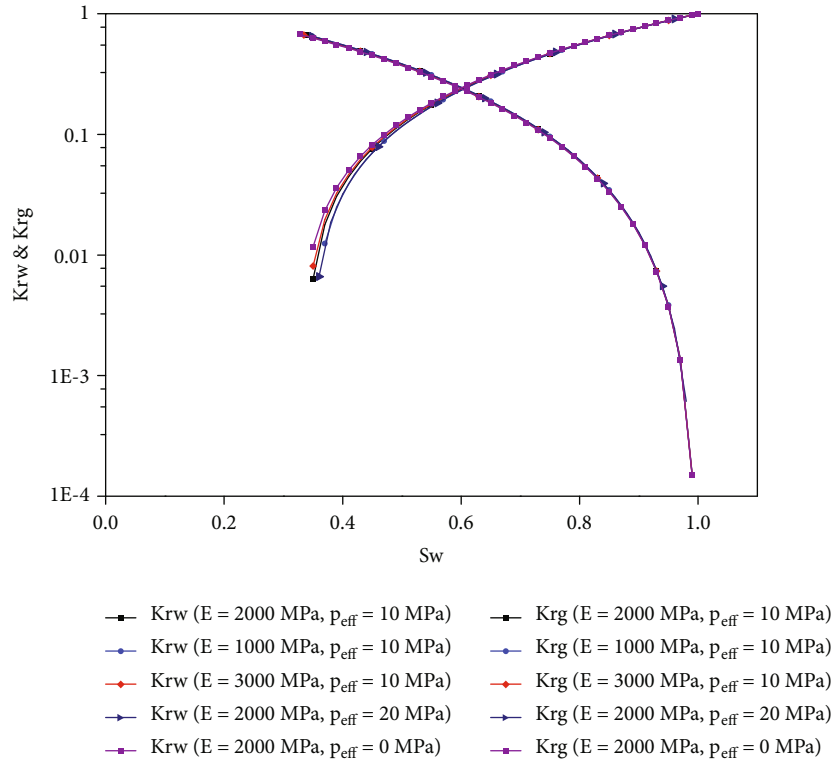


FIGURE 5: Relative permeability curve under different elastic modulus and effective stress.

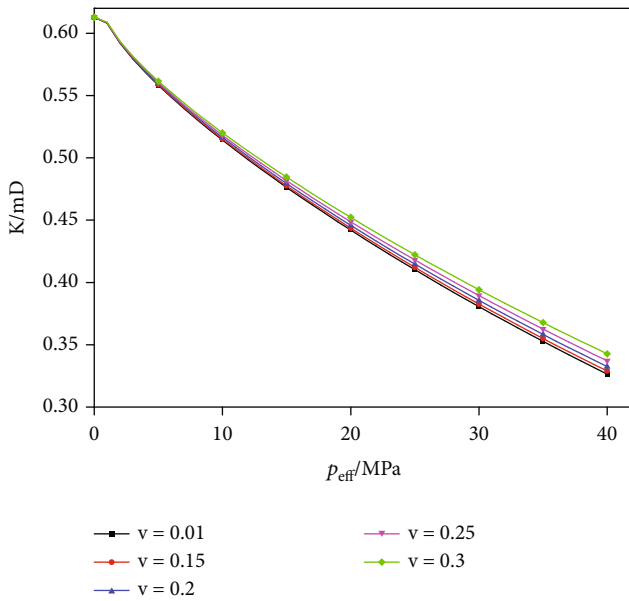


FIGURE 6: Relationship curve between permeability and effective stress under different Poisson's ratio.

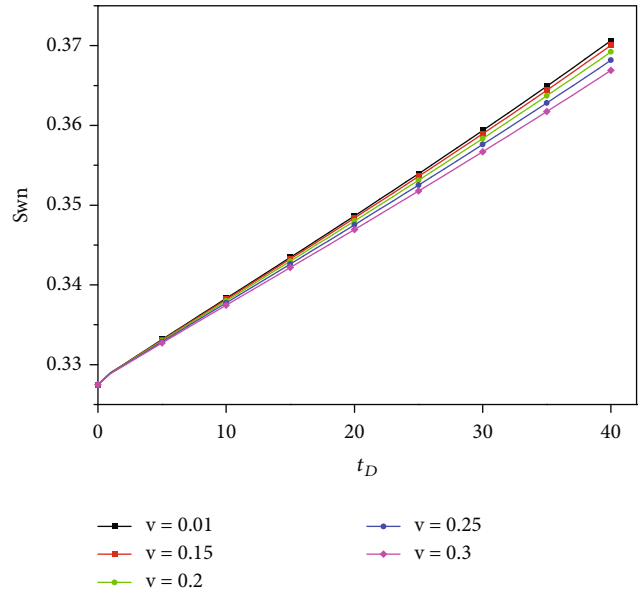


FIGURE 7: Relation curve between irreducible water saturation and effective stress under different Poisson's ratio.

of pores is in rock, and the flow capacity is enhanced, so the permeability is increased (Figure 8). The smaller the ratio of the maximum pore radius to the minimum pore radius is, this means that the pore radius is concentrated in the minimum pore radius' accessories. When the displacement pressure is constant, the minimum capillary radius which can be driven is a certain value, the more

bundle of capillary in the minimum pore channel and the minimum pore channel size space is, and therefore, the irreducible water saturation is higher (Figure 9). Figure 10 shows the curves of relative permeability under different ratios of the maximum pore radius to the minimum pore radius. The smaller the ratio is, the greater the irreducible water saturation is, the more the isotonic point moves to

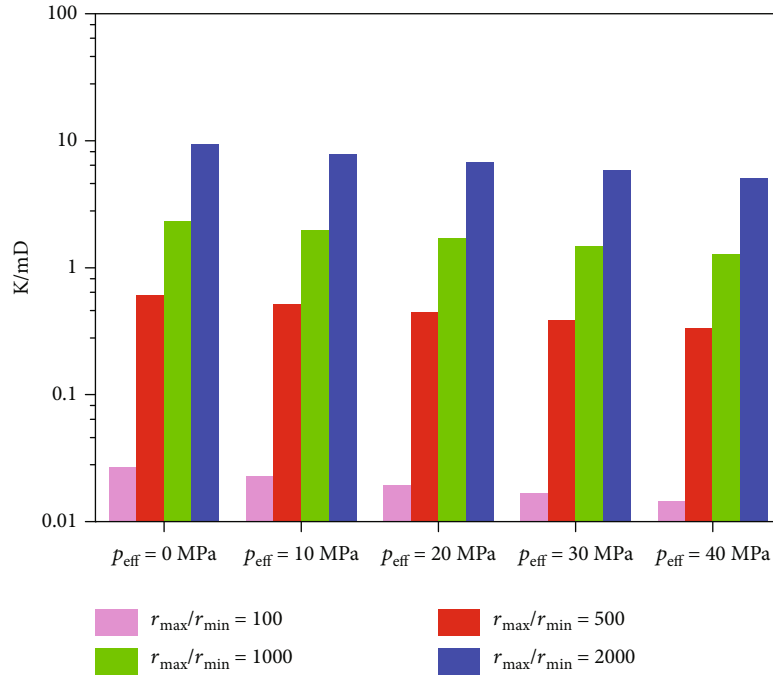


FIGURE 8: Permeability with different ratios of maximum pore radius to minimum pore radius.

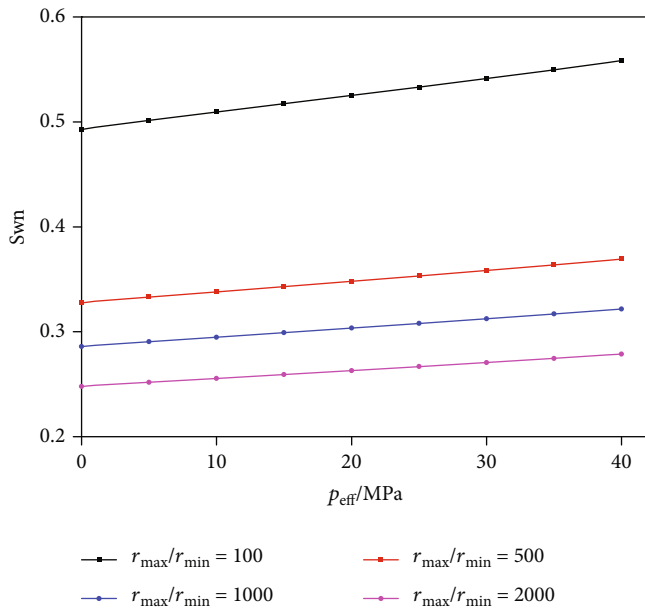


FIGURE 9: The relationship curve between irreducible water saturation and effective stress under different ratios of the maximum pore radius to the minimum pore radius.

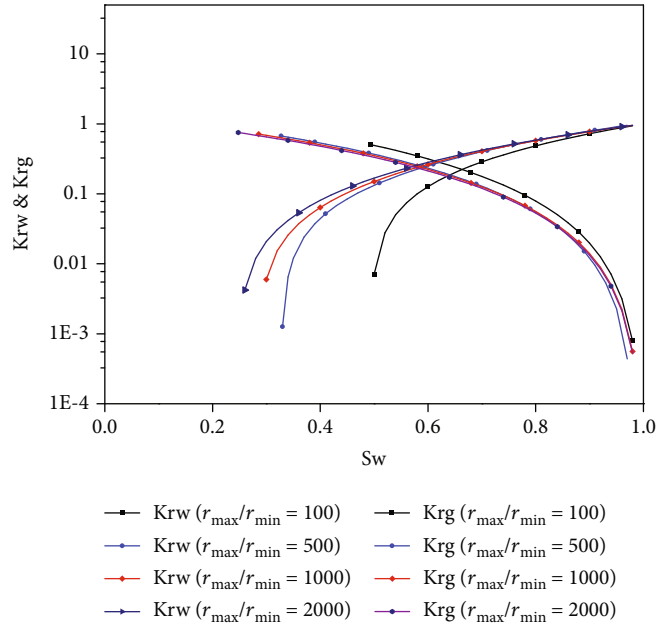


FIGURE 10: Curves of relative permeability under different ratios of the maximum pore radius to the minimum pore radius.

the right direction, the smaller the two-phase flow interval is, and the worse the flow capacity is.

**4.4. Minimum Flow Channel Radius.** In the reservoir, the minimum flow channel radius is mainly controlled by the displacement pressure difference. The larger the displacement pressure is, the smaller the minimum flow channel radius is. When the effective stress is constant, the displace-

ment pressure has no effect on the permeability. Therefore, the minimum flow channel radius has no effect on the rock permeability. The radius of minimum flow channel is larger, the more capillary bundles do not flow, therefore, the irreducible water saturation is greater (Figure 11). While the effective stress increases, the capillary bundle becomes small. When the minimum flow channel radius is constant, the effective stress increases, and the irreducible water saturation



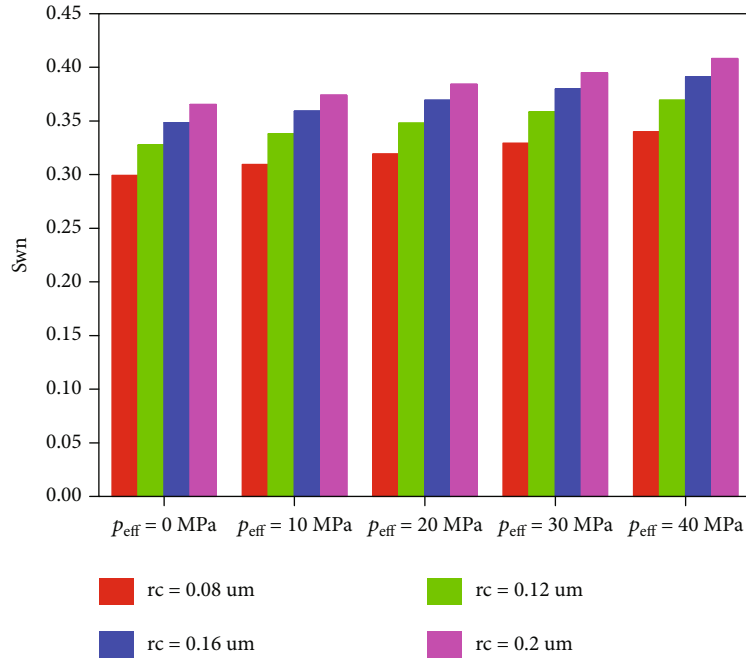


FIGURE 11: Irreducible water saturation under different minimum flow channel radius.

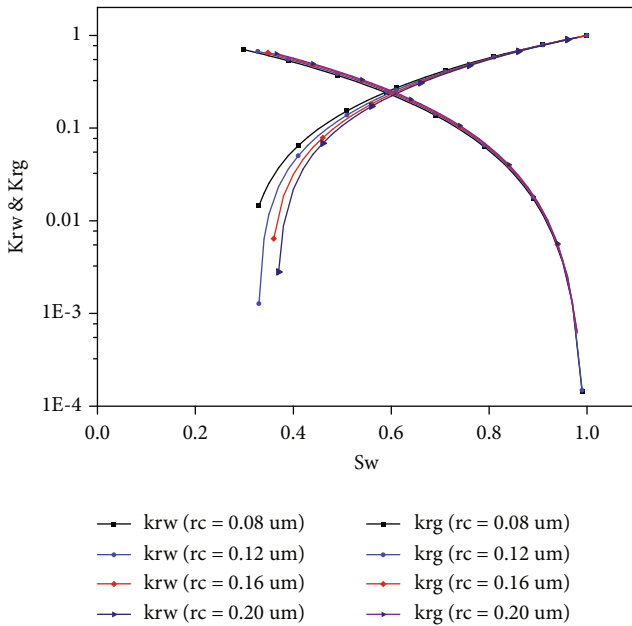


FIGURE 12: Relative permeability curves with different minimum flow channel radius.

increases. Figure 12 shows the two-phase relative permeability curves under different minimum flow channel radius. The smaller the minimum flow channel is, the greater the displacement pressure is, which mainly affects the two-phase flow space of the relative permeability curve.

### 5. Conclusion

Based on capillary bundle model and fractal theory, the model of irreducible water saturation, the permeability

model, and the relative permeability model are built in tight gas reservoirs, which can consider the effects of water film and stress sensitivity at the same time. The influence of some parameters is analyzed, which includes elastic modulus and Poisson’s ratio on irreducible water saturation, core permeability, and relative permeability curves. Through above works, some conclusions can be drawn:

- (1) Based on capillary bundle model and fractal theory, the model of irreducible water saturation, the permeability model, and the relative permeability model are constructed with the influence of irreducible water film and stress sensitivity. The above models can analyze some changes of irreducible water saturation, permeability, and relative permeability with formation pressure, which overcomes the fact that these parameters are regarded as pressure independent variables in most current studies
- (2) As the elastic modulus of rock increases, the stress-sensitive effect of reservoir is weakened. In the process of increasing effective stress, the increase in irreducible water saturation becomes smaller, the little in permeability decreases, and the relative permeability curve does not change much
- (3) Poisson’s ratio has little influence on irreducible water saturation, stress sensitivity effect, and relative permeability curve
- (4) When the porosity is constant and there are some large pores, the permeability increases significantly, the irreducible water saturation decreases significantly, and the two-phase flow interval increases. When the displacement pressure increases, the irreducible water saturation decreases

- (5) These models are only applicable to single porous media of reservoirs, and these application needs further research in fractured reservoirs

## Data Availability

The data in this manuscript will be available upon the readers' request.

## Conflicts of Interest

We declare that we have no competing interests.

## Acknowledgments

This work was supported by the Open Foundation of State Key Laboratory of Shale Oil and Gas Enrichment Mechanisms and Effective Development (GSYKY-B09-32).

## References

- [1] W. S. Spencer, "Geologic aspects of tight gas reservoirs in the Rocky Mountain region," *Journal of Petroleum Technology*, vol. 37, no. 7, pp. 1308–1314, 1985.
- [2] R. Rezaee, A. Saeedi, and B. Clennell, "Tight gas sands permeability estimation from mercury injection capillary pressure and nuclear magnetic resonance data," *Journal of Petroleum Science & Engineering*, vol. 88–89, pp. 92–99, 2012.
- [3] L. D. Sun, C. N. Zou, A. L. Jia et al., "Development characteristics and orientation of tight oil and gas in China," *Petroleum Exploration and Development*, vol. 46, no. 6, pp. 1015–1026, 2019.
- [4] H. Q. Song, Y. Cao, M. X. Yu, Y. H. Wang, J. E. Killough, and J. Leung, "Impact of permeability heterogeneity on production characteristics in water-bearing tight gas reservoirs with threshold pressure gradient," *Journal of Natural Gas Science and Engineering*, vol. 22, pp. 172–181, 2015.
- [5] H. Zhang, L. Wang, X. Wang et al., "Productivity analysis method for gas-water wells in abnormal overpressure gas reservoirs," *Petroleum Exploration and Development*, vol. 44, no. 2, pp. 280–285, 2017.
- [6] Y. F. Meng, C. B. Luo, G. Li, and H. B. Liu, "An experimental study on stress sensitivity of tight sandstone gas reservoirs during nitrogen drilling," *Arabian Journal of Geosciences*, vol. 12, no. 18, pp. 576–586, 2019.
- [7] A. P. S. Selvadurai, D. J. Zhang, and Y. L. Kang, "Permeability evolution in natural fractures and their potential influence on loss of productivity in ultra-deep gas reservoirs of the Tarim Basin, China," *Journal of Natural Gas Science and Engineering*, vol. 58, pp. 162–177, 2018.
- [8] Y. Wang, L. Jeannin, F. Agostini, L. Dormieux, F. Skoczylas, and E. Portier, "Experimental study and micromechanical interpretation of the poroelastic behaviour and permeability of a tight sandstone," *International Journal of Rock Mechanics and Mining Sciences*, vol. 103, pp. 89–95, 2018.
- [9] N. I. Christensen and H. F. Wang, "The influence of pore pressure and confining pressure on dynamic elastic properties of Berea sandstone," *Geophysics*, vol. 50, no. 2, pp. 207–213, 1985.
- [10] F. O. Jones and W. W. Owens, "A laboratory study of low-permeability gas sands," *Journal of Petroleum Technology*, vol. 32, no. 9, pp. 1631–1640, 1980.
- [11] P. Guo, J. Zhang, J. F. Du, Y. G. Xu, and G. S. Wu, "Study on core stress sensitivity for gas reservoir with two experiment method," *Journal of Southwest Petroleum university*, vol. 29, no. 2, pp. 7–9, 2007.
- [12] W. L. Xiao, M. Li, J. Z. Zhao, L. L. Zheng, and L. J. Li, "Laboratory study of stress sensitivity to permeability in tight sandstone," *Rock and Soil Mechanics*, vol. 31, no. 3, pp. 775–779, 2010.
- [13] W. Xiao, T. Li, M. Li, J. Zhao, L. Zheng, and L. Li, "Evaluation of the stress sensitivity in tight reservoirs," *Petroleum Exploration and Development*, vol. 43, no. 1, pp. 115–123, 2016.
- [14] P. F. Worthington, "The effect of scale on the petrophysical estimation of intergranular permeability," *Petrophysics*, vol. 45, no. 1, pp. 59–72, 2004.
- [15] F. M. Tiller, "The role of porosity in filtration part I: numerical methods," *Chemical Engineering Progress*, vol. 46, pp. 467–479, 1953.
- [16] R. W. Ostensen, "The effect of stress-dependent permeability on gas production and well testing," *SPE Formation Evaluation*, vol. 1, no. 3, pp. 227–235, 1986.
- [17] Q. Lei, W. Xiong, C. Yuan, and Y. S. Wu, "Analysis of stress sensitivity and its influence on oil production from tight reservoirs," in *Presented at the SPE Eastern Regional Meeting*, pp. 17–19, Lexington, Kentucky, 2007.
- [18] N. Cao and G. Lei, "Stress sensitivity of tight reservoirs during pressure loading and unloading process," *Petroleum Exploration and Development*, vol. 46, no. 1, pp. 138–144, 2019.
- [19] J. X. Xu, L. F. Yang, Y. H. Ding, Z. Liu, R. Gao, and Z. Wang, "Stress sensitivity analysis of the shalereservoir by the quartet structure generation set," *Natural Gas Science*, vol. 30, no. 9, pp. 1341–1348, 2019.
- [20] F. Civan and E. C. Donaldson, "Relative permeability from unsteady-state displacements with capillary pressure included," *SPE Formation Evaluation*, vol. 4, no. 2, pp. 189–193, 1989.
- [21] J. C. Xu, C. H. Guo, R. Z. Jiang, and M. Z. Wei, "Study on relative permeability characteristics affected by displacement pressure gradient: experimental study and numerical simulation," *Fuel*, vol. 163, pp. 314–323, 2016.
- [22] W. C. Yan, J. M. Sun, H. M. Dong, and L. K. Cui, "Investigating NMR-based absolute and relative permeability models of sandstone using digital rock techniques," *Journal of Petroleum Science and Engineering*, vol. 207, 2021.
- [23] G. Lei, P. C. Dong, Z. S. Wu et al., "A fractal model for the stress-dependent permeability and relative permeability in tight sandstones," *Journal of Canadian Petroleum Technology*, vol. 54, no. 1, pp. 36–48, 2015.
- [24] B. V. Derjaguin and N. V. Churaev, "Structural component of disjoining pressure," *Journal of Colloid and Interface Science*, vol. 49, no. 2, pp. 249–255, 1974.
- [25] Y. L. Su, J. G. Fu, L. Li et al., "A new model for predicting irreducible water saturation in tight gas reservoirs," *Petroleum Science*, vol. 17, no. 4, pp. 1087–1100, 2020.
- [26] P. Xu, S. Qiu, B. Yu, and Z. Jiang, "Prediction of relative permeability in unsaturated porous media with a fractal approach," *International Journal of Heat and Mass Transfer*, vol. 64, pp. 829–837, 2013.
- [27] B. M. Yu, "Fractal character for tortuous streamtubes in porous media," *Chinese Physics Letters*, vol. 22, no. 1, pp. 158–160, 2005.
- [28] B. M. Yu and J. H. Li, "A geometry model for tortuosity of flow path in porous media," *Chinese Physics Letters*, vol. 21, no. 8, pp. 1569–1571, 2004.

- [29] J. S. Yang and J. Y. Liu, *Practical Calculation of Gas Production*, Petroleum Industry Press, 2011.
- [30] S. Gupta, R. Helmig, and B. Wohlmuth, “Non-isothermal, multi-phase, multi-component flows through deformable methane hydrate reservoirs,” *Computational Geosciences*, vol. 19, no. 5, pp. 1063–1088, 2015.
- [31] G. Lei, Z. Z. Dong, W. R. Li, Q. Z. Wen, and C. Wang, “Theoretical study on stress sensitivity of fractal porous media with irreducible water,” *Fractals*, vol. 26, no. 1, 2017.
- [32] Z. Harari, W. Shu-Teh, and S. Salih, “Pore-compressibility study of arabian carbonate reservoir rocks,” *SPE Formation Evaluation*, vol. 10, no. 4, pp. 207–214, 1995.
- [33] Y. K. Zhang, H. B. Luan, Y. G. Si, J. G. Wang, and W. Q. Wang, “The fundamental parameters determining method for the well test analysis in the waterflood reservoir,” *Well Testing*, vol. 10, no. 6, pp. 23–25, 2001.
- [34] K. W. Li and R. N. Horne, “Comparison of methods to calculate relative permeability from capillary pressure in consolidated water-wet porous media,” *Water Resources Research*, vol. 42, no. 6, pp. 285–293, 2006.
- [35] F. Mo, X. L. Peng, D. Devegowda et al., “Permeability jail for two-phase flow in tight sandstones: formulation, application and sensitivity studies,” *Journal of Petroleum Science and Engineering*, vol. 184, 2020.
- [36] M. L. Delli and J. Grozic, “Experimental determination of permeability of porous media in the presence of gas hydrates,” *Journal of Petroleum Science & Engineering*, vol. 120, pp. 1–9, 2014.
- [37] K. Chen, H. Chen, and P. Xu, “A new relative permeability model of unsaturated porous media based on fractal theory,” *Fractals*, vol. 28, no. 1, article 2050002, 2020.
- [38] C. D. Tsakiroglou, “A method to calculate the multiphase flow properties of heterogeneous porous media by using network simulations,” *AIChE Journal*, vol. 57, no. 10, pp. 2618–2628, 2011.
- [39] T. J. Miao, A. M. Chen, Y. Xu, S. J. Cheng, and K. D. Wang, “A permeability model for water-gas phase flow in fractal fracture networks,” *Fractals*, vol. 26, no. 6, article 1850087, 2018.
- [40] S. P. Ojha, S. Misra, A. Sinha et al., “Relative permeability and production-performance estimations for Bakken, Wolfcamp, Eagle Ford, and Woodford shale formations,” *SPE Reservoir Evaluation & Engineering*, vol. 28, no. 2, pp. 307–324, 2018.

## Research Article

# Study on a Novel Water-Soluble Hydrophobically Associating Polymer as an Enhanced Heavy Oil Recovery Agent

Dongyu Qiao,<sup>1</sup> Zhongbin Ye ,<sup>1,2</sup> Xindong Wang,<sup>3</sup> Yiping Zheng,<sup>3</sup> Lei Tang,<sup>1</sup> and Nanjun Lai <sup>1,2</sup>

<sup>1</sup>School of Chemistry and Chemical Engineering of Southwest Petroleum University, Chengdu, 610500 Sichuan, China

<sup>2</sup>Oil & Gas Field Applied Chemistry Key Laboratory of Sichuan Province, Chengdu, 610500 Sichuan, China

<sup>3</sup>Engineer Technology Research Institute, CNPC Xibu Drilling Engineering Company Limited, Urumqi 830001, China

Correspondence should be addressed to Zhongbin Ye; yezb@swpu.edu.cn and Nanjun Lai; lainanjun@126.com

Received 8 September 2021; Accepted 30 September 2021; Published 3 November 2021

Academic Editor: Qingwang Yuan

Copyright © 2021 Dongyu Qiao et al. This is an open access article distributed under the Creative Commons Attribution License, which permits unrestricted use, distribution, and reproduction in any medium, provided the original work is properly cited.

In this study, emulsion-free radical reaction was applied to synthesize a novel sulfomethylating hydrophobically associating copolymer (HPDS) by using acrylamide, acrylic acid, NaHSO<sub>3</sub>, HCHO, and a laboratory-made N,N-divinylnonadeca-1,10-dien-2-amine to enhance heavy-oil recovery. The structure and properties of HPDS were characterized by a range of experiments, which showed that HPDS had better stability and enhanced heavy-oil recovery capacity than hydrolyzed polyacrylamide (HPAM). One-dimensional flooding experiments illustrated that HPDS performed better in establishing resistance factor (RF) and residual RF (RRF), and approximately 19.8% oil recovery could be enhanced by injecting 1500 mg/L of HPDS solution compared with that of HPAM at only 14.1%. HPDS has a promising application prospect in enhancing heavy-oil recovery.

## 1. Introduction

Heavy-oil reservoirs are one of the most important unconventional resources, with an enormous economic value and an abundant quantity of reserves. The application of thermal methods to enhance heavy-oil recovery has some crucial challenges due to economic and environmental obstacles [1, 2]. For example, SAGD is a thermal process requiring energy to turn water into steam, and it is commercially expensive. In addition, fresh water supply is another environmental issue inhibiting the application of thermal methods [3, 4].

Water flooding is a commonly used secondary recovery method in the industry because it is economically advantageous for the development of oil reservoirs; however, more than 60% of the heavy oil in place is usually still left after the technique is conducted [5, 6]. Polymer flooding is a technology wherein high-molecular-weight, water-soluble polymers are added to the injection water to increase the viscosity and reduce the mobility ratio of the injection water

and the crude oil to be displaced [7, 8]. One of the most commonly used polymers is the partially hydrolyzed polyacrylamide (HPAM) due to its rapidly soluble and large hydrodynamic volume, which could greatly enhance solution viscosity. Given the high sensibility of the HPAM chain in aqueous solution at high temperature and high salinity, a considerable loss in viscosity is possible owing to its molecules' random/coil conformation [9, 10].

In recent years, several efforts have been exerted to develop new polymers with superior performance at high temperature and high salinity, and some progresses have been made [11, 12]. Two approaches could be mainly used to make new polymers with preferable performance in harsh environments. The first is the introduction of hydrophobic groups [13–15]. An effective method to improve polymer salt tolerance and thermal stability is by increasing polymer hydrophobic interaction by introducing hydrophobic groups into the molecular chains. Polymers with hydrophobic groups exhibit similar viscosities in fresh and saline waters. The second is the introduction of salt-tolerant groups

[16–18]. The carboxyl groups in HPAM could easily react with  $\text{Ca}^{2+}$  and  $\text{Mg}^{2+}$  ions in the solution and form precipitate, resulting in phase separation or formation damage. If  $-\text{SO}_3\text{H}$  groups could be introduced to acrylamide (AM), the polymer could exhibit good thermal stability and increased tolerance with divalent and multivalent metal ions. In addition, the  $-\text{SO}_3\text{H}$  group is a strong polar group, and its strong hydrophilic interaction and electrostatic repulsion increase the water solubility of copolymers and the fluid volume of the molecular chain [19–21].

Inspired by predecessors' methods, a novel thermal stable and salt-tolerant polymer referred to as HPDS was synthesized by introducing sulfonic acid groups to a water-soluble hydrophobically associating polymer referred to as HPDN, which was prepared from AM, acrylic acid (AA), and another laboratory-made agent N,N-divinylnonadecan-1, 10-dien-2-amine (DNDA) in emulsion-free radical reaction. Then, a series of work was conducted to HPDS, such as characterization and performance testing.

## 2. Experimental

### 2.1. Materials

**2.1.1. Drugs.** AM was obtained commercially and purified by crystallization from a water-ethanol mixture. NaOH, AA,  $\text{NaHSO}_3$ ,  $(\text{NH}_4)_2\text{S}_2\text{O}_8$ , alkylphenol ethoxylates (OP-10), NaCl,  $\text{MgCl}_2 \cdot 6\text{H}_2\text{O}$ ,  $\text{CaCl}_2$ , and other chemicals were commercially available and used directly without further purification. DNDA was prepared in accordance with literature [22, 23]. Crude oil and HPAM came from Shengli Oilfield in Dongying (Shandong Province, China). Water was doubly distilled and deionized by passing through an ion exchange-column. All the other chemicals were of analytical grades, unless otherwise noted.

**2.1.2. Instrument.** WQF-520 infrared spectrometer (Beijing Rayleigh Analytical Instrument Co., Ltd.), Bruker AC-E 200 (Bruker BioSpin, Switzerland), S-3000 N scanning electron microscopy (SEM, Hitachi, Japan), Brookfield DV-III rheometer, HAAKE RheoStress 6000 rotational rheometer (Thermo Fisher Scientific, Waltham/Massachusetts), and Waring stirrer (LB20EG laboratory blender) were used in this study.

**2.2. Preparation of the HPDS.** Copolymerization of HPDN was carried out by emulsion-free radical polymerization. Seven grams of AM, 3 g of AA, 0.0361 g of DNDA, emulsifier (0.3 wt.%), and  $\text{NaHSO}_3$ - $(\text{NH}_4)_2\text{S}_2\text{O}_8$  initiator (0.2 wt.% and 1 : 1 mol ratio) were taken along with deionized water in a three-necked flask assembled with a nitrogen inlet. The reactor was kept in a water bath with magnetic stirring arrangement. Copolymerization was carried out at  $40^\circ\text{C}$  under  $\text{N}_2$  atmosphere for 10 h. The pH of the reaction was 7. The polymer was then isolated by precipitation with acetone or water-ethanol and dried in a vacuum oven at  $40^\circ\text{C}$  for 7 h to yield the corresponding copolymer.

A new sulfonylurea methylation modification displacing agent was synthesized through the reaction with HCHO and  $\text{NaHSO}_3$ . HPDN dissolved to 1 wt.% with deionized water

was taken along with  $\text{NaHSO}_3$  and HCHO (7.5 wt.% and 3 : 1 mol ratio) in a three-necked flask assembled with a nitrogen inlet. The reactor was kept in a water bath with magnetic stirring arrangement. Reaction was carried out at  $70^\circ\text{C}$  under  $\text{N}_2$  atmosphere. The pH of the reaction was 11. The polymer then was isolated by precipitation with acetone or water-ethanol and dried in a vacuum oven at  $40^\circ\text{C}$  for 7 h to yield the corresponding HPDS. The synthesis route of HPDS is shown in Scheme 1.

**2.3. Characterization.** HPDN and HPDS were characterized by WQF-520 infrared spectroscopy. The  $^1\text{H-NMR}$  spectra of HPDS were recorded on Bruker AC-E 200 (Bruker BioSpin, Switzerland) spectrometer by dissolving the samples in  $\text{D}_2\text{O}$  and being operated at 200 MHz.

HPDS was dissolved in degassed and distilled water (solution concentration = 2000 mg/L, HPAM concentration = 2000 mg/L) to observe the microscopic structures. SEM images were taken by S-3000 N SEM (Hitachi, Japan). The SEM resolution was  $3\ \mu\text{m}$ , and the magnifying multiple ranged from 3 to 30,000. Analysis was conducted at 20 kV acceleration voltage and 120–500 Pa pressure in the sample chamber.

**2.4. Intrinsic Viscosity.** The intrinsic viscosity  $[\eta]$  of HPDS was measured with Ubbelohde's viscometer (diameter: 0.3 mm, length: 12.15 cm) at  $30^\circ\text{C}$ . The solvent (1 mol/L NaCl) efflux time was greater than 100 s. Therefore, no kinetic energy corrections were made on the observed data. The temperature was controlled using a Cannon constant-temperature bath. Triplicate records were taken at each concentration using a stopwatch with an accuracy of 0.2 s. At each concentration, the reduced viscosity ( $\eta_{\text{sp}}/c_r$ ) and inherent viscosity ( $\ln \eta_r/c_r$ ) were determined from the passing time of polymer solutions, and then, they were plotted against the concentration of polymer solutions. Extrapolation was used to gain the intercept ( $H$ ). Then, the inherent viscosity of HPDS was calculated using the following equation:

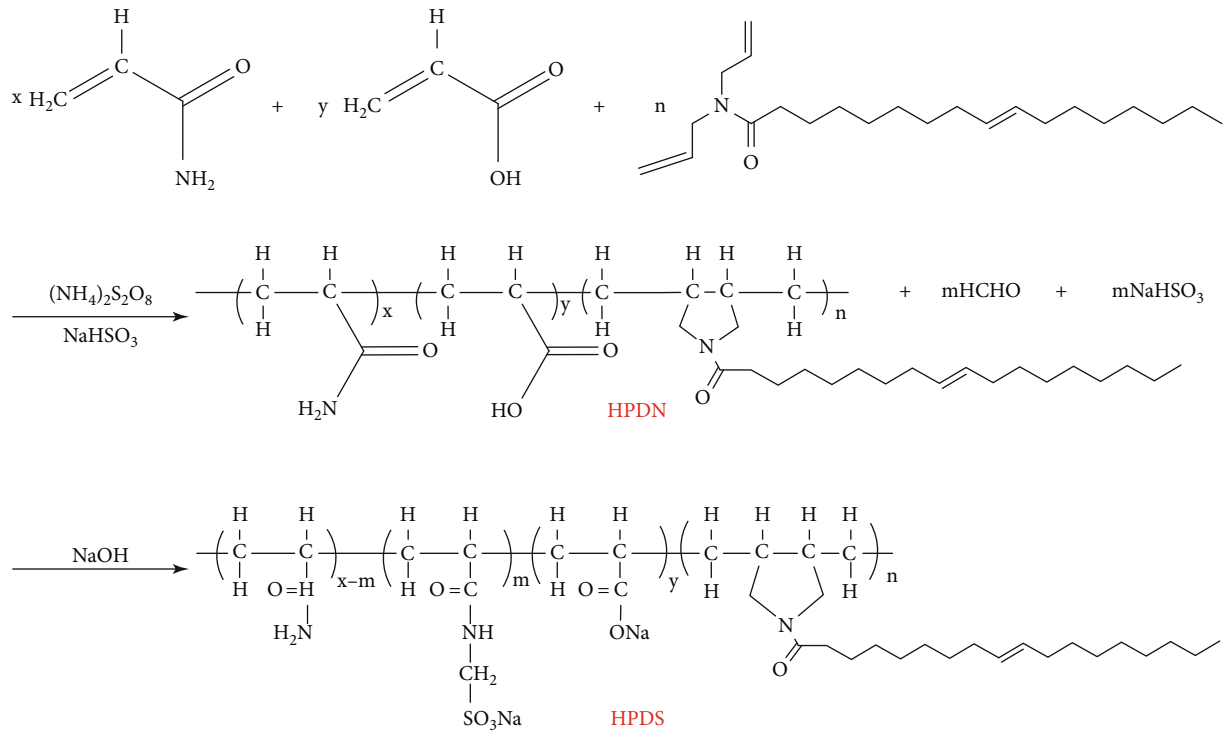
$$[\eta] = \frac{H}{c_0}, \quad (1)$$

where  $[\eta]$  is the intrinsic viscosity, mL/g;  $H$  is the intercept of y axis; and  $c_0$  is the initial concentration of polymer solution, g/mL.

**2.5. Viscosity in Different Concentrations.** HPDS and HPAM solutions with different concentrations were established (polymer dilute solution was diluted by mother liquor, the same as below), and the apparent viscosities of the solutions were measured by Brookfield DV-III rheometer at  $25^\circ\text{C}$ .

**2.6. Rheology Test.** The rheological properties of polymer solution are closely related to its solution properties. They are the integrated embodiment of solution's microphase structure and functions. Thus, the investigation of rheological property was repeatedly utilized to study whether the polymer solution met the requirement of the oil displacement in





SCHEME 1: The synthesis of HPDS.

previous studies. HAAKE RheoStress 6000 rotational rheometer (Thermo Fisher Scientific, Waltham/Massachusetts) was used to study the rheological character of the HPDS (1500 mg/L) and HPAM (1500 mg/L) solutions at 30°C.

**2.7. Stability Experiments.** When injected into the formation, the polymer solution could be subjected to different types of shearing, such as the shearing of pipelines and formation. Waring stirrer (LB20EG laboratory blender) was used to simulate the shearing in the injection process. Different concentrations of HPAM and HPDS were sheared for 30 s (5000 r/min) [24]. The viscosities of the polymers were determined after 30 min.

Temperature rises as the depth of oil or gas well/reservoir increases, thus making the viscosity of the polymer flood agent decreased remarkably. Brookfield DV-III rheometer was utilized to measure the apparent viscosity of HPDS solutions (1500 mg/L) in comparison with that of HPAM solutions (1500 mg/L). Then, temperature resistance and salt tolerance were tested repeatedly with the increase in temperature and salinity.

**2.8. Physical Simulation Experiments.** Sand-pack models were used in the physical simulation experiments to test the capacity of HPDS to establish resistance factor (RF) and residual RF (RRF), which were the measurements of injectability and profile controlling. A single homogeneous core was present in the sand-pack model with a diameter of 2.5 cm and a length of 50 cm. The permeability of the models was in the range of 2.0–3.0  $\mu\text{m}^2$  by packing with some quartz sand, which was washed by hydrochloric acid solution and distilled water several times. In the physical

simulation experiment, the core was saturated with 5000 mg/L NaCl brine. Then, 1500 mg/L polymer solution was injected until the pressure of the core was stable. Afterwards, water was injected into the core until the pressure became stable again [25, 26]. The RF and RRF of the polymer solution were calculated using Equations (2) and (3), respectively, as follows:

$$RF = \frac{K_w \mu_p}{K_p \mu_w} \quad (2)$$

$$RRF = \frac{K_{wa}}{K_{wb}} \quad (3)$$

where RF and RRF are the resistance factor and residual resistance factor of the polymer solution, respectively;  $K_p$  and  $K_w$  are the permeability of polymer injection and water injection,  $\mu\text{m}^2$ ;  $\mu_p$  and  $\mu_w$  are the viscosity of injected polymer and water, mPa-s; and  $K_{wb}$  and  $K_{wa}$  are the permeability before and after injection of polymer,  $\mu\text{m}^2$ .

The permeability of the sand-pack models was determined using Darcy's law as follows:

$$K = \frac{\mu L Q}{\Delta P A} \quad (4)$$

where  $K$  is the permeability of the sand-pack model,  $\mu\text{m}^2$ ;  $\mu$  is the viscosity of the injected fluid,  $\mu\text{m}^2$ ;  $A$  is the inner cross-sectional area of the sand-pack model,  $\text{cm}^2$ ;  $Q$  is the flow rate of the fluid, mL/s;  $\Delta P$  is differential pressure, atm; and  $L$  is the length of the sand-pack model, cm.

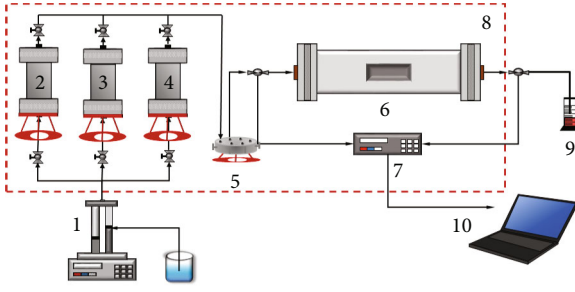


FIGURE 1: One-dimensional sand-packed model for EOR. 1: ISCO pump; 2: heavy oil; 3: polymer solution; 4: NaCl solution; 5: valves; 6: one-dimensional sand packed model; 7: pressure acquisition system; 8: constant temperature box; 9: sample device; 10: computer.

A two-layer model with two parallel homogeneous cores with different permeabilities was also utilized in the flooding experiments to simulate the nonhomogeneity of the reservoir. Every core had a diameter of 2.5 cm and a length of 25 cm. The permeability of the two layers was in the ranges of 1.2–1.8 and 0.4–0.6  $\mu\text{m}^2$ , respectively. In the flooding tests, the two cores were saturated with 5000 mg/L NaCl brine. Then, crude oil (apparent viscosity was 58.2 mPa·s at 60°C) was injected into the cores to saturate until no brine flowed from the end of the two cores. After aging (24 h), brine was injected into the cores saturated with oil until the water cut reached 95%. After the brine flooding, 0.3 pore volume ( $V_p$ ) of polymer solution was injected into the two-layer model. Then, subsequent water continued to be injected until the water cut reached 95% again. All of the experiments were carried out at 60°C. The injecting velocity of oil, brine, and flooding agent was 3 mL/min. The EOR of polymer solutions were calculated using Equation (5) as follows:

$$\text{EOR} = E_p - E_w, \quad (5)$$

where EOR is the enhanced oil recovery of polymer solution, %;  $E_p$  is the total recovery of flooding process, %; and  $E_w$  is the oil recovery of the water flooding process, %. Figure 1 shows the equipment used in the flooding test.

### 3. Results and Discussion

**3.1. IR Spectroscopy Analysis.** The structure of HPDN and HPDS was confirmed by IR spectroscopy (as shown in Figure 2). In the IR spectrum, certain groups of chemical bonding gave rise to bands at or near the same frequency, regardless of the rest structure of the molecule. The major functional groups identified in the spectrum of HPDN included N-H stretching vibration ( $3408\text{ cm}^{-1}$ ) and C=O deformation of the saturate ( $1675\text{ cm}^{-1}$ ). The peaks at 2945 and  $2921\text{ cm}^{-1}$  indicated the presence of  $-\text{CH}_2-$  groups, and the peak of C double-bond stretching vibration appeared at  $1660\text{ cm}^{-1}$ . As expected, the IR spectra confirmed the presence of different monomers in the copolymer HPDN. The peaks at 630, 1045, and  $1198\text{ cm}^{-1}$  indicated the presence of sulfonic acid groups. The IR spectrum of HPDN

and HPDS indicated that sulfonic acid groups were successfully connected to the polymer chain as expected.

**3.2.  $^1\text{H-NMR}$  Analysis.** The  $^1\text{H-NMR}$  spectra of HPDS are shown in Figure 3. The chemical shift value at 5.96 ppm was assigned to the protons of  $-\text{NH}_2$ . The protons of C-C double bonds appeared at 5.59 ppm, and the protons of  $-\text{CH}_2-$  in the  $\alpha$ -position to the sulfonic acid groups appeared at 5.57 ppm. The chemical shift value at near 3.41 and 3.39 ppm could be assigned to the protons of  $-\text{CH}_2-$  of nitrogen heterocyclic ring. The broad signals at 2.11 ppm could be attributed to methylene protons. The shift value near 1.11 ppm was assigned to methyl. Other shift values at 1.11, 3.57, and 4.70 ppm were assigned to the protons of  $\text{H}_2\text{O}$  and ethanol. Thus, the  $^1\text{H-NMR}$  spectra of HPDS indicated that sulfonic acid groups and DNDA were successfully connected to the polymer chain as expected.

**3.3. Environmental SEM (ESEM) Images.** ESEM was utilized to study the morphology of the HPDS and HPAM solutions at concentrations of 1500 mg/L. As shown in Figure 4, the observation accuracy of (a) and (b) was 20  $\mu\text{m}$ , and the magnification of (a) and (b) was 5000 times. The network structure could be easily observed, and HPDS showed a stronger link and better dimensional network structure than HPAM due to the association action. The network structure could prevent further degradation of the molecular chains, hence more shear, temperature, and salt resistances.

**3.4. Intrinsic Viscosity of HPDS.** Intrinsic viscosity was measured in accordance with the previous experimental plan, and the result of HPDS was 388.15 mL/g. Figure 5 shows that the  $\eta_{sp}/c_r$  and  $\ln \eta_r/c_r$  of HPDS had a good linear relationship with  $c_r$ . The  $\eta_{sp}/c_r$  of general polymers decreases with the decrease in  $c_r$ , and  $\ln \eta_r/c_r$  increases with the decrease in  $c_r$ . The  $\eta_{sp}/c_r$  of HPDS decreased linearly with the decrease in  $c_r$ , similar to the reported viscosity behavior of conventional polymer solutions.

**3.5. Rheological Properties of Polymer.** Rheological properties were investigated using HAAKE RheoStress 6000 rotational rheometer (as shown in Figure 6). The HPDS aqueous solution inherently showed better viscosity than the HPAM solution under the same concentration, indicating that the HPDS solution had a perfect property of retaining viscosity and strong non-Newtonian behavior.

**3.6. Stability Experiments.** The effect of concentration on the apparent viscosity of HPDS and HPAM solutions was determined (as shown in Figure 7). With the increase in polymer solution concentration, the apparent viscosity mounted, and the viscosity of HPDS was lower than that of HPAM before 1500 mg/L. Meanwhile, with the accretion of polymer solution concentration, the apparent viscosity of HPDS solution sharply increased. At low concentrations, the association of polymer was mainly intramolecular association. When the concentration was greater than CAC, the intermolecular association formed a transient network structure, which could increase the hydrodynamic radius of polymer. With

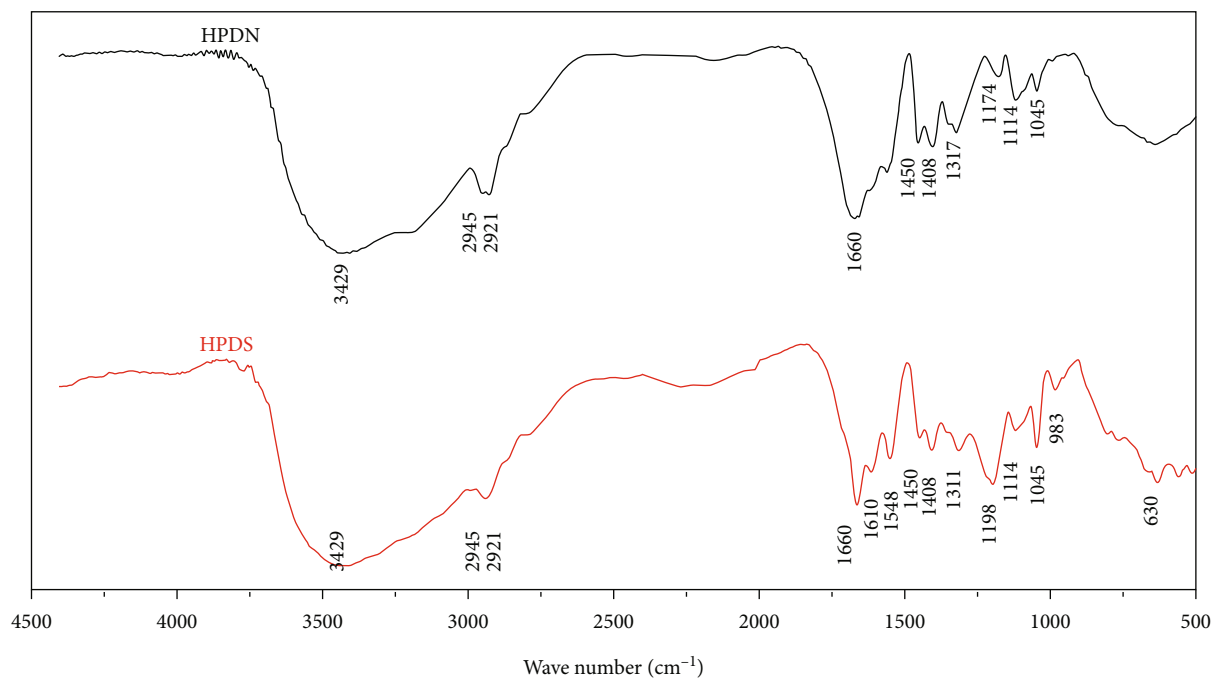


FIGURE 2: IR spectra of HPDN and HPDS.

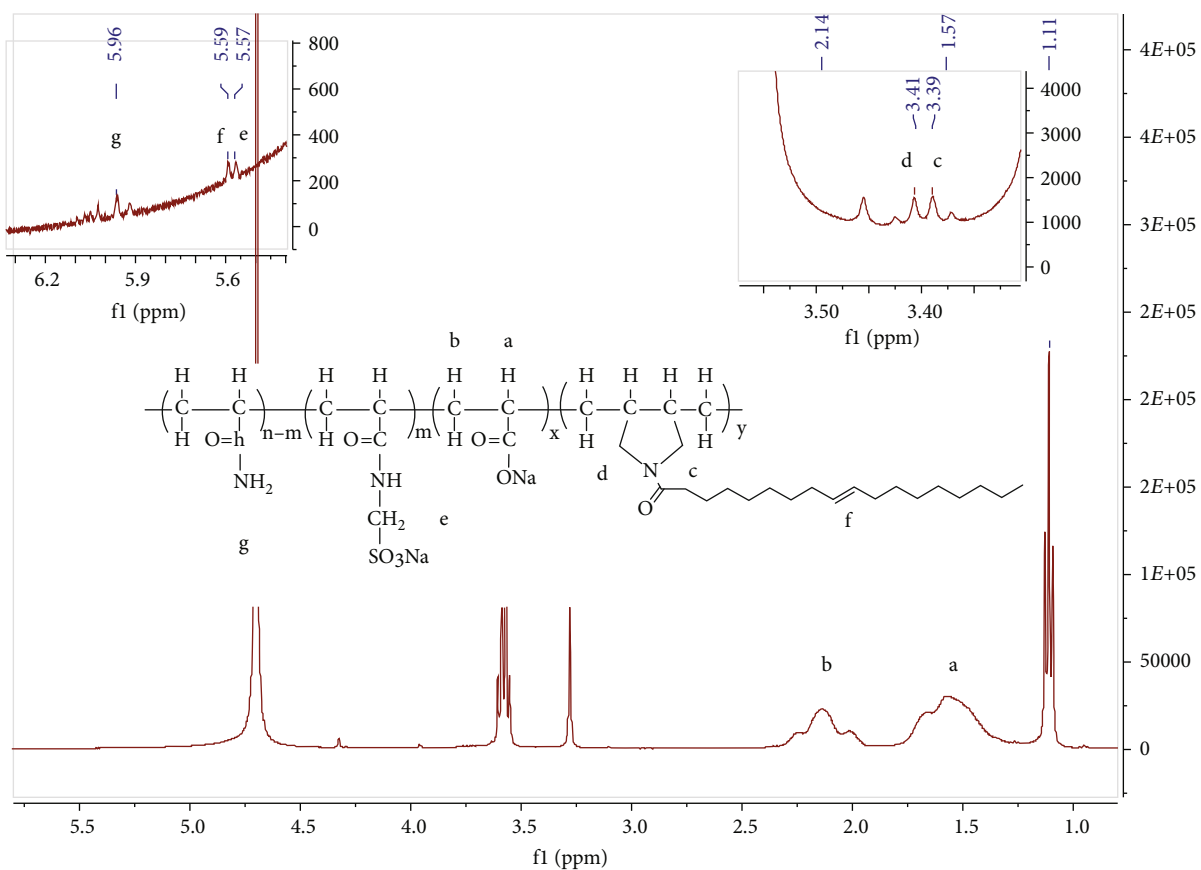


FIGURE 3:  $^1\text{H-NMR}$  spectra of HPDS.

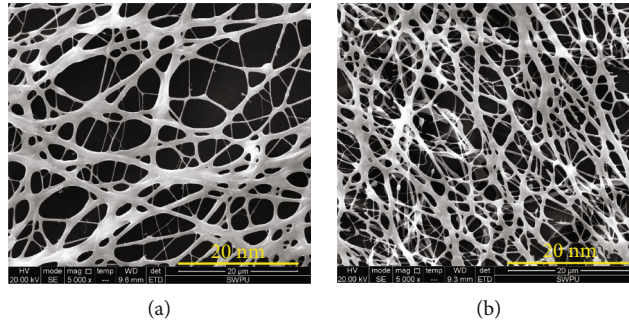


FIGURE 4: Structure of HPAM (a) and HPDS (b) solution.

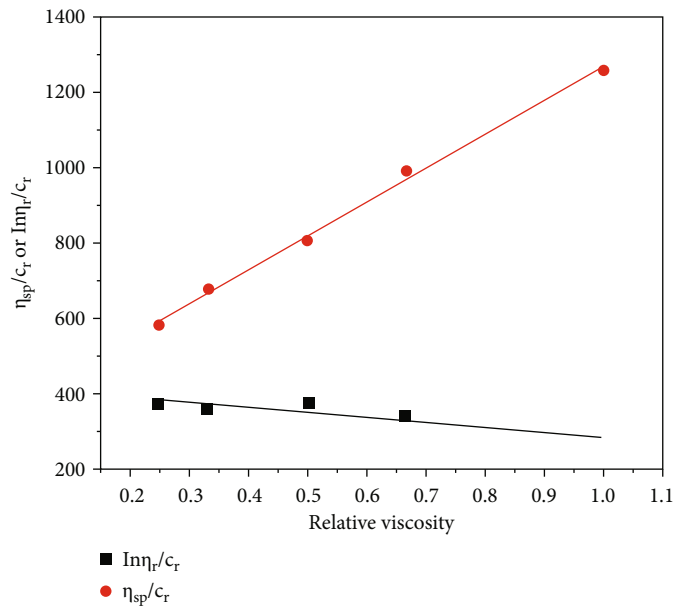


FIGURE 5: Relationship between  $\eta_{sp}/c_r$  or  $\ln \eta_r/c_r$  and relative viscosity.

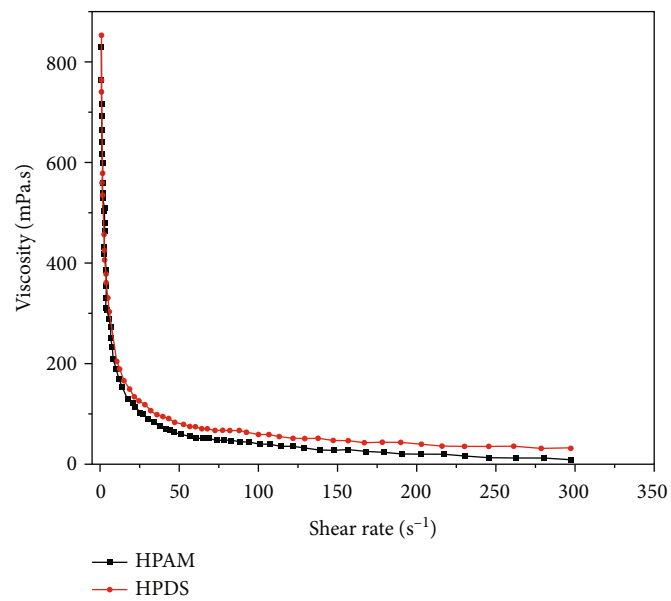


FIGURE 6: Relationship between apparent viscosity and shear rate.

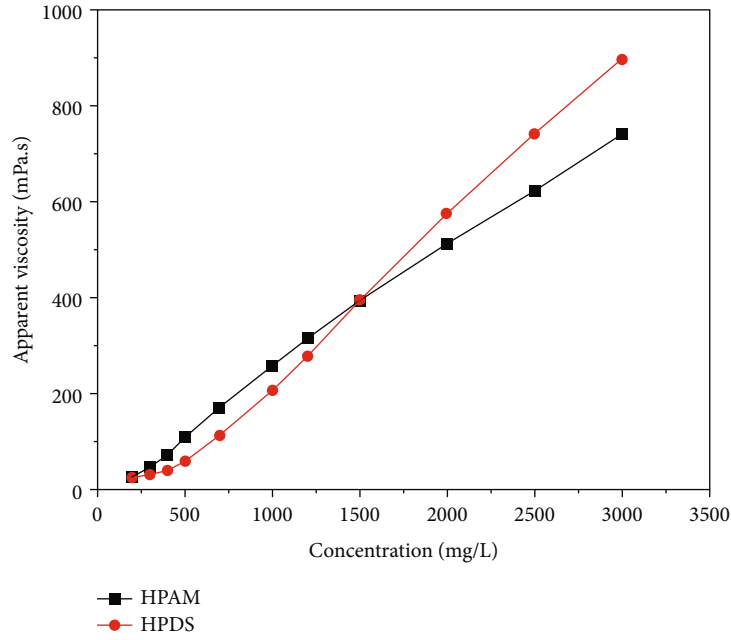


FIGURE 7: Relationship between apparent viscosity and concentration.

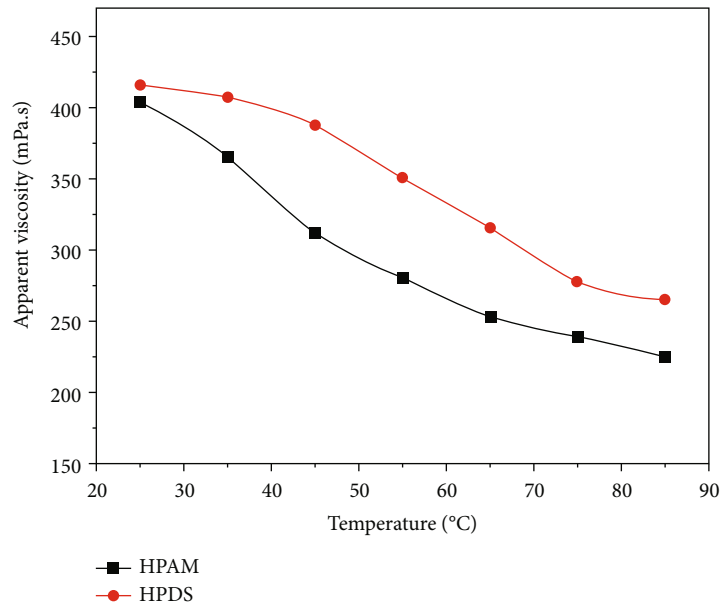


FIGURE 8: Relationship between apparent viscosity and temperature.

the further increase in concentration, the intermolecular association formed more intermolecular structures. Thus, the apparent viscosity of HPDS solution was much thicker. The critical association concentration was approximately 500 mg/L (as shown in Figure 7).

The effect of temperature on polymer solution was investigated (Figure 8). The general trend indicated an apparent viscosity decrease with increasing temperature. The phenomenon may be attributed to the effect of temperature. A large number of associating groups aggregate together to form reversible supermolecular structures via strong van der Waals' interactions, and polymer chains entangle with

TABLE 1: Data of HPDS and HPAM shear resistance test.

Shear conditions	Polymer types	Polymer concentration (mg/L) and viscosity (mPa.s)			
		500	1000	1500	2000
Before shearing	HPDS	58.9	205.1	395.3	575.2
	HPAM	108.7	257.3	391.5	511.3
After shearing	HPDS	40.5	103.6	298.8	445.2
	HPAM	89.4	150.8	211	266.9



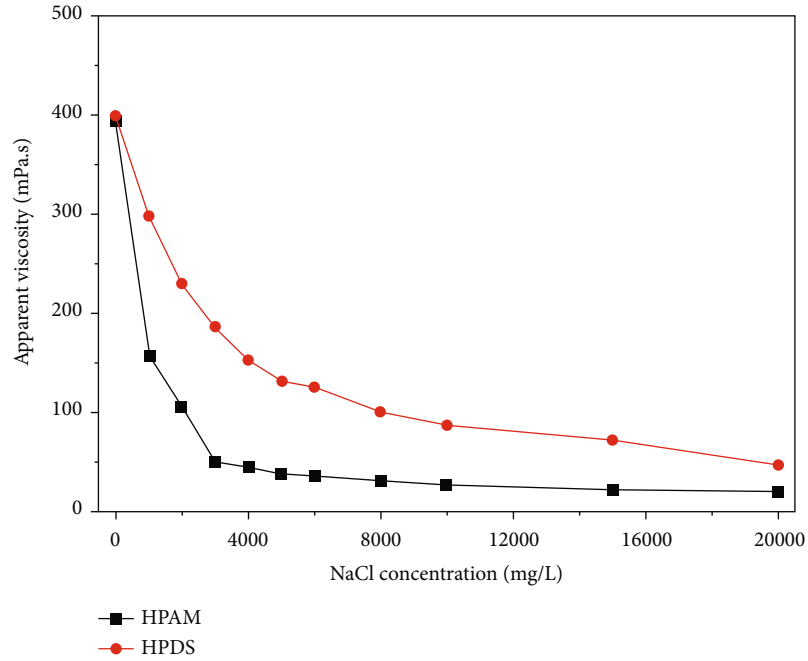


FIGURE 9: Effect of NaCl concentration on the apparent viscosity of polymer aqueous solution. The apparent viscosity was tested by Brookfield DV-III rheometer at  $7.34 \text{ s}^{-1}$ .

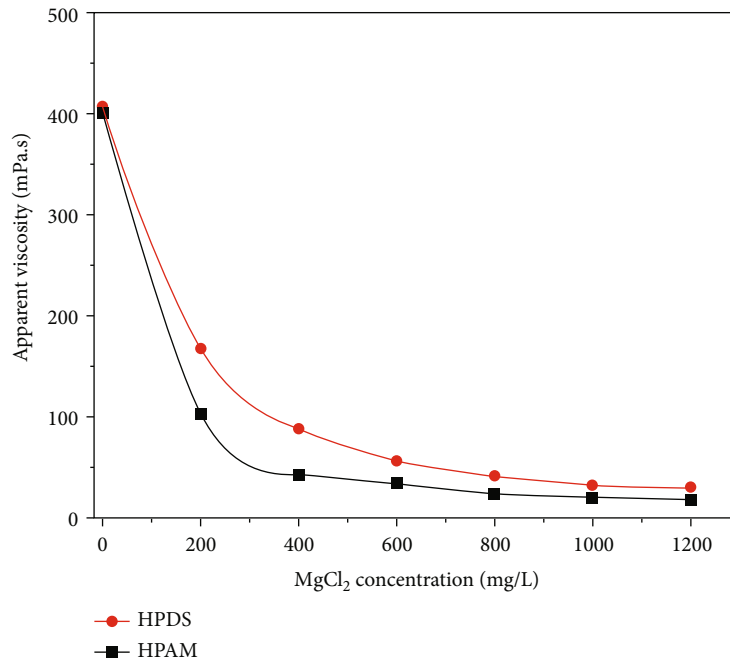


FIGURE 10: Effect of  $\text{MgCl}_2$  concentration on the apparent viscosity of polymer aqueous solution. The apparent viscosity was tested by Brookfield DV-III rheometer at  $7.34 \text{ s}^{-1}$ .

one another by hydrogen-bond interactions in the aqueous solution [27, 28]. However, the intermolecular interaction was unstable, especially under high temperature, resulting in the apparent reduction. However, at any temperature, the viscosity of HPDS was higher than that of HPAM, demonstrating that HPDS revealed better temperature tolerance.

As shown in Table 1, the viscosity after the shearing of HPDS was higher than that of HPMA, especially in high-concentration solution, mainly due to the hydrophobic association among HPDS molecules. When the solution is at high shear rates, most of the network structures and supramolecular aggregations split up. However, when the

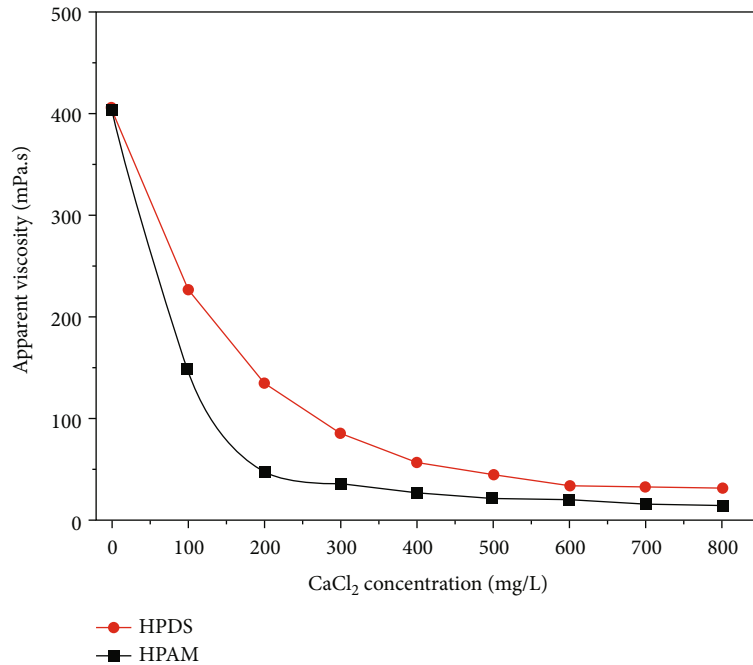


FIGURE 11: Effect of CaCl<sub>2</sub> concentration on apparent viscosity of polymer aqueous solution. The apparent viscosity was tested by Brookfield DV-III rheometer at 7.34 s<sup>-1</sup>.

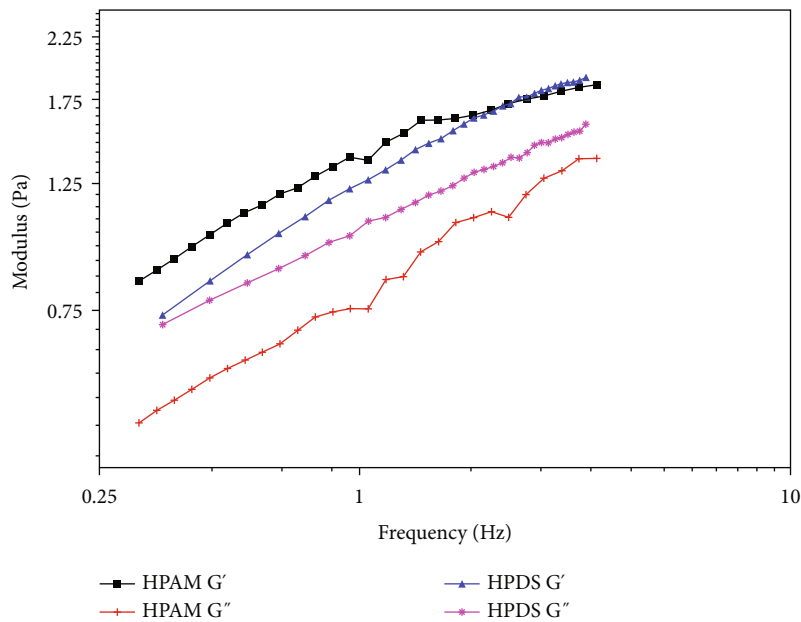


FIGURE 12: Relationship between modulus and frequency.

shear conditions revoke, the molecular chains form new association aggregations and network structures. Due to the large molecular weight and long molecular chain length, at high shear conditions, the HPAM molecular chains are likely to be split into a number of small segments. Thus, the apparent viscosity greatly decreased. The above results demonstrated that HPDS has desirable shear resistance.

The salts, such as NaCl, CaCl<sub>2</sub>, and MgCl<sub>2</sub>, abounding in the formation usually result in high salinity of the reservoir water, a crucial problem for flooding polymer. The relation-

ship between brine concentration and apparent viscosity is shown in Figures 9–11. HPDS exhibited higher viscosity under any salinity than HPAM, thereby demonstrating that HPDS was more tolerant to salt brine. The result also revealed that HPDS possessed salt tolerance structures. A possible mechanism is that hydrophobic groups generate association structures with the increase in salt solution polarity, especially among the molecules, which are able to moderate viscosity decline caused by molecular chain curling. Meanwhile, the introduction of salt-insensitive

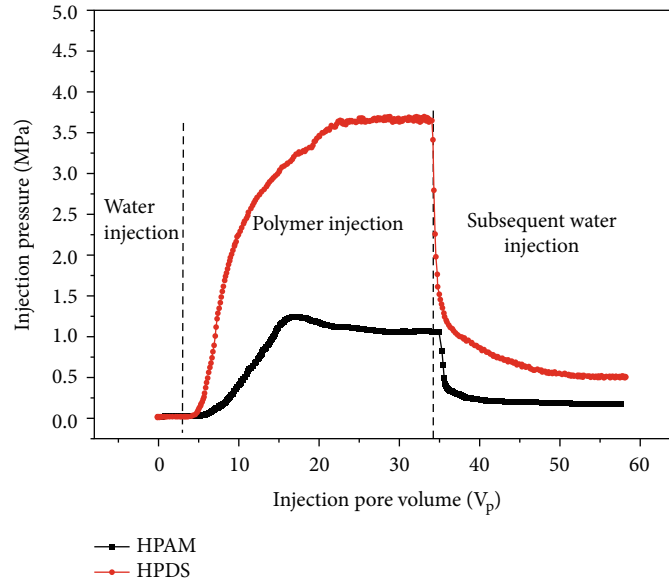


FIGURE 13: Relationship between injection pressure and injection pore volume.

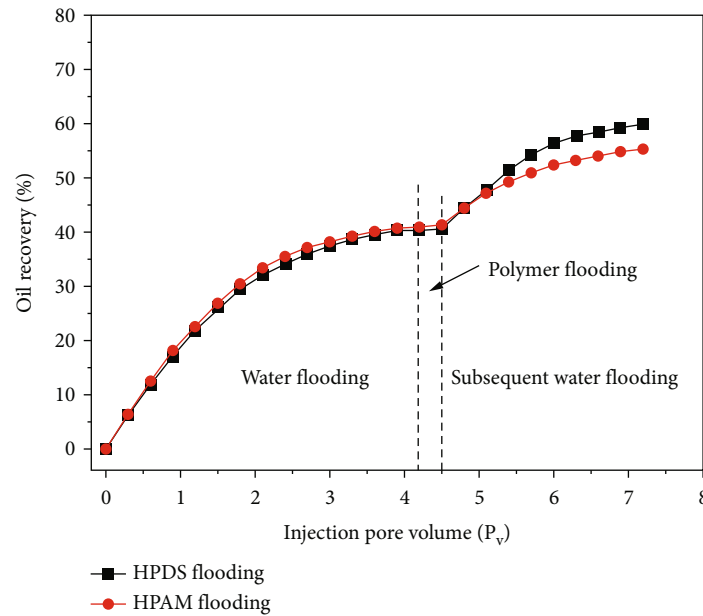


FIGURE 14: Relationship between oil recovery and injection pore volume.

sulfonic groups to the backbone could assemble more bound water molecules to weaken the dehydration of the inorganic salt, thereby causing observable salt-tolerance enhancement [21, 29].

**3.7. Viscoelasticity of HPDS.** Figure 12 shows the viscoelasticity of polymer HPDS and HPAM. The elastic modulus ( $G'$ ) of HPDS was lower than that of HPAM in low frequency; with the increase in frequency, it showed a sharp increasing trend. When the frequency was higher than 2.3 Hz, the viscous modulus of HPDS was higher than that of HPAM. Comparison of the loss modulus ( $G''$ ) of HPDS and HPAM showed that both of them increased with the

increase in frequency, and the trend of the former was higher. Therefore, HPDS represented better viscoelasticity.

**3.8. Physical Simulation Experiments Analysis.** Similar concentrations of HPDS and HPAM solutions and sand-pack models were used in the physical stimulation experiments. As shown in Figure 13, the injection pressure was recorded, and then, RF and RRF were calculated. When the HPDS solution flowed through the sand pack, RF equaled 200.5 and RRF equaled 27.9, while upon injecting HPAM solution, RF equaled 42.4 and RRF equaled 6.8. This finding implied that HPDS was better at establishing flow resistance to control profile in polymer flooding than HPAM, thus expanding the sweep efficiency and improving the ultimate recovery.

As shown in Figure 14, oil recovery changed when water or polymer solution was injected in the two different homogeneous cores (initial oil saturation of 71.2%), which were used to simulate the nonhomogeneity of the reservoir. The experiment results showed that HPDS and HPAM flooding could increase oil recovery, and HPDS flooding performed better by comparison. The first water flooding recoveries of the two experiments were 40.1% and 41.3% when water cut reached 95%. Then, flooding agent and subsequent water were injected into the core. Under the same condition, the ultimate recoveries of HPDS and HPAM flooding were 59.9% and 55.4%, respectively, and their EORs were 19.8% and 14.1%, respectively. When injected into the stratum, the polymer solution first entered the layers with high permeability. Then, the water-oil mobility ratio decreased and the injecting pressure rose, which forced more displacement agents to access low-permeability layers that contained much untapped oil. Thus, the sweep efficiency improved and oil recovery increased. The phenomenon above may indicate that HPDS has stronger shear resistance, temperature resistance, salt tolerance, and higher viscosifying ability than HPAM.

#### 4. Conclusion

This work introduced a novel polymer HPDS as a flooding polymer. Studies on the properties of this water-soluble polymer revealed that it had good viscosity performance, and the viscosity sharply increased with the increase in concentration, especially when the aqueous solution concentration was thicker than CAC. With the increase in temperature, the polymer viscosity was reduced, while the range was much smaller than that of HPAM, thus displaying great temperature resistance. Meanwhile, the viscosity of HPDS was comparatively higher at any share rate. Considering the hydrophobic groups and sulfonic groups embedded in the polymer backbone, the novel polymer had more diastolic chain segment and network structure than HPAM in brine. In addition, HPDS represented better anchoring ability, especially in high frequency. The simulation experiments showed that HPDS performed better at establishing flow resistance to control profile in polymer flooding, and the oil recovery was up by 19.8% under 5000 mg/L NaCl brine at 60°C. These findings showed that the novel hydrophobically associating polymer could be an ideal candidate as an EOR chemical to satisfy high-temperature and high-density reservoirs.

#### Data Availability

All the data are listed in the manuscript.

#### Conflicts of Interest

The authors declare that there is no conflict of interests regarding the publication of this paper.

#### Acknowledgments

This work was funded by the Sichuan Science and Technology Program (Applied Basic Research) (2018JY0515), Open Foundation of State Key Laboratory of Oil and Gas Geology and Exploitation (Chengdu University of Technology) (PLC20180103), and Opening Project of Oil and Gas Field Applied Chemistry Key Laboratory of Sichuan Province (YQKF202010).

#### References

- [1] X. Zhou, Q. Jiang, Q. Yuan et al., "Determining CO<sub>2</sub> diffusion coefficient in heavy oil in bulk phase and in porous media using experimental and mathematical modeling methods," *Fuel*, vol. 263, p. 116205, 2020.
- [2] Z. Zargar, S. M. Razavi, and S. M. F. Ali, "Analytical model of steam-assisted gravity drainage (SAGD) process in relation to constant injection rate," *Fuel*, vol. 265, article 116772, 2020.
- [3] D. Belivean, "Waterflooding viscous oil reservoirs," *SPE Reservoir Evaluation & Engineering*, vol. 12, no. 5, pp. 689–701, 2009.
- [4] Z. Q. Li, J. Hou, W. Liu, and Y. Liu, "Multi-molecular mixed polymer flooding for heavy oil recovery," *Journal of Dispersion Science and Technology*, vol. 2021, article 1878902, 9 pages, 2021.
- [5] Z. Song, Z. Li, F. Lai, G. Liu, and H. Gan, "Derivation of water flooding characteristic curve for high water-cut oilfields," *Petroleum Exploration and Development*, vol. 40, no. 2, pp. 216–223, 2013.
- [6] Z. Song, Z. Li, C. Yu et al., "D-optimal design for rapid assessment model of CO<sub>2</sub> flooding in high water cut oil reservoirs," *Journal of Natural Gas Science and Engineering*, vol. 21, pp. 764–771, 2014.
- [7] X. Zhang, C. Lin, Y. Wu et al., "Experimental investigation of the effects of water and polymer flooding on geometric and multifractal characteristics of pore structures," *Energies*, vol. 13, no. 20, p. 5288, 2020.
- [8] H. He, Y. Chen, Q. Yu, X. Wen, and H. Liu, "Optimization design of injection strategy for surfactant-polymer flooding process in heterogeneous reservoir under low oil prices," *Energies*, vol. 12, no. 19, p. 3789, 2019.
- [9] A. M. Firozjahi and H. R. Saghafi, "Review on chemical enhanced oil recovery using polymer flooding: fundamentals, experimental and numerical simulation," *Petroleum*, vol. 6, no. 2, pp. 115–122, 2020.
- [10] F. Wang, H. Yang, H. Jiang et al., "Formation mechanism and location distribution of blockage during polymer flooding," *Journal of Petroleum Science and Engineering*, vol. 194, p. 107503, 2020.
- [11] Q. Yu, Y. Liu, S. Liang, S. Tan, Z. Sun, and Y. Yu, "Experimental study on surface-active polymer flooding for enhanced oil recovery: a case study of Daqing placanticline oilfield, NE China," *Petroleum Exploration and Development*, vol. 46, no. 6, pp. 1206–1217, 2019.
- [12] L. Xue, U. S. Agarwal, and P. J. Lemstra, "Shear degradation resistance of star polymers during elongational flow," *Macromolecules*, vol. 38, no. 21, pp. 8825–8832, 2005.
- [13] R. Zhang, Z. Ye, L. Peng, N. Qin, Z. Shu, and P. Luo, "The shearing effect on hydrophobically associative water-soluble polymer and partially hydrolyzed polyacrylamide passing

- through wellbore simulation device,” *Journal of Applied Polymer Science*, vol. 127, no. 1, pp. 682–689, 2013.
- [14] Y. J. Che, J. Cao, H. J. Gong, G. Y. Xu, and Y. Tan, “Dilational rheological properties of fluorocarbon modified poly(acrylamide)s at the air/water surface,” *Journal of Dispersion Science and Technology*, vol. 32, no. 2, pp. 174–184, 2011.
- [15] X. J. Liu, W. Jiang, S. Gou et al., “Synthesis and evaluation of novel water-soluble copolymers based on acrylamide and modular  $\beta$ -cyclodextrin,” *Carbohydrate Polymers*, vol. 96, no. 1, pp. 47–56, 2013.
- [16] Z. B. Ye, G. J. Gou, S. H. Gou, W. C. Jiang, and T. Y. Liu, “Synthesis and characterization of a water-soluble sulfonates copolymer of acrylamide and N-allylbenzamide as enhanced oil recovery chemical,” *Journal of Applied Polymer Science*, vol. 128, no. 3, pp. 2003–2011, 2013.
- [17] X. J. Liu, W. C. Jiang, S. H. Gou, Z. B. Ye, and X. D. Xie, “Synthesis and evaluation of a water-soluble acrylamide binary sulfonates copolymer on MMT crystalline interspace and EOR,” *Journal of Applied Polymer Science*, vol. 125, no. 2, pp. 1252–1260, 2012.
- [18] X. J. Liu, W. Jiang, S. Gou, Z. Ye, and C. Luo, “Synthesis and clay stabilization of a water-soluble copolymer based on acrylamide, modular  $\beta$ -cyclodextrin, and AMPS,” *Journal of Applied Polymer Science*, vol. 128, no. 5, pp. 3398–3404, 2013.
- [19] A. Mehrdad, “Effect of HCl and solution concentration on the ultrasonic degradation of aqueous solutions of poly (ethylene oxide),” *Journal of Polymer Engineering*, vol. 28, no. 9, pp. 597–610, 2008.
- [20] S. Y. Shao, J. Ding, L. Wang, X. Jing, and F. Wang, “Highly efficient blue electrophosphorescent polymers with fluorinated poly(arylene ether phosphine oxide) as backbone,” *Journal of the American Chemical Society*, vol. 134, no. 37, pp. 15189–15192, 2012.
- [21] A. Sabhapondit, A. Borthakur, and I. Haque, “Water soluble acrylamidomethyl propane sulfonate (AMPS) copolymer as an enhanced oil recovery chemical,” *Energy & Fuels*, vol. 17, no. 3, pp. 683–688, 2003.
- [22] C. McCormick and L. Salazar, “Water soluble copolymers: 46. Hydrophilic sulphobetaine copolymers of acrylamide and 3-(2-acrylamido-2-methylpropanedimethylammonio)-1-propanesulphonate,” *Polymer*, vol. 33, no. 21, pp. 4617–4624, 1992.
- [23] N. Lai, W. Dong, Z. Ye et al., “A water-soluble acrylamide hydrophobically associating polymer: synthesis, characterization, and properties as EOR chemical,” *Journal of Applied Polymer Science*, vol. 129, no. 4, pp. 1888–1896, 2013.
- [24] X. Y. Wang, *Effect of Shear on Microstructure of Polymer Solution*, Southwest Petroleum University, 2014.
- [25] N. J. Lai, L. Tang, N. Jia et al., “Feasibility study of applying modified nano-SiO<sub>2</sub> hyperbranched copolymers for enhanced oil recovery in low-mid permeability reservoirs,” *Polymers*, vol. 11, no. 9, p. 1483, 2019.
- [26] Y. Zhang, X. Li, X. Ma, S. Bai, J. Zhang, and R. Guo, “Critical phase separation concentration of acrylamide and 2-acrylamido-2-methylpropanesulfonate copolymers in ammonium sulfate aqueous solution and its influence factors,” *Colloids and Surfaces A: Physicochemical and Engineering Aspects*, vol. 590, p. 124485, 2020.
- [27] N. Seetapan, N. Limparyoon, and S. Kiatkamjornwong, “Effect of fire retardant on flammability of acrylamide and 2-acrylamido-2-methylpropane sodium sulfonate copolymer composites,” *Polymer Degradation and Stability*, vol. 96, no. 10, pp. 1927–1933, 2011.
- [28] C. S. Yang, K. Shin, and H. K. Jeong, “Thermal analysis of poly(sodium 4-styrenesulfonate) intercalated graphite oxide composites,” *Chemical Physics Letters*, vol. 517, no. 4–6, pp. 196–198, 2011.
- [29] D. A. Z. Wever, F. Picchioni, and A. A. Broekhuis, “Polymers for enhanced oil recovery: a paradigm for structure-property relationship in aqueous solution,” *Progress in Polymer Science*, vol. 36, no. 11, pp. 1558–1628, 2011.



## Review Article

# Advancement of Hydraulic Fracture Diagnostics in Unconventional Formations

Ali Mahmoud,<sup>1</sup> Ahmed Gowida,<sup>1</sup> Murtada Saleh Aljawad <sup>1,2</sup> Mustafa Al-Ramadan,<sup>1,2</sup> and Ahmed Farid Ibrahim <sup>1,2</sup>

<sup>1</sup>Department of Petroleum Engineering, King Fahd University of Petroleum & Minerals, Dhahran, Saudi Arabia

<sup>2</sup>Center for Integrative Petroleum Research, King Fahd University of Petroleum & Minerals, 31261 Dhahran, Saudi Arabia

Correspondence should be addressed to Murtada Saleh Aljawad; [mjawad@kfupm.edu.sa](mailto:mjawad@kfupm.edu.sa)

Received 12 August 2021; Accepted 19 October 2021; Published 2 November 2021

Academic Editor: Qingwang Yuan

Copyright © 2021 Ali Mahmoud et al. This is an open access article distributed under the Creative Commons Attribution License, which permits unrestricted use, distribution, and reproduction in any medium, provided the original work is properly cited.

Multistage hydraulic fracturing is a technique to extract hydrocarbon from tight and unconventional reservoirs. Although big advancements occurred in this field, understanding of the created fractures location, size, complexity, and proppant distribution is in its infancy. This study provides the recent advances in the methods and techniques used to diagnose hydraulic fractures in unconventional formations. These techniques include tracer flowback analysis, fiber optics such as distributed temperature sensing (DTS) and distributed acoustic sensing (DAS), tiltmeters, microseismic monitoring, and diagnostic fracture injection tests (DFIT). These techniques are used to estimate the fracture length, height, width, complexity, azimuth, cluster efficiency, fracture spacing between laterals, and proppant distribution. Each technique has its advantages and limitations, while integrating more than one technique in fracture diagnostics might result in synergies, leading to a more informative fracture description. DFIT analysis is critical and subjected to the interpreter's understanding of the process and the formation properties. Hence, the applications of machine learning in fracture diagnostics and DFIT analysis were discussed. The current study presents an extensive review and comparison between different multistage fracture diagnostic methods, and their applicability is provided. The advantages and the limitations of each technique were highlighted, and the possible areas of future research were suggested.

## 1. Introduction

Hydraulic fracturing is a well stimulation technique for enhancing hydrocarbon production from reserves. It relies on creating high-conductivity fractures propagated from the wellbore out into the formation [1]. The proppant fills the created fracture so that the fracture remains open when the fluid's pressure is reduced. As a result, a conductive path for hydrocarbons to flow from the reservoir into the wellbore is created. Hydraulic fracturing treatment, while appearing to be simple, offers many complications. Uncertainties exist regarding reservoir characteristics, fracture growth patterns, and fluid and proppant placement, which jeopardize the treatment's effectiveness [2, 3]. Fracture diagnostic techniques have proven to be effective in addressing

difficulties related to the design, execution, and monitoring of the fracture stimulation treatments [4]. There are several techniques for obtaining subsurface understanding into fracture dimensions, growth behavior, and interactions with the surrounding reservoir following treatment [5]. The crucial economic assessment of the potential outcomes is conducted based on the information received from these diagnostics, and optimal treatments are achieved [6].

Technological advances in well drilling, completion, and stimulation have resulted in record production and considerable growth in unconventional global markets. While these advancements are already having an impact, there is still a lack of understanding of important subsurface information, such as the created hydraulic fracture shape near and beyond the wellbore [7]. Hydraulic fracture diagnostics,

visualization of the created hydraulic fractures, and identifying proppant deep in the formation, further from the wellbore, are likely to be game-changers in releasing more hydrocarbons from unconventional reservoirs and improving well economics [8].

Unconventional resources expansion has made considerable strides in recent decades, thanks to game-changing advances in horizontal drilling and hydraulic fracturing. These previously uneconomic tight, low-permeability oil, and gas reservoirs are now an essential element of the energy mix necessary to meet the world's energy demands. Increased contact of fracture surface area and formation through innovative horizontal drilling and multistage fracturing completion method is a significant contributor to the success of unconventional hydrocarbon production [9]. Regions rich in conventional resources are actively exploring methods to demonstrate the potential for unconventional resources for future generations. Despite the availability of various diagnostic tools, the problems remain, particularly with the advancement of horizontal drilling and growing interest in the exploitation of unconventional [10, 11]. Hence, novel diagnostic methodologies are required to address the emerging challenges. This research discusses different diagnostic techniques and recent changes made to the conventional methods for application in unconventional reservoirs.

## 2. Literature Review

**2.1. Fracture Diagnostics Using Tracers.** The application of radioactive tracers combined with spectral gamma ray logging for fracture diagnosis is well established [12, 13]. Tracers that emit gamma rays are either injected into the fracturing fluids or coated on the proppant. Following the completion of the hydraulic fracturing treatment, logging is conducted to establish the near-wellbore fracture propped and unpropped heights. Radioactive (R/A) proppant tracers provide an approximation of the fracture height near the wellbore. RA tracers use embedded tracers, which can be ceramic materials, and provide quantitative information when assessing critical characteristics around the wellbore using gamma ray [5, 14]. There are different R/A tracers available that can be distinguished from one another using the logging tools; hence, by employing different tracers at different periods throughout the treatment, it may be possible to determine which perforations were receiving fluid at a given point in the treatment. These instruments have been widely used in both offshore and onshore applications to improve perforation efficiency and optimal proppant placement [15]. This technique has several advantages, including its relatively low cost, low reactivity with the reservoir fluids and rocks, similar transport behavior with the injected fluids, and ease of measuring with a high accuracy detection level [16]. However, the use of radioactive tracers raises environmental and safety problems for operators. Tracers are also restricted in their ability to provide information for regions far from the wellbore and fracture height in highly deviated wells [14, 17]. Radioactive tracers are being phased out in favor of chemical tracers, which are more environ-

mentally friendly and allow for longer-term data collection of in-well tracer flowback and communication within reservoir wells.

Chemical tracers are compounds that are either liquid or solid and are soluble in water, oil, or gas. The best chemical tracers must possess the following characteristics: be stable under reservoir conditions, have minimum partitioning into the nonsoluble phases, no adsorption on the reservoir rock, have a very low limit of detection, and have minimal to no environmental impacts [18]. Tracers used in multistage hydraulic fracturing are often classified as emulsion tracers, perforation tracers, and controlled release tracers. Tracer types and characteristics are summarized in Table 1.

[20] described the use of a nonradioactive tracer to assess the fracture height. The authors presented case studies as well as a comparison of nonradioactive and radioactive tracers. The nonradioactive tracer presented is a high thermal neutron capture cross-section tracer (HTNCC) that is placed into ceramic proppant grains during manufacture [21]. The HTNCC is added at very low concentrations that there is no noticeable change in the mechanical or physical properties of the proppant as a result of the addition. These tracers can be placed in either every grain for treatments that use 100% ceramic proppant or in treatments that use sand or other nonceramic proppant, ceramic grains having higher concentrations of the HTNCC can be mixed in and replace a small portion (5%) of the designed proppant. A pre- and postfrac neutron log is run across the zones of interest in both cases, and the difference in neutron response gives an estimate of proppant location. The primary advantage of this method is that the tracer is not radioactive; therefore, no special handling is required. Furthermore, because the tracer is a component of the proppant grains, the well can be logged at any time in the future. The cost may be higher depending on the fracture design and corresponding proppant requirements. Furthermore, this method is dependent on the depth of investigation of the logging tools. The radius of investigation is usually limited to no more than 24 in. from the wellbore, which means that the propped fracture profile outside 18-24 in. remains unknown. The accuracy of these methods is limited to a positive response only—if the proppant is not detected in a set of perforations or is not seen near the wellbore in a vertical well, it does not necessarily mean the proppant did not enter that set of perforations, or that the fracture did not grow higher. The fracture and proppant may be merely outside the radius of investigation. The inability of tracers to provide information on fracture dimensions far from the wellbore (greater than 24 in. from the wellbore) has been highlighted by Palisch et al. [22]. The authors described a method for far-field detection of the placed proppant. The method relies on electromagnetic technology to locate a detectable proppant.

In unconventional reservoirs, tracer flowback analysis is frequently used to determine hydraulic stimulation effectiveness, understand fracture communication with offset wells, and estimate fracture volume, correlate relative fracture contribution to the overall flow, and the connectivity of the fractured matrix created, etc. The combination of horizontal well drilling and multistage hydraulic fracturing treatment

TABLE 1: Tracers types and their characteristics modified after [19].

Tracer type	Uses	Advantages	Disadvantages
Perforation	1 Understanding the effectiveness of perforation.	1 The effectiveness of perforation treatment. 2 Inflow attributes.	1 Tracer volume restrictions.
Emulsion	1 Interwell communication. 2 Determining the strength of the fracture. 3 Evaluating the flow patterns.	1 Completion and zonal purposes. 2 Migration of fracturing fluids.	1 Possibility for faulty readings. 2 Tracer volume restrictions. 3 Short life period.
Controlled release	1 Inflow assessment.	1 Long-term inflow monitoring. 2 Accurate representation of zonal inflow.	1 Single-well characterization.

is widely used to increase production in unconventional and tight reservoirs. It is critical to evaluate the fracture networks developed to accurately predict hydrocarbon production. Several advantages have been found for fracture characterization using tracer flowback. Firstly, injecting different tracers into each fracture can effectively distinguish individual stages. Because these tracers will not become reactive with each other, the trace flowback analysis may be utilized to predict the fracture parameters at each stage. Secondly, since only a limited amount of tracers are injected, the concentration of tracers produced decreases over time, and the best tracer analysis would occur at the start of production. As a result, the collected tracer flowback data will most likely provide the earliest opportunity to evaluate a single-stage fracture network that contributes to the production of hydrocarbon (production allocation per stage). Finally, the tracer flowback test is fairly cost-effective, and its data is very multifunctional [23].

The general procedure for performing tracer flowback in a multistage hydraulically fractured well mainly consists of four steps, as shown in Figure 1 [23].

- (1) Tracer is injected with the fracturing fluid down into the reservoir
- (2) Tracer-free fracturing fluid is injected into the reservoir to drive the tracer slug into the fractures and matrix further (also known as the chase period).
- (3) During flow shut down, a downhole packer is introduced into the well to prop the next fracture
- (4) Opening the well (injector is being changed into a producer), the tracer can now be flown back with the fracturing fluid

Salman et al. [19] discussed the analysis of chemical tracers in flowback samples from unconventional reservoirs to determine the effectiveness of the treatment. They presented the flowback results for a multistage completion and concluded that tracer analysis can be used to assess the fractured system in the stimulated reservoir volume (highly fractured vs. sparsely fracture). [24] provided an analytical approach for quantifying fractures in a tight oil reservoir by using an early-time tracer poststimulation flowback profile. The authors determined that tracer dispersion,

adsorption, and the difference between the injection and flowback rates affect tracer flowback profiles (TFPs). Tian et al. [25] used synthetic numerical simulation to examine the chemical tracer selection criteria for fracture volume diagnosis in a shale gas reservoir. The authors found that the tracer partitioning coefficient had a considerably greater influence on fracture volume calculation than the tracer adsorption rate. As a result, the tracer adsorption effect on fracture volume calculations is dismissed, and the partitioning coefficient is the most important factor for tracer selection in fracture volume diagnosis. Based on the tracer data, the increase of the tracer partitioning coefficient will improve the accuracy of the estimated swept volume. [26] proposed a new numerical simulation method for analyzing chemical tracer data to help in estimating connectivity between the wellbore and the open connected fractures. As the fracture pressure falls during flowback, the induced unpropped (IU) fracture will close over time, causing the tracer to remain in the reservoir and the fractures. Based on the tracer response curve (TRC), it is clear that the IU fracture closure has a significant impact on the recovery of the tracer. The multiple peaks in the TRC can be explained by the closure of IU fractures during flowback. Early peaks in the production profile can be attributed to fracture closure near the wellbore, while late time peaks are due to the flowback of tracers from fractures connected to the wellbore through IU fractures. The area under the early time peak is directly related to the sections of fractures that are well hydraulically connected to the wellbore, while the area under the later peaks is related to the part of the fracture connected to the wellbore through IU fractures.

*2.2. Fracture Diagnostics Using Fiber Optics.* The use of fiber optics in well stimulation treatments has increased recently. The optical cable is deployed downhole, allowing for continuous monitoring of the treatment. Depending on the application, the cable installation can be temporary (coiled tubing or wireline conveyed) or permanent (installed behind the casing), and multiple sensors can be distributed along with the cable Figure 2. DTS and DAS are the two most common measuring techniques used with fiber optics. Monitoring the acoustic and temperature-related activity from an offset well-instrumented with a fiber optic cable in a multi-well hydraulic fracture stimulation can provide valuable

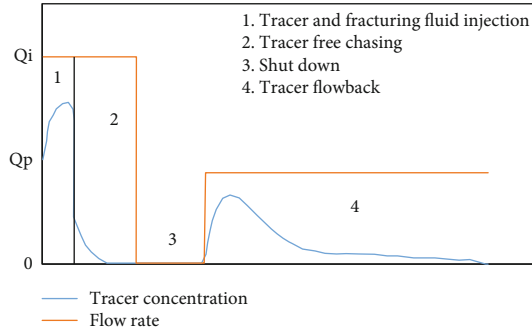


FIGURE 1: Schematic of the general process for performing tracer flowback in a multistage hydraulically fractured well modified after [23].

insight into fracture diagnostics for stimulated wells. Due to the reservoir complexity, determining the optimal completion and stimulation design to enhance fracturing efficiency and production performance in unconventional reservoirs remains difficult. Unconventional fiber optic applications have focused on fiber-based pressure gauges and cluster efficiency calculations using near-wellbore DAS and DTS obtained via permanent casing installations or DTS wireline logs run after treatment [27–30]. Fiber optics technology has been recognized as a potential option for establishing consistent production profiles in unconventional wells [30]. Fiber optics have brought new insights through real-time monitoring and integrated diagnostics in this aspect.

**2.2.1. Distributed Temperature Sensing (DTS).** DTS monitors wells by measuring wellbore temperature fluctuations. Whether gas, oil, or water enters the wellbore, a particular heat signature will be generated [32]. DTS can also be used for well integrity diagnostics. Fluid entering a wellbore can be quantified; fluid leaving or entering from a nonproductive zone can also be detected using temperature readings. Sierra et al. [31] described the details of the data acquisition and interpretation of the DTS results during fracturing treatments. The temperature profile can be used to monitor the cooling during injection and the warm-back during shut-in Figure 3. The authors highlighted the advantages of the permanent installation of the cable. Furthermore, they suggested the use of thermal tracers with faster interpretation capabilities in situations when cables are installed in flow paths. DTS has shown to be a successful method for injection/production allocation in unconventional wells. It can be used to evaluate fluid distribution across several clusters during fracturing stimulations and to monitor inflow distribution along the horizontal producer using absolute temperature data [33–35] and to track the distribution of inflows along with the horizontal producer [36–38]. DTS has also been used in assessing production from fractured wells during production [39]. Holley et al. [40] described the specific application of DTS in open hole packer completion for a tight gas reservoir. With the challenge of low permeability in tight gas reservoirs, the open hole completion is expected to provide greater access to the reservoir. Based on the case studies, the authors demonstrated the value of DTS monitor-

ing in providing insight into treatment effectiveness, the number, the location of initiation of fractures, and postfracture crossflow. Yoshida et al. [41] developed a two-phase linked wellbore and reservoir model that numerically simulates temperature throughout the injection, warm-back, and production phases. By using DTS data, they evaluated the cluster efficiency for one stage during the warm-back time. [38] established a black-oil thermal model that provides the cluster efficiency for a horizontal well with multistage fractures by evaluating DTS data during oil-water production. Aljawad [42] showed that DTS could be used after acid stimulation to identify a layered formation mineralogy. Another issue addressed by DTS is zonal isolation. In most cases, these reservoirs are accessed through multistage horizontal wells where zonal isolation between different stages is imperative. Several published case studies [36, 43–45] demonstrate how DTS was able to diagnose a failure in isolation in horizontal wells. DTS is useful for identifying communication between stages. During hydraulic fracture stimulation, the entire well cools down to the last perforation taking fluid [46].

**2.2.2. Distributed Acoustic Sensing (DAS).** This technology, which is relatively recent in comparison to DTS, is based on the measurement of the acoustic energy emitted during the treatment [47]. DAS surveys record the acoustic activity at various stages of the well's life. These recordings can then be used to provide information such as fluid and proppant distributions for different perforation clusters along the wellbore during stimulation [8]. DAS applications such as ball tracking, injection/production profiling, cluster efficiency evaluation, and interstage communication rely on signal intensity in high-frequency bands [44, 48, 49]. DAS may also be used to conduct time-lapse vertical seismic profiles [50–52], to monitor microseismic events [53–55], and to measure cross-well strain variations [56]. One of the most important applications of DAS technology is the diagnosis of multistage fracture treatment in horizontal wells [57]. DAS can also be used to conduct time-lapse vertical seismic (VSP) profiles [50–52] and to monitor microseismic events [53–55]. These findings have been used to quantify and estimate the geometry of far-field hydraulic fractures. DAS can provide production allocation estimates for specific types of unconventional wells over the life cycle of the well [30, 58]. DTS can be utilized to determine stage isolation and plug integrity during stimulation. It may also be used to forecast production allocation during peak periods [59]. By monitoring formation warmback after stimulation, DTS data can also help to restrict the geometry of near-wellbore fractures [30, 60]. DAS enabled the prediction of dominant fractures locations to optimize and improve future treatments [46, 57]. Compared to DTS, DAS has the advantage of faster diagnosis of immediate changes in the flow [61]. Furthermore, the thermal conductivity of the tubular and the fiber does not affect DAS measurements. [62] discussed the application of real-time DAS measurement for fracturing a horizontal well in tight sand. In gas-producing wells, successful production profiling using DAS has been reported by [30] presented DAS strain front analysis from hundreds



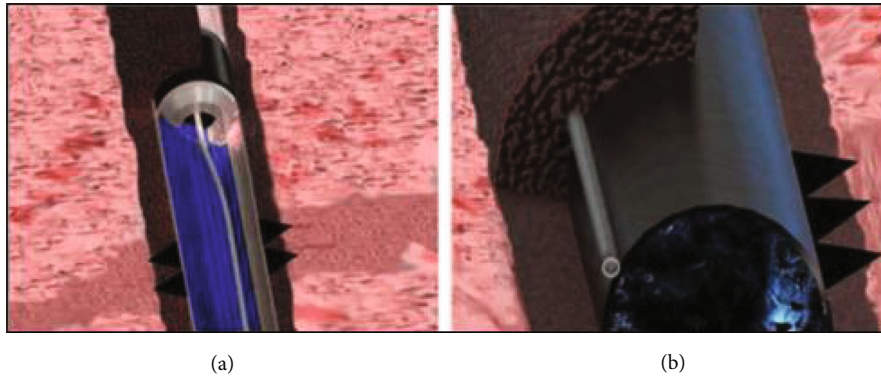


FIGURE 2: Installation of the optical cable (a) along the flow path (b) and behind the casing modified after [31].

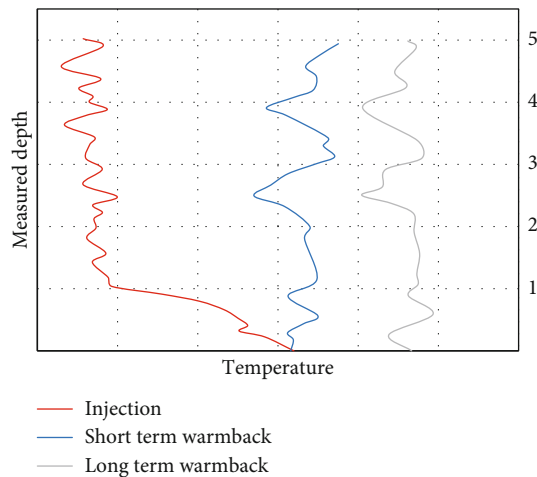


FIGURE 3: DTS measured temperature profile during injection and shut-in, indicating the flow distribution across the stage modified after [44].

of stages across a range of completion systems, with the results allowing for improved well azimuth techniques and stage offsetting. DAS is frequently used to integrate with other diagnostic tools, such as downhole pressure gauges. DAS responses often indicate fluid communication between current treatment stages and those previously stimulated, and bottom hole pressure gauges provide the ability to determine how far the current stage may be propagating. Figure 4 shows the pressure response of the pressure gauge due to several approaching stages (i.e., hydraulic connection). Monitoring the acoustic, temperature, and strain-related activity from an offset well-instrumented with a fiber optic cable can provide valuable insight into fracture diagnostics for stimulated wells. In unconventional reservoirs, DAS is utilized in time-lapse VSP seismic monitoring [63]. One challenge of DAS is the huge amount of data collected during the measurements. The discovery of low-frequency DAS (LF-DAS) of correlating fracture contacts from offset completions has increased the industry's use of fiber optics [56, 64, 65]. Jin and Roy [56] showed the application of an LF-DAS to monitor strain perturbation caused by hydraulic fracture propagation at offset monitor wells. The authors demonstrated the application of LF-DAS to monitor pro-

gressive strain perturbations caused by fracture propagation during hydraulic stimulation of a plug and perf (PnP) well. The spatial resolution of LF-DAS is limited by the system's gauge length configuration, which is generally more than a meter to offer a suitable signal-to-noise ratio and signal quality. The vast majority of LF-DAS studies in unconventional reservoirs have focused on strain changes at offset monitor wells during stimulation. The present interpretation of LF-DAS data is primarily concerned with mechanically induced rock deformation (i.e., fracture opening/closing). In contrast, LF-DAS signals are sensitive to both mechanical and thermal strains. It is critical to measure the influence of temperature changes on LF-DAS data [56].

DAS coupled with DTS has been used to evaluate completions parameters to save future expenses and improve well plans by optimizing injection profiles during treatment. [67] discussed the application of both techniques in a horizontal tight gas well with multiple clusters and stages. The measured data revealed that fracture initiation does not occur in all the clusters. The number of clusters that receive fluid is determined by stress interference and near-wellbore and tortuosity friction. Using multiple short-duration transient DTS and DAS signals, generating clusters may be identified and production profiles can be created [68, 69]. Diversion treatments can be used in multistage fracturing to ensure uniform distribution of the fracturing fluid and proppant. Fiber optic measurements can also provide information on the success of different treatments [43, 45, 57]. Fiber optics are generally much more expensive than other diagnostic methods. Furthermore, the fluid and proppant profiles are limited to near-wellbore measurements. However, the fiber optic glass crystals along the fiber make it ideal to understand well conditions in real time and allow for near-wellbore fracture quantification analysis. Jin et al. [58] generated a production allocation profile across an entire well using a combined inverted DTS transient temperature signal and DAS flow-velocity data.

Although the mechanism behind fiber optics makes it very effective for accessing the fracturing fluid taken by each cluster, its ability to evaluate proppant distribution is still under debate. Fluid transport is not the same as proppant transport. Proppant has been shown to only reach a portion of the induced fracture, which is dependent on many parameters including injection rate and fluid rheology [70]. In



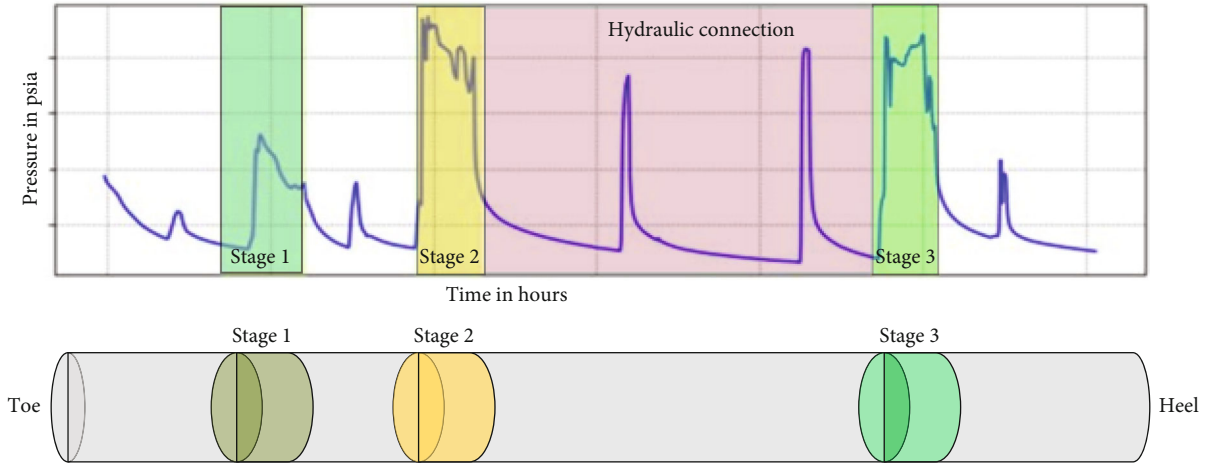


FIGURE 4: Gauge pressure recordings showing the hydraulic connection between stages modified after [66].

addition, simulations reveal a substantial heel bias in proppant distribution in the majority of the stages [23, 71]. Furthermore, DTS and DAS are unable to track the lateral extension of the proppant. As a result, fiber optic monitoring is ineffective for direct far-field mapping of the proppant distribution.

**2.3. Fracture Diagnostics Using Tiltmeters.** When a hydraulic fracture forms, the parting along the fracture causes deformation. These deformations are measured as tilt fields and can be utilized to diagnose fractures using inversion methods (Figure 5). Surface tiltmeters can be used to determine the azimuth, dip, and complexity of a fracture. The fracture dimensions can be determined using downhole tiltmeters.

**2.3.1. Surface Tiltmeters.** The depth of the fracture, as described by [17], was regarded as a major challenge for the application of the surface tiltmeters. Initially, the limitations were thought to be around 5,000 ft. However, recent advancements, as mentioned by [73], have overcome these challenges significantly, and measurements for depths greater than 10,000 ft have been reported. The limitations were attributed to the resolution of the instruments and the noise in the background, which were solved using improved instrumentation.

The data inversion process is an important aspect of tilt field diagnosis. The mathematical geophysical inversion is based on obtaining the best fit from the minimization of the difference between the forward model predictions and measured data. The residual error in the best fit can be representative of secondary fractures [73]. This is an important finding for the fracture diagnosis. One of the most distinguishing features of hydraulic fracturing in unconventional reservoirs is the growth of complex fracture networks, different from conventional treatments that create planar biwing fractures are formed and unconventional reservoirs have many intersecting nonplanar fractures. Furthermore, the network can contain both natural and induced fractures. The interaction of the hydraulic fracture with preexisting rock-fabric heterogeneity, such as natural fractures, fissures,

or cleats, is usually linked with complexity. Understanding and modeling the process of hydraulic-natural fracture interactions is critical for explaining fracture complexity and microseismic events seen during hydraulic fracturing treatments, therefore correctly predicting fracture geometry and, ultimately, reservoir production [7, 74–78]. Dahi-Taleghani and Olson [79] developed a numerical model to study the interactions between tensile fractures, induced shear fractures, and preexisting natural fractures in multi-stage hydraulic fracturing operations. The authors concluded that the fracture complexity was controlled by the geometry of the natural fractures, as well as the magnitudes, directions, and anisotropy of the principal stresses. An important application example for Eagle Ford shale formations has been discussed by [80] where an approach is described for determining the fracture network growth. They reported expanded steps in the geomechanical inversion technique for determining the areal extent of the fracture network. Similarly, [81] presented a case study for a tight gas reservoir with a cluster of horizontal wells. They found that the tiltmeter could monitor the fracture network growth during synchronous fracturing across multiple wells. [82] reported a new technique for assessing fracture complexity using surface tiltmeters, in which three additional parameters are specified to characterize the complexity in shale, coalbed, and sandstones.

Another application that benefits from surface tiltmeter diagnostics are reorientation refracturing [83–85]. The direction of the maximum principal stress changes in depleted reservoirs, causing fracture growth during refracturing to occur in a different direction from the original fracture. The change in the orientation of the fracture leads to more reservoir contact. Since the tiltmeter can monitor the azimuth of the fracture growth, the reorientation during treatment, and the additional reservoir contacted can be estimated.

**2.3.2. Downhole Tiltmeters.** Surface tiltmeters cannot provide information about the fracture dimensions because the dimensions cannot be resolved using the fields when the distance between the point of measurement and the

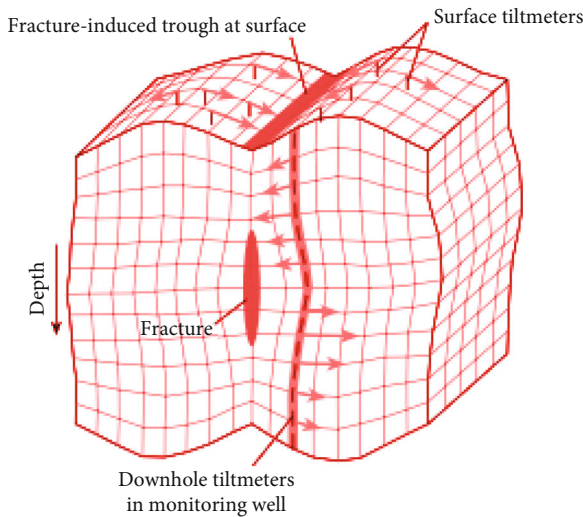


FIGURE 5: Schematic of tilt fields generated from deformation during fracturing modified after [72].

fracture is much larger than the fracture dimension. Downhole tiltmeter mapping is used to overcome this limitation. Tiltmeters are installed in offset wells rather than on the surface. The downhole tiltmeter and its implementation were reported by [73]. The downhole tiltmeter's fracture mapping principle is similar to that of a surface tiltmeter. Deformation fields are generated as a result of the induced fractures and are analyzed using inversion methods.

Figure 6 shows the influence of fracture length on deformation magnitude. The downhole tiltmeter arrays were previously installed in an offset observation well. Later advancements, however, were made to obtain data from the treatment well itself using tiltmeters. Although downhole tiltmeters are significantly more sensitive to fracture dimensions than surface tiltmeters, they do not offer direct information regarding proppant distribution [73]. As a result, they are rarely the primary choice to infer propped fracture geometries [84, 86] described the treatment well tiltmeters concept. They presented case studies in which the fracture height and width in deviated wellbores were measured in real-time. However, the technique was limited to treatments without proppants. Mayerhofer et al. [87] evaluated and used downhole tiltmeters in the treatment well to map fractures for propped treatments.

The ability to assess the vertical evolution of fracture-induced stresses and quantify fracture height is an advantage of downhole tiltmeters [88–92]. The tilt gradient displacement is orthogonal to the direction of displacement and can be used to identify how the rock formation is distorting [93]. Tiltmeters are also subjected to external disturbance, such as noise which can corrupt the data collected from the tiltmeters and distort the data of the actual fracture [94]. Surface tiltmeters are primarily used to determine fracture azimuth, dip, and complexity whereas downhole tiltmeters are used to obtain fracture dimensions. Furthermore, using the fracture mapping results, over a specified time interval, a deformation map can be generated outlining how the fracture network is formed and couple the results

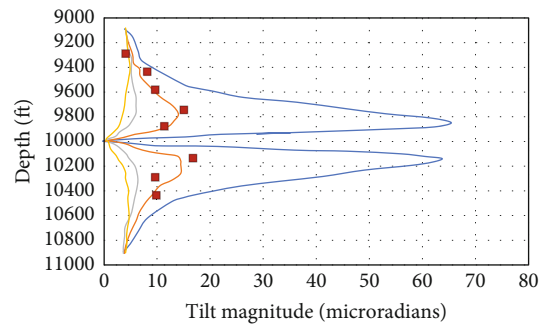


FIGURE 6: Effect of fracture length on the tilt magnitude modified after [73].

with a specified forward model will allow for approximation regarding the orientation of the fracture, the fracture volume, and the potential understanding of the fracture geometry by an inversion process [95]. Inverse problems with multiple solutions can be ill posed, and determining fracture properties such as width and shape can be difficult if the tiltmeters are located far away from the fracture plane [96].

#### 2.4. Fracture Diagnostics Using Microseismic Monitoring.

This approach for fracture mapping is based on the measurement of the seismic waves generated as a result of a hydraulic fracturing treatment. Microseisms emit elastic waves of two types: p waves (compressional) and s waves (shear). The emissions are attributed to the changes in pore pressure and stress during the treatment.

Microseismic monitoring is a common hydraulic fracturing surveillance technique that detects and records small earthquakes caused by hydraulic stimulation using surface, shallowly buried, or downhole geophones [97]. The magnitude and frequency of microseismic events are utilized to assess the growth of hydraulic fractures. Microseismic monitoring of a fracturing treatment yields information on fracture length, height, azimuth, and location around the wellbore [75]. According to [98], understanding fracture networks and growth allows for a more efficient treatment. Furthermore, tight reservoirs that have extremely low permeabilities will not be economical to recover, which is why understanding fracture propagation is critical to economic success [99].

The application of microseismic monitoring in modeling in the Barnett Shale has been discussed by [100–103] detailed the results of the stimulation treatment monitoring, as well as the resulting fracture network and stimulated reservoir volume (SRV) in the Sichuan shale. Accurate determination of far wellbore fracture geometry is an advantage of this approach. As a result, diversion treatments aiming at inducing far-field fracture complexity can also be monitored. Waters et al. [104] discussed the use of real-time monitoring for restimulation and far-wellbore diversion in Barnett Shale. East et al. [105] reported the use of this technique combined with net pressure analysis to monitor real-time far-field diversion and modify the treatment to achieve high complexity and maximum reservoir contact.

The data acquisition of the microseisms is an essential aspect of this method. Initially, measurements were obtained

using sensors installed downhole in an offset well. According to [5], the observation is reliant on the ability of the formation to transmit acoustic energy. It is preferable to have the measurements as close to the center of the fracture as possible. An offset well, on the other hand, may not be within the visible limits; therefore, new observation wells might not be desirable. Peyret et al. [106] discussed the possibility of monitoring from the surface. The authors compared the surface and downhole observations. They reported that by using surface and shallow grid observations, they were able to identify microseismic events with high accuracy. Similarly, [107] compared the downhole deployment in the treatment and offset wellbores. They discussed the triaxial borehole seismic technique for monitoring treatment wells. The authors reported that the treatment well monitoring system was able to record more data compared to the remote observation well. This treatment well recording, however, could only be done during the shut-in period following the injection treatment.

Recent advances in complex fracture modeling using microseismic modeling have enabled the prediction of fracture propagation in unconventional reservoirs using sophisticated models [75, 78, 108–110]. [111, 112] developed a fully coupled flow and geomechanics model was to identify the poroelastic behavior of multiphase fluid diffusivity and rock deformation of interwell fracturing interference in Eagle Ford unconventional reservoirs using the finite-element method (FEM) and multifracture propagation using the displacement discontinuity method. Nagel et al. [113] conducted studies on fracture complexity using higher viscosity fracture fluids, different proppant sizes, and natural fractures to investigate the interaction between a single dominant vertical hydraulic fracture and preexisting fracture networks.

Microseismic modeling is not without difficulties and geophone placement, monitoring array, is critical in the location selection of the monitoring array, how to deal with noise, and determining the suitable velocity structure ([114]. The seismic signal received by geophones are typically very weak and exhibit a low signal-to-noise ratio, introducing significant uncertainty about the location of the events, which is typically calculated by time separation of the P (primary) wave and S (secondary) wave, and these wave signals can also aid in rock formation identification [106]. The spatial distribution of microseismicity reveals information on fracture geometry and fracture development; however, it does not provide detailed information about the fracturing process, other than what is determined from the locations of the microseismic events [115]. Furthermore, microseismic measurements capture only a portion of the rock failure events and the results can be easily biased by adopting inaccurate velocity models. Moreover, this technique solely considers seismic events associated with shear failure [114, 116], without considering fluid and proppant transport. As a result, this technique provides very limited information into the propped fracture geometry, which is the primary factor controlling the effectiveness of a hydraulic fracturing job.

*2.5. Diagnostic Fracture Injection Tests (DFITs).* Diagnostic fracture injection tests (DFITs) basically comprise pump-

ing fluids into the subsurface formations to create a hydraulic fracture whereby important data can be gathered to help design hydraulic-fracturing treatments and characterize the subject reservoir as well. Historically, DFITs in conventional reservoirs focused on acquiring specific data that are essentially required for the treatment design, i.e., leak-off coefficient values and fluid efficiencies [3, 117]. This role has been then extended to acquire more data such as formation stresses, leak-off mechanisms, closure pressure, and transmissibility that can be correlated to reservoir permeability. More value was added to DFITs; when it comes to unconventional reservoirs characterization, it is found that most of the information obtained from such tests are comparable to those gained from the traditional pressure tests that are usually impractical to implement in tight, unconventional reservoirs [118]. Therefore, DFITs are recently employed to get an analyzable pressure response from such tight formations and characterize its in situ stresses.

DFITs are pump-in treatments in which small volumes of slick-water (usually KCl water) are pumped at constant low rates for a short time, creating a small fracture after exceeding the formation breakdown pressure [119]. After pumping for a certain time, the well is shut-in, and the pressure starts to fall off. After the well shut-in, the collected pressure transient data (PTA) are analyzed to identify the fracture closure pressure that is typically considered the formation minimum horizontal stress (Shmin). Figure 7 shows a typical bottom-hole pressure vs. time profile for the DFIT test.

*2.5.1. Common Data Acquisition Issues.* There are some common issues associated with DFITs either in the data acquisition stage or the analysis process. Regarding the data acquisition process, Newtonian, nonwall-building fluid should be used while pumping the treatment to get some other properties of the reservoir from the test. On the other hand, the after-closure pressure gradient can be disrupted, and the formation flow capacity can be masked in case of using gelled or other non-Newtonian fluids. While dealing with low-permeability formations, DFITs should be conducted as a pulse test which will not allow the superposition of multiple injections to have a valid analysis. In other words, if the first treatment is not pumped properly, there will be no point in injecting a second immediate attempt because the reservoir conditions have been altered by the first treatment. In such a condition, it is recommended to wait for a sufficient time for the reservoir to dissipate the pressure transient and reach unperturbed conditions [118].

Another common acquisition issue is not recording the falloff data for enough time. Depending on the type of the reservoir, the falloff recording period would differ but generally, it would be longer than the period that the pumping equipment could be available on site. After the pumping equipment move, the pumping gauges are usually replaced by secondary gauges to record the pressure. However, being calibrated in a different way than the primary pumping gauges, the secondary gauges could cause a difference in

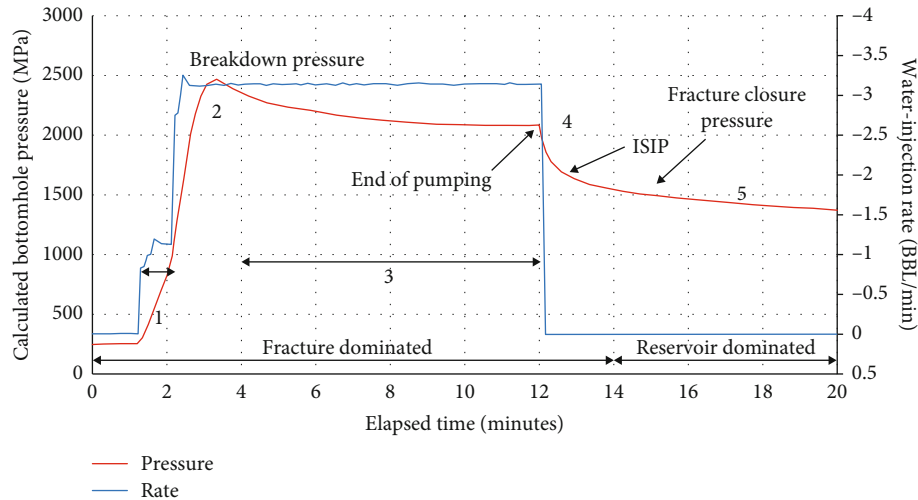


FIGURE 7: Typical bottom-hole pressure vs. time for DFIT test. The plotted lines represent the surface pressure (red line) and the injection rate (black line) modified after [120].

the readings which in turn affects the pressure derivatives and slopes [118, 121]. This may lead to false interpretation results while analyzing the recorded data. Generally, the pressure gauges should be adjusted in the way that it is highly sensitive and only reflects the response of the fracture and the formation.

**2.5.2. DFIT Data Analysis.** DFIT pressure data after shut-in can be categorized into two main groups: before and after the fracture closure (closure pressure). Nolte (1979, 1986, 1988) pioneered the before closure analysis (BCA) by introducing a dimensionless function called “G-function” that represents the elapsed time after shut-in normalized to the fracture extension duration. The G-function concept was developed based on Carter’s (1957) leak-off model and the material balance to build his approach for interpreting the data to get the fracture closure pressure, fluid efficiency, and fluids leak-off coefficients. In 1987, Castillo used the developed G-function to introduce a plot of the pressure vs. the G-function. In this plot, it is expected that the pressure data would form a straight line before deviation at the closure pressure. Often, pressure vs. G-function plot yields plots with multiple inflection points that interpret the pressure data difficult to identify the closure pressure. This can be attributed to nonideal leak-off behavior conditions, especially with unconventional reservoirs. [122] introduced two other plots including the first derivative ( $dP/dG$ ) and diagnostic derivative of the G-function ( $GdP/dG$ ) vs. the G-function. For the latter type, the ( $GdP/dG$ ) should yield a straight line passing through the origin before deviation at the closure pressure. The conventional analysis of the DFIT pressure decline data is ideally valid under some assumptions and simplifications that could introduce some errors when they are violated. Some of these assumptions are as follows:

- (i) Isotropic and homogenous reservoir
- (ii) Incompressible fracturing fluid

- (iii) Symmetric biwing fracture geometry
- (iv) Constant fracture height
- (v) Fracture growth stops immediately when pumping is stopped
- (vi) During DFIT, continuous stable fracture propagation is attained
- (vii) Constant pressure injection of a power law fluid
- (viii) Complete (unobstructed) closure of the fracture
- (ix) Constant fracture compliance (or stiffness) during closure

**2.5.3. Challenges with DFIT Data Analysis in Unconventional Reservoirs.** Being petrophysical complex systems, variations in the DFIT pressure decline behavior in the unconventional reservoirs compared to the conventional ones. In the case of unconventional reservoirs, it is not common to have such symmetric biwing fractures. Also, the fracture extension does not necessarily stop after pumping because of the accumulated pressure in the fracture during injection that may be released after pumping. This accumulation may occur due to the low fluids leak-off and the extremely low matrix permeability [120]. Consequently, the implementation of the DFIT pressure decline based on the standard assumptions makes it susceptible to noticeable errors in the interpretation of the fracture closure pressure and the formation properties as well.

For such nonideal leak-off behaviors with unconventional reservoirs, Barree et al. [123] introduced signature G-function plots considering different nonideal leak-off cases such as pressure-dependent leak-off, fracture tip extension, closing of secondary transverse fractures, and fracture height recession.

For unconventional reservoirs, it is common to have continued fracture extension or natural fracture activation. This is due to the stored pressure in the fracture, as a result



of extremely low leak-off coefficient for such reservoirs, during injection that tends to be redistributed toward the fracture tip and may cause fracture extension. Such extension may increase the fluid loss rate in such cases and can be observed as a steeper slope of the  $G$ -plot compared to the constant leaking-off area cases. Such considerations should be considered during the estimation of the fluid loss parameters using basic pressure decline analysis.

McClure et al. [124] investigated the fracture closure behavior using numerical simulation and concluded that the application of the conventional  $G$ -function diagnostic plot (the tangent line technique) underestimates the closure pressure. Therefore, they introduced another approach called the “compliance method” for interpreting the DFIT data to identify the closure pressure on the  $G$ -function plot at the point at which the fracture stiffness starts to increase. The fracture compliance can be defined as the derivative of fracture closure with respect to effective normal stress or pressure [125]. The fracture compliance is equal to the reciprocal of the fracture stiffness. This method is based on understanding how fracture stiffness (compliance as well) change due to fracture closure.

Another fracture model was then introduced by [126] to investigate the behavior of the fracture closure. They confirmed the observation of McClure et al. [124] which states that the fracture closure pressure may be underestimated when the DFIT data are interpreted using the tangent line method, and they recommended the compliance method as a more reliable approach. However, closes from its edges to the center in a progressive way, the fracture compliance keeps changing since it does not close all at once [119]. In such a case, the fracture closure pressure interpreted using this method might be larger than the minimum principal stress. Wang and Sharma [127] proposed the “variable compliance method,” and they suggested to pick an average of the dimensionless  $G$ -time of the tangent line method and compliance method as a reliable way for estimating the minimum in situ stress when a concave pressure derivative exists.

Generally, after conducting DFITs, the collected data are then analyzed to characterize the reservoir. Fracture closure pressure is one of the main objectives of such analysis to optimize the hydraulic fracturing treatment and its execution as well. Different analytical methods are commonly used for determining the closure pressure such as  $G$ -function plot,  $G$ - $dP/dG$  plot, and square-root of time approach, and fracture compliance method. However, one of the main issues associated with the data analysis process is the pressure curve interpretation especially in the case of unconventional reservoirs. Solid experience and good understating of the process is an essential requirement for identifying the straight-line sections for plotting slopes. Being solely based on human decision, such analysis is more likely to be subjective. Therefore, such analysis is very critical, and it might be sometimes biased by the human interpreter’s understanding of the process and the formation properties [128].

*2.5.4. Machine Learning (ML) Applications.* Given such criticality and importance of accurate fracture closure pressure

makes it is worthwhile for continued improvements for the followed analysis techniques to reduce the subjectivity of the analysis. Therefore, new approaches were introduced to implement the machine learning approaches to help analyze the DFIT data and identify the fracture closure pressure more accurately. Such machine learning-based approaches are recently supported by the availability of a huge amount of data besides the powerful capabilities of computers nowadays. Such models basically learn from the patterns observed in the input data to create the optimized network that can accurately predict the desired output, i.e., the fracture closure pressure. Having such models does not mean replacing the existing analytical methods but it could help identify the different fracture properties, i.e., fracture closure pressure.

Nande [128] introduced a new model to predict the fracture closure pressure ( $P_c$ ) using a supervised learning technique: artificial neural network (ANN). The proposed model was developed based on field data measured during in situ minifrac tests, from several wells within the same field. Linear regression and multilayer perceptron (MLP) algorithms were also presented as viable ML approaches to predict  $P_c$  based on field DFIT test results [129]. For such approaches, the data collected from the field tests, i.e., DFIT and mini-fract test, were analyzed carefully using different analytical techniques, i.e.,  $G$ -function and the squared-time plot, to assure the accuracy of the interpreted  $P_c$  values before being fed as output features for the ML models [128, 130].

Moreover, the ML applications are extended to detect the fracture hits at offset monitoring wells based on optical fiber-based distributed acoustic sensors (DAS) signals [58]. The developed model fitted the manually picked fracture hits using ANN to eventually result in fracture-hit probability in unconventional reservoirs. ML approaches could also help boost the event detection accuracy upon microseismic monitoring for hydraulic fracturing. Zhang et al. [131] developed a neural-network-based microseismic event detection model combined with a convolutional neural network (CNN), long short-term memory (LSTM), and a probability inference. The model was able to improve the efficiency of real-time microseismic monitoring significantly even in case of poor signal-to-noise ratio (SNR). Generally, it should be highlighted that the larger the field data available for developing such ML models are, the better the expected reliability and robustness of such models are for interpreting fracture diagnostic data with accepted accuracy. This in turn could help overcome the limitation of the subjectivity and personal biases and avoid misleading conclusions.

### 3. Comparative Analysis

Different fracture diagnosis techniques have been successfully applied to fracture treatment. However, each of them has certain advantages and disadvantages. Depending on the quality and type of information required for treatment, appropriate techniques should be evaluated and used. Analyses of the fracture diagnostic methods have also been performed previously [5, 17, 132, 133]. These studies have detailedly compared the characteristics and limitations of



TABLE 2: Application of fracture diagnostics for characterizing fracture parameters.

Parameter	High applicability	Limited applicability
Created length	Surface microseismic	When installed downhole can measure created length; the observation well monitoring should be within three times the fracture length
	Downhole microseismic	
Height	Downhole microseismic	DTS
	Surface tiltmeter	Data acquired during and after treatment; applicable to the vertically oriented wellbore
	Downhole tiltmeters	
Width	Downhole tiltmeter	DAS
		Diagnostic DAS data combined with fracture model to estimate fracture growth
Complexity	Surface tiltmeter	Pressure diagnostics
		Net pressure data and minifrac decline can also give estimates of fracture complexity when the maximum stress is known
Cluster efficiency	DTS	Information obtained posttreatment; real-time diagnosis cannot be performed to modify the treatment on-the-fly
	DAS	
Azimuth	Surface tiltmeter	Provides estimates of fracture azimuth when employed in the offset well
	Surface microseismic	
	Downhole microseismic	
Proppant distribution	RA tracers	Provides an estimate of proppant distribution in multiple fractures from different clusters assuming relative fluid and relative proppant distribution are the same
	HTNCC proppants	
	EM-based detectable proppants	
Asymmetry	Surface microseismic	The tiltmeter arrays should be in proximity to the propagating fracture
	Downhole microseismic	

the techniques for fracture dimensions, azimuth, and dip. For unconventional reservoirs, the fracture growth is not a planar fracture, but a complex fracture network. Therefore, in the case of unconventional reservoirs, it is necessary to characterize the complexity of the fracture. Warpinski et al. [11] compared different techniques, including the parameters of fracture complexity and multistage effectiveness and isolation. Table 2 presents a similar summary, comparing different diagnostic methods and their applicability to determine the important parameters of different stimulation treatments.

Through this analysis, it is obvious that no single diagnostic provides enough information to fully understand and optimize fracturing. Therefore, the combined application of multiple diagnostic methods may be the most appropriate strategy to characterize the fracturing treatment.

#### 4. Integration of Different Diagnostic Methods

[134] presented an example of integrating different diagnostic methods. The authors reported a case study in which DTS technology and microseismic mapping were used for the diagnosis of shale fractures. The limitation of microseismic mapping in resolving the near-wellbore fluid distribution is highlighted. In the case of multiple clusters, it can be assumed that the distribution of fluids among all clusters is equal. However, due to factors such as near-hole friction, in situ stress heterogeneity, and stress interference, all clusters might not receive fluid and fracture initiation might

not occur in all clusters. The assumption of equal distribution can lead to misunderstandings about microseismic events. The real-time fluid distribution monitoring using DTS can provide a better near-wellbore resolution and thus can provide more accurate information about fracture initiation. Examples of fluid entry through perforations, flow behind casing, fault reactivation, and stage isolation highlight the benefits of applying DTS and microseismic mapping at the same time.

Holley et al. [40] combined microseismic mapping and DTS to diagnose hydraulic fracturing networks. Microseismic usually cannot capture near-well fractures and reservoir conditions, while DTS can only obtain information from near-well formations. The integration of these two methods can provide real-time and comprehensive monitoring of hydraulic fracturing operations, as well as interpretation and analysis after fracturing. In addition, these two fracture diagnosis tools are linked with production log data to obtain accurate flow distribution results.

McCullagh et al. [135] discussed the application of the microseismic data to improve the results obtained through the DTS surveys for Eagle Ford shale. The far-field information obtained from the microseismic data is used to calibrate the fluid distribution and related thermal models to accurately determine fluid distribution.

The application of the microseismic mapping of the fracturing treatment in the Biyang shale in China was discussed by Yang et al. [136]. In an attempt to improve the accuracy of the estimated SRV, they used a reservoir model based on

geological logs and well log data. Based on the model, the areas with high probability and low probability of forming fractures in the near-wellbore area are determined. When the uncertainty is high, model-based indexing is used to filter the microseismic monitoring data.

The combined application of surface and downhole microseismic monitoring along with surface tiltmeters to monitor the fracturing treatment in Eagle Ford shale was described by [137]. The purpose of the monitoring was to determine the SRV and the fracture network geometry. The results of each of the diagnostic led to a more conclusive interpretation. The tiltmeter results showed the horizontal fractures dominate the near-wellbore fracture network. The difference in microseismic activity between the early and late periods was observed. The comprehensive interpretation of surface and downhole microseismic events refutes the assumptions of observation bias and background noise and points out that changes in geomechanical properties are possible causes. To determine the advantages of the combined application of tiltmeters and microseismic monitoring, [138] described the hybrid downhole tiltmeter and microseismic array. The authors also discussed the method for the inversion of the acquired data.

As a cost-saving advantage, it is mentioned that a single well is used to monitor and obtain a single result instead of two separate results. The literature also describes the application of various diagnostic methods, including RA tracers and chemical tracers [14]; [10], demonstrating the advantages of integrated fracture diagnosis.

Rate transient analysis (RTA) and pressure transient analysis (PTA) are indirect methods that can be used for fracture diagnostics and estimate the fracture and formation parameters. RTA has been used to estimate the stimulated surface area in many multistage fractured horizontal wells. Different authors combined the chemical tracer analysis with RTA to convert the producing SRV for the whole well to SRV for each stage. This combination helps to allocate the production at the stage level, in addition, to investigate the fracture operations for each stage [139]. Lately, PTA was conducted in readily available fall-off data after each stage completion to estimate the created SRV during the fracturing process. This method provides a free and real-time investigation method to estimate the fracture geometry and a measure of completion efficiency [140, 141]. However, the results from these techniques are still under debate and open more room for research.

## 5. Conclusions

- (i) Individual methods have limitations preventing a thorough characterization of the fracture network created. Using multiple diagnostic techniques (pressure diagnostics, microdeformation monitoring, microseismic monitoring, DTS/DAS fiber optics, and tracers) at the same time might result in synergies, leading to a more informative fracture description

- (ii) When utilized for diagnostic design and interpretation, advanced mathematical modeling can be useful. Data inversion for fracture asymmetry from surface tiltmeter monitoring, reservoir geomechanical model for complementing mitigating uncertainties in microseismic monitoring, and DTS inversion for real-time fluid distribution monitoring are some examples
- (iii) DFIT is one of the common fracture diagnostic tools. However, its results might be biased by the human interpreter's understanding of the process and the formation properties
- (iv) The main issue associated with the data analysis process is the pressure curve interpretation especially in the case of unconventional reservoirs due to the complex fracture matrix created and the associated nonideal leak-off behavior. Therefore, solid experience and good understating of the process is an essential requirement for identifying the fracture closure pressure accurately. Such an issue can be quietly resolved by implementing more than one technique while interpreting the pressure decline data to confirm the value of the interpreted
- (v) AI and machine learning can play a significant role in the digital transformation of the oil and gas industry which includes the improvement of pre-existing diagnostic techniques by overcoming previous limitations by utilizing the wealth of data available from field operations
- (vi) The automation of the operations using intelligent methods that exist in AI can lead to dramatically reduce the costs incurred by the personnel and equipment in the field operations, hence improving the economics of the service providers

## Conflicts of Interest

The authors declare that they have no conflicts of interest.

## References

- [1] M. B. Smith and C. Montgomery, *Hydraulic fracturing*, Crc Press, 2015.
- [2] C. L. Cipolla, N. R. Warpinski, and M. J. Mayerhofer, "Hydraulic fracture complexity: diagnosis, remediation, and exploitation," in *SPE Asia Pacific Oil and Gas Conference and Exhibition*, Perth, Australia, 2008.
- [3] D. P. Craig and T. A. Blasingame, "Application of a new fracture-injection/falloff model accounting for propagating, dilated, and closing hydraulic fractures," in *SPE Gas Technology Symposium*, Calgary, Alberta, Canada, 2006.
- [4] S. C. Maxwell, C. K. Waltman, N. R. Warpinski, M. J. Mayerhofer, and N. Baroumand, "Imaging seismic deformation induced by hydraulic fracture complexity," *SPE Reservoir Evaluation and Engineering*, vol. 12, no. 1, pp. 48–52, 2009.
- [5] R. D. Barree, M. K. Fisher, and R. A. Woodroof, "A practical guide to hydraulic fracture diagnostic technologies," in

- Proceedings-SPE annual technical conference and exhibition*, pp. 983–994, San Antonio, Texas, 2002.
- [6] N. Warpinski, “Microseismic monitoring: inside and out,” *JPT, Journal of Petroleum Technology*, vol. 61, no. 11, pp. 80–85, 2009.
- [7] M. J. Mayerhofer, E. P. Lonon, C. Rightmire, D. Walsler, C. L. Cipolla, and N. R. Warpinski, “What is stimulated reservoir volume?,” *SPE Production and Operations*, vol. 25, no. 1, pp. 89–98, 2010.
- [8] M. M. Molenaar, D. J. Hill, P. Webster, E. Fidan, and B. Birch, “First downhole application of distributed acoustic sensing for hydraulic-fracturing monitoring and diagnostics,” *SPE Drilling and Completion*, vol. 27, no. 1, pp. 32–38, 2012.
- [9] P. Saldungaray and T. Palisch, “Hydraulic fracture optimization in unconventional reservoirs,” in *Offshore Mediterranean conference and exhibition 2013*, pp. 1–15, OMC, 2013.
- [10] M. P. Scott, T. Stephens, R. H. Durant, J. M. McGowen, W. W. Thom, and R. A. Woodroof, “Investigating hydraulic fracturing in tight gas sand and shale gas reservoirs in the Cooper Basin,” in *Society of Petroleum Engineers-Asia Pacific Unconventional Resources Conference and Exhibition 2013: Delivering Abundant Energy for a Sustainable Future*, vol. 2, pp. 731–756, Brisbane, Australia, 2013.
- [11] N. R. Warpinski, M. J. Mayerhofer, E. J. Davis, and E. H. Holley, “Integrating fracture diagnostics for improved microseismic interpretation and stimulation modeling,” *Society of Petroleum Engineers-SPE/AAPG/SEG Unconventional Resources Technology Conference*, vol. 2013, pp. 1–19, 2016.
- [12] L. L. Gadeken and H. D. Smith, “Relative distance indicator from gamma ray spectroscopy measurements with radioactive tracers,” in *SPE Middle East Oil Technical Conference and Exhibition Proceedings: Society of Petroleum Engineers*, pp. 357–364, Manama, Bahrain, 1989.
- [13] G. L. Gore and L. L. Terry, “Radioactive tracer techniques,” *Journal of Petroleum Technology*, vol. 8, no. 9, pp. 12–17, 1956.
- [14] R. L. Johnson, M. P. Scott, R. G. Jeffrey et al., “Evaluating hydraulic fracture effectiveness in a coal seam gas reservoir from surface tiltmeter and microseismic monitoring,” in *Society of Petroleum Engineers-SPE Asia Pacific oil and gas conference and exhibition 2010*, pp. 714–741, Florence, Italy, 2010.
- [15] N. Stegent, R. Dusterhoft, and H. Menon, “Insight into hydraulic fracture geometries using fracture modeling honoring field data measurements and post-fracture production,” in *SPE Europec Featured at 81st EAGE Conference and Exhibition*, London, England, UK, 2019.
- [16] Y. Du and L. Guan, “Interwell tracer tests: lessons learned from past field studies,” in *SPE Asia Pacific Oil and Gas Conference and Exhibition-Proceedings*, pp. 211–219, Jakarta, Indonesia, 2005.
- [17] N. R. Warpinski, “Hydraulic fracture diagnostics,” *JPT, Journal of Petroleum Technology*, vol. 48, no. 10, pp. 907–910, 1996.
- [18] H. Ron and L. Lake, *Petroleum Engineering Handbook, Volume V (B)*, Reservoir Engineering and Petrophysics, 2007.
- [19] A. Salman, B. Kurtoglu, and H. Kazemi, “Analysis of chemical tracer flowback in unconventional reservoirs,” *Society of Petroleum Engineers-SPE Canadian Unconventional Resources Conference 2014*, vol. 2, no. 1, pp. 1067–1088, 2014.
- [20] A. D. Grae, R. J. Duenckel, J. R. Nelson, H. D. Smith, X. Han, and T. T. Palisch, “Field study compares fracture diagnostic technologies,” in *Society of Petroleum Engineers-SPE Hydraulic Fracturing Technology Conference*, pp. 397–408, The Woodlands, Texas, USA, 2012.
- [21] R. J. Duenckel, H. D. Smith, W. A. Warren, and A. D. Grae, “Field application of a new proppant detection technology,” in *Proceedings-SPE annual technical conference and exhibition*, pp. 2471–2485, Denver, Colorado, USA, 2011.
- [22] T. Palisch, W. Tailji, L. Bartel, C. Cannan, M. Czapski, and K. Lynch, “Recent advancements in far-field proppant detection,” *Society of Petroleum Engineers-SPE Hydraulic Fracturing Technology Conference, HFTC*, vol. 2016, 2016.
- [23] L. Li, H. Jiang, J. Li, K. Wu, F. Meng, and Z. Chen, “Modeling tracer flowback in tight oil reservoirs with complex fracture networks,” *Journal of Petroleum Science and Engineering*, vol. 157, pp. 1007–1020, 2017.
- [24] L. Li, H. Jiang, J. Li, and L. Zhao, “Fracture quantitative characterization using tracer flowback for multistage fracturing horizontal well in tight oil,” in *All Days*, Moscow, Russia, 2016.
- [25] W. Tian, X. Wu, T. Shen, and S. Kalra, “Estimation of hydraulic fracture volume utilizing partitioning chemical tracer in shale gas formation,” *Journal of Natural Gas Science and Engineering*, vol. 33, pp. 1069–1077, 2016.
- [26] A. Kumar and M. M. Sharma, “Diagnosing fracture-wellbore connectivity using chemical tracer flowback data,” in *SPE/AAPG/SEG Unconventional Resources Technology Conference*, Houston, Texas, USA, 2018.
- [27] I. Pakhotina, S. Sakaida, D. Zhu, and A. Daniel Hill, “Diagnosing multistage fracture treatments with distributed fiber-optic sensors,” *SPE Production and Operations*, vol. 35, no. 4, pp. 0852–0864, 2020.
- [28] P. Richter, T. Parker, C. Woerpel, W. Wu, R. Rufino, and M. Farhadiroushan, “High-resolution distributed acoustic sensor using engineered fiber for hydraulic fracture monitoring and optimization in unconventional completions,” *SEG International Exposition and Annual Meeting*, vol. 2020, pp. 4874–4878, 2019.
- [29] P. F. Stark, N. C. Bohrer, T. T. Kemner, J. Magness, A. Shea, and K. Ross, “Improved completion economics through real-time, fiber optic stimulation monitoring,” in *SPE Hydraulic Fracturing Technology Conference and Exhibition*, OnePetro, 2019.
- [30] G. A. Ugueto, F. Todea, T. Daredia et al., “Can you feel the strain? DAS strain fronts for fracture geometry in the BC Montney, Groundbirch,” in *Proceedings-SPE Annual Technical Conference and Exhibition*, Calgary, Alberta, Canada, 2019.
- [31] J. Sierra, J. Kaura, D. Gualtieri, G. Glasbergen, D. Sarkar, and D. Johnson, “DTS monitoring data of hydraulic fracturing: experiences and lessons learned,” *Proceedings-SPE Annual Technical Conference and Exhibition*, vol. 5, no. 1, pp. 3461–3475, 2008.
- [32] C. Cipolla, S. Maxwell, M. Mack, and R. Downie, “A practical guide to interpreting microseismic measurements,” in *Society of Petroleum Engineers-SPE/EAGE European Unconventional Resources Conference and Exhibition*, pp. 49–76, The Woodlands, Texas, USA, 2012a.
- [33] X. Li, J. Zhang, M. Grubert et al., “Distributed acoustic and temperature sensing applications for hydraulic fracture diagnostics,” in *SPE Hydraulic Fracturing Technology Conference and Exhibition*, OnePetro, 2020.



- [34] X. Li and D. Zhu, "Temperature behavior during multistage fracture treatments in horizontal wells," *SPE Production & Operations*, vol. 33, no. 3, pp. 522–538, 2018.
- [35] M. Tabatabaei and D. Zhu, "Fracture-stimulation diagnostics in horizontal wells through use of distributed-temperature-sensing technology," *SPE Production & Operations*, vol. 27, no. 4, pp. 356–362, 2012.
- [36] P. Huckabee, "Optic fiber distributed temperature for fracture stimulation diagnostics and well performance evaluation," *Society of Petroleum Engineers-SPE Hydraulic Fracturing Technology Conference*, 2009, pp. 74–93, The Woodlands, Texas, USA, 2009.
- [37] H. Sun, W. Yu, and K. Sepehrnoori, "A new comprehensive numerical model for fracture diagnosis with distributed temperature sensing DTS," in *Proceedings-SPE Annual Technical Conference and Exhibition, 0(Nolte 1979)*, San Antonio, Texas, USA, 2017.
- [38] S. Zhang and D. Zhu, "Efficient flow rate profiling for multiphase flow in horizontal wells using downhole temperature measurement," in *International Petroleum Technology Conference*, Beijing, China, 2019.
- [39] S. Gorgi, J. F. Joya, A. Al-Ebrahim et al., "Case history: real-time fiber-optic technology maximizes tight carbonate formation returns in Kuwait, multistage acid fracturing diagnostics, post-treatment flowback allocation, and production profiling," in *International Petroleum Technology Conference 2019*, Beijing, China, 2019.
- [40] E. H. Holley, M. M. Molenaar, E. Fidan, and B. Banack, "Interpreting uncemented multistage hydraulic-fracturing completion effectiveness by use of fiber-optic DTS injection data," *SPE Drilling and Completion*, vol. 28, no. 3, pp. 243–253, 2013.
- [41] N. Yoshida, A. D. Hill, and D. Zhu, "Comprehensive modeling of downhole temperature in a horizontal well with multiple fractures," *SPE Journal*, vol. 23, no. 5, pp. 1580–1602, 2018.
- [42] M. S. Aljawad, "Identifying formation mineralogy composition in acid fracturing from distributed temperature measurements," *SPE Reservoir Evaluation & Engineering*, vol. 23, no. 1, pp. 200–211, 2020.
- [43] A. Gustavo, C. Ugueto, P. T. Huckabee, and M. M. Molenaar, "Challenging assumptions about fracture stimulation placement effectiveness using fiber optic distributed sensing diagnostics: diversion, stage isolation and overfishing," in *Society of Petroleum Engineers-SPE Hydraulic Fracturing Technology Conference*, pp. 357–368, The Woodlands, Texas, USA, 2015.
- [44] E. H. Holley and N. Kalia, "Fiber-optic monitoring: stimulation results from unconventional reservoirs," in *Society of Petroleum Engineers-Unconventional Resources Technology Conference*, San Antonio, Texas, USA, 2015.
- [45] B. Wheaton, K. Haustveit, W. Deeg, J. Miskimins, and R. Barree, "A case study of completion effectiveness in the Eagle Ford shale using DAS/DTS observations and hydraulic fracture modeling," *Society of Petroleum Engineers-SPE Hydraulic Fracturing Technology Conference, HFTC*, vol. 2016, 2016.
- [46] G. A. Ugueto, M. Ehiwario, A. Grae et al., "Application of integrated advanced diagnostics and modeling to improve hydraulic fracture stimulation analysis and optimization," *Society of Petroleum Engineers-SPE Hydraulic Fracturing Technology Conference*, vol. 2014, pp. 347–360, 2014.
- [47] R. Cannon and F. Aminzadeh, "Distributed acoustic sensing: state of the art," in *Society of Petroleum Engineers-SPE Digital Energy Conference and Exhibition*, pp. 51–60, The Woodlands, Texas, USA, 2013.
- [48] C. Ugueto, G. A. Huckabee, P. T. Molenaar, M. M. Wyker, and K. Somanchi, "Perforation cluster efficiency of cemented plug and perf limited entry completions; insights from fiber optics diagnostics," in *Spe Hydraulic Fracturing Technology Conference*, OnePetro, 2016.
- [49] P. Webster, J. Wall, C. Perkins, and M. Molenaar, "Microseismic detection using distributed acoustic sensing," in *In SEG Technical Program Expanded Abstracts 2013*, pp. 2459–2463, Society of Exploration Geophysicists, 2013.
- [50] G. Binder and D. Chakraborty, "Detecting microseismic events in downhole distributed acoustic sensing data using convolutional neural networks," in *SEG International Exposition and Annual Meeting*, pp. 4864–4868, San Antonio, Texas, USA, 2019.
- [51] G. Byerley, D. Monk, P. Aaron, and M. Yates, "Time-lapse seismic monitoring of individual hydraulic frac stages using a downhole DAS array," *The Leading Edge*, vol. 37, no. 11, pp. 802–810, 2018.
- [52] A. Titov, G. Binder, G. Jin et al., "Analysis of scattered waves observed in inter-stage DAS VSP data from zipper-fracturing operations," in *In SEG Technical Program Expanded Abstracts 2020*, pp. 3793–3797, Society of Exploration Geophysicists, 2020.
- [53] S. Cole, M. Karrenbach, D. Kahn, J. Rich, K. Silver, and D. Langton, "Source parameter estimation from DAS microseismic data," in *SEG technical program expanded abstracts 2018*, pp. 4928–4932, Anaheim, California, USA, 2018.
- [54] M. Karrenbach, D. Kahn, S. Cole et al., "Hydraulic-fracturing-induced strain and microseismic using in situ distributed fiber-optic sensing," *The Leading Edge*, vol. 36, no. 10, pp. 837–844, 2017.
- [55] I. Vera Rodriguez and A. Wuestefeld, "Strain microseismics: radiation patterns, synthetics, and moment tensor resolvability with distributed acoustic sensing in isotropic media," *Geophysics*, vol. 85, no. 3, pp. KS101–KS114, 2020.
- [56] G. Jin and B. Roy, "Hydraulic-fracture geometry characterization using low-frequency das signal," *The Leading Edge*, vol. 36, no. 12, pp. 975–980, 2017.
- [57] M. M. Molenaar, E. Fidan, and D. J. Hill, "Real-time downhole monitoring of hydraulic fracturing treatments using fibre optic distributed temperature and acoustic sensing," *Society of Petroleum Engineers-SPE/EAGE European Unconventional Resources Conference and Exhibition*, vol. 2012, pp. 726–738, 2012.
- [58] G. Jin, K. Mendoza, B. Roy, and D. G. Buswell, "Machine learning-based fracture-hit detection algorithm using LFDAS signal," *The Leading Edge*, vol. 38, no. 7, pp. 520–524, 2019.
- [59] G. Jin, K. Frieauf, B. Roy et al., "Fiber optic sensing-based production logging methods for low-rate oil producers," in *SPE/AAPG/SEG Unconventional Resources Technology Conference*, Denver, Colorado, USA, 2019a.
- [60] K. Raterman, Y. Liu, and L. Warren, "Analysis of a drained rock: an Eagle Ford example," in *SPE/AAPG/SEG Unconventional Resources Technology Conference*, Denver, Colorado, USA, 2019.

- [61] J. Williams, "Distributed acoustic sensing for pipeline monitoring," *Pipeline and Gas Journal*, vol. 239, no. 7, pp. 24–26, 2012.
- [62] W. MacPhail, B. Lisoway, and K. Banks, "Fiber optic distributed acoustic sensing of multiple fractures in a horizontal well," in *Society of Petroleum Engineers-SPE Hydraulic Fracturing Technology Conference*, pp. 531–550, The Woodlands, Texas, USA, 2012.
- [63] J. Andres Chavarria, D. Kahn, D. Langton, S. Cole, and X. Li, "Time-lapse WAW VSP imaging of an unconventional reservoir using DAS fiber optics," in *Proceedings of the 7th Unconventional Resources Technology Conference*, pp. 1–9, Denver, Colorado, USA, 2020.
- [64] Y. Wu, P. Richter, R. Hull, and M. Farhadiroushan, "Hydraulic frac-hit corridor (FHC) monitoring and analysis with high-resolution distributed acoustic sensing (DAS) and far-field strain (FFS) measurements," *First Break*, vol. 38, no. 6, pp. 65–70, 2020.
- [65] S. Zhang, H. Tang, R. Hurt, V. Jayaram, and J. Wagner, "Joint interpretation of fiber optics and downhole gauge data for near wellbore region characterization," in *Society of Petroleum Engineers-SPE hydraulic fracturing technology conference and exhibition 2020, HFTC 2020*, The Woodlands, Texas, USA, 2020.
- [66] Z. Zhang, Z. Fang, J. Stefani et al., "Modeling of fiber-optic strain responses to hydraulic fracturing," *Geophysics*, vol. 85, no. 6, pp. A45–A50, 2020.
- [67] P. A. Sookprasong, C. C. Gill, and R. S. Hurt, "Lessons Learned from DAS and DTS in multi cluster, multistage horizontal well fracturing: interpretation of hydraulic fracture initiation and propagation through diagnostics," in *Society of Petroleum Engineers-IADC/SPE Asia Pacific Drilling Technology Conference 2014: Driving Sustainable Growth Through Technology and Innovation*, pp. 432–440, Bangkok, Thailand, 2014.
- [68] A. Attia, J. Brady, M. Lawrence, and R. Porter, "Validating refrac effectiveness with carbon rod conveyed distributed fiber optics in the Barnett Shale for Devon Energy," in *SPE Hydraulic Fracturing Technology Conference and Exhibition.*, The Woodlands, Texas, USA, 2019.
- [69] M. Lawrence and A. Attia, "Comparing and combining camera, tracer and distributed temperature and acoustic sensing DAS+DTS for a holistic understanding of stimulation and production performance," in *SPE Hydraulic Fracturing Technology Conference and Exhibition.*, 2021Virtual.
- [70] C. A. Blyton, D. P. Gala, and M. M. Sharma, "A comprehensive study of proppant transport in a hydraulic fracture," in *SPE Annual Technical Conference and Exhibition*, Houston, Texas, USA, 2015.
- [71] C.-H. Wu, S. Yi, and M. M. Sharma, "Proppant distribution among multiple perforation clusters in a horizontal wellbore," in *Day 1 Tue, January 24, 2017*, The Woodlands, Texas, USA, 2017.
- [72] L. Bennett, J. L. Calvez, D. R. R. Sarver et al., "The source for hydraulic fracture characterization," *Oilfield Review*, vol. 17, no. 4, pp. 42–57, 2005.
- [73] C. A. Wright, E. J. Davis, W. A. Minner et al., "Surface tiltmeter fracture mapping reaches new depths -10, 000 feet, and beyond?," in *Proceedings-SPE Annual Western Regional Meeting*, Denver, Colorado, 1998.
- [74] C. L. Cipolla, M. J. Williams, X. Weng, M. Mack, and S. Maxwell, "Hydraulic fracture monitoring to reservoir simulation: maximizing value," in *Second EAGE Middle East Tight Gas Reservoirs Workshop*, p. 244, Manama, Bahrain, 2010.
- [75] C. Cipolla, X. Weng, M. Mack et al., "Integrating microseismic mapping and complex fracture modeling to characterize fracture complexity," in *SPE/EAGE European Unconventional Resources Conference & Exhibition-from Potential to Production*, p. 285, Vienna, Austria, 2012b.
- [76] S. C. Maxwell, X. Weng, O. Kresse, and J. Rutledge, "Modeling microseismic hydraulic fracture deformation," in *Proceedings-SPE Annual Technical Conference and Exhibition*, vol. 4, pp. 2792–2801, New Orleans, Louisiana, USA, 2013.
- [77] C. M. Sayers and J. Le Calvez, "Characterization of microseismic data in gas shales using the radius of gyration tensor," in *SEG Technical Program Expanded Abstracts 2010*, Denver, Colorado, 2010.
- [78] X. Weng, O. Kresse, C. E. Cohen, R. Wu, and H. Gu, "Modeling of hydraulic fracture network propagation in a naturally fractured formation," in *SPE Hydraulic Fracturing Technology Conference. Society of Petroleum Engineers*, The Woodlands, Texas, USA, 2011.
- [79] A. Dahi-Taleghani and J. E. Olson, "Numerical modeling of multistranded-hydraulic-fracture propagation: accounting for the interaction between induced and natural fractures," *SPE Journal*, vol. 16, no. 3, pp. 575–581, 2011.
- [80] D. K. Astakhov, W. H. Roadarmel, and A. S. Nanayakkara, "A new method of characterizing the stimulated reservoir volume using tiltmeter-based surface microdeformation measurements," in *Society of Petroleum Engineers-SPE hydraulic fracturing technology conference 2012, (Mayerhofer 2010)*, pp. 21–35, The Woodlands, Texas, USA, 2012.
- [81] J. Zhou, Y. Zeng, T. Jiang, B. Zhang, and X. Zhang, "Tiltmeter hydraulic fracturing mapping on a cluster of horizontal wells in a tight gas reservoir," in *Society of Petroleum Engineers-SPE/IATMI Asia Pacific Oil and Gas Conference and Exhibition, APOGCE 2015*, Nusa Dua, Bali, Indonesia, 2015.
- [82] X. Wang, Y. Ding, N. Xiu, and Z. Wang, "A new method to interpret hydraulic fracture complexity in unconventional reservoir by tilt magnitude," in *Society of Petroleum Engineers-International Petroleum Technology Conference 2013, IPTC 2013: Challenging Technology and Economic Limits to Meet the Global Energy Demand*, vol. 6, pp. 5011–5025, Beijing, China, 2013.
- [83] Y. Fei, W. Dingwei, L. Yang, Y. Yongbo, and H. Feng, "Reorientation refracturing case study," in *SPE production and operations symposium, proceedings*, pp. 230–235, Oklahoma City, Oklahoma, USA, 2007.
- [84] E. Siebrits, J. L. Elbel, R. S. Hoover et al., "Refracture reorientation enhances gas production in Barnett Shale tight gas wells," in *Proceedings of the annual southwestern petroleum short course*, pp. 192–202, Dallas, Texas, 2001.
- [85] S. Wolhart, M. Zoll, G. McIntosh, and L. Weijers, "Surface tiltmeter mapping shows hydraulic fracture reorientation in the Codell formation," in *Proceedings-SPE Annual Technical Conference and Exhibition*, vol. 3, pp. 1763–1770, Wattenberg Field, Colorado, 2007.
- [86] C. A. Wright, E. J. Davis, J. F. Ward et al., "Real-time fracture mapping from the "live" treatment well," in *Proceedings-SPE annual technical conference and exhibition*, pp. 2811–2817, New Orleans, Louisiana, 2001).
- [87] M. J. Mayerhofer, H. L. Stutz, E. Davis, and S. L. Wolhart, "Optimizing fracture stimulation using treatment-well



- tiltmeters and integrated fracture modeling,” *SPE Production and Operations*, vol. 21, no. 2, pp. 222–229, 2006.
- [88] A. Daneshy, “Dynamic interaction within multiple limited entry fractures in horizontal wells: theory, implications and field verification,” in *SPE Hydraulic Fracturing Technology Conference*, The Woodlands, Texas, USA, 2015.
- [89] A. Daneshy, C. Touchet, F. Hoffman, and M. McKown, “Field determination of fracture propagation mode using downhole pressure data,” in *SPE Hydraulic Fracturing Technology Conference*, The Woodlands, Texas, USA, 2015.
- [90] M. Dawson and G. Kampf, “Breakthrough in hydraulic fracture & proppant mapping: achieving increased precision with lower cost,” in *Unconventional Resources Technology Conference*, pp. 438–458, San Antonio, TX, USA, 2016.
- [91] G. Kampf and M. Dawson, “A novel approach to mapping hydraulic fractures using poromechanic principles,” in *50th US rock mechanics/Geomechanics symposium*, Houston, Texas, 2016.
- [92] N. P. Roussel and S. Agrawal, “Introduction to poroelastic response monitoring-quantifying hydraulic fracture geometry and SRV permeability from offset-well pressure data,” in *SPE/AAPG/SEG Unconventional Resources Technology Conference*, OnePetro, 2017.
- [93] J. L. Miskimins, *Hydraulic Fracturing: Fundamentals and Advancements*, Society of Petroleum Engineers, 2019.
- [94] V. Pandurangan, A. Peirce, Z. R. Chen, and R. G. Jeffrey, “Tiltmeter mapping of measured nonsymmetric hydraulic fracture growth in a conglomerate/sandstone formation using the implicit level-set algorithm and the extended Kalman filter,” *SPE Journal*, vol. 23, no. 1, pp. 172–185, 2018.
- [95] B. Lecampion and J. Gunning, “Model selection in fracture mapping from elastostatic data,” *International Journal of Solids and Structures*, vol. 44, no. 5, pp. 1391–1408, 2007.
- [96] B. Lecampion, R. Jeffrey, and E. Detournay, “Resolving the geometry of hydraulic fractures from tilt measurements,” *Pure and Applied Geophysics*, vol. 162, no. 12, pp. 2433–2452, 2005.
- [97] S. Maxwell, *Microseismic Imaging of Hydraulic Fracturing: Improved Engineering of Unconventional Shale Reservoirs*, 2014, Society of Exploration Geophysicists.
- [98] G. E. King, L. Haile, J. A. Shuss, and T. Dobkins, “Increasing fracture path complexity and controlling downward fracture growth in the Barnett Shale,” in *SPE Shale Gas Production Conference*, Fort Worth, Texas, USA, 2008.
- [99] R. P. Sutton, S. A. Cox, and R. D. Barree, “Shale gas plays: a performance perspective,” in *Tight Gas Completions Conference*, Society of Petroleum Engineers, 2010.
- [100] D. Denney, “Optimizing horizontal completions in the Barnett Shale with microseismic fracture mapping,” *Journal of Petroleum Technology*, vol. 57, no. 3, pp. 41–43, 2005.
- [101] D. Denney, “Hydraulic fracturing: compensation of surge and swab pressures in floating drilling operations,” *Journal of Petroleum Technology*, vol. 60, no. 3, pp. 57–60, 2008.
- [102] S. C. Maxwell, T. I. Urbancic, N. Steinsberger, and R. Zinno, “Microseismic imaging of hydraulic fracture complexity in the Barnett Shale,” in *Proceedings-SPE Annual Technical Conference and Exhibition*, pp. 965–973, San Antonio, Texas, 2002.
- [103] F. Dwan, J. Qiu, M. Zhou et al., “Sichuan shale gas microseismic monitoring: acquisition, processing, and integrated analyses,” in *Society of Petroleum Engineers-International Petroleum Technology Conference 2013, IPTC 2013: Challenging Technology and Economic Limits to Meet the Global Energy Demand*, pp. 1097–1112, Beijing, China, 2013.
- [104] G. Waters, H. Ramakrishnan, J. Daniels, D. Bentley, J. Belhadi, and D. Sparkman, *Utilization of Real Time Microseismic Monitoring and Hydraulic Fracture Diversion Technology in the Completion of Barnett Shale Horizontal Wells*, pp. 1–11, 2009.
- [105] L. East, M. Y. Soliman, and J. Augustine, “Methods for enhancing far-field complexity in fracturing operations,” *SPE Production & Operations*, vol. 26, no. 3, pp. 291–303, 2011.
- [106] O. Peyret, J. Drew, M. Mack, K. Brook, and S. Ma, *SP subsurface to surface microseismic monitoring for hydraulic fracturing*, 2012.
- [107] K. D. Mahrer, R. J. Zinno, and J. R. Bailey, “Simultaneous recording of hydraulic-fracture-induced microseisms in the treatment well and in a remote well,” in *SPE-Hydraulic Fracturing Technology Conference 2007, 2007*, pp. 132–135, College Station, Texas, USA, 2007.
- [108] M. K. Rahman, M. M. Hossain, and S. S. Rahman, “A shear-dilation-based model for evaluation of hydraulically stimulated naturally fractured reservoirs,” *International Journal for Numerical and Analytical Methods in Geomechanics*, vol. 26, no. 5, pp. 469–497, 2002.
- [109] W. Xu, M. J. Thiercelin, U. Ganguly et al., “Wiremesh: a novel shale fracturing simulator,” in *International Oil and Gas Conference and Exhibition in China. Society of Petroleum Engineers*, Beijing, China, 2010.
- [110] W. Xu, M. J. Thiercelin, and I. C. Walton, “Characterization of hydraulically-induced shale fracture network using an analytical/semi-analytical model,” in *SPE Annual Technical Conference and Exhibition. Society of Petroleum Engineers*, New Orleans, Louisiana, 2009.
- [111] X. Guo, K. Wu, J. Killough, and J. Tang, “Understanding the mechanism of interwell fracturing interference with reservoir/geomechanics/fracturing modeling in eagle ford shale,” *SPE Reservoir Evaluation & Engineering*, vol. 22, no. 3, pp. 842–860, 2019.
- [112] X. Guo, K. Wu, C. An, J. Tang, and J. Killough, “Numerical investigation of effects of subsequent parent-well injection on Interwell fracturing interference using reservoir-geomechanics-fracturing modeling,” *SPE Journal*, vol. 24, no. 4, pp. 1884–1902, 2019.
- [113] N. B. Nagel, M. A. Sanchez, and B. Lee, *Gas shale hydraulic fracturing: a Numerical evaluation of the effect of geomechanical parameters*, SPE Hydraulic Fracturing Technology Conference, Society of Petroleum Engineers, 2012.
- [114] L. Eisner, T. Fischer, and J. H. Le Calvez, “Detection of repeated hydraulic fracturing (out-of-zone growth) by microseismic monitoring,” *The Leading Edge*, vol. 25, no. 5, pp. 548–554, 2006.
- [115] N. R. Warpinski, J. Du, and U. Zimmer, “Measurements of hydraulic-fracture-induced seismicity in gas shales,” in *SPE Hydraulic Fracturing Technology Conference. Society of Petroleum Engineers*, The Woodlands, Texas, USA, 2012.
- [116] N. R. Warpinski and J. Du, “Source-mechanism studies on microseismicity induced by hydraulic fracturing,” in *SPE Annual Technical Conference and Exhibition. Society of Petroleum Engineers*, Florence, Italy, 2010.

- [117] R. D. Barree, "Applications of pre-frac injection/falloff tests in fissured reservoirs-field examples," in *SPE Rocky Mountain Regional/Low-Permeability Reservoirs Symposium*, Denver, Colorado, 1998.
- [118] R. D. Barree, J. L. Miskimins, and J. V. Gilbert, "Diagnostic fracture injection tests: common mistakes, misfires, and misdiagnoses," *SPE Production & Operations*, vol. 30, no. 2, pp. 84–98, 2015.
- [119] H. Wang and M. M. Sharma, "A non-local model for fracture closure on rough fracture faces and asperities," *Journal of Petroleum Science and Engineering*, vol. 154, pp. 425–437, 2017.
- [120] M. I. Mohamed, M. Salah, Y. Coskuner, M. Ibrahim, C. Pieprzica, and E. Ozkan, "Investigation of non-ideal diagnostic fracture injection tests behavior in unconventional reservoirs," in *SPE Hydraulic Fracturing Technology Conference and Exhibition. Society of Petroleum Engineers*, The Woodlands, Texas, USA, 2019.
- [121] D. D. Cramer and D. H. Nguyen, "Diagnostic fracture injection testing tactics in unconventional reservoirs," in *Society of Petroleum Engineers-SPE Hydraulic Fracturing Technology Conference*, pp. 517–559, The Woodlands, Texas, USA, 2013.
- [122] R. D. Barree and H. Mukherjee, "Determination of pressure dependent leakoff and its effect on fracture geometry," in *SPE Annual Technical Conference and Exhibition*, Denver, Colorado, 1996.
- [123] R. D. Barree, V. L. Barree, and D. P. Craig, "Holistic fracture diagnostics: consistent interpretation of prefrac injection tests using multiple analysis methods," *SPE Production & Operations*, vol. 24, no. 3, pp. 396–406, 2009.
- [124] M. W. McClure, H. Jung, D. D. Cramer, and M. M. Sharma, "The fracture-compliance method for picking closure pressure from diagnostic fracture-injection tests," *SPE Journal*, vol. 21, no. 4, pp. 1321–1339, 2016.
- [125] J. C. Jaeger, N. G. W. Cook, and R. Zimmerman, *Fundamentals of Rock Mechanics*, Wiley-Blackwell, 4th edition, 2007.
- [126] B. Zanganeh, C. R. Clarkson, and R. V. Hawkes, "Reinterpretation of fracture closure dynamics during diagnostic fracture injection tests," in *SPE Western Regional Meeting. Society of Petroleum Engineers*, Bakersfield, California, 2017.
- [127] H. Wang and M. M. Sharma, "New variable compliance method for estimating in-situ stress and leak-off from DFIT data," in *SPE Annual Technical Conference and Exhibition. Society of Petroleum Engineers*, San Antonio, Texas, USA, 2017b.
- [128] S. Nande, *Application of machine learning for closure pressure determination*, SPE Annual Technical Conference and Exhibition, Society of Petroleum Engineers, 2018.
- [129] M. Ibrahim, D. Mehta, and E. Ozkan, "Advanced machine learning methods for prediction of fracture closure pressure," in *SPE Western Regional Meeting*, 2021aVirtual.
- [130] A. F. Ibrahim, M. Ibrahim, M. Sinkey, T. Johnston, and W. Johnson, "Unique fall off signatures for stage fracture characterization, actual field cases," in *Paper presented at the SPE Western regional meeting, virtual*, 2021bVirtual.
- [131] X. Zhang, J. Lin, Z. Chen, F. Sun, X. Zhu, and G. Fang, "An efficient neural-network-based microseismic monitoring platform for hydraulic fracture on an edge computing architecture," *Sensors*, vol. 18, no. 6, p. 1828, 2018.
- [132] C. L. Cipolla and C. A. Wright, "Diagnostic techniques to understand hydraulic fracturing: what? Why? And how?," in *Society of Petroleum Engineers-SPE/CERI gas technology symposium 2000*, pp. 1–13, The Woodlands, Texas, USA, 2020.
- [133] C. L. Cipolla and C. A. Wright, "State-of-the-art in hydraulic fracture diagnostics," in *SPE-Asia Pacific Oil and Gas Conference*, pp. 649–663, Brisbane, Australia, 2000b.
- [134] E. H. Holley, U. Zimmer, M. J. Mayerhofer, and E. Samson, "Integrated analysis combining microseismic mapping and fiber-optic distributed temperature sensing (DTS)," in *Society of Petroleum Engineers-Canadian Unconventional Resources and International Petroleum Conference*, pp. 295–308, Calgary, Alberta, Canada, 2010.
- [135] C. L. McCullagh, A. N. Tutuncu, and T. H. Song, "Coupling distributed temperature sensing (DTS) based wellbore temperature models with microseismic data for enhanced characterization of hydraulic fracture stimulation," *48th US Rock Mechanics/Geomechanics Symposium 2014*, vol. 1, pp. 76–90, 2014.
- [136] S. Yang, Z. Chen, W. Wu, Y. Zhang, X. Zhang, and H. Deng, "Addressing microseismic uncertainty from geological aspects to improve accuracy of estimating stimulated reservoir volumes," *Europe*, vol. 2015, pp. 1–13, 2015.
- [137] R. Velasco, K. Chambers, and S. Wilson, "The characterization of fracture mechanisms using a combination of surface microseismic imaging, microdeformation modelling, and downhole microseismic mapping: an examination of the value of moment tensor microseismic imaging," in *Society of Petroleum Engineers-SPE/AAPG/SEG Unconventional Resources Technology Conference*, Denver, Colorado, USA, 2016.
- [138] N. R. Warpinski, L. G. Griffin, E. J. Davis, and I. Grant, "Improving hydraulic frac diagnostics by joint inversion of downhole microseismic and tiltmeter data," in *Proceedings-SPE annual technical conference and exhibition*, vol. 4, pp. 2744–2753, San Antonio, Texas, USA, 2006.
- [139] M. Salah and S. Ibrahim, "Engineered fracture spacing staging and perforation cluster spacing optimization for multi-stage fracturing horizontal wells," in *Paper presented at the SPE annual technical conference and exhibition*, Dallas, Texas, USA, 2018.
- [140] G. Liu, T. Zhou, F. Li, Y. Li, and C. A. Ehlig-Economides, "Fracture surface area estimation from hydraulic-fracture treatment pressure falloff data," *SPE Drilling & Completion*, vol. 35, no. 3, pp. 438–451, 2020.
- [141] M. Ibrahim Mohamed and E. Ozkan, "State of the Art in Characterization of Frac Stage Geometry and Conductivity Using Pressure Leakoff," in *SPE Western Regional Meeting*, OnePetro Virtual, 2021.

## Research Article

# Production Analysis for Fractured Vertical Well in Coal Seam Reservoirs with Stimulated Reservoir Volume

**Chen Li** 

CNOOC Research Institute Ltd., CNOOC Building, Yard 6, Taiyanggong South Street, Chaoyang District, Beijing, China

Correspondence should be addressed to Chen Li; [lichen1125@foxmail.com](mailto:lichen1125@foxmail.com)

Received 11 August 2021; Revised 17 September 2021; Accepted 27 September 2021; Published 1 November 2021

Academic Editor: Jinjie Wang

Copyright © 2021 Chen Li. This is an open access article distributed under the Creative Commons Attribution License, which permits unrestricted use, distribution, and reproduction in any medium, provided the original work is properly cited.

The development and utilization of coalbed methane is of great significance to reduce carbon dioxide emission. Through the research, this paper presents a fast analytical solution method for the productivity of coalbed methane reservoir with finite-conductivity fractured well and stimulated reservoir volume region. Based on the dual-porosity flowing mechanism, combined with the Langmuir adsorb equation, Fick diffusion law, and Darcy law, a mathematical model considering diffusion in matrix and transport in natural fracture system is established, using spherical matrix to describe the transient steady-state sorption, and using cubic matrix to describe the pseudosteady-state sorption. Then, combined with the inner system and outer system, the analytical solution was obtained. Furthermore, the accuracy of the solution was validated against a numerical simulation. According to the Duhamel principle, the effect of wellbore storage and skin factor was got. Due to the SRV region, the linear flow and radial flow will appear before the pressure wave reach the outer region. And then, based on the pressure analysis result, we will have made the sensitivity analysis with different influence parameter. The result reveals that storage coefficient and conductivity factor mainly influence the early time; the permeability ratio and dimensionless SRV region radius mainly influence the property of SRV region. Finally, the analytical solution of the new model was applied to field history match. This model takes into account the adsorption and desorption characteristics of coalbed methane, as well as the SRV zones generated during fracturing. The calculation speed of the new model is increased while the calculation accuracy is retained, and the intensity of software application is reached. The model achieves the purpose of rapid evaluation and accurate prediction of gas well productivity and obtains a set of productivity evaluation method suitable for coalbed methane reservoir with fractured vertical well, which provides a basis for the development and productivity evaluation of coalbed methane reservoir in domestic and international cooperation.

## 1. Introduction

Coalbed methane refers to methane gas in coal seams. There are two main ways of occurrence of coalbed methane in coal seams: free and adsorption. The existence form of free gas is the same as conventional gas reservoir. Adsorbed gas is adsorbed in the matrix of coal seam in a dynamic equilibrium way. In the process of exploitation, with the decline of formation pressure, the adsorbed gas is gradually resolved from the adsorbed state and becomes free gas. Therefore, when analyzing the pressure change in coal seam, the desorption of adsorbed gas and the migration of free gas must be considered [1, 2].

The main method to develop the coalbed methane was stimulated reservoir volume (SRV) and hydraulic fractured. Due to the fragility of coal seam, with the fracturing fluid injected in to the formation, it will crush the coal around the injection point. Based on this process, the seepage environment around the injection point has been changed. Especially the stimulated reservoir volume, its purpose was improving the seepage environment around the injection point. With the fracture width decrease and effective length increase, we cannot ignore the fracture conductivity. So, it is necessary to establish the new model that has the different seepage environment in the inner region and outer region with the finite-conductivity fracture.

The pressure analysis model and productivity analytical solution model of coalbed methane are based on the classical dual-porosity model of conventional gas reservoirs proposed by Warren-Root's regular hexahedron model (1963) [3], De Swaan-A' spherical model (1976) [4], and Kazemi's stick model (1992) [5]. In the Laplace space, production multiplied by the pressure is equal to the image variable of Laplace transformation. So, mathematically, pressure analysis is actually productivity analysis [6, 7]. At present, the main means of pressure analysis and productivity evaluation are numerical simulation and analytical solution simulation [7–9]. Anbarci et al. introduced Langmuir isothermal adsorption equation to describe the desorption process of adsorbed gas in coalbed methane reservoir and introduced Fick diffusion law to describe the diffusion process of free gas in matrix [1]. For the fractured well, Gringarten et al. [10] studied the pressure performance during the production process and type curve analysis. In their model, the gas reservoirs are averaged, and the hydraulic fracture is the infinite-conductivity fracture. However, for the soft reservoir of coalbed methane, the attribute of the reservoir is nonmean, fracture conductivity is often small, and its conductivity factor cannot reach the magnitude of infinite conductivity. To solve this problem, Cinco-Ley et al. [11, 12] developed a semianalytical solution. In terms of production prediction, Clarkson et al. [13] presented typical production curves for fractured vertical wells and staged fractured horizontal wells in coalbed methane reservoirs. Zhao et al. [14] use the composite model to discuss the infinite-conductivity fracture with SRV region in coalbed methane and get the pressure behavior in the button hole. Wang et al. [15] use the semianalytical simulation to calculate the production rate with complex fracture network and stress-sensitive conductivity. [16] use source and Green's function to establish framework model for complex fracture network. Huang [17] using the point source function and pressure superposition theory gained the mathematical model of production decline. Zhu [18] proposed an automatic segmentation trend tracking model for the CBM production forecast. His work based on the production data and is more robust for the complex production condition. Yan et al. [19] gained the semianalytical mathematical model that considers the self-regulating effects of coal reservoirs. Jiang et al. [20] studied the unsteady productivity model of multilateral horizontal wells based on point source function. The stress sensitivity effect is considered in the model. Wu et al. [21] studied the pressure performance of multistage fractured horizontal well with the rectangular SRV region and adsorbed gas. Shang et al. [22] studied the gas-water two-phase flow in coalbed with single layer and multilayer. The influence of coal seam pressure difference on single well production is demonstrated. Tian et al. [23] studied the flow characteristics of horizontal well with multiple fracture wings. The semianalytical solution model of horizontal well with multiple fracture wings is established, and the flow stage of the model is defined. The influencing factors of production capacity are evaluated.

Most of the above literature cannot completely describe the model with all factor. Especially the stimulated reservoir

volume in coal seam, very few people work with it. However, the elastic modulus of coal seam is small, and natural fractures are developed in coal seam, even hydraulic fracturing always generates a network fracture around the well, not to mention stimulated reservoir volume. On the other hand, with the fracture width decrease and length increase, we cannot ignore the fracture conductivity. So, SRV model with the finite-conductivity fracture in the coalbed was the important model for the production; it is a suitable model for the really geologic condition. In order to accurately describe the characteristics of coalbed methane reservoirs, the purpose of this paper is to establish a productivity evaluation model considering hydraulic fractures and SRV region.

A new mathematical model in this paper was established and solved. The new model comprehensively considers the desorption and adsorption effect of coalbed methane, the diffusion process of matrix, and the conductivity of fracture. Firstly, the transient steady-state, pseudosteady-state sorption, and diffusion models will be discussed in this specific flow model. Secondly, the analytical results of the model are verified by a commercial numerical simulator. The degenerate model of the model is verified by the classical model. Thirdly, the different diffusion models were analyzed. There is different pressure performance with different flow stage between the transient steady-state and pseudosteady-state sorption and diffusion models. Finally, the new model is used to analyze the bottom hole pressure and flow rate of production wells in the southern Qinshui Basin, and the calculated results are well fitted.

## 2. Mathematical Models and Analytical Solutions

*2.1. Methodology.* In order to simplify the seepage model, important assumptions need to be made:

- (1) The reservoir is cylindrical; the producing well is located in the center of the gas reservoir. The well perforated throughout the reservoir
- (2) The inner boundary has either constant pressure or constant flow rate
- (3) The reservoir has the cylindrical SRV region, using the composite model to describe the reservoir, and the inner region can be treated as the SRV region caused by hydraulic fracturing (Figure 1)
- (4) Gas is adsorbed in the matrix of coal seam under original condition; as the development goes on, the gas desorption from the matrix diffuses into the natural fracture system, flows into the hydraulic fracture, and eventually flows into the wellbore (Figure 2)
- (5) Hydraulic fractures are finite-conductivity fracture (Figure 3)
- (6) The sorption and diffusion model of the matrix divide into the unsteady state and pseudosteady state, the unsteady state uses spherical matrix



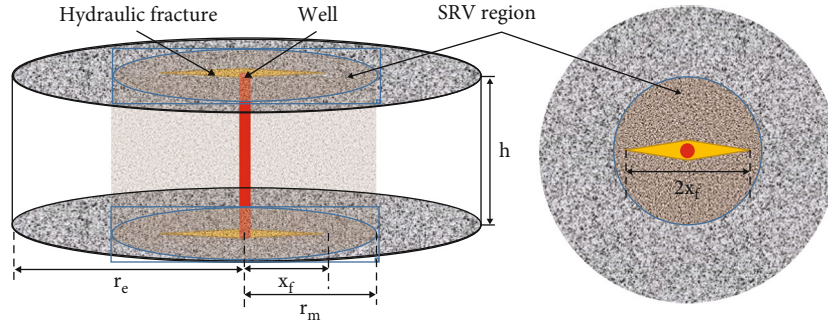


FIGURE 1: Reservoir model with SRV.

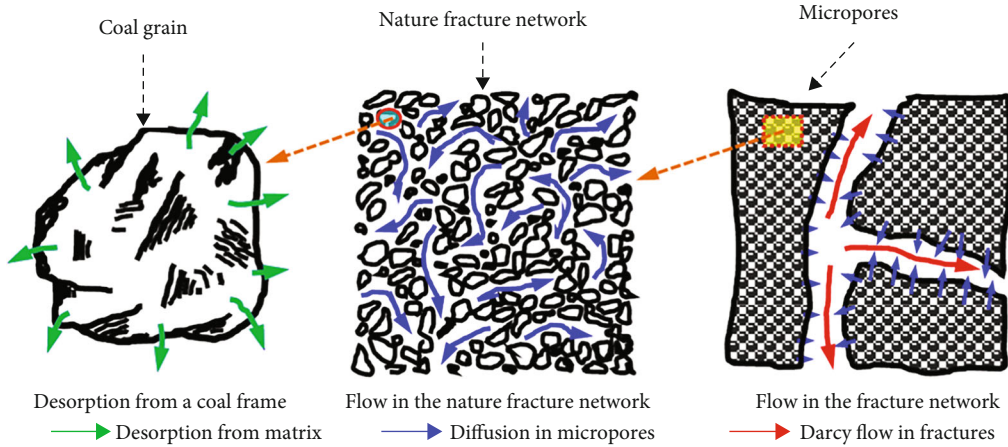


FIGURE 2: Desorption and diffusion in the matrix and Darcy flow in the fracture.

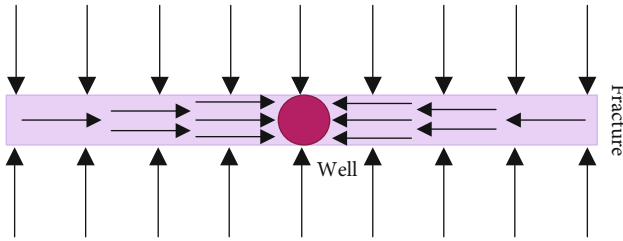


FIGURE 3: The flow rate distribution in the finite-conductivity fracture.

expressed and the pseudosteady state uses the cube matrix expressed (Figure 4)

- (7) The initial reservoir is uniform
- (8) Skin effect and wellbore storage effect are not negligible

**2.2. Model Establishment and Solution.** Anbarci and Ertekin [1] proposed a coalbed methane reservoir seepage model based on the conventional double-porosity model. However, this model can only consider the mean gas reservoir, and its hydraulic fractures are infinite-conductivity fractures. In this article, fractured well with finite conductivity in coalbed with stimulated reservoir volume region is discussed, using the spherical matrix to describe the transient steady-state sorp-

tion and the cubic matrix to describe the pseudosteady-state sorption.

**2.3. Modeling Flow in the Nature Fracture.** Different from conventional gas reservoirs, free gas and desorbed adsorbed gas flow together in coalbed methane reservoirs. This makes the material balance equation become nonlinear equation.

The control equation in the nature fracture system in SRV region:

$$\frac{1}{r} \frac{\partial}{\partial r} \left( r \frac{p_{1nf}}{\mu_1 Z} \frac{\partial p_{1nf}}{\partial r} \right) = \frac{\phi_{1nf} c_g p_{1nf}}{k_{1nf} Z} \frac{\partial p_{1nf}}{\partial t} + \frac{p_{sc} T}{k_{1nf} T_{sc}} \frac{\partial V_{1nf}}{\partial t} \quad (1)$$

The control equation in the nature fracture system in outer region:

$$\frac{1}{r} \frac{\partial}{\partial r} \left( r \frac{p_{2nf}}{\mu_2 Z} \frac{\partial p_{2nf}}{\partial r} \right) = \frac{\phi_{2nf} c_g p_{2nf}}{k_{2nf} Z} \frac{\partial p_{2nf}}{\partial t} + \frac{p_{sc} T}{k_{2nf} T_{sc}} \frac{\partial V_{2nf}}{\partial t} \quad (2)$$

For a well with an infinite, closed, or constant pressure boundary, we have



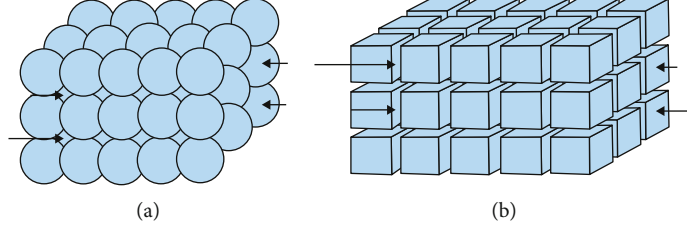


FIGURE 4: Unsteady-state (a) and pseudosteady-state (b) sorption/diffusion.

$$\begin{aligned}
 p_{2nf}(r, t) \Big|_{r \rightarrow \infty} &= p_i \text{ infinite boundary,} \\
 \frac{\partial p_{2nf}}{\partial r} \Big|_{r=r_e} &= 0 \text{ closed boundary,} \\
 p_{2nf} \Big|_{r=r_e} &= p_i \text{ constant pressure boundary.}
 \end{aligned} \quad (3)$$

The well was produced at constant flow rate:

$$\frac{k_{1nf}h}{\mu_1} \left( r \frac{\partial p_1}{\partial r} \right) \Big|_{r \rightarrow 0} = q_{sc} \frac{Z p_{sc} T}{p_{1nf} T_{sc} \Lambda L^2}. \quad (4)$$

At the junction between the SRV region and outer region:

$$\begin{aligned}
 p_{1nf}(r, t) \Big|_{r=r_m} &= p_{2nf}(r, t) \Big|_{r=r_m}, \\
 p_{1nf} \frac{\partial p_{1nf}}{\partial r} \Big|_{r=r_m} &= \frac{p_{1nf}}{M_{12}} \frac{\partial p_{2nf}}{\partial r} \Big|_{r=r_m}.
 \end{aligned} \quad (5)$$

The initial condition of natural fracture system:

$$p_{1nf}(r, 0) = p_{2nf}(r, 0) = p_i. \quad (6)$$

According to Al-Hussainy et al. [24] and Agarwal [25], the pseudopressure and pseudotime are defined as

$$\begin{aligned}
 \psi &= 2 \int_0^p \frac{p}{\mu Z} dp, \\
 t_a &= \int_{t_0}^t \frac{1}{\mu c_g} dt.
 \end{aligned} \quad (7)$$

The dimensionless group is defined as follows:

$$\begin{aligned}
 t_D &= \frac{k_{2nf} t_a}{\Lambda L^2}, \quad \psi_{1nfD} = \frac{k_{2nf} h T_{sc}}{p_{sc} T} \Delta \psi_{1nf}, \quad M_{12} = \frac{k_{1nf}}{k_{2nf}}, \quad r_{mD} \\
 &= \frac{r_m}{L_f}, \quad \omega_1 = \frac{\phi_1 \mu_{gi} c_{t1}}{\Lambda}, \quad r_{Dm} = \frac{r_m}{R_m}, \quad \omega_2 = \frac{\phi_2 \mu_{gi} c_{t2}}{\Lambda},
 \end{aligned}$$

$$\sigma = \frac{V_L \psi_L(p_{nf})}{[\psi_L(p_{nf}) + \psi(p_{nf})] [\psi_L(p_{nf}) + \psi(p_i)]} \frac{q_{sc} p_{sc} T}{k_{2nf} h T_{sc}}, \quad r_D = \frac{r}{L_f},$$

$$\Lambda = \begin{cases} (\phi \mu c_i) + \frac{6k_{2nf}h}{q_{sc}} & \text{TSS,} \\ (\phi \mu c_i) + \frac{3k_{2nf}h}{q_{sc}} & \text{PSS,} \end{cases} \quad \lambda = \begin{cases} \frac{k_{2nf}\tau}{\Lambda L^2} & \text{TSS,} \\ \frac{k_{2nf}\tau}{6\Lambda L^2} & \text{PSS,} \end{cases} \quad \tau = \begin{cases} \frac{R_m^2}{D} & \text{TSS,} \\ \frac{R_m^2}{\pi^2 D} & \text{PSS.} \end{cases} \quad (8)$$

Sorption equation for transient steady state and pseudosteady state:

$$\frac{\partial V}{\partial t} = \frac{3D}{R_m} \frac{\partial V}{\partial r_m} \Big|_{r_m=R_m} \quad \text{for TSS,} \quad (9)$$

$$\frac{\partial V}{\partial t} = \frac{6D\pi^2}{R_m^2} (V_E - V) \quad \text{for PSS.} \quad (10)$$

Combined with the diffusion equation, the control equation in the nature fracture system becomes as follows.

Inner boundary:

$$\frac{1}{r_D} \frac{\partial}{\partial r_D} \left( r_D \frac{\partial \tilde{\psi}_{1nf}}{\partial r_D} \right) = f_1(s) \tilde{\psi}_{1nf}. \quad (11)$$

Outer boundary:

$$\frac{1}{r_D} \frac{\partial}{\partial r_D} \left( r_D \frac{\partial \tilde{\psi}_{2nf}}{\partial r_D} \right) = f_2(s) \tilde{\psi}_{2nf}, \quad (12)$$

where

$$f_1(s) = \begin{cases} \frac{\omega_1 s}{M_{12}} + \frac{\beta_1 \sigma}{\lambda M_{12}} \left[ \sqrt{\lambda s} \coth(\sqrt{\lambda s}) - 1 \right] & \text{TSS,} \\ \frac{\omega_1 s}{M_{12}} + \frac{\beta_1 \sigma s}{M_{12} \lambda s + 1} & \text{PSS,} \end{cases} \quad (13)$$

$$f_2(s) = \begin{cases} \omega_2 + \frac{\beta_2 \sigma}{\lambda} \left[ \sqrt{\lambda s} \coth(\sqrt{\lambda s}) - 1 \right] & \text{TSS,} \\ \omega_2 s + \beta_2 \frac{\sigma s}{\lambda s + 1} & \text{PSS,} \end{cases} \quad (14)$$

$$\beta_1 = (1 - \omega_1 - \omega_2)(1 - \phi_1), \quad (15)$$

$$\beta_2 = (1 - \omega_1 - \omega_2)(1 - \phi_2). \quad (16)$$

Through Equations (13) and (14), combined with the definite condition, we can get the solution as follows:

$$\begin{aligned}\tilde{\psi}_{1nf} &= A_1 I_0 \left( \sqrt{f_1(s)} r_D \right) + B_1 K_0 \left( \sqrt{f_1(s)} r_D \right), \\ \tilde{\psi}_{2nf} &= A_2 I_0 \left( \sqrt{f_2(s)} r_D \right) + B_2 K_0 \left( \sqrt{f_2(s)} r_D \right).\end{aligned}\quad (17)$$

We want to get the pressure performance at bottle hole. So, combining with the inner boundary condition and interface condition, we can get the  $A_1$  and  $B_1$ .

In the infinitely boundary:

$$\begin{aligned}B_1 &= q_{sc} \frac{p_{sc} T k_{2nf}}{T_{sc} \Lambda L^2 k_{1nf} h}, \\ A_1 &= B_1 \frac{M_{12} \sqrt{f_1(s)} K_1 \left( \sqrt{f_1(s)} r_{mD} \right) K_0 \left( \sqrt{f_2(s)} r_{mD} \right) - \sqrt{f_2(s)} K_0 \left( \sqrt{f_1(s)} r_{mD} \right) K_1 \left( \sqrt{f_2(s)} r_{mD} \right)}{M_{12} \sqrt{f_1(s)} I_1 \left( \sqrt{f_1(s)} r_{mD} \right) K_0 \left( \sqrt{f_2(s)} r_{mD} \right) + \sqrt{f_2(s)} I_0 \left( \sqrt{f_1(s)} r_{mD} \right) K_1 \left( \sqrt{f_2(s)} r_{mD} \right)}.\end{aligned}\quad (18)$$

In the closed boundary and constant pressure boundary, it has the same  $B_1$  with the infinitely boundary, the  $A_1$  as

$$A_1 = B_1 \frac{K_0 \left( \sqrt{f_1(s)} r_{mD} \right) + \varepsilon \sqrt{f_1(s)} K_1 \left( \sqrt{f_1(s)} r_{mD} \right)}{\varepsilon \sqrt{f_1(s)} I_1 \left( \sqrt{f_1(s)} r_{mD} \right) - I_0 \left( \sqrt{f_1(s)} r_{mD} \right)}, \quad (19)$$

where

$$\begin{aligned}\varepsilon &= \frac{M_{12} \left( \eta I_0 \left( \sqrt{f_2(s)} r_{mD} \right) + K_0 \left( \sqrt{f_2(s)} r_{mD} \right) \right)}{\eta \sqrt{f_2(s)} I_1 \left( \sqrt{f_2(s)} r_{mD} \right) - \sqrt{f_2(s)} K_1 \left( \sqrt{f_2(s)} r_{mD} \right)}, \\ \eta_{cb} &= \frac{K_1 \left( \sqrt{f_2(s)} r_{eD} \right)}{I_1 \left( \sqrt{f_2(s)} r_{eD} \right)}.\end{aligned}\quad (20)$$

The constant pressure boundary has the same theory with the closed boundary, only different with  $\eta$ :

$$\eta_{cpb} = - \frac{K_0 \left( \sqrt{f_2(s)} r_{eD} \right)}{I_0 \left( \sqrt{f_2(s)} r_{eD} \right)}.\quad (21)$$

Generally, we can get the solution for the nature fracture system as

$$\tilde{\psi}_{1nf} = \frac{p_{sc} T q_{sc}}{T_{sc} k_{1nf} h} \left( K_0 \left( \sqrt{f_1(s)} r_D \right) + \Omega I_0 \left( \sqrt{f_1(s)} r_D \right) \right).\quad (22)$$

According to the dimensionless group,

$$\tilde{\psi}_{1Dnf} = \int_{-1}^1 \frac{1}{M_{12}} \tilde{q}_{Dnf} \left( K_0 \left( \sqrt{f_1(s)} r_D \right) + \Omega I_0 \left( \sqrt{f_1(s)} r_D \right) \right) dr_D,\quad (23)$$

where

$$\Omega = \begin{cases} \frac{M_{12} \sqrt{f_1(s)} K_1 \left( \sqrt{f_1(s)} r_{mD} \right) K_0 \left( \sqrt{f_2(s)} r_{mD} \right) - \sqrt{f_2(s)} K_0 \left( \sqrt{f_1(s)} r_{mD} \right) K_1 \left( \sqrt{f_2(s)} r_{mD} \right)}{M_{12} \sqrt{f_1(s)} I_1 \left( \sqrt{f_1(s)} r_{mD} \right) K_0 \left( \sqrt{f_2(s)} r_{mD} \right) + \sqrt{f_2(s)} I_0 \left( \sqrt{f_1(s)} r_{mD} \right) K_1 \left( \sqrt{f_2(s)} r_{mD} \right)} & \text{infinitely boundary,} \\ \left. \frac{K_0 \left( \sqrt{f_1(s)} r_{mD} \right) + \varepsilon_x \sqrt{f_1(s)} K_1 \left( \sqrt{f_1(s)} r_{mD} \right)}{\varepsilon_x \sqrt{f_1(s)} I_1 \left( \sqrt{f_1(s)} r_{mD} \right) - I_0 \left( \sqrt{f_1(s)} r_{mD} \right)} \right|_{x=cb \text{ or } cpb} & \text{closed and constant pressure boundary.} \end{cases}\quad (24)$$

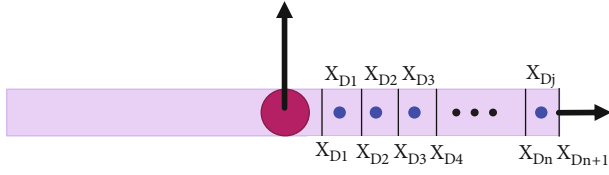


FIGURE 5: Disperse the finite-conductivity fracture.

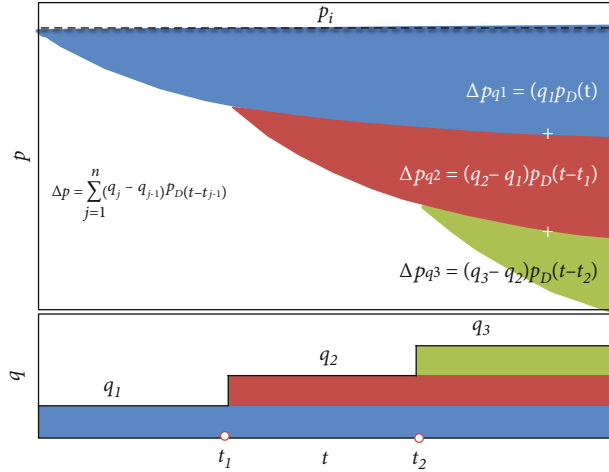


FIGURE 6: The process of Duhamel convolution.

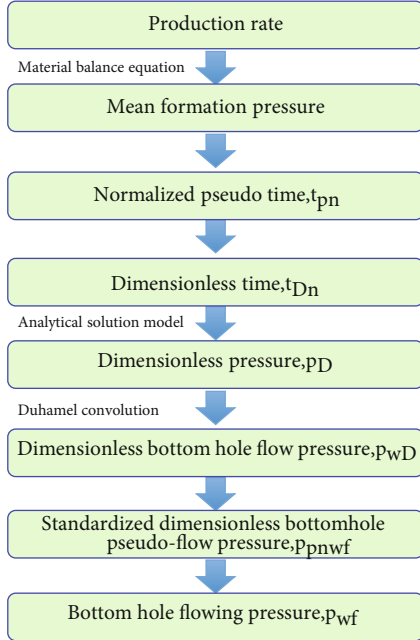


FIGURE 7: The Duhamel convolution is used to obtain pressure.

2.4. *The Model Flow in the Hydraulic Fracture.* In a similar way to Equation (23), we can get the control equation in the hydraulic fracture. In the finite-conductivity fracture, the  $\tilde{q}_{Dnf}(s)$  was different with different place in the hydraulic fracture (Figure 3).

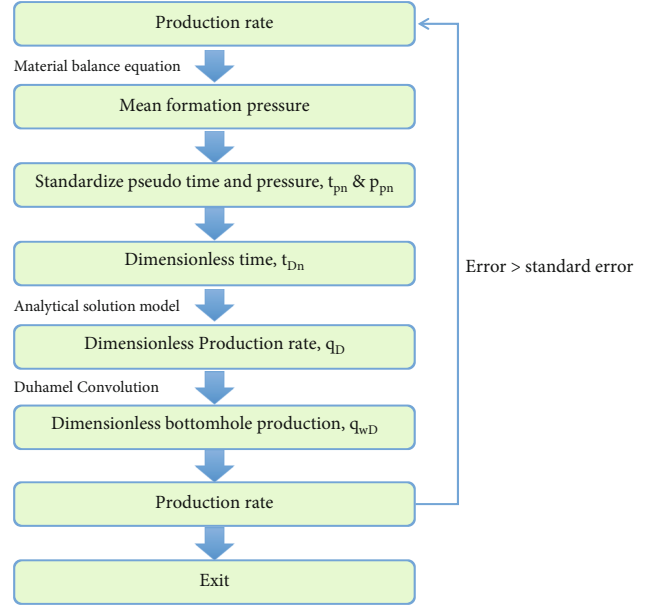


FIGURE 8: The Duhamel convolution is used to obtain production rate.

TABLE 1: The basic data to verify the result.

$\tau = 328990$ hr	$r_w = 0.5$ ft
$\mu = 0.01082$ cp	$c = 0.002234$ psia <sup>-1</sup>
$T = 530$ R	$z = 0.9404$
$q_{sc} = 0.2$ MMscf/d	$V_L = 18.632$ scf/ft <sup>3</sup>
$p_{ic} = 447.7$ psia	$k = 26$ md
$\varphi = 0.01$	$h = 6$ ft
$x_f = 100$ ft	$P_L = 167.58$ psi

$$\frac{\partial^2 \tilde{\psi}_{Dnf}}{\partial x_D^2} + \frac{2}{C_{fD}} \frac{\partial \tilde{\psi}_D}{\partial y_D} \Big|_{y_D=0} = 0 \quad 0 < x_D < 1, \quad (25)$$

$$\tilde{q}_{Dhf}(x_D, s) = -\frac{2}{\pi} \frac{\partial \tilde{\psi}_D}{\partial y_D} \Big|_{y_D=0}, \quad (26)$$

$$\frac{\partial \tilde{\psi}_{fD}}{\partial x_D} \Big|_{x_D=0} = -\frac{\pi}{s C_{fD}}. \quad (27)$$

Through Equations (25), (26), and (27), we can get

$$\tilde{\psi}_{wD} - \tilde{\psi}_{Dnf}(x_D, y_D = 0, s) = \frac{\pi}{s C_{fD}} \left[ x_D - s \int_0^{x_D} \int_0^\eta \tilde{q}_{Dhf} dx_D d\eta \right]. \quad (28)$$

Dispersing Equation (28) according to Figure 5,

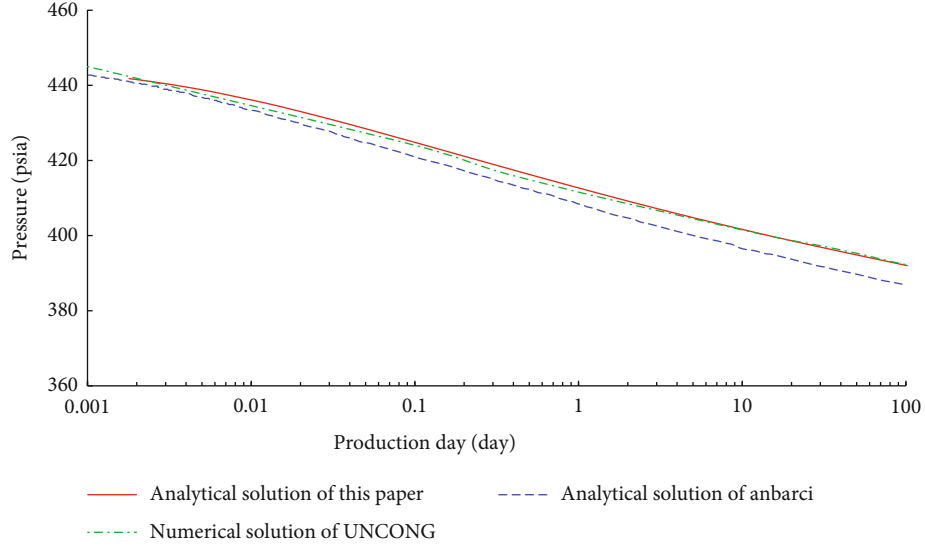


FIGURE 9: The comparison between classical literature and commercial numerical simulator.

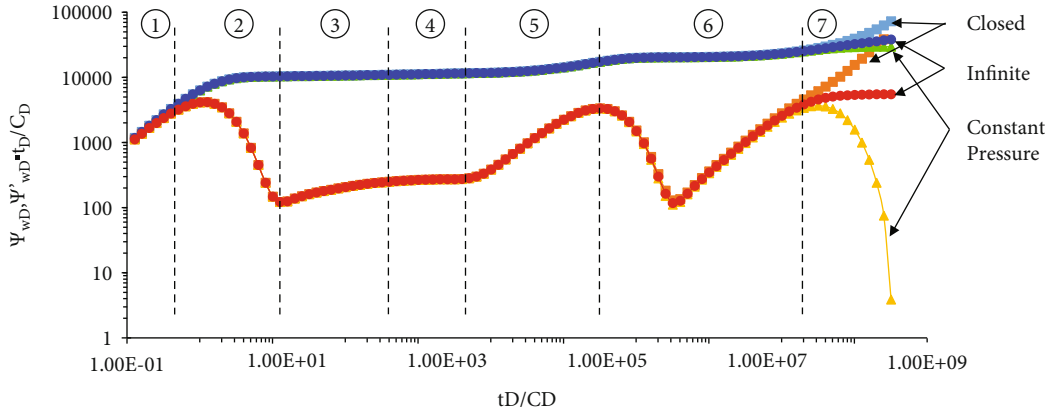


FIGURE 10: Flow stage divided for rectangle coal reservoirs.

$$\left[ \begin{aligned} & \tilde{\Psi}_{wD} - \frac{1}{2} \sum_{i=1}^n \tilde{q}_{fDi} \int_{x_{Di}}^{x_{Di+1}} \left[ K_0 \left( |\bar{x}_{Dj} + \xi| \sqrt{f(s)} \right) + K_0 \left( |\bar{x}_{Dj} - \xi| \sqrt{f(s)} \right) \right] d\xi + \\ & \frac{\pi}{C_{fD}} \left\{ \sum_{i=1}^j \tilde{q}_{fDi} \left[ 0.5 \Delta x_{Dj}^2 + \Delta x_{Dj} (\bar{x}_{Dj} - i \Delta x_{Dj}) \right] + \tilde{q}_{fDj} \frac{\Delta x_{Dj}^2}{8} \right\} \\ & = \frac{\pi}{s C_{fD}} x_{Dj} \end{aligned} \right] \quad (29)$$

TABLE 2: The basic data of the curves.

$\Phi_1 = 0.2$	$\omega_1 = 0.5$	$M_{12} = 10$	$r_{md} = 10$
$\Phi_2 = 0.1$	$\omega_2 = 0.1$	sk = 1	$\lambda = 1000$
$C_{fd} = 10\pi$	$C_D = 0.0001$	$r_{ed} = 60$	$\sigma = 100$

$$\tilde{\Psi}_{wD} = \frac{1}{s^2 C_D + s/[s\tilde{\Psi}_{wD}(s) + S_k]} \quad (31)$$

In the Laplace space, the sum of all the flow rate in every part is  $1/s$ :

$$\Delta x \sum_{k=1}^n \tilde{q}_{Dhfk}(s) = \frac{1}{s} \quad (30)$$

To obtain the solution including wellbore storage and skin effect, we need the relationship given as

**2.5. History Matching and Duhamel Convolution.** In the process of solving the theoretical analytical solution, it is necessary to assume that the inner boundary condition is constant to obtain the particular solution of the analytical solution. But in the actual production process, because of the influence of production conditions, the output and pressure are generally changed. Duhamel convolution is required to superimpose varying production or pressure. Theoretical analytical solutions under variable yield and pressure can be obtained. The theoretical analytical solution is fitted with

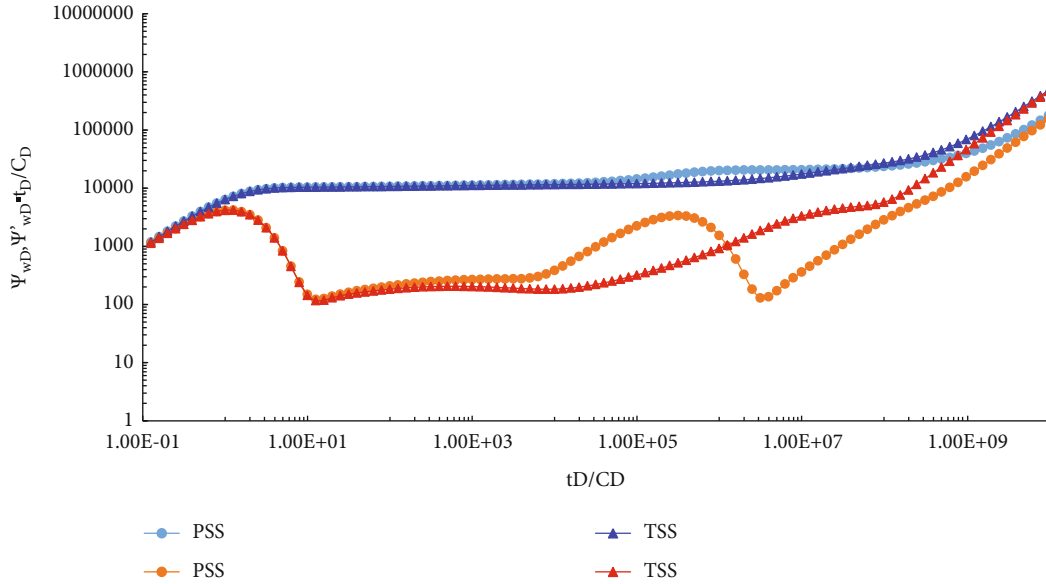


FIGURE 11: Comparison with the transient steady-state and pseudosteady-state models.

TABLE 3: Basic data of production well.

$p_{ic}$ (psia)	160	$s$	0.12
$k_{in}$ (md)	6.13	$k_{out}$ (md)	3
$\rho_b$ (g/cm <sup>3</sup> )	1.47	FCD	100
$r_{in}$ (ft)	800	$r_{out}$ (ft)	840
$h$ (ft)	21.3	$C_t$ (psi <sup>-1</sup> )	0.025
$R_w$ (ft)	0.3	$T$ (F)	57.2
$\varphi$	0.12	$V_L$ (scf/ton)	318
$L_f$ (ft)	262.5	$P_L$ (psi)	116.03

the actual production data. On the basis of fitting, the productivity evaluation and production forecast of gas well are finally realized (Figure 6).

The principle of variable pressure yield calculation or variable pressure yield calculation is similar; the only difference is that in variable pressure yield calculation, as the yield is unknown, it is necessary to assume a yield to calculate the average pressure, and the final output needs to be calculated iteratively (Figures 7 and 8).

**2.6. Model Verification.** Due to the complexity of the model considered in this paper, there is no classical literature to compare. On the one hand, the model presented in this paper is reduced to a simpler mean value and infinite diversion fracture model for comparison with Anbarci's work (1992). For comparison purposes, we set a large enough fracture conductivity factor and same permeability with inner and outer region. On the other hand, a commercial simulator (UNCONG) [26] is used to build the model same with Anbarci's work, and the analytical solution results in this paper are compared with those in a commercial numerical simulator. Basic data from Anbarci's paper are listed in Table 1.

Comparison with the analytical solution of Anbarci and solution from this paper was better fitting with the numeri-

cal solution (Figure 9). Anbarci's solution was relatively small compared with the numerical solution.

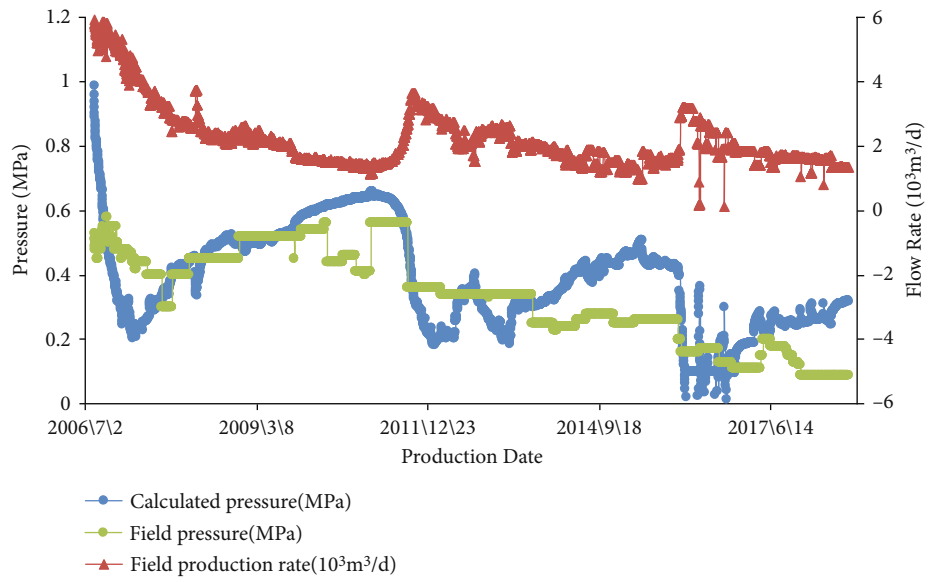
### 3. Result and Discussion

**3.1. Flow State Analysis for Composite Coal Reservoirs.** Because of the composite, the pressure will through the SRV region firstly and then through the outer region. Under this condition, the flow state will differ from the homogeneous coal seam. It can be divided into seven stages (Figure 10). The value of the figure is shown in Table 2.

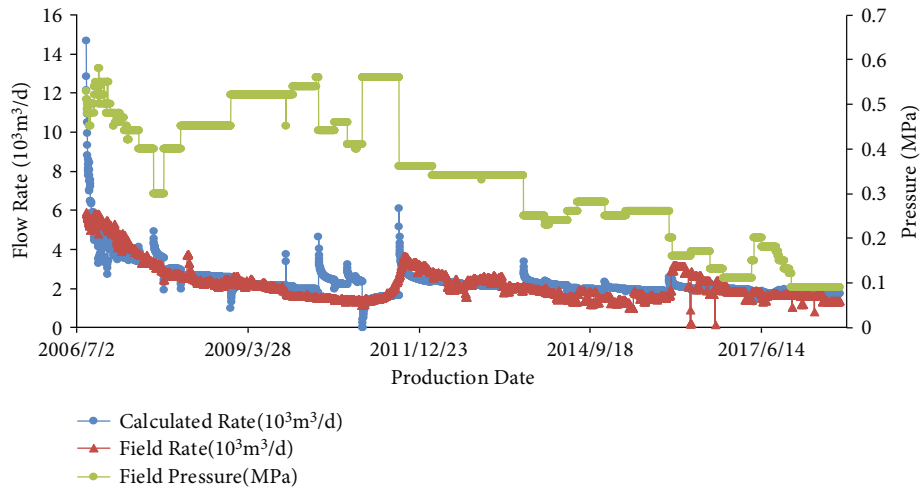
The flow stage divides its characteristics as follows:

- (1) Wellbore storage stage. The seepage characteristic curve of coalbed methane reservoir in this stage is consistent with that of conventional gas reservoir
- (2) Transition stage of wellbore storage. Wellbore storage effect gradually decreases. Because of the high permeability in the inner zone, the formation fluid flow is radial flow. Formation fluid flows from the SRV zone to the wellbore
- (3) Linear flow in SRV region. The duration time of this stage always short. Sometimes, it was concealed by the wellbore storage stage when the  $C_D$  was large. The duration time depends on the length of the fracture and the  $C_D$
- (4) Radial flow in SRV region. This stage will appear when the ratio of the SRV region radius and the fracture length reach the relatively large level. The characteristic of this stage was the horizontal line. The value of this line was  $1/(2 \times M_{12} \times C_D)$
- (5) Linear flow in coal seam. When the pressure wave reaches the outer region, the linear flow in the whole reservoir appeared. The characteristic of this stage

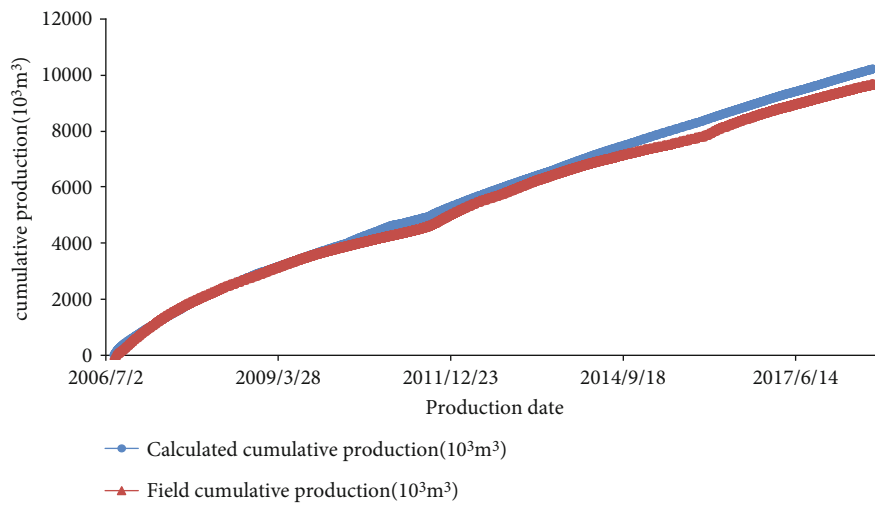




(a) Bottom hole pressure history fitting



(b) Flow rate history fitting



(c) Cumulative gas production history fitting

FIGURE 12: History match result.

was the half slope in pseudopressure derivative curves on the log-log scale

- (6) Desorption and diffusion stage. With the pressure and gas concentration decrease, the desorption becomes more and more obviously. The adsorbed gas in the matrix is gradually desorbed from the coal rock matrix into free gas. The increase in gas concentration in the matrix results in a concentration difference with the natural fracture system, and the gas diffuses from the matrix to the natural fracture system. The derivative curve of the pressure was appearing the “V” shape at this stage. The depth and time of “V” shape are influenced by the desorption coefficient, storage coefficient, cross flow coefficient, and the wellbore storage coefficient. This stage is also the unique pressure response stage of coalbed methane, which reflects the unique adsorption and desorption effect of coalbed methane
- (7) Boundary control flow stage. At this stage, the pseudopressure nearly becomes horizontal line with the infinite boundary, the pseudopressure and pseudopressure derivative were upwarp with closed boundary, the pseudopressure derivative falls, and pseudopressure becomes horizontal line with constant pressure boundary

**3.2. Comparison of PSS and TSS.** Figure 11 showed the transient steady-state and pseudosteady-state sorption and diffusion models with the parameters from Table 2. The pseudosteady diffusion ignores the spatial variation of coalbed methane concentration and focuses on the temporal variation. The pseudosteady-state diffusion assumes that the concentration of methane in the diffusion space is consistent at each time point. This will speed up the calculation, but will lead to calculation errors. The two models show some difference with the same parameters. In the wellbore storage stage, the dimensionless pseudopressure and pseudopressure derivative curves of two models exhibit good agreement with a unit slope straight line. This condition continued to the end of the linear flow stage in SRV region. The PSS model experiences a shorter radial flow in SRV region compared with the TSS model. The dimensionless pseudopressure and pseudopressure derivative curves of PSS model are large than the TSS model at flow in this stage. This is because of the difference of the geometry of two models. The TSS model has the stronger diffuse capacity at earlier stage that can supply to the natural fractured network leading the smaller pressure decline in natural fractured network at this time. This condition will continue to the linear flow in the coal seam, and the gap between the dimensionless pseudopressure derivative curves reaches the peak. In the desorption and diffusion stage, because the desorption and diffusion in the TSS model accomplish instantaneously much of the gas diffusion before, the desorption and diffusion characteristics do not show in this model and continue the reservoir linear until the boundary of the control flow stage. But with the PSS model, the desorption and diffusion reached the peak to supply the natural fractured network

leading the smaller pressure decline in natural fractured network. Eventually, the dimensionless pseudopressure derivative curves of PSS model will be under the TSS model; it will continue to the rest of the time. This difference directs us to control the decrease speed of pressure when we develop the coalbed methane; this will use the reservoir energy efficiently. The difference between the PSS and TSS is that PSS was the cube matrix (Figure 4(b)) and the TSS was the spherical matrix (Figure 4(a)). The ultimate difference with the PSS and TSS reflects Equations (9) and (10). Using TSS model and PSS model, we obtain the control equation with Equations (13) and (14).

## 4. Field Application

In the fracturing process of coal, due to the soft coal seam, a lot of fracturing sand will be embedded in the coal seam, which will lead to the obstruction of fracture extension. Most of the fracturing sand is accumulated around the wellbore, forming SRV zone. Surface microseismic monitoring shows that most fractures form only around the wellbore during coal fracturing. Lv et al. [27] based on the information from underground mining in coal mines found most hydraulic fractures extend only 5 to 10 meters.

**4.1. Basic Data.** The proposed model is used in this paper to validate the model in this paper local in Qinshui Basin. The well was stimulated reservoir volume and hydraulically fractured. Qinshui Basin is located in Shanxi Province of China. Dynamic data mainly include daily gas production data, bottom hole flow pressure data, and other reservoir parameters that represent the geological characteristics of the reservoir (Table 3). The model provided in this paper is used to fit the dynamic parameters.

**4.2. History Match Result.** Through the principle of time superposition, the analytic solution model is fitted with the actual production data, and the fitting result is finally obtained. Figure 12(a) showed the pressure matching. The average error was 22%. Because of some engineering factors in the well, the data was not fitted well at the end of the match.

The average fitting error of the flow rate shown in Figure 12(b) is 17%. The flow rate fitting effect is better than the pressure fitting effect. Figure 12(c) showed the actual cumulative gas production and the calculated cumulative gas production of the producing well. The fitting error between the calculated value and field value is small, and the fitting effect is good.

## 5. Conclusion

In this paper, we investigated a stimulated reservoir volume model for finite-conductivity fractured well in a coal seam. With the Laplace transformation, the solutions of this model at a constant production rate or bottom-hole pressure are obtained. Through the above analysis, the following conclusions can be summarized.

- (1) Through a comparison of the equivalent infinite boundary model with infinite-conductivity fracture in homogeneous coal seam, compared with the classical analytical solution, using the new method to solve the fractured model is more accurate and has the better fitting effect with the numerical solution
- (2) Compared with the homogeneous coal seam, the composite reservoir has the linear flow and radial flow in SRV region and manifests on the type curves. The value of radial flow in type curves was  $1/(2 \times M_{12} \times C_D)$
- (3) The PSS model experiences a shorter radial flow in SRV region compared with the TSS model. The desorption and diffusion characteristics do not show in this model and continue the reservoir linear until the boundary of control flow stage. Before the desorption and diffusion stage, the pressure of PSS model decreases quickly, but after this stage, the TSS model decreases quickly. Eventually, pressure decrease of PSS model is smaller than the TSS model; it will continue to the rest of the time. This difference directs us to control the decrease speed of pressure when we develop the coalbed methane; this will use the reservoir energy efficiently
- (4) The influence of the storage coefficient will be ignored in the line flow because of the flow condition has been improved in the SRV region. The ratio of permeability influences the radial and line flow in SRV region, including the value of radial flow in type curves and the duration time. The well storage coefficient makes the flow stage directly into the matrix methane diffusion phase when it reached a certain value. Conductivity factor mainly influence the early time; after that, the gas from the nature fracture decreases and can flow into the wellbore quickly; the hydraulic fracture is equivalent for the infinity conductivity fractured. The dimensionless SRV region radius mainly influences the end time of the radial flow in SRV region

## Symbol

### Symbol in Article

- $r$ : Radius of coalbed methane reservoir, m  
 $p$ : Pressure, MPa  
 $t$ : Time variable, h  
 $t_a$ : Agarwal time  
 $t_0$ : Initial time of Agarwal integral, h·MPa/cp  
 $r_{Dm}$ : Dimensionless matrix radius  
 $R_m$ : External radius of the matrix block, m  
 $r_m$ : Radial distance of the SRV region, m  
 $\psi$ : Pseudopressure, MPa<sup>2</sup>/cp  
 $L$ : Reference length, in this paper  $L$  equal to half of the fracture length, m  
 $x$ : Length of the  $x$  coordinates, m  
 $y$ : Length of the  $y$  coordinates, m

- $\mu$ : Gas viscosity, MPa·s  
 $j$ : Summation variable in the hydraulic fracture system  
 $k$ : Summation variable in the hydraulic fracture system  
 $Z$ : Gas deviation factor, dimensionless  
 $\phi$ : Reservoir porosity, dimensionless and decimal  
 $c_g$ : Coal compressibility, MPa<sup>-1</sup>  
 $k$ : Reservoir permeability, D  
 $T$ : Temperature, K  
 $V$ : Average matrix gas concentration, m<sup>3</sup>/m<sup>3</sup>  
 $V_E$ : Volume of gas adsorbed per unit volume of the coal grain in equilibrium at pressure  $p$ , m<sup>3</sup>/m<sup>3</sup>  
 $C$ : Volumetric gas concentration in the microspores, m<sup>3</sup>/m<sup>3</sup>  
 $D$ : Diffusion coefficient, m<sup>2</sup>/s  
 $p_L$ : Langmuir pressure, MPa  
 $s$ : Laplace variable, dimensionless  
 $R$ : External radius of matrix, m  
 $L_f$ : Half-length of hydraulic fracture, m  
 $C_D$ : Dimensionless wellbore storage coefficient  
 $C_{fD}$ : Dimensionless fracture conductivity  
 $M_{12}$ : Ratio of the permeability between the SRV region and outer region  
 TSS: Abbreviation of the transient steady state  
 PSS: Abbreviation of the pseudosteady state  
 cb: Abbreviation of the closed boundary  
 cpb: Abbreviation of the constant pressure boundary.

### Subscripts and Superscripts

- $D$ : Dimensionless property  
 $e$ : Boundary property  
 $g$ : Gas property  
 $t$ : Total property  
 $L$ : Factor of the Langmuir equation  
 $w$ : Wellbore property  
 $i$ : Initial condition  
 $sc$ : Standard condition  
 $f$ : Fracture property  
 $1$ : SRV region property  
 $2$ : Outer region property  
 $\sim$ : Image function of Laplace transform  
 $\bar{\cdot}$ : Average property  
 $nf$ : Natural fracture system  
 $hf$ : Hydraulic fracture system.

### Intermediate Variable

- $\sigma = p_L V_L p_i^2 q_D / (p_L + p)(p_L + p_i)(p_i + p)$   
 $\Lambda = \phi \mu c_g + (p_{sc} T \mu z / T_{sc} q_D p_i^2)$   
 $\omega = \phi \mu c_g / \Lambda$   
 $\tau = R^2 / D$   
 $\lambda = k \tau / \Lambda L_f^2$   
 $\gamma = \sqrt{f(s)}$

### Dimensionless

- $\psi_D = (\pi k h T_{sc} / p_{sc} q_{sc} T)(\psi_i - \psi)$   
 $t_D = k t / \Lambda L_f^2$   
 $L_D = L / L_f$

## Data Availability

The verification data in this paper can be found in this paper: Anbarci and Ertekin [1] A comprehensive study of pressure transient analysis with sorption phenomena for single-phase gas flow in coal seams, SPE Annual Technical Conference and Exhibition of the Society of Petroleum Engineers, New Orleans, Louisiana, September 23-26. The rest of the data are all original; if you need any data in the article, please send me an email, Email address: lichen1125@foxmail.com.

## Conflicts of Interest

The authors declare that they have no conflicts of interest.

## References

- [1] K. Anbarci and T. Ertekin, "A comprehensive study of pressure transient analysis with sorption phenomena for single-phase gas flow in coal seams," in *Paper SPE 20568-MS Presented at the SPE Annual Technical Conference and Exhibition*, New Orleans, Louisiana, USA, 1990.
- [2] K. Anbarci and T. Ertekin, "Pressure transient behavior of fractured wells in coalbed reservoirs," in *Paper SPE 24703-MS Presented at the SPE Annual Technical Conference and Exhibition*, Washington, D.C., USA, 1992.
- [3] J. E. Warren and P. J. Root, "The behavior of naturally fractured reservoirs," *Society of Petroleum Engineers Journal*, vol. 3, no. 3, pp. 245–255, 1963.
- [4] A. De Swaan, "Analytic solutions for determining naturally fractured reservoir properties by well testing," *Society of Petroleum Engineers Journal*, vol. 16, no. 3, pp. 117–122, 1976.
- [5] H. Kazemi, J. R. Gilman, and A. M. Eisharkawy, "Analytical and numerical solution of oil recovery from fractured reservoirs with empirical transfer functions (includes associated papers 25528 and 25818)," *SPE Reservoir Engineering*, vol. 7, no. 2, pp. 219–227, 1992.
- [6] W. J. Mcguire and V. J. Sikora, "The effect of vertical fractures on well productivity," *Journal of Petroleum Technology*, vol. 12, no. 10, pp. 72–74, 1960.
- [7] R. Raghavan, G. V. Cady, and H. J. Ramey, "Well-test analysis for vertically fractured wells," *Journal of Petroleum Technology*, vol. 24, no. 8, pp. 1014–1020, 1970.
- [8] G. R. King, T. Ertekin, and F. C. Schwerer, "Numerical simulation of the transient behavior of coal-seam degasification wells," *SPE Formation Evaluation*, vol. 1, no. 2, pp. 165–183, 1986.
- [9] R. Jiang, X. Liu, X. Wang, Y. Gao, and Y. Huang, "Unsteady productivity model for multi-branched horizontal wells in coalbed methane reservoir," *Petroleum Geology and Recovery Efficiency*, vol. 27, no. 3, pp. 48–56, 2020.
- [10] A. C. Gringarten Jr., H. J. Ramey, and R. Raghavan, "Applied pressure analysis for fractured wells," *Journal of Petroleum Technology*, vol. 27, no. 7, pp. 887–892, 1975.
- [11] H. Cinco-Ley, V. F. Samaniego, and A. N. Dominguez, "Transient pressure behavior for a well with a finite-conductivity vertical fracture," *Society of Petroleum Engineers Journal*, vol. 18, no. 4, pp. 253–264, 1978.
- [12] H. Cinco-Ley and H. Z. Meng, "Pressure transient analysis of wells with finite conductivity vertical fractures in double porosity reservoirs," in *Paper SPE 18172-MS Presented at the 63rd Annual Technical Conference and Exhibition of the Society of Petroleum Engineers*, Houston, Texas, USA, 1988.
- [13] C. R. Clarkson, C. L. Jordan, D. Ilk, and T. A. Blasingame, "Production data analysis of fractured and horizontal CBM wells," in *Paper SPE 125929-MS Presented at the SPE Eastern Regional Meeting*, Charleston, West Virginia, USA, 2009.
- [14] Y. Zhao, L. Zhang, G. Feng, B. Zhang, and B. Kang, "Performance analysis of fractured wells with stimulated reservoir volume in coal seam reservoirs," *Oil and Gas Science & Technology*, vol. 71, no. 1, pp. 1–28, 2016.
- [15] J. Wang, A. Jia, Y. Wei, W. Luo, and H. Yuan, "Semi-analytical simulation of transient flow behavior for complex fracture network with stress-sensitive conductivity," *Journal of Petroleum Science and Engineering*, vol. 171, no. 2018, pp. 1191–1210, 2018.
- [16] J. Wang, A. Jia, and Y. Wei, "A generalized framework model for simulating transient response of a well with complex fracture network by use of source and green's function," *Journal of Natural Gas Science and Engineering*, vol. 55, no. 2018, pp. 254–275, 2018.
- [17] D. Huang, J. Yang, H. Yu, and W. Li, "Study on production decline law of multilateral horizontal well in coalbed methane reservoirs," *IOP Conference Series: Earth and Environmental Science*, vol. 300, no. 2, pp. 1–4, 2019.
- [18] Q. Zhu, H. Du, Q. Hu, B. Fan, J. Wang, and J. Yu, "Automatic trend tracking model for coalbed methane production forecast," *Journal of Physics: Conference Series*, vol. 1894, no. 1, pp. 1–5, 2021.
- [19] X. Yan, S. Zhang, S. Tang, Z. Li, and J. Wang, "A prediction model for pressure propagation and production boundary during coalbed methane development," *Energy & Fuels*, vol. 35, no. 2, pp. 1219–1233, 2021.
- [20] R. Jiang, X. Liu, and X. Wang, "Transient pressure analysis of multilateral horizontal well in coal bed methane reservoir with two regions," *Journal of Xi'an Shiyou University (Natural Science Edition)*, vol. 35, no. 4, pp. 53–62, 2020.
- [21] J. Wu, J. Zhang, C. Chang, and W. T. W. Xie, "A model for a multistage fractured horizontal well with rectangular SRV in a shale gas reservoir," *Geofluids*, vol. 2020, no. 1, Article ID 8845250, p. 18, 2020.
- [22] X. Shang, Z. Zhang, Y. Niu, X. Yang, and F. Gao, "Analytical solutions for gas-water two-phase flow in multiseam coalbed methane production," *Geofluids*, vol. 2021, no. 8, Article ID 6690218, p. 15, 2021.
- [23] Q. Tian, Y. Cui, W. Luo, P. Liu, B. Ning, and E. Sciuabba, "Transient flow of a horizontal well with multiple fracture wings in coalbed methane reservoirs," *Energies*, vol. 13, no. 6, 2020.
- [24] R. Al-Hussainy, H. Jr, and P. B. Crawford, "The flow of real gases through porous media," *Journal of Petroleum Technology*, vol. 18, no. 5, pp. 624–636, 1966.
- [25] R. G. Agarwal, "Real gas pseudo-time" - a new function for pressure buildup analysis of MHF gas wells," in *Paper SPE 8279-MS Presented at SPE Annual Technical Conference and Exhibition*, Las Vegas, Nevada, USA, 1979.
- [26] X. Li, D. Zhang, and S. Li, "A multi-continuum multiple flow mechanism simulator for unconventional oil and gas recovery," *Journal of Natural Gas Science and Engineering*, vol. 26, no. 2015, pp. 652–669, 2015.
- [27] S. Lv, S. Wang, H. Liu et al., "Analysis of the influence of natural fracture system on hydraulic fracture propagation morphology in coal reservoir," *Journal of China Coal Society*, vol. 45, no. 7, pp. 2590–2601, 2020.

## Research Article

# A Semianalytical Model for Analyzing the Infill Well-Caused Fracture Interference from Shale Gas Reservoirs

Sidong Fang,<sup>1,2</sup> Yonghui Wu ,<sup>3</sup> Cheng Dai,<sup>1,2</sup> Liqiang Ma ,<sup>3</sup> and Hua Liu<sup>1,2</sup>

<sup>1</sup>State Key Laboratory of Shale Oil and Gas Enrichment Mechanisms and Effective Development, Beijing, China

<sup>2</sup>Sinopec Key Laboratory of Shale Oil/Gas Exploration and Production Technology, Beijing, China

<sup>3</sup>Key Laboratory of Deep Coal Resource Mining (China University of Mining & Technology), Ministry of Education, China

Correspondence should be addressed to Yonghui Wu; wuyonghuijr@cumt.edu.cn

Received 13 September 2021; Accepted 19 October 2021; Published 1 November 2021

Academic Editor: Xiang Zhou

Copyright © 2021 Sidong Fang et al. This is an open access article distributed under the Creative Commons Attribution License, which permits unrestricted use, distribution, and reproduction in any medium, provided the original work is properly cited.

Drilling infill well has been widely used in many plays to enhance the recovery of shale gas, but the infill well-caused fracture interference is a very important issue that should be taken into consideration. The well interference makes it difficult for the conventional models to make production predictions, fracture characterization, and production data analysis. In this paper, a semianalytical model is proposed for this purpose by discretizing the whole control volume of the parent and infill wells into several linear flow zones. In this way, three important issues can be further handled very naturally, including fracture connection between the parent and infill wells, different SRV properties for zones with different distances to the wellbore, and different production times for adjacent wellbores. The approximate expressions for different flow regimes are used in making production predictions in the time domain, and a flowing material balance method and a simple iteration are used to update the model parameters step by step. The proposed model is shown to be reasonable and accurate for handling multiwell interference problems after comparing with the commercial numerical simulator tNavigator. The synthetical cases show that the fracture parameters, SRV properties, and well infill time have a significant influence on the production performance of both the parent and infill wells. The results show that the production of the parent well will be dramatically enhanced when it is connected with the infill well via high-conductive hydraulic fractures. Longer unconnected fractures and more fracturing stages/clusters for the infill well will result in higher production for the infill well, but a negative effect is observed for the parent well. The permeability of the distant well SRV has a similar influence on the parent and infill wells. The results also show that late time well interference will result in a more significant increase in production rate on the log-log plots for the severe depletion around the parent well. Finally, the proposed model is used to analyze the production data of a field case from Fuling shale in Southwestern China. After analyzing the production data, several parameters can be obtained for both parent and infill wells, including the fracture lengths and conductivities, numbers of connected fractures, and the near and distant well permeabilities of the SRV. This gives a basic and practical technique for production prediction, formation and fracture evaluation, and well connectivity analysis from shale gas wells with fracture connection.

## 1. Introduction

With the development of the technology in drilling long horizontal wells and multiple-stage hydraulic fracturing, unconventional shale gas resources have been economically developed in many counties around the world, such as the USA, China, and Canada [1]. However, the recovery of shale gas is quite low at present because of the high decline rate in shale gas production. At present, several

techniques are presented for this problem, including CO<sub>2</sub> sequestration in the shale formation [2–4] and refracturing and drilling infill wells [5, 6]. In particular, drilling infill wells are widely used in many plays and the well spaces have been tightened to 200–300 meters. A major concern of drilling an infill well is the infill well-caused well interference, which makes it difficult for making production predictions and interpreting the fracture parameter and evaluating the well connectivity.



Many researchers have reported the well interference phenomenon from several aspects, including fracture propagation simulation, field microseismic monitoring, and production and pressure tests. Fracture propagation studies show that fractures growing from adjacent wells tend to attract each other and result in fracture connections [7]. Field microseismic data also show that the phenomenon of fracture connection between adjacent wells is quite common, especially for infill well cases, where there is pressure sink in the formation after the long-time production [8, 9]. Production and pressure tests show that the pressure, and gas, and water production of a parent well will dramatically change after the hydraulic fracturing of an adjacent infill well [10–12]. Therefore, it is of great importance to analyze the effects of infill well-caused fracture interference for shale gas reservoirs.

Numerical models are quite comprehensive and robust for fracture interference analysis for their ability in handling complex fracture networks, nonlinearities, heterogeneities, and other complex problems. The present numerical models mainly include discrete fracture models (DFM) and embedded discrete fracture models (EDFM) [13–19]. The EDFM is quite efficient in analyzing the effects of infill well-caused fracture interference because the time-consuming grid system is not needed to be discretized two times after adding the infill well. Green element method- (GEM-) based discrete fracture model is another efficient method for unconventional reservoir simulation, which borrows the advantages of EDFM in discretization and the boundary element method (BEM) in precision [20, 21]. By using numerical models, several studies have studied the effects of well interference on the production and pressure performance [22–25]. In these studies, the wells are assumed to be connected with low-conductivity reactivated natural fractures and high-conductivity hydraulic fractures.

Because numerical models are often time-consuming in matching the production and pressure data when there are many fractures in the model, analytical models are still often used in reservoir engineering. The analytical models for unconventional oil and gas reservoirs are often based on linear flow assumptions for the long-time linear flow regimes observed in the field. In the linear flow models, the reactivated natural fractures are treated using the SRV concept and the analytical solutions can be derived by discretizing the whole control volume of the wellbore with several linear flow zones [26–28]. Several studies also enriched the analytical models to more complex problems, such as the two-phase flow in retrograde gas and condensate oil reservoirs, and early-time two-phase flow back data analysis [29, 30]. Some studies also use this concept to approximately analyze the production data for wells with fracture interference [12, 31–33]. The slopes exhibited by the pressure and rate curves on the log-log plots are used to diagnose the well interference. It is reported that well interference will increase the decline rate on the type curves. However, the present analytical model can only be used for production decline analysis qualitatively. In addition, the wells are assumed to start producing at the same time, so the problem of infill well-caused fracture interference is not considered in these models.

In this paper, we will present a semianalytical model for production prediction and production data analysis based on the linear flow assumptions. This model mainly handled three important problems concerning the well interference, including different production times for different wells, well connections with part of the fractures, and different formation properties for near and distant well SRV regions. In the following, we first presented the mathematical fundamentals of the semianalytical model. Then, the proposed model is benchmarked with a commercial simulator and several synthetic cases are used to analyze the effects of different parameters. Finally, a field case is used to show the application of the proposed model.

## 2. Methodology

*2.1. Physical Model.* For shale gas reservoirs, as shown in Figure 1, multiple high-conductive fractures and an SRV will be generated after hydraulic fracturing. Before adding the infill well and there is no well interference, the SRV is near the parent well, just like SRV<sub>1</sub> in Figure 1(a) and SRV<sub>1</sub> and SRV<sub>5</sub> in Figure 1(b). After the hydraulic fracturing of the infill well, SRV can be generated near the infill well, just like SRV<sub>3</sub> in Figure 1(a) and SRV<sub>3</sub> in Figure 1(b). In addition, the distant well area can also be stimulated because the depletion around the parent well and the hydraulic fractures are tending to propagate into the SRV of the parent well. Therefore, some fractures will be connected between the parent and infill wells and the distant well SRV can be generated, just like SRV<sub>2</sub> in Figure 1(a) and SRV<sub>2</sub> and SRV<sub>4</sub> in Figure 1(b).

In this paper, we assume that part of the distant well SRV will contribute to the parent well and the other part will contribute to the infill well. The distant well SRV, including SRV<sub>2</sub> in Figure 1(a) and SRV<sub>2</sub> and SRV<sub>4</sub> in Figure 1(b), contribute to both the parent and infill wells, so there should be a contribution ratio to the parent well, which can be defined using the fracture length. Based on this assumption, the representative zones can be obtained in Figure 1 for both parent and infill wells. For the two-well case shown in Figure 1(a), zones A and B are the representative zones of the parent well and the whole control volume of the parent well can be formed with the combinations of A and B. For the infill well shown in Figure 1(a), zones C and D can be regarded as the representative zones. One should note that zones A and C are different models because the near and distant well SRVs are not starting produce at the same time. In the same way, we can analyze the three-well case shown in Figure 1(b). Another assumption is that the unstimulated reservoir volume is not considered in this model because the production contribution from the unstimulated reservoir is not significant. In addition, this contribution cannot be observed on log-log plots in late flow regimes.

Taking half of the representative zones shown in Figure 1, as shown in Figure 2, we can further extract the basic linear flow models, including the two-region linear flow model, convergence linear flow model, and single-linear flow model. In this way, we can simplify the complex multiwell interference model to basic linear flow models. In

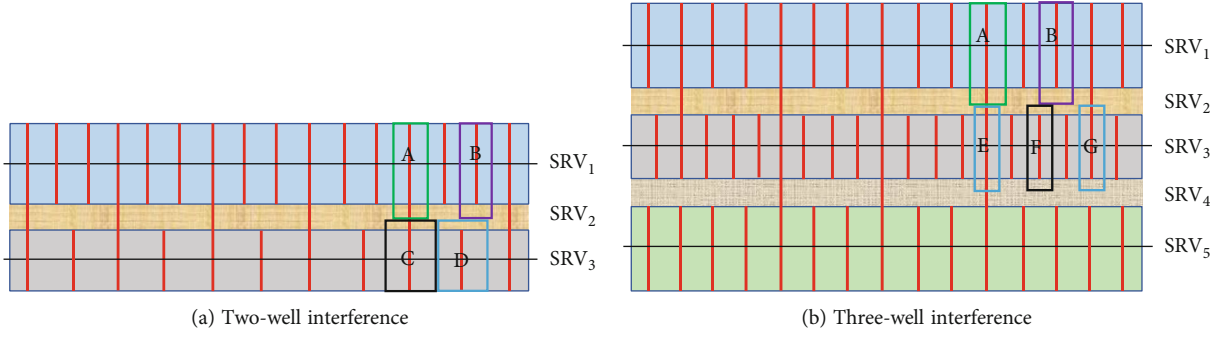


FIGURE 1: Schematic of a well pad with fracture connection between the parent and infill wells.

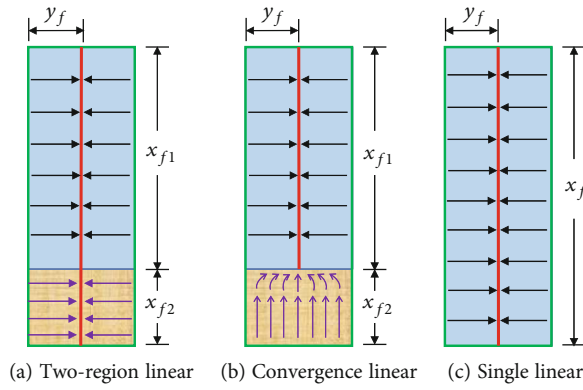


FIGURE 2: Schematic of the typical flow models for analyzing the infill well-caused fracture interference.

Section 2.2, we will present the mathematical fundamentals for the physical model.

2.2. Mathematical Model

2.2.1. Analytical Solution in Linear Systems. For the single-linear flow, taking the schematic shown in Figure 2(c) for example, the governing equation can be given by

$$\frac{\partial^2 \psi_D}{\partial y_D^2} = \frac{1}{\eta_D} \frac{\partial \psi_D}{\partial t_D}. \quad (1)$$

It should be noted that the gas desorption from the tight matrix pores is considered using desorption compressibility, which is defined by  $c_d = ((p_{sc} Z T) / (\phi Z_{sc} T_{sc})) ((V_L p_L) / (p(p_L + p)^2))$  in our previous work [34]. Here, we should state that the geomechanics and complex transport mechanisms in the shale nanopores are not seriously considered in this analytical model [35–42]. In this model, these transport mechanisms can be characterized using apparent permeability and handled with the pseudopressure approximately in the analytical model. The pseudopressure can be defined with  $\psi = 2 \int_0^p ((f_{app} p) / (\mu Z)) dp$ , where  $f_{app}$  is a permeability modifier.

The definitions of the dimensionless variables are shown in Table 1.

The initial condition is given by

$$\psi_D|_{t_D=0} = 0. \quad (2)$$

The inner boundary condition is

$$\frac{\partial \psi_D}{\partial y_D} \Big|_{y_D=y_{fD}} = 0. \quad (3)$$

The outer boundary condition is coupled with the hydraulic fractures. Since infinite-conductivity fracture is assumed in this model, the inner boundary condition can be written as

$$\psi_D|_{y_D=0} = 1 + s_c. \quad (4)$$

Laplace transformation can be used to obtain the analytical solution of the single-linear flow model shown in equations (1)–(3). According to our previous work [43], the production solution can be directly given by

$$\bar{q}_D = \frac{1 + s_c}{s} \frac{k_D x_{fD}}{\pi} \sqrt{\frac{s}{\eta_D}} \tan h \left( \sqrt{\frac{s}{\eta_D}} \cdot y_{fD} \right). \quad (5)$$

It should be noted that the numerical algorithm proposed by Stehfest should be used to obtain the solution of equation (5) in the time domain [44]. Because there are mainly two flow regimes for the infinite conductive fracture

TABLE 1: Definitions of the dimensionless parameters used in the model derivation.

Variables	Definition	Variables	Definition
Dimensionless pressure for gas (at constant rate)	$\psi_D = (k_r H(\psi_i - \psi)) / (1.291 \times 10^{-3} q_{sc} T)$	Dimensionless pressure for gas (at constant BHP)	$\psi_D = (\psi_i - \psi) / (\psi_i - \psi_{wf})$
Dimensionless rate for oil (at constant rate)	$\psi_D = (k_r H(p_i - p)) / (1.842 q_{sc} B\mu)$	Dimensionless pressure for oil (at constant BHP)	$\psi_D = (p_i - p) / (p_i - p_{wf})$
Reference diffusivity ( $10^6$ mD/s)	$\eta_r = 0.0864 k_r / (\phi c_t \mu)_r$	Dimensionless time	$t_D = (\eta_r / L_r^2) t$
Dimensionless length: $x$ direction	$x_D = x / L_r$	Dimensionless length: $y$ direction	$y_D = y / L_r$
Dimensionless diffusivity	$\eta_D = (\eta / \eta_r) = (1 / \eta_r) (0.0864 k / \phi c_t \mu)$	Dimensionless permeability	$k_D = k / k_r$

model, linear flow regime, and boundary dominated flow regime, the regional approximate solutions [45] can be used to simplify the solution.

For the linear flow regime, the solution for the constant bottom hole pressure condition case is given by

$$\frac{1}{q_D} = \frac{1}{1 + s_c} \frac{\pi}{2k_D x_{fD}} \sqrt{\pi \eta_D t_D}. \quad (6)$$

Taking the dimensionless variables into equation (6), we can obtain

$$q_{sc} = \frac{2(1 + s_c)kH(\psi_i - \psi_{wf})x_f}{\pi \cdot 1.291 \times 10^{-3} T \sqrt{\pi \eta t}}. \quad (7)$$

For the long-term boundary-dominated flow regime, the solution can be written as

$$q_{sc} = \alpha_g \frac{\pi kH(\bar{\psi} - \psi_{wf})x_f}{2 \cdot 1.291 \times 10^{-3} T y_f}. \quad (8)$$

$\alpha_g$  is a factor, which makes the production rate curves continuous at the connection of the two flow regimes. The value of  $\alpha_g$  can be determined using the following expression

$$q_{sc}|_{\text{linear flow}, t_{\text{elf}}} = q_{sc}|_{\text{boundary dominated flow}, t_{\text{elf}}}, \quad (9)$$

where  $t_{\text{elf}}$  is the time of deviation from the linear flow regime to the boundary-dominated flow regime and it can be estimated as follows:

$$t_{\text{elf}} = \frac{\phi \mu_i c_{ti}}{k} \left( \frac{y_f}{0.5836} \right)^2. \quad (10)$$

The bilinear flow may occur when the permeability of the SRV is high and the fracture cannot be regarded as infinitely conductive. In this case, the approximation of the production [43] can be given as

$$\frac{1}{q_D} = \frac{1}{1 + s_c} \frac{1.2254\pi}{\sqrt{k_D k_{fD} \omega_{fD}}} \sqrt[4]{\eta_D t_D}. \quad (11)$$

Taking the dimensionless variables into equation (11),

we can obtain

$$q_{sc} = 201.4 \sqrt{k k_f \omega_f} \frac{(1 + s_c) H(\psi_i - \psi_{wf})}{T \sqrt[4]{\eta t}}. \quad (12)$$

**2.2.2. Average Pressure Calculation.** We can find that some parameters in equations (7) and (8) are average pressure dependent, such as  $\bar{\eta}_i$  and  $\bar{\psi}$ . Therefore, to obtain the production solution of the system, another step is to obtain the average pressure. In this section, the flowing material balance equations are used for this purpose. According to equation (10), the distance of investigation can be written as

$$y_{\text{inv}} = 0.5836 \sqrt{\frac{kt}{\phi \mu_i c_{ti}}}. \quad (13)$$

Therefore, for the single-linear flow system, the control volume of the fracture can be given by

$$V_{\text{inv}} = 4x_f y_{\text{inv}} H \phi. \quad (14)$$

Using the material balance method, we can obtain

$$G_p = \text{IGIP} - \text{RGIP}. \quad (15)$$

In which,  $G_p$  is the cumulative gas production, IGIP is the initial gas reserve, RGIP is the remaining gas reserve, and they can be calculated with

$$G_p = \int_0^t q_{gsc} dt, \quad (16)$$

$$\text{IGIP} = V_{\text{inv}} \left( \frac{S_{gi}}{B_{gi}} + \frac{V_L p_i}{p_L + p_i} \right), \quad (17)$$

$$\text{RGIP} = V_{\text{inv}} \left( \frac{S_{gi}}{B_g} + \frac{V_L \bar{p}}{p_L + \bar{p}} \right). \quad (18)$$

It should be noted that the water in the formation is irreducible, so the initial gas saturation is used in equation (18).

Taking equations (16)–(18) into equation (15), we can obtain

$$\frac{S_{gi}}{\bar{B}_g} + \frac{V_L \bar{p}}{p_L + \bar{p}} = \frac{S_{gi}}{B_{gi}} + \frac{V_L p_i}{p_L + p_i} - \frac{G_p}{V_{inv}}. \quad (19)$$

Equation (19) can be rewritten as

$$f(\bar{p}) = \frac{S_{gi}}{\bar{B}_g} + \frac{V_L \bar{p}}{p_L + \bar{p}} + \frac{G_p}{V_{inv}} - \frac{S_{gi}}{B_{gi}} - \frac{V_L p_i}{p_L + p_i} = 0. \quad (20)$$

Taking the derivation of Eq. (20), we obtain

$$f'(\bar{p}) = -\frac{S_{gi} dB_g}{\bar{B}_g^2 dp} + \frac{V_L p_L}{(p_L + \bar{p})^2}. \quad (21)$$

We can use the Newton-Raphson iteration to solve equations (20) and (21). The iteration equation can be written as

$$\bar{p}_{k+1} = \bar{p}_k - \omega \frac{f(\bar{p}_k)}{f'(\bar{p}_k)}, \quad (22)$$

where  $\omega$  depends on the iteration steps  $n$ ,  $\omega = 1/2^{n-1}$ .

**2.2.3. Production Prediction for Different Regions.** For the cases shown in Figure 1, the whole reservoir can be characterized with representative regions, including A–G. In addition, each region is combined with the typical flow models shown in Figure 2.

For the model shown in Figure 1(c), the solution can be obtained using the mathematical derivations shown in Sections 2.3.1 and 2.3.2. The detailed procedure can be concluded in Figure 3.

Using the procedure for a single-linear flow, we can obtain the production of the typical regions and the horizontal wells. Table 2 shows the composition of different regions shown in Figure 1. For the parent and infill wells, the total gas production is the summation of different typical regions. It should be noted that the production times for the parent and infill wells are different, so this should be considered in predicting the production of the parent wells.

### 3. Results and Discussion

In this section, we will first validate the proposed semianalytical model by using the commercial numerical simulator tNavigator. Then, we will analyze the effects of the connection condition between the parent and infill wells on the production performance. Finally, a field case from the Fuling shale gas field in Southwestern China is provided to show the application of the proposed model. Because only a two-well interference field case is accessible at present, the case shown in Figure 1(a) is analyzed in this section. However, the same method can be used for cases shown in Figure 1(b).

**3.1. Model Validation.** In this section, two cases are used to validate the proposed semianalytical model, the single-linear flow case and two-well interference case. In the follow-

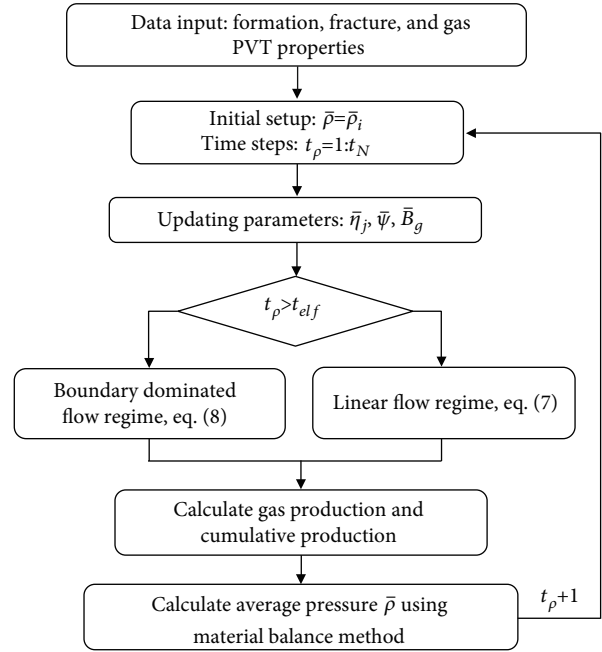


FIGURE 3: The procedure to predict the production for a single-linear flow model.

ing, we first use the single-linear flow case shown in Figure 2(c) to validate the model in the calculation, and then, a two-well interference case shown in Figure 1(a) is used to validate the model in model assumptions. For the two cases, the reservoir and fracture properties are shown in Table 3 and the gas PVT properties are calculated using the method proposed by Lee et al. [46] and shown in Figure 4(a).

The validation result of the single-linear flow case is shown in Figure 4(b). We can find that the proposed semianalytical model has a good match with the numerical simulation results. In addition, for this case, there are mainly two flow regimes exhibited by the gas production curves on the log-log plot—the formation linear flow and boundary-dominated flow regimes. This shows that the computation of the semianalytical model is reliable.

We further analyzed the validity of the assumptions of the regional linear flow model in handling infill well-caused fracture interference. In this case, the infill well is assumed to start to produce 720 days later than the parent well. Figure 5 shows the validation result, which shows that good matches are obtained for both the parent and infill wells. Figure 5(a) shows that the parent well has been in the boundary-dominated flow regime when it gets interfered by the infill well. It should be noted that the flow regimes after the infill time are composite for the parent well. The flow for the old SRV, the  $x_{f1}$  part shown in Figures 2(a) and 2(b), is under the boundary-dominated flow regime, while the new SRV generated by the fracturing of the infill well is under a linear flow regime. Two methods can be used to analyze this combined flow regime. The first method is by history matching, which will be presented in Section 3.3. The other method is by straight line analysis after processing the production data by deducting the contribution from the

TABLE 2: The composition of the typical sections shown in Figure 1.

Typical region	Composition	Production time
A	Linear (Figure 2(c) )+two – region linear (Figure 2(a))	At a different time
B	Linear (Figure 2(c) )+convergence linear (Figure 2(b))	At a different time
C	Linear (Figure 2(c) )+two – region linear (Figure 2(a))	At the same time
D	Linear (Figure 2(c) )+convergence linear (Figure 2(b))	At the same time
E	Two-region linear (Figure 2(a) )+two – region linear (Figure 2(a))	At a different time
F	Convergence linear (Figure 2(b) )+convergence linear (Figure 2(b))	At a different time
G	Two-region linear (Figure 2(a) )+convergence linear (Figure 2(b))	At a different time

TABLE 3: Parameters for the validation case.

Parameter	Value	Parameter	Value
Initial pressure (MPa)	75	Formation temperature (K)	408
Initial water saturation (irreducible)	0.56	Formation thickness (m)	25
Matrix permeability (mD)	$1 \times 10^{-5}$	Porosity of the matrix	0.051
Rock compressibility ( $\text{MPa}^{-1}$ )	$8 \times 10^{-5}$	Hydraulic fracture porosity	0.3
Hydraulic fracture width (m)	0.01	Bottom hole pressure (MPa)	5
Hydraulic fracture permeability (mD)	10000	Fracture half-length of the infill well (m)	82.5
Fracture half-length of the parent well (m)	122.5	Number of fractures for the infill well	11
Number of fractures for the parent well	16	Number of connected fractures	6
Permeability of the region between the two wells (mD)	$3 \times 10^{-5}$	Well space (m)	300
Permeability of the SRV for the parent well (mD)	$1 \times 10^{-4}$	Permeability of the SRV for the infill well (mD)	$6 \times 10^{-5}$

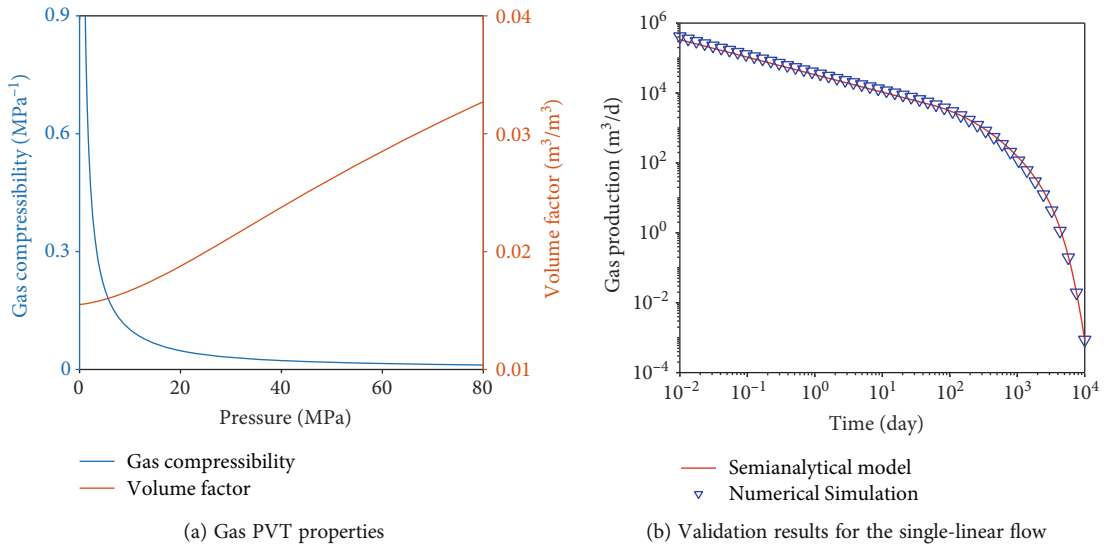


FIGURE 4: The procedure to predict the production for a single-linear flow model.

near-well SRV, but this will be our future work. One should also notice that the time shown in Figure 5(b) is the production time of the infill well, which is 720 days later than the production time of the parent well. The flow regimes cannot be exhibited by the log-log plots if the production time of the parent well is used, just like the late flow regimes shown in Figure 5(a).

3.2. *Synthetic Case Study.* In this section, we will analyze the infill well-caused well interference on the production performance of both the parent and infill wells. The analyzed parameters include the numbers of the connected fractures between the parent and infill wells, the length of the unconnected fractures for the infill well, the fracture numbers of the infill well, the permeability of the new SRV region



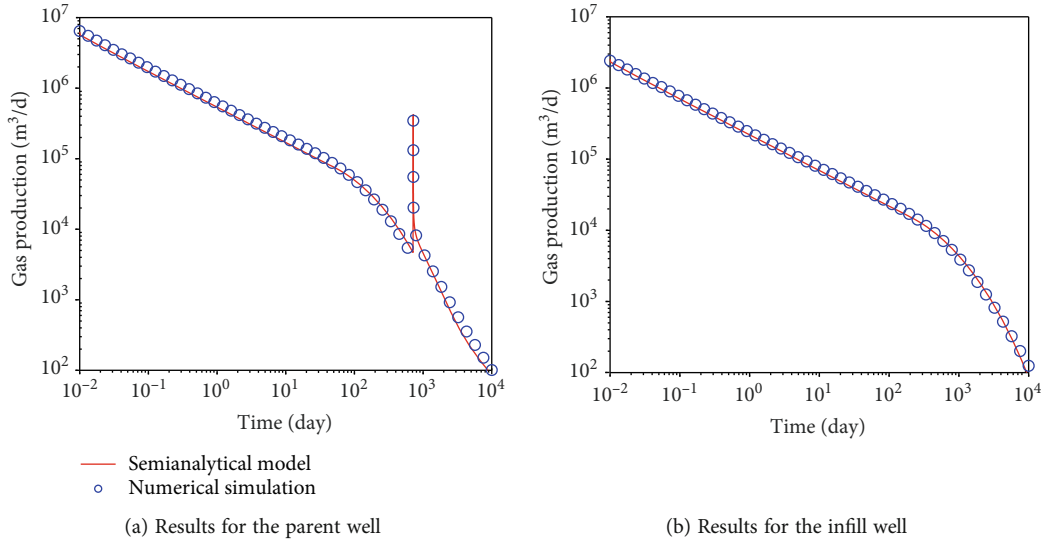


FIGURE 5: The gas production comparison results for the two-well interference case.

TABLE 4: The analyzed parameters for the synthetic cases.

Parameter	Value	Parameter	Value
Fracture half-length of the parent well (m)	120	Number of fractures for the parent well	40
Permeability of the near-well SRV (mD)	$1 \times 10^{-4}$	Infill time (day)	360/540/ <b>720</b> /900
Number of connected fractures	10/ <b>20</b> /30/40	Number of fractures for the infill well	20/30/ <b>40</b> /50
Permeability of the distant well SRV ( $\times 10^{-5}$ mD)	1, 3, 6, 10	Fracture half-length of the infill well (m)	40/80/ <b>120</b> /160

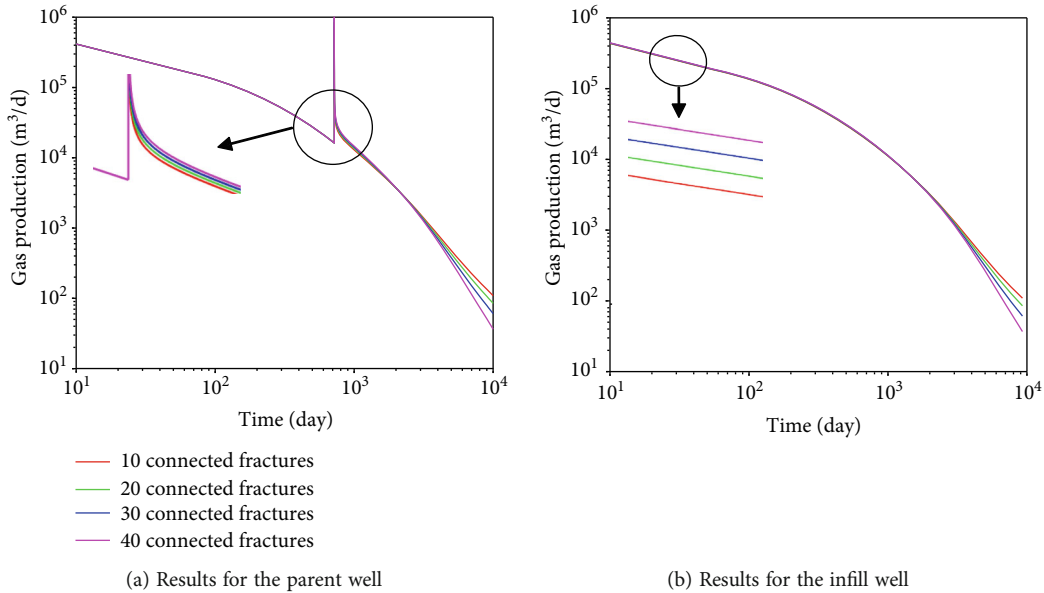


FIGURE 6: The effects of connected fracture numbers on the gas production of both parent and infill wells.

between the parent and infill wells, and the well infill time. In this section, the fracture and SRV properties of the parent well are assumed to be the same for all the studied cases. Table 4 shows the analyzed parameters, and other parameters are shown in Table 3. One should note that the values in bold font in Table 4 are the default value for the parameters.

3.2.1. *The Effect of the Connected Fracture Numbers.* Figure 6 shows the effects of connected fracture numbers on the production of the parent and infill wells. The results show that the production of the parent well will be significantly enhanced when it gets fracture interference from the infill well. This is because of the gas contribution from the far well SRV, which is generated after the hydraulic fracturing of the

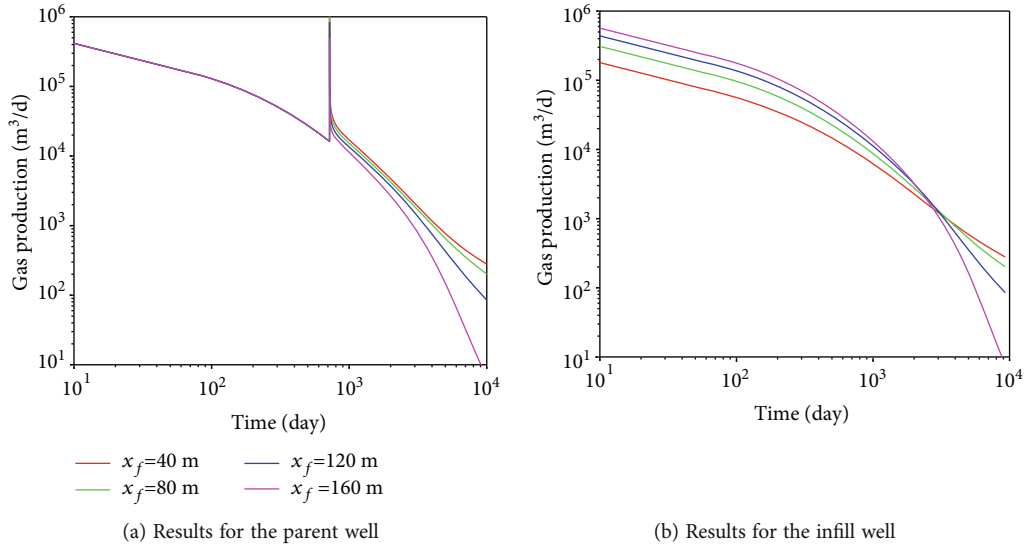


FIGURE 7: The effects of the unconnected fracture length on the gas production of both parent and infill wells.

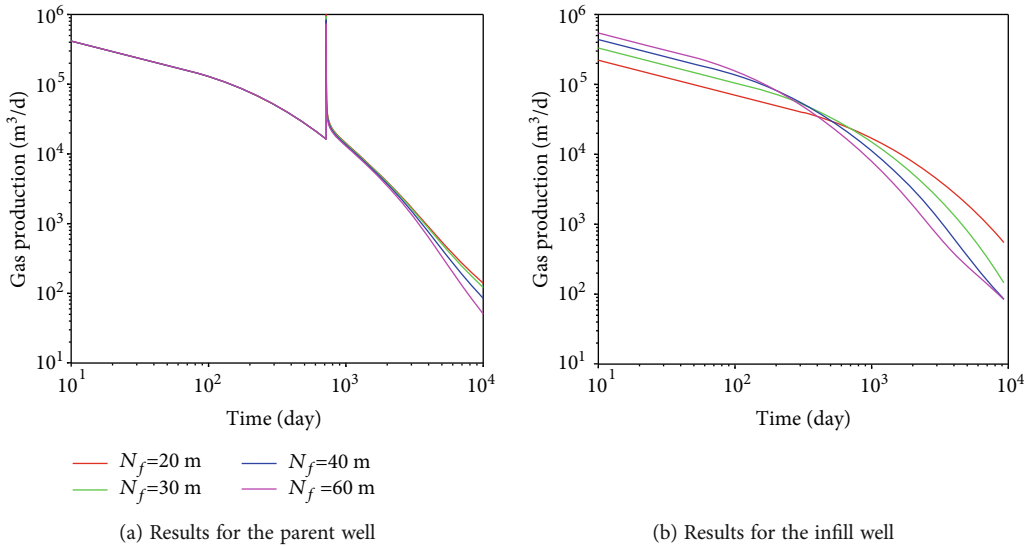


FIGURE 8: The effects of fracture stages/clusters on the gas production of both parent and infill wells.

infill well. The results also show that the production of both parent and infill wells will be higher with more connected fractures at early flow regimes, while lower production rates are observed for late flow regimes. This shows that the remaining gas in the formation will be extracted by the wells earlier with more connected fractures.

**3.2.2. The Effect of the Length of Unconnected Fractures.** In this case, the length of the parent well is given a constant value and the length of the unconnected fractures for the infill well is given as 40, 80, 120, and 160 m to analyze the effects of well interference.

As shown in Figure 7, the length of the unconnected fractures has a significant influence on the production of both the parent and infill wells. For the infill well, much larger SRV and control volume can be obtained with longer fracture, so the production of the infill well is significantly enhanced.

For the parent well, fracture connection can increase the gas production for all the cases but higher production will be obtained with shorter unconnected fractures. This is because a longer fracture of the infill well will increase the near SRV of the infill well and reduce the distant well SRV, which causes the production increase for the parent well.

**3.2.3. The Effect of the Fracture Stages/Clusters.** Figure 8 shows the effects of the fracture stages/clusters of the infill well on shale gas production. The results show that the fracture stages of the infill well have limited influence on the production of the parent well. This is because the connected fracture number is given as 20 for all the scenarios, while this may be not true in the field. Because it is more possible to have more fractures connected with the parent well if more stages/clusters are used in the hydraulic fracturing of the infill well. For the infill well, more fracture stages/clusters

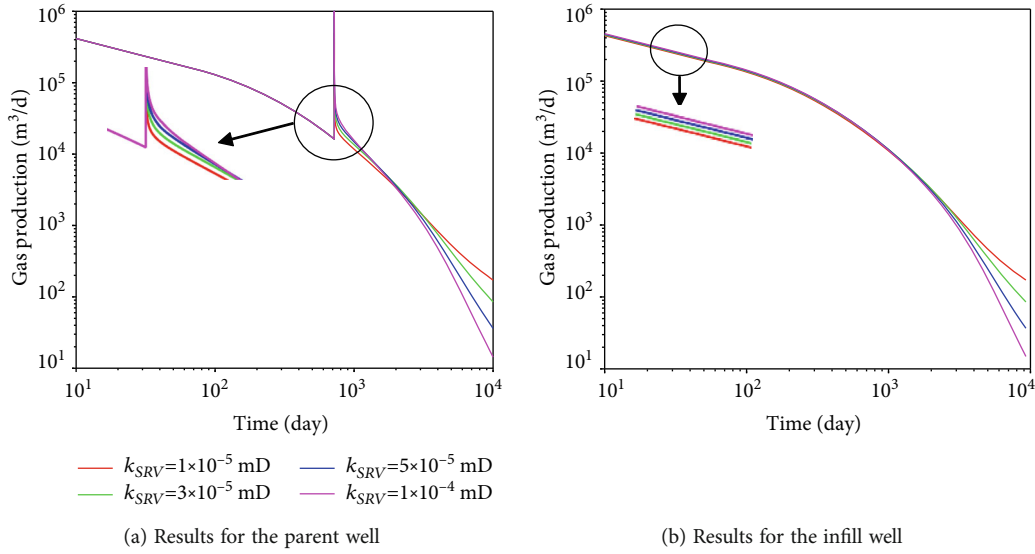


FIGURE 9: The effects of the SRV permeability on the gas production of both parent and infill wells.

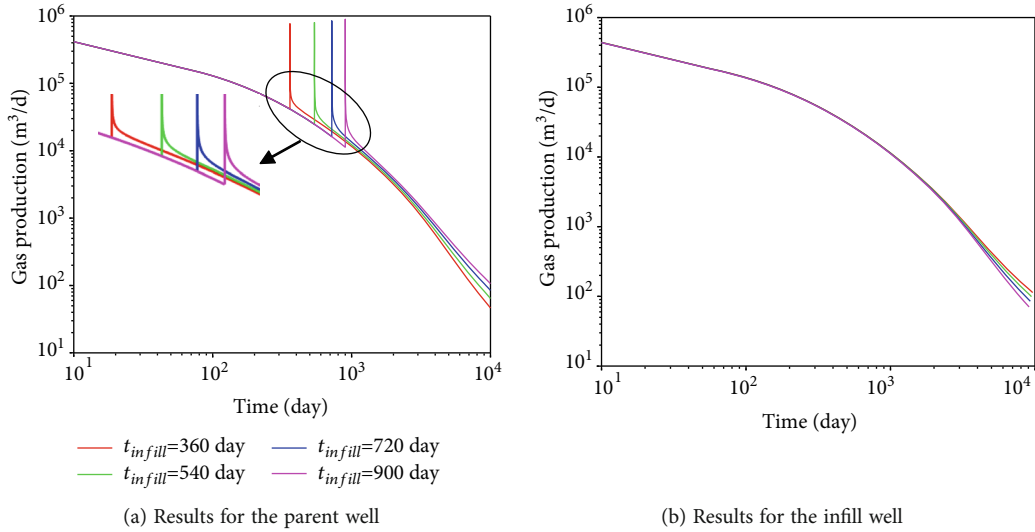


FIGURE 10: The effects of the well infill time on the gas production of both parent and infill wells.

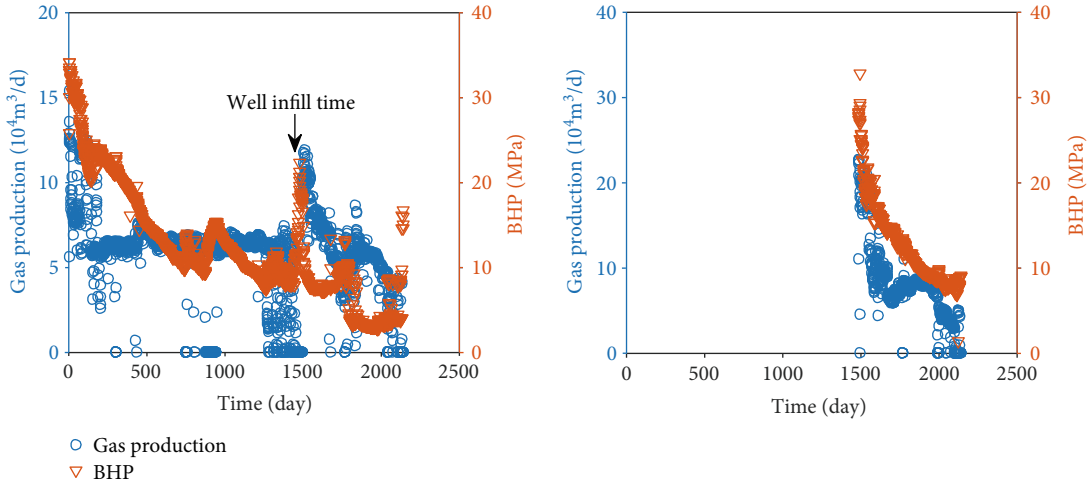
will result in higher gas production in the early flow regimes and lower in the late flow regimes. This is quite like the influence of the fracture length shown in Figure 7(b), but the influence of the fracture length is more significant with the studied parameters.

**3.2.4. The Effect of the SRV Permeability.** In this section, we are focused on analyzing the effects of the permeability of the distant well SRV generated during the stimulation of the infill well. For comparison, the permeability of the near well SRV for both the parent and infill wells is given as  $1 \times 10^{-4}$  mD. Figure 9 shows that the influence of the SRV permeability on the parent and infill well is quite similar. In the early flow regimes, larger production rates are obtained with higher SRV permeabilities, while an opposite influence is observed on the curves for the late flow regimes.

This is because more gas reserves are produced from the wells with higher SRV permeabilities and left limited remain reserves for the late flow regimes.

**3.2.5. The Effect of the Well Infill Time.** In this section, we assume that the infill well starts to fracture and produce at 360, 540, 720, and 900 days after the parent well.

Figure 10(a) shows that well interference in later flow regimes will result in higher production “pick” when the parent well gets interfered by the infill well. In addition, the amount of production increase will be larger with later fracture interference. This is because the depletion in the control volume of the parent well is more severe and a larger proportion of the distant well SRV will contribute to the parent well. Therefore, in Figure 10(b), we can find that the production of the infill well will be lower when the infill well is added into the well pad at a later time.

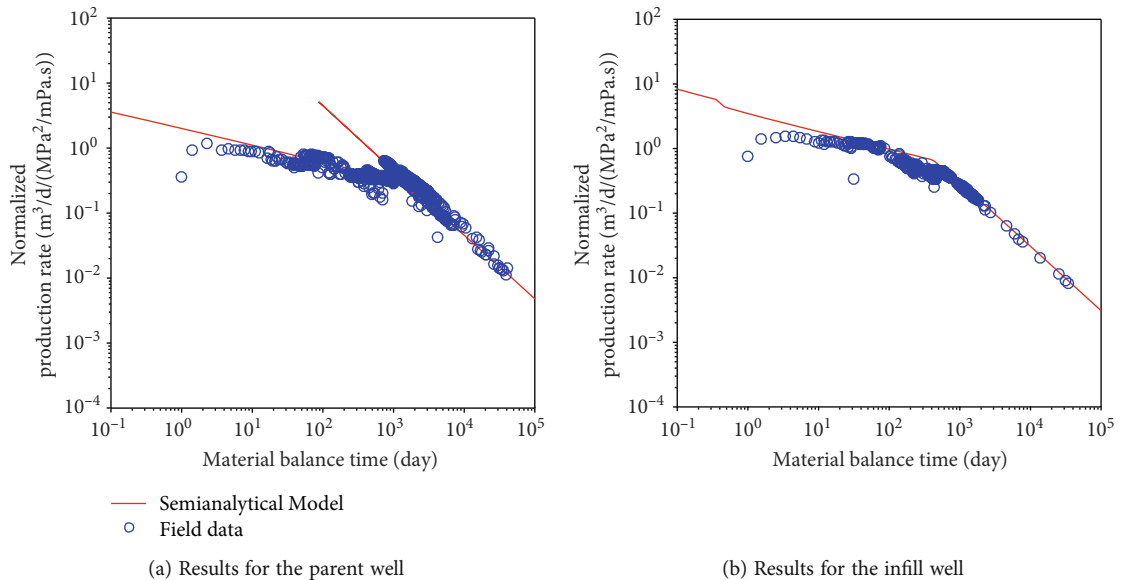


(a) Performance of the parent well (b) Performance of the infill well

FIGURE 11: The production performance of the parent and infill wells for the field case.

TABLE 5: The formation properties and fitted parameters using the semianalytical model.

Parameter	Value	Parameter	Value
Initial pressure (MPa)	75	Formation temperature (K)	408
Initial water saturation (irreducible)	0.56	Formation thickness (m)	25
Matrix permeability (mD)	$1 \times 10^{-5}$	Porosity of the matrix	0.051
Rock compressibility ( $\text{MPa}^{-1}$ )	$8 \times 10^{-5}$	Hydraulic fracture porosity	0.3
Well space (m)	300	Permeability of the distant well SRV (mD)	$5 \times 10^{-5}$
Langmuir pressure (MPa)	5	Langmuir volume ( $\text{m}^3/\text{t}$ )	3
*Hydraulic fracture conductivity (D-cm)	0.05	*Number of connected fractures	15
*Number of fractures for the parent well	15	*Number of fractures for the infill well	25
*Half-length of the fractures for the parent well (m)	140	*Half-length of the fractures for the infill well (m)	90
*Permeability of the near-well SRV (mD)	$5 \times 10^{-4}$	*Contribution ratio to the parent well	0.7



(a) Results for the parent well (b) Results for the infill well

FIGURE 12: The production analysis results for the parent and infill wells.

**3.3. Field Case Study.** To further benchmark the proposed semianalytical model, a field case from Southwestern China is used in the analysis. The parent well is 1450 meters long and hydraulically fractured with 15 stages. After producing for 1484 days, an infill well is fractured and starts to produce. The distance between the parent and infill wells is 300 meters. Figure 11 shows the production performance of both the parent and infill wells. Significantly, there is a boom in the gas production for the parent well when the infill well is added to the well pad. Therefore, in this case, we will use the proposed semianalytical model to analyze the production data and inverse the fracture properties and evaluate the inter-well connectivity by using history matching. Some of the formation properties are shown in Table 5.

Because the production data is under variable BHP and rate conditions, we should use the normalized production rate and material balance time to process the production data. The production data obtained using the proposed semianalytical model is also handled using this concept because of the nonlinearity of the semianalytical model. In this paper, both the production data and the semianalytical results are handled in this way. The history matching results are shown in Figure 12. For both the parent and infill wells, there are mainly two flow regimes exhibited in the log-log plots. The first flow regime is a bilinear flow regime, which is characterized by a 1/4 slope on the log-log plots. The second flow regime is a boundary-dominated flow regime, which has a slope of 1. Therefore, the approximated expressions, equations (8) and (12), are used in the semianalytical model. The history matching results show that a good match to the field data is obtained. The fitted parameters are shown in Table 5, in which character “\*” is used to mark the fitted parameters. We should admit that this may be not the only one to match the field data because of the uncertainties in the model. It should be noted that the dimensionless fracture conductivity is about  $2\pi$ , so the early flow regime is bilinear flow. This is following the assumption for using the bilinear flow model. One should also note that the contribution ratio to the parent well, shown in Table 5, is obtained by history matching for field cases.

## 4. Conclusions

In this paper, a practical semianalytical model is proposed to analyze the infill well-caused fracture interference on the gas production performance. Based on the studies in this paper, the following conclusions are guaranteed:

- (1) Strict analytical models cannot handle the problem of infill well-caused fracture interference because the parent and infill wells are not in production at the same time, which makes the analytical model nonlinear and nonhomogeneous. The validation over the numerical simulator shows that this problem can be handled by dividing the whole model into several linear flow regions and the production of the wellbore can be obtained by adding the production contribution from all the parts

- (2) When two wells are connected with high-conductivity fractures, the production of the parent well will significantly increase when the parent well gets interfered. The production rates of the wells are influenced by the fracture parameters, including the numbers of connected fractures, the length of the unconnected fractures, and fracturing stages/clusters for the infill well. Although similar effects are observed on the production rates curves, the length of the fractures and fracturing stages/clusters are particularly significant
- (3) The production is also affected by the SRV permeability and well infill time, which influence the production contribution from the distant well SRV by changing the properties and the production contribution ratio to the parent well. The production increase of the parent well upon getting fracture interference will be more significant in late time infill well production
- (4) The normalized production rate and material balance time can be used to analyze the production data for multiwell cases with fracture connections. The interwell connection conditions and the fracture properties of the parent and infill wells can be interpreted with the proposed semianalytical model

## Nomenclature

$B$ :	Fluid volume factor, $\text{m}^3/\text{m}^3$
$c_i$ :	Total compressibility, $\text{MPa}^{-1}$
$f_{\text{app}}$ :	Permeability modifier, dimensionless
$G_p$ :	Cumulative gas production, $\text{m}^3$
$H$ :	Formation thickness, m
$k$ :	Permeability, mD
$k_f$ :	Permeability of the hydraulic fracture, mD
$k_r$ :	Reference permeability, mD
$L_r$ :	Reference length, mD
$p$ :	Pressure, MPa
$p_i$ :	Initial pressure, MPa
$p_L$ :	Langmuir pressure, MPa
$p_{\text{wf}}$ :	Flowing pressure, MPa
$q_{sc}$ :	Flow rate at the surface condition, $\text{m}^3/\text{d}$
$S_g$ :	Gas saturation
$s$ :	Laplace constant
$s_c$ :	Skin factor caused by the choking effect
$t$ :	Time, day
$t_p$ :	Time step
$T$ :	Temperature, K
$V_{\text{inv}}$ :	Investigation volume, $\text{m}^3$
$V_L$ :	Langmuir volume, $\text{m}^3/\text{m}^3$
$w_f$ :	Fracture aperture, $\text{m}^3/\text{m}^3$
$x$ :	$x$ direction, m
$x_f$ :	Half-length of hydraulic fractures, m
$y$ :	$y$ direction, m
$y_f$ :	Half-length of fracture space, m.

## Greeks symbols

$\Psi$ :	Pseudopressure of gas $\text{MPa}^2/\text{mPa}\cdot\text{s}$
----------	--



$\eta_r$ : Reference diffusivity, mD·MPa/mPa·s

$\eta$ : Diffusivity, mD·MPa/mPa·s

$\Phi$ : Porosity, m<sup>3</sup>/m<sup>3</sup>

$\mu$ : Fluid viscosity, mPa·s

$\omega$ : Coefficient.

### Superscripts

$\bar{\phantom{x}}$ : Laplace transform.

### Subscripts

$D$ : Dimensionless

$f$ : Hydraulic fracture

$i$ : Initial condition

elf: End of linear flow

sc: At standard surface condition

$r$ : Reference variable

inv: Investigation area

wf: Flowing variable of the wellbore.

## Data Availability

The data used to support the findings of this study are included in the article.

## Conflicts of Interest

The authors declare that they have no conflicts of interest.

## Acknowledgments

The authors acknowledge that this study was partially supported by the Fundamental Research Funds for the Central Universities (2021QN1005) and the Natural Science Foundation of Jiangsu Province (BK20210520).

## References

- [1] C. L. Cipolla, E. P. Lolon, J. C. Erdle, and B. Rubin, "Reservoir modeling in shale-gas reservoirs," *SPE Reservoir Evaluation & Engineering*, vol. 13, no. 4, pp. 638–653, 2010.
- [2] L. Huang, W. Zhou, H. Xu, L. Wang, J. Zou, and Q. Zhou, "Dynamic fluid states in organic-inorganic nanocomposite: implications for shale gas recovery and CO<sub>2</sub> sequestration," *Chemical Engineering Journal*, vol. 411, article 128423, 2021.
- [3] X. Zhou, Q. Yuan, Y. Zhang, H. Wang, F. Zeng, and L. Zhang, "Performance evaluation of CO<sub>2</sub> flooding process in tight oil reservoir via experimental and numerical simulation studies," *Fuel*, vol. 236, pp. 730–746, 2019.
- [4] X. Zhou, Q. Yuan, and X. Peng, "A critical review of the CO<sub>2</sub> huff 'n' puff process for enhanced heavy oil recovery," *Fuel*, vol. 215, pp. 813–824, 2018.
- [5] R. Safari, R. Lewis, X. Ma, U. Mutlu, and A. Ghassemi, "Fracture curving between tightly spaced horizontal wells," in *Presented at the unconventional resources technology conference*, San Antonio, Texas, USA, 2015.
- [6] R. Malpani, S. Sinha, L. Charry, B. Sinosis, B. Clark, and K. Gakhar, "Improving hydrocarbon recovery of horizontal shale wells through refracturing," in *Presented at SPE/CSUR unconventional resources conference*, Calgary, Alberta, Canada, 2015.
- [7] K. Wu, B. Wu, and W. Yu, "Mechanism analysis of well interference in unconventional reservoirs: insights from fracture-geometry simulation between two horizontal wells," *SPE Production & Operations*, vol. 33, no. 1, pp. 12–20, 2018.
- [8] J. P. Detring and G. Michael, "Using microseismicity to understand subsurface fracture systems and to optimize completions: eagle ford shale, TX," in *Presented at the unconventional resources technology conference*, Denver, Colorado, USA, 2014.
- [9] E. A. Ejofodomi and F. Silva, "Using a calibrated 3D fracturing simulator to optimize completions of future wells in the Eagle Ford Shale," in *Presented at the unconventional resources technology conference*, San Antonio, Texas, USA, 2015.
- [10] H. Lawal, G. Jackson, N. Abolo, and C. Flores, "A novel approach to modeling and forecasting frac hits in shale gas wells," in *Presented at EAGE Annual Conference & Exhibition*, London, United Kingdom, 2013.
- [11] B. Kurtoglu and A. Salman, "How to utilize hydraulic fracture interference to improve unconventional development," in *Presented at international petroleum exhibition and conference*, Abu Dhabi, UAE, 2015.
- [12] A. Ataei, E. Motaei, M. E. Yazdi, R. Masoudi, and A. Bashir, "Rate transient analysis RTA and its application for well connectivity analysis: an integrated production driven reservoir characterization and a case study," in *Prepared at the SPE Asia Pacific oil & gas Conference and exhibition*, Brisbane, Australia, 2018.
- [13] H. Hoteit and A. Firoozabadi, "Multicomponent fluid flow by discontinuous Galerkin and mixed methods in unfractured and fractured media," *Water Resources Research*, vol. 41, no. 11, pp. 274–282, 2005.
- [14] L. Li and S. H. Lee, "Efficient field-scale simulation of black oil in a naturally fractured reservoir through discrete fracture networks and homogenized media," *SPE Reservoir Evaluation & Engineering*, vol. 11, no. 4, pp. 750–758, 2008.
- [15] A. Moinfar, A. Varavei, K. Sepehrnoori, and R. T. Johns, "Development of an efficient embedded discrete fracture model for 3D compositional reservoir simulation in fractured reservoirs," *SPE Journal*, vol. 19, no. 2, pp. 289–303, 2014.
- [16] X. Rao, L. Cheng, R. Cao et al., "An efficient three-dimensional embedded discrete fracture model for production simulation of multi-stage fractured horizontal well," *Engineering Analysis with Boundary Elements*, vol. 106, pp. 473–492, 2019.
- [17] H. Liu, X. Rao, and H. Xiong, "Evaluation of CO<sub>2</sub> sequestration capacity in complex-boundary-shape shale gas reservoirs using projection-based embedded discrete fracture model (pEDFM)," *Fuel*, vol. 277, article 118201, 2020.
- [18] X. Rao, L. Xin, Y. He et al., "Numerical simulation of two-phase heat and mass transfer in fractured reservoirs based on projection-based embedded discrete fracture model (pEDFM)," *Journal of Petroleum Science and Engineering*, vol. 208, article 109323, 2022.
- [19] Y. Wu, L. Cheng, J. Killough et al., "Integrated characterization of the fracture network in fractured shale gas reservoirs—stochastic fracture modeling, simulation and assisted history matching," *Journal of Petroleum Science and Engineering*, vol. 205, article 108886, 2021.
- [20] Y. Wu, L. Cheng, S. Fang, S. Huang, and P. Jia, "A green element method-based discrete fracture model for simulation of the transient flow in heterogeneous fractured porous media," *Advances in Water Resources*, vol. 136, article 103489, 2020.

- [21] Y. Wu, L. Cheng, S. Fang, K. John, S. Huang, and P. Jia, "A novel edge-based green element method for simulating fluid flow in unconventional reservoirs with discrete fractures," *SPE Journal*, vol. 25, no. 2, pp. 842–866, 2020.
- [22] C. Xiao, Y. Dai, L. Tian et al., "A semianalytical methodology for pressure-transient analysis of multiwell-pad-production scheme in shale gas reservoirs, part 1: new insights into flow regimes and multiwell interference," *SPE Journal*, vol. 23, no. 3, pp. 885–905, 2018.
- [23] W. Yu, Y. Xu, R. Weijermars, K. Wu, and K. Sepehrnoori, "A numerical model for simulating pressure response of well interference and well performance in tight oil reservoirs with complex-fracture geometries using the fast embedded-discrete-fracture-model method," *SPE Reservoir Evaluation & Engineering*, vol. 21, no. 2, pp. 489–502, 2018.
- [24] H. Tang, B. Yan, Z. Chai, L. Zuo, J. Killough, and Z. Sun, "Analyzing the well-interference phenomenon in the Eagle Ford Shale/Austin chalk production system with a comprehensive compositional reservoir model," *SPE Reservoir Evaluation & Engineering*, vol. 22, no. 3, pp. 827–841, 2019.
- [25] Y. He, S. Cheng, J. Qin et al., "Interference testing model of multiply fractured horizontal well with multiple injection wells," *Journal of Petroleum Science and Engineering*, vol. 176, pp. 1106–1120, 2019.
- [26] H. A. Al-Ahmadi and R. A. Wattenbarger, "Triple-porosity models: one further step towards capturing fractured reservoirs heterogeneity," in *Presented at the SPE/DGS Saudi Arabia section technical symposium and exhibition*, Al-Khobar, Saudi Arabia, 2011.
- [27] M. L. Brown, E. Ozkan, R. S. Raghavan, and H. Kazemi, "Practical solutions for pressure-transient responses of fractured horizontal Wells in unconventional shale reservoirs," *SPE Reservoir Evaluation & Engineering*, vol. 14, no. 6, pp. 663–676, 2011.
- [28] K. Stalgorova and L. Mattar, "Analytical model for unconventional multifractured composite systems," *SPE Reservoir Evaluation & Engineering*, vol. 16, no. 3, pp. 246–256, 2013.
- [29] Y. Wu, L. Cheng, L. Ma et al., "A transient two-phase flow model for production prediction of tight gas wells with fracturing fluid-induced formation damage," *Journal of Petroleum Science and Engineering*, vol. 199, article 108351, 2021.
- [30] Y. Wu, L. Cheng, S. Huang et al., "An approximate semianalytical method for two-phase flow analysis of liquid-rich shale gas and tight light-oil wells," *Journal of Petroleum Science & Engineering*, vol. 176, pp. 562–572, 2019.
- [31] H. Chu, X. Liao, Z. Chen, and W. J. Lee, "Rate transient analysis of a multi-horizontal-well pad with a semi-analytical method," in *Prepared at the unconventional resources technology conference*, Austin, Texas, USA, 2020.
- [32] M. Eghbal, A. Abdolrahim, and Y. M. Ebrahim, "Production analysis PA and application of rate transient analysis RTA in carbonate oil reservoirs for reservoir characterization and connectivity," in *Presented at the Offshore Technology Conference Asia*, Kuala Lumpur, Malaysia, 2018.
- [33] H. Yadav and S. Motealleh, "Improving quantitative analysis of frac-hits and refracs in unconventional plays using RTA," in *Presented at the SPE hydraulic fracturing technology conference and exhibition*, The woodlands, Texas, USA, 2017.
- [34] Y. Wu, L. Cheng, S. Huang et al., "A practical method for production data analysis from multistage fractured horizontal wells in shale gas reservoirs," *Fuel*, vol. 186, pp. 821–829, 2016.
- [35] J. Wang, L. Yu, and Q. Yuan, "Experimental study on permeability in tight porous media considering gas adsorption and slippage effect," *Fuel*, vol. 253, pp. 561–570, 2019.
- [36] Q. Yuan, X. Zhou, J. Wang, F. Zeng, K. D. Knorr, and M. Imran, "Control of viscous fingering and mixing in miscible displacements with time-dependent rates," *AIChE Journal*, vol. 65, no. 1, pp. 360–371, 2019.
- [37] T. Zhang, F. Javadpour, Y. Yin, and X. Li, "Upscaling water flow in composite nanoporous shale matrix using lattice Boltzmann method," *Water Resources Research*, vol. 56, article e2019WR026007, 2020.
- [38] Z. Sun, X. Li, W. Liu, T. Zhang, M. He, and H. Nasrabadi, "Molecular dynamics of methane flow behavior through realistic organic nanopores under geologic shale condition: pore size and kerogen types," *Chemical Engineering Journal*, vol. 398, article 124341, 2020.
- [39] H. Xiong, D. Devegowda, and L. Huang, "EOR solvent-oil interaction in clay-hosted pores: insights from molecular dynamics simulations," *Fuel*, vol. 249, pp. 233–251, 2019.
- [40] H. Xiong, D. Devegowda, and L. Huang, "Water bridges in clay nanopores: mechanisms of formation and impact on hydrocarbon transport," *Langmuir*, vol. 36, no. 3, pp. 723–733, 2020.
- [41] H. Wu, D. Ma, and A. J. S. Spearing, "Fracture phenomena and mechanisms of brittle rock with different numbers of openings under uniaxial loading," *Geomechanics and Engineering*, vol. 25, no. 6, pp. 481–493, 2021.
- [42] P. Yu, D. Dempsey, and R. Archer, "A three-dimensional coupled thermo-hydro-mechanical numerical model with partially bridging multi-stage contact fractures in horizontal-well enhanced geothermal system," *International Journal of Rock Mechanics and Mining Sciences*, vol. 143, article 104787, 2021.
- [43] Y. Wu, L. Cheng, S. Huang, S. Fang, P. Jia, and X. Rao, "An analytical model for analyzing the impact of fracturing fluid-induced formation damage on rate transient behavior in tight formations," *Journal of Petroleum Science and Engineering*, vol. 179, pp. 513–525, 2019.
- [44] H. Stehfest, "Algorithm 368: numerical inversion of Laplace transforms [D5]," *Communications of the ACM*, vol. 13, no. 1, pp. 47–49, 1970.
- [45] R. A. Wattenbarger, A. H. El-Banbi, M. E. Villegas, and J. B. Maggard, "Production analysis of linear flow into fractured tight gas wells," in *Presented at the SPE Rocky Mountain regional/low-permeability reservoirs symposium*, Denver, Colorado, USA, 1998.
- [46] A. L. Lee, M. H. Gonzalez, and B. E. Eakin, "The viscosity of natural gases," *Journal of Petroleum Technology*, vol. 18, no. 8, pp. 997–1000, 1966.

## Research Article

# Synthesis of a Novel Filtrate Reducer and Its Application in Water-Based Drilling Fluid for Ultra-High-Temperature Reservoirs

Dongyu Qiao,<sup>1,2</sup> Zhongbin Ye <sup>1,3</sup> Lei Tang,<sup>1</sup> Yiping Zheng,<sup>2</sup> Xindong Wang,<sup>2</sup> and Nanjun Lai <sup>1,3</sup>

<sup>1</sup>School of Chemistry and Chemical Engineering of Southwest Petroleum University, Chengdu, 610500 Sichuan, China

<sup>2</sup>Engineer Technology Research Institute, CNPC Xibu Drilling Engineering Company Limited, Urumqi 830001, China

<sup>3</sup>Oil & Gas Field Applied Chemistry Key Laboratory of Sichuan Province, Chengdu, 610500 Sichuan, China

Correspondence should be addressed to Zhongbin Ye; [yez@swpu.edu.cn](mailto:yez@swpu.edu.cn) and Nanjun Lai; [lainanjun@126.com](mailto:lainanjun@126.com)

Received 11 September 2021; Accepted 1 October 2021; Published 29 October 2021

Academic Editor: Jinjie Wang

Copyright © 2021 Dongyu Qiao et al. This is an open access article distributed under the Creative Commons Attribution License, which permits unrestricted use, distribution, and reproduction in any medium, provided the original work is properly cited.

The high-temperature stability and filtration property controlling of ultra-high-temperature water-based drilling fluids is a worldwide problem. To resolve this problem, a high-temperature-resistant quaternary copolymer (HTRTP) was synthesized based on molecular structure optimization design and monomer optimization. The physical and chemical properties were characterized by infrared spectroscopy, thermal weight, and spectrophotometry, and their temperature and salt resistance was evaluated in different drilling fluids, combined with adsorption, particle size analysis, and stability test. The results show that the thermal stability of HTRTP is very strong, and the initial temperature of thermal decomposition is above 320°C. The salt resistance of HTRTP is more than 162 g/L, and the calcium resistance is more than 5000 mg/L, which is equivalent to the foreign temperature-resistant polymer DCL-a, and is superior to the domestic metal ion viscosity increasing fluid loss agent PMHA-II for drilling fluids. It has excellent high-temperature resistance (245°C) and fluid loss reduction effect in fresh water base mud, fresh water weighted base mud, saturated brine base mud, and composite salt water base mud, which is better than foreign DCL-a (245°C) and domestic PMHA (220°C). The adsorption capacity of HTRTP on clay particles is large and firm, and the adsorption capacity changes little under the change of chemical environment and temperature. Both before and after HTRTP aging (245°C/16 h), the permeability of filter cake can be significantly reduced and its compressibility can be improved. By optimizing the particle size gradation of the drilling fluid and enhancing the colloid stability of the system, HTRTP can improve the filtration building capacity of the drilling fluid and reduce the filtration volume. The development of antithermal polymer provides a key treatment agent for the study of anti-high-temperature-resistant saline-based drilling fluid.

## 1. Introduction

The fluid loss additive, also known as the fluid loss control preparation and water loss additive, is an important drilling fluid treatment agent to ensure the stability of drilling fluid performance, reduce the loss of harmful fluids to the formation, stabilize the well wall, and ensure the well diameter rule [1, 2]. At present, the following categories of fluid loss agents are used at home and abroad: (1) modified lignite [3]; (2) modified starch [4]; (3) modified cellulose [5]; (4) modified resin [6]; and (5) olefin monomer polymers [7]. With the

development of the depth of petroleum exploration and development, the drilling depth keeps deepening and the bottom hole temperature is getting higher and higher, which puts forward higher requirements for the control of drilling fluid filtration and rheological properties [8, 9]. Commonly used natural and natural modified fluid loss reducers could not meet the needs of deep and ultradeep well drilling. Polymer fluid loss additive not only reduces fluid loss but also regulates rheological properties [10, 11]. It is an indispensable key treatment agent for high-temperature and ultra-high-temperature water-based drilling fluids [12, 13]. Since

the 1970s, the new synthetic polymer drilling fluid treatment agent which is resistant to high temperature and electrolyte pollution has been studied at home and abroad and has been applied in deep and ultradeep well drilling [14, 15]. With excellent performance of resistance to high temperature and salt resistance, the treatment agent has the following several kinds: Oseh et al. [16] on synthesizing a polypropylene-silica nanocomposite (PP-SiO<sub>2</sub> NC) using hot-emulsion sol-gel method as a viscosity modifier and filtration control agent for WBMs. PP-SiO<sub>2</sub> NC is spherical, with a particle size distribution between 80 and 390 nm, finely dispersed; a stronger resistance from 430°C to 485°C; and better filtration control and rheological properties, and plastic viscosity is reduced by 22.7%. Chang et al. [17] have developed a new environmentally friendly fluid loss agent nano-LS (nano-LS) with good thermal stability, salt tolerance, and calcium resistance. The water-based drilling fluid prepared with it maintains its stability at 200°C and can control the water loss at 7.5 mL. The high-temperature- and salt-resistant polymer DCL-a, developed by Philips and Chevron, can effectively reduce the high-temperature and high-pressure filtration of drilling fluid. The temperature resistance is more than 230°C, and it has strong salt and calcium resistance. At present, the thermal resistance of polymer filtrate reduction agents at home and abroad still cannot meet the requirements of ultra-high-temperature filtration control in deep and ultradeep well drilling [18, 19]. Therefore, this paper carried out the synthesis and characterization of high-temperature- and salt-resistant quaternary polymer, evaluation of filtration loss performance and stability in drilling fluid, and analysis of its action mechanism [20, 21].

## 2. Experimental

**2.1. Material.** Anhydrous sodium carbonate, 2-methyl-2-acrylamide propanesulfonic acid (AMPS), N-vinylpyrrolidone (NVP), N, N-diethylacrylamide (DEAM), and dimethyldiallylammonium chloride (DMDAAC) are all industrial products for the industrial pilot amplification production [22, 23]. The initiator and sodium hydroxide were analytical pure. Drilling fluid with metal ions increased sticky fluid loss agent PMHA from the Xinjiang oil field (high-temperature-resistant polymer DCL-a, foreign ConocoPhillips company).

IRAffinity-1 Fourier Transform Infrared Spectrometer (Shimadzu Corporation, Japan), HTG-1 thermogravimetric analyzer (Beijing Hengjiu Scientific Instrument Factory), Model 722 UV-Vis Spectrophotometer (Shanghai Precision Instrument Co., Ltd.), ZNS2 medium pressure filter loss instrument (Qingdao Haitongda Special Instrument Co., Ltd.), and ZNN-D6 model six-speed rotary viscometer (Qingdao Haitongda Special Instrument Co., Ltd.) were the materials used.

### 2.2. Synthesis of Quaternary Copolymer

#### 2.2.1. Synthesis Principle

(1) *Competitive Rate of Polymer.* The reactivity rate is the ratio of the rate constants of homopolymer (self) growth

and copolymer (cross) growth. The reactivity ratios of the designed high-temperature-resistant quaternary copolymers can be estimated using the  $-e$  equation proposed by Alfrey and Price. The calculated values of the reactivity ratios of the four monomers (Table 1) show that the product of the reactivity ratios between the monomers is less than 1, indicating that the nonideal copolymerization occurs in this synthesis [24].

(2) *Structural Formula.* According to the principle of polymerization reaction, the possible structural formula of HTRTP is shown in Figure 1.

**2.2.2. Synthesis.** The reaction monomers (AMPS : DEAM : DMDAAC : NVP = 6 : 3 : 3 : 1) were added in the four-point flask, and then, the reaction monomers were added in turn. The pH value of the system was adjusted to 7.0 with 30% NaOH solution, and the temperature was raised to 60°C. The initiator of 0.1% of the total monomer was added, and the viscous liquid product was obtained by stirring for 4 h. The product was dried and crushed at 105°C to obtain HTRTP in powder form.

### 2.3. Characterization

**2.3.1. Composition and Molecular Weight.** Acetone was used as precipitant, and HTRTP was purified and dried by solution precipitation. The structure of HTRTP was analyzed by Fourier transform infrared spectroscopy (FT-IR) with KBr.

The “one-point method” was used to determine the intrinsic viscosity of the polymer (fluid loss additive), and the viscosity average molecular weight of the polymer was estimated by the Mark-Houwink empirical formula [25]. The calculation is as follows:

$$M = \sqrt[\alpha]{\frac{\sqrt{2[(\tau/\tau_0) - 1] - \ln(\tau/\tau_0)}}{kc}}, \quad (1)$$

where  $C$  is solute concentration, g/mL;  $M$  is the molecular weight of the solute; and  $K$  and  $\alpha$  are constants related to the determination conditions and polymer structure, and the value of  $K$  is  $3.684 \times 10^{-2}$ , and the value of  $\alpha$  is 0.646.

**2.3.2. Resistance to Temperature.** In N<sub>2</sub> atmosphere, the purified HTRTP was subjected to thermogravimetric analysis on a thermogravimetric analyzer at a temperature of 29°C-800°C and a heating rate of 5°C/min [26].

With 0.2 mol/L NaCl solution as solvent, 0.2% HTRTP and DCL-a solutions were prepared, and their intrinsic viscosities after aging at different temperatures for 8 hours were measured by an ohmmeter.

**2.3.3. Ability to Antisalt.** The salting-out resistance of high-temperature-resistant quaternary copolymer was tested and evaluated by UV-visible photometry [27]. In making polymer aqueous solution (PMHA, DCL-a, and HTRTP), the concentration is 0.5%. Add different amounts of distilled water and 180 g/L sodium chloride solution to a test tube



TABLE 1: Estimation results of monomer's reactivity ratio.

Monomer	Q value	e value	Competitive rate of poly	Competitive rate product
NVP	0.15	-1.2	$r_{12} = 0.05; r_{13} = 0.008; r_{14} = 0.002$	$r_{12}r_{21} = 0.059$
AMPS	0.38	0.46	$r_{21} = 1.180; r_{23} = 0.487; r_{24} = 0.096$	$r_{13}r_{31} = 0.002$
DEAM	1.16	1.32	$r_{31} = 0.278; r_{32} = 0.981; r_{34} = 0.174$	$r_{14}r_{41} = 0.005$
DMDACC	5.46	1.17	$r_{41} = 2.274; r_{42} = 6.261; r_{43} = 5.61$	$r_{23}r_{32} = 0.478$
				$r_{24}r_{42} = 0.601$
				$r_{34}r_{43} = 0.976$

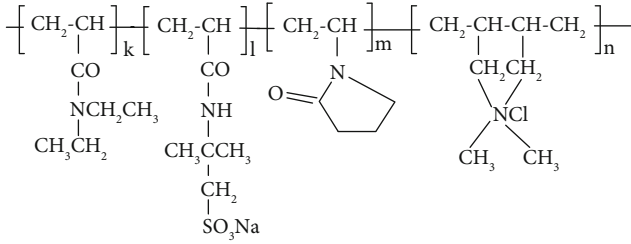


FIGURE 1

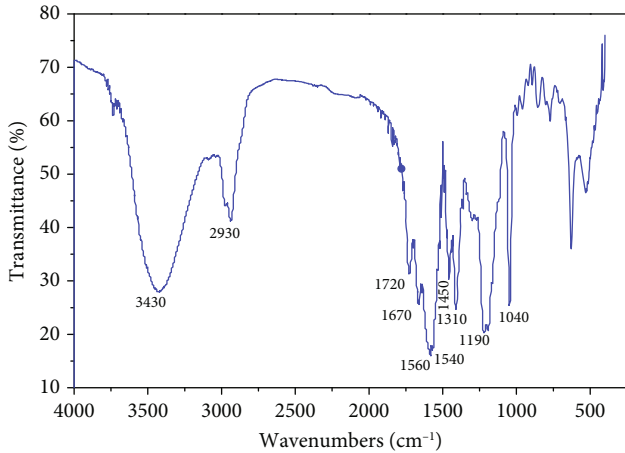


FIGURE 2: Infrared spectrogram of HTRTP.

containing 1.0 mL sample solution, and shake well. Distilled water was used as blank experiment, and the transmissivity of each solution was measured with a 722 spectrophotometer. After salting out, the solution becomes turbid, which causes the change of transmission ratio of the solution. Therefore, when the salt in the solution reaches or exceeds the turbidity point, the transmission ratio of the solution is significantly reduced, and the turbidity point salinity of the copolymer is determined.

#### 2.4. Evaluation of Filtration Loss Reduction Effect

**2.4.1. Evaluation of Fluid Loss Reduction Effect in Fresh Water Base Slurry.** The experimental base slurry is composed of 400 mL tap water + 0.8 g anhydrous sodium carbonate + 4% secondary bentonite + 3% evaluation soil, respectively, to the early hydration good base paste to add 1% of the sample evaluation (PMHA, DCL-a, and HTRTP), stirring evenly, measuring the rheological property and filtration [28]. The experimental slurry was then

put into a high-temperature aging tank and rolled at 220°C and 245°C for 16 h, respectively. The rheological properties and filtration loss of the slurry were measured by the same method.

**2.4.2. Effect of Fluid Loss Reduction in Fresh Water Weighted Base Slurry.** The experimental base slurry is composed of 400 mL tap water + 1.2 g anhydrous sodium carbonate + 6% secondary bentonite + 5% evaluation soil + 30% barite, respectively, to the early hydration good base paste to add 1% of the sample evaluation (PMHA, DCL-a, HTRTP), stirring evenly, into the high-temperature aging tank, respectively, under 220°C and 245°C hot rolled out after 16 h, measuring the rheological property and filtration.

**2.4.3. Effect of Fluid Loss Reduction in Saturated Salt-Water-Based Slurry.** The experimental base slurry is composed of 400 mL tap water + 1.2 g anhydrous sodium carbonate + 6% secondary bentonite + 10% evaluation soil + 30% sodium chloride, respectively, to the early hydration good base paste to add 1.5% of the sample evaluation (PMHA, DCL-a, HTRTP), stirring evenly, into the high-temperature aging tank, respectively, under 220°C and 245°C hot rolled out after 16 h, measuring the rheological property and filtration.

#### 2.5. Research on Mechanism of Action

**2.5.1. Adsorption Characteristics on Clay Particle Surface.** A known amount of polymer solution was added to 4 wt % calcium montmorillonite (purified with 15 wt % H<sub>2</sub>O<sub>2</sub>) suspension and then diluted with 50 mL distilled water. The initial concentration of polymer was recorded as  $c_0$ . The suspension was agitated vigorously and then left to stand for 20 min to allow the adsorption process of the quadripolymer to complete at given temperature. The suspension was subsequently centrifuged for 30 min at a speed of 1000 rpm using a KUBOTA 3500 centrifuge. The concentration of unadsorbed quadripolymer,  $c_1$ , located in the clear centrifuged supernatant was measured via absorbance at wavelengths of 390 nm and 330 nm for polymer solution using an ultraviolet spectrophotometer (722, Shanghai Yuanxi Instruments Co., Ltd., China). Applying material balance of the polymer, the adsorption of polymer on clay particles can be calculated via

$$\tau = \frac{v(c_0 - c_1)}{G}, \quad (2)$$



TABLE 2: Testing results of intrinsic viscosity and molecular weights.

Sample	Concentration (g/100 mL)	0.1	0.2	0.3	Average intrinsic viscosity (mL/g)	Molecular weight
HTRTP	Average outflow time (s)	76.13	98.68	123.24	284.06	1040322
	Intrinsic viscosity (mL/g)	279.06	288.29	284.87		
DCL-a	Average outflow time/s	79.92	107.69	141.06	339.78	1372721
	Intrinsic viscosity (mL/g)	332.72	341.59	345.04		

where  $\tau$  is the mass of polymers absorbed onto specific weight calcium montmorillonite, mg/g;  $v$  is volume of solution, L;  $c_0$  and  $c_1$  are polymer concentration before and after polymer absorbed onto calcium montmorillonite, mg/L; and  $G$  is the mass of calcium montmorillonite, g.

**2.5.2. Influence on Filter Cake Quality.** The effect of its addition in fresh water base slurry on the permeability of filter cake was investigated. After measuring the API filtration loss, carefully remove the substrate slurry on the surface of the filter cake [29], replace it with distilled water, measure the volume of water for 30 min, measure the thickness of the filter cake with a steel plate ruler, and calculate the permeability  $K$  of the filter cake according to the following formula:

$$K = 0.175vh \times 10^{-6}, \quad (3)$$

where  $K$  is the permeability of mud cake,  $\mu\text{m}^2$ ;  $v$  is the effluent volume, mL;  $h$  is the thickness of mud cake, mm; and 0.175 is the conversion factor (0.07 for high temperature and high pressure).

The effect of several treatment agents on the compressibility of base mud was investigated by using the "two-stage water loss method" which is simple, feasible, and reliable. If other factors are set to be constant, the compressibility of filter cake can be expressed by a simple proportional relationship of filtration rate at 500 psi and 100 psi:

$$R = \frac{V_{500}}{V_{100}}, \quad (4)$$

in which  $R$  is the compressibility coefficient of the filter cake and  $V_{500}$  and  $V_{100}$  are static filtration loss under pressure difference of 500 psi and 100 psi, respectively.

**2.5.3. Particle Size and Specific Area Measurements of Calcium Clay.** The suspensions were prepared by mixing deionized water, 4% ( $w/v$ ) calcium montmorillonite, and 0.3% ( $w/v$ ) viscosity breaker (XY-28, sulfonated tannin and quadripolymer separately), stirring for 20 minutes at a high speed of 10,000 rpm and aging for 24 hours at room temperature. Aging experiments of suspensions were carried out in a XGRL-4A-type rolling oven through hot rolling at 220°C (XY-28) or 245°C (sulfonated tannin and quadripolymer) for 16 hours. Concentrated NaOH (10 mol/L) and HCl (6 mol/L) solutions were used to change pH so as not to cause excessive dilution of samples. The size distribution and specific area of clay particles in suspension were determined using a Bettersize2000 laser particle analyzer.

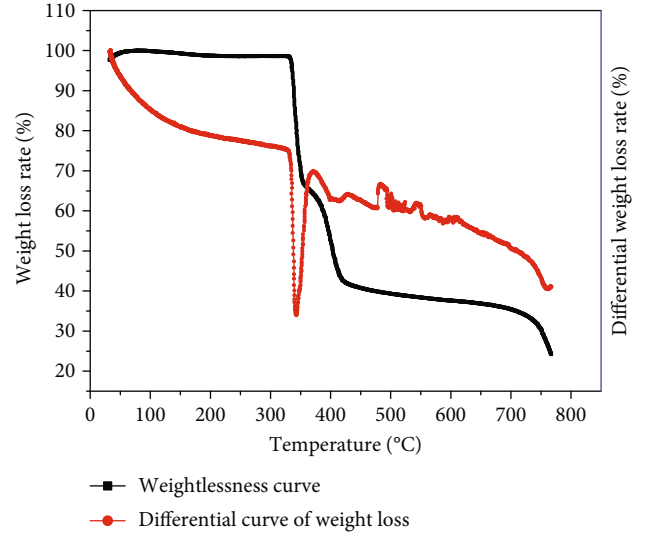


FIGURE 3: Curves of TG and DTA of HTRTP in nitrogen gas ambience.

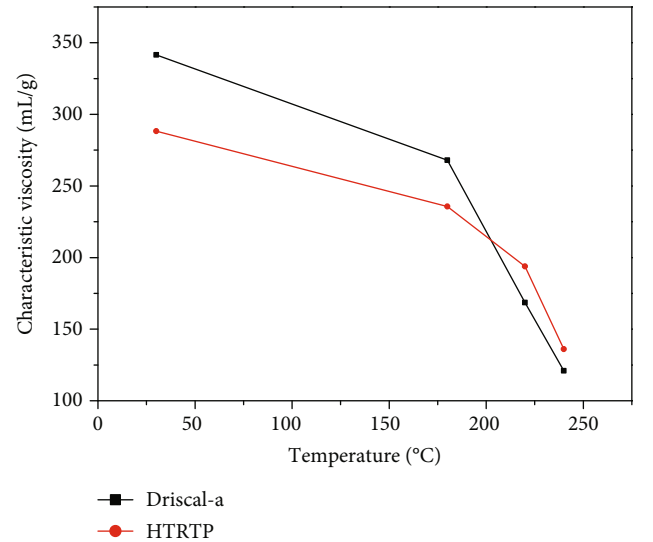


FIGURE 4: Viscosity-temperature curves of HTRTP and DCL-a.

**2.5.4. Influence on Stability of Fresh Water Base Slurry Colloid.** Turbiscan, an infrared scanning dynamic stability tester, can quantitatively evaluate the stability of dispersion systems such as colloid, foam, and suspension. The effects of 0.1%, 0.2%, and 0.3% HTRTP on the colloidal stability of 3% bentonite slurry before and after aging (245°C/16h) were investigated.

TABLE 3: Experimental results of antisolting out of PMHA.

Concentration of Cl <sup>-</sup> (g/L)	0	90	108	126	144	162
Solution transmission ratio of PMHA	98.8	98.6	98.3	97.9	95.1	94.3
Solution transmission ratio of DCL-a	99.0	98.9	98.7	98.5	98.3	98.0
Solution transmission ratio of HTRTP	98.3	98.2	98.1	98.0	97.7	97.4

TABLE 4: Experimental results of antisolting out of PMHA.

Concentration of CaCl <sub>2</sub> (mg/L)	0	500	1500	2500	4000	5000
Solution transmission ratio of PMHA	98.8	98.4	98.0	96.2	95.4	94.5
Solution transmission ratio of DCL-a	99.0	99.0	98.8	98.6	98.4	98.1
Solution transmission ratio of HTRTP	98.3	98.2	98.1	98.0	97.8	97.5

TABLE 5: Comparison of fluid loss controlling of fluid loss agents in fresh water slurry.

Experimental slurry	Test conditions	AV (mPa-s)	PV (mPa-s)	YP (Pa)	API (mL)
3-1 basic slurry	Room temperature	8.5	3	5.5	24.0
	Room temperature after 220°C/16 h	7	3	4	34.0
	Room temperature after 245°C/16 h	8.5	8	0.5	41.0
Basic slurry + 1%PMHA	Room temperature	60	30	30	8.4
	Room temperature after 220°C/16 h	4	1	3	12.4
Basic slurry + 1%DCL - a	Room temperature	53	21	32	10.6
	Room temperature after 245°C/16 h	11	10	1	20.6
Basic slurry + 1%HTRTP	Room temperature	40	28	12	7.8
	Room temperature after 245°C/16 h	17	14	3	11.0

TABLE 6: Comparison of fluid loss controlling of fluid loss agents in weighted fresh water slurry.

Experimental slurry	Test conditions	AV (mPa-s)	PV (mPa-s)	YP (Pa)	API (mL)
3-2 basic slurry	Room temperature after 220°C/16 h	35	16	19	16.0
	Room temperature after 245°C/16 h	38	26	12	21.0
1% PMHA	Room temperature after 220°C/16 h	33.5	27	6.5	8.4
1% DCL-a	Room temperature after 245°C/16 h	45	35	10	6.6
1% HTRTP	Room temperature after 245°C/16 h	41	32	9	6.0

TABLE 7: Comparison of fluid loss controlling of fluid loss agents in saturated brine slurry.

Experimental slurry	Test conditions	AV (mPa-s)	PV (mPa-s)	YP (Pa)	API (mL)
Basic slurry	Room temperature after 220°C/16 h	18	8	10	124
	Room temperature after 245°C/16 h	17.5	6	11.5	143
1.5% PMHA	Room temperature after 220°C/16 h	16.5	9	7.5	49
1.5% DCL-a	Room temperature after 245°C/16 h	40	19	21	24
1.5% HTRTP	Room temperature after 245°C/16 h	45	24	21	18

### 3. Results and Discussion

#### 3.1. Characterization

**3.1.1. Composition and Molecular Weight.** It can be seen from Figure 2 that the stretching vibration absorption peak at 3450 cm<sup>-1</sup> is N-H; 3060 cm<sup>-1</sup> is the absorption peak of stretching vibration of C-H bond of -CH<sub>2</sub>- in the ring. 2960 cm<sup>-1</sup> is the characteristic absorption peak of C-H bond of -CH<sub>3</sub>. 2920 cm<sup>-1</sup> is the absorption peak of stretching

vibration of C-H bond of -CH<sub>2</sub> in chain. At 1730 cm<sup>-1</sup>, there is a stretching vibration absorption peak with C=O. The characteristic absorption peaks of -C(O)NH- are at 1660 cm<sup>-1</sup> and 1540 cm<sup>-1</sup>. At 1520 cm<sup>-1</sup>, there is the vibration absorption peak of N-H bond deformation. The absorption peak of bending vibration of C-H bond of -CH<sub>2</sub> is at 1460 cm<sup>-1</sup>. At 1300 cm<sup>-1</sup>, =C=N- stretching vibration absorption peaks. The characteristic absorption peaks of SO<sub>3</sub><sup>-</sup> are at 1190 cm<sup>-1</sup> and 1040 cm<sup>-1</sup>. The results show that

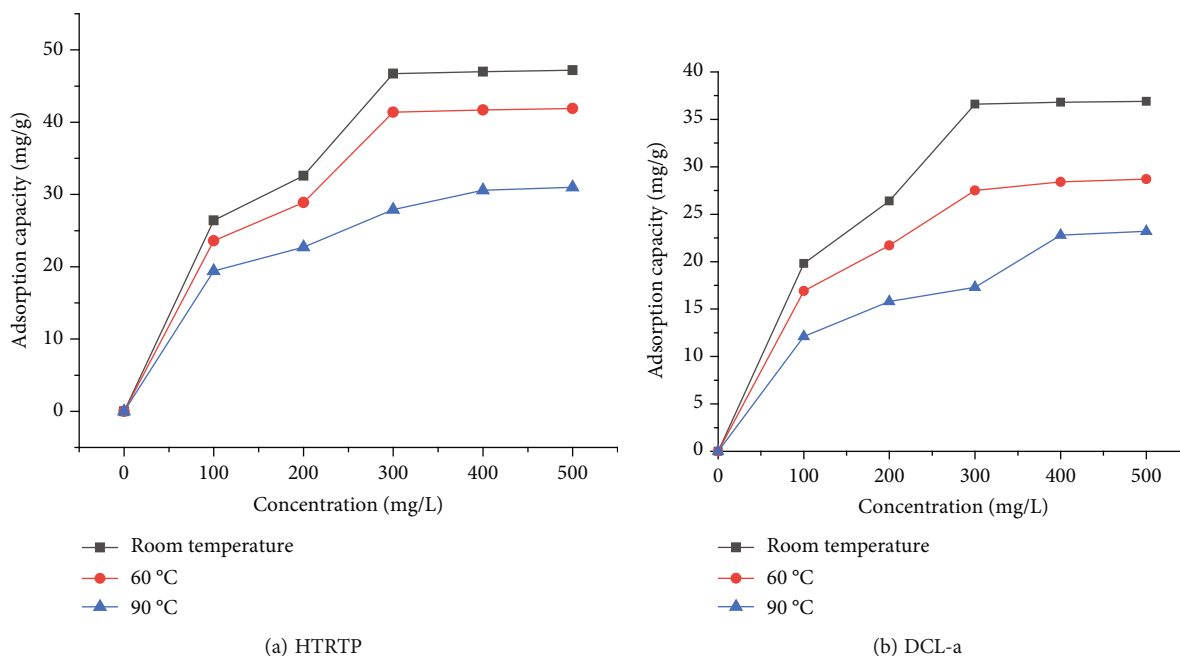


FIGURE 5: Effect of temperature on adsorption quantity of DCL-a and HTRTP.

the molecular chain of the product has the predicted group of molecular structure design, which verifies the correctness of the molecular structure design and the correctness of the HTRTP synthesis reaction scheme.

It can be seen from the test results in Table 2 that the molecular weight of HTRTP is about 1.04 million, which is smaller than that of high-temperature-resistant polymer DCL-a, and its influence on drilling fluid viscosity will be smaller than that of DCL-a.

**3.1.2. Temperature Resistance.** It can be seen from the thermal difference curve in Figure 3 that the thermal decomposition process of HTRTP can be divided into many stages, of which there are two main pyrolysis stages. The first stage occurs between 320 and 360°C with a weight loss rate of 20%-25%, which is mainly the decomposition of carboxylic acid group 9 and sulfonic acid group on the side chain. The second stage, which occurs above 400°C, is mainly the decomposition of the backbone chain of polymerization. The total weight loss rate of these two stages is 52.41%. It can be seen that the high-temperature-resistant quaternary copolymer HTRTP has strong thermal stability.

As shown in Figure 4, with the increase of aging temperature, the intrinsic viscosity of HTRTP decreased more slowly than that of DCL-a, indicating that HTRTP had better temperature resistance than DCL-a in aqueous solution.

**3.1.3. Resistance to Salting Out.** It can be seen from Table 3 that when the  $\text{Cl}^-$  concentration of PMHA increases from 126 g/L to 144 g/L, the transmittance of PMHA solution changes suddenly, indicating that the solution begins to become cloudy; that is, the antisolting out ability of PMHA (calculated by  $\text{Cl}^-$ ) is between 126 g/L and 144 g/L. At the  $\text{Cl}^-$  concentration of 162 g/L, the transmittance of DCL-a

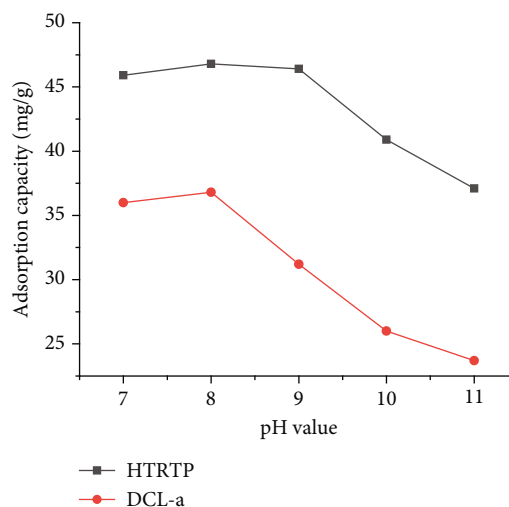


FIGURE 6: Effect of pH value on adsorption quantity of DCL-a and HTRTP.

solution and HTRTP solution still has no obvious change, indicating that the solutions have not become turbid; that is, the salting-out resistance of DCL-a and HTRTP (calculated by  $\text{Cl}^-$ ) is greater than 162 g/L.

It can be seen from Table 4 that when the concentration of  $\text{CaCl}_2$  increases from 1500 mg/L to 2500 mg/L, the transmittance of PMHA solution changes suddenly, indicating that the solution begins to become cloudy; that is, the calcium resistance of PMHA (calculated by  $\text{CaCl}_2$ ) is between 1500 mg/L and 2500 mg/L; with the increase of  $\text{CaCl}_2$  concentration, the transmittance of DCL-a solution and HTRTP solution has no significant change. When  $\text{CaCl}_2$  concentration reached 5000 mg/L, the transmittance did not change

obviously, which indicated that the solutions did not become turbid; that is, the calcium resistance of DCL-a and HTRTP (calculated by  $\text{CaCl}_2$ ) was greater than 5000 mg/L.

### 3.2. Evaluation of Fluid Loss Reduction Effect

**3.2.1. Evaluation of Fluid Loss Reduction in Fresh Water Base Slurry.** As shown in Table 5, the API filtration loss of HTRTP was the lowest before and after aging, and the viscosity changed the least before and after aging. The filtration loss of fresh water base slurry treated with 1% HTRTP decreased from 41 mL to 11 mL after aging at 245°C/16 h at high temperature. 1% PMHA was processed in fresh water slurry in 220°C/16 h after high-temperature aging filtration quantity from 34 mL of 12.4 mL, but after aging experiment, paste viscosity decreased; treatment may have serious degradation. When the fresh water base slurry treated with 1% DCL-a was aged at 245°C/16 h, the filtrate loss reduction effect was not as good as that of HTRTP. The results indicated that HTRTP not only had a good filtration loss reduction effect but also had a better temperature resistance in fresh water base slurry.

**3.2.2. Effect of Fluid Loss Reduction in Fresh Water Weighted Base Slurry.** As can be seen from Table 6, API filtration loss of experimental slurry after aging is low, among which the experimental slurry treated by 1% HTRTP has the lowest filtration loss, which is 6.0 mL. It was shown that in fresh water increased base slurry, HTRTP fluid loss effect is better than PMHA and DCL-a.

**3.2.3. Effect of Fluid Loss Reduction in Saturated Salt-Water-Based Slurry.** It can be seen from Table 7 that, compared with the base slurry, the API filtration loss of the aging experimental slurry treated with filtration reduction agent was significantly reduced, among which the experimental slurry treated with 1.5% HTRTP had the lowest filtration loss, which was 18.0 mL. It is shown that the filtration reduction effect of HTRTP is better than that of PMHA and DCL-a in saturated salt-water-based slurry.

### 3.3. Study on Mechanism of Action

#### 3.3.1. Adsorption Properties on the Surface of Clay Particles

(1) *Influence of Temperature.* As can be seen from Figure 5, at the same temperature, with the increase of HTRTP and DCL-a concentration, their adsorption capacity on clay particles increased. With the increase of temperature, the adsorption amount decreased. It can also be seen from the figure that both HTRTP and DCL-a have different adsorption isotherms at different temperatures. The reason is that adsorption is an exothermic reaction, and increasing temperature is conducive to equilibrium in the direction of desorption. In addition, when the temperature rises, the thermal movement of clay particles intensifies, which is not conducive to adsorption.

(2) *Influence of pH.* As can be seen from Figure 6, when pH is 8, the adsorption capacity of the two polymers on the surface of clay particles reaches the maximum. When pH

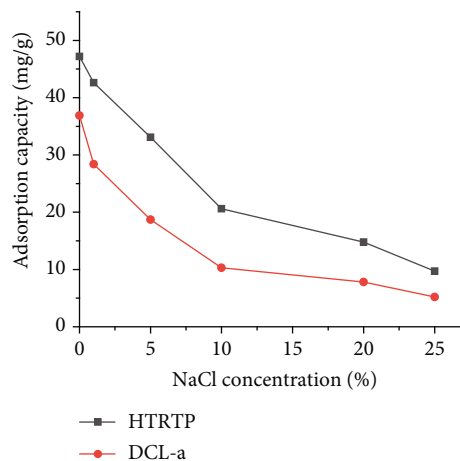


FIGURE 7: Effect of NaCl content on adsorption quantity of DCL-a and HTRTP.

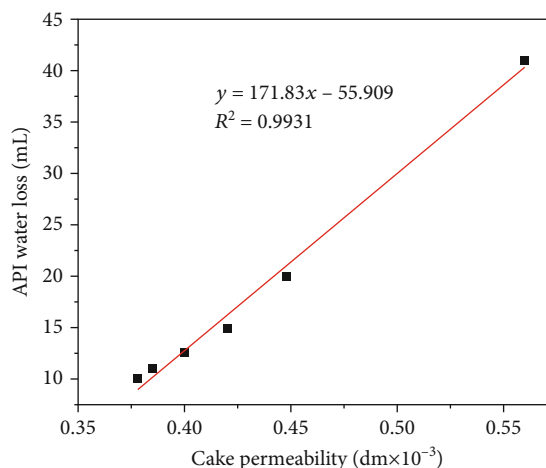


FIGURE 8: Relation between filter cake permeability and API filtration under different HTRTP contents.

is higher or lower than this value, the adsorption capacity decreases. Within the test range, the higher the pH value, the lower the adsorption capacity. The reason is that when the pH is 8, the clay particles are fully dispersed and the negative charge on the surface of the particles is moderate. When pH becomes lower, it is not conducive to the full dispersion of clay particles, which can be used for adsorption of small surface area; when the pH value is higher than this value, more  $\text{OH}^-$  is adsorbed on the surface of clay particles, which further enhances the electronegativity of the surface. The electrostatic action is not conducive to the adsorption of polymer molecules. As can be seen from the figure, not only is the adsorption capacity of HTRTP greater than that of DCL-a, but with the increase of pH, the adsorption capacity of HTRTP on the surface of clay particles decreases more slowly than that of DCL-a. This is because certain cationic groups are introduced into HTRTP molecules, which can weaken the influence of the increase of electronegativity on the surface of clay particles on adsorption.

TABLE 8: Test results of filter cake compressibility.

Formula	Test conditions	$V_{100}$ (mL)	$V_{500}$ (mL)	R
	Room temperature	22	43	1.95
Basic slurry: 4%bentonite + 3%evaluation of soil	Room temperature after 220°C/16 h	34	72	2.12
	Room temperature after 245°C/16 h	42	90	2.14
Basic slurry + 1%PMHA	Room temperature	8.6	16	1.86
	Room temperature after 220°C/16 h	12	23.4	1.95
Basic slurry + 1%DCL – a	Room temperature	12	21	1.75
	Room temperature after 245°C/16 h	20	36	1.80
Basic slurry + 1%HTRTP	Room temperature	8	12.8	1.60
	Room temperature after 245°C/16 h	11.6	19	1.64

(3) *Effect of Sodium Chloride Addition on Adsorption Capacity.* It can be seen from Figure 7 that with the increase of sodium chloride dosage, the adsorption amount of HTRTP and DCL-a on clay particles decreases. This is because, after adding sodium chloride, a large amount of  $\text{Na}^+$  accumulates near clay particles, compressing their diffusion electric double layer; the  $\zeta$  potential decreases; the repulsive force weakens; the agglomeration of clay particles increases; and the surface area decreases. In addition, the addition of sodium chloride affects the extension of polymer molecular chain, which is not conducive to adsorption. Therefore, in sodium chloride brine drilling fluids, the contribution of polymer plugging and improving filtrate viscosity to fluid loss reduction performance is increased.

3.3.2. *Influence on the Quality of Filter Cake.* It can be seen from Figure 8 that there is a good linear relationship between filter cake permeability and API filtration amount. With the increase of HTRTP addition, API filtration amount decreases before and after experimental slurry aging, and the permeability of filter cake also decreases.

It can be seen from Table 8 that the compressibility coefficient of the experimental slurry before aging is lower than that after aging, indicating that high temperature will cause the compressibility reduction of the drilling fluid filter cake. The compression coefficient of experimental slurry with filtrate loss additive before and after aging is lower than that of base slurry, which indicates that improving the compressibility of filter cake is also one of the action mechanisms of filtrate loss additive. The filter cake added with HTRTP slurry has the lowest compressibility coefficient, which is consistent with the best filtration loss reduction effect.

3.3.3. *Effect on Particle Size Distribution of Fresh Water Base Slurry.* As can be seen from Figure 9, after aging, the proportion of particles with smaller particle size in the experimental slurry decreases, while the content of particles with larger particle size increases; both particle size and distribution become larger, which is one of the reasons for the increase of filtration loss after aging. The mean particle size of different suspensions was 1.7  $\mu\text{m}$ , 21.5  $\mu\text{m}$ , 7.5  $\mu\text{m}$ , and 17.6  $\mu\text{m}$ , respectively (tagged in Figure 9). After adding HTRTP, both before and after aging, the particle size distribution of exper-

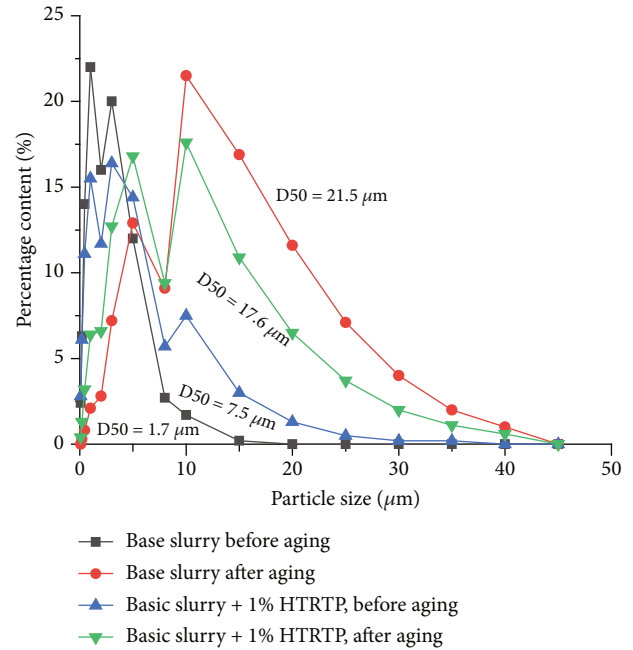


FIGURE 9: Test results of particle size distribution.

imental slurry is wider and the grading is more reasonable, so the filtration loss of experimental slurry is reduced.

3.3.4. *Effect on Stability of Fresh Water Base Slurry Colloids.* As can be seen from Figure 10, the colloidal stability of the experimental slurry was significantly better than that of the base slurry after the addition of HTRTP, and the colloidal stability of the experimental slurry increased with the increase of the amount of HTRTP. After aging at 245°C/16 h, high temperature promoted the hydration and dispersion of bentonite. In the experiment, it was measured that the thickness of the upper “clear liquid” of the aging base slurry was 0.30 mm after standing for 24 h, 0.1 mm when adding 0.1% HTRTP, 0.06 mm when adding 0.2% HTRTP, and 0.04 mm when adding 0.3% HTRTP. Combined with the previous particle size test results, it can be seen that for the base slurry with low bentonite content, the contribution of adhesive protection of HTRTP to filtration loss reduction is greater than that after aging. After aging, the mechanism



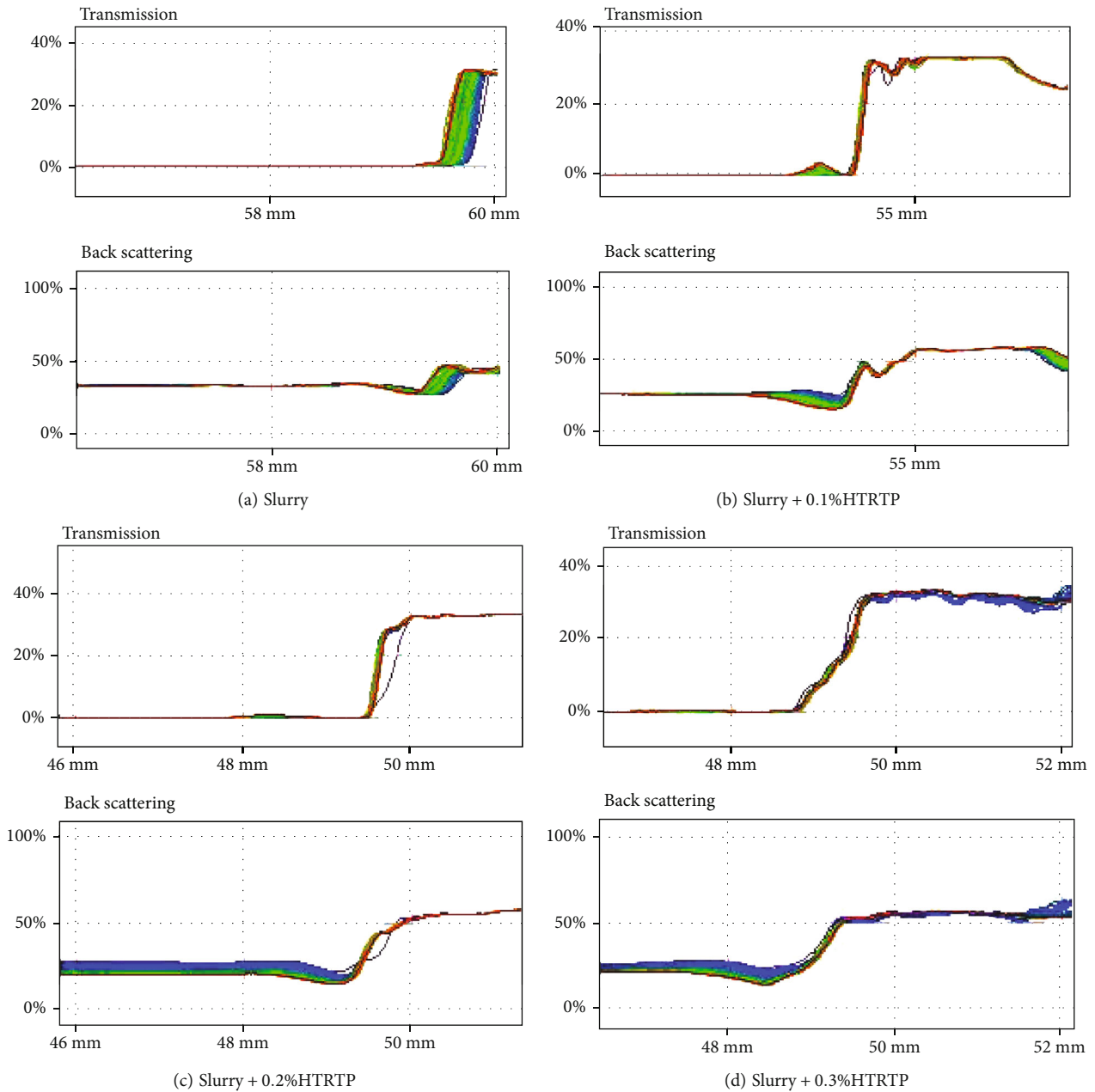


FIGURE 10: Effect of HTRTP on colloid stability of bentonite grouting (after aging).

of HTRTP reducing filter cake permeability by improving particle size grading in the system and enhancing the compressibility of filter cake is more important.

The action mechanism of high-temperature-resistant quaternary copolymer HTRTP is as follows:

- (1) Temperature resistance mechanism: the molecular structure difference is the main factor that determines the temperature resistance of the fluid loss agent. High-temperature-resistance quaternary copolymer HTRTP molecule main chain is C-C bond and has the internal structure of high temperature resistance; C-S and C-N bonds are used between the main chain and the side chain, and the

thermal stability of the main chain and the side chain is strong

- (2) Mechanism of salt resistance and calcium resistance: the hydrophilic group is the sulfonic acid group ( $-\text{CH}_2\text{SO}_3^-$ ), which has strong hydration ability and can thicken the hydration film on the surface of clay particles with strong salt resistance. The sulfonic acid group does not react with  $\text{Ca}^{2+}$  to form precipitation, which has a strong anticalcium ability. In addition, the side groups introduced into the HTRTP chain (e.g.,  $-\text{CONHC}(\text{CH}_3)_2\text{CH}_2\text{SO}_3^-$ ) are large and rigid, and the chain is not easy to curl in electrolyte solutions (salt solutions)

- (3) Adsorption mechanism: in addition to the phthalamine group ( $-\text{CON}(\text{CH}_2\text{CH}_3)_2$ ), the cationic adsorption group ( $-\text{CH}_2\text{N}^+(\text{CH}_3)_2\text{CH}_2-$ ) is also introduced into the HTRTP molecular chain.  $-\text{CON}(\text{CH}_2\text{CH}_3)_2$  is adsorbed by hydrogen bond, which has strong adsorption stability and is not easy to be desorbed under temperature change.  $-\text{CH}_2\text{N}^+(\text{CH}_3)_2\text{CH}_2-$  is chemisorbed through static ion bonds, and the adsorption is stronger
- (4) Mechanism of filtration loss reduction: firstly, HTRTP is adsorbed on the surface of clay particles to form an adsorption layer, which prevents flocculation of clay particles from becoming larger. At the same time, it stabilizes the fine particles separated by stirring so as not to become larger. So it can improve clay particle grading in drilling fluid. It has excellent protective adhesive effect, forming thin and compact filter cake, reducing filtration loss. Secondly, HTRTP increases the degree of hydration by adsorbing on clay particles, so that the hydration film on the surface of clay particles is thickened to enhance the compressibility of the filter cake and reduce the permeability of the filter cake, thus reducing the filtration loss. Thirdly, the molecular size of HTRTP is just within the range of colloidal particles, and the molecular chain wedges into the pores of the filter cake or curls into a ball to block the micropores of the filter cake, making the filter cake thin and compact, thus reducing the filtration loss. Finally, HTRTP is a high molecular weight polymer that is added to the drilling fluid to increase the viscosity of the filtrate and thus reduce filtration loss

#### 4. Conclusions

The high-temperature-resistant quaternary copolymer HTRTP was synthesized by molecular structure optimization and monomer optimization. The viscosity average molecular weight of HTRTP was about 1 million, which had less effect on the viscosity of drilling fluid than DCL-a. HTRTP molecular structure has good thermal stability, temperature resistance in drilling fluid up to 245°C, salt resistance and calcium resistance, and good compatibility with fresh water and salt water experimental base slurry. The performance of fluid loss reduction, temperature resistance and salt and calcium resistance in drilling fluid is better than that of foreign temperature resistance polymer DCL-a and domestic similar products. The adsorption capacity of HTRTP on clay particles is higher than that of foreign anti-temperature polymer DCL-a. In the case of chemical environment and temperature change, the adsorption amount changed little and was still higher than that of DCL-a, and the adsorption was firm. Before and after aging (245°C/16h), HTRTP can significantly reduce the permeability and improve the compressibility of filter cake. Improving the particle size grading in drilling fluid system and enhancing the colloidal stability of the system are the important mechanisms of high-temperature-resistant qua-

ternary copolymers. The quad-element polymer reducer was suitable for fresh water-based drilling fluid and low-mineralized saline drilling fluid.

#### Nomenclature

AMPS:	2-Acrylamido-2-methyl-1-propane sulfonic acid
API:	American Petroleum Institute
AV:	Apparent viscosity
DEAM:	N, N-Diethyl acrylamide
DMDAAC:	Dimethyl diallyl ammonium chloride
FT-IR:	Fourier transform infrared spectroscopy
NVP:	N-Vinyl pyrrolidone
PV:	Plastic viscosity
TGA:	Thermogravimetric analysis
YP:	Dynamic shear forces.

#### Data Availability

All data and research results are listed in the manuscript.

#### Conflicts of Interest

The authors declare that they have no conflicts of interest.

#### Acknowledgments

This work was financially supported by the Open Foundation of State Key Laboratory of Oil and Gas Geology and Exploitation, Chengdu University of Technology (PLC20180103), and Opening Project of Oil and Gas Field Applied Chemistry Key Laboratory of Sichuan Province (YQKF202010).

#### References

- [1] A. R. Ismail, W. R. Wan Sulaiman, M. Z. Jaafar, I. Ismail, and E. Sabu Hera, "Nanoparticles performance as fluid loss additives in water based drilling fluids," *Materials Science Forum*, vol. 864, no. 1, pp. 189–193, 2016.
- [2] A. Nasiri, M. J. AMERI Shahrabi, M. A. Sharif NIK, H. Heidari, and M. Valizadeh, "Influence of monoethanolamine on thermal stability of starch in water based drilling fluid system," *Petroleum Exploration and Development*, vol. 45, no. 1, pp. 167–171, 2018.
- [3] H. Zhong, G. Shen, Z. Qiu et al., "Minimizing the HTHP filtration loss of oil-based drilling fluid with swellable polymer microspheres," *Journal of Petroleum Science and Engineering*, vol. 172, pp. 411–424, 2019.
- [4] X. Ma, M. Yang, and M. Zhang, "Synthesis and properties of a betaine type copolymer filtrate reducer," *Chemical Engineering and Processing-Process Intensification*, vol. 153, article 107953, 2020.
- [5] F. Dugonjic-Bilic and J. Plank, "Polyelectrolyte complexes from polyethylene imine/acetone formaldehyde sulfite polycondensates: a novel reagent for effective fluid loss control of oil well cement slurries," *Journal of Applied Polymer Science*, vol. 121, no. 3, pp. 1262–1275, 2011.

- [6] X. Yang and Z. Wang, "Molecular design of polymer treatment agent used for drilling fluid," *Fine and Specialty Chemicals*, vol. 18, pp. 14–18, 2010.
- [7] Z. Y. Chang, D. L. Breeden, and M. J. McDonald, "The use of zinc dialkyl dithiophosphate as a lubricant enhancer for drilling fluids particularly silicate-based drilling fluids," in *SPE International Symposium on Oil Field Chemistry*, The Woodlands, Texas, USA, 2011.
- [8] X. Bai, Y. Yang, D. Xiao, X. Pu, and X. Wang, "Synthesis, characterization, and performance evaluation of the AM/AMPS/DMDAAC/SSS quadripolymer as a fluid loss additive for water-based drilling fluid," *Journal of Applied Polymer Science*, vol. 132, no. 14, article 41762, 2015.
- [9] J. Su, Q. Chu, and M. Ren, "Properties of high temperature resistance and salt tolerance drilling fluids incorporating acrylamide/2-acrylamido-2-methyl-1-propane sulfonic acid/N-vinylpyrrolidone/dimethyl diallyl ammonium chloride quadripolymer as fluid loss additives," *Journal of Polymer Engineering*, vol. 34, no. 2, pp. 153–159, 2014.
- [10] P. W. Livanec, G. P. Perez, and J. P. Deville, "Methods of preventing emulsification of crude oil in well bore treatment fluids," 2012, U.S. Patent No. 9,051,508.
- [11] J. B. Wen, H. J. Luo, and Z. Q. Long, "Emulsification behaviors of crude oil-water system and its quantitative relationship with exergy loss rate," *Journal of Petroleum Science & Engineering*, vol. 176, pp. 502–508, 2019.
- [12] X. I. N. Haipeng, Z. E. N. G. Jianguo, Z. O. U. Jianlong, Z. H. A. O. Baohui, and S. U. N. Fuquan, "Laboratory study on comb-like polycarboxylic acid friction reducer," *Drilling Fluid and Completion Fluid*, vol. 34, pp. 72–76, 2017.
- [13] G. Duan, G. Huang, A. Li, Y. Zhu, and Y. Gong, "A study of supermolecular polarization of comb-like polycarboxylate admixtures synthesized with polyoxyethylene macromolecules," *Journal of Molecular Liquids*, vol. 174, pp. 129–134, 2012.
- [14] Q. Jiang, G. Jiang, C. Wang et al., "A new high-temperature shear-tolerant supramolecular viscoelastic fracturing fluid," in *IADC/SPE Asia Pacific Drilling Technology Conference*, Singapore, 2016.
- [15] W. Li, J. Liu, X. Zhao et al., "Development and screening of additives for biodiesel based drilling fluids: principles, strategies and experience (Conference Paper)," in *Proceedings-SPE International Symposium on Oilfield Chemistry*, Texas, USA, 2019.
- [16] J. O. Oseh, M. N. A. Mohd Norddin, I. Ismail, A. O. Gbadamosi, A. Agi, and H. N. Mohammed, "A novel approach to enhance rheological and filtration properties of water-based mud using polypropylene-silica nanocomposite," *Journal of Petroleum Science and Engineering*, vol. 181, article 106264, 2019.
- [17] X. F. Chang, J. S. Sun, Z. Xu et al., "Synthesis of a novel environment-friendly filtration reducer and its application in water-based drilling fluids," *Colloids and Surfaces A: Physicochemical and Engineering Aspects*, vol. 568, pp. 284–293, 2019.
- [18] X. Liu, B. Xie, Y. Gao et al., "Development of low toxicity and high temperature polymer drilling fluid for environmentally sensitive offshore drilling," in *IADC/SPE Asia Pacific Drilling Technology Conference and Exhibition*, Bangkok, Thailand, 2018.
- [19] L. Long, X. Xianguang, Z. Jinzhi et al., "Application of innovative high-temperature high-density oil-based drilling fluid technology in the efficient exploration and development of ultra-deep natural gas resources in West China," in *International Petroleum Technology Conference*, Bangkok, Thailand, 2016.
- [20] H. Shen, K. Lv, X. Huang et al., "Hydrophobic associated polymer-based laponite nanolayered silicate composite as filtrate reducer for water-based drilling fluid at high temperature," *Journal of Applied Polymer Science*, vol. 137, no. 5, 2020.
- [21] D. V. Kosynkin, G. Ceriotti, K. C. Wilson et al., "Graphene oxide as a high-performance fluid-loss-control additive in water-based drilling fluids," *ACS Applied Materials and Interfaces*, vol. 4, no. 1, pp. 222–227, 2012.
- [22] H. Shen, K. Lv, X. Huang et al., "Hydrophobic-associated polymer-based laponite nanolayered silicate composite as filtrate reducer for water-based drilling fluid at high temperature," *Journal of Applied Polymer Science*, vol. 137, no. 18, article 48608, 2020.
- [23] H. A. Craddock, "Oilfield chemistry and its environmental impact," *John Wiley & Sons*, pp. 21–110, 2018.
- [24] G. Pan, J. Chen, C. Zhang et al., "Combined technology of weak gel flooding assisting thermal huff and puff enhances oil recovery for offshore heavy oil field," in *SPE Annual Technical Conference and Exhibition*, Dubai, UAE, 2016.
- [25] M. X. Li, S. C. Xie, H. Zhang, X. G. Wang, and Q. Z. Jin, "Effect of mechanical stirring rate on the texture, rheological property and microstructure of gel-like oil," *Journal of Food Science and Biotechnology*, vol. 32, pp. 393–398, 2013.
- [26] R. Jain, T. K. Mahto, and V. Mahto, "Rheological investigations of water based drilling fluid system developed using synthesized nanocomposite," *Korea Australia Rheology Journal*, vol. 28, no. 1, pp. 55–65, 2016.
- [27] K. K. Chandan and G. P. Karmakar, "Drilling fluid waste treatment using polysaccharide-grafted copolymers," *The APPEA Journal*, vol. 59, no. 1, pp. 34–46, 2019.
- [28] P. Dejtardon, H. Hamidi, M. H. Chuks, D. Wilkinson, and R. Rafati, "Impact of ZnO and CuO nanoparticles on the rheological and filtration properties of water-based drilling fluid," *Colloids and Surfaces A: Physicochemical and Engineering Aspects*, vol. 570, pp. 354–367, 2019.
- [29] B. Xie, X. Zhang, Y. Li, W. Liu, and M. Luo, "Application a novel thermo-sensitive copolymer as a potential rheological modifier for deepwater water-based drilling fluids," *Colloids and Surfaces A: Physicochemical and Engineering Aspects*, vol. 581, article 123848, 2019.

## Research Article

# Experimental Study on Enhanced Condensate Recovery by Gas Injection in Yaha Condensate Gas Reservoir

Yiming Wu,<sup>1</sup> Kun Yao,<sup>1</sup> Yan Liu,<sup>1</sup> Xiangyun Li,<sup>2</sup> Mimi Wu,<sup>1</sup> Ronghong Cheng,<sup>1</sup> and Bo Wang<sup>3</sup>

<sup>1</sup>Research Institute of Exploration and Exploitation, Petro-China Tarim Oilfield Company, Korla 841000, China

<sup>2</sup>CNPC USA Corporation, Beijing 100028, China

<sup>3</sup>Petroleum Systems Engineering, Faculty of Engineering and Applied Science, University of Regina, Regina, Saskatchewan S4S 0A2, Canada

Correspondence should be addressed to Bo Wang; [wbg373@uregina.ca](mailto:wbg373@uregina.ca)

Received 8 August 2021; Revised 8 September 2021; Accepted 20 September 2021; Published 14 October 2021

Academic Editor: Jinjie Wang

Copyright © 2021 Yiming Wu et al. This is an open access article distributed under the Creative Commons Attribution License, which permits unrestricted use, distribution, and reproduction in any medium, provided the original work is properly cited.

A condensate gas reservoir is an important special oil and gas reservoir between oil reservoir and natural gas reservoir. Gas injection production is the most commonly used development method for this type of gas reservoir, but serious retrograde condensation usually occurs in the later stages of development. To improve the recovery efficiency of condensate oil in the middle and late stages of production of a condensate gas reservoir, a gas injection parameter optimization test study was carried out, taking the Yaha gas condensate reservoir in China as an example. On the premise that the physical experimental model and key parameters met the actual conditions of the formation, the injection method, injection medium, injection-production ratio, and other parameters of the condensate gas reservoir were studied. Research on the injection method showed that the top injection method had a lower gas-oil ratio and higher condensate oil recovery. The study of injection medium showed that the production effect of carbon dioxide (CO<sub>2</sub>) injection was the best injection medium, and the maximum recovery rate of condensate oil was 95.11%. The injection-production ratio study showed that the injection-production ratio was approximately inversely proportional to the recovery factor of condensate gas and approximately proportional to the recovery factor of condensate oil. When the injection-production ratio was 1 : 1, the maximum recovery rate of condensate oil was 83.31%. In summary, in the later stage of gas injection development of the Yaha condensate gas reservoir, it was recommended to choose the development plan of CO<sub>2</sub> injection at the top position with an injection-production ratio of 1 : 1. This research can not only provide guidance for the later formulation of gas injection plans for Yaha condensate gas reservoirs but also lay a foundation for the research of gas injection migration characteristics of other condensate gas reservoirs.

## 1. Introduction

With the continuous improvement of the level of exploration technology and exploration degree at home and abroad, the proportion of condensate gas reservoirs discovered is increasing year by year. Therefore, condensate gas fields occupy a particularly important position in the development of gas fields in the world. Condensate gas reservoir is different from ordinary oil reservoir or gas reservoir; it has the dual characteristics of oil reservoir and gas reservoir [1]. Due to the special fluid phase characteristics, its extraction technology and development difficulty are much more com-

plicated than general gas reservoirs and oil reservoirs [2–4]. During the development of condensate gas reservoirs, when the reservoir pressure is lower than the dew point pressure, serious retrograde condensation will occur in the reservoir. In other words, condensate oil will separate out of the gas phase and accumulate in a large amount in the near-wellbore zone, which will block the original seepage pores, thereby reducing the final recovery rate of condensate gas and condensate oil [5–9].

Compared with natural gas, condensate oil has extremely high economic value. At present, there are two main methods to improve the recovery rate of condensate

TABLE 1: Condensate gas reservoir parameters and content.

Category	Parameter	Numerical	Unit
Condensate gas properties	Density	0.63~0.67	kg/m <sup>3</sup>
	CO <sub>2</sub>	<1	%
	N <sub>2</sub>	3~8	%
	C <sub>1</sub>	85	%
Condensate oil properties	Density	0.78~0.83	kg/m <sup>3</sup>
	Freezing point	9~36	°C
	Sulfur content	<0.12	%
	Wax content	5.74~13.77	%
	Wax-off point	9~20.5	°C
	Gum and asphalt content	Low content	—
Formation water properties	Density	1.08~1.44	kg/m <sup>3</sup>
	Salinity	137752~214209	mg/l
	Condensate oil content	600~700	g/m <sup>3</sup>
Gas reservoir properties	Maximum reverse condensation pressure	25~30	MPa
	Maximum reverse condensate volume	30	%

TABLE 2: Geological characteristic parameters of condensate gas reservoirs.

Reservoir location	Thickness (m)	Average thickness (m)	Porosity (%)	Average porosity (%)	Permeability (10 <sup>-3</sup> μm <sup>2</sup> )	Average permeability (10 <sup>-3</sup> μm <sup>2</sup> )	Multiple of permeability	Average multiple of permeability
Paleogene	0.2~3.4	0.9	16.4~21.21	17.9	120.7~2257.7	641.4	2.6~7.6	3.4
Cretaceous	0.2~1.6	0.5	11.2~18.34	16	33.6~233.9	89.3	2.6~6.2	3.4

TABLE 3: Experimental program.

Experiment category	Experiment grouping	Experiment content	Experimental program	Experimental parameters
1	1	Gas injection method	Side gas injection	Temperature:137.8°C Pressure:54.94 MPa Initial pressure:60 MPa Injection speed:0.2 ml/min Injection and mining method: one injection and one mining
	2		Bottom gas injection	
	3		Shaft gas injection	
	4		CH <sub>4</sub>	
2	5	Gas injection medium	On-site gas	
	6		CO <sub>2</sub>	
	7		0.5:1	
3	8	Injection-production ratio	0.75:1	
	9		1:1	

oil: one is continuous depletion development, and the other is gas injection to maintain pressure. In the process of depletion mining, natural energy is gradually released and pressure-free replenishment system. The injection pressure-holding mining method is to inject gaseous media into the reservoir to supplement the formation energy to reduce retrograde condensate damage [10–12]. Scholars at home and abroad have conducted in-depth discussions on these two methods. For example, Jingsong et al. [13] used reservoir numerical simulation methods to analyze the sensitivity of injection parameters for cyclic gas injection devel-

opment of condensate gas reservoirs, focusing on evaluating the impact of injection methods, gas injection timing, and injection-production ratios on the development effects of condensate gas reservoirs. The results show that for condensate gas reservoirs rich in condensate oil and with a large ground pressure difference, the development effect of the top cycle gas injection after depletion development to the dew point pressure is better. Dong et al. [14] took the Yaha-5 condensate gas reservoir as an example. The three production methods of exhaustion, water injection, and gas injection were compared and analyzed by component





FIGURE 1: Schematic diagram of the core sample.

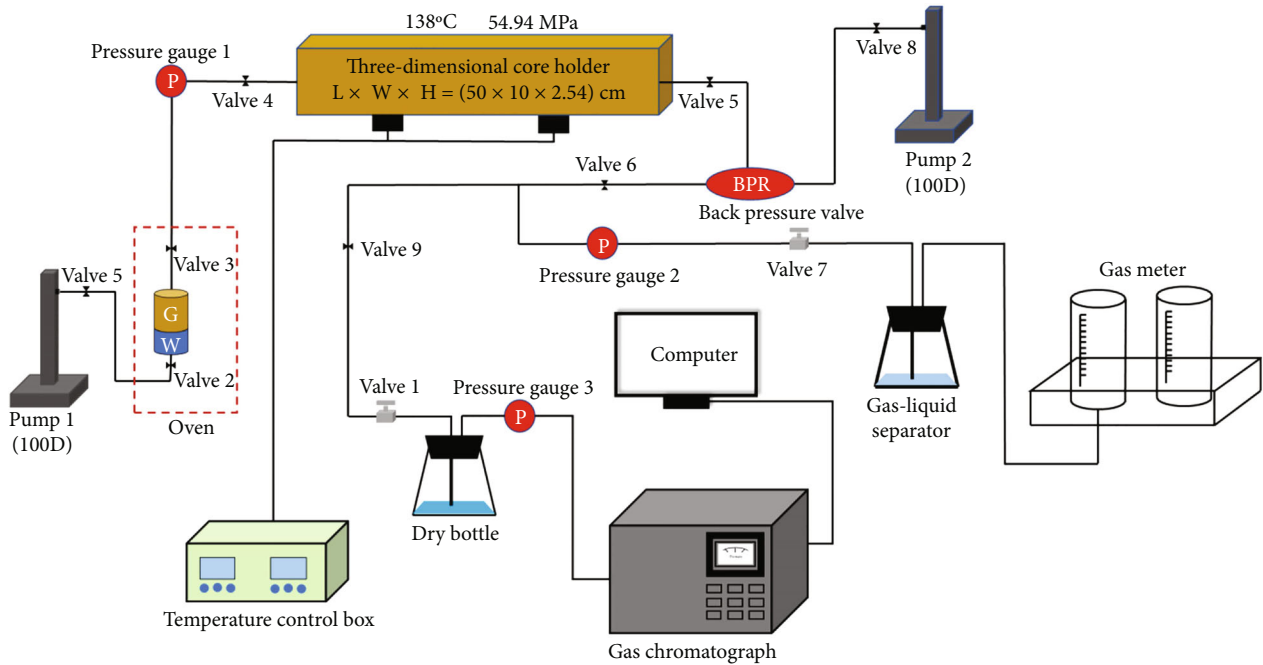
numerical simulation. The research results show that water injection and gas injection are better than depletion mining, and gas injection is better than water injection. In particular, the large well spacing gas injection development method can not only delay gas channeling and improve gas injection efficiency but also greatly increase the degree of condensate oil recovery. Lu [15] took Dalaoba No. 2 condensate gas reservoir with high condensate oil content as an example. The gas injection state and seepage mechanism are analyzed, and pilot experiments are carried out. The research results show that when entering the middle and late stages of mining, the formation pressure drops faster, the retrograde condensation phenomenon is serious, and the formation edge water is active. Therefore, it is not appropriate to choose depletion mining or water injection development in the middle and late stages of mining, and gas injection and pressure-maintaining development methods should be considered. Lu [16] made a comparative analysis and summary of the current recovery methods of condensate gas fields and discussed the strategies for optimizing gas injection production methods. The research results indicate that the optimization of production system, gas injection method, and stop injection time should be strengthened in the development process to improve the recovery rate of condensate gas fields. Through research, it can be found that the depletion mining cost is low and the process is relatively simple, so this method is widely used in the development of condensate gas reservoirs. The method of gas injection to maintain pressure is the most important method to improve the recovery of condensate, especially for condensate gas reservoirs with high condensate oil content, because injecting gas into the reservoir can not only increase the formation pressure in the retrocondensation zone but also reduce the antievaporation effect of the condensate oil. Therefore, the condensate oil is more easily produced. If pressure-holding mining is not carried out, the loss of condensate oil will even reach more than 60% to 70% of the original reserves [17–20].

Following the above research, most foreign scholars have conducted in-depth discussions on various issues under the conditions of gas injection. Through literature research, the methods of research problems can be roughly divided into two categories: one is reservoir numerical simulation methods, and the other is experimental analysis and research. For numerical simulation research methods, He

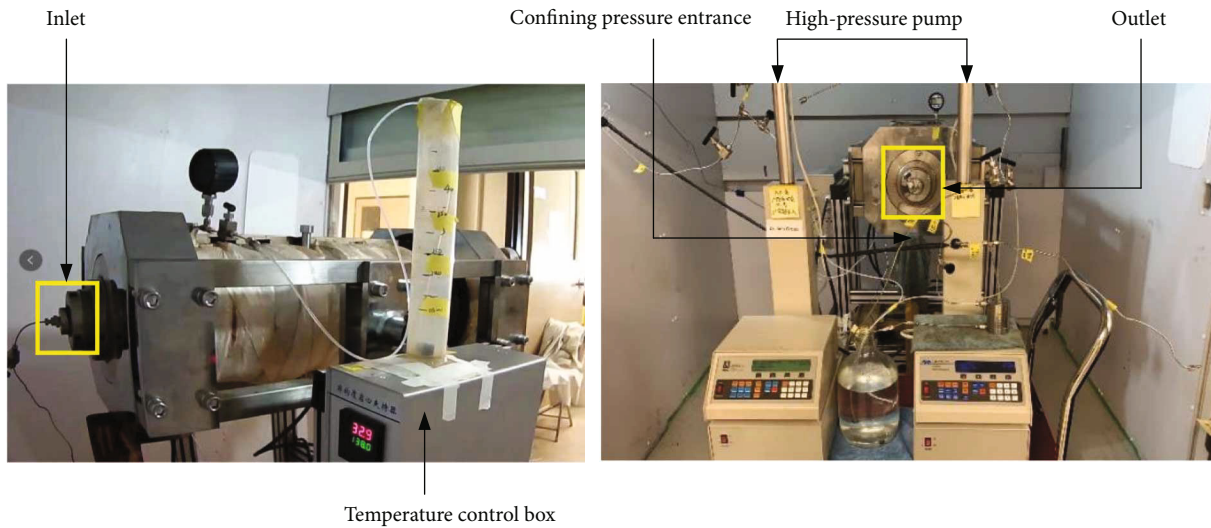
TABLE 4: Laboratory compound condensate gas composition table.

Component	Actual		Laboratory			
	Mole fraction (mol%)		Mole fraction (mol%)			
N <sub>2</sub>	3.26%	79.85%	CH <sub>4</sub>	81.44%		
CH <sub>4</sub>	76.59%					
CO <sub>2</sub>	0.62%					
C <sub>2</sub> H <sub>6</sub>	8.90%					
C <sub>3</sub> H <sub>8</sub>	1.83%					
iC <sub>4</sub>	0.48%					
nC <sub>4</sub>	0.71%				C <sub>2</sub> H <sub>6</sub>	13.66%
iC <sub>5</sub>	0.34%					
nC <sub>5</sub>	0.34%					
C <sub>6</sub>	0.59%					
C <sub>7</sub>	1.10%					
C <sub>8</sub>	1.12%	On-site condensate	4.90%			
C <sub>9</sub>	0.59%			6.34%		
C <sub>10</sub>	0.48%					
C <sub>11</sub> <sup>+</sup>	3.05%					

et al. [21] took the condensate gas reservoir in the southern part of Rangnar A as an example, applied phase equilibrium theory and reservoir numerical simulation technology, and studied the mechanism and effect of CO<sub>2</sub> huff and puff to increase gas well condensate production. The research results show that when the amount of CO<sub>2</sub> injected is small, the capacity of CO<sub>2</sub> vaporization and condensate is limited. To ensure the effect of CO<sub>2</sub> huff and puff to increase oil, the periodic injection of CO<sub>2</sub> should exceed  $500 \times 10^4 \text{ m}^3$ . Hassan et al. [22] used thermochemical treatment methods to treat the near-well zone and used reservoir simulation methods to simulate oil and gas recovery. The research results show that this method can significantly improve oil and gas recovery, and the main reason for this phenomenon is that this method can reduce capillary pressure and viscosity of condensate oil well. Wan and Mu [23] took the Eagle Ford shale gas condensate gas reservoir as an example, used numerical simulation to study the effect of carbon dioxide steam huff and puff injection on slowing down the accumulation of condensate around the induced fractures, and conducted in-depth discussions on the molecular scale. The research results show that the use of CO<sub>2</sub> huff and puff gas injection is more conducive to improving the recovery of rich condensate oil. Jiang and Younis [24] used a multicomponent molecular simulation method to perform a numerical analysis on the enhanced oil recovery of carbon dioxide steam huff and puff in a complex fractured condensate gas reservoir. On this basis, several design elements such as the number of cycles and the length of the injection period in the steam stimulation process are briefly studied. For experimental analysis and research methods, Feng et al. [25] took Sulige tight sandstone condensate gas reservoir in Ordos Basin as an example. Based on the results of PVT phase experiments, core gas injection displacement experiments were carried out. An in-depth study of continuous gas



(a) Schematic diagram of theoretical model



(b) Schematic diagram of actual device

FIGURE 2: Schematic diagram of experiment setup.

injection, gas injection huff and puff and pulse gas injection condensate recovery degree, and the change characteristics of average condensate oil saturation in the core was conducted, and then, the best gas injection method to improve the condensate oil recovery was optimized. Yuan et al. [26] took the Zhongyuan Oilfield high-pressure and high-saturation condensate gas reservoir as the research object. The laboratory test study of methane ( $\text{CH}_4$ ) injection for enhanced oil recovery in high-pressure and high-saturated condensate gas reservoirs has been carried out. The research results show that for high-pressure and high-saturation condensate gas fields, first depletion production to a certain extent and then gas injection can also achieve higher

recovery. Hou [27] used the fully visible mercury-free high-temperature and high-pressure multifunctional formation fluid PVT analyzer to conduct an experimental study on the phase behavior of an offshore high-carbon dioxide condensate gas well. The experimental results show that the higher the  $\text{CO}_2$  content, the higher the condensate oil-gas-oil ratio, the greater the condensate density, the higher the condensate dew point pressure, the larger the relative volume of condensate, and the smaller the amount of reverse condensate. Therefore, carbon dioxide injection can improve the recovery efficiency of condensate oil. For this conclusion, some scholars have also verified this view [8, 28].

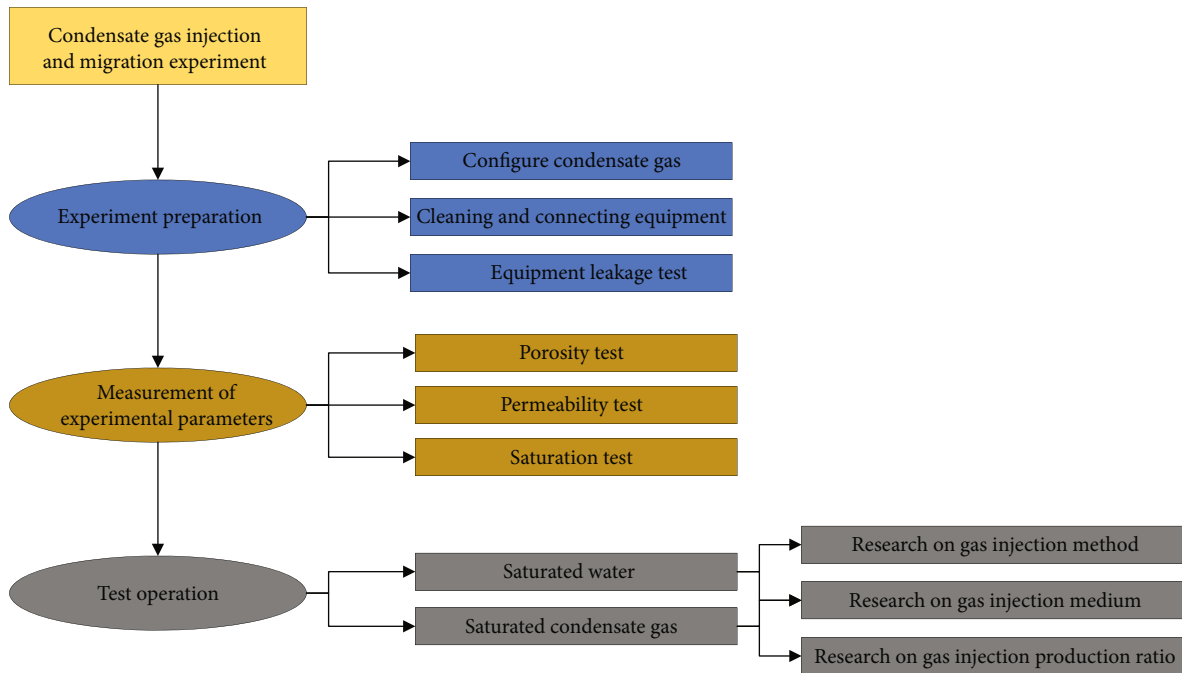


FIGURE 3: Experiment procedure flowchart.

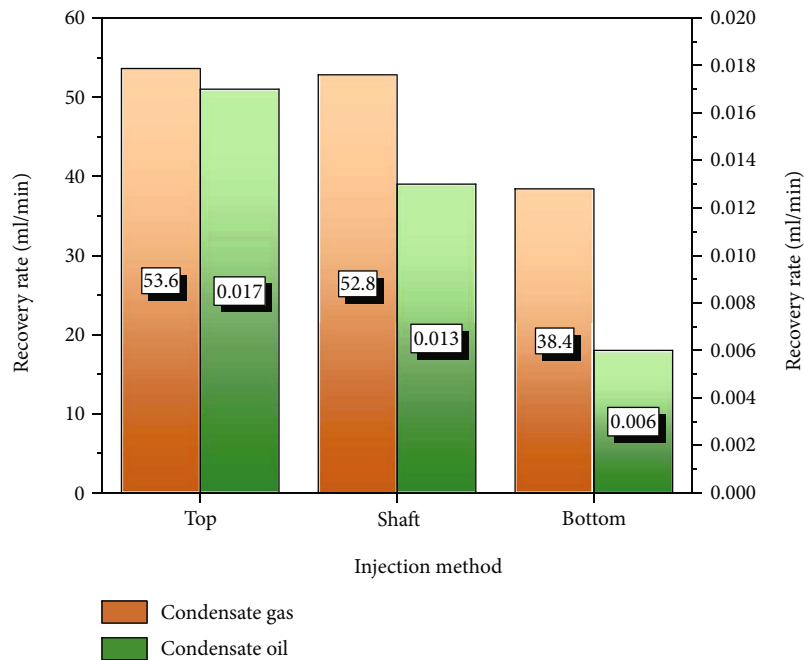


FIGURE 4: Histogram of the average recovery rate of different gas injection methods.

According to the above analysis, the research on improving the condensate gas reservoir by gas injection and maintaining pressure mainly uses numerical simulation methods and focuses on the elimination of retrograde condensate theory and complex phase transition issues. For experimental research, most of the research focuses on the selection of gas injection medium and the discussion of gas injection methods. There are few reports on the analysis of key parameters and variables in the development method

of gas injection and pressure maintenance. However, studying the migration mechanism and law of injected gas has become an urgent problem to be solved to improve the recovery rate of gas injection in condensate gas reservoirs. In-depth study of the migration law of injected gas in condensate gas reservoirs is the key to increasing gas injection utilization and improving development effects.

To sum up, to research the gas injection migration characteristics of the Yaha condensate gas reservoir and improve

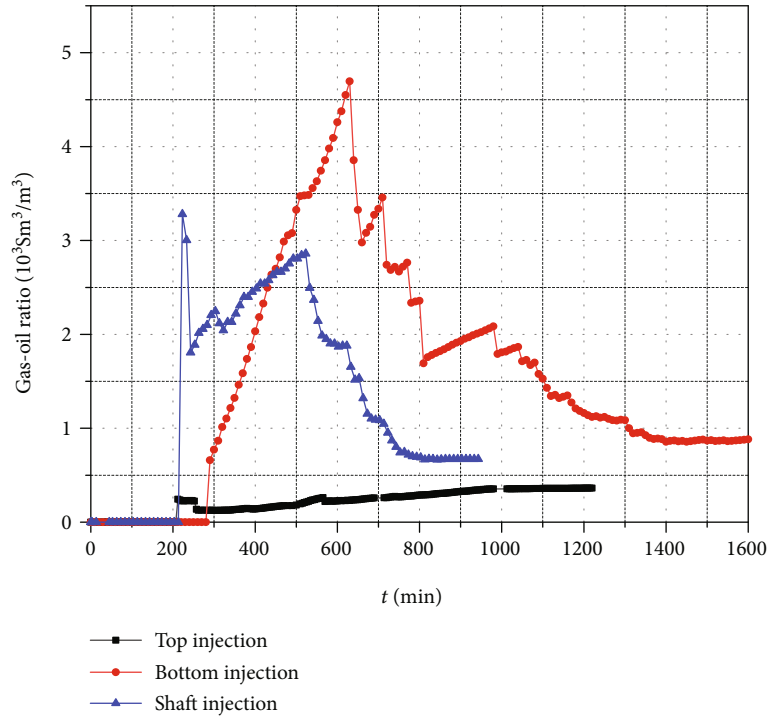


FIGURE 5: Gas-oil ratio curves produced by different gas injection methods.

the oil recovery in the later stage of the oilfield development, this research is based on the oilfield site and conducted indoor physical model experiments. First, the gas reservoir and geological profile are described. Then, the condensate gas injection and migration experiments are carried out. Finally, by changing the gas injection method, gas injection medium, and injection-production ratio, the influence of various variables on the enhanced oil recovery of condensate gas injection was clarified. This research can not only provide guidance for the later formulation of gas injection plans for Yaha condensate gas reservoirs but also lay a foundation for the research of gas injection migration characteristics of other condensate gas reservoirs.

## 2. Gas Reservoir Overview and Geological Characteristics

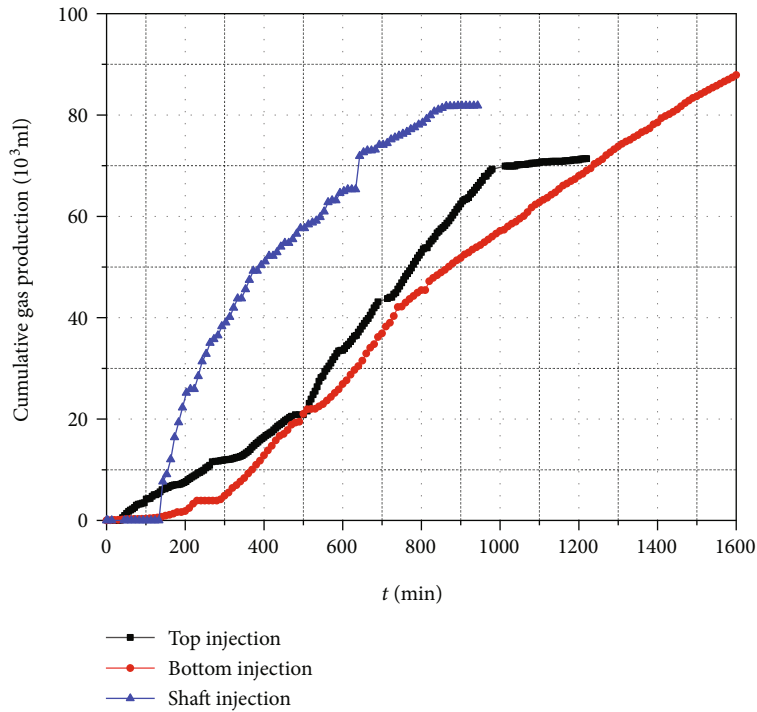
**2.1. Condensate Gas Reservoir Overview.** The Yaha condensate gas reservoir is located in Kuqa County, Xinjiang Uygur Autonomous Region, China, with an altitude of 967~1033 m. This gas reservoir is the largest condensate gas reservoir developed by cyclic gas injection in China. The gas reservoir structure is located on the Yaha fault structural belt in the Tarim Basin, distributed from northeast to southwest. The formation pressure of the gas reservoir is 53~56 MPa, the ground pressure difference is 2~4 MPa, and the condensate oil content is relatively high (500~5600 g/m<sup>3</sup>). It is a high-pressure condensate gas reservoir close to saturation with high condensate oil content. The condensate oil in the gas reservoir has low density, low viscosity, low content of colloidal asphalt, high wax content, and high freezing point. The H<sub>2</sub>S content in the con-

densate gas is very small, the CO<sub>2</sub> content is low, and the N<sub>2</sub> content is high. The specific conditions of condensate gas reservoirs are shown in Table 1.

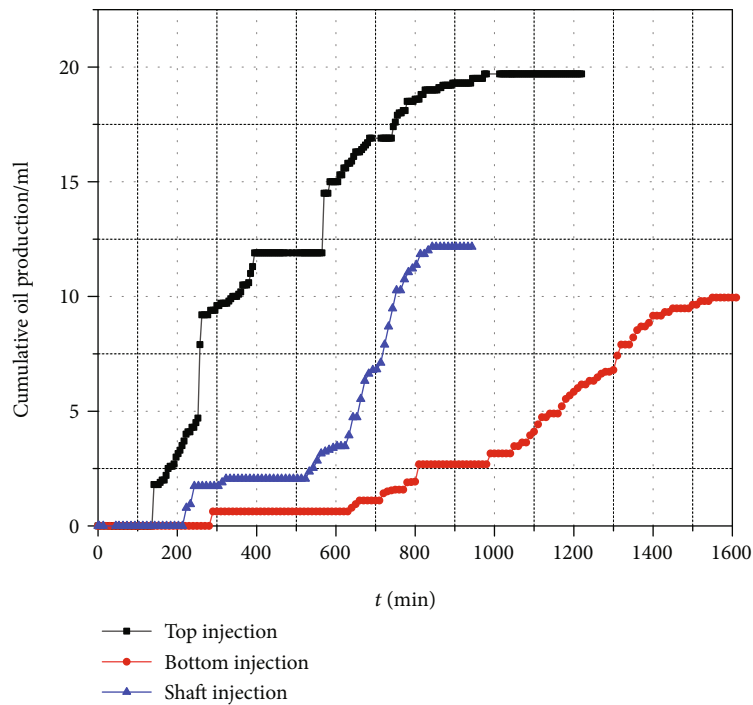
**2.2. Geological Characteristics.** The Yaha condensate gas reservoir is vertically divided into two gas layer groups: the bottom sandstone of the Paleogene and the top sandstone of the Cretaceous (Table 2). The above two condensate gas layers are both massive bottom water condensate gas reservoirs rich in condensate oil. The Paleogene gas reservoir is dominated by gray-brown fine sandstone, followed by coarse sandstone, medium sandstone, and gypsum sandstone. The Paleogene gas reservoir has low shale content and belongs to a chemically cemented reservoir. The Cretaceous gas reservoir is brown-red and brown siltstone, medium-fine sandstone with brown-red mudstone, and argillaceous siltstone. The Cretaceous gas reservoir is a lime mud cemented reservoir. Therefore, the Yaha condensate gas reservoir has the characteristics of deep burial, high formation pressure, small ground pressure difference, high condensate oil content, maximum retrograde condensate pressure, and high maximum retrograde condensate liquid volume.

## 3. Experiment Overview

Based on the actual geology of the Yaha condensate gas reservoir, this experiment conducted a study on the characteristics of gas injection migration. Under the condition that the core properties, fluid properties, initial conditions, and experimental procedures remain unchanged, the gas injection method, gas injection medium, and injection-production ratio are changed, and the gas injection scheme



(a) Cumulative gas production curve



(b) Cumulative oil production curve

FIGURE 6: Cumulative production curve of different injection methods.

is optimized to improve the recovery effect of the condensate gas reservoir. The experiment designed 3 types (9 groups) of programs; the specific conditions are shown in Table 3.

**3.1. Experiment Materials.** The core used in the experiment was provided by China Chengdu Core Technology Com-

pany, as shown in Figure 1. The core sample is a homogeneous low-permeability core slab manufactured artificially, and its size is  $L \times W \times H = 50 \times 10 \times 2.54$  (cm).

Based on the actual situation of the oil field, using CMG WinProp software, according to the mole fraction, the condensate gas composition and dosage used in the experiment



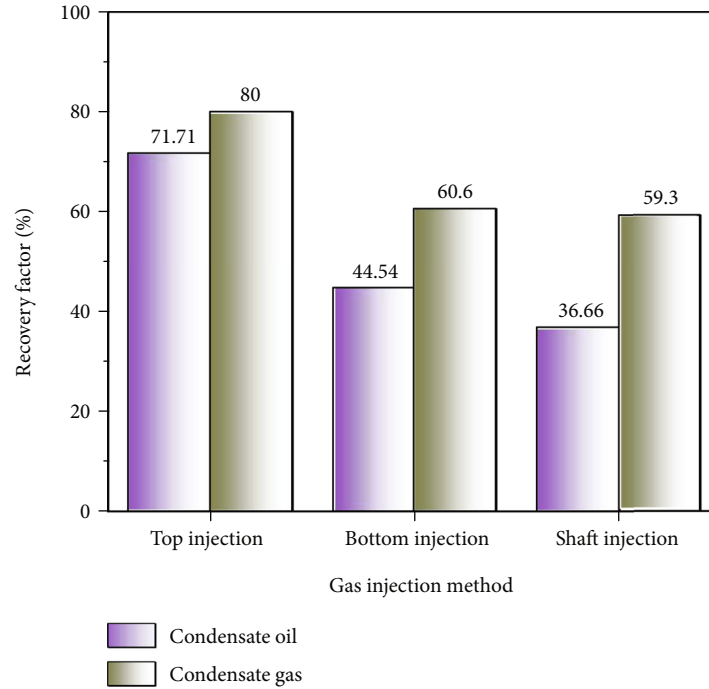


FIGURE 7: Histogram of final recovery factor of different gas injection methods.

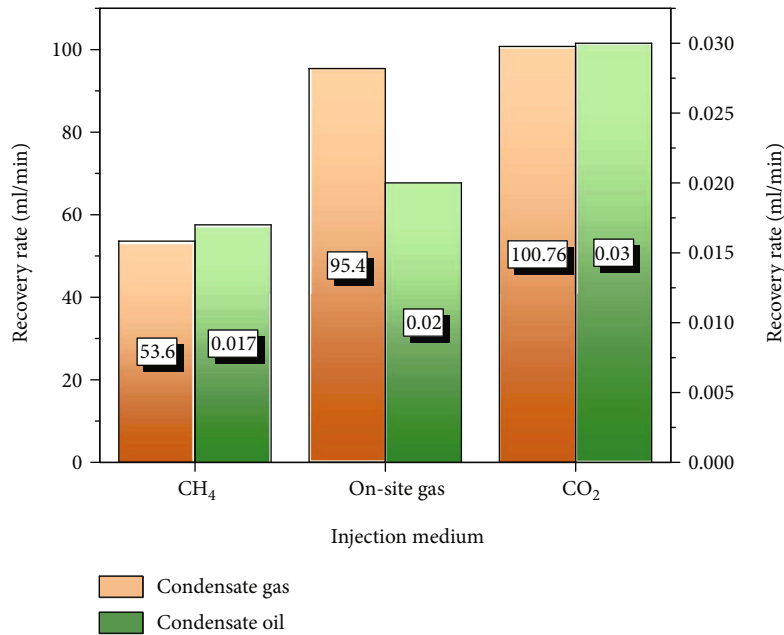


FIGURE 8: Histogram of average recovery speed of different gas injection media.

were determined. The properties of the actual fluid on site and the fluid configured in the laboratory are shown in the table. It can be seen from Table 4 that the actual condensate gas in the reservoir is mainly composed of methane (76.59%), ethane (83.9%), and macromolecular liquid hydrocarbon compounds. To ensure the feasibility and accuracy of the experiment, similar condensate gas components are used for coordination and modulation. It is finally deter-

mined that the condensate gas composition is methane (81.44%), ethane (13.66%), and condensate oil (4.90%). The gas raw materials prepared by the condensate gas are provided by Praxair Canada Inc., and the purity is as high as 99.99%.

**3.2. Experiment Setup.** The experiment setup of the gas injection migration experiment in the condensate gas reservoir is

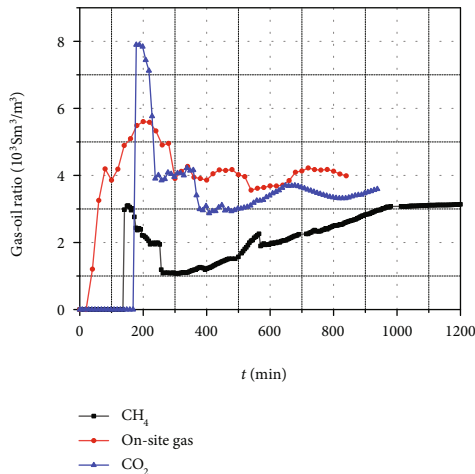


FIGURE 9: Curves of gas-oil ratio produced by different gas injection media.

shown in Figure 2. Among them, Figure 2(a) is a theoretical schematic diagram, and Figure 2(b) is an actual device diagram.

It can be seen from Figure 2 that the physical simulation experiment in this research mainly includes a three-dimensional core holder, a high-temperature and high-pressure intermediate container, and a high-pressure injection pump. Among them, the three-dimensional core holder is selected from Hai'an Petroleum Instrument Factory, with a maximum pressure of 70 MPa and a maximum temperature of 200°C. In order to meet the needs of the experiment, it uses fluorine rubber special core rubber sleeve inside. Two types of high-temperature and high-pressure resistant intermediate containers are selected, 206 ml and 1000 ml, and their maximum pressure is 70 MPa and the maximum temperature is 200°C. The high-pressure injection pump adopts ISCO-100DX model produced by Teledyne, USA, and the maximum injection pressure is 71 MPa.

**3.3. Experiment Procedure.** In this research, the experiment includes three parts: experiment preliminary preparation, experimental parameter determination, and test operation. The specific situation is as shown in Figure 3.

In the stage of experiment preliminary preparation, the condensate gas used in the experiment is configured according to the actual parameters in the oilfield reservoir. Then, the experimental platform is assembled according to the experimental plan, and the ethanol solution is used to clean and leak test it.

In the stage of experimental parameter determination, deionized water is used to test the porosity of core samples. The porosity is calculated based on the ratio of water absorption to model volume. Then, the permeability test of the core sample is carried out. The permeability is calculated according to the water injection speed and pressure difference using Darcy's law. Finally, we vacuum the model and wait for the formal test.

In the test operation stage, the core saturated water treatment is performed according to the oilfield geological data,

and the initial irreducible water saturation is 30%. Then, the core is treated with saturated condensate gas. Finally, the physical model is used to study the characteristics of gas injection migration in condensate gas reservoirs. By changing the gas injection method, gas injection medium, and injection-production ratio, the optimal condensate gas injection program is further optimized and designed.

## 4. Results and Discussion

**4.1. Gas Injection Method.** The use of different gas injection methods in condensate gas reservoirs will have a serious impact on the recovery rate and recovery rate of condensate gas and condensate oil. To study the best gas injection method for the Yaha condensate gas reservoir, shaft injection, top injection, and bottom injection were selected for comparative analysis. The experimental gas injection medium is methane, and the injection-production ratio is 0.5:1. Other specific experimental parameters are shown in Table 3.

The average recovery rate of condensate gas and condensate oil for different gas injection methods is shown in Figure 4.

It can be seen from Figure 4 that for the average recovery rate of condensate gas, the effects of top gas injection and shaft gas injection are approximately the same, but both are much greater than bottom gas injection. For the recovery rate of condensate oil, the top gas injection has the best effect, with a recovery rate of 0.017, followed by shaft gas injection with a recovery rate of 0.013, and finally bottom gas injection with a recovery rate of 0.006. Therefore, through comparative analysis, it can be known that whether it is the average recovery rate of condensate gas or the average recovery rate of condensate oil, the top gas injection method is the best choice.

To analyze the recovery rate of condensate gas and condensate oil during the entire recovery process, the production gas-oil ratio curves of three different injection methods are drawn, as shown in Figure 5.

It can be seen from Figure 5 that the production gas-oil ratio of the top gas injection method is always the lowest, so the condensate recovery effect of this method is the best. The production gas-oil ratio curves of the shaft gas injection method and the bottom gas injection method roughly show a trend of rising first and then falling. This shows that in the early stage of production, the condensate gas recovery effect of this gas injection method is better. And in the later stage of production, the recovery effect of condensate gas gradually declines, and the recovery effect of condensate oil gradually strengthens, but the effect of condensate oil in the entire production cycle is still lower than that of the top gas injection method.

The cumulative production curves of condensate gas and condensate oil for different gas injection methods are shown in Figure 6.

It can be seen from Figure 6(a) that under the same production pressure, the cumulative gas production curves of the three gas injection methods are quite different, but they all show a gradually increasing trend. In the early stage of

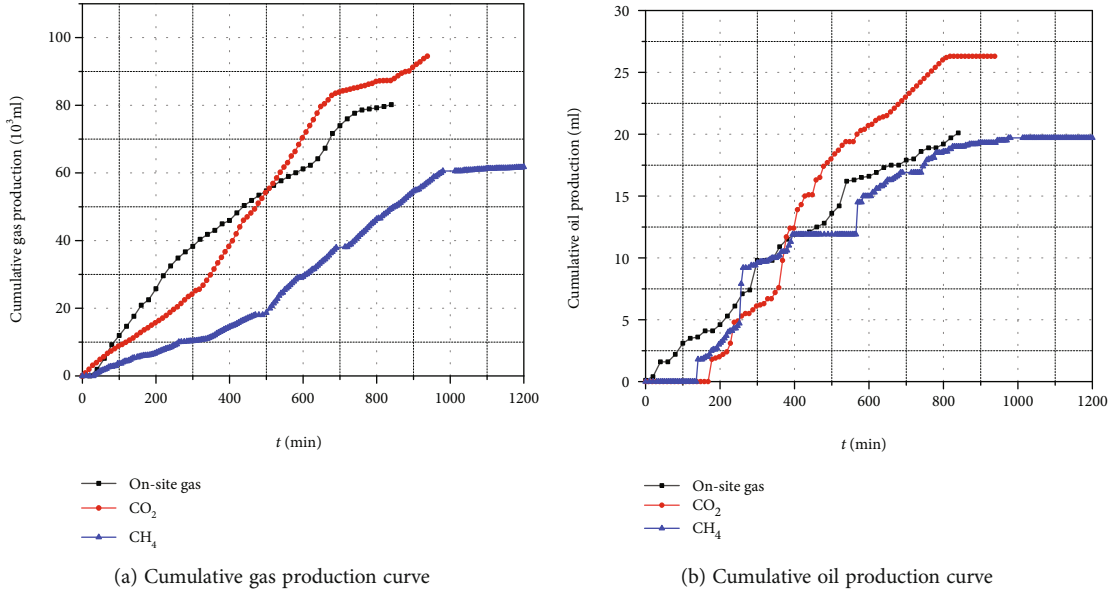


FIGURE 10: Cumulative production curve of different injection media.

gas production ( $t < 500$  min), the shaft gas injection has the fastest gas production speed, followed by bottom gas injection, and top gas injection has the slowest gas production speed. In the middle stage of gas production ( $t = 500 \sim 900$  min), the gas production rate of shaft gas injection rises rapidly, which is roughly the same as the gas production rate of shaft gas injection, and the gas production rate of bottom gas injection is the slowest. In the later stage of gas production ( $t > 900$  min), the axial gas injection method reached the peak point first, with a peak value of about  $80 \times 10^3$  ml, followed by the top gas injection method, with a peak value of about  $70 \times 10^3$  ml. Although the bottom gas injection method has a slower gas production rate, the gas production time is the longest, with a peak value of about  $90 \times 10^3$  ml.

It can be seen from Figure 6(b) that under the same production pressure, the cumulative oil production curves of the three different gas injection methods are quite different, but the overall trend is gradually increasing. In the early stage of oil production ( $t < 400$  min), the oil production rate and cumulative oil production of the top gas injection method increase rapidly, and they are much higher than the other two gas injection methods. In the mid-stage ( $t = 400 \sim 800$  min); although the oil production rate of the shaft gas injection method increases rapidly, the cumulative oil production is still much smaller than the top gas injection method, and the bottom gas injection method has the lowest oil production rate and oil production. In the later stage ( $t > 800$  min), the shaft gas injection method stops oil production at the earliest time, and the cumulative oil production finally stabilizes around 12.33. The second is the top gas injection method, which stops oil production after the mining time is about 1200 minutes, and the final oil production stabilizes around 19.78. The last to stop oil production is the bottom gas injection method. Although this method has the longest cumulative oil production time, the cumulative oil production is the smallest, and the final oil produc-

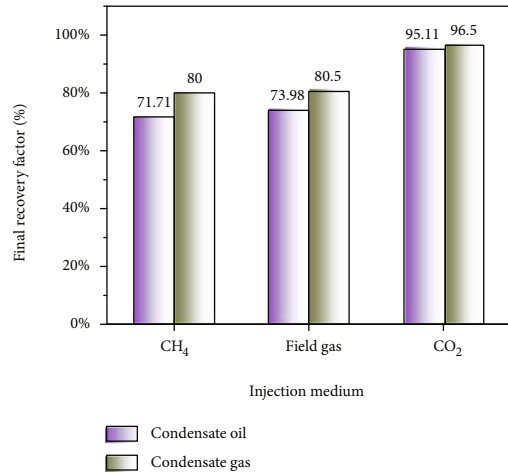


FIGURE 11: Histogram of the final recovery factor with different injection media.

tion is stable around 10.00. Therefore, through the abovementioned comparative analysis, it can be known that among the three gas injection methods, the top gas injection method is most conducive to improving the condensate oil recovery of the Yaha condensate gas reservoir.

The final recovery factor histogram of different gas injection methods is shown in Figure 7.

It can be seen from Figure 7 that the recovery efficiency of condensate oil and condensate gas using the top gas injection method is the highest, with values of 80% and 71.71%. The condensate recovery factor of bottom gas injection and shaft gas injection is basically the same, but the condensate recovery factor of bottom gas injection is slightly greater than that of shaft gas injection. Therefore, through comparative analysis, it can be known that the best gas injection

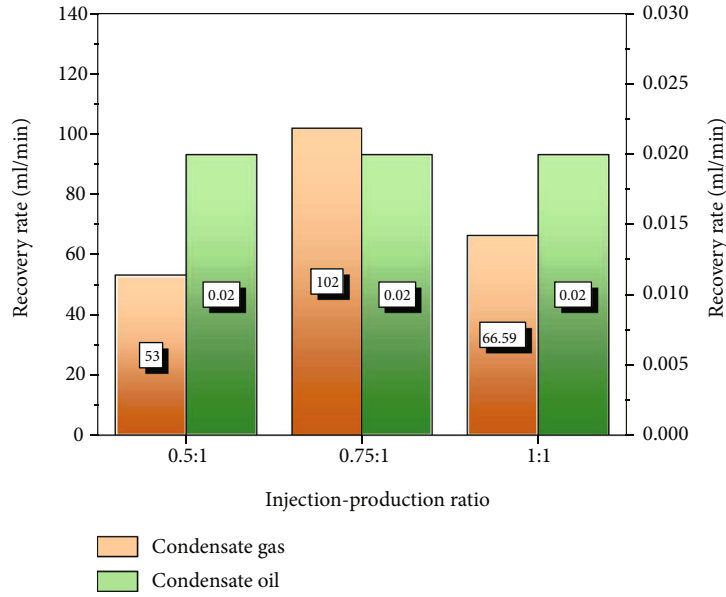


FIGURE 12: Histogram of the average recovery speed with different injection-production ratios.

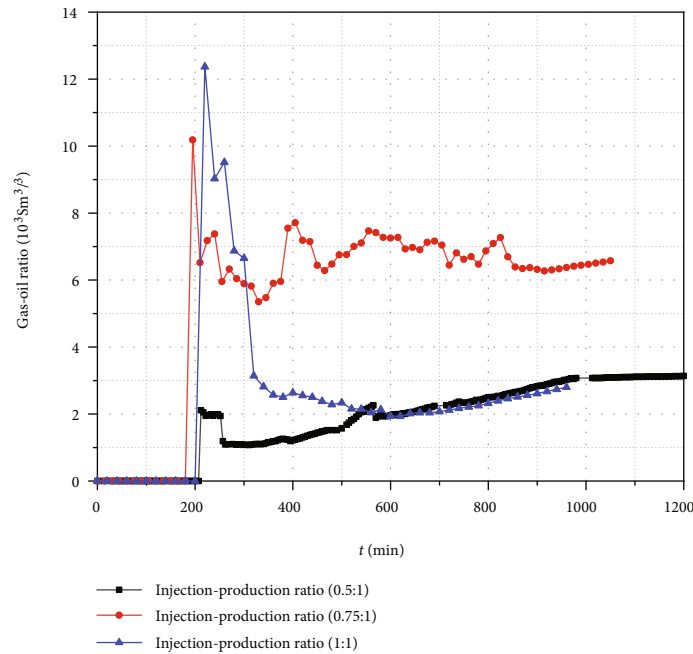


FIGURE 13: Production gas-oil ratio curves with different injection-production ratios.

method for the Yaha condensate gas reservoir is top gas injection.

**4.2. Injection Medium.** When studying the migration law of injected gas in the formation, it is necessary to consider the important factor of injected fluid characteristics. Because the physical properties of reservoir fluid and injected gas are quite different, the interaction between the two will seriously affect the migration of injected gas. Therefore, three gas injection media were selected for comparative analysis, and the injection media were CH<sub>4</sub>, CO<sub>2</sub>, and on-site gas.

The experimental gas injection method is shaft gas injection, and the injection-production ratio is 0.5:1. Other specific experimental parameters are shown in Table 3.

The average recovery rate of condensate gas and condensate oil for different gas injection methods is shown in Figure 8.

It can be seen from Figure 8 that for the average recovery rate of condensate gas, the effects of on-site gas injection and carbon dioxide injection are approximately the same, and both are much greater than methane gas injection. For the recovery rate of condensate oil, carbon dioxide injection

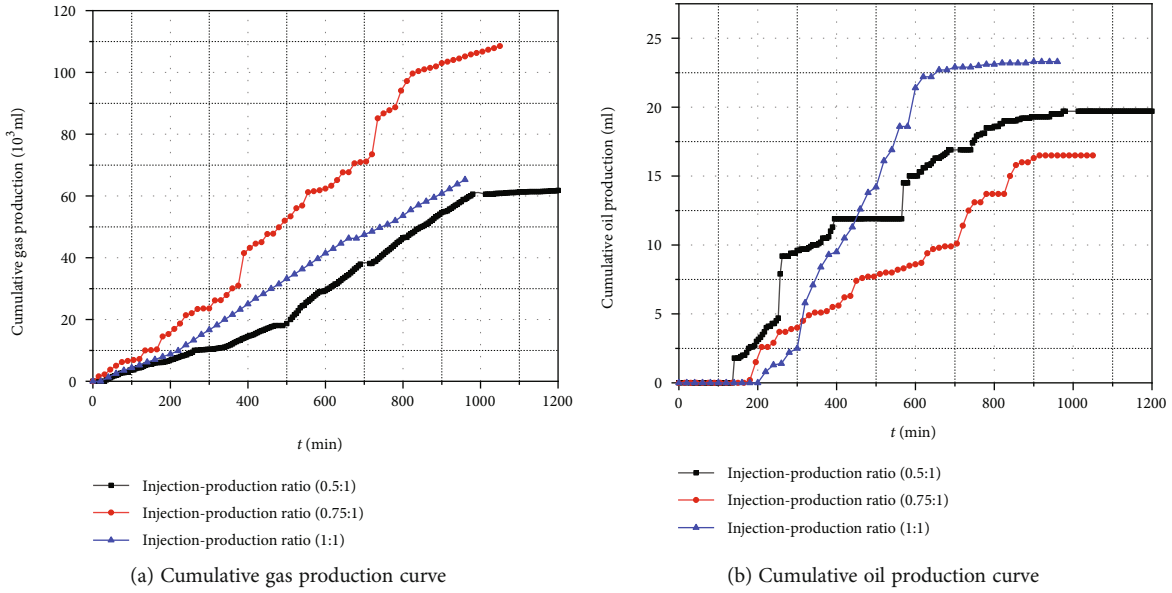


FIGURE 14: Cumulative production curve of different injection-production ratios.

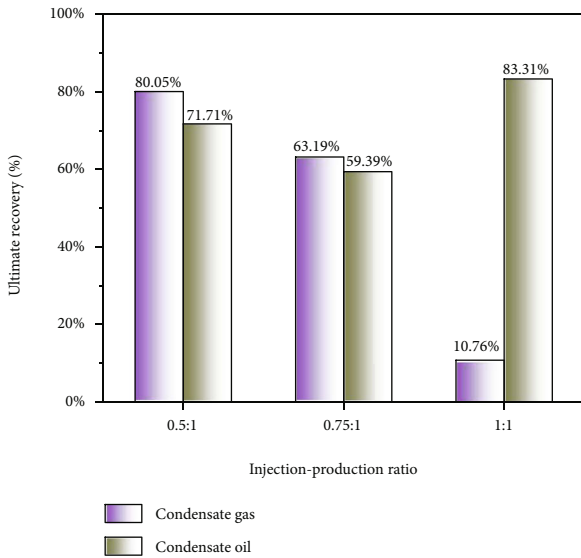


FIGURE 15: Histogram of the final recovery factor with different injection-production ratios.

has the best effect with a value of 0.03, followed by on-site gas injection with a value of 0.02, and finally methane injection with a value of 0.017. Therefore, in order to improve the recovery of condensate gas and condensate oil, carbon dioxide injection is the best injection medium.

The production gas-oil ratio curves of different gas injection media are shown in Figure 9.

It can be seen from Figure 9 that the changing trends of the produced gas-oil ratio curves of different gas injection media are approximately the same, and they all show a trend of first rising rapidly and then falling and finally tending to stabilize. However, the production gas-oil ratio curve of carbon dioxide injection increased the most in the early stage, the maximum value was close to  $8 \times 10^3 \text{ Sm}^3 \cdot \text{m}^{-3}$ , and finally

stabilized near  $3.7 \times 10^3 \text{ Sm}^3 \cdot \text{m}^{-3}$ . This is because it is affected by phase changes in the early stage of production, and even if condensate is precipitated in the later stage of production, the precipitated condensate is mixed with carbon dioxide, and the condensate is displaced by the mixed phase of carbon dioxide. On the whole, the average production gas-oil ratio of on-site gas injection is the largest, followed by carbon dioxide injection, and finally methane injection.

The cumulative production curves of condensate gas and condensate oil for different gas injection media are shown in Figure 10.

It can be seen from Figure 10(a) that under the same production pressure, the cumulative gas production curves of the three different gas injection methods are quite different, but they all show a trend of gradually increasing and then becoming stable. In the early stage of gas production ( $t < 500 \text{ min}$ ), the gas production rate of on-site gas injection first increases and then decreases, while the gas production rate of carbon dioxide injection first decreases and then increases. And the cumulative gas production of on-site gas injection is greater than the cumulative gas production of carbon dioxide injection, and the gas production rate and cumulative gas production of methane gas injection are the smallest. In the middle stage of gas production ( $t = 500 \sim 800 \text{ min}$ ), the gas production rate and cumulative gas production of carbon dioxide injection increase rapidly, which is much greater than the situation of on-site gas injection and methane gas injection. In the later stage of gas production ( $t > 800 \text{ min}$ ), the gas production rate of carbon dioxide injection is still further increasing, so the cumulative gas production is also gradually increasing. However, the production of on-site gas and methane gas was gradually stopped. The cumulative production of on-site gas was finally stabilized at about  $80 \times 10^3 \text{ ml}$ , and the cumulative



production of methane gas was finally stabilized at about  $60 \times 10^3$  ml.

It can be seen from Figure 10(b) that under the same production pressure, the cumulative oil production curves of the three different gas injection methods are quite different, but they all show a trend of increasing first and then becoming stable. In the early stage of oil production ( $t < 400$  min), the oil production rate and cumulative production of on-site gas injection are greater than those of carbon dioxide and methane injection. In the middle stage ( $t = 400\sim 800$  min), the oil production rate and cumulative production of carbon dioxide injection gradually increase and eventually exceed the gas production rate and cumulative oil production of on-site gas injection. In the later stage ( $t > 800$  min), the output of carbon dioxide injection gradually reaches its maximum value, which is about 27.5 ml. The second is the cumulative oil production of on-site gas injection, while methane gas injection ends the oil production process earliest and the cumulative oil production is the lowest. Therefore, through the abovementioned comparative analysis, it can be known that among the three gas injection methods, carbon dioxide injection is most conducive to improving the recovery of condensate oil in the Yaha condensate gas reservoir, followed by on-site gas injection, and finally methane gas injection.

The final recovery factor histogram of different gas injection methods is shown in Figure 11.

It can be seen from Figure 11 that the final recovery efficiency of condensate gas and condensate oil under different gas injection medium conditions is more obvious. Among them, the production effect of carbon dioxide injection is the best. The final recoveries of condensate gas and condensate oil under this condition are both higher than 90%, with values of 95.11% and 96.5%, respectively. The final recovery efficiencies of methane injection and on-site gas injection are approximately the same. Therefore, in order to further improve the ultimate recovery of condensate gas and condensate oil, the most suitable gas injection medium should be selected.

**4.3. Injection-Production Ratio.** The injection volume of gas injection wells and production wells of condensate gas reservoirs directly affect the changes in gas layer pressure gradient, and pressure changes have a great impact on gas reservoir recovery. Therefore, a reasonable injection-production ratio is a key factor to ensure oil and gas recovery. In order to analyze the influence of injection-production ratio on the Yaha condensate gas reservoir, three physical simulation experiments of injection-production ratio were selected, which were 0.5:1, 0.75:1, and 1.1. The experimental gas injection medium is methane, and the gas injection method is shaft gas injection. Other specific experimental parameters are shown in Table 3.

The average recovery rate of condensate gas and condensate oil for different gas injection-production ratios is shown in Figure 12.

It can be seen from Figure 12 that for the average recovery rate of condensate gas, when the injection ratio is 0.75:1, the average recovery rate is the largest, with a value of

102 ml·min<sup>-1</sup>. The second is the injection ratio of 0.5:1, and the last is the injection ratio of 1:1. For the recovery rate of condensate oil, the average recovery rate of the three injection-production ratios is the same, which is 0.02.

The production gas-oil ratio curves of different gas injection-production ratios are shown in Figure 13.

It can be seen from Figure 13 that the changing trends of the produced gas-oil ratio curves of different gas injection media are approximately the same. The curves all show a rapid rise first, then fall, and finally stabilize. As the injection-production ratio increases, the production gas-oil ratio curve fluctuates more violently in the early production stage, and the peak value reached is higher. Through comparative analysis, it can be known that when the injection-production ratio is 1:1, the maximum gasoline production ratio is about  $12.5 \times 10^3 \text{ Sm}^3 \cdot \text{m}^{-3}$ . In the later stages of production, the production gas-oil ratio curve with an injection-production ratio of 0.75:1 is significantly higher than the other two cases. The production gas-oil ratio curves with injection-production ratios of 0.5:1 and 1:1 are approximately coincident and are stable around  $3.1 \times 10^3 \text{ Sm}^3 \cdot \text{m}^{-3}$ . Therefore, it can be seen that the production effect of the injection-production ratio of 0.5:1 and 1:1 is better than that of the injection-production ratio of 0.75:1.

The cumulative production curves of condensate gas and condensate oil with different gas injection ratios are shown in Figure 14.

It can be seen from Figure 14(a) that under the same production pressure, the cumulative gas production curves of the three different gas injection methods are quite different, but they all show an increasing trend. With the gradual extension of the production time, the gas production rate with an injection-production ratio of 0.75:1 is the fastest and the cumulative gas production always remains the largest, followed by the injection-production ratio 1:1. The gas production rate and cumulative gas production with an injection-production ratio of 0.5:1 is the lowest. Therefore, through comparative analysis, it can be known that the gas production effect with an injection-production ratio of 0.75:1 is the best.

It can be seen from Figure 14(b) that under the same production pressure, the cumulative oil production curves of the three different gas injection methods are quite different, but they all show a trend of increasing first and then becoming stable. In the early stage of oil production ( $t < 300$  min), the oil production rate and cumulative oil production with an injection-production ratio of 0.5:1 are greater than those of the other two groups. Moreover, the oil production rate and cumulative oil production with an injection-production ratio of 0.75:1 are greater than the case where the injection-production ratio is 1:1. In the middle and late stages ( $t = 400\sim 800$  min), the oil production rate and cumulative oil production of 1:1 injection-production ratio gradually increase, and the final oil production stabilizes at around 23.3 ml. The cumulative oil production under this condition surpasses the other two injection-production ratios, which means that the condensate recovery effect is the best under this condition.

The final recovery factor histogram of different gas injection methods is shown in Figure 15.

It can be seen from Figure 15 that as the injection-production ratio increases, the condensate gas recovery factor gradually decreases, while the condensate oil recovery factor gradually increases. When the injection-production ratio is 0.5 : 1, the recovery factor of condensate gas reaches its maximum value, which is 80.05%. When the injection-production ratio is 1 : 1, the condensate recovery rate reaches the maximum value, which is 83.31%. Therefore, through comparative analysis, it can be known that the increase of injection-production ratio is beneficial to the improvement of condensate oil recovery.

## 5. Summary and Conclusions

- (1) Different gas injection methods have different effects on improving the recovery of condensate oil. The top gas injection has a high oil production rate and a low gas-oil ratio. When the production pressure is reduced from 58 MPa to 39 MPa, oil is produced rapidly and the cumulative oil production is the largest. Therefore, under the same production conditions, top gas injection is the best choice, followed by shaft gas injection, and bottom gas injection has the worst effect
- (2) The conclusions obtained from the comparative analysis of gas injection media are basically consistent with those obtained by previous scholars. When the pressure drops below the dew point pressure, the output of condensate increases sharply, the production effect of carbon dioxide injection is the best, and the condensate recovery rate reaches the maximum with a value of 96.5%
- (3) The higher of the injection-production ratio, the more stable the production and recovery rate of condensate oil and gas. The injection-production ratio and the recovery factor of condensate gas change in inverse proportion, and it is in direct proportion to the recovery factor of condensate oil. When the injection-production ratio is 1 : 1, the condensate recovery rate reaches the maximum value of 83.31%
- (4) The research in this paper is based on the Yaha condensate gas reservoir. Therefore, the conclusions obtained in this research can provide certain reference value and guiding significance for the injection parameters of similar gas reservoirs

## Data Availability

The (data type) data used to support the findings of this study are available from the corresponding author upon request.

## Additional Points

**Highlights.** (1) The Yaha gas condensate reservoir will appear reversed condensate in the later stage of exploitation.

(2) Indoor physical model research helps to understand the mechanism of gas migration. (3) Optimizing the condensate gas injection scheme helps to improve the recovery efficiency in the later stages of development.

## Conflicts of Interest

The authors declare that they have no conflicts of interest.

## Acknowledgments

This study was supported by the China Petroleum Major Science and Technology Project (Phase III) (No. 2018E-1804).



## References

- [1] Z. Su, Y. Tang, H. J. Ruan, Y. Wang, and X. Wei, "Experimental and modeling study of CO<sub>2</sub> - Improved gas recovery in gas condensate reservoir," *Journal of Petroleum*, vol. 3, no. 1, pp. 87–95, 2017.
- [2] Z. Xie, H. Y. Deng, and W. Lei, "Study on phase characteristics of condensate gas reservoir with oil ring," *Drilling & Production Technology*, vol. 32, no. 2, 2009.
- [3] P. Guo and Z. C. Li, "Study on the phase behavior of formation fluid in Nanyishan-E3 condensate gas reservoir," *Natural Gas Industry*, vol. 19, no. 5, pp. 43–46, 1999.
- [4] L. X. Zhou and X. B. Chu, "Study on the phase behavior of Fengshen-1 condensate gas reservoir," *Journal of Southwest Petroleum University*, vol. 30, no. 3, pp. 81–84, 2008.
- [5] H. J. Lu, *Study on the Distribution of Favorable Sedimentary Facies Belts in the Upper Paleozoic in Block Zhao 51 of Sulige Gas Field*, Northwest University, Xi'an, 2014.
- [6] R. Q. Ming, H. Q. He, and Q. F. Hu, "A new method for prediction of water breakthrough time in bottom water condensate gas reservoir," *Special Oil and Gas Reservoirs*, vol. 25, no. 5, pp. 99–103, 2018.
- [7] R. Q. Ming, H. Q. He, and Q. F. Hu, "A new model for predicting water breakthrough time of high-yield wells in edge water condensate gas reservoirs," *Special Oil and Gas Reservoirs*, vol. 25, no. 2, pp. 76–79, 2018.
- [8] Y. Tang, Z. M. Du, Z. L. Qi, S. L. Li, and L. Sun, "Current status and future development of the study on removal of near-wellbore damage in low-permeability gas condensate wells," *Natural Gas Industry*, vol. 27, no. 6, pp. 88–92, 2007.
- [9] J. J. Sheng, "Increase liquid oil production by huff-n-puff of produced gas in shale gas condensate reservoirs," *Journal of Unconventional Oil and Gas Resources*, vol. 11, pp. 19–26, 2015.
- [10] S. L. Li, Y. Pan, and L. Sun, "New ideas for improving the recovery efficiency of condensate gas reservoirs," *Natural Gas Industry*, vol. 28, no. 9, 2008.
- [11] H. Lu, G. Ma, L. Cao, and M. Azimi, "Optimization of light hydrocarbon recovery system in condensate gas field," *Energy Reports*, vol. 5, pp. 1209–1221, 2019.
- [12] M. Wang, S. Chen, and M. Lin, "Enhancing recovery and sensitivity studies in an unconventional tight gas condensate reservoir," *Petroleum Science*, vol. 15, no. 2, pp. 305–318, 2018.
- [13] L. Jingsong, L. Xiangfang, K. Xiaodong, T. Min, and Z. Yongyi, "New method of cyclic gas injection for condensate gas reservoirs," *Natural Gas Industry*, vol. 24, pp. 76–79, 2004.

- [14] P. C. Dong, T. W. Jiang, M. L. Tang, and W. Xie, "Optimization of Yaha-5 condensate gas reservoir development method," *Daqing Petroleum Geology and Development*, vol. 26, no. 3, pp. 51–54, 2007.
- [15] F. Lu, *Gas injection enhanced oil recovery phase behavior and seepage mechanism of Dalaoba condensate gas reservoir*, Journal of Southwest Petroleum University, Chengdu, 2019.
- [16] C. W. Lu, "Optimize gas injection to improve the recovery rate of condensate gas field," *Petrochemical Technology*, vol. 23, no. 1, 2016.
- [17] Y. L. Hu, B. Z. Li, and Z. D. Sun, "Selection of mining methods for condensate gas reservoirs," *Natural Gas Geoscience*, vol. 14, no. 5, pp. 398–401, 2003.
- [18] J. Liu, *Fine description of gas reservoirs in Wenjisang Gas Field*, Northwest University, Xi'an, 2007.
- [19] J. P. Shao and B. R. Niu, "Low-permeability condensate gas reservoir development technology," *China Petroleum and Petrochemical*, vol. 1, no. 1, pp. 62–63, 2007.
- [20] C. F. Hu, K. Zheng, and X. P. Hu, "Application of reservoir numerical simulation technology in the development of condensate gas reservoirs with oil rings," *Petroleum Geology and Engineering*, vol. 24, no. 3, pp. 46–49, 2010.
- [21] A. He, C. Zou, Y. Cui, J. Yan, H. Zhang, and Y. Tang, "Research on increasing the production of condensate with CO<sub>2</sub> huff and puff in South A condensate gas reservoir of Zanarol Oilfield," *Reservoir Evaluation and Development*, vol. 10, no. 3, 2020.
- [22] A. Hassan, M. Abdalla, M. Mahmoud, G. Glatz, A. al-Majed, and A. al-Nakhli, "Condensate-banking removal and gas-production enhancement using thermochemical injection: a field-scale simulation," *Processes*, vol. 8, no. 6, p. 727, 2020.
- [23] T. Wan and Z. J. Mu, "The use of numerical simulation to investigate the enhanced Eagle Ford shale gas condensate well recovery using cyclic CO<sub>2</sub> injection method with nano-pore effect," *Fuel*, vol. 233, pp. 123–132, 2018.
- [24] J. Jiang and R. M. Younis, "Compositional modeling of enhanced hydrocarbons recovery for fractured shale gas-condensate reservoirs with the effects of capillary pressure and multicomponent mechanisms," *Journal of Natural Gas Science and Engineering*, vol. 34, pp. 1262–1275, 2016.
- [25] Q. H. Feng, B. B. Deng, Y. Z. Yang, J. C. Zhang, X. H. Peng, and J. K. Yuan, "Reasonable and efficient gas injection development method for tight sandstone condensate gas reservoirs in Ordos Basin," *Daqing Petroleum Geology and Development*, vol. 39, no. 6, pp. 55–62, 2020.
- [26] G. H. Yuan, R. J. Wang, S. G. Luo, L. Shang, and X. Z. Wang, "Laboratory test study on enhanced oil recovery by methane injection in highly saturated condensate gas reservoirs," *Inner Mongolia Petrochemical Industry*, vol. 34, no. 11, pp. 21–22, 2008.
- [27] D. L. Hou, *Study on the mechanism and storage of CO<sub>2</sub> enhanced oil recovery in near-critical condensate gas reservoirs*, Southwest Petroleum University, Chengdu, 2014.
- [28] S. L. Sui, P. Guo, J. F. Du, and L. X. Xiao, "The experiment of gas condensate depletion in low-permeability porous medium," *Journal of Southwest Petroleum University*, vol. 32, no. 3, pp. 97–100, 2010.

## Research Article

# A New Method of Central Axis Extracting for Pore Network Modeling in Rock Engineering

Xiao Guo <sup>1</sup>, Kairui Yang <sup>1</sup>, Haowei Jia,<sup>1</sup> Zhengwu Tao,<sup>2</sup> Mo Xu,<sup>1</sup> Baozhu Dong,<sup>3</sup> and Lei Liu<sup>4</sup>

<sup>1</sup>State Key Laboratory of Oil and Gas Reservoir Geology and Exploitation, Southwest Petroleum University, Chengdu, China

<sup>2</sup>Research Institute of Exploration and Development Korla, PetroChina Tarim Oilfield Co., Korla, China

<sup>3</sup>Kenli 3-2 Oilfield, Bonan Operation Company, Tianjin Branch of CNOOC (China) Co., Ltd., Tianjin, China

<sup>4</sup>Sichuan Baoshihua Xinsheng Oil and Gas Operation Service Co., Ltd. of Southwest Oil and Gas Field Branch, China

Correspondence should be addressed to Kairui Yang; 201511000118@stu.swpu.edu.cn

Received 14 July 2021; Revised 30 August 2021; Accepted 7 September 2021; Published 12 October 2021

Academic Editor: Chao Zhang

Copyright © 2021 Xiao Guo et al. This is an open access article distributed under the Creative Commons Attribution License, which permits unrestricted use, distribution, and reproduction in any medium, provided the original work is properly cited.

Characterizing internal microscopic structures of porous media is of vital importance to simulate fluid and electric current flow. Compared to traditional rock mechanics and geophysical experiments, digital core and pore network modeling is attracting more interests as it can provide more details on rock microstructure with much less time needed. The axis extraction algorithm, which has been widely applied for pore network modeling, mainly consists of a reduction and burning algorithm. However, the commonly used methods in an axis extraction algorithm have the disadvantages of complex judgment conditions and relatively low operating efficiency, thus losing the practicality in application to large-scale pore structure simulation. In this paper, the updated algorithm proposed by Palágyi and Kuba was used to perform digital core and pore network modeling. Firstly, digital core was reconstructed by using the Markov Chain Monte Carlo (MCMC) method based on the binary images of a rock cutting plane taken from heavy oil reservoir sandstone. The digital core accuracy was verified by comparing porosity and autocorrelation function. Then, we extracted the central axis of the digital pore space and characterize structural parameters through geometric transformation technology and maximal sphere method. The obtained geometric parameters were further assigned to the corresponding nodes of pore and throat on the central axis of the constructed model. Moreover, the accuracy of the new developed pore network model was measured by comparing pore/throat parameters, curves of mercury injection, and oil-water relative permeability. The modeling results showed that the new developed method is generally effective for digital core and pore network simulation. Meanwhile, the more homogeneity of the rock, which means the stronger “representative” of binary map the rock cutting plane, the more accurate simulated results can be obtained.

## 1. Introduction

Porous media, such as metal, wood, soil, and rock, is one of the most common substances in daily life [1–3]. The common character of all porous materials is that the internal pore structure usually governs the flow of fluid and electric current inside the media [4–6]. Even for the two materials with equal porosity, the fluid flow behaviors may be still different because of the different spatial distribution of internal pore structures, the connection types, and the shape or size of the pore and throat [7–9]. Therefore, in order to comprehensively study porous media, characterizing pore network

structures is of significant importance. This is typically true for petroleum/reservoir engineering, as pore network structures determine the capacity of hydrocarbon accumulation and also the flow behavior.

As we are approaching the end of conventional hydrocarbon resources, a giant potential of unconventional resources of energy has been manifested. However, there are difficulties with unconventional resources in exploitation, such as the very low permeability of tight oil/gas reservoir and the high viscosity of heavy oil in heavy oil reservoir. So much attention and research have been paid to heavy oil reservoirs, as it accounts for a large proportion



in oil and gas resources. Since reservoir macroscopic properties (i.e., permeability and capillary pressure) are controlled by its microstructure, especially for heavy oil reservoirs where the oil viscosity is so high, it is necessary to examine the characteristics of pore networks at microscale and eventually improve oil and gas recovery. Thus, in order to provide efficient production from heavy oil reservoirs, sufficiently reliable information about the pore structure of the hosting rock is required.

In fact, due to specially designed experimental setups and complicated operation procedures, traditional rock mechanics and geophysical experiments are usually difficult and time-consuming methods to extract pore network [10]. Meanwhile, the rapid development of computer technology and the explosive growth of computing power make it possible to perform large-scale simulations using rock digital geometric data [11, 12]. The digital core modeling can provide detailed information on rock internal pore network, and the simulation results can be also compared with laboratory observations to comprehensively understand rock microstructures.

The current computational study method focuses on rock microstructures mainly and consists of (i) digital core model and (ii) pore network model. For the digital core model, it can accurately capture the pore network properties based on the numerical reconstruction of data obtained from rock geophysics tests. Specifically, the reconstructed digital core using data from X-ray CT scanning could present almost the same statistical characteristics as the real core. Therefore, the modeling results via this type of digital core can truly reflect the rock microscopic properties. Given the natural features for capturing all detailed microstructures, the reconstructed pore networks by X-ray CT scanning are very complex. This raises some difficulties for core-scale numerical simulation (i.e., seepage simulation and acoustic and electrical characteristic simulation), as it needs very high computation to reflect every detail of microstructures while has very limited contribution for accuracy improvement [13–15]. Therefore, urgent needs are calling to develop a new method which can retain the topological geometry properties of real core pore space and with far less computing power to improve modeling efficiency.

The pore network model is one of such promising models that is efficient and accurate [16, 17]. By reasonably simplifying the microscopic details of pore space, the pore network model can achieve similar topological and geometric structures as digital core while requiring much less computing power [18–20]. Since the first two-dimensional pore network model introduced by Fatt [21–23] in 1956, a wide range of pore network models have been developed, which are mainly divided into two categories: (1) regular topological pore network model and (2) real topological pore network model. The regular topological pore network model consists of pores and throats that are regularly arranged in plane or space. By assigning different values of pore/throat shape and size, this model could present a certain degree of heterogeneity. However, the uniform distributions of pores and throats in the regular topological network cannot represent the high complexity of pore structures within the real

rock, which constrains the application in numerical simulation. On the other hand, the real topological pore network model is developed on the basis of digital core. Therefore, it has the equivalent topological structure of digital/real pore space and is more accurate for pore network modeling. Previously, a variety of methods were proposed to construct this type of model. For example, Zhao et al. [24] proposed a multidirectional slice scanning method to characterize the values of internal pore/throat. They defined the located in situ minimum value as throat while pores were hardly detected. Lindquist et al. [25], Sheppard et al. [26], and Prodanovic et al. [27] used the pore central axis method to characterize the topological structure of pore space, as the central axis can accurately represent the characteristics of topological networks. The internal pores were defined as the nodes on the central axis, and the nodes with minimum area were defined as the throat. Later, Delerue and Perrier [28] developed a method that can build Voronoi polyhedron in any type of pore space and subsequently form pore networks based on the established polyhedron. This method was applied by Okabe and Blunt [29] to establish pore networks for Berea sandstones, but they found that the generated topological networks were poorly structured and concluded that the Voronoi polyhedron method is not a suitable tool for the pore network modeling of digital core. Silin et al. [30] established a pore network model on Fontainebleau sandstones by using the maximum sphere method, and they calculated the mercury injection capillary pressure (MICP). They reported that although the developed model with the maximum sphere method seems to be reasonable, the connectivity number (the number of throats connected with a pore) of pore/throat was still relatively higher than the actual value.

It is worth mentioning that the combination of the central axis method and maximum sphere method has been widely applied to characterize pore space topological structure and identify pores and throats. The central axis can be obtained through thinning algorithm [31, 32] and burning algorithm [33]. However, the complicated judgment conditions of these algorithms usually present relatively low running efficiency. Meanwhile, the central axis extraction algorithm proposed by Palágyi and Kuba [34] only requires to judge the neighborhood relationship of pore voxel, so that it dramatically reduces the system calculation amount. In the discrete system, a voxel has no more than 6, 18, and 26 neighboring voxels, when the distance between neighboring voxels is defined as no more than 1,  $\sqrt{2}$ , and  $\sqrt{3}$  unit lengths. Therefore, when extracting the central axis with the algorithm proposed by Palágyi and Kuba, only 27 neighboring voxels at most rather than all points or many points of local area need to be analyzed in one iteration. Furthermore, six deletion templates in the algorithm simplify the analysis of neighboring voxels, thus making this central axis method computationally effective. While this method has been widely used in the study of heart and cerebral vessels [35–37] and pulmonary vessels [38, 39] of human, early embryonic mouse heart [40], and plants [41] and shows satisfactory results, to the best of our knowledge, it has not ever been applied petroleum engineering for core-scale pore network simulation.



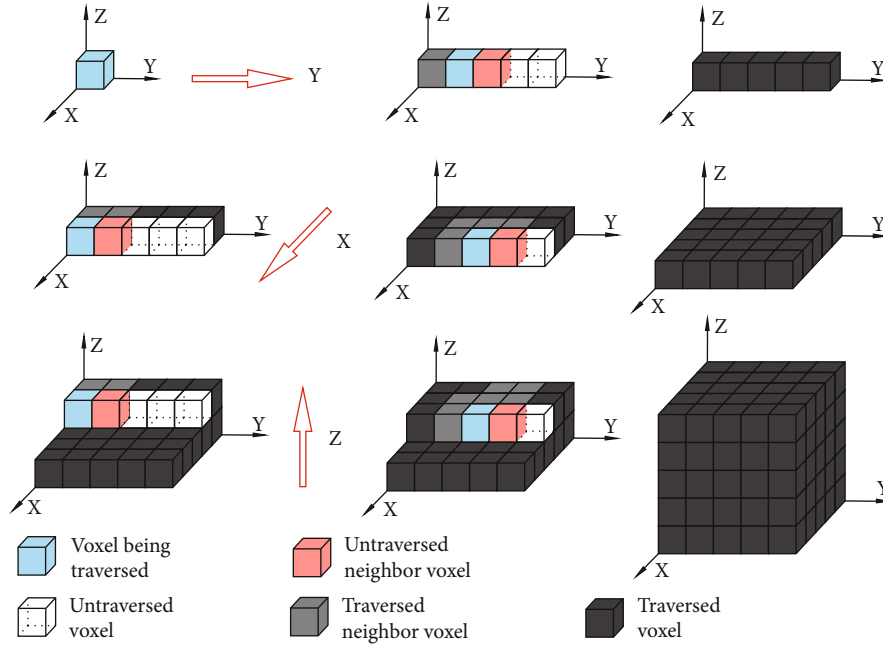


FIGURE 1: Reconstruction of digital core based on the MCMC method [43].

Therefore, in this paper, we try to use this central axis extraction algorithm to extract the pore topological structure of reservoir rock and compare the modeling results with the curves of MICP and oil-water relative permeability. Firstly, four images of binary cutting plane from four individual sandstones were used for the reconstruction of digital core with the MCMC (Markov Chain Monte Carlo) method [42]. Then, pore axis networks were extracted by applying the refinement algorithm proposed by Palágyi and Kuba. Finally, pore networks were obtained by adding the identified pore throat information on the pore central axis network. In order to construct the digital core and pore network model, Visual Basic 6.0 was used.

## 2. Methodology

**2.1. Reconstruction of Digital Core.** Markov chain describes a state sequence that has lack-of-memory or memoryless properties, where the value of each state depends on the previous finite states and is independent of other states. The probability of this state is called the transfer probability. The calculating transfer probability is the core in the application of Markov chain, but the calculation procedures are very complex. To address this issue, Wu et al. [43] introduced the neighborhood concept, namely, that the state of a certain point only depends on the states of several nearby points. In this work, we use a traversal scanning algorithm (based on the MCMC method) to generate sufficient image size to ensure the formed digital core has the same statistical characteristics with the original image. In general, the MCMC method requires three different two-dimensional images as input files to build digital cores on the corresponding three coordinate axis planes. But when the core presents high homogeneity or lacks images of good

quality, the identical image can be also used to construct a 3D digital core.

The procedure's steps of 3D digital core construction through the MCMC method are listed as follows (Figures 1 and 2); the  $n$ -neighborhood, which consists of one voxel being traversed, traversed voxels, and one untraversed voxel adjacent (component of partial  $n$ -neighborhoods) to the voxel being traversed, denotes that the number of voxels involved in one iteration of simulation is  $n$ .

- (1) Use calculated porosity from core scanning images as the conditional probability of the first voxel state
- (2) Generate voxels on the first row of the first layer along  $Y$  axial direction. The second voxel state in the first row is simulated by the 2-neighborhood, and the next voxel is simulated by 3-neighborhood. Their condition probabilities are derived from the 6-neighborhood of core scanning image in  $XY$  plane
- (3) Repeat step (2) to form voxels in  $X$  axial direction. The edge voxels are simulated by 3-neighborhood and 4-neighborhood, whereas the inner voxels are simulated by 5-neighborhood and 6-neighborhood. Their condition probabilities are also derived from the 6-neighborhood of core scanning image in  $XY$  plane
- (4) Repeat step (3) to form voxels in  $Z$  axial direction. From the second row of the second layer, the edge voxels are simulated by 9-neighborhood and 10-neighborhood, and the inner voxels are simulated by 14-neighborhood and 15-neighborhood. Their condition probabilities are obtained from the combination of 6-neighborhood systems of three planar core scanning images

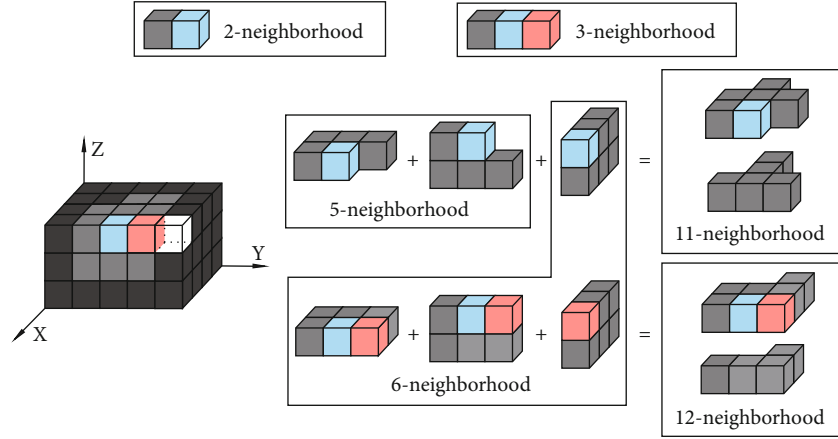


FIGURE 2: The  $n$ -neighborhoods contained in 15-neighborhood (synthesized from 11-neighborhood and 12-neighborhood).

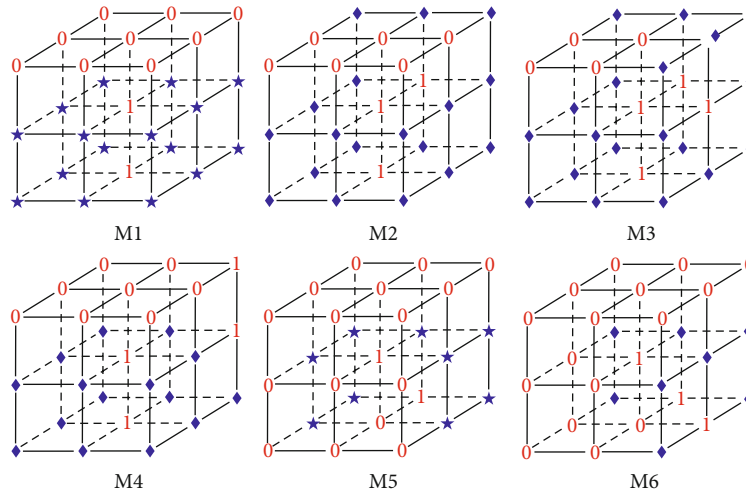


FIGURE 3: Deletion templates along the  $U$  direction. “★,” “1,” “0,” and “◆” represent the points that at least one of them is black, black point, white point, and the point either black or white, respectively [34].

**2.2. Correction of Digital Core.** Considering the intrinsic properties of the image segmentation process and reconstruction algorithm, isolated skeleton and pores often exist in the reconstructed digital core [44]. The isolated skeleton needs to be removed as it would form redundant pores and faulty connecting channels, which actually do not exist. For the isolated pores, they may exist in real cases, but the contribution of these pores to fluid flow is negligible. Besides, these isolated pores could affect the simulated results of core pore topological structure, the calculation of pore structure parameters, and the simulation of microscopic seepage. Therefore, these pores also need to be corrected.

In this paper, we used the Seed Filling Method to delete isolated skeleton and unreasonable isolated pores. The adjacent skeleton voxels or pore voxels are firstly put into a set  $\Omega$ . Then, we count the number of elements in set  $\Omega$  and compare the number with threshold  $x$  to determine whether the set belongs to an isolated skeleton voxel set or an isolated pore voxel set. The detailed procedures of removal of

isolated pores (similar steps can be used for isolated skeleton correction) are explained as the following:

- (1) Set the threshold  $x$  (the value of  $x$  varies with target cores)
- (2) Travers all pore voxels of digital core until finding the pore voxel A without a label
- (3) Take A as seed and assign it with a label. Then, push all pore voxels of the seed but without a label, back to the stack
- (4) Pop up the top element B, assign it with the same label, and store it in the set  $\Omega$ . Then, put all pore voxels in the 26-neighborhood of element B but without the label in the set  $\Omega$
- (5) If the number of elements in set  $\Omega$  is greater than the threshold  $x$ , go back to step (2). Otherwise, repeat step (4) until the stack is empty. Then, a connected pore space containing A in the digital core can be

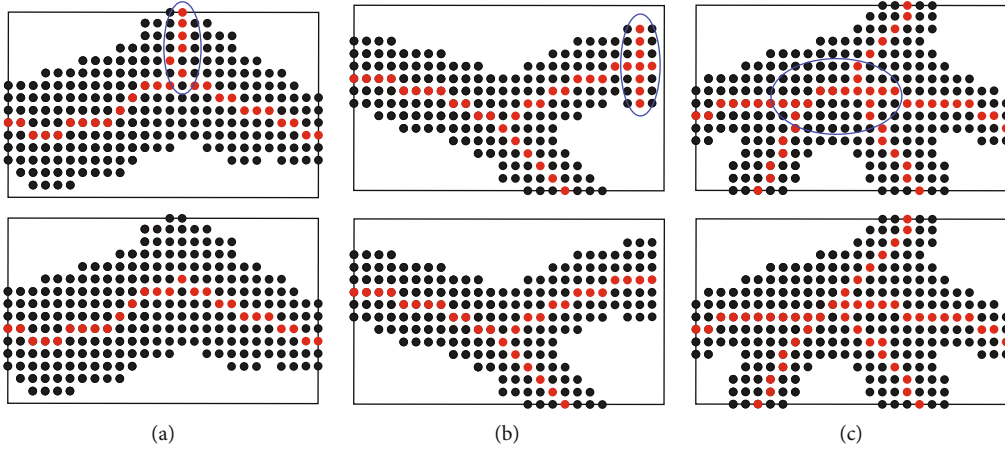


FIGURE 4: Optimization of pore axis: (a) optimization of short branch central axis; (b) correction of boundary central axis; (c) correction of central axis node.

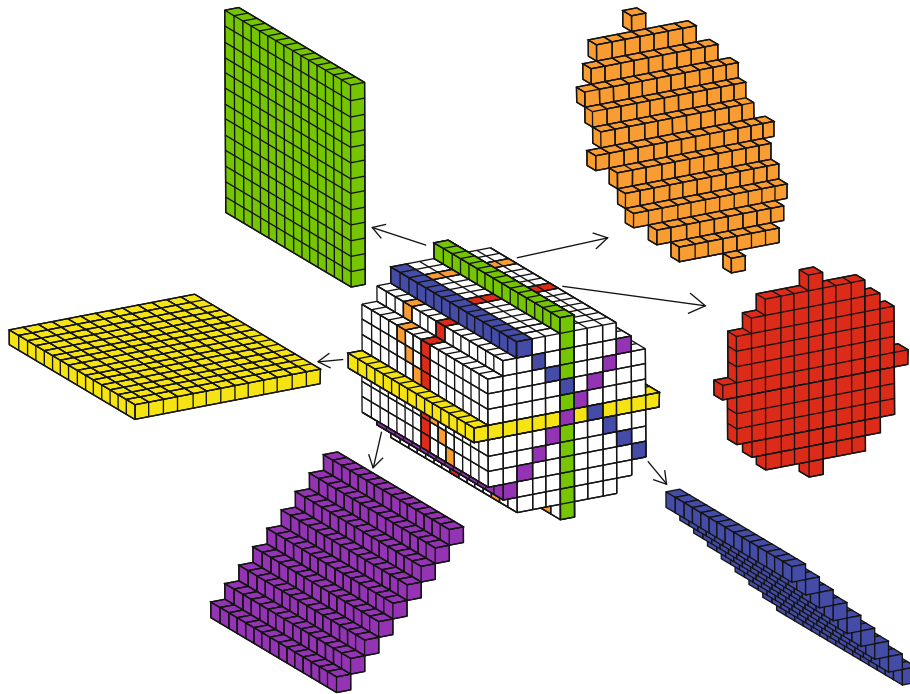


FIGURE 5: Section with different cutting angles.

found, and the pore voxels in this area are all marked with the label

- (6) If the number of elements in set  $\Omega$  is less than the threshold  $x$ , delete all the pore voxels (converted into skeleton voxels) belonging to the set  $\Omega$ . Otherwise, return to step (1) until all pore voxels are marked with the label

2.3. *Extraction of Pore Axis.* The theory and criterion proposed by Bakken and Eliassen [45], Kong and Rosenfeld [46], and Ma [47] lay the foundation for the pore axis extraction. Later, Palágyi and Kuba [34] developed a refinement

algorithm based on delete template. Besides, Wildenschild and Sheppard [32] developed a fully parallel refinement algorithm which is on the basis of theory of Ma [47], and Lee et al. [48] proposed another refinement algorithm (the LKC algorithm) with consideration of the octree algorithm. Among these extraction algorithms, the method developed by Palágyi and Kuba only requires to consider the neighborhood relationship information, which is more efficient than other algorithms.

The core concept of this algorithm is to transform the black points (pore voxels) that match deletion conditions into white points (skeleton voxels), while keeping other original white points the same. Whether the black points match

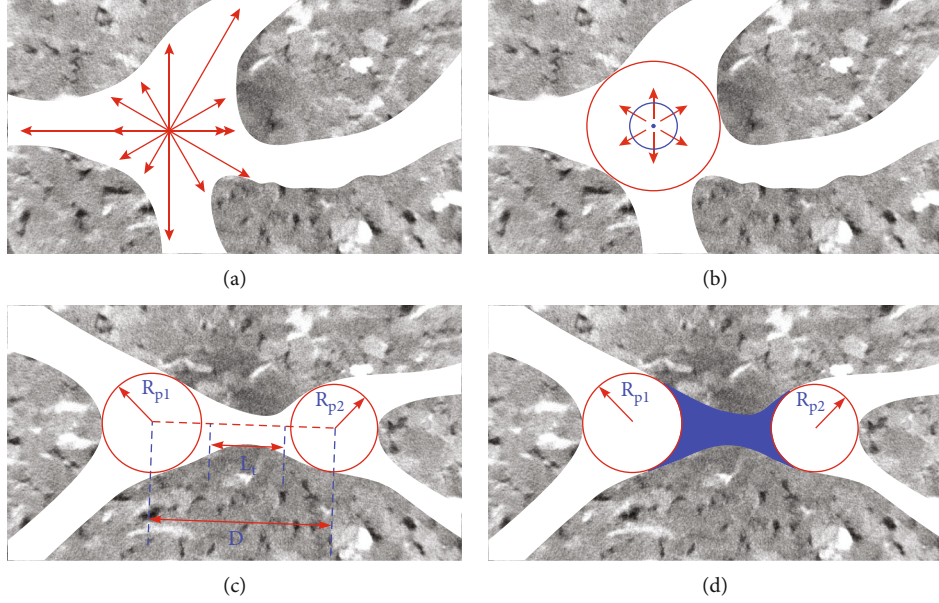


FIGURE 6: Method for analyzing pore-throat parameters: (a) ray emits in cutting plane; (b) maximum sphere method; (c) length of throat measurements; (d) throat section (blue plane).

TABLE 1: Scanning parameters of each core sample.

	Sandstone a	Sandstone b	Sandstone c	Sandstone d
Diameter (mm)	2.00	2.00	2.00	2.00
Length (mm)	2.60	2.80	2.70	2.80
Porosity (%)	26.90	18.82	19.93	14.07
Pixel size ( $\mu\text{m}$ )	2.25	2.25	2.25	2.25

the deletion conditions or not is mainly determined by the definition of connectivity in a discrete medium. In a 3D discrete system, voxels of different phases (skeleton and pore in this work) should have maximum and minimum number of connected neighboring voxels in the same phase correspondingly to avoid situations where voxels of both phases are disconnected or connected. When voxels of one phase have the maximum number of connected voxels, i.e., 26, they may connect with each other in the form of a point or a line, which do not occur between solid-phase voxels. Considering rock skeleton is solid and the simple point described by Bakken and Eliassen [45], in this work, we define that the pore voxel is connected with 26 nearby pore voxels at most and the rock skeleton voxel is connected with 6 nearby skeleton voxels at most. Therefore, the condition to delete black point depends on the relationship in its 26-neighborhood voxels. Palágyi and Kuba [34] introduced six deletion templates to judge whether the black point  $P$  should be deleted or not, and these templates actually describe six types of 26-neighborhood relations. These templates vary with deletion direction ( $U$ ,  $D$ ,  $N$ ,  $S$ ,  $E$ , and  $W$ ), whereas the deletion direction is determined by the 6-neighborhood relationship. For example, if the black point  $P$  lacks of 6-neighborhood neighbors in the  $U$  direction, then, the deletion direction is  $U$ . Figure 3 shows the

deletion templates M1 to M6 in the  $U$  direction. M1 to M6 combined with the rotation around the  $U$  direction axis (angles of rotation are  $90^\circ$ ,  $180^\circ$ , and  $270^\circ$ ) form the final deletion templates along the  $U$  direction. The meaning of each symbol in the figure is as follows: at least one “ $\star$ ” is a black point, “1” is a black point, “0” is a white point, and “ $\blacklozenge$ ” is a black or white point.

The detailed procedures for black points processing based on the aforementioned deletion principle are shown as follows:

- (1) Import binary image of the digital core into the voxel set  $P$
- (2) Select a black point  $p$  from set  $P$  to judge whether it matches deletion condition along the  $U$  direction. If  $p$  satisfies one or more neighborhood relations along the  $U$  direction, then delete  $p$ ; otherwise, keep  $p$ . Repeat this process until all black points are traversed
- (3) Change the deletion direction and select a black point  $q$  to judge whether it matches the deletion condition in that direction. If  $q$  satisfies one or more neighborhood relations in this direction, then delete  $q$ ; otherwise, keep  $q$ . Repeat this process until all black points are traversed

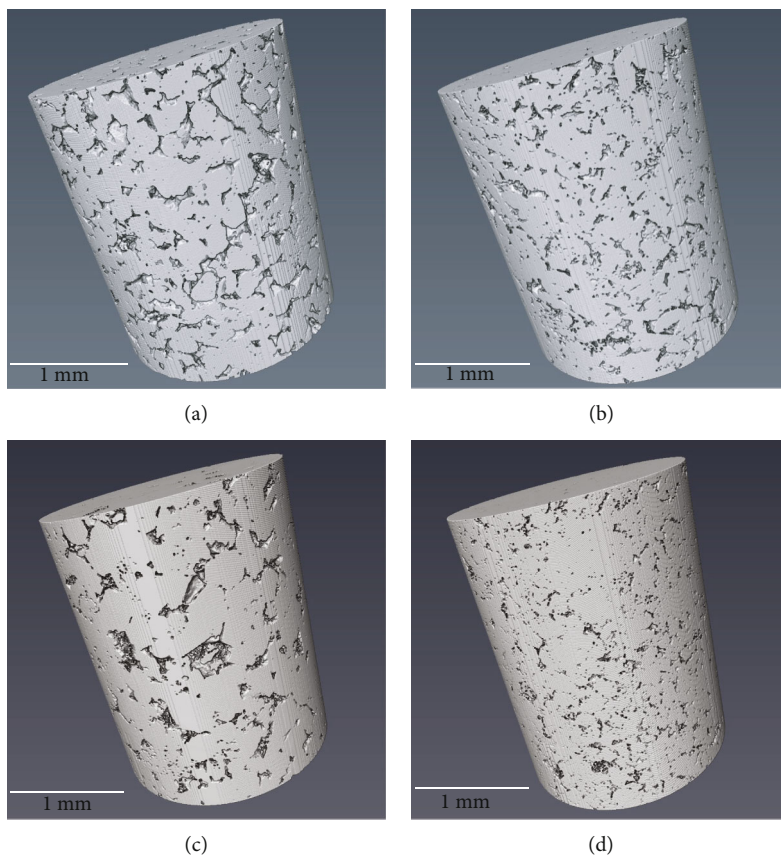


FIGURE 7: Binarized scanning result of sandstones: (a) sandstone a; (b) sandstone b; (c) sandstone c; (d) sandstone d.

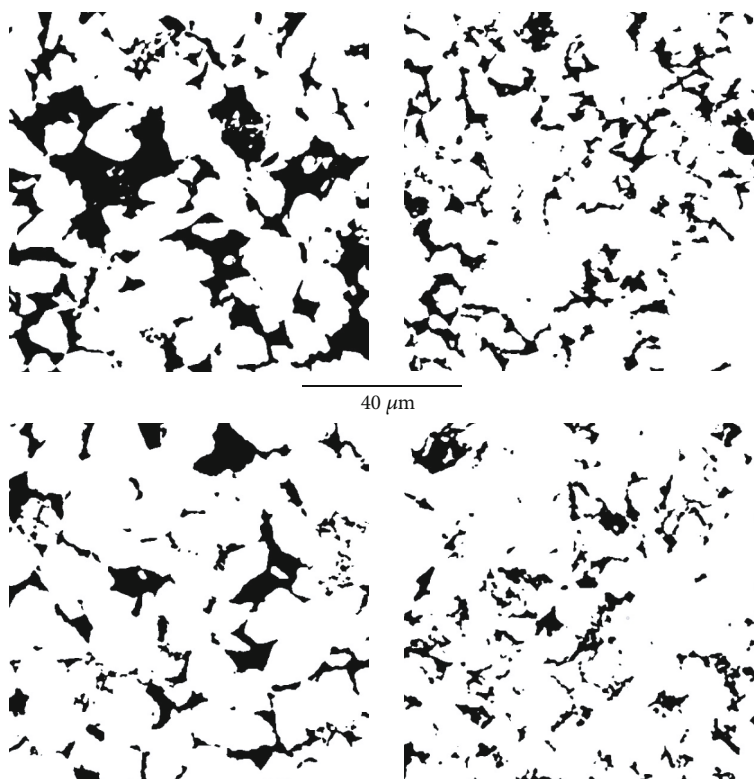


FIGURE 8: Binary section image of sandstones: (a) sandstone a; (b) sandstone b; (c) sandstone c; (d) sandstone d.



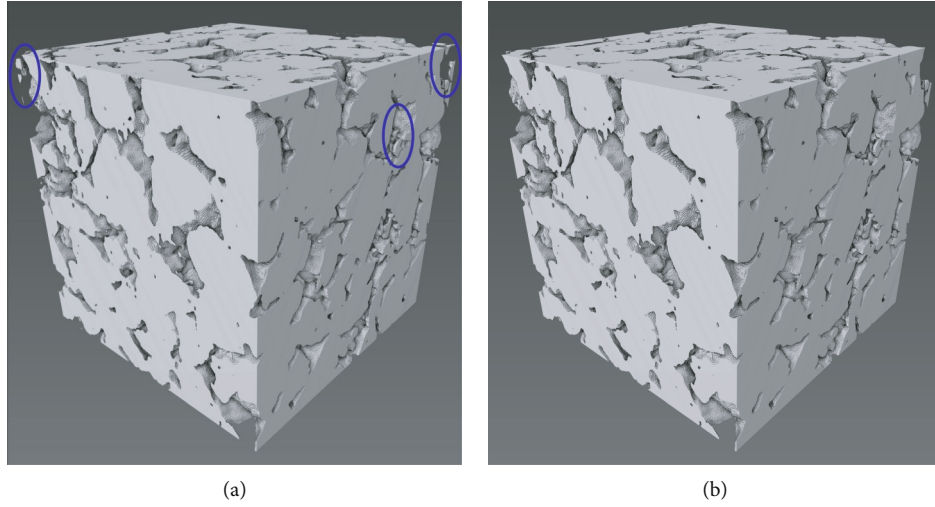


FIGURE 9: (a) Digital core a and (b) corrected digital core a.

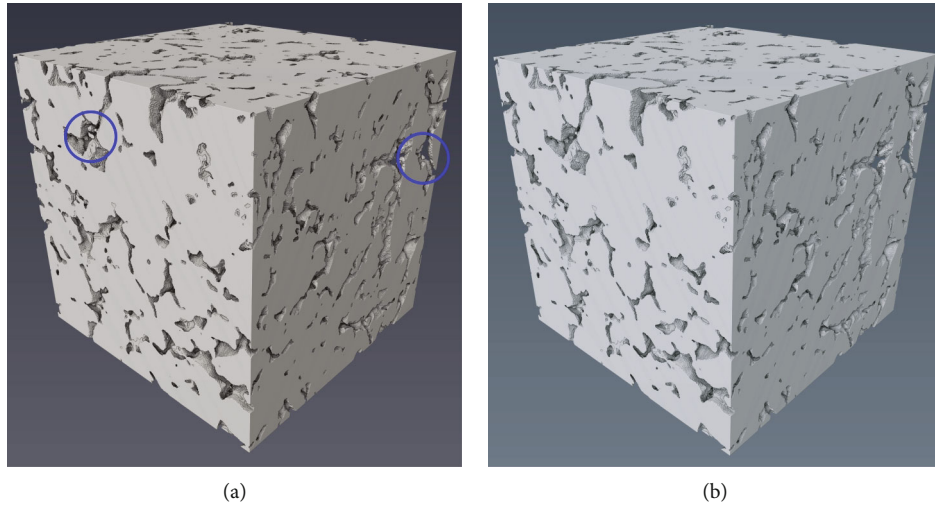


FIGURE 10: (a) Digital core b and (b) corrected digital core b.

- (4) Repeat step (2) until all black points are traversed
- (5) Repeat step (3) until the deletion process traversed along all directions
- (6) If the black points in set  $P$  do not change anymore, the deletion process ends, and all black points in set  $P$  are the central axis voxels; otherwise, repeat step (2) until black points in set  $P$  do not change (no more black points need to be deleted)

**2.4. Optimization of Pore Axis.** The aforementioned refinement algorithm would extract the central axis of pores very well, but there are some unreasonable outcomes, caused by surface noise, limit size of digital core, and complex pore structure, that could still exist. These unwanted outcomes are namely unreasonable short branches, redundant branches on the boundary, and multiple central axis nodes in a single pore. The existing of unreasonable microstructures

cannot accurately reflect the topological structure of pore space. Therefore, we need to further modify these unreasonable microstructures. In this paper, the processing method proposed by Jiang et al. [49] was applied for pore axis correction, which is explained as the following:

- (1) Delete short branch on the central axis: given the influence of surface noise, some unreasonable short branches may appear in the upper part of the pore (as shown in Figure 4(a), the black point represents the pore point, and the red point represents the central axis point). It is necessary to delete these short-axis branches where the number of black points is less than a certain threshold or the pore node radius
- (2) Correct the boundary central axis: the size limitation of digital or real core could lead to extra generation of unreasonable boundary pores and boundary central axis, as shown in Figure 4(b). To eliminate the

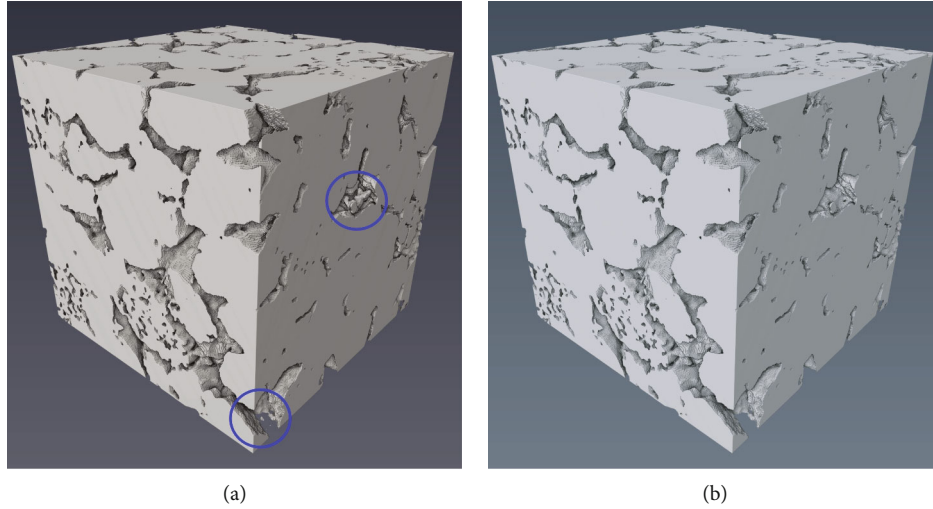


FIGURE 11: (a) Digital core c and (b) corrected digital core c.

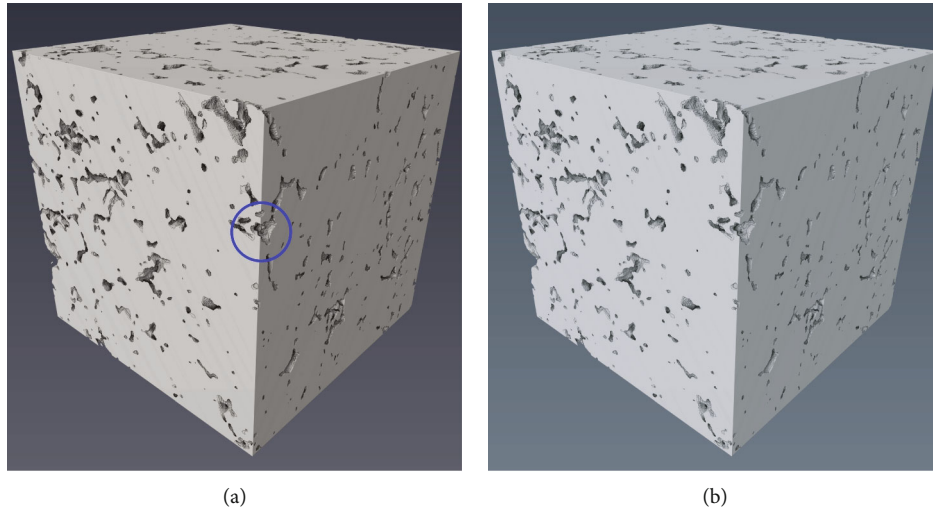


FIGURE 12: (a) Digital core d and (b) corrected digital core d.

effect of undesired central axis, we first add several layers that have the same properties of the outermost layer of digital cores, then extract the central axis, and remove the added parts

- (3) Correct central axis node: Figure 4(c) shows the complex pore structure could trigger the multiexisting of several nodes in one pore. To ensure the accurate and reasonable corresponding relationship between pore node and core pore, it is necessary to appropriately merge multiple nodes which exist in the same pore

**2.5. Construction of the Pore Network Model.** To properly develop the pore network model, the key step is to assign the geometric parameters of the pore and throat nodes on the central axis at the corresponding position; thus, the central axis network of the pore space is transformed

into the pore network model. During this construction process, the pore space geometric parameters need to be correctly identified.

The maximum sphere method is one of the most commonly used methods to analyze pore and throat parameters. However, the length of the segmented pore is usually way too large and affects the accuracy of parameters of other pores and throats. Therefore, in this paper, we applied a geometric transformation method [50] combined with the maximum sphere method [51] to segment pore space. Meanwhile, the OTSU method [52], a method to obtain the threshold value leading to the maximum between-cluster variance, was used to determine the pore/throat length and throat shape factor.

To effectively determine the pore length, geometric transformation has been widely used to cut pore space in a certain angle at the pore point (central axis node) to form a series of cutting planes, as shown in Figure 5. Then, on all cut planes, rays are emitted from the pore point at a

TABLE 2: Parameters of the sandstones.

Porosity (%)	Core a	Core b	Core c	Core d
Real core	26.90	18.82	19.93	14.07
Digital core	27.70	19.11	19.57	14.05
Digital core after correction	28.10	18.87	19.23	14.06

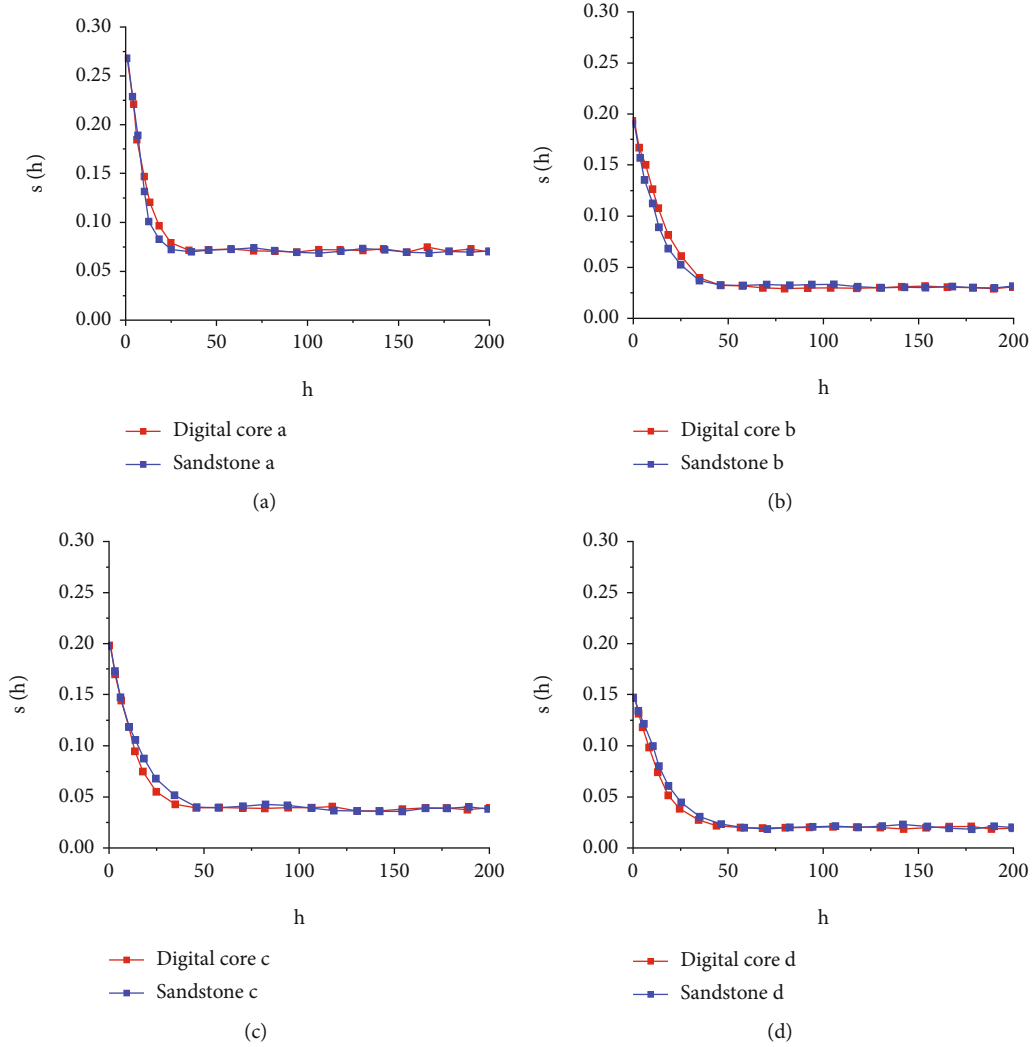


FIGURE 13: Autocorrelation functions: (a) digital core a and sandstone a, (b) digital core b and sandstone b, (c) digital core c and sandstone c, and (d) digital core d and sandstone d.

certain angle. As Figure 6(a) shows, the emitted ray would keep extending until reaching the skeleton voxel and then record the length of all line segments. These line segments can form a single set, and the pore length can be determined by the OTSU method using optimal segmentation.

The pore radius can be determined by the maximum sphere method. Taking pore point as the sphere center, the radius of the sphere is kept increasing until reaching the skeleton voxel and forms an inscribed sphere. Therefore, the pore radius is equivalent to the radius of the largest sphere, as shown in Figure 6(b).

Figure 6(c) shows that throat length  $L_t$  is given by the difference of the distance  $D$  between adjacent pore points and their respective pore radius  $R_{p1}$  and  $R_{p2}$ , i.e.,  $L_t = D - R_{p1} - R_{p2}$ . The throat radius can be also determined through the maximum sphere method which is similar to pore radius estimation. The difference is that the throat radius is the minimum value of the maximum sphere radius within the throat length.

The last parameter is the throat shape factor. We first get several cutting planes of the throat along different directions using image transformation, as shown in Figure 6(d). The



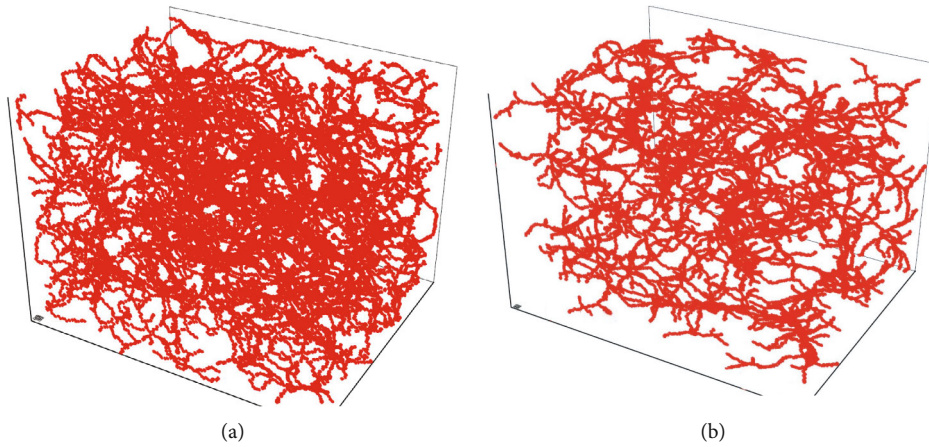


FIGURE 14: (a) Central axis network and (b) optimized central axis network of digital core a.

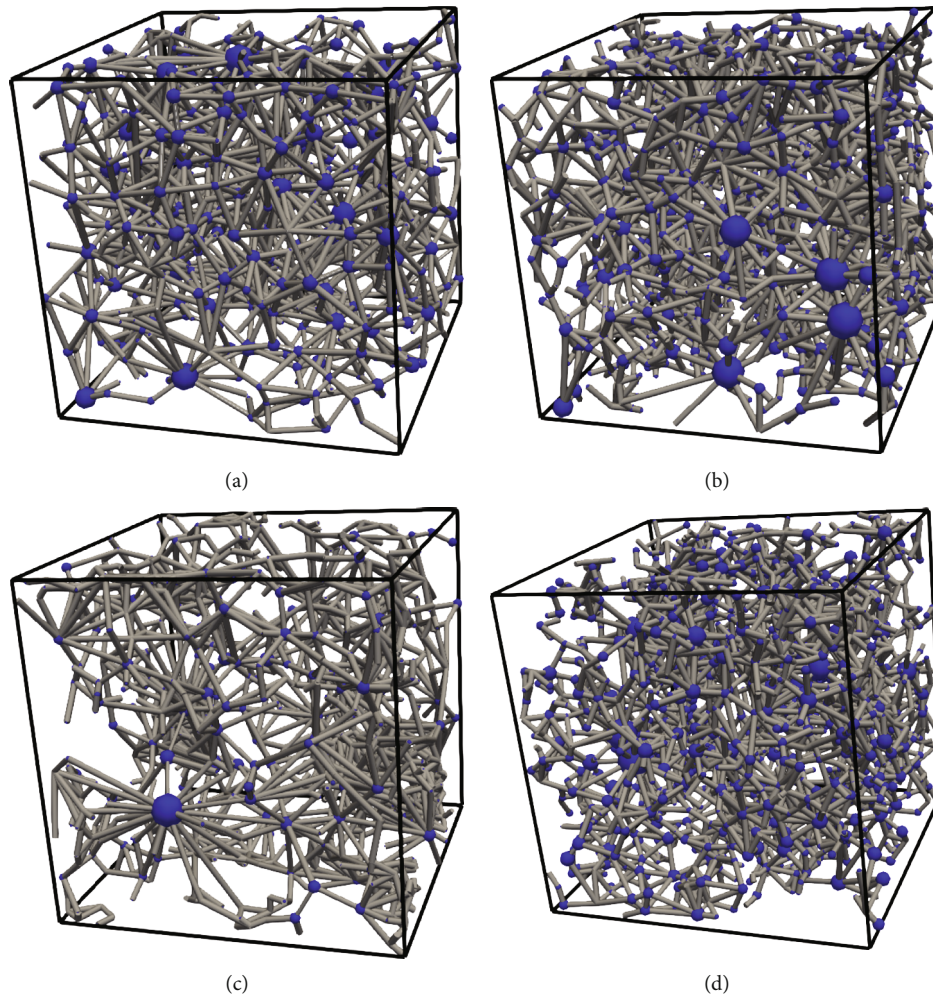


FIGURE 15: Pore network model of (a) digital core a, (b) digital core b, (c) digital core c, and (d) digital core d.

perimeter of the cutting planes can be obtained by counting boundary voxels, and the corresponding area can be obtained by counting all voxels on the plane. The shape factor of a single cutting plane can be then calculated via the shape factor calculation formula. Consequently, the shape factor of the

throat can be calculated by counting obtained shape factors of all cutting planes using the OTSU method.

Finally, we construct the pore network model by assigning the aforementioned pore structure parameters to the corresponding position on the central axis of the pore space.

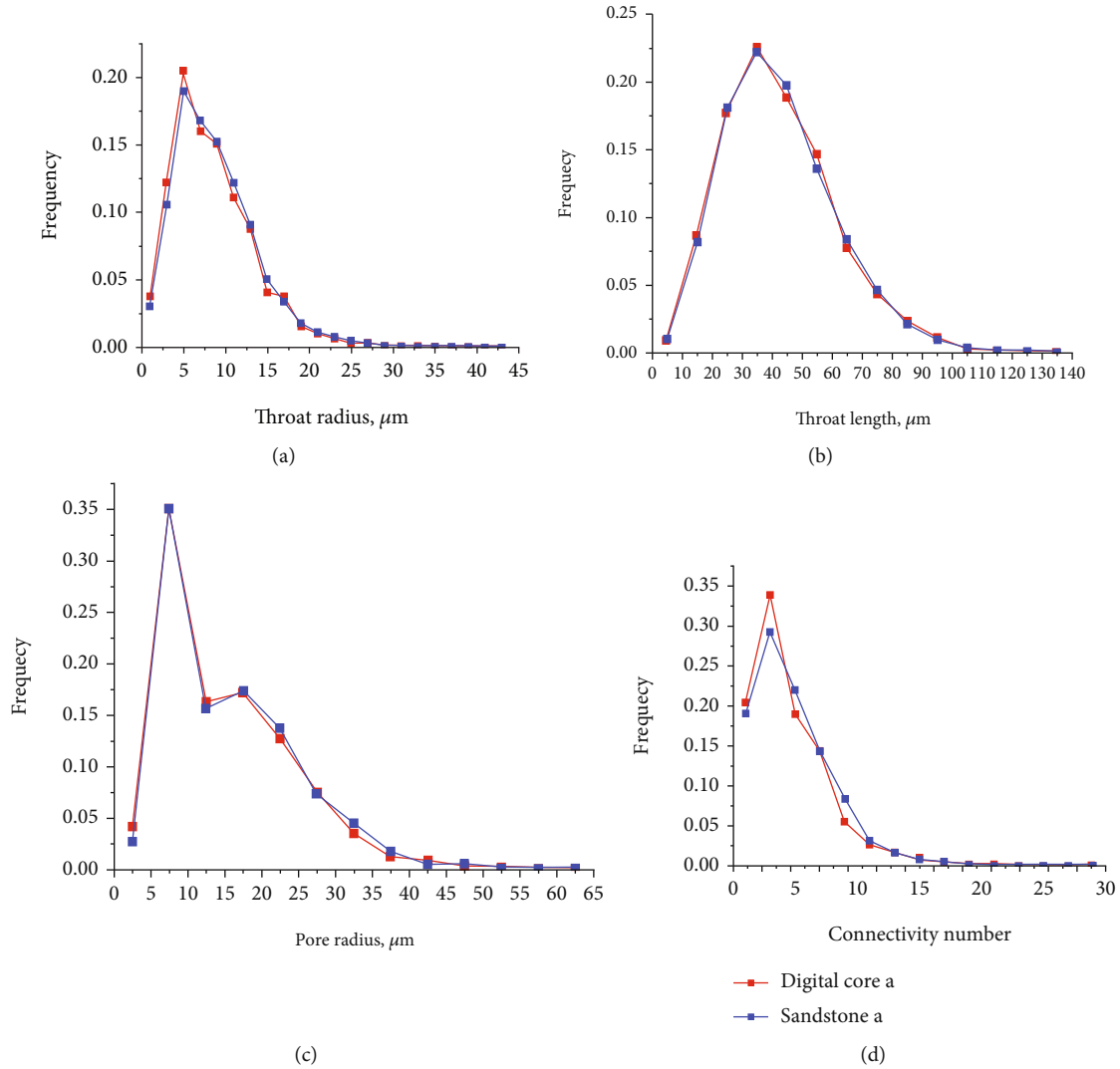


FIGURE 16: Pore-throat parameters of digital core a and sandstone a: (a) throat radius; (b) throat length; (c) pore radius; (d) connectivity number.

### 3. Validation

As aforementioned, although the digital core reconstructed by CT scanning has almost the same pore structure characteristics as the real core, the expensive cost and long consuming time still limit its application. On the other hand, the numerical reconstruction based on series of pore structure parameters or cutting plane pictures can effectively avoid these issues while presenting satisfactory running results.

In this paper, four individual core samples of heavy oil reservoir sandstones (named as sandstone a, sandstone b, sandstone c, and sandstone d) were used in X-ray CT scanning experiment. The lab equipment used for CT scanning is the Xradia MicroXCT-400 CT scanner. Basic parameters of the five cores of the CT scanning are shown in Table 1, and the binarized scanning results of four core samples are shown in Figure 7.

The initial input files for the digital core modeling method used in this work are four binary images (as shown

in Figures 8(a)–8(d)) from the CT scanning result of sandstone a, sandstone b, sandstone c, and sandstone d. And all the parameters of the control group (sandstones a, b, c, and d) of digital cores reconstructed later are all processed from the CT scanning results.

Figures 9(a), 10(a), 11(a), and 12(a) show the reconstructed digital cores with the size of  $400 \times 400 \times 400$  voxel<sup>3</sup> using the MCMC method, i.e., digital core a, digital core b, digital core c, and digital core d, respectively. Given the intrinsic properties of the image segmentation process and reconstruction algorithm, isolated skeleton and pores may exist in the reconstructed digital core. We then use the Seed Filling Method to remove these unreasonable isolated skeletons isolated pores (the modified sections are indicated by blue circles in Figures 9(b), 10(b), 11(b), and 12(b)).

In fact, the removal of redundant isolated skeleton pore can make digital core more concise and realistic. The corrected skeleton voxels and pore voxels can transform into each other. Besides, the proportion of the modified skeleton/pore voxel points in the whole digital core is very low so



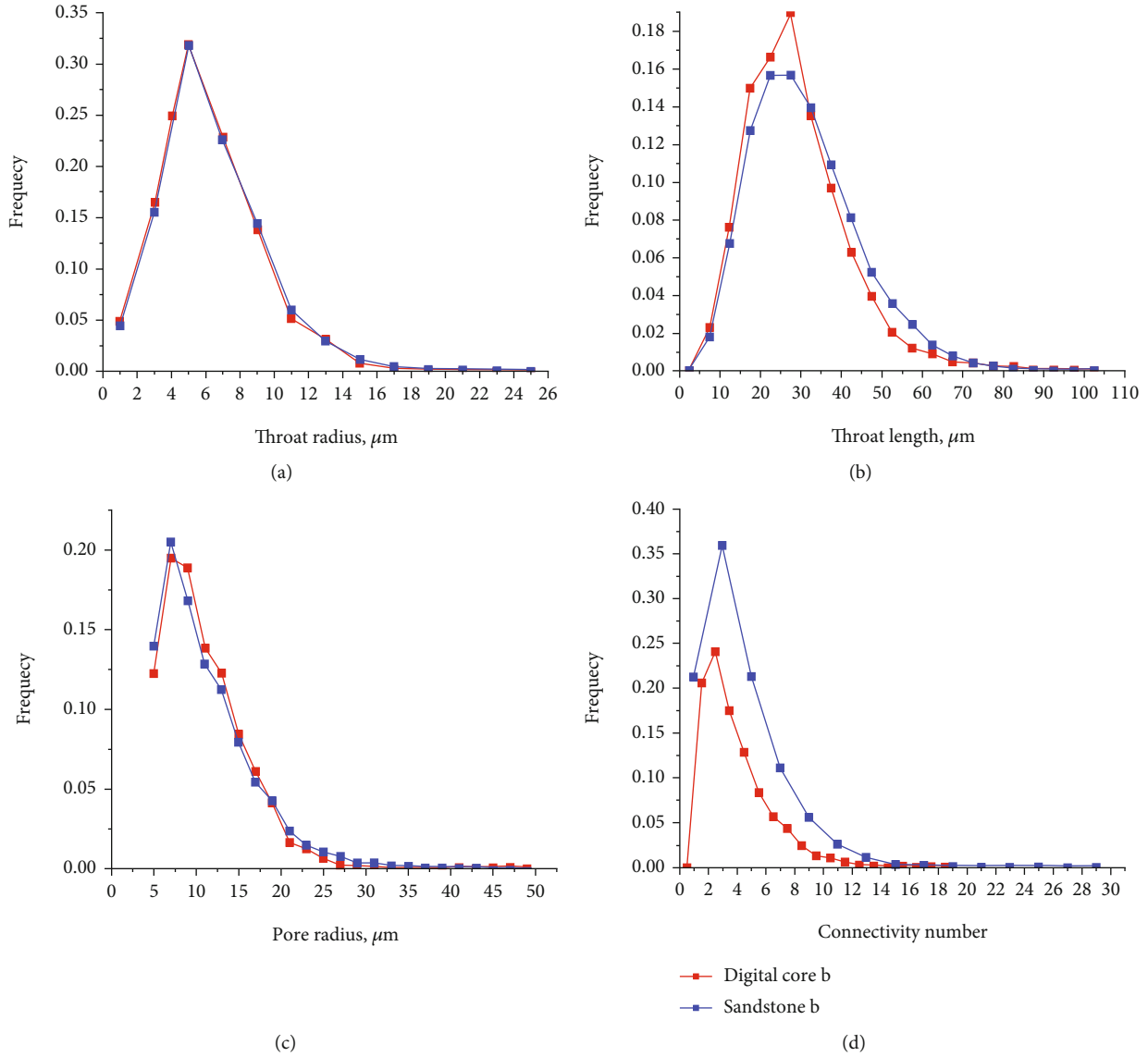


FIGURE 17: Pore-throat parameters of digital core b and sandstone b: (a) throat radius; (b) throat length; (c) pore radius; (d) connectivity number.

that the porosity before and after correction should roughly remain the same value. For example, the porosity of sample A of the real core, digital core, and corrected digital core is 26.90%, 27.70%, and 28.10%, respectively, which only gives 0.4% difference before and after correction (Table 2). If only referring to porosity data, the reconstructed and corrected digital core are in line with the original core. However, as said, the internal microstructures of two porous media with exactly the same porosity could still behave differently. To further examine the conformity between constructed core and real core, we used autocorrelation function to characterize pore space properties. The autocorrelation function [53] is widely used to evaluate image structural properties. It represents the probability that any two points in the image are in the same phase (i.e., skeleton or pore):

$$S(h) = Z(r_i) \times \bar{Z}(r_i + h), \quad (1)$$

where  $S(h)$  is the value of autocorrelation function,  $r_i$  is the coordinate of point  $i$ ,  $Z(r_i)$  is the observation value at the coordinate  $r_i$ ,  $Z(r_i + h)$  is the observation value at coordinate  $r_i + h$ , and  $h$  is the distance between two observation coordinates in  $\mu\text{m}$ .

Figure 13 shows the calculated autocorrelation function varies with  $h$ . It can be clearly seen that the variation trends of autocorrelation functions of reconstructed cores and original cores for all sandstones are very similar, indicating a high similarity of pore structure characteristics between reconstructed cores and real cores. With consideration of similar porosity of real and digital cores, it can be concluded that the digital core reconstructed in this paper has high accuracy compared to raw core, and the reconstruction algorithm and correction process are trustworthy.

The next step is to construct the final pore network model. We first extract the central axis of pore space based on the reconstructed digital core and identify corresponding

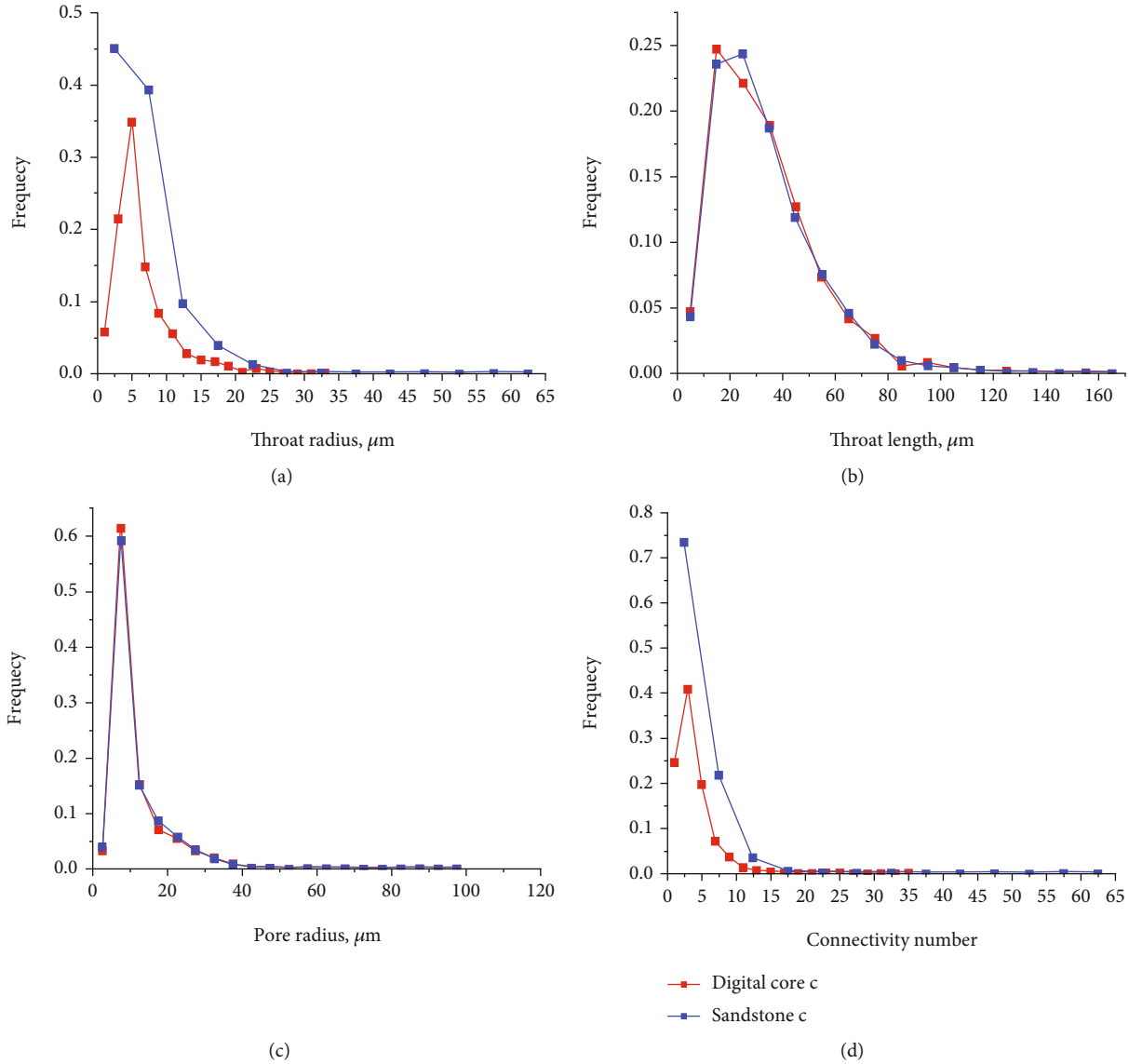


FIGURE 18: Pore-throat parameters of digital core c and sandstone c: (a) throat radius; (b) throat length; (c) pore radius; (d) connectivity number.

geometric parameters using geometric transformation technology, maximum sphere method, and OTSU method. Then, the desired pore network model can be obtained once assigning geometric parameters to the corresponding position of central axis node. Figures 14(a) and 14(b) show the central axis network of digital core a before and after correction, respectively.

Figures 15(a)–15(d) show the final pore network models for all candidate cores. It can be qualitatively seen that core a has relatively larger pore size compared to the rest of the cores. For core b, a small portion of pores is large, but in general, they seem to be smaller and more densely distributed than core a. Core c has the worst uniformity of pore distribution, where the pore size is generally small but large pores could be locally present. The average pore size of core d is the smallest among all samples, and it is in fine distribution. Considering the high match of aforementioned digital

core characteristics with the properties of the raw cutting plane binary map, we believe that the extracted pore network model can accurately reflect the microstructure of the real core.

To further validate the accuracy of the extracted pore network, we compare microstructure parameters of the pore network model with the same parameters of the original core, including throat radius, throat length, pore radius, and connectivity number, as shown in Figures 16–19. It is worth noting that the biggest difference among all microstructure properties between digital cores and real core is the connectivity number. The main reason is that compared to the rest of parameters, the connectivity number is spatially more sensitive, so that the three-dimensional space position changes would significantly affect the value of connectivity number. Since the initial input file for reconstruction modeling is a two-dimensional binary cutting

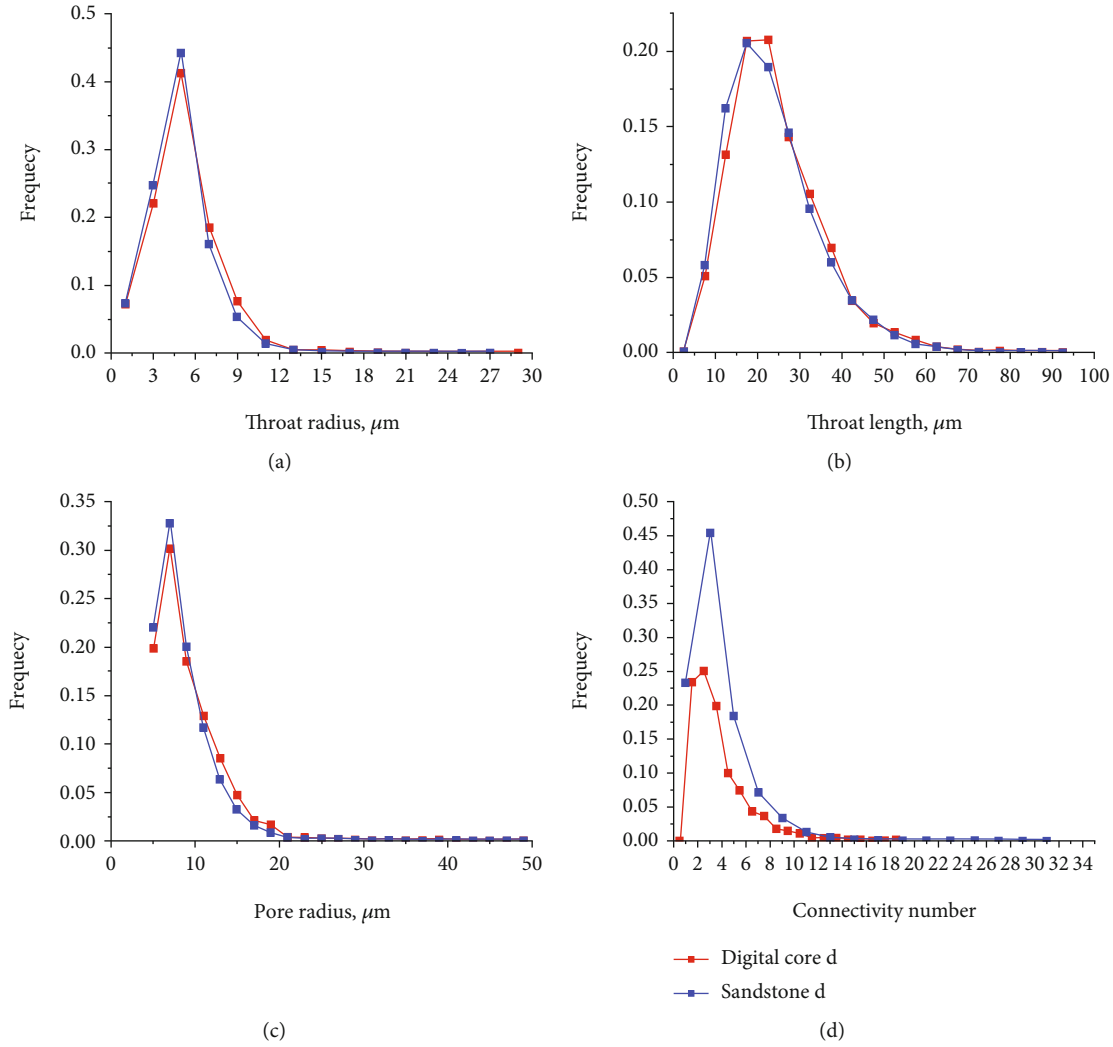


FIGURE 19: Pore-throat parameters of digital core d and sandstone d: (a) throat radius; (b) throat length; (c) pore radius; (d) connectivity number.

plane image, the information contained in this image will largely determine the microstructure parameters of reconstructed digital core and pore networks. Given one two-dimensional image cannot completely and accurately reflect the pore throat coordination number which is significantly affected by the spatial position, the obtained coordination numbers of digital cores are therefore slightly lower than the original cores' values.

For core a and d, the throat radius, throat length, and pore radius are almost identical; for core b, the throat length of digital core is slightly concentrated at relatively smaller sizes than sandstone, while throat radius and pore radius are almost identical; for core c, there is the biggest difference in the length of throat among these 4 cores, while throat radius and pore radius are almost identical. In general, except for coordination number, the other three parameters of digital core are almost in line with the real core. Among them, pore and throat radius have higher consistency than throat length. Particularly the throat length, core c shows the largest difference between digital core and real core, which is

followed by core b. The rest two cores have very well consistency of throat lengths between digital core and real core.

From the above results, we can observe that the parameters of reconstructed digital core, such as throat radius, throat length, pore radius, and connectivity number, are generally in line with the real core. Therefore, we conclude that the modeling method used can capture the same microstructure properties from real core to reconstructed digital core or/and pore network model. On the other hand, the main purpose of digital core and pore network model construction is to replace the physical experiment of the real core with numerical simulation. However, the accuracy of the established digital core and pore network model is yet to be totally assured of this replacement. To achieve this, the digital core and pore network model should have the same micropore structures and internal flow behaviors as real core. Therefore, to further validate the proposed modeling method, we performed simulations on mercury injection and oil-water two-phase flow based on the extracted pore network model.

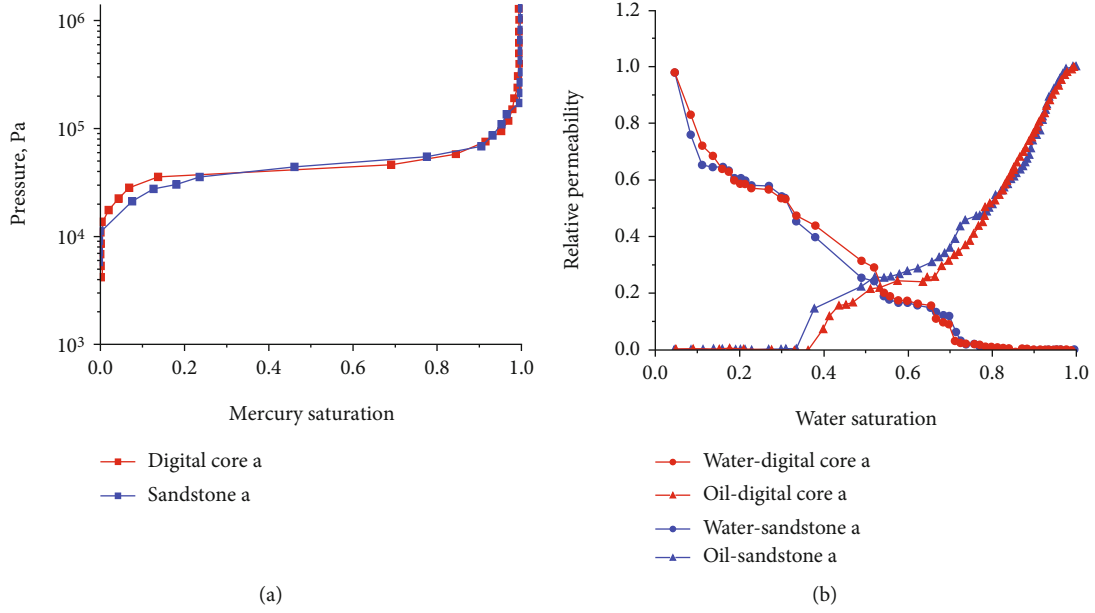


FIGURE 20: (a) Mercury injection and (b) oil-water two-phase flow simulation of digital core a and sandstone a.

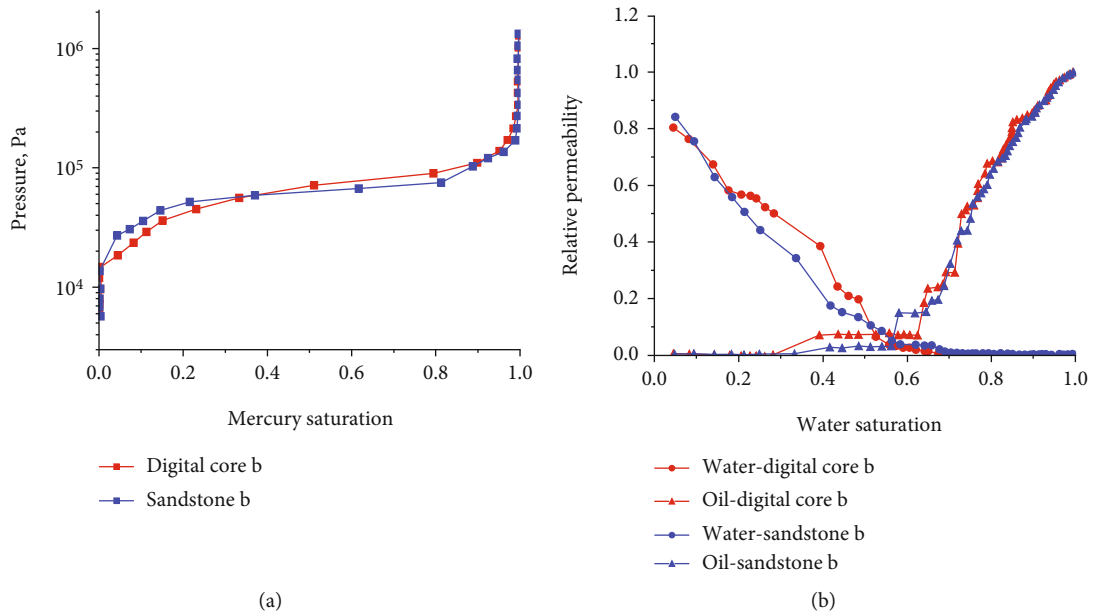


FIGURE 21: (a) Mercury injection and (b) oil-water two-phase flow simulation of digital core b and sandstone b.

The basis of flow (both single-phase and multiphase) simulations in the pore network model is the Hagen–Poiseuille model for hydraulic conductance between two pores:

$$q = \frac{g}{L} \Delta p, \quad (2)$$

where  $q$  is the flux between pores connected via throat,  $g$  is the fluid conductance of the pore-throat-pore,  $L$  is the length of path between pore body centers, and  $\Delta p$  is the pressure difference between pores. The computation of the hydraulic

conductance for any 2D cross-section (or fluid menisci for multiphase flow)  $g$  is based on the dimensionless conductance model of Patzek and Silin [54]:

$$g = \frac{A^2 \tilde{g}}{\mu}, \quad (3)$$

where  $A$  is the area of a cross-section,  $\tilde{g}$  is the dimensionless hydraulic conductance (rigorously established for circle, square, and triangle within a circle-triangle-square model), and  $\mu$  is the fluid viscosity.

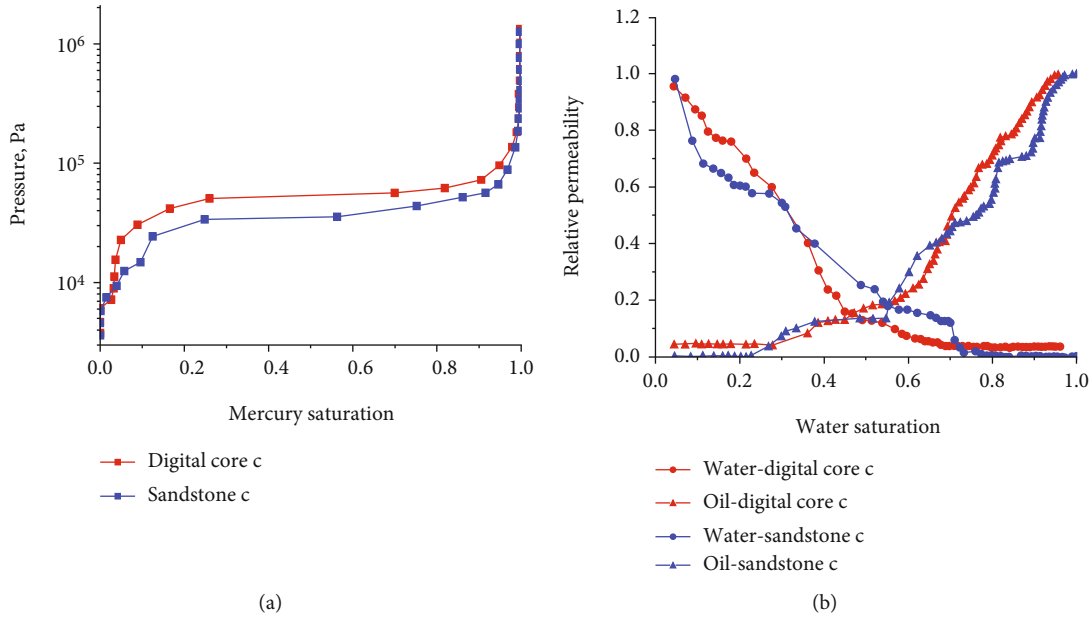


FIGURE 22: (a) Mercury injection and (b) oil-water two-phase flow simulation of digital core c and sandstone c.

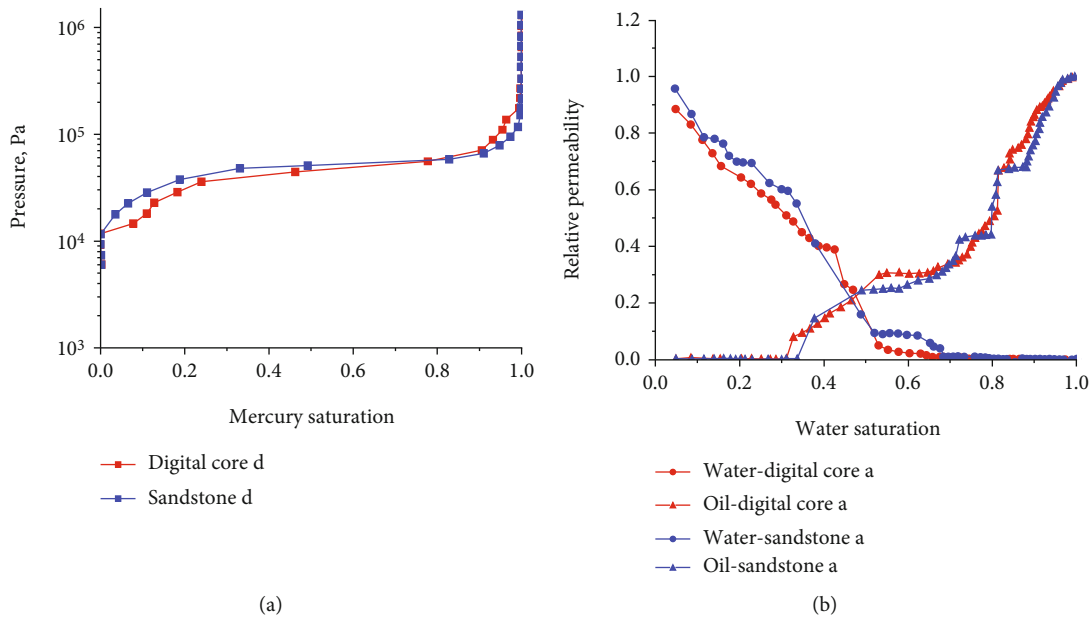


FIGURE 23: (a) Mercury injection and (b) oil-water two-phase flow simulation of digital core d and sandstone d.

As shown in Figures 20–23, it can be observed that the fluid flow behaviors in digital cores and pore network models are basically consistent with the corresponding real cores by comparing the mercury injection curves and oil-water relative permeability of digital cores and real cores. Mercury injection curves show better consistency than the relative permeability curves of oil-water two-phase flow, which could be explained by the more complex force in multiphase flow than that in single-phase flow. To be more specific, the sequence of consistency of relative permeability

curves between digital cores and real cores is core a/d > core b > core c, which is in line with the results from pore and throat microstructure parameters. In other words, when the other parameters show high consistency (except connectivity number), the throat length of digital core b is slightly less consistent with real core b and worse for core c compared to core a and core d. Nevertheless, we observed high accuracy between digital cores and real cores. Therefore, we can conclude that the method used for digital core/pore network reconstructions in this paper can fully reflect the



microstructure characteristics of real core, which gives convenience and paves the road for large-scale fluid flow simulation in oil/gas reservoirs.

#### 4. Conclusions

In this work, we developed a new method for digital core and core network modeling based on the algorithm proposed by Palágyi and Kuba and also the Markov Chain Monte Carlo (MCMC) method.

- (1) The modeling results show that the digital core of heavy oil reservoir sandstone reconstructed with this digital core modeling method can accurately reflect the microstructure characteristics of the real core. Moreover, the accuracy could be further improved when three representative images on the three vertical coordinate planes are available in the digital core modeling
- (2) Considering the low initial input requirement, which is one binary image of the core cutting plane for the least and the image can be easily obtained from X-ray CT scanning, casting thin section imaging or scanning electron microscope, etc., and high accuracy of simulation results, the new proposed method for digital core/pore network modeling in rock engineering should have wide applied future
- (3) As the microstructure properties of core cutting plane binary image, the only input in the modeling directly governs the corresponding pore network characteristics of the reconstructed digital core/pore network model. Therefore, the quality of input image highly determines the accuracy of reconstruction results. In general, the more homogeneous the rock behaves, the more precise the produced binary map section will be and the modeling results will be more accurate. As in this paper, the sequence of homogeneity of sandstones is  $\text{core a/d} > \text{core b} > \text{core c}$ , so the reconstructed digital core a and d presents higher accuracy than digital core b and c
- (4) In this work, we extracted the pore network model based on the obtained digital core. The results of pore/throat microstructure parameters and flow behavior simulation between extracted pore network and real core show a high consistency. Therefore, the modeling method of pore network in rock engineering presented in this paper is accurate and can be used to extract the pore network model of any other digital core

#### Data Availability

The data used to support the finding of this study are included within the article.

#### Conflicts of Interest

The author declares no conflict of interest regarding the publication of this manuscript.

#### Acknowledgments

This research was funded by the National Natural Science Foundation of China (No. 51874249), the National Key Research and Development Program of China (No. 2019YFC0312304-4), and the National Science and Technology Major Project of China (2016ZX05015-002) Open Fund (PLN201914) of State Key Laboratory of Oil and Gas Reservoir Geology and Exploitation (Southwest Petroleum University).

#### References

- [1] H. Chen, M. H. Yang, K. Chen, and C. Zhang, "Relative permeability of porous media with nonuniform pores," *Geofluids*, vol. 2020, Article ID 5705424, 14 pages, 2020.
- [2] X. Zhou, Q. Jiang, Q. Yuan et al., "Determining CO<sub>2</sub> diffusion coefficient in heavy oil in bulk phase and in porous media using experimental and mathematical modeling methods," *Fuel*, vol. 263, article 116205, 2020.
- [3] A. Salama, S. Y. Sun, M. F. el Amin, Y. Wang, and K. Kumar, "Flow and transport in porous media: a multiscale focus," *Geofluids*, vol. 2017, Article ID 7579015, 3 pages, 2017.
- [4] X. Zhou, F. Zeng, L. Zhang et al., "Experimental and mathematical modeling studies on foamy oil stability using a heavy oil-CO<sub>2</sub> system under reservoir conditions," *Fuel*, vol. 264, article 116771, 2020.
- [5] J. B. Nielsen, R. L. Hanson, H. M. Almughamsi, C. Pang, T. R. Fish, and A. T. Woolley, "Microfluidics: innovations in materials and their fabrication and functionalization," *Analytical Chemistry*, vol. 92, no. 1, pp. 150–168, 2020.
- [6] Y. Du, J. Chen, and T. Zhang, "Reconstruction of three-dimensional porous media using deep transfer learning," *Geofluids*, vol. 2020, Article ID 6641642, 22 pages, 2020.
- [7] J. T. Gostick, "Versatile and efficient pore network extraction method using marker-based watershed segmentation," *Physical Review E*, vol. 96, no. 2, article 023307, 2017.
- [8] W. P. Yang, J. W. Brownlow, D. L. Walker, and J. Lu, "Effect of surfactant-assisted wettability alteration on immiscible displacement: a microfluidic study," *Water Resources Research*, vol. 57, no. 8, 2021.
- [9] W. P. Yang, C. L. Fu, Y. du et al., "Dynamic contact angle reformulates pore-scale fluid-fluid displacement at ultralow interfacial tension," *SPE Journal*, vol. 26, no. 3, pp. 1278–1289, 2021.
- [10] L. Zhang, Q. J. Kang, J. Yao et al., "Pore scale simulation of liquid and gas two-phase flow based on digital core technology," *SCIENCE CHINA Technological Sciences*, vol. 58, no. 8, pp. 1375–1384, 2015.
- [11] M. J. Blunt, B. Bijeljic, H. Dong et al., "Pore-scale imaging and modelling," *Advances in Water Resources*, vol. 51, pp. 197–216, 2013.
- [12] G. Zhang, B. Liu, A. G. Xu, Y. M. Shan, and Y. J. Li, "Morphology effect of surface structures on microchannel flow using lattice Boltzmann method," *Geofluids*, vol. 2019, Article ID 3475872, 14 pages, 2019.
- [13] L. Wang, S. H. Wang, R. L. Zhang et al., "Review of multi-scale and multi-physical simulation technologies for shale and tight gas reservoirs," *Journal of Natural Gas Science and Engineering*, vol. 37, pp. 560–578, 2017.

- [14] P. Tahmasebi, F. Javadpour, M. Sahimi, and M. Piri, "Multi-scale study for stochastic characterization of shale samples," *Advances in Water Resources*, vol. 89, pp. 91–103, 2016.
- [15] S. W. Zhou, G. Yan, H. Q. Xue, W. Guo, and X. B. Li, "2D and 3D nanopore characterization of gas shale in Longmaxi formation based on FIB-SEM," *Marine and Petroleum Geology*, vol. 73, pp. 174–180, 2016.
- [16] Y. B. Gong and M. Piri, "Pore-to-core upscaling of solute transport under steady-state two-phase flow conditions using dynamic pore network modeling approach," *Transport in Porous Media*, vol. 135, no. 1, pp. 181–218, 2020.
- [17] Y. B. Gong, M. Sedghi, and M. Piri, "Dynamic pore-scale modeling of residual trapping following imbibition in a rough-walled fracture," *Transport in Porous Media*, 2021.
- [18] Y. J. Liu, F. Meirer, C. M. Krest, S. Webb, and B. M. Weckhuyzen, "Relating structure and composition with accessibility of a single catalyst particle using correlative 3-dimensional microspectroscopy," *Nature Communications*, vol. 7, no. 1, 2016.
- [19] M. Aghighi, M. A. Hoeh, W. Lehnert, G. Merle, and J. Gostick, "Simulation of a full fuel cell membrane electrode assembly using pore network modeling," *Journal of the Electrochemical Society*, vol. 163, no. 5, pp. F384–F392, 2016.
- [20] J. Zeng, Y. C. Zhang, J. S. Ma, C. L. Liu, and Z. Cao, "Investigating the influences of pore-scale characteristics on tight oil migration by a two-phase pore network model," *Geofluids*, vol. 2020, Article ID 4890758, 13 pages, 2020.
- [21] I. Fatt, "The network model of porous media I. Capillary pressure characteristics," *Transactions of the AIME*, vol. 207, pp. 144–159, 1956.
- [22] I. Fatt, "The network model of porous media II. Dynamic properties of a single size tube network," *Transactions of the AIME*, vol. 207, pp. 160–163, 1956.
- [23] I. Fatt, "The network model of porous media III. Dynamic properties of networks with tube radius distribution," *Transactions of the AIME*, vol. 207, pp. 164–181, 1956.
- [24] X. C. Zhao, J. Yao, and Y. J. Yi, "A new stochastic method of reconstructing porous media," *Transport in Porous Media*, vol. 69, no. 1, pp. 1–11, 2007.
- [25] W. B. Lindquist, S. M. Lee, D. A. Coker, K. W. Jones, and P. Spanne, "Medial axis analysis of void structure in three-dimensional tomographic images of porous media," *Journal of Geophysical Research: Solid Earth*, vol. 101, no. B4, pp. 8297–8310, 1996.
- [26] A. P. Sheppard, R. M. Sok, and H. Averdunk, "Improved pore network extraction methods," in *Proceedings of the International Symposium of the Society of Core Analysts*, pp. 21–25, Toronto, Canada, 2005.
- [27] M. Prodanovic, W. B. Lindquist, and R. S. Seright, "Porous structure and fluid partitioning in polyethylene cores from 3D X-ray microtomographic imaging," *Journal of Colloid and Interface Science*, vol. 298, no. 1, pp. 282–297, 2006.
- [28] J. F. Delerue and E. Perrier, "DXSoil, a library for 3D image analysis in soil science," *Computers & Geosciences*, vol. 28, no. 9, pp. 1041–1050, 2002.
- [29] H. Okabe and M. J. Blunt, "Prediction of permeability for porous media reconstructed using multiple-point statistics," *Physical Review E*, vol. 70, no. 6, article 066135, 2004.
- [30] D. B. Silin, G. Jin, and T. W. Patzek, "Robust determination of pore space morphology in sedimentary rocks," in *In proceedings of SPE Annual Technical Conference and Exhibition*, Denver, Colorado, U.S.A, October 2003.
- [31] Q. R. Xiong, T. G. Baychev, and A. P. Jivkov, "Review of pore network modelling of porous media: experimental characterisations, network constructions and applications to reactive transport," *Journal of Contaminant Hydrology*, vol. 192, pp. 101–117, 2016.
- [32] D. Wildenschild and A. P. Sheppard, "X-ray imaging and analysis techniques for quantifying pore-scale structure and processes in subsurface porous medium systems," *Advances in Water Resources*, vol. 51, pp. 217–246, 2013.
- [33] L. M. Anovitz and D. R. Cole, "Characterization and analysis of porosity and pore structures," *Reviews in Mineralogy and Geochemistry*, vol. 80, no. 1, pp. 61–164, 2015.
- [34] K. Palágyi and A. Kuba, "A 3D 6-subiteration thinning algorithm for extracting medial lines," *Pattern Recognition Letters*, vol. 19, no. 7, pp. 613–627, 1998.
- [35] T. Dunås, A. Wåhlin, K. Ambarki et al., "Automatic labeling of cerebral arteries in magnetic resonance angiography," *Magnetic Resonance Materials in Physics, Biology and Medicine*, vol. 29, no. 1, pp. 39–47, 2016.
- [36] T. Dunås, A. Wåhlin, K. Ambarki, L. Zarrinkoob, J. Malm, and A. Eklund, "A stereotactic probabilistic atlas for the major cerebral arteries," *Neuroinformatics*, vol. 15, no. 1, pp. 101–110, 2017.
- [37] T. Dunås, M. Holmgren, A. Wåhlin, J. Malm, and A. Eklund, "Accuracy of blood flow assessment in cerebral arteries with 4D flow MRI: evaluation with three segmentation methods," *Journal of Magnetic Resonance Imaging*, vol. 50, no. 2, pp. 511–518, 2019.
- [38] D. A. Moses, L. Dawes, C. Sammut, and T. Zrimec, "Peripheral bronchial identification on chest CT using unsupervised machine learning," *International Journal of Computer Assisted Radiology and Surgery*, vol. 13, no. 9, pp. 1379–1395, 2018.
- [39] K. Pluta, M. Janaszewski, and M. Postolski, "New algorithm for modeling of bronchial trees," *Image Processing & Communications*, vol. 17, no. 4, pp. 179–190, 2012.
- [40] V. Olejníčková, B. Šaňková, D. Sedmera, and J. Janáček, "Trabecular architecture determines impulse propagation through the early embryonic mouse heart," *Frontiers in Physiology*, vol. 9, no. 9, p. 1876, 2019.
- [41] Y. Bao, L. Tang, S. Srinivasan, and P. S. Schnable, "Field-based architectural traits characterisation of maize plant using time-of-flight 3D imaging," *Biosystems Engineering*, vol. 178, pp. 86–101, 2019.
- [42] J. P. Muhirwa, S. I. Mbalawata, and V. G. Masanja, "Markov chain Monte Carlo analysis of the variable-volume exothermic model for a continuously stirred tank reactor," *Engineering, Technology & Applied Science Research*, vol. 11, no. 2, pp. 6919–6929, 2021.
- [43] K. J. Wu, N. Nunan, J. W. Crawford, I. M. Young, and K. Ritz, "An efficient Markov chain model for the simulation of heterogeneous soil structure," *Soil Science Society of America Journal*, vol. 68, no. 2, pp. 346–351, 2004.
- [44] R. Bostanabad, Y. C. Zhang, X. L. Li et al., "Computational microstructure characterization and reconstruction: review of the state-of-the-art techniques," *Progress in Materials Science*, vol. 95, pp. 1–41, 2018.
- [45] R. H. Bakken and L. M. Eliassen, "Real-time three-dimensional skeletonisation using general-purpose computing on graphics processing units applied to computer vision-based human pose estimation," *The International Journal of High Performance Computing Applications*, vol. 31, no. 4, pp. 259–273, 2017.

- [46] T. Y. Kong and A. Rosenfeld, "Digital topology: introduction and survey," *Computer Vision, Graphics, and Image Processing*, vol. 48, no. 3, pp. 357–393, 1989.
- [47] C. M. Ma, "On topology preservation in 3D thinning," *CVGIP: Image Understanding*, vol. 59, no. 3, pp. 328–339, 1994.
- [48] T. C. Lee, R. L. Kashyap, and C. N. Chu, "Building skeleton models via 3-D medial surface axis thinning algorithms," *CVGIP: Graphical Models and Image Processing*, vol. 56, no. 6, pp. 462–478, 1994.
- [49] Z. Jiang, K. Wu, G. Couples, M. I. J. van Dijke, K. S. Sorbie, and J. Ma, "Efficient extraction of networks from three-dimensional porous media," *Water Resources Research*, vol. 43, no. 12, pp. 2578–2584, 2007.
- [50] M. W. Graham, J. D. Gibbs, D. C. Cornish, and W. E. Higgins, "Robust 3-D airway tree segmentation for image-guided peripheral bronchoscopy," *IEEE Transactions on Medical Imaging*, vol. 29, no. 4, pp. 982–997, 2010.
- [51] P. Mostaghimi, M. J. Blunt, and B. Bijeljic, "Computations of absolute permeability on micro-CT images," *Mathematical Geosciences*, vol. 45, no. 1, pp. 103–125, 2013.
- [52] R. F. Hamade and A. M. R. Baydoun, "Nondestructive detection of defects in friction stir welded lap joints using computed tomography," *Materials & Design*, vol. 162, pp. 10–23, 2019.
- [53] Y. F. Hou, W. B. Hu, X. Wang, T. T. Hou, and C. L. Sun, "Damage identification of ancient timber structure based on autocorrelation function," *Advances in Civil Engineering*, vol. 2021, Article ID 6683666, 2021.
- [54] T. W. Patzek and D. B. Silin, "Shape factor and hydraulic conductance in noncircular capillaries: I. One-phase creeping flow," *Journal of Colloid and Interface Science*, vol. 236, no. 2, pp. 295–304, 2001.

## Research Article

# Experimental Study of Hydraulic Fracture Propagation Behavior during Multistage Fracturing in a Directional Well

Yongtao Zhang,<sup>1</sup> Hao Jin,<sup>1</sup> Bumin Guo,<sup>2</sup> Shoumei Qiu ,<sup>2</sup> Peng Yang,<sup>3</sup> Shili Qin,<sup>1</sup> Yantao Xu,<sup>2</sup> and Qiang Zhang<sup>1</sup>

<sup>1</sup>Shenzhen Branch of CNOOC (China) Co. Ltd., Shenzhen, Guangdong 518054, China

<sup>2</sup>China Oilfield Services Ltd., Oilfield Production Division, Tianjin 300459, China

<sup>3</sup>China University of Petroleum (Beijing), Beijing 102249, China

Correspondence should be addressed to Shoumei Qiu; [marchisio7@163.com](mailto:marchisio7@163.com)

Received 31 July 2021; Revised 9 September 2021; Accepted 20 September 2021; Published 4 October 2021

Academic Editor: Jinjie Wang

Copyright © 2021 Yongtao Zhang et al. This is an open access article distributed under the Creative Commons Attribution License, which permits unrestricted use, distribution, and reproduction in any medium, provided the original work is properly cited.

Due to the limited space of offshore platform, it is unable to implement large-scale multistage hydraulic fracturing for the horizontal well in Lufeng offshore oilfield. Thus, multistage hydraulic fracturing technology in directional well was researched essentially to solve this problem. Modeling of fracture propagation during multistage fracturing in the directional and horizontal wells in artificial cores was carried out based on a true triaxial hydraulic fracturing simulation experiment system. The effects of horizontal stress difference, stage spacing, perforation depth, and well deviation angle on multifracture propagation were investigated in detail. Through the comparative analysis of the characteristics of postfrac rock and pressure curves, the following conclusions were obtained: (1) multistage fracturing in horizontal wells is conducive to create multiple transverse fractures. Under relatively high horizontal stress difference coefficient (1.0) and small stage spacing conditions, fractures tend to deflect and merge due to the strong stress interference among multiple stages. As a consequence, the initiation pressure for the subsequent stages increases by more than 8%, whereas in large stage spacing conditions, the interference is relatively lower, resulting in the relatively straight fractures. (2) Deepening perforation holes can reduce the initiation pressure and reduce the stress interference among stages. (3) When the projection trace of directional wellbore on horizontal plane is consistent with the direction of the minimum horizontal principal stress, fractures intersecting the wellbore obliquely are easily formed by multistage fracturing. With the decrease of well deviation angle, the angle between fracture surface and wellbore axis decreases, which is not conducive to the uniform distribution of multiple fractures. (4) When there is a certain angle between the projection trace of directional wellbore on horizontal plane and the direction of minimum horizontal principal stress, the growth of multiple fractures is extremely ununiform and the fracture paths are obviously tortuous.

## 1. Introduction

With the development of unconventional oil and gas reservoirs and the advancement of technology, directional wells, horizontal wells, and multistage fracturing technology are combined to increase the drainage area of the reservoir, hence to improve oil recovery and economic benefits. Currently, multistage fracturing is the main stimulation technology for unconventional resources; the principle of which is to enlarge the oil and gas discharge area by forming dense transverse fractures that are perpendicular to the wellbore [1–4]. However, due to the limited area of offshore plat-

forms, high equipment operating costs, and high operational safety risks, it is difficult to apply mature onshore staged fracturing technologies to offshore oilfields. Meanwhile, the development of offshore horizontal staged fracturing technologies is far behind that of onshore oilfields [5]. In order to adapt to the characteristics of offshore platforms and treat more production zones at the same time, the research on multistage fracturing technology in directional wells is of great importance.

Series of theoretical studies on hydraulic fracture initiation and propagation in directional wells have been conducted [6–10]. The models of stress distribution near the



wellbore of directional wells under different conditions have been established, and formulas of fracture initiation pressure and fracture initiation angle have been deduced. Zhou et al. [11] proposed the prediction model of fracture initiation by establishing the distribution model of stress field in the surrounding rock of directional wellbore and pointed out that the initiation mode of hydraulic fractures was affected by the azimuth of wellbore, in situ stress difference, and well deviation angle. Since the hypotheses of theoretical researches often somewhat differ from the actual conditions and studies of fracture propagation morphology are usually based on simplified two-dimensional or three-dimensional models, the results obtained have limitations to a certain degree. In addition to the theoretical model research, the physical simulation experiment is also an important means to study fracture initiation and propagation. Physical hydraulic fracturing simulation experiments of directional wells conducted by domestic and foreign scholars showed [12–17] that the controlling factors of hydraulic fracture initiation in directional wells mainly include well deviation angle, borehole azimuth, horizontal stress difference, and perforation parameters, and the fracture propagation is easy to deflect to produce complex forms. However, the earlier experiments mainly focused on the study of a single fracture in directional wells and did not take into account the interaction of simultaneous propagation of multiple fractures in directional wells. Many studies have shown that multifracture propagation tends to be unbalanced [4] due to the influence of (1) reservoir characteristics such as natural fractures, in situ stress distribution, and rock mechanical properties, (2) well completion factors such as stage spacing and cluster spacing, (3) perforation parameters, and (4) stress interference between fractures. The smaller the cluster spacing, the stronger the “stress shadow” effect between fractures, and the greater the influence on fracture propagation and fracture width [18–27]. In addition, some scholars established a finite element model for directional well fracturing based on the basic finite element theory and studied the propagation morphology of single fracture under uneven confining pressure [28, 29]. Although many theoretical and experimental studies have been carried out on hydraulic fracture initiation and propagation in directional wells and horizontal wells, most of the physical simulation experiments on fracture initiation and propagation in directional wells were carried out under the condition of single-fracture or multifracture fracturing in a single stage, and there were few studies on the fracture propagation of multistage fracturing in directional wells. Therefore, the propagation morphology of fractures formed in multistage fracturing under stress interference among stages in directional wells was not taken into account, and treating parameter optimization of multistage fracturing in directional wells still lacks direct experimental evidence.

To shed a light on the problem mentioned above, this paper presents the physical simulation research of staged fracturing and multifracture propagation in horizontal and directional wells using the true triaxial hydraulic fracturing physical simulation experiment system. Then, we compared and analyzed the influence factors that affect multifracture

initiation and propagation of two types of wells. The effects of horizontal stress difference, perforation depth, stage spacing, well deviation angle, and wellbore azimuth (the angle between projection of wellbore axis in the horizontal plane and the direction of maximum horizontal principal stress) on fracture propagation morphology and pressure curve characteristics of multistage fracturing were considered.

## 2. Experimental Method

*2.1. Sample Preparation.* The research area is located in the south of Lufeng Sag of Zhu I Depression, Pearl River Mouth Basin, South China Sea. The facies of research formation are shallow shore lake and braided river delta, with buried depth of 3563–4272 m. The reservoir varies greatly in vertical and horizontal directions, including silty mudstone, siltstone, and fine sandstone, with strong heterogeneity. The reservoir rocks have elastic modulus of 21.3–34.4 GPa, Poisson’s ratio of 0.18–0.31, tensile strength of 2.1–4.6 MPa, maximum horizontal principal stress of 78.4–86.6 MPa, and minimum horizontal principal stress of 64.1–70.3 MPa.

The experimental samples were cement cubes (G grade cement, quartz sand, and water in a 3 : 1 : 1 ratio) with a side length of 30 cm (Figure 1(a)). The physical properties were similar to those of the reservoir lithology. The wellbores were prefabricated in the cement. Each wellbore was divided into three sections (one perforation cluster in each section and four perforations in each cluster) to facilitate staged fracturing in horizontal and directional wells [4]. Since the size of the core samples and wellbores was limited and the effect of stress interference among stages on fracture propagation morphology can be reflected by the model with single cluster in each stage, the design of single cluster in each stage was adopted. Each wellbore was composed of three parts: outer casing, inner wellbore, and fluid injection pipelines. The inner wellbore was a steel pipe with an outer diameter of 1.5 cm, an inner diameter of 0.8 cm, and a length of 20.0 cm. The outer casing was a steel pipe with an outer diameter of 2.0 cm, an inner diameter of 1.6 cm, and a length of 20.0 cm, and a certain number of thread grooves were processed on its outer surface to strengthen the bond between the casing and cement. Four drain holes with a diameter of 3 mm were drilled on the outer casing in each section. A steel tube with the same diameter as the holes was welded perpendicularly at the position of each hole to simulate the perforation process. The annulus of each stage was sealed off with a gasket to simulate stage packer. Each stage in the inner wellbore was sealed by a steel plate and linked with an injection line which connected to an individual intermediate vessel. A six-way valve was connected between the injection lines and three intermediate vessels to control the injection. The staged fracturing can be achieved by operating the valves to have one injection line and one intermediate vessel connected at one time, while keeping the others closed.

Figures 1(b) and 1(c) show the layout of horizontal and directional wellbores inside the sample, respectively. The well deviation angle ( $\alpha$ ) is the angle between the axis of the wellbore and the direction of overburden stress ( $\sigma_v$ ), and



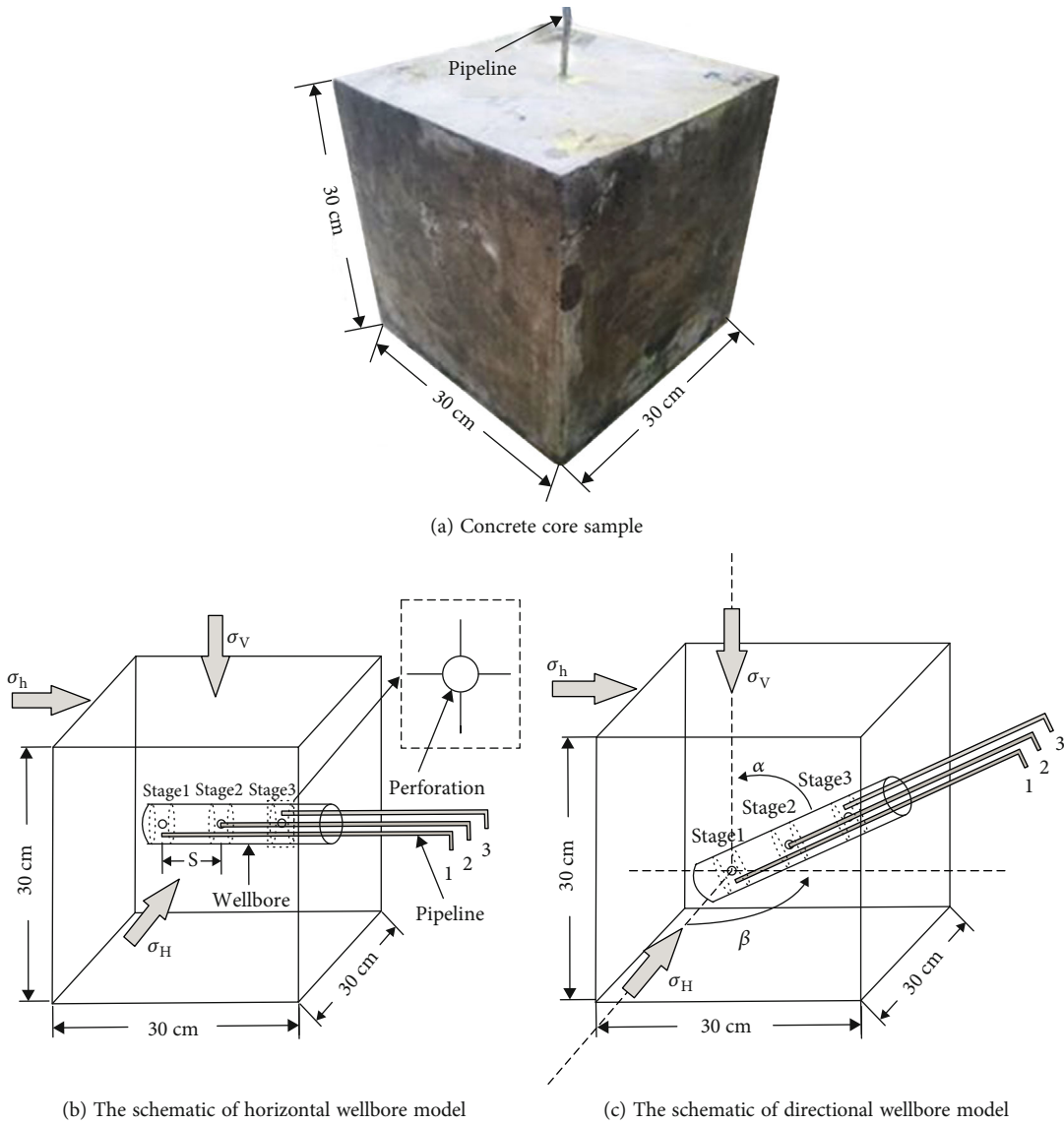


FIGURE 1: Concrete artificial core sample and well type.

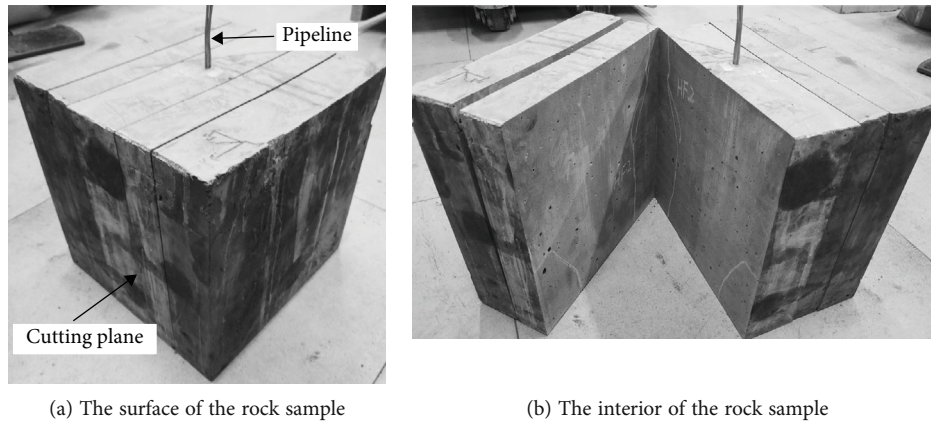


FIGURE 2: Rock specimen dissection after fracturing.

TABLE 1: Experimental parameter settings.

Sample number	In situ stress state				Stage spacing (cm)	Perforation depth (cm)	Well type	Deviation angle (°)	Azimuth angle (°)
	$\sigma_v$ (MPa)	$\sigma_H$ (MPa)	$\sigma_h$ (MPa)	$K_h$					
1	20.0	10.0	8.0	0.25	2.0	5.0	Horizontal	90	90
2	20.0	10.0	8.0	0.25	5.0	1.0	Horizontal	90	90
3	20.0	16.0	8.0	1.0	2.0	1.0	Horizontal	90	90
4	20.0	10.0	8.0	0.25	2.0	1.0	Directional	60	90
5	20.0	10.0	8.0	0.25	2.0	1.0	Directional	30	90
6	20.0	10.0	8.0	0.25	2.0	1.0	Vertical	0	90
7	20.0	10.0	8.0	0.25	2.0	1.0	Directional	30	60
8	20.0	10.0	8.0	0.25	5.0	1.0	Directional	30	60

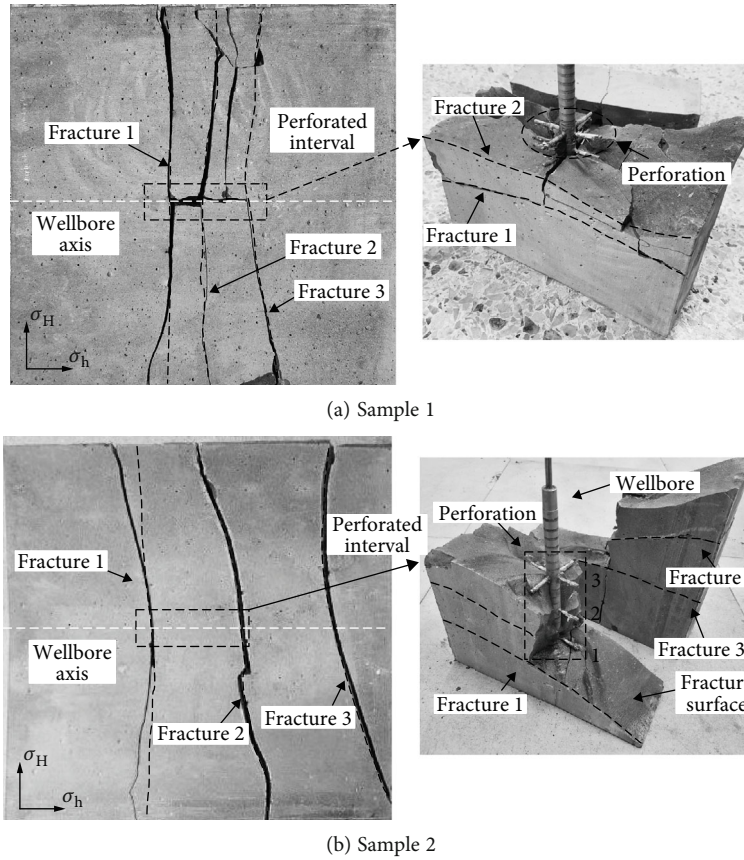


FIGURE 3: Fracture morphology for horizontal well under different stage spacing and perforating depth (samples 1 and 2).

the azimuth ( $\beta$ ) is the angle between the projection trace of the wellbore on horizontal plane and the direction of maximum horizontal principal stress ( $\sigma_H$ ). The deviation angle of horizontal wells was  $90^\circ$ , and the azimuth was set at  $90^\circ$ . The deviation angle of directional wells varied from  $0^\circ$  to  $90^\circ$ , and the azimuths were  $60^\circ$  and  $90^\circ$ .

**2.2. Experimental Procedures and Parameters.** A true triaxial hydraulic fracturing simulation system was used in fracturing experiments [4]. The experimental steps included the following. (1) Place the sample into the sample chamber in

the preset direction and use hydraulic pump set to apply triaxial stress to the rock sample to simulate the real reservoir stress condition according to the real in situ stress. (2) Connect three intermediate vessels which were filled with fracturing fluids mixed with blue, green, and red dye, respectively, and three injection lines to the six-way valve. (3) During staged fracturing, switch off all valves except the one connected with the injection line of first stage and the other one connected with the corresponding intermediate vessel. Then, inject a certain amount of fracturing fluid at a constant displacement rate. Meanwhile, monitor the wellhead

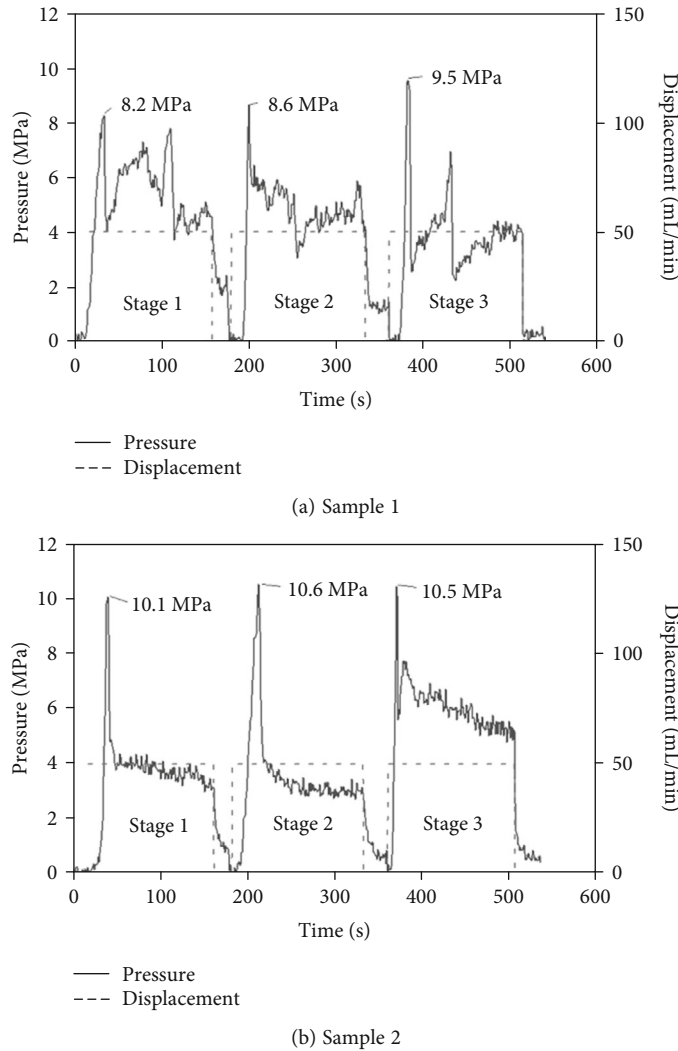


FIGURE 4: Treating pressure curve for horizontal well under different stage spacing and perforating parameters (samples 1 and 2).

pressure. Repeat the process above until all stages were completed. (4) After fracturing, observe and distinguish fractures of different sections in the rock sample by the different colors of the dye. Then, cut the fractured rock samples into pieces by the linear cutting machine (see Figure 2) to further identify the morphology of fractures inside the rock samples.

The stress state of the sample and the injection parameters were determined according to the parameters of experimental instruments and similarity criteria [4, 30]. In the experiment, the in situ stress difference coefficient (horizontal stress difference coefficient  $K_h = (\sigma_H - \sigma_h) / \sigma_h$ ) was taken into account to simulate the real formation stress environment. The fracturing fluid viscosity was 63 mPa·s, the pumping rate was 50 mL/min, and the cumulative pumping volume of a single group of experiments was 120-200 mL. Actual stage spacing in the field was mostly within the range of 30-100 m, which was converted to 1.75-5.6 cm (symbol  $s$  in Figure 1(b)). In order to facilitate experimental comparison, small stage spacing was set at 2 cm and large stage spacing was set at 5 cm, which were equivalent to 30 m and 80 m of actual stage spacing in the field. In order to reduce the

impact of additional wellbore stress field on fracture initiation, the perforation depth was 1-5 times of the wellbore diameter, namely, 1-5 cm [4]. A total of 8 rock samples were designed and their experimental parameters are shown in Table 1.

### 3. The Fracture Morphology and Pressure Curve Characteristics

#### 3.1. Fracture Characteristics of Staged Fracturing in Horizontal Wells

**3.1.1. The Influence of Stage Spacing and Perforating Depth.** The stage spacing of sample 1 and sample 2 was set at 2 cm and 5 cm, respectively, and the horizontal stress difference coefficient was 0.25. The experimental results showed that stage spacing was an important factor affecting fracture propagation. The propagation direction in the second and third stages (fractures 2 and 3) of sample 1 diverged from that of fractures in the first stage (fracture 1) (Figure 3(a)). This was because the induced stress field generated by the

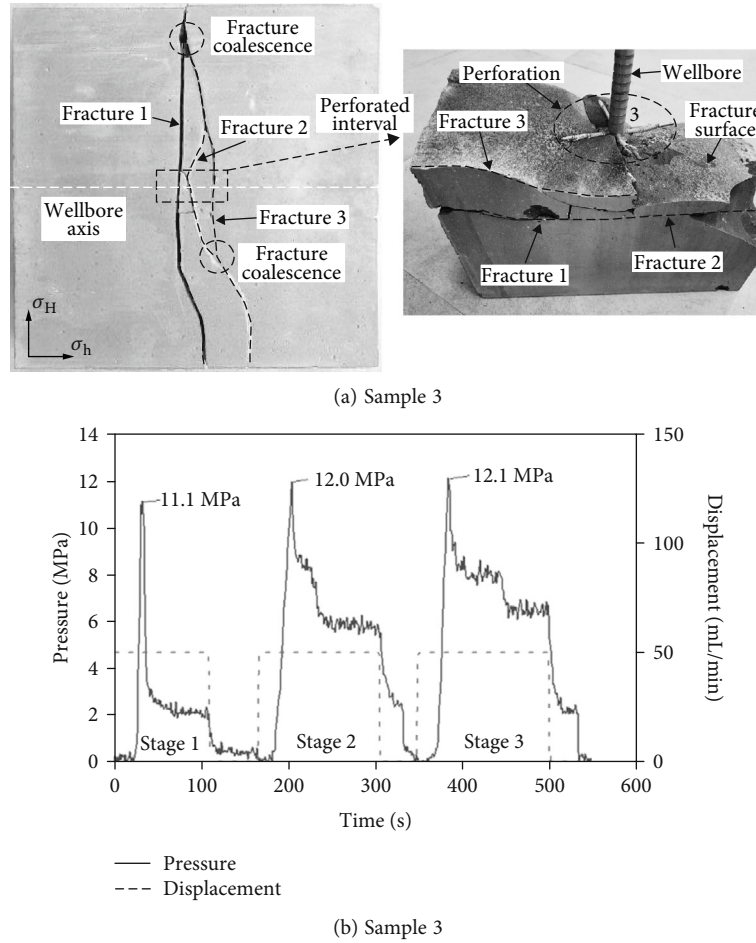


FIGURE 5: Fracture morphology and pressure curve of sample 3 (stress difference coefficient of 1.0).

first fracture changed the distribution of the original in situ stress and formed stress interference so that the subsequent fracture propagation paths were no longer parallel to the first fracture, but deflected at a certain angle. However, the fractures in the first and second stages of sample 2 with larger stage spacing were approximately perpendicular to the horizontal wellbore, while the fractures in the third stage were deflected at a certain angle from the fractures in the first two stages (Figure 3(b)). The stress interference decreased with the increase of stage spacing. For example, no obvious stress interference was found in the fracture of the second stage in sample 2. However, due to the superposition of the stress interference of the first two stages, the fracture propagation in the third stage showed a certain angle deflection. By comparing the fracture curves of sample 1 and sample 2, it can be found that the smaller stage spacing, the stronger the stress interference. The propagation pressure of each fracture in rock sample 1 fluctuated sharply and was about 1-2 MPa higher than that of sample 2 (Figures 4(a) and 4(b)). It also can be found in sample 1 that the fractures were more tortuous and the width of the fractures was smaller.

In addition, perforating depth was an important factor affecting the fracture initiation pressure. The perforation depths of sample 1 and sample 2 were 5 cm and 1 cm,

respectively. According to the pumping pressure curves of sample 1 and sample 2, the initiation pressures of each stage of sample 2 were 23.2%, 23.2%, and 10.5% higher than those of sample 1, respectively (Figure 4). As perforation depth increased, the area of the perforation hole on which fluid pressure acted increased, and the energy used for fracturing formation increased, resulting in the increase of the circumferential stress of the hole and the decrease of the breakdown pressure [31]. Smaller stage spacing is equivalent to high density perforation. The higher the perforation density, the stronger the stress concentration effect, and the greater the stress near the perforations. Therefore, the reduction of initiation pressure can be attributed to the result of stress concentration caused by multiple holes on an infinite object [32]. As a result, high density and deep penetration perforations can be used in the field to reduce the initiation pressure.

**3.1.2. The Influence of Horizontal Stress Difference.** The horizontal stress difference coefficient was set at 1.0. The stage spacing of sample 3 was 2.0 cm, and the perforation depth was 1.0 cm. The first fracture (fracture 1) formed in stage 1 was a transverse fracture perpendicular to the axis of the wellbore. The second fracture (fracture 2), formed in stage 2, deflected near the wellbore and merged with fracture 1 on the upper side distally, while its lower side propagated



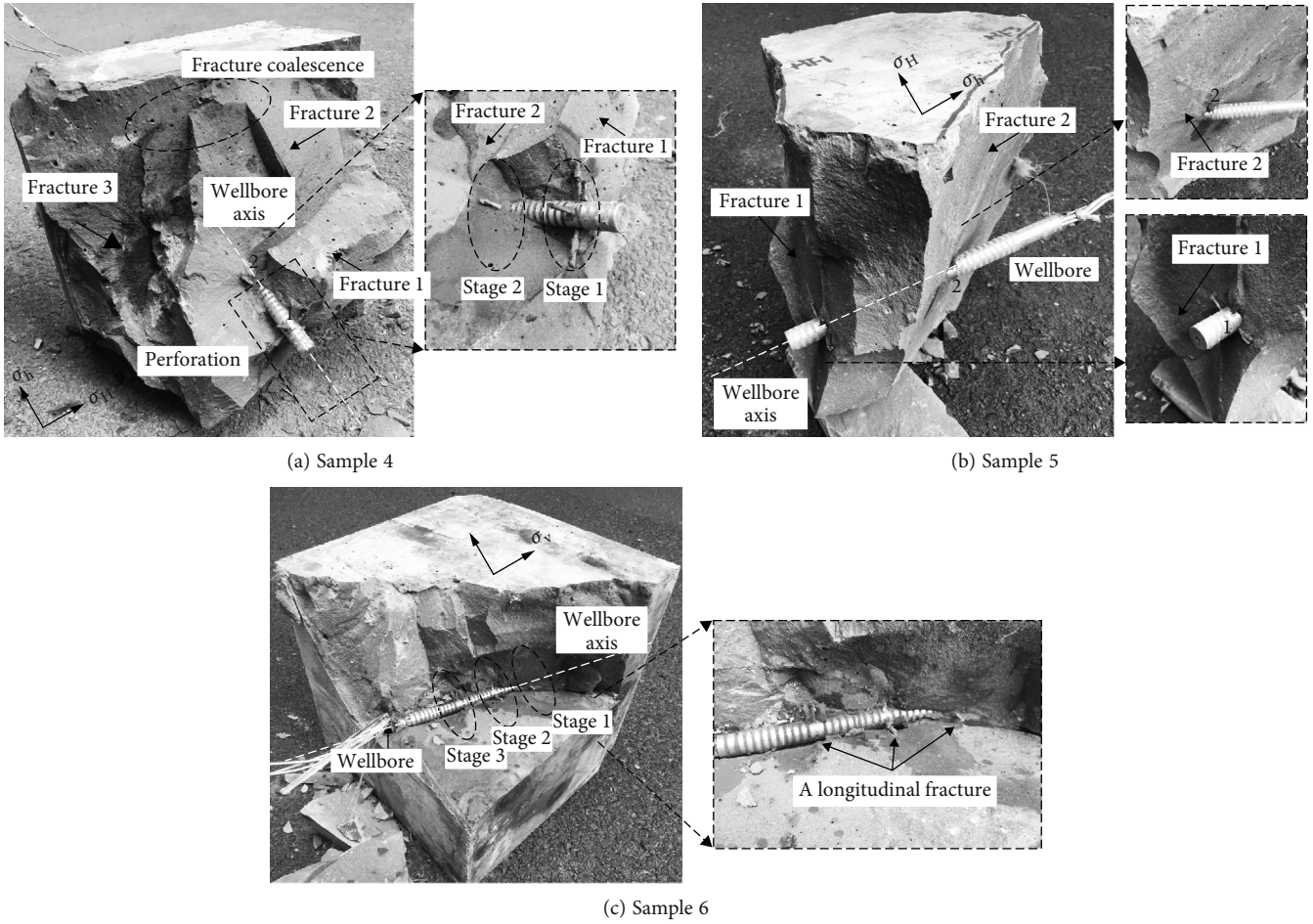


FIGURE 6: Fracture morphology of directional well with different deviation angles (azimuth angle 90°).

toward the direction of the original maximum horizontal principal stress distally. For the fracture in the third stage (fracture 3), it propagated a short distance near the wellbore, and then, both the upper and lower sides of it merged with fracture 2 (Figure 5(a)), which indicated that under the condition of high horizontal stress difference and small stage spacing, multiple fractures may merge in staged fracturing in horizontal wells. The fracture tip of the first stage may close under the action of fluid friction and filtration effect, which changed the distribution of induced stress field and made the maximum horizontal principal stress near the fracture surface deflected to fracture 1 by a certain angle. Because of the small stage spacing, fracture 2 merged with fracture 1 after propagating a certain distance, and fracture 3 merged with fracture 2 immediately after initiation.

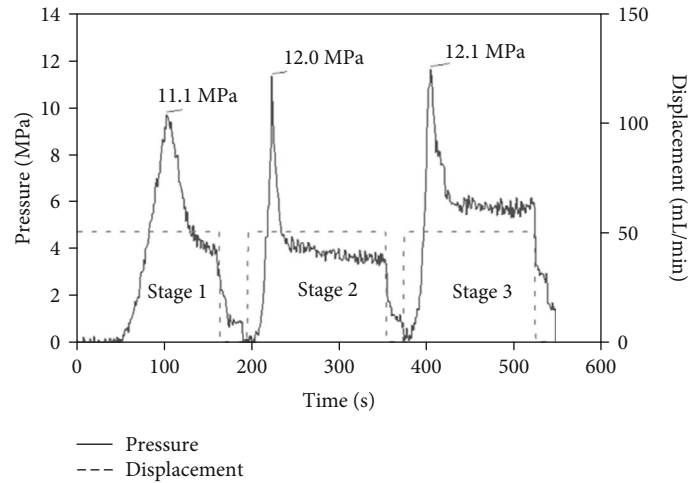
Under the influence of the superposition of induced stress field, the initiation pressure of subsequent fractures showed a gradually increasing trend. According to the pressure curve of sample 3 (Figure 5(b)), when the dimensionless net pressure in the first fracture was 0, the initiation pressures of the last two fractures in sample 3 were 8.1% and 9.0% higher than those of the first fracture, respectively. Moreover, the propagation pressures of the last two stages were more fluctuating than those of the first stage. Due to the influence of stress interference on the last two fractures,

the fractures became narrower and more complex in shape, thus resulting in greater flow resistance to the fluid. Therefore, the pumping pressure curve could reflect the state of stress interference, fracture initiation, and propagation and has important guiding significance for the optimization of treating parameters.

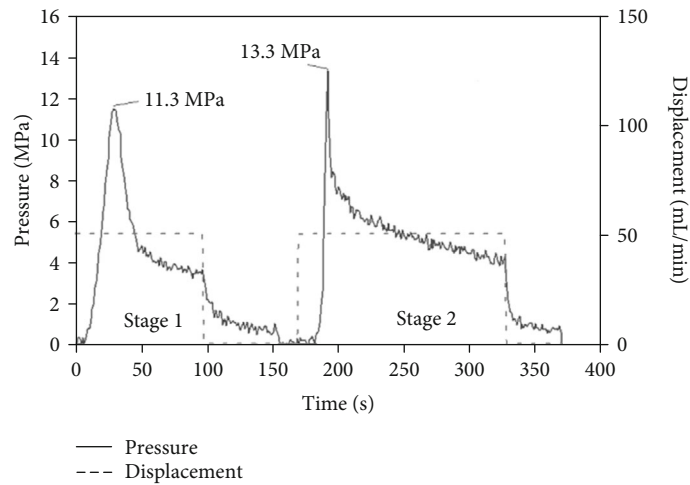
### 3.2. Fracture Characteristics of Staged Fracturing in Directional Wells

3.2.1. *The Influence of Well Deviation Angle When Azimuth Is 90°.* The horizontal stress difference coefficient was set at 0.25. The stage spacing was 2.0 cm, and the perforation depth was 1.0 cm. When the directional wellbore azimuth was 90° (the projection trace of directional wellbore on horizontal plane was consistent with the direction of the minimum horizontal principal stress), the effect of different well deviation angle on the fracture morphology and pressure curve characteristics of multistage fracturing was analyzed. As shown in Figure 6, as the deviation angle decreased, the multiple fractures obliquely intersected with the wellbore during staged fracturing became a single longitudinal fracture propagating along the wellbore. There were three transverse fractures obliquely across the wellbore in sample 4 and the wellbore deviation was 60°. The upper side of the fracture

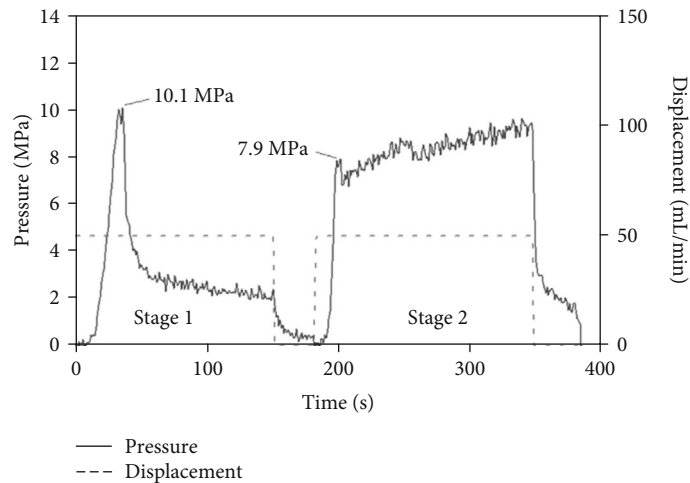




(a) Sample 4



(b) Sample 5



(c) Sample 6

FIGURE 7: Pressure curve of directional well under different deviation angles (azimuth angle  $90^\circ$ ).

in the second stage was deflected toward the wellhead due to the influence of the fracture of the first stage, while the upper side of the fracture of the third stage was merged with the that of the second stage when it was far away from the well-

bore (Figure 6(a)). Accordingly, the pressure curve showed that the initiation pressure and propagation pressure in the third stage gradually increased (Figure 7(a)). The well deviation angle of sample 5 was  $30^\circ$ , and the first and second

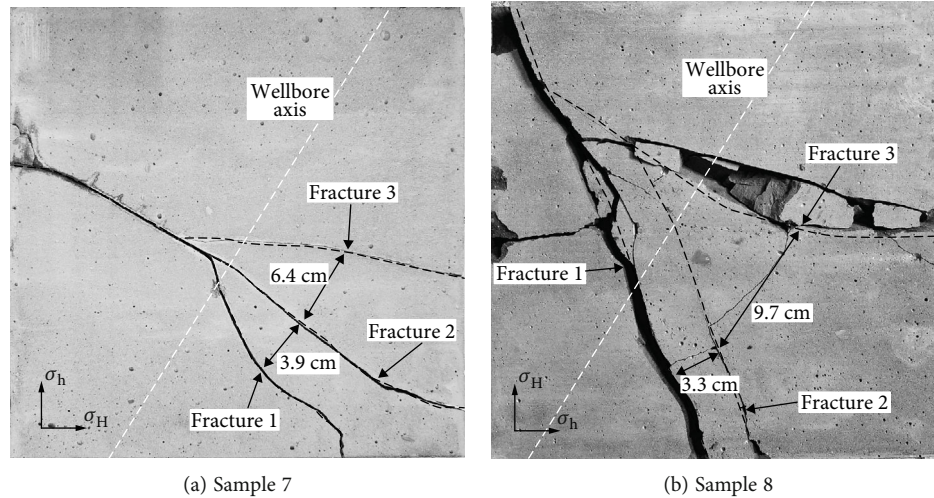


FIGURE 8: Fracture morphology in directional wells (azimuth angle  $60^\circ$ ) under different stage spacing.

stages each had a transverse fracture obliquely intersecting with the wellbore. However, it can be seen that the angle between the fracture in the second stage and the wellbore was relatively small (less than  $20^\circ$ ), which led to the perforation hole in the third stage being connected to fracture 2 and unable to initiate new fractures (Figure 6(b)). In addition, the initiation pressure of the second stage was 2 MPa higher than that of the first stage, while there was no initiation pressure at the third stage (Figure 7(b)). The well deviation angle of sample 6 was  $0^\circ$  (vertical well), and a single longitudinal fracture propagating along the wellbore was formed in the first fracturing stage. As a result, fractures cannot be formed in the next two stages (Figure 6(c)). The pressure curve showed that there was no significant initiation pressure in stage 2 (only 7.9 MPa), while there was no initiation pressure in stage 3 (Figure 7(c)). Fractures formed in directional wells with an azimuth angle of  $90^\circ$  propagated along the direction of the maximum horizontal principal stress on the whole, but the stress interference was obviously enhanced, and the subsequent fractures diverted significantly.

**3.2.2. The Influence of Stage Spacing When Azimuth Is  $60^\circ$ .** For sample 7 and sample 8, the stage spacing was set at 2 cm and 5 cm, respectively. Other variables of those two samples were the same: the horizontal stress difference coefficient was 0.25, perforation depth was 1 cm, well deviation was  $30^\circ$ , and azimuth was  $60^\circ$ . As shown in Figure 8(a), there were three fractures obliquely across the wellbore in sample 7, and the fractures were relatively tortuous. The fractures in the second and third stages (fractures 2 and 3) merged with the fractures in the first stage on the upper left side of the wellbore, while the fractures of three stages on the lower right side of the wellbore were mutually repellent. The spacing between fractures (3.9 cm between fractures 1 and 2, 6.4 cm between fractures 2 and 3) was significantly larger than the stage spacing (2 cm). In sample 8, the stage spacing was increased to 5 cm. Three fractures obliquely across the wellbore were also formed. Similar to sample 7, the three fractures formed in sample 8 had obvious deflection. The

fractures in the second and third stages (fractures 2 and 3) merged with fracture 1 on the upper left side of the wellbore, while the fractures of the three stages on the lower right side of the wellbore were mutually repellent (Figure 8(b)). Overall, compared with the directional well whose azimuth angle was  $90^\circ$ , fractures formed in directional wells whose azimuth angle was  $60^\circ$  more likely exhibited uneven distribution (merger or repulsion) under the condition of small stage spacing, resulting in more tortuous and complex fractures. In particular, for subsequent fractures, they were more likely to initiate along the direction perpendicular to the wellbore and then deflected substantially to propagate in the direction of the maximum horizontal principal stress.

## 4. Conclusions

Based on the true triaxial hydraulic fracturing simulation experiment system, multifracture propagation and pressure curve of staged fracturing in horizontal well and directional well were investigated. The understandings and suggestions are as follows:

- (1) In horizontal wells, under the conditions of high horizontal stress difference coefficient (1.0) and small stage spacing, multiple fractures tend to merge, and stress interference among multistage is obvious. As a response, the increase of initiation pressure for the subsequent stages is more than 8%. The degree of stress interference is low for large stage spacing, resulting in relatively straight fractures. Deepening penetration hole can reduce the initiation pressure by more than 10% and reduce the stress interference among stages
- (2) When the projection trace of directional wellbore on horizontal plane is consistent with the direction of the minimum horizontal principal stress, multiple fractures intersecting the wellbore obliquely are easily formed by staged fracturing. With the decrease

of well deviation, the angle between fracture surface and wellbore axis decreases, which is not conducive to the uniform distribution of multiple fractures. Only one vertical fracture extending along the wellbore is formed for the extreme case that the well deviation angle is 0 degree (namely, vertical well)

- (3) When there is a certain angle between the projection trace of directional wellbore on horizontal plane and the direction of minimum horizontal principal stress, the propagation of multiple fractures is extremely ununiform and the fracture paths are obviously tortuous. When the stage spacing is small, multiple fractures tend to merge near the upper part of wellbore or repel far away from the lower part of wellbore and deflect to the direction of maximum horizontal principal stress. The initiation pressure increases significantly stage by stage and the propagation pressure is relatively high

## Nomenclature

- $s$ : Stage spacing (cm)  
 $d$ : Perforation depth (cm)  
 $\sigma_h$ : Minimum horizontal principal stress (MPa)  
 $\sigma_H$ : Maximum horizontal principal stress (MPa)  
 $\sigma_v$ : Vertical stress (MPa)  
 $K_h$ : Horizontal stress difference coefficient, dimensionless.

## Data Availability

The data that support the findings of this study are available on request from the corresponding author. The data are not publicly available due to privacy or ethical restrictions.

## Conflicts of Interest

The authors declare that they have no conflicts of interest.

## References

- [1] Q. Wu, Y. Xu, X. Wang, T. Wang, and S. Zhang, "Volume fracturing technology of unconventional reservoirs: connotation, design optimization and implementation," *Petroleum Exploration and Development*, vol. 39, no. 3, pp. 377–384, 2012.
- [2] Y. Xu, M. Chen, Q. Wu et al., "Stress interference calculation model and its application in volume stimulation of horizontal wells," *Petroleum Exploration and Development*, vol. 43, no. 5, pp. 849–856, 2016.
- [3] C. L. Cipolla, N. R. Warpinski, M. J. Mayerhofer, E. P. Lolon, and M. C. Vincent, "The relationship between fracture complexity, reservoir properties, and fracture treatment design," *SPE Production & Operations*, vol. 25, no. 4, pp. 438–452, 2010.
- [4] N. Liu, Z. Zhang, Y. Zou, X. Ma, and Y. Zhang, "Propagation law of hydraulic fractures during multi-staged horizontal well fracturing in a tight reservoir," *Petroleum Exploration and Development*, vol. 45, no. 6, pp. 1129–1138, 2018.
- [5] F. Du, J. Huang, X. Ru, Y. Ga, and Z. Yu, "Status and prospect of offshore horizontal well staged fracturing technology," *Offshore Oil*, vol. 41, no. 1, pp. 22–26, 2021.
- [6] C. Mian, C. Zhixi, and H. Rongzun, "Hydraulic fracturing of highly deviated wells," *Journal of the University of Petroleum, China*, vol. 19, no. 2, pp. 30–35, 1995.
- [7] G. Jianchun, D. Yan, and Z. Jinzhou, "Study on breakdown pressure of hydraulic fracturing for extended reach wells with perforation completion," *Natural Gas Industry*, vol. 26, no. 6, pp. 105–107, 2006.
- [8] L. Hailong, Z. Lei, X. Tao, Z. Yuchen, and W. Xiaopeng, "Study on hydraulic fracturing initiation pressure of oriented perforating," *China Petroleum Machinery*, vol. 46, no. 9, p. 63, 2018.
- [9] C. H. Yew, J. H. Schmidt, and Y. Li, "On Fracture Design of Deviated Wells," in *Paper presented at the SPE Annual Technical Conference and Exhibition*, pp. 211–224, San Antonio, October 1989.
- [10] M. M. Hossain, M. K. Rahman, and S. S. Rahman, "A Comprehensive Monograph for Hydraulic Fracture Initiation From Deviated Wellbores Under Arbitrary Stress Regimes," in *Paper presented at the SPE Asia Pacific Oil and Gas Conference and Exhibition*, pp. 1–11, Jakarta, Indonesia, April 1999.
- [11] D. Zhou, J. C. Guo, J. Z. Zhao, and Y. Deng, "Study of fracture initiation of the extended reach wells with open-hole completion," *Journal of Southwest Petroleum Institute*, vol. 24, no. 6, pp. 32–35, 2006.
- [12] C. G. Jia, M. Z. Li, and J. G. Deng, "Large-scale three dimensional simulation test for directional perforation and fracturing in deflected well," *Journal of Southwest Petroleum University*, vol. 29, no. 2, pp. 135–137, 2007.
- [13] B. Hou, M. Chen, C. Diao, L. C. Li, and M. J. Cheng, "True triaxial experiment study of hydraulic fracture penetrating sand and mud interbedding in deviated wellbore," *Science Technology and Engineering*, vol. 15, no. 26, pp. 54–59, 2015.
- [14] H. Bing, Z. Ruxin, D. Ce et al., "Experimental study on hydraulic fracture propagation in highly deviated wells," *China Offshore Oil and Gas*, vol. 28, no. 5, pp. 85–91, 2016.
- [15] B. X. Dong, L. Yang, W. Li, X. Zhou, and H. Y. Xu, "Physical simulation of fracture initiation and propagation in horizontal well fracturing," *Special Oil and Gas Reservoirs*, vol. 26, no. 8, pp. 151–157, 2019.
- [16] Z. Liu, Y. Jin, M. Chen, and B. Hou, "Analysis of non-planar multi-fracture propagation from layered-formation inclined-well hydraulic fracturing," *Rock Mechanics and Rock Engineering*, vol. 49, no. 5, pp. 1747–1758, 2016.
- [17] P. Tan, Y. Jin, B. Hou, K. Han, Y. Zhou, and S. Meng, "Experimental investigation on fracture initiation and non-planar propagation of hydraulic fractures in coal seams," *Petroleum Exploration and Development*, vol. 44, no. 3, pp. 470–476, 2017.
- [18] C. K. Miller, G. A. Waters, and E. I. Rylander, "Evaluation of production log data from horizontal wells drilled in organic shales," in *Paper presented at the North American Unconventional Gas Conference and Exhibition*, pp. 1–23, The Woodlands, Texas, USA, June 2011.
- [19] N. R. Warpinski and P. T. Branagan, "Altered-stress fracturing," *Journal of Petroleum Technology*, vol. 41, no. 9, pp. 990–997, 1989.
- [20] M. Y. Soliman, J. L. Hunt, and A. M. el Rabaa, "Fracturing aspects of horizontal wells," *Journal of Petroleum Technology*, vol. 42, no. 8, pp. 966–973, 1990.
- [21] J. E. Olson and A. D. Taleghani, "Modeling simultaneous growth of multiple hydraulic fractures and their interaction with natural fractures," in *Paper presented at the SPE*

- Hydraulic Fracturing Technology Conference*, pp. 1–7, The Woodlands, Texas, January 2009.
- [22] G. A. Waters, B. K. Dean, R. C. Downie, K. J. Kerrihard, L. Austbo, and B. McPherson, “Simultaneous hydraulic fracturing of adjacent horizontal wells in the Woodford Shale,” in *Paper presented at the SPE Hydraulic Fracturing Technology Conference*, The Woodlands, Texas, 2009SPE 119635.
- [23] A. P. Bunger, R. G. Jeffrey, J. Kear, X. Zhang, and M. Morgan, “Experimental investigation of the interaction among closely spaced hydraulic fractures,” *Strength of Materials*, vol. 19, no. 8, pp. 1160–1165, 2011.
- [24] K. Wu and J. E. Olson, “Simultaneous multi-fracture treatments: fully coupled fluid flow and fracture mechanics for horizontal wells,” in *Paper presented at the SPE Annual Technical Conference and Exhibition*, pp. 1–14, New Orleans, Louisiana, USA, September 2013.
- [25] L. Pan, S. Zhang, L. Cheng, Z. Lu, and K. Liu, “A numerical simulation of the inter-cluster interference in multi-cluster staged fracking for horizontal wells,” *Natural Gas Industry*, vol. 34, no. 1, pp. 74–79, 2014.
- [26] G. Jianchun, Z. Xinhao, and D. Yan, “Distribution rules of earth stress during zipper fracturing of shale gas horizontal cluster wells,” *Natural Gas Industry*, vol. 35, no. 7, pp. 44–48, 2015.
- [27] Z. Jinzhou, C. Xiyu, L. Changyu, L. Yongming, L. Hui, and C. Xuejun, “The analysis of crack interaction in multi-stage horizontal fracturing,” *Natural Gas Geoscience*, vol. 26, no. 3, pp. 533–538, 2015.
- [28] P. Gupta and C. A. Duarte, “Coupled hydromechanical-fracture simulations of nonplanar three-dimensional hydraulic fracture propagation,” *International Journal for Numerical and Analytical Methods in Geomechanics*, vol. 42, no. 3, pp. 1–38, 2018.
- [29] P. Gupta, *A Generalized Finite Element Method for the Simulation of Nonplanar Three-Dimensional Hydraulic Fracture Propagation*, University of Illinois at Urbana-Champaign, 2016.
- [30] L. Gonghui, P. Fei, and C. Zhixi, “Similarity criterion in simulation experiment of hydraulic fracturing,” *Journal of China University of Petroleum (Edition of Natural Science)*, vol. 24, no. 5, pp. 45–48, 2000.
- [31] H. O. U. Bing, C. H. E. N. Mian, L. I. Zhimeng, W. A. Yonghui, and D. I. Ce, “Propagation area evaluation of hydraulic fracture networks in shale gas reservoirs,” *Petroleum Exploration and Development*, vol. 41, no. 6, pp. 763–768, 2014.
- [32] G. Li, L. Liu, Z. Huang, and J. Niu, “Study of effect of hydraulic perforating on formation fracturing pressure,” *Journal of China University of Petroleum (Edition of Natural Science)*, vol. 30, no. 5, pp. 42–45, 2006.